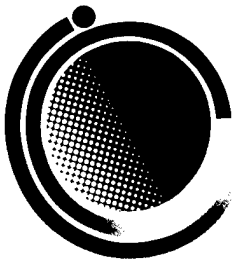

IGARSS'97

1997 International Geoscience and Remote Sensing Symposium

03-08 August 1997

Singapore International Convention & Exhibition Centre • Singapore

Remote Sensing -- A Scientific Vision for Sustainable Development

Volume II

IEEE Catalog Number: 97CH36042
Library of Congress Number: 97-70575

1997 IEEE INTERNATIONAL GEOSCIENCE AND REMOTE SENSING SYMPOSIUM

Editor: Tammy I. Stein
Production: IEEE Publications

IEEE Catalog Number:	97CH36042 (softbound) 97CB36042 (casebound)
Library of Congress Number :	97-70575
ISBN Softbound:	0-7803-3836-7
ISBN Casebound:	0-7803-3837-5
ISBN Microfiche:	0-7803-3838-3
CD-ROM:	0-7803-3839-1
ISSN:	N/A

Additional copies of this publication are available from the following source:

IEEE Operations Center
P. O. Box 1331
445 Hoes Lane
Piscataway, NJ 08855-1331 USA

1-800-678-IEEE
1-908-981-1393
1-908-981-9667 (FAX)
833-233 (Telex)
email: customer.services@ieee.org

IGARSS'97

1997 International Geoscience and Remote Sensing Symposium

03-08 August 1997

Sponsors

IEEE Geoscience and Remote Sensing Society

Centre for Remote Imaging, Sensing and Processing
The National University of Singapore

National Aeronautics and Space Administration (NASA)

National Oceanic and Atmospheric Administration (NOAA)

Office of Naval Research (ONR)

International Union of Radio Science (URSI) ... Technical Sponsor

ORGANIZING COMMITTEE

Hock Lim
General Chairman

Tat Soon Yeo
Janet Nichol
Jian Kang Wu
Dayalan Kasilingam
Technical Co-Chairmen

Leong Keong Kwoh
Finance Chairman

Karen Wong
Publicity Chairman

Choong Weng Mak
Ngi Kun Chng
Exhibits Co-Chairmen

Jonnovan Hong
Chiat Keng Yew
Fen He
Local Arrangements Co-Chairmen

Tammy Stein
GRSS
Director of Conferences and Information Services

TECHNICAL COMMITTEE

Alpers, Werner
Aschbacher, Josef
Bechacq, Yves
Blanchard, Andrew J.
Boerner, Wolfgang-Martin
Cracknell, Arthur
Chan, Philip
Chappelle, Emmett W.
Chen, A.J.
Choi, Soon Dal
Chua, Poh Kian
Chuah, Hean Teik
Cumming, Ian
D'Aranjo, Wesley Gerard
Duchossois, G.
Durana, Jim
Forster, Bruce
Friedman, Ami Ben-Shalom
Fung, Adrian
Gasiewski, Albin J.
Gatlin, James A.
Goodenough, David
Guo, Huadong
Gupta, Avijit
Hallikainen, Martti T.
Hardesty, R. Michael
Ho, Anthony
Hong, Ye
Ishimaru, Akira
Jackson, Thomas J.
Kam, Suan-Pheng
Keydel, Wolfgang
Khazenie, Nahid
Khorram, Siamak
Kong, J.A.
Kuga, Yasuo
Lau, William K.M.
Le Toan, Thuy
Lee, Jong-Sen
Lewis, Anthony J.
Liew, Soo Chin
Lin, I-I
Lu, Yi Hui
Lui, Pao Chuen
Luther, Charles
Mariton, Michel
Massonet, Didier
Milne, Anthony K.
Moon, Wooil M.
Murai, Shunji
Nik Nasruddin Mahmood
Njoku, Eni
Ong, Jin Teong
Pampaloni, Paolo
Prati, C.
Quegan, Shaun
Quek, Gim Pew
Rais, Jacob
Reagan, John
Rees, W.G.
Salomonson, Vincent
Schumann, Robert
Shimoda, Haruhisa
Shu, Peter K.
Sieber, Alois
Singh, Kuldip
Su, Guaning
Takagi, Mikio
Tan, Bernard T.G.
Tilton, James C.
Tomiyasu, Kiyo
Tsang, Leung
Ulaby, Fawwaz
Wiesbeck, Werner
Winebernner, Dale
Zhang, Cheng Bo

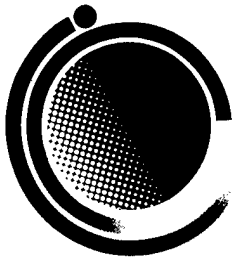

IGARSS'97

1997 International Geoscience and Remote Sensing Symposium

03-08 August 1997

Table of Contents

Interactive Area 1: Aerosols

Interactive Area 2: Applications of Radar and SAR Techniques

"NA" indicates not available at time of printing.

Interactive Area 3: Applications of Remote Sensing

Interactive Area 4: Atmospheric Sounding

"NA" indicates not available at time of printing.

Interactive Area 8: Detection of Buried Objects and Voids

Interactive Area 9: Detection and Monitoring of Ships and Ocean Pollution

"NA" indicates not available at time of printing.

Interactive Area 10: Emission and Scattering

Interactive Area 11: Geology and Geomorphology

"NA" indicates not available at time of printing.

"NA" indicates not available at time of printing.

Interactive Area 16: Optical Measurement of the Ocean

Interactive Area 17: Remote Sensing Data Processing Techniques

"NA" indicates not available at time of printing.

Interactive Area 20: Snow and Glaciers

"NA" indicates not available at time of printing.

Interactive Area 21: Lidars

Interactive Area 22: SAR Interferometry

"NA" indicates not available at time of printing.

"NA" indicates not available at time of printing.

Interactive 33: General Applications

"NA" indicates not available at time of printing.

A01: Remote Sensing of Snow and Glaciers

A02: Image Processing Techniques

"NA" indicates not available at time of printing.

"NA" indicates not available at time of printing.

A08: Properties and Processing of SAR Speckle

A09: Radar Observations of Forest

A10: Coastal Environments

B01: Marine Biochemistry

B02: Clouds and Precipitation I

"NA" indicates not available at time of printing.

B03: Remote Sensing and Urban Planning

B04: Educational Initiatives/Student Programs

B05: Remote Sensing of Sea Ice

B06: SAR Interferometry: Phase Unwrapping

B07: Remote Sensing of Coral and Coastal Environments

B08: Monitoring Urban Settlements

B09: Microwave Emission & Scattering from Rough Surfaces

"NA" indicates not available at time of printing.

"NA" indicates not available at time of printing.

"NA" indicates not available at time of printing.

"NA" indicates not available at time of printing.

IGARSS'97 DIGEST VOLUME III

D01: Soil Moisture I

D02: Remote Sensing of Precipitation

H08: Aerosols

H09: Advance Sensors and Sensor Calibration II

"NA" indicates not available at time of printing.

D05: Remote Sensing of Mesoscale Features

D06: SAR Image Filters & Non-Bayesian Classification Techniques

D07: Neural Network Applications in Remote Sensing

D08: Satellite and Airborne Missions

"NA" indicates not available at time of printing.

D09: Surface Temperature: Observations and Applications

D10: Data Standards and Distributions

E01: Soil Moisture II

E02: Hydrological Cycle

"NA" indicates not available at time of printing.

E03: Detection of Buried Objects and Voids II

E04: Sea Ice Remote Sensing and Applications to Global Change Detection

"NA" indicates not available at time of printing.

E07: Terrain Scattering Models and Their Applications

E08: Advance Sensors and Sensor Calibration I

"NA" indicates not available at time of printing.

IGARSS'97 DIGEST VOLUME IV

F01: Global Monitoring and Remote Sensing for Climate Studies

F02: Clouds and Precipitation II

"NA" indicates not available at time of printing.

F04: Data Processing

F05: Remote Sensing of the Ocean by Radar Techniques

F06: SAR Interferometry: Systems and Applications

F07: Tropical Forest Monitoring

"NA" indicates not available at time of printing.

F08: Interferometric and Differential Interferometric SAR

F09: PS-PR Polarimetric Propagation and Scattering, Sounding and Radiometry

F10: Surface Backscatter Modeling

G01: Soil and Vegetation Biophyscial Properties I

"NA" indicates not available at time of printing.

"NA" indicates not available at time of printing.

G07: Ecosystem Studies with Microwave Remote Sensing

G08: Remote Sensing of Clouds and Aerosols

"NA" indicates not available at time of printing.

"NA" indicates not available at time of printing.

H04: Scattererometer Applications

H05: Radar Measurements of Ocean Winds

"NA" indicates not available at time of printing.

H06: Application of SAR/INSAR in Forestry

H07: Atmospheric Radiation

H08: Advance Sensors and Sensor Calibration II

H09: Aerosols

"NA" indicates not available at time of printing.

H10: Weather Information Systems & Data Analysis Methods

I01: Soil and Vegetation Process Model

I02: Atmospheric Processing and Dynamics

I03: Remote Sensing Research in China

"NA" indicates not available at time of printing.

I04: Data Compressson Techniques and Visualization

I05: Sea Surface Temperature and Its Validation

I06: SAR Techniques

I07: Crop Monitoring and Classification

"NA" indicates not available at time of printing.

I08: SAR Image Processing

I09: ADEOS

I10: Atmospheric Profile

Author's Index

"NA" indicates not available at time of printing.

Improving the MODIS Global Snow-Mapping Algorithm

Andrew G. Klein, USRA
Dorothy K. Hall, NASA Goddard Space Flight Center
George A. Riggs, Research and Data Systems Corporation

Hydrological Sciences Branch Mail Code 974
Laboratory for Hydrospheric Processes
NASA/Goddard Space Flight Center, Greenbelt, MD 20771
tel: 301-286-3314 fax: 301-286-1758 email: aklein@glacier.gsfc.nasa.gov

Abstract -- An algorithm (Snowmap) is under development to produce global snow maps at 500 meter resolution on a daily basis using data from the NASA MODIS instrument. MODIS, the Moderate Resolution Imaging Spectroradiometer, will be launched as part of the first Earth Observing System (EOS) platform in 1998. Snowmap is a fully automated, computationally frugal algorithm that will be ready to implement at launch. Forests represent a major limitation to the global mapping of snow cover as a forest canopy both obscures and shadows the snow underneath. Landsat Thematic Mapper (TM) and MODIS Airborne Simulator (MAS) date are used to investigate the changes in reflectance that occur as a forest stand becomes snow covered and to propose changes to the Snowmap algorithm that will improve snow classification accuracy forested areas.

INTRODUCTION

In the Northern Hemisphere winter, over 40% of the globe may be covered with seasonal snow. The high albedo of snow coupled with its large areal extent make it a strong influence on the Earth's radiation budget. Snow cover also has important societal ramifications. Runoff from snowmelt is an important water resource in many regions of the world and heavy late season snowfalls can cause disastrous flooding [1]. However monitoring of snow cover extent is not currently performed on a global basis.

MODIS, The Moderate Resolution Imaging Spectroradiometer, is scheduled for launch in 1998 aboard the first NASA Earth Observing System (EOS) platform. MODIS is designed to provide quantitative measurements of important geophysical parameters on a global basis [2]. Its high spatial resolution and numerous spectral bands in the 0.4 to 2.5 μm wavelength region allow for more accurate monitoring of snow cover than is possible using currently operational satellites. A prototype algorithm (Snowmap) has been developed to produce daily snow maps with 500 meter resolution at the global scale using MODIS visible to short-wave infrared reflectances [3].

Aside from cloud cover, forests present the most serious limitation to monitoring snow-cover extent using visible to short-wave infrared satellite imagery as much of the world's seasonally snow-covered area contains forests. For example, in North America 40% of the area north of the continental snowline is forest covered. Validation efforts using Landsat Thematic Mapper (TM) and MODIS Airborne Simulator (MAS) images indicate that classification accuracy in forests, especially dense forests, is lower than in biomes where vegetation is sparse or of low stature. Because of their large extent, accurate snow mapping in forests is vital to maximize the accuracy of mapping snow cover in forests.

THE SNOWMAP ALGORITHM

Snowmap is a fully automated and computational frugal algorithm that will be ready to implement by the launch of the EOS AM-1 spacecraft in 1998 [3]. It builds on nearly on two decades of remote sensing research and represents a significant improvement over existing operational products because of the cloud screening ability of MODIS, its unique spectral bands and the planned 500 m resolution of the future MODIS snow cover products Snowmap uses at-satellite reflectances in the 0.4 to 2.5 μm wavelengths (Fig. 1) to determine if a pixel is snow-covered using two classification criteria. The first is a Normalized Difference Snow Index (NDSI) value of greater or equal to 0.40. The NDSI is akin

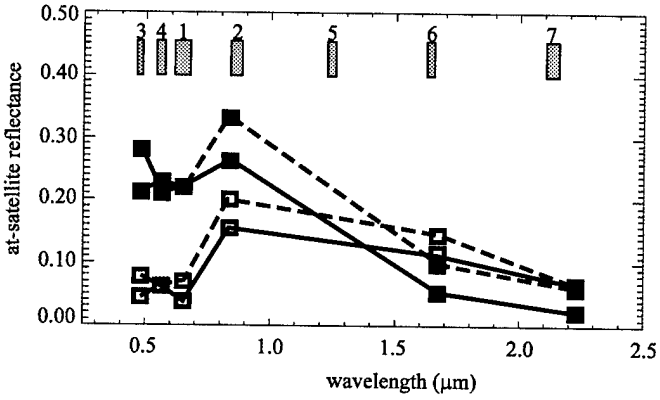

Fig. 1: Observed (solid line) and modeled (dashed line) spectra for a leafless deciduous forest stand. Open symbols are for snow free conditions and filled symbols for snow covered conditions. The model results were produced using the GeoSAIL model for a leafless aspen stand and illumination conditions corresponding to the August and February TM acquisitions. MODIS bands are indicated by the gray boxes

to the Normalized Difference Vegetation Index (NDVI) and is calculated using MODIS bands 4 and 6. Such a combination of visible and short-wave infrared wavelengths has a long history of use in snow classification and provides good discrimination of snow over a wide range of conditions. In addition, only pixels with a reflectance at 0.9 μm, (MODIS band 2) of greater than 11% are considered snow. This effectively excludes water which may have high NDSI values.

FOREST STAND REFLECTANCE

A forest canopy affects the stand reflectance as it obscures and shadows the snow cover underneath. Thus the reflectance of a forest stand with a snow cover beneath (a snow-covered forest) will differ considerably from that of a pure snowpack. The reflectance of a forest stand is determined by the reflectance, transmittance, geometry and areal extent of the canopy, properties of the canopy, the areal extent of the canopy, the surface cover and the solar illumination conditions which determine the proportion of shadowed and sunlight areas.

Landsat TM images from Prince Albert National Park, Saskatchewan, and Glacier National Park, Montana, and MAS images from central Alaska were used to observe how the reflectance of snow-covered and snow-free forests differ. GeoSAIL, a forest canopy model [4] was used to investigate how the reflectance of a forest stand would be expected to vary due to changes in the canopy and background, solar zenith angle, and snow grain size. Both observed and modeled spectra of a forest stand indicate a snow cover under a forest canopy will produce significant changes in the spectral reflectance of the forest stand that can be used to distinguish snow-covered from snow-free conditions (Fig. 1).

The most obvious reflectance change is an increase in the visible reflectances. In some species, short-wave infrared (1.6 μm) reflectances may also decrease. Combined, these changes will cause a snow-covered forest to have a higher NDSI than a snow-free forest, though not as high as for a pure snow cover and in many cases too low to be classified as snow in Snowmap. In addition, the red reflectance of forest is closer to its near-infrared reflectance if a snow cover is present. This makes the NDVI for a snow-covered forest lower that that of a snow-free forest.

PROPOSED ADDITIONS TO THE SNOWMAP ALGORITHM

These observed and modeled reflectance differences are used to propose improvements to the current Snowmap algorithm that enable improved detection of snow under forested conditions. To maintain Snowmap's simplicity and frugality and to speed possible implementation, the proposed additions are designed as additions to the existing algorithm, not as a complete redesign of the algorithm.

The first is the addition of a NDSI-NDVI field (Fig. 2) that captures the observed differences between snow-covered and snow-free forests better than does the current algorithm. Taken together, the NDVI and NDSI allow for robust discrimination between snow-free and snow-covered forests. The new field is designed to capture as much of the variation in NDSI-NDVI values observed in the snow-covered forests as possible while minimizing inclusion of non-forested pixels. Existing or future MODIS derived vegetation maps may also be used to apply the additional criteria only to forested pixels.

Another possible improvement that has been explored is using MODIS band 7 instead of MODIS band 6 to calculate the NDSI. MODIS band 6 was originally selected because of its history of use in cloud detection. However, the reflectance of some forest species, primarily deciduous species, is much higher than snow in MODIS band 6 which causes forest stands to have lowered NDSI values.

The GeoSAIL was used to model the NDSI values using TM 5 and 7 as surrogates for MODIS band 6 and 7, respectively. For both coniferous and deciduous species, using band 7 results in higher NDSI values, especially for more closed canopies. However, there are two drawbacks to using band 7 in the NDSI calculation. The first is that modeled NDSI values using band 7 for snow-covered coniferous forests are much closer to snow-free conditions than if band 6 is used. Secondly, use of band 7 would require recalculation of the original NDSI threshold. While using MODIS band 7 to calculate the NDSI shows promise for some deciduous canopies, application in a global algorithm is not warranted until comparisons can be made with the MAS data in areas where adequate canopy information is available.

Some tree species, most notably black spruce, have very

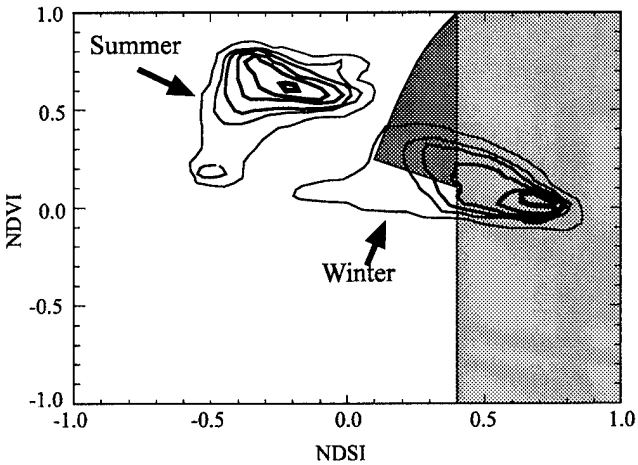

Fig 2: The light gray area indicates NDSI values that are considered snow in the current Snowmap algorithm. The dark gray shaded area indicates the proposed additional field for improved mapping of snow-covered forests. NDSI and NDVI values are contoured for an area surrounding Glacier National Park, Montana, for winter and summer. Thicker lines indicate a higher values of the 2-D probability density function.

low reflectances in the 1.6 μm wavelength region (MODIS band 6). These low reflectances cause the denominator in the NDSI to be quite small, and only small increases in the visible wavelengths are required to make the NDSI value high enough to be classified as snow. To prevent forest stands with very low visible reflectances from being classified as snow, a 10% reflectance in the green (MODIS band 4) is used as a lower limit. A similar visible criteria has been proposed previously [5]. One potential drawback to using the visible threshold is that some snow-covered forests on slopes that either face away from the sun or are topographically shadowed may have a visible reflectance under ten percent.

ACCURACY ASSESSMENT AND CONCLUSIONS

To quantitatively assess the improvements in snow classification accuracy that are made by the proposed changes, both the original and revised Snowmap algorithms were run on a subsection of five TM scenes surrounding Prince Albert National park. Because validation of actual snow cover extent was not possible, snow cover is assumed to be 100% in the three winter and spring scenes and 0% for the two summer and fall scenes. The algorithms were compared for three forest classes (wet coniferous, dry coniferous, and deciduous). These classes were selected from the land cover map produced from the August 6, 1990 TM scene by F.G. Hall (NASA/Goddard Space Flight Center). Overall, the proposed modifications increase the percentage of total area mapped as snow-covered in the winter scenes and decrease the area incorrectly mapped as snow in the summer and fall scenes (Table 1).

Because forests comprise a large percentage of the seasonally snow-covered portion of the globe, accurate mapping of snow in forests is essential for producing reliable estimates of global snow cover extent using MODIS. Detection of snow in forests is more difficult than other biomes because a forest canopy obscures and shadows the snow underneath. However, in many instances, snow-covered forests can be distinguished from snow-free forests. Minor changes to the current Snowmap algorithm enable more accurate classification of snow cover in forests without sacrificing its simplicity and computational frugality.

REFERENCES

[1] J. L. Foster and A. T. C. Chang, "Snow cover," in R. J. Gurney, C. L. Parkinson and J. L. Foster (eds.) *Atlas of Satellite Observations Related to Global Change*, Cambridge University Press, Cambridge, pp. 361-370, 1993

[2] V. V. Salomonson, D. L. Toll, and W. T. Lawrence, "Moderate resolution imaging spectroradiometer [MODIS] and observations of the land surface," presented at International Geoscience and Remote Sensing Society Annual Meeting (IGARSS'92), Houston, TX, pp. 549-551, 1992.

[3] D. K. Hall, G. Riggs, A., and V. V. Salomonson, "Development of methods for mapping global snow cover using moderate resolution imaging spectroradiometer data," *Remote Sensing of Environment*, vol. 54, pp. 127-140, 1995.

[4] K. F. Huemmrich, "A simple addition to the SAIL model to describe discontinous canopy reflectance: the GeoSAIL model," unpublished.

[5] J. Dozier, "Spectral signature of alpine snow cover from the Landsat Thematic Mapper," *Remote Sensing of Environment*, vol. 28, pp. 9-22, 1989.

Table 1: Mapping accuracy of the revised Snowmap algorithm. The first column for each date indicates the percentage of each cover type mapped as snow while values in parentheses indicate the percentage change in area between the revised and original algorithms. Positive values indicate more area mapped as snow in the revised algorithm, and negative values less area mapped as snow in the revised algorithm.

	18-Jan-93		**06-Feb-94**		**29-Mar-95**		**06-Aug-90**		**21-Sep-95**	
Wet Conifer	99.9	(0.3)	91.6	(15.8)	89.3	(-1.3)	0.00	(0.00)	0.10	(0.00)
Dry Conifer	99.9	(0.1)	93.3	(10.4)	96.4	(0.8)	0.15	(0.07)	0.15	(0.02)
Mixed	99.7	(1.4)	86.1	(37.4)	87.3	(14.8)	0.00	(0.00)	0.00	(-0.04)
Deciduous	99.6	(1.6)	56.6	(33.9)	89.34	(6.3)	0.00	(0.00)	0.00	(0.00)

The HUT brightness temperature model for snow-covered terrain

Martti Hallikainen, Jouni Pulliainen, Lauri Kurvonen, and Jochen Grandell[1]
Laboratory of Space Technology, Helsinki University of Technology
P.O. Box 3000, FIN-02015, Finland
Telephone +358-9-451 2371, Fax +358-9-451 2898, E-mail Martti.Hallikainen@hut.fi
[1]Presently with the Finnish Geodetic Institute

Abstract -- The Helsinki University of Technology (HUT) semiempirical model to describe microwave emission from snow-covered terrain is discussed. The model treats the snowpack as a single layer above the ground and it takes into account the contributions from the ground, snowpack, forest canopy, and atmosphere.

DESCRIPTION OF MODEL

The HUT snow model consists of the following components:

- emission from the snow layer, $T_{Bs,up}$ and $T_{Bs,down}$
- emission from the ground, T_{Bg}
- contribution from the atmosphere, T_{Ba}
- effect of forest canopies.

The terms $T_{Bs,up}$ and $T_{Bs,down}$ describe the upwelling and downwelling radiation from the snowpack, respectively. The total brightness temperature excluding vegetation is

$$T_B = T_{Bs,up} + T_{Bs,down} + T_{Bg} + T_{Ba}. \quad (1)$$

The upward welling radiation just below the snow-air boundary from a snowpack of depth d is the sum of brightness temperature contributions due to emission and scattering,

$$T_{Bs,up-} = T_{B,e} + T_{B,sc}. \quad (2)$$

For a homogeneous snowpack (2) simplifies to

$$\begin{aligned} T_{Bs,up-} = {} & T_s \frac{\kappa_a}{\kappa_e}(1-\exp(-\kappa_e d \sec(\Theta)) \\ & + qT_s\left[1-\exp(-\kappa_a d \sec\Theta)\right] \\ & - qT_s\left[\frac{\kappa_a}{\kappa_e}(1-\exp(\kappa_e d \sec\Theta))\right], \end{aligned} \quad (3)$$

where Θ is the propagation angle in the snowpack, κ_a and κ_e are the absorption coefficient and extinction coefficient, respectively, and T_s is the physical temperature of snow. The term q takes into account multiple scattering within the snowpack. In the case of perfect forward scatter, $q = 1$. Based on our ground-based radiometer mesurements of snow-covered terrain over a period of one winter [1], the optimum value is $q = 0.7$. This means that forward scatter dominates in $T_{B,sc}$. (3) can also be written in terms of the snow water equivalent W_{eq} and, further, in terms of the snowpack extinction coefficient L_e and attenuation coefficient L_a,

$$\begin{aligned} T_{Bs,up-} = {} & T_s \frac{\kappa_{am}}{\kappa_{em}}(1-\frac{1}{L_e}) \\ & + qT_s\left[(1-\frac{1}{L_a}) - \frac{\kappa_{am}}{\kappa_{am}}(1-\frac{1}{L_e})\right], \end{aligned} \quad (4)$$

where κ_{am} and κ_{em} are the mass absorption and extinction coefficients, respectively.

The brightness temperature due to downwelling radiation just above the ground-snow boundary is

$$T_{Bs,down+} = T_{Bs,up-}. \quad (5)$$

Upwelling radiation from snow is

$$\begin{aligned} T_{Bs,up} = {} & T_{Bs,up-}(1-\Gamma_{as})F_1 + \\ & qT_{Bs,up-}(1-\Gamma_{as})\Gamma_{as}\Gamma_{sg}F_2, \end{aligned} \quad (6)$$

where Γ_{as} and Γ_{sg} are the reflectivities of the air-snow and snow-ground boundary, respectively, and functions F_1 and F_2 take into account multiple reflections within the snowpack.

The reflectivity of the air-snow boundary can be obtained using the approach employed in [2]. The approach leads to unrealistically small values for the surface roughness in order to provide results that agree with experimental data. Hence, the surface roughness factor presented in [2] should be

0-7803-3836-7/97/$10.00 © 1997 IEEE

taken, rather, as an experimental coefficient for accounting for a non-specular air-snow surface.

A better approach [3] employs the incoherent IEM surface scattering and transmission coefficient equations and a coherent transmissivity [4]. This approach leads to realistic values for the surface roughness.

Similarly to (4), the emission contribution from the ground can be written just below the air-snow boundary as

$$T_{Bg-} = e_g T_g \left[\frac{1}{L_e} + q\left(\frac{1}{L_a} - \frac{1}{L_e}\right) \right], \tag{7}$$

where T_g and e_g are the temperature and emissivity of the ground.

The ground-emitted brightness temperature is then

$$T_{Bg} = T_{Bg-}(1-\Gamma_{as})F_1 + qT_{Bg-}(1-\Gamma_{as})\Gamma_{as}\Gamma_{sg}F_2, \tag{8}$$

where functions F_1 and F_2 take into account multiple reflections within the snowpack.

Similarly to (6) and (8), the brightness temperature contribution from the snowpack, due to downwelling radiation, is

$$T_{Bs,down} = T_{Bs,down+}\frac{(1-\Gamma_{as})\Gamma_{sg}}{L_e}F_1 + qT_{Bs,down-}(1-\Gamma_1)\Gamma_2 F_2. \tag{9}$$

The effective emissivity of snow-covered terrain can be defined as

$$e_{eff} = \frac{T_{Bg} + T_{Bs,up} + T_{Bs,down}}{T_{eff}}, \tag{10}$$

where T_{eff} is the effective physical temperature of snow-covered terrain. In the case of dry snow cover,

$$T_{eff} \approx T_g. \tag{11}$$

The downwelling atmospheric brightness temperature contribution $T_{Ba,down}$ is reflected from the snow-ground surface and the contribution just above the air-snow surface is

$$T_{Ba} = (1-e_{eff})T_{Ba,down}. \tag{12}$$

By grouping the terms in the above equations properly, the following brightness temperature contributions can be defined:

- Directly transmitted brightness temperature from snow
- Multiply-reflected brightness temperature from snow
- Directly transmitted brightness temperature from ground
- Multiply-reflected brightness temperature from ground.

For calculations, the scattering properties of dry snow are modelled using equations from [5], the real part of snow permittivity using equations from [6], the imaginary part of snow permittivity using the Polder-van Santen mixing model [7], and the ice permittivity using equations from [6].

Fig. 1 shows the modeled behavior of snowpack and ground contributions as a function of frequency, when the new approach to treating the surface roughness is used. The frequency response in Fig. 1 is realistic. The results also demonstrate that multiple reflections are negligible.

The tranmissivity of a boreal canopy is modeled as a function of frequency and stem volume, based on helicopter-borne microwave radiometer measurements (frequency range 24 to 94 GHz) conducted in the Sodankylä test site in northern Finland [8]. The total attenuation of forest canopies with stem volumes (maximum 150 m^3/ha) was observed to be up to 2.7 dB, depending on frequency.

CONCLUSIONS

The HUT semiempirical snow emission model is based, in addition to the radiative transfer theory, on ground-based and helicopter-borne microwave radiometer measurements for snow-covered terrain in open and forested areas, and experimental observations on the dielectric and scattering properties of snow.

REFERENCES

1. Hallikainen, M. and V. Jääskeläinen, "Microwave emission behavior of snow," Digest IEEE IGARSS'88, pp. 437-438, Edinburg, Scotland, 13-16 September 1988.

2. Choudhury, B.T., T. Schmugge, A. Chang, and R.W. Newton, Effect of surface roughness on the microwave emission from soils," J. Geophys. Res., vol. 84, pp. 5699-5706, 1979.

3. Pulliainen, J., K. Tigerstedt, H. Wang, M. Hallikainen, C. Mätzler, A. Wiesmann, U. Wegmuller, Retrieval of geophysical parameters with integrated modelling of land

surfaces and atmosphere, Interim Report, ESA ESTEC Contract No. 11706/95/NL/NB(SC), December 1996.

4. Fung, A., Microwave Scattering and Emission Models and Their Applications, Artech House, 573 p., 1994.

5. Hallikainen, M., F.T. Ulaby, T.E. van Deventer, "Extinction behavior of dry snow in the 18 to 90 GHz range," IEEE Trans. Geoscience and Remote Sensing, vol. 25, no. 6, pp. 737-745, 1987.

6. Mätzler, C., "Applications of interactions of microwaves with the natural snow cover, " Remote Sensing Reviews, vol. 2, pp. 259-387, 1987.

7. Hallikainen, M., F.T. Ulaby, and M. Abdelrazik, "Dielectric properties of snow in the 3 to 37 GHz range," IEEE Trans. Antennas and Propagation, vol. 34, no. 11, pp. 1329, 1340, 1986.

8. Kurvonen, L. and M. Hallikainen, "Influence of land-cover category on brightness temperature of snow," IEEE Trans. Geoscience and Remote Sensing, vol. 35, no. 2, pp. 367-377, 1997.

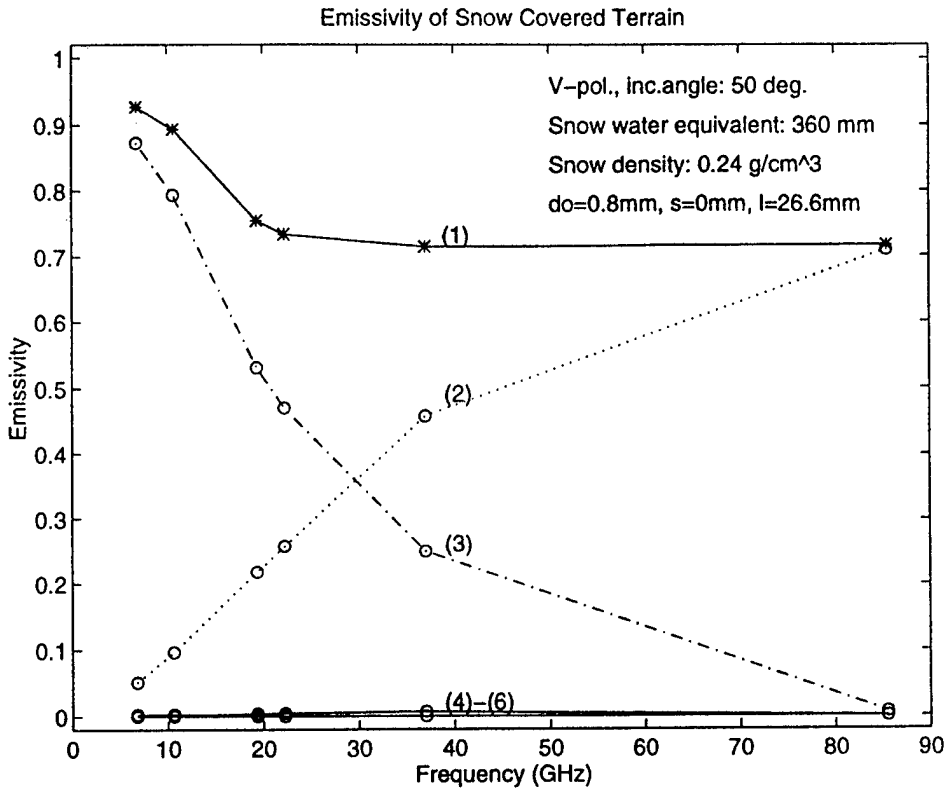

Fig. 1. Modeled snowpack emission contributions in the case of rough air-snow boundary. The temperature of snow and ground is -5 C. The snow grain diameter 0.8 mm, surface roughness rms height 1.4 mm, and surface correlation length 26.6 mm.
The contributions are: (1) : total emissivity
(2) : direct snowpack contribution
(3) : direct ground contribution
(4) - (6) : multiply-reflected contributions from snow and ground.

Snow Crystal Shape and Microwave Scattering

J.L. Foster, D.K. Hall and A.T.C. Chang
NASA Goddard Space Flight Center, Code 974
Hydrological Sciences Branch
Laboratory for Hydrological Processes
Greenbelt, MD 20771
phone: 301-286-7096, fax: 301-286-1758
e-mail: jfoster@glacier.gsfc.nasa.gov

A. Rango, W.Wergin and E. Erbe
U.S. Department of Agriculture, Hydrology Laboratory
Agricultural Research Service
Beltsville, MD

INTRODUCTION AND BACKGROUND

No two snow crystals look exactly the same because their histories are different. Precipitating snow crystals grow into forms according to how water molecules fit together as they fall through the atmosphere and encounter different temperature, pressure and humidity conditions. Impurities or defects on the surface of the crystals affect their growth by helping them to attract water vapor more efficiently. The crystals may take the form of plates, columns, needles, or dendrites, all of which are based on a hexagonal lattice structure. Competition for water vapor plays a big role in determining the shape of the falling crystals [1]. This is also the case for snow crystals which survive their fall to the ground, where the process of constructive metamorphism increases their size and alters their shape. In addition, the constant jostling of the crystals within the snowpack (destructive metamorphism) result in shapes having fewer protuberances.

Microwave emission from a layer of snow over a ground medium consists of contributions from the snow itself and from the underlying ground. Both contributions are governed by the transmission and reflection properties of the air-snow and snow-ground boundaries and by the absorption/emission and scattering properties of the snow layer [2]. Most of the attention in algorithm development has been directed towards the effects of snow crystal size and effective size [3] in scattering microwave energy, and relatively little effort has been given to the role that crystal shape plays in this regard. A better understanding of the physics of snow and how microwave energy interacts with snow crystals is needed to make the snow/microwave algorithms more reliable.

In this study, which is a follow-up of the work presented at the 1996 IGARSS meeting in Lincoln, Nebraska [4], a hand-held 35 GHz radiometer was used to make microwave measurements of snowpacks in both north-central Wisconsin and west-central Wyoming. Because the climate conditions are different for these areas, the characteristics of the snow crystals are somewhat different in regards to their shape and size. Microwave brightness temperatures (TB), in each area were related to physical properties of the snow, including snow depth, snow density, snow water equivalent (SWE) , and crystal size and shape. Coincident with the field observations, an aircraft instrumented with a gamma-ray sensor made measurements of the SWE of the snowpack. These measurements are compared with the SWE as derived using the passive microwave techniques and the "ground truth" measurements.

A particle scattering model is used to assess the scattering properties of differently-shaped snow crystals and to determine if spherically-shaped crystals adequately mimic the extinction and absorption of microwave energy. Crystals were collected from the field sites and brought to a scanning electron microscopy (SEM) laboratory in order to examine and measure them in detail.

A cryosystem has been developed [5] to preserve snow crystals collected in the field (Figure 1) so that they can be imaged using low-temperature SEM. This technique uses liquid nitrogen as a coolant and special pre-cooled dewars to store and transport the snow crystal samples, which are virtually undisturbed, to the SEM laboratory in Beltsville, Maryland.

OBJECTIVE

The goal of this study is to determine how the shape of snow crystals affects the response of microwave radiation emanating from below and within the snowpack and to determine whether or not the use of spheres is suitable for modeling how this radiation is scattered. This information will be useful in producing more reliable snow cover and snow depth passive microwave algorithms. At the time of this writing, the laboratory analysis and the analysis of the field data are not yet complete, thus the emphasis here is on results from modeling.

MODELING RESULTS

In terms of modeling snow crystals, although it may be that spheroids are adequate substitutes for actual snow and ice particles in radiative transfer calculations , it is not known with a high degree of certainty whether or not differently shaped crystals of a given size range will affect how microwave radiation is scattered. To address this concern a discrete dipole model [6] is used to approximate the scattering of idealized snow crystals having various shapes. The shapes can be hexagonal, cubic, cylindrical, elliptical, etc., or clusters of two or more crystals, and are modeled as an array of point dipoles. The electromagnetic scattering problem for the arrays is then solved , essentially exactly, using a Fortran program called DDSCAT [6].

DDSCAT is very versatile and can be used to approximate the scattering from snow crystals or even interstellar dust. The version of the program used here uses the discrete dipole approximation formulae [7]. The code incorporates fast fourier transform methods [8], and a lattice dispersion relation prescription is used for determining dipole polarization possibilities.

For this DDSCAT program the wavelength selected was 8100 microns (0.81 cm), corresponding to 37 GHz, and a value of 1.78 is used for the real part of the refractive index of ice, and 0.0024 is used for the imaginary part. Particles were modeled having effective radius (radii of a sphere of equal volume) of 0.3 mm, 0.5 mm, and 1.0 mm. The shapes modeled included spheroids, ellipsoids, cylinders and hexahedrons. There are three different target orientations with calculations for two incident polarization states. Scattered intensities are computed for two scattering planes at intervals of 30 degrees in the scattering angle theta.; phi = 0 for the x-y plane, and phi = 90 for the x-z plane.

Using this model with an effective radius of 0.3 mm and with the above inputs, the average extinction efficiency is equal to 1.432E-03 (Qscattering = Qextinction - Qabsorption). This compares very favorably to Mie calculations (also with a radius of 0.3 mm), which give a value for the extinction efficiency of 1.40E-03. Table 1 gives scattering values for the different shapes and particle sizes. In general, there are only small differences between results for spherical crystals and crystals having other shapes. The size of the crystal has little consequence on how different shapes scatter microwave energy.

DISCUSSION

The microwave radiation emitted by a snowpack is dependent on the physical temperature, crystal characteristics and density of the snow. A basic relationship between these snow properties and the emitted radiation can be derived by using the radiative transfer approach. The lack of precise information about snow crystal size and shape is compensated for by using an average size of 0.3 mm (radius), a density of 300 kg m^{-3}, an assumed spherical shape for the snow crystals, and the assumption that the crystals scatter radiation incoherrently and independently of the path length between scattering centers. These quantities are then used in radiative transfer equations to solve the energy transfer through the snowpack. If the crystals differ significantly from the averages and assumptions, then poor SWE values will result.

The effects of shape on extinction efficiency can be used as a measure of the effectiveness of different shaped scatterers. It was shown [4] that the extinction response for a cylinder is somewhat higher, though not significantly different from that of a sphere. Modeling of other shapes, ie. ellipsoid, and hexahedron, gives more credence to this observation.

When examining snow crystals in the field with a loop, it is apparent that they consist of a myriad of shapes and sizes. Because the edges or branches are quickly worn-off, the shapes become more and more rounded as the snow season progresses. The process of freezing and thawing (metamorphism) further rounds the crystals. Thus, the spherical shape used in the radiative transfer approximations is representative of what is observed in the field. Of course, when viewed with an electron microscope, the detail is so great that it becomes difficult to ascribe any crystal with a standard shape and the variation between even adjacent crystals can be substantial. Regardless, though, the size of the crystal and the effective particle size [3] are so dominant in scattering, that the cumulative contribution of other structural features, such as shape, is overwhelmed.

CONCLUSIONS AND FUTURE PLANS

While crystal size and correlation length are strongly related to microwave brightness temperature, it appears from the modeling results of this study that the shape of the snow crystal is of little consequence in accounting for the transfer of microwave radiation (at 0.81 cm) from the ground through the snowpack. Analyzing the results for this past winter of the data collected in Wisconsin and Wyoming, will be useful in evaluating how accurately the model matches the observations.

TABLE 1

	extinction efficiency
sphere	
0.3 mm	1.432E-03
0.5 mm	1.134E-02
ellipsoid	
0.3 mm	1.454E-03
0.5 mm	1.253E-02
cylindrical	
0.3 mm	1.313E-03
0.5 mm	1.014E-02
hexahedron	
0.3 mm	2.076E-03
0.5 mm	1.676E-02

FIGURE 1

REFERENCES

1. Hallett, J., "Freeze Frame," The Sciences, Nov./Dec., 22-26, 1996.

2. Chang, A.T.C., J.L. Foster and D.K.Hall, "Nimbus-7 SMMR derived global snow cover parameters," Annals of Glaciology, Vol. 9, 39-44, 1987.

3. Matzler, C., "Autocorrelation functions of granular media with arrangement of spheres, spherical shells or ellipsoids. Journal of Applied Physics, Vol. 3, 1509-1517, 1997.

4. Foster, J, D.Hall, A. Chang, A. Rango, W. Wergin, and E. Erbe, "Observations of snow crystal shape in cold snowpacks using scanning electron microscopy," Proceedings of the IGARSS 1996, Vol. 4, 2011-2013, Lincoln, NE, 1996.

5. Wergin, W.P., A.Rango and E.F. Erbe, "Observations of snow crystals using low-temperature scanning electron microscopy," Scanning, Vol. 17, 41-49, 1995.

6. Draine, B. and P. Flatau, "Discrete dipole approximation for scattering calculations," Journal of the American Optical Society, Vol. 11, 1491-1499, 1994.

7. Draine, B., "The discrete dipole approximation and its application to interstellar graphite grains," Journal of Astrophysics, Vol. 33, 848-872, 1988.

8. Goodman, J., B. Draine, and P. Flatau, P., "Applications of FFT tecniques to the discrete dipole approximation," Optical Letters, Vol. 16, 1198-1200, 1991.

Mapping Snow Cover With Repeat Pass Synthetic Aperture Radar

Jiancheng Shi, Scott Hensley, and Jeff Dozier*

Institute For Computational Earth System Science (ICESS)
University of California, Santa Barbara, CA 93106, U.S.A
Tel:805-893-8116, Fax:805-893-2578, E-mail:shi@icess.ucsb.edu
**NASA/Jet Propulsion Laboratory*

ABSTRACT

In hydrological investigations, modeling and forecasting of snow melt runoff requires information about snowpack properties and their spatial variability. This study demonstrates a technique to map snow cover with both the backscattering and coherence (with and without snow covered images) measurements. We found the coherence measurements provide a much easier way to map snow covered area. For validation of this method, we compared classification result with that derived from TM imagery. A accuracy of better than 86 % can be achieved if we consider the classification result from TM imagery as the ground truth.

INTRODUCTION

Recently, there are several methods have been developed to map snow cover in alpine regions. (1) using single pass, single frequency and polarization SAR image[1-2]; (2) using single pass but polarization property or frequency ratio measurements [3]; (3) using single frequency and polarization with repeat passes [4]; and (4) using single pass but multi-frequency and polarization [5]. Except the last technique, all above methods are restricted to map wet snow-cover since it is difficult to discriminate dry snow cover with bare ground and short vegetation. In the recent study using SIR-C/X-SAR data to map snow cover [5], we found that wet snow cover has very similar backscattering intensity and polarization characteristics with smooth bare surface at C-band and X-band. For instance, the backscattering from wet snow-cover are very similar to those from smooth dry soil, alluvial surfaces, and relative rough water surface under windy condition. At drainage basin or regional scales where many different targets are within a scene, above techniques might not be reliable. For same reason, the change detection measurement from backscattering more unreliable since the similar change in backscattering could be caused by different natural environment change for different targets. In order to develop a large scale snow mapping technique we need other measurement to discriminate snow with other targets.

A interferometric radar technique for topographic mapping of surfaces not only promises a high-resolution digital elevation models but also permits inference of changes in the surface over the orbit repeat cycle from the correlation properties of the radar echoes. Measurement of interferometer correlation provides the amount of surface changes over time describes processes occurring on the time scales of the orbit repeat time and size scales on the order of a radar wavelength, such as vegetation growth, glacier motion, permafrost freezing and thawing, and soil moisture induce effects. The coherence measurement between two repeat-pass, therefore, provides another useful measurement in addition to backscattering intensities in each scene and their changes between two passes, and makes it possible to develop an algorithm for mapping both dry and wet snow covers over large area.

This study evaluates the usage of the interferometric measurements, mainly the coherence measurements with and without snow covered SAR imageries, in terms of mapping snow covered area. We will demonstrate the principle for snow mapping by using both backscattering and coherence measurements with repeat passes SIR-C image data from Mammoth Mtn., California.

The Mammoth Mountain SIR-C/X-SAR site, at 37°N 119°W on the eastern slope of the Sierra Nevada, is typical of much of the alpine region of the range. The study site includes a range of climatic zones only a few kilometers apart, from the heat and dryness of the high

0-7803-3836-7/97/$10.00

desert at 1,000–2,000 m elevation to the cold and snow of the alpine zone above 3,000 m.

Each climatic zone has its own assemblage or community of plants and soil types. Tree line is at about 3,000 m. Below tree line the forest type progresses through high mountain mixed forest. The short vegetation in the study site varies from the sagebrush in Long Valley, patchy grass along the Owens River, to the alpine cold of the Sierran Montane Chaparral. The soils of the study site are young and undeveloped, consisting of pumice ash, glacial till, and lava, with little organic material. At low elevations, most of bare surfaces are pumice ash, glacial till, and poorly developed soil with smooth surface roughness.

CHARACTERISTICS OF COHERENCE MEASUREMENTS

We evaluated the coherence measurements between two repeat-pass SIR-C image data from its first mission in April (has snow) and second mission in October (without snow), 1994. This measurement indicates that If the ground is completely undisturbed between viewings the signals will be highly correlated. Otherwise, the decorrelation will occur. Figure 1 shows the coherence measurements of L-band VV polarization as y-axis and VH polarization ratio of L-band to C-band as x-axis from 5 targets - snow as shown by character *s*, lake - *w*, bare surface - *b*, short vegetation - *v*, and forest - *f*. The reason why we select the VH polarization ratio of L-band to C-band is that this measurement can be obtained without requiring terrain correction and also provide a good seperation between the bare surface, short vegetation, and forest. It can be clearly seen that lake and snow cover have very low coherence between two data-takes with and without snow cover. For lake, the decorrelation between two data-takes is mainly resulted from the changes of the lake surface roughness characteristics, due to different windy conditions, such as wind speed and direction. For dry snow case, even the dominant scattering at L-band is from the interface of snow-ground, in addition to the change of the dielectric contrast from air-ground to snow-ground, existing dry snow cover will result in large decorrelation due to change in local incidence angle when radar signal passes through snow layer which will cause a spatial baseline decorrelation. We also expect that the radar echoes will be close to completely decorrelated when measuring correlation between wet snow-cover and bare ground passes. This is because the radar signal in snow-covered pass can only penetrate a few centimeters so that the radar senses two different targets. The coherence measurements from the bare surface are significantly higher that those from lake and snow as shown in Figure 1. For the bare surface, a change of soil moisture will result in a decorrelation. However, the amount of decorrelation is expected to be relative smaller because radar senses a same target with a same scattering mechanism (only change in magnitude). The short vegetation (mainly sagebrush and grass in our study area) has very similar coherence measurements with that from the bare surface mainly due to the dominant scattering source is from the ground surface at L-band. However, the coherence measurements from forest can have very low values - similar as those from snow and lake, especially from dense forest.

CLASSIFICATION AND VALIDATION

Figure 1. indicates that the coherence measurement between a snow covered scene and one without snow and provide a very good separation between snow cover and bare surface as well as short vegetation. These two targets are most difficult to discriminate with snow cover. Thus, the correlation measurement provides a significant information to map snow covered area. We could use the coherence measurements to discriminate forest, open water, and snow with short vegetation and bare ground. Then using backscattering intensities to separate forest and open water with snow.

We used decision tree classifier (DTC) to establish a pixel-based classifier based on training sets. In order to verify the classification results, we acquired a cloud-free Landsat Thematic Mapper scene on April 14, 1994 (the SIR-C/X-SAR data-take on April 13, 1994). We classified the TM data using same technique. We geocoded the TM classification map and projected (or co-registered) them to the slant range presentation of the SAR images by using the Shuttle ephemeris data and ground control points. In the classification of the TM scene, there are only four target categories: lake, snow, forest, and range land, which includes bare ground and short vegetation. Figure 2 shows the SAR classification map on top and TM classification map at

bottom. The comparison of this two results indicated that 86 % accuracy can be obtained for snow cover area under consideration of the TM classification map as the ground truth.

CONCLUSIONS

This paper demonstrated SAR on mapping snow in an alpine region by means of the repeat pass SAR measurements. For large scale snow mapping, the major problem is topographic effect since accurate high resolution DEM data are not available for most of world. Mapping snow in remote alpine regions by a conventional SAR backscattering measurements requires the topographic information in order to remove the topographic effects on the radiometric properties measured from SAR imagery. With the coherence measurements by repeat passes (with and without snow cover), both dry and wet snow can be mapped without requiring any topographic information. The validation, compared with TM classification result, indicates that a better than 86 % can be achieved.

REFERENCES

[1] Rott, H., C. Mätzler, D. Strobl, S. Bruzzi, and K. B. Lenhart, Study on SAR land applications for snow and glacier monitoring, Technical Report 6618/85/F/FL(SC), European Space Agency, 1988.

[2] J. Shi and J. Dozier, Measurements of snow- and glacier-covered areas with single-polarization SAR, *Annals of Glaciology*, vol. 17, pp. 72-76, 1993.

[3] Shi, J., J. Dozier and H. Rott, Snow mapping in alpine regions with synthetic aperture radar, *IEEE Trans. Geosci. Remote Sens.*, 32(1):152-158, 1994.

[4] H. Rott and T. Nagler, Capabilities of ERS-1 SAR for snow and glacier monitoring in alpine areas, *Proc. Of Second ERS-1 Symposium,*. ESA SP-359, pp 1-6, 1993.

[5] J. Shi and J. Dozier, "Capability of SIR-C/X-SAR Mapping Seasonal Snow Cover in Moutainous Areas", In press, *Remote Sensing Environment*, 1997.

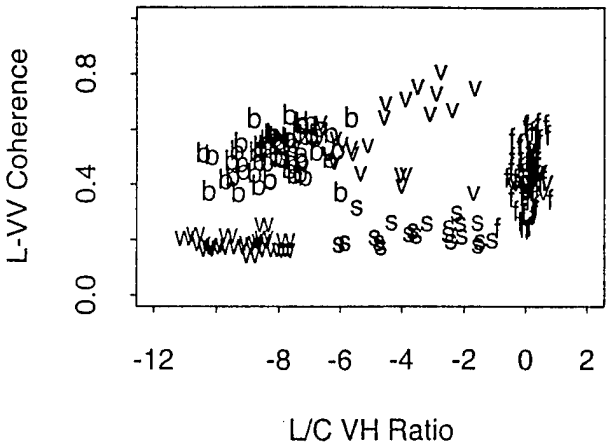

Figure 1 shows the coherence measurements of L-band VV polarization as y-axis and VH polarization ratio of L-band to C-band as x-axis from 5 targets - snow as shown by character *s*, lake - *w*, bare surface - *b*, short vegetation - *v*, and forest - *f*.

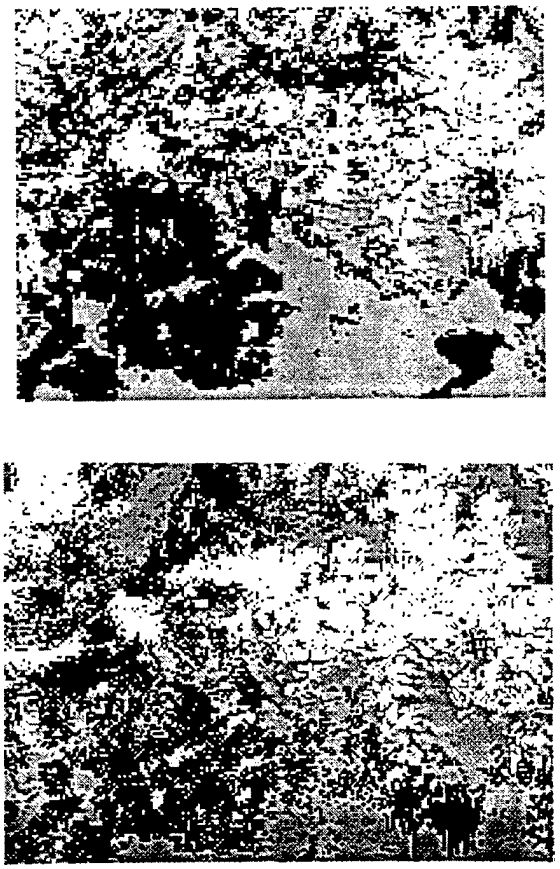

Figure 2. *Comparison of SAR (top) and TM (bottom) derived classification maps. Black - Forest and Lake, gray - bare surface and short vegetation, white - snow.*

Snow Monitoring Using EMISAR and ERS-1 Data within the European Multi-sensor Airborne Campaign EMAC-95

Tore Guneriussen, Harald Johnsen, Rune Solberg[1] and Espen Volden[1]

NORUT IT Ltd., Tromsoe Science Park, 9005 Tromsoe, Norway
Telephone: + 47 77 62 94 00/Fax: + 47 77 62 94 01/E-mail: tore.guneriussen@itek.norut.no
[1]Norwegian Computing Center P.O. Box 114 Blindern N-0314 Oslo, Norway

ABSTRACT

Results from analysis of data obtained in the Snow and Ice experiment within the European Multi-sensor Airborne Campaign (EMAC'95) [2] are presented in this paper. The study area is located in Norway, 66° N, 14° E.
Fully polarimetric C- and L-band SAR data from EMISAR, a airborne instrument operated by the Danish Centre for Remote Sensing, combined with ERS SAR, airborne photos and field data were analyzed in order to determine the capabilities for snow parameter estimation in mountainous areas.
The backscatter statistics of EMISAR C-band data from two areas partly covered with wet snow was studied. There was a difference in mean values between the two areas of up to 4.4 dB for snow and up to 1.3 dB for bare ground. For the purpose of classification, this indicates that local class statistics has to be applied. A classification test on a small area of K-means clustering showed that the best results was obtained for VV polarization with an error rate of 7.2%. All error rates were between 7.2 and 12.2%. The C-band polarization responses derived from the snowcover corresponds to smooth surface scattering.
The extent of the wet snowcover observed by ERS SAR correspond to EMISAR observation.

INTRODUCTION

The weather dependencies of the optical instruments, in particular the cloud cover, significantly reduce their applicability for operational monitoring of snow cover. Studies have demonstrated the capability of C-band SAR for detecting the extent of wet snow cover (e.g. [5], [3]). The scattering from a wet snow covered area is a combination of surface and volume scattering, and the relative strength between the two components depends on the snow properties- liquid water content, density ice particle size and shape and surface roughness [6]. The dielectric loss within the wet snow volume is high and the scattering contribution from the snow- ground interface may be neglected.
For a homogenous dry snow cover the absorption loss within the snow is low, and the snow cover is tranparent leaving the snow ground interface as the significant scattering source. In mountainous areas SAR data are radiometrically and geometrically distorted due to topography, and the data must be geometric corrected and calibrated using a Digital Elevation Model (DEM).

The EMAC-95 EXPERIMENT

The Norwegian test area is located at Kongsfjellet and at the Okstindan glacier, Norway, 66° N, 14° E. The snow test field cover elevations from about 400 m to 1100 m and contains different vegetation types varying from sparsely forested peatland to exposed rock. Three combined remote sensing and ground data acquisition campaigns were conducted at March 22- 23, May 1-3 and July 5-6. Fully polarimetric C- and L-band airborne SAR data were acquired using the EMISAR

The EMISAR polarimeter measures the four elements (hh, hv, vh and vv) of the scattering matrix from an area of the earth's surface. The EMISAR polarimeter data are one look slant range complex data focused to a resolution of 2 m x 2 m, motion compensated, imbalance compensated and absolute calibrated [1]. The incidence angle varies from 35° to 60° at the near and far range respectively. In Fig. 1 the EMISAR C-vv backscattering coefficient image from July 6 are shown. We clearly observe the the extent of the wet snow cover in white (low backscatter).

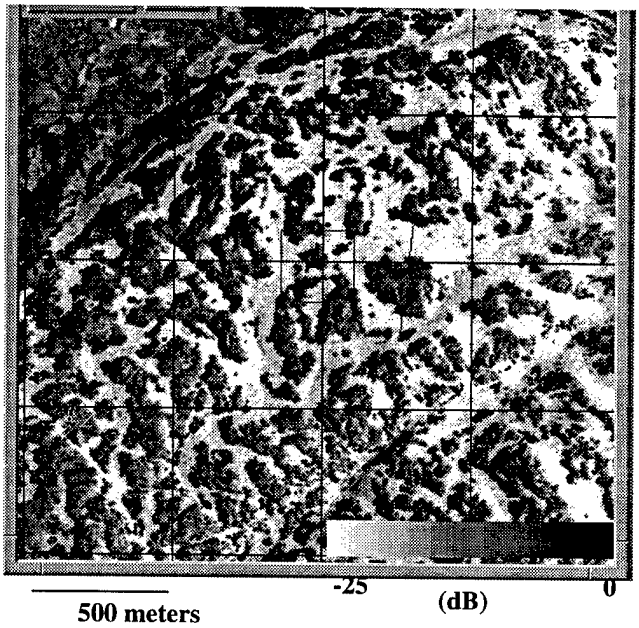

Figure 1. EMISAR C-vv backscattering coefficient image from Kongsfjellet July 6 1995.

0-7803-3836-7/97/$10.00 © 1997 IEEE

The ground measurements include measurements of snow density, snow grain size, snow liquid water content and surface roughness. Air- and snow temperature data are also available. Several trihedral corner reflectors were deployed within the field for calibration and georeferencing purposes. The field measurements are georeferenced using GPS. One aerial photo of the test site was taken July 14. The field was completely covered with snow on March 22 and on May 1-3, while in July the field was nearly snowfree.

The calibration of the EMISAR data have been verified using the radar cross section and the polarization responses from a 0.7 and 1m trihedral corner reflectors deployed within the area.

CLASSIFICATION EXPERIMENT

One experiment using the EMISAR C-band data from July 1995 data set is presented here. Data was extracted from three test areas, two areas for investigation of snow and bare ground backscatter statistics.
Area 1 is located about 550 m.a.s.l., while Area 2 is located about 1000 m.a.s.l. The aerial photo was co-registered with Area 3 EMISAR data using a second-degree control-point transformation. An accurate snow cover mask was extracted from the aerial image based on thresholding.

In Fig. 2 the Co-polarization responses from snow covered areas are shown for C- and L-band, extracted from two different range positions. The C-band polarization responses correspond to theoretical smooth surface scattering responses. No range variation are observed. The polarization response at L-band have a higher pedestal, i.e a show a higher degree of diffuse scattering than at C-band. This is explained by the higher penetration depth of the L- band resulting in scattering contribution from within the snow volume We clearly observe a range difference.
For the statistical investigation, "safe" snow and bare areas were selected. Due to the uncertainty in the co-registration, the areas defined were all well within the border of each snow and bare ground area. The statistics are shown in Table 1. For Area 1, we see that the difference between the mean values of the two classes (between-class distance) is of the order 1.0-1.5 standard deviations. For Area 2, the between-class distance is about 2.0 standard deviations. This means that the two classes should be well separable in a classification for Area 2, but less separable for Area 1. Comparing the two areas for snow for each class, we see that the backscatter level is about 4.4 dB higher in Area 2 for co-polarization and 1.8 higher for cross-polarization. For bare ground, there is a change of less than 1 dB for co-polarization and about 1.3 dB for cross-polarization. The ground truth measurements of snow show that water contents and surface roughness are almost equal for the two areas. For bare ground, the type of vegetation cover is different and may influence on the backscatter level. However, both areas have only low alpine vegetation. It is more likely that the main differences in backscatter levels are due to the variations in local incidence angle. The angle was about 45 for Area 1 and 55 for Area 2.

Table 1: Backscatter statistics for Area 1 and 2. The values are given in dB.

	Area 1	Area 1	Area 2	Area 2
Class	**Mean**	**St. dev.**	**Mean**	**St. dev.**
Snow HH	-15.8	2.8	-20.1	3.1
Bare gr.HH	-12.7	3.0	-13.6	3.4
Snow VV	-15.1	2.8	-19.6	3.1
Bare gr. VV	-12.6	3.0	-12.5	3.3
Snow HV	-21.4	2.9	-23.2	2.8
Bare gr. HV	-16.5	3.1	-18.0	3.1
Snow VH	-21.2	2.9	-23.0	2.9
Bare gr. VH	-16.4	3.1	-17.7	3.1

To obtain a more accurate investigation of the discrimination which could be expected for Area-2 conditions, Area 3 was investigated further. A K-means clustering algorithm [7] was applied. Data from the entire West Profile, including Area 1 and 2, were speckle filtered by a 3 × 3 mean filter and applied for the clustering.

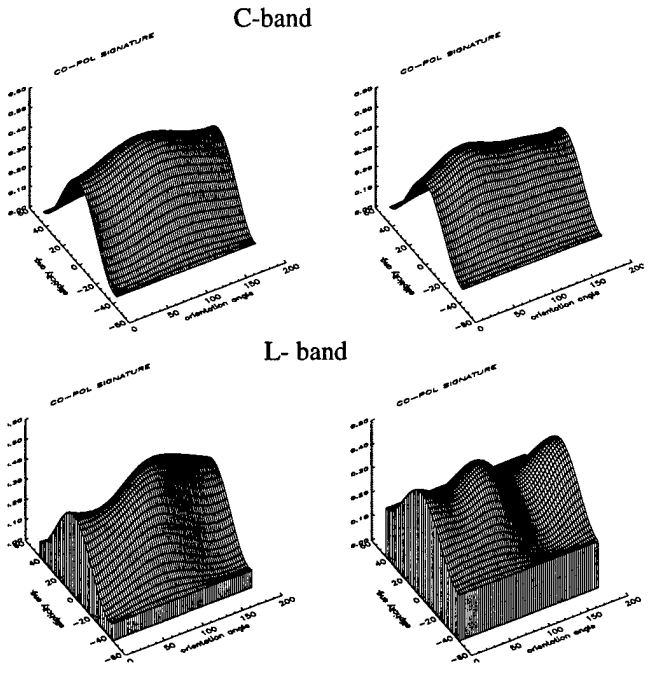

Figure 2. Snow Co-polarization responses for C- and L-band. Left) near range, right) far range.

Area 3 was used for investigation of the classification results. The results are shown in Table 2. The table shows that clustering of VV data gave the best results with an error rate of 7.2%. The least good results were obtained for cross-polarization with an error rate of 12.2%.

ERS DATA

ERS-1 SAR PRI datasets from 29 March, 6 June, 11 July and 12 July have been calibrated and processed into terrain corrected images in Universal Transverse Mercator (UTM) map projection by applying high resolution (5m x5m) DEM data and geocoding software [4]. The DEM is derived from airphoto. A 3x3 Lee filter was applied to the data before conversion to dB.

In Fig. 3 the mean ERS-1 SAR backscattering coefficient for from, 29 March, 6 June, 11 July and 12 July, respectively, are shown for two areas close to the previously defined areas are used. A decrease of 4 dB in backscattering coefficient is observed for the high mountainous area between 29 March to 6 July. This change is related to the change in snow properties. In 29 March the area is covered with dry snow while in June the area is covered with wet snow. We clearly observe a change between the ascending 11 July and descending 12 July ERS pass. This is caused by the difference in viewing geometry giving rise to different local incidence angle.

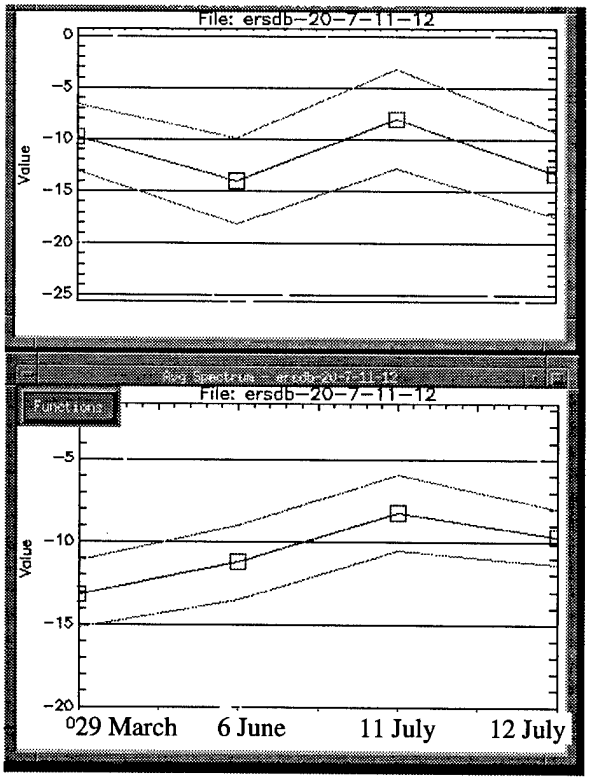

Figure 3. ERS mean backscattering coefficient from two areas for March 29, June 6, July 11 and July 12, respectively. The standard deviation is also shown.

DISCUSSION AND CONCLUSIONS

The backscatter statistics of two areas with an elevation difference of about 450 m was studied. The difference of the mean of the class snow between the two areas were largest for co-polarization with about 4.4 dB. Correspondingly, it was 1.8 dB for cross-polarization. For bare ground, the corresponding numbers were less than 1.0 and 1.3 dB. Since the ground conditions for snow were very similar in the two areas, the main reason for the change of the backscatter level is probably the incidence angle. For the purpose of classification, a preliminary conclusion is that local classstatistics must be applied. If the reason for variation is mainly due to the incidence angle parametrized class models may be designed. A classification test using K-means clustering showed best results with an error rate of 7.2% for VV polarization. All error rates were between 7.2 and 12.2. An investigation of a larger area is necessary in order to draw more clear conclusions.

EMISAR C-band polarization responses from wet snow correspond to theoretical responses from smooth surfaces. The polarization response at L-band show a higher degree of diffuse scattering than C-band.

REFERENCES

[1] J. Hall, EMISAR data description, Electomagnetics Institute, Technical University of Denmark report, IR 701, 1995.

[2] M. Hallikainen et al., Results from EMAC'95 Snow and Ice Experiment in Finland, IEEE Proc. of IGARSS'96, 1996

[3] T. Guneriussen, Backscattering properties of a wet snow cover derived from DEM corrected ERS-1 SAR data, Int. J. Remote Sensing, vol 18, No 2, 1997, pp. 375-392

[4] H Johnsen, I. Lauknes and T. Guneriussen, Geocoding of Fast-Delivery SAR Image Mode Product Using DEM Data, Int. J. Remote Sensing, vol 6, No 11, 1995

[5] H. Rott, and Th. Nagler, Snow and Glacier Investigations by ERS-1 SAR - First Results, Proceedings First ERS-1 Symposium, ESA SP-359, 1993

[6] J. Shi. and Dozier, Inferring Snow Wetness Using C-band Data from SIR-C's Polarimetric Synthetic Aperture Radar, IEEE Trans. Geosci. Remote Sensing, vol. 33, No 4, pp 905-914, 1995

[7] A.K. Jain & R.C. Dubes 1988: Algorithms for Clustering Data, Prentice Hall, New Jersey.

ACKNOWLEDGMENT

Parts of this work is carried out within SNOW-TOOLS, a Environment and Climate project funded by Commision of the European Community Contract no ENV4-CT96-0304. Thanks to all members of the field team.

Ground Penetration Radar and ERS SAR Data for Glacier Monitoring

Svein-Erik Hamran[1], Tore Guneriussen[2], Jon Ove Hagen[3] and Rune Ødegård[4]

[1]Norwegian Defence Research Establishment, Division for Electronics, 2001 Kjeller, Norway
Phone +47 63 80 70 00, E-mail: Svein-Erik.Hamran@ffi.no
[2]NORUT Information Technology Ltd. N-9005 Tromsø, Norway
[3] Dept. of Physical Geography, University of Oslo, 0316 Oslo, Norway
[4] Hoegskolen i Gjoevik, BMS, 2801 Gjoevik, Norway

Abstract

Ground Penetrating Radar (GPR) data from the upper 30 meters is used in the interpretation of ERS-1 SAR data from the accumulation area of Finsterwalderbreen (77° 30'N , 15° 20' E), Svalbard. An effective relative backscatter coefficient at the surface is calculated based on the GPR profiles. These profiles are compared with the backscatter coefficients measured by the ERS-1 SAR along the GPR profiles. The results indicates that the SAR penetrates the cold surface layer, but not into the temperate ice. The SAR can distinguish between the superimposed ice zone and the wet snow zone.

Introduction

Several studies investigating the potential of utilizing spaceborne Synthetic Aperture Radar (SAR) for snow and glacier parameters extraction have been carried out during the recent years [1]. The GPR-technique, also called radio-echo sounding in glaciological literature, has proven useful in studying poly-thermal glaciers and characterizing the different zones on a glacier [2]. HF-frequency radar penetrates the glacier and maps the ice/rock bottom interface. UHF-frequency radar waves are scattered from the free water inclusions inside the temperate parts of the glacier, making it possible to map the cold/temperate interface. High resolution microwave GPR gives information on the upper 30 meters of the glacier showing the last year snow thickness together with scattering from firn layers from previous years in the accumulation area. There is some uncertainty to what depth the ERS-1 SAR penetrates and to what depth the inhomogeneities contributes to the backscattering crossection. This depends on the number of scatterers and absorption in the surface layer. In this paper a comparison of high resolution GPR data of the upper 25 meters of the glacier is compared with ERS-1 data giving indication of what contributes to the backscattering coefficient and to what depth. In the case of backscattering, the normalized backscattering coefficient, radar cross section per unit area or backscattering coefficient, σ^0, is used to describe the backscattering.

For a wet snow cover the surface scattering component from the air-snow interface is significant and the dielectric loss within the snow volume is high. The penetration depth at C-band is 0.05 m for a volumetric content of water in the snow, W = 5 % and density equal 0.5 g/cm3. The scattering from a wet snow covered area is a combination of surface and volume scattering, and the relative strength between the two components depends on the snow properties; liquid water content, density ice particle size and shape and surface roughness [3].

For a dry snow cover the surface scattering component is low and the absorption loss within the snow is low resulting in a penetration depth of 20 m at C-band.

In this study the snowcover is dry with temperatures from -1 to -4 degrees [4] and the volume scattering is significant. The volume scattering from a dry snow cover may be modeled as cloud of spherical stutterer (ice) in a background media (air). In the case of infinite depth of the snow cover the backscattering coefficient is given by:

$$\sigma_o(0) = 0.5\Upsilon^2\cos(0)\frac{Q_b}{Q_e} \qquad (1)$$

Where Q_b and Q_e is the backscattering cross section and extinction cross section for an spherical scatterer, respectively. T is the transmissivity of the snowpack, and 0 the incidence angle.

Table 1. Backscattering coefficient (dB)

Ice size	5.3 GHz	0.5 GHz
r = 1 mm	-7.5	-22
r = 2 mm	-6.5	-31

Table 1 gives the backscattering coefficient for a infinite depth snowcover consisting of ice particles with radius 1 mm and 2 mm, complex dielectric constant $\varepsilon = 3.15 - j\,5*10^{-5}$ at 5.3 GHz and 500 MHz, respectively.

GPR estimation of scattering crossection

The major difference between the GPR data and the ERS-1 data, beside the frequency, are that the SAR gets a two dimensional image where the depth is integrated out, while the GPR integrates along the spherical phase front of the probing wave, and gets a depth versus distance image. The antenna to medium transfer function is however not known making it impossible to get calibrated scattering cross sections.

The received power from depth R_0 is given as:

0-7803-3836-7/97/$10.00 © 1997 IEEE

$$P(R_0) \approx \frac{C\sigma(R_0)}{R_0^2}(-4\alpha_{GPR}R_0) \quad (2)$$

Where C is a constant, σ is the backscattering coefficient, R_0 is the depth to the scattering volume and α is the absorption coefficient. An estimation of the radar crossection observed by a SAR having the same frequency as the GPR is given by:

$$\sigma_{GPR} = \int_0^{R_{Max}} P_r(R_0)R_0^2 dR_0 \quad (3)$$

where the power in depth has been integrated to give an effective scattering coefficient at the surface. This scattering crossection can only be used to measure relative changes as a function of position and not for calibration purposes. The radar will more or less only see scatterers which are larger than the wavelength. This means that if the GPR "sees" the scatterers they will also be visible by the SAR. Thus all the scatterers recorded in the GPR image will also contribute to the SAR reflection. Only scatterers smaller than the GPR wavelength will be present in the SAR image but not in the GPR.

Data acquisition

The area under study is the accumulation area of Finsterwalderbreen, see Fig. 1. The figure show the different surface zones obtained from summer in-situ inspections of the glacier. Two GPR profiles, one running through stake 9 to 13 and the other through F9E to FE3 where recorded on May 1st. 1995. The same area was imaged by the ERS-1 SAR on the April 12 1995. No melting occurred between the SAR-data and the GRP-recordings, this is also observed in the GPR measurements where no internal layers in the snow-pack are seen.

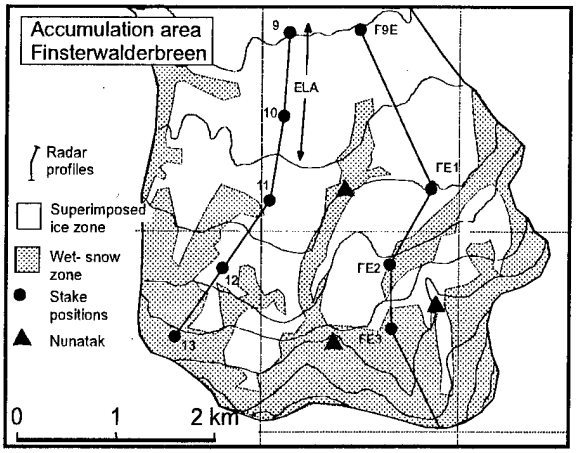

Figure 1. Accumulation area of Finsterwaldbreen.

ERS-1 SAR 3-look Fast Delivery (FD) data set from April 12 1995 acquired and processed at Tromsø Satellite Station (TSS), Norway has been used in the study. The SAR FD product has been geometric corrected using DEM, calibrated and processed into terrain corrected images in Universal Transverse Mercator (UTM), zone 33 and ED50 datum map projection using geocoding software [5]. The geocoding software corrects the data for variations in SAR parameters and converts SAR FD products into σ^0, values by first correcting the intensity in the FD image for antenna gain and propagation loss. Corrections are also made for the variations in physical size of the scattering area due to local topographic variations. Fig. 2 show the SAR derived backscattering coefficient image. By comparing the map and the SAR image we find that the areas defined as wet snow in the map appear dark in the SAR image, i.e. high backscatter. Thus the ERS-1 SAR data discriminate between the superimposed ice zone and the wet snow zone. This has been reported by several investigators [1].

Figure 2. ERS SAR backscattering coefficient image.

GPR-field measurements

The two profiles shown in Fig. 1 were recorded using a step-frequency radar system [7]. The radar system was mounted on a sled pulled by a snow scooter. 201 frequencies were transmitted over the frequency range 600-1000 MHz giving a depth resolution in free-space of 37.5 cm. Fig. 3 show the GPR recording of the eastern profile running over stake F9E through F3E. The plot show received power in logarithmic dB scale as a function of depth and surface distance from stake 9. The plot is intensity modulated were darker areas indicate high backscattered signal.

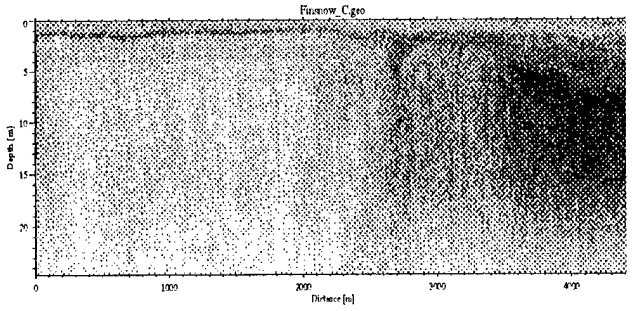

Figure 3. GPR image from east profile.

The first 2.4 km show a nice reflection stemming from the snow/ice interface. The snow thickness is varying from 1.5 m to 2.5 m. From 2.4 km and up strong scattering at increasing depth is clearly seen. This agrees well with the map in Fig. 1 indicating that the wet snow zone starts close to FE2. A closer look show that stronger scattering at depths from 5-20 m starts at 3.3 km. This is believed to be scattering from free water in the temperate ice.
The UHF-radar profile (not shown here) show that from 3.4 to 3.7 km and up the glacier is temperate almost from the surface to the bottom [5].

Fig. 4 show the SAR backscatter coefficient profile and the GPR relative backscatter coefficient long the eastern profile. The GPR relative backscatter coefficient is calculated from (3).
The general trend in the GPR profile is the same as Fig. 3 with an increase starting at 2.2 km. There is a fairly flat plateau until 3.4 km where another increase of 8 dB take place. An explanation for the increase at 3.2 km can be found looking at Fig. 3. At 3.4 km the temperate ice rise to the surface giving increased scattering at depths greater than 5 m, see Fig. 3. This scattering is believed to stem from free water particles inclusions in the ice.

The SAR profile in Fig. 4 is relatively flat until 2 km where an increase of 10 dB takes place. The backscattering coefficient from 2.7 km and to the end of the profile is approximately 8 dB higher than at the first part of the profile.

The GPR and the SAR profile in Fig. 4 show the same behavior up to 2.4 km. In particular the increase in GPR backscattering from 3.3 km is not observable in the SAR profile. This may be explained by the increased dielectric absorption between the GPR and SAR frequency when free water is present in the ice/snow.

If the SAR only penetrates the cold surface layer and very little down into the temperate layer, then the SAR image only shows the difference between the superimposed ice zone and the wet snow zone, and not where the layer comes up to the surface.

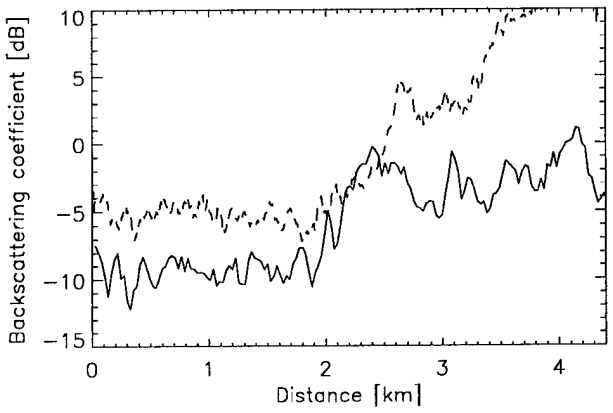

Figure 4. SAR σ^0 (solid) and GPR profile.

Conclusion

A comparison between GPR shallow sounding and ERS-1 SAR data indicates that the SAR only penetrates the cold surface layer down to approximately 5 meters. The SAR data reveals the superimposed ice and wet snow zones but can not indicate where the temperate layer hits the surface. The SAR will still be a powerful tool in glacier study with its potential in mapping the different snow zones. A lower frequency SAR than the ERS-1 SAR could however also map the structures at greater depths such as the temperate and cold-ice zones on a poly thermal glacier.

References

[1] W. G Rees, J. A Dowdeswell and A. D Diament, Analysis of ERS-1 SAR data from Nordaustlandet, Svalbard, IJRS vol 16, No.5, 1996, pp. 905-924

[2] J. L. Bamber, Ice/bed interface and englacial properties of Svalberd ice masses deduced from, airborne radio-echo data, Journal of Glaciology, 35, no 119, 1989, pp. 30-37

[3] Shi J. and Dozier, Inferring Snow Wetness Using C-band Data from SIR-C's Polarimetric Synthetic Aperture Radar, IEEE Trans. Geosci. Remote Sensing, vol. 33, No 4, 1995, pp 905-914

[4] R. Ødegård, J. O. Hagen and S-E. Hamran, Comparison of radio-echo sounding (30 MHz - 1000 MHz) and high resolution temperature measurements at Finsterwalderbreen, southern Spitsbergen, Svalbard, Annals of Glaciology, 1996, In Press

[5] H. Johnsen , I. Lauknes and T.Guneriussen, Geocoding of Fast-Delivery SAR Image Mode Product Using DEM Data, Int. J. Remote Sensing, vol 6, No 11,1995

[6] S-E. Hamran, D.T. Gjessing, J. Hjelmstad and E. Aarholt, 1995 Ground penetration synthetic pulse radar Dynamic range and modes of operation, Journal of Applied Geophysics, 33, pp. 7--14

Comparison of Ranging Scatterometer and ERS-1 SAR Microwave Signatures over Boreal Forest Zone during Winter Season

Jarkko Koskinen, Jouni Pulliainen, Marko Mäkynen, Martti Hallikainen
Helsinki University of Technology, Laboratory of Space Technology
Otakaaari 5A, 01250 Espoo, Finland, Fax: +358-0-4512898, email jarkko@avasun.hut.fi

Abstract -- A set of ERS-1 SAR images along with airborne non-imaging ranging scatterometer (HUTSCAT) measurements and *in-situ* surveys has been obtained from the Sodankylä test site in Northern Finland. A total of 5 measurement campaigns have been organized during years 1991 to 1993. 19 test lines have been selected from the test site to represent different land-use classes. Microwave signatures representing the test lines have been extracted from ERS-1 SAR images and HUTSCAT measurements. The behaviour of these signatures has been compared to each other and with boreal forest semi-empirical backscattering model. The results indicate that the behaviour of ERS-1 SAR derived microwave signatures are similar to those of HUTSCAT even in the presence of forest canopies. By using the semi-empirical model the ERS backscattering is divided into two contributions 1) contribution from top of the canopy and 2) contribution from ground, trunks and ground-canopy reflections. This can be used for analyzing forest backscattering mechanism under various conditions

INTRODUCTION

Airborne or ground based scatterometers are often used to make reference measurements for spaceborne radars. With airborne or ground based radars the measurement conditions can be better controlled than in case of spaceborne radars. By employing airborne or ground based radar and comparing the results with spaceborne radar:

1) more exact understanding of the backscattering from snow and vegetation can be obtained and
2) better theoretical and semi-empirical models can be validated / developed.

In this study a comparison of helicopter-borne non-imaging ranging C-band scatterometer and ERS-1 SAR is conducted. All measurements have been conducted in controlled conditions and extensive information has been collected from ground, snow and vegetation. The conditions include 1) snow free wet ground (and canopy), 2) snow free frozen ground, 3) dry snow, 4) wet snow and 5) partially melted wet snow.

TEST LINE AND DATA DESCRIPTION

Our test site is located in northern Finland around the town of Sodankylä. The land-use of the test site consist of sparsely forested areas (pine, mixed forest and mires) and open areas (bogs, lakes and clear-cut areas). A total of 19 test lines with a total length of over 9 km were selected for airborne and ground truth measurements. The properties of the forest canopies along the test lines were measured. During the airborne campaigns ground truth measurements were conducted along the test lines.

ERS-1 SAR data set consists of 5 SAR images (19 Sep. 1992, 23 Oct. 1991, 20 Jan. 1993, 1 May 1992 and 6 May 1993). The original SAR images, delivered in PRI format by ESA, were rectified and geocoded by the Technical Research Center of Finland [1]. The rectified images were undersampled into 25 m resolution.

HUTSCAT [2] data set consists of backscattering coefficients along each test line. For forested test lines, in addition to the total backscattering coefficients, the ground and canopy backscattering coefficients were also determined. The backscattering coefficients were measured using incidence angle of 23°. HUTSCAT sampling interval on ground was about 1.5 m and the illuminated area on ground was less than 15 m. For comparison with ERS-1 SAR backscattering coefficients the HUTSCAT backscattering coefficients were averaged for 25 m interval.

COMPARISON OF REMOTELY SENSED DATA AND SEMI-EMPIRICAL MODEL FITTINGS

In the comparison of HUTSCAT and ERS-1 SAR a mean of backscattering coefficients was calculated for every land-use class. The average number of independent samples in case of ERS-1 SAR image was 100-300 while in case of HUTSCAT more than 1000 samples. In four cases the time difference between HUTSCAT and ERS measurements was within few hours but at 5 May 1993 it was one day. The comparison of ERS-1 SAR and HUTSCAT is performed using the mean backscattering coefficients for each land-use class.

The comparison of remotely sensed data with boreal forest backscattering model benefit from the HUTSCAT's ability to distinguish the forest floor backscattering contribution from that originating from the tree canopy. Hence, the HUTSCAT data can be directly compared with the semi-empirical model which predicts the levels of forest canopy backscatter, forest canopy transmissivity and forest floor backscatter [3], [4]. The semi-empirical forest backscattering model describes the backscattering coefficient (σ^o) as a function of forest stem volume, vegetation moisture and soil moisture [3], [4]. Even though the model does not include the effect of snowpack properties it is possible to employ it for snow covered ground conditions, since the snow covered terrain can be usually considered as a forest floor layer with a constant σ^o for a certain measurement event. The results for both comparisons are explained below.

Snow free wet ground

Fig. 1a depicts the behaviour of ERS-1 SAR and HUTSCAT backscattering coefficients under snow free conditions. Both forest canopy and ground are wet due to the heavy rain (21 mm). The general backscattering level is also high due to the wet soil and forest canopy. The σ^o curves of ERS-1 SAR and HUTSCAT

0-7803-3836-7/97/$10.00 © 1997 IEEE

follow each other well throughout all land-use classes. At the time of measurements there was no wind, hence, the water was quite calm which causing a mirror-like reflection and therefore a low value of backscatter. Fig. 2a depicts the results for the comparison of ERS-1, HUTSCAT and semi-empirical model. Both ERS-1 SAR and HUTSCAT data indicate that the response of σ^o to forest biomass is constant, which is typical phenomenon for wet soil conditions. The model fitting suggest a relative high value for soil moisture which appears to be quite realistic according to weather statistics. The estimate for forest canopy moisture ($m_{v,v} = 60\%$) is a somewhat higher value than typical values for dry summer conditions (the nominal model parameters are supposed to correspond to conditions $m_{v,v} = 53\%$). In general, the model appears to agree very well with observations. HUTSCAT observations for three stem volume classes ($V = 19, 85$ and $136 m^3/ha$) were used in model fitting.

Snow free frozen ground

The total backscattering level in Fig. 1b and Fig. 2b is remarkably lower than in Fig. 1a due to the low backscattering contribution from frozen ground. Also in this case the backscattering curves of ERS-1 and HUTSCAT follow each other well. HUTSCAT has a clear correlation between stem volume and backscattering coefficient which is not the case with ERS-1 SAR derived results. The ERS results indicate almost no difference in the mean σ^o values as a function of stem volume. The level of soil backscatter is extremely low (Fig. 2b). Thus, the equivalent soil moisture value obtained $m_{v,s}$ is only 3.2%. The canopy moisture estimate $m_{v,v}$ is also quite low (43%) indicating a partially frozen tree cover. The decrease of backscatter has been the most drastic in the forest floor backscattering contribution. Hence, the canopy contribution overcomes the ground contribution at a lower level of stem volume (90 m^3/ha) than in the case of unfrozen soil (130 m^3/ha).

Cold mid-winter dry snow conditions

The test lines in Fig 1c and Fig. 2c were covered by thick snow layer and the temperature has been well below zero for a long time period. Therefore the forest canopy is frozen. The results show a higher total backscattering level than in case of frozen snow-free ground. This is caused by increased volume scattering inside the snow pack. The general behaviour of backscattering curves of both instruments follow each other well. The backscattering contribution originating from forest floor is extremely high compared with forest canopy backscattering contribution (Fig 2c). Because the canopy is frozen the equivalent forest canopy moisture value is low. The total level of backscatter is slightly lower than that observed under wet unfrozen soil conditions. The model-based curve for forest floor backscattering contribution differs slightly from HUTSCAT observations.

Wet (melting) snow conditions

The air temperature was daytime above zero and the snow cover is wet. Although the snow melt period has already begun the whole test site is covered by thick wet snow layer. The general backscattering coefficient is low in non forested areas due to the high absorption caused by wet snow (Fig. 1d). The correlation between HUTSCAT and ERS results is not so strong as for the previous cases. The correlation of σ^o with the stem volume is slightly positive (Fig. 2d) and the level of σ^o at low stem volumes is 2.5 dB lower than for dry snow cover, whereas at high stem volumes the level of σ^o is about the same. This is due to the fact that the $m_{v,v}$-value is relatively high indicating non-frozen forest canopy.

Partially melt-off snow conditions

The Fig. 1e shows the ERS-1 and HUTSCAT signatures in situation where the snow has melted from some areas. Thus, terrain is a mosaic of open ground and snow. This can be easily seen as an increased level of backscatter for open areas when compared to Fig. 1d. Although the ERS-1 SAR image was take one day before the HUTSCAT measurements took place the results follow each other extremely well. The correlation between stem volume and σ^o can be observed but it is not that strong as in Fig. 1d due to the fact that 95 % of forest floor was covered by wet snow layer in contrast to open areas. Also the canopy backscatter has a lower level which indicates that the tree canopy may be partially frozen.

CONCLUSIONS

In this study, the comparison of the microwave signatures of ranging scatterometer HUTSCAT and those of spaceborne SAR was conducted. The results indicate that the behaviour of ERS-1 SAR microwave signatures are similar to those of HUTSCAT measurements for various conditions. By applying this result together with the boreal forest semi-empirical backscattering model, the ERS-1 SAR backscattering coefficient were divided into two partitions backscattering contribution from (1) forest canopy layer and (2) ground. This novel method offers us new knowledge about the division of backscatter between forest canopy and ground under different weather conditions. Also as a result of the model an estimate related to changes in the canopy and soil moisture and freezing/thawing of soil and vegetation can be obtained.

REFERENCES

[1] Y. Rauste, " Methods for Analyzing SAR Images", *Report no. 612, Laboratory of Instrument Technology, National Research Centre*, Espoo, 99 p., 1989.

[2] M. Hallikainen, J. Hyyppä, J. Haapanen, T. Tares, P. Ahola, J. Pulliainen, and M. Toikka, "A Helicopter-borne eight-channel ranging scatterometer for remote sensing - Part I: system description," *IEEE Transaction on Geoscience and Remote sensing*, Vol 31, pp. 161 - 169, 1993.

[3] J. Pulliainen, "Investigation on the Backscattering Properties of Finnish Boreal Forests at C- and X-band: a Semi-empirical Modelling Approach", *Thesis, Report 19. Laboratory of Space Technology, Helsinki University of Space Technology*, Espoo, 199 p., 1994.

[4] J. Pulliainen, P. Mikkelä, M. Hallikainen, J-P. Ikonen, " Seasonal Dynamics of C-band Backscatter of Boreal Forests with Application to Biomass and Soil Moisture Estimation", *IEEE Trans. on Geoscience and Remote Sensing*, Vol. 34, No. 3, 1996.

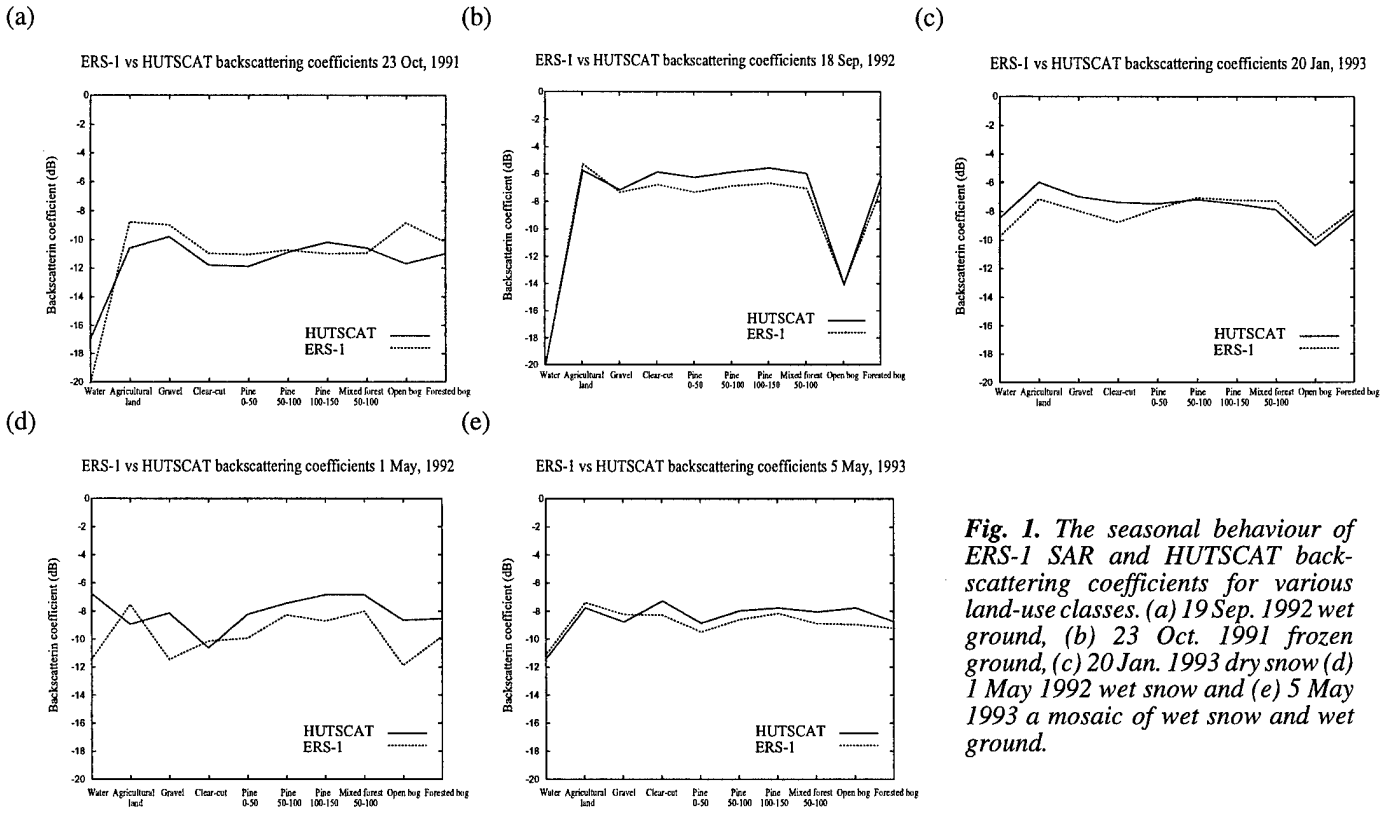

Fig. 1. The seasonal behaviour of ERS-1 SAR and HUTSCAT backscattering coefficients for various land-use classes. (a) 19 Sep. 1992 wet ground, (b) 23 Oct. 1991 frozen ground, (c) 20 Jan. 1993 dry snow (d) 1 May 1992 wet snow and (e) 5 May 1993 a mosaic of wet snow and wet ground.

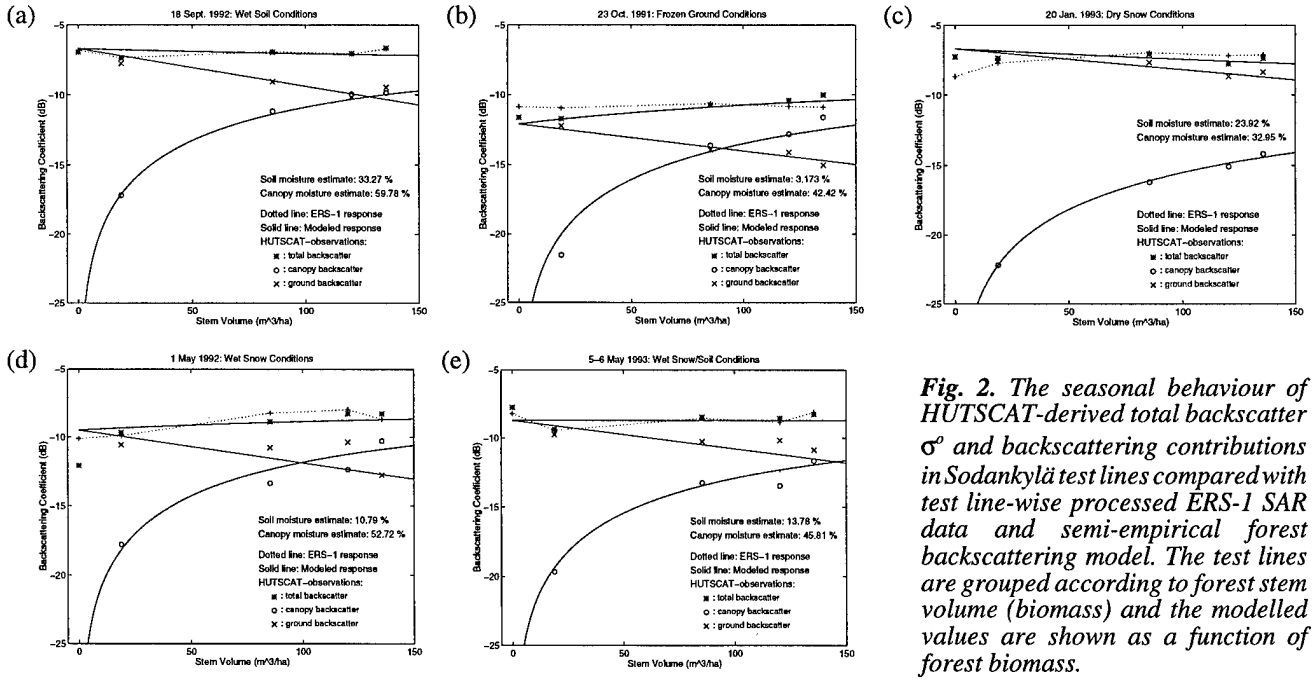

Fig. 2. The seasonal behaviour of HUTSCAT-derived total backscatter σ^o and backscattering contributions in Sodankylä test lines compared with test line-wise processed ERS-1 SAR data and semi-empirical forest backscattering model. The test lines are grouped according to forest stem volume (biomass) and the modelled values are shown as a function of forest biomass.

MULTI-SOURCE SNOW COVER MONITORING IN THE SWISS ALPS

Jens Piesbergen and Harold Haefner
Remote Sensing Laboratories, Department of Geography, University of Zurich
Winterthurerstrasse 190, CH-8057 Zurich - Switzerland
fax: +41 1 362 52 27, email: {piesi, haefner}@geo.unizh.ch

ABSTRACT

Methods for the application of ERS-1 SAR and L-5 TM imagery to monitor and map the snow cover in high mountain areas are presented. Snow monitoring using SAR data considering the multitemporal optimal resolution approach MORA results in a sequence of wet snow cover maps. The climbing of the snow-line could clearly be detected. Furthermore snow cover maps based on L-5 TM imagery are discussed. Considering spectral reflectances of snow a simple snow cover maps were derived. Analyzing advantages and disadvantages of the use of SAR or EO sensors, finally, a data fusion model was used to evaluate the potential of data fusion techniques for the retrieval of geoecological parameters, eg. snow. Including the SAR γ-values in a RGB-YUV-RGB-model results show more textural information in snow covered areas while edge information originates from the TM imagery. The information content of the calculated image is increased. The potentials and limitations of the approaches are discussed.

Keywords: snow cover mapping and monitoring, SAR and EO data, geometric and radiometric rectification, data fusion

1. INTRODUCTION

Snow cover variations significantly influence the hydrological circulation. Remote sensing data and related techniques offer the opportunity to continuously monitor the snow cover over large areas. Results of snow cover mapping and water equivalent estimation showed the usefulness of electro-optical (EO) data over large alpine basins [1]. However, the use of optical satellite sensors can lead to lack of information, due to bad weather conditions. To overcome this problem interpolations to bridge the missing link between consecutive satellite images are required. Another possibility is to rely on radar sensors. In terrain with pronounced relief variations, radar backscatter becomes strongly distorted, exhibiting changes in local mean intensity. Furthermore, layover and radar shadow effects produce signals without interpretable thematic information.

Therefore it becomes necessary to use the optimal resolution approach ORA to combine SAR data of crossing orbits for each acquisition day [2], [3]. This method produces synthetic images to reduce the layover areas and improve the local mean resolution. Furthermore theses images are more easily interpretable than the originals in the initial SAR geometry. Applying the multitemporal aspect of ORA to several ascending and descending image pairs (MORA) a sequence of "wet snow cover" maps can be derived [4].

The purpose of this paper is to present methods on snow cover mapping and monitoring with ERS single frequency SAR mangitude data and Landsat-5 Thematic Mapper (TM) imagery in high alpine basins. In addition we evaluate data fusion techniques for a natural, well distributed features.

This work consists of three thematic parts, namely the monitoring of the snow cover applying the multitemporal aspect of ERS-1 SAR data analysis, the derivation of snow cover maps based on L-5 TM imagery, as well as some aspects of data fusion techniques. Results show that the monitoring of wet snow cover based on SAR is practicable and give good results concerning a qualitative wetness distribution while EO derived maps indicate the local distribution of the overall snow coverage. First results on data fusion are presented. Several limitations will be discussed.

2. DATASETS

For this study 12 ERS-1 SAR PRI scenes covering a part of Eastern Switzerland (1260km^2) acquired in a 35-day repeat orbit cycle between January 1993 and July 1993 from ascending and descending orbits were used. The satellite overflight of the ascending swath (21:30 UTC) and the descending swath (10:10 UTC) took place on the same date (Figure 1). Two Landsat-5 Thematic Mapper (TM) scenes dated 15.02.93 and 22.05.93 (09:10 UTC) are also available (Figure 4).

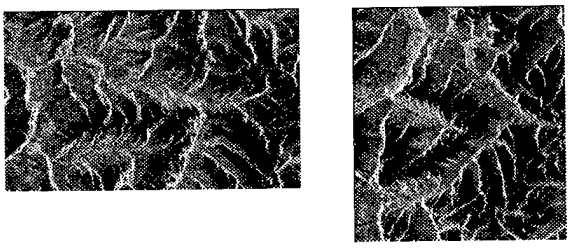

Figure 1: Subset of ERS-1 PRI imagery 01.05.93, descending orbit (left), ascending orbit (right)

For this project a digital elevation model (DHM25) with a grid size of 25m and a height resolution of 0.1m is available [5]. Meteorological data (air temperature, cloud coverage, precipitation, wind velocity) and snow parameters (snow temperature, snow depth, density, grain size and type, snow surface type, and the load-bearing capacity) were collected during the field mea-

surements on the January, February and March overflights.

3. BASIC CONCEPT

The concept is based on three main pillars. First, snow cover monitoring is performed using SAR magnitude data. Second, the local snow coverage distribution is mapped based on EO imagery. Finally, the sensor specific snow maps are used as input in a simple fusion model to overcome the sensor specific disadvantages (SAR: no non-snow/snow discrimination; EO: no wetness information). Figure 2 illustrates the data processing scheme.

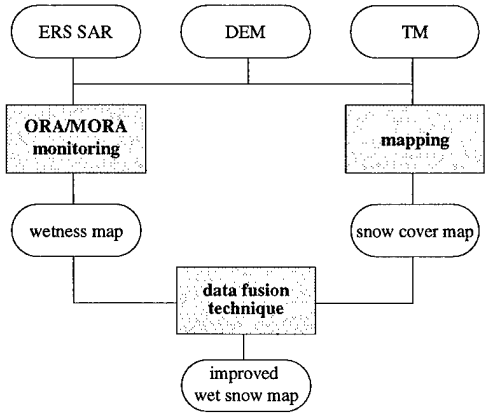

Figure 2: Basic concept of snow cover mapping and monitoring based on SAR and EO data

MORA is based on the optimal resolution approach ORA, which allows the radiometric calibration of the SAR data in the initial original geometry (slant range or ground range representation), as well as the combination of ascending and descending orbit imagery in a cartographic reference system using the highest local ground resolution. Layover areas are dramatically reduced (from 38% to 5% remaining layover areas) and the extraction of thematic information is significantly improved. Prerequisites are a DEM and a precise terrain geocoding [6]. Wet snow cover mapping is done by calculating the ratio between the backscattering coefficient values of the synthetic SAR images and that of a snow-free reference scene as proposed in [7]. The ratio of the backscattering coefficients corresponds to the difference between the γ-values expressed in dB. For each synthetic scene the ratio to a reference scene is calculated. As reference dates for the thematic interpretation the acquisition dates of 16.01.93 and 10.07.93 were chosen because the first had relatively dry snow conditions and in the latter most parts of the scene were snow free except some areas near ridges with permanent snow coverage.

TM derived snow cover mapping is based on a simple RGB composite of geometrically and radiometrically corrected imagery. The choice of the optimal TM channels is depending on the spectral refectance of snow. Therefore, channels 4 (nir) as red, 3 (red) as green and 5 (mir) as blue were used [8]. They are used due to the significantly different reflectance of several snow types in the channels 4 and 5. A separation of snow and clouds can only be done with channel 5. Reflectance values in the visible part of the spectra (blue, green, red) are used for a simple separation of snow-/non-snow covered areas because of the relatively high contrast between snow and bare soil/forest (channel 3).

To be able to fuse SAR and EO data, both image types have to be referenced to the same geodetic/cartographic reference system. One of the most simple fusion methods is to display the data in a RBG-color cube. Applying a RGB-YUV-RGB color transformation the calculated original Y-channel is replaced by the normalized SAR backscatter values γ. The YUV-model corresponds to a intensity-hue-saturation (IHS)-model used for video signals. So, only a visual interpretation is preferred. Finally, the resulting RGB imagery includes the orignally detected snow coverage as well as information on the wetness conditions.

4. RESULTS

The multitemporal dataset printed in Figure 3 are sequences of "wet snow coverage" based on ERS SAR data. The grayscale values indicate the increase of wetness and ranges from -0.5dB to -12dB and were applied to guarantee comparable results to [3]. The extent of the snow coverage is strongly correlated to the topography during the melting season, especially seen in May and June. January and February are relatively dry. Within the March scene an increase of the wetness conditions can be notified. Between the May and the June date the snow-line moved to higher altitudes. July is snowfree but the remaining wetness indicate wet soil conditions.

Figure 4 shows the RGB-435-composites of both TM acquistion dates. Remarkable is the strong influence of illumination effects due to the rugged terrain and the sun position (15.02.93). Most parts of the scene are snow covered (medium and light grey resp. green/yellow) while forested areas are appearing in very dark grey resp. very dark green. For the May scene a significant difference between bare soil/forest (medium and dark values resp. bordeaux and blue) and snow covered areas (very bright gray values resp. green and yellow) is recognized. Snow is represented on sunny slopes as yellow, while in shadowed part and not directly illuminated slopes the green color dominates. Saturated pixel values are appearing in each dataset in TM-channel 3.

Figure 5 illustrates the data fusion result. As a first step, using TM scene of 22.05.93 a RGB-YUV transformation was calculated. The dynamically strechted 8bit-γ-values of SAR scene 01.05.93 were used to replace the Y-information for backward transformation (YUV-RGB). Comparing the subsets of the original 435-input image with the resulting fused output image visually following remarks can be made: a) saturated pixels in snow covered areas are gone, b) more textural information is appearing in snow covered areas, c) a clear border between dark grey and light gray values (blue/violet and light blue/red) can be detected, d) bare soil and forested areas are no more easily detectable. The border can be interpreted as a no-snow/snow zone, which includes dry snow conditions in upper altitudes as well as wet snow conditions in lower parts near snow free areas. The γ-information of the included SAR image dominates the resulting image while edge information originate mainly from the EO data.

5. DISCUSSION AND CONCLUSIONS

Methods for mapping and monitoring wet snow cover in alpine terrain were presented. Analyzing advantages and disadvantages of the use of EO or SAR sensors, in general it can be concluded that EO data are more suitable for snow cover mapping purposes. On the other hand SAR systems are absolute necessary to retrieve certain snow parameters and to monitor the melting process. However, there is still a great unrealised poten-

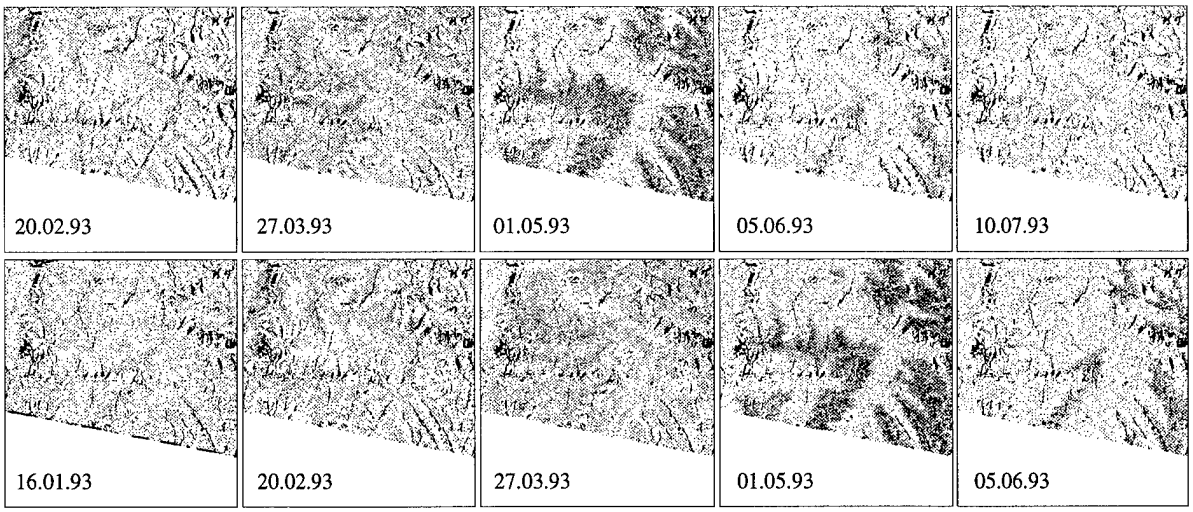

Figure 3: Sequences of wet snow coverage based on SAR data: ratio values relative to 16.01.93 and 10.07.93, dark values indicate wetness

tial in analysing multitemporal and multisource data for geoecological applications as well as for natural features using data fusion techniques. Following achievements and limitations have to be mentioned and taken into account:

- The optimal resolution approach ORA increases the availability of thematic SAR imagery in mountainous regions dramatically. The multitemporal optimal resolution approach MORA is a practicable method for change detection using ERS magnitude data. A dry-snow or snow-free reference scene for calculating the ratio within the MORA results in qualitatively comparable results [4].
- Snow/no-snow maps based on SAR PRI data cannot directly be calculated. Nevertheless, a coarse discrimination of wet snow can only be made in wide open areas and together with additional information, i.e. meteorological data and specific thematic parameters.
- Snow mapping based on EO imagery has to consider spectral reflectance characteristics of snow. Wetness information can not be retrieved. Saturated image pixels limit the retrieval of snow pack parameters.
- A simple RGB-YUV-RGB fusion model was used to show the potential of fusion techniques. Results are promising but more investigations considering numerical aspects and other fusion methods have to be carried out.
- Vegetation changes have also to be considered.

REFERENCES

[1] Seidel, K., Ehrler, C., Martinec, J., Turpin, O.: Derivation of statistical snowline from high resolution snow cover mapping; Proceedings of EARSeL Workshop "Remote Sensing of Land Ice and Snow"; Freiburg, Germany, 17-18 April, 1997

[2] Haefner, H., Holecz, F., Meier, E., Nüesch, D., and Piesbergen, J.: Capabilities and Limitations of ERS-1 SAR Data for Snowcover Determination in Mountainous Regions; Proc. Second ERS-1 Symposium, Hamburg, pp. 971-976, 1993

[3] Piesbergen, J., Holecz, F., Haefner, H.: Snow cover monitoring using multitemporal ERS-1 SAR data; In: Proc. IGARSS'95, Florence, pp. 1750-1752, 1995

[4] Piesbergen, J., Holecz F., Haefner H.: Multi-source snow cover monitoring in Eastern Switzerland. Proc. 3rd ERS Symposium, Florence,1997

[5] Swiss Federal Office of Topography: Das digitale Höhenmodell des Bundesamtes fuer Landestopographie; Wabern, Switzerland, 1996

[6] Meier, E., Frei, U., and Nüesch, D.: Precise Terrain Corrected Geocoded Images, Chapter 7 in: SAR-Geocoding - Data and Systems, Wichmann-Verlag, edited by Schreier, G., pp. 173-185, 1993

[7] Rott, H., and Nagler, T.: Capabilities of ERS-1 SAR for Snow and Glacier Monitoring in Alpine Areas; Proc. Second ERS-1 Symposium, Hamburg, pp. 965-970, 1993

[8] Guck, U.: Auswertung von digitalen, multitemporalen LANDSAT-5-Thematic-Mapper-Daten zur Erfassung der Schneefläche und anderer Oberflächenarten im hinteren Ötztal unter besonderer Berücksichtigung der wasserwirtschaftlichen Bedeutung von Schneeflächendaten, Forschungsbericht, DFVLR-FB 86-46, Oberpfaffenhofen, Germany, 1986

ACKNOWLEDGMENTS

This work has been supported by the Swiss Academy of Science (Project 20-41889.94). The ERS-1 SAR data were made available for AO.CH2 experiment by the European Space Agency ESA. Landsat-5 Thematic Mapper data provided by Eurimage. Digital terrain model (DHM25): © Swiss Federal Office of Topography (1637a).

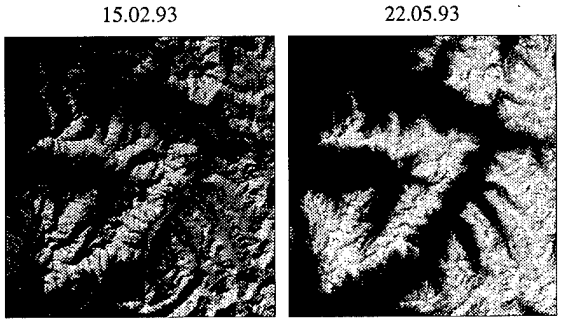

Figure 4: 435-RGB composites of TM imagery; explanation see text; coloured images: http://www.geo.unizh.ch/rsl/projects/

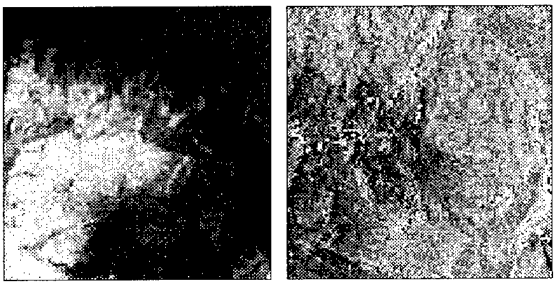

Figure 5: Subsets of RGB images before (left) and after data fusion process (right); explanation see text coloured images: http://www.geo.unizh.ch/rsl/projects/

The use of Mathematical Morphology for accurate detection and Identification of Microwave Images in the K-Space Domain

Paul Gader
Andrew J. Blanchard

Office of the Dean
University of Missouri-Columbia
W1024 EBE
Columbia, Missouri
Voice (573) 884-7872
FAX (573) 882=2490
E Mail ajb@ecvax2.ecn.missouri.edu

Abstract -- The use of holography in imaging is generally confined to the optical regime. Recent advances in microwave techniques have allowed the use of multi-frequency and multi-geometry to collect phase information that can be used to construct two and three dimensional information sets. The use of longer wavelengths allows flexible configurations and applications that can penetrate propagation media and in some cases the target of interest. Microwave radiation has not been used extensively in imaging three dimensional structure using holographic approaches. The use of tomographic processing requires that data be collected at sufficient resolution to allow unambiguous slices to be constructed. This differs from interferometric techniques where there is some ambiguity (phase) that must be handled to properly reconstruct the final three dimensional image.

INTRODUCTION

The difficulty in using these image construction techniques lies in the fact that the inversion is a linear process. The scattering mechanism is driven by non-linear behavior (multiple scatter, polarization coupling, near field effects, etc.). When decision processing mechanism are developed for images the characteristics inherent in the image generation process must be included in the algorithm design. There are two phenomena that must be modeled and accounted for in the development process, 1) the scattering information base and 2) the image generation attributes. One would like to develop decision processes that are invariant to the image generation process. These robust algorithms could then be used with a variety of measurement system architectures and not be impacted by imaging constructs. We would also be able to include the non linear processes as part of the decision making scheme.

The development of Imaging processes use the process of acquiring information in the K or time space domain to recover the effective spatial domain construct. The measurement space is illustrated in Figure 1. Information can be acquired in the frequency domain, and the geometric domain. In many cases the frequency domain is used to acquire data because the acquisition time is generally much less than that required for acquisition in the geometric domain. The relationship between the acquired data in the measurement space and the scattered field is given by (1)

$$-\oiint_{S_M}\left[\phi_S(\overline{R}',\omega)\frac{\partial G^*}{\partial \hat{n}'}-G^*(\overline{R}-\overline{R}',\omega)\frac{\partial \phi_S}{\partial \hat{n}'}\right]dS'$$

$$=j2\int_{-\infty}^{\infty}\iiint q_Q(\overline{R}',\omega)\,\mathrm{Im}\{G(\overline{R}-\overline{R}',\omega)\}\,d^3\overline{R}' \qquad \text{EQ (1)}$$

In this expression the convenient inversion of the measured parameters to the field image values require several linearizing assumptions. The most convenient assumption is the far field measurement configuration.

0-7803-3836-7/97/$10.00 © 1997 IEEE

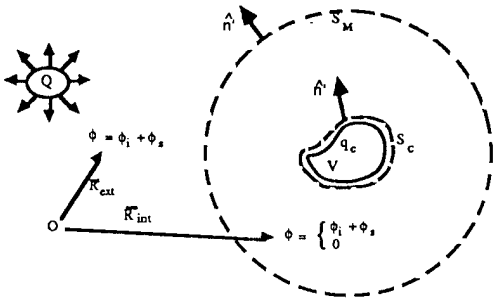

Figure 1 Measurement Configuration

In most radar applications this limitation does not impose a significant difficulty for practical application of the image inversion process. The application of the process on reflective surface or objects does require that the curvature of the surface be convex, single scatter process describe the interaction, and polarization independence. The last three can pose several difficulties in creating image that are recognizable in the optical sense. Multiple scatter processes can not correctly identify the interaction location of the multiple bounce phenomena. This makes the image look different than the physical structure of the object of interest. The convex surface requirement can also pose some problems given the general nature of natural and man-made objects. Finally in many cases polarization processes are couples and cannot be separated. By linearizing the interaction process the full descriptive nature of the object interaction process is not available. When these assumptions are made the expression relating measured data to inversion data becomes:

$$q_c(\bar{R}) = -\frac{R}{2\pi^2}\iiint_{-\infty}^{\infty} \frac{\phi_s^{far}(\bar{K})e^{-j\bar{k}_i\cdot\bar{R}}}{k^2} e^{j(\bar{k}_r-\bar{k}_i)\cdot\bar{R}}\, d^3\bar{K} \qquad \text{EQ (2)}$$

This expression is the recognizable form of the Fourier Transform

$$q_c(\bar{R}) = -\frac{R}{2\pi^2} F_{3D}^{-1}\left\{\frac{\phi_s^{far}(\bar{K})e^{-j\bar{k}_i\cdot\bar{R}}}{k^2}\right\} \qquad \text{EQ (3)}$$

Where the Fourier variable is

$$\bar{K} = \bar{k}_r - \bar{k}_i$$

NON-LINEAR EFFECTS

These nonlinear effects are not confined to the frequency spectrum, as polarization is also a coupled process. The linearizing assumptions described in (3) are significant for all forms of nonlinear coupling. When multiple scatter is present the interpretation of the scattering point is confused. A simple example is the scatter from a spherical object. The largest and most significant scattering phenomena is the direct scatter from the orthogonal point of the sphere. If we map this scattering point as a function of geometry the spatial scattering function paints the surface scatter magnitude on the physical surface of the sphere. The response of a sphere is well quantified, however, it is probably easier to identify the behavior in the frequency domain, rather than the time or space domain. The secondary interaction scattering function causes some ambiguity in the space domain (looks like two individual scatterers rather than one). It is much easier to define the nature of the interaction in the frequency domain because we know the nature of the scattering process and its frequency response. The linearization of the scattering process causes this ambiguity in the space domain.

NON-LINEAR PROCESSING

Mathematical morphology is a nonlinear processing paradigm that provides a firm mathematical basis for a class of nonlinear filtering and detection schemes. Morphological processing can be generalized to include robust statistical operators and can be incorporated into neural network architectures [1,2].

Mathematical morphology involves translation-invariant, non-linear convolution type operations based on fundamental operations of erosion and dilation. Erosion and dilation are operations that involve probing the image with sets, called *structuring elements*. Morphological processing is used to derive shape information from the image. This information is dependent on the structuring elements. The structuring elements are analogous to linear filters.

Let **X** be a subset of n-dimensional Euclidean space, and let f:**X**→**R** be a real valued function on **X**. Generally n is 2 and f represents a digital

image. Let $f_{\mathbf{z}}(\mathbf{x}) = f(\mathbf{x}-\mathbf{z})$ denote the spatial translation of f and let the reflection of f be defined by $f^*(\mathbf{x}) = -f(-\mathbf{x})$.
The gray-scale *erosion* of a function f by a structuring element g is defined by

$$(f \ominus g)(\mathbf{x}) = \min \{f(\mathbf{z}) - g_{\mathbf{x}}(\mathbf{z}) : \mathbf{z} \in D[g_{\mathbf{x}}]\}. \quad \text{EQ (4)}$$

This operation measures the minimum difference between $f(\mathbf{z})$ and $g_{\mathbf{x}}(\mathbf{z})$ for $\mathbf{z} \in D[g_{\mathbf{x}}]$ and is equivalent to measuring the maximum amount that the structuring element $g_{\mathbf{x}}$ can be translated vertically and still lie beneath f. It indirectly measures how well the shape represented by g fits under f but the output value is not invariant to shifts because if λ is a number, then

$$(f + \lambda \ominus g)(\mathbf{x}) = (f \ominus g)(\mathbf{x}) + \lambda. \quad \text{EQ(5)}$$

The gray-scale *dilation of* a function f by a structuring element g is defined by

$$(f \oplus g)(\mathbf{x}) = \max \{f(\mathbf{z}) - (g^*)_{\mathbf{x}}(\mathbf{z}) : \mathbf{z} \in D[(g^*)_{\mathbf{x}}]\} \quad \text{EQ(6)}$$

The gray-scale dilation is the dual of the erosion and indirectly measures how well the structuring element fits above f in the same sense that erosion measures the fit below f. An operation which measures both the fit above and below is the gray-scale *hit-miss transform*, which is defined as:

$$f \otimes (h,m) = (f \ominus h) - (f \oplus m^*) \quad \text{EQ(7)}$$

This definition is motivated by the *umbra transform* [1]. The hit-miss transform measures how the shape h fits under the function f and how the shape m fits above f. Higher values indicate good fits. If $f \otimes (h,m)(\mathbf{x}) > 0$, then there exists a set of vertical shifts for which both shapes h and m closely fit the function f. If the structuring elements match the shape of an image over a region I, the hit-miss transform will produce a peak where the shape occurs.

These nonlinear detection filters can be used in place of linear detection filters. We have empirical results that indicate that morphological filters produce images with better entropy than linear filters.

[1] E. R. Dougherty, *An Introduction to Morphological Image Processing*. Bellingham WA: SPIE, 1992.

[2] Y. Won. P. Gader, and P. Coffield, "Morphological Shared-Weight Networks with Applications to Automatic Target Recognition", IEEE Trans Neural Networks (Accepted for Publication).

NEW CLASSIFICATION TECHNIQUES FOR ANALYSIS OF REMOTE SENSING INTEGRATED DATA

Elena Console*, Marie Catherine Mouchot**
*** T.E.A. s.a.s.**
Via Bruno Chimirri 28, 88100 - Catanzaro (Italy)
phone: +39.961.74.75.28, fax: +39.961.72.56.36, e-mail: console_e@abramo.it
**** Département I.T.I., ENST de Bretagne**
Technopole de Brest-Iroise, BP 832, 29285 Brest Cedex (France)
phone: +33.298.00.13.58, fax: +33.298.00.10.98, e-mail: mc.mouchot@enst-bretagne.fr

Abstract -- The aim of this work is the application of techniques based on fuzzy logic for integrating and classifying spectral data and spatial information. The analysis was performed on a Landsat-TM image and on a set of map field data.

Firstly fuzzy membership values of Landsat image pixels were calculated and a buffer area was defined around map field data for each considered class.

The membership values were then modulated using spatial information derived from known targets.

Finally the accuracy of the classification was assessed on a set of test data. The obtained results shown a significant improvement compared to more traditional methods of classification.

INTRODUCTION

Adequation of techniques for processing remote sensing imagery improves the knowledge of Earth' surface and contributes remarkably to the development of policies for planning and monitoring of environmental resources. The possibility of using different type of data can increase our ability to visually discriminate between different ground targets.

The fusion techniques of optical imagery with other information require appropriate procedures for data analysis. Furthermore it becomes necessary to determine suitable methodologies of classification which take into account the heterogeneity of the acquired data and the indeterminateness of considered targets.

In this work we used fuzzy logic for integrating and classifying spectral and spatial information. More particularly the analysis was performed on a Landsat-TM image of Southern Italy and on cartographic data.

The map field data are represented by geographical coordinates of training pixels and by vector files of hydrography of the considered area.

These known targets were used for modulating the fuzzy membership values of all pixels located in their neighbourhood. The size of the neighbourhood was defined differently for each class according to the experts's opinion.

The steps of the applied methodology were the followings:

a) choice of fuzzy membership function and membership values computing;
b) estimation of buffer around the set of known targets;
c) modulation of membership values in buffer areas;
d) hard classification from fuzzy classification;
e) accuracy assessment
f) mixed classification.

APPLIED METHODOLOGY

The chosen membership function for computing fuzzy membership values of each pixel to considered class has been the following (Figure 1):

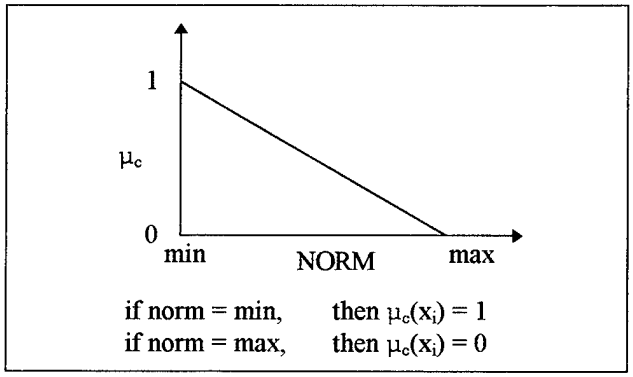

Figure 1: Membership function

The adopted norm is defined as the absolute distance from the mean of the considered class normalized by the standard deviation:

$$norm(x_{i,c}) = \sum_{b=1}^{6} \frac{\left| x_{i,b} - \bar{x}_{c,b} \right|}{\sigma'_b}$$

where:
i = *ith* considered pixel
c = c*th* considered class
b = b*th* considered band

$\bar{x}_{c,b}$ = mean of c*th* class in the b*th* band

$\sigma'_b = \frac{\sigma_b}{\sum_{b=1}^{6} \sigma}$ normalized standard deviation

σ_b = standard deviation of the b*th* band.

Next, the physical distances of each pixel from map field data have been calculated (Figure 2a).

For each class a buffer area around the set of know targets (training pixels and hydrographic vector files) were defined on the ground based on expert's knowledge (Table 1). These windows delimit the pixels which the membership to the considered class is most probable (Figure 2b).

Table 1

DIMENSION OF BUFFER AREA FOR EACH CLASS			
Class	**meters**	**Class**	**meters**
Grass covered area	200	Cultivated area	250
Orchards	250	Forest	100
Non vegetated area	100	Road network	60
Shady forest	500	Urban area	150
Hydrography	100		

We assigned these pixels to values between 0 (assigned to the central pixel of the buffer area) and 1 (assigned to the pixels of external edge) defined as modulation values, *m.v.* (Figure 3).

In order to integrate the spectral and the spatial information we assumed that the pixels located around the known targets belong most likely to the same class of the target. Hence the membership values of these neighbour pixels were modified using the modulation values drawn from spatial data:

$$\textit{final membership value} = \mu_c(x_i)^{m.v.}$$

The resulting images have been filtered applying a median filter, which size was identical to the class buffer size.

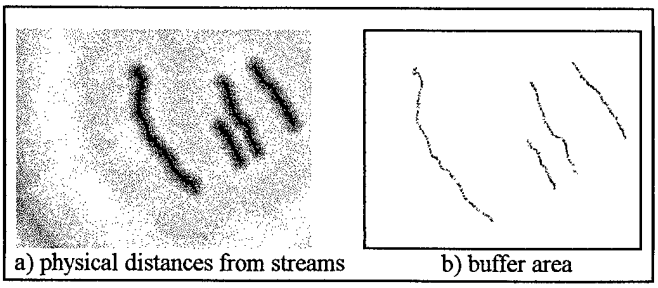

a) physical distances from streams b) buffer area

Figure 2: Hydrographic network

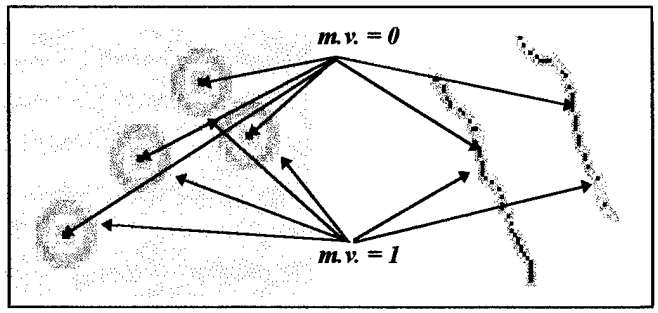

Figure 3 - Modulation values

RESULTS

In order to verify the accuracy of results, the error matrix and the K indices have been computed on hard classification derived from fuzzy classification against a sample of ground truth pixels.

The hard classification was produced by assigning each pixel to the class having the highest membership value. We considered a fixed threshold value, under which the pixel was labelled non classified:

$$\text{if } \mu_c(x_i) = \max_{c=1}^{8} \mu(x_i), \qquad \text{then } x_i \in \text{class c}$$

The results were compared with conventional classifications (minimum distance and maximum likelihood) and hard classification not integrating spatial information.

In the Table 2 we have reported the values of global index K and the conditional index K for classes "Urban area" and "Road Network". These two classes were chosen more particularly because they prove to exhibit a fairly high rate of false classifications in prior studies.

One can see that the integration of the spatial information significantly improved the accuracy of the classification both in term of global K and conditional K.

Table 2

COMPARISON OF RESULTS			
Algorithm	**Global K**	**Conditional K**	
		Urban a.	***Road netw.***
Minimum distance	0.37	0.26	0.27
Maximum likelihood	0.46	0.33	0.25
Fuzzy cl. non integrated with spatial information	0.30	0.44	0.19
Fuzzy cl. integrated with spatial information	**0.42**	**0.60**	**0.28**

Finally the mixed classification was considered; the mixed classes are represented by the combination of the two classes having the highest fuzzy membership values.

Superimposing the mixed classification image on the official cartography of the considered area it becomes obvious that correspondence is better than with maximum likelihood classification.

It is then confirmed that the "Urban area" and "Road Network" classes are better identified (Figure 4).

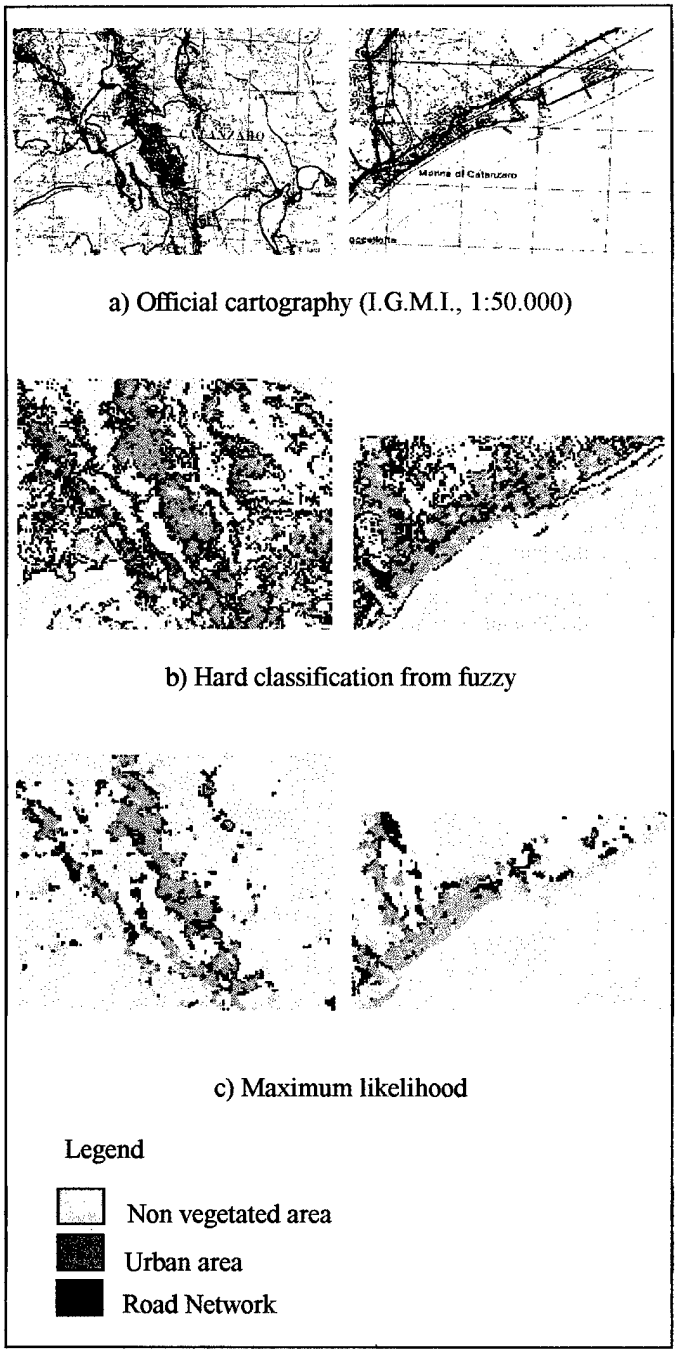

Figure 4: Comparison of results

CONCLUSIONS

The use of different data sources and their integration significantly improved the performance of the adopted fuzzy classification technique. In particular, the applied methodologie, by allowing the modulation of membership values of each class, enhanced its ability to discriminate among all considered soil coverage, especially in the difficult case of the urban agglomerates.

REFERENCES

[1] D. Altman, "Fuzzy Set Theoretic Approaches for Handling Imprecision in Spatial Analysis", Int.Journal of Geographical Information Systems, vol. 8, n. 3, pp. 271-289, 1994

[2] S. Aronoff, "Classification Accuracy: a User Approach", Photogrammetric Engineering and Remote Sensing, vol. 48, n. 8, pp. 1299-1307, 1982

[3] E. Console and M.C. Mouchot, "Fuzzy Classification Techniques in the Urban Area Recognition"", in Proceeding of IGARSS'96 - Remote Sensing for a Sustainable Future, IEEE Publications, vol.II, pp. 1373-1375, 1996

[4] L.A. Zadeh, "Fuzzy Sets", Inf. Control., vol. 8, pp. 338-353, 1965

Hughes Phenomenon in the Spatial Resolution Enhancement of Low Resolution Images and Derivation of Selection Rule for High Resolution Images

Ryuei Nishii

Faculty of Integrated Arts and Sciences, Hiroshima University
Kagamiyama 1-7-1, Higashi-Hiroshima 739, JAPAN
Phone: +81-824-24-6474, Fax: +81-824-24-0756, E-mail: nishii@mis.hiroshima-u.ac.jp

Saeko Kusanobu and Noriyuki Nakaoka
Graduate School of Engineering, Hiroshima University

Abstract — The Landsat TM sensor for thermal infrared measurements, Band 6, has lower resolution than those of other six Bands. Nishii et al (1996) proposed a statistical method to improve Band 6 by the linear combination of other six band data. In this case, we observe a subset of high-resolution bands provide a better predictor than that based on all high-resolution bands. This may be Hughes phenomenon. We will propose the way to select the best subset of high-resolution bands based on the information theoretic criterion called AIC.

1 INTRODUCTION

The Band 6 of the TM sensor equipped by the Landsat 5 observes heat radiation, which is physically important. Unfortunately, its spatial resolution on the earth is of 120m × 120m, whereas those of other six Bands are of 30m×30m. Thus, it is a key problem to enhance the spatial resolution of Band 6. [2] proposed a statistical procedure to enhance the low-resolution image. By employing conditional expectations of multivariate normal distributions, Band 6 is improved by the linear combination of other six bands. The coefficients of the linear combination are estimated by the covariance matrix among seven band data.

Of course, every band with high-resolution has information on Band 6 to a greater or less degree. However, the linear combination of all high-resolution bands may give a poor correction than that of some of high-resolution bands. This is shown by actual images.

In [2], four prediction procedures of Band 6 are suggested. We examine the performance of the block and global predictors through the sum of squared errors (SSE). Further, the usefulness of a subset of high-resolution bands for predicting Band 6 is verified through Akaike's information criterion (AIC) by [1]. It is shown that AIC provides a similar performance of SSE and needs less computation.

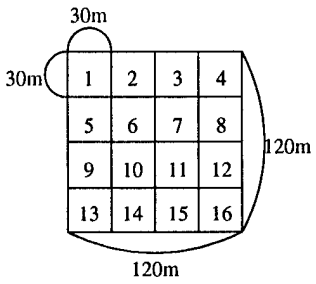

Figure 1: Pixels in the local window

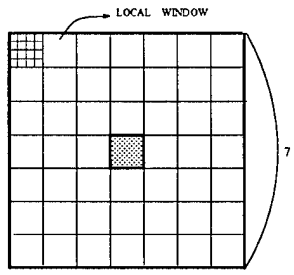

Figure 2: Block consisting of 49 local windows

2 PREDICTORS FOR BAND 6

A region consisting of pixels numbered from $i = 1$ to 16 at which Band 6 is observed is called a local window. Let X_{bi} be a random variable of Band $b(= 1, \ldots, 5, 7)$ observed at the i-th pixel of the local window. Its observation, say x_{bi}, is placed as $\boldsymbol{x}_i \equiv (x_{1i}, \ldots, x_{5i}, x_{7i})^T$. Let Y_i be an unobservable random variable of Band 6, but the averaged value $\sum_{i=1}^{16} Y_i/16 = \overline{Y}$ is observed, say $\overline{y}$. Assume that the random vectors $(\boldsymbol{X}_i^T, Y_i)^T$ are independently distributed as a 7-variate normal distribution with mean $(\boldsymbol{\mu}^T, \nu)^T$ and covariance matrix $\Sigma = \begin{pmatrix} \Sigma_{xx} & \boldsymbol{\sigma}_{xy} \\ \boldsymbol{\sigma}_{yx} & \sigma_{yy} \end{pmatrix}$. The mean and covariance matrix are supposed to be common in the local window. Then, the value of Band 6 is predicted by the conditional expectation. Here, we consider the following two predictors of Band 6 depending on estimation methods of the covariance matrix Σ.

1. **The block predictor $\widetilde{Y}_i^{\text{block}}$**
   Consider a block consisting of ℓ^2 local windows, see Fig. 2 with $\ell = 7$. Deriving the mean of 7-dimensional observations in each local window, we calculate a sample covariance matrix based on ℓ^2 mean vectors which would give an estimate for $(1/16)\Sigma$.

2. **The global predictor $\widetilde{Y}_i^{\text{global}}$**
   Choose only one observed vector in each local window. Then, calculate a sample covariance matrix based on all selected vectors.

3 NECESSITY OF BAND SELECTION

The necessity of band selection is shown by the Landsat TM image of Hiroshima Bay, JAPAN (2,000 rows × 2,000 columns). This is verified by the following steps.

1) 4 × 4 average one out of these bands.

2) Certain band values are again averaged in 4×4 pixels in order to simulate the resolution of Band 6.

3) Choose a subset of high-resolution bands and fix the block size $\ell = 3(2)11$. Then, predict the low-resolution band y_i by the block predictor $\tilde{Y}_i^{\text{block}}$.

4) Compare the sum of squared errors (SSE) between predicted and observed values.

Let RSSE be a ratio of SSEs: $\sum^* \sum_{i=1}^{16} (y_i - \tilde{Y}_i^{\text{block}})^2 / \sum^* \sum_{i=1}^{16} (y_i - \bar{y})^2$, where $\sum^*$ extends over all local windows. The small RSSE means a satisfactory result.

Table 1 tabulates RSSEs of Band 3 predicted by linear combinations of all possible subset of Bands 1,2,4,5,7. The numerals in the bold face denote the minimum values among five block sizes, and band combinations are sorted in the increasing order of the minimum RSSEs. This shows that Band 3 is very accurately predicted by remaining high-resolution bands. Further, the linear combination of Bands 2,4,7 provides a better predictor than that of Bands 1,2,4,5,7 for any block size.

Table 1. RSSEs of block predictors of Band 3 based on subsets of Bands 1,2,4,5,7 with sample size = 500×500

Selected Bands	Block Sizes				
	3	5	7	9	11
2 4 7	.0676	.0569	**.0565**	.0570	.0575
2 4	.0598	**.0579**	.0594	.0606	.0615
2 4 5	.0707	.0587	**.0584**	.0588	.0592
1 2 4 7	.0867	.0595	**.0588**	.0595	.0603
2 4 5 7	.0932	.0612	**.0589**	.0589	.0591
1 2 4 5	.0902	.0605	**.0597**	.0601	.0608
1 2 4 5 7	.1313	.0632	**.0605**	.0606	.0610
2 7	.0664	.0607	**.0605**	.0607	.0610
1 2 7	.0773	.0614	**.0606**	.0607	.0611
2 5 7	.0781	.0618	**.0606**	.0606	.0607
2 5	.0659	**.0607**	.0613	.0619	.0624
1 2 4	.0724	**.0609**	.0620	.0633	.0647
1 2 5	.0777	.0616	**.0612**	.0617	.0623
1 2 5 7	.0999	.0644	**.0625**	.0628	.0633
2	**.0642**	.0653	.0671	.0679	.0684
1 2	.0716	**.0665**	.0676	.0686	.0695
1 4 7	.1358	**.1148**	.1165	.1189	.1212
1 4	.1202	**.1196**	.1244	.1282	.1309
1 4 5	.1447	**.1229**	.1259	.1301	.1342
1 4 5 7	.1926	.1304	**.1291**	.1320	.1354
1 5	.1457	**.1362**	.1372	.1379	.1382
1 5 7	.1804	.1426	.1401	.1398	**.1397**
1 7	.1553	**.1442**	.1455	.1467	.1473
1	**.1738**	.1779	.1820	.1842	.1859
4 7	.3970	**.3944**	.4150	.4332	.4495
4 5 7	.5176	**.4045**	.4094	.4220	.4319
7	.5063	**.4973**	.4994	.5011	.5024
5 7	.5768	.5151	.5077	**.5074**	.5092
4	**.5560**	.5651	.5848	.6040	.6201
4 5	**.5622**	.5730	.6195	.6578	.6912
5	.5947	**.5796**	.5828	.5860	.5890

Table 2 gives RSSEs of Band 6 predicted by linear combinations of subsets of Bands 1 – 5, 7. Some digits exceed one, which means the enhanced image becomes worse than the 4 × 4 averaged image. Unfortunately, the linear combination of all high-resolution bands makes the result worse. This is also true for the sum of absolute errors. Hence, both selections of bands and of block sizes are inevitable.

Table 2. RSSEs of block predictors of Band 6 based on subsets of Bands 1 - 5, 7 with sample size = 500×500

Selected Bands	Block Sizes				
	3	5	7	9	11
1	**.6595**	.7070	.7426	.7759	.8024
1 4	.7224	**.7209**	.7679	.8007	.8285
2	**.7211**	.7634	.8013	.8283	.8543
1 5	**.7259**	.7259	.7746	.8103	.8354
3	**.7473**	.7810	.8145	.8415	.8725
1 3 4	.8805	**.7733**	.8170	.8589	.8887
2 4	**.7881**	.7928	.8459	.8806	.9127
7	**.7917**	.8267	.8620	.8949	.9359
1 3 5	.9748	**.7966**	.8273	.8643	.8877
1 3	.8533	**.7995**	.8297	.8577	.8842
1 7	.8058	**.8028**	.8544	.9077	.9430
1 4 5	.9210	**.8064**	.8616	.9147	.9443
1 2	.8659	**.8068**	.8339	.8304	.8504
1 4 7	.9190	**.8094**	.8686	.9284	.9656
1 2 4	.9946	**.8191**	.8534	.8701	.8824
3 4	**.8240**	.8257	.8791	.9170	.9533
1 2 5	1.0682	**.8294**	.8468	.8524	.8628
5	**.8298**	.8689	.9032	.9326	.9664
1 5 7	.9418	**.8319**	.8921	.9557	.9978
2 5	.8542	**.8456**	.9038	.9446	.9770
1 2 4 7	1.3319	**.8585**	.8801	.9219	.9391
1 3 4 7	1.2479	**.8585**	.8757	.9206	.9498
1 3 4 5	1.2650	**.8593**	.8838	.9317	.9545
3 5	.8794	**.8651**	.9245	.9650	.9983
1 2 4 5	1.3211	**.8701**	.8952	.9361	.9543
1 3 5 7	1.3077	**.8739**	.8875	.9352	.9615
1 2 7	1.0946	**.8750**	.8855	.9152	.9357
1 2 5 7	1.3329	**.8894**	.9144	.9548	.9694
4 7	.9277	**.8921**	.9444	.9941	1.0478
2 4 7	1.0357	**.9058**	.9473	1.0048	1.0436
1 2 3 5	1.3960	**.9069**	.9566	.9957	.9962
2 3 4	1.0711	**.9070**	1.0136	1.1029	1.1240
1 4 5 7	1.3289	**.9090**	.9466	.9877	1.0125
1 3 7	1.1174	**.9204**	.9283	.9564	.9749
2 4 5	1.0649	**.9214**	.9789	1.0328	1.0649
1 2 3 4	1.4298	**.9248**	.9871	1.0223	1.0284
5 7	.9660	**.9366**	1.0329	1.0958	1.1519
2 7	.9674	**.9444**	.9910	1.0505	1.0874
4 5	1.0183	**.9501**	.9951	1.0392	1.0855
1 2 3	1.1367	**.9521**	.9925	1.0105	1.0111
4	.9906	**.9577**	.9599	.9693	.9892
2 3 5	1.1658	**.9618**	1.0440	1.1346	1.1553
2 5 7	1.1107	**.9765**	1.0309	1.0853	1.1219
1 3 4 5 7	2.0349	.9988	**.9860**	1.0109	1.0313
3 4 5	1.1514	**.9887**	1.0475	1.1026	1.1414
1 2 4 5 7	2.4716	**.9930**	.9959	1.0224	1.0382
2 3	1.0347	**.9931**	1.0957	1.1828	1.1852
3 4 7	1.1559	**1.0074**	1.0479	1.1127	1.1674
1 2 3 4 5	2.2289	**1.0163**	1.0345	1.0603	1.0525
1 2 3 5 7	2.2757	1.0289	**1.0187**	1.0324	1.0416
1 2 3 7	1.5727	**1.0205**	1.0242	1.0551	1.0467
1 2 3 4 7	2.3151	1.0431	**1.0312**	1.0396	1.0388
3 7	1.0526	**1.0350**	1.0935	1.1724	1.2325
2 4 5 7	1.4996	**1.0503**	1.0836	1.1272	1.1529
3 5 7	1.2478	**1.0595**	1.1015	1.1622	1.2141
2 3 4 7	1.6185	**1.0784**	1.0978	1.1319	1.1247
2 3 4 5	1.6470	**1.0997**	1.1566	1.1850	1.1730
1 2 3 4 5 7	5.2273	1.1309	**1.1068**	1.1189	1.1169
2 3 7	1.3683	**1.1100**	1.1536	1.2366	1.2548
2 3 5 7	1.7200	1.1415	**1.1156**	1.1399	1.1477
4 5 7	1.3160	**1.1173**	1.2435	1.3486	1.4206
3 4 5 7	1.6859	**1.1672**	1.1913	1.2268	1.2544
2 3 4 5 7	2.5159	**1.2187**	1.2261	1.2478	1.2342

4 SELECTION OF BANDS BY AIC

The redundancy of a subset of full-resolution bands is evaluated through Akaike's information criterion [1] under the null hypothesis such that the subset has no additional information. This is formulated as follows.

Partition the high-resolution bands as $\boldsymbol{X}_i^T = (\boldsymbol{X}_{1i}^T, \boldsymbol{X}_{2i}^T)$. The mean and covariance matrix are partitioned in the similar manner as $\boldsymbol{\mu}^T = (\boldsymbol{\mu}_1^T, \boldsymbol{\mu}_2^T)$, $\boldsymbol{\sigma}_{yx} = (\boldsymbol{\sigma}_{y1}, \boldsymbol{\sigma}_{y2})$ and $\Sigma_{xx} = \begin{pmatrix} \Sigma_{11} & \Sigma_{12} \\ \Sigma_{21} & \Sigma_{22} \end{pmatrix}$. Now, we consider the following null hypothesis:

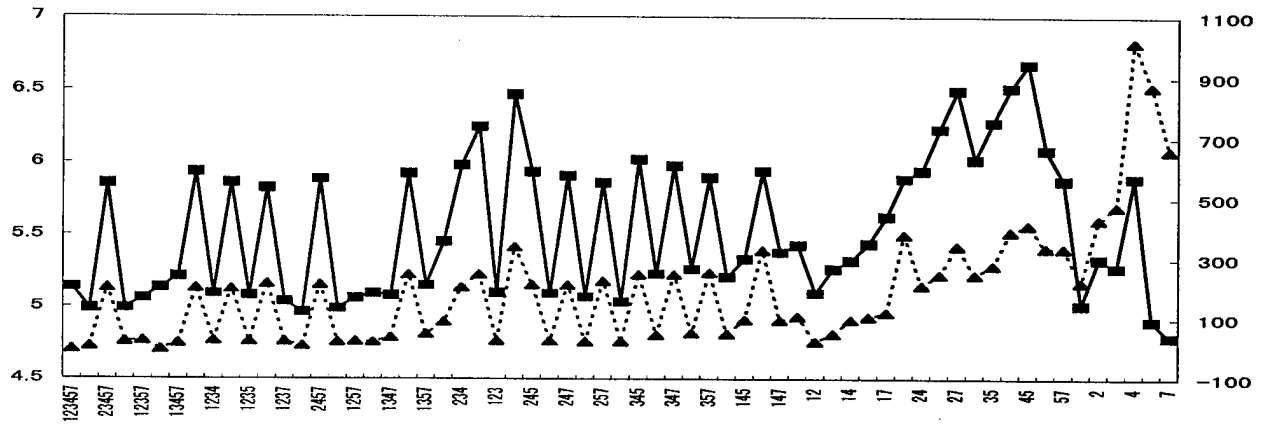

Figure 3: SSE (solid line) and AIC* (dotted line) of global predictors of Band 6 with sample size 140×104 (The horizontal axis is corresponding to subsets of full-resolution Bands 1 – 5, 7)

H_0: Subvectors $\boldsymbol{X}_{2i} : q \times 1$ $(i = 1, \ldots, 16)$ in all local windows have no additional information for predicting Band 6

against the hypothesis:

H_1: All full-resolution bands $\boldsymbol{X}_i : 6 \times 1$ have information for predicting Band 6.

The conditional expectation of Y_i:

$$E[Y_i|\boldsymbol{X}_i = \boldsymbol{x}_i] = \nu + \boldsymbol{\gamma}_1^T(\boldsymbol{x}_{1i} - \boldsymbol{\mu}_1) + \boldsymbol{\gamma}_2^T(\boldsymbol{x}_{2i} - \boldsymbol{\mu}_2)$$

with $\boldsymbol{x}_i^T = (\boldsymbol{x}_{1i}^T, \boldsymbol{x}_{2i}^T)$ and $\boldsymbol{\gamma}^T = (\boldsymbol{\gamma}_1^T, \boldsymbol{\gamma}_2^T) = (\boldsymbol{\sigma}_{y1}, \boldsymbol{\sigma}_{y2})\begin{pmatrix} \Sigma_{11} & \Sigma_{12} \\ \Sigma_{21} & \Sigma_{22} \end{pmatrix}^{-1}$ leads that H_0 is naturally formulated by $\boldsymbol{\gamma}_2 = (0, \ldots, 0)^T$. After some algebra, it is shown that this is equivalent to $\boldsymbol{\sigma}_{y2} = \boldsymbol{\sigma}_{y1}\Sigma_{11}^{-1}\Sigma_{12}$. Then, the conditional distribution of Y_i is given by

$$Y_i|\{\boldsymbol{X}_i = \boldsymbol{x}_i\} \sim N(\nu + \boldsymbol{\gamma}_1^T(\boldsymbol{x}_{1i} - \boldsymbol{\mu}_1),\ \sigma_{yy\cdot 1}),$$

where $\boldsymbol{\gamma}_1 = \Sigma_{11}^{-1}\boldsymbol{\sigma}_{1y}$ is a regression coefficient vector and $\sigma_{yy\cdot 1} = \sigma_{yy} - \boldsymbol{\sigma}_{y1}\Sigma_{11}^{-1}\boldsymbol{\sigma}_{1y}$ is a conditional variance. We use the global estimate for Σ. Then, AIC for the conditional random variables is obtained as

$$\mathrm{AIC}(H_0) = N \log s_{yy\cdot 1} + N \log(2\pi e) + 2 \times 8 - 2q,$$

where N is a sample size, $s_{yy\cdot 1} = s_{yy} - s_{y1}S_{11}^{-1}s_{1y}$ with

$$\begin{pmatrix} S_{xx} & s_{xy} \\ s_{yx} & s_{yy} \end{pmatrix} = \frac{16}{N} \sum{}^{*} \begin{pmatrix} x - \bar{\bar{x}} \\ y - \bar{\bar{y}} \end{pmatrix} \begin{pmatrix} x - \bar{\bar{x}} \\ y - \bar{\bar{y}} \end{pmatrix}^T,$$

$S_{xx} = \begin{pmatrix} S_{11} & S_{12} \\ S_{21} & S_{22} \end{pmatrix}$ and $s_{yx} = (s_{y1}, s_{y2})$. Here, $(\boldsymbol{x}^T,\ y)$ denotes an observation selected in each local window, $\bar{\bar{x}}$ denotes an average of $\boldsymbol{x}$ and $\sum^*$ extends over all local windows. Among all possible subsets of full-resolution bands, the subset which minimizes AIC is considered as optimal.

We here note that finding of the minimum $\mathrm{AIC}(H_0)$ is equivalent to that of $\mathrm{AIC}(H_0) - \mathrm{AIC}(H_1)(\equiv \mathrm{AIC}^*$, say) which is simply equal to

$$\mathrm{AIC}^* = N \log \frac{s_{yy\cdot 1}}{s_{yy\cdot x}} - 2q \quad \text{with} \quad s_{yy\cdot x} = s_{yy} - \boldsymbol{s}_{yx}S_{xx}^{-1}\boldsymbol{s}_{xy}.$$

In Fig.3, AIC* and SSE of a subregion of the TM image used in Section 3 are calculated. The subregion is of size 560×416, and it is 4×4 averaged. The horizontal axis of Fig.3 denotes 63 combinations of full-resolution bands from $\{1, 2, 3, 4, 5, 7\}$ to $\{7\}$. The vertical scales in the left hand side and in the right hand side are used for SSE and AIC*, respectively. This shows that AIC has a similar performance of SSE.

5 CONCLUSION

We have shown that band selection is necessary and useful for predicting Band 6. Of course, SSE may be a natural measure for evaluating the goodness of subsets of high-resolution bands. We proposed an alternative procedure based on AIC. Features of our procedure are as follows:

- AIC shows the similar performance of SSE.
- AIC can be obtained when the covariance matrix is estimated. AIC needs calculations of order O(1), whereas SSE needs $O(N)$ for each band combination.

The efficient procedure for finding the optimal block size with less effort is also another important problem.

References

[1] H. Akaike, "A new look at the statistical model identification," IEEE Trans. Auto Control, AC-19, pp. 716–723, 1974.

[2] R. Nishii, S. Kusanobu and S. Tanaka, "Enhancement of low spatial resolution image based on high resolution bands," IEEE Trans. Geosci. Remote Sensing, 34, pp. 1151–1158, 1996.

Forming digital elevation models from single pass SPOT data: results on a test site in the Indian Ocean

DIDIER MASSONNET
ALAIN GIROS
ERIC BRETON
Centre National d'Etudes Spatiales
18 Avenue E. Belin, 31401 Toulouse cedex 04, France
Phone: (33) 5-61-27-34-18 Fax: (33) 5-61-27-31-67
Didier.Massonnet@cnes.fr
Alain.Giros@cnes.fr
Eric.Breton@cnes.fr

Digital Elevation Models are significant elements in most of the remote sensing field, mostly as auxiliary data and sometimes as primary source of scientific or commercial information. The use of SPOT data opened a new era in the DEM computing business by allowing the construction of good precision DEMs (typically 10m rms.) thanks to its side-looking capability. Alternate techniques are now available, such as SAR interferometry, which is highlighted by the upcoming Shuttle Radar Topographic Mission to be launched around the year 2000 in order to compute a global DEM. Not all applications, however, require high precision DEM. Here we report the accuracy of a DEM made from two images acquired by the same optical instrument at the same time (single pass stereoscopy). This experiment is characterized by a very small forward baseline of about 15 km. The geometric performance is attenuated by a factor of about 100 with respect to conventional SPOT stereoscopy. Another potential difficulty is the different nature of the two images : 20m single band image and 10m panchromatic image. On the other hand, single pass operation guarantees a very good similarity between the images and a minimal influence of cloud cover. The concept has been tested using data acquired over l'ile de la Reunion, off the coast of Madagascar, a typical area where collecting stereoscopic data is difficult. We use a high performance image correlator we developed, which compensates partially for the poor baseline available. We discuss the quality of the result, which is compared to a conventional DEM, as well as the potential of this new product, from the point of view of the applications and of the design of future missions.

BACKGROUND

Digital elevation models (DEM) are crucial to a number of activities. They are directly used as input for geosciences, as witnesses of fault activity; their accuracy is essential in the assessment of the effort necessary for public works (road building, dams...); they are pivotal for the use of terrain following, advanced weapons and, in general, the protection of aircraft from detection; they find an application in hazard maps either directly (flooding) or indirectly (assessment of slopes for protecting against landslides). Last but not least, they are used as auxiliary data for proper positioning of any kind of data that can enter a geographical information system. In this sense, DEM give a better value to any geographical data, which is especially true for remotely sensed data.

In the recent years, the use of SAR interferometry as a unique technique for the determination of displacement fields has added a new application of DEMs, since it is necessary to remove, sometimes with high accuracy, a topographic contribution from a radar interferogram before the displacement of the terrain is revealed, sometimes with centimeter-size accuracy.

DEMs can be computed in a variety of ways, including the digitization of existing maps. The global result is, however, very heterogeneous both in terms of accuracy and in terms of reliability. Furthermore, the DEMs are not always openly accessible. In the US, the Defense Mapping Agency created a global DEM with a sampling of 1200 points per degree of latitude or longitude and a credited accuracy of 30 m rms. However, even if the part of this product covering the US territory is freely accessible, this is not the case elsewhere.

The SPOT system offered in the mid-80s a solution for global DEM thanks to its lateral pointing capability. A number of areas, and sometimes whole countries, were successfully covered by this means, with a good and controllable accuracy in the range of 10 m rms. However, two passes are required for lateral stereoscopy, which leads to a low probability of success for areas with frequent cloud cover. Let P be the probability of having a cloud free acquisition over a given area, the probability of having two such acquisitions is P squared, not a matter of concern when P is 70%, but a miracle if P is only a few percent.

To overcome this situation, plans have been made to use forward-backward stereoscopy in future satellites, or to synchronize several satellites in order to correlate the

0-7803-3836-7/97/$10.00 © 1997 IEEE

probabilities of cloud cover for the two passes, for instance if the two satellites are only a few minutes apart.

In the mid-90's another solution emerged thanks to the interferometric technique. Various studies showed that the interferometric signal had a potential for meter-size accuracy. Using radar data such as the ones ERS-1 had made available almost everywhere on earth could lead, in principle, to a global DEM. In an effort to reduce the time separation between images, the European Space Agency synchronized its two ERS satellites, creating the "tandem" mission. However, as we recognized early in our studies dealing with displacement fields, there is a strong atmospheric contribution to an interferogram. This contribution leads to artifacts that we have learned to recognize in order to avoid misinterpreting geophysical signals. However, to build a DEM requires not only to recognize, but also to correct the artifacts. This is the reason why radar interferometry is more useful, now, for validation of existing DEMs rather than for creating new ones. Hopefully, further signal processing improvement might solve the problem using several interferograms on the same spot.

The inconvenient of radar interferometry disappears if one considers a simultaneous acquisition of the two radar images. However, this requires a specific radar mission with two antennas on the same craft. Despite the cost involved, the Defense Mapping Agency and NASA designed the Shuttle Radar Topography Mission, intended to deliver a DEM between plus and minus 60 degrees of latitude at the turn of the century. The results of this mission will certainly improve the situation a lot, however, part of the data will remain classified and efforts to solve the problem of global DEM by other means are still welcome.

Here we discuss the first results of a test conducted with SPOT data, using a specific feature of the data from SPOT 1, 2 or 3: the slight forward-backward stereoscopic difference between high resolution (10 m), black and white data (panchromatic) and lower resolution (20 m) spectral bands (XS).

USING PANCHROMATIC AND XS STEREOSCOPY

It results from the design of SPOT 1,2,3 instrumental focal plane that corresponding panchromatic and XS data are not acquired at exactly the same time. The panchromatic data is acquired about 2 seconds sooner than the XS data because the CCD line matrix which creates the XS data is behind the CCD line matrix of the panchromatic data. As a result, there is a tiny stereoscopic effect between the two data sets, which corresponds to a baseline on the ground of about 15 km combined with a distance of observation of about 832 km. This effect is responsible for a well known artifact in the combination of the two channels into a single image: landscapes with large elevation range occasionally create slight mis-registrations.

We decided to attempt exploiting this stereoscopic effect for DEM production, which raises several questions:

1) the stereoscopic effect is tiny, the baseline ratio is 15/832 and we are forced to use the 20 m data as reference. The net result is that we are approximately 100 times less sensitive to topography than 10 m data used with a baseline ratio of one

2) we attempt to correlate data of different physical meaning. XS data represent only a fraction of the spectrum observed by panchromatic data

3) the instrumental responses are not the same for both kind of data. It suffices to notice that the resolutions are not the same, however, more factors of difference may come into play

4) at the level of "pixel slicing" envisioned for our application, structured noise sources can be predominant (shift between neighbor CCD sub-matrixes, irregular matrix grid, very low amplitude vibrations, etc.). No one knows if these artifacts can be successfully modeled and removed.

On the other hand we have two trumps:

1) Having such a slight difference between images, furthermore acquired at the same time, may boost the performance of the procedure of correlation

2) Our group at CNES is experienced with high performance image comparison techniques. In particular, we recently developed a new concept of precise image comparison.

The only way to answer fully these questions was to experiment.

DATA SELECTION AND ANALYSIS

The ideal test site must have several qualities: 1) availability of combined panchromatic and XS data, 2) easy horizontal reference in order to bypass possible problems with biases in the attitude angles of the satellite, 3) availability of a DEM of good quality for the assessment of the results, and 4) the test site must be relevant, that is typical of a situation where conventional stereoscopy is likely to fail.

For these reasons we selected La Réunion, which is part of France, and a volcanic island is the Indian Ocean. We have a

good quality, 100 m sampled, DEM computed by IGN (the French Geographical Institute). Besides, the island is under investigation as part of our RADARSAT proposal, which intends to monitor ground displacements of the main volcano: Piton de la Fournaise, using radar interferometry based on RADARSAT data. The site is relevant as a typical tropical area and working with an island about the size of SPOT frame gives an easy horizontal reference.

We selected two image pairs which could both be used for our purpose. None of the pair was acquired vertically. The mirror of SPOT was tilted for each pair, selected from archived data. By chance, the two pairs could also be used for conventional stereoscopy since their angular biases are opposite. We used one pair as a reference and the other as a backup.

Applying the latest image comparison techniques we have resulted, in an automated way, in a disparity image featuring a typical dispersion of 2% of a pixel, which is equivalent to a dispersion of 20 m in elevation.

Several problems were discovered and corrected in the image comparison procedure, which is a first valuable result of the experiment. The technique had not been used in such a challenging context before. It seems possible to improve further on the quality and having a final 10 m accuracy is within reach.

However, the main challenge is not in the accuracy, but in the separation of topography from artifactual contributions. We observed well known phenomena such as differences between adjacent matrix bars and, more generally, differences linked the layout of the various detectors used. These biases can, however, be mapped and accurate geometric calibration could correct them.

More difficult is the short period oscillations of the satellite attitude, which cannot be easily modeled from auxiliary data because these are poorly sampled, and thus aliased, in the frequency range of interest. This is not a system design error, but a specification choice linked to the extremely low amplitude expected at these frequencies, which goes unnoticed for any conventional application.

DISCUSSION

The study is now focused on the modeling of the attitude aliasing and the perfection of the geometric model. The latter could actually help a great deal the former : one may think, for instance, of using lateral deformation as a calibration source for the geometric setting of the data take, where the useful data are mainly based on the forward deformation. This study will be followed along two axes:

On the short term, we intend to turn this experiment into the development of an industrial software product, which would create DEMs of satisfactory accuracy (in the 10-20 meter range)

On the long term, the results will be used as a driver for new missions as well as a way to revise the technical specifications of future missions.

A Mixed Fractal/Wavelet Based Approach For Characterization of Textured Remote Sensing Images

A. Marazzi*, P. Gamba*, A. Mecocci ,E. Costamagna*.**
***Dip. Di Elettronica, Università di Pavia, Via Ferrata 1, 27100 Pavia, Italy**
Tel. ++39 382 505923 Fax++39 382 422583, E-mail: maraz@comel1.unipv.it
****Fac. Di Ingegneria, Università di Siena, Via Roma 77, 55300 Siena, Italy**

ABSTRACT

One of the problems encountered in the field of remote sensing image characterization, is the choice for the right features. The addition of textures as a discriminating parameter is a good help in the step of segmentation of different zones. In this work we present an approach that is a mix between a wavelet multiscale analysis and a fractal characterization, in order to exploit both the main characteristic of the two approaches and to override the limitations of the two techniques. The chain was applied to different textured images showing an improvement respect to other methods based on wavelet transform and fractal approach alone.

1. INTRODUCTION

Most traditional statistical approaches to texture are restricted to the analysis of spatial interactions over relatively small neighborhoods. The recent advent of texture multiscale analysis, leading with the simple wavelet transform [1] to the more complete packet wavelet approach [2][3][4], permits to overcome the problem due to the intrinsic limitations of a single scale analysis. With a different approach several researchers have investigated the possibility of the use of fractals to study textured patterns, with the aid of the fractal dimension and some features related [5][6] or the recent multifractal dimension [7]. It is well known that the use of the simple fractal dimension does not provide sufficient information to describe and to segment natural textures, because different fractal sets may share the same dimension and have a different visual appearance. The addition of the wavelet tools allows to override the problem due to rotation invariance of the fractal dimension; the multichannel approach is able to change the distribution of the information in such a way that is possible a discrimination based on the simple fractal dimension. So, the use of a wavelet transform applied to the original image before performing the computation of the fractal parameters permits to improve the results.

2. FRACTAL GEOMETRY

Fractal geometry was developed by Mandelbrot [7] and is an interesting mathematical approach to give a description of natural scenes ; the basic idea is that an object has fractal properties when is Hausdorff-Besicovitch dimension is greater than its topological dimension. It is so possible to give a degree of complexity for irregular shapes that is called fractal dimension. In order to calculate the dimension, we can exploit the concept of self-similarity. Rake a bounded set A in the Euclidean n-space: This set is considered self-similar when is the union of N distinct copies of itself, each of which has been scaled down by a ratio r in all the coordinates. The fractal or similarity dimension of A is given by the relation :

$$D = \frac{\log\left(N_r\right)}{\log\left(\frac{1}{r}\right)} \qquad (1)$$

This concept of self -similarity can not be applied in a straightforward way for natural surfaces because they do not posses a deterministic self-similarity (only some specific natural surfaces is strictly self-similar), but an other kind of self-similarity called statistical self-similarity can be considered with a mathematical definition equal to the FD shown in (1).
Several approaches exist to estimate the FD in image like as [9][10][11], they differ for the computational weight , for the complexity and for the efficiency.

3. THE WAVELET TRANSFORM

Several studies has proven the utilities of the wavelet transform with application to texture. With the 2-D wavelet technique an image is decomposed in a set of subimages with a reduced dimension and with a narrow and more defined bandwidth. While in the classical transform this process of filtering and decimation is iterated only in the base-band, in the more complete packet wavelet the filtering process is applied to all the subimages, obtaining a number of pictures

0-7803-3836-7/97/$10.00 © 1997 IEEE

equal to 4^n where n is the level of decomposition. This last kind of technique is quite useful to define textures because they can be generally modeled as a quasi-periodic signal with dominant frequencies in the middle frequency channels. The basic transform can be seen as tensor product of two 1-D wavelet basis along the horizontal and vertical directions ; the corresponding coefficients can be expressed as :

$$h_{LL}(k, l) = h(k)\, h(l), \qquad h_{LH}(k, l) = h(k)\, g(l),$$
$$h_{HL}(k, l) = g(k)\, h(l), \qquad h_{HH}(k, l) = g(k)\, g(l), \tag{2}$$

where the first and second subscript denote the low-pass and high-pass filtering along the x and y directions. Different kind of filter (corresponding to different wavelet basis) can be easily found in literature with different characteristic and utilization.

4. THE MIXED APPROACH

As discussed in the introduction the basic idea is to apply a wavelet/packet wavelet algorithm before to perform the calculation of the fractal dimension. The dimension is considered as a features in the segmentation step.
Different basis were here applied and the best result were found with the Battle-Lemarie'. The fractal dimension were calculated with the classical differential box counting algorithm [9] that seems to give the best fractal approximation with low computational cost.

The algorithm works as follows:

1 - apply a 2D wavelet transform to an image with different textures and obtain the filtered subimages. With this first step, that can be iterated with a packet wavelet transform, the frequency information is separated in different channels and it is easier to discriminate the different textured patterns.

2 - compute the fractal dimension for each subimage. A moving window is shift along all the images in order to built the histogram of the fractal dimension. A this point we have a number of subimages, dependent on the choice of the level of the wavelet transform, where the gray level is replaced by the local fractal dimension. Note how there is a reduction of the dimension of the images because the border is lost in the process of the computation of FD.

3 - apply an unsupervised K-means clustering to the images using the fractal dimensions as features in the multidimensional space.

The application of the wavelet transform allows to identify the fractal information related to each textured patterns; in fact textures with the same fractal dimension often show a different fractal behavior in each wavelet subband. With usual wavelet 2D techniques, where an horizontal and vertical filtering is performed, textures with patterns mainly referring to these directions are recognized by fractal dimension very well.
The algorithm was tested with different basis and with different levels of wavelet transform; good results were found with the application of a complete decomposition stage with a packet wavelet algorithm.

5. RESULTS AND DISCUSSION

Here are shown some results obtained by testing the algorithm on a mosaic with 4 textures. In fig.1a are shown the test patterns built with a set of 4 textures with the same fractal dimension. A comparison is made between the result obtained with the application of the algorithm [6] and the application of our mixed approach. It is easy to notice how the addition of a wavelet decomposition permits to improve the segmentation results both in the two cases. The application of this kind of approach to a remote sensing textured image is a straightforward consequence of what we have discussed in the previous section where different patterns are easily distinguishable by this mixed approach.

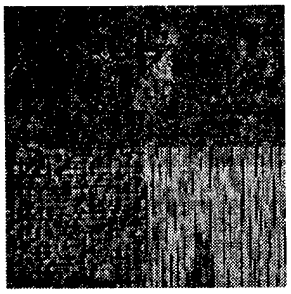

a)

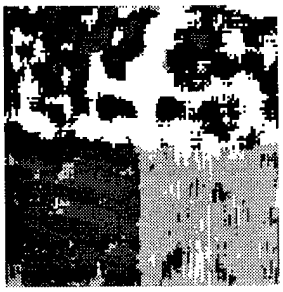

b)

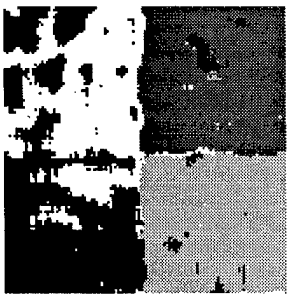

c)

fig.1 a)mosaic of 4 textures with the same fractal dimension b)result of the segmentation with the C&S algorithm c)result of the segmentation with the mixed wavelet/fractal approach

REFERENCES

[1] S.G. Mallat, "A theory of Multiresolution Signal Decomposition: the Wavelet Representation", *IEEE Trans. Patt. Anal. Mach. Intell*, vol. PAMI-11, pp. 674-693, 1989

[2] M.Unser, "Texture Discrimination Using Wavelets" Proc. of 1993 *IEEE Conference on Computer Vision and Pattern Recognition*, pp. 640-641, New York City June 1993

[3] A.Laine and J.Fan, "Texture Classification by Wavelet Packet Signatures",", *IEEE Trans. Patt. Anal. Mach. Intell*, vol. PAMI-15, pp. 1186-1191, Nov. 1993

[4] A.Mecocci, P.Gamba, A.Marazzi, M.Barni, "Texture Segmentation in Remote Sensing Images by Means of Packet Wavelets and Fuzzy Clustering" *Proc. of 2nd ESSRS SPIE*, pp. 142-151, Vol. 2584 Paris, Sept. 1995

[5] J.M.Keller, S.Chen and R.M.Crownover, "Texture Description and Segmentation through Fractal Geometry" *Comp. Graph. Im. Proc.* pp. 150-166 Vol. 45 1989

[6] B.B. Chaudhuri and N. Sarkar, "Texture segmentation Using Fractal Dimension", *IEEE Trans. Patt. Anal. Mach. Intell*, vol. PAMI-17, pp. 72-77, Jan. 1995

[7] S.Fioravanti "Multifractals. Theory and Application to Image Texture Recognition, in *Proc. of the Congress on Fractals in Geoscience and Remote Sensing,* EUR Report 16092 EN, Vol. I, pp. 152-175, 1994

[8] B. B. Mandelbrot *"Fractals: Form, Chance and Dimension"*, W. H. Freeman, San Francisco, CA, 1977.

[9] N. Sarkar and B.B.Chaudhuri, "An Efficient Approach to Estimate Fractal Dimension of Texture Image", *Pattern Recognition*, Vol. 25, pp. 1035-1041, 1992

[10] A. P. Pentland, "Fractal-based description of natural scenes", *IEEE Trans. Pattern Anal. Machine Intell.* **6**, 661-674, 1984.

[11] J. J. Gangepain and C. Rocques-Carmes. "Fractal approach to two dimensional and three dimensional surface roughness", *Wear* 109, 119-126, 1986.

Significance-Weighted Classification by Triplet Tree

Masanobu Yoshikawa*, Sadao Fujimura**, Shojiro Tanaka*, and Ryuei Nishii***
* Faculty of Engineering, Yamanashi University
** Faculty of Engineering, University of Tokyo
*** Faculty of Integrated Arts and Sciences, Hiroshima University
* Takeda 4-3-11, Kofu-shi, Yamanashi 400, Japan
Phone: +81 552 20 8491, FAX: +81 552 20 8776, E-mail: yoshi@esi.yamanashi.ac.jp

Abstract – An efficient classification method using a triplet tree is proposed for target land-cover categories with significance weight. The weights are determined by user in the view of importance in actual classification. In the proposed method, a triplet tree classifier for land cover classification is used. The triplet tree classifier has two types of nodes. It generates two nodes for 'definite nodes' and one optional 'indefinite node' at every node segmentation.

Tree design procedure uses the weights in the two meanings. Firstly, significant categories are assigned with high priority in the selection of splitting patterns. Categories with higher priority are separated from other categories at the upper nodes. Secondly, a node for heavily weighted categories are designated with little classification error at every decision of boundaries.

Experiment about real remotely sensed images was executed to show the performance of the proposed method. The results of classification were compared with the standard Bayesian classifier or other multistep methods.

The classification accuracy about heavy weighted categories by this method is higher than a conventional classifier without weights. The computing cost for this method is small because this approach is based on a decision tree method.

INTRODUCTION

In many cases of classification of remotely-sensed image, several categories are highly interested categories. For example, the target category is an agricultural field or forest area. In such case, classification accuracies of the other categories is less important and precise classification of such categories are sometimes unnecessary. Traditional classifiers are not always suitable for this objective. They are designed for averaged performance about all categoried in the image. An effective method has been proposed for a successive feature extraction method designed for significance-weighted supervised classification[2]. That method has intended for hyperdimensional data.

This paper proposes another simplified approach with a triplet tree classifier. We already proposed a triplet tree classifier for land cover classification [1]. The triplet tree is an extension of binary decision tree. It generates two types of nodes in each step: two 'definite nodes,' which are nodes for definitely-classified samples, and one 'indefinite nodes,' which is a node for indefinitely-classified samples. Data with uncertain spectral features are classified to indefinite nodes and processed repeatedly in the tree. In this triplet tree, single category may appear as plural terminal nodes. In the proposed method, these weights are utilized in the design process of the triplet tree.

In a step of tree design, one binary segmentation pattern of the group of categories is selected as label-set of child nodes. And two boundaries in the feature space are decided based on the data histograms and the specified error tolerance about training samples. These two boundary generates triplet nodes, two are definite nodes and one is an indefinite node.

In this paper, highly interested categories are heavyly weighted in the triplet tree design. Significance-weighted triplet tree focuses highly interested categories in two ways.

- At the selection of splitting pattern of nodes, the most important category is tried firstly to separated from the other categories. If it works well, other patterns will not be checked.
- At the decision of two boundaries, error tolerance about training samples are calculated considering total weights for two definite child nodes.

SIGNIFICANCE-WEIGHT OF CATEGORIES

The significance is defined as a weight for each category determined in the view of importance in classification. Important categories have larger weights and less important categories have smaller weights.

Suppose g identification classes are given. Importance of category i is denoted by weight w_i. Several assumption enables to help formalization of the method. The value of weights are determined by user following to the interests or objectives of classification under the following definitions.

For normalization, let weight w_i $(i = 1 \ldots g)$ conform to $\sum_{i=1}^{g} w_i = 1$. Assume that there are $G(G \leq g)$ interested categories and their priority queue is denoted as (p_j). One type of weight for this case is defined by the next equation:

$$w_j = \frac{(p_j)^{-1}}{\sum_{i=1}^{G}(p_i)^{-1}}. \quad (1)$$

0-7803-3836-7/97/$10.00 © 1997 IEEE

Here we define that some category i and some groups of category $J \subseteq \{1, 2, \ldots, g\}$ are *informative* or *not-informative* as follows:

$$(D1)\begin{cases} i & \text{is } informative & \text{if} & w_i \geq W, \\ i & \text{is } not-informative & \text{if} & w_i < W, \end{cases}$$

$$(D2)\begin{cases} J & \text{is } informative & \text{if} & \sum_{j\in J} w_j \geq W, \\ J & \text{is } not-informative & \text{if} & \sum_{j\in J} w_j < W, \end{cases}$$

where $W = \frac{1}{G \cdot \sum_{i=1}^{G}(i)^{-1}}$. W is the minimum value of (1) in simple case that $(p_j) = [1, \ldots, G]$.

SIGNIFICANCE-WEIGHTED CLASSIFICATION

Triplet Tree Method

A triplet tree method has been proposed by Yoshikawa et al.[1] to make flexible and robust classification of feature space. The tree of the method is an extension of binary decision tree and third segmentation of indefinite category groups are not executed. Thus the classifier is almost as simple as binary decision tree, while the accuracy is much improved. The overview of the mechanism is as follows.

1. A binary segmentation with one optional node is selected by group distance criterion.
2. Two 'definite nodes' and one 'indefinite node' are generated as child nodes.
3. Samples definitely classified are assigned to 'definite nodes'.
4. The uncertain samples are assigned to 'undetermined node' labeled as the same categories as the parent node.
5. Two boundaries in the feature space for the division of nodes are decided based on the data histograms about training samples. Specified error tolerance parameter τ is used as criterion.

Error tolerance parameter $\tau(\%)$ is determined at the beginning of design. Let N be the number of training samples for a parent node. Then two boundaries are selected to satisfy the condition that error classified samples for two definite nodes are less than $\lfloor N * \tau/100 \rfloor$.

Definite part of data are classified as fast as binary decision tree. Categories with uncertain parts have plural terminal nodes according to the nature of training data. The decision of binary segmentation pattern and two boundaries are executed in the bottom-up manner with training data. The advantage of the triplet tree appears when categories are diversified in nature or training samples have poor representabilities[1]. Several terminal nodes have plural categories for uncertain samples by the definition of division. They are indefinite terminal nodes with labels of candidate categories. If single classification category for all data is needed, triplet tree without indefinite terminal nodes can be made by applying majority rule about training samples to such nodes.

Processing about Weights in the Tree

Several devices are introduced to the design process of the triplet tree classifier. Let the group of category $J = \{j_1, j_2, \ldots, j_k\}\,(k \leq g)$ be included in a parent node and let J_A and J_B be categories for two child definite nodes A and B respectively. Assume that N be the number of samples in the parent node, and that N_A and N_B be the number of samples about J_A and J_B respectively.

(a) **τ and weights of categories**
The upper limits of error classified samples are calculated not only by the size and τ, but the total weights for J_A and J_B are also considered. The upper limits L_A for A is in inverse ratio to total weights:

$$L_A = \lfloor N_A * \sum_{i\in J_B} w_i * \tau/100 \rfloor, \quad (2)$$

$$L_B = \lfloor N_B * \sum_{i\in J_A} w_i * \tau/100 \rfloor. \quad (3)$$

(b) **Top-down strategy in binary splitting**
Target categories with large weight are assigned with high priority in the selection of splitting patterns. Such categories are separated from other categories at the upper nodes and early classification is executed. When j_1 is the most informative category in J, the first candidate for binary splitting pattern is $J_A = \{j_1\}, J_B = \{j_2, \ldots, j_k\}$, Then, this pattern is adopted when the node division for this pattern is well-constructed in the sense of accuracy and size as follows:

- Error tolerance criterion is applied severely than (a). In this case, N_A is number of samples for category 1 in J. The upper limits of error classified samples for A and B are decided only by the size for highly interested category.

$$L_A = \lfloor N_A * \sum_{i\in J_B} w_i * \tau/100 \rfloor, \quad (4)$$

$$L_B = \lfloor N_A * w_1 * \tau/100 \rfloor. \quad (5)$$

- Samples of category j_1 in J_A is more than presetted portion of samples of j_1 in J. This parameter was equal to 10(%) in the experiment.

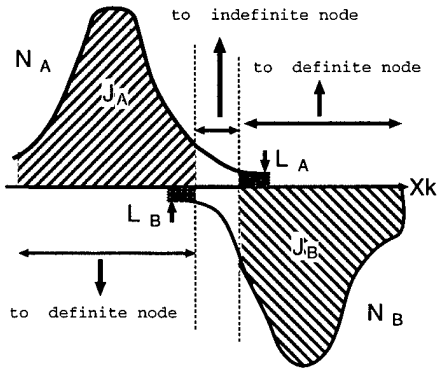

Fig.1. Segmentation to child nodes: sample histogram and boundaries (using feature x_k)

(c) **Weighted majority rule**
When a triplet tree without indefinite terminal nodes is needed, a weighted majority rule is utilized. Let n_i be the number of samples for category i in A, the category $j_A = \max_{i \in J_A} w_i n_i$ is selected.

(d) **Division for not-informative nodes**
When the total weight for J is not-informative, further division of this node is found to be useless. In the method, such nodes are omitted to classification and remains to be indefinite terminal nodes.

EXPERIMENTAL RESULTS

Test Image

Triplet tree classifier was designed for a real remotely-sensed image. Error tolerance parameter τ was selected as 3%. For the comparison, traditional quadratic discriminant function method (QDF) was applied to the same data.

The used image was geocoded six bands of Landsat TM data in December 2, 1989. The field of image was 16km×12km area. The test fields has the following categories with widely varied frequencies: Residential area(C1), Developed area(C2), and Barren(C3), Farm and Grassland(C4), Paddy field(C5) and Water surface(C6).

The sample sizes in the whole data (12004 pixels) are:

Class	C1	C2	C3	C4	C5	C6
pixels	2111	1798	1167	3162	2748	1018

300 pixels for each category were selected as training data. The design process was tested by assigning two types of priority to categories. The priority [A] was $\{C4 > C5 > C2 > C1 > C6 > C3\}$, and the priority [B] was$\{C4 > C5 > C6 > C1 > C2 > C3\}$. In these cases, the main targets of classification were agricultural fields. The weights were calculated by equation (1) with $G = 6$, so that all categories were informative.

Classification Results

Each sample was forced to be classified to single category in this experiment by two reasons. At first, all appeared nodes included categories with informative total weight. Secondly, majority rule with significance weight was applied.

Table 1 describes comparisons of accuracies. Accuracy about each category, overall accuracy, averaged accuracy for all categories are shown. Average2 is averaged accuracies about first and second informative categories. AverageA3 and AverageB3 are averaged accuracy about three highly weighted categories respectively.

Proposed triplet tree was better than QDF about averaged accuracy for larger weighted categories(Average2, AverageA3 and AverageB3), while QDF was better in terms of averaged accuracy. Compared with two most informative categories, advantages of triplet trees were over five percent. Compared with the overall accuracy, tree methods were about equivalent performance to QDF in this case.

Table 1: Accuracies for TEST Image (%)

CLASS	Triplet Tree [A]	Triplet Tree [B]	QDF
C1	85.8 (4)	82.5(4)	83.8
C2	37.3 (5)	46.7(3)	40.7
C3	55.8 (6)	54.0(6)	87.8
C4	89.4 (1)	90.5(1)	75.7
C5	94.8 (2)	93.1(2)	94.0
C6	73.6 (3)	63.9(5)	73.6
Overall	76.7	77.3	77.1
Average	71.0	71.7	75.9
Average2	92.1	91.8	84.8
AverageA3	82.5	–	81.1
AverageB3	–	76.7	70.1

(Digits in parentheses are priority of category.)

CONCLUSION

Triplet tree considering weights was proposed and actual classification was tested. Highly interested categories are included many nodes in the tree, and they are fast and accurately classified. Triplet tree is robust about sample distribution because the decision of boundary are independent of distribution functions. It was found by experimental result that proposed method had apparent advantages in accuracies for larger weighted categories.

The triplet tree has multistep process with redundancy about categories. Proposed triplet tree method has advantages when target categories are diversified in nature or training samples for target categories have poor representabilities.

References

[1] M. Yoshikawa et al., "Design Method of Triplet Decision Tree Classifier with Division-Wait Mechanism ," Proc. of SPIE, vol.2955, 52-62, 1996.

[2] S.Fujimura and S. Kiyasu, "Significance-Weighted Feature Extraction from Hyper-Dimensional Data and its Applications," the 2nd International Airborne Remote Sensing Conference and Exhibition, III, 288-297, 1996.

[3] B. Kim and D. A. Landgrebe, "Hierarchical Classifier Design in High-Dimensional, Numerous Class Cases," IEEE Trans. on Geoscience and Remote Sensing, vol.29, 518-529, 1991.

[4] Wang Ru-Ye, "An Approach to Tree-Classifier Design Based on a Splitting Algorithm," Int. J. Remote Sensing, vol.7, 89-104, 1986.

On-line System for Monitoring and Forecasting Earth Surface Changes Using Sequences of Remotely-Sensed Imagery

Lee Sanghoon
Department of Industrial Engineering, KyungWon University
SeongNam-Shi, KyungKi-Do, Korea
Tel: 82-342)750-5367 Fax: 82-342)750-5273
Email: shlee@main.kyungwon.ac.kr

ABSTRACT - Irregular temporal sampling is a common feature of geophysical and biological time series in remote sensing. This study develops an on-line system for monitoring and forecasting ground surface changes by adaptively generating an appropriate synthetic time series at regular interval with recovering missing measurements for sequential images that are compiled at irregular time interval from earth ground. The proposed system integrates an adaptive reconstruction technique and a classification algorithm. The reconstruction method incorporates temporal variation according to physical properties of targets and anisotropic spatial optical properties into image processing techniques. The classification algorithm segments each image frame by partitioning into physically meaningful regions whose statistics are expected to depend on the physical properties of the region. This adaptive approach allows successive refinement of the structure of objects that are barely detectable in the observed series and monitoring of temporal variation in surface characteristics by observing statistical changes between contiguous image frames in the adaptive system.

INTRODUCTION

In this study, a Gibbs Random Field (GRF) is used to represent the spatial dependency of the digital image structure, while a polynomial model is employed to track the underlying variation through time. Because simultaneous modeling of the spatial and temporal components is extremely complex, the feedback scheme using multiple filters is utilized to separate the operations on these components. An anisotropic diffusion approach is employed to restore mean intensity image from spatially-contaminated observation. This approach is an iterative smoothing technique which adaptively selects the GRF coefficients according to the intensity difference between the center and neighbor pixels at each iteration. Temporal variation in remotely-sensed image process is represented with a polynomial time series model. For a realization sequence of the intensities, the estimates of the polynomial coefficients are sequentially updated over time using the exponentially weighted least squares criterion. The parameter values related to the class characteristics continuously change over time. An unsupervised classification method is thus applied for the multitemporal analysis. The integrated system sequentially collects the estimated results from the individual filters and then statistically analyzes them to monitor and forecast the change in surface characteristics.

IMAGE MODEL

Most physical processes observed in remote sensing data usually exhibit systematic trends in properties over a long period time. This type of variation is most apparent in the mean intensity. In this study, the mean intensity variation is represented by a polynomial function of time. Let $\mathbf{X}_t$ and μ_t be the variables of the observed intensity image and the mean intensity image at time t respectively. The image process of n pixels can be modeled as

$$\begin{aligned} \mathbf{X}_t &= \mu_t + \mathbf{e}_t \\ \mu_t &= \left\{ \mu_{t,i} \,|\, \mu_{t,i} = \textstyle\sum_{k=0}^{p} a_{i,k} t^k, \, i \in \mathbf{I}_n \right\} \end{aligned} \tag{1}$$

where $\mathbf{I}_n = \{1,2,\cdots,n\}$ be a set of indices of pixels and $\mathbf{e}_t$ is a Gaussian random noise with zero mean.

This study uses a particular class of GRF to represent the spatial dependency of the mean intensity process in neighboring regions. The energy function of the GRF is expressed in terms of "pair potentials" [1] which are a family of symmetric functions

$$\left\{ V_{(r,s)}(\mu) \,|\, V_{(r,s)} = V_{(s,r)} \text{ and } V_{(r,s)} = 0 \text{ if } r = s, (r,s) \subset \mathbf{I}_n \right\}.$$

The pair potential, which is only dependent on the values of pixel pair in the associated clique, can be defined as a function of the quadratic distance between the mean intensities of the associated pixel-pair:

$$V_{(r,s)}(\mu) = \alpha_{rs} \left(\mu_r - \mu_s \right)^2 \tag{2}$$

where $\alpha_{rs} = \alpha_{sr}$ is the nonnegative coefficient which represents "bonding strength" between the rth and sth pixels. Specification of the energy function with the pair potentials of (2) quantifies the local smoothness in the image spatial structure such that neighboring pixels have closer intensity

0-7803-3836-7/97/$10.00 © 1997 IEEE

levels with higher probability. The related GRF defines a probability structure of the mean intensity process:

$$P(\mu) = \kappa^{-1} \exp\left[E_p(\mu)\right]$$
$$E_p(\mu) = \sum_{(r,s)\in \mathbf{C}} \alpha_{rs}\left(\mu_r - \mu_s\right)^2 \quad (3)$$

where κ is a normalizing constant and $\mathbf{C}$ is the set of cliques.

BAYESIAN MEAN INTENSITY ESTIMATION USING ANISOTROPIC DIFFUSION

For a probability structure of μ, a class of Gibbs measures is specified with the energy function $E_p(\mu)$ of (3) which can be expressed for the periodic boundary as

$$E_p(\mu) = \mu' \mathbf{A}\, \mu$$

where $\mathbf{A}=\{A_{ij},\ i,j\in \mathbf{I}_n\}$ is the matrix related to the bonding strength coefficients such that

$$A_{ij} = \begin{cases} \sum_{k\in R_i} \alpha_{ik}, & \text{if } j = i \\ -\alpha_{ij}, & \text{if } j \in R_i \\ 0 & \text{otherwise} \end{cases}$$

where R_i is the index set of neighbors of the ith pixel. Given the random noise variance Σ = diagonal$\{\sigma_i^2,\ i\in \mathbf{I}_n\}$, the posterior probability of the mean intensity conditioned on the observation process $\mathbf{X} = \mathbf{x}$ is then

$$f(\mu|\mathbf{x}) \propto \exp\left[(\mathbf{x}-\mu)'\, \Sigma^{-1}(\mathbf{x}-\mu) + \mu' \mathbf{A}\, \mu\right],$$

and the log likelihood equation is

$$\Sigma^{-1}(\mathbf{x}-\mu) - \mathbf{A}\,\mu = 0. \quad (4)$$

Equation (4) can be rewritten as

$$\mu = \mathbf{D}^{-1}\mathbf{S}\,\mu + \mathbf{D}^{-1}\Sigma^{-1}\mathbf{x} \quad (5)$$

where

$$\mathbf{D} = \left\{D_{ij},\ i,j \in \mathbf{I}_n | D_{ii} = \sigma_i^{-2} + A_{ii} \text{ and } D_{ij} = 0 \text{ for } i \neq j\right\}$$
$$\mathbf{S} = \left\{S_{ij},\ i,j \in \mathbf{I}_n | S_{ii} = 0 \text{ and } S_{ij} = A_{ij} \text{ for } i \neq j\right\}$$

Applying an iterative approach similar to the point-Jacobian iteration method [2] to (5), the mean intensity image is iteratively obtained. At the hth iteration,

$$\hat{x}_i^h = D_{ii}^{-1}\left(\sigma_i^{-2} - \sum_{j\in R_j} S_{ij}\hat{x}_j^{h-1}\right),\ \forall\, i \in \mathbf{I}_n.$$

This iteration converges to a unique solution since

$$D_{ii}^{-1}\sum_{j\in R_j} S_{ij} < 1,\ \forall\, i \in \mathbf{I}_n.$$

Unfortunately the bonding strength coefficients $\{\alpha_{rs},\ (r,s)\in \mathbf{C}\}$ are unknown in most practice. This study employs an approach of anisotropic diffusion [3] which adaptively choose the coefficients at each iteration. The coefficients are updated at every iteration as a function of the brightness gradient:

$$\alpha_{rs}^h = g\left(\left|\nabla_{rs} X_{rs}^h\right|\right) = g\left(\left|x_r^h - x_s^h\right|\right),\ \forall\, (r,s) \in \mathbf{C}\ .$$

As in [3], two functions generating different scale-spaces are considered for $g(\cdot)$:

$$g(\nabla X) = \exp\left[-\left(\left|\nabla X\right| / K\right)^2\right] \text{ and } g(\nabla X) = \frac{1}{1+\left(\left|\nabla X\right| / K\right)^2}$$

where K is a constant which determines the magnitude of discontinuities to be preserved during the smoothing process. The one privileges high-contrast discontinuities over low-contrast ones, while the other privileges wide regions over smaller ones.

SEQUENTIAL IMAGE SEGMENTATION

Let $\mathbf{J}_m = \{1,2,\cdots,m\}$ be a set of region indices associated with a partition of $\mathbf{I}_n$. The closest neighbor of region j is defined as

$$CN(j) = \min_{k\in N_j}\left\{d(j,k)\right\}$$

where N_j is the index set of neighboring regions of the jth region and $d(j,k)$ is the dissimilarity measure between region j and region k. These regions are referred to as mutually closest neighbors (MCN) iff k = CN(j) and j = CN(k). If a cutting rule is given as the merging condition for two regions, for arbitrary region j_0 that satisfies the merging condition with CN(j_0), a CN-chain is established as the sequence of regions

$j_0, j_1 = \text{CN}(j_0), j_2 = \text{CN}(j_1), \cdots, j_{k-1} = \text{MCN}(j_k)$

such that the last two regions constitute an MCN pair. The CN-chain spatial clustering algorithm [4] provides the unique optimal solution for the spatial constraint of merging if the dissimilarity measures satisfies the following condition, referred to as regional reducibility:

$$d(p\cup q, k) > d(p,q),\ k \in \left\{N_p \cup N_q\right\}$$

where p = MCN(q). Using intra-cluster sample variance which is a typical measure satisfying the reducibility, the measure of inter-cluster dissimilarity is defined as

$$d(j,k) = n_j n_k (\hat{\mu}_j - \hat{\mu}_k)^2 \Big/ (n_j + n_k)$$

where n_j and $\hat{\mu}_j$ are the number of pixels and the sample average of the jth region respectively.

All the pixels in the sample space are initially considered to be separate regions in the clustering algorithm. It results in computational complexity for sequential imagery analysis. Instead, at each iteration, the algorithm is used for the initial configuration which is modified from the segmentation map generated at the previous contiguous time step.

ADAPTIVE POLYNOMIAL PREDICTION

If the mean intensity process is only signal-dependent, the

intensity variable can be considered separately for each pixel. Given a realization sequence $\{\mu_\tau,\ \tau = \tau_0, \tau_1, \cdots, \tau_k\}$ and a weight factor for the unit time, $0 < \lambda \le 1$, the estimate of the polynomial coefficients are sequentially updated over time using the exponentially weighted least squares criterion [5]: for $k \ge p$

$$\left(\hat{a}_{t_k,0}\ \hat{a}_{t_k,1}\cdots\hat{a}_{t_k,p}\right)' = \begin{bmatrix} \phi_0(t_k) & \cdots & \phi_p(t_k) \\ \vdots & \ddots & \vdots \\ \phi_p(t_k) & \cdots & \phi_p(t_k) \end{bmatrix}^{-1} \begin{pmatrix} \varphi_0(t_k) \\ \vdots \\ \varphi_p(t_k) \end{pmatrix} \quad (6)$$

and $k \ge 0$

$$\phi_j(t_k) = \lambda^{(t_k - t_{k-1})}\phi_j(t_{k-1}) + t_k^j, \qquad j = 0,\cdots,2p$$

$$\varphi_j(t_k) = \lambda^{(t_k - t_{k-1})}\varphi_j(t_{k-1}) + t_k^j \mu_{t_k}, \quad j = 0,\cdots,p$$

where $\phi_j(t_{-1}) = \varphi_j(t_{-1}) = 0, \forall j$. Using the estimated coefficients, the mean at the present time can be predicted on the basis of the temporal trend in previous history.

DYNAMIC COMPOSITING

Image compositing is a procedure in which geographically registered data sets which are collected over a sequential period time are compared and the best value of a defined measurement is selected to represent the conditions observed during that time period. Successively observing images from the same area over time, the compositing procedure can be dynamically done by fitting observations to the adaptive polynomial functions of (6). At time t_k, the fitted value for a pixel is

$$\tilde{x}_{t_k} = \sum_{i=0}^{p} \tilde{a}_{t_k,i} t_k^i$$

where $\left(\tilde{a}_{t_k,0}\ \tilde{a}_{t_k,1}\cdots\tilde{a}_{t_k,p}\right)'$ is computed by substituting $\tilde{\phi}$ and $\tilde{\varphi}$ for ϕ and φ in (6):

$$\tilde{\phi}_j(t_k) = \tilde{\lambda}_{t_k}\phi_j(t_{k-1}) + t_k^j$$

$$\tilde{\varphi}_j(t_k) = \tilde{\lambda}_{t_k}\varphi_j(t_{k-1}) + t_k^j y_{t_k}$$

where $\tilde{\lambda}_t$ is a compositing factor and y_t is the present observation. Factor $\tilde{\lambda}_t$ indicates a tradeoff between information in the present value and temporal tendency. As a compositing technique, $\tilde{\lambda}_t$ is set to relatively a small value if data is good, while a larger $\tilde{\lambda}_t$ is used if necessary to achieve consistency with temporal trend. For a missing pixel, the predicted value from the polynomial function or the spatially-interpolated value [5] can be used for y_t. Alternatively, missing values can be estimated by using spatial compositing based on the segmentation map of the scene at previous contiguous time step under the assumption that region classes are smoothly changed over time. It is effective for large missing area.

MONITORING AND FORECASTING SYSTEM

Given an observed image as an input signal to the system, the system initially performs the dynamic compositing, and the mean image is then restored by the Bayesian estimation. Next, the restored image is segmented by the CN-chain spatial clustering algorithm and the adaptive polynomial coefficients are updated using the segmentation results. For the Bayesian estimation of the mean intensity process, the variance matrix can be adaptively estimated in the integrated system using the composite values and the restored values. Difference between the segmentation maps at contiguous time steps can be utilized to monitor changes in land use on ground.

The estimated polynomial parameters for each pixel represents a local temporal trend at the corresponding site for the mean signature related only to the target characteristics. Using these estimates, an image series with regular time interval can be generated. If a feature is shifting over time, temporal variation of the response in a image series is more rapid at the sites around its boundary. Therefore, the pixels associated with the track of the feature's boundary have relatively steeper temporal trends compared to the inner regions. The amount of temporal trend change in a pixel can be represented by gradient that is the first derivative with respective to time for the estimated polynomial function. The gradient image shows the trace of the feature movement in recent observations, thereby resulting in predicting the future track of target feature.

REFERENCES

[1] H.O.Geergii, *Canonical Gibbs Measure*, Springer-Verlag, Berlin, 1979.

[2] R.S.Varga, *Matrix Iterative Analysis*, Prentice-Hall Inc., 1962.

[3] P.Perona and J.Malik, "Scale-space and edge detection using anisotropic diffusion," *IEEE Trans. Pattern Anal. Machine Intell.*, vol. 12, pp. 629-639, 1990.

[4] S. Lee and M.M.Crawford, "Multistage unsupervised classification of spatially continuous Imagery," *Proc. IGARSS'95*, vol. 2, pp1165-1167, Firenze, Italy.

[5] S. Lee, M.M.Crawford and S. Gallegoes, "Statistical reconstruction and feature tracking of temporally irregular data sequences," *Proc. IGARSS'95*, vol. 1, pp352-354, Firenze, Italy.

Effect of Scale on the Information Content in Remote Sensing Imagery.

K.O. Niemann[1,4], D.G. Goodenough[2,3], G.J. Hay[1]

[1] Spatial Sciences Laboratory, Department of Geography, University of Victoria, Victoria B.C. Canada, V8W 3P5
[2] Pacific Forestry Centre, Natural Resources Canada, Victoria, B.C. Canada.
[3] Department of Computer Science, University of Victoria, Victoria, BC Canada, V8W 3P6
[4] Corresponding author: e-mail address: oniemann@office.geog.uvic.ca, fax: (250) 721-6216,telephone: (250) 721-7329

I. Introduction

Over the next few years a large number of satellites designed to image the earth's surface will be launched. These satellites, quite commonly, will have a large range in spatial as well as spectral resolutions. The potential for users to become overwhelmed, not only by the quantity of data, but also by the problem of multiple pixel sizes is very real. Second, individual platforms and sensors will have the ability to image at multiple resolution simultaneously. It may therefore be useful and necessary to integrate, or fuse, the images from a number of sources into a single data set.

The approach taken in this study is that high resolution data should be degraded when fused with coarser data, rather than the more common approach of "sharpening" coarser imagery. This approach is at odds with the more common attitude but conforms with the generally accepted notion that one cannot introduce detail into a generalized data set.

II. Research Questions

A number of research questions can be developed as a result of the anticipated increase in the number of sensors. These include:

- Do we need to collect data at a variety of scales or can we collect imagery at a single resolution and degrade the data set to the desired resolution?
- Can we incorporate more relevant information into a pixel which has been upscaled (degraded) than one which has been collected at coarser scales?
- Can we combine the data collected by multiresolution sensor packages, such as MODIS, into a single image?
- Is it reasonable to collect data at a certain scale/resolution for process models generated at an entirely different resolution?

III. Project Description

A project was developed to address the research questions outlined above. This project has a number of objectives. These include:

- the assessment of resampling strategies for upscaling;
- the assessment of changing information content of varying resolution remote sensing imagery;
- automated cartographic generalization coincidental with image upscaling;
- the development of expert systems to help resolve scale/resolution/application questions.

Multiresolution, multi sensor data been collected over three separate forested sites on Vancouver Island, British Columbia. These sites represent a range of oldgrowth and regeneration conditions. Two of these sites are located on the west coast near Tofino. The first site, located on Flores Island, is covered by an unmodified oldgrowth west coast temperate rain forest. The species composition is dominated by both Western Red-cedar (*Thuga plicata* Donn *ex.* D. Don in Lambert) and Yellow-cedar (*Chamaecyparis nootkatatensis* [D. Don in Lambert] Spac). The second site, centered on Tofino Creek Watershed, is substantially drier, and has a greater elevation range, extending above tree line (approximately 1000m). The species composition is dominated by cedar (both Yellow- and Western Red-cedar) with lesser quantities of Sitka Spruce (*Picea sitchensis* [Bongrad] Carriere). There is substantially less precipitation at this site so that the similarly aged trees are significantly smaller than at the Flores Island site. Also there has been a substantial amount of clearcutting and regeneration yielding a range in forest stand age classes. Both the Flores Island and the Tofino sites start at sealevel The third site is located on southeastern Vancouver Island in the Sooke Watershed. This is a substantially drier site that the previous two. As a result the predominant species is Coastal Douglas Fir (*Pseudotsuga mensiesii* [Mirbel] Franco) with

0-7803-3836-7/97/$10.00 © 1997 IEEE

minor inclusions of Western Hemlock (*Tsuga heterophylla* [Rafinesque] Sargent [T. Mertensiana (Gordon) Carriere]) and Western Red-cedar. Logging activities, as well as an active fire history over the past 50 years has resulted in a range of age classes from less than 10 years to oldgrowth greater than 160 years. The topography in this site is less rugged than the coastal sites with a relief of less than 500 metres.

The remote sensing data collected for each of these sites is itemized in Table 1. The data collected over the three sites represents three seasons of imaging. The first was 1993 when AVIRIS and MEIS data were acquired for the Sooke and Tofino sites. Landsat Thematic Mapper data from those years were also acquired. During the second season, 1994, AVIRIS data were acquired over the Flores Island site. The third season was summer 1996 when CASI data were flown over the Flores Island site.

Table 1

Flores Island
1 m. Orthophoto (pan)
2 m CASI (15 bands)
4 m KFA1000 (pan)
10 m SPOT (pan)
20 m SPOT (4 bands)
20 m AVIRIS (224 bands
30 m Landsat TM (7 bands)
50 m Landsat MSS (4 bands)
1000 m AVHRR (5 bands)
Tofino Creek
1 m. Orthophoto (pan)
4 m MEIS (8 bands)
4 m KFA1000 (pan)
10 m SPOT (pan)
20 m SPOT (4 bands)
20 m AVIRIS (224 bands
30 m Landsat TM (7 bands)
50 m Landsat MSS (4 bands)
50 m MAS (11 bands)
50 m AOCI (11 bands)
1000 m AVHRR (5 bands)
Sooke
1 m. Orthophoto (pan)
1 m MEIS (8 bands)
20 m AVIRIS (224 band)
30 m Landsat TM (7 bands)
50 m Landsat MSS (4 bands)
1000 m AVHRR (5 bands

IV. Project Components

To achieve the stated objectives, a number of different facets are being undertaken. These include:

1. Evaluation of a number of approaches to upscaling (resampling);
2. Assessment of the information transfer between images;
3. Generalization of cartographic products to reflect the varying scales.

1) Upscaling:

A number of different approaches to degrading the resolution of remotely sensed data are being assessed. These include the more traditional approaches commonly incorporated into the image processing packages: nearest neighbour, bilinear interpolation, cubic convolution and nonoverlapping averaging. In addition we are investigating the potential of using a variance based approach (4) which works on the premise that there are scene objects which are not all the same size. This is in contrast with the approach outlined by Woodcock and Strahler (6) whose assumption was that an optimal pixel size could be identified to represent for objects. This project recognizes that forest objects (including trees as well as areas with shrub and herbaceous cover and no cover at all) are represented by varying sizes, so that a representative pixel size may not be realistic.

2) Assessment

The upscaled images created by applying the various resampling methods will be assessed through the application of a number of strategies. These include global methods such as the Wald-Wolfowitz test (1, 5), a nonparametric test used to assess the degree of randomness, or the existence of spatial trends, in a sequence of numbers or pixels. This test does not address the image qualities, or give an impression of local variations within the image. Histogram moments were used to achieve this local evaluation (3) The moments are defined as:

$$\mu_n(z) = \sum_{i=1}^{L} (z_i - m)^n p(z_i),$$

where $p(z_i)$, i=1,2,3,...,L for the corresponding histogram, where L is the number of distinct histogram values, and n is the moment. The mean pixel value (m) is defined as:

$$m = \sum_{i=1}^{L} z_i p(z_i)$$

The second moment, variance, is especially important in that it relates to the contrast within the kernel. The third moment is a measure of skewness, while the fourth is the relative flatness, or kurtosis.

To investigate the degree of similarity between images of varying resolutions, the use of a Principal Component Analyses is being investigated. In the cases where the degraded images do not change substantially a high correlation between the images is encountered. Where the images have experienced a substantial degree of change there will be less redundancy.

An alternative assessment strategy will be to segment the images into individual forest objects at the highest resolution, and track the statistical characteristics of the objects with decreasing spatial resolution. This will also allow for the effective application of spectral unmixing in the image and the investigation of the statistical behaviour of the objects with changing resolutions.

The images that will be evaluated will include the resampled images as well as the images collected at similar resolutions but by different sensors. The correspondence of the images is being assessed.

A final assessment as to correspondence will be in the classification accuracy of the various images generated. The class resolution as well as classification accuracy will be investigated. The classifications will be based on and compared to the Forest Inventory and ecological land evaluation maps for the study areas.

3) Cartographic Generalization

In an effort to develop maps which are representative of the various resolutions being produced, or processes being modeled, a cartographic generalization strategy has also been implemented in ARCINFO. The intent is that thematic maps originally produced at scales of 1:20,000 will be generalized to representative scales of 1:50,000, 1:100,000, or 1:250,000. Three cartographic issues have being addressed: polygon size, class definition, and line generalization.

- Polygon size: a minimum polygon size that will be cartographically reproduced can be specified. This is operator specific but should follow standard cartographic protocol.
- Class definition: as the scale of the map changes, so does the label that can represent the cover class. Smaller scales will have a less detailed class definition.
- Line generalization: as the cartographic scale becomes smaller the number of points used to define boundaries and features become fewer as the level of detail decreases. The generalization approach adopted for this study allows for the reduction of points according to the Douglas and Poiker (2) method.

V. Conclusions

The project that has been described addresses some of the issues relevant to the successful fusion of multiscale and multi resolution data sets. The results of the study will enable the user of multiresolution data to merge these data using the most appropriate procedures possible.

VI. References

[1] Chen, R., D.L. Jupp, C.E. Woodcock, and A.N. Strahler (1993) Nonlinear estimation of scene parameters from digital images using zero-hit run-length statistics. IEEE Trans. Geosci. Remote Sens. GE-31:735-746

[2] Douglas, D. and T. Poiker (1973) Algorithms for the reduction for the number of points required to represent a digitized line or its caricature. *The Canadian Cartoigrapher*, 10:112-122.

[3] Gonzalez, R.C. and P. Wintz (1987) Digital Image Processing. Addison-Wesley publishing Company. 503pp.

[4] Hay, G.J., K.O. Niemann, and D.G. Goodenough Spatial Thresholds, Image-Objects and Upscaling: A Multi-Scale Evaluation. (Accepted and in press) Remote Sensing Environ.

[5] Marceau, D.J., P.J. Howarth, and D.J. Gratton (1994) Remote sensing and the measurement of geographical entities in a forested Environment. 1. The scale and spatial aggregation problem. Remote Sensing Environ. 49:93-104

[6] Woodcock. C.E. and A.N. Strahler (1987) The factor of scale in remote sensing. Remote Sensing Environ.21:311-332

VII. Acknowledgments

The authors wish to thank Forest Renewal British Columbia for funding support. As well, support was provided by NASA's Applied Information System Research Programme.

Multisensor Classification of Wetland Environments Using Airborne Multispectral and SAR Data

Michael R. Ricard[1], Amy L. Neuenschwander[1], Melba M. Crawford[1], and James C. Gibeaut[2]
[1]Center for Space Research, University of Texas at Austin, 3925 W. Braker Ln., Suite 200, Austin, TX 78759-5321
[2]Bureau of Economic Geology, University of Texas at Austin, Campus Mail Code: E0630, Austin, TX 78712
Ph: (512) 471-5573 Fax: (512) 471-3570 E-mail: ricard@csr.utexas.edu

Abstract - Near concurrent airborne data were acquired over the wetlands of the Bolivar Peninsula on the Texas coast by the NASA/JPL AIRSAR (June 28, 1996) and NASA/Stennis Space Center Calibrated Airborne Multispectral Scanner (CAMS) (July 3, 1996), both at 4m spatial resolution. Several approaches which utilize information from both sensors are investigated for classifying the landcover in these data sets. Differences in statistical characteristics of the data necessitate individual parametric models for observations from each sensor, so data are initially classified separately, then a final classification is obtained by combining results from the statistical models using different multisensor integration techniques. These integrated results are compared to single-sensor classification results, as well as to a multisensor classification based on artificial neural networks.

INTRODUCTION

The primary objective of classification of remotely sensed data is often to map landcover. Because different information is provided by various sensors, it can be advantageous to jointly utilize the information of the multisensor data in the classification process. In order to optimally exploit this potentially expanded information set in the classification framework, issues of sensor characteristics, differences in time of acquisition, and target/sensor dependent information content must be addressed.

Over the past several years, a significant amount of research has focused on multisource and/or multisensor classification for remote sensing applications. In [1] and [2], the authors classify multisource data consisting of digital imagery (Landsat MSS) and ancillary information (elevation, slope, and aspect data). Since these data cannot be represented by a single multivariate statistical model, the authors utilize consensus theoretic methods to combine the results of single-source statistical classifiers. In [3], the authors classify multisensor data (optical and SAR) using structured classifiers based on artificial neural networks, thus avoiding the need for modeling the statistical distribution of the data and treating each source or sensor separately.

Based on these issues, there were three objectives of this study. The first was to classify the landcover present in a wetland environment using remotely sensed data from several sensors. Part of this process involved assessing the accuracy of single-sensor classification, as well as determining the advantages and potential problems associated with the use of data from each sensor. By performing multisensor integration of single-sensor classifier outputs, it could be determined whether an improved classification was achieved, as well as whether sensor integration enabled the detection of "hard" classes, i.e. those classes which had lower probabilities of correct classification for a given sensor. The final objective was to determine, based on the data and single-sensor classifier architecture adopted, how to best integrate the multisensor data for classification of the study area.

The following sections contain descriptions of the test site, the multisensor data acquired for the project, and the methodology used to combine the information from these data sets for the purpose of multisensor classification, as well as preliminary results from analysis of the imagery.

STUDY SITE

Bolivar Peninsula is part of the low relief barrier islands of the Texas coast located at the mouth of Galveston Bay. The test site chosen for this study consists of a salt marsh located at a washover fan on southern Bolivar Peninsula.

For classification purposes, this salt marsh study area is characterized in terms of sub-environments defined by wetland maps [4]. The various landcover types present in these environments include low proximal marsh, high proximal marsh, high distal marsh, and spoil/barren flats, as well as areas consisting of water and trees. The low proximal marsh corresponds to tidal flats comprised of *spartina alterniflora* which experience frequent flooding. High proximal marsh is defined as more continuos areas of *spartina alterniflora* and *salicornia virginica* and are less frequently flooded. High distal marsh is comprised of *spartina patens, salicornia virginica, juncus roemerianus* and lies adjacent to barren sand flats. This area is flooded less frequently than proximal marshes.

MULTISENSOR DATA DESCRIPTION

Two near concurrent airborne data sets were acquired over the study site for the purpose of mapping wetland vegetation. Both 20 MHz and 40 MHz AIRSAR data were acquired by NASA/JPL on June 28, 1996 with a ground resolution of approximately 8m and 4m respectively. Additionally, Calibrated Airborne Multispectral Scanner (CAMS) was flown by NASA/Stennis Space Center on July 3, 1996 with

This work was supported in part by the NASA Topography and Surface Change Program (Grant NAG5-2954) and by the NASA National Space Grant Consortium (Grant NGT40003).

0-7803-3836-7/97/$10.00 © 1997 IEEE

approximately 4m spatial resolution. The CAMS data and the 40 MHz AIRSAR data were selected for multisensor classification due to their common coverage and comparable spatial resolution. The multisensor classification system analyzed data from three sensors: optical, thermal, and radar. The "optical sensor" consisted of the six Landsat bands of the CAMS instrument (Blue-NIR) plus a vegetation index, the thermal sensor recorded the ninth band of the CAMS data, and the NASA AIRSAR system acquired two frequency bands (C,L) of fully polarimetric radar data (six channels total).

CLASSIFICATION METHODOLOGY

An ensemble based approach was adopted for classification of the test site data. Data from each sensor were classified separately, then single-sensor classifier outputs were combined at the sensor integration stage.

Pre-Processing

During the pre-processing phase, radiometric and geometric corrections were applied to the data sets. The CAMS Optical data were corrected for bi-directional reflectance The CAMS Thermal data were empirically corrected for radiometric curvature present as a function of scan angle. The AIRSAR data was passed through a 5x5 enhanced Lee filter to reduce the effects of speckle in the imagery. Geometrically, the AIRSAR data was slant-to-ground range corrected. To enable multisensor classification, the three sensor data sets were co-registered. Finally, each sensor band was normalized to zero mean and standard deviation one for input to the classifiers.

Single-Sensor Classifier

For each sensor, the modular classifier architecture employs an expert classifier trained for each output class. The modularized class-specific expert classifiers are chosen to increase the rate of correct classification since the sensor classifier is not trained to solve the whole problem, just to identify a particular class from all the remainder [5].

A separate radial basis function (RBF) network, based on a mixture of Gaussians distribution for each sensor's class, is used to obtain an estimate of the posterior probability for each class

$$P(C_k|\mathbf{x}) = \sum_{j=1}^{M} w_{kj}\phi_j(\mathbf{x}) \qquad (1)$$

where $\phi_i(\mathbf{x})$ are the local basis functions, w_{kj} are the weights of the network, and M is the number of basis functions [6]. These class distributions are modeled as local kernel functions, in this case as mixtures of Gaussians. Based on this framework, each class-specific RBF network was trained to provide estimates of the posteriors using Moody-Darken three-phase learning.

Sensor Integration

Sensor integration techniques are investigated as ensemble approaches to combining classifiers with the goal to incorporate information from each sensor and thereby increase the performance over that achieved by single-sensor classifiers [5]. Since the classifiers utilized for this study provide estimates of the posterior probabilities for each class, information can be combined via either the sum rule or the product rule [1,7]. The sum rule, or weighted average, is based on a weighted sum of the posterior probabilities of a class for each sensor, whereas the product rule is based on a weighted product of the posterior probabilities of a class for each sensor. The weights can either be chosen to be equal for each sensor, in which case just a simple average of the posteriors is performed, or they can be chosen to represent, for instance, the reliability of a given sensor [1]. A further extension would be to weight the posteriors by the sensor's reliability for a given class, not just its overall reliability.

The final technique employed for sensor integration utilizes an artificial neural network, here an RBF network, trained on the outputs of the single-sensor classifiers.

Multisensor Classifier

For comparison to ensemble based sensor integration techniques, a multisensor classifier was tested to determine if information was lost through the single-sensor classification process. Since the data from each sensor were modeled using a mixture of Gaussians model, a classifier using an expert RBF network for each class was again used to classify the multisensor data jointly from a single input vector.

RESULTS

Single-sensor classifiers based on RBF networks and multisensor integrated classifiers based on ensemble approaches to combining classifiers were used for the classification of the CAMS Optical, CAMS Thermal, and AIRSAR data sets. These results are shown in Table 1.

Single-Sensor Classification

Each single-sensor classifier was trained, validated, and tested on separate data sets consisting of 267 ground truth points collected from each of the six classes: water (1), low proximal marsh (2), high proximal marsh (3), high distal marsh (4), spoil/barren flats (5), and trees (6).

The CAMS Optical data and AIRSAR data were both trained using expert RBFs with a total of 50 basis functions for each, while the CAMS Thermal data were trained using expert RBFs with a total of 40 basis functions for each.

Overall, CAMS Optical performed the best of three sensors, with the only difficulty coming in misclassifying 8% of the low proximal marsh as water. Given the amount of water in the low marshes, this is not surprising.

AIRSAR classified water and trees reasonably well, but had trouble separating both the high proximal marsh from the high distal marsh, as well as, separating the spoil/barren flats from the three marsh types. The similar moisture content and vegetation geometry in the high proximal marsh and high distal marshes are likely the cause of this result.

The CAMS Thermal sensor had trouble separating water and high proximal marsh, separating low proximal marsh and high distal marsh, and performed poorly for trees.

Multisensor Integration Results

A simple average and simple product of the single-sensor classifier results were computed with equal weights for each sensor, 95.2% and 94.9% overall classification rate respectively. Both performed better than the best single-sensor classifier, CAMS Optical, indicating the potential increase in performance through combining classifiers for different sensors, even with naive rules.

A weighted average and weighted product were then computed, with the weights for each sensor based on reliability factors obtained from the validation set's overall classification accuracy for each sensor. These sensor weighted results showed improvement over their equally weighted counterparts, thereby giving credence to influencing the sensor integration process based upon the reliability of a given sensor. Weights based on the reliability of a sensor for a given class were also chosen from the sensor validation set's probability of correct classification for that class. There was no significant improvement in results.

Another sensor integration technique involved using a single RBF network with 100 basis functions trained on the outputs of the single-sensor classifiers. These results were comparable overall to both sensor weighted results.

The final multisensor classification results were obtained from combining the single-sensor data prior to classification and then using them as inputs to the class-specific expert RBF classifiers. The results from this method were the best overall at 96.0%. This is because no information was lost from each of the sensors by classifying them separately.

By utilizing the multisensor data, noticeable improvements were made in the classification accuracy for high proximal marsh, high distal marsh, and trees. This is due to the added information AIRSAR and CAMS Thermal data provide about these classes when used in conjunction with CAMS Optical.

Table 1. Classification Accuracy for Test Sets

	Probability of Correct Classification Class						
Classifier	1	2	3	4	5	6	Overall
CAMS Optical	97.4	86.5	95.9	89.5	97.8	92.1	93.2
AIRSAR	94.0	72.7	68.9	72.3	53.9	82.0	74.1
CAMS Thermal	61.8	33.0	50.2	67.0	77.2	39.7	54.8
Sensor Wgt. Average	98.9	92.1	94.8	93.6	97.8	97.4	95.8
Sensor Wgt. Product	98.9	93.6	94.8	93.3	97.0	97.8	95.8
RBF Network	96.6	93.6	94.8	91.8	98.5	99.3	95.8
Joint Classifier	98.9	92.5	95.9	93.6	97.0	98.7	96.0

CONCLUSIONS

Remotely sensed data from multiple sensors were classified both on a single-sensor and multisensor basis. Of the single-sensor classifiers, the CAMS Optical performed the best for each individual class and overall. When multisensor integration was performed on single-sensor classifiers, increases in classification rates were obtained for all techniques when compared to the best single-sensor classifier, CAMS Optical. This highlights the fact that additional information can be gained by combining the results from the classification of individual sensors.

Comparing the multisensor integration techniques, sensor weighted sum and product rules performed better than their equally weighted versions, demonstrating the need for utilizing sensor reliability measures into the classification scheme. Of these sensor integrated results, in addition to the RBF network integrator, all produced comparable results.

The best overall classification rate was obtained from the joint classification of the three sensors using an RBF network based on a mixture of Gaussians distribution for each class. While the percent increase was not sizable, it shows that some information was lost in classifying each sensor separately; that by combining the three sensors into a single classifier input vector, the CAMS Thermal and AIRSAR were able to provide useful information to the classification of the CAMS Optical data set. However, in general, flexibility is lost in classification of a combined data set in terms of the potential use of statistical classification techniques in conjunction with fusion of results via neural networks.

REFERENCES

[1] J.A. Benediktsson and P.H. Swain, "Consensus Theoretic Classification Methods", *IEEE Transactions on Systems Man and Cybernetics*, vol. 22, no. 4, pp. 688-704, July/August 1992.

[2] J.A. Benediktsson, J.R. Sveinsson, and P.H. Swain, "Hybrid Consensus Theoretic Classification", In *Proceedings of International Geoscience and Remote Sensing Symposium*, vol. III, pp. 1848-1850, 1996.

[3] S.B. Serpico and F. Roli, "Classification of Multisensor Remote-Sensing Images by Structured Neural Networks", *IEEE Transactions on Geoscience and Remote Sensing*, vol. 33, no. 3, pp. 562-578, May 1995.

[4] W.A. White, T.R. Calnan, R.A. Morton, R.S. Kimble, T.G. Littleton, J.H. McGowen, H.S. Nance, and K.E. Schmedes, *Submerged Lands of Texas, Galveston-Houston Area*, Bureau of Economic Geology, University of Texas at Austin, 1985.

[5] A.J.C. Sharkey, "On Combining Artificial Neural Nets", *Connection Science*, 8(3/4), 1996.

[6] C.M. Bishop, *Neural Networks for Pattern Recognition*, Oxford: Clarendon Press, 1995.

[7] J. Kittler, M. Hatef, and R.P.W. Duin, "Combining Classifiers", In *Proceedings of International Conference on Pattern Recognition*, vol. II, pp. 897-901, 1996.

Automated Forest Inventory Update with SEIDAM

David G. Goodenough[1,4], Daniel Charlebois[2], A.S. (Pal) Bhogal[1], Stan Matwin[3], and Nigel Daley[1,4]

[1]Pacific Forestry Centre, Natural Resources Canada, Victoria, B.C
[2]Université du Québec à Hull, Hull, Québec
[3]Department of Computer Science, University of Ottawa, Ottawa, Ont..
[4]Department of Computer Science, University of Victoria, Victoria, BC, Canada
{dgoodenough, pbhogal, ndaley}@ pfc.forestry.ca
daniel_charlebois@uqah.uquebec.ca
stan@csi.uottawa.ca

ABSTRACT – As part of the Applied Information Systems Research Program sponsored by NASA, a System of Experts for Intelligent Data Management, SEIDAM, has been created. As a component of SEIDAM, a case-based reasoning system called PALERMO was developed in order to reason about the process of digital forest inventory update. SEIDAM uses a set of software agents that carry out tasks such as translate point elevation data into a digital terrain model or import polygonal information from a geographical information file into an image format or ingest remote sensing data and update meta data databases. In this paper we discuss the new agents that were created for automatic classification and the ease with which they were added to the SEIDAM environment.

INTRODUCTION

Due to the ever increasing exploitation of natural resources, it has become crucial that decision makers have a clear and concise picture of the actual state of the environment that falls within their jurisdiction. They can rely on modern database systems and geographical information systems (GIS) as a storage base for the information. In Canada, for instance, forest inventories stored in GIS are used by the provincial governments in order to issue tree farm licenses, logging permits, etc. In the province of British Columbia, forest products are one of the main economic resources. The province of British Columbia contains more than 40% of Canada's marketable timber. The main problem with electronic forest inventories is that they are seldom current to the present year and, therefore, may provide decision makers with inaccurate data.

In 1991, we began the creation of a System of Experts for Intelligent Data Management (SEIDAM) that could use remote sensing data to update existing digital forest inventories [2]. SEIDAM addresses several problems, two of which are intelligent data management and the processing of forest inventory and remote sensing information. As a component of SEIDAM, a case-based reasoning system called PALERMO (Planning And LEarning for ResOurce Management and Organization) was developed in order to reason about digital forest inventory update. SEIDAM uses a set of software agents that carry out tasks.

SEIDAM agents when activated in the proper sequence, can integrate automatically a topographic GIS file with a digital forest cover GIS file, and remote sensing imagery, such as from LANDSAT Thematic Mapper. Previously, once the integration was complete, the SEIDAM user was asked to manually digitize new clear cuts onto the digital map while using the image as a backdrop. After digitizing, SEIDAM activated another set of software agents in order to update the forest cover map given the newly digitized clear cut polygons. Since 1995, more software agents have been created. They now allow the user to use automatic classification algorithms and segmentation rather than carry out manual digitizing. The processing of these data requires expertise in several different fields: forestry engineering, database systems, GIS, remote sensing and digital image analysis. SEIDAM uses artificial intelligence technologies to perform both the management and processing of GIS and remote sensing data with a case-based reasoning system to assemble plans that can be executed to create integrated products [1,2].

SEIDAM: THE SYSTEM

SEIDAM components are shown in Figure 1. In this diagram, data are stored in repositories shown outside the gray box. These data are the raw and processed forest inventory and remote sensing data as well as metadata describing the data sources. GIS metadata are stored in accordance with the FGDC standard and image metadata are stored following our standard. Inside the box, there are seven individual components: the SEIDAM expert system, the reasoning system, the smart access software agents, the image processing software agents, the GIS software agents, the SEIDAM knowledge base and the case base. A complete description of these components and the PALERMO reasoning system can be found in [1, 2].

0-7803-3836-7/97/$10.00 © 1997

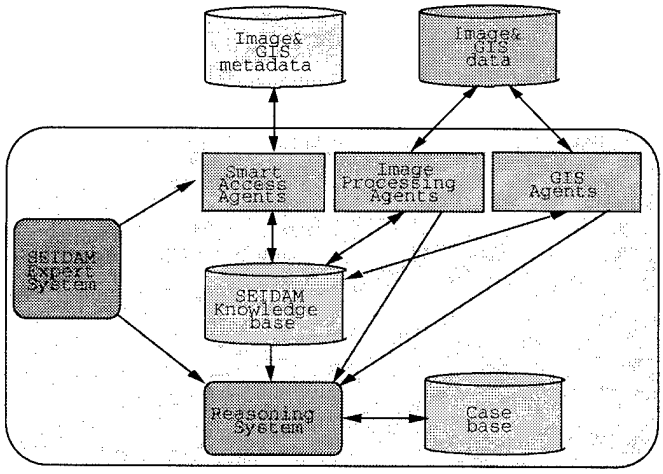

Figure 1. SEIDAM Architecture.

The Smart Access software agents utilize the user's goal statement to create SQL queries into the image and GIS metadata databases. The objective of these queries is to extract all of the information contained in the databases that is relevant to the user's goal. This information is placed in the SEIDAM knowledge base and is used by the reasoning system as its initial world. Software agents used by SEIDAM were specifically designed to work in conjunction with the problem solver. Each software agent is composed of: an expert system, a knowledge-base, a Prolog module containing a set of operators and a set of programs (software packages such as PCI image analysis or ESRI Arc/Info GIS). All of the agents were created with our training system called PAROT. This ensures that all agents are consistent with the requirements of PALERMO. The expert system component of the agent uses a set of procedural rules or sequences of steps that represent states and state transitions. A procedural rule normally fires an operator and then sets the next state according to the reaction of the program (a transition). This behaviour is a finite state machine (FSM) where each transition is deterministic.

PLANNING

Table 1 describes how the SEIDAM environment maps into the requirements of a planning system. Let us recall the definition of planning:

Given:

- an initial world described by a set of facts (object-attribute-value triplets),
- a set of planning operators that have a pre-condition list, a delete list and an add list that describe: what facts must hold for the operator to be applicable, what facts will be deleted and what facts will be added,
- a goal statement containing the facts that must hold to satisfy the user's goal.

Find:

- a partially ordered set of operators that, if successfully applied, will ensure that the goal statement is satisfied.

Table 1. Problem solving in SEIDAM

Planning	SEIDAM	Example
goal statement	product description	updated forest cover map
planning operators	SEIDAM agents	trim2dem: extracts a digital elevation model from a terrain resource information map trim2dem:: if frame_get(current_map,name,A) and frame_get(working_dir,path,B) then delete [map(A,dem_file,C)] add [trim_to_dem, map(A,dem_file,dem)]
initial world	image and GIS metadata	digital elevation model filename /dwarf/robot/data/gis/092f013/dem

In the context of SEIDAM, the initial world is described by the information contained in the metadata databases (e.g.: a digital elevation model exists in the file /dwarf/robot/data/gis/092f013/dem). Each operator in the set of planning operators describes how a software agent behaves (e.g.: the trim2dem software agent requires a terrain resource information map, TRIM, and produces a digital elevation model). The user's goal statement describes a product that would allow her to make a land use decision (e.g.: requires an updated forest cover map to determine whether or not to allow logging in a certain area; to create this product the goal would be that a forest cover file exists).

In a typical scenario for SEIDAM, a user selects a product used to make land use decisions via a graphical user interface. A product can be a digital forest cover map updated with TM imagery in order to determine change in the total area. The creation of this product becomes the goal that SEIDAM will submit to the reasoning system. SEIDAM's main expert system will then activate the smart access software agent that retrieves the relevant metadata from the remote sensing image and GIS metadata databases and stores the information in SEIDAM's knowledge-base. SEIDAM then submits the goal statement describing the product to the reasoning system. The reasoning system then creates a plan to satisfy the user's goal. If the reasoning system is successful, the plan is executed. The execution of the plan entails activating each agent in the order prescribed by the ordering constraints included in the plan. As the agents execute, they access, process and create new image and GIS data. After the successful activation of all of the agents, a product satisfying the user's goal has been created, and there is new information contained in the knowledge-base that must be stored in the metadata databases. SEIDAM will therefore activate the smart access agent to update the metadata databases.

FOREST INVENTORY UPDATE

In [2], we showed how SEIDAM creates and executes a plan that integrates forest GIS files and LANDSAT TM imagery in order to allow users to manually digitize new clear cuts. This process is completely automatic and requires user input for digitizing only. The data integration and digitizing process is:

- `copy_files_to_working_dir`: this agent will copy the TM image and GIS files from the robotic mass storage device to a working directory on disk.
- `trim_to_dlg`: this agent translates TRIM GIS data into the digital line graph standard readable by Arc/Info.
- `import_hydrology`: this agent creates an Arc/Info hydrology coverage.
- `erdascp_lakes`: this agent translates the hydrology coverage into a PCI image file.
- `sieve_lakes`: since the hydrology data contains many small lakes, a smoothing filter is used to remove any lake smaller than nine pixels or 5500 m^2.
- `lakes_to_bitmap`: convert the smoothed hydrology image into a bit map.
- `trim_to_dem`: creates a point elevation file readable by Arc/Info from TRIM data.
- `create_tin`: create a DEM from a triangulated irregular network constructed with the point elevation file and place the result in an Erdas file format for input to PCI.
- `erdascp_dem`: create a PCI image file from the Erdas DEM file.
- `copy_bitmap`: copy the hydrology bit map into the .DEM image file.
- `set_georeference_tm_large`: get geo-reference information from the TM image file and DEM image file and place it in SEIDAM's knowledge base.
- `create_tm_small`: create a small TM file that fits over the current map and copy a subset image from the original TM image file.
- `dem_to_pix_image_match`: copy DEM into small TM file.
- `set_georeference_tm_small`: add geo-reference information to small TM file.
- `tercom`: apply topographic relief to small TM file.
- `export_clear_cuts_to_pci`: export old clear cut vectors from Arc/Info to PCI.
- `digitize_clear_cuts`: allow user to digitize new clear cuts.
- `export_clear_cuts_to_arc`: export the new clear cut vectors from PCI to Arc/Info.
- `generate_products`: create any paper maps or tabular summaries of forest cover changes.

This process has been successfully applied. However, there are proven automatic classification methods, such as segmentation, that require even less user intervention. Indeed, once a segmented image has been created, the user need only select segments for clustering in order to produce a classified image. User intervention is reduced from manually digitizing cut block boundaries to pointing and clicking on clear cut segments.

The approach presented in [2, 3], shows that software agents can be trained to carry out the tasks listed in the process above. By using the same training interface, PAROT (PALERMO Agent ResOurce Trainer), it becomes a simple matter of training the system to perform cut block identification via segmentation classification. We have carried out this training and SEIDAM can now produce the a plan similar to the previous plan, but with the `digitize_clear_cuts` replaced with

```
create_gradient_image,
segment_gradient_image,
identify_cut_blocks,
cluster_image,
export_clear_cuts_to_arc,
```

Rather than performing manual digitizing, the user is now asked to assist during the classification process. The new steps are:

- `create_gradient_image`: the agent generates a gradient image using edge operators applied to six TM bands.
- `segment_gradient_image`: the gradient image is segmented and the segment boundaries overlaid on the image.
- `identify_cut_blocks`: the user identifies segments which are over new cut blocks.
- `cluster_image`: the segments are clustered and the new cut blocks are labeled.

We present an example of the automated capability within SEIDAM for forest inventory update using GIS and remotely sensed data from the primary SEIDAM test site, the Greater Victoria Watershed District (GVWD). Forest cover GIS files for the Greater Victoria Watershed District (GVWD) on Vancouver Island in southwestern British Columbia are used. The boundaries can be used as a mask to geographically constrain the remotely sensed data to the appropriate area. A LANDSAT TM image, shown in Figure 2 as bands 3 (R), 4(G), and 5(B), is fused with the GIS file.

The constrained image is segmented. Classification on this segmented image can help to ascertain certain structural units such as forest at various stages of growth, rock outcrops, and areas of forest cover change. Such a result from the segmentation process is shown in Figure 3. Structural units are clearly visible in the image as polygons. After classification, we obtain the result shown in Figure 4. In the final step of updating the polygon attribute database, the forest cover change polygons of Figure 4 are exported to the GIS data.

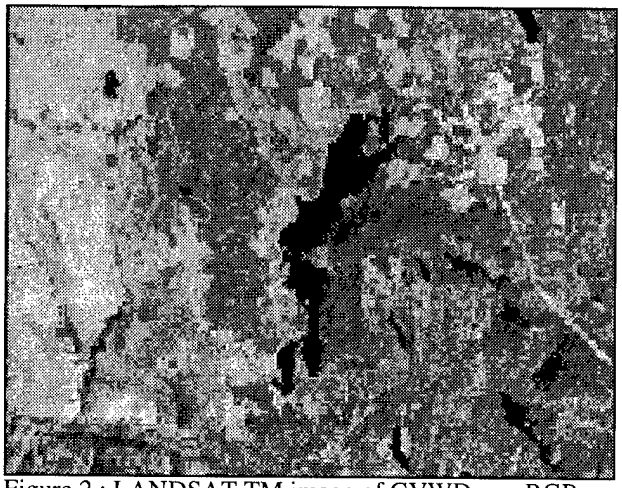

Figure 2 : LANDSAT TM image of GVWD as a RGB emulation with channels 3, 4 and 5 respectively.

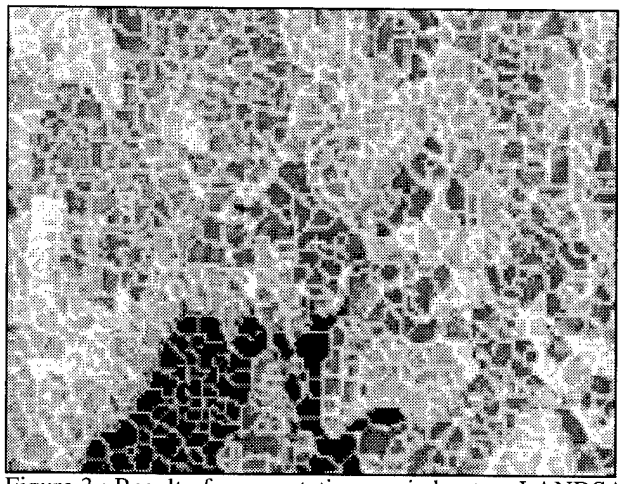

Figure 3 : Result of segmentation carried out on LANDSAT TM image of Figure 2 above. The segments are clearly visible in this result prior to classification.

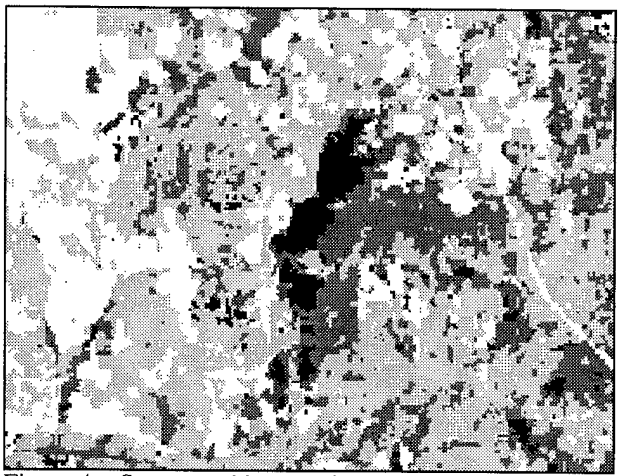

Figure 4 : Segmented image after user-assisted classification. Old growth appears as dark gray, younger vegetation areas appear as lighter shades of gray, and recent cut-blocks and rock outcrops appear as white. Water appears as black.

CONCLUSIONS

SEIDAM can now execute forest inventory update using remote sensing imagery with automated image segmentation. The updated GIS files are stored in ARC/Oracle together with metadata conforming to FGDC standards. A CD-ROM has been created containing SEIDAM software and a test data set. The next version of SEIDAM will incorporate processing threads for AVIRIS and AIRSAR. Intelligent information systems make it much easier for users to use remote sensing data in their GIS environments.

ACKNOWLEDGMENTS

We gratefully acknowledge support from Natural Resources Canada and the Natural Sciences and Engineering Research Council of Canada. We also thank our co-investigators in SEIDAM and NASA for their contributions to the project. Additional information can be found at http://www.aft.pfc.forestry.ca.

REFERENCES

[1] D. Charlebois, D. G. Goodenough, S. Matwin, A. S. P. Bhogal, and H. Barclay, "Planning and Learning in a Natural Resource Information System," presented at Canadian AI, Toronto ON Canada, 1996, pp.187-199.

[2] D. Charlebois, D. G. Goodenough, P. Bhogal, and S. Matwin, "Case-based Reasoning and Software Agents for Intelligent Forest Information Management," presented at 1996 International Geoscience and Remote Sensing Symposium IGARSS'96, Lincoln, Nebraska, USA, pp. 2302-2306, 1996.

[3] S. Matwin, D. Charlebois, and D. G. Goodenough, "Training Agents in a Complex Environment," presented at IEEE: Conference on Artificial Intelligence for Applications, Los Angeles, CA, 1995.

Modelling Soil Erosion Hazard by Using a Fuzzy Knowledge-based Approach

G. I. Metternicht
Curtin University of Technology, School of Surveying and Land Information,
GPO Box U 1987, Perth 6001, Western Australia
TE: + 618 9266 3935 - Fax: +618 9266 2703 - Email:Metternicht@cage.curtin.edu.au

Abstract -- Land degradation as the result of water erosion represents a serious environmental threat. The erosion processes are complex and depend in many factors, determined on turn by a set of characteristics. Fuzzy knowledge-based exploratory models are designed to investigate the susceptibility to erosion by incorporating expert knowledge, in the sense that information on soil properties and/or landscape elements assumed to control accelerated soil erosion are incorporated into the modelling process. Fuzzy boundaries are applied to rank the landscape factors used in modelling the likelihood of an area to be affected by different erosion degrees. Although the model provides qualitative estimations, it reveals very useful to explore indicators-causes-processes relationships. In addition, it allows to test the importance of individual landscape elements related to soil erosion, and select those suggested as best predictors.

INTRODUCTION

Many of the traditional tools for formal modelling, reasoning and computing are crisp, deterministic, and precise in character. However, in land degradation research, real situations are very often not crisp and deterministic, hence impeding precise description. In addition, certain indicators of land degradation are not measurable, or the relationship between degradation processes and indicators are not exactly known, or the analytical models to express these relations are missing. For instance, values of variables such as the abundance of rock fragments on the soil surface, or the strength of the soil structure can only be approximated or evaluated using expert's experience. A soil surveyor can describe the grade of the soil structure in terms of *weak, moderate* or *strong*. Though these data are valuable for soil degradation studies, the main question resides on how to use and processes this information.

Accordingly, this paper presents a model for land degradation hazard prediction, based on expert knowledge, which is also often not sharp, not precise, but can be formalised using fuzzy sets, fuzzy logic and exploratory models.

THE MODELLING PROCESSES

The construction of a fuzzy knowledge-based exploratory model requires determination of the model structure; formulation of the fuzzy knowledge base; selection of fuzzy knowledge processing methods; calibration and validation [4].

The model structure comprises the selection of the input and output variables, the number of sub-models and the connection between them. Knowledge formalisation in the form of a knowledge base requires definition of the rules and determination of the fuzzy sets used to describe the values of the model variables, such as *moderately*, *slightly* or *strongly*. Yet the main problem in fuzzy modelling is to find an appropriate set of linguistic rules describing the phenomenon to be modelled. They can be taken directly from the expert experience, but sometimes the expert knowledge is too complex to be expressed in a limited set of rules. Moreover, the set of linguistic rules has to be complete and provide a correct answer for every possible input values. Obviously, the formulation of these rules as well as the definition of fuzzy sets has a subjective character.

The fuzzy sets and rules and the data set are the main components of the fuzzy knowledge-based model, as illustrated in figure 1. Using membership functions and operators, the fuzzy knowledge is processed and output values corresponding to certain input values are computed. The input values can take a crisp, that is numerical, or fuzzy (ie. certainty factors) form. Linguistic terms are also allowed for the input, as could be the case of a *moderately saline class*, represented by the intersection of the fuzzy sets saline and non saline. The output values are fuzzy sets, which can be transformed into numerical values by applying a membership function, or approximated to one of the linguistic terms defined for the output variables. During the calibration process, selected parameters are adjusted to improve the model performance. Assessing the spatial coincidence between the results and the reality, in terms of areal extent, carries out final model validation.

AN EXAMPLE TO ASSESS SOIL EROSION HAZARD

A fuzzy model was designed to answer common user's question such as:

(a) What is the hazard to accelerated soil erosion in area A', located in the distal part of an alluvial fan, with a slope of about 20%, vegetation coverage less tan 30% and 50% of rock fragments on the terrain surface?

(b) What degree of erosion can be expected to occur in an area where the vegetation cover is lower than 80%?

What is the best set of soil degradation indicators to predict soil erosion hazard in a selected area?

(d) Where high erosion can be expected to occur?

The model explores cause-effect relationships on the basis of the general knowledge about causes and the specific relation between processes and indicators of water erosion. The model was designed to investigate the susceptibility of

0-7803-3836-7/97/$10.00 © 1997 IEEE

specific areas to erosion by incorporating expert knowledge, in the sense that information on soil properties and landscape elements assumed to control accelerated soil erosion could be incorporated into the modelling process. The model is therefore considered region-oriented and exploratory. Fuzzy boundaries were applied to rank the landscape factors, used in modelling the likelihood of an area to be affected by different erosion degrees. For instance, if the user observes highly eroded areas to be strongly related to slope percentage, landscape position and surface rock fragments, these landscape factors can be used to 'explore' the susceptibility to erosion hazard. The model can be formulated as a state factor equation, where

Hazard to accelerated erosion = f (Climate, A, B, C, ...n)

Where *A, B, C, ... n* represent erosion-promoting landscape elements, together with climate, a non-differentiating factor in the selected area.

The fuzzy knowledge-based model requires the expertise to decide on the following items:

- Erosion-related landscape elements
- The primary terms to represent the susceptibility to soil erosion hazard (eg. low, moderate, high)
- Type and set of parameters of the membership function. Membership functions can adopt trapezoidal, triangular or sigmoidal shapes. The function is used to compute the certainty factor of the erosion-related parameters to the fuzzy sets representing low, moderate and high hazard degrees.
- The fuzzy production rules (IF-THEN statements). They are implemented by means of fuzzy operators [6].

Soil erosion hazard was ranked in five classes, namely very low, low, moderate, high and very high. Three fuzzy sets (low, moderate and high) were determined and the qualitative labels 'very low' and 'very high' were derived by concentration of the fuzzy membership functions low and high, as described by [6], [5] and [2].

Not all the model inputs were quantitative, thus needing the use of linguistic variables such as 'very low', 'low', 'moderate', 'high'. These variables have to be mapped into a range of numbers where the user defines a series of basic parameters required to build up the membership function representing, for example, the linguistic variable 'moderate'.

The membership function

An S-shaped function, as described by [1], was used to determine the degree of membership of the selected parameters. This is a significant step because the membership degree of the selected landscape elements to the low, moderate and high erosion hazard sets depends on the correct determination of the parameters characterising the membership function, that is interval, sharpness and inflection points (figure 2).

The model was implemented in a geographic information system. Vegetation coverage, rock fragment density, abundance of whitish topsoils, reddish brown topsoils assumed to reflect the absence of erosion, landscape position and slope gradient were the landscape elements selected to map soil erosion hazard [3]. The inputs for the first four elements were proportion maps derived from the spectral unmixing of a Landsat TM data set [7], while landscape position was obtained from a geopedologic map and slope gradient computed from a digital elevation model. For each selected parameter, five intervals were derived from the membership functions as shown in figure 3. For instance, the model considers that surface rock fragments protect the soil surface against raindrop impact and water entrainment. Therefore, a surface covered by 20% of rock fragments will be more exposed to surface erosion than other having 70% of rock fragments on its surface. When applying the fuzzy operators a 'very low' erosion label is ranked as 1, while 5 characterise areas having a 'very high' susceptibility to erosion.

Knowledge-based exploratory models were build up and implemented by using IF-THEN statements. For instance, considering the following model:

Soil erosion severity = *f (vegetation coverage, surface rock fragments, landscape position),* the model would be implemented as:

> IF *the vegetation coverage is very high* AND *the surface rock fragments are moderately dense* AND *the landscape position is very low*, THEN *the soil erosion hazard is very low.*

The statement is computed using a fuzzy minimum operator. This means:

$$\mu_{soil\ erosion\ hazard}(x) = min\ [(\mu_{vegetation}(x), \mu_{surface\ rock\ fragment}(x), \mu_{landscape\ position}(x))]$$

$$\mu_{soil\ erosion\ hazard}(x) = min\ (very\ high, moderate, very\ low)$$

$$\mu_{soil\ erosion\ hazard}(x) = min\ (5,3,1) => \mu_{soil\ erosion\ hazard}(x) = 1$$

The area is mapped as prone to very low soil erosion, that is, the ground cell (x) takes the label resulting from applying a minimum operator to the selected landscape elements.

CONCLUSIONS

A fuzzy knowledge model was designed to investigate the susceptibility of specific areas to erosion by incorporating expert knowledge, in the sense that information on soil properties and landscape elements assumed to control accelerated soil erosion could be incorporated into the modelling process. Fuzzy boundaries were applied to rank the landscape factors used in modelling the likelihood of an area to be affected by different erosion degrees.

Soil erosion hazard was ranked in five classes, namely very low, low, moderate, high and very high. Three fuzzy sets (low, moderate and high) were determined and the qualitative labels 'very low' and 'very high' were derived by concentration of the fuzzy membership functions low and high.

Although the model provided only qualitative estimations, it showed very useful to explore indicators-causes-processes relationships. In addition, it allowed testing the importance

of the individual landscape elements related to soil erosion and selecting those that best predict soil erosion hazard in the area.

REFERENCES

[1] J. Dombi, 'Membership function as an evaluation'. Fuzzy sets and systems. Vol. 35, pp.1-21, 1990.

[2] B. Jiang, 'Fuzzy overlay analysis and visualisation in Geographic Information Systems. PhD thesis, Utrecht University, The Netherlands, 165 pages, 1996.

[3] G. Metternicht, 'Detecting and monitoring land degradation features and processes in the Cochabamba valleys, Bolivia. A synergistic approach'. PhD thesis, State University of Gent, 399 pages. ITC publication No.36, 1996.

[4] A. Salski, 'Fuzzy knowledge-based models in ecological research'. Ecological modelling, vol. 63, pp.103-112, 1992.

[5] K. Schmucker, 'Fuzzy sets, natural language computations and risk analysis'. Computer Science Press, 189 pages, 1982.

[6] L. Zadeh, 'Fuzzy sets'. Information and control, vol. 8, pp.338-353, 1965.

[7] G. Metternicht and A. Fermont, 'Spectral unmixing and mapping of surface features related to soil erosion', IGARSS'97, in press.

Figure 1: Information flow in the fuzzy knowledge-based model

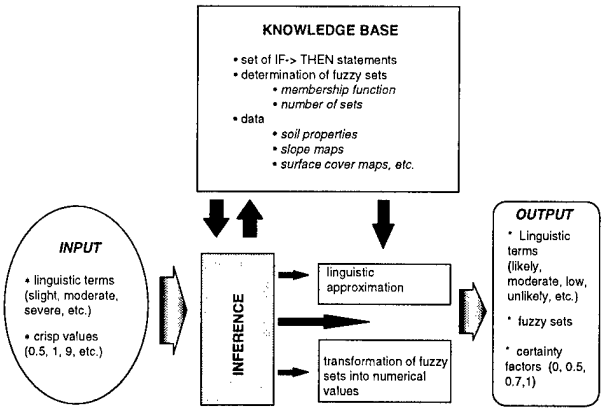

Figure 2: An S-shaped function with variations in sharpness (s) and inflection (i)

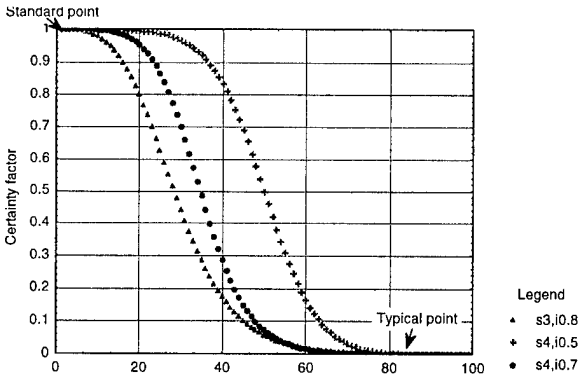

Figure 3: Flow chart of the procedure followed to develop exploratory models suitable to map soil erosion hazard

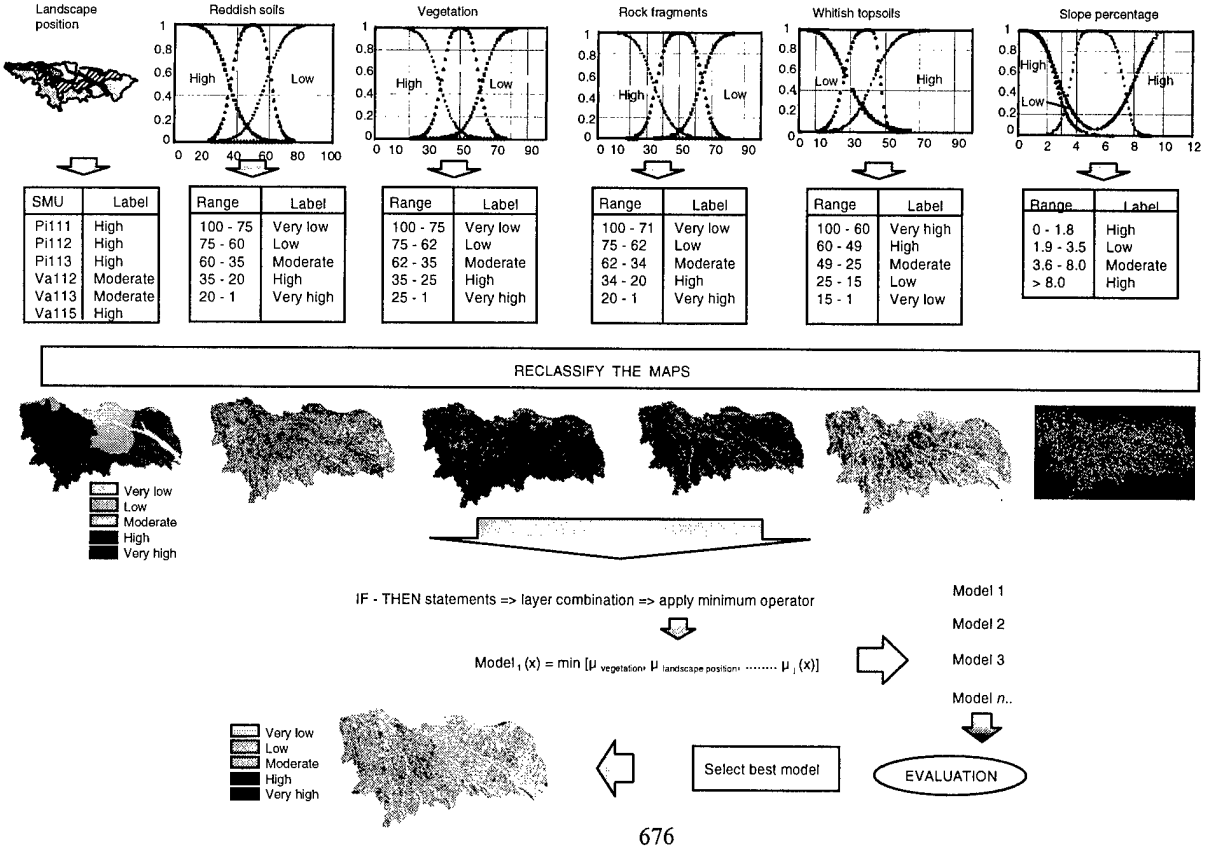

Comparing Raster and Object Generalization

Nigel Daley [1,2], David G. Goodenough [1,2], A.S. (Pal) Bhogal [1], Quetzalcoatl Bradley [2], and Z. Yin [2]

[1]Pacific Forestry Centre, 506 West Burnside Rd, Victoria, BC, Canada, V8Z 1M5
[2]University of Victoria, Dept. of Computer Science, P.O. Box 1700, Victoria, BC, Canada, V8W 2Y2
Contact: ndaley@pfc.forestry.ca, 250-363-0153, fax: 250-363-0775

Abstract – Digital interpretation of imagery produces descriptions of the earth's surface, each description relying on the inherent resolution of the original image. Forest cover geographic information (GIS) files have been produced by interpretation of aerial photography. Common mapping scales in Canada for representing land information are 1:20,000 and 1:250,000. This paper discusses two methods to automatically generalize GIS from higher spatial resolution scales to lower scales. These two methods are a raster method (MapGen) for generalization developed by Pamap and the BC Ministry of Forests, and an object-oriented method (ObjectGen). The GIS data set consists of topographic data and forest cover files, both at 1:20,000 scale and placed on the same datum. In this presentation we compare the results for generalizing forest objects by these different methods. This work leads to segmentations of remote sensing images, at corresponding resolutions to the GIS files, being used to constrain the generalizations.

INTRODUCTION

Remote sensing data is available from satellites and aircraft at multiple resolutions from 1 m to 1 km. For each application, there is a need to assess the utility of acquiring data at a wide variety of resolutions. In particular, can imagery at 1 m be used to derive digital interpretations appropriate for coarser resolutions? We chose to begin our investigation of how to generalize image objects by investigating the generalization of geographic information (GIS) files produced from interpretation of aerial photography. Our interest in this paper is in methods to automatically represent GIS information at other scales. We have implemented a raster method (MapGen) for generalization developed by Pamap and the BC Ministry of Forests (BCMOF) [1], and an object-oriented method described by Richardson [2]. The GIS data set consists of topographic data and forest cover files, both at 1:20,000 scale. In this presentation we compare the results for generalizing forest objects by these two different methods. The primary scales used for this test are 1:20,000 and 1:250,000. For remote sensing data, we will be segmenting images from the following sensors: MEIS (1 m), AVIRIS (20 m), TM (30 m), and AVHRR (1 km) for two test sites on Vancouver Island.

THE DATA SETS

Forest cover and hydrology GIS data are available for British Columbia at 1:20,000 scale. We worked with 3 mapsheets, 082E062, 082E072, and 083E073, which cover the Okanagan Mountain Park area just south of Kelowna, BC. Forest cover data came from BCMOF in IGDS/Forest Inventory Planning Data Exchange Format (FIPDEF). These data files were digitized from 1994 airphotos on the NAD27 datum. The *Projected Type ID* attribute is used by BCMOF to generalize forest cover data. Values and descriptions for this attribute can be found in table 1.

Hydrology data (lakes and rivers) came from the BC Ministry of Environment, Lands, and Parks (BCMELP) Terrain Resource Information Management (TRIM) initiative. These data were digitized from airphotos using the NAD83 datum. They were converted to NAD27 to be compatible with the forest cover data.

GENERALIZATION METHODS

Two methods of automated generalization systems were compared: raster generalization (MapGen) and object generalization (ObjectGen).

Raster Generalization

MapGen, developed by Pamap (PCI Pacific) and BCMOF, is an automated raster generalization system. It is based on a set of polygon and vector generalization rules. Each polygon rule specifies how to combine neighbouring polygons. From

Table 1. Generalized Classes & MapGen Rules

Class	Rule	Min Size	Merge List
0 Water			
1 Immature (stocking class 0)	PROJTYPEID = 1	15	3,2,4,9,5,6,8
2 Mature	PROJTYPEID = 2	15	1,3,4,9,5,6,8
3 Immature Residual	PROJTYPEID = 3	15	1,2,4,9,5,6,8
4 NSR	PROJTYPEID = 4	15	9,1,3,2,5,6,8
5 Non Commercial	PROJTYPEID = 5	15	6,4,9,1,3,2,8
6 Non Productive	PROJTYPEID = 6	15	5,4,9,1,3,2,8
8 No Typing	PROJTYPEID = 8	15	6,5,4,9,1,3,2
9 Silviculture NSR	PROJTYPEID = 9	15	4,1,3,2,5,6,8

0-7803-3836-7/97/$10.00 © 1997

table 1, a class 2 polygon (Project Type ID = 2) smaller than the minimum size will be merged with an adjacent class 1 polygon if it exists. If not, it will be merged with a class 3 polygon, and so on down the list. Vector rules specify the vector features to be displayed on the generalized map and a weeding tolerance for vector simplification. Feature attributes are stored in Oracle for fast sorting and selection.

After selecting input mapsheets and rules, MapGen appends and converts the IGDS files into Pamap GIS files and the FIPDEF attribute files into Oracle tables. Forest cover polygons are then converted from a vector representation to a raster representation, merged according to the polygon rules, and then re-vectorized. Vectors layers, such as rivers, are simplified using the weeding tolerance with the Douglas-Poiker Algorithm [1]. The result is a Pamap GIS file with a layer for generalized forest cover polygons and layers for each vector generalization layer.

Object Generalization

ObjectGen [3] is a modified implementation of the automated spatial and thematic generalization method outlined in [2] and [4]. ObjectGen uses an object class hierarchy to partition features into hierarchies of objects, classes and superclasses. In our implementation the forest cover superclass was divided into the 8 classes shown in table 1 and the hydrology superclass was divided into rivers and lakes. Objects of these classes were individual forest cover polygons, river segments, or lakes.

This data structure supports generalization at the superclass, class, or object levels by ordering the objects according to common superclass, class, or object attributes and applying a removal threshold. Richardson [2] calls this threshold the necessity factor and calculates it based on a matrix of map theme, target generalization scale, map object requirement (MOR) and map object functionality (MOF). MOF defines an object's usefulness in supporting and assisting in map reading and use. For example, map objects such as rivers, roads, and boundaries assist users in reading a map because they provide the reader with a sense of orientation, among other things. MOR defines the degree of need for an object class to appear on a map at a particular scale.

These two measures, ranging from 0 to 100, are quantification's of a map object's usefulness and necessity and are specific to each map theme. They are mathematically combined together to form the necessity factor (NF) which is applied to the data as a threshold, above which features are dynamically selected.

Our implementation [3] is a two phase process: data preparation and feature selection. Phase one has three steps: lakelines are automatically generated for lakes that have one inflowing and outflowing stream and manually digitized for the rest; Strahler stream orders [5] are calculated for the river network and lakelines; object attributes are transferred to Oracle. Phase two has four steps: necessity factors for each class are calculated based on MOF and MOR tables; forest cover is generalized at its superclass level; hydrology is generalized at its object level; the resulting generalization is viewed in ArcView. Phase two can be run repeatedly with attenuation factors applied to the necessity factor calculations. In forest cover superclass generalization the class partitions are ignored and objects are ordered by area, smallest to largest. The mean necessity factor, calculated as the mean of the 8 class necessity factors, is taken as the percentage of polygons to be generalized starting at the smallest.

In hydrology object generalization, each object is ordered in its class, and its necessity factor is applied to that class' objects only. Rivers are ordered first by stream order then by length. Lakes are ordered by area. If a lake is removed it is automatically replaced by its lakeline.

RESULTS

The 8 classes are an aggregation of original polygons which contained descriptions of forest species, volume, site index, height, and so forth. These classes correspond to the standard followed by BCMOF for representation of forest cover at 1:250,000 scale. Our initial hypothesis was that object generalization would yield more accurate results than raster generalization. The results of the generalization are shown in table 2. The table lists the classes, the original area of the classes at 1:20,000 scale in hectares, the percentages of the original area by class, and the percentages of the original area by class for MapGen and ObjectGen after generalization to 1:250,000 scale. No significant difference in areas as a function of generalization method was seen. The 1:20,000 scale maps contained 520 polygons corresponding to the 8 classes. MapGen reduced this number to 160 polygons and ObjectGen reduced this number to 150 polygons. The loss of 370 polygons did not impair the visual result of the generalization as shown in Figure 1.

Table 2. Percentage Areas by Class and Generalization

	Class	Original (ha)	Map Gen	Original	Object Gen
0	Water	10,263	21.4%	21.3%	21.3%
1	Immature 0	11,333	24.8%	23.5%	24.1%
2	Mature	13,366	27.6%	27.8%	27.8%
3	Immature R	454	0.9%	0.9%	0.9%
4	NSR	1,494	2.9%	3.1%	2.9%
5	Non Comm	132	0.0%	0.3%	0.2%
6	Non Prod	10,910	22.0%	22.7%	22.3%
9	Silvi NSR	182	0.4%	0.4%	0.4%
Subtotal		**48,132**	**100%**	**100%**	**100%**
Number of polygons			**160**	**520**	**150**

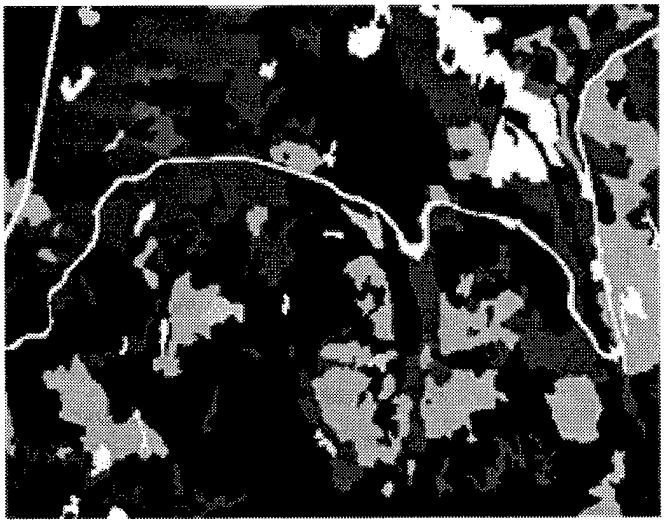

Figure 1a. Portion of 1:20,000 scale original forest cover data covering an area 8 km by 6 km.

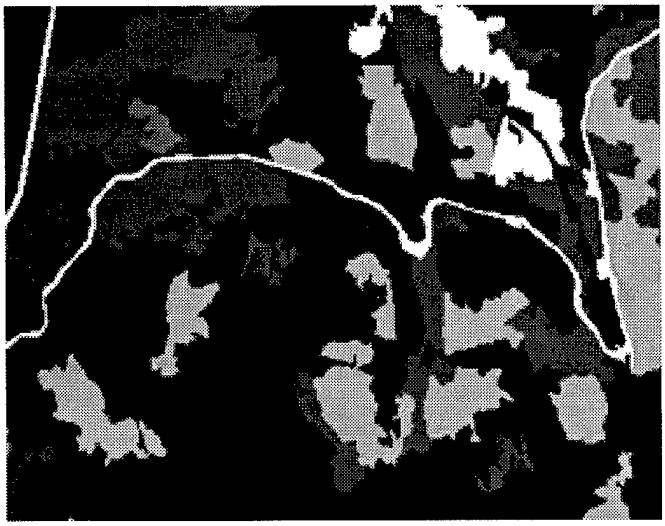

Figure 1b. 1:250,000 scale MapGen generalization of Fig 1a.

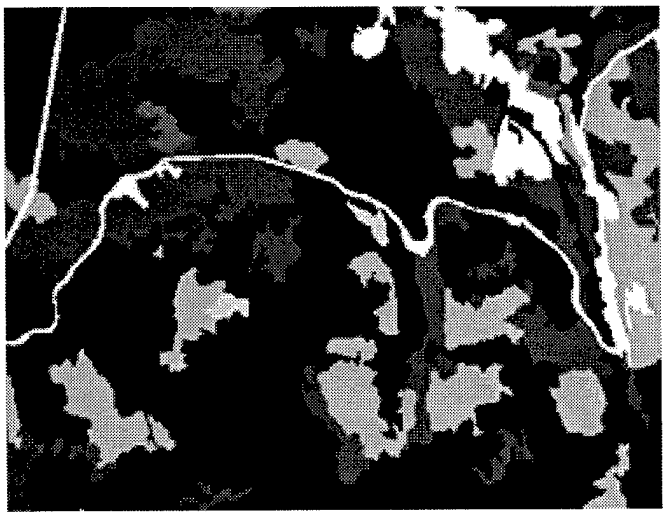

Figure 1c. 1:250,000 scale ObjectGen generalization of Fig 1a.

CONCLUSIONS

Two methods of generalization were implemented, a raster generalization (MapGen) and an object generalization (ObjectGen). These methods were applied to three forest cover maps to create broad classes. There were no significant differences in class areas between the two generalizations and the original areas. Reductions in the original number of polygons of over 72% were achieved without significant errors in class areas. We are now investigating segmentation of remote sensing imagery, conversion of segments to labeled objects, and generalization of these objects.

ACKNOWLEDGMENTS

This research was supported by the Natural Sciences and Engineering Research Council (NSERC) of Canada under grant OGP0184109, and by the Pacific Forestry Centre, Natural Resources Canada. We thank the Resources Inventory Branch of BCMOF and the Geographic Data BC Branch of BCMELP for their ongoing support.

REFERENCES

[1] Pamap Technologies Corporation, "Map Generalization User Guide," PCI Pacific, Victoria, BC, Canada May 1994.

[2] D. E. Richardson, "Automated Spatial and Thematic Generalization Using a Context Transformation Model," Ph.D. thesis, University of Wageningen, Wageningen, The Netherlands, 1993.

[3] N. M. A. Daley and Q. Bradley, "Automated Spatial and Thematic Generalization: an implementation," University of Victoria, Victoria. BC, Canada http://www.aft.pfc.forestry.ca/ndaley/objgen/index.html, April 18 1997.

[4] D. E. Richardson, "Rule Based Generalization for Base Map Production," M.Sc. thesis, International Institute for Aerospace Survey and Earth Sciences, Enschede, The Netherlands, 1988.

[5] A. N. Strahler, "Quantitative Geomorphology of Drainage Basins and Channel Networks," in *Handbook of Applied Hydrology*, V. T. Chow, Ed., 1964.

Expert maps: an alternative for integrating expert knowledge in satellite imagery classification

‡ Manuel L. Campagnolo [1] and Mario Caetano[2]
[1] Dep. of Mathematics, I.S.A. , Lisbon University of Technology
Tapada da Ajuda 1399 Lisboa Codex, Portugal.
Tel: 351 1 3638161; Fax: 351 1 3630723; e-mail: mcampagnolo@isa.utl.pt
[2] National Center for Geographic Information (CNIG)
Rua Braamcamp, 82, 1 dto., 1200 Lisboa, Portugal.
Tel: 351 1 3860011; Fax: 351 1 386287; e-mail: mario@helios.cnig.pt

Abstract: A new classification method which permits the integration of expert knowledge in satellite image classification is presented. This approach differs from other knowledge based ones for the following reasons: 1) it is a low-cost procedure; 2) it allows that the available experts explicitly express all their knowledge on the area to be classified, and 3) it does not have to face the problem of rule generalization over the whole area. The method is applied to a real image data set and it is shown that the achieved classification is more accurate than the classification just based on spectral data.

INTRODUCTION

The use of expert knowledge has been widely used in the last decade for improving the accuracy of remote sensing derived land cover maps (see [6], [1]). The knowledge has been represented as a set of evidential rules which encompasses classes and surface attributes at a pixel level and also, in more recent studies, at a spatial context level. Knowledge based methods are usually used to improve, *via* Bayesian [4] or Dempster-Sheffer [5] evidences combination, land cover maps generated from spectral data.

However, the proposed approaches for expert knowledge integration have performed worse than expected when applied to complex rural landscapes. We believe that this is related to two intrinsic features of the approaches that have been proposed: (1) it is assumed that the rules are valid within the whole study area, and (2) it is assumed that the expert is able to translate his knowledge into a rule format. As a consequence, relevant knowledge which does not verify the above assumptions cannot be inserted in the knowledge base. For exemple, if an expert states that "if the altitude is greater than 600 meters there is no eucalyptus forest" it is assumed that this is true in the whole area to be classified. As a consequence the expert will not take the risk of stating that the threshold is, instead, 500 meters even if this last value seems more likely to him, because this last statement could not be always true. He could, as an alternative, establish a probability distribution instead of a simple threshold but then there will arise two related problems. Even if the expert is familiar with the concept of probability distribution it will be difficult (and boring) for him to define that distribution. If he his not familiar with that concept it will be almost impossible to him to define it without the help of another expert in data analysis. Furthermore, the rules like the previous one are very hard to gather from experts, specially in the case where experts haven't any kind of mathematical background. For instance, in land cover mapping from satellite imagery in rural landscapes, the useful experts are, in general, forestry an agricultural agents which have o good knowledge of the area but who are not able to express it in rule format.

METHODOLOGY

Expert Maps

To overcome the limitations mentioned above we propose a new methodology for the integration of expert knowledge. Our goal is to extend the ability of the classification process to gather relevant expert knowledge.

To obtain the additional input needed in this methodology, people acquainted with the study area are asked to spatially locate known land uses on a satellite image color composite. This map is obtained from the satellite imagery and can be completed with non spectral data like roads and rivers networks if available. These maps, which are given to experts of the study area, will be used as the frame for the encapsulation of their knowledge. The expert is asked to draw on that map the borders of the areas that he thinks that correspond to a particular land cover class in the field.

We designate this kind of knowledge representation by *experts maps*. For integration with satellite imagery, expert maps are digitized into a Geographic Information System. The classification procedure that we propose has the following steps: (1) calculate from the expert maps and for each pixel a likelihood for each class; (2) calculate, for each pixel, the expert maps entropy, to evaluate the disparity among them; (3) integrate the likelihood for each class, calculated in step one, with spectral and ancillary data in a pixel-level classification procedure.

Formal Statement of the Method

Suppose we know that there m different land cover classes $w_1, \ldots, w_m$ in the area to be classified and we dispose of a random sample of classified pixels $(x_1,\ldots,x_N)$. Each x_i represents a vector of spectral values of the i-th pixel, $x_i=(x_{i1},\ldots,x_{ip})$, for p dimensional data. If we use a minimum Bayes risk classifier we will obtain, under certain hypoteses (see [2] or [3] for details), for each pixel i, a vector of probabilities of belonging to the different classes $(p_1,\ldots,p_m)$, where $p_k=P(w_k/x_i)$. In hard classification approaches the pixel is then allocated to a unique class: the one for which the probability value is larger, that is, x is allocated to w_k if $p_k \geq p_j$, for all j in $\{1,\ldots,m\}$.

‡ This work was partially suported by ISA/DGOT/JNICT contract 28/94.

0-7803-3836-7/97/$10.00 © 1997 IEEE

In our approach we dispose, also, of one other probability value that a pixel belong to a class. If l of the total number of experts, that we will denote by t, have labeled a particular pixel (note that each expert don't have to cover the whole area) we can estimate the experts' probability q_k of that pixel belongs to class w_k. It will be the number of experts that indicated the class w_k over l.

Furthermore, there can be discrepancies among experts. We will assume that the experts' information is more reliable when a large number of experts indicate the same class. This will be measured by an entropy measure. This measure was originally proposed by Shannon in 1949 in the context of a general theory of communication. The entropy for a probability vector (for a given pixel) is defined by

$$E = -\sum_{k=1}^{m} q_k \log_2 q_k, \text{ with } q_k \log q_k = 0 \text{ if } q_k=0.$$

The entropy takes it maximum value (maximum uncertainty on the pixel's allocation), 1, when all the probabilities are $1/m$ and takes its minimum value (maximum certainty), 0, when one of the p_k is 1 and the others are 0. We will consider, in fact, a modified formula for the entropy:

$$E' = E + q' \log q' \qquad (1).$$

In (1) the additional term q' denotes the proportion of experts that do not indicate any class for the pixel. If we didn't consider this additional term, a pixel for which just one expert (of, say, six experts) indicate a class could have a much smaller entropy, E=0, than another pixel for which, for instance, five experts agree and one disagrees, E=0.65. Using the modified entropy we would get E'=0.43 for the first case and E'=0.65 as before for the second case. Note that usually the entropy is calculated for a fixed number of information items. Here we have a variable number: the number of experts that indicate one of the classes for a given pixel.

Finally we have to integrate spectral evidence (x) with experts' evidence (e) on the pixel allocation. We will use a rather empirical approach for that purpose: the probability of belonging to a certain class will be the geometrical mean, weighted by the entropy, between $P(w_k/x)$ and q_k. Formally, and representing q_k by $P(w_k/e)$,

$$P(w_k/x,e) = P(w_k/x)^{(1-E')} P(w_k/e)^{E'} \qquad (2).$$

REAL DATA APPLICATION

Study Area

The proposed method is tested in the Monsanto area, near Lisbon, Portugal, with SPOT-XS data from the summer of 1990. We have only considered four classes: water, urban areas, forested areas and agricultural areas. We asked five experts to draw experts maps on a color composite of the SPOT imagery on which we had superimposed the roads network. It is a small area of 2580 meters by 1940 meters covered by 12513 pixels. We used a random sample of 500 pixels (approximately 4% of the total) for the training of the classifier. We knew exactly the land cover map from the photo-interpretation of aerial photographs of the same year. That map is shown in Fig. 1.

Fig 1. Land cover map (black: water; light gray: urban; dark gray: forest; white: agriculture).

Results

From the exploratory analysis of the distribution of pixels in the three dimensional spectral space we realized that the data could be considered to fit the hypotheses of quadratic discriminant rule (QDR): multinormal distribution and unequal variance-covariance matrixes for the four classes. That classifier was trained with the 500 pixels sample and achieved the classification shown in Fig. 2. The confusion matrix is shown in Table 1. The percentage numbers in Table 1. are the classes accuracies for the user (last column) and for the producer (last row). Note that the confusion matrix is build over the totality of the pixels and not over a test sample.

The global accuracy is then 79.83% for QDR. The class for which the precision is lower is the agriculture because the spectral signatures of the individuals of that class are close to the ones of the urban class. Since this last class has a more spread distribution and a larger a priori probability the classifier tends to allocate the agriculture pixels to it.

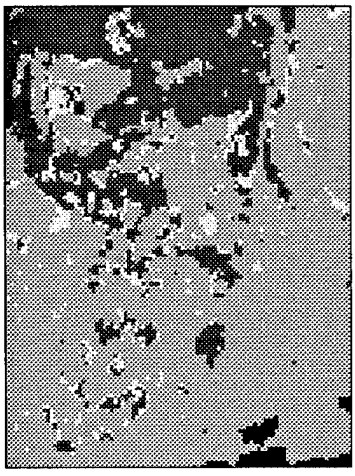

Fig. 2. Land cover map from QDR classifier (black: water; light gray: urban; dark gray: forest; white: agriculture).

Table 1. Confusion matrix for the QDR classifier.

Number of pixels		real classes				
		agric.	water	forest	urban	
predicted classes	agric.	208	0	294	361	863 (24%)
	water	0	140	0	65	205 (68.2%)
	forest	319	1	2337	269	2926 (79.8%)
	urban	820	35	359	7305	8519 (85.7%)
		1347 (15.5%)	176 (79.5%)	2990 (78.2%)	8000 (91.3%)	12513

The five experts didn't cover the whole study area. In Fig. 3 we show the number of experts (from 0 to 5) who indicated a class. Note that approximately one quarter of the whole area wasn't covered by any expert. In that area the classification hasn't be revised and the final classification has been exactly the same that the one achieved by QDR.

The expert maps were digitized and the expert probability for each pixel and each class was estimated. Then, we calculated the modified entropy using equation (1) and the revised probabilities using equation (2). Finally, each pixel was reallocated to the class for which the revised probability was larger. The resulting map is shown in Fig. 4. The final confusion matrix is shown in Table 2.

Table 2. Confusion matrix for the classification after integrating spectral and experts' evidence.

Number of pixels		real classes				
		agric.	water	forest	urban	
predicted classes	agric.	807	0	61	319	1187 (67.9%)
	water	0	153	0	74	227 (67.4%)
	forest	404	6	2744	473	3627 (75.6%)
	urban	136	17	185	7134	7472 (95.5%)
		1347 (60%)	176 (87%)	2990 (91.7%)	8000 (89.1%)	12513

The global accuracy is 86.6%. Note that a large improvement was reached both for the user's and producer's accuracies of the agriculture class.

CONCLUSION

Although the expert maps do not cover the entire study area, we have shown that (a) in the area covered by the expert maps, our method is an efficient way for solving several types of class assignment ambiguities, and (b) in the remaining area, the expert maps unavailability does not impede that the classification procedure run with the available information. In this particular experiment, the classification accuracy increased for all classes, reaching increasing values as high as 44% for the agriculture class.

This study shows that it is possible to make use of knowledge that hasn't been used in former knowledge based approaches. In fact, the information contained in the expert maps not only is useful, at a pixel level, to correct some misclassifications but contains, also, a relevant spatial component very important in image analysis. As it can be seen comparing Fig. 2 and Fig. 4, the final land cover map (Fig. 4) is spatially more homogeneous although we used a pixel level classification procedure.

Fig. 3. Number of experts (black:0,...,white:5).

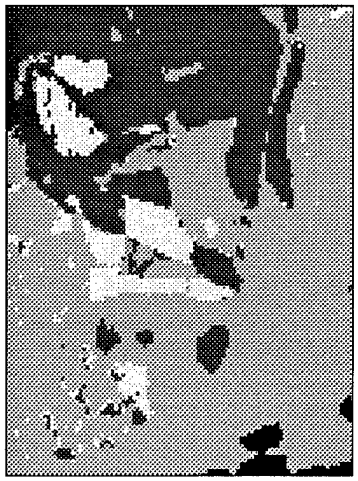

Fig. 4. Land cover map after integration of spectral and experts' evidence (black: water; light gray: urban; dark gray: forest; white: agriculture).

ACKNOWLEDGMENTS

We would like to thank I. Faria, J. Casquilho, J. Cadima, F. Valente, I. Martins and J. Martins for their expertise.

REFERENCES

[1] Bolstad, P.V. and Lillesand, T.M. "Rule-based classification models: flexible integration of satellite imagery and thematic spatial data", Photog. Eng. and Remote Sensing, vol. 58, No. 7, pp. 965-971, July 1992.

[2] McLachlan, G.J., Discriminant Analysis and Statistical Pattern Recognition, Wiley, 1992.

[3] Schalkoff, R., Pattern Recognition, Wiley, 1992.

[4] Skidmore, A.K., "An expert system classifies eucalypt forest types using thematic mapper data and a digital terrain model", Photog. Eng. and Remote Sensing, vol. 55, No. 10, pp. 1449-1464, October 1989.

[5] Srinivasan, A. and Richards, J.A., "Knowledge-based techniques for multi-source classification", Int. J. Remote Sensing, vol 11, No. 3, pp. 505-525, 1990.

[6] Wilkinson, G. "Reasoning with geographic knowledge in satellite image understanding", in New Tools for Spatial Analysis, Office for Official Publications of the European Communities, 1994.

Infusion of Altimeter Data to Same Spatial, Temporal Resolution Infrared Images to Improve the Accuracy of the Classification of Images and DEM

Liu Zhen Li Shukai

Institute of Remote Sensing Applications, Chinese Academy of Sciences
PBX 9718, Beijing 100101, PRC. Tel:+86-10-6491-9232 Email:sfdirsa@public3.bta.net.cn

ABSRTACT—Topographic effect and radiation effect are two key elements which affect the accuracy of classification of the remote sensing image. Topographical Normalization is a valuable tool by use of DEM. Because the time, when image is acquired, differs from that of DEM, new error was induced in the procedure of topographical normalization. It is obvious that the accuracy of classification of image and DEM can be improved by use of the same spatial temporal and spatial resolution image and DEM. The DEM help radiation correction, on the other hand, the image provide some information on earth objects to restore DEM. A new system was developed, which can provide high accurate DEM and remote sensing image synchronically. A series of research were conducted by use the same spatial and temporal resolution image and DEM.

INTRODUCTION

The system, which integrates differential GPS receiver, INS, Scanning Laser Ranger and Infrared Sensor, is loaded on a specially developed platform. The optical axis of IS and that of SLR are coupled in the same optical axis, so every SLR point fit in a pixel of inferred image accurately. The integrated INS and GPS system can provide high accurate position and attitude parameters of the platform. DEM is generated form INS, GPS and SLR data. Because SLR point fit in a pixel of inferred image accurately, every DEM data have a corresponding image pixel. These points have the same function as the GCPs. It is easy to correct the error of images. On the other hand, generating DEM need some information of earth surface, which can be drawn from images. It is useful to restore more accurate DEM and correct some error in DEM generated. Obviously, the system has many advantages than the old method can, because the error induced by different spatial and temporal resolution is got rid of.

PRINCIPLE OF THE SYSTEM

G, P is one point in space and ground respectively. If the coordinates $G(Xg,Yg,Zg)$ are given, and the vector $\overline{GP}$ from G to P are given, then the coordinates of P can be obtained. The parameters of optical center are drawn from GPS data, INS provide three angle of the vector: sidespin α, angle of pitch ω and angle of yaw κ。 SLR records the length of the vector: the range S is G to P.

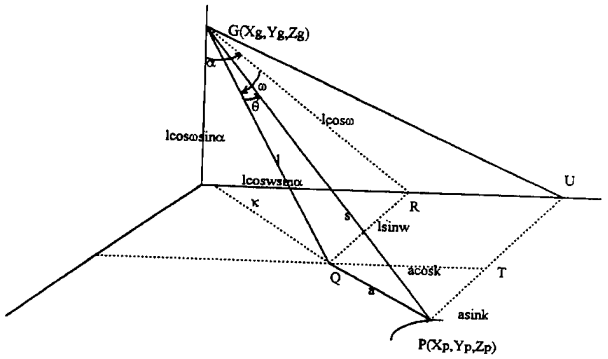

Figure 1 Principle of the System

$$\begin{cases} Xp = Xg + (S\cos\theta - \dfrac{S\sin\theta}{\sqrt{1-b^2}})\cos\omega\sin\alpha + \dfrac{S\sin\theta}{\sqrt{1-b^2}}\cos\kappa \\ Yp = Yg + (S\cos\theta - \dfrac{S\sin\theta}{\sqrt{1-b^2}}\,b)\sin\omega + \dfrac{S\sin\theta}{\sqrt{1-b^2}}\sin\kappa \\ Zp = Zg(S\cos\theta - \dfrac{S\sin\theta}{\sqrt{1-b^2}}\,b)\cos\omega\cos\alpha \end{cases} \quad (1)^{[1]}$$

Where θ is the angle between scanning line and vertical line.

The DEM can be obtained after interpolation and resample. All information, such as slope degree and relative height, can be calculated.

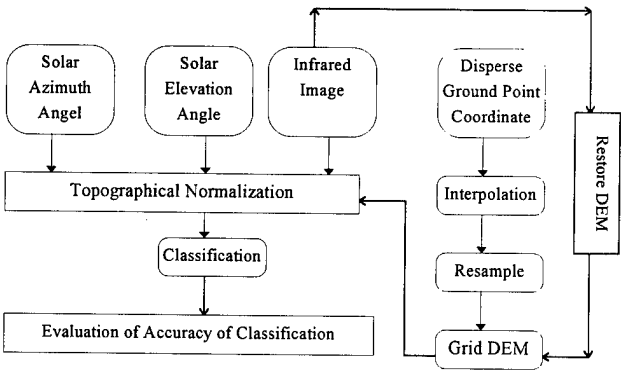

Figure 1 Conception of Model

CONCLUSION AND DISCUSSION

0-7803-3836-7/97/$10.00 © 1997 IEEE

CONCLUSION AND DISCUSSION

Test Site: Datangshan test site locate at Changping County, Beijing, north edge of North China plain, 116°18'45"–116°22'30"E , 40°10'40"–40°12'30"N. It cover 25 km. There is a hill which is 120 meter high in test site.

Picture 1 is the original image, picture 2 is the classification of the original image. Picture3 is the result of classification after normalization by use of DEM, which has different temporal resolution from the original images. Picture 4 is the result of classification by use of same spatial and temporal resolution images and DEM. The picture 4 has better accuracy of classification than picture2 and picture 3 have.

There are a lot of research to be conducted:

- Draw earth information from image to aid restore DEM automatically.
- Develop new algorithm for the data process to improve the effect of topographical normalization.

ACKNOWLEDGEMENTS

We thanks all people conduct different research in the project, they are Prof. Xue Yongqi, Prof. Guo Huadong, Prof. Qian Yuhua, Mr. Liu Tong, Mr. You Hongjian, Dr. Jiang Yuesong, Mr. Chen Jiping, Mr. Shen Zaixun, Miss Ma Jingzhi, Mr. Jin Dondhua, Mr. Su Rong, Dr. Shao Hui, Mr. Liu Jianmin.

Pic1 Original Image

Pic2 Classification of Original Image

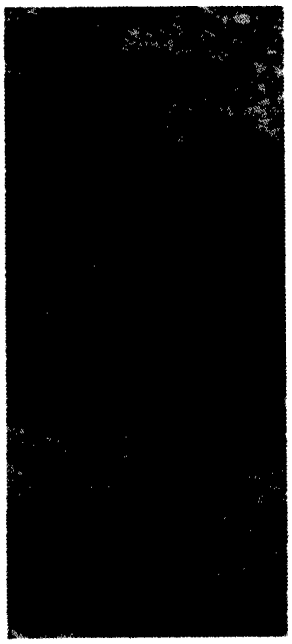

Pic3 Classification of after Normalization, Different Resolution

Pic3 Classification of after Normalization Same Resolution

NASA'S Mission to Planet Earth Invests in the Future Through a Broad National Education Program

Dr. Nahid Khazenie
NASA-Goddard Space Flight Center
Mission To Planet Earth Program Office
Code 170
Greenbelt, MD 20771
Phone: 703-917-8655
Fax : 703-917-8656
khazenie@istbsun.gsfc.nasa.gov

Stephanie Stockman
NASA-Goddard Space Flight Center
Mission To Planet Earth Program Office
Code 921
Greenbelt, MD 20771
stockman@core2.gsfc.nasa.gov
301-286-3181
301-286-1616 FAX

Abstract -- NASA's Mission to Planet Earth Program (MTPE) is a long-term research program to examine the global effects of human-induced and natural influences on the Earth's interacting physical, biological, and chemical systems. MTPE's Earth Observing System (EOS) is a comprehensive system which consists of a set of Earth-observing instruments on spacecraft and in situ to collect the data needed for the research, and a data and information system to process, store, distribute, and make accessible the acquired instrument data.

While the most significant and visible goal of MTPE is increased scientific understanding, education, in its broadest form, has become an extremely important part of the program, and is embedded in our goals and success criteria. One goal of the MTPE program is to "foster the development of an informed and environmentally aware public." Within this context, contributions by MTPE to the advancement of formal education are a major aspect of how the success of the program will be measured.

The MTPE educational programs and resources are designed with the following objectives: 1) train next generation of scientists to use an interdisciplinary, Earth system science approach; 2) continue to educate and train educators as research evolves and capabilities change; 3) raise awareness of policy makers and citizens to enable prudent policy determination regarding global change; 4) improve science and math literacy; 5) improve interface between educators and scientists; 6) explore mechanisms to leverage the development of materials; and 7) educate the populace to be better caretakers of Earth for future generations.

As a response to the above objectives several key national educational programs have been identified and implemented. These include: 1) Teacher Preparation Programs; 2) Curriculum Support Materials Development; 3) Systemic Change - US Global Change Education Workshops; and 4) Global Learning and Observations to Benefit the Environment (GLOBE).

INTRODUCTION

MTPE's formal education efforts have sought to reach the education community at all levels, from K-12 to colleges and universities. MTPE supported faculy and teacher enhancement programs include insevice and preservice teacher initiatives as well as college and university faculty and teaching assistant enhancement programs. Earth System Science curriculum support materials have been developed using the National Science Standards as a framework to guide the development of lessons and activities. These materials are disseiminated via NASA's Educators Resoursce Networks, through the Internet via NASA's Space Link, through NASA CORE and via inservice and preservice teacher workshops. Systemic change initiatives have targeted both undergraduate curricullum reform and K-12 reform through state systemic iniatives. At the K-12 level, GLOBE has involved thousands of schools throughtout the world in the Earth System Science research in colloboration with scientists.

FACULY AND TEACHER ENHANCEMENT PROGRAMS

Teacher enhancement activities are the primary focal point of the MTPE strategy. By reaching teachers, as opposed to individual students, the multiplier effect occurs. In times of increased demands for information and declining budgets, it is essential to leverage the impact that teachers and curriculum

developers make on the formal education system. Therefore, an increased emphasis on "training the trainers" has developed within the MTPE Education Program. Pre-service teacher training provides an opportunity for Earth system science to be introduced as part of a teacher's degree program or certification. This increases the opportunity for future teachers to incorporate Earth system science into their integrated curricula.

Inservice Teacher Enhancement Through Distance Learning

The NASA Classroom of the Future at Wheeling Jesuit University has nearly completed its first version of the online middle school teachers earth systems science course. This 16 week course engages groups of teachers in online discussions concerning the impact of major earth events. Events, such as volcanoes or hurricanes are explored in a systems context. Teachers conduct individual research, contribute to group discussions, and collect, post and share earth systems science resources. Most importantly, participants come away with increased knowledge concerning the complexity of the earth and its processes. An additional benefit comes through the sharing and testing of classroom applications.

The course will be offered online during fall 1997 through the University of Idaho. The COTF is also designing an online K-4 teachers earth systems science course. The first offering of this course will be in January 1998.

Preservice Teacher and College Faculy Enhancement

Project NOVA has been created to develop and disseminate a national framework for enhancing science, mathematics and technology literacy for teachers in the 21st century. The Project NOVA consortium, consisting of the University of Alabama, Fayetteville State University (NC), University of Idaho, and James Madison University, is working to produce enhanced scientific, math and technology literacy for new teachers. This effort will be accomplished through the demonstration of an undergraduate science or math course framework, examples of successful course models, and a mentoring support system for faculty wishing to implement new courses or modify existing courses at their universities. The framework uses interactive learning and integrates science, mathematics and technology as a means of developing a new paradigm for educating teachers. Project NOVA invites the participation of science, engineering, technology, mathematics and education faculty who are concerned with how universities prepare new teachers.

Using the NASA mission, facilities and resources, Project NOVA provides faculty with enhanced knowledge and skills to implement change in university courses.

Project Nova will disseminate a national preservice model that is based on national standards and benchmarks for mathematics, science and technology and involves the research and development areas of NASA which:

- encourage collaboration between school of education and science/engineering faculties to develop innovative approaches to teacher preparation for student learning;
- through a world wide web server, link all sites together and provide a means for facultand students to exchange and have access to the model, materials, activities, and updated information;
- utilize interactive technologies in learning;
- make use of instructional strategies that are not common in traditional education courses;

and

- be compatible with new teacher certification.

DISSEMINATION OF CURRUCULUM SUPPORT MATERIALS

Training of Trainors

In December, 1996 twenty-nine representatives from NASA's Educators' Resource Center Network (ERCN) and the NASA Aerospace Education Services Program (AESP) attended the pilot MTPE Education Products Workshop. The workshop was held at Goddard Space Flight Center and provided training in the science of MTPE and selected education products. The three-day program was intended to provide these educators with the resources they needed to each present a minimum of three MTPE-related teacher enhancement activities over the coming year.

A range of MTPE education activities are blossoming across the country, as a direct result of this small, but very significant group. These activities include presentations at national and regional conferences, teacher workshops at ERCs and Regional ERCs, and graduate education courses. There are many creative approaches, such as team presentations, presenations to state and regional Science and Mathematics Education conferences, workshops with presercice teachers, and activities under development.

SYSTEMIC CHANGE INIATIVES

To raise the awareness of Earth system science on a broad scale, simultaneous efforts from the bottom up and from the top down are needed. Formal education is driven by a systemthat varies, depending on state, locality, and institutional setting. Therefore, a series of parallel activities must take place to work within the existing university and precollege systems to influence degree plans and curriculum standards.

Undergraduate Systemic Change

Since 1991, the ESSE program has worked to help establish a national academic underpinning for earth system science and global change education. The program recognizes that for the interdisciplinary approach to earth science to succeed, mechanisms are yet needed that stimulate scientific collaboration among scientists, and departments within universities, among universities, and between university and government science communities. The ESSE program offers financial incentives to universities that are willing to participate cooperatively with other universities and NASA in undergraduate curriculum development activities. As a requirement for their participation, each ESSE school develops and offers an interdisciplinary survey and senior level course in earth system science based upon their in-house capabilities, but drawing upon the collective experience of other participants.

Twenty-two universities were selected in 1991 to participate in the original ESSE program. By 1994, nearly 4000 students/year were enrolled in ESSE courses, with over 100 faculty and teaching assistants directly involved. In 1995 twenty-two new colleges and universities were selected to participate in the program through the year 2000. The second group of ESSE schools includes a broader array of institutions in terms of size and emphasis on teaching versus research. The primary initiative of the second phase of the ESSE program is to promote the cooperative development of flexible education modules and resources for use in earth system science courses. These materials would be designed for electronic delivery among ESSE participants and to a broad community of educators via the internet.

K-12 Systemic Change

U.S. Global Change Education State Teams, representing all 50 United States, are forming strategies to infuse global change science and issues into state curricula. Twenty-five of the teams have also been funded by the National Aeronautics and Space Administration (nineteen projects) and the Environmental Protection Agency (six projects) to develop teacher workshops, training materials, and other resources- all focusing on global environmental change topics.

Teachers, curriculum specialists, informal educators, and scientists all play an active role in these teams, which are a major component of the US Global change Research Program's (USGCRP) education initiative.

STUDENT ENRICHMENT ACTIVITIES

Global Learning Through Observations to Benefit the Environment (GLOBE)

The GLOBE program is a hands-on international environmental science and education program. GLOBE links students, teachers, and the scientific research community in an effort to learn more about the environment through student data collection and observation. GLOBE fosters the creation of a worldwide research team comprised of students and teachers in collaboration with scientists for the purpose of generation knowledge of the Earth as an interconnected system. Students from ages five through eighteen years in 3000 schools in 51 countries throughout the world conduct a continuing program of scientifically meaningful environmental measurements. The measurement protocols were designed by teams of scientists and educators to be appropriate for primary and secondary students and to generate accurate and reliable measurements for use by the international science community. GLOBE students transmit their data to a central data processing facility via the Internet, receive vivid images composed of their data, and data from other GLOBE schools worldwide, acquire information from a variety of sources, and collaborate with scientists and other GLOBE students and communities worldwide in using these data for education and research.

FUTURE INITIATIVES: TARGETING AREAS OF NEED

Last fall (1996) NASA's Mission to Planet Earth (MTPE) Program announced its first National Research Announcement specifically focused on education, NRA-96-MTPE-07, "Opportunities to Participate in NASA's Mission to Planet Earth Education Program." This announcement, developed in conjunction with the NASA Education Division, sought to round out and strengthen the MTPE Education Program by soliciting unique and innovative proposals from a broad range of education and research professionals to address two specific areas. Those two areas were Earth system science education for the pre-service teaching community and support of undergraduate student research opportunities in Earth system science.

A total of sixty-one proposals, from over fifty different institutions, were received in response to this NRA. Using a peer review process which included both science and education professionals, eighteen proposals were selected for funding at a level of nearly $700 thousand per year for the next three years. This group includes twelve pre-service teaching proposals and six undergraduate student support proposals.

What is Earth System Science?

Donald R. Johnson, Martin Ruzek, Michael Kalb
Universities Space Research Association
7501 Forbes Blvd., Suite 206, Seabrook, MD 20706-2253
301-805-8396 FAX 301-805-8466
donj@ssec.wisc.edu, ruzek@usra.edu, mkalb@gvsp.usra.edu

Abstract - Given the concerns that humankind is impacting the earth's physical climate system, a broader concept of the earth as a system is emerging. Within this concept, knowledge from the traditional earth science disciplines of geology, meteorology and oceanography along with biology is being gleaned and integrated to form a physical basis for Earth System Science. The broader concept of Earth System Science has also come to include societal dimensions and the recognition that humanity plays an ever increasing role in global change.

The Earth System Science concept fosters synthesis and the development of a holistic model in which disciplinary process and action lead to synergistic interdisciplinary relevance. However, the development both conceptually and physically of the earth system model and its quantitative assessment in the classroom and laboratory is a continuing, formative processes which requires nurturing and commitment to eclectic learning beyond one's discipline. The intersection of disciplinary specialties often provides the most fertile and interesting fields for study, but is easily sidetracked by traditional disciplinary interests and limited understanding.

In its purest sense there should be no conflict between a discipline's interests with emphasis on specifics and depth and the demands for the interdisciplinary focus for Earth System Science and Global Change. Addressing the scientific issues of Earth System Science demands both breadth across disciplines and depth within disciplines to meet the future extremely difficult challenges of Agenda 21. In the emergence of Earth System Science as an effort to address Agenda 21 challenges, there is also an overriding need to embrace the interests of a broader range of disciplines than those which traditionally have represented earth science.

For the past six years the Cooperative University-based Earth System Science Education Program (ESSE) has been developing undergraduate Earth System Science courses, curricula and degree programs at forty-four colleges and universities throughout the country. The experience from these efforts has helped to create content and the means by which Earth System Science is being offered successfully at the college and university level. Earth System Science courses offer unusual opportunities to incorporate fundamental understanding with a broad appreciation of systems concepts and observational dimensions. In this paper trans-disciplinary concepts and applications to the Earth System are examined, and a strategy to build a repository of educational resources which bridge across disciplines is examined.

THE CHALLENGE OF AGENDA 21

Agenda 21 represents an international consensus on actions necessary to move the world towards the goal of truly sustainable development. It is an agenda for the 21st Century, as adopted by the United Nations Conference on Environment and Development (UNCED) at the "Earth Summit" meeting in June 1992 in Rio de Janeiro, Brazil. Agenda 21 takes a holistic approach to sustainable development and recognizes the interrelationships between people, the environment, and the economy [1].

There is a critical need for creating an orderly, comprehensive, interdisciplinary Earth System Science and Global Change curriculum in order to develop and evolve the underlying science and knowledge that forms the foundation for understanding and policy discussion by the government, economic, industrial, agricultural, regulatory and other societal interests as referenced in Agenda 21. The current state of insight into global sustainability within our society is minimal with respect to factual information and its interpretation. The aim must be to develop understanding of the interplay among the relevant societal endeavors of Global Change in relation to the Earth System and global sustainability.

As an abstract entity, the multi-dimensional nature of the knowledge space of the Earth System Science and Global Change setting remains to be determined. Clearly, the geosciences and other relevant disciplines have explored the subspace of their individual interests. However, the subspaces embodied within the larger setting that form the intersection among the disciplines are the fertile ones which need to be traversed and studied extensively. The only means of traversing these interesting intersecting subspaces is for disciplinary scientists to lock arms and through exchange of past, current and future information and creative insight develop all the dimensions of the knowledge space needed for Earth System Science and Global Change. The necessary talent that spans the range of disciplines and interests needed for this effort does not reside within any single government agency, university, small group of universities or regional activity. The development of an ordered and comprehensive Earth System Science and Global Change curriculum over the coming decade can only be accomplished through broadly based collaboration.

The objectives of this paper are twofold: One is to summarize certain underlying tensions that exist in developing the larger dimensions of Earth System Science

0-7803-3836-7/97/$10.00 © 1997 IEEE

within universities and between disciplines; the other is to describe an approach to creating a repository of education resources in Earth System Science which avoids disciplinary barriers by focusing on topics which bridge across disciplines and utilizes data bases and information from NASA's Mission to Planet Earth. The overall strategy of the ESSE Program, in effect, creates the Senate of the Interested in Earth System Science and Global Change education by engaging participants from the larger university setting who actively commit their time and energy in classroom instruction and shared curriculum development. A decade of effort or more will be needed before the integration of specific disciplinary interests into a comprehensive Earth System Science discipline relating to Global Change emerges. While many faculty are interested, the actual percentage of faculty who are committed to the pursuit of Earth System Science education is still relatively small.

EARTH SYSTEM SCIENCE EMERGES

A major effort of NASA's Office of Mission to Planet Earth (MTPE) is to provide for a global observational capability and to ensure that the data collected bear on the scientific and societal challenges that attend Earth System Science and Global Change. The acquisition of a global database for the Earth System is a massive undertaking in itself. The interpretation and utilization of global datasets are equally demanding. Data are meaningful and useful insofar as information is gained concerning structure and/or process within the Earth System. A key determining factor as to whether data provides information is an underlying framework or model - physical, biological, economic, statistical, etc. The model may be a simple understanding of cause and effect from experience or it may be based on the governing equations of physics where cause and effect stem from first principles. Apart from whether there is information in data, the framework or model to describe a system state and process which evolves is essential. Not only is it important for advancing scientific understanding and reducing uncertainty, but it is equally important for meaningfully informing society.

To realize the potential benefits from NASA's effort requires an informed society that understands and appreciates the interdependency of the Earth's physical climate system with all of life. Clearly classroom education within the nation's colleges and universities is an important dimension leading to an informed society concerning the Earth System. To achieve the larger need of developing a knowledge base for Earth System Science, an infrastructure within education is required that fosters collaboration and integrates relevant knowledge and resources currently residing within many different disciplines. The NASA/USRA Cooperative University-based Program in Earth System Science Education provides an infrastructure which brings together scientific talent and interests of various disciplines in the classroom, the laboratory and the workplace and ensures integration of knowledge in the classroom from both disciplinary and interdisciplinary research efforts [2, 3]. Key resources are emerging through collaborative efforts involving broadband communications, Internet, computer networking and electronic libraries with archives for large earth science and other data bases.

The point of departure of the ESSE Program for the development of educational resources in Earth Systems Science was the NASA document "Earth System Science: A Closer View" [4]. In this document the "Bretherton Diagram", as it has come to be known, provided a structure which emphasized the physical climate system and biogeochemical cycles. Within these two broad areas, the emphasis was on physical, dynamical and chemical interactions within the state of the system, as represented by the atmosphere, the hydrosphere and the lithosphere. The emergence of the human dimension of global environmental change expanded greatly the breadth needed in offering Earth System Science and Global Change Science within universities. Here, the following definition of Global Change has proven to be useful for two reasons.

> Global Change is concerned with the nature and consequences of anthropogenic perturbations in the interacting physical, chemical and biological and social systems that regulate the environment supporting human life and influence the quality of that life on planet Earth [5].

One, although this definition broadens the scope of interests, the thrust is bounded in the sense that the emphasis is on anthropogenic perturbations involving interacting physical, chemical, biological and social systems that regulate the environment. Two, there is a mandate that the knowledge required to address Earth System Science and Global Change is broader than that which is gained from any one discipline or for that matter group of disciplines such as that represented by the geosciences; meteorology, oceanography, geology, hydrology, glaciology etc. Still the knowledge residing in the geoscience disciplines is central to emergence of Earth System Science as a holistic discipline. At the moment, there is considerable tension within and among disciplines within the university system as to how to incorporate Earth System Science and Global Change in course offerings and degree programs, even within the geoscience disciplines.

To a certain degree the tension is useful, since it brings about change. Inherent university traditions and practices still for the most part fail to emphasize interdisciplinary efforts in education directed towards Earth System Science and Global Change. This problem stems from the emphasis given to competitive strengths of disciplines, as opposed to the emphasis needed for collaborative interests across disciplines.

There is a danger, however, of the Earth System Science concept becoming diluted by generalities without gaining meaningful insight into the fundamental physical processes which govern the system. Historical, descriptive observations are critical aspects in understanding the physical basis for the Earth system, and have contributed enormously with such basic concepts as the heliocentric solar system and plate tectonics. However, physics, mathematics and chemistry are still the fundamental disciplines upon which quantitative

analysis and process must be based. Fundamentals from these disciplines provide the necessary foundation for theory, modeling and applications in the geoscience disciplines and for understanding the physical, chemical and biological core of land, ocean, atmosphere and life processes which constitute the Earth System. A combination of fundamental and applied interdisciplinary knowledge provides fruitful avenues to explore the interface of the known and the unknown and thus understand the system as a whole.

A MODULE APPROACH TO EARTH SYSTEM SCIENCE AND LEARNING

Based on experiences among the ESSE participants over several years, it is apparent that the definitions of Earth System Science and Global Change are evolving and will continue to evolve, since the needs, perspectives and expectations of those who desire to integrate such topics and themes in their courses are extremely diverse. Thus, it is unrealistic to attempt to impose a single view of an organization and content for Earth System Science that would serve the needs of faculty whose perspectives could range anywhere from environmental economics to physical oceanography. Global change, especially, is not as much a fixed set of ideas that define a single curriculum, as it is a perspective.

In August, 1996, ESSE participants initiated a formal collaborative effort to create Earth System Science educational modules for utilization by ESSE participants, faculty, teaching assistants and students with the primary users of the ESSE modules being university and college faculty developing Earth System Science and Global Change courses. Fourteen teams of 3 - 5 ESSE faculty and teaching assistants are now creating flexible educational materials to be accessed electronically [6]. Module topics include:

Observing Systems and Remote Sensing
The Biosphere
Atmospheric Ozone
Economics, Sustainability and Nat Resources
The Antarctic
Earth Energy Budget
El Niño - Southern Oscillation
Hydrological Cycle
Earth System History
Biogeochemical Cycles
Human Population - Environment Interactions
Health and Climate Change
Soil Processes, Land Use, Land Cover Change
System Concepts and the Earth System

These materials are to be specifically designed for eventual electronic delivery through the ESSE sever [7]. In previous years, various strategies for organizing ESSE educational resource materials had been discussed, including the familiar disciplinary components of the geosphere, atmosphere, hydrosphere, biosphere and anthroposphere. However, the development around interdisciplinary topics was considered by ESSE participants to be the means of ensuring an interdisciplinary perspective. Other ways for conceptually organizing topics and content among and within modules may become apparent with time and experience. However, an advantage of computer-based and linked materials is that alternative conceptual frameworks are easily accommodated through customized indexing even after materials are created.

At the moment, modules are best viewed as organized collections of "useful" instructional resources organized around fourteen interdisciplinary topics. The number of module topics is expandable, as is the content within each. Structurally, each module is divided into a number of key issues or sub-topics as a second level of organization (Fig. 1). A module sub-topic is populated with resources or instructional materials designed to impart specific concepts or skills. A resource can be anything that has proven to be useful based on experience in undergraduate instruction, and can be applied directly in the classroom by others. Resources are written background materials, bibliographies, annotated images, lab or model exercises, demonstrations, activities broadly defined and documented, etc. A resource could be something newly developed in response to need, or could be existing materials from among ESSE or collaborating schools. A resource could be the modification, adaptation, compilation or presentation in a unique and particularly useful way of currently available materials, concepts or data, but would not duplicate materials already easily available from non-ESSE sources. ESSE modules would acknowledge and point to existing materials on the internet or elsewhere.

While each ESSE team has flexibility in their development of focus, approach and content, each module is expected to share certain attributes. Each module will contain resource materials that are developed, presentable and adaptable to undergraduate students at various levels of intellectual readiness, survey to senior. Module content will be scientifically accurate. Either the module or subtopics will be readily applicable in the classroom or lab and will include substantive components of the human and social dimensions of global change wherever possible. Materials will be suitably formatted for electronic delivery, and be innovative in their use of internet-based resources and computer-based tools, applications, and models. No specific size limits are placed on any resource except those dictated by reason and time constraints. The overarching criteria for a resource to be included in an ESSE module (directly or indirectly through web links) are content applicability and educational utility. Being central to NASA's mission in Earth System Science, *Remote Sensing, Systems Concepts, and Understanding Models* will be common threads that run through all modules. All ESSE resources will be considered in the public domain.

Efforts are being made to ensure professional input on pedagogical considerations and assessments for the program. Education specialists within ESSE, as well as outside collaborators, are available to advise the program and teams in these areas. With many approaches facilitating effective learning, there is a need for flexibility. No single pedagogical approach is being promoted or considered. However, each team is to consider effective and cohesive pedagogical approaches. An ESSE shell or template surrounding all

modules and resources will offer a common user interface that provides entry documentation explaining the context, purpose and use of the material, and will include lists of key concepts and questions in the spirit of inquiry-based learning.

SUMMARY

In recognition of the diversity of interests and expertise concerning Earth System Science that reside within universities and research organizations and the need to develop breadth and depth that reside within disciplines, a strategy adopted within the ESSE program for the development of classroom educational resources is to create electronic modules based upon topics that are of central importance to Earth System Science. The emphasis on topics of importance avoids the compartmentalization of teaching Earth System Science by "subdisciplines", since in all cases the topics focus on critical issues that bridge across the geosciences and other relevant disciplines. There is emphasis on evolving course content as the underlying knowledge base develops through acquisition, analysis and interpretation of global data. This ensures the development of holistic perspectives of Earth System and Global Change Science and introduces students to the underlying important issues and challenges of Agenda 21.

ACKNOWLEDGMENTS

The authors acknowledge the contributions of time and expertise of the participants at the ESSE Module Development Workshop in Coolfont, WV August 12 - 16, 1996. The NASA/USRA Cooperative University-based Earth System Science Education Program is supported by a grant from NASA's Mission to Planet Earth (NAGW-4831)

REFERENCES

[1] "Agenda 21", UNCED Summit, Rio de Janeiro, 1992 http://www.igc.apc.org/habitat/agenda21/

[2] D. R. Johnson, M. Ruzek, M. Kalb, "Earth System Science Education - An Internet-based Electronic Curriculum" in *Proceedings of the 1995 International Geoscience and Remote Sensing Symposium (IGARSS '95)*, Florence, Italy pp. 572-574

[3] D. R. Johnson, M. Ruzek, M. Kalb, "Earth System Science Education: A Continuing Collaboration" in *Proceedings of the 1996 International Geoscience and Remote Sensing Symposium (IGARSS '96)*, Lincoln, NE pp. 1175 - 1177

[4] "Earth System Science - A Closer View" Report of the Earth System Science Committee NASA Advisory Council, May, 1986

[5] "International Networks for Addressing Issues of Global Change", Sigma Xi, 1994

[6] M. Kalb, D. Johnson, M. Ruzek "Evolution of the Cooperative University-based Program in Earth System Science Education", Proceedings of the American Meteorological Society Sixth Symposium on Education Long Beach, CA, February, 1997 pp. J1-4

[7] The Earth System Science Education WWW Home Page http://www.usra.edu/esse

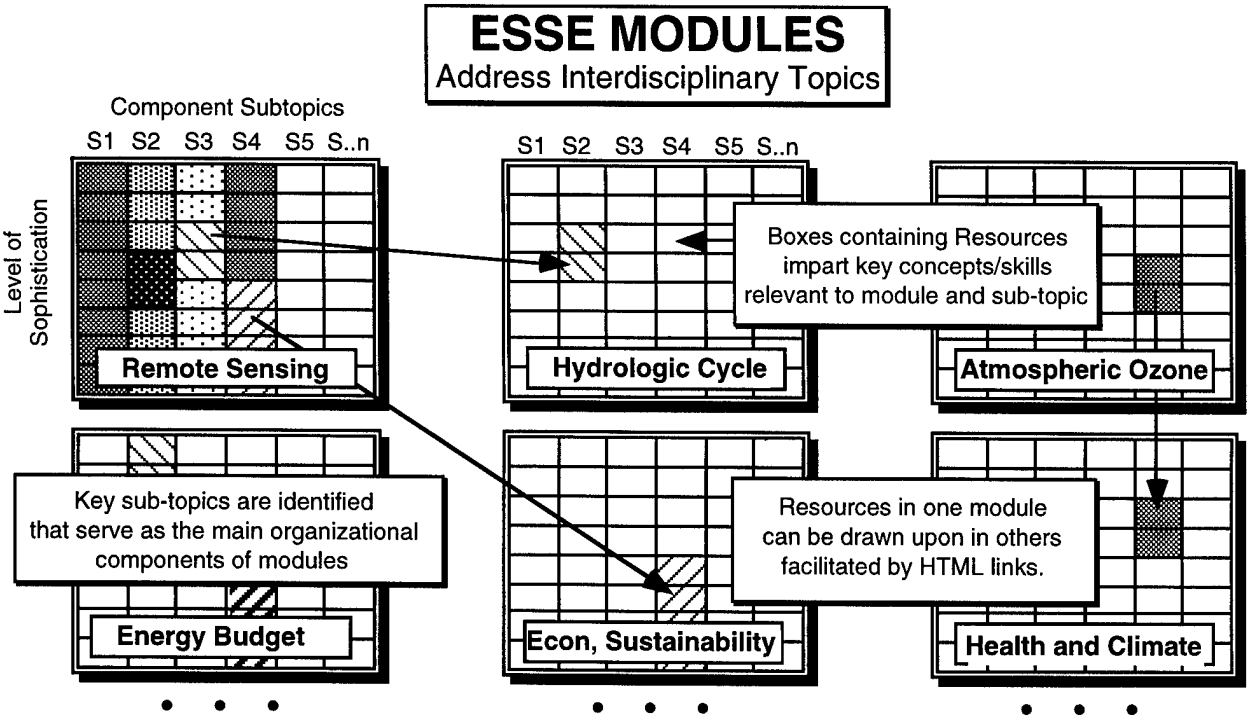

Figure 1

A Web-Based Earth Systems Science Graduate Course for Middle School Teachers

Robert J. Myers, Ph.D.
NASA Classroom of the Future

Edwin L. Shay, Ph.D.
Earth Systems Science Consultant
P.O. Box 496, Langley, WA 98260

Hilarie B. Davis Ed.D.
Technology for Learning Consortium
P.O. Box 2163, Flemington, NJ 08822

James A. Botti, Ph.D.
NASA Classroom of the Future
Wheeling Jesuit University
Wheeling, WV 26003

bmyers@cotf.edu; phone (304) 243-2388, fax (304) 243-2497

On-line courses consisting of communities of learners are experiencing increasing use and credibility. This paper outlines the design, development and implementation of a middle school teachers' earth systems science graduate course. This 16-week course was developed at the Center for Educational Technologies, Wheeling Jesuit University, under the sponsorship of the National Aeronautics and Space Administration's Mission to Planet Earth. The themes of earth system science content and collaborative, inquiry-based science education prevailed within an electronic environment where teacher participants took responsibility for their learning within a structure of clear expectations.

The course was delivered through the World Wide Web (WWW) and featured collaborative exercises and threaded discussion. This on-line asynchronous environment was chosen to accommodate teachers in remote locations and those whose schedules did not provide for on-campus attendance. Participants were chosen for the course based on access to the WWW and their stated interest in helping refine the course for future iterations. The course also addressed the US National Research Council's standard for using inquiry-based approaches in science teaching. This was accomplished by modeling a collaborative, student-centered environment in which teachers relied on each other to develop knowledge.

A primary concern during course design was to create an on-line learning environment where interdependence among participants provided the necessary glue for a successful community of learners. Davis's [1] recipe for building a self-sustaining community included shared goals, challenges that cause relationships to form through exchanges of ideas, regular reflection for developing shared understanding, and an infrastructure or set of places that defined the way for the virtual community to form and interact. One means of following this recipe is to have participants focus on independent information collection, then enter "virtual space" to test ideas and ask questions of each other and the mentors. Rogers and Laws [2] addressed the challenge of building a community through extensive on-line discussions and providing opportunities for cooperative learning to support participation.

Cooperative learning is a successful teaching strategy in which small teams use a variety of learning activities to improve their understanding of a subject. Each team member is responsible not only for learning but also for helping others. This paradigm rejects the idea of competition in the classroom and promotes teamwork among learners by defining a variety of roles and by setting shared goals. It is important for each team member to take responsibility for the progress of the whole group -- sharing ideas, materials and resources -- and sharing equally in the rewards of a successfully completed assignment [3]. A variant of cooperative learning is the jigsaw method in which participants are sent to new teams where each individual becomes an "expert" in a certain area. These experts then return to their original teams where information is shared with other team members in creating a product, in this case, an earth systems diagram [4, 5].

DEVELOPMENT TEAM AND PARTICIPANTS

The development team included instructional designers, earth systems scientists, a graphic designer, and a web master. The inclusion of an expert in on-line collaborative environments and the web master proved to be crucial in the design and implementation. Two sections of participants (teachers) enrolled in the course (N=44). Each

0-7803-3836-7/97/$10.00 © 1997 IEEE

section had two mentors, a master teacher and an earth systems scientist. The mentors guided discussions by interjecting when necessary, responding to weekly discussions, and replying to students' journal entries.

Participants came from across the United States and had diverse backgrounds in earth systems science and on-line experience. All except two were practicing teachers; of the two, one is returning to the classroom; the other is a curriculum specialist.

IMPLEMENTATION

The on-line environment was seen as a place for collaboration and knowledge building, not as a repository for earth systems content. With this view in mind, participants were mailed necessary background reading materials, CD-ROMS, and other supporting materials. The on-line site was limited to week by week instructions, information about grading, how to thrive in on-line communities, and the discussion area itself.

Design of the first three weeks allowed participants to become acclimated before plunging fully into collaborative activities. During this time most discussion occurred in "Course Space" (Figure 1). Starting slowly had several advantages. It allowed non-technical users to learn about cyberspace and for everyone to become accustomed to the site. During weeks two and three participants learned about the others assigned to their teams, and they were introduced to earth systems science.

During week two, the 1988 Yellowstone National Park fires were used as an event that impacted upon earth's interacting and interdependent spheres (i.e., atmosphere, biosphere, hydrosphere, and lithosphere.) Using a graphic depiction, participating teachers were presented with a tutorial on how to examine positive and negative feedback loops and dynamic equilibrium. During week three participants worked within their teams in designing a new earth systems diagram. The meteorite impact on the Yucatan Peninsula was used as the earth event for this diagram. Participants also reflected on their progress in content knowledge and posed questions in the "Journal Space." This was a weekly requirement and served as a space in which one-on-one discussions could be made with the course mentors.

Week four signaled the start of what would be four, three-week series, during which time deforestation, volcanoes, sea ice change, and hurricanes provided the events for group discussion and earth system diagram construction. This paper elaborates on the first, three-week series. To begin the deforestation discussion, each section of approximately 20 participants was broken into new "Sphere Space" teams. This meant, for example, that in a group of four, one person went to the

Fig. 1, Collaboration Space

atmosphere sphere group discussion, one to the biosphere group discussion, and so on. The objective of the sphere group discussion was for each member to become as knowledgeable as possible about deforestation's impact on his or her sphere. At the end of the week, each participant had collected and discussed information concerning his or her sphere and then returned to the cooperative team to help with the construction of the earth systems diagram.

During week five the original cooperative teams reformed and work began on the earth systems diagram. This work was completed in "Event Space" (see Figure 1). Each member was counted on for knowledge developed during the previous week's sphere group discussion. Mentors watched the discussion, intervening only to ask thought-provoking questions or respond to requests. Week six provided teacher participants opportunities to think about and share classroom activities they would use with their middle school students. This information was recorded in "Classrooms Applications Space."

REQUIREMENTS AND EVALUATION

Course developers provided participants rubrics as guides for course expectations and grading purposes. Participants were graded on their contributions to Sphere Space, Event Space, and Classroom Activities. Points were also awarded for journal entries and for the final project. For the final, participants could develop an earth systems diagram based

on theories about geoengineering, or they could submit an article to Science Activities magazine.

RECOMMENDATIONS

Who succeeded in this course? Based on the low drop out rate (5 of 44), and the end-of-course surveys from participants, most succeeded. One participant noted in an email that she hoped the course would never end. Some individuals dominated discussion and some shied away, remaining aloof and laconic, much like face-to-face discussions would be. Rogers and Laws [6] suggest that students who succeed in asynchronous, distance learning courses tend to be more self-disciplined learners. McClure [7], in discussing development of the WELL, said developers thought the best participants would be intelligent people with diverse backgrounds and who were sufficiently outgoing and extroverted. The jigsaw design with well-defined spaces for public, private, large and small group activities was designed to mitigate against an "extroverts only" environment.

The course was extremely rigorous and time-consuming for teacher and mentors alike. It was designed to be this way, yet many teachers had not anticipated the heavy workload. Five quit. Two or three were talked into continuing through intervention by mentors or course developers. This is similar to the negotiations likely to ensue in on-campus, face-to face courses.

Having a master teacher and an earth system scientist was a luxury that not many universities could afford. If this becomes too problematic, course developers could elect to spread the scientist's workload over multiple sections. A frequently asked questions (FAQ) area could also be developed to tap their content expertise.

Even with two mentors per approximately 20 students, the mentors' workload was huge. Developers would do well to keep the number of students in these classes at no more than 24. Based on what was observed in this course, raising the number of students is likely to detract from students' learning.

Developers envisioned all course coordination, communications, and discussions happening in asynchronous, virtual space. This proved to be overly optimistic; many phone calls and emails were used to provide scaffolding and support. One team of teachers formed their own synchronous, online chat sessions in order to facilitate timely construction of their earth system diagram. It is likely that in order to overcome the gap created in distance education, multiple means are not only likely, but necessary.

The groupware used for this course did not allow the participants to display graphics, pictures, or images, unless the web master assisted. The cooperative team mentioned above put their systems diagram on their own web site.

The web master's role was essential. The groupware used for the course needed a great deal of tweaking early in the course and he was called upon time after time to address users' technical problems. Many of these problems resulted from incompatibilities between browsers, versions of the browsers, and differences in users' platforms (Macintosh or Windows).

Giving teachers weekly tasks and deadlines paid off, especially in this asynchronous environment. The best weekly time frame was Monday morning through Sunday night; teachers liked to have the whole weekend to complete assignments.

SUMMARY

An overriding objective in the development of this on-line course was to create "reasons" for individuals to engage in the material. The population consisted of very busy classroom teachers. Course developers purposely designed the structure to be student-centered so that participants relied on each other for input. As discussed above, this was accomplished through the jigsaw strategies that made participants depend on each other for essential information in creating the earth systems diagrams. There is always room for improvement and fine tuning, but developers have been pleased with the implementation of this course. After minor tuning, it will soon be offered again and will provide a model for development of other on-line courses.

REFERENCES

[1] H. B. Davis, "Building virtual communities: Parallel universes of the mind," http://www.eclipse.net/~hilaried/parallel.html, January 15, 1997.

[2] C. S. Rogers and P. Laws, "Successes and lessons learned in an on-line course on socioemotional development," http://leahi.kcc.hawaii.edu/org/tcc-conf/pres/rogers.html, May 1, 1997.

[3] R. E. Slavin, "Research on cooperative leaning: Consensus and controversy," Educational Leadership, vol. 47, pp. 52-54.

[4] D. Grisham, and P. Molinelli, Cooperative learning, Westminister, CA: Teacher Centered Materials (1995).

[5] M. S. Leighton, "Cooperative learning," in Classroom Teaching Skills J. M. Cooper, Ed., Lexington, MA: D. C. Heath and Company, 1990, pp. 307-334.

[6] Rogers and Laws, op. cit.

[7] K. Hafner, "The epic saga of the WELL," WIRED, May 1997, pp. 98-142.

System Thinking and System Modeling in the Earth System Science Classroom

Farzad Mahootian, Ph.D., Earth System Science Community Co-Investigator
Gonzaga College High School, 19 Eye St., N.W., Washington D.C. 20001, USA
(202)966-8588, fax (202)336-7164
farzad@circles.org

INTRODUCTION AND CONTEXT

Earth system science (ESS) is a holistic study of the Earth. ESS marshals the resources a variety of scientific and technical fields to explore interactions among the Earth's component subsystems in order to understand the Earth as a system, to explain Earth dynamics and Earth evolution, and to address the problem of the effects of human actions on global change. We have begun to understand that because the Earth is a system, our local actions have global effects, that human society has the power to change the world, for better or worse. It is of great importance, both for the sake of the Earth and for the sake of our own future, to understand the Earth for what it is: a complex system of interlaced and interacting subsystems.

In order to investigate the Earth system, teachers and students need access to expertise in a broad variety of disciplines: chemistry, physics, computer science, biology, mathematics, statistics, and political science. A variety of relatively new skills are also required: networked computing, tools and techniques for retrieving, visualizing, and analyzing remote sensing data, and building dynamic systems models. The question of systems modeling became a central issue in curriculum development efforts of the Earth System Science Community (ESSC), a three-year project supported by NASA's Information Infrastructure Technology and Applications and High Performance Computing and Communication programs.

The thrust of the curriculum development effort was to enable students and teachers to conduct investigations in global change topics using remote sensing data gathered by NASA and other science agencies. The curriculum was project-based [1], with the intention of producing an authentic and living sense of understanding and participation in science research [2], [3]. Students and teachers were to collaborate on-line with their peers in other schools, and with scientists/mentors in universities and government science agencies. In this effort students and teachers become researchers and learn to design and carry out a research strategy, involving the proposal and articulation of a hypothesis, the building of a system model, and the search, retrieval, manipulation, visualization and analysis of appropriate data. Students conclude their research by testing their hypothesis with available data, using visualization software, and information available in print and on-line. Finally, students communicate the results of their research by publishing their reports, data, data products, and systems models. To date, over sixty reports have been published on the project website (http://www.circles.org/).

The curriculum content and pedagogy was designed and implemented during the 1993-94 pilot phase in adherence to the science strategy of NASA's Mission to Planet Earth, and to the (U.S.) National Research Council's (NRC) National Science Education Standards which were in draft form at the time [4].

THE ESSC PROJECT IN RETROSPECT

The original purpose of the Earth System Science Community was to build an investigation-oriented Earth system science curriculum in which high school and university students could conduct research projects on global change issues using Earth observation data and information over the Internet. Three integrated components were proposed: 1) an Earth system science curriculum, 2) an information system over the Internet to support the curriculum and access to remote sensing data, and 3) a pilot community of educators, students and scientists who would help define requirements for improving the curriculum and information system.

While the first two goals were achieved with a significant degree of success, it has become clear that the requirements of a successful on-line community were underestimated. In this respect, the main lesson learned was that, with proper encouragement and cultivation, communities can grow organically from a pre-existing nutritive substrate. The "substrate" here refers to long-term institutional commitment to supporting innovative (i.e., non-traditional) courses and teachers. A paradigm case of such commitment is represented in the (U.S.) National Science Foundation's *"systemic* initiatives" for science education reform. But in the absence of such a substrate, the simple influx of temporary dollars for teacher training and partial release time is an insufficient and ineffectual way to build on-line communities.

SYSTEM MODELING AND STUDENT LEARNING

A. Introduction

The two most difficult aspects of teaching ESS are the visualization, analysis, and interpretation of data, on the one hand, and the use and construction of system models on the other. The problem of data visualization, in the ESSC context, is the topic of another paper in this volume ("Issues of WWW-Based Data Visualization for the Earth System Science Classroom").

Systems thinking is "the art and science of making reasonable inferences about behavior by developing an increasingly deep understanding of underlying structure." [5] To add a more technical dimension to this definition, we may define system dynamics as "a method for studying the world around us. It deals with understanding how complex systems change over time. Internal feedback loops within the

0-7803-3836-7/97/$10.00 © 1997 IEEE

structure of the system influence the entire system behavior." [6]

It is important to point out that in the ESSC visual models were used, rather than models that describe the phenomena mathematically in symbolic language. While both types of models may produce their result as visualizations, the former embeds the mathematical relations within an object-oriented environment that displays objects and object-interactions in a manner that is more like the kind of diagram students and scientist are apt to draw or think of when discussing systems. The benefits of using modeling and visual simulation in science education are manifold, and to a large extent mirror the benefits of this technique in science research: namely, these tools enhance the ability to observe, think about, experiment with, and discover patterns and relations that are inaccessible because of spatio-temporal scale (nanotech or planetary-scale), or inhospitable environments (the Earth's interior).

B. The Form and Content of Systems Thinking

Earth system science represents a significant departure from classical science and science education. Not only does Earth system science require an interdisciplinary and holistic approach, it also requires a new focus on the *interrelation of Earth processes*. The integrity of the Earth as a system consists of the interrelatedness of its component subsystems: hydrosphere, atmosphere, biosphere, lithosphere and cryosphere. To understand the Earth as a system one must understand not only the fundamentals about each component subsystem, but also the processes that interconnect them. The Earth is not a static system; without the understanding of *process* we would miss the underlying causes of both natural and anthropogenic global environmental *change*. In short, Earth system science without system modeling is impossible.

The best way for students to gain a working knowledge of such complex interrelations is to build and interact with Earth system models. For example, after learning about the Earth energy budget and then playing with an Earth energy model, and altering the cloud amount, and other values, the student's mind resonates with an intellectual satisfaction that results from this correspondence of form and content -- simultaneously learning about the system model and the modeled system.

The use of modeling software to instruct students about the Earth system is consistent with the "constructivist" theory of learning, and with the inquiry- and discovery-based mode of learning advocated by the NRC [7]. The NRC makes explicit reference to studying the Earth as a system [8], and to the use of models in secondary school science education [9].

C. The Construction of Knowledge

Aside from the fact that the form and content of learning are well-matched, as they are in the case of system modeling and ESS, what is chief cognitive benefit of using modeling in education? To paraphrase the great 18th century German epistemologist, Immanuel Kant, "models without data are empty, and data without models are blind." In Kant's theory of knowledge [10], "categories of understanding" (i.e., causality, composition, etc., which collectively lay the foundation for the "laws of nature") provide conceptual connectivity to the "forms of perception" (i.e., the ordering principles of space and time, which apply to all objects and events). Scientific consciousness, according to Kant, is constructed by one's appropriate use of the categories of understanding in association with the forms of perception. In his philosophy, Kant demonstrated that all knowledge -- indeed, all experience-- is an active, on-going construction. In this respect the contemporary constructivist theory of learning [11] finds its ancestry in Kant's philosophy.

In the context of our discussion of Earth system science, the forms of perception are analogous to the archives of data of the Earth's systems --blind data without meaning or connection-- while the categories of understanding are embodied in our system models --which, without data, are conceptual structures devoid of significance. In their use of system models and data archives students begin to germinate scientific consciousness. In their effort to define and understand the limitations and omissions in their models, and to refine these in the face of research, data and criticism, they begin to attain scientific self-consciousness.

Kant's immediate successor in the German philosophical tradition, Georg Hegel, rendered the static scheme of his predecessor dynamic. Hegel elaborated the developmental emergence of scientific consciousness and self-consciousness as stages in the development of *mind* [12]. In his theory of knowledge the categories of understanding are not given, as in Kant's scheme: the categories are themselves *constructed*. For Hegel, consciousness emerges from one stage to the next by realizing and outgrowing the limitations of the previous stage, and constructing the framework of the next stage around the content of the new discovery. What this means in the context of the Earth system science classroom is that when students construct their own models they learn something about their own process of learning.

In directing high school students' research projects over the course of the year, I have seen this process embodied repeatedly at each phase of their research. However, nowhere is the development of consciousness and self-consciousness more clearly facilitated or more readily observable than in student's use of models and modeling software. "Models, and the arguments that students use to explain them, provide nice windows to the evolution of student thinking" [13]. The struggle to make systems models is the struggle to think about the whole and the dynamic relations among its parts. This messy and painful process is the first step in attaining a broad understanding of science as a living force that grows when scientists discover nature's data and find their own errors.

SYSTEMS THINKING AND SYSTEMS MODELING EXAMPLES IN EDUCATION

While some good examples of it exist in the undergraduate context, systems modeling is generally

reserved for graduate and post-graduate research, where it is an essential component of many science disciplines. Earth system science is not possible without modeling. University Space Research Association's cooperative program in Earth System Science Education (ESSE) has been actively promoting the use of modeling in college ESS courses for the past six years, and has begun to create a library of system models (http://www.usra.edu/esse/learnmod.html).

Examples of systems thinking and systems modeling in the pre-college context can be found in a number of places: 1) The Massachusetts Institute of Technology's System Dynamics in Education Project, whose Road Maps project is a study guide with examples [14]; 2) Bolt, Baranek, and Newman System Technologies, Inc. (BBN), has produced a number of modeling and simulation applications for elementary through high school students [15]. BBN's research on the efficacy of using model-based inquiry is extremely valuable in this context [16]; 3) the U. of Michigan HI-C research group's Model-It "enables middle and high school students to construct dynamic, visualizable and photo-realistic models", and allows students to put simple relationships (increases, decrease) between system components [17]. 4) The Ohio State Univ.'s Earth System Education (ESE) Project (http://www.ag.ohio-state.edu/~earthsys/esehome.html) has put the systems emphasis in Earth science since 1987.

The modeling software used in the ESSC was STELLA, which stands for "Structural Thinking, Experiential Learning Laboratory with Animation." [18]. This is a tool of considerable sophistication which has been used in college courses in Earth system science in the U.S.A. (see ESSE, above). STELLA models can be simplified to a level appropriate for high school students and teachers without sacrificing the software's capability to add complexity to the model. It can be used simply to create elegant qualitative concept-maps that display the student's understanding of the system in question. More advanced students can set about the task of building equations and data in to the model to create a running quantitative model. For the most part, students used quantitative models that have been built by experts [18], and build qualitative models to display their understanding of the system which they are investigating. An added benefit of using STELLA's in high school is that the same software is currently in use in many of the ESSE partner universities and colleges. This provides high school educators with an excellent pool of experts in using Earth system modeling.

REFERENCES

[1] Blumenfeld, Soloway, Marx, et al, "Motivating Project-Based Learning: Sustaining the Doing, Supporting the Learning," Educational Psychologist, 26 (1991), pp.369-398.

[2] Whitehead, A. N., The Aims of Education, New York: McMillan, 1929.

[3] Edelson, D. C., "Realizing Authentic Science Learning through Adaptation of Scientific Practice," in Tobin, K., and Fraser, B., International Handbook of Science Education. Dordrecht: Kluwer, 1997 (in press).

[4] Nat'l Research Council, National Science Education Standards (NSES). Washington,D.C: Nat'l Acad. Press, 1996.

[5] B.Richmond, "System Dynamics/Systems Thinking: Let's Just Get On With It." http://www.hps-inc.com/st/paper.html

[6] "System Dynamics in Education," http://sysdyn.mit.edu/

[7] (NSES) p. 20.

[8] (NSES) pp. 158-160.

[9] (NSES) p. 175.

[10] Immanuel Kant, The Critique of Pure Reason (1781). Translated by N. K. Smith. New York: St. Martin's, 1965.

[11] Yager, R.E., "The Constructivist Learning Model," The Science Teacher, September 1991.

[12] Georg W. F. Hegel, The Phenomenology of Mind (1807). Translated by J. B. Baillie, New York: Harper Colophon, 1967.

[13] Richard Lehrer, quoted in S. Foster, "Center Research on Student Understanding", Principled Practice in Math and Science Education. Vol. 1, No. 1, Spring 1997

[14] Jay Forrester, et al, "Road Maps: A guide to Learning System Dynamics," http:// sysdyn.mit.edu/road-maps/home.html

[15] Wallace Feurzeig, "Visualization in Educational Computer Modeling", in The Use of Computer Models for Explication, Analysis, and Experiential Learning, ed., Towne, D., de Jong, T., & Spada, H., NY: Springer-Verlag, 1994.

[16] Horwitz, P., Linking Models to Data: Hypermodels for Science Education, The High School Journal, Vol. 79, No. 2, Dec. 1995, Jan. 1996. A well-developed product in this effort is "*GENSCOPE*:: Multi-Level Science", http://copernicus.bbn.com/genscope/index.html.

[17] http://hi-c.eecs.umich.edu/research/model_it.html

[18] See the High Performance Systems, Inc., www-site at http://www.hps-inc.com/st/resources.html

[19] A. Few, System Behavior and System Modeling, Global Change Instruction Program, Boulder: UCAR,1993. http://www.ucar.edu/ucargen/education/gcmod/currmat.html

Practical Uses of Math And Science (PUMAS)

Web Site: http://pumas.jpl.nasa.gov

Ralph Kahn
Jet Propulsion Laboratory/California Institute of Technology, MS 169-237, 4800 Oak Grove Drive, Pasadena, CA 91109. Tel.: 818-354-9024; FAX: 818-393-4619; e-mail: ralph.kahn@jpl.nasa.gov

Practical Uses of Math And Science [PUMAS (**poo'** • mas)] -- the On-line Journal of Math and Science Examples for Pre-College Education -- is a collection of one-page examples of how math and science topics taught in K-12 classes can be used in interesting settings, including everyday life. The examples are written primarily by scientists and engineers, and are available to teachers, students, and other interested parties via the PUMAS Web Site. Our goal is to capture, for the benefit of pre-college science education, the flavor of the vast experience that scientists have with interesting and practical uses of math and science...

All examples are peer-reviewed by at least one scientist, with a relevant background, and at least one teacher, at an appropriate grade level. Once accepted, the example is a citable reference, in a refereed journal of science education. PUMAS examples may be activities, anecdotes, descriptions of "neat ideas," formal exercises, puzzles, or demonstrations. They may be written in any style that serves the material well.

Teachers already have textbooks. But the exercises in them are often routine and uninteresting, written by people with only limited experience at actually using the ideas presented. The intention of PUMAS is to give teachers a resource to supplement the textbook. So a teacher who has taught "cosines" for thirty years, but never actually used a cosine for anything except to teach it, can benefit from the ways scientists describe how they use cosines.

Teachers can search the PUMAS collection based on curriculum topic, grade level, subject keywords (such as airplanes or dinosaurs), or any other parameters in the example headers. They then scan through the relevant examples, and develop ideas of their own about how to use the material to enrich their presentations. This relieves scientists of the obligation to develop "curricula," which few of us are equipped to do. It puts the job of "integration into the lesson plan" on the teacher, who is in the best position to judge the students' needs, abilities, and interests, as well as the teacher's own interests and proclivities.

There are several mechanisms for obtaining feedback from users. A "Comments" file is attached to each example; teachers can submit comments on particular examples, such as experiences with the example in the classroom. Subsequent users can view all previously posted comments. There is also an "Examples Wanted" Bulletin board, where requests for new examples can be posted, and a formal "On-line Teachers' Assessment Form."

We began designing the PUMAS Web Site in the spring of 1996. **We are currently in need of examples**, and anticipate opening the Site to general users in late 1977, once the collection contains a number of entries. The "Contributors' Page" on the PUMAS Web Site describes how to use the automatic submission process. K-12 teachers and scientists are also needed now, to serve in the pool of PUMAS reviewers. The on-line "Participant Volunteer/Update Form" can be found from the Navigation portion of the Help page, or from the hyperlink at the top of the PUMAS Examples Search page.

ACKNOWLEDGMENTS

This work is performed at the Jet Propulsion Laboratory, California Institute of Technology, under contract with the National Aeronautics and Space Administration.

0-7803-3836-7/97/$10.00 © 1997 IEEE

An Earth System Science Education and Training Program for the Inter American Institute for Global Change Research (IAI)

Donald R. Johnson, Martin Ruzek, Michael Kalb
Universities Space Research Association
7501 Forbes Blvd., Suite 206, Seabrook, MD 20706-2253
301-805-8396 FAX 301-805-8466
donj@ssec.wisc.edu, ruzek@usra.edu, mkalb@gvsp.usra.edu

Abstract - The Inter-American Institute for Global Change Research (IAI) is an international cooperative effort among 17 countries in the Americas seeking to improve understanding of global change. The 1992 United Nations Conference on Environment and Development (UNCED) focused attention on global change as one of the most critical challenges facing the world today. Natural and human induced changes such as ozone depletion, loss of biodiversity and changing climatic conditions are evidenced throughout the world, without respect for geopolitical boundaries. In recognition of the importance of a regional approach to the study of global change, the Institute's science agenda involves environmental issues which affect the sustainability of regional resources and socioeconomic systems of the IAI Member Nations. Education and training are a component of the overall IAI effort, and the USRA Earth System Science Education (ESSE) Program was selected to develop further the concept of an ESSE counterpart in the IAI structure. Central to the common interests of both ESSE and IAI are the educational challenges and opportunities which Earth System Science and Global Change present. The ongoing Cooperative University-based ESSE Program is proposed to be a model for the development of similar collaborative efforts within the IAI member countries, but tailored to the specific technical capabilities and scientific interests of the IAI participants. A planning meeting was held in January 1997 to assess the educational needs of the IAI, inventory the existing capabilities and resources, and prepare a course of action that provides for collaborative university efforts to address these needs. The meeting served to exchange information about current educational programs and formed the nucleus of a network of educators, researchers, students and other individuals interested in Earth System Science and Global Change education topics which will be applied to the needs of the IAI member countries. Working groups were formed to discuss and recommend approaches to a variety of IAI related topics including networking, workshops, partners and mentors, distance learning, professional development and training, environmental policy, human dimensions and an assessment of current educational resources. A core educational program in Global Change is being proposed which would establish a working relationship between the current ESSE community and IAI member educators and researchers and include the creation of a WWW server specifically for the needs of the IAI. The overall effort will facilitate contact and dialog between individuals and foster partnerships among institutions focused on understanding the Earth as a sustainable system.

BACKGROUND

The Inter American Institute for Global Change Research is an intergovernmental organization chartered in 1992 to address the global change research needs of the seventeen participating countries in North , Central and South America. The IAI has identified seven science themes pertaining to global change, the study of which will provide national and international policy and decision makers accurate information concerning global and regional effects of change. The program also aims to increase the scientific capacity and international cooperation among member nations [1].

The seven science themes (see Table 1) concerning global change are linked by crosscutting themes that span the IAI effort, including Networks, Education and Training, Modeling, and the Human Dimensions of Global Change. While embracing several crosscutting themes, the ESSE/IAI workshop recommendations concerning the Earth System Science education and training activities for the IAI are the primary subject of this paper.

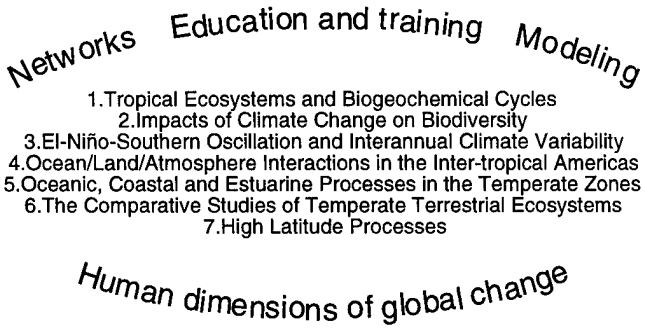

Table 1 - The IAI's Seven Science Themes

The Cooperative University-based Program for Earth System Science Education (ESSE) is an ongoing effort funded by NASA through USRA which emphasizes classroom education, collaborative learning, a network of faculty and students focused on the scientific and human dimensions of global change, and a shared repository of teaching resources [2,3]. The ESSE Program develops and facilitates cooperative efforts among scientists and departments within universities, among universities and between university and government science communities in areas relevant to Earth System Science and Global Change education. ESSE participants design and offer survey and senior level courses on Earth System Science topics. A scientist/faculty exchange

0-7803-3836-7/97/$10.00 © 1997 IEEE

component of the program brings to the classroom expertise and perspectives different from those at the host campus. Hands-on workshops and tutorials are held each year for faculty and teaching assistants to exchange and develop content and familiarize the group with new software tools and methods for the classroom. The overarching objective of ESSE is to accelerate development of an academic base for Earth System and Global Change science within and among colleges and universities. The Program has involved 44 colleges and universities since 1991, and is forming partnerships with other institutions and organizations with complementary educational goals [4].

In 1995, USRA submitted a proposal to the IAI to plan for an extension of the ESSE concept to advance the education and training needs of the IAI. The proposal was accepted in mid 1996 as an IAI Startup Grant.. In coordination with the first IAI science team meeting, a group of 35 researchers and educators representing ESSE participants and eight IAI member countries met in San Diego, CA in January 1997 to discuss the IAI's education and training needs.

The primary goal of the proposed effort is to accelerate the development of Earth System Science and Global Change Education through collaboration within the IAI consortium, increase understanding of Earth System and Global Change Science, and thus ultimately impact education throughout the Americas in the coming century. To reach this goal, the experience and needs of IAI members and partners must be incorporated in a strategy that addresses Earth System Science and Global Change education and training topics through alliances and collaboration. The USRA proposal which offers the ongoing ESSE Program as a model, is a starting point to begin this process. However, modifications and additions need to be made in view of the diversity of educational institutions. It's direction and implementation depend largely upon the input of participating educators and researchers.

Workshop participants were given the opportunity for short presentations about their interests and institutional background. A short description of the ESSE program was also presented, before the participants divided into working groups to consider options and formulate a response to the call to prepare recommendations for an IAI education and training strategy building upon the ESSE experience. Working group organization, draft reports and a list of participants can be found at http://www.usra.edu /iai/iai.html.

WORKING GROUP RECOMMENDATIONS

Working groups were asked to identify the issues and needs for an IAI education and training program, the problems that must be overcome, and recommendations for action, keeping in mind what is tractable within the scope and budget of the IAI.

Working group boundaries were not defined rigidly, so several groups identified similar themes for the IAI education and training effort. There was a general agreement among the groups that talented Latin American students must be attracted to graduate study of Earth System Science in order for the IAI research objectives to be met over the next decade. Training and education in global environmental and climate change issues must also support several levels of learning - teachers, technicians, engineers, students - to meet their needs in public and academic sector projects, and to effectively impact the political and economic aspects of environmental management. The inherent interdisciplinary nature of global change studies was recognized, including the human element, as well as the need to shift perceptions of the environment from local to regional and global scales. Many of the IAI institutions could benefit from background exposure to topics such as collaborative learning and teaching, new pedagogical methodologies, active and interactive learning, integration of technology and teaching, computer data analysis and visualization tools, etc. English was recognized as the common language for science being generally appropriate for specific lectures and modules, especially among faculty workshop participants. However, the need for quality technical translations to Spanish and Portuguese was recognized as a priority for classroom undergraduate education.

Workshops, Courses, and Learning Module Development

Each working group recognized workshops as a primary means to educate and train faculty about Earth System Science and Global Change topics. The goals of the workshops will be:

- Build scientific capacity among the IAI community by extending and developing Earth System Science and Global Change courses and educational materials with emphasis on the content of the seven IAI science themes
- Establish a collaborative network of IAI educators and researchers within the Americas utilizing a shared repository of education and research materials via the Internet

Within the workshop, interdepartmental faculty teams of two or three per home institution will interact with teams from other institutions in developing course content and educational resource. Subject matter for the workshops will involve global change science and issues from the IAI research themes and elsewhere, classroom educational materials, technological tools such as Internet applications, geographic information systems, remote sensing and image processing, STELLA modeling software, etc. The workshop will also incorporate pedagogical techniques that aid faculty delivery and student learning of the materials.

Upon returning to their home institutions, participants will develop undergraduate and beginning graduate level courses dealing with Earth System Science and Global Change topics, drawing upon materials, ideas and personal contacts acquired during the workshop. In addition to the course, participants may also choose to develop interactive multimedia learning modules and engage in activities which aid in teaching Earth System Science. Multimedia instructional technology has the potential to foster interest in science among a more diverse student population. These modules will be shared among participants, and will form the basis for a broader curriculum focused on IAI and Earth Systems topics. Rather than offering a limited curriculum in global change studies, the

modular nature of these resources will allow faculty to select and organize educational topics which best suit their needs for a particular course. Given the diversity and emphasis of faculty from different institutions, the capability to select from a menu of topics is a strength of the program.

Communications, Connectivity and Networking

The early development of an infrastructure to address the challenges of IAI global change science focused on education for IAI researchers, educators and students, including a WWW server, is essential. The infrastructure will contribute to the scientific capacity of the IAI, and the creation of a diverse community of talented individuals who will be prepared to make informed policy and social decisions well into the next century. The Internet is a powerful tool which will aid in the implementation of international collaboration. The WWW server, as an active repository with common contributors, is an excellent and essential mechanism for scientists and educators to build capacity and community in the areas of Earth System Science and Global Change.

The working groups emphasized the need for IAI faculty, researchers and students to communicate actively and effectively in sharing Earth System Science and Global Change concepts and learning resources. Students and faculty from across the IAI should be given the opportunity to work together via high-bandwidth video and teleconferencing technologies, either for specific events (e.g. a lecture) or for ongoing collaboration via the Internet on research or education topics.

The availability of computer and communication technology to IAI participants varies greatly from country to country. However, accessibility is steadily improving in most areas, and their recommendation was to plan for tomorrow and not be constrained by today's limited capabilities.

Field Studies

Interdisciplinary hands-on activities and field studies were given high priority by the working groups, and should include faculty and students from all IAI member countries. A range of field activities should be considered, from day trips to extended courses working in IAI study areas. Field trips should emphasize "hands on" activities with students and as much interdisciplinary professional interaction as possible. Field courses visiting research projects should produce "virtual field trips"(data, video, still imagery, etc.) and case studies for dissemination via the Internet to others interested in the area. Field experiences connecting "hard science" to human dimensions (sustainability of agriculture, public health, etc.) should be encouraged.

Standardized Databases

The working groups expressed the need for standardized cross-platform climatological databases, both textual and graphical, for use in an IAI educational context. The databases will provide students the opportunity to learn analysis methods while working on locally relevant problems. Such databases could be made available via the WWW or CD-ROM, and would include good multilingual documentation.

SUMMARY

Recognizing that no individual university or institution has the diversity of expertise and experience that is needed for global change education, the most significant result of the proposed effort will be the early establishment of a collaborative network of IAI educators and researchers, integrated with ongoing international research and educational activities such as ESSE. The cooperative involvement of IAI scientists and educators focused on Earth System and Global Change Science, education and training is fundamental to building research and education capacity and the establishment of a functional network within the IAI.

The overall USRA/IAI education and training plan prepared by the working groups emphasizes the collaborative development of classroom educational resources. Support should be provided for classroom education, workshops and field trips with a WWW presence including home pages, a repository for resources and translated materials, listserves, video and teleconferences, etc. This effort will contribute within the Americas to an awareness , appreciation and understanding of the earth system. This increased awareness, appreciation and understanding will benefit society and the future of the earth system, and lead to a more educated and considered response by humankind.

ACKNOWLEDGMENTS

The authors acknowledge the contributions of time and expertise of the participants at the Global Change Research Education and Training Planning Workshop for the Inter American Institute in San Diego, CA January 30 - February 1, 1997. This effort is supported by a planning grant from NSF/IAI, and by the NASA/USRA ESSE Program.

REFERENCES

[1] The Inter-American Institute WWW Home Page http://geoserver.geo.nsf.gov/iai/

[2] Johnson, D. R., M. Ruzek, M. Kalb, 1995: "Earth System Science Education - An Internet-based Electronic Curriculum" in *Proceedings of the 1995 International Geoscience and Remote Sensing Symposium (IGARSS '95)*, Florence, Italy pp. 572-574

[3] Johnson, D. R., M. Ruzek, M. Kalb "Earth System Science Education: A Continuing Collaboration" in *Proceedings of the 1996 International Geoscience and Remote Sensing Symposium*, Lincoln, NE pp. 1175 - 1177

[4] The Earth System Science Education WWW Home Page http://www.usra.edu/esse

Application of an Extended IEM To Multiple Surface Scattering and Backscatter Enhancement

Chin-Yuan Hsieh1 and Adrian K. Fung2
1E.C.E. Dept., National Kaohsiung Marine Institute of Technology, Kaohsiung, Taiwan
Tel:+886-7-3451711, FAX:+886-7-3452492
2E.E. Dept., Box 19016, University of Texas at Arlington, TX 76019
Tel: 817-2733422, FAX 817-273-3443, eefung@uta.edu

Abstract- In the late 1980s backscattering enhancement and strong depolarization of waves scattered from randomly rough Gaussian surfaces with large rms slopes were observed in optical and millimeter measurements. It was noted that backscattering enhancement was most prominent, when the surface rms slope was of the order of unity, a condition under which multiple surface scattering may dominate. In this study an extended IEM model which includes surface multiple scattering called integral equation model with multiple scattering (IEMM) is applied to interpret this phenomenon. According to this model the conditions for significant multiple surface scattering to occur are (1) the normalized surface height $k\sigma > 1$ and (2) the surface rms slope > 0.5. In the analysis of multiple scattering from very rough surfaces it is found that there is a sharp but small peak in the specular direction also. This observation comes directly from the IEMM model and is partially confirmed by the data reported by Ishimaru. Further comparisons of IEMM with experimental data acquired from very rough surfaces show excellent agreements in bistatic scattering including backscattering enhancement.

INTRODUCTION

The surface scattering model based on an integral equation method [1] was extended to include multiple surface scattering [2] for surfaces with significant rms slopes and roughness by considering the propagation effects due to the phase term in the Green's function. This allows the upward and downward scattered fields to be identified and consequently properly shadowed to produce the correct amount of multiple scattering. Comparisons were made over a significant range of frequency and angles with data collected under controlled conditions from statistically known surfaces which confirm the extended model.

In this paper we want to establish some guidelines regarding the condition under which multiple surface scattering would be significant and verify the phase interference effect due to the multiple-scattered waves that generate the phenomenon known as backscattering enhancement in the literature. The expressions for the surface scattering coefficients for like and cross polarizations of moderately rough surfaces can be found in [2]. The bistatic scattering coefficients for surfaces with large rms height and correlation length relative to the incident wavelength are given in the next section.

SCATTERING COEFFICIENT

In this section we provide the multiple scattering terms of the bistatic scattering coefficient for randomly rough surfaces with large surface roughness parameters. The readers are referred to [1] for single scattering terms in the same scattering coefficient and to [2] for the bistatic scattering coefficients for moderately rough surfaces.

Expressions For Large Roughness Condition

We let the surface rms slope be $rss = \sigma\sqrt{|\rho''(0)|}$, $cs = \cos\theta$ and $css = \cos\theta_s$. To restrict to radiation modes we require $cs > q, cs > qp$, $css > q, css > qp$ and $qp \geq 0$.. Now, let θ denote the incident angle along the reference azimuthal plane, $\phi = 0$; and θ_s, ϕ_s denote the scattering direction. Furthermore, let

$$s = \sin\theta,\quad ss = \sin\theta_s,\ sfs = \sin\phi_s,\quad csfs = \cos\phi_s$$

$$c1[q, qp] = (cs + q)(cs + qp)$$

$$c2[q, qp] = (cs + q)(css - qp)$$

$$c3[q, qp] = (css - q)(css - qp),$$

$$c4[q, qp] = (css - q)(cs + qp).$$

$$rr1[q] = c1[q, css],\ rr2[q] = c3[q, -cs]$$

$$\arg 1 = \frac{(ss\ \text{csfs} + u)^2 + (ss\ \text{sfs} + v)^2}{2(rss)^2}$$

$$\arg 2 = \frac{(s + u)^2 + v^2}{2(rss)^2},$$

$$ar[q, qp] = -(k\sigma)^2(css - cs - q - qp)^2 \text{ and}$$

$$qp = \sqrt{1 - (u + ss\ \text{csfs+s})^2 - (v + ss\ \text{sfs})^2}.$$

Then, the multiple scattering terms in the bistatic scattering coefficient are given by the sum of the three terms,

$$\sigma_{qp}^{m} = \sigma_{qp}^{kcm} + \sigma_{qp}^{c1m} + \sigma_{qp}^{c2m} \tag{1}$$

where

$$\sigma_{qp}^{kcm} = \frac{S(\theta)S(\theta_s)Re\{f_{qp}{}^{*}}{4\pi(rss)^4}\iint F_{qp}(u, v)$$

$$\left\{\left[\frac{0.5}{c1[css,css]c2[q,q]}\right][1-S(u,v)]\right.$$

$$Exp\left[-\frac{\arg 1}{rr2[q]}-\frac{\arg 2}{rr1[q]}\right]$$

$$+\left[\frac{0.5}{c1[css,css]c2[-q,-q]}\right]S(u,v)$$

$$\left.Exp\left[-\frac{\arg 1}{rr2[-q]}-\frac{\arg 2}{rr1[-q]}\right]\right\}dudv\Bigg\} \tag{2}$$

$$\sigma_{qp}^{c1m}=\frac{0.25S(\theta)S(\theta_s)}{16\pi(rss)^4}\{\int\int|F_{qp}(u,v)|^2$$

$$\left\{\left(\left[\frac{S(u,v)}{c1[-q,-q]c3[-q,-q]}\right]exp\left[-\frac{\arg 1}{c3[-q,-q]}-\frac{\arg 2}{c1[-q,-q]}\right]\right.\right.$$

$$+\frac{S(u,v)}{c1[-q,q]c3[-q,q]}exp\left[-\frac{\arg 1}{c3[-q,q]}-\frac{\arg 2}{c1[-q,q]}\right]\Bigg)$$

$$+\left(\frac{[1-S(u,v)]}{c1[q,-q]c3[q,-q]}exp\left[-\frac{\arg 1}{c3[q,-q]}-\frac{\arg 2}{c1[q,-q]}\right]\right.$$

$$\left.\left.+\frac{[1-S(u,v)]}{c1[q,q]c3[q,q]}exp\left[-\frac{\arg 1}{c3[q,q]}-\frac{\arg 2}{c1[q,q]}\right]\right)dudv\right\} \tag{3}$$

$$\sigma_{qp}^{c2m}=\frac{0.25(S(\theta)S(\theta_s))}{16\pi(rss)^4}\{$$

$$\int\int F_{qp}(u,v)F_{qp}(-u-ss\ \mathrm{csfs}-s,-v-ss\ \mathrm{sfs})$$

$$\left\{\left(\left[\frac{exp\{ar[-q,-qp]\}}{c2[-q,-qp]c4[-q,-qp]}\right]\right.\right.$$

$$exp\left[-\frac{\arg 1}{c4[-q,-qp]}-\frac{\arg 2}{c2[-q,-qp]}\right]$$

$$+\frac{exp\{ar[-q,qp]\}}{c2[-q,qp]c4[-q,qp]}$$

$$\left.exp\left[-\frac{\arg 1}{c4[-q,qp]}-\frac{\arg 2}{c2[-q,qp]}\right]\right)S(u,v)$$

$$+\left(\frac{exp\{ar[q,-qp]\}}{c2[q,-qp]c4[q,-qp]}exp\left[-\frac{\arg 1}{c4[q,-qp]}-\frac{\arg 2}{c2[q,-qp]}\right]\right.$$

$$\left.+\frac{exp\{ar[q,qp]\}}{c2[q,qp]c4[q,qp]}Exp\left[-\frac{\arg 1}{c4[qp,q]}-\frac{\arg 2}{c2[q,qp]}\right]\right)$$

$$\left.[1-S(u,v)]dudv\right\} \tag{4}$$

Multiple surface scattering terms appear in the form of a two dimensional integration with respect to the spectral variables u and v. These variables originate from the Green's function and can be interpreted to represent the direction of scattering. In this case the cotangent in the shadowing function should be represented by [Fung, 1994]

$$\cot\theta=\sqrt{(k^2-u^2-v^2)/(u^2+v^2)} \tag{5}$$

To remind the reader of this change we have used the symbols $S(\theta)$ and $S(u,v)$ to distinguish the two forms of the shadowing function needed in the average power expressions.

THEORETICAL RESULTS

In Fig. 1 we show calculations of the scattering coefficients including and excluding the multiple scattering terms with several values of the rms height normalized to the wave number, $k\sigma$. It is seen that the multiple scattering terms do not contribute to 1 dB or more until this parameter exceeds 1. In Fig. 2 we show another plot where we vary the rms slope of the surface. For the multiple scattering terms to contribute to a dB or more we see that the rms slope must be at least 0.5 or more.

COMPARISONS WITH DATA

In Fig. 3 and 4 we show comparisons with like and cross bistatic scatterings from a randomly rough surface with parameters as indicated on the figures. It is clear that for such a rough surface there is a clear narrow peak in the backscattering direction for both the like and the cross polarizations. It is believed that this is due to coherent interference in a constructive way that is repsonsible for the peak. The theoretical scattering coefficient given in (1) indicates that there is actually a smaller peak in the specular direction also due to a similar physical mechanism as the one causing the backscattering enhancement.

CONCLUSIONS AND DISCUSSION

The above results indicate that for very rough surfaces some spots on the surface may act as a corner reflector which causes a strong reflection in the backscattering direction. For this to occur the roughness must be larger than the incident wavelength and there must be a rms slope around 0.5 or more. As in the case of a corner reflector having a large slope alone is not enough. We need the surface parameters to be large relative to the incident wavelength also.

[1] A.K.Fung, "Microwave Scattering and Emission Models and Their Applications", Artech House, 1994

[2] C.Y. Hsieh, A. K. Fung, G. Nesti, A. Sieber and P. Coppo, "A further study of the iem surface scattering model",IEEE GRS 1997 in press.

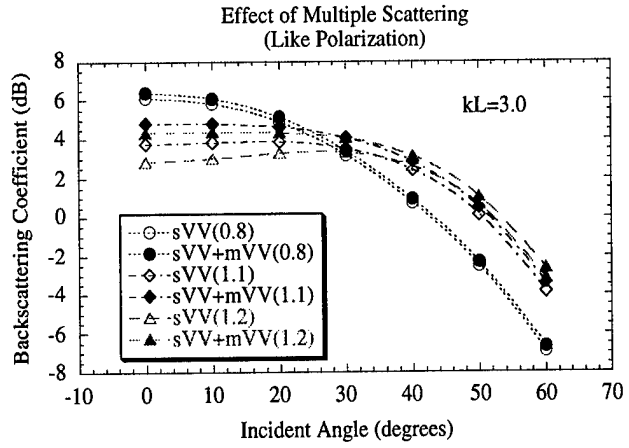

Figure 1. The normalized rms height $k\sigma$ is changing from o.8 to 1.2 in vertical polarization.

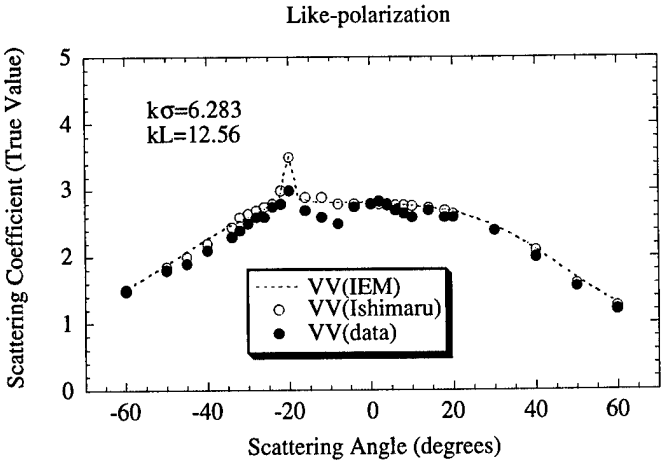

Figure 3. Comparison with millimeter wave data taken from perfectly conducting surface with rms slope of 0.7.

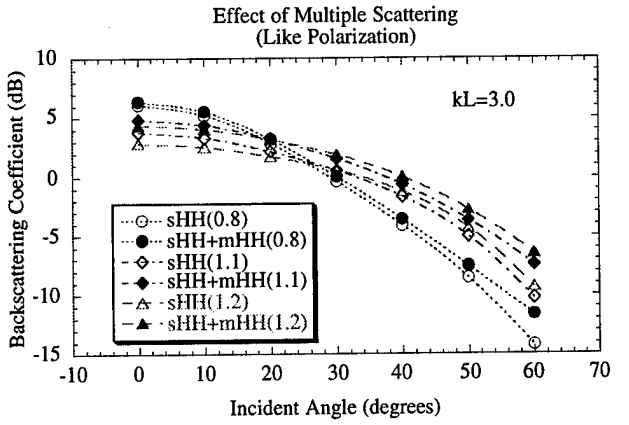

Figure 2. Three surface rms slopes, 0.38, 0.52, and 0.57, are shown

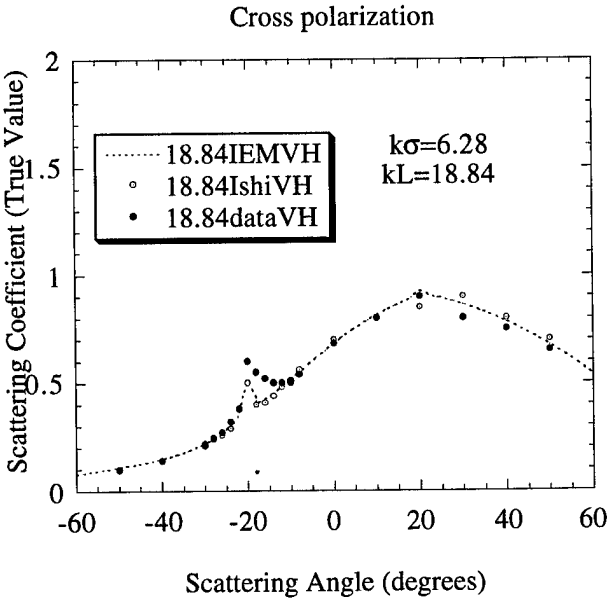

Figure 4. Comparison with millimeter wave data taken from perfectly conducting surface with rms slope of 0.47.

Numerical Study of Shadowing in Electromagnetic Scattering from Rough Dielectric Surfaces

James C. West, J. Michael Sturm
School of Electrical and Computer Engineering
Oklahoma State University, 202ES, Stillwater, OK 74078, USA
Voice: 405/744-6096, FAX: 405/7555-9198, Email: jwest@master.ceat.okstate.edu

Abstract— **A numerical study has been performed to examine the effects of surface self-shadowing on the electromagnetic scatter from rough dielectric interfaces. A hybrid numerical technique combining the moment method and geometrical theory of diffraction was used in the numerical calculations. This technique was first extended to be applicable to general dielectric media as well as perfectly conducting and high loss, high permittivity surfaces. The numerical calculations show that weakly shadowed small-scale roughness can contribute significantly to the backscatter at extreme grazing angles. This effect is more pronounced at VV polarization than at HH polarization when the surface is perfectly conducting, but is approximately the same at both polarizations when a finite-conductivity interface is considered. Scattering models that depend on a shadowing function based on geometrical optics are likely to fail at extreme grazing angles for lossy dielectric as well perfectly conducting scattering surfaces.**

INTRODUCTION

We have performed a numerical study to investigate the validity of geometrical-optics based shadowing theory when applied to surfaces whose dielectric properties approximate both that of soil of differing moisture content as well as that of sea water. A numerical approach based on the hybrid MM/GTD technique was used to find the scattering from two-scale rough surfaces that allowed the shadowing to be controlled. The numerical technique was first extended to allow the application to low-loss, homogeneous dielectric scattering media. It was then applied to two-scale rough interfaces that had random small-scale roughness superimposed on a deterministic large-scale displacement. The scattering with small-scale roughness both included and not included in the shadowed regions was calculated and compared, giving an estimate of the importance of the shadow-region roughness.

This work was supported in part by the Air Force Office of Scientific 1995 Summer Research Extension Program and the Office of Naval Research under contract N00014-96-1-0075.

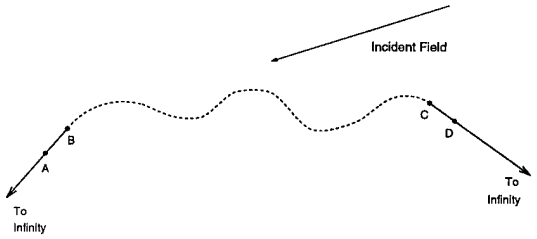

Figure 1. Arbitrary scattering surface.

NUMERICAL TECHNIQUE

The numerical technique used is a hybrid approach that extends the moment method using the geometrical theory of diffraction (MM/GTD technique). It is applied to one-dimensionally rough surfaces of the form shown in Fig. 1. The extension of the surface to infinity eliminates the artificial edges that limit the application of standard MM to moderate grazing incidence angles. MM is extended using GTD to treat the infinitely extending surface. Three different implementations of the technique are used in this work. The first is designed for perfectly conducting surfaces while the second treats high dielectric constant, high conductivity surfaces using impedance boundary conditions. These are described in detail by West [1] and West *et al.* [2] respectively.

A third implementation of the hybrid MM/GTD technique was developed for treating the scattering from low dielectric constant and/or low conductivity scatterers. In this case the surface is treated using the approach of Arvas *et al.* [3], as shown in Fig. 2. The scattering problem, shown in the left illustration of Fig. 2, is separated into external and internal equivalents, as shown in the middle and right illustration, respectively. The scattering problem is divided into internal and external equivalent problems. In the external problem the region is homogeneous with the dielectric properties of free space. Equivalent electric (**J**) and magnetic (**M**) surface currents are chosen on the obstacle boundary to yield the scattered field outside the obstacle and zero field inside. Similarly, a homogeneous medium with the properties of the scattering obstacle are

0-7803-3836-7/97/$10.00 © 1997 IEEE

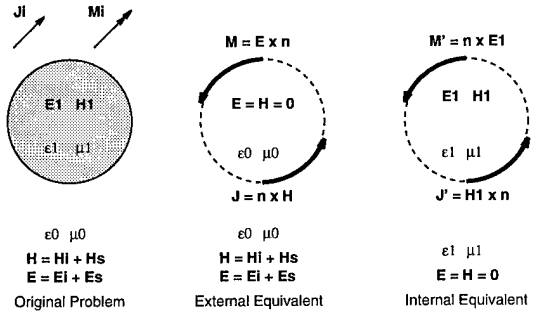

Figure 2. External and internal equivalent problems.

used in the internal equivalent. Equivalent currents ($\mathbf{J}'$ and $\mathbf{M}'$) are chosen to give the correct internal field with zero external field. Application of the surface boundary conditions shows that $\mathbf{J} = -\mathbf{J}'$ and $\mathbf{M} = \mathbf{M}'$, so only $\mathbf{J}$ and $\mathbf{M}$ need be determined.

The moment method is used to solve for both $\mathbf{J}$ and $\mathbf{M}$. The interaction matrix is established to force the sums of the incident fields (both electric and magnetic) and the fields radiated by $\mathbf{J}$ and $\mathbf{M}$ to be zero just within the obstacle in the external problem and the fields radiated by $-\mathbf{J}$ and $-\mathbf{M}$ to be zero just outside the obstacle in the internal problem. Solving both the internal and external problems simultaneously gives $\mathbf{J}$ and $\mathbf{M}$. The integral equations that give the correct scattered fields are given by Arvas *et al.* [3].

In a hybrid MM/GTD implementation of the Arvas *et al.* technique, little is known about the currents between points A and D in Fig. 1, so the standard MM approach of using pulse basis functions and point matching is used to describe the currents in this region. Beyond these points the fields in the vicinity of the extensions can be accurately described from GTD as the sum of the geometrical optics incident and reflected fields (assuming the extension is not shadowed from the incident field) plus a field diffracted from point B or C. The diffracted field is known from GTD to be ray optical sufficiently far from the diffraction point. Application of the surface boundary conditions to these fields on the extensions gives the physical optics (PO) currents (known *a priori*) plus currents (electric and magnetic) associated with the diffracted the field. Since the PO currents are known they need not be described by MM basis functions; they are entirely accounted for by treating their re-radiation as a field source term. On the other hand, the diffracted field currents are not entirely known and must be described by basis functions. Applying the boundary conditions to the GTD ray optical fields shows that they may be entirely described to infinity by the basis functions

$$J^d_{VV}, M^d_{HH} = \frac{e^{-jkr}}{\sqrt{r}}, \quad (1)$$

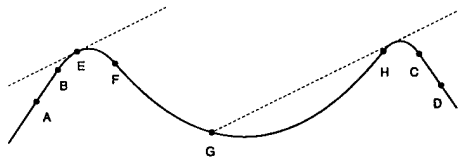

Figure 3. Large-scale scattering surface. The dashed lines show the shadow boundaries with 10° grazing illumination.

$$J^d_{HH}, M^d_{VV} = \frac{e^{-jkr}}{r^{1.5}}, \quad (2)$$

where VV indicates vertical incident and scattered polarization, HH is horizontal polarization, k is the electromagnetic wave number, and r is the distance from the diffraction point to the point on the extension. The computational overhead of the MM/GTD approach compared to standard MM is only moderate since single basis functions are used to describe the unknown currents to infinity.

The validity of the arbitrary-dielectric MM/GTD technique was confirmed by comparison with the scattering predicted by the impedance-boundary implementation under conditions where both are expected to be valid. The scattering from a rounded-apex dielectric wedge (internal angle of 120° and apex radius of 1 λ, $\epsilon_R = 30 - j1$) agreed to within 0.5 dB under most incident angles of interest. The maximum difference observed was only 1.5 dB, and occurred when the backscattering was due to very small back-diffraction from the rounded apex at horizontal polarization. This small discrepancy likely occurs because the impedance boundary condition implementation of the technique is only marginally valid with this dielectric constant.

RESULTS

The scattering calculations were applied to two-scale rough surfaces of the same type used by West [1]. The large-scale displacement is shown in Fig. 3. The distance from crest to crest is 25 λ, and the height and radius of curvature of the shadowing obstacle are 3 λ and 2 λ respectively. Scattering calculations were performed with a Gaussian spectral small-scale roughness extending both from point F to point H (rough-in-shadow) and from point F to point G (smooth-in-shadow). The results are shown

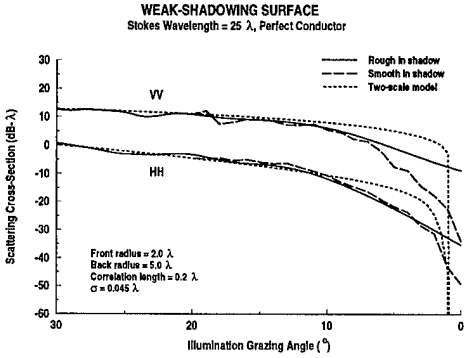

Figure 4. Backscattering from perfectly surface.

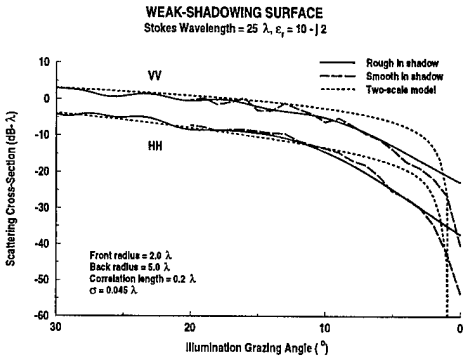

Figure 6. Backscattering with $\epsilon_r = 10 - j2$.

in Figs. 4 through 7. First examining the perfectly conducting surface (equivalent to an infinite dielectric constant), it makes little difference whether or not the small-scale roughness is included in the shadowed area when the grazing angle is above 7° and 2.5° at VV and HH polarization respectively. A GO-based shadowing function should prove adequate under these conditions. Below this angle the slightly shadowed roughness on the back crest yields significant backscatter. When the surface dielectric constant is changed to $35 - j5$ the smooth-in-shadow and rough-in-shadow scattering agrees to 2.5° grazing at both polarizations. This also proves true with a dielectric constant as low as $\epsilon_r = 3 - j0$. Also, as the dielectric constant drops the relative levels of the VV and HH backscatter become more nearly equal.

CONCLUSIONS

The numerical calculations show that weakly shadowed surface roughness can contribute to the backscatter from a rough surface at both VV and HH polarizations. This effect is most severe with perfectly conducting surfaces at VV polarization, and is approximately equal at VV and HH polarization when the surface has finite conductivity. Use of a GO-based shadowing function in a scattering theory is likely to yield inaccurate results at the smallest grazing angles.

REFERENCES

[1] J. C. West, "Effect of shadowing on electromagnetic scattering from rough ocean-wave-like surface at small grazing angles", *IEEE Transactions on Geoscience and Remote Sensing*, vol. 35, no. 2, pp. 293–301, Mar. 1997.

[2] J. C. West, J. M. Sturm, and S. Ja, "Low-grazing scattering from breaking water waves using an impedance boundary mm/gtd approach", *IEEE Transactions on Antennas and Propagation*, 1997, under review.

[3] E. Arvas, S. M. Rao, and T. K. Sarkar, "E-field solution of tm-scattering from multiple perfectly conducting and lossy dielectric cylinders of arbitrary cross-section", *IEE Proceedings*, vol. 133, Pt. H, no. 2, pp. 115–121, Apr. 1986.

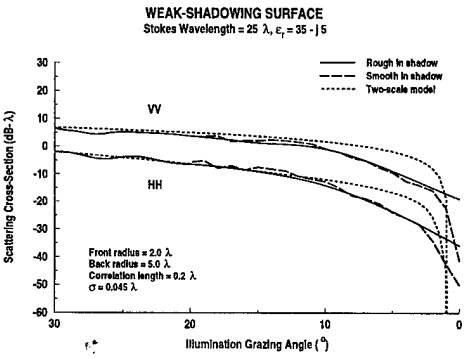

Figure 5. Backscattering with $\epsilon_r = 35 - j5$.

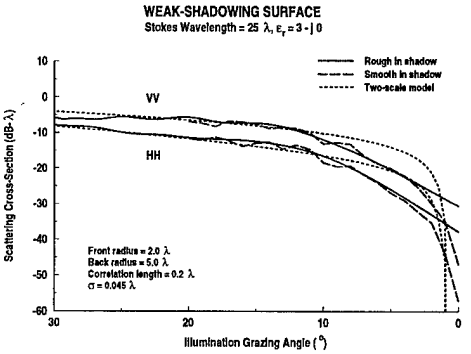

Figure 7. Backscattering with $\epsilon_r = 3 - j0$.

Precise Estimation of Surface Roughness Parameters from Field-Measured Ground Truth Data

Yisok Oh
School of Electronic and Electrical Engineering , Hong-Ik University
72-1 SangSu-dong, MaPo-gu, Seoul, Korea (121-791)
Tel:+82-2-320-1481; e-mail: yisokoh@wow.hongik.ac.kr

Abstract: Whereas it is well known that electromagnetic scattering by a random, rough surface is strongly influenced by the surface height correlation function, it is not clear as to how long a surface height profile is needed and at what interval it should be sampled in order to experimentally quantify the correlation function of a real surface. This paper presents the results of a Monte Carlo simulation conducted to answer these questions. It was determined that in order to measure the surface parameters with a precision of $\pm 10\%$, the surface segment should be at least $40\bar{l}$ - long, where $\bar{l}$ is the mean (or true) value of the surface correlation length. Shorter segment lengths can be used if multiple segments are measured and then the estimated values are averaged. The second part of the study focused on the relationship between sampling interval and measurement precision. It was found that in order to estimate the surface roughness parameters with a precision of $\pm 5\%$, it is necessary that the surface be sampled at a spacing no longer than 0.2 of the correlation length.

1. INTRODUCTION

Extraction of soil-moisture and vegetation-biomass information from imaging radar data has been a subject of intense interest for a long time. However, the technique has not been very successful, in part because of the complexity of natural soil surfaces; specifically, the difficulty estimating the surface roughness and the inhomogeneity of the soil moisture. Furthermore, theoretical and numerical models, while well suited for ideal rough surfaces, are not easy to implement for natural soil surfaces. An attempt has been made to retrieve soil moisture and surface roughness together from polarimetric radar scattering data through the use of an inversion algorithm [1]. Because the dynamic range of the backscattering coefficient associated with the surface roughness is comparable to or larger than that associated with the soil moisture, the surface roughness should be estimated accurately for retrieving the soil moisture with good accuracy. In this paper, the effect of surface roughness on radar scattering from soil surfaces is discussed, and the results of a simulation study aimed at quantifying criteria for accurate estimation of surface roughness parameters are presented.

According to experimental observations[1], whereas the height distribution of natural soil surfaces are characterized by Gaussian density functions, the measured correlation functions of the surface height profiles more closely resemble exponential functions. The angular responses of the *vv*-polarized backscattering coefficients for the exponential and Gaussian correlation functions were computed and are shown in Fig. 1 for a surface with ks=0.2, kl=2.9 and ε_r=(10,2) using the small perturbation method (SPM), where k is the wavenumber, s is the rms height, and l is the correlation length. The large difference in trend between the two curves, particularly in the higher angular range, shows the importance of the shape of the correlation function on the backscattering coefficient.

2. SIMULATION PROCEDURE

In order to examine the surface characteristics of random surfaces, several randomly rough surfaces are generated using the technique given in [2] as follows;

$$Z(k) = \sum_{j=-M}^{M} W(j)\, X(j+k) \tag{1}$$

where $Z(k)$ is the surface height distribution, $X(i)$ is a Gaussian random deviate $N(0,1)$, and $W(j)$ is the weighting function given by

$$W(j) = F^{-1}\left[\sqrt{F\left[\, C(j) \,\right]}\,\right] \tag{2}$$

where $C(j)$ is the correlation function and $F[\ ]$ denotes the Fourier transform operator. For a one-dimensional rough surface characterized by a Gaussian or an exponential correlation function, given respectively by

$$C_G(j) = s^2 \exp\left[-\left(\frac{j\Delta x}{l}\right)^2\right] \text{ and}$$

$$C_e(j) = s^2 \exp\left[-\frac{|j|\Delta x}{l}\right], \tag{3}$$

the corresponding weighting functions are given by

$$W_G(i) = \left(\frac{2\,\Delta x}{\sqrt{\pi}\ l}\right)^{1/2} s \exp\left[-2\left(\frac{i\,\Delta x}{l}\right)^2\right] \text{ and}$$

$$W_e(i) = \left(\frac{\sqrt{2\,\Delta x}}{\pi\sqrt{l}}\right) s\, K_0\left[\frac{i\,\Delta x}{l}\right], \tag{4}$$

where Δx is the sampling distance and $K_0[\ ]$ is the modified Bessel function of the second kind.

Using the above equations, randomly rough surfaces were generated for several rough surfaces. The profiles shown in Fig. 2 are for surfaces with s=0.032λ and l=0.46λ for Gaussian and exponential correlation functions, both with a Gaussian height distribution.

3. SIMULATION RESULTS

The simulation procedure described in the preceding

0-7803-3836-7/97/$10.00 © 1997 IEEE

section was used to generate surfaces of various rms heights and correlation lengths. In each case the surface profile was 1000λ long, where λ is the wavelength. These profiles were then used to determine:

(a) the relationships between the measurement precision associated with estimating the surface roughness parameters (rms height s and correlation length l) and the length of the surface height profile L (by using only specific segment lengths of the total generated profile),

(b) the improvement provided by averaging multiple segments on the estimates of s and l, and

(c) the relationship between measurement precision and sampling interval Δx.

3.1 Dependence on Segment Length

Figure 3(a) shows plots of two correlation functions calculated as in [3] for the same surface, but on the basis of segments of different lengths. It is clear from the plots that the 400λ long segment produces an exponential looking correlation function, whereas the short segment (L=10λ) produces an oscillatory function and it is accurate only for displacements shorter than 0.5λ. By repeating the process for many different surface segments of the same surface, and then calculating the rms height (standard deviation of surface height) and correlation length (displacement $j\Delta x$ such that the normalized correlation function $C_e(j)/s^2 = e^{-1}$), it was possible to calculate the standard deviations σ_s and σ_l associated with the estimates of s and l (as percentages of the true means $\bar{s}$ and $\bar{l}$). The results are displayed in Figure 3(b) which shows that σ_s and σ_l decrease in an exponential-like manner with segment length L. To determine s with $\sigma_s/\bar{s} \le 0.1$, it is sufficient to use a single segment $40l$ in length, but to estimate l with $\sigma_l/\bar{l} \le 0.1$, the segment length has to be at least $200l$ in length.

The measurement precision is improved by averaging multiple equal-length segments of the same surface. However, averaging multiple segments does not necessarily result in the same correlation function, even when the total segment length is the same. This is illustrated by the plots in Figure 4 which include the correlation function of a single 1000λ-long segment, the correlation function obtained by averaging the correlation functions of 50 segments, each 20λ in length, and by averaging the correlating functions of 100 segments with each being 10λ in length. The shorter the segment length is, the shorter is the estimated value of the correlation length.

3.2 Sampling Distance

The precision associated with the measurements of the roughness parameters s and l is also dependent on the sampling distance Δx. According to the results shown in Fig. 5, which displays the estimated values of l (in Fig. 5(a)) and s (in Fig. 5(b)) as a function of Δx (measured in units of $\bar{l}$) for a segment 1000λ in length, Δx should be no more than $0.2\bar{l}$ in order to keep the error in estimating l to within ± 5% and no more than $0.5\bar{l}$ for the same error bound when estimating s.

4. CONCLUSIONS

Simulations were generated for many random surfaces, all characterized by the same exponential correlation function. The surface rms height, s, surface correlation function and associated correlation length, l, were then evaluated numerically for surface segments extending in length from 10λ to 1000λ (correlation length of simulated surface was slightly shorter than 1λ). Based on the simulation study involving the generation of random surfaces, it is recommended that in order to measure the surface roughness parameters with a precision of about ± 10% of their mean values, the minimum segment length should be $40\bar{l}$, the total segment length (segment length L multiplied by the number of segments) should be at least $400\bar{l}$ and the sampling distance Δx should be no more than $0.2\bar{l}$ in length, where $\bar{l}$ is the true correlation length of the surface.

REFERENCES

[1] Y. Oh, K. Sarabandi, and F.T. Ulaby, "An empirical model and an inversion technique for radar scattering from bare soil surfaces", *IEEE Trans. GeoScience Remote Sensing*, vol. 30, pp. 370-382, March 1992.

[2] A.K. Fung and M.F. Chen, "Numerical simulation of scattering from simple and composite random surfaces", *J. Opt. Soc. Am. A*, vol. 2, no. 12, pp. 2274-2284, December 1985.

[3] F.T. Ulaby, M.K. Moore and A.K. Fung, Microwave Remote Sensing, Active and Passive, vol.2, Ch.11 and 12, Artech House, Norwood, MA, 1986.

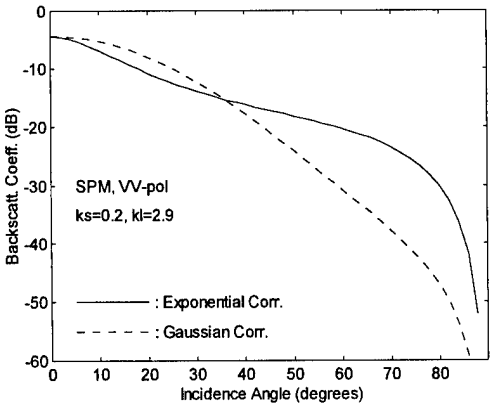

Figure 1. The effect of the correlation function on the backscattering coefficient.

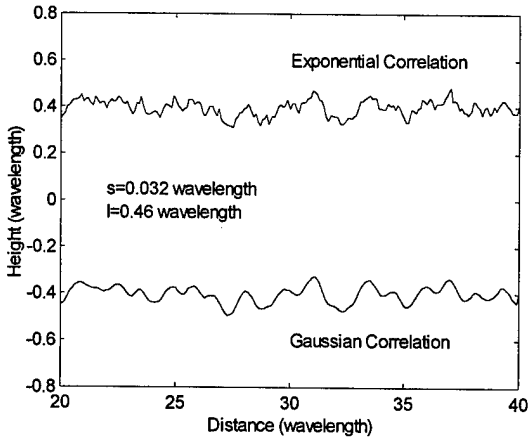

Figure 2. Surface profiles generated for both a Gaussian and an exponential correlation function.

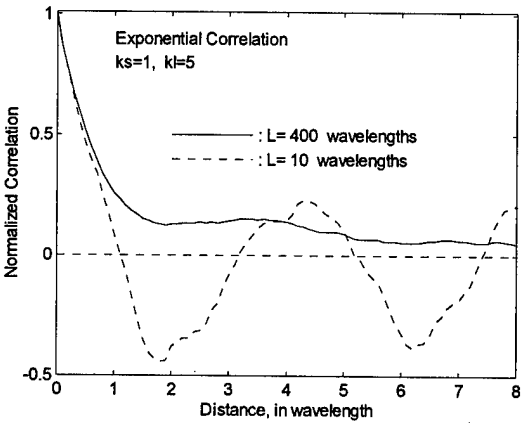

(a)

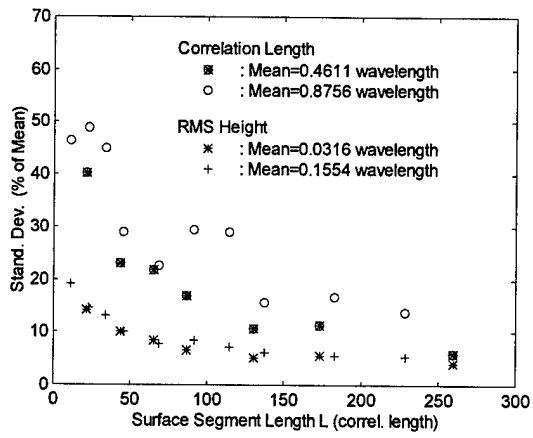

(b)

Figure 3. An exponential correlation function, (a) for two different segment sizes, and (b) standard deviations of the correlation length and the rms height as a function of segment length.

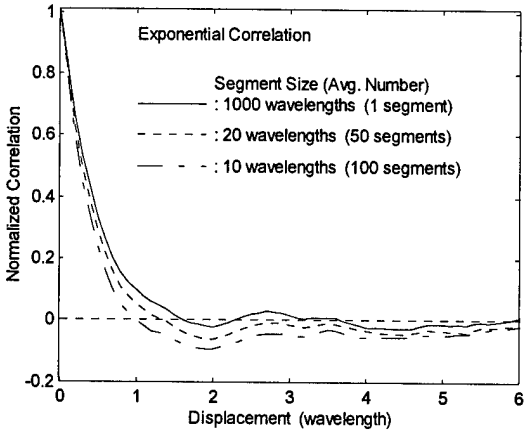

Figure 4. The dependence on segment size when generating the correlation function of the surface.

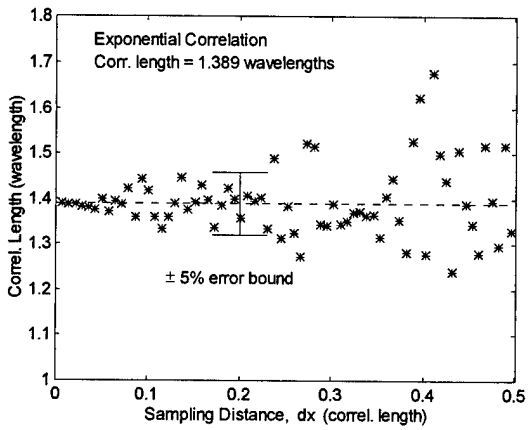

(a)

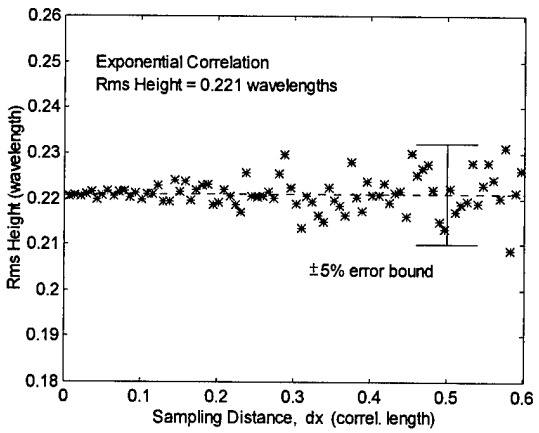

(b)

Figure 5. The effect of the sampling distance for (a) the correlation length l and (b) the rms height s.

Laboratory Study of Polarized Microwave Scattering from Steep Waves at Grazing Incidence

A. Rozenberg, D. Quigley, M. Ritter and W. K. Melville
Scripps Institution of Oceanography
University of California, San Diego, La Jolla, CA 92093-0213.
Ph. (619) 534-40478, Fax (619) 534-7132, email:melville@ucsd.edu

Abstract Laboratory measurements of the fine space-time structure of short gravity-capillary waves, as well as Ku-band scattering at grazing incidence in mechanical and wind-generated waves are presented. This study was stimulated by the need to verify the impact of nonlinear features of the surface that contribute to scattering at grazing incidence.

A scanning laser slope gauge (SLSG) was used for measuring short waves of length 0.2-20cm, and frequencies up to 150Hz. A dual polarized (VV, HH) coherent pulsed Ku-band scatterometer with 3ns temporal resolution was used to obtain Doppler spectra of the scattered signals. The simultaneous time-series for wave slope and the scattered signal, both the local Doppler frequency and amplitude, were measured along a long wave profile. Due to their different phase velocities, two-dimensional space-time filtering could be used to separate the free and bound capillary waves,

Both types of waves were found to co- and counter-propagate relative to the direction of the dominant wave propagation. Measurements of the Doppler frequency and amplitude of a scattered signal are consistent with this classification of the wave field and reveal Bragg-scattering for both types of waves. Wave breaking at the crests of the long wave packets is a possible source of the observed scatterers.

INTRODUCTION

This study is a continuation of previous laboratory measurements in the SIO wind-wave tank of dual-polarized Ku-band scattering at grazing incidence (Rozenberg et al.,1995,1996) [1,2]. Recent laboratory measurements of Ku-band scattering at grazing incidence from wind waves showed that the Doppler spectra of a scattered signal have a bimodal structure. While the first low-frequency part of the spectrum corresponds to the Bragg scattering from the free capillary waves, the high-frequency part appears to be associated with scattering from bound capillary waves at the crests of the dominant waves. To verify this interpretation and better understand scattering from the bound waves, laboratory measurements of Ku-band scattering at grazing incidence from steep short waves, as well as the fine space-time structure of the waves were made in wind-wave channels at Scripps Institution of the Oceanography (SIO) and Delft Hydraulics Laboratory. The primary goal of the present study is to measure simultaneously the parameters of the scattered signal and the fine space-time structure of the short waves, with the aim of separating free and bound waves. This work was done in several stages. At first mechanically-generated steep periodic (4 to 6Hz) waves were used to generate bound parasitic capillary waves in the SIO channel. Next wind-generated bound parasitic waves in SIO channel were produced. Finally, like Trizna et al.,1993 [3], who used a combination of 1s paddle waves and wind waves to accentuate the non-linear features of the short waves, located on the crests of the long waves, we used a combination of 3s long waves and wind waves to provide non-linear short waves in the 100m-long Delft Hydraulic channel.

EXPERIMENTAL METHODS

The experiments were conducted in the SIO glass-walled channel, which is 28.7 m long, 0.5m wide, and filled to a depth of 0.6m with fresh water, and in the Delft Hydraulics Laboratory channel, which is 100m long, 8m wide, and 2.65m in height. A coherent, 14 GHz (λ=2.1cm), dual-polarized, pulsed (3ns pulse width) scatterometer was used for obtaining the amplitude and frequency of the scattered signal. The scatterometer is described in detail in Rozenberg et. al.[1]. The scatterometer's antennas were fixed 40 - 140 cm above the water surface, with the grazing angle varying from 6 to 45 degrees. The SLSG was designed for measuring short waves with lengths from 0.1 to 20 cm and frequencies up to 150Hz. The SLSG consists of an underwater laser and scanner assembly, and the position-sensor assembly above the water surface. The 60kHz sampling rate produced two 50x300 pixel space-time images every second.

RESULTS

a) Periodic bound parasitic waves Measurements for both VV and HH polarizations and upwave-downwave directions of illumination at grazing angles from 5 to 30 degrees and 4, 5, and 6Hz waves with steepness AK up to 0.5 were taken. Typical samples of simultaneous time series from the laser slope gauge and HH and VV scattered signals for 5Hz initial waves, 15 degrees grazing angle and upwave direction of illumination are presented in Fig.1a. Note the presence of parasitic capillary waves for the slope time series: sets of very short and steep waves near the crest of each longer wave (Longuet-Higgins, 1995; Fedorov & Melville, 1997) [3,4]. The presence of high intensity harmonics (up to the 16th) is typical for slope spectra for such waves (see Fig.1a). The

0-7803-3836-7/97/$10.00 © 1997 IEEE

presence of higher harmonics is noticeable also in the time-series and spectra for HH and VV signals, but differences are also obvious. While the harmonics of the slope spectrum decrease monotonically out to the fifth harmonic, in the scattered signals the intensity of the Bragg component (n=4, λB=1.25 cm.) for both HH and VV is dominant. The wavelength of Bragg-resonant component and its Doppler shift can be found from the equations:

$$\lambda_o = 2\lambda_B \cos\psi \qquad F_D = \frac{2C}{\lambda_o}\cos\psi = F_B$$

where λ_O is the microwave length, λ_B is the Bragg-resonant wavelength, ψ is the grazing angle, F_D is the Doppler shift, and C and F_B are the phase velocity and frequency of the Bragg-resonant waves. In every case, both HH and VV scattering by parasitic bound waves is consistent with Bragg-resonance.

b) Wind generated bound parasitic waves

The corresponding data for wind waves generated by a $5ms^{-1}$ wind at 6m fetch is shown in Fig.1b. Here again the presence of bound waves on the primary wind waves is evident (see slope time series in Fig.1b). In this case, due to the quasi-random nature of the wind-waves, the harmonics in the slope spectra are not as well-defined as in the case of the mechanically-generated periodic waves (Fig.1a), but 2-D X-T images from the SLSG (not shown here) reveal the presence of "fast" bound waves. Both the time series and the Doppler spectra for the scattered signals again show strong evidence of Bragg scattering dominating around n=4, λB=1.25cm and FB=25Hz.

c) Wind- and Mechanically-Generated Waves (Delft Hydraulics channel) Measurements for both VV and HH polarizations and upwind-downwind directions of illumination at grazing incidence angles from 6 to 25 degrees, wind speeds from 2 to 12.5 ms^{-1} and 3-sec long waves with AK = 0.05, 0.1, 0.15 were made. A sample of simultaneous time series of the laser slope gauge, HH and VV scattered signals, as well as corresponding spectra, are presented in Fig.1c (upwind look direction , AK=0.1, wind speed $5ms^{-1}$). The existence of both free short waves in the trough of long waves and strongly nonlinear bound waves in areas associated with the front slope of the long waves can be observed in the 2-D X-T images from the SLSG (not shown here). It should be noted that the phase velocity of these short waves is equal to (bound to) the phase velocity of the initial 3Hz long waves. The HH and VV mean Doppler spectra (Fig.1c) are very broad; a result of the presence of many spreading factors (random wind-wave field, orbital velocity of the long waves, shadowing, ...) and Doppler peak frequencies, corresponding to free and bound waves cannot be easily separated. A spectrographic presentation (local Doppler spectra versus time) reveals the Bragg-resonant nature of scattering for both free and bond waves in this case

CONCLUSION

1. Laboratory measurements of Ku-band scattering at grazing incidence, as well as fine space-time structure of the short surface waves are presented.

2. Mechanically-generated periodic bound parasitic waves, wind generated free and bound waves in a small wind-wave channel, and combined mechanically-generated long waves and wind waves in a large wind-wave channel were used as sources of scattering.

3. It was found that the short surface wave slope field could be separated into short fast bound parasitic waves, and free gravity-capillary waves. Measurements of the Doppler frequency and amplitude of the scattered signal are consistent with this classification of the wave field and reveal Bragg-scattering for both types of waves.

REFERENCE

[1] A. D. Rozenberg, D. C. Quigley and W. K. Melville, 1995, Laboratory study of polarized scattering by surface waves at grazing incidence: Part I - wind waves, IEEE Geoscience and Remote Sensing , (33), 1037-1046.

[2] A. D. Rozenberg, D. C. Quigley, and W. K. Melville, 1996, Laboratory study of polarized scattering by surface waves at grazing incidence: Part II: the influence of long waves, IEEE Geoscience and Remote Sensing, (34), 1331-1342.

[3] D. B. Trizna, J. P. Hansen, P. Hwang, and J. Wu, 1993, Ultra wideband radar studies of steep crested waves with scanning laser measurements of wave slope profiles, Dyn. Atmosph. and Ocean., (20), 33-53.

[4] M.S.Longuet-Higgins, 1995 parasitic capillary waves: a direct calculation. J. Fluid Mech. 301, 79-107.

[5] A.V. Fedorov and W.K. Melville, 1997 Nonlinear gravity-capillary waves with forcing and dissipation. J. Fluid Mech., sub judice.

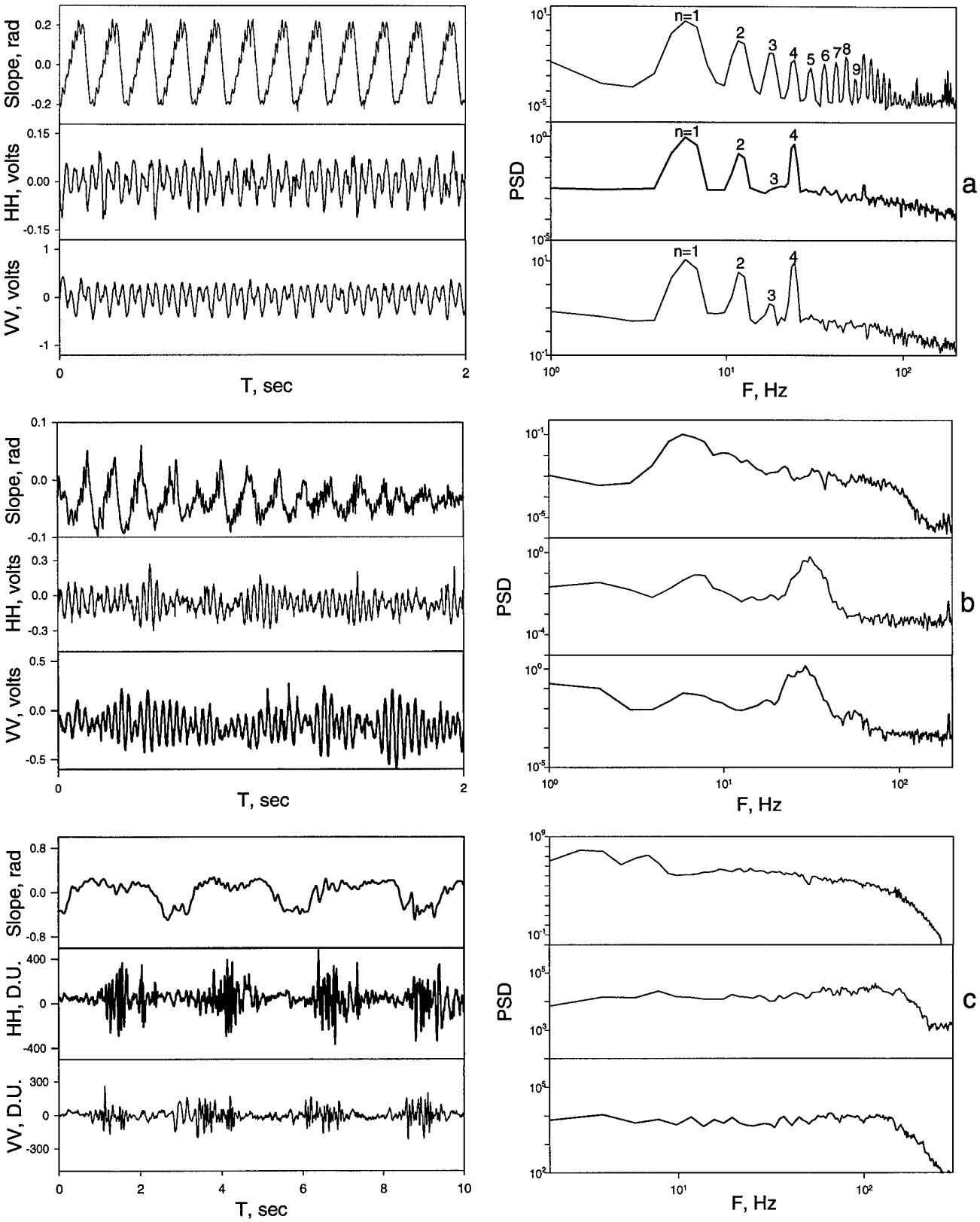

Fig. 1. Slope, HH, and VV time series (left) and spectra (right) for periodic bound waves (a), wind waves (b), and imposition of long 3sec waves and wind (c).

Inside the Sea-Spike:
Low Grazing Angle Radar Imaging of Laboratory Waves Repeatedly Breaking in Wave Groups

Jörn Fuchs, Sam Welch, Takuji Waseda, Dominic Regas and Marshall P. Tulin

Ocean Engineering Laboratory, University of California, Santa Barbara, Ca 93106
Telephone 805.893.4945, Fax 805.893.4945, E-mail joern@vortex.ucsb.edu

ABSTRACT

Backscatter characteristics of 2.3m waves breaking in wave groups have been investigated with a c-band FMCW radar (7.5cm range resolution) in the large wind-wave tank of the University of California, Santa Barbara. The purpose of these experiments was to determine the hydrodynamic sources of the sea spike and its structure. This paper covers the experimental subset of mechanically generated breaking waves with the 15% highest radar cross sections (RCS) in horizontal copolarization (HH). Four phases of the breaking process with distinct hydrodynamic characteristics were identified and correlated with synchronous radar data.

In addition to RCSs of more than $1m^2$ the breaking waves displayed concurrent copolarization ratios (HH/VV) exceeding 20dB. Synchronous high speed video images showed that these peak values appear just after a plunging jet developed at the breaker crest, well before it hit the front face of the wave. Focusing of the electromagnetic energy on the jet by the parabolic front face of the breaking wave is suggested as a mechanism yielding both high HH returns and high HH/VV ratios. The Doppler speed of the HH peaks is 80% of the initial wave speed c_0.

INTRODUCTION

"Seaspikes" are events of high radar cross section and short duration observed in low grazing angle radar backscatter from the ocean surface. They are also called "anomalous returns" because their high σ_{HH}/σ_{VV} (HH/VV) ratio cannot be explained with the standard composite model for ocean backscatter. It is known that seaspikes are associated with breaking waves, and sometimes with wave group breaking [1], and that they have their own characteristic structure [2], but details are missing. To investigate both the cause and structure of sea spikes, backscatter experiments in fresh water have been conducted in the controlled environment of the UCSB-Ocean Engineering Laboratory large wind-wave tank, 4.3m wide and 53m long, Fig. 1, utilizing waves from 1-4m long, breaking in wave groups. For these experiments a high resolution, polarimetric FMCW radar [3], at a grazing angle of 6° was used, close to the minimum reflection coefficient of vertical polarized electro-magnetic waves at 5 GHz, the radar center frequency.

The specific purpose of these experiments was to correlate high-resolution polarized backscatter with detailed observations of the wave processes as they occurred, and thereby to determine as precisely as possible the hydrodynamic sources of the sea spike and its temporal structure.

INSTRUMENTATION

The FMCW c-band radar [7], is calibrated, linearly polarized, and has a range resolution down to 3.75cm. In the experiments described here the radar was used with a chirp from 4-6 GHz, corresponding to a range resolution of 7.5cm. Horizontal and vertical polarizations are transmitted alternately, with a combined pulse repetition rate of 1kHz. The 3dB beam width is 0.5m at the center of the footprint at 10m range.

Radar synchronous surface truth instrumentation consisted of a side looking 1kfps digital video camera, two regular 60 Hz video cameras, a 5fps 35mm camera and a wave wire array with 14 wires. The high-speed camera focused at the center of the tank at 10m range and covered an area of roughly 0.5m in range. The wave wire array was at the side of the tank allowing us to profile the waves at 8-12m range from the radar.

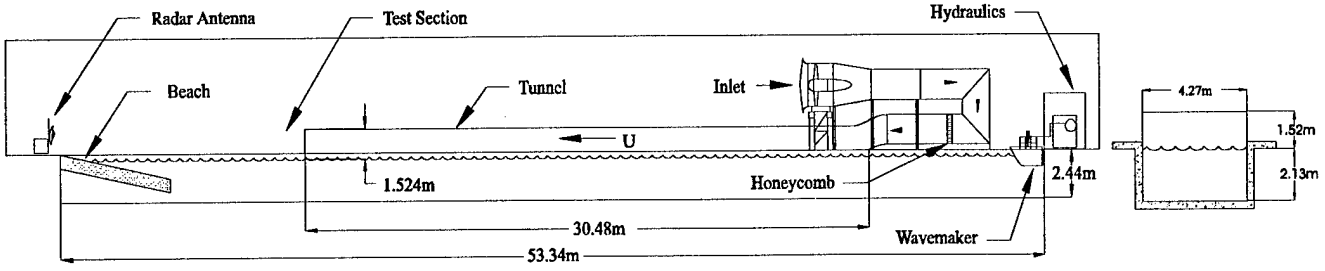

Figure 1: Large Wind-Wave-Tank at the University of California, Santa Barbara. The radar test section is at 10m range.

0-7803-3836-7/97/$10.00 © 1997 IEEE

WAVES

A programmable wavemaker generated three free gravity waves, including an initially dominant central (carrier) wave plus two low energy sidebands differing from the carrier frequency by (±) about 10%. This three wave system evolves continuously down tank as a consequence of non-linear (Benjamin-Feir) instability [4], the sidebands gaining energy at the expense of the carrier waves; strongly modulated wave groups result, each containing about five waves, depending on wave steepness. Individual waves passing through the strong central peak of these wave groups, are caused to deform with strong front face steepening and then to break [5], with the formation of small plunging jets at the wave crest, Fig 2.

The initial sideband steepness, $(ak)_0$, was adjusted so that the waves broke energetically at fetch 40m (10m range to the radar) as well as repeatedly at somewhat shorter fetches. Observations show that after some duration of wave making the strength of these breaking events and the appearance of the breakers varies widely, and seems determined both by the phase of the individual wave relative to the wave group peak, and by turbulent scars left in the water by previous breakers. Neither do the waves generally break in a strictly two dimensional pattern across the tank, cyclical patterns being observed in which alternate breaking occurs at the sides and then at the tank center in the narrow radar footprint. The center breakers were energetic and strongly resemble the kind of three-dimensional breakers observed in the open ocean, [6], and these were used during the present tests.

In the process of breaking at the group peaks, the waves first deform, the front face steepening and becoming increasingly concave and eventually vertical near the crest, which continually sharpens, with the eventual formation of small transverse scallop-like instabilities; this we call the STEEPENING-CRESTING phase, Fig. 2a. This is followed by the PLUNGING JET phase, wherein a small jet forms at the crest, Fig. 2b, grows, Fig. 2c, and plunges downward until it touches the concave front surface of the wave, Fig. 2d, at a point generally lower than the crest by not more than 40% of the total wave height, depending on the breaker strength. This begins the SPLASHING-PLOUGHING phase, Fig. 2e, wherein the plunging jet, with a severity depending on its strength, enters the water moving forward and downward, entraining air to some depth, and ahead of it throwing water upwards and forward due to a strong plowing action, Fig. 2f. The now submerged jet in this way creates a new front ahead of it, followed by a strongly turbulent region between this new front and the old wave crest, Fig. 2g. With the subsidence of the active splashing jet and its turbulent underwater structure, a weaker turbulent DECAYING SCAR phase ensues in the water, Fig. 2h, in which the scar moves more and more slowly and less energetically relative to the wave, resulting finally in quieting of the surface and the formation in the ocean of a thin foam layer until another breaking cycle occurs in the same vicinity.

EXPERIMENTS

A large number of synchronized experiments using waves from 1-4m long, and initial steepnesses, $(ak)_0$, from 0.12 to 0.20 have been carried out, and the statistical variation in returns studied, including some effects of wind. For present purposes, a data subset of the 15% highest radar cross sections (RCSs) of 2.3m waves, $(ak)_0 = 0.165$, no wind, were used. These generally produced maximum RCSs well above $1m^2$ in HH (equivalent in these experiments to normalized cross sections over 30dB) with concurrent HH/VV ratios exceeding 20dB, which correlated with the appearance of energetic breaking jets.

RESULTS

Surface truth data, such as photos and video images have been omitted from this paper for space reasons. Instead Fig. 2 shows silhouettes of a typical breaking wave from the data subset described here. The letter indices are used to correlate the wave shapes with the range-time diagrams in Figs. 3-6.

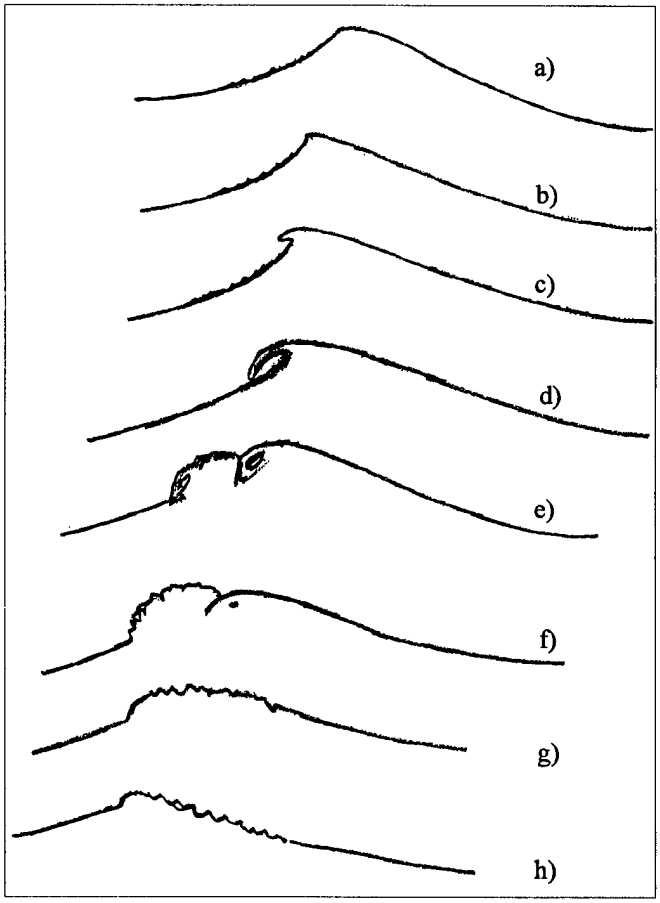

Figure 2: Different phases of the breaking process of a 2.3m plunging breaker. The shapes were sketched from video images.

Figs. 3-7 show radar data of a single breaking wave. Figs. 3-6 show range-time diagrams of amplitude and speed of the copolarizations,. Fig. 7 shows range integrated cross-sections of HH and VV on top and the HH/VV ratio on the bottom.

In the STEEPENING-CRESTING phase, non-compact targets first appear in a spatial region around and in front of the wave crest, which narrows with time as jet inception is approached, Figs. 2a and 4, coincident with rapid steepening of the front face of the wave; the peak RCS in this region rises some 15dB above background in HH and 10dB in VV, while HH/VV rises quickly to about 0dB, Fig. 7. This is accompanied by an increase in both HH and VV Doppler speeds from the speed of Bragg waves in the wave troughs, to values consistent with Bragg wave convection by increasing orbital velocities near the steepening crest. This is followed by a further increase of above 10dB in HH, 5dB in HH/VV, and increases in Doppler speed to about 80% of the linear wave speed, c_0 (1.89m/sec for a 2.3m wave), while a compact target emerges somewhere near the wave crest.

Peak HH and HH/VV ratios appear in the PLUNGING JET phase, in which there occurs within 5-10% of a wave period a rapid rise of over 10dB in HH to RCSs between 1-10m^2, with rises in local HH/VV to over 25dB, while the Doppler speed remains at about $0.8c_0$. This initial peak is often but not always followed by several concurrent oscillations in both HH and HH/VV, which however always remains well above 0dB, and an increase in Doppler speed to values around c_0. See Figs. 5 and 6. The target is compact throughout (3dB width in range is about 7.5cm).

In the SPLASHING-PLOUGHING phase, multiple targets appear in range within a slowly widening region, which can be somewhat correlated with the splash structure on the water between the original crest and the new front. The HH Doppler speeds remain around c_0 and partially higher, while the VV speeds later in the phase, decline from that value. The highest Doppler speeds of the breaking process, reaching $1.3c_0$, are seen in front of the track, with cross sections in HH 5-10dB below the peaks in the previous phase. The HH and VV returns seem to de-correlate, a stronger structure appearing in HH. Returns in HH drop into a range roughly between 0.1 and 1m^2 and about 10dB lower in VV and even 20dB lower at HH peaks. Unusually large HV/VV ratios of 0dB are observed.

As the deformed, broken wave disappears in the DECAYING SCAR phase to be replaced by an HH invisible, unbroken wave, cross-sections slowly return to background values, somewhat faster in HH, and the HH/VV ratio returns to values between 0 and -10dB. The Doppler speed drops to below 1m/sec.

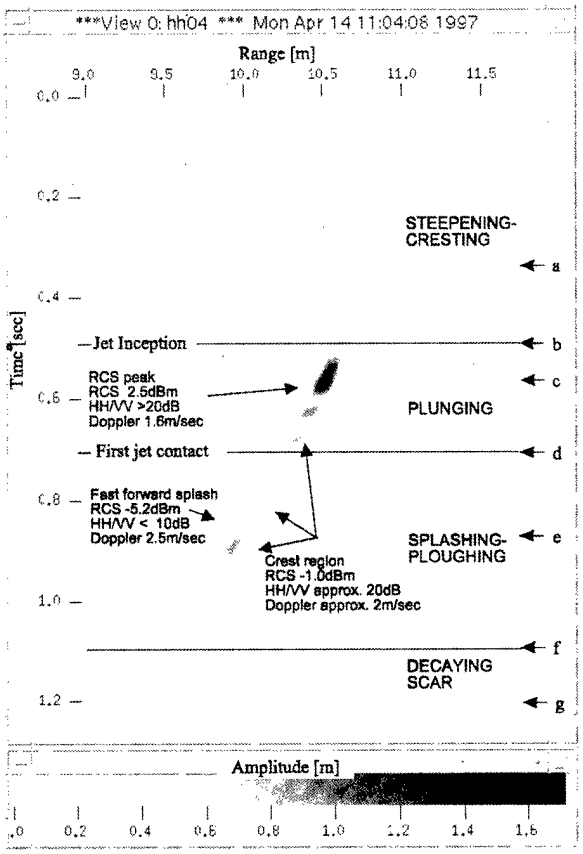

Figure 3: Range-Time-Amplitude diagram of the HH backscatter of a 2.3m breaking wave, c_0=1.89m/sec.

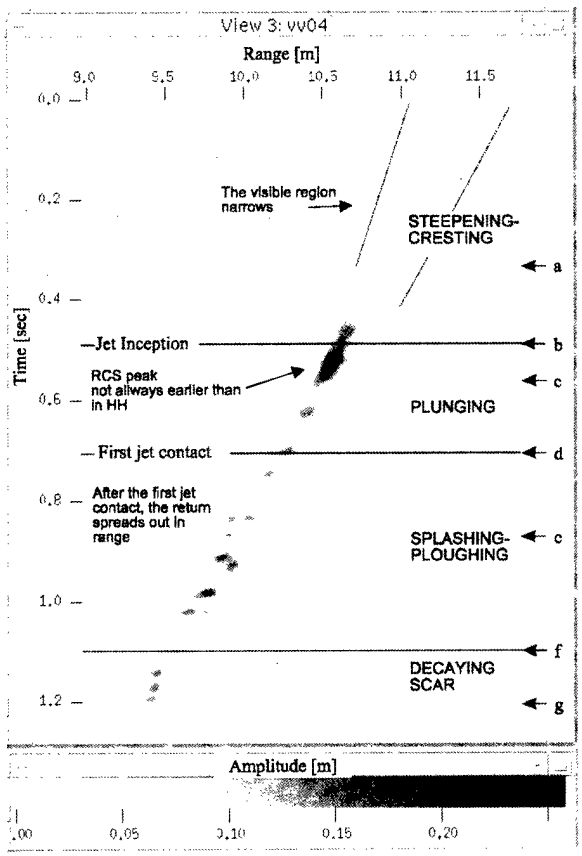

Figure 4: Range-Time-Amplitude diagram of the VV backscatter of a 2.3m breaking wave, c_0=1.89m/sec.

INTERPRETATION and CONCLUSIONS

At the onset of wave deformation and front face steepening, between points (1) and (2) in Fig. 7, HH & VV Bragg return from the turbulence ruffled wave face, in a narrowing but finite region, in front of the wave crest, Fig. 2a, grows rapidly as the incidence angle between the radar vector and the front face of the wave increases. The fact that the steepening wave is almost invisible in HH in early CRESTING is due to the small scale of the surface roughness and the low angle of incidence. The only cause of roughness in the absence of wind being previous breakers, these relatively small disturbances can only be detected with VV because the sensitivity to Bragg of VV exceeds HH at small angles of incidence by several orders of magnitude. The growing Doppler speed in this region is evidence of the increase in wave orbital velocities as the wave steepens. Eventually HH/VV approaches 0dB suggesting incidence angles well beyond 45°; the concurrent HH RCS is about 0.01 m^2.

With the sharpening of the wave crest, and as the front face approaches 90° incidence locally below the wave crest, and with the appearance of vertical, instability structures at the crest, the RCS in both HH and VV increases substantially beyond the Bragg return, see pt. (3) in Fig. 7. We hypothesize that this is due to scattering from the wave crest region, which appears as a compact target, resulting in HH/VV somewhat greater than 0dB and with HH RCS around 0.1m^2. This ends the STEEPENING-CRESTING phase.

The VV RCS reached at the end of this last phase are on average not enhanced in the next, PLUNGING-JET phase, suggesting a continuation of direct scattering from the crest region, but now including the jet which emerges there. In contrast to VV, however, the rapidly enhanced HH RCS (1-10 m^2) and extremely high HH/VV ratios (exceeding 27dB locally) which accompany jet plunging, see pt. (4) in Fig. 7, suggest a different HH scattering source and mechanism than in previous phases. This compact source of scattering seems most likely to be the plunging jet itself, which has a thickness of the order of 1 cm and lengths from 1-10 cm, although subject to aeration and fragmentation.

The continuous rise in HH, combined with extremely high values of HH/VV virtually guarantee that this compact target is being observed by the radar in HH along multiple paths, involving reflection between the radar and the target from the water surface, while VV is absorbed at these low grazing angles. This explanation of the "anomalous" HH/VV ratios was offered long ago [8]. The simplest multiple path model, an isotropic target above flat water, with Brewster damping, predicts a maximum HH/VV cross section ratio of about 14dB. This old model has been cited very recently in an investigation of sea clutter [9]. The observation of HH/VV ratios as high as 27dB in these experiments, with frequent observations of range integrated values of 20dB at HH peaks

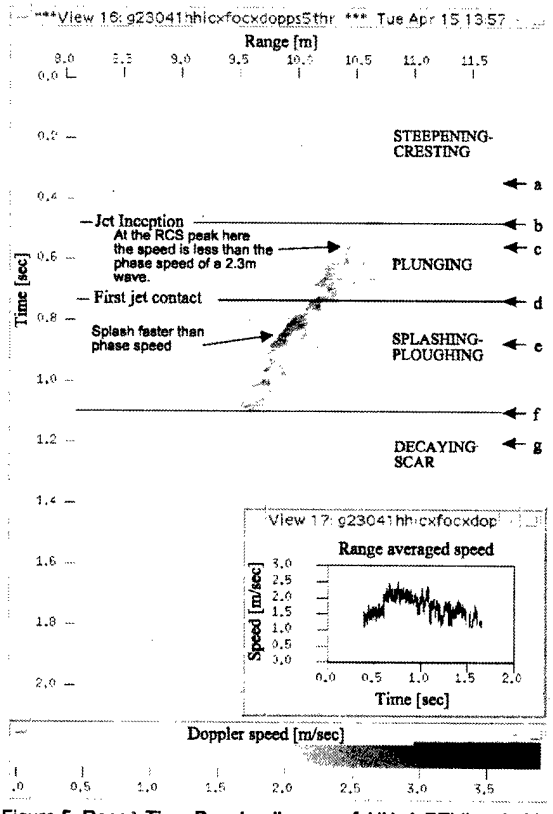

Figure 5: Range-Time-Doppler diagram of HH. A RTI threshold of -23 dbm^2 was used to eliminate weaker signals.

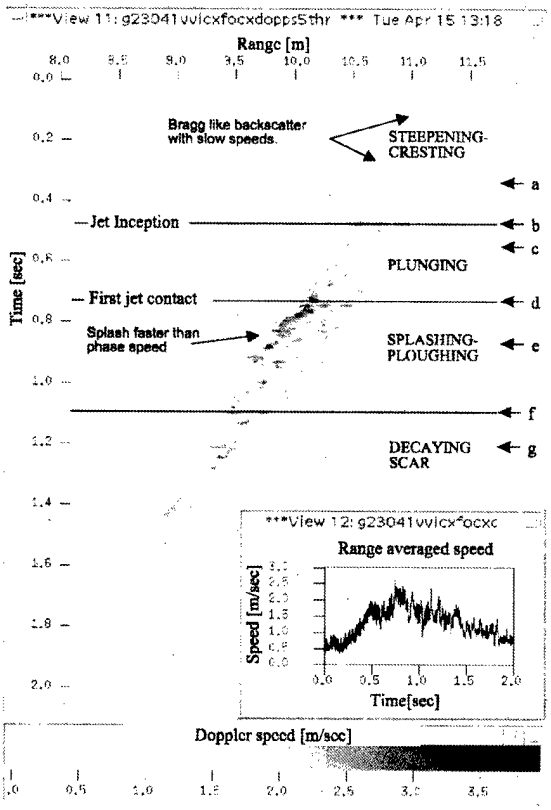

Figure 6: Range-Time-Doppler diagram of VV. A RTI threshold of -40 dbm^2 was used. Letters on the right correspond to Fig.2.

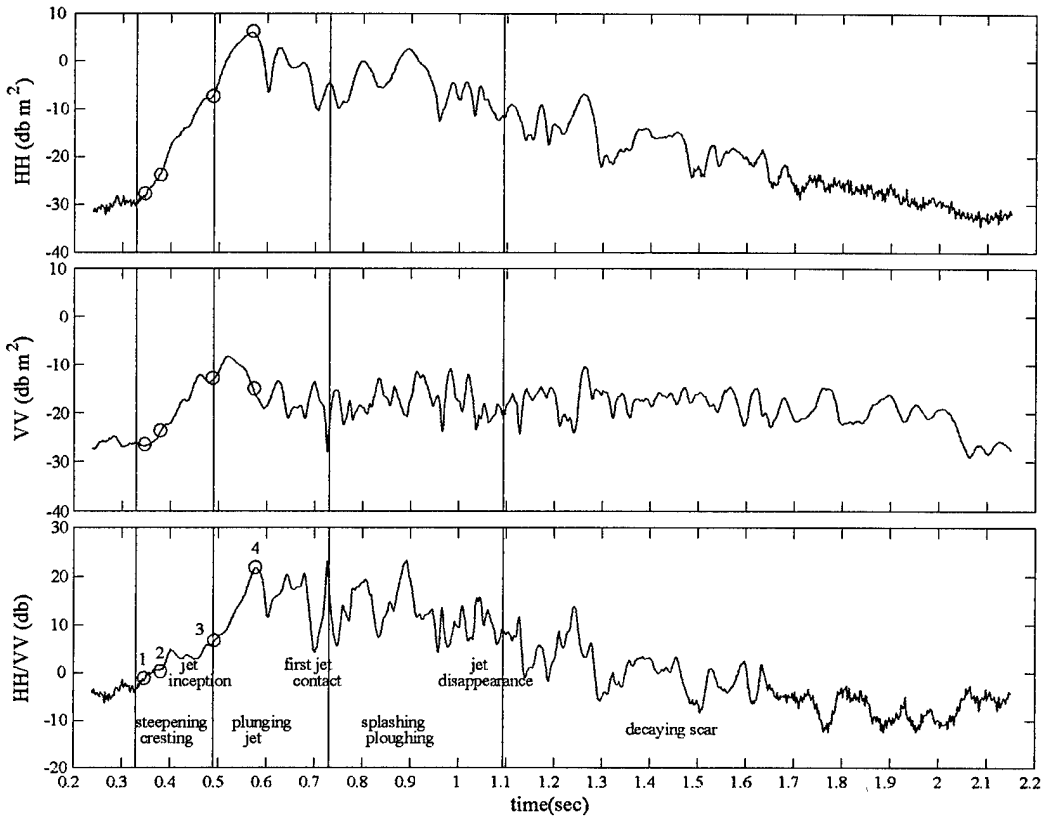

Figure 7: Range integrated cross sections of the wave in figure 4-6. Bottom HH/VV ratio.

following jet formation, requires an additional and separate explanation. Here the existence of a continuously concave front face of the breaking wave, approximating a parabola, with the plunging jet passing through the focal region, suggests a strong focusing effect of incident HH radiation near the surface of the wave face and in the region of the jet. The effect of focussing varies substantially from wave to wave depending on the shape of the front face and the strength of the breaker.

The SPLASHING-PLOUGHING phase displays the highest Doppler speeds of the breaking process, reaching $1.3c_0$. These high speeds, seen in the front of the target track, are caused by the water thrown forward by the ploughing jet. The large HH returns and structures often seen in this phase are caused by various parts of the breaking wave. Early on, they originate from the jet, later they are associated with the formation of the new wave crest which has been ploughed upwards by the submerging jet, Fig. 2e&f. This crest can be seen in HH and VV moving forward down the concave wave face, followed by a highly turbulent region visible as oscillatory VV return.

ACKNOWLEDGMENT

This investigation was sponsored by the ASAP program of ISSO (DoD), contract SP4700-97-C-0002, and until Dec. 1996 by the Ocean Imaging program of LLNL (under contract to DoD), contract B-218685. The authors appreciate help and encouragement from many persons, including J.Brase, D.Holliday, D.Kulla, R.Twogood, K.Ward, B.Werle, and R.York.

REFERENCES

[1] B.Werle, IEEE Int. Radar Conf. 1995

[2] B.L.Lewis, I.D.Olin, Experimental Study and Theoretical Model of High-Resolution Backscatter from the Sea, Radio Science, Vol. 15, No 4, p. 815-828, July-August 1980

[3] D.Mensa, High Resolution Radar Cross-Section Imaging, Artech House: Boston 1991

[4] T.B.Benjamin, J.E.Feir, The Disintegration of Wave Trains on Deep Water, Part 1, Theory, J.Fluid Mech. 27, p. 417-430.

[5] Y.Yao, P.Wang, M.P.Tulin, Wave Groups, Wave-Wave Interaction and Wave Breaking: Results of Numerical Experiments. Proc. of the 20th Symposium on Naval Hydrodynamics; Santa Barbara, 1994, National Academy Press, Washington, 1996

[6] A.T.Jessup, C.J.Zappa, M.R.Loewen, V.Hesany, Infrared Remote Sensing of Breaking Waves, Nature, Vol. 385, 2 January 1997

[7] J.Fuchs, K.D.Ward, M.P.Tulin, R.York, Simple Techniques to Correct for VCO Nonlinearities in Short Range FMCW Radars, IEEE MTTS 1996

[8] M.Long, Radar Reflectivity of Land and Sea, p. 135ff., Artech House, Boston 1983

[9] M.Sletten, D.Trizna, Ultrawide-Band Radar Observations of Multipath Propagation over the Sea Surface. IEEE Transaction on Antennas and Propagation, Vol. 44, No 5, p. 646-651, May 1996

Monte Carlo Simulation of Backscattering from Natural Soil Surfaces

D. Casarano (1), F. Posa (1), F. Mattia (2), G. De Carolis (2), J.C. Souyris (3), T. Le Toan(3), G. Pasquariello (4)

(1) Dipartimento Interateneo di Fisica - Bari, via Amendola 173, 70125 Bari (Italy), Ph. +39 80 5443171, Fax. +39 80 5442434, e-mail: posa@ba.infn.it
(2) Istituto di Tecnologia Informatica Spaziale (ITIS)- CNR, c/o GCS-ASI Loc. Terlecchia, 75100 Matera (Italy),
(3) Centre d'Etudes Spatiales de la BIOsphere (CESBIO), 18 av Edouard Belin bpi 2801, 31401 Toulouse Cedex 4 (Fr),
(4) Istituto di Elaborazione Segnali ed Immagini (IESI) - CNR, via Amendola 166/5, 70125 Bari (Italy),

Abstract -- The objective of this paper is to investigate the impact of a multiscale roughness description on the surface radar backscattering response. Surfaces are generated using a 2-D fractional Brownian motion process. A Monte-Carlo e.m. simulation based on the Kirchhoff tangent plane approximation is used to derive the backscattering coefficient. Numerical results are compared with backscattering coefficients obtained by means of the IEM model. Exponential, Gaussian and Hybrid autocorrelation functions are considered.

INTRODUCTION

Over the past few years, the e.m. backscattering from rough surfaces has been extensively investigated for the interpretation of Synthetic Aperture Radar (SAR) data in remote sensing applications. Rough surfaces have been traditionally described as bidimensional stationary Gaussian random process with an associated autocorrelation function. According to this description, statistical parameters characterizing the e.m. response of random surfaces are the height profile std (s) and the correlation length (l). However, the analysis of ground measurements carried out over different European test sites indicates that natural surfaces generally show *self similarity* properties [1].

The objective of this paper is to investigate the effect of a more realistic roughness description on the surface backscattering response. To reach this goal, a Monte Carlo simulation based on the Kirchhoff e.m. approximation has been implemented. However, Kirchhoff approximation approach requires to restrict the study to the case of moderately smooth surfaces. They are generated as a fractional Brownian motion (fBm) processes by using the *successive random addition algorithm* (*sraa*) [2]. Copolarized backscattering coefficients for a set of different geometrical and physical surface states are numerically derived. In order to assess to what extent backscattering from *self-similar* surfaces may be correctly described by classical asymptotic e.m. models, a comparison between numerical results and backscattering coefficients based on Integral Equation Model (IEM) [3] is carried out.

The next section addresses the surface generation and concurrent statistics. Subsequently, the Monte Carlo approach is presented. Finally, results are discussed and compared with IEM.

SURFACE GENERATION

Using the *sraa*, a set of fBm surfaces with Hurst exponent H=0.4 were generated on *1024 x 1024* square grids.

Bidimensional fBm is a random process $z = z(\vec{x})$ $\left(\vec{x} = (x, y)\right)$ with the following variance

$$\left\langle \left[z(\vec{x}_2) - z(\vec{x}_1) \right]^2 \right\rangle = s^2 \left| \vec{x}_2 - \vec{x}_1 \right|^{2H} \qquad (1)$$

where s is a constant and $0<H<1$ is called the Hurst exponent. The important property of such a process is that its increments are *self-similar* with parameter H:

$$\forall r > 0 \;\; z(\vec{x}) - z(\vec{x}_0) \text{ and } \frac{z(r\vec{x}) - z(\vec{x}_0)}{r^H}$$

are statistically indistinguishable $\forall \vec{x}_0$ and $\forall \vec{x}$.

Basically, the two dimensional *sraa* consists of calculating the appropriate altitudes on corners and midpoints of the initial square grid and then keeping on repeating the procedure for each sub square obtained by subdividing the initial grid. More precisely, at the generic n^{th} subdivision, firstly the midpoint height of each square is determined by averaging the corresponding corner altitudes, secondly a Gaussian random variable x having variance

$$\left\langle \xi^2 \right\rangle = s^2 r^{2nH} \qquad (2)$$

is added to all points. As discussed in [2], the algorithm permits a degree of freedom by choosing r which determines the sharpness of surface peaks, to a certain extent.

0-7803-3836-7/97/$10.00 © 1997 IEEE

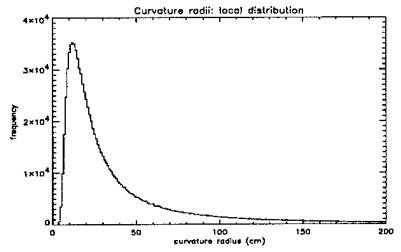

*Fig. 1: Distribution of curvature radii (1024*1024 points)*

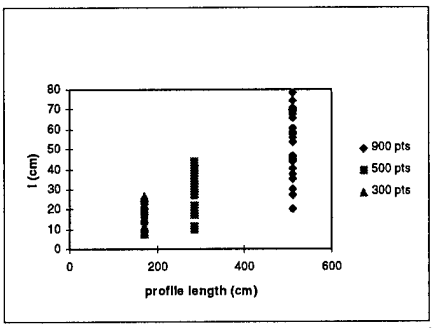

Fig.2: Estimated correlation length over different spatial scales

In our case, a value of r=1/2 was selected. For the selected Hurst exponent and when s =2.5, 2, 1.5, 1 and 0.5 cm, a value of r=1/2 provides surfaces with estimated average radius of curvature of 8.0, 10.0, 13.3, 20 and 40 cm respectively. As an example, Fig. (1) shows the measured distribution of radii of curvatures for s=1 cm. A consequence of the surface self similarity properties is that a fundamental spatial scale characterizing the surface does not exist. In fact, the classical statistical parameters estimates, namely profile height std and correlation length, are dependent on the profile length over which they are estimated. Fig. (2) shows the estimated correlation lengths over different spatial scales.

MONTE CARLO SIMULATION

Scattering coefficient can be defined in terms of the incident and scattered electric field by the expression:

$$\sigma^0_{pq} = \frac{4\pi R_0^2 \,\mathrm{Re}\left\{\left\langle \left|\mathbf{E}^s_{pq}\right|^2 \right\rangle / \eta_s^*\right\}}{A_0 \,\mathrm{Re}\left\{\left|E_0\right|^2 / \eta_1^*\right\}} \qquad (3)$$

where A_0 is the illuminated area, R_0 is the distance from the point of observation. s indicates the quantities related to the scattered wave and the scattering medium, h_1 and h_s are the intrinsic impedances of the media.

For an e.m. wave scattered by a generic surface S, the far field expression is:

$$\mathbf{E}^s = K\hat{\mathbf{n}}_s \times \int\left[\left(\hat{\mathbf{n}}\times\mathbf{E} - \eta_s\hat{\mathbf{n}}_s\times(\hat{\mathbf{n}}\times\mathbf{H})\right)\right] e^{jk_s\,\mathbf{r}\cdot\hat{\mathbf{n}}_s} dS \quad (4)$$

where $\mathbf{E}$ and $\mathbf{H}$ are the total electric and magnetic field vectors at the surface boundary, $K = -jk_s e^{-jk_s R_0}/(4\pi R_0)$, k_s and $\hat{\mathbf{n}}_s$ are the incident radiation wavenumber and the scattered wave unit vector, respectively. The vector $\hat{\mathbf{n}}$ is the normal of the surface element dS.

The Kirchhoff approximation is based on the assumption that at any boundary position, the surface S may be locally well approximated by its tangent plane. Under this hypothesis, fields at the boundary may be calculated as the sum of the incident and geometrically reflected fields. In fact, they depend only on a local process and every interaction between fields in different points of the surface, like multiple scattering, is not accounted for.

However, such an approximation is valid only if the curvature radii is larger than incident wavelength. Assuming $\mathbf{E}^i = \hat{\mathbf{a}}E_0 \exp(-jk\hat{\mathbf{n}}_i\cdot\mathbf{r})$ is the incident electric field and considering the local coordinate system given by

$$\hat{\mathbf{t}} = \hat{\mathbf{n}}_i \times \hat{\mathbf{n}} / \left|\,\hat{\mathbf{n}}_i \times \hat{\mathbf{n}}\,\right|$$
$$\hat{\mathbf{d}} = \hat{\mathbf{n}}_i \times \hat{\mathbf{t}}$$
$$\hat{\mathbf{n}}_i = \hat{\mathbf{t}} \times \hat{\mathbf{d}},$$

the tangential components of surface fields are:

$$\hat{\mathbf{n}}\times\mathbf{E} = [(1+R_h)(\hat{\mathbf{a}}\cdot\hat{\mathbf{t}})(\hat{\mathbf{n}}\times\hat{\mathbf{t}}) - (1-R_v)(\hat{\mathbf{n}}\cdot\hat{\mathbf{n}}_i)(\hat{\mathbf{a}}\cdot\hat{\mathbf{d}})\hat{\mathbf{t}}]E_0 \quad (5)$$

$$\eta_1(\hat{\mathbf{n}}\times\mathbf{H}) = -[(1-R_h)(\hat{\mathbf{n}}\cdot\hat{\mathbf{n}}_i)(\hat{\mathbf{a}}\cdot\hat{\mathbf{t}})\hat{\mathbf{t}} + (1+R_v)(\hat{\mathbf{a}}\cdot\hat{\mathbf{d}})(\hat{\mathbf{n}}\times\hat{\mathbf{t}})]E_0 \quad (6)$$

where R_h and R_v are the Fresnel coefficients for the local incidence angle.

In the simulation, a numerical integration over surfaces *100* λ *x 100* λ has been performed to calculate (4). A surface sampling of $\lambda/10$ has been found to provide the best balance between computing time and accuracy. In addition, a Gaussian tapering function has been used to overcome the effects of the truncated surface edge.

The backscattering response of a random surface is a stochastic process such as real and imaginary part are independent Gaussian variables (although the distribution can be not Gaussian under specific assumption). The scattering coefficient σ^0 is then exponentially distributed (i.e. $P(\sigma^0) = \frac{1}{\bar{\sigma}^0} e^{-\sigma^0/\bar{\sigma}^0}$). To obtain an acceptable estimates of σ^0, many values over independent samples must be averaged. The independent samples are obtained by using different realizations of a given statistics. If the surface dimensions are much larger than the wavelength and than the correlation length, independent samples may be also obtained by imaging the surface with different

azimuth angles. In our simulation, each value of σ^0 results from the average of 24 realizations.

Since the average of n exponential distributed variables is distributed like a $2n$-degrees of freedom chi-square, averaging cross section over 24 realizations gives a 95% degree of confidence between the interval σ_0–1.8 and σ_0+1.6 dB.

The simulation was preliminary validated over a set of Gaussian correlated surfaces by comparing numerical results with backscattering values derived by means of IEM.

RESULTS AND DISCUSSION

For different roughness and dielectric conditions of *self similar* surfaces, numerical estimates of copolarized backscattering coefficients at 5.3 GHz have been computed. The angular range between 10° and 50° has been investigated. In order to compare the numerical results with IEM, profile *std* and correlation length have been estimated over three different spatial scales: *170 cm*, *300 cm* and *560 cm*. To get reliable estimates the used s and l values have been averaged over a large number of independent samples. In addition, three different autocorrelation function have been considered, namely Gaussian, exponential and hybrid function. The hybrid case is intermediate between Gaussian and exponential. It is characterized by two correlation lengths, namely l_G and l_E. This degree of freedom permits the use of one correlation length as a fitting parameter.

As general result, a better agreement has been found for s and l estimated over *170 cm*. However, significant differences are observed between numerical results and IEM whatever the correlation function (ACF) is. As an example, for *HH* polarization Figs. (3) and (4) display the comparison between simulated data and IEM (with exponential ACF), in the case of $s=1$ *cm* and $s=2$ *cm*, respectively. In both cases, simulated σ_0 decrease faster than those predicted by IEM at small angles and slower at large angles. In addition, IEM backscattering values calculated for a Gaussian autocorrelation function are much lower than simulated data. For *VV* polarization the trend is the same. Finally, for $s=2$ *cm* Fig (5) shows the comparison between simulated and IEM results in the case of hybrid ACF. Two different values of l_G have been tested: $l_G=0.3\ l$ and $l_G=0.6\ l$. In both cases important differences still remain.

In conclusion, our results show that when assuming a self similar roughness state the backscattering trend shows significant differences from the trend shown by classical e.m. models coupled with the standard roughness description. Future work will be dedicated to improve direct forward models incorporating appropriate description of natural surfaces.

REFERENCES

[1] Mattia, F., Souyris, J.C., Le Toan, T., Casarano, D., Posa, F., Borgeaud, M.,"On the surface roughness characterizationfor SAR data analysis", Proc. IGARSS'97, Singapore, 4-8 August, 1997

[2] R.F. Voss, "Random Fractal Forgeries", in "Fundamental Algorithms for Computer Graphics", ed. E. Earnashaw, Springer-Verlag, Berlin, 1985

[3] A.K. Fung, "Microwave Scattering and Emission Models and their Applications", Artech House, 1994

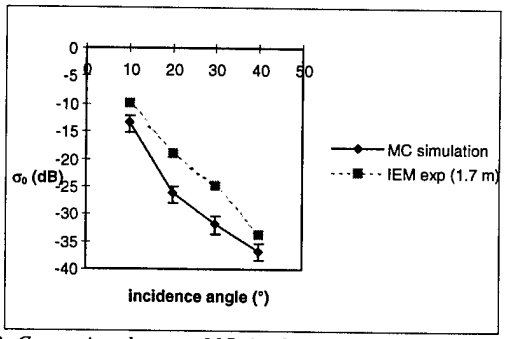

Fig. 3: Comparison between MC simulation and IEM model. s=1 cm, ε_r=6.5+1.5i, Pol. HH. Exponential ACF.

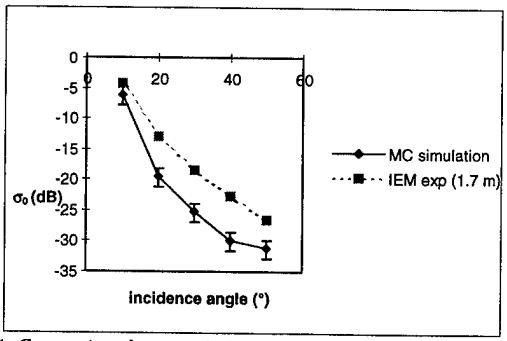

Fig. 4: Comparison between MC simulation and IEM model. s=2 cm, ε_r=6.5+1.5i, Pol. HH. Exponential ACF.

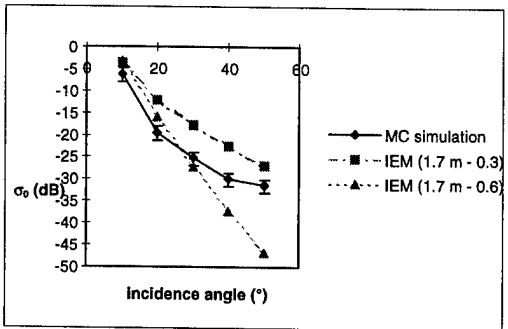

Fig.5: Comparison between MC simulation and IEM model. s=2 cm, ε_r=6.5+1.5i, Pol. HH. Hybrid ACF with $l_G=al$ (a=0.3, 0.6)

A PROCESSING ALGORITHM FOR THE ENVISAT ALTERNATING POLARIZATION MODE SINGLE LOOK COMPLEX PRODUCT

David Stevens, Frank Wong and Paul Lim

MacDonald Dettwiler and Associates, Richmond, B.C., Canada
tel: 604-278-3411 fax: 604-278-0531 drs@mda.ca

Yves-Louis Desnos

ESA/Estec, ENVISAT System Division, P.O. Box 299, 2200 AG Noordwijk
tel: +31 71 565 4927 fax: +31 71 565 5617 ydesnos@yw.estec.esa.nl

ABSTRACT:— This paper discusses the choice of a processing algorithm for the ENVISAT Alternating Polarization (AP) mode Single Look Complex (SLC) product to be used for Interferometric SAR. The chosen algorithm is a modified phase preserving Range Doppler approach. The processed Doppler bandwidth is made equal to four burst bandwidths (multi-burst processing) so as to keep as much of the signal information as possible while maintaining radiometric quality. The resulting product has a modulated impulse response but contains all the necessary information required for Interferometric SAR.

1 INTRODUCTION

This paper discusses the choice of processing algorithm for the Alternating Polarization (AP) mode Single Look Complex (SLC) product to be generated by the ENVISAT Advanced Synthetic Aperture Radar (ASAR) generic processor. The ASAR generic processor is part of the ESA ENVISAT Payload Data Handling Station. The requirements for this product will be discussed in light of Interferometry (InSAR) being the primary application. In the ENVISAT AP mode the ASAR sensor operates in a single swath burst mode within any one of the seven possible swaths. The polarization of the transmitted pulses are selectable but fixed for a scene and the received bursts alternate between polarizations. The resulting possible polarization combinations for the two channel product are (HH, VV), (HH, HV), and (VV, VH) where V is vertical polarization and H is horizontal.

There are unique complications and limitations inherent to burst mode data, especially when precision phase preservation is required. In addition, when the AP SLC products are "systematically" generated by the ASAR processor there is no specific knowledge of what other data set this product may be paired with at some future time to do InSAR. This requires that the product be as versatile as possible. For example, InSAR can be done with two suitably aligned AP SLC products or one AP SLC and one non-bursty (image mode) SLC of the same beam.

Two classes of processing algorithms were evaluated as candidates for processing the AP SLC product within the ASAR processor: single burst, and multi-burst approaches.

Single burst algorithms only use one of possibly several bursts to generate each output image point [1]. Multi-burst approaches use more than one, summed coherently, which results in more Doppler bandwidth being processed for each target in the image [2].

2 AP SLC PRODUCT REQUIREMENTS

The image quality requirements for the AP SLC product are derived from the typical requirements for a non-bursty SLC product which includes phase preservation and adequate focusing. Many SAR processing algorithms claim that they are "phase preserving", meaning that the phase is preserved only at the peak of the impulse response, but the phase may have undesirable properties across the impulse response. For InSAR, this phase variation across the impulse response is also an important consideration, and it is necessary at least to have a common variation in the two SLC products. Furthermore, the Doppler spectrum that is used for processing must be common to both images in order to maximize the inter-channel correlation. Any disjoint portions of the spectra will degrade the performance of the interferometer.

The following features are therefore desirable for the AP SLC product: 1) the phase is preserved at the peak of the impulse response. 2) The phase and frequency are continuous functions across the impulse response. 3) All

0-7803-3836-7/97/$10.00

the required Doppler spectrum information for successful interferogram generation is available. 4) The impulse response shape and radiometry is appropriate for image interpretation and information extraction.

It has been determined that it is not possible to fully satisfy all these requirements simultaneously by a single algorithm. This is due to fundamental limitations in the burst mode data and the operational scenario of the AP SLC product. This will be discussed in the following sections.

3 SINGLE BURST PROCESSING

In the case of the AP mode, the azimuth aperture covers a little more than five burst durations. Any one target is captured from two to three bursts in the same polarization. Due to the time-frequency coupling inherent to linear FM signals the spectrum for a given ground target is also bursty. The location of the bursts in the spectra for a particular target depend upon the relative location of the target to the burst train in the time domain. In single burst processing algorithms only one of the possible bursts are used to focus any given ground point. In this case, the Doppler centroid (effective energy centroid) for a given ground target will depend upon the relative location of the target to the burst time-line and the choice of the burst for focusing that target. In the case of Range Doppler (RD) processing the slope of the phase ramp across the impulse response depends upon the Doppler centroid frequency. Therefore, for bursty data processed using an RD type single burst approach, the slope of the phase ramp will change along the image.

Any single burst processing algorithm, such as the modified RD [1], or the single look SPECtral ANalysis (SPECAN), can output a series of targets along azimuth from a burst but then the processing has to skip to another burst to output the next series of targets. Since the spectrum has gaps, there are discontinuities in the Doppler centroid along the image. This leads to phase and frequency discontinuities across the impulse response.

If a single burst algorithm is used to "systematically" process two passes of AP mode data independently, the skips in the Doppler spectrum will, in general, occur at different locations. This results in periodic strips in the images where the Doppler spectra are disjoint and InSAR can not be performed. For this reason single burst algorithms are not suitable for this operational scenario. Single burst approaches can be appropriate for the case where both data sets are processing from the raw data with a priori knowledge of the other burst train and Doppler centroid, or when the AP SLC is paired with a non-bursty SLC product.

4 MULTI-BURST PROCESSING

Another approach is to focus all the available bursts for a given output point simultaneously (in other words, process the full Doppler bandwidth). This ensures that all the Doppler spectrum available is maintained for a given target. This can, and in the ASAR processor case must, be done independently for both passes. But, there will still be disjoint portions of the spectrum due to burst timing misalignment and differences in the Doppler centroid between passes. During InSAR processing, azimuth varying bandpass filters can be used to select out common continuous spectral regions from each image [3].

In the range Doppler implementation of this approach the alternate polarization raw data lines are zeroed out prior to the azimuth Fast Fourier Transform (FFT) (only one polarization is processed at a time). The non-zero bursts are coherent because of the uniform pulse repetition frequency for AP mode. Azimuth processing proceeds with a forward FFT, followed by a matched filter multiply and an inverse FFT. This is similar to the multi-burst algorithm proposed in [2]. Since all the Doppler spectrum information is maintained InSAR processing can perform azimuth varying bandpass filtering of two passes to extract common continuous Doppler spectra.

This approach satisfies the requirements for InSAR processing but the impulse response of the product suffers from modulation artifacts in the form of spikes bounded by an envelope equal to the ideal impulse response obtained by processing one burst [2]. The modulation arises from the fact that the spectrum of each target is segmented in the inverse FFT. The modulation disappears in the InSAR filtered images because the filtering selects out a single continuous spectrum for each target which restores the sinc-like impulse response.

The AP SLC product will suffer from radiometric scalloping if the full Doppler bandwidth is processed. This is due to there being a different number of bursts or partial bursts used to focus the targets. This banding can be removed by modifying the processed azimuth bandwidth with range. If the processed bandwidth is exactly four times the burst bandwidth then there will always be the energy from two bursts captured. Therefore, when the inverse beam pattern is applied and there is no weighting applied to the matched filter the total energy processed for each target will be the same. The truncation of the spectrum by the rectangular window will either capture two complete bursts or will capture one complete burst and two partial bursts. In the latter case the two partial bursts add up to a full burst of energy. Since the burst bandwidth is range dependent, the processed bandwidth must be adjusted across range. This results in less of the total available Doppler bandwidth being retained for InSAR.

Bandwidth adjustment leads to a more limiting constraint on the possible differences in the Doppler centroid between two AP SLC products that can be used for InSAR. In order for InSAR to proceed it is necessary to have an overlap between the processed bandwidths of the two images that is greater than two burst bandwidths plus the overlap of the bursts. This can be observed by comparing the two image spectra for a series of good targets. For example, if the bursts overlap by 75% then the necessary overlap in the processed bandwidths must be 2.75 burst bandwidths. Clearly, if there is no burst overlap then InSAR is not possible.

If the full five burst bandwidths are processed and assuming 100% alignment then the Doppler centroids between the two products can vary by up to two burst bandwidths. When bandwidth adjustment is used it can only vary by up to one burst bandwidth (this corresponds to about 250 Hz). Given the typically small changes in Doppler centroids between passes this limitation is not expected to pose a problem.

In order to support InSAR azimuth varying bandpass filtering it is necessary to supply the following parameters in the product annotation: burst return time, time of the start of a burst for a specified polarization, Doppler centroid coefficients, azimuth FM rate coefficients, and zero Doppler time of the first output line.

5 EXPERIMENTAL RESULTS

The modified RD algorithm with bandwidth adjustment was implemented in the ASAR processor and tested using simulated point target data as well as reconditioned ERS data (to have AP characteristics). The impulse response characteristics were consistent with the analysis. For targets where two complete bursts were processed the expected single burst impulse response was modulated by a cosine with a frequency equal to the burst bandwidth. This results in a main lobe 3-dB width in seconds of about $0.242/W$ where W is the burst bandwidth. The phase was linear across the main lobe. The maximum sidelobe level was about -3.5 dB. The integrated side lobe ratio was less than about 0 dB (large due to very high sidelobes). There were small perturbations about these numbers for targets which had only one complete burst and two partial bursts processed.

The radiometric error was less than 0.15 dB in integrated point target energy compared between polarizations. When the ERS data was processed there was no scalloping.

The "phase offset test" was also conducted. This involves processing two products where the only difference between the two is the location of the raw data within the input processing window. The input data is offset in both range and azimuth. The resulting images are then registered by an integral shift and the differential phase is computed and analyzed. For the case of a 200 sample and 200 line offset the resulting standard deviation of the phase was less than 1 degree for a typical ERS scene and the mean was negligible (less than 0.004 degrees). When the phase offset test was performed on point target data sets the differential phase at the peak of the impulse responses was less than 0.05 degrees. This is similar to results obtained using non-bursty data sets which demonstrates the phase preservation of the algorithm.

6 CONCLUSIONS

In general, algorithms can be classified as either processing one burst per output point or algorithms that process multiple bursts. The single burst processing algorithms can maintain image quality but can lose vital spectral information required for InSAR. Multiple burst algorithms are more suitable for "systematically" generated AP SLC products but have a modulated impulse response that varies along the image.

For the specific case of the Alternating Polarization SLC product to be generated within the ENVISAT ASAR generic processor, a multi-burst modified RD algorithm has been selected, implemented and tested. It has been shown to satisfy the requirements of InSAR which is the target application.

References

[1] F. Wong, D. Stevens, and I. Cumming, "Phase Preserving Processing of ScanSAR Data by Modifying the Range Doppler Algorithm," *IGARSS'97*, Singapore, August 1997.

[2] R. Bamler and M. Eineder, "ScanSAR Processing Using Standard High Precision SAR Algorithms," *IEEE Trans. Geoscience and Remote Sensing*, vol. 34, Jan. 1996.

[3] A. Monti-Guarnieri and C. Prati, "ScanSAR Focusing and Interferometry," *IEEE Trans. Geoscience and Remote Sensing*, vol. 34, pp. 1029–1038, July 1996.

Phase-Preserving Processing of ScanSAR Data with a Modified Range Doppler Algorithm

Frank Wong and David Stevens
MacDonald Dettwiler and Associates, Richmond, B.C., Canada
tel: 604-278-3411 fax: 604-278-0531 fhw@mda.ca

Ian Cumming*
Dept. of Electrical and Computer Engineering
The University of British Columbia, Vancouver, BC, Canada
tel: 604-822-4623 fax: 604-822-5949 ianc@ee.ubc.ca

ABSTRACT:— This paper presents a phase-preserving algorithm for processing ScanSAR data, based on modifications to the well-known RD algorithm. The azimuth compression stage is modified to isolate each target's energy within the burst regimes. Analysis and simulations verify the phase accuracy of the modified algorithm.

1 INTRODUCTION

Burst-mode or ScanSAR data collection is used in several SAR systems, such as Radarsat and ENVISAT, and a phase-preserving processing algorithm is needed if this data is to be used for interferometry [1].

For efficiency reasons, the SPECtral ANalysis (SPECAN) algorithm [2] is usually recommended for processing burst-mode data. SPECAN can be made to be phase preserving at the peak of the impulse response. However, the azimuth sample spacing is a function of the azimuth FM rate.

The Range Doppler (RD) algorithm [3] is well proven for its efficiency and accuracy, including its ability to preserve phase. In this paper we describe a modification to the RD algorithm to allow it to process burst-mode data with accurate phase.

2 ALGORITHM DESCRIPTION

The basic RD algorithm is generally used to process continuous data. In this case, the phase of any target is preserved at the peak of the impulse response, and is a ramp function across the impulse response, with the slope of the ramp being a function of the Doppler centroid. A key point to note here is that all targets exhibit the same frequency versus time characteristics, since each target is swept by the same antenna beam in which the target is illuminated continuously. Therefore, ignoring the azimuth variation of the Doppler centroid, all targets in the same range gate occupy the same range of frequencies in the Doppler spectrum. As a result, each compressed target has the same phase ramp in the continuous mode.

2.1 Spectrum of ScanSAR Targets

This subsection examines the target spectrum for burst-mode data, and explains why the basic RD algorithm is not optimal in this case. Understanding the spectrum characteristics leads to the proposed algorithm.

In this discussion, the burst arrangement of the ENVISAT AP mode is used as an example. Let T_b be the burst duration as well as the burst separation, and let the beamwidth be $5T_b$. Consider 16 equally-spaced targets that lie in the same range gate after RCMC, denoted by T_1 to T_{16} in Figure 1. The frequency excursions of these targets are shown in Figure 2. It is assumed that the PRF equals the full target bandwidth. Because of the data gaps, the spectrum of each target is segmented.

To use the standard single-look RD algorithm, the data gaps must be zero padded. However, the following problems are encountered:

- The impulse response exhibits a "spiky" appearance [4] due to the rectangular modulation of the input signal. The modulation is caused by processing across the zero padding, and the phase changes by $\pm\pi$ whenever the amplitude crosses zero.
- The range of frequencies covered by each target is different as shown in Figure 2. In the RD algorithm, the same weighted matched filter is applied to all the targets, resulting in each target being weighted differently.

With modifications to the basic RD algorithm, these problems can be solved.

*This work was supported by the MDA/NSERC Industrial research Chair in Radar Remote Sensing

0-7803-3836-7/97/$10.00 © 1997 IEEE

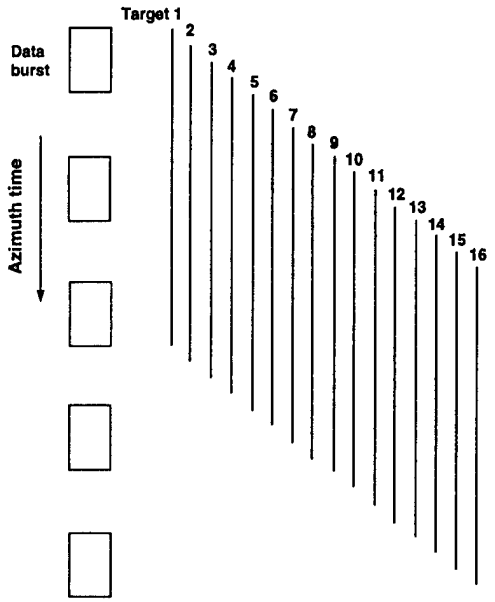

Figure 1: Burst and Target Arrangements

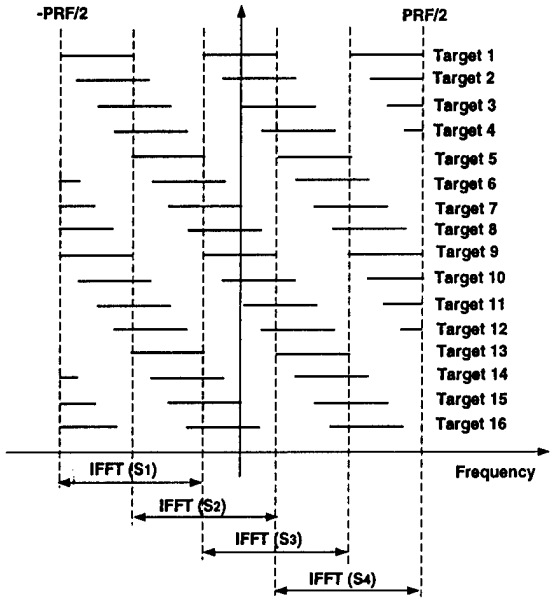

Figure 2: Target Spectrum

2.2 The Modified RD Algorithm

In the RD algorithm, the inverse transform part of the azimuth compression stage extracts target energy from selected stationary parts of the Doppler spectrum. In the modified algorithm, the IFFTs are placed so as to follow the specific time-frequency pattern of the burst mode cycles shown in Figure 2. The IFFT length is chosen so that if one full burst of a target is captured, no other energy of that target is present. The choice of IFFT length involves an efficiency/oversampling tradeoff, with zero padding and decimation used as appropriate [5].

Returning to the previous example, let ΔF be the frequency excursion of each target in a burst. Also, let four short IFFTs, each of duration $2\Delta F$, be positioned as in Figure 2. The IFFTs are denoted by S_1 to S_4.

In S_1, Targets T_1 to T_5 and T_9 to T_{13} have one *contiguous* set of Doppler frequencies (one burst bandwidth) within the IFFT. After the matched filtering and IFFT, these complete targets will be kept as "good" ones and the other incomplete targets thrown away. Specifically, the good points to keep are: T_1 to T_4 and T_9 to T_{12} in S_1 and S_3, and T_5 to T_8 and T_{13} to T_{16} in S_2 and S_4.

Note that only two IFFTs are needed to give complete coverage of the ground in this case, for example, the sets S_1 and S_2, S_2 and S_3, S_3 and S_4, or S_4 and S_1. The data of the chosen pair is then stitched together to form a final Single Look Complex (SLC) product. At this point, three possibilities of data utilization are available:

1. use one set only for an SLC product,
2. coherently add each set to achieve interferometric phase smoothing, or
3. detect and add each set to form a look-summed product for non-interferometric use.

The placement of the IFFTs and the IFFT length can be adjusted to accommodate the various RADARSAT and ENVISAT burst arrangements.

The short IFFTs have a time varying band pass filtering effect, but without having to implement this time consuming filter in the time domain. Also, since the IFFTs capture the full burst energy of each good target in the Doppler spectrum there is no additional radiometric artifact due to the processor.

3 ANALYSIS OF RESULTS

Using mathematical analysis, an expression can be found for the amplitude and phase of the compression of an arbitrarily-placed point target. The phase of a point target, after processing by the modified RD algorithm, was found to have the following properties:

- The phase is preserved at the target peak.
- The phase is a linear ramp across the impulse response, with a negligible quadratic component, but the slope of the ramp varies between targets. This slope change is due to the spectral location of the acquired data, rather than the processing.
- After the stitching, some targets may have phase and phase slope discontinuities at the stitching boundaries. This happens when stitched portions are taken from different burst cycles.

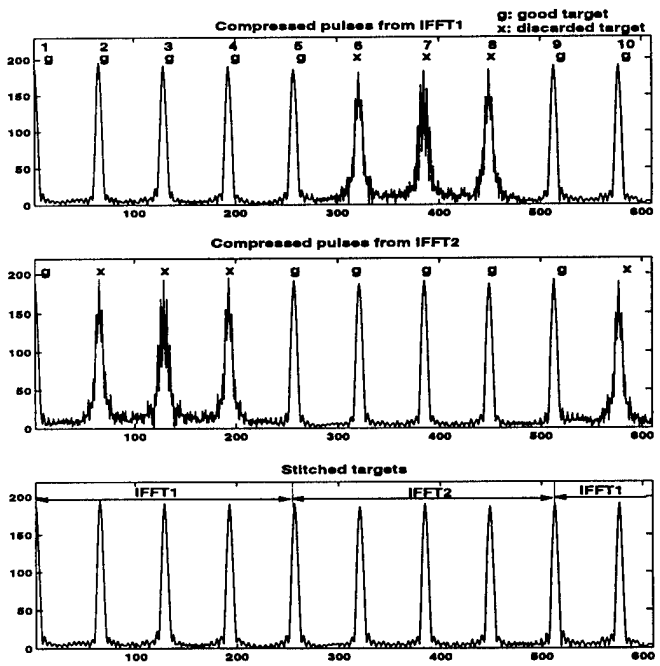

Figure 3: Three groups of targets stitched together

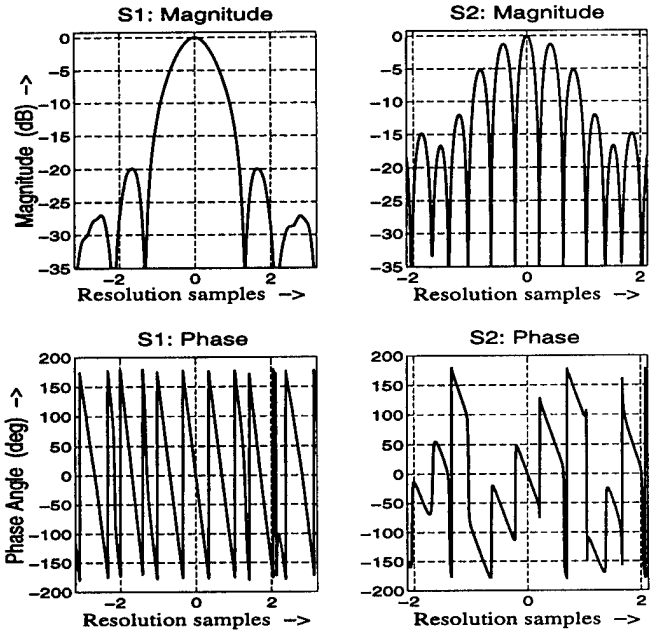

Figure 4: Impulse Response of Target T_3

4 EXPERIMENTS

A simulation experiment was performed to verify the performance of the proposed algorithm. 16 equally-spaced targets were placed in the same range gate as shown in Figure 1. A Kaiser window was applied to each burst in the processing. Image quality parameters of the good targets such as impulse response width, maximum side lobe ratio, geometric registration, and phase at the theoretical peak position were measured. It was found that these parameters agreed with their theoretical values.

Figure 3 shows part of the output from IFFTs 1 & 2, corresponding to targets 1 to 10. Two divisions where the targets change from complete to incomplete are shown, at targets 5 & 9. The good targets are then selected from each IFFT, as shown in the bottom part of Figure 3.

Figure 4 shows the impulse response of Target T_3 in S_1 and S_2. From the figure, it is clear why this target is a good one in S_1, but rejected in S_2.

5 CONCLUSIONS

This technical note has presented a phase-preserving algorithm to process ScanSAR data. It is based on the RD algorithm, using a combination of weighting, zero padding and FFTs to achieve the desired phase properties. The look placement and data selection are modified to accommodate the unique pattern of energy received in burst mode, in a similar way as the SPECAN algorithm. The modifications build upon the well-proven attributes of the RD algorithm, and unifies the treatment of continuous-mode and burst-mode data.

Mathematical analysis and simulation experiments were performed, and image quality parameters were measured. The measurements agreed with the theoretical values, thus verifying that the proposed algorithm can be used to process ScanSAR data with high phase fidelity.

References

[1] A. Monti-Guarnieri and C. Prati, "ScanSAR Focusing and Interferometry," *IEEE Trans. Geoscience and Remote Sensing*, vol. 34, pp. 1029–1038, July 1996.

[2] M. Sack, M. Ito, and I. Cumming, "Application of Efficient Linear FM Matched Filtering Algorithms to SAR Processing," *IEEE Proc-F*, vol. 132, no. 1, pp. 45–57, 1985.

[3] I. G. Cumming and J. R. Bennett, "Digital processing of SEASAT SAR data," in *IEEE 1979 International Conference on Acoustics, Speech and Signal Processing*, (Washington, D.C.), April 2-4, 1979.

[4] R. Bamler and M. Eineder, "ScanSAR Processing Using Standard High Precision SAR Algorithms," *IEEE Trans. Geoscience and Remote Sensing*, vol. 34, Jan. 1996.

[5] I. Cumming, Y. Guo, and F. Wong, "Analysis and precision processing of Radarsat ScanSAR data," in *Geomatics in the Era of Radarsat*, (Ottawa, Canada), May 25–30, 1997.

Synthetic Aperture Radar Out of Slant Plane Motion Compensation

N.J.S. Stacy
Microwave Radar Division, Defence Science and Technology Organisation,
Building 180L, PO Box 1500, Salisbury SA 5108, Australia
ph: +61-8-82597191, fax: +61-8-82595200, email: nick.stacy@dsto.defence.gov.au

Abstract -- Compensation of out of slant plane motion for synthetic aperture radar systems is essential for fine resolution focused imagery. It is shown here that a time domain approach, that corrects the phase of each range bin, is equivalent to the polar format processing approach of projecting the range spectral data onto the ground focusing plane, with the two motion compensation approaches linked by a Fourier transform. It is also shown that these methods are equivalent to the spectral shift identified in multiple pass interferometric data.

INTRODUCTION

Motion compensation of synthetic aperture radar (SAR) data, particularly that acquired from airborne platforms, is essential for forming focused fine resolution radar images. Typically airborne SAR systems use inertial navigation equipment to acquire a swath of data in a known geometry, usually with respect to some reference collection path at the aircraft altitude and a reference image line or image point on the surface of the Earth. The plane that contains this reference collection line and image location is referred to as the reference *slant plane*. Changes in range between the SAR system and reference image line or point can generally be accommodated by changing the transmit to receive delay during acquisition or processing. If the SAR data acquisition system moves out of the reference slant plane (e.g. from changes in the aircraft altitude), then the change in range between the aircraft and different points across the image swath are significantly different and can not be compensated by a single range delay offset. Consequently motion out of the slant plane requires a compensation procedure that is a function of position within the image swath.

This paper examines the algorithms typically used for compensating motion of the SAR system out of the reference slant plane for stripmap and spotlight data with the assumption of a flat Earth and narrow swath. Motion compensation of stripmap SAR data can be implemented by scaling the range sampling and applying a range dependent phase correction to the range compressed time domain data. Often the differential change in range across the swath for the synthetic aperture time is significant compared to the radar wavelength but much less than the range resolution, so the compensation can be approximated by the phase correction alone. Motion compensation of spotlight SAR data processed by the polar-format [1] or equivalent tomographic [2] method can be implemented by projecting the range compressed signal spectrum onto the ground plane or the reference slant plane [1]. This paper shows the equivalence of the two approaches for small swath widths (where the variation in incidence angle across the swath is small), that is, the time domain sample scaling and phase correction is equal to the frequency domain spectral projection. The out of slant plane motion compensation is also equivalent to the range wavenumber scale and shift as a function of incidence angle, previously identified for increasing range resolution [3] and improving SAR interferometry data processing [4].

IMAGING GEOMETRY

The SAR imaging geometry for the spotlight mode is shown in Fig. 1. The reference collection path and reference image point for spotlight mode define the reference slant plane, at incidence angle θ to the vertical. The actual SAR collection "slant plane" surface has a complicated shape defined by the

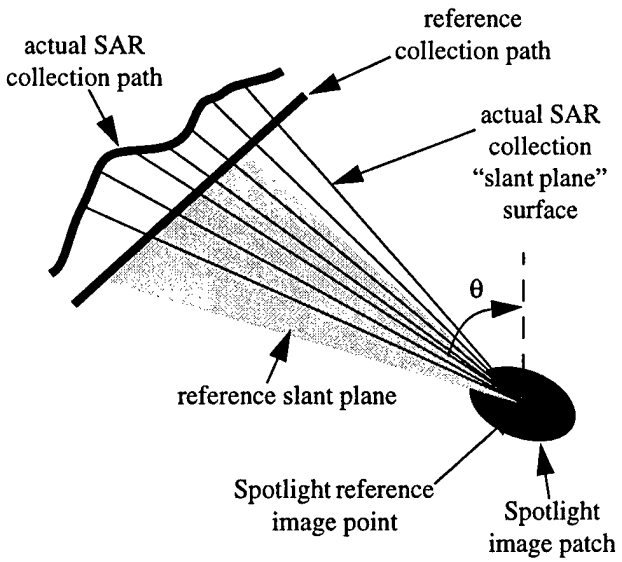

Figure 1. Spotlight mode reference slant plane (shaded) at incidence angle θ and the actual SAR collection "slant plan" surface (represented by the sequence of lines).

0-7803-3836-7/97/$10.00 © 1997 IEEE

actual path of the radar system and the reference image point. A similar geometry exists for stripmap SAR which has a reference image line associated with the data collection swath.

Fig. 2 shows the geometry associated with a vertical slice through Fig. 1 for the circumstance of a simple out of slant plane offset Δs between the reference and actual paths. The range to the image swath center, point A from the actual data collection path is,

$$r_A' = \sqrt{r_A^2 + \Delta s^2} = r_A + \frac{\Delta s^2}{2r_A} - \frac{\Delta s^4}{8r_A^3} + \dots \quad . \tag{1}$$

Similarly the range from the actual path to point B, offset from the image center is,

$$r_B' = \sqrt{(r_B - \Delta s \sin\alpha)^2 + (\Delta s \cos\alpha)^2}$$
$$= r_B - \Delta s \sin\alpha + \frac{\Delta s^2}{2r_B} + \dots \quad . \tag{2}$$

The difference in range between image swath points A and B from the actual data collection path is,

$$\Delta r' = r_B' - r_A' = \Delta r - \Delta s \sin\alpha - \frac{\Delta s^2}{2}\left(\frac{\Delta r}{r_A r_B}\right) + \dots \quad , \tag{3}$$

where $\Delta r = r_B - r_A$ is the difference in range to the reference path. For small angles α the change in range to the reference line,

$$\Delta r = r_A \sin\alpha \tan\theta \quad , \tag{4}$$

when substituted into (3) yields,

$$\Delta r' = \Delta r\left(1 + \frac{\Delta\theta}{\tan\theta}\right) \quad , \tag{5}$$

where $\Delta\theta = \theta' - \theta$ is the change in the center swath incidence angle approximated by $-\Delta s / r_A$ and higher order terms have been ignored. In summary, small changes in the observation geometry due to out of slant plane motion scales the range distance between fixed points on the ground by (5).

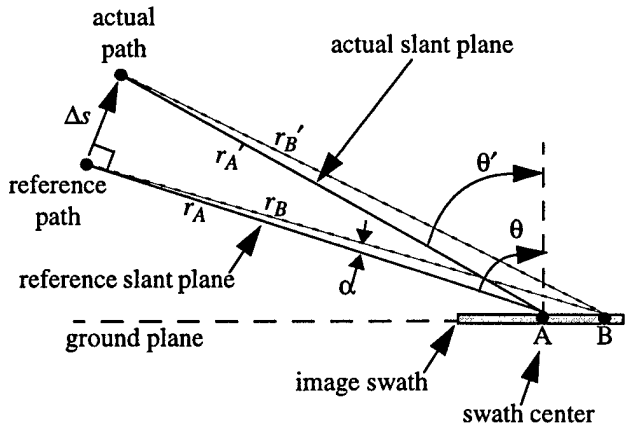

Figure 2. Cross section through the data collection path showing the reference ranges to the image swath center at point A, (r_A), and to point B offset from the center (r_B) and the actual ranges (r_A' and r_B') for an out of slant plane offset Δs. Also shown is the reference and actual incidence angles (θ and θ') and α the angle between r_A and r_B.

TIME DOMAIN MOTION COMPENSATION

The change in range between fixed points in the swath due to out of plane motion can be corrected in the time domain signal by scaling the sampling rate and applying a range dependent phase correction. Scaling the sampling rate in proportion to (5) will maintain the separation between points A and B at a fixed number of range samples. Since this scaling will alter the sampling frequency in proportion to $1/(1 + \Delta\theta/\tan\theta)$, the width of the fixed bandwidth transmit signal within the extent of the sampled spectrum will be scaled in proportion to (5). If the transmit signal has narrow bandwidth compared to the center frequency, f_0, then the phase correction is approximated by,

$$\Delta\phi = e^{j2\pi f_0 \frac{\Delta\theta}{\tan\theta} t} \quad , \tag{6}$$

where $t = 2\,\Delta r / c$ is the range dependent time delay. This time domain phase shift is equivalent to a shift in the transmit signal spectrum from f_0 to $f_0(1 + \Delta\theta/\tan\theta)$. The combined effect of the sample scaling and phase correction is the shifting of frequency f in the transmit signal to,

$$f\left(1 + \frac{\Delta\theta}{\tan\theta}\right) \quad . \tag{7}$$

POLAR FORMAT MOTION COMPENSATION

The spotlight SAR polar format data processing algorithm forms a focused image by arranging the two-dimensional data spectrum onto a polar grid and applying an inverse Fourier transform [1]. Motion compensation for movement of the collection system out of the slant plane is corrected by projecting the spectrum of the range data from the collection slant plane onto a focusing plane [1]. The ground plane (Fig. 2) is typically chosen to be the focusing plane. For data

collection along the actual path this projection moves the spectra frequency f to $f \sin\theta' = f \sin(\theta + \Delta\theta)$. Once compensated for out of slant plane motion the data can be reprojected onto any display plane. If the original reference slant plane is chosen to be the display plane then the compensated location of frequency f is,

$$f\left(\frac{\sin(\theta + \Delta\theta)}{\sin\theta}\right) = f\left(1 + \frac{\Delta\theta}{\tan\theta}\right) \quad , \tag{8}$$

equal to the time domain compensation in (7).

COMPARISON WITH INTERFEROMETRIC WAVENUMBER SHIFT

Interferometric observations of a scene are usually acquired with a non-zero separation between the two data acquisition paths, referred to as the interferometric baseline. The data acquisition geometry is similar to that shown in Fig. 2 where the "reference" and "actual" paths are the two data collection paths and Δs is the interferometric baseline. The baseline separation results in the two observations being acquired at slightly different incidence angles. The resulting range spectra have a relative shift given by (7) [4]. This spectra shift can be used to improve the range resolution [3] and the quality of SAR interferometry data processing [4].

DISCUSSION

Movement of the data collection system out of the reference slant plane changes the observation incidence angle of a scene. The resulting change in data collection geometry changes the sampling distance between fixed points on the ground by the amount in (5). This change in geometry can be corrected by applying a time domain sample scaling and phase correction or by shifting and scaling the frequency domain spectrum given in (7). These corrections are equivalent to the spectral shift identified in interferometry.

The two motion compensation and the interferometric approaches provide different perspectives to the same phenomenon. The change in observation incidence angle changes the projection of the radar probing wavelength onto the ground surface. Consequently small changes in the incidence angle results in the surface reflectively function being sampled over a slightly different range of frequencies. This means the sampled spectrum from different incidence angles corresponds to a different set of ground reflectivity spectral components. For narrow swaths the two out of slant plane motion compensation procedures apply an equivalent spectral shift to the sample data to align common spectral components in the range direction, permitting accurate cross range data processing and, hence, well focused imagery.

REFERENCES

1. Walker, J.L., "Range-Doppler Imaging of Rotating Objects", *IEEE Trans. Aerospace & Electronic Systems*, Vol. AES-16, No. 1, Jan. 1980, pp. 23-52.
2. Munson, D.C., Jr., J.D. O'Brien, and W.K. Jenkins, "A Tomographic Formulation of Spotlight-Mode Synthetic Aperture Radar", *Proceedings of the IEEE*, Vol. 71, No. 8, Aug. 1983, pp. 917-925.
3. Prati, C., and F. Rocca, "Range resolution enhancement with multiple SAR surveys combination", in *Proc. IGARSS'92*, Houston, TX, May 1992, pp. 1576-1578.
4. Gatelli, F., A.M. Guarnieri, F. Parizzi, P. Pasquali, C. Prati, and F. Rocca, "The Wavenumber Shift in Interferometry", *IEEE Trans. Geoscience and Remote Sensing*, Vol. 32, No. 4, July 1994, pp. 855-864.

A Comparison of Phase-Preserving Algorithms for Burst-Mode SAR Data Processing

Ian Cumming and Yi Guo*

Dept. of Electrical and Computer Engineering
The University of British Columbia, Vancouver, BC, Canada V6T 1Z4.
tel: 604-822-4623 fax: 604-822-5949 ianc@ee.ubc.ca yig@ee.ubc.ca

Frank Wong

MacDonald Dettwiler and Associates, Richmond, B.C., Canada
tel: 604-278-3411 fax: 604-278-0531 fhw@mda.ca

ABSTRACT: — Burst-mode data is obtained when a SAR system is operated in ScanSAR mode. Missing data in the burst gaps makes it difficult to use traditional phase-preserving algorithms to produce single look complex (SLC) data. In this paper, three phase-preserving algorithms for burst-mode data compression are examined and compared to find the best algorithm for precision processing applications such as interferometry.

1 INTRODUCTION

With the increasing interest in SAR interferometry (InSAR), it is important that SAR processing algorithms be phase preserving. In the last few years, many sophisticated phase-preserving SAR algorithms, such as classical Range Doppler (RD), modified RD, SPECAN (de-ramp and FFT) and chirp scaling have been published. These algorithms work well on continuous-mode data, but have to be modified when applied to burst-mode data, because the spectrum of the data varies with time.

This paper will discuss three phase-preserving algorithms for burst-mode data, two modified from the RD algorithm, and one from the SPECAN algorithm. We show the simulation results using these algorithms, and by comparing these results, the best algorithm will be recommended.

2 BURST-MODE DATA

Burst-mode data is obtained when SAR works in a ScanSAR mode. In this mode, the satellite antenna scans through different range subswaths in order to image a larger area. In each subswath, the received range signal is the same as the continuous range signal, however, in azimuth direction, the data is blocked into bursts.

*This work is supported by the NSERC/MDA chair in Radar Remote Sensing.

Fig. 1 shows the difference between continuous-mode and burst-mode data. The Doppler spectrum of a continuous-mode target covers the full antenna bandwidth, the same for each target. However, in burst mode, different targets will have a different spectral distribution, depending on the target's azimuth location.

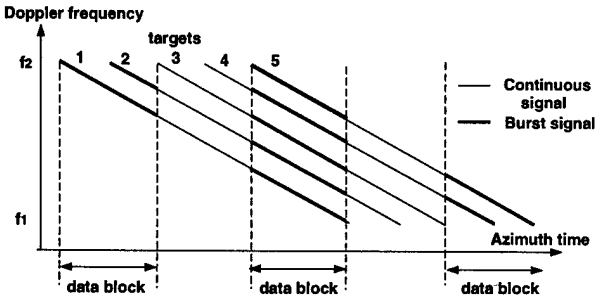

Figure 1: Target spectral distribution in continuous and burst mode

This discontinuous, non-stationary Doppler spectrum makes it difficult to apply traditional phase preserving compression algorithms. Modifications of the algorithms are necessary for the compression of burst-mode data.

3 MODIFIED RD ALGORITHMS

In this section, two modifications of the RD algorithm will be discussed.

3.1 The range/Doppler algorithm

The traditional range/Doppler (RD) algorithm consists of the following steps [1, 2]:

1. Range compression.
2. Azimuth FFT.
3. Range cell migration correction (RCMC).

0-7803-3836-7/97/$10.00 © 1997 IEEE

4. Azimuth matched filter multiplication.

5. Complete azimuth compression using IFFTs.

In continuous mode, the compressed signal from the RD algorithm has stationary phase properties: the phase slope is constant for all the targets, and at the peak, the phase information of the target is preserved. When data is collected in burst mode, as the effective Doppler centroid frequency varies with targets, the RD algorithm will result in a non-stationary compressed signal.

3.2 Bamler's algorithm

Bamler's algorithm directly applies the RD algorithm to the burst-mode data [3]. If a point-target azimuth signal is:[1]

$$s(\eta) = \sum_i rect\left(\frac{\eta - \eta_{bc}(i)}{T_b}\right) \exp\left(-j\pi K_a(\eta - \eta_a)^2\right) \quad (1)$$

where K_a is the azimuth FM rate, η_a is the zero Doppler time of the target, η_{bc} is the time of the centre of the burst, and T_b is the burst duration, Bamler's compression result is the same as coherently adding the RD compression results of all the bursts.

The compressed pulse of a single burst is a *sinc* function, its phase has a linear slope depending on the burst center frequency and a negligible quadratic component, and phase is preserved at the peak (the peak phase is zero). When such pulses from all bursts are added coherently, the resulting pulse still preserves the phase at the peak, but the magnitude curve is spiky due to the different phase slopes from each burst. This compressed phase slope at the peak is proportional to the target's effective Doppler centroid frequency, however the phase value frequently jumps by $\pm\pi$ whenever the amplitude crosses zero.

3.3 The SIFFT algorithm

The SIFFT algorithm developed at MDA [4] is also a modification of the RD algorithm. At the last step of the RD algorithm, part of the spectrum is extracted using a short IFFT, and by doing several such short IFFTs, the complete array of compressed targets can be obtained by stitching the short IFFT results together.

If f_1 and f_2 are the burst spectrum boundaries, and the short IFFT is taken between f_a and f_b, where $f_a \leq f_1 < f_2 \leq f_b$, then the SIFFT output from this burst after phase compensation is:

$$\begin{aligned} c_1(\eta) &= \exp\left[j\pi\left(K_a(\eta - \eta_a)^2 - (\eta - \eta_a)(f_2 + f_1)\right)\right] \\ &\quad sinc\left[(\eta - \eta_a)(f_2 - f_1)\right] \end{aligned} \quad (2)$$

[1] A phase term due to the slant range R_0 and its amplitude which is only a multiplicative constant are ignored in equations (1) to (3).

This compressed pulse is a *sinc* function with resolution depending on the burst bandwidth, $(f_2 - f_1)$. It preserves the phase at the compressed peak. Also, the phase is a linear ramp with a slope proportional to the burst center location, plus a small quadratic component.

4 SPECAN ALGORITHM

The generic SPECAN algorithm includes deramping and DFT operations [5, 6]. When applied to burst-mode data, the reference function is the same, and the DFT is simply aligned to each burst segment.

Using the same example as in the SIFFT algorithm, in which $f_1 = K_a(\eta_1 - \eta_a)$, and $f_2 = K_a(\eta_2 - \eta_a)$, where η_1 and η_2 are the burst boundaries in azimuth time, and the de-ramp function orgin is at $\eta = 0$, the SPECAN output after phase compensation is:

$$\begin{aligned} c_2(\eta) &= \exp\left[j\pi K_a\left((\eta - \eta_a)^2 - (\eta - \eta_a)(\eta_1 + \eta_2 - 2\eta_a)\right)\right] \\ &\quad sinc\left[K_a(\eta - \eta_a)(\eta_2 - \eta_1)\right] \end{aligned} \quad (3)$$

As with the SIFFT algorithm, the phase at the peak of the compressed pulse is preserved, and a phase slope proportional to the target-dependent burst Doppler centroid is present at the peak. In addition, similar to the SIFFT algorithm, a small quadratic phase term exists.

5 SIMULATION RESULTS

The above three algorithms are all modified from algorithms for continuous data. By compressing only one burst for each target, both the SIFFT and SPECAN results results show a linear phase plus a small quadratic component. On the other hand, the Bamler's algorithm compresses the whole spectrum of a target at once, but gives a spiky result. In this section, we will compare the simulation results of the three algorithms.

5.1 The SIFFT and SPECAN algorithms

Here the simulation results of the SIFFT algorithm and the SPECAN algorithm are compared. Consider a target exposed by 3 bursts, with a distribution of spectral energy shown in Fig. 2. We compute the compressed pulse properties from IFFT2 in the SIFFT method, and from the second burst in the SPECAN method.

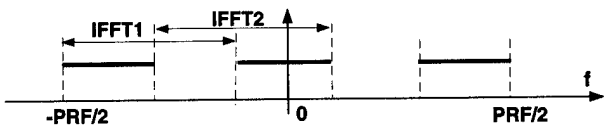

Figure 2: Doppler spectrum of a burst-mode target

The magnitude curves of the two results are the same, as the resolution is related to the burst bandwidth in each

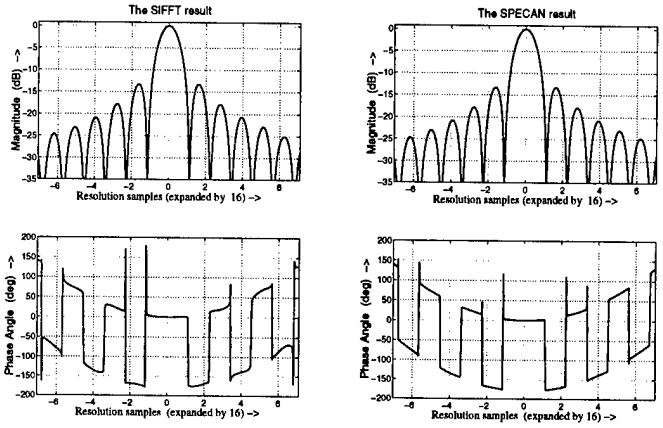

Figure 3: The compressed pulses from the SIFFT algorithm (left) and the SPECAN algorithm (right)

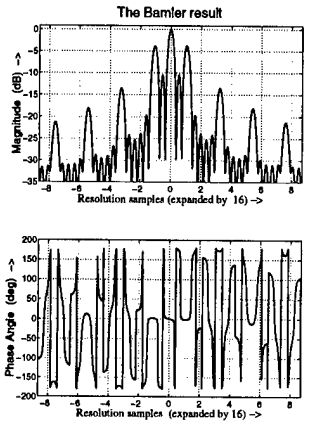

Figure 4: The compressed pulse in Bamler's algorithm

case. The phase is preserved at the peak of the pulse in each case. Since in this example, the center frequency of the compressed burst spectrum is at the origin, the phase slope at the peak is zero in the two results. As described in the mathematical analysis, the same quadratic component exists in the two results.

It is also interesting to examine the average phase across the peak of the compressed pulse, within the -3dB margins of the peak amplitude. The quadratic phase component takes the average phase away from zero by a small amount in either case. In the current example, the average phase shift is 0.3^o.

5.2 Bamler's and SIFFT algorithms

Using the same Doppler spectrum in Fig. 2, Bamler's algorithm will compress the whole data at once, with the result shown in Fig. 4. The SIFFT magnitude in Fig. 3 is the envelope of Bamler's result (note that the sampling rate is twice as fast in Fig. 4). The spikes in the compressed pulse makes the phase jump frequently.

The advantage of Bamler's algorithm is that it uses all the information in the data. However in InSAR processing, when bursts are misregistered in the two passes, the interferogram is more susceptible to errors due to a rapidly changing phase, and the spikes will add more noise to the interferogram. The spatial averaging inherent in the SIFFT algorithm, and the subsequent phase smoothing will give a less noisy result for interferometry use.

6 CONCLUSIONS

In this paper, we have analyzed and compared three modified algorithms for precision processing burst-mode data. Bamler's algorithm uses all the data information, but gives a spiky pulse. Comparing these three algorithms, we can conclude that the SIFFT and SPECAN algorithms are favored for interferometric application of burst-mode data. Out of the two, the SIFFT algorithm has the advantage that it follows the heritage of RD, and that the azimuth spacing in SPECAN is a function of the azimuth FM rate.

References

[1] I. G. Cumming and J. R. Bennett, "Digital processing of SEASAT SAR data," in *IEEE 1979 International Conference on Acoustics, Speech and Signal Processing*, (Washington, D.C.), April 2-4, 1979.

[2] C. Wu, K. Y. Liu, and M. J. Jin, "A modeling and correlation algorithm for spaceborne SAR signals," *IEEE Trans. on Aerospace and Electronic Systems*, vol. AES-18, pp. 563–574, Sept. 1982.

[3] R. Bamler and M. Eineder, "ScanSAR Processing Using Standard High Precision SAR Algorithms," *IEEE Trans. Geoscience and Remote Sensing*, vol. 34, Jan. 1996.

[4] F. Wong, D. Stevens, and I. Cumming, "Phase-Preserving Processing of ScanSAR Data with a Modified Range Doppler Algorithm," in *Proceedings of the International Geoscience and Remote Sensing Symposium, IGARSS'97*, (Singapore), August 4–8, 1997.

[5] I. Cumming and J. Lim, "The design of a digital breadboard processor for the ESA remote sensing satellite synthetic aperture radar," tech. rep., MacDonald Dettwiler, Richmond, BC, Canada, July 1981. Final report for ESA Contract No. 3998/79/NL/HP(SC).

[6] M. Sack, M. Ito, and I. Cumming, "Application of Efficient Linear FM Matched Filtering Algorithms to SAR Processing," *IEEE Proc-F*, vol. 132, no. 1, pp. 45–57, 1985.

Precision Two-Dimensional Focusing of Spaceborne Synthetic Aperture Radar Data With Range-Varying Doppler Centroid

Alice Wang-Cheng Heng
Department of Computational Science, The National University of Singapore, 10 Kent Ridge Cresent, Singapore 119260. Telephone: (65)-772 2878. Facsimile: (65)-774 6756. Email: cschwc@nus.sg

Hock Lim, Soo Chin Liew and Bernard T.G. Tan
Centre for Remote Imaging, Sensing and Processing, The National University of Singapore, 10 Kent Ridge Cresent, Singapore 119260. Telephone: (65)-772 3220. Facsimile: (65)-775 7717. Email:phylimh@nus.sg

Abstract – An efficient two-dimensional synthetic aperture radar (SAR) processing algorithm based on the exact transfer function is presented. The approximations made are similar to those in the chirp-scaling algorithm but it works with range-compressed data and can easily handle systems with range-varying Doppler centroids. The range-dependent migration is treated as a small perturbation from that of a given range position. This small deviation is corrected by resampling whilst the main migration factor (large in cases of large Doppler centroids) is corrected by a two-dimensional phase multiply. The azimuth compression filter is range-dependent and implemented as in the range-Doppler algorithm. This algorithm can be easily incorporated into SAR processors using the classical range-Doppler algorithm. We tested the algorithm on the Seasat Goldstone scene, ERS-1 and RADARSAT data. The interferometric offset tests show that the algorithm is phase-preserving.

INTRODUCTION

The two-dimensional and range-variant nature of the synthetic aperture radar (SAR) point target response poses a great challenge to an efficient implementation of an accurate two-dimensional matched filter. Various approximations have been proposed to handle the range-variant correlation kernel. These approximations have been systematically documented and compared using the exact transfer function[1]. The chirp-scaling algorithm[2] has been found to be most faithful in handling the range-variation in the two-dimensional matched filter. It has the advantage of not requiring explicit interpolation of data points. However, to be efficient, the chirp-scaling algorithm requires the transmitted pulse to be a linear chirp and range compression is not carried out prior to computing the Fourier transform in the azimuth direction.

A careful examination of the exact transfer function shows that the main difficulty with processing spaceborne SAR data with high Doppler centroids lies in the large and range variant range migration of the Doppler history. Moreover, one difficulty associated with handling a range-variant Doppler centroid is the spectral folding due to sampling of the Doppler spectrum at close to Nyquist rate[3]. However, these two problems can be solved using a differential range correction (DRC) method which is presented in this paper. In the following sections, we will discuss the theoretical derivation of the DRC algorithm and present results of our work.

THEORETICAL CONSIDERATIONS

DRC algorithm for constant Doppler centroid

Following Chang, Jin and Curlander[4], the two-dimensional SAR exact transfer function can be written as:

$$H(f_x, f_y; r_o) = \exp\left\{ j\pi \left[-\frac{f_c}{(f_y + f_c) f_r} f_x^2 + 2\frac{f_d}{f_r} f_x - \frac{(f_y + f_c) f_d^2}{f_c f_r} \right] \right\} \quad (1)$$

where f_c, f_x, f_y and f_d are the carrier, Doppler, signal and Doppler centroid frequencies respectively, r_0 the range distance to the point target when it is at the centre of the antenna pattern and f_r the Doppler frequency rate can be approximated by:

$$f_r = -\frac{2V^2 f_c}{c r_0} \quad (2)$$

with V being the relative speed between the SAR platform and point target . By expanding the term in f_x^2/f_r using Binomial expansion:

$$\left(1 + \frac{f_y}{f_c}\right)^{-1} \approx 1 - \frac{f_y}{f_c} + \left(\frac{f_y}{f_c}\right)^2 - \cdots \quad (3)$$

and keeping up to the quadratic term, we obtain from (1) and (2) the following range-variant two-dimensional transfer function:

0-7803-3836-7/97/$10.00 © 1997 IEEE

$$H(f_x,f_y;r_0)\approx \exp\left\{j\pi\frac{cr_0}{2f_cV^2}(f_x-f_d)^2\right\}$$
$$\exp\left\{-j2\pi\frac{cr_0}{4f_c^2V^2}(f_x^2-f_d^2)f_y\right\}$$
$$\exp\left\{j\pi\frac{cr_0}{2f_c^3V^2}f_x^2f_y^2\right\} \quad (4)$$

The three phase factors can be easily associated with the azimuth chirp, the range migration and the secondary range compression factors respectively. We first design a two-dimensional matched filter using the following phase factors:

$$M(f_x,f_y)=\exp\left\{j2\pi\frac{cr_A}{4f_c^2V^2}(f_x^2-f_d^2)f_y\right\}$$
$$\exp\left\{-j\pi\frac{cr_A}{2f_c^3V^2}f_x^2f_y^2\right\} \quad (5)$$

The result of applying the matched filter (5) to (4) is:

$$H_M(f_x,f_y;r_0)=\exp\left\{j\pi\frac{cr_0}{2f_cV^2}(f_x-f_d)^2\right\}$$
$$\exp\left\{-j2\pi\frac{c}{4f_c^2V^2}(r_0-r_A)(f_x^2-f_d^2)f_y\right\}$$
$$\exp\left\{j\pi\frac{c(r_0-r_A)}{2V^2f_c^3}f_x^2f_y^2\right\} \quad (6)$$

The second phase factor in (6) can be interpreted to be a Doppler frequency dependent differential range shift – a shift by an amount which is proportional to the difference between a chosen reference range r_A and the actual range r_0. This differential range shift is corrected using chirp-scaling interpolation in the chirp scaling algorithm but it can be easily corrected by any interpolation method as it is quite small. The phase aberration in the quadratic factor, unfortunately, is not easily corrected. However, by proper choice of the reference range, this phase error can be minimised.

Range varying Doppler centroid

One problem associated with a range varying Doppler centroid is the spectral folding. For a given Doppler centroid, it is quite possible to 'unfold' the Doppler spectrum to yield a correct Doppler spectrum within the sampled Doppler bandwidth. But with a range-varying Doppler centroid, the folding frequency will be different for different range. When a wrong Doppler centroid is used, the azimuth spectrum will not be correctly reconstructed. This will result in loss of energy in that range line and part of the data will be brought to a wrong range during the range migration correction. The latter will lead to artefacts in the final processed image. However, we observe that for small errors in the Doppler centroid, the Doppler frequencies at which the wrong data get shifted are near the edges of the Doppler bandwidth. Therefore these aliased components have low energies and can be quite easily filtered off.

Suppose a block of range pixels is chosen such that the variation in the Doppler centroid is not more than 10 % of the pulse repetition rate. We apply a two-dimensional matched filter similar to (5) to this block with a Doppler centroid chosen to be between the minimum and maximum of the Doppler centroids in this block. For range lines whose Doppler centroids differ from this value, there will be aliased errors – but these will be outside the 80% of the central bandwidths and can therefore be filtered off.

The residual phase that must be corrected for each range in this case will be:

$$d(f_x,f_y;r_0)=\exp\left\{-j2\pi\frac{c}{4f_c^2V^2}(r_0-r_A)(f_x^2-f_d^2)f_y\right\}$$
$$\exp\left\{-j2\pi\frac{cr_A}{4f_c^2V^2}(f_{dA}^2-f_d^2)f_y\right\} \quad (7)$$

where f_{dA} is the Doppler centroid at the chosen reference range. The additional second phase factor in (7) is just a shift to correct for the different Doppler centroid used in the two-dimensional range migration correction.

A block diagram illustrating the processing steps based on the above concepts is shown in Fig. 1.

IMPLEMENTATION RESULTS

Performance of the algorithm on simulated point targets and the Seasat Goldstone scene has been reported in [5]. The results are practically identical to those obtained using the chirp-scaling algorithm.

To check if the algorithm is phase preserving, we have carried out interferometric offset tests[6] on ERS-1 and RADARSAT (S7 mode) data. The test scenes were non-homogeneous areas, consisting of a mix of urban, vegetative and sea surfaces. The block size used was 4096 (azimuth) by 1024 (range). The results as shown in Table 1 indicate that the algorithm is phase-preserving.

We note that the size of the final ERS-1 image used in the interferometric offset test is much smaller than a typical ERS-1 scene. But the resulting coherence magnitude is much higher than that reported in [6] and the standard deviation of of the phase is much lower (0.09 degrees compared to 0.6

degrees).

The RADARSAT scene had a range-varying Doppler centroid and though the mean and standard deviation of the phase are on the high side, they are within the recommended criteria[6] of 0.1 and 5.0 degrees respectively.

CONCLUSION

The DRC algorithm is a two-dimensional phase-preserving SAR algorithm that is adaptive to the range variant nature of the SAR transfer function. It is relatively simple to implement.

Compared with the classical range-Doppler algorithm, it will only incur extra phase multiplies in the two-dimensional transform domain, as well as two additional Fourier transforms in the range direction. But it is well-suited for processing systems with high and range-varying Doppler centroids.

ACKNOWLEDGMENT

We thank Mr Kwoh Leong Keong for making available the raw SAR data for our study.

REFERENCES

[1] R.Bamler, "A comparison of range-Doppler and wavenumber domain SAR focusing algorithms", IEEE Transactions on Geoscience and Remote Sensing, vol. 30, pp. 706-713, July 1992.

[2] R.K.Raney, H.Runge, R.Bamler, I.G.Cumming and F.H.Wong, "Precision SAR processing using chirp scaling", IEEE Transactions on Geoscience and Remote Sensing, vol. 32, pp. 786-799, July 1994.

[3] C.Prati and F.Rocca, "Focusing SAR data with time-varying Doppler centroid", IEEE Transactions on Geoscience and Remote Sensing, vol. 30, pp. 550-558, May 1992.

[4] C.Y.Chang,M.Y.Jin and J.C.Curlander,"SAR processing based on the exact two-dimensional transfer function", Proc. IGARSS '92, pp. 355-359.

[5] A.Heng, H.Lim, S.C.Liew and B.T.G.Tan, "Precision focussing algorithms for spaceborne synthetic aperture radar (SAR)", International Journal of Remote Sensing, vol. 17, pp. 629-635, 1996.

[6] B.R.Tell and H.Laur, "Phase preservation in SAR processing: The interferometric offset test", Proc. IGARSS'96, pp.477-480.

Table 1 Results of interferometric offset tests

	ERS-1	RADARSAT
Image size (azimuth x range)	2200x2876	2800 x 2660
Azimuth offset (lines)	452	150
Range offset (pixels)	124	112
Coherence(mag)	0.999966	0.9924
Coherence(arg) (deg.)	0.000011	0.0256
Mean phase (deg.)	0.000039	0.0113
Phase std. dev. (deg.)	0.0937	1.59

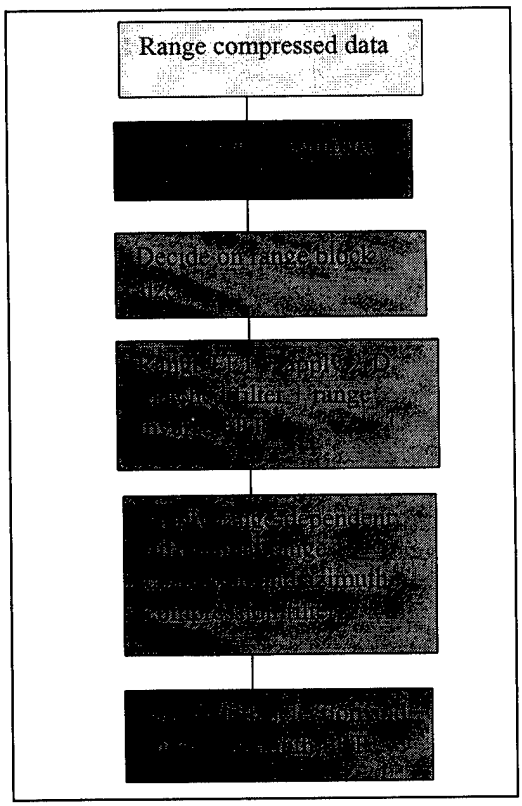

Fig. 1 Block diagram illustrating the DRC algorithm

SAR Image Interpretation Based on Markov Mesh Random Fields Models

P.C. Smits[1], F. Giorgini[1], A. Martuccelli[1], M. Petrou[2], and S.G. Dellepiane[1]

[1]University of Genoa - Department of Biophysical and Electronic Engineering
Via all'Opera Pia 11A, I-16145 Genova – Italy
smits@dibe.unige.it, silvana@dibe.unige.it

[2]University of Surrey – Department of Electronic and Electrical Engineering
Guildford Surrey GU2 5XH
m.petrou@ee.surrey.ac.uk,

Abstract - In this paper, an unsupervised segmentation approach is presented for the analysis of intensity synthetic aperture radar (SAR) images. It utilizes Hidden Markov Mesh Random Fields (HMMRF), assuming that the image elements have a causal relationship: a pixel's past is considered more important than its future, a hypothesis that is of particular interest to SAR images, given the way these images are generated. The approach is build upon the HMMRF theory of Devijver (1993), substituting his Gaussian distribution with the Gamma distribution, using an new initial image segmentation algorithm. The method is suited for real time image analysis, making the method powerful in, for instance, SAR image interpretation and data base browsing.

INTRODUCTION

Automated analysis of Remote Sensing (RS) imagery has become important in order to cope with the large quantities of data that become available every day. Among automatic and semi-automatic approaches for RS data analysis, those based on Markov random fields (MRFs) have proven to be very useful, especially when it comes to the segmentation of synthetic aperture radar (SAR) data with its typical speckle noise [1].

However, due to the heavy iterative character of the non-causal MRF models, these methods are in general non suited for real time implementations. This drawback may be overcome by using Pickard random fields and hidden Markov mesh random fields (HMMRFs). Devijver [2] showed that computational problems in implementing HMMRFs can be overcome, and that the HMMRF approach can be very efficient, making it suited to real-time implementation.

The method proposed in [2] is based on the assumption that the image data is characterized by Gaussian statistics. Adapting the approach to images that are characterized by a Gamma distribution would make the HMMRF approach suited to SAR data, offering processing speed and user-friendliness, since for the Gamma model no parameters are to be set but the estimated number of looks.

The objective of this paper is twofold. First the modified HMMRF approach is presented, and secondly suggestions are made for the initial segmentation that is required by the HMMRF method.

METHOD OVERVIEW

We will follow the terminology and notation used in [2]. The basic idea is to group pixels into clusters based on local properties and neighborhood relationships. The role of the Markov component of the image model is to account for those neighborhood relationships.

The strong point of the used HMMRF approach lies in the handling of the prior information embodied in the Markov mesh model and in an original clustering technique that is used for estimating the model parameters. Pixel clusters are then mapped back to the original spatial domain on a maximum, marginal, a posteriori probability basis.

OBSERVATION MODEL

In this section, we are concerned with the observation model, i.e., the relation between the intensity data I and the image labels L.

The observation model or class conditional grey-level distribution implemented in [2] has been the Gaussian distribution, given by:

$$p(I_s / L_s) = \frac{1}{\sqrt{2\pi\sigma}} \exp\left(- \frac{I_s - \langle I \rangle_l}{2\sigma} \right)^2$$

where s is the index for the location, I is the intensity of the SAR data at s, and L the label. $\langle I \rangle_l$ is the mean intensity for class l.

In the literature agreement exists on the gamma distribution being one of the most suitable statistical

This work was supported by the European Community program Training and Mobility for Researchers (Marie Curie Fellowship) under contract ERBF MBICT 95257, and by grants from the Erasmus program.

0-7803-3836-7/97/$10.00 © 1997 IEEE

models for SAR data. The distribution for multilook intensities can be modeled as ([1],[3]):

$$p(I_s / L_s) = \frac{N^N I_s^{N-1}}{\langle I \rangle_l^N \Gamma(N)} \exp\left(-\frac{NI_s}{\langle I \rangle_l}\right), \qquad (1)$$

where N is the number of independent one-look samples used to form each multilook intensity sample I_s and $\Gamma(N) = (N-1)!$. A well known problem with SAR data is that the real number of looks is not necessarily the effective number of looks. In what follows, the estimation of the number of looks has been optimized, based on the χ^2 goodness-of-fit test [4]. Suppose that p_1, p_2, .., p_k are the probabilities of the grey-levels within the k classes with $\sum_{i=1}^{k} p_i = 1$. Then, considering the total number of pixels of a class as m experiments performed, the expected number of occurrencies of the i-th outcome is given by $e_i = mp_i$. Denoting the observed frequency of the i-th outcome by o_i, the distribution of

$$\chi_0^2 = \sum_{i=1}^{k} \frac{(o_i - mp_i)^2}{mp_i}$$

is approximately that of a χ^2 random variable with (k-1) degrees of freedom. Now, given the number of classes, we can vary the number of looks N, in order to fit the model to the histogram, i.e., to minimize the difference between χ_0^2 and χ^2 over the entire histogram.

INITIAL SEGMENTATION

In the HMMRF approach proposed by Devijver [1] it is necessary to have an initial segmentation of the image, from which the initial statistical parameters (the mean values of every class) are obtained. This first segmentation is important, since it influences strongly the efficiency of the rest of the algorithm. For that reason it may be wise to invest some computation time in this first step, for instance by using a more precise model, risking to spend more time correcting the parameters if doing otherwise.

In the literature, many algorithms have been presented that may help in finding the best thresholds in the histogram in order to segment images affected by Gaussian noise. Only few methods presented in the literature work efficiently on speckled images. When it comes to An easy and fast method that moreover gives satisfying results has been presented in []. The method assumes that the classes in the image have all the same probability. Defining the quantity Q=(number of pixels / 2n), with n the number of classes, the grey-level histogram is delimited by the values f_k, such that

$$\int_{f_{k-1}}^{f_k} \rho(x)dx = Q$$

with k=0..(2n-1) and $f_0 = 0$, computing the mean values of the classes simply counting grey-levels: $\mu_i = f_{2i-1}$. The only drawback of this method is that all classes are assumed to have the same probability; however, being an initial segmentation this limitation does not have too big an influence on the final result.

HMMRF WITH GAMMA DISTRIBUTION

Not being able to go too much into detail, we limit ourselves to a brief, general summary, that reports the most relevant characteristics.

The very basis of the HMMRF approach is the definition of a third-order MMRF [5]: A third-order MMRF is defined by the property

$$P(\lambda_{m,n} / \{\lambda_{k,l} | k < m \text{ or } l < n\}) = P\left(\lambda_{m,n} / \begin{matrix} \lambda_{m-1,n-1} & \lambda_{m-1,n} \\ \lambda_{m,n-1} & \end{matrix}\right)$$

for any $1 < m \le M$ and $1 < n \le N$ for an image MxN. λ.. indicate the labels. This definition relates the label of a pixel to its past, i.e., to all the labels sites above or to the left of (m,n). It is stressed that the Markovian relation is defined on the label image, and not on the observations.

It is well known that the correlation between the observations in SAR data is very low [8], which is a *conditio sine qua non* for Devijver's algorithm.

Now, using an image model in the form of the class conditional distribution of our observations X based on (1), we are able to compute the maximum *a posteriori* probability (MAP) estimates. In order to avoid iterative techniques such as the *iterated conditional mode* or *simulated annealing*, the MAP is estimated based on the marginal distribution $P(\lambda_{m,n} / X_{m+1,n+1})$. This marginal distribution is recursively computed, estimating its parameters from the initial segmentation.

EXPERIMENTAL RESULTS

Data description: In order to assess the usefulness of the proposed method, experiments have been done on various SAR images. In this paper, results are reported using a portion of a San Francisco scene. The intensity image is shown in Fig. 1a.

Comments on results: In the original intensity image, mainly three land-cover types can be observed: water, urban areas, and vegetation. These classes are detected

well in Fig. 1b. Fig. 1c shows the segmentation result with the algorithm looking for four classes.

DISCUSSION AND CONCLUSIONS

In this paper, an approach has been presented for the analysis of synthetic aperture radar (SAR) images based on hidden Markov mash random fields and Gamma image statistics. This resulted in a new algorithm that is more suited to the processing of SAR images than the classical HMMRF model. The results obtained by the proposed approach are very promising. Moreover, no parameter setting is required but the number of classes and the estimated number of looks, making the algorithm interesting to a wide range of end-users that work with SAR data.

ACKNOWLEDGMENT

The authors wish to thank Dr. J.S. Lee (Remote Sensing Devision, Naval Research Laboratory, Washinton, DC) for providing the San Francisco Scene.

REFERENCES

[1] Rignot E. and R. Chellappa, "Segmentation of polarimetric synthetic aperture radar data," IEEE Transactions on Image rocessing, Vol. 1, No. 3, pp. 281-300, July 1992.

[2] P.A. Devijver, Hidden Markov mesh random field models in image analysis, In: K.V. Mairia and G.K. Kanji (Eds.) Advances in applied statistics, Statistics and Images 1. Adhigdon: Carfax Publ. Cy. 1993, pp. 187-227.

[3] Goodman J.W. (1975), Statistical properties of laser speckle patterns, in Laser Speckle and related phenomena, J.C. Dainty, ed., Vol. 9 of Topics in Applied Physics (Springer Verlag, New York, 1975), pp. 9-75.

[4] C. Chatfield, Statistics for technology. Third edition, 1983.

[5] K. Abend, T.J. Harley, and L.N. Kanal, Classification of binary random patterns, IEEE Trans. on Information Theory, IT-11, pp. 538-544.

[6] N. Otsu, A threshold selection method from gray-level histograms, IEEE Transactions on Systems, Man and Cybernetics, Vol. 9, No. 1, 1979, pp. 64-66.

[7] C. Fassnacht, P.A. Devijver, A unilateral Markov field applied to image segmentation, Report RR-94029-ITI, Télécom Bretagne, Département Image et Traitement de l'Information, Oct. 1994.

[8] J.-S. Lee, M.R. Grunes, Feature classification using multi-look polarimetric SAR imagery, 91-72810/92 IEE 1992.

a.

b.

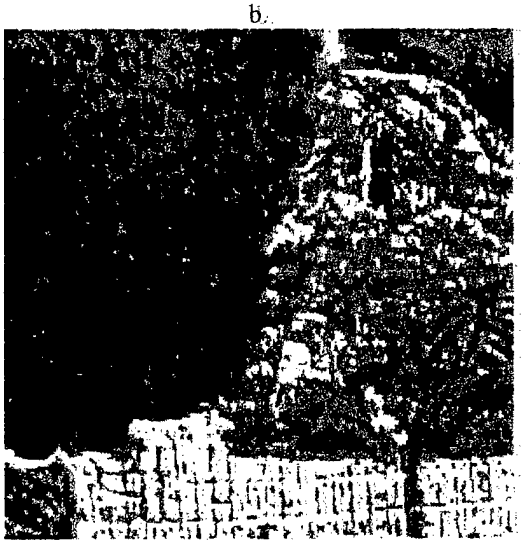

c.

Fig. 1. Results. a) original San Francisco SAR image. Estimated nr. looks 9. b) 3 classes. c) 4 classes.

The Spaceborne SAR Imaging Algorithms Research

Li,Gang Zhu,Minhui Zhu,Xixing
(Institute of Electronics, Academia Sinica, Beijing, China, 100080)
(Telephone: -86-010-62565121, Fax: -86-010-62567363, E-mail: gangl@ie0.ie.ac.cn)

Abstract--In this paper, we mainly discuss some efficient imaging and speckle noise restriction algorithms in the Spaceborne SAR Azimuthy Imaging Processing (SSARAIP) based on the analyses of the spectral characteristics of Spaceborne SAR Echo Signals (SSARES), Range Migration (RM) and Speckle Noise (SN). On the basis of the imaging models of targets on the ground, we also contrast the Customed Imaging Mode (CIM) for fixed-targets and the Moving-target's Imaging Mode (MIM) in detail.

INTRODUCTION

The high imagery resolutions of Synthetic Aperture Radar (SAR) rely on the pulse compression in both range and azimuth directions. The range reference function is determined by parameters such as the Chirp FM Rate of the transmitting pulse etc, and the azimuthy reference function is due to the moving state of radar platform and the azimuthy beamwidth. The main differences between Airborne SAR and Spaceborne SAR lie in their moving states of radar platform. In general, the range pulse compression is accomplished by SAW in antenna part of radar, so the efficient azimuthy imaging algorithms and SN restriction algorithms will be the key to SSARAIP. Under the current hardware conditions, we must improve the efficiency of these algorithms and reduce the complexity of computation as soon as possible to get the accurate images from SSARES quickly. In this paper, we will firstly analyze the basic imaging and moving compensation theorems in SSARAIP based on some basic concepts about SSARES, and then introduce some efficient imaging and SN restriction algorithms, by analyzing the differences between fixed-targets and moving-targets, we develop a kind of efficient azimuthy imaging method with the compitablity for both CIM and MIM.

BASIC CONCEPTS ON SPACEBORNE SAR IMAGING

The Spectral Characteristics of SSARES

The phase change of SSARES can be expressed by the Range Doppler History (RDH) of the relative motion between the radar carrier and targets. To ground fixed-targets, the corresponding RDH is: $R(t)\approx|\vec{R}|+[(\vec{V}\cdot\vec{R})t]/\vec{R}+[(|\vec{V}|^2+\vec{A}\cdot\vec{R})t^2]/2|\vec{R}|$ (1)
$\vec{R}=\vec{R_s}-\vec{R_t}$, $\vec{V}=\vec{V_s}-\vec{V_t}$, $\vec{A}=\vec{A_s}-\vec{A_t}$, where $\vec{R_s},\vec{R_t}$ are position vectors of the satellite and the ground target respectively, $\vec{V_s},\vec{V_t}$ and $\vec{A_s},\vec{A_t}$ are velocity and acceleration vectors of the satellite and the ground target respectively, the instantaneous phase is: $\varphi(t)=4\pi R(t)/\lambda=4\pi[|\vec{R}|+(\vec{V}\cdot\vec{R})t/|\vec{R}|+(|\vec{V}|^2+\vec{A}\cdot\vec{R})t^2/2|\vec{R}|]/\lambda$ (2)
the instantaneous frequency is:

$$f(t)=-1/2\pi\cdot d\varphi(t)/dt=f_{DC}+f_{DR}t \tag{3}$$

where $f_{DC}=-2(\vec{V}\cdot\vec{R})/(\lambda|\vec{R}|)$, $f_{DR}=-2(|\vec{V}|^2+\vec{A}\cdot\vec{R})/(\lambda|\vec{R}|)$

To the ground moving-targets, the corresponding RDH is:

$$R(t)\approx R_0-V_r t+[(V_a-V_c)^2-R_0 a_r]t^2/2R_0 \tag{4}$$

where R_0 is the original distance (t=0) between the radar platform and the targets, V_r is the range velocity of the target, a_r is its range acceleration, V_c is the azimuthy velocity of the target, a_c is the azimuthy acceleration, V_a is the velocity of the radar carrier itself and T is the effective focus time of the antenna. So the phase of RDH is: $\varphi(t)=4\pi R(at)/\lambda$ (5)

Obviously, the SSARES is a kind of scaling Chirp FM signal, two parameters which are the Doppler centroid f_c and Chirp FM rate f_r will determine targets' positions and their moving states: $f_c=2V_r/\lambda$, $f_r=2[(V_a-V_c)^2-R_0 a_r]/\lambda R_0$ (6)

On the basis of the spectral analyses, the range velocity V_r will determine the moving state of the target, to the ground fixed-targets, V_r=0, CIM will focus on the Doppler Spectral Deviation (DSD) caused by the motion of the radar carrier itself only, the images of fixed-targets will concentrate on the clutter area, to the contrary, the DSD caused by the motion of the ground moving-targets (V_r>0) are different, which cause the Doppler centroid's displacement to the MTI area, so the echo spectrums should include both processing areas for fixed-targets and moving-targets simultaneously.

The Imaging Model For Spaceborne SAR [1]

0-7803-3836-7/97/$10.00 © 1997 IEEE

Because of the influence from RM, the mathematical model for SSARES will be more complex than the airborne SAR's. By the analyses of SAR theorem, we develop that the SSARES $S_r(r,x)$ can be expressed as the 2-D convolution between the Backward Scattering Characteristic Function (BSCF) $\sigma(r,x)$ of target backscatter and two 2-D impulse response function (IRF) ($h_r(r,x)$ and $h_a(r,x)$):

$$S_r(r,x) = \sigma(r,x) * [h_r(r,x) * h_a(r,x)] \quad (7)$$

In fact, the SSARES can be taken as the BSCF $\sigma(r,x)$ of ground target through a linear system which IRF is:

$$h(r,x) = h_r(r,x) * h_a(r,x) \quad (8)$$

where: $h_a(r,x) = W_a(x)\delta(r - R(x)) \cdot \exp\{-j4\pi R(x)/\lambda\}$

$$h_r(r,x) = A(2r/c)\delta(x) \cdot \exp\{-j\alpha(2r/c)^2/2\} \quad (9)$$

$W_a(x)$ is the azimuthy weighting function of the antenna, A(.) is the amplitude function with respect to the distance and c is the transmitting velocity of light, α is the chirp FM rate of the transmitting pulse. In fact, the whole procedure of SSARAIP is the 2-D convolution process, and the imaging procedure is to get the function $\sigma(r,x)$. Because of the difference in the range velocity of targets and the influence caused by the moving state of the radar carrier itself, the above mathematical model of the SSARAIP procedure will have some change while for MIM and CIM.

Range Migration and Speckle Noise [2]

SSARAIP must solve the RM effect in azimuth processing and take Multi-Look Processing (MLP)to restrict SN.

Range Migration

From the expression of the instantaneous RDH, we can develop the RM equation as: $R(t) = \lambda(f_{DC}t + f_{DR}t^2/2)/2$ (10)

So the curve of RM is the quadric curve of time, the linear part and the quadric part in the above equation are Range Walk and Range Curvature which are caused by the self-rotation of the earth and the shape of the transmitting wave respectively. The frequency-domain expression of RM is:

$$R(f) = \lambda\{f_{DC} \cdot (f - f_{DC})/f_{DR} + f_{DR} \cdot [(f - f_{DC})/f_{DR}]^2/2\}/2 \quad (11)$$

The Characteristics of Speckle Noise

SN is caused by the random phase of the coarse surface illuminated by the radar interference wave. The brightness of SAR image satisfies the negative exponential distribution, and we often take MLP methods to restrict the influences from speckle noise.,

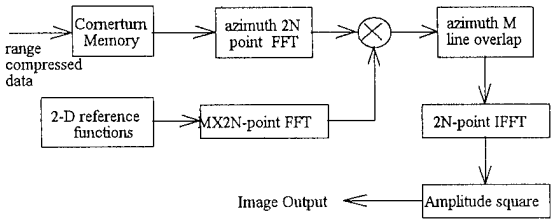

Fig 1. Algorithm Frame of Time-Frequency Hybric Spaceborne SAR Imaging Processing

SPACEBORNE SAR IMAGING ALGORITHMS

Range Migration Correction Algorithm for Fixed-targets

In SSARAIP, we usually take the following algorithms to realize 2-D inverse convolution computation of the echos: Time-domain correlation; Frequency-domain correlation; Time-Frequency Hybric correlation (TFHC); Hierarchial transform methods and Basic-frequency analyzing methods etc. Considering characteristics of SSARAIP and the flexibility of hardware realization, we usually take TFHC (Quick correlation) to correct the RM effect in SSARAIP. The TFHC algorithm is the direct frequential realization of the time correlation algorithm, that is to say, the azimuthy correlation is accomplished in frequency domain, and the RM correction is accomplished by the range correlation processing in time domain, the azimuthy compression processing of SAR is accomplished by FFT in frequency domain. The azimuthy compression processing based on the TFHC algorithm is:

$$I(x,r) = s_a(x,r) \oplus h'_a(x,r) = \iint s_a(x'+x, r'+r)h'_a(x,r)dx'dr' \quad (12)$$

The reference function after range discretization is:

$$h'_a(x,r) = \sum_{i=1}^{M} W_a(x)\exp\{-j4\pi R(x)/\lambda\} \cdot \{[\sin C_0(r_i - R(x))]/[C_0(r_i - R(x))]\} \cdot \delta(r - r_i)$$

Moving-Targets Imaging Algorithms

To moving-targets' imaging and detection, the model of radar echo signal is: $x(t) = s(t) + c(t) + n(t)$, where x(t) is radar echo signal, s(t) is moving-target signal, c(t) is clutter signal, n(t) is noise of system. That is to say, the echo signal of radar can be described as the overlap of moving-targets' signals and noise signals (which include clutters and noise from the system), so the process of moving-targets' abstraction from backscatters can be regarded as the detecting process of moving-targets from noise, and the imaging process can be taken as the Doppler Parameters Estimation Process (DPEP) to unknown-parameters signals.

Usually, the spectrums of moving-targets and fixed-targets mix together in original SARES, we must separate them effectively to get their accurate images respectively and display together. The key to these is the efficient spectrums separation between moving-targets and fixed-targets. In SSARAIP, the main difference between moving-targets and fixed-targets is their radial velocity. The radial velocity of fixed-targets is decided only by the moving state of radar platform, the moving-targets' spectrums transfer in a different way from fixed-targets' within the range of the whole aperture because of the existence of their own radial velocitys corresponding to the position of radar. In original SSARES, moving-targets can be divided into slowly moving-targets and fastly moving-targets according to their velocities corresponding to the velocity of radar platform. To fastly moving-targets, the echo density of fixed-target is usually stronger than moving-target's, so we can use an adaptive filtering method to separate the fastly moving-targets' spectrums from fixed-targets'. To slowly moving-targets, we can implement the separation by means of antenna array (which the echos received by neighboring antenna units at the neighboring time can be canceled), and we can also use Time-Spatial Shift Filters to eliminate the effects from the velocity changes of SAR in a small scope. The key to the above problem is the selection of adaptive flitering weight factor, which is usually determined by the correlative matrix R of echoes, the exactitude of weights in weighting matrix is proportional to the correlativity of echoes. At the same time, to moving-targets' imaging, we should estimate their Doppler parameters accurately. The first step of DPEP is clutters' suppression, that is to say, we must separate the spectrums of clutters from the original echos effectively, there are some kinds of clutters' suppression algorithms, which are: DPCA, AMTI, ADPCA and 2-D time-frequency filtering algorithm etc[3]. The next step is to estimate parameters of moving-targets in clutters-suppressed area to image for moving-targets finally. There are two kinds of important parameters for moving-targets imaging processing, Doppler centroid frequency and Chirp FM rate, and the efficiency of DPEP will determine the exactitude of the final images of moving-targets. We usually take some kinds of 2-D time-frequency distributions such as: Wigner-Ville Distribution (WVD), Extended WVD (EWVD) [4] or Wavelet Transform (WT) etc. to solve resolution conflicts between time and frequency domains. But their final results are different: WVD can't be suitable for multi-moving-targets condition because of its double linearity which will occur some false images caused by the cross-part of WVD, EWVD and CWT which both have linear property can image for moving-targets accurately, and CWT has a better time-frequency resolution than EWVD theoretically, but its complexity of algorithm is also higher than EWVD's, so in practical DPEP, we usually use EWVD.

In order to get the final synthetic images accurately and clearly, we must restrict the speckle noise efficiently.

SPECKLE NOISES RESTRICTION ALGORITHMS

Based on the characteristics of SN, we often take some Multi-look filtering algorithms to restrict SN, and there are some efficient SN restricting algorithms such as Multi-look Whitening Filtering, Multi-look Polar Whitening Filtering and Orthogonal Wavelet Transform [5] etc. Here we won't offer some more detailed discussion and their comparisons on these SN restricting algorithms which are presented in another paper [6] of the author in detail.

REFERENCES

[1] Huang, Yonghong., "Spaceborne SAR Imaging Processing and Moving Compensation", Degree paper for Ph.D of Beijing Airspace and Aerospace University, 1992.

[2] Wu, C., Liu, K.Y., Jin, M., "Modeling and A Correlation Algorithm for Spaceborne SAR Signals", IEEE Tran. on Aerospace and Electronic Systems AES-18, 1982, pp563-575.

[3] Ender, J., "Detection and Estimation of Moving Target Signals by Multi-Channel SAR", Proc. EUSAR'96, Germany, 1996, pp411-417.

[4] Wang Tao., "Synthetic Aperture Radar Moving-Targets Imaging Research", Degree paper for M.S. on Electronics of The Chinese Academy, 1995.

[5] Jinhao Yang, Jianguo Wang, Shunji Huang, "Speckle Filtering for SAR Images Based on Orthonormal Wavelet Transofrm", Proc. EUSAR'96, Germany, 1996, pp151-154.

[6] Li Gang, "The Comparisons of SAR Speckle Noises Restriction Algorithm", to be pressed on the "Journal of Electronics " of China.

MULTISENSORAL APPROACH FOR STUDYING THE GEOLOGY AND TECTONICS OF THE DEAD SEA RIFT /ISRAEL

Bodechtel J.[1], Frei M.[1]., Tretter, W. [1], Wever T.[1], Kaufmann H.[2], Xia Y.[2], Beyth M.[3]

[1]Working Group Remote Sensing, Institute for General and Applied Geology, University of Munich, Luisenstr.37
80333 München, T: ++49 89 5203-222 F: -393
E-mail: Johann.Bodechtel@iaag.geo.uni-muenchen.de. 37,
[2] GeoResearchCenter Potsdam, Telegraphenberg A 17, 14473 Potsdam,
T: ++49-28179-31 F: -11 E-mail: charly@gfz-potsdam.de
[3] Geological Survey Israel, 30 Malkhe Yisrael Str., Jerusalem, Israel
T: ++972-2-314246 F: *972-2-380688 E-mail: beyth@netvision.net.il

Abstract -- The ERS-1/2 tandem mission opened a new dimension in the detection of recent displacements of active tectonic structures like the Dead Sea Rift in Israel. The investigations are mainly concentrated on the northern coastal plains of the Golf of Aqaba and the Wadi Araba. The test site is part of the Aqaba-Levant-Structure situated in the Israel/Jordan/Egypt triangle. It is an active fracture zone with continuous seismic activity. Existing faults developed parallelly and vertically to the major stress component are reactivated and vertical and horizontal movements can be observed. Displacements can be expected twice or even more times a year. ERS-1/2 data were studied to detect reactivated fracture zones and corresponding displacement caused by the earthquake of November 1995.

For studying of the recent displacements ERS-1/2 data sets before and after the earthquake of November 1995 were analysed using the differential interferometry approach. First results will be demonstrated and displacements of several cm will be discussed. Additionally, optical and microwave data like TM and SIR-C/X-SAR were analysed intensively for studying the complete geologic and tectonic framework of the Dead Sea Rift.

For an overall understanding of the process and the interpretation of these remote sensing data, especially the interferometrically processed SAR data, small scale geological, tectonic, soil and land-use maps and DTMs have to be set up. The relevant parameters are extracted from the remote sensing data and completed by ground-truth data. The scientific goal of the project focuses on the evaluation of remote sensing data for a better understanding of the movements along the Dead Sea Rift.

In general it can be stated that radar data are an excellent tool for the detection of structural elements especially in areas were faults are covered by loose sediments. Recent small scale displacements caused by earthquakes can be detected using the phase information of the radar signal whereas the geological setting caused by the tectonic displacements can be detected by optical data.

INTRODUCTION

Optical remote sensing is able to provide a large part of information needed for tectonic investigations. Nevertheless optical data are limited to the surface and monitoring with a high repetition rate using optical data is not realistic. A lack of information about soil conditions can be stated. Especially these restrictions can can be overcome to considerable extent by integrating ERS-1/2 radar data into the present investigations. An important factor for the solution of the above mentioned problems is the integrated use of optical and radar data. An essential improvement is expected by the combination of spectral signatures derived from optical data and physical properties extracted from radar signatures.

Recently different algorithms for the processing of radar data, especially advanced filtering techniques and texture recognition software as well as new methods for the modelling of surface roughness and soil moisture were developed by the working group. Additionally, the application of automatic classification procedures and/or alternative image processing techniques are under investigation.

Another promising technique for the application of ERS-1/2 radar data is the use of interferometry. Using this method, detailed and accurate three-dimensional relief maps of the Earth's surface can be produced directly from SAR-data. In addition, as an extension of the basic technique, the detection of very small vertical changes (mm-scale) of land-surface changes is possible by using the differential interferometry. These possibilities open up many potential applications in the field of geoscientific monitoring for change detection investigations of spaceborne SAR data. In this case ERS-1/2 data before and after the earthquake of November 1995 were investigated to detect reactivated fracture zones and corresponding displacement. First results will be demonstrated and displacements of several cm will be discussed.

The parameters extracted from remote sensing data and other data sources will be stored, analysed and displayed in a geographic information system. A GIS serves as a basis for planning activities, and a modelling of series of scenarios can be done to show the proposed impacts of e.g. tectonic activities to certain regions. The monitoring of movements along fracture zones has become well known since the displacement zone along the San Andreas fault [1] could be shown by specially processed ERS data. The majority of movements along active fracture zones spread on the earth

0-7803-3836-7/97/$10.00 © 1997 IEEE

crust are less sensational, but nevertheless of high importance for long term planning activities. The present investigation area is situated in such an active zone. The horizontal overall displacement is about 107 km on the left and the movement is still continuing. The use of interferometry opens up a new dimension for the observation of small scale movements. For the overall understanding of the process and the interpretation of remote sensing data especially the interferometrically processed SAR data, small scale geological, tectonic, soil and land-use maps and DTM's have to be set up or updated. The relevant parameters will be extracted from various optical and microwave remote sensing data (e.g. ERS. Landsat-TM, SPOT, MOMS-02) and completed by ground-truth data.

TEST SITE

The Aqaba-Levant-Structure [2] is situated along the boarder line of Israel and Jordan: The preliminarily investigated area of the Wadi Araba exeeds from the northern edge of the Gulf of Aqaba to the southern edge of the Dead Sea (180 km).
The structure is considered a left-hand shear zone with 107 km displacement orientated in N 20° E direction. The Aqaba-Levant-Structure is interpreted as a transform fault to the Red Sea rift. The movement of Arabia in relation to the Sinai-Palestine is believed to have taken place intermittently during two principal phases between which there was a prolongated pause. The first phase is considered to be early Miocene or late Oligocene. The last movement is considered to be in Plio-Pleistocene and still continuing.
There are manifold geological features to manifest these displacements. Two regions where studied extensively. The Timna Valley (western bank of the Gulf of Aqaba) and Wadi Fenan (east of Wadi Araba).
Both sides of the Wadi Araba are built up alternating by Lower to Middle Cambrian layers of shales and siltstones. These sequences are underlain by lower Cambrina arkoses and overlain by variegated sandstones and shales of Middle Cambrian age. The precambrian basement underlying the entire area mainly consists of aplitic leucogranites and porphyrites. The sequences are in parts surrounded or overlain by dolomite-silt-conglomerate-sandstone layers of Mesozoic to quaternary age. The plains and wadis are covered by the host-rock depending alluvium fans.
In the vicinity of the northern edge of the Gulf of Aqaba and the southern Dead Sea salt-industry is situated, several mining areas are active, and along the Wadi and west of the Wadi irregated agricultural land use is dominant.
The potential of TM data for the detection of these lithological units could be demonstrated in extent. The detection of fracture zones belonging to the transform-fault structure sometimes shows high correlation to lithological units and are widespread on both sides of the Wadi Araba.

METHODOLOGY OF THE INVESTIGATION

For the general extraction of information from the different imaging sensors distinct processing steps are mandatory. Before merging the data additional pre-processing steps are necessary. The digital data from different sensors or seasons have to be geometrically registered. The data with the lower spatial resolution have to be resampled to the data with the highest resolution. This means that e.g. Landsat-TM data will be digitally enlarged to generate a pixel size similar to the ERS-1/2 data. Within areas with greater relief differences terrain geocoded ERS data were used in accordance with [3]. In a next step, image-to-image control points were selected to register the Landsat data to geocoded ERS data.
The information contents concerning spatial and spectral differences were mixed to generate a single data set with optimal synergism of input data. To merge multisenor data the Intensity-Hue-Saturation (IHS) [3] procedure provides best results in comparison to other well known algorithms. The optical data were processed with common, well known image processing procedures like stretching, rationing, principal component analysis before transferring to the IHS-colour space.
The preprocessing of the ERS-1/2 data is different as for optical data, other and /or additional processing algorithms had to be used, e.g. advanced filter algorithms for the reduction of the radar noise (speckle).
An additional approach for surface change detection and small scale tectonic movements was done by interferometry. Surface changes can be detected by conventional multi-temporal amplitude SAR images as well as by coherence images representing pre-products of interferometry. Tectonic movements can be measured by using differential interferometry.

RESULTS

The SAR differential interferometry technique is a powerful tool to measure small scale movements on the earth e.g. [4]. In this case ERS-1/2 data were investigated to detect small fracture zones and corresponding displacement caused by the 1995 earthquake. The reference topography was calculated from the interferogram phase derived from the ERS-1/2 data pair Aug. 16, 1995 and Sep. 21, 1995 while the phase from D-INSAR between reference topography and interferogram phase was derived from data pair Aug. 16, 1995 and Nov., 29, 1995. First results demonstrate the high potential of the D-INSAR technique but also some problems which have to be considered. Often the orbit parameters are not known with a sufficient accuracy and also atmospheric distortions can occur. Furthermore a three-month-difference between August and November can lead to some changes on the

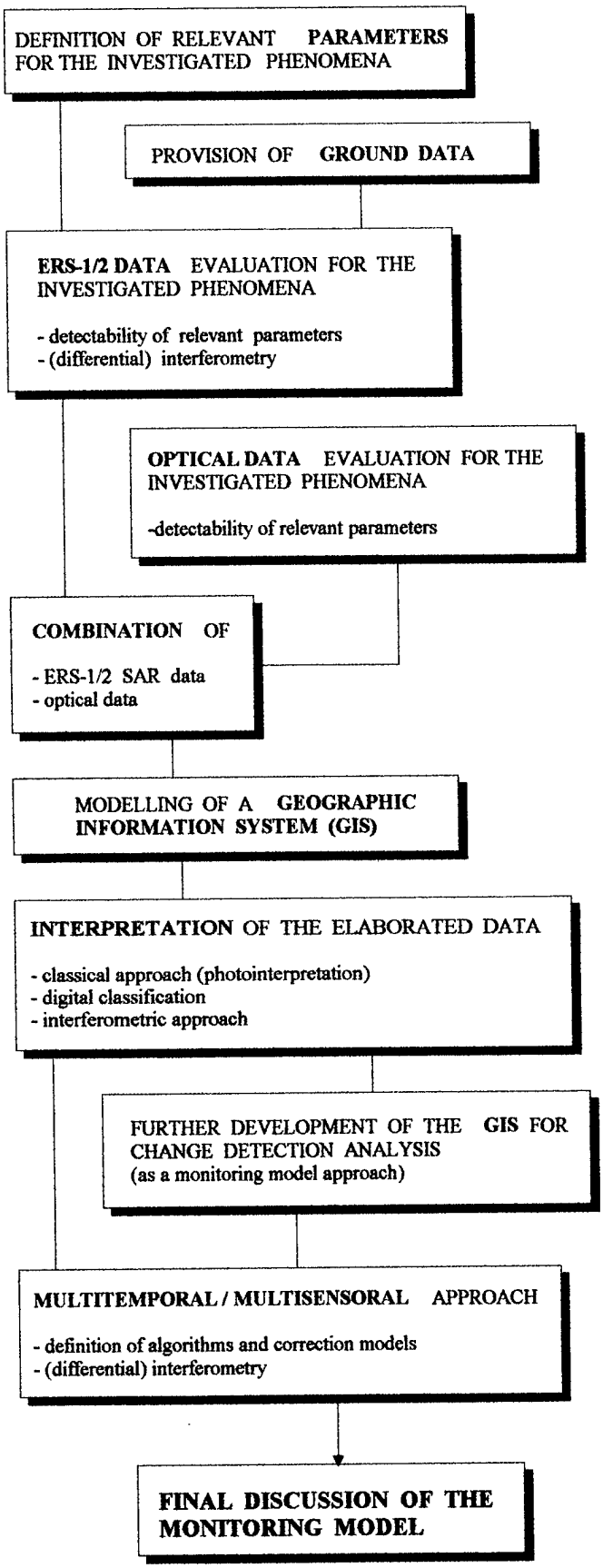

ground due to sediment transpositions which makes the differentiation between tectonical and sedimentary displacement difficult.

For the overall understanding of the processes and the interpretation of the remote sensing data, especially the interferometrically processed SAR data, geologic, tectonic, soil and landuse maps as well as DEMs had to be considered. The relevant parameters were extracted from various maps as well as from optical and microwave remote sensing data. The scientific investigations presented here mainly focus on the characterization of lithological and soil parameters as well as landuse to monitor dynamic physical properties e.g. erosional features via tectonic movements.

The first goal of this project in the near future focuses on the evaluation of the different remote sensing data for the determination of spatially distributed and different order input parameters for a dynamic geo-tectonic model.

The presented study is an example for the integration of ERS-1/2 data into an pre-operational application project of high relevance: Small scale movements along fracture zones. Active tectonic zones are of high interest and have to be discussed by different planning authorities (e.g. mining authorities, roads department, ministry for energy and power plants, water resources department).

REFERENCES

[1] MASSONNET D., ROSSI M., CARMONA C., ADRAGNA F., PELZER G., FELGL K. & RABAUTE T., 1993, The displacement field of the Landers earthquake mapped by radar interferometry, Nature, Vol.364, pp.138-142.

[2] KAUFMANN H., 1988, Mineral Exploration along the Aqaba-Levant Structure by Use of TM-data- Concepts, Processing and Results. International Journal of Remote Sensing, 9, 10-11, pp. 1639-1658.

[3] MEIER E.,FREI U. & NÜESCH D., 1993, Precise Terrain Corrected Geocoded Images. Editor: Schreier G., SAR Geocoding: Data and Systems, Wichmann Verlag, Karlsruhe., pp.173-185.

[4] HENKEL J., 1986, Vergleich der RGB-Farbmischung bei der Verknüpfung unterschiedlicher Informationsebenen in der Bildverarbeitung, Proc. Nutzung von Fernerkundungsdaten in der BRD, BMFT Statusreport, DGLR, Bonn, pp. 443-446.

[5] PRATI C., ROCCA F., MONTI GUARNIERI A., 1993, SAR Interferometry Experiments with ERS-1, Proc. of the First ERS-1 Symp. - Space at the Service of our Environment, Cannes, France, 4-8 Nov. 1992, ESA SP-359, pp. 211-218.

Volcanic Mapping with SIR-C/X-SAR Data for Western Kunlun of China

Changlin Wang, Huadong Guo and Jinjuan Liao
Institute of Remote Sensing Applications, Chinese Academy of Sciences
P.O. Box 9718, Beijing 100101, China
Tel: (86)-10-64917351-3292, Fax: (86)-10-64915035
Email: Guohd@sun.ihep.ac.cn

Abstract - This paper presents a comparative study with SIR-C/X-SAR and Landsat TM data for detecting volcanoes in the northeast of Aksayqin Lake, western Kunlun Mountain. The study shows that these two remote sensing techniques are complementary to each other, and the LHV image can be used best for identifying cinder cones and other features, while, Landsat TM data provide the compositional information of rocks which are not shown on SAR images.

INTRODUCTION

The western Kunlun Mountain in Xinjiang province of China is an east-west mountain range marking the limit between the Tarim basin and the high Tibetan plateau, which was formed in the late Paleozoic and has been reactived since the India-Eurassia collision[1]. Extensive volcanism has existed in the Tibetan area over the last 100 Ma, and volcanism since Cenozoic dominates the volcanic activities in the northern part of Tibetan plateau. A group of volcanoes about 50 km northeast of Aksayqin lake in the western Kunlun was studied with SIR-C/X-SAR data, and field visit was made during a joint field expedition by the scientists from the Jet Propulsion Laboratory and the Institute of Remote Sensing Applications, Chinese Academy of Sciences in August 1995. The paper describes the results of our further study to the volcanoes with both SIR-C/X-SAR data and Landsat TM data.

The study area is arid, with elevation more than 5000m above sea level, and vegetation is very rare. Geological survey is poorly conducted for the area due to its high relief, remote and poor working conditions, and only 1/2000000 scale geological map is available [2]. Prior to our study, the volcanoes were discovered during the survey mapping [2][3], but the spatial distribution and morphology of the lava flows as well as cinder cones presented in the area have not been reported. This study allows more detailed recognition of the volcanic features, and to compare the signatures of these features imaged by both optical and microwave remote sensing sensors, so as to reveal the abilities of these sensors in detecting volcanoes. Rock samples were collected during the field trip and were analysed for its chemical composition and dating their ages.

GEOLOGICAL SETTING

The study area is situated in the highland plateau of Kunlun Mountain, where at least three major crustal blocks (named Kunlun Block, Qantang block and Lhassa block) have been sutured together [4]. The area is bounded by Altyn Tagh fault to the north and Karakorum fault to the south, both of strike-slip fault nature. The Altyn Tagh fault is a left-lateral strike-slip fault, extending about 2000 km along the edges of the Tarim basin. West of longitude 82°E, the fault becomes westly oriented, and runs through Karakax Valley which shows a most prominent linear feature on the remote sensing imagery (e.g. Landsat MSS, TM, SPOT, ERS-1 and SIR-C/X-SAR). The portion of the fault along the Karakax Valley is called Kangxiwar fault in Chinese literature [3]. Studies from satellite images have revealed that the fault is very active with a slip rate between 20 and 30 mm/yr [5]. Indeed, earthquakes have happened 9 times since 1900 along the faulting belt [6], and one of the volcanoes in the Ashikule basin about 120 km northeast of this study area erupted in 1951. To the west of the study, the Dahongliutan fault extends north-westly, and jointed with Karakax fault. There are also many unnamed faults running through the study area, which spatially control the distribution of the volcanoes in this study. In fact, the volcanoes northeast of Aksayqin lake, similar to those of Ashikule basin, are controlled by triangular faulting zones (Dahongliutan fault - Karakax fault - southwestly extension of Altyn Tagh fault), which is obviously favourable for magma movement. The strata rocks in the area are mainly of upper Triassic meta-sediments. The volcanics described in this paper unconfomably lie above the strata.

DATA ACQUISITION AND PROCESSING

The western Kunlun area was imaged by SIR-C/X-SAR in 1994, on board the shuttle "Endeavour". The following data are used in this study: SIR-C data take 111.41, SRL-1 (mode 11, LHH, LHV, CHH, CHV incidence angle at image center 50.4°, pixel spacing rng 12.5m/az 12.5m), X-SAR data take 127.61, SRL-1, (XVV, incidence angle at image center 50.0°, pixel spacing rng 12.5m/az 12.5m). In addition to SIR-C/X-SAR data, Landsat TM 5 with bands 1, 2, 3, 4, 5, 7 are used to show the volcanic features in terms of

0-7803-3836-7/97/$10.00 © 1997 IEEE

reflectance (dominated by the composition of surface materials) versus the intensity of radar backscattering from the surface (influenced by imaging geometry, band and polarization, surface roughness, dielectric constant of surface materials).

X-SAR data and TM data are registrated to SIR-C data, so that all pixels on the images presented in this paper have the same pixel spacing 12.5m x 12.5m in range and azimuth directions. Fig.1a gives a composite color image from LHH (red), LHV (green) and CHV (blue), and Fig.1b shows a composite color image from TM bands 7 (red), band 5 (green) and band 4 (blue). It can be seen from these two figures that although the spatial distribution pattern of the volcanic features are similar, there are considerable differences in the appearances of cinder cones and lava flows, due to the difference of their imaging methods and the nature of the energy received from the sensors (reflectance vs backscattering). In order to integrate these two types of data, principal component analysis (PCA) was made for six TM bands, and also for four SIR-C channels respectively. The first eigenvector of TM PCA analysis was then replaced by the first eigenvector of SIR-C analysis, and then ran PCA again (with PCI software). The resulting image produce an image with integrated features from both SIR-C and TM.

CHARACTERISTIZATION OF VOLCANIC FEATURES

Cinder Cones

In Figs.1a and 1b, the largest cinder corn is apparent above the center of the images. The crater wall facing towards the top of the image was illuminated in SIR-C image, because of the steepness of the wall, the backscattering radar return is very intensive, therefore, it is very bright, however, the brightness makes the island-like feature in the middle of the depressed crater unclear, which is clearly shown in Fig. 1b. On the left side of this cone, SIR-C image shows two small cone-like feature, however, they are apparently two holes originated from the same cone described above, which were mapped as two separate cones in [8]. The signatures for the second largest cone can also be discriminated from Figs.1a and 1b. Geological study in [2][3] suggests that the cones mainly consist of dacite, pumice and minor volcanic breccia.

Apart from the above apparent cinder cones, there are several cones distributed in the lava flow. A comparative study has been made for a portion of lava flow with LHH, LHV, CHH, CHV, XVV and TM band 7 images (Fig. 2). Three large circular features can be recognized from these images, in particular, from LHV image. The circular features are also cinder cones, but they have been considerably degraded. The results suggest that LHV image can best discriminate the cone features due to clear contrast between the apparence of lava flows and cone features. The CHV image also shows better ability to identify cone features than that of CHH image, whereas XVV image is similar to CHH image. As the backscatter coefficients for HV are lower than that for HH [8], depolarization must play an important role. The cone features in TM band 7 appears bright, indicating the presence of light color rocks around the cones, but the circular features are not as clear as that of LHV image. This further suggests that side looking radar can accentuate terrain features such as these degraded circular cones.

Lava Flow

Field survey has confirmed the presence of pahoehoe and block (aa) lava in the area. The pahoehoe lave appears dark in SIR-C and X-SAR image due to its smooth surface, while, aa lava appears bright due to its rougher surface. The aa lava are mostly present around the cinder cone south of the second largest cone (Fig.1a). The original rope surface of pahoehoe lava are not presented, weathering with times degraded the surface which has been filled with eolian sediments. Although no much difference of the pahoehoe lava flow can be identified from the SAR images, the TM band 7 image reveals bright reflectance around the middle of the image (Fig. 2) and also some darker reflectance in the vicinity of the bright features, indicating the composition changes from light color rocks to dark color rocks.

GEOLOGICAL STUDY

The K-Ar isotopic dating for the rocks collected from the field suggest the ages from 7.45 to 3.97Ma [8], i.e. from Miocene to Pliocene epoches. The rocks belong to the shoshonitic series. The study in [2] suggests three phases of eruptions, the eruptive intensities of which were discreased with time. The three phases are: 1) large scale basaltic lava sheets, 2) basaltic andesite around cones, 3) dacite at craters.

CONCLUSIONS

This study has shown that SIR-C/X-SAR and Landsat TM data are two complementary remote sensing techniques for studying volcanic features. The LHV image can best identify cinder cones in this study, which may due largely to the depolarization effect, whereas Landsat TM data can reveal better the distribution of rocks with different compositions.

REFERENCES

[1] Tapponnier, P., and P. Molnar, Active faulting and tectonic s of China, J. Geophys. Res. 82, 2905-2930, 1977.

[2] Bureau of Geology and Mineral Resources of Xinjiang, Geological map of Xinjiang-Uygur Autonomous Region, scale 1/2000000, 1993.

[3] Zhang, Z. D., Li, G. L., and Yang, D. P., , The geological characteristics, formation and development of Kangxiwa fault, Xinjiang Geology, 5(3): 50-57, 1987.

[4] Arnaud, N.O., Vidal, Ph., Tapponnier, P., matte, Ph., and Deng, W.M., The high K_2O volcanism of northwestern Tibet: Geochemistry and Tectonic implications, Earth and Planetary Science Letters, 111, 351-367, 1992.

[5] Peltzer, G. P. Tapponnier, and R. Armijo, Magnitude of late Quaternary left-lateral displacements along the north edge of Tibet, Science, 246, 1285-1298, 1989.

[6] Seismic Institute, Bureau of State Seismology, Altas of Landsat imagery of main active fault zones in China, 147pp., 1989.

[7] Liu, J. and Yi, M., Quaternary volcanic distribution and K-Ar isotopic ages in western Kunlun Mountain, Chinese Science (B), 2: 180-187, 1990.

[8] Guo Huadong, Liao Jingjuan, Wang Changlin, Wang Chao, Thomas G. Farr and Diane L. Evans, Use of multifrequency, multi-polarization shuttle imaging radar for volcano mapping in the Kunlun Mountains of western China, Remote Sensing of Environment, Vol. 59 (2), 364-374, 1997

Fig.2 Comparison of SIR-C LHV with TM band 7

Fig. 1a Upper, SIR-C LHH, LHV, CHH (RGB)
Fig. 1b Lower, Landsat TM 7, 5, 4 (RGB)

Viewing China With the ERS-1 WSC Data

Wang Xiangyun[1,2], Wang Chao[1], Guo Huadong[1]

1. Institute of Remote Sensing Application, Chinese Academy of Science, (Beijing, 100101)

2. Department of Earth science, Nanjing University, (Nanjing, 210093)

Abstract----This paper analyses the distributive characteristic of China land surface backscatter coefficient with ERS-1 WSC data. Results show that China land surface backscatter coefficient image is the synthesis of vegetation map and terrain map. From the image, at the first eye, the vast Takla Makan deserts, the reach to the sky Qingzang plateau, ringlike Chengdu basin, and a chain of undulating southern China hills greet one's eye. Insight into the image, a lot of information can be acquired, for example, the tectonic sketch of China, the distribution of vegetation and deserts. It is a very important source to study the tectonics, the coverage of vegetation, and desertification. The statistical study of the typical terrain shows that using the WSC data could discriminate six types of main land surface coverage including: deserts; Gobi; plateau and basin; mountains; vegetation; and snow-covered field. On the whole, backscatter coefficient σ° value range from -30—-5 dB. The lowest value corresponds to desert of Takla Makan, Badain Jaran, Tengger. The highest value corresponds to snow-covered regions of Himalaya mountains and Tianshan mountains.

1. INTRODUCTION

The objective of this paper is to insight the capabilities of the C-band scatterometer for monitoring land surface. The emphasis is put on the land surface coverages of China. The major feature of the scatterometer is that the backscatter coefficient values(σ^{0}) of terrain can be quantitatively measured.

The normalized radar backscatter coefficient at C-band , VV polarization, depends mainly on the moisture content of the soil and the vegetation, the vegetation types and coverage, and the surface roughness[1]. The radar backscatter coefficient increase with soil moisture and moisture content of the vegetation, for small incidence angle the radar backscatter coefficient is sensitive to soil moisture and decrease with surface roughness. For larger incidence angles (40^{0}-45^{0}) the radar backscatter coefficient increases with surface roughness and, in the presence of vegetation, with biomass. In arid regions the radar backscatter coefficient mainly depend on surface roughness, dielectric constant, and penetration depth[2].

2. DISTRIBUTIVE CHARACTERISTICS OF BACKSCATTER COEFFICIENT OVER CHINA LAND SURFACE

Fig. 1 show the distribution of backscatter coefficient over China land surface. On the whole, backscatter coefficient σ^{0} value range from -30 to -5 dB. The lowest value corresponds to Badain Jaran, Takla Makan, Tengger deserts, the highest value correspond to snow-covered regions . The most striking feature is the synthesis of vegetation and terrain map[3]. Overall, six types of surface can clearly be distinguished: deserts; Gobi; plateau and basin; mountains; vegetation; snow-covered field . The range of distribution for these six types can be identified from coloration.

It is common knowledge that C-band, VV polarization system mainly sensitize to soil moisture content, vegetation covering, and surface roughness, these characteristics are fully demonstrated over the image of China backscatter coefficient. Chinese geographer subdivided the land into four different parts by the factor of dryness, such as wet, subwet, subdry, and dry area[4]. From the range of distribution both map of dryness factor and backscatter coefficient, one can find out the relationship of dryness factor k and σ^{0} as follows:

wet area $k<1.0$ σ^{0}=-7--10dB

0-7803-3836-7/97/$10.00 © 1997 IEEE

subwet area	k=1.0-1.5	σ^0=-12--13dB
subdry area	k=1.5-2.0	σ^0=-14--16dB
dry area	k>2.0	σ^0=-17--30dB

By combining the subwet and subdry area into one, and naming it as a transitional belt, we can obtain a map of China land soil moisture acquired by ERS-1 WSC data, which would probably be the sources of information for studying the variation of atmosphere and soil moisture.

China is a mountainous country, the bedrock, snow-covered area or vegetation on the mountains contribute very strong backscatter coefficient, the σ^0 value is -11dB. Excepting the southeast China, almost all of the mountains are easily identified from the image.

Mountains are the resultant of geological tectonic, so, it is also the source of information for studying geological tectonics.

As far as vegetation, the forest resources in China are very rich, and are mainly located in the southeast of China. Bounding in above-cited wet area, in north of the boundary, the main types of the forest are deciduous, on contrary, in south of the boundary, the main types of forest are evergreen broad-leaf forest and tropic rain forest. Its backscatter coefficient values ranging from -10 to -7dB, are mainly located in the wet area.

3. CONCLUSION

Above analytical results show that six types of main land surface coverage can be identified based on distribution character of China backscatter coefficient. This paper demonstrate the high capability of ERS-1 WSC data for monitoring land coverage at regional scales.

ACKNOWLEDGMENT

The authors thank the ESA for providing us the ERS-1 WSC data by project A02. RC101.

REFERENCES

[1] F. T. Ulaby, R. K. Moor, A. K. Fung, 1986, Microwave Remote Sensing, Active and Passive, Vol. II .

[2] Volkmar R. Wisman, kai Boehnke, and Christiane Schmullius, 1995, Monitoring Ecological Dynamics in Africa with the ERS-1 Scatterometer, IGARSS'95, 0-78032567-2/95.

[3] Huang Xiulian, Shen Wenxuan, 1992 , The Newest Map Atlas of the World, China map Press.

[4] Zhu Kezhen, 1985, Physiographic of China, Science Press.

The Image of ERS-1 WSC Backscatter Coefficient over China in March, 1996

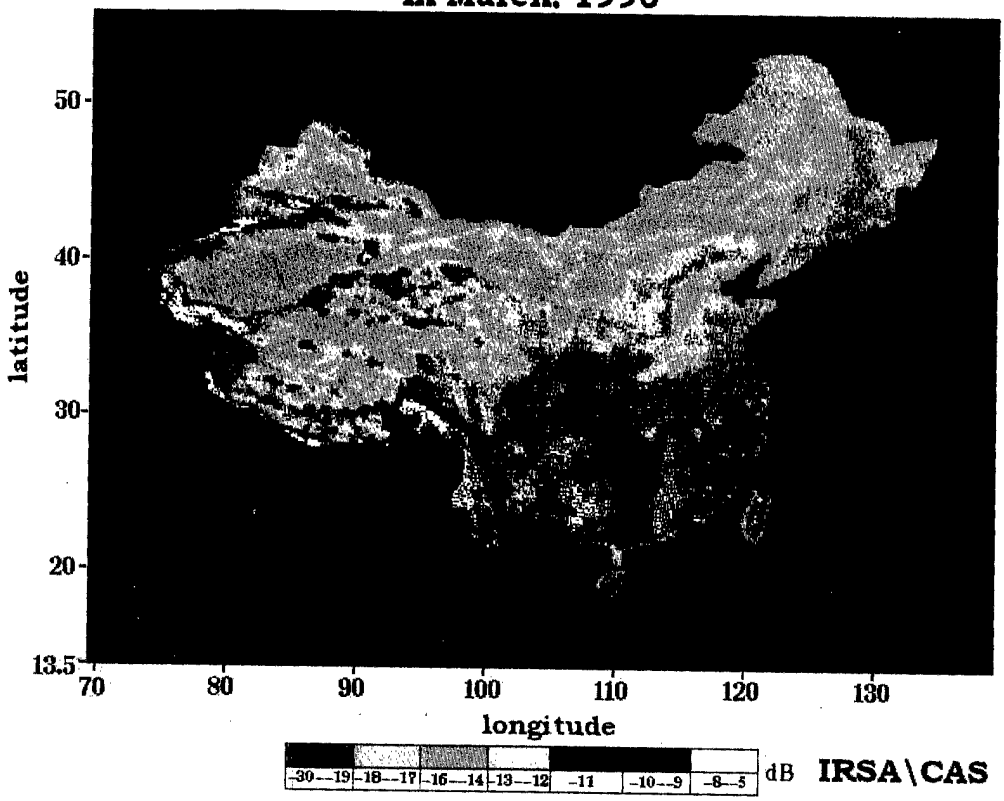

EFFECTS OF TERRAIN TYPES ON THE SELECTION OF RADARSAT BEAM MODES FOR GEOLOGICAL MAPPING

Vern Singhroy
Canada Centre for Remote Sensing
588 Booth Street
Ottawa, Ontario, Canada K1A 0Y7
Telephone: (613) 947-1215/Fax: (613) 947-1385/Email: vern.singhroy@ccrs.nrcan.gc.ca

Abstract -- RADARSAT has 35 different beam and incidence angle positions with spatial resolution varying from 10-100m. In order to maximize its use for geological and geomorphological mapping, it is necessary to evaluate the various beam modes and report on their suitability.
Our results have shown that selected RADARSAT viewing geometry is significant for the delineation of geological structures, lithological units, landforms and terrain types. In mountainous terrains, incidence angles varying from 40-59 degrees, are suitable for structural and geomorphic mapping. Small incidence angles, varying from 20-31 degrees, are suitable for the Precambrian shield terrains. A wide range of incidence angles, varying from 25 to 45 degrees, is suitable for the flat and rolling prairies.

INTRODUCTION

The effects of SAR viewing geometry for geological mapping are significant. This is based on the fact that the effects of terrain and surface roughness on RADARSAT backscatter varies with different viewing geometry. Geologists identify structures and landforms from changes in topography and textural patterns. In barren environments, surficial materials and rock types are identified by their surface roughness characteristics. The different ways the SAR views the terrain naturally affects the geological interpretation in terms of the delineation of geological structures, surficial materials, rock units and landforms.
Recent studies have focused on evaluating the relative benefits of the viewing geometry of CCRS airborne SAR, ERS-1 and JERS-1 for geologic mapping. Results have shown that the SAR viewing geometry and surface cover are significant in the delineation of geological structures, surficial materials, lithologic units and landforms [1, 2, 3, 4]. In addition, [5] have shown that the effects of terrain slope on radar backscatter is significant with different viewing geometry.

This investigation provides some general guidelines for the use of selected RADARSAT beam modes for representative geological terrains in Canada.

STUDY AREAS

The study areas were selected to represent different terrain types and surfaces in Canada. The terrain types represent high, moderate and low relief. The study areas are representative of these terrain types. They are:
the rugged forested mountainous terrains in the Canadian Cordillera with relief varying from 1800-3800 meters.
the variable glaciated forested and moderate relief within the Canadian Shield. The relief varies from 325 to 400 meters.

The low rolling prairie terrain which varies from 275- 375 meters.

DISCUSSION

For the most part the RADARSAT images were interpreted for surficial geological information. It is clear that orthogonal viewing, which is determined by the local slope is the most suitable for geological mapping. An interpretation of the RADARSAT image in relation to viewing geometry is briefly described for each test site.
In the *Fraser Valley*, within the Cordillera, thirty-five large landslides ranging in size from at least 1 million to more than 500 million cubic metres have been identified.

An interpretation of Standard beam mode, S1 (20-27 degrees), and an Extended high beam mode, EH6 (57- 59 degrees) was done for mapping landslide features (see Table I). The landslide features on the steep slopes of the Fraser valley are more easily recognized on the EH6 images than from the S1 image. The eastern slopes where most of the slides are occurring has a local slope which vary from 40-60 degrees, and as such are suitable for RADARSAT viewing at the higher angles between 40 and 60 degrees. The significance of identifying the characteristic landslide features is that they provide clues on the nature of motion and therefore indicate potential hazards along transportation routes and where protective measures should be made. In comparison, the S1 image with its steep viewing geometry resulted in considerable layover, which restricts interpretation of landslide features.

In general, the Precambrian shield has the local slope which varies from 10 to 35 degrees with sharp breaks in the terrain because of differential erosion and deposition from glaciation.

The RADARSAT backscatter is primarily from the canopy of the boreal forest cover. Topographic variations are enhanced by the large number of steep but small breaks in the terrain. These breaks are very significant from a geological standpoint. They represent the slopes of glacial and linear

0-7803-3836-7/97/$10.00 © 1997 IEEE

features and edges of outcrops. RADARSAT S1 or S2 (20-31 degrees) are the most suitable to recognize geological features in most Canadian Shield terrains. A comparison of Standard beam S2 (24-31 degrees) and S6 (41-46) shows that more linears and glacial features are clearly recognised from the S2 image than the S6. A summary of features recognized is included in Table 1. It is important to note that S6 and other higher incidence angles are also useful for geological mapping in this terrain but the S1 and S2 beams (20-31 degrees) provide a more useful image.

In the low prairie terrains both the RADARSAT S2 (24-31 degrees) and the S7 (45-49 degrees) images were useful in mapping strandlines flow slides and drainage patterns. In this area the local slope varies from 5 to 30 degrees, but unlike the Canadian Shield the topographic breaks are less abrupt and are enhanced by local landuse patterns. For this reason a variety of RADARSAT viewing geometry are useful for surficial geologic mapping. For example the S1 is suitable for the subtle topographic breaks and the S7 is suitable for the landuse patterns (see Table I). Because the geomorphology is related to landuse the S7 appears to be a more useful image.

With the exception of stereo-viewing, there are no strict guideline for the use of ascending and descending mode for geological mapping. Their use is based on the direction of the structures and landforms needed to be interpreted. The maximum information is obtained only when the feature is perpendicular to the SAR viewing geometry. However, stereo-viewing is an additional technique which provides a better rendition of the geologic features than monoscopic viewing. Depending on the nature of the interpretation the additional image needed for the stereo radar interpretation can be costly. The best results are obtained from same-side stereo (ascending/ ascending or descending/ descending) with large overlaps and stereo intersection angles (e.g. S1/S6 or S2/S7) [6].

CONCLUSION

The guidelines developed from this study will be of use in similar terrains outside Canada. The interpretation of several RADARSAT beam modes and their uses to surficial geological mapping, and geohazard assessment in different Canadian terrains has shown the following.

Different RADARSAT viewing geometry exhibits significant differences in images for the delineation of geological structures, lithological units, landforms and terrain types.

In mountainous terrains, incidence angles varying from 40-59 degrees, are suitable for structural and geomorphic mapping.

Small incidence angles, varying from 20-31 degrees, are suitable for the Precambrian Shield terrains.

A wide range of incidence angles, varying from 25 to 45 degrees, are suitable for the flat and rolling prairies.

REFERENCES

[1] Singhroy .V 1996 Environmental and Geological site characterization in vegetated areas : Image enhancement guidelines. *Remote Sensing and GIS: Applications and Standards. ASTM Special Technical Publication #1279. V. Singhroy, D. Nebert. and A. Johnson, Eds., American Society for Testing and Materials*. pp.5-17.

[2] Singhroy. V. Kenny F. and P Barnett.1992. Radar Imagery for Quaternary geological lapping in Glaciated Terrains. *Canadian Journal of Remote Sensing* Vol 18 # 2 pp 112-117.

[3] Singhroy, V.H., Slaney R., P. Lowman Jr., Harris J., and W. Moon, 1993. "Radarsat and Radar Geology in Canada". *Canadian Journal of Remote Sensing, Vol* 19, pp. 338-351.

[4] Lowman, Paul D. Jr., 1994: Radar Geology of the Canadian Shield: a ten year review, *Canadian Journal of Remote Sensing*, Vol. No. 3, pp 198-209.

[5] Ahern, F.J. and R.K. Raney, 1993 An Almaz / ERS-1 Comparison demonstrates incidence angle effects in Orbital SAR Imagery. *Canadian Journal of Remote Sensing,* Vol 19 #3 pp 259- 262.

[6] D'Iorio, M., A, P. Budkewitch and N.N. Mahmood. 1997. Practical considerations for geological investigations using RADARSAT-1 stereo image pairs in tropical environments. GER'97. 8p.

Table 1: Summary of selected RADARSAT beam modes for geological mapping

Area	Relief	Surface Cover	Recommended Viewing Geometry	Features Identified
Cordillera- Fraser Valley	1800-3800m 40-60 degrees slope with large terrain breaks.	forest, mainly conifers	40-60 degrees	• Block slide • Ridges • Scarp • Faults
Precambrian Shield. Geraldton Mineral Belt	325-400m 10-35 degrees slope with numerous small terrain breaks due to differential erosion and deposition	Mixed forest	20-35 degrees	• Faults • Fluted surfaces • Eskers • Thick till • Thin till • Organic terrain • Some lithotectonic units
Prairies Morden, Manitoba.	275-375m 5-30 degrees slope with minor breaks from streams.	Mainly Agriculture	20-50 degrees	• Strandlines • Flow slides • Drainage patterns and associated alluvium

Title: Influence of Canopy Shape on SAR Speckle Distributions over Woodland

Mark L. Williams
Defence Research Agency
R117, St Andrews Road, Malvern, Worcs. WR14 3PS, UK.
Tel: +44 (0)1684-894671, Fax: +44 (0)1684-894481, Email: mark@sar.dra.hmg.gb

Abstract -- A first order, mean field model for scattering from a woodland canopy is developed in the distorted Born approximation. The model is applied to simulated mixed woodland. Full account is taken of shading, shadowing and the SAR imaging process. Resulting simulated SAR images are barely distinguishable from real C-band SAR images of woodland, and show intensity speckle distributions that are well modelled by the K distribution at low to moderate resolutions. Speckle distribution shape is revealed to depend upon resolution, incidence angle, canopy topography and instrument function and the physical origins of these dependencies are identified within the context of the model.

INTRODUCTION

The intensity distribution in synthetic aperture radar (SAR) images has been used to discriminate woodland [1]. However, the speckle distribution for woodland is observed to depend upon imaging conditions and canopy type [2]. It is important, therefore, to understand the physical origins of intensity speckle distributions in order to access the information they contain. Previous work with discrete scatterer vegetation models [1] has shown that cross section fluctuations, and number fluctuations can influence intensity distributions. However, these cannot account in full for observed distribution moments. It has been speculated that shadowing effects in woodland canopies are the main influence on intensity distributions but until now no physical model has been available to investigate this idea. A model for scattering at short wavelength from an undulating woodland canopy is developed in this paper. The model is fundamentally a first order, mean field model and as such is only proposed for the modelling of copolar backscatter since cross-polar backscatter calculations require second order models or higher [3]. The theory, briefly outlined in the following section, is formulated in terms of the distorted Born approximation (DBA) for an isotropic canopy [4].

THEORY

Scattering from a flat vegetation half-space

Discrete scatterer vegetation models employing the DBA make use of the concept of scatterers embedded in a flat, half-space, effective medium [4]. The introduction of what is an essentially artificial boundary plays an important role: it fixes the incidence angle and determines transmission coefficients. In addition, the electric field boundary conditions determine the mean field decay constant. The boundary also provides a height reference. The half-space model is applicable when the canopy depth far exceeds the decay constant e.g. in a green woodland canopy at C-band [1]. The DBA is encapsulated in a single equation for the scattered field [4, equation 60]:

$$E_s \approx \sum_n G_{eff}\, S_n < E > \qquad (1)$$

Using in (1) the Foldy-Lax approximation [1,4] for the permittivity of the effective medium comprised of Rayleigh-Gans [3] scatterers with scattering operators S_n, and employing expressions from [5] for the effective Green's function G_{eff} and mean field $< E >$ for an isotropic half-space, it can be shown that the backscatter cross-section per unit area of surface is [1]

$$\sigma^o = \rho \cos\theta < \sigma_n^o >_n T(\delta / 4) \qquad (2)$$

where ρ is the number of scatterers per unit volume, θ is the incidence angle, $< \sigma_n^o >_n$ is the mean scatterer cross-section, T is the two-way power transmission coefficient and δ is the mean field decay constant or penetration depth.

Scattering from an uneven vegetation canopy

The flat canopy model is a poor approximation for a woodland where the canopy height fluctuates on a scale commensurate with the SAR resolution. However, we make the approximation of local flatness on a scale *less* than the SAR resolution (see Fig.1). The woodland canopy is divided into flat facets, with dimensions smaller than the SAR resolution, but greater than the radiation wavelength.

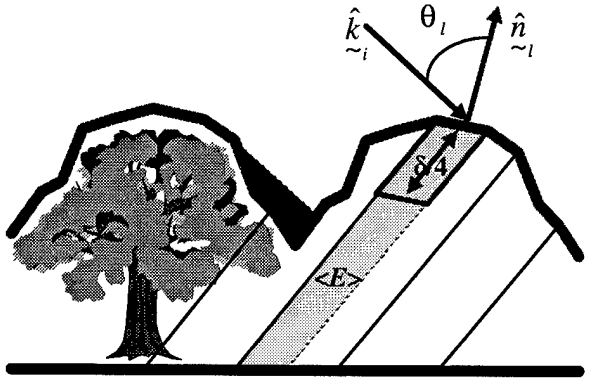

Figure 1. Discrete woodland canopy and imaging model

0-7803-3836-7/97/$10.00 © 1997

Each facet cross section may be approximated using (2) if we replace the global incidence angle, θ, with a local incidence angle, θ_l, determined from the facet normal, $\hat{n}_l$ and the incident wave vector, $\hat{k}_i$. In addition a facet is taken to contribute zero cross section if a) local incidence is greater than 90° (shading), or b) it is geometrically obscured by another element of canopy (shadowing).

Account is taken of the SAR imaging process by projecting the mean facet cross sections onto the SAR imaging plane using the concept of range gates. In keeping with the first order, mean field scatter nature of the model, the mean facet cross sections should be determined by summing (1) over the corresponding range volume and averaging the backscattered intensity. However (2) is used to approximate this process using the concept of local flatness. The instrument function is incorporated by allowing each mean facet cross section to contribute to neighbouring SAR pixels with the appropriate weighting. In this way, and uniquely, a mean cross section SAR image is generated. The projection process has the effect of 'compressing' a bright leading edge into a small image space, and of 'stretching' shadowed/shaded areas across larger image spaces.

To obtain the single point speckle distribution two techniques are used. The first simply assumes that the speckle is 'locally Gaussian' and replaces each SAR pixel in the mean intensity image with a random number taken from an exponential distribution with the given mean. This technique is the most efficient but it does not preserve the correlations in the speckled image and for this a second technique is used. Returning to the generation of the mean image, if instead of summing facet mean cross sections into SAR pixels we sum complex realisations of the facet scattered *field*, again 'locally Gaussian', then a speckled image results which preserves image correlations. That the two techniques yield the same single point speckle distributions is readily proved provided that the mean number of facets per SAR resolution cell is large (≥ 9).

Simulation of a woodland canopy

A simulated woodland has been used with the model. Trees of varying diameters were arranged randomly on a periodic flat surface. Crown shapes were either conical for pine trees or ellipsoidal for deciduous trees. Crown size was linked to the tree's nearest neighbour separation and crowns overlapped for high cover. Gaussian correlated height noise was added to the crown shapes to degrade their regularity and to mimic the trees' internal structure. The canopy was then discretized for use in the SAR simulation. Examples of height profiles taken through a mixed canopy of some 900 trees in an area 120m by 120m are displayed in Fig.2.

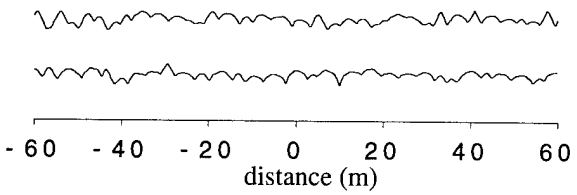

Figure 2. Simulated woodland height profiles.

RESULTS

Fig.3 shows images generated from the simulated canopy which has a height standard deviation of 0.9m. Fig.3(a) is a projection of the canopy surface cross section which reveals the shadowing and shading (looking left to right). Fig.3(b) is the mean intensity SAR image and Fig. 3(c) is the correlated speckle image produced by summing field returns. The resolution is 1.6m in azimuth and range, and the incidence angle is 55°. Topographic features apparent in Fig.3(a) are preserved to some extent in the mean image but are disguised by speckle. At higher resolutions topographic features are recognisable in speckled images. Fig.3(d) is a section of a real SAR image of mixed woodland at the same incidence and resolution which has the same textural properties as the simulated image.

The model has been used to investigate the dependence of texture on resolution and incidence for a mixed canopy. A measure of texture is the normalised second intensity moment, $I^{(2)} = \langle I^2 \rangle / \langle I \rangle^2$.

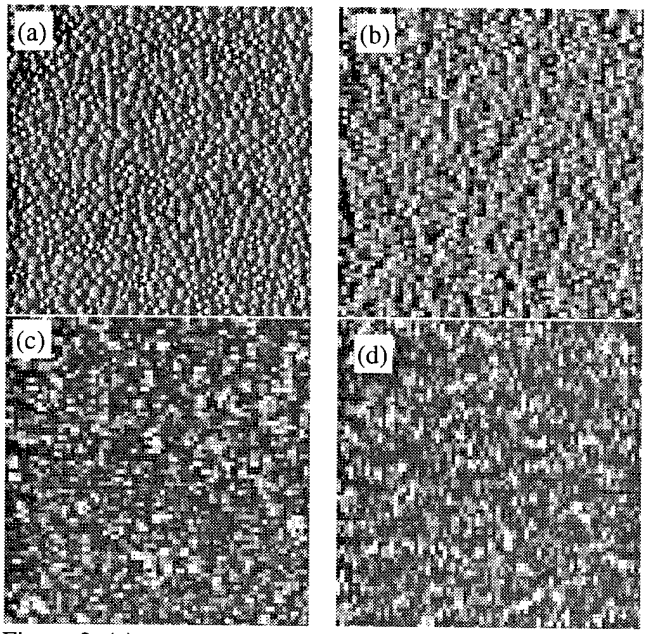

Figure 3. (a) mean canopy cross section map, (b) mean SAR intensity, (c) speckled SAR intensity, (d) SAR intensity image from *real* observation of woodland.

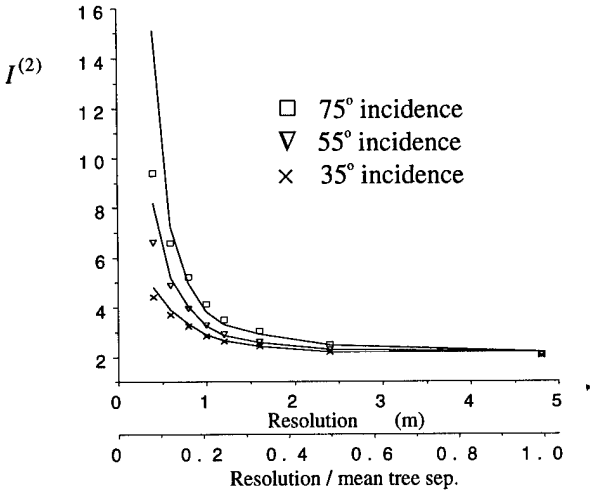

Figure 4. Normalised second intensity moment v resolution. Symbols: data, full lines: estimate from best fit K-dist'n.

For exponentially distributed, fully developed speckle $I^{(2)} = 2$ .The value of $I^{(2)}$ in Fig.3(c) and Fig.3(d) is 2.6 and the intensity in both these images is K-distributed. Fig.4 shows the variation of $I^{(2)}$ with resolution. At a low resolution of 4.8m (~ mean tree separation) the images display little texture and intensity distributions are exponential. At all incidences the normalised moments increase monotonically and more rapidly with improving resolution. The simulated intensity distributions are found to be K-distributed at moderate resolution, but depart from K significantly as the resolution is increased. It is interesting to note that whilst the fit to K-distribution in the speckled image is generally exceptionally good, the underlying mean image is not so well approximated by the corresponding Γ-distribution. The values obtained from simulation are in very good agreement with observations. Moments are also seen to increase with increasing incidence angle as is more clearly revealed in Fig.5.

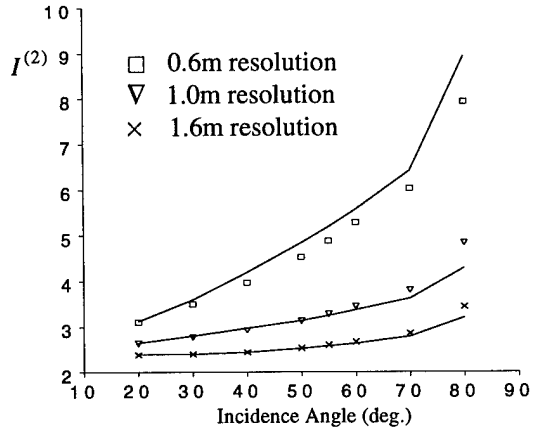

Figure 5. Normalised second intensity moment v incidence angle. Symbols: data, full lines: est. from best fit K-dist'n.

DISCUSSION

The model reveals the dependence of intensity speckle distributions upon both canopy topography and the imaging process. The distribution of cross section values on the canopy surface is very different from that in the mean SAR image as a result of the imaging process. Long, bright leading canopy edges are compressed into single SAR pixels and shadowed areas tend to occupy a greater extent of the final image. This has the effect of stretching the bright end of the intensity distribution and raising the dark end, aiding the transition from exponential to K-distribution. Intensity moment values obtained from simulations are in good agreement with observations, implicating topography and imaging as the main influences on speckle distributions.

Global incidence angle dependence can be traced to the variation in shadow length and the change in distribution of local incidence angle. At low resolution the effects of local slope variation are averaged out and the intensity is exponentially distributed. Local slope effects become apparent as the resolution improves. This behaviour reveals information about the canopy height correlation length, which in turn is linked to the distribution of tree separations. So intensity distributions contain information about the distribution of trees and their crown shapes and sizes. That intensity is K-distributed at moderate resolution is verified observationally. The model predicts a trend away from the K-distribution at higher resolutions.

Verification of the woodland canopy model is desirable. Forest type discrimination, cover estimation and speckle correlations are under investigation. Estimates of mean backscatter cross section can vary significantly between the flat canopy model and the undulating canopy model. The model will be extended to anisotropic canopies, cross-polar backscatter and shallow canopies/longer wavelengths.

ACKNOWLEDGMENTS

MLW thanks D. Blacknell, A. Blake, C. J. Oliver, S. Quegan, and R. White.

REFERENCES

[1] M. L. Williams, S. Quegan & D. Blacknell, "Distribution of backscatter...", Waves in Random Media, in press.

[2] S. Quegan & I. Rhodes, Int. J. Remote Sens., vol. 16, p.1183, 1995.

[3] M. L. Williams & S. Quegan, "Modelling microwave backscatter...", Waves in Random Media, April 1997.

[4] R. H. Lang & Sidhu, IEEE Trans. Geosci. & Remote Sensing, vol. 21, p.62, 1983.

[5] J. K. Lee & J. A. Kong, "Active remote sensing...", Electromagnetics, vol. 3, p.111, 1985.

Prior Scene Knowledge for the Bayesian Restoration of Mono- and Multi-Channel SAR Images

Edmond Nezry, *Armand Lopes, Francis Yakam-Simen

PRIVATEERS NV, Private Experts in Remote Sensing
42 De Weaver Drive, Philipsburg, Sint Marteen, Netherlands Antilles; c/o 21 via Carducci, 21027 Ispra, Italy
Phone/Fax: (+39) 332-781494; E-mail, via: http://www.treemail.nl/privateers/

*CESBIO (UMR 5639 CNES/CNRS/UPS), 18 Av. E. Belin, BP 2801, 31401 Toulouse Cedex 4, France
Phone: (+33) 5-61558539; Fax: (+33) 5-61558500; E-mail: armand.lopes@cesbio.cnes.fr

ABSTRACT

Ideally, using SAR data in combination with optical data or to invert of a physical backscattering model, prior scene knowledge is introduced in adaptive speckle filters to aim at restoration of radar reflectivity *i.e.* of the physical quantity, proportional to the backscattering coefficient, that is measured by a SAR instrument. Introduction of A Priori knowledge or A Priori guess implies generally the use of Bayesian methods in the processing of SAR images. In this paper, we analyse how prior knowledge, or prior guess, of the first order and of second order statistics of the imaged scene has been gradually introduced in the development of adaptive speckle filters. It is shown how these scene statistical models are used, in particular in a Bayesian Maximum A Posteriori (MAP) inference process. These Bayesian filters, that present the structure of control systems, are analysed in terms of stability and commandability.

1. INTRODUCTION

Fifteen years ago, speckle filtering was generally considered as a simple image enhancement operation, which could be done using heuristic filters (block averaging, median filter, etc.). In the last years, speckle filtering was slowly reconsidered as an operation dedicated not only to remove "speckle noise" in SAR images, but also to prepare such images for data fusion with optical data or for the inversion of a physical backscattering model. In this framework, the introduction of prior scene knowledge in speckle filters became a domain of growing interest.

In presence of scene texture, to preserve the useful spatial resolution, *e.g.* to restore the spatial fluctuations of the radar reflectivity (texture), an A Priori first order statistical model is needed. With regard to SAR clutter, it is now well accepted that the Gamma-distributed scene model is the most appropriate [1-3]. The Gamma-distributed scene model, modulated by, either an independent complex-Gaussian speckle model (complex SAR images), or by a Gamma speckle model (multilook detected SAR images), gives rise to a K-distributed clutter. Nevertheless, the Gaussian-distributed scene model remains still popular, mainly for mathematical tractability of the inverse problem in case of multi-channel SAR images (multivariate A Priori scene distributions).

2. BAYESIAN MAP SPECKLE FILTERING

To account optimally for non-linear effects of the scene/speckle combination giving rise to an actual SAR image, introduction of A Priori knowledge or A Priori guess implies the use of a Bayesian method to solve an inverse problem, such as the restoration of the radar reflectivity in speckled SAR images. As an example, lets consider the case of a multi-channel detected SAR image. The inference mechanism, that enables, at the lowest error cost, to deduce conditional A Posteriori radar reflectivity vector R/I from its speckled observation I uses the Bayes theorem:

$$P(R/I) = P(I/R) \,.\, P(R) \,/\, P(I) \qquad (1)$$

where $P(I/R)$ is the joint probability density function (pdf) of speckle, and $P(R)$ is the joint pdf of the radar reflectivity, introduced as statistical A Priori information. Eq.(1) combines A Priori knowledge $P(R)$ and new knowledge given by the observation I. Clearly, the A Posteriori estimation of R is influenced by the prior knowledge (or prior guess) of the statistical properties of R.

The MAP estimate corresponds to the maximum of the A Posteriori distribution $P(R/I)$:

$$\partial \mathrm{Ln}(P(I/R))/\partial R_i + \partial \mathrm{Ln}(P(R))/\partial R_i = 0 \quad \text{for } R_i = \hat{R}_{i\,MAP} \qquad (2)$$

The first (Maximum Likelihood) term of Eq.(2), accounts for effects of the compound imaging system. The second (Maximum A Priori) term represents our prior statistical knowledge of the imaged scene (cf. [4]).
A major advantage of the MAP restoration process is that non-linear system and scene effects are taken into account by the restoration process. Therefore, MAP speckle filtering can be considered as a controlled restoration of R, where A Priori knowledge controls the inference process, and allows an accurate estimation of radar reflectivities R_i, and of their fluctuations due to scene texture in all image channels i.

0-7803-3836-7/97/$10.00 © 1997 IEEE

3. PRIOR KNOWLEDGE/GUESS AND MAP FILTERS

* Mono-channel detected SAR images:

The choice of P(R) as a Gamma pdf (K-distributed clutter) gives rise to the Gamma-Gamma MAP filter [5-7]. Additional MAP filters have already been developed, with prior P(R) defined as: a Gaussian pdf [8], a Beta pdf [5,6], a triangular pdf [6], a Weibull pdf [6], and a LogNormal pdf [6]. Comparison of results given by these filters shows that MAP filtering presents a good robustness to local errors in the A Priori guess of P(R), unless the scene becomes very heterogeneous. This justifies using geometrical refinements [7] or refined texture analysis that involves the use of second order statistics [9], to identify and isolate the sources of strong heterogeneity.

* Multi-channel detected SAR images:

No analytic multivariate Gamma pdf is available to describe first order statistical properties of a natural scene as viewed by diverse SAR sensors (different physical features of the scene), or at different dates (scene evolution over time) Therefore, a multivariate Gaussian pdf was chosen as analytic multi-channel scene statistical model [10].
Two MAP filters have been recently developed to restore the radiometry of all image channels in a SAR dataset, for the respective cases of correlated and uncorrelated speckle between SAR image channels. The performances of these two new filters are reported in [10], and an example of results is shown in Fig.1.

* Mono-channel complex SAR images:

Luttrell [4] has developed a MAP filter to perform the specific task of super-resolution in complex SAR images. His MAP filter produces a detected image at enhanced spatial resolution. A Priori knowledge is introduced under the form of a Gaussian scattering model.

* Separate Complex Looks:

Gaussian-Gamma MAP for separate complex multilook SAR images [11] has been developed to produce a detected filtered multilook image, from original separate complex looks. A Priori knowledge of P(R) as a Gamma pdf (K-distributed clutter) is introduced in the Bayes equation.

* Polarimetric SAR images:

The fully polarimetric Wishart-Gamma MAP for polarimetric SAR data [12] bases on the two hypothesis that: 1) the normalized number N of scatterers within the resolution cell might remain constant whatever the configuration of polarization; 2) P(N) is assumed a Gamma pdf. At this point, the filter performs a local estimation of N. Although this filter gives apparently very good results, at the light of more recent work [13], it appears that the guess that N might remain constant while changing polarization is not a robust statement. As a consequence, more sophisticated MAP polarimetric filters have to be developed.

4. MAP FILTERS AND CONTROL SYSTEMS

Nevertheless, the most remarkable feature is that they present the structure of control systems. As an example, the two MAP filters for multi-channel detected SAR images can both be easily rewritten as Riccati's algebraic equations:

$$- A X - X {}^{t}A - Q + X {}^{t}C P^{-1} C X = 0 \qquad (3)$$

Eq. (3) represents the optimal controlled reconstruction at constant gain of linear invariant processes (R and textures of the channels) perturbed by white noises (speckle, pixel spatial mismatch between channels). It can be shown that the scene A Priori model acts as a command, and that the covariance matrices act as multipoles or controls. It is also noticeable that MAP elaboration of information generates automatically feedback processes that enable to control the filtering process itself. In addition, Riccati's theorem stipulates the existence of a unique positive definite solution for Eq.(3). Therefore, this property holds also for the corresponding MAP filters.

5. CONCLUSION

In this paper, we have presented a non-exhaustive review of existing MAP speckle filters to illustrate the interest of prior knowledge in SAR image restoration, restraining to "point restoration" filters. For example, MAP segmentation of SAR images (*e.g.* DRA's work in the UK) is out of our scope.
In addition, among Bayesian methods, alternatives to the MAP approach exist, according to the final goal of the treatment. Such a valid alternative, the A Posteriori Mean (APM) speckle filtering is presented in [14]. All these Bayesian filtering methods take non-linear effects into account, giving rise to SAR clutter, while restoring radar reflectivity, and above all, texture. In restoring scene texture, they prove superior to heuristic filtering, or adaptive filtering based on frequentist approaches. Even if some other methods, such as LMMSE filters derived from [15-17], implicitly assume some A Priori knowledge, forced linearization of their filtering processes does not allow using it. However, Bayesian filters are commandable through the weighting of A Priori knowledge in the induction process. In addition, they present the form of stable control systems, that can be extended to real applications. A demonstration of the application of the control systems principles for retrieval of geophysical parameters is presented in [18], to illustrate the potential of this approach.

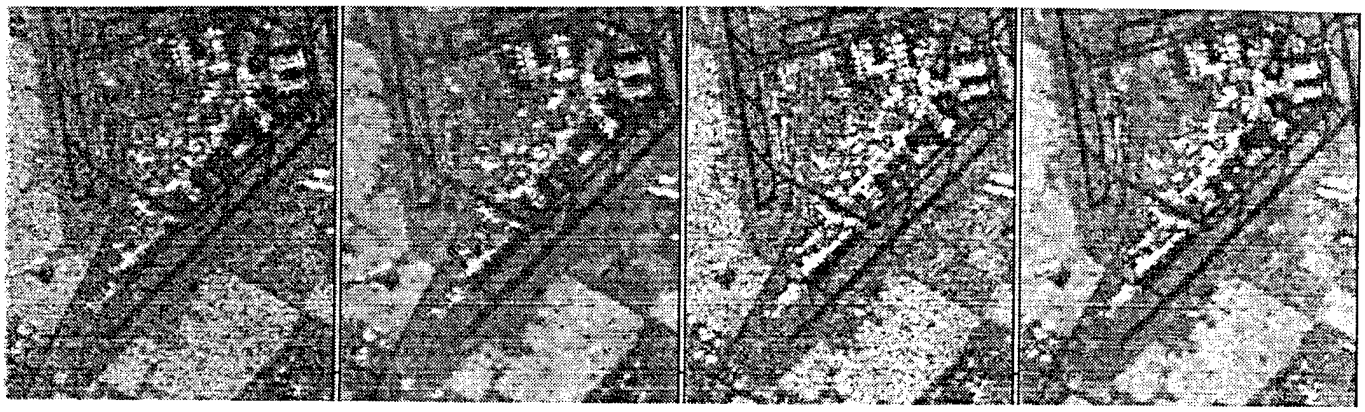

Figure 1: From left to right: ERS PRI image (©Eurimage 1996) and filtered version. RADARSAT Std Beam S1 image (©RADARSAT Int. 1996) and filtered version (Gaussian-Gaussian MAP filter for multi-channel detected multilook images).

ACKNOWLEDGMENTS

The ERS and Radarsat images have been provided by the European Space Agency (Pilot Project PE-FRNE2) and by the Canadian Space Agency (Pilot Project ADRO#581).

REFERENCES

[1] E. Jakeman, P.N. Pusey, 1976: "A model for non-Rayleigh sea echo", *IEEE Trans. on AP*, Vol.AP-24, n°6, pp.804-814.

[2] C.J. Oliver, 1986: "The interpretation and simulation of clutter textures in coherent images", *Inverse Problems*, Vol.2, pp.481-518.

[3] E. Jakeman, R.J.A. Tough, 1987: "Generalized K distribution: a statistical model for weak scattering", *J. Opt. Soc. Am. A.*, Vol.4, n°9, pp.1764-1772.

[4] S.P. Luttrell, 1991: "The theory of super-resolution of coherent SAR images: a review", *Int. J. Rem. Sens.*, Vol.12, n°2, pp.303-314.

[5] A. Lopes, E. Nezry, R. Touzi, H. Laur, 1990: "Maximum A Posteriori speckle filtering and first order texture models in SAR images", *Proc. of IGARSS'90*, Washington, Vol.3, pp.2409-2412.

[6] E. Nezry, 1992: "Restauration de la reflectivite radar pour l'utilisation conjointe des donnees radar et optiques en teledetection", Ph.D. dissertation, n°1236, University Toulouse, 3 July 1992.

[7] A. Lopes, E. Nezry, R. Touzi, H. Laur, 1993: "Structure detection and statistical adaptive speckle filtering in SAR images", *Int. J. Rem. Sens.*, Vol.14, n°9, pp.1735-1758.

[8] D.T. Kuan, A.A. Sawchuk, T.C. Strand, 1987: "Adaptive restoration of images with speckle", *IEEE Trans. on ASSP*, Vol.ASSP-35, n°3, pp.165-177.

[9] E. Nezry, M. Leysen, G. De Grandi, 1995: "Speckle and scene spatial statistical estimators for SAR image filtering and texture analysis: some applications to agriculture, forestry, and point targets detection", *Proc. of SPIE*, Vol.2584, pp.110-120.

[10] E. Nezry, F. Zagolski, A. Lopes, F. Yakam-Simen, 1996: "Bayesian filtering of multi-channel SAR images for detection of thin structures and data fusion", *Proc. of SPIE*, Vol.2958, pp.130-139.

[11] A. Lopes, E. Nezry, S. Goze, R. Touzi, G. Solaas, 1992: "Adaptive multilook processing of complex SAR images", *Proc. of IGARSS'92*, Houston, Vol.2, pp.890-892.

[12] A. Lopes, S. Goze and E. Nezry, 1992: "Polarimetric filters for SAR data", *Proc. of IGARSS'92*, Houston, Vol.1, pp.80-82.

[13] G. De Grandi, E. Nezry, J.S. Lee, D. Schuler, 1995: "On the statistics of polarimetric synthesized images", *Proc. of IGARSS'95*, Vol.2, pp.1418-1421.

[14] A. Lopes, J. Bruniquel, F. Sery, D. Ducrot-Gambart, E. Nezry, 1997: "Optimal Bayesian texture estimators for speckle filtering and classification of polarimetric data", *Proc. of IGARSS'97*, this issue.

[15] J.S. Lee, 1980: "Digital image enhancement and noise filtering by use of local statistics", *IEEE Trans. on PAMI*, Vol.PAMI-2, n°3, pp.165-168.

[16] D.T. Kuan, A.A. Sawchuk, T.C. Strand, P.Chavel, 1985: "Adaptive noise smoothing filter for images with signal-dependent noise", *IEEE Trans. on PAMI*, Vol.PAMI-7, n°2, pp.165-177.

[17] V.S. Frost, J.A. Stiles, K.S. Shanmugan, J.C. Holzman, 1982: "A model for radar images and its application to adaptive digital filtering of multiplicative noise", *IEEE Trans. on PAMI*, Vol.PAMI-4, n°2, pp.157-166.

[18] E. Nezry, F. Zagolski, F. Yakam-Simen, I. Supit, 1997: "Control systems principles applied to speckle filtering and geophysical information extraction in multi-channel SAR images", *Proc. of IGARSS'97*, this issue.

Statistical Properties of Speckle and Full Polarimetric Filters in SAR

Franck Séry and Armand Lopès

CESBIO (UMR 5639 CNES/CNRS/UPS), 18 Avenue Edouard Belin BP 2801 - 31401 Toulouse Cedex 4, France
***Telephone :* (33) 5 61 55 64 84, *Fax :* (33) 5 61 55 85 00, *E-mail :* sery@cesbio.cnes.fr**

Abstract. Reducing the speckle effects in polarimetric data implies the use of statistical models for the speckle. A well known model is the product model which assumes the same texture variable for all the elements of the Covariance Matrix (CM). We present here 2 models which allow differences between channels. For each model, a filtering technique is also presented. Finally, an analysis of texture variations is realized on several natural and non natural clutters.

1 .- INTRODUCTION

For a surface with fully developed speckle, the polarimetric vector of measures, ${}^t\mathbf{Z} = (z_{hh}, z_{hv}, z_{vh}, z_{vv})$, is a 4-dimensional (3-dimensional for reciprocal data) jointly circular gaussian complex vector with mean Covariance Matrix (CM) $\mathbf{C_Z}$.
The sample CM of a L-look polarimetric data :

$$\Sigma_Z = \frac{1}{L}\sum_{m=1}^{L} \mathbf{Z}_m \, {}^t\mathbf{Z}_m^*$$

is shown to be Wishart distributed :

$$p(\Sigma_Z / \mathbf{C}_Z) = \frac{L^{Lp}\left|\Sigma_Z\right|^{L-p} e^{-LTr(\mathbf{C}_Z^{-1}\Sigma_Z)}}{\pi^{p(p-1)/2}\Gamma(L)\ldots\Gamma(L-p+1)\left|\mathbf{C}_Z\right|^{L}} \qquad (1)$$

In single or multilook cases, the polarimetric information of the surface is entirely contained in $\mathbf{C_Z}$ which is the only variable to estimate.

For homogeneous surfaces, $\mathbf{C_Z}$ is suppose to be constant from a resolution cell to another and the Maximum Likelihood (ML) estimate of $\mathbf{C_Z}$ is given by the sample mean of the sample CM's of all the resolution cells defining the surface. For non-homogeneous surfaces, $\mathbf{C_Z}$ has to be estimated for each resolution cell or set of resolution cells. We first present 2 general models to estimate $\mathbf{C_Z}$ on heterogeneous areas. These models are generalizations of the well known product model [5,6,9] :

$$\mathbf{C_Z} = \mu.\mathbf{C_{zh}}$$

with $\mathbf{C_{zh}} = E(\mathbf{C_Z}) = E(\Sigma_Z)$, mean CM of an equivalent homogeneous area, and μ normalized texture ($E(\mu) = 1$).
An analysis of the textural variations between polarization intensities is realized for some natural and non natural clutters. This analysis will permit to define the proper model to use for each clutter type.

2 .- Matrix direct product model and linear Minimum Mean Square Estimate (LMMSE) of $\mathbf{C_Z}$

Such an estimator was first proposed for 1 look data in [1] and extended to L-look data in [2].

The model used was :

$$\Sigma_Z = \Sigma_F \otimes \mathbf{C}_Z \qquad (2)$$

($\otimes$: matrix direct product)
with Σ_F Wishart distributed with mean CM $\mathbf{C_F}$:

$$\mathbf{E}(\Sigma_F) = \mathbf{C_F} = \begin{pmatrix} 1 & \rho'_{hhhv^*} & \rho'_{hhvv^*} \\ \left(\rho'_{hhhv^*}\right)^* & 1 & \rho'_{hvvv^*} \\ \left(\rho'_{hhvv^*}\right)^* & \left(\rho'_{hvvv^*}\right)^* & 1 \end{pmatrix}$$

Pierdicca *et al.* [3] pointed out that this model implies, for homogeneous areas :

$$\mathrm{Var}(z_{pq}z_{kl}^*) = E(|z_{pq}z_{kl}^*|^2)/L \qquad p,q,k,l \text{ in } \{h,v\} \qquad (3)$$

Their experiments prove that (3) is not verified, but another relation is observed :

$$\mathrm{Var}(z_{pq}z_{kl}^*) = E(|z_{pq}|^2)E(|z_{kl}^*|^2)/L \qquad p,q,k,l \text{ in } \{h,v\} \qquad (4)$$

Their explanation is that an additive noise is superimposed to the multiplicative speckle noise.

To fit to the experimental observations of Pierdicca *et al.* [3], we propose another model (« matrix direct product model »):

$$\Sigma_Z = \Sigma_F \otimes \Sigma_R \qquad (5a)$$

$$\mathbf{C_Z} = \mathbf{C_{zh}} \otimes \Sigma_R \qquad (5b)$$

with Σ_F, Wishart distributed with a mean CM : $\mathbf{C_{zh}}$. Σ_R is a matrix containing the normalized texture value of each element of Σ_Z :

$$\Sigma_R[i,j] = \mathbf{C_Z}[i,j]/\mathbf{C_{zh}}[i,j] = \mathbf{C_Z}[i,j]/E(\mathbf{C_Z}[i,j])$$

We don't relate it to a vector of complex texture variables and hence Σ_R is not considered here as a covariance matrix even though the off-diagonal elements may be complex. It is a spatially varying matrix variable with mean : $\mathbf{1_{3x3}}$ ($\mathbf{1_{4x4}}$ for non-reciprocal data). Σ_F and Σ_R are independent random variables.
For homogeneous areas, Σ_R is constant ($\Sigma_R = \mathbf{1_{3x3}}$) over all the pixels of the surface and this model is equivalent to (1) . Theoretical variances derived from distribution (1) (see [2]) conduct to relation (4). The LMMSE estimate of [1] and [2] give then estimates of Σ_R for each pixel of the surface. The estimate of $\mathbf{C_Z}$ is constructed by :

$$\hat{\mathbf{C}}_Z = \hat{\mathbf{C}}_{zh} \otimes \Sigma_{RLMMSE}$$

0-7803-3836-7/97/$10.00 © 1997 IEEE

3 .- Multiplicative model on all synthesized powers

Polarimetric synthesis defines isomorphism's between the elements of the CM and some synthesized powers. In [4], such an isomorphism is given for the reciprocal case :

$$\{|hh|^2, |hv|^2, |vv|^2, Re(hhhv^*), Im(hhhv^*), Re(hhvv^*), ...\}$$
$$\Leftrightarrow \quad \{P_{hh}, P_{hv}, P_{vv}, P_{vf}, P_{vl}, P_{hf}, P_{hl}, P_{fl}, P_{fo}\}$$

(f is the 45° linear, o, the 135°, and l, the left circular polarization)

Multiplicative model is used for each power :

$$P_{pq} = R_{pq}.F_{pq} \quad , (p,q) \text{ in } \{h,v,f,o,l\}$$

with R_{pq} scene reflectivities and F_{pq} speckle intensities.

R_{pq} may differ from a power to another. The main difference between this model and the matrix direct product model (5) is that no complex texture variable is used.

Filtering speckle effects under this model can be done with any of the existing multi-channels filters. To keep the polarimetric specificity of the data, we propose a combined use of the Polarimetric Whitening Filter (PWF) [5,6] and the optimal summation with textural compensations [7]. The original method of [7] calculates a channel of minimum variance. Here, the PWF gives the channel of minimum standard-deviation-to-mean ratio. The CM equivalent to the set of filtered powers has been shown to keep mean polarimetric information's of the surface.

4 .- Texture analysis of natural and non natural clutters

The « product model » is the particular case of model (5) where all the elements of Σ_R are equal, real and positive, but also a particular case of model of part 3, with a same R for all powers. For the product model, several estimates of $\mathbf{C}_z$ are given in [8]. This simplified model is not verified for some clutters and models of part 2 and 3 have to be used. The aim of this part is to test the product model on some natural and non natural clutters.

N°	Clutter type	sample size
1	calm water	3248
2	wet sand (low tide)	3245
3	young planted forest of pines	2215
4	old planted forest of pines	2724
5	natural forest	2130
6	culture	1537
7	irrigated culture	1473
8	urban	518
9	mixed urban-forest	1312

Table 1 .- Names and sample sizes of the 9 clutters

A great variety of such tests were proposed in [9] and more recently in [10]. Two of these tests are realized here on a SIR-C single look data taken in April 1994 over the region of Les Landes (south-west of France). The scene is a coastal region with a site of planted pine forest in its center. A large sample has been taken for 9 different clutters (table 1).

To reduce the number of tables, results are presented for L band data only.

4. 1 .- Order parameter variations

All the clutters are supposed K-distributed (Gamma-distributed texture variable). For each polarization intensity, the Maximum likelihood (ML) estimate of the order parameter α of the corresponding K distribution is numerically approached using the method described in [10]. A KS test verifies the fit of the experimental distribution to the K distribution. If the 4 polarization intensity channels represent 4 realizations of speckle on the same texture channel (product model), α will have gaussian variations (for sufficiently large samples, see [10]). For L=1, results from [11] show that, for $\alpha<10$, the theoretical variance of the ML estimate is well approached by the variance of the estimate using the mean of the log, and that, for $\alpha>10$, it is well approached by the variance of the contrast estimator. We use these approximations here.

	H H		H V		V H		V V	
N°	α	KS	α	KS	α	KS	α	KS
1	**50**	0.88	**37.2**	0.95	**50**	0.94	**50**	0.99
2	**1.8**	0.03	**31.4**	0.80	**50**	0.62	**1.4**	0.00
3	**50**	0.65	**10**	0.66	**9.9**	0.99	**32**	0.92
4	**17.9**	0.97	**18.1**	0.92	**17.3**	0.65	**21.6**	0.77
5	**11**	0.96	**13.6**	0.64	**13.2**	0.95	**21.2**	0.51
6	**8.9**	0.75	**50**	0.49	**50**	0.35	**9.2**	0.43
7	**5.2**	0.98	**50**	0.78	**38.3**	0.50	**25.6**	0.77
8	**0.81**	0.00	**0.71**	0.00	**0.67**	0.00	**0.81**	0.00
9	**1.9**	0.01	**4.8**	0.63	**3.6**	0.87	**3.2**	0.13

Table 2 .- Estimates of α and corresponding KS probabilities for the intensities of the 4 polarization's

As expected, calm water (N°1) may be considered as a purely gaussian clutter (for α=50, KS test compares experimental distribution with the exponential distribution). A doubt is permitted for the HH channel, with a KS probability of only 0.88 . The sand discovered by the low tide (N°2) has a highly textured surface which gives rise to double bounce effects. In this case, fit of co-pol intensities to the K distribution with low order parameter is poor. For cross-pol intensities, no real variation of α is observed but the fits are poorer. Backscattering from young forest (N°3) is dominated by surface scattering from ground. In this case, a significant difference appears between the order parameters of co- and cross-pol, but it may be due to gaussian variations of mean $E(\alpha)$=25 and theoretical standard deviation $std(\alpha)$~15. Product model is not statistically rejected for sample 3, but it seems that texture has to be analyzed separately for co- and cross polarization's. Older forests (4 and 5) have a dominant volume scattering, coherent with the product model. Cultures (6 and 7) are similar to N°2 with highly textured surface (just

planted cultures). Fits of co-pol intensities are nevertheless better for these 2 cases. Urban (N°8), dominated by double bounce and surface scattering, shows very low estimates of α for all polarization, without fitting to K distribution. Mixed urban-forest, with some volume scattering, is closer to the product model but poor fits are still observed on co-polarized channels.

4.2 .- Ratios of intensities

The texture variable, μ, is supposed to have the same value in each polarization channel. This is a consequence of the product model. Ratios of channel's ML estimators of texture (normalized intensity for the single channel case [6]), are compared to the theoretical distribution of the ratio of 2 correlated exponential random variables with means 1 [9] :

$$p(r) = \frac{(1-|\rho|^2)(1+r)}{\left((1+r)^2 - 4|\rho|^2 r\right)^{3/2}}$$

For each sample, the ML estimate of the correlation coefficient of the intensities, $|\rho|^2$, is evaluated by numerically finding the one which maximizes the log-likelihood function in the range 0.001 to 0.999 by step 0.001.

N°	(hh,hv)	(hh,vh)	(hh,vv)	(hv,vh)	(hv,vv)	(vh,vv)
1	0.95	0.56	0.28	0.90	0.99	0.86
2	0.00	0.00	0.002	0.79	0.00	0.00
3	0.34	0.24	0.72	0.79	0.33	0.65
4	0.87	0.84	0.92	0.94	0.78	0.77
5	0.65	0.32	0.12	0.92	0.54	0.74
6	0.53	0.86	0.66	0.29	0.42	0.07
7	0.16	0.03	0.003	0.35	0.995	0.95
8	0.03	0.004	0.53	0.01	0.007	0.003
9	0.00	0.00	0.002	0.16	0.78	0.76

Table 3 .- KS probabilities of the fit of experimental distributions of ratios

Some of the results of table 3 are somewhat suprising. For the assumed purely gaussian clutter (N°1), the poorest fit is observed for the couple of co-polarized channels ($|\rho_{hhvv}|$ ~ 0.11, $|\rho_{hvvh}|$ ~ 0.12). From table 2, we see that KS probability of the HH channel is just sufficient to conclude to the exponential distribution. Here this bad fit appears clearly and this sample may not present purely gaussian variations. Sample 2 ($|\rho_{hhvv}|$ ~ 0.85) clearly don't verify the test of the product model, excepted, perhaps, for the couple of cross-polarized channels ($|\rho_{hvvh}|$ ~ 0.15). For the young planted forests, textures are different between co and cross polarized channels ($|\rho_{hhvv}|$ ~ 0.78, $|\rho_{hvvh}|$ ~ 0.96, $|\rho_{hhhv}|$ ~ 0.00). It confirms the necessary separation of these 2 textures. Old planted forest can be assumed to verify the product model, but natural forest show some differences between channels. This may be due to the greatest heterogeneity of the covers of natural forests. Cultures are clearly not verifying the test. For these clutters, models of part 2 and 3 have to be used. This second test confirms that urban or mixed urban-forest are also clutters for models of part 2 and 3.

CONCLUSION

In this paper, we have proposed 2 models to use when the product model doesn't apply. For these two general models, some methods are given to estimate the mean CM $\mathbf{C}_z$. A comparison between these models is necessary and will be the point of future studies. Here we limited our investigations to the assessment of the product model. The tests we made have shown that only 2 of the 9 clutters we've chosen, can be assumed verifying this model. The general models appear necessary in the other cases. A future step of this study will be to rely the backscattering mechanisms to the model type in order to automatically (using methods like [12]) choose the right model to apply.

Acknowledgments. The authors would like to thank Thuy Le Toan (CESBIO) and NASA JPL for providing the data.

References :

[1] Goze S. & Lopès A., A MMSE speckle filter for full resolution SAR polarimetric data, *JEWA* , Vol. 7 n°5, 717-737, 1993.

[2] Lopes A. & Séry F., 1994, The LMMSE polarimetric Wishart ..., *Proc. of IGARSS'94*, pp 2143-2145, JPL Pasadena USA.

[3] Pierdicca *et al.*, 1995, Classification of multifrequency radar polarimetric data: role and contribution of vectorial filters, *Proc. of the IGARSS'95*, pp 1915-1917, Firenze, Italia.

[4] Séry *et al.*, 1996, Multisource classification of SAR ..., *Proc. of SPIE Europto'96*, Image and Signal Proc. III, pp 186-197, Taormina , Italia.

[5] Novak L.M. & Burl M.C., 1990, Optimal speckle reduction in polarimetric SAR imagery, *IEEE Trans. on AES*, Vol.26 n°2, 293-305.

[6] Lopès A. and Séry F., 1997, Optimal speckle reduction for the product ..., *IEEE Tr. on GRS*, Vol.35 n°3.

[7] Bruniquel J. & Lopès A., 1997, Multi-variate optimal speckle reduction in SAR imagery, *IJRS*, Vol.18, N°3, pp 603-627.

[8] Lopès *et al.*, 1997, Optimal bayesian texture estimators for speckle filtering, *Proc. of IGARSS'97*, Singapore.

[9] Quegan S. and Rhodes I., 1995, Statistical models for polarimetric data : consequences, testing and validity, *IJRS*, Vol.16 n°7, pp 1183-1210.

[10] Blacknell D. and Blake A. P., 1997, Single point and spatial statistics of polarimetric SAR imagery, *IJRS*, Vol.18 n°3, pp 629-649.

[11] Blacknell D., 1994, Comparison of parameter estimators for K-distribution, *IEE Proc. Radar Sonar Navig*, Vol.141, N°1.

[12] Cloude S.R. & E. Pottier, 1997, An entropy based classification scheme for land applications of polarimetric SAR, *IEEE Trans. on GRS*, Vol. 35 n°1, pp. 68-78.

Effects of parameter tuning and de-speckle filtering on the accuracy of SAR image classification based on gray-level co-occurrence matrix features

L. Bruzzone[1], S.B. Serpico[1], and G. Vernazza[2]

(1) Dept. of Biophysical and Electronic Engineering - D.I.B.E.
University of Genoa, Via Opera Pia, 11a, I-16145 Genova (Italy)
Phone: +39-10-3532672; Fax.: +39-10-3532134; E-mail: lore@dibe.unige.it

(2) Dept. of Electrical and Electronic Engineering
University of Cagliari, Piazza d'Armi, I-09123 Cagliari (Italy)

Abstract -- In this paper, the results of an experimental investigation of the use of textural features computed from the Gray-Level Co-occurrence matrix for Synthetic Aperture Radar (SAR) image classification are reported and discussed. The investigation, carried out on SAR images acquired with the SIR-C/X-SAR sensor in an Italian agricultural area, makes it possible to derive interesting information about the computation modalities and the effectiveness of the above textural features.

INTRODUCTION

SAR images are characterized by a large spatial variability (resulting from their high spatial resolution and from the presence of speckle), which makes it useful to exploit texture information for classification purposes [1].

In the literature, many techniques for characterizing remote-sensing image textures have been proposed [1,2]. Among the most widely used, there is the technique based on the Gray-Level Co-occurrence (GLC) matrix [3]. This technique relies on the assumption that the texture information present in an image can be described by the spatial relationships among the grey levels. Such relationships are associated with the GLC matrix, from which several textural features can be computed (in the following, we shall refer to these features as GLC features).

Many papers have been presented, dealing with the application of GLC features to the classification of remote-sensing optical images [2,4]. From such papers, interesting information on how to perform feature computation and on the effectiveness of the above features for classification purposes can be derived.

On the other hand, the papers that address the application of GLC features to SAR data do not report similar investigations, and the different nature of SAR data does not allow one to extend results obtained by optical data.

The main purpose of this paper is to describe the results of an experimental investigation of the use of GLC features for SAR image classification. Experiments were carried out in order to obtain information about the best values of the parameters for the GLC matrix computation, to assess the effectiveness of the most commonly used de-speckle filters as a preprocessing of SAR images before extracting GLC features, and to identify the best GLC features for land-cover classification. A data set composed of SIR-C/X-SAR images acquired in an agricultural area in the north of Italy has been used.

DATA SET DESCRIPTION

The study region was an agricultural site in the Oltrepo Pavese area (in northern Italy). We selected a section of 512×512 pixels of a scene acquired with the SIR-C/X-SAR installed on board of the Space Shuttle Endeavour. The acquisition took place in April 1994. In order to reduce the computational load of our experiments, we focused our attention on a four-look image acquired in the C band, polarization HV, as we found that the texture in such a channel was very effective to discriminate among different land-cover classes.

For our experiments, we considered the following six numerically most representative classes present in the image: poplar-grove, wheat, tobacco, herbaceous, water, and urban. The image regions of each land-cover class were randomly subdivided into two disjoint sets; 6190 training samples were taken from the regions of one set and 6916 test pixels from the regions of the other set.

EXPERIMENTS

Experimentation planning

The dynamics of the above described image was compressed from the original 256 levels to 128 levels by using an equal-probability quantizing algorithm [3]. This allowed us to reduce the load of GLC feature computation to an acceptable level. Twelve GLC features were used to characterize the pixels of the analyzed image. The classification accuracy provided by a k-nearest neighbour (k-nn) classifier [5] was used to assess the effectiveness of these features with respect to the conditions considered to compute the GLC matrix.

Three main experiments were carried out.

The first experiment was aimed at investigating what information can be derived about the selection of suitable values of the parameters for the GLC matrix computation for SAR images. In particular, we focused on the two main parameters for to the GLC matrix computation, i.e., the window size and the interpixel distance [3].

0-7803-3836-7/97/$10.00 © 1997 IEEE

The target of the second experiment was to investigate on the capability of the most common de-speckle filters [6] to reduce the effects of speckle without reducing the information provided by texture. Several trials were carried out by using different filters on the considered SAR image as a pre-processing for the GLC matrix computation.

The third experiment was designed to identify the most effective subsets of GLC features for SAR image classification. To this end, we performed our analysis by using a feature-selection criterion. Among the criteria proposed in the literature [7], we adopted the maximization of the Jeffreys-Matusita (J-M) distance, as it is one of the most effective criteria.

Results and discussion

Preliminary tests on the considered data set were carried out in order to select the value of the k parameter of the k-nn classifier to be used in all the scheduled experiments. As a result, we chose k=11, since high and stable classification accuracies were obtained by a k parameter equal or close to this value.

Concerning the first experiment, Fig.1 shows the overall accuracies provided by the k-nn classifier on the test set with respect to the values of the window size and of the interpixel distance used to compute the GLC matrix (the direction 0° was considered as a visual inspection of the image did not reveal any particular dominant texture orientation). Small interpixel distances are the most effective. In particular, the best accuracy was obtained for an interpixel distance equal to 1, with a window size of 25×25 pixels. As regards the choice of the interpixel distance, results were in agreement with the general hints given by Haralick *et al.* [3]. They suggested to adopt, as an upper bound to the distance, the value at which the normalized autocorrelation function of the image becomes small. For SAR images, this upper bound is usually equal to only a few pixels, as the correlation among neighbouring pixels is strongly reduced by the presence of speckle. Concerning the window size, the best classification accuracies were obtained by using intermediate values. These values represent a good compromise between two opposite trends. Due to the low signal-to-noise ratios of SAR images, in order to allow the GLC matrix to provide a reliable estimate of the second-order statistics of spatial variability, the matrix computation must be based on a large number of textural units (i.e., on quite a large window). On the other hand, when the window size becomes too large (i.e., larger than 27×27 in our experiments), the overall classification accuracy decreases as the influence of different areas increases (a large analysis window can include pixels from more than one class). According to the information provided by the first experiment, for the next experiments we chose an interpixel distance equal to one pixel and a window size equal to 25×25.

In the second experiment, for all the filters considered (see Table 1) [6], we chose a 5×5 size for the sliding window, as this value represents a good compromise in order to have a sufficient statistics and to limit the computational load. For each of the filters considered, we applied only one filtering iteration to the original image; then, we computed the GLC matrix of the filtered image and extracted the GLC features. The classification accuracies obtained for the test set by using different filters are shown in Table 1. The analysis of results highlights that only the lee filter significantly increases the effectiveness of GLC features, as it provide an overall classification improvement of 3.6%. Slight improvements (i.e., in the range from 0.3 % to 1.6%) were also provided by the local region filter, the frost filter and the sigma filter. On the contrary, all the other filters decreased the classification accuracy.

Finally, let us analyze the results of the third experiment to assess the effectiveness of the different GLC features. The experiment was performed by selecting the optimal subsets of GLC features on the basis of the average J-M distance in the training set. In particular, the optimal features subset was identified for each value of the number of features in the optimal subset. Fig.2 depicts the behaviour of the average J-M distance for an optimal subset of GLC features with respect to the number of features in the subset. The most

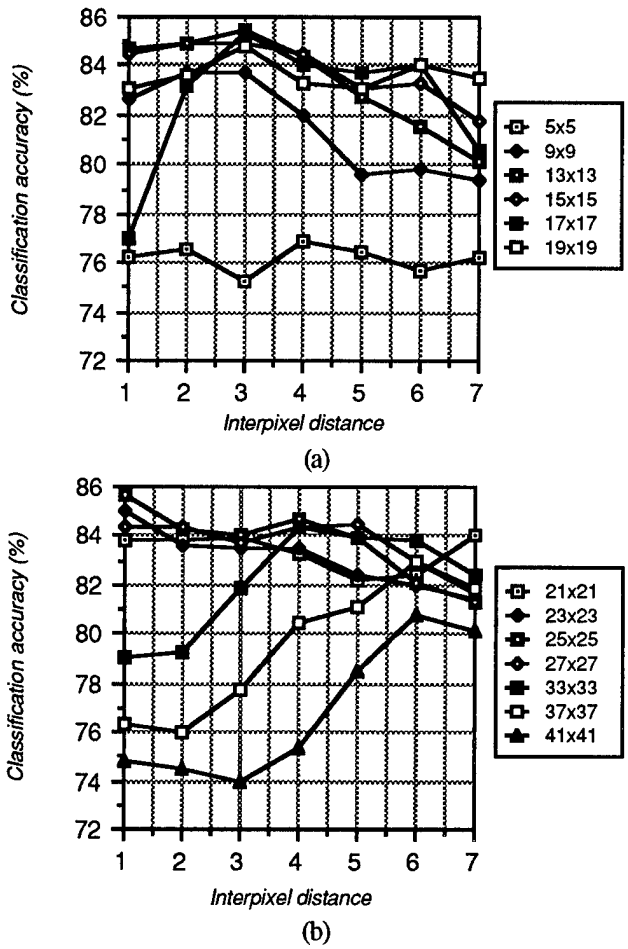

Fig. 1 - Overall classification accuracy provided by the k-nn classifier of the test set as a function of both the interpixel distance and the window size: (a) window sizes from 5×5 to 19×19 pixels; (b) window sizes from 21×21 to 41×41 pixels.

discriminant feature is the "inverse difference moment"; however, it is not able to distinguish each class. To reach a classification accuracy close to that obtained by considering all the features, at least four features are necessary. The best subset of four features is composed of "sum variance", "correlation", "entropy", and "difference entropy" which provide an average J-M distance equal to 1.08 and a classification accuracy of 83.1 %. Fig.2 shows that the addition of other features does not significantly improve the class separability. This confirms that a strong correlation exists among some of the twelve GLC features used in our experiments.

CONCLUSIONS

In this paper, an experimental investigation of the effectiveness of textural features computed from the GLC matrix for the classification of a four-look SAR image has been described.

Some suggestions were derived as to how to perform the GLC matrix computation. In particular, the results of our experiments showed that the size of the analysis window is an important parameter, as low overall classification accuracies were obtained by a window size smaller than 9×9 and larger than 33×33 pixels. Also the interpixel distance turned out to be an important parameter. Our analysis highlighted that small interpixel distances (i.e., from one to four pixels) are the most effective for SAR data.

The tests we performed also pointed out that the use of de-speckle filtering techniques (e.g., the lee filter) as a pre-processing for GLC matrix computation may improve classification accuracy. However, a careful use of these filters has to be made, since some of the filters considered (i.e., the mean, median, and MAP filters) damage the texture information extracted by means of GLC features and reduce the possibility of discriminating among different classes.

Finally, the experiment concerning the most effective subsets of textural features for classification purposes highlighted the usefulness of some features usually not considered in the literature. However, as certain information about the importance of the various GLC features is not available, it is recommended to consider a large set of such features and then to perform a feature selection step.

ACKNOWLEDGMENTS

This research was funded by the Italian Ministry for the University and Scientific Research, whose support is gratefully acknowledged. The authors wish to thanks Dr. M.A. Gomarasca (C.N.R. - I.R.R.S. - Telerilevamento, Milan, Italy) for providing the Thematic Mapper data and for assisting in the related agronomic interpretation.

REFERENCES

[1] F.T. Ulaby, F. Kouyate, B. Brisco, and T.H.L. Williams, "Texture information in SAR images," IEEE Trans. on Geoscience and Remote Sensing, vol. 24, pp. 235-245, 1986.

[2] D.J. Marceau, P.J. Howarth, P.J. Dubois, and D.J. Gratton, "Evaluation of the grey-level co-occurrence matrix method for land-cover classification using SPOT imagery," IEEE Trans. on Geoscience and Remote Sensing, vol. 28, pp. 513-518, 1990.

[3] R.M. Haralick, K. Shanmugan, and I. Dinstein, "Textural features for image classification," IEEE Trans. on System, Man and Cyber., vol. 3, pp. 610-621, 1973.

[4] R.W. Conners, M.M. Trivedi, and C.A. Harlow, "Segmentation of a high-resolution urban scene using texture operators," Computer Vision, Graphics and Image Processing, vol. 25, pp. 273-310, 1984.

[5] R.O. Duda and P.E. Hart, Pattern classification and scene analysis, New York: John Wiley and Sons, 1973.

[6] J.S. Lee, I. Jurkevich, P. Dewaele, P. Wambacq, and A. Oosterlinck, "Speckle filtering of Synthetic Aperture Radar images: a review," Remote Sensing Reviews, Vol. 8, pp. 313-340, 1994.

[7] P.H. Swain and S.M. Davis, Remote Sensing: The Quantitative Approach, New York: MCGraw-Hill, 1978.

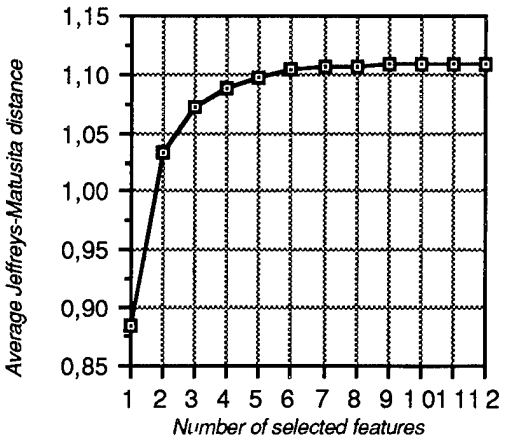

Fig. 2 - Average J-M distance of the optimal subsets of GLC features in the training set as a function of the number of features in such optimal subsets.

Table 1 - Overall classification accuracies obtained by filtering the original image with the mean, median, local region, lee, sigma, frost and MAP filters.

Filter	Classification accuracy (%)
Mean	82.78
Median	73.18
Local region	86.61
Lee	88.61
Frost	86.06
Sigma	85.31
MAP	80.39
Without filter	85.01

Bayesian Approach to SAR Image Reconstruction

M. Walessa, M. Datcu

German Aerospace Research Establishment DLR
German Remote Sensing Data Center DFD
Oberpfaffenhofen, D - 82234 Wessling
Phone +49 8153 28 1413 / Fax +49 8153 28 1448 / Email {walessa, datcu}@dfd.dlr.de

Abstract -- An approach for reconstruction of speckled SAR images is presented. This approach is based upon Bayes' rule obtaining the maximum a posteriori estimate of the underlying radar cross section. The prior used for the reconstruction is modelled by Gibbs random fields reflecting the existing texture characteristics, while the system transfer function of the SAR signal processing together with the speckle noise is accounted for by the likelihood distribution. The solution of this optimization problem is obtained by relaxation methods such as simulated annealing using the prior information as a constraint to limit the optimization space.

INTRODUCTION

In general, textures are represented by a difficult to handle two-dimensional Markov random field. Due to the known equivalence between Markov and Gibbs random fields, texture attributes can be encapsulated by different energy functions of a Gibbs distribution. This is done by defining a distinct neighbourhood for each pixel so that correlation between neighbouring pixels can be modelled. It can be demonstrated that the texture complexity or the degree of the Markov field depends on the size of the neighbourhood although correlations over long ranges are represented in terms of propagation between different neighbourhoods during the generation process. Hence, basic textures as they may appear in SAR imagery can be synthesized given the corresponding Gibbs random field by using a stochastic relaxation technique such as simulated annealing. If the texture parameters of a SAR scene are known, e.g. by maximum likelihood estimation, further image reconstruction and better despeckling without loss of textural information is assumed to be possible. In this way, texture in SAR imagery may be preserved by a despeckling process with simultaneous texture segmentation, further improving the analysis by image understanding and interpretation algorithms.

This paper is organized as follows: In the next section we present a short overview of the assumed degraded image model and point out the differences between conventional despeckling techniques and the proposed approach. Then, in the main section of this paper, the texture modelling, the introduction of the SAR system transfer function and our approach used for optimization are described. Finally, we conclude with experimental results and give some proposals how to extend this work in the near future.

DEGRADED IMAGE MODEL

The radar cross section σ which we want to estimate from our observation, i.e. from the intensity SAR image I, is subject to several transformations. Due to SAR signal processing, σ is convolved with a system transfer function h, which is generally sinc-shaped. Furthermore, we assume a non-linear transformation by a function ψ for generality. The obtained noisefree signal u is affected by the well-known speckle noise which is multiplicative and follows a negative exponential distribution. This degraded image model, as introduced in [2], may be written as:

$$I = \Psi(h \otimes \sigma) \cdot n = u \cdot n \qquad (1)$$

The problem to be solved is the reconstruction of the original radar cross section σ out of I which is known as inversion problem. Unlike conventional techniques which only remove speckle noise, thus estimating u, the inversion approach takes into account the SAR image formation for image reconstruction.

BAYESIAN IMAGE INVERSION

In order to obtain the cross section which best explains our observed image, i.e. getting the MAP estimate, we have to rely on Bayes' equation

$$p(\sigma|I) = \frac{p(I|\sigma) \cdot p(\sigma)}{p(I)} \qquad (2)$$

which includes our texture model in $p(\sigma)$ and the transformation process from σ to I as some noise dependent norm in $p(I|\sigma)$. However, in contrast to conventional optimization techniques, used to find the global optimum of $p(\sigma|I)$ as one single expression, we adopted a different approach.

0-7803-3836-7/97/$10.00 © 1997 IEEE

Optimization

Sampling new values for σ from the posterior distribution, as described in [2], instead of using the Metropolis algorithm [7], we noticed very high computation times due to the influence of the likelihood term which encapsulates the system transfer function h. As a result we decided to use a modified technique for optimization by separating the model and the likelihood terms:

- Sample new values for σ from the prior distribution, i.e. make minor changes to the estimate, determined by the model characteristics limiting the optimization space
- Evaluate the resulting change in the likelihood term using a Metropolis-like algorithm, thus minimizing the noise-dependent norm

Besides the increased computation speed, this algorithm has the advantage that it is also suitable for prior models that cannot be described by a distribution $p(\sigma)$, e.g. fractal models.

Prior Model

For our prior model we make the assumption that each pixel in σ is conditioned by a limited neighbourhood system forming a Gibbs random field given by:

$$p(\sigma) = \frac{1}{Z} EXP\left(-\sum_i \theta_i V(\sigma, \sigma_i)\right) \qquad (3)$$

Depending on the parameters of $p(\sigma)$ a large number of different textures can be described. Using these texture models as prior for the inversion enables us to reconstruct the original textured cross section σ. For the texture of the underlying cross section is unknown and hidden by speckle in the beginning, the model parameters θ have to be estimated during the inversion process [4], [5].
In fact, this is where the main problem for real SAR images arises. Since real SAR scenes consist of different regions with presumably different textures, a combined segmentation, parameter estimation and inversion has to be employed which is not only computationally an extremely difficult task. Of course, further questions arise concerning the neighbourhood size and the choice of the potential function V.

However, in absence of suitable prior knowledge for the whole image with different textures, one can make use of the principle of maximum entropy to regularize the reconstruction [11]. It is clear that this approach does not meet the goal of full texture preservation but is a good compromise until more about simultaneous segmentation and restoration is known.

Likelihood Function

The part of the Bayes equation which embeds the transformation process from the cross section σ to the SAR intensity image I is the likelihood term $p(I|\sigma)$. This term which encapsulates our knowledge about the SAR system transfer function and the speckle noise has to be maximized constrained by our model. As already mentioned, we use the likelihood function to evaluate the current realisation of our model with regard to the observed data.

EXPERIMENTAL RESULTS

We present some results by showing the filtered image of a well-known speckle reduction technique and compare this to our reconstruction. The image in Fig 2. shows a small part of a X-SAR scene of Munich, Germany, which we took for our despeckling experiments. Fig. 3 represents the following results:

- The first image a) is the result of the GMAP filter [6] applied to our test image. We observe that the image is blurred a lot and that image details are not clearly visible any more.
- Image b) was obtained by using the bayesian image inversion approach which was constrained by the principle of maximum entropy as prior. Speckle is nicely reduced without significantly blurring the image. The visual impression remains good
- For image c) a Gibbs model was used for reconstruction. Speckle is completely reduced and image details become more visible.

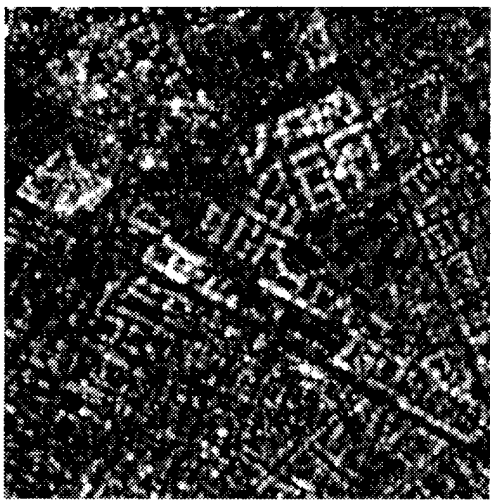

Fig. 2: Part of a X-SAR scene of Munich, Germany

Fig.3: a) GMAP filtered image, b) image inversion constrained by maximum entropy, c) image inversion with Gibbs model

CONCLUSION

We have seen that it is possible to reconstruct fine details from SAR images. However, the quality of the obtained results is largely dependent on the choice of the prior knowledge. As a consequence, the use of a predefined and constant model will give poor results so that a recursive model estimation during the inversion is needed. By combining this approach with simultaneous segmentation, we expect a reconstruction algorithm in the future which not only despeckles the image but also preserves its different textures [9] to a certain extend. However, until now the bayesian reconstruction constrained by maximum entropy also remains a good choice.

REFERENCES

[1] H. Derin, H. Elliott, "Modeling and Segmentation of Noisy and Textured Images using Gibbs Random Fields," IEEE Trans. PAMI, vol. PAMI-9, pp. 39-55, Jan. 1987.

[2] S. Geman, D. Geman, "Stochastic Relaxation, Gibbs Distributions and the Bayesian Restoration of Images," IEEE Trans. PAMI, vol. 6, No.6, Nov. 1984.

[3] D. Geman, "Random Fields and Inverse Problems in Imaging," Lecture Notes in Mathematics, Springer-Verlag, 1988, pp. 117-193.

[4] P.A. Kelly, H. Derin, "Adaptive Segmentation of Speckled Images using a Hierarchical Random Field Model," IEEE Trans. ASSP, vol. 36, No. 10, Oct. 1988.

[5] S. Lakshmanan, H. Derin, "Simultaneous Parameter Estimation and Segmentation of Gibbs Random Fields Using Simulated Annealing," IEEE Trans. PAMI, vol. 11, No. 8, Aug. 1989.

[6] A. Lopez, E. Nezry, R. Touzi, H. Laur, "Structure Detection and Statistical Adaptive Speckle Filtering in SAR Images," Int. J. Remote Sensing, vol. 14, No. 9, pp. 1735-1758, 1993.

[7] N. Metropolis, A.W. Rosenbluth, M.N. Rosenbluth, A.H. Teller, E. Teller, "Equations of State Calculations by fast Computing Machines", J. Chemical Physics, 21, 1953, pp.1087-1091.

[8] C.J. Oliver, "Information from SAR Images," J. Phys. D: Appl. Phys. 24, 1991, pp. 1493-1514.

[9] C.J. Oliver, A. Blake, R.G. White, "Optimum Texture Analysis of Synthetic Aperture Radar Images," SPIE vol. 2230, pp. 389-398.

[10] M. Schroeder, "Gibbs Random Field Models for Image Content Characterization," to be published in Proceedings IGARSS '97.

[11] C.E. Toma, M. Datcu, "Maximum Entropy and Minimum Cross-Entropy Methods in Image Processing," Proc. SPIE, vol. 1827, Nov. 1992, pp. 133-144.

Validation of Segmentation Techniques for SAR Images

M. I. Preston & S. Quegan
Sheffield Centre for Earth Observation Science,
The University of Sheffield, Hicks Building, Sheffield S3 7RH, UK.
Tel: +44 114 2223710, Fax: +44 114 22223739. Email: M.I.Preston@sheffield.ac.uk

Abstract – Segmentation is a vital technique in describing the structure of SAR images and in combating the effects of speckle that dominate such images. The performances of five segmentation algorithms are assessed and compared using real and simulated SAR data. The 'best' algorithm is sought using objective measures based on segment homogeneity and shape measures. These measures are compared to theoretical values and visual impressions of the images.

INTRODUCTION

Many applications of SAR require an image to be divided into regions (segments) corresponding to fields, ice floes, water bodies, etc. By segmenting an image a structure is imposed which can be used, for example, in classification, matching and detecting changes between images. Segmentation of an image is both hindered by the noise-like effect known as speckle, which arises because SAR is a coherent imaging system and provides a means of combating speckle by allowing meaningful area averages to be taken.

In this paper, the performance of a selection of automatic segmentation algorithms is compared using real and simulated SAR data. The method used to model a SAR image is presented along with a very brief description of the algorithms under investigation. The validation and comparison techniques are described and results are presented and discussed.

DATA MODEL

A SAR intensity image, I, can be described by a multiplicative model

$$I = \sigma n, \tag{1}$$

where σ is the radar cross section (RCS) and n represents the speckle, with σ and n assumed to be statistically independent. It is well accepted that n is Gamma distributed [1] and we assume that it is spatially uncorrelated. Real SAR data often violates this assumption but methods exist to remove or reduce correlation [2]. For the RCS a 'cartoon model' is used, where the RCS is thought of as regions of constant intensity bounded by abrupt edges. Fluctuations within a segment due to texture are not represented by this model. In segmentation the aim is to partition an image into regions that are consistent with this model. Agricultural sites, such as Feltwell, UK provide suitable SAR data to test segmentation algorithms as the fields allow the eye to segment the images easily. Fig.2(a) shows an ERS-1 SAR image of Feltwell taken on 6^{th} June 1992.

In addition, since for real SAR data the RCS is not known, simulated SAR images are useful to test the algorithms. To create them, RWSEG [3], described later, was used to segment Fig.2(a) to obtain an RCS map, which will be referred to as the ideal segmentation. Ten realisations of unit mean gamma distributed data were generated and multiplied by the RCS map to simulate SAR images, one of which is shown in Fig.1(a). Creating the simulated data in this fashion ensures that there is some reflection of the characteristics of images encountered in practice such as shape and RCS variations. The edge map of Fig.1(a) is depicted in Fig.1(b).

SEGMENTATION ALGORITHMS

Five segmentation algorithms are currently under investigation; merging only, RWSEG, ANNEAL [4], MUM [5] and split & merge. All the algorithms, with the exception of MUM, use merging as a final stage, to ensure that adjacent segments are statistically distinct. Merging is performed by attaching a probability to the existence of an edge and deleting it if the probability is greater than an input threshold. MUM performs a similar task by using the statistical moments of segments to form a criterion for merging. RWSEG is based on an iterative edge detection and segment growing process. The iteration continues while a homogeneity measure is decreasing. A global maximum *a posteriori* approach is adopted by ANNEAL. Split & merge divides segments if their CV^2, defined below, is greater than 3 standard deviations from their theoretical value. The input parameters for each algorithm were selected to give approximately the same mean segment area as the ideal.

VALIDATION TECHNIQUES

Three issues are of concern when validating SAR segmentation algorithms: visual quality (conformity with expectation), agreement with the model (homogeneity) and the preservation of segment shapes. To obtain a feel of realism about the performance of image segmentation a visual comparison must be undertaken. The most meaningful representation of a segmented image is that of its edge map. Segment boundaries can be easily seen and hence comparisons can be drawn. However, this could lead to divided opinion as to the 'best' segmentation.

Statistical representations of the homogeneity of a segmentation can be obtained by considering the coefficient

of variation (CV^2) of each segment, defined for the k^{th} segment as

$$CV_k^2 = \frac{\sigma_k^2}{\mu_k^2}, \quad (2)$$

where μ_k and σ_k are the mean and standard deviation of the pixels in the segment. For the whole segmentation the weighted average of the CV^2 is then

$$\text{Average } CV^2 = \sum_{k=1}^{m} \frac{n_k}{n} CV_k^2, \quad (3)$$

with n corresponding to the total number of pixels in the image, m the number of segments and n_k the number of pixels in the k^{th} segment. A theoretical value for the CV^2 can be calculated which is based solely on the distribution of the n_k's [6].

Further performance measures are introduced by considering the complexity of the shape of each segment. By stepping around the boundary and building up a boundary chain, various measures have been developed. These include perimeter, eccentricity (maximum radius/minimum radius), roundness (area/4πperimeter) and the number of corners (changes in direction). Once obtained, for a segmentation, the distribution of the values of each measure can be compared to the distributions in the ideal segmentation. This comparison is carried out by performing a Kolmogorov-Smirnov goodness of fit (K-S) test on the two distributions. Note that, unlike the homogeneity test, this requires prior knowledge of the correct segments and hence cannot be applied to real data.

RESULTS

Fig.1 shows the edges obtained from segmenting the simulated image (a) with the algorithms RWSEG (c), ANNEAL (d), MUM (e) and split and merge (f). A cursory glance at the edge maps suggests that RWSEG and ANNEAL produce the best results. Closer inspection of the output of MUM and split & merge reveals that some structure has been retained but most edges in the ideal have not been found. The differences between Fig.1(b), Fig.1(c) and Fig.1(d) are much more subtle. The large triangular region at the top right, for example, shows up very well in all three maps. Conversely, the small vertical edge in the bottom left corner of the ideal has not quite been reproduced by either RWSEG or ANNEAL. Clearly, although giving some guidance on relative performance, visual inspection is subjective and more objective methods must be used.

To assess the homogeneity of the segmentations the mean segment CV^2 is recorded in Table 1. Each value is averaged over the ten simulated images and over the number of pixels in each image. The final column in Table 1 shows the difference of the observed value of the CV^2 from the expected value normalised by the standard deviation. It can be seen that all algorithms produce results that are at most 1.86 standard deviations away from their expected values. RWSEG is the closest to its expected value and is also the closest to the ideal. Despite the apparent success of ANNEAL, according to its edge map, it appears to be less successful than most other methods in producing homogeneous segments.

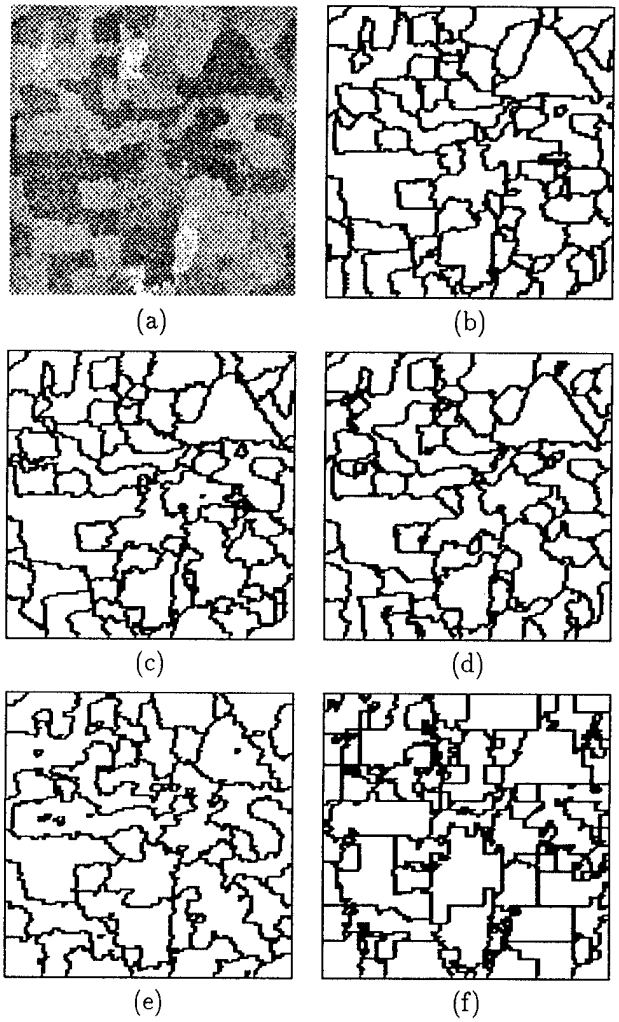

Figure 1: Simulated SAR data (a), with the ideal edge map (b) and edge maps from segmenting with RWSEG (c), ANNEAL (d), MUM (e) and split and merge (f).

Shape preservation is assessed by comparing the size distribution of segments to the ideal by means of the K-S fit, with results shown in Table 2. It is clear that RWSEG and ANNEAL perform much better than the other algorithms. This is in agreement with the visual impression obtained from the edge maps.

When real data are used, the edge maps are much more complex. Those obtained from segmenting the real SAR image in Fig.2(a) using RWSEG (b), ANNEAL (c) and MUM (d) are shown. All three edge maps depict many more segments than the eye detects. An alteration of

Table 1: The observed mean and standard deviation of the CV^2 along with the expected values and normalised difference for simulated data.

Method	Obs. CV^2	Exp. CV^2	s.d. CV^2	Diff. CV^2
RWSEG	0.1973	0.19880	0.002407	-0.089
ANNEAL	0.1927	0.19881	0.002407	-0.379
MUM	0.2034	0.19888	0.002409	1.861
MERGE	0.1929	0.19879	0.002406	-0.133
SPLIT	0.2005	0.19873	0.002406	-0.161
IDEAL	0.1988	0.19878	0.002406	0.017

Table 2: Values of the K-S fit for each shape measure to the ideal; values near 1 imply a good fit.

Method	Area	Perim	Eccen	Round	Corn
RWSEG	0.930	0.963	0.815	0.741	0.513
ANNEAL	0.741	0.768	0.708	0.405	0.660
MUM	0.002	0.003	0.011	0.017	0.002
MERGE	0.655	0.000	0.000	0.000	0.000
SPLIT	0.198	0.166	0.008	0.001	0.200

the input parameters would reduce the amount of segmentation - here they were fixed at the same values as were used for the simulated data. Fig.2 shows that the performance of MUM is much more comparable with the other methods when tested with real data. Table 3 contains the CV^2 of the segmentations for the real data. The observed values of CV^2 are markedly larger for the real data than in the simulated cases for RWSEG and ANNEAL. Conversely, MUM has performed better with the real data and has obtained a CV^2 closer to the expected value than both the other algorithms.

CONCLUSIONS

All algorithms succeed in producing homogeneous segments when simulated data is used. RWSEG and ANNEAL achieve better results in the other tests with RWSEG out-performing ANNEAL in all but one of the K-S fit tests. MUM creates a greater spread in the distribution of segment size by generating more small and more large segments than RWSEG and ANNEAL. This accounts for the poor values seen in Tables 1 and 2. Results obtained with real data show MUM to be a serious contender as it out-performs the other methods in

Table 3: The observed mean and standard deviation of the CV^2 along with their expected values and the difference in terms of standard deviations for real data.

Method	Obs. CV^2	Exp. CV^2	s.d. CV^2	Diff. CV^2
RWSEG	0.3517	0.19735	0.002390	8.478
ANNEAL	0.2238	0.19713	0.002388	1.131
MUM	0.2091	0.19726	0.002390	0.619

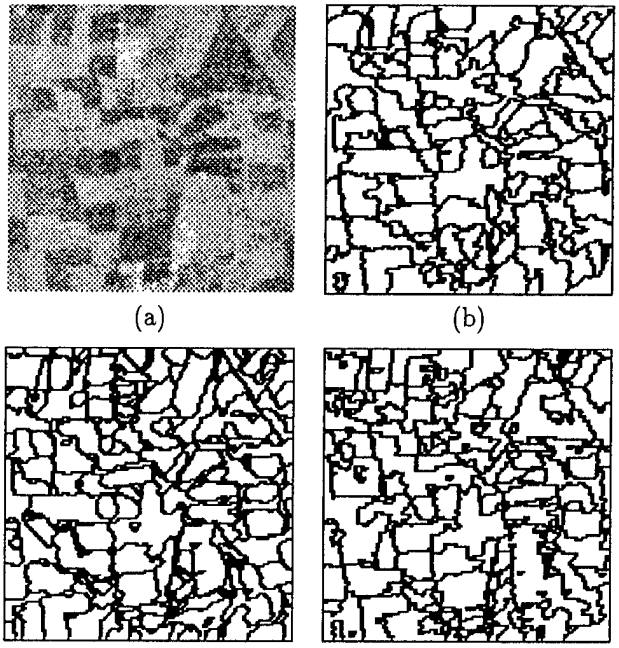

Figure 2: Real SAR data (a) and edge maps from segmenting with RWSEG (b), ANNEAL (c), MUM (d).

producing homogeneous segments and has an edge map similar to them. Current results fail to highlight one algorithm as being superior, but Fig.2 does indicate that the best algorithms produce results which are reasonably consistent with the visual inspection of the real image. It is important at this stage that the value of such algorithms in applications (for example, mapping, classification) be tested.

REFERENCES

[1] F. T. Ulaby, R. K. Moore and A. K. Fung, *Microwave Remote Sensing*, vol. 3, Dedham, MA: Artech House, 1986.

[2] C. J. Oliver and S. Quegan, *Information in SAR Images: Methods and Models for Understanding SAR Data*, Artech House, 1997.

[3] R. G. White, "Low level segmentation of noisy imagery," Tech. Rep. 3900, Roy. Signals and Radar Estab., Malvern, UK, 1986.

[4] R. Cook, I. McConnell, D. Stewart and C. J. Oliver, "Segmentation and Simulated Annealing," Tech. Rep., NA Software, Roscoe House, 62 Roscoe St., Liverpool, UK, 1996.

[5] R. Cook, I. McConnell, C. J. Oliver and E. Welbourne, "MUM (Merging Using Moments) Segmentation for SAR Images," in *SAR Data Processing for Remote Sensing*, (Rome, Italy), SPIE, 1994.

[6] R. G. Caves, S. Quegan and R. G. White, "Quantitative comparison of the performance of SAR segmentation algorithms," *IEEE Trans. Image Processing*, (submitted), 1997.

The Effect of Forest Understory on Synthetic Aperture Radar Backscatter

Tiago A. M. Silva and José M. B. Dias
Instituto de Telecomunicações and
Departamento de Engenharia Electrotécnica e de Computadores.
Instituto Superior Técnico
1096 Lisboa Codex, PORTUGAL.
Email:edias@beta.ist.utl.pt Phone: +351 1 8418466 Fax: +351 1 8418472

Abstract–This paper studies the effect of the understory on radar backscatter from forest stands. The purpose is to understand in what extent the understory presence modifies the backscatter composition. In order to account for the understory, a third layer of scattering media, just above the ground, is added to the *Michigan Microwave Scattering* model. The model is parametrized with experimental data gathered at a forest site, constituted by typical Portuguese forest stand of maritime pine plantations, and published data on North American trembling aspen forest. A sensitivity analysis is conducted in order to evaluate the effect of the understory at L, C and X bands and different polarizations. Simulation results show the importance of the forest understory on the backscattering process, and suggest the feasibility of inverting the proposed model for understory parameter inference.

I. Introduction

Microwave remote sensing is a powerful tool for studying scattering properties of objects, areas, or phenomena, namely those of forests. The availability of high resolution *synthetic aperture radar* (SAR) images of huge areas has fostered research towards understanding the relations between scene parameters (e.g., constitutive, geometrical, structural, biophysical, etc.) and microwave backsatteering. In the case of forest ecosystems these relations has been put in evidence in several works, namely estimation of biomass [1], *leaf area index* (LAI) [2], and soil water contents [3], only to name a few.

Different scattering models have been developed to predict the scattered energy from forested scenes, as well as to assist in real data interpretation. The *radiative transfer* (RT) theory [4], [5], has been the theoretical framework underlaying most models. This theory assumes that there is no correlation between the scattered fields of each scene component, and therefore the addition of power, rather than the addition of fields, holds. The RT theory, despite of being heuristic, has proved to be powerful in many propagation problems in random media [5], without being too heavy from the computational point of view.

Recently, vegetation scattering models have become more realistic and complex as more structural elements are included, and more interactions calculated. The *Michigan Microwave Scattering* Model (MIMICS) [6] is one of the most realistic and extensively tested models presented. The forest is represented by two layers of dielectric elements over a rough surface: the top layer uses dielectric cylinders modeling branches and needles or leafs; the bottom layer contains near vertical cylinders representing the tree trunks; a rough surface models the ground. The presence of shrubby vegetation underneath the crown (understory) has not been contemplated, although some authors (e.g., [7]) have suggested that its presence might have a non-negligible effect on the forest backscatter.

This study aims at the evaluation of the forest understory effect on the total backscatter. This effect, if significant, can degrade the *quality* of biophysical parameter estimates. On the other hand, the estimation of understory parameters, if possible, would be of great value, for instance, for the elaboration of fire behaviour models, and fire risk maps [8].

In order to study the role of the understory in forest backscatter, an extra layer above the ground is added to the two layers of MIMICS model. The scattering elements used in the understory layer are those present the MIMICS crown layer (with different sizes, densities and spatial distributions), and the trunks also present in the trunk layer.

The paper is organized as follows: section II introduces notation and formulates the problem in terms of the radiative transfer theory; in section III the first order solution of the RT differential equation is presented, and its terms are interpreted as forest element contributions; simulation results and the respective discussion are presented in section IV.

II. Problem Formulation

Figure 1 schematizes the proposed three layer forest model. The ground is modelled by a rough surface at $z = -(d + H_t)$. The understory is modelled by a layer with height H_u. The remaining layers are the crown and trunk, of heights d and $H_t - H_u$, respectively.

The two upper layers are identical to the ones included in the MIMICS model. The crown layer includes large cylinders for simulating branches of various sizes, disks (very short and large cylinders) to simulate leafs, and long

0-7803-3836-7/97/$10.00 © 1997 IEEE

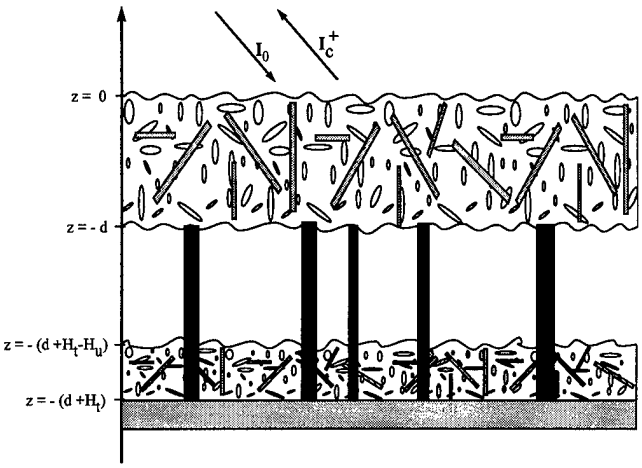

Figure 1: Three layer forest model.

and thin cylinders for simulating tree needles (for a more detailed description see [6]). Each structural element is distributed in size and orientation according to given probability density functions. The trunk layer is constituted by near vertical cylinders of a fixed height but of size and orientation also given by probability density functions.

The bottom layer, introduced in this paper, standing between the trunk and the ground surface, simulates the understory in a similar way the upper layer simulates the crown; as structural elements it uses dielectric cylinders as branches, leafs, and needles. In addition, it also includes large cylinders as the trunks which are exactly parametrized as the trunk layer (see Fig. 1).

It is assumed that the media substratum of the three layers is the vacuum, and that each layer is homogeneous (in a statistical sense) at planes $z = c^{te}$. Defining $\mu = \cos\theta$, where θ is the colatitude angle[1], the vector differential equation for the *specific intensity*

$$\mathbf{I}(\mu,\phi,z) = \begin{bmatrix} I_v \\ I_h \\ U \\ V \end{bmatrix} \tag{1}$$

is given by (see, e.g. [6], for further details)

$$\frac{d\,\mathbf{I}(\mu,\phi,z)}{dz} = -\frac{\boldsymbol{\kappa}_e}{\mu}\mathbf{I}(\mu,\phi,z) + \frac{1}{\mu}\mathbf{F}(\mu,\phi,z), \tag{2}$$

where $\boldsymbol{\kappa}_e$ is the extinction matrix, that accounts for volume absorption and total scattering, and $\mathbf{P}(\mu,\phi,\mu',\phi')$ is the *phase matrix* for incident radiation in the direction (μ',ϕ') and scattered radiation in the direction (μ',ϕ'). Matrix

$$\mathbf{F}(\mu,\phi,z) \equiv \int_{4\pi} \mathbf{P}(\mu,\phi,\mu',\phi')\mathbf{I}(\mu',\phi',z)\,d\Omega'. \tag{3}$$

[1]The lateral coordinates herein used are $(\theta,\phi) \equiv$(colatitute, longitude).

is the so-called *source function*, and represents the total radiation, per volume element, scattered in the direction (θ,ϕ) due incident energy from all directions.

To derive the solution of (2) the boundary conditions must be stated. At $z = 0$ the specific intensity in the direction (μ_0,ϕ_0) is imposed; for diffuse boundaries, at $z = -d$ and $z = -(d + H_t - H_u)$, the specific intensity vector is continuous; the scattering by the rough surface at $z = 0$ is described by the scattering matrix $\mathbf{P}_g$. In conclusion, the following boundary conditions must be satisfied:

$$\mathbf{I}(\mu,\phi,0) = \mathbf{I}_0\delta(\mu-\mu_0,\phi-\phi_0) \tag{4}$$
$$\mathbf{I}(\mu,\phi,-d^+) = \mathbf{I}(\mu,\phi,-d^-) \tag{5}$$
$$\mathbf{I}(\mu,\phi,-z_1^+) = \mathbf{I}(\mu,\phi,-z_1^-) \tag{6}$$
$$\mathbf{I}(\mu,\phi,-z_2) = \mathbf{P}_g(\mu,\phi,\mu'\phi')\mathbf{I}(\mu',\phi',-z_2), \tag{7}$$

where $z_1 = (d + H_t - H_u)$ and $z_2 = (d + H_t)$.

The proposed model is an extension to the MIMICS, from which the layered architecture is adopted. Although, the radiative transfer equation has to be solved from scratch for the three layer case, MIMICS package was still used for calculating the extinction and phase matrices of all forest elements.

III. First order solution

Different methods have been proposed to determine the solution of RT differential equation (2) [9]. Here we adopt the iterative method, which computes a sequence $\{\mathbf{I}^{(n)}, n = 0,1,\ldots,\}$, such that, under weak conditions, $\mathbf{I} = \lim_{n\to\infty}\mathbf{I}^{(n)}$. Term $\mathbf{I}^{(n+1)}$ is obtained by introducing $\mathbf{I}^{(n)}$ in (3), and then solving equation (2) with respect to $\mathbf{I}$.

In the present approach the initial *condition* $\mathbf{I}^{(-1)}$ is given by (4). The zero order solution $\mathbf{I}^{(0)}$ then computed, is simply the reduced incident intensity (due to absorption and scattering), which decays exponentially inside the medium. The first order solution $\mathbf{I}^{(1)}$ is given by a sum of terms each one corresponding to a first order interaction between the specific intensity and scene elements. The interactions corresponding to each term are illustrated in Fig. 2, where letters G, U, T, and C stand for ground, understory, trunk, and crown, respectively.

Generically, the n-order solution $\mathbf{I}^{(n)}$ contains interactions of order $n, n-1,\ldots,1$ between the specific intensity and scene elements.

It has been shown that the first order solution $\mathbf{I}^{(1)}$ approximates well $\mathbf{I}$, when scatterers density is *tenuous* [5]. This is, approximately, the case in the present case. On the other hand, the computational burden of the first order solution is quite acceptable when compared, for instance, with the second order solution. The first order solution is therefore adopted in these work.

Concerning the ground, it is assumed that it has a nearly specular behaviour. This assumption simplifies, in a great extent, the first order solution. Nevertheless, a term corresponding to the direct scattering from the

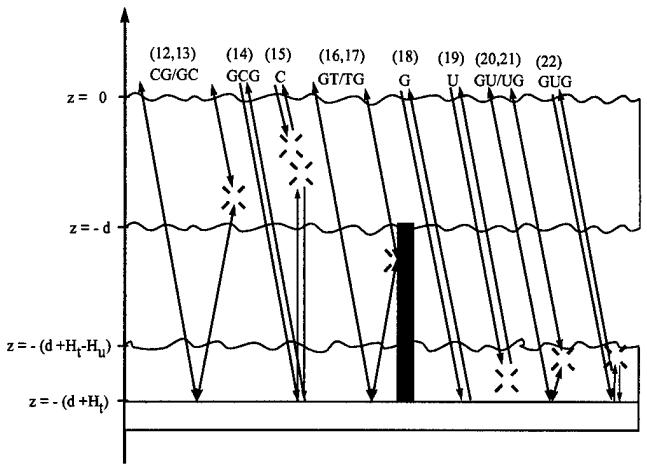

Figure 2: Scattering decomposition of first order solution given by the iterative method.

ground (term G in Fig. 2) is added to the final solution (see e.g., [6] for details).

The following notation is introduced for compactness:

$$\boldsymbol{\alpha}_l^{\pm} \equiv e^{-\frac{\boldsymbol{\kappa}_l^{\pm} H_l}{\mu}} \quad (8)$$

$$\mathbf{R}_{ug} \equiv \boldsymbol{\alpha}_u^{+}\mathbf{R}\boldsymbol{\alpha}_u^{-} \quad (9)$$

$$\mathbf{R}_{tg} \equiv \boldsymbol{\alpha}_t^{+}\mathbf{R}_{ug}\boldsymbol{\alpha}_t^{-} \quad (10)$$

$$\mathbf{R}_{cg} \equiv \boldsymbol{\alpha}_c^{+}\mathbf{R}_{tg}\boldsymbol{\alpha}_c^{-}, \quad (11)$$

where $\boldsymbol{\alpha}_l^{\pm}$ is the attenuation suffered by upward (+) or downward (−) going radiation, crossing layer l with height H_l, and $\mathbf{R} \equiv \mathbf{P}_g(-\mu_0, \phi_0, \mu_0, \phi_0)$ is the ground reflexion matrix. Matrices $\mathbf{R}_{ug}$, $\mathbf{R}_{tg}$, and $\mathbf{R}_{cg}$ denote the total attenuation along the path layer-ground-layer for the understory, trunk, and crown layers, respectively.

After a simple but lengthy computation, one is led to the following solution:

$$\begin{aligned}
\mathbf{I}(\mu,\phi,0) = & \\
+ \ & \boldsymbol{\alpha}_c^{+}\mathbf{R}_{tg}\mathbf{S}_c(-,-) && (12)\\
+ \ & \mathbf{S}_c(+,+)\mathbf{R}_{tg}\boldsymbol{\alpha}_c^{-} && (13)\\
+ \ & \boldsymbol{\alpha}_c^{+}\mathbf{R}_{tg}\mathbf{S}_c(-,+)\mathbf{R}_{tg}\boldsymbol{\alpha}_c^{-} && (14)\\
+ \ & \mathbf{S}_c(+,-) && (15)\\
+ \ & \boldsymbol{\alpha}_c^{+}\mathbf{S}_t(+,+)\mathbf{R}_{ug}\boldsymbol{\alpha}_u^{-}\boldsymbol{\alpha}_t^{-}\boldsymbol{\alpha}_c^{-} && (16)\\
+ \ & \boldsymbol{\alpha}_c^{+}\boldsymbol{\alpha}_t^{+}\mathbf{R}_{ug}\mathbf{S}_t(-,-)\boldsymbol{\alpha}_c^{-} && (17)\\
+ \ & \boldsymbol{\alpha}_c^{+}\boldsymbol{\alpha}_t^{+}\boldsymbol{\alpha}_u^{+}\mathbf{R}_g(+,-)\boldsymbol{\alpha}_u^{-}\boldsymbol{\alpha}_t^{-}\boldsymbol{\alpha}_c^{-} && (18)\\
+ \ & \boldsymbol{\alpha}_c^{+}\boldsymbol{\alpha}_t^{+}\mathbf{S}_u(+,-)\boldsymbol{\alpha}_t^{-}\boldsymbol{\alpha}_c^{-} && (19)\\
+ \ & \boldsymbol{\alpha}_c^{+}\boldsymbol{\alpha}_t^{+}\mathbf{S}_u(+,+)\mathbf{R}\boldsymbol{\alpha}_u^{+}\boldsymbol{\alpha}_t^{-}\boldsymbol{\alpha}_c^{-} && (20)\\
+ \ & \boldsymbol{\alpha}_c^{+}\boldsymbol{\alpha}_t^{+}\boldsymbol{\alpha}_u^{+}\mathbf{R}\mathbf{S}_u(-,-)\boldsymbol{\alpha}_t^{-}\boldsymbol{\alpha}_c^{-} && (21)\\
+ \ & \boldsymbol{\alpha}_c^{+}\boldsymbol{\alpha}_t^{+}\boldsymbol{\alpha}_u^{+}\mathbf{R}\mathbf{S}_u(-,+)\mathbf{R}\boldsymbol{\alpha}_c^{-}\boldsymbol{\alpha}_t^{-}\boldsymbol{\alpha}_c^{-} && (22)
\end{aligned}$$

where

$$\mathbf{S}(s_\mu, s_{\mu_0}) \equiv \int_l \boldsymbol{\alpha}_l^{s_\mu}(z)\mathbf{P}_l(s_\mu, s_{\mu_0})\boldsymbol{\alpha}_l^{s_{\mu_0}}(z)dz,$$

with $s_\mu, s_{\mu_0} \in \{+-\}$, accounts for backscattering and attenuation in one layer.

Figure 2 schematizes all the first order interactions within the forest canopy. The numbers over each interaction refer to the term with the same number of the first order solution. Interactions from (12) to (18) have a one to one correspondence to those of MIMICS. The understory introduces interactions (19) to (22).

IV. Simulation Results

In order to study the effect of understory presence, two forests were simulated: the *trembling aspen* and the Portuguese maritime pine (*Pinus pinaster*). For comparison purposes, the trembling aspen forest, simulated without understory in [6], is used. The maritime pine forest, is the most common and widespread forest in Portugal, and may contain dense undergrowth depending on its management. The main forest parameters, like tree height, crown width, *diameter at breast height* (DBH), density, etc., were obtained from field measurements of a monospecific, even aged, mature (36 to 38 years old) forest located in Cantanhede, central Portugal [10]. Table 1 shows the main parameters used in both forests. Table 2 shows the main parameters for the understory vegetation. All the simulations were made for an incidence angle of 30°. Values close to this one are widely used in spaceborne sensors and suits well forestry remote sensing.

For L-band VV without understory, the most important contributions from the maritime pine forest are the near dihedral corner reflections on the trunks and ground (GT/TG component), followed by the direct scattering from the crown (C component). This can be read from Fig. (3) at $H_u = 0$. For 1m high undergrowth, the direct backscatter from this layer (U term) codominates with the crown contribution. Also for L-band VH, the understory contribution becomes dominant over the crown contribu-

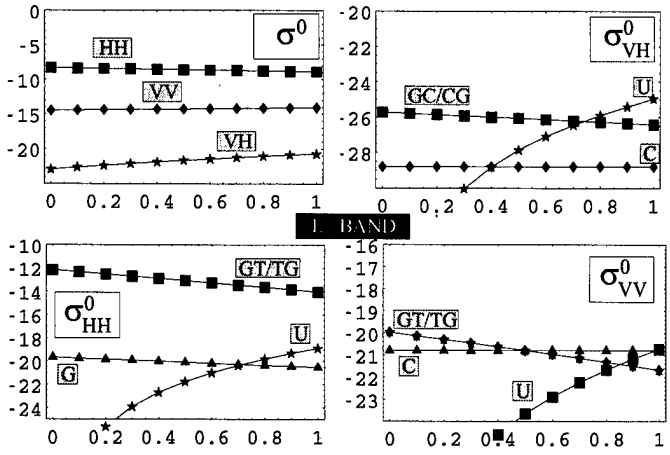

Figure 3: L-band maritime pine forest backscattering coefficient, in decibels, for a 30° incidence angle, as function of the understory height H_u in meters.

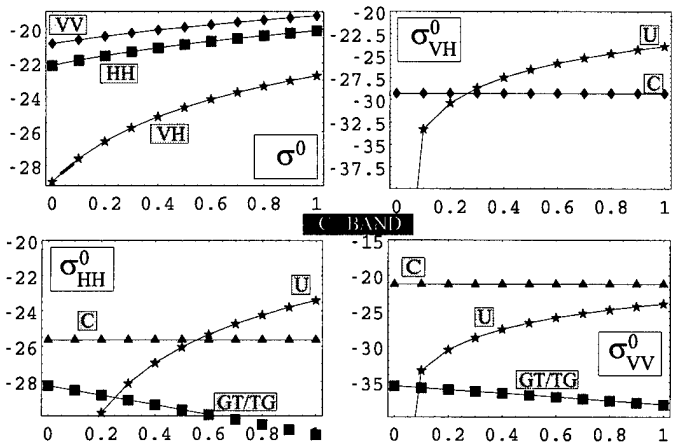

Figure 4: C-band maritime pine forest backscattering coefficient, in decibels, for a 30° incidence angle, as function of the understory height H_u in meters.

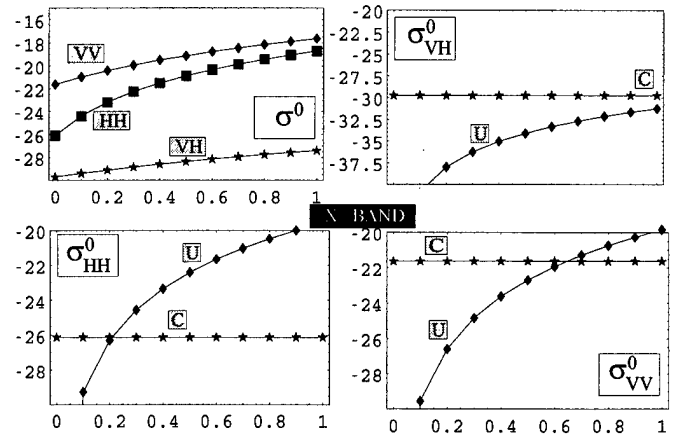

Figure 5: X-band maritime pine forest backscattering coefficient, in decibels, for a 30° incidence angle, as function of the understory height H_u in meters.

tions for $H_u \geq 0.7\ m$. Still reading L-band results, notice that the GT/TG component decreases with H_u due to understory attenuation. For example, the GT/TG component is attenuated, approximately, 2 dB when $H_u = 1\ m$. This effect is quite magnified as the understory density increases.

At higher frequencies the relative weight of the understory backscatter becomes noticeable. At C-band and X-band, with 1m high understory, this contribution is comparable or higher than the most important contributions, and lead to an increase in the total backscatter for all polarizations. The variation of the total backscatter when the understory height varies from 0 to 1m ranges from almost null to 6-7 dB at X-band and HH polarization.

The trembling aspen forest is significantly different in structure. The trees have thinner branches, laminar leafs instead of needles, and the stands have higher densities. Once again the effect of the understory is noticeable for the considered wavelengths, but especially for C-band

Parameters	Tremb. as.	Mari. pi.
Tree den. (m^{-2})	0.11	0.04
Canopy hei. (m)	2	5.65
Trunk hei. (m)	8	9.68
Trunk dia. (cm)	24	28.2
Pri. branch den. (m^{-3})	4.1	0.5
Pri. branch len. (m)	0.75	1.5
Pri. branch dia. (cm)	0.7	5
Sec. branch den. (m^{-3})	-	1
Sec. branch len. (m)	-	0.7
Sec. branch dia. (cm)	-	1
Leaf/needle den. (m^{-3})	830	500
Leaf/needle dia. (cm)	6.18	0.2
Leaf thi./needle len. (cm)	0.03	18
Soil model	Phy. op.	Phy. op.
Soil rms hei. (cm)	1.0	1.0
Soil corr. length (cm)	15	15
Surface dielec.	5.68-j1.13	5.68-j1.13
Wood dielec.	28-j7.8	28-j7.8
Leaf/needle gravi. cont.	0.8	0.61

Table 1: Parameters for Trembling aspen and Maritime pine forests.

Parameters	Understory
Needle den. (m^{-3})	2000
Needle dia. (cm)	0.10
Needle length (cm)	2.0

Table 2: Parameters for understory.

(5.7cm). At this frequency and for cross-polarization, the understory is responsible for an increase of the total backsatter of more than 10 dB.

In short, the effect of the understory, for the studied forests, is twofold:

(a) **Attenuation of the GT/TG backscatter component**
Apart from the direct crown scattering, all the other contributions must cross the understory, thus suffering increased attenuation with the understory biomass and height. This effect is stronger at L-band and can degrade severely the estimation forest parameters such as height, biomass, LAI, DBH, and basal area;

(b) **Added backscatter from the understory**
The understory is responsible for backscattering directly or indirectly (components U, UG, GU, GUG of Fig. 2). If any of these components becomes dominant, it might be possible to infer understory parameters. This is the case of the U-component in the maritime pine forest studied for C-band VH and $H_u \geq 0.2\ m$, and X-band HH and $H_u \geq 0.2\ m$.

V. Concluding Remarks

In this paper, the first order solution of radiative transfer differential equation was derived for a three layer architecture. Each layer models a horizontal set of structural elements in a forest. From top to bottom each layer accounts for crown, trunks, and understory. The three layers stands over a rough surface. The studied structure is an extension to the MIMICs model, in which the understory is not present.

Simulations were made at L, C and X band at 30° incidence angle for a coniferous and a deciduous forest: a Portuguese maritime pine and North American trembling aspen forest to which understory was added. It was found that the backscattered predictions are sensitive to understory presence, for all the considered wavelengths and most polarization configurations. Considering understory heights from 0 to 1 m resulted in a variation of the total backscatter ranging from -2 dB to 10 dB. The rationale underlying this behaviour is roughly the following:

(a) attenuation of the ground-trunk/trunk-ground backscatter component:

(b) added backscatter from the understory.

The balance between this two mechanisms can result in an increase or in an decrease of the total forest backscatter. At lower frequencies (L-band) mechanism (a) dominates, while at higher frequencies (C and X bands) mechanism (b) dominates.

The implication of the previous conclusions on forest parameters estimation is twofold:

(a) at L-band, estimation of forest parameters such as tree height, biomass, LAI, DBH, and basal area can be severely corrupted;

(b) at C and X bands, it may be possible to infer understory parameters.

ACKNOWLEDGMENT

The authors acknowledge using MIMICS software kindly made available by Radiation Laboratory of the University of Michigan.

References

[1] Y. Hussin, R. Reich, and R. Hoffer, "Estimating slash pine biomass using radar backscatter", *IEEE Trans. Geosci. Remote Sensing*, vol. 29, pp. 427–431, 1991.

[2] S. Paloscia, "An empirical approach for retrieving leaf area index from multifrequency sar data", *in IEEE International Geoscience and Remote Sensing Symposium- IGARSS'95*, pp. 967–969, Florence, Julv 1995.

[3] K. McDonald, M. Dobson, and F. Ulaby, "Using MIMICS to model L-band multiangle and multitemporal backscatter from a walnut orchard", *IEEE Trans. Geosci. Remote Sensing*, vol. 28, pp. 477–491, 1990.

[4] S. Chandrasekhar, *Radiative Transfer*, Oxford University Press, London, New York and Dover, 1950.

[5] A. Ishimaru, *Wave Propagation and Scattering in Random Media*, vol. 1, Academic Press, New York, 1978.

[6] F. Ulaby, K. Sarabandi, K. McDonald, M. Whitt, and M. Dobson, "Michigan microwave canopy scattering model", *Int. J. Remote Sensing*, vol. 11, pp. 1223–1253, 1990.

[7] T. Le Toan, A. Beaudoin, J. Riom, and Guyon, "Relating forest biomass to SAR data", *IEEE Trans. Geosci. Remote Sensing*, vol. 30, pp. 403–411, 1992.

[8] M. Vasconcelos and D. Guertin, "Firemap - simulation of fire growth with a geographic information system", *Int. J. of Wildland Fire*, vol. 2, pp. 87–96, 1992.

[9] F. Ulaby and Elachi (eds.), *Radar Polarimetry for Geoscience Applications*, Artech House, Boston, 1990.

[10] Anonymous, "Inventário florestal do PDR do Baixo Mondego e Gândaras", Technical report, Instituto Florestal de Portugal, 1996.

Block-Based Maximum Likelihood Classification For Hyperspectral Remote Sensing Data

Xiuping Jia
School of Electrical Engineering
University College, The University of New South Wales
Australian Defence Force Academy, ACT 2600, Australia
Tel: +61 6 2688202, Fax: +61 6 2688443, Email: x-jia@adfa.oz.au

Abstract -- In this paper, a block-based maximum likelihood classification is developed. The proposed method is based on individual class statistics to break the complete set of bands into several highly correlated subgroups. By ignoring low correlations between subgroups, the maximum likelihood methods is then employed for each subgroup independently. To accommodate the flexibility of using different segmentations for different classes, a progressive two-class decision procedure is used. This method also overcomes the problem caused by inadequate training samples for small classes. Experiments using a hyperspectral remote sensing data set were carried out. The results show that the block-based maximum likelihood method is an effective and practical alternative to conventional maximum likelihood classification for small class identification. The classification accuracies given by the proposed method are significantly higher than using a minimum distance classifier, which is one of the only viable techniques for hyperspectral data sets.

INTRODUCTION

Airborne imaging spectrometers, such as AVIRIS, acquire images with high spatial and spectral resolutions. Therefore, fine detailed characteristics of solar reflectance of various ground cover types can be derived and used for class identification. However, the enormous data sets generated have a major impact on traditional supervised statistical image processing techniques, such as maximum likelihood classification, due to long processing times and the difficulty in training on small classes.

Conventional maximum likelihood classification is based on the assumption that the probability distribution for each spectral class is of the form of a multivariate normal model with dimensions which equal the number of spectral bands. When equal prior probabilities are assumed for all the classes, this leads to the discriminant function [1]

$$g_i(\mathbf{x}) = -\ln|\Sigma_i| - (\mathbf{x}-\mathbf{m}_i)^t \Sigma_i^{-1}(\mathbf{x}-\mathbf{m}_i) \qquad i = 1, \ldots, M \qquad (1)$$

The decision rule is:

$$\mathbf{x} \in \omega_i \ \ if \ \ g_i(\mathbf{x}) > g_j(\mathbf{x}) \ \ for \ all \ \ j \neq i \qquad (2)$$

where represent $\mathbf{x}$ a unknown pixel vector, and ω_i, $i = 1, 2, \ldots, M$, represent the classes for an image. M is the total number of classes. The mean vector and covariance matrix, $\mathbf{m}_i$ and Σ_i, are estimated from the training pixels, and used as class signatures.

This model works well only if class statistics are estimated reliably; this requires a large number of training pixels for each class. The rule of thumb is that the number of training pixels per class should be at least 10 times the number of bands used [2]. However, the number of training pixels is always limited in remote sensing image classification, since training pixel identification is a time-consuming step and can be very costly. Particularly, for hyperspectral image data, small classes may not have enough training pixels available for reliable maximum likelihood estimates.

Various techniques have been developed for dealing with small class training. For instance, class statistics can be effectively enhanced by using the extra information provided by unlabelled data other than training samples from the class of interest [3]. A statistical multisource analysis method [4] was applied to hyperspectral data classification by assuming that a hyperspectral data set consists of several independent data sources [5]. Jia and Richards developed a simplified maximum likelihood classification method, in which several subgroups are formed from the complete set of spectral bands in the data, based on properties of the global correlation among the bands. Subgroups which are poorly correlated with each other are treated independently using conventional maximum likelihood classification. However, the band grouping may not reflect the class data statistics. In this paper, individual class data's statistics is examined and used to determine the segmentation. To accommodate this flexibility in using different band segmentations for different classes, a progressive two-class decision procedure [7] is used. Experiments using an AVIRIS data set were carried out. The results show that the performance of the block-based maximum likelihood method is significantly better than minimum distance classifier and can be used as an effective and practical alternative to conventional maximum likelihood classification when small classes do not have enough training pixels.

METHODS

The Scheme

It has been observed that for AVIRIS or other airborne optical remote sensing data, correlations between neighbouring spectral bands are generally higher than for bands further apart and that high correlations appear in blocks as shown in Fig. 1 [6, 8]. The bright diagonal blocks in Fig. 1 indicate the high correlations among that group of bands.

0-7803-3836-7/97/$10.00 © 1997 IEEE

By ignoring low correlations between subgroups, that is, assuming subgroups of bands are independent, the block-based maximum likelihood classification method is developed.

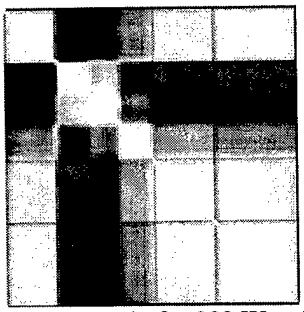

Fig. 1. Correlation Matrix for 202 Wavebands for an AVIRIS Image (White=1 or -1; black=0).

Selection of Blocks

Block-based maximum likelihood classification exploits the partitioning of the complete set of spectral bands into several subgroups. A subgroup is selected so that the correlations are high among the spectral bands in the subgroup and low to the remaining bands. Such a subgroup appears as a diagonal block in data's correlation matrix. Therefore, the subgroups to use are generally guided by observation of the boundaries of the bright blocks along the principal diagonal of the correlation matrix. The number of blocks and the sizes of each block may be different for different classes and different images.

The block size will need to be limited by the number of training pixels per class available. Reliable statistics for maximum likelihood classification, as noted earlier, require at least ten times the number training pixels as bands being used in *the biggest subgroup*. In this case, some relatively high correlations may have to be ignored. However, this approach will still be better than traditional minimum distance classification (often used when training pixels are limited) since at least some correlations are included.

Selection of blocks can be based on global data statistics [6] or based on class data correlation properties. The former involves a smaller work load, and a single stage classification scheme can be used. The latter is sensitive to the class data structure and allows the use of bigger block sizes for those classes which have large numbers of training pixels. However, a multilayer classification procedure is required.

Multilayer Block-based Maximum Likelihood Classification

A progressive two-class decision classifier [7], illustrated in Fig. 2, converts a multiclass classification problem into a several independent two-class separations.

$\mathbf{x}$ is an N-dimensional pixel vector. Suppose there are six classes, represented by ω_a, ω_b, ω_c, ω_d, ω_e, and ω_f. The scheme focuses on one class pair at a time (at a node). The function of the very first layer is to check the potential membership of $\mathbf{x}$ to class ω_a and class ω_b and the vector is classified temporarily as either class ω_a or class ω_b using the decision rule, D_{ab}. Class ω_b will be rejected for further consideration for those vectors labelled into the ω_a category, and class ω_a is rejected for further consideration for those vectors labelled into the ω_b category. At the second layer, there are two nodes, and two new class pairs (ω_a and ω_c for the left side node and ω_b and ω_c for the right side node) are considered, respectively. This process continues until a pure class labelling has been reached at the last layer, which is the final assignment.

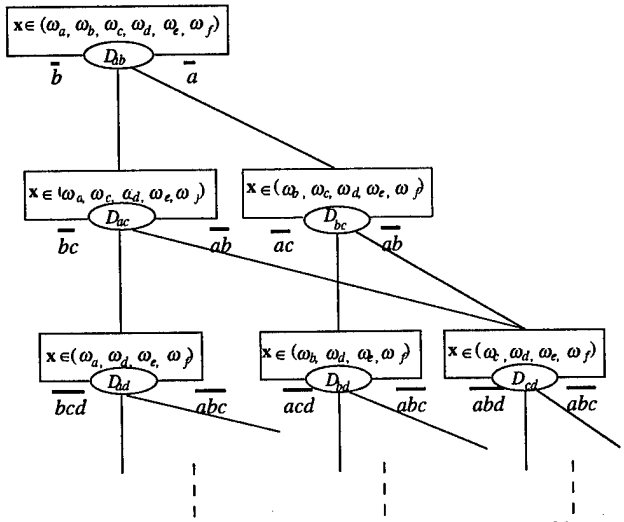

Fig. 2. A Schematic Chart for Progressive Two-Class Decision Classifier.

One of the advantages of this scheme is that it allows the use of different band segmentations for different class pairs. Let classes A and B be the class pair to consider at a node. Referring to class A data's correlation matrix among the complete set of N bands, for example, as shown in Fig. 3 (a), K_a subgroups are formed corresponding to K_a distinguishable diagonal blocks as shown in Fig. 3 (b). Similarly, referring to class B data's correlation matrix, K_b subgroups are formed. To make a same degree of approximation to both classes, an unified segmentation with K_{ab} subgroups is required. K_{ab} is formed by adopting the larger blocks between the two segmentations. If the number of training pixels is inadequate, the smaller of the two should be adopted instead. As a result, $K_{ab} < K_a + K_b$ when there are some overlapping blocks. By ignoring the off-diagonal block correlation, an assumption of normality is made for each class within each subgroup k, $k = 1, 2, \ldots, K_{ab}$. The discriminant function (1) becomes:

$$g_i(\mathbf{x}) = -\sum_{k=1}^{K_{ab}} \left\{ \ln|\Sigma_{ik}| + (\mathbf{x}_k - \mathbf{m}_{ik})^t \Sigma_{ik}^{-1} (\mathbf{x}_k - \mathbf{m}_{ik}) \right\} \quad (3)$$

In (3), the dimensions of $\mathbf{x}_k$, $\mathbf{m}_{ik}$, and Σ_{ik} are reduced to n_k ($n_k < N$), the size of the k th subgroup, so that advantage can be taken of the corresponding quadratic reduction in classification time. Also, the number of training pixels

required per class, which is linked with the size of *the biggest subgroup*, is much smaller than when all bands are used.

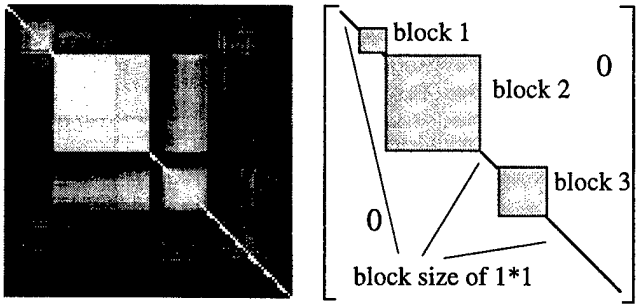

(a) (b)

Fig. 3. (a) A Class Correlation Matrix. (b) Block Selections.

EXPERIMENTS

The AVIRIS image data used for this test is from an area of mixed agriculture and forestry in Northwestern Indiana, USA. Water absorption bands, bands 104 to 108 and 150 to 162, were removed, leaving 202 bands. The global data's correlation matrix is as shown in Fig. 1 previously. Four classes are selected based on the ground truth map, and the correlation matrix for each class is examined. Table 1 gives details of class selection and band segmentations. Each subgroup of bands corresponds to a diagonal block in the covariance matrix. The block size must be limited to 20 by 20 for class Hay and 10 by 10 for the remaining 3 classes, since there are 200 and 90 or 100 training pixels available, respectively.

Three tests were carried out: (i) the minimum distance classification (MD); (ii) single layer block-based maximum likelihood classification with uniform subgroup of size 10 (BML.U10); 20 blocks of size 10 by 10 are formed; and (iii) the multilayer block-based maximum likelihood methods with segmentation as shown in Table 1 (BML.VSize). As results of these band segmentations, 11, 12 and 16 blocks of size 10 by 10 are used in 1, 2 and 3 class pairs separations, respectively. The classification result comparison is given in Table 2.

The classification accuracies achieved from the two tests on the block-based method are both significantly higher than using a minimum distance classifier, since some second degree of statistics have been taken into account. Although the size of each block used in BML.VSize is smaller or equal to the block used in BML.U10, the classification accuracy given by the BML.VSize method is very close to that given by BML.U10. This result indicates that the class sensitive method is more effective.

DISCUSSION AND CONCLUSIONS

While the block-based maximum likelihood classification method is not identical to the original maximum likelihood classification, it provides an effective and practical alternative method for handling small class training problems. The segmentation based on individual class correlation matrix, generally, is more flexible and effective than based on global data statistics. This becomes a significant advantage when class correlation properties are very different from class to class. When the blocks are limited to small sizes as in the above experiments, the segmentation for each class becomes similar, therefore, global data' correlation matrix can be simply used.

Table 1 Block Selections For Each Class

No. of Pixels for Training/Testing		Band Segmentation†
wood	90/50	19-28; 33-102 by 10; 110-139 by 10
hay	200/70	9-28; 33-92 by 20; 93-102; 110-129; 130-139
pasture	90/57	19-28; 33-102 by 10; 110-139 by 10
grass	100/68	9-28 by 10; 33-102 by 10; 110-139 by 10; 156-195 by 10

† The subgroups of size one are not listed.

Table 2 Classification Result Comparison

Methods	MD	BML.U10	BML.VSize
Training Data	80.2%	98.5%	98.1%
Testing Data	86.9%	97.1%	96.5%

ACKNOWLEDGMENT

The author wishes to thank to Prof. J. Richards of School of Electrical Engineering, University College, the University of New South Wales for his valuable discussions and help in manuscript preparation. Thanks also goes to Dr. D. Landgrebe of School of Electrical Engineering, Purdue University for providing the AVIRIS data set.

REFERENCES

[1] J.A. Richards, Remote Sensing Digital Image Analysis: an Introduction. 2nd ed., Springer-Verlag: Berlin and Heidelberg, 1993.

[2] P.H. Swain and S.M. Davis, Remote Sensing: The Quantitative Approach, New York: McGraw-Hill, 1978.

[3] B.M. Shahshahani and D.A. Landgrebe, "The effect of unlabeled samples in reducing the small sample size problem and mitigating the Hughes phenomenon", IEEE Trans. on Geos. Remote Sensing, vol.32, pp. 1087-1095, 1994.

[4] T. Lee and J.A. Richards, "Piecewise linear classification using seniority logic committee methods, with application to remote sensing", Pattern Recognition. 17: 453-464, 1984.

[5] J.A. Benediktsson and P.H. Swain, "Consensus theoretics classification methods", IEEE Trans. on Systems, Man and Cybernetics, vol 22, pp. 688-704, 1992.

[6] X. Jia and J.A. Richards, "Efficient maximum likelihood classification for imaging spectrometer data sets", IEEE Trans. on Geos. Remote Sensing, vol.32, pp. 274-81, 1994.

[7] X. Jia and J.A. Richards, "Feature reduction using a supervised hierarchical classifier", 8th Australasian Remote Sensing Conference, Canberra, March 25-29, pp. 32, 1996.

[8] X. Jia, "Classification techniques for hyperspectral remote sensing image data", PhD Thesis, School of Electrical Engineering, University College, ADFA, The University of New South Wales, 1996.

SAR Image Analysis Methods for Forest Applications

Shaun Quegan and Jiong Jiong Yu
Sheffield Centre for Earth Observation Science, University of Sheffield,Sheffield, S3 7RH,UK
Tel: +44 114 2223778 (Professor S.Quegan),Fax: +44 114 2223803,Email: S.Quegan@sheffield.ac.uk

ABSTRACT

Forest information can be inferred from a wide range of SAR systems and data types, each of which brings its own requirements for parameter estimation. These parameters and the current state of knowledge on their estimation properties are summarised in a unified approach, in the main based on the product model for multi-channel data. The possible need to modify this model for long wavelength data is described.

1. INTRODUCTION

In order to the assess the value of SAR to forestry applications, it is necessary to consider a wide range of data types, including polarimetric, multi-frequency, multi-temporal, interferometric, high resolution and combinations of these. Experimental and modelling studies try to establish which forest properties give rise to measurable effects in these different types of data. The image analysis task is to relate these effects to parameters and to treat the images in such a way as to bring out these parameters to best advantage. Image analysis can also precede physical understanding: for example, the physical basis for texture is only just becoming well understood [1], although its image manifestation is well known (see Section 4). This paper reviews what we know about the relevant parameters and methods to estimate them. The only new results are in Section 2, but we attempt to present the material in a way which brings out commonality of approach.

Image analysis must start from a data model. We assume that the basic data type for a homogeneous distributed target observed in M channels is a complex M-vector, **S**, with the following statistical properties:

(i) if the data is polarimetric or single-pass interferometric,

$$\mathbf{S}=T\mathbf{Y} \qquad (1)$$

where **Y** is Gaussian, and T is a positive scalar texture variable [2];

(ii) if the data is multi-temporal or repeat-pass interferometric, each channel of the data vector is independently textured

$$S_k=T_kY_k \qquad 1\le k\le M \qquad (2)$$

We first deal with untextured data, i.e., $T_k\equiv 1$ for all *k;* texture is discussed in Section 4. In this case, **S** is Gaussian and completely described by its covariance matrix, *C*, where $C_{ij}=\langle S_iS_j^*\rangle$. Hence <u>all</u> the information about the target is carried by the covariance terms, and the basic problem is to provide good local estimates of them. The maximum likelihood estimator (MLE) of C is well-known when pixels are independent, as we will assume: it is the sample covariance matrix [3].

An important classification of data types is into those exhibiting inter-channel correlation (polarimetry, interferometry) and those not doing so (multi-temporal, multi-frequency). We first deal with the latter, focusing on multitemporal data.

2. MULTITEMPORAL DATA

When the channels are uncorrelated, the covariance matrix is diagonal, so that all the information is contained in the channel powers. Each channel has an independent Gaussian (or, if multi-looked, independent gamma) distribution, and the complete information vector is the vector $\left(\sigma^o_1,\ldots,\sigma^o_M\right)$ of backscattering coefficients at each pixel. Exploitation of this information to distinguish forest types or forest from non-forest should optimally be approached through Bayesian methods, but more ad hoc methods based on change detection have proved useful [4,5].

Because of the multiplicative nature of speckle, a constant false alarm rate change detector must operate on image ratios, not differences [6] (although this is equivalent to differencing log images). The maximum likelihood estimator of the intensity ratio of two regions is given by $Z\equiv \bar{I}_1/\bar{I}_2$, where $\bar{I}_k$ denotes the observed average intensity in region k. (For multitemporal data, the region is the same but the times are different). Assuming that the data are L-look and that each region contains N pixels, then Z has a probability density function given by [7]:

$$p(Z)=\frac{\Gamma(2M)}{\Gamma^2(M)}\gamma^M Z^{M-1}(\gamma+Z)^{-2M} \qquad (3)$$

where M is the total number of looks, i.e. $M=NL$, $\gamma=\langle I_1\rangle/\langle I_2\rangle$ denotes the true intensity ratio of the regions, and $\langle I_k\rangle$ denotes the mean intensity in region k. For a chosen threshold T and fixed γ, the probability that a change will be detected is given by:

$$P_d(T,M)=P\{Z>T\}=\int_T^\infty p(Z)dZ$$
$$=\frac{\Gamma(2M)}{\Gamma^2(M)}\sum_{p=0}^{M-1}\binom{M-1}{p}\frac{(-1)^{D-M}}{D}(1+R)^{-D} \qquad (4)$$

where D=2M-p-1 and R=T/γ. An efficient reduction formula for P_d(T,M) is given by:

0-7803-3836-7/97/$10.00 © 1997 IEEE

$$P_d(T,M+1)=P_d(T,M)+X(R,M)$$
$$=P_d(T,M)+\frac{2R(2M-1)X(R,M-1)}{M(1+R)^2} \quad (5)$$

where $P_d(T,1) = (1+R)^{-1}$ and $X(R,1)=R(1-R)(1+R)^{-3}$. The probability of false alarm, P_{fa}, which also depends on M and T, is calculated by using the same formula for P_d but with $\gamma=1$:

$$P_{fa}(T,M)=P_d(T,M|\gamma=1) \quad (6)$$

For given P_d and γ, the decision threshold T as a function of M can be determined numerically by using (5). The corresponding P_{fa} can then be worked out by substituting the same M and T into (6). A convenient approach is to plot a look-up graph; an example with $P_d=0.99$ and $\gamma=2$ is shown in Fig.1.

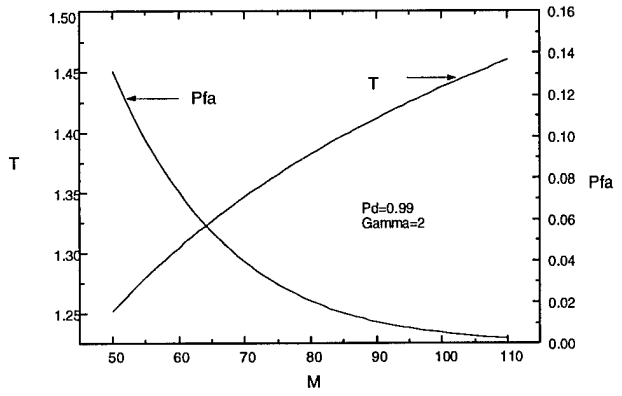

Figure 1. Look-up graph of the probability of false alarm (P_{fa}) and the threshold (T) against the number of looks (M) for $P_d=0.99$ and $\gamma=2$

Studies [4] and [5] indicated that it is necessary to detect changes of ~2-3 dB for discrimination of tropical forest at C band. Graphs like Fig.1 provide a simple way to select the corresponding number of looks and the threshold, in order to give a desired P_{fa}, for the given P_d and γ. For example, in Fig.1, it can be seen that in order to satisfy the requirement of $P_d=0.99$, $P_{fa}=0.01$ and $\gamma=2$, the required number of looks is 92 and the corresponding threshold 1.41 (1.49dB). The forest in Thetford, UK, was stable though the year, with the temporal change around 1.5 dB as in the tropics, while the surrounding agriculture areas showed variation of up to 5 dB, allowing discrimination of the two cover types.

3. POLARIMETRIC AND INTERFEROMETRIC DATA

For polarimetric data the covariance matrix has the form

$$C=\begin{pmatrix} \sigma_{hh} & 0 & \sqrt{\sigma_{hh}\sigma_{vv}}\rho \\ 0 & \sigma_{hv} & 0 \\ \sqrt{\sigma_{hh}\sigma_{vv}}\rho^* & 0 & \sigma_{vv} \end{pmatrix} \quad (7)$$

as long as the forest exhibits azimuthal symmetry. Here $\sigma_{pq}=\left\langle |S_{pq}|^2 \right\rangle$ and $\rho=\left\langle S_{hh}S_{vv}^* \right\rangle / \sqrt{\sigma_{hh}\sigma_{vv}}$. The symmetry condition is likely to be met in natural forest but may be violated in plantations. In the latter case, sensitivity to asymmetry may depend on wavelength; the canopy may be essentially symmetric while the soil and trunk structure may be asymmetric. Short wavelengths scattering in the canopy will then have a covariance matrix of the form (7) while longer wavelengths may require the cross-polarised term to be included. (Although examination of AirSAR data revealed no significant correlation between the like and cross polarised channels at any of C, L or P bands in coniferous plantation forest.) For two channel interferometric data, we have a similar form to (7) but omitting the second row and column of C. The estimation properties, which we describe below, are then identical.

The properties of the sample covariance matrix are described by the complex Wishart distribution [3], from which the important marginal distribution can be derived. The $\hat{\sigma}_{pq}$ are gamma distributed (where ^ denotes MLE, in this case the spatial average), so their sampling properties are well known. Since ρ is a function of covariance terms, its MLE is given by the corresponding function of the MLEs, i.e.

$$\hat{\rho}=\hat{r}e^{i\hat{\phi}}=\frac{\sum_1^M S_{hh}S_{vv}^*}{\left(\sum_1^M |S_{hh}|^2 \sum_1^M |S_{vv}|^2\right)^{1/2}} \quad (8)$$

where M denotes the number of independent samples averaged. The distribution of the multi-look phase difference, $\hat{\phi}$, can be described by elementary functions [2]. Its essential properties are that it is unimodal with mode given by $\angle\rho$ and it becomes more concentrated on $\angle\rho$ as $|\rho|$ increases. There are no analytic expressions for its mean and variance except in the case N=1. However, as noted in [9] these are not good descriptors unless the distribution has mode near 0° and is reasonably narrow. In forestry, modes well in excess of 90° are common and specific phase statistics may be preferred [10].

The distribution of coherence, $\hat{r}$, is given by

$$p(\hat{r})=2\hat{r}(M-1)\left(1-|\rho|^2\right)^M\left(1-\hat{r}^2\right)^{M-2}$$
$$\times {}_2F_1\left(M,M,1,\hat{r}^2|\rho|^2\right) \quad (9)$$

where ${}_2F_1$ is a hypergeometric function. Expressions for the moments of $\hat{r}$ are readily calculated but rely on the generalised hypergeometric function ${}_3F_2$ hence are not easy to handle. An important point is that, although $\hat{r}$ is an asymptotically unbiased estimate of $|\rho|$, it can exhibit substantial bias for small values of $|\rho|$. In fact, if $|\rho| = 0$, $\langle \hat{r} \rangle \approx \sqrt{\pi / M}$ [2], so that at least 314 samples are needed to reduce the bias to less than 0.1. Perhaps more important than (9) is the posterior PDF of $|\rho|$ given the estimate $\hat{r}$, $p(|\rho| \,|\hat{r})$, which is proportional to the PDF in (9) for $0 \le |\rho| \le 1$ and zero otherwise. The use of this distribution for setting confidence intervals on $|\rho|$.is described in [11].

4. High Resolution Data

High resolution data from forests often display significant texture, so that the variable T in (1) needs to be considered. A gamma distribution for T, leading to a K distribution for **S** has been shown to be particularly useful in describing texture. This requires an extra parameter, the order parameter υ of the gamma distribution, to be estimated. Simple methods based on the moment relation

$$\langle I^2 \rangle / \langle I \rangle^2 = 2\left(1+\upsilon^{-1}\right) \qquad (10)$$

can be used but better is to invert the equation

$$\langle \ln I \rangle - \ln \langle I \rangle = \varphi^{(0)}(\upsilon) - \ln \upsilon - \gamma_E \qquad (11)$$

where $\varphi^{(0)}$ is the digamma function and γ_E ~ 0.5772 is Euler's constant [2]. Relation (10) has the advantage of being meaningful even if the data are not K distributed, but (11) provides better classification performance. Both have been used to good effect in forest studies [12,13].

5. Long Wavelength Data

The previous sections have been based on the product model (1) but the validity of the model will break down if the mean number of scatterers is small or (in the polarimetric case) if different polarizations effectively scatter from different layers in the canopy [1,2]. In the former case, which may be appropriate to forest scattering at long wavelengths, such as those used by CARABAS, the speckle/texture model needs to be replaced by a treatment specific to small numbers of scatterers, for example that described in [14]. In this case, the data histogram contains information on the number of scatterers (in the forest case, tree density), and it is therefore important to examine in detail the distributional forms displayed by CARABAS and comparable systems. However, the theoretical treatment is not complete because it currently does not deal with the case of number variation between resolution cells. Hence the inversion to number density may be difficult.

6. Concluding Remarks

This paper has concentrated on the statistical bases of any attempt to derive information from SAR data. Most of the important PDFs for parameter estimation are noted or are to be found in the referenced papers. Such operations as filtering, segmentation and classification need to be based on these foundations. This is discussed at length in [2].

REFERENCES

[1] M.L.Williams, S.Quegan and D.Blacknell, "Distribution of backscatter intensity in the distorted Born approximation: application to C-band SAR Images of woodland ", Waves in Random Media, 1997 (in press)

[2] C.J. Oliver and S. Quegan, Information in SAR Images: Methods and Models for Understanding SAR Data, Artech House, 1997.

[3] N.R. Goodman, " Statistical analysis based on a certain multivariate Gaussian distribution (an Introduction)," Ann.math.Stat. **34**, pp.152-177, 1963.

[4] T. Le Toan, F. Ribbes, N. Floury and U. R. Wasrin, "Use of ERS-1 SAR data for forest monitoring in South Sumatra", Final Report for Trees Project.

[5] K. Grover, S. Quegan and C. Yanasse, " Quantitative estimation of tropical forest cover by SAR", IEEE Trans. Geosci. Remote Sensing, 1997 (submitted)

[6] E.J.M.Rignot and J.J.van Zyl, "Change detection techniques for ERS-1 SAR data", IEEE Trans. Geosci. Remote Sensing, vol.31, pp.897-905, 1993.

[7] R. Touzi, A. Lopes and P. Bousquet, "A statistical and geometrical edge detection for SAR images", IEEE Trans. Geosci. Remote Sensing, vol.26,pp.765-773,1988.

[8] R.J.A.Tough, D.Blacknell and S.Quegan, "A statistical description of polarimetric and interferometric synthetic aperture radar data,"

[9] S. Quegan, L. V. Dutra and K. D Grover, "Phase measurements in MAESTRO polarimetric data from the UK test sites", Int Jnl Remote Sensing vol.15, pp. 2719-2736, 1994.

[10] N.I.Fisher, Statistical analysis of circular data, Cambridge University Press, Cambridge, 1993.

[11] M.R.Foster and J.Guinzy, "The coefficient of coherence, its estimation and use in geophysical data processing", Geophysics, vol.32, pp.602-616,1967.

[12] C.J. Oliver, "Optimum texture estimators for SAR clutter", J. Phys. D, vol.26, pp.1824-1835, 1993.

[13] A. Beaudoin, M.Deshayes, S.Hardy, T. le Toan and D. Girou, "Use of airborne SAR data for the mapping of shifting cultivation in French Guiana", Proc. SAREX-92 Workshop, ESA WPP-76, pp. 185-191,1993.

[14] P.N. Pusey, D.W.Schaefer and D.E.Koppel, "Single-interval statistics of light scattered by identical independent scatterers", J.Phys.A: Math.Nucl.Gen.vol. 7, pp.530 -540, 1975.

On the Coupling of Backscatter Models with Tree Growth Models : Part 1 : A Realistic Description of the Canopy using the AMAP Tree Growth Model

T. Castel*, A. Beaudoin*, J.F. Barczi**, Y. Caraglio**, N. Floury***, T. Le Toan*** and L. Castagnas*

* LCT Cemagref-ENGREF, 500 rue J.F. Breton, 34093 Montpellier cedex 05, France
tél: (33) 4.67.54.87.52 / fax: (33) 4.67.54.87.00 / e-mail: castel@teledetection.fr
** CIRAD, Unité de Modélisation des Plantes, BP 5035, 34032 Montpellier, France
tél : (33).4.67.61.65.38 / e-mail: barczi@cirad.fr
*** CESBIO, 18 Ave Edouard Belin, bpi 2801, 31055 Toulouse, France
tél: (33) 5.61.55.66.71 fax: (33) 5.61.55.85.00 / e-mail: thuy.letoan@cesbio.cnes.fr

Abstract- In this paper, we present a method using the AMAP architectural tree growth model to describe the 3D canopy architecture, towards forest backscatter modelling. This method allows to 1) fully describe a tree as a collection of dielectric cylinders and 2) obtain histograms and statistics of the cylinder parameters within the canopy layers. The usefulness of this method is illutrated in southern France on Austrian pine trees, where the parameters in the crown layer show a variability with age and canopy depth that should be considered in RT modelling.

1. INTRODUCTION

Biomass retrieval is a promising application of SAR remote sensing, considering the numerous results recently reported in the literature. In particular, we conducted an experiment in southern France (Mende forest, Lozère) on Austrian pine plantations, towards the assessment of biomass retrieval over hilly terrain. The experimental set-up along with significant relationships between relief-corrected SIR-C L-band forest backscatter and forest parameters were reported in [1].

In a joint paper [2], radiative transfer (RT) modelling is considered to interpret the link between the L-band σ° and the pine forest biomass. It requires a detailed description of the canopy as a collection of dielectric cylinders embedded within a multi-layer discrete random media. Even though part of this characterization can be obtained from *in situ* measurements of usual forest parameters (tree and crown height, trunk diameter and density), the crown characterization through measurements and/or allometric equations (see for example [3]) is tedious, time-consuming and usually destructive. Therefore, other realistic description methods and associated tools are needed to get proper input parameters to RT models.

To this aim, we present a method based on an architectural tree growth model called AMAP [4]. It is illustrated on homogeneous even-aged Austrian pine (*pinus nigra nigricans*) plantations found in various topographic situations (Mende state forest). Stand ages extend from 0 to 140 years, with bole volume reaching up to 800 m^3/ha.

2. METHOD FOR CANOPY DESCRIPTION

The method is based on three characterization steps : 1) AMAP modelling of the tree architecture, 2) generic description of the tree as a collection of cylinders and 3) specific adaptation to the MIT/CESBIO RT model.

1) The AMAP model relies on both qualitative and quantitative architectural tree growth description. Detailed botanical observations allowed to develop an architectural typology used in the modelling [5]. Specific botanical measurements are then necessary to calibrate the model for a given species in its environmental conditions. They are performed on tree shoots called *growth units* (GU), which are produced by the terminal meristems and build the tree architecture. Parameters of theoretical distribution (binomial and geometric laws) for GU characteristics and branching process (growth, interruption or mortality) are obtained from fittings with the measurements.

Then, tree architectural simulation for a given age is realized through Monte-Carlo technique and Markov process, allowing to reproduce i) the meristem activity and ii) the branching process and associated geometry (angle, length, diameter) of GU's. The result is a realistic 3D tree stored in a file, such as the 40 years old Austrian pine (without needles) in Fig. 1a.

Finally, the canopy natural variability is reproduced through successive random AMAP simulations. A set of these simulations is performed for each growth stage of interest (age).

2) An interface was developed to transform these 3D trees into a collection of cylinders representing the various tree elements : trunk, branches and needles, with their geometric characteristics : (x,y,z) position, diameter, length and orientation angles. A branch is considered as a collection of successive cylinders of varying dimensions and orientation, to take into account tapered and curved branches (Fig. 1b).

0-7803-3836-7/97/$10.00 © 1997 IEEE

3) An additional step is to adapt this description to the specific MIT/CESBIO RT model, including the branching model [6]. It describes the canopy as a n-layer discrete random media, where the tree crown is characterized as a multi-scale cluster of dielectric cylinders. In our case, up to five scales represent the trunk, increasing orders of branches and needles.

The interface first splits the canopy into n horizontal layers, using a fixed vertical interval or a variability criteria. For each branch order, successive cylinders forming a given branch are transformed in a single approximated cylinder, as sketched in Fig. 1c, since curved and tapered branches are not yet taken into account. From there, cylinders at each cluster scale (branch order BR1 to BR4) are characterized by mean length, diameter, linear density and branching angle (Fig.1c), after averaging over 20 simulated trees. In addition, histograms of all these parameters are available.

3. RESULTS AND DISCUSSION

For validation purposes, AMAP-derived parameters such as tree height, diameter and length of primary branches (10 and 20 years old stands) are compared to those measured at the whorl level (mean values). This is illustrated in Fig. 2 where a satisfactory agreement is reached, although some observed dispersion still has to be explained. Also, this validation will need to be extended to all other parameters.

Fig. 3 includes vertical profiles of cylinder parameters (4-scale cluster for branches) : number, diameter and length averaged over twenty 40 years old trees (as in Fig. 1a). Number of branches is quite constant for 1st order whereas it is high for 2nd and 3rd orders. Branch length and diameter, which are highly correlated, increase rapidly in the first top meters to reach a relatively constant value within the deeper layers (except for the 2nd order). From these profiles, it is obvious that more than one layer should be considered in RT modelling.

Fig. 4 includes the histogram of branching angle within the crown layer. Considering the sensitivity of L-band backscatter to this structural parameter [6], the use of such histograms should improve the computation of averaged scattering amplitudes in RT models. This could be useful also for other cylinder parameters.

4. CONCLUSION

The results show that the AMAP model can provide a realistic and complete 3D canopy description as a collection of dielectric cylinders. The AMAP model has been calibrated up to a tree age of 50 years (close to the L-band saturation level) and will be extrapolated to older trees. Further measurements and improvements are needed for the needle modelling found on various orders of branches.

Most backscatter models can not yet fully accomodate such a detailed description, a degradation of the architectural information is necessary to feed them. Hopefully, this description should be very helpful to point out future modelling improvements related to scattering from curved branches, layered canopy, 2nd order effects, etc.

In a joint paper [2], encouraging RT modelling results obtained at L-band after the coupling with the AMAP model are presented over the Mende forest.

ACKNOWLEDGMENTS

We would like to thank various French institutes for their financial support : CNES, PNTS and ADEME. Special thanks go to the CIRAD-AMAP team and the French forestry board (ONF) for their contribution.

REFERENCES

[1] Beaudoin, A., T. Castel, M. Deshayes, N. Stussi and T. Le Toan, 1995. Forest biomass retrieval over hilly terrain from spaceborne SAR data, *Proc. on Int. Symp. on Retrieval of bio- and geophysical parameters from SAR data for land applications*, Toulouse, France, 10-13 Oct. 1995, p. 131-141.

[2] N. Floury, G. Picard, T. Le Toan, J.A. Kong, T. Castel, A. Beaudoin and J.F. Barczi, 1997. On the coupling of backscatter models with tree growth models : Part 2 : RT modelling of forest backscatter, *IGARSS'97 Proceedings*, Singapore, August 4-8, 1997.

[3] Kasischke, E.S., N.L. Christensen and E.M. Haney, 1994. Modeling of geometric properties of loblolly pine tree and stand characteristics for use in radar backscatter studies, *IEEE Trans. Geo. Remote Sensing*, Vol. 32, No. 4, 800-822.

[4] de Reffye, P., F. Houllier, F. Blaise, D. Barthelemy, J. Dauzat and D. Auclair, 1995. A model simulating above- and below-ground tree architecture with agroforestry applications, *Agroforestry systems*, Vol. 30, 175-197.

[5] Jaeger, M., and P. de Reffye, 1992. Basic concepts of computer simulation of plant growth, *J. Bioscience.*, No 17, pp. 275-291.

[6] Hsu, C.C., C.H. Han, R.T. Shin, J.A. Kong, A. Beaudoin and T. Le Toan, 1994. Radiative transfer theory for polarimetric remote sensing of pine forest at P band, *Int. Journal of Remote Sensing*, Vol. 15 no 14 , pp. 2943-2954.

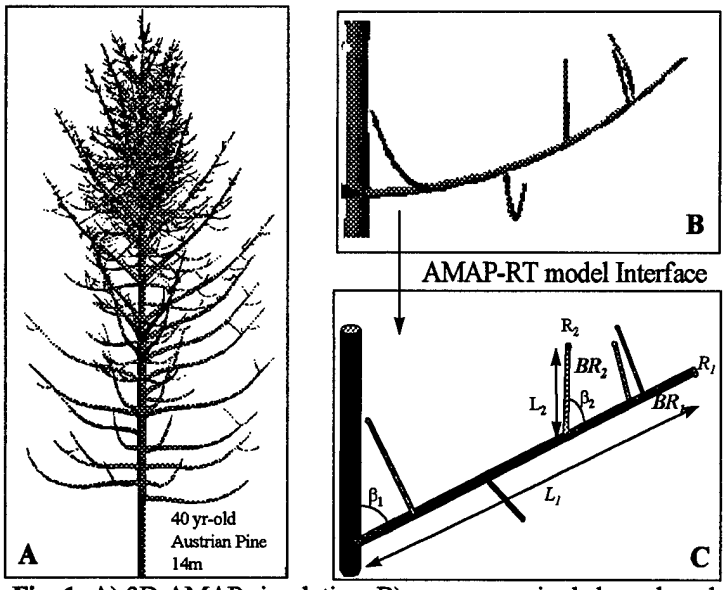

Fig. 1: A) 3D AMAP simulation, B) zoom on a single branch and C) description as a cylinder collection, with cylinder length L, diameter R and branching angle β for 2 branch orders.

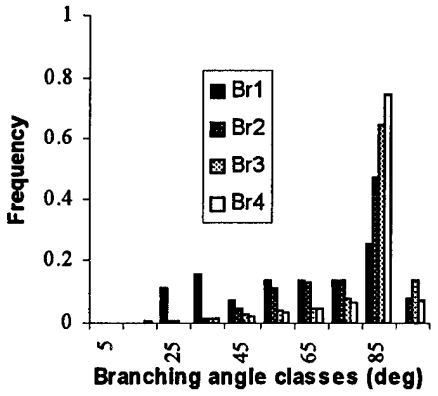

Fig 4 : Histogram of branching angle β for the 4 branch orders in the crown.

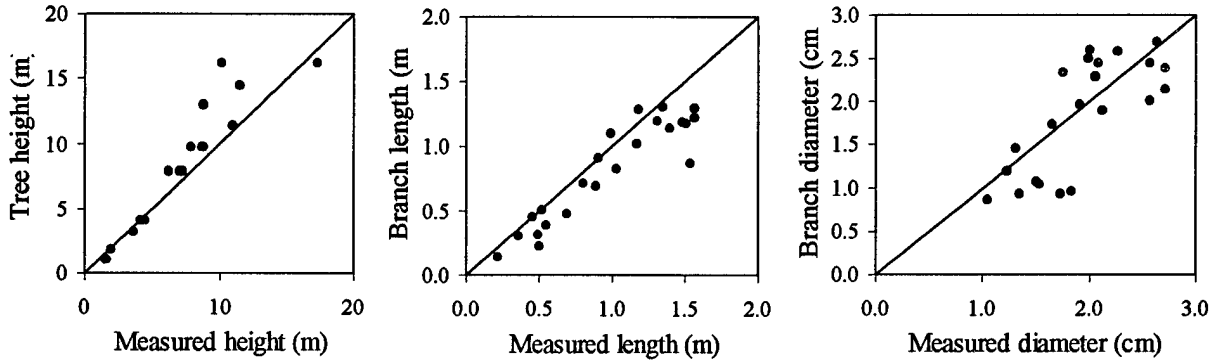

Fig. 2 : Comparison of AMAP-derived forest parameters with measurements (10 and 20 year-old trees). Diameter and length are for primary branches (comparison at the whorl level).

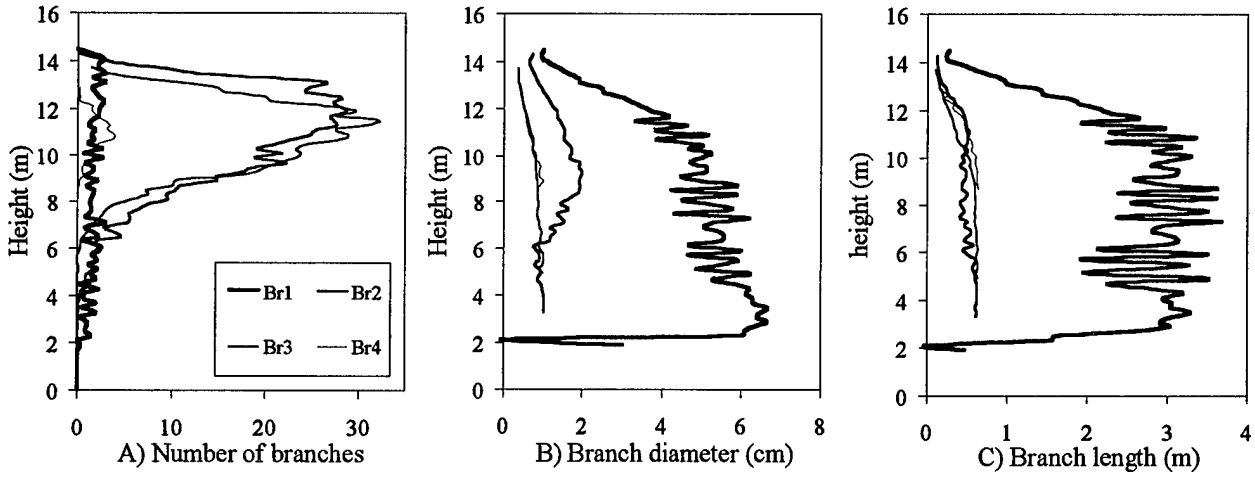

Fig. 3 : Vertical profiles within the canopy of mean cylinder parameters for RT modelling : A) number of branches, B) diameter and C) length, representing the 4 branch orders in the crown layer of a 40 years old stand of Austrian pine.

ON THE COUPLING OF BACKSCATTER MODELS WITH TREE GROWTH MODELS : 2) RT MODELLING OF FOREST BACKSCATTER

N. Floury*, G. Picard*, T. Le Toan*, J.A. Kong**, T. Castel***, A. Beaudoin***, J.F. Barczi****
* CESBIO, 18 avenue Edouard Belin, bpi 2801, 31400 Toulouse cedex 4, France
tel : (33).5.61.55.66.71 fax : (33).5.61.55.85.00 / e-mail : floury@cesbio.cnes.fr
** Massachusetts Institute of Technology, Cambridge, USA
***LCT Cemagref-ENGREF, 500 rue J.F. Breton, 34039 Montpellier cedex 05, France
tel : (33).4.67.54.87.52 / fax: (33).4.67.54.87.00 / e-mail: castel@teledetection.fr
**** CIRAD, Unité de Modélisation des Plantes, BP 5035, 34032 Montpellier, France

ABSTRACT

In this paper, the use of an architectural tree growth model as a generator of input parameters for a forest backscatter model is investigated. This is shown to be a useful method to (1) provide input data which are otherwise tedious to obtain, (2) describe the canopy with an enhanced precision which may be useful to explain physical mechanisms involved in the interaction between the electromagnetic wave and the forest.

1. INTRODUCTION

Theoretical modelling of the forest backscatter is a powerful tool towards the development of quantitative forest applications such as biomass retrieval from SAR data. RT models usually describe the forest canopy as a discrete multi-layer random media containing different classes of dielectric cylinders for the vegetation elements. One of the actual major limitations of RT modelling is the difficulty to obtain a realistic and complete canopy architectural description as a function of growth stage. In particular, tree crown parameters, through which backscatter usually correlates to above-ground biomass, are very difficult to measure or estimate. Allometric equations offer an alternative but are often not available for the species under study and crown parameters of interest. An alternative is to develop a new approach making use of the available tree growth models to derive input parameters to RT models.

In this paper, we illustrate a new approach based on the coupling of a RT model to an architectural tree growth model providing a detailed 3D canopy description. We present preliminary results applied to SIR-C L-band backscatter (HH and HV at 55° incidence angle) of Austrian pine (*Pinus nigra*) plantations over hilly terrain in southern France. The experimental set-up along with significant relationship between relief-corrected forest backscatter and forest parameters were reported [1].

In this study, the RT branching model [6] is used and coupled to the AMAP architectural tree growth model [7], through an interface allowing to extract the tree architecture as multi-scale clusters of dielectric cylinders [2].

2. CANOPY DESCRIPTION FROM AMAP

The Mende forest under investigation is composed of 500 large stands (5-15 ha) of homogeneous even-aged Austrian pine plantations found in various topographic situations. Stand age extend from 0 to 140 yr-old, with bole volume reaching up to 800 m^3/ha. 60 stands were sampled for basic forest parameters : age, dbh, tree and crown height, tree density and bole volume. In addition, the AMAP tree growth model was validated for this site through specific botanical calibration measurements, allowing to reconstruct 1) the 3D tree architecture, as in Fig. 1 for a 40 yr-old tree (needles not represented), and 2) to extract forest geometric parameters according to the following canopy description used in the MIT RT model.

For a stand at a given age, the canopy is described as a 2-layer discrete random media (crown and trunk) over a rough surface, as sketched in Fig. 1. At this stage, we consider only one crown layer but according to the vertical variability of the simulated tree architecture in Fig. 1, it is clear that probably at least 2 layers will be considered later.

In the top layer, the tree is described as a 5-scale cluster of dielectric cylinders, where the different scales account for the

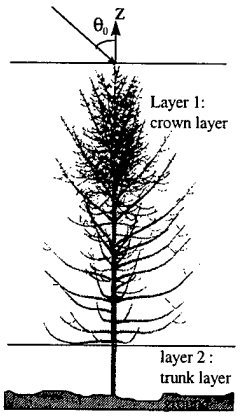

Fig. 1 : 2-layer configuration and 40 yr-old tree simulation (17m high) from AMAP

vegetation element of increasing order (1 : primary branches, 2 : secondary branches, etc.), up to the 5^{th} scale being the needle clusters. Cylinders at each scale are described by mean length, diameter, linear density and branching angle relative to the lower scale. Pdf of these parameters can also be considered. At this stage, we consider only the pdf of the branching angle of the primary branches.

Statistics of cylinder parameters were obtained in the following manner using the AMAP interface. For each age, 20

0-7803-3836-7/97/$10.00 © 1997 IEEE

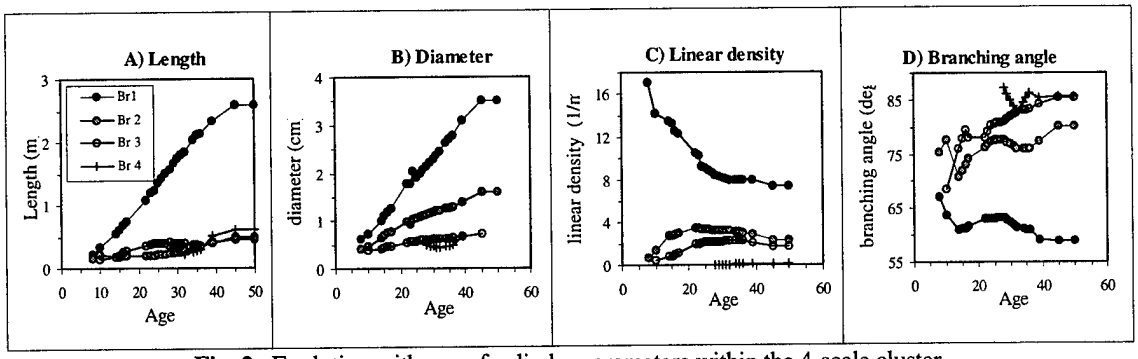

Fig. 2 : Evolution with age of cylinder parameters within the 4-scale cluster, describing the 4 branch orders (Br1 to Br4) within the tree crown (mean values)

independent 3D trees were simulated using the AMAP model to account for natural architectural variability. Then, a specific interface allows to describe a given tree as a collection of (x,y,z) positioned cylinders for each order of branch, in addition to trunk and needles. For example, the 40yr-old tree in Fig. 1 includes more than 80000 cylinders (without the needles). Then, 1st order statistics of these parameters are obtained from averaging over the 20 trees.

Fig. 2 includes the evolution with stand age of the geometric parameters of cylinders for increasing order of branches. Diameter and length are correlated and linearly increase with age, whereas linear density and branching angle have a more complex behaviour. Needle clusters are the most difficult to characterise; at this stage, a mean cluster is used with needle diameter, length, density and branching angle respectively of 1 mm, 8 cm, 16 / cm and 33°.

In addition to geometric parameters, dielectric constant of the soil, trunk, branch and needles were derived from field measurements of water content WC. These were found quite stable as a function of growth stage.

3. RT MODEL DESCRIPTION

The RT model developed at MIT [6] includes three layers: a crown layer, a trunk layer and a ground surface. The trunks, branches and needles are modelled as circular cylinders where finite cylinder approximation is used [4]. The bottom rough surface is described by its rms height and its correlation length. The Kirchhoff approximation is used to calculate the scattering from the random rough surface. The scattering properties of structured pine trees are taken into account by incorporating the branching model [5] into the phase matrix of the RT equation (1).

$$\cos\theta \frac{d\bar{I}(\theta,\phi,z)}{dz} = -\bar{\kappa}_e(\theta,\phi,z).\bar{I}(\theta,\phi,z) + \int_{4\pi} d\Omega' \bar{\bar{P}}(\theta,\phi,\theta',\phi').\bar{I}(\theta',\phi',z) \qquad (1)$$

Where the Stokes vector $\bar{I}$ contains information regarding field intensity and phase relation of the two orthogonal polarisations. The extinction matrix $\bar{\bar{k}}_e$ represents the attenuation due to both scattering and absorption, and can be obtained through the optical theorem in terms of forward scattering functions. The phase matrix $\bar{\bar{P}}(\theta,\phi,\theta',\phi')$ characterises the scattering of the Stokes vector from (θ',ϕ') direction into (θ,ϕ) direction. The phase matrix can be formulated in terms of the scattering functions of the randomly distributed discrete scatterers

4. RESULTS

In the following, modelling results are compared to backscatter measurements at L and C-band obtained from SIR-C data acquired over the Mende test-site during the SRL-2 mission in October 94, in dual-pol mode (HH and HV) at 55° incidence angle. The data set was radiometrically corrected for slope effects and ortho-rectified in the Lambert II projection [3].

The overall agreement between experiment and theory is good. Fig. 4 presents the experimental and simulated backscattering coefficients at C-HH and L-HV. These preliminary results do not include simulated values of young stands, due to the lack of appropriate soil surface characterization. The RT model can be used to identify the major scattering mechanisms. Fig. 5 presents the main contributions of the tree element classes at C-HH.

Some differences remain between experimental and simulated results. For example, L-HV simulated values decrease for stands older than 24 years whereas a slight increase is observed experimentally. One of the possible causes is the assumption of homogeneity whithin the crown layer by a RT model. As an example, fig. 6 shows the histogram of primary branches angle vs the stand age (high values are bright, low values are dark). It can be observed that at about 24 years there is a change of the dominant angle from 70° to 80°, and also appearance of lower angles of about 30°. This indicates the need to take into account the vertical variability within the canopy by using the AMAP output to increase the number of layers in the RT model.

5. CONCLUSION

This study has shown the usefulness of using a tree growth model such as AMAP to provide input parameters for a backscatter model. The tree growth model can provide missing data or measurements difficult to acquire.

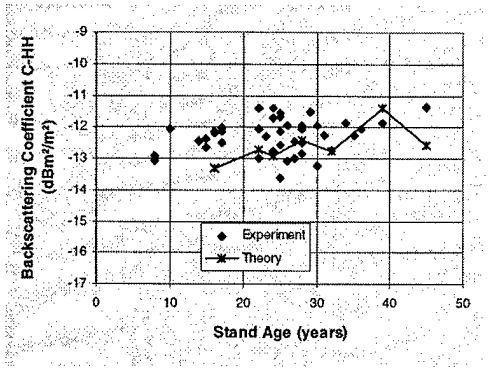

(a)

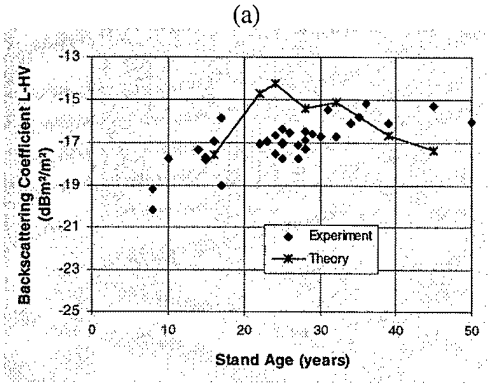

(b)

Fig. 4: Comparison theory-experiment for (a) CHH and (b) LHV

Moreover, the flexibility of AMAP to provide information on any part of the canopy may help providing inputs to more detailed description improved backscatter models, such as considerating more layers in the crown canopy or curved branches.

6. ACKNOWLEDGMENTS

This work has been conducted in the frame of the European Union DG XII EUFORA project, French National remote Sensing Program (PNTS) and French Space Agency (CNES). Warmest thanks go to all the people involved in the intensive ground truth collection. Thanks also to the AMAP team and the French forestry board (ONF). Nicolas Floury receives a grant from CNES and Alcatel Espace.

7. REFERENCES

[1] Beaudoin, A., T. Castel, M. Deshayes, N. Stussi and T. Le Toan, 1995. Forest biomass retrieval over hilly terrain from spaceborne SAR data, Proc. on Int. Symp. on Retrieval of bio- and geophysical parameters from SAR data for land applications, Toulouse, France, 10-13 october 1995, p. 131-140.

[2] Castel, T., A. Beaudoin, J.F. Barczi, Y. Caraglio, N. Floury and T. Le Toan,n 1997. On the Coupling of Backscatter Models with Tree Growth Models :1) A Realistic Description of the Canopy using the AMAP Tree Growth Model, IGARSS'97 Proceedings, Singapore, August 4-9 1997.

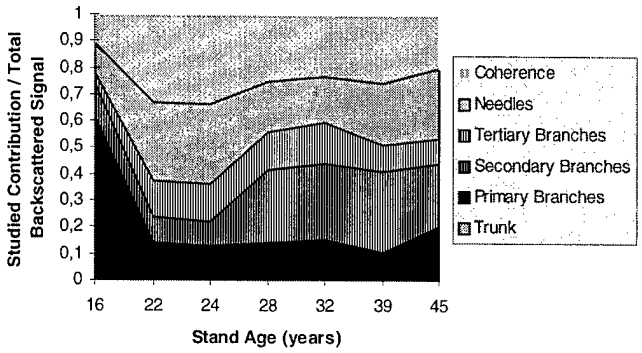

Fig. 5: Relative contributions of the scattering elements in the total backscattered signal, C-HH configuration.

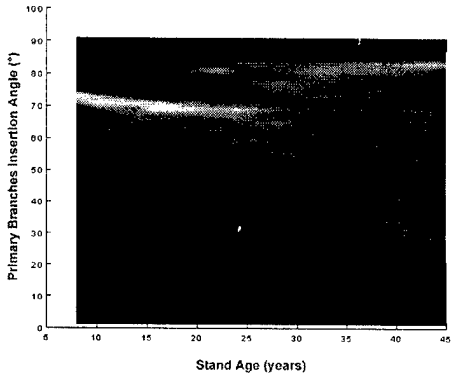

Fig. 6: Histogram of the primary branches angle vs stand age

[3] Stussi, N., A. Beaudoin, T. Castel and P. Gigord, 1995. Radiometric correction of multi-configuration spaceborne sar data over hilly terrain, Proc. on Int. Symp. on Retrieval of bio- and geophysical parameters from SAR data for land applications, Toulouse, France, 10-13 october 1995, p. 469-478.

[4] Karam, M.A., A.K.Fung, and Y. M. M.Antar, "Electromagnetic scattering from a layer of finite length, randomly orientated, dielectric, circular cylinders over a rough interface with application to vegetation", *IJRS, Vol. 9, No. 6, 1109-1134,* 1988.

[5] Yueh, S.H., J.A. Kong, J.K. Jao, R.T. Shin and T. Le Toan, « Branching model for vegetation », *IEEE Trans. on Geoscience and Remote Sensing, vol.30, no.2, pp. 390-402*, March 1992.

[6] C.C.Hsu, H.C.Han, R.T.Shin, J.A.Kong, A. Beaudoin and T. Le Toan: « Radiative transfer theory for polarimetric remote sensing of pine forest at P band », IJRS, Vol. 15, No. 14, September 1994, pp 2943-2954.

[7] de Reffye, P., Houllier, F., Blaise, F., Barthelemy, D., Dauzat, J., and Auclair, D., 1995. A model simulating above- and below-ground tree architecture with agroforestry applications, *Agroforestry systems*, Vol. 30, 175-197.

Forest applications of ERS, JERS, and SIR-C SAR interferometry

Urs Wegmüller, Tazio Strozzi, and Charles Werner
Gamma Remote Sensing AG
Thunstrasse 130, CH-3074 Muri b. Bern, Switzerland
Tel: +41(0)31-951.70.05, Fax: +41(0)31-951.70.08, email: gamma_rs@pingnet.ch

Abstract – In the past interferometric analysis of ERS-1/2 SAR data demonstrated a high potential for forest applications. In this study, the dependence of the SAR interferometric signatures on radar frequency, incidence angle, and polarization, and acquisition time interval were investigated. The results are used to discuss the feasibility of forest applications using SAR data of the Japanese Remote Sensing Satellite JERS, and the Shuttle Imaging Radar SIR-C.

Keywords: SAR interferometry, forest, ERS, JERS, SIR-C

INTRODUCTION

As a part of the methodological research project EUFORA (European Forest Observations using Radars), in the frame of the Environment and Climate Programme of the European Union, forest applications of spaceborne SAR data were investigated.

In recent years the available space borne SAR systems allowed the development and application of a new remote sensing technique, SAR interferometry (INSAR). One area where repeat-pass SAR interferometry showed very promising results were forest applications. Based on ERS-1 data acquired during 3-day repeat orbits it was found that the interferometric correlation is not just a measure of the phase noise of the interferogram but a valuable source of information on scene properties which can be used to map forest [1,2].

The ERS Tandem data were found to be very useful for forest mapping. Validation of the classification results based on the interferometric correlation, and the two backscatter intensities of an interferometric pair against a landuse inventory demonstrated the robustness and accuracy of the approach [3]. With the nearly global coverage of 35-day repeat-orbits of the two satellites the interferometric techniques can be widely applied.

In this study here it was investigated how well the techniques developed for ERS data may be transferred to other spaceborne sensors and how they need to be adjusted for the different sensor configuration. In addition the question was addressed if other information than what was found based on the ERS data might become available for the other sensor configurations.

Based on data availability the study concentrated on SIR-C and JERS data. The signature investigation was mainly based on SIR-C data because of its polarimetric and multi-spectral capacity which allowed a direct comparison of the signatures at different frequencies and polarization using identical test areas. JERS data were then investigated to determine how well the results found for SIR-C L-band may be transferred to JERS data, in spite of its much longer acquisition time interval.

SIR-C INSAR FOR FOREST APPLICATIONS

The shuttle imaging radar SIR-C was flown, together with the X-SAR, during two missions. A part of the experiment was devoted to interferometry. In spite of the short mission duration and therefore limited data acquisition the data is of strong interest as SIR-C/X-SAR was up to now the only space-borne mission including multi-spectral (L-, C-, and X-bands), as well as fully polarimetric capability. In our study we used interferometric data over Switzerland and Raco, MI, USA, focusing in particular on the investigation of the influence of the frequency and polarization on the observed signatures, in particular the interferometric coherence. Using SIR-C data allowed a direct comparison of the spectral and polarization dependence of the signatures. Combining data acquired by different satellites requires availability of data over identical test sites and refined registration capability. In addition, temporal change occurring between the acquisitions, of the ERS and JERS data may are expected to change the signatures.

Spectral dependence of interferometric signatures

The spectral dependence of the backscattering and the interferometric coherence were investigated based on SIR-C L- and C-band data over Yverdon, Switzerland. The acquisition time intervals of the investigated interferometric pairs were short (one and two days).

Here, the spectral dependence of the backscattering is not discussed in detail here, as this was covered in other publications. In summary it can be said that the backscattering at C-band originates mainly from small twigs and branches. Nevertheless, leaves and needles have an important influence, mainly through absorption. At L-band thicker branches dominate the scattering. Contributions from the ground surface and the trunk-ground multiple scattering term become more important. While the backscattering varies very little over forest at C-band a much increased sensitivity is observed at L-band allowing to retrieve stand density and

0-7803-3836-7/97/$10.00 © 1997 IEEE

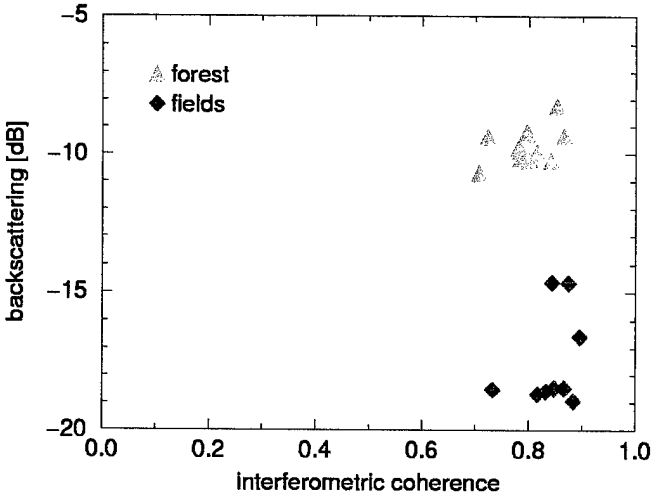

Figure 1: SIR-C L-band backscattering intensity [dB] versus interferometric coherence for forest and non-forest (agricultural fields) at Yverdon test-site.

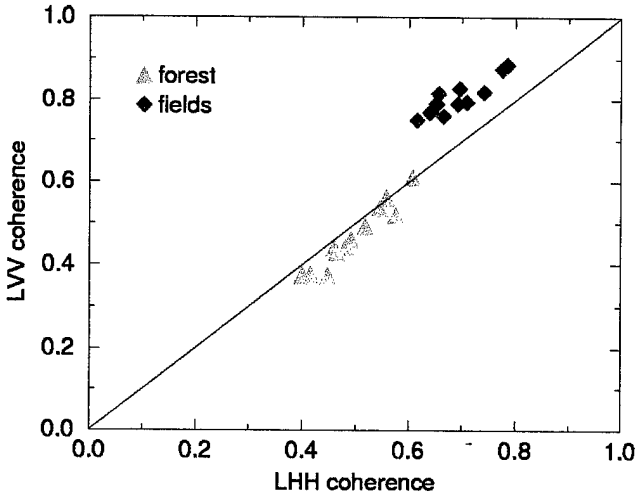

Figure 3: SIR-C L-band VV-pol. coherence versus HH-pol. coherence for forest and non-forest (fields) at Raco test-site.

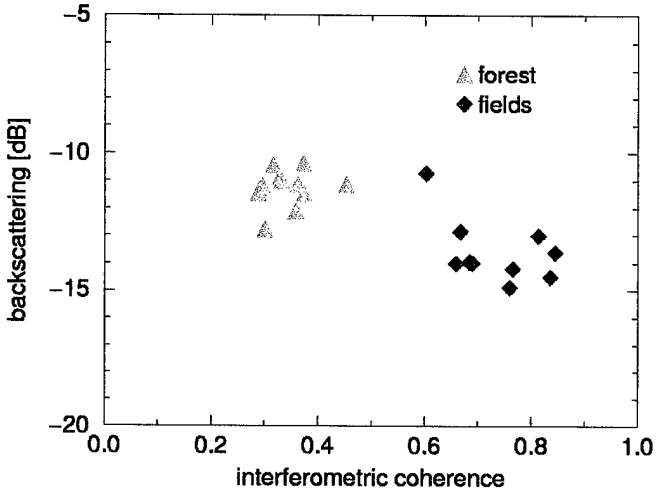

Figure 2: SIR-C C-band backscattering intensity [dB] versus interferometric coherence for forest and non-forest (agricultural fields) at Yverdon test-site.

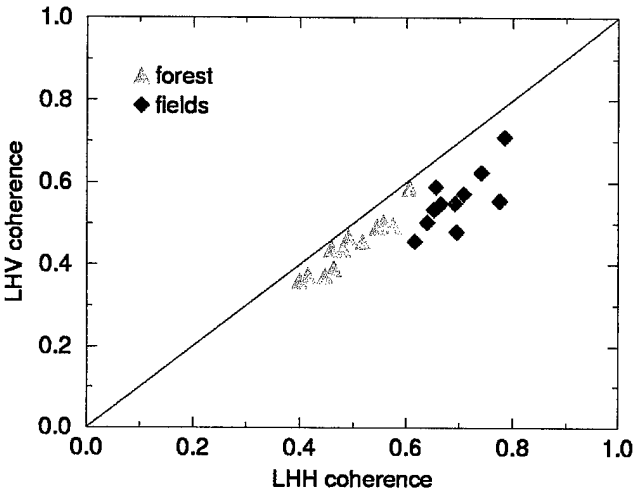

Figure 4: SIR-C L-band cross polarization (HV-pol.) coherence versus HH-pol. coherence for forest and non-forest (fields) at Raco test-site.

biomass information, as demonstrated in the past by several authors. At L-band the backscattering over forested areas is several dB higher than over low vegetation (grass land, agricultural fields), while similar backscatter levels are observed over these categories at C-band. As a consequence, L-band backscattering supports forest mapping much better than C-band backscattering.

The interferometric coherence is a measure of random displacement of the scatterers, weighted by the scatterers relative contribution to the to scattering. At C-band the dominating scatterers (small twigs and branches) are small. As a result of wind, solar illumination and plant growth the position of these small scatterers changes with a high probability. In addition, the propagation through the even less stable leaves and needles may cause temporally changing phase distortions, which also reduce the interferometric coherence. The dominant scatterers at L-band are larger and therefore more stable. In addition, ground and trunk-ground scattering contribute to a higher interferometric coherence. As a result, the observed interferometric coherence is higher at L-band than at C-band. The average interferometric coherence and backscattering extracted for forest stands and agricultural fields at the Yverdon test-site are shown in Figures 1 and 2, for L- and C-band, respectively.

Polarization dependence of interferometric signatures

The polarization dependence of the backscattering is not discussed in detail here as this was covered in other

publications. One important point is that the backscattering at cross polarization is significantly lower than the backscattering at like polarization. Several authors found that the backscattering at L-band, in particular at cross-polarization, was related to canopy biomass.

To investigate the polarization dependence of the interferometric coherence a polarimetric - interferometric SIR-C data set over Raco, Michigan, USA was used. Interferograms were generated for like and cross-polarization channels [4]. Coherence estimates extracted for forest and non-forest (fields) areas are presented in Figures 3, and 4. Similar coherence values at HH and VV like polarization, were observed, with slightly higher VV coherence over fields and slightly higher HH coherence over forest. A very interesting and somewhat unexpected finding was that the coherence at cross-polarization was only slightly below the levels observed at like polarization (Figure 4). The relatively high interferometric coherence at L-band cross-polarization found over forest (0.3 - 0.5) and fields (0.4 - 0.6) told us that even at cross-polarization a large fraction of the backscattering obviously originates from relatively stable scatters.

Consequences for forest mapping and parameter retrieval

Both, L- and C-band data could successfully be used to map forest. At L-band the distinction between forest and non-forest was mainly based on the high backscattering over forest. At C-band the result was based on the low interferometric coherence, in combination with low backscatter change and intermediate backscattering.

With respect to forest biomass retrieval those parameters which change the most between forest and non-forest seem to be the most promising to be further investigated. In addition to the well known potential of L-band backscattering, the coherence at both C- and L-band shows a promising potential with respect to forest biomass retrieval. From the current findings and earlier results based on ERS data we expect that the C-band coherence has its highest sensitivity to forest biomass at low biomass levels, especially if the acquisition time intervals are longer than 3 days. At L-band the coherence variation between forest and non-forest is much smaller than at C-band but still significant. Even with its reduced overall variation between forest and non-forest the L-band coherence may be as promising as the C-band coherence because much less saturation effects are expected at the biomass levels typically encountered in closed forest canopies.

JERS INSAR APPLICATIONS OVER FOREST

Based on experience gained with the C-band SAR on the ERS satellites the 44 days repeat orbit interval of the L-band SAR on JERS may seem to be rather long for interferometric applications over forest. Data analysis showed, nevertheless, that the longer acquisition time intervals are not such a severe problem because of the longer wavelength. The reduced coherence decrease with time is a consequence of the more stable scatterers which dominate the scattering at L-band and the fact that the distance a scatterer has to move to decorrelate is about four times larger than at C-band. The investigated JERS data examples showed that even for dense tropical forest a certain coherence level was maintained, in spite of longer acquisition time intervals. Applying advanced processing techniques [4] allowed us, for example, to generate interferometric height maps, even over tropical forest.

As discussed based on SIR-C L-band data JERS backscattering and interferometric coherence have a good potential for forest applications.

CONCLUSIONS

SIR-C and JERS interferometric signatures were investigated with respect to forest applications. With each of these sensors the combined interpretation of backscattering and interferometric coherence allowed to distinguish forest from non-forest (agricultural fields, grass-land). At C-band forest is classified mainly based on its low interferometric coherence, at L-band based on its high backscattering. For C- and L-band coherence a potential for forest parameter retrieval was identified. Similar LHH and LVV coherence levels were found over forest and non-forest . For the same landuse categories the cross polarized coherence was only slightly below the like polarized coherence. Because of the longer wavelength JERS interferometry has a potential for forest applications in spite of longer acquisition intervals as a consequence of the 44 day repeat-orbit mode.

ACKNOWLEDGMENTS

This work was supported by the Swiss Federal Office for Education and Science in the frame of the European Union Research Project EUFORA.

REFERENCES

[1] Wegmüller U., Werner C. L., 1995: SAR interferometric signatures of forest, *IEEE Geosci. Remote Sensing*, 33(5), 1153-1161.

[2] Wegmüller U., Werner C. L., 1997a: Retrieval of vegetation parameters with SAR interferometry. *IEEE Geosci. Remote Sensing*, 35(1), 18-24.

[3] Strozzi T. and U. Wegmüller, Forest mapping with ERS SAR interferometry, Proceedings 3rd ERS Scientific Symposium, Florence, Italy, 17-20 March 1997, http://florence97.ers-symposium.org/papers/

[4] Wegmüller U., Werner C. L., 1997b: Gamma SAR Processor and Interferometry Software. *3rd ERS Symposium*, Florence, 18-21 March, http://florence97.ers-symposium.org/papers/.

Use of ERS SAR Interferometry for Monitoring Clear-cutting of Forests

G. Smith and J. Askne

Remote Sensing Group
Department of Radio and Space Science,
Chalmers University of Technology,
S-412 96 GÖTEBORG, Sweden
Telephone: +46-31-772 1844,
Facsimile: +46-31-164513
email:smith@rss.chalmers.se

ABSTRACT

Clear-cut monitoring is an important application for space-borne SAR systems. With 17 ERS interferograms from the boreal forest of Sweden, obtained over a 3 year period, this paper investigates the use of coherence information for identifying clear-cuts. It is shown that coherence performs significantly better in separating clear-cuts from forest than intensity data, and can be used with a resolution about twice that possible for backscatter measurements based on a single image. The minimum area of cutting that can reasonably be detected is about 3 ha. The detection of clear-cuts tends to deteriorate with increased time between images. This is particularly significant for 13 interferograms from the rain forest of Brazil which have also been studied. These show generally lower separability than the results from Sweden.

INTRODUCTION

Regular updating of clear-cut maps is of importance for regulating forestry operations, particularly for the rapid identification of illegal cuttings in protected areas, or for the less urgent needs of tax investigation. High-resolution optical imagery is sufficient for mapping of clear-cuts, however, the frequency with which these maps can be updated is limited by the need for cloud-free images. This is a problem for boreal and tropical forests where the climate generally limits the possibility of acquiring cloud-free images, resulting in updates every 3 to 5 years [1].

To meet these requirements for continuous monitoring, the use of satellite-borne SAR systems has been suggested. To improve classification, temporal sequences of images have been used (for example [2, 3]). An alternative approach is to use SAR interferometry, which can achieve 91% accuracy when discriminating between forest and non-forested areas [4].

This work investigates the potential of SAR interferometry for clear-cut mapping, addressing the issues of discrimination between different types of clear-cuts, the time period of their visibility in the images, and the relationship between spatial resolution and probability of correct classification. The results indicate that clear-cutting of areas greater than about 3 ha can be spotted using coherence images.

TEST-SITES AND IMAGE DATA

Most of the results in this study come from an area in northern Sweden, just south of Skellefteå. The land is covered by boreal forest, with the most common tree species being pine, spruce and birch in that order. The topography of the region is reasonably flat, with altitudes up to 150m.

Single look complex (SLC) images from the ERS-1 and ERS-2 SAR systems were studied. To observe changes occurring over a number of years, 11 images from the 3-day repeat cycles of ERS-1 in the winters of 1992 and 1994 were used, as well as 2 pairs from the tandem mission in the summer of 1995. From these images, 17 interferograms were produced (the remaining combinations being impossible to use due to problems with long baselines, or simply too much temporal decorrelation).

A total of 8 clear-cuts of various ages were chosen for the study. They were selected as being on relatively flat land, with similar soil characteristics, and similar densities of plants growing on them (around 2000 trees per hectare). The areas were split into three classes, the properties of which are shown in table 1.

Table 1 Clear-cut classes

Class	Years of cutting	Average tree height/ m		
		1992	1994	1996
1	1993	N/A	0	0.1
2	1982-1983	1.2	1.8	2.5
3	1978-1981	2.2	3.0	3.9

0-7803-3836-7/97/$10.00 © 1997 IEEE

Along with the Swedish test-site, 6 SLCs from March 1994 taken over the rain forest to the north-east of Manaus in Brazil, were used. A total of 13 interferograms were processed using these images. No ground truth was available, however, the coherence images consistently showed an area with higher coherence than the surrounding forest. Combined with a low-resolution image from JERS-1, it was believed that the area is one of less dense tree cover than the surrounding forest.

IMAGE PROCESSING

The interferograms were produced using the ISAR toolbox provided by ESA. Coherence was estimated over a window of 5 by 25 pixels in the original SLC images (corresponding to about 100 m in both range and azimuth respectively). This was estimated to give a minimum measurable coherence (bias level) of about 0.27.

RESULTS

The coherence measurements for the three classes of clear-cut, along with representative values for fields and forests, are shown in Fig. 1. The study areas were identified visually by comparing aerial photographs of the studied areas with a filtered, false-colour image produced using both intensity and coherence information. It can be seen that clear-cut classes 2 and 3 are in most cases virtually indistinguishable from fields. For the 1992 results, class 1 (at that time uncut forest) has similar coherence values to other forested areas. But after the trees were felled in 1993, class 1 became indistinguishable from the other clear-cut areas.

To illustrate the use of the coherence measurements for identifying the cutting, the Jeffreys-Matusita distance has been used [5]. This is defined as:

$$J_{ij} = \iint \left(\sqrt{p_i(x,y)} - \sqrt{p_j(x,y)} \right)^2 dxdy \qquad (1)$$

where p_i is the probability distribution of class i (shown in this case as a function of two variables, for example intensity and coherence). This distance measure can be related to the limits for the probability of correct classification for a maximum-likelihood classifier operating on Normally distributed data [6].

The probability density functions were estimated numerically, which led to errors in the estimation of J of about 0.2 for low values, improving to about 0.1 at higher values. This was due to the discretisation of a limited number of samples. A J-value greater than 1 represents good separability, whilst below about 0.5 is virtually useless for classification.

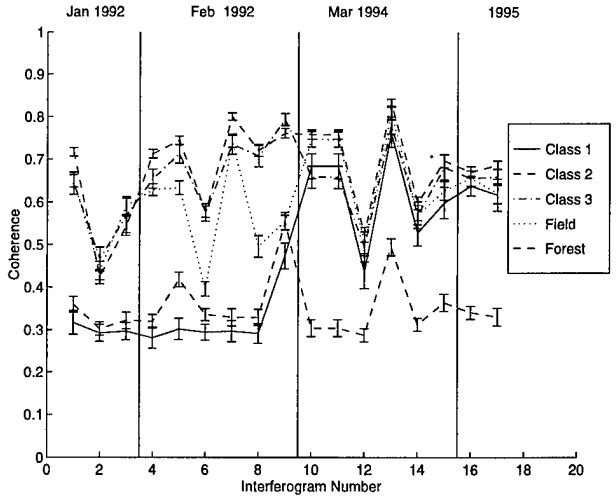

Fig. 1. Coherence measurements for different classes. Errorbars indicate one standard error of the estimate for the class above and below the mean.

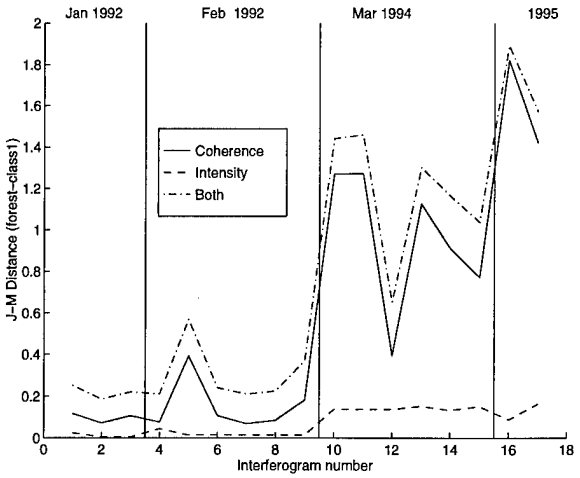

Fig. 2. The J-M distance between forest and class 1, calculated using coherence (solid line), intensity (dashed line) and using the joint distribution of coherence and intensity (dot-dashed line).

DISCUSSION

The calculated separabilities between forest and class 1 are shown in Fig. 2. Before 1993, class 1 is indistinguishable from other forested areas. After the cutting in 1993 it remains difficult to use the intensity to separate class 1 from forest, but in most cases it would be possible using the coherence. Using both intensity and coherence information gives only a slight improvement in separability. The variability in separability is a result of weather-related temporal changes

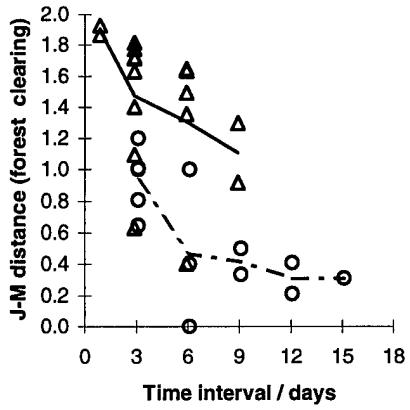

Fig. 3. Showing how the separability of clear-cuts and forest vary with time interval between the images. Triangles show measurements from Sweden, circles from Brazil. The lines join the mean values for each test-site at each time interval.

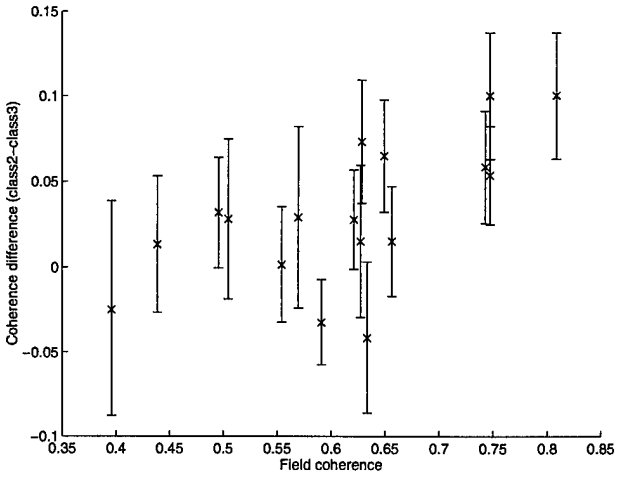

Fig. 4. The difference between classes 2 and 3 as a function of field coherence. Errorbars show one standard error of the estimate above and below.

The separabilities between forest and clear-cuts for the Swedish and Brazilian test-sites are shown in Fig. 3 (using class 2 for the Swedish test-site, and the suspected clear-cut in Brazil). It can be seen that the distance between the classes is generally higher in the boreal area. For the tropical region the separability decreases rapidly with larger time intervals between the images, due to temporal decorrelation [7].

To investigate the possibility of using coherence measurements to monitor the growth of vegetation, the difference between the coherence values of classes 2 and 3 were compared. This method has the advantage of comparing coherence measurements within a single interferogram, as comparisons between interferograms are very sensitive to unknown temporal decorrelations [8]. Fig. 4 shows the difference between the coherence values, as a function of the open field coherence. Although the measurement errors are relatively large, there is an apparent trend towards increased difference in coherence with larger field coherence. This is qualitatively in agreement with a model of the coherence for boreal forests [9], and is explained by the increased influence of the ground coherence (assumed proportional to that of open fields) in class 2, where the trees are smaller.

RESOLUTION OF CLEAR-CUTS

Coherence appears better than intensity measurements for separating clear-cuts from forest, but, the classification accuracy based on backscatter could be improved by averaging the data. For the coherence measurements some averaging was necessary simply to be able to calculate coherence values. To compare resolutions, imagine the following scenario for a managed forest. The manager knows the boundaries of a particular stand, and is interested in knowing if it has been cut since last checked. The ability to distinguish between the two possibilities depends on the measured parameter (coherence or intensity), the variation of the measured parameter, and the number of independent samples.

For coherence measurements, a clear-cut with a coherence of about 0.7 would require averaging over about 3.5 ha to be distinguishable at the 95% level (considering the forest to have a Normally distributed coherence with mean value of 0.3). In the case of intensity measurements, where the mean intensity for a clear-cut is assumed to be about 2 dB greater than that of the background forest, it would require averaging over about twice this area (~6.5 ha) to reach the same significance (assuming that the intensity is also Normally distributed at this level of averaging). This is the kind of resolution that would be achievable if the clear-cut coherence was decreased to about 0.5.

CONCLUSIONS

We have shown that clear-cutting events are much easier to detect using coherence measurements than intensity measurements, and that using both together produces only slightly better results than using coherence alone. It is difficult to detect any difference between classes 2 and 3 (class 3 having trees about twice the size of class 2), although this separation did increase with increased coherence of the ground. This is in-line with model results and will be investigated further. A difference could be used to supplement intensity measurements when monitoring re-growth of cut areas. The technique used in this study, i.e. observing different areas within each interferogram, as opposed to studying the same area in different interferograms, has the advantage of removing some of the effects of temporal decorrelation (assuming the areas are affected in the same way by temporal decorrelation). The significance of results obtained in this manner will be investigated further as a means of comparing measurements with the model.

The results presented in this paper are largely based on studies of boreal forest, but results from the rain forest of Brazil indicate that coherence may still be useful for clear-cut identification. The separabilites are shown to be quite unstable, and it appears that short time periods between the repeat-passes are necessary. This is true for both study areas, but the time periods required are shorter for tropical regions due to the greater temporal decorrelation.

ACKNOWLEDGMENTS

The authors would like to express their thanks to Johan Fransson for the collection of the ground-truth used for the Swedish test-site, and to Adrian Luckman for providing a low-resolution JERS-1 image of the Brazilian test-site. This work has been carried out as part of the European Union EUFORA project. and with support from the Swedish National Space Board.

REFERENCES

[1] P. R. Coppin and M. E. Bauer, "Digital change detection in forest ecosystems with remote sensing imagery," Remote Sensing Reviews, vol. 13, pp. 207-234, 1996.

[2] S. Quegan and K. D. Grover, "Change detection and backscatter modeling applied to forest monitoring by SAR," Proceedings of SPIE - The International Society for Optical Engineering, vol. 2584, pp. 241-251, 1995.

[3] T. LeToan, F. Ribbes, T. Hahn, N. Floury, and U. R. Wasrin, "Use of ERS-1 SAR data for forest monitoring in South Sumatra," International Geoscience and Remote Sensing Symposium (IGARSS), vol. 2, pp. 842-844, 1996.

[4] U. Wegmuller and C. Werner, "Retrieval of vegetation parameters with SAR interferometry," IEEE Transactions on Geoscience and Remote Sensing, vol. 35, pp. 18-24, 1997.

[5] P. H. Swain, "Fundamentals of Pattern Recognition in Remote Sensing," in Remote Sensing: The Quantitative Approach, P. H. Swain and S. M. Davis, Eds. New York: McGraw-Hill, 1978, pp. 170-174.

[6] S. M. Yatabe and D. C. Leckie, "Clearcut and forest-type discrimination in satellite SAR imagery," Canadian Journal of Remote Sensing, vol. 21, pp. 455-467, 1995.

[7] J. A. Askne, D. P, and S. G, "Interferometric SAR observations of forested areas," 3rd ERS Symposium, Florence, 1997.

[8] G. Smith, P. B. G. Dammert, and J. Askne, "Decorrelation Mechanisms in C-Band SAR Interferometry over Boreal Forest," European Symposium on Remote Sensing III, Taormina, Italy, pp. 300-310, 1996.

[9] J. I. H. Askne, P. B. G. Dammert, L. M. H. Ulander, and G. Smith, "C-band repeat-pass interferometric SAR observations of the forest," IEEE Transactions on Geoscience and Remote Sensing, vol. 35, pp. 25-35, 1997.

Analysis of CARABAS VHF SAR data from BALTASAR-96

L.M.H. Ulander, P.O. Frölind, A. Gustavsson, H. Hellsten, T. Jonsson, B. Larsson, and G. Stenström
Defence Research Establishment (FOA)
P.O. Box 1165, S-581 11 Linköping, Sweden
Phone: (+46)-13-318044, Fax: (+46)-13-318100, email: ulander@lin.foa.se

Abstract -- CARABAS-II is a new airborne ultra-wideband and widebeam SAR which operates in the lower VHF band (20-90 MHz). Its design has been based on the experiences and insights gained from the earlier CARABAS system. The initial radar test flights were conducted during October-November 1996 which included a flight campaign as part of BALTASAR-96. The subsequent data analysis has resulted in a number of processed images with good image quality over a forested area in southern Sweden. The resolution of the imagery has been measured to 3 x 3 m^2. The present limitation before full performance can be achieved is due to uncompensated antenna characteristics.

INTRODUCTION

The CARABAS-II system is an airborne ultra-wideband and widebeam (UWB) SAR operating in the lower VHF band, i.e. 20-90 MHz. This new system is based on the design of its predecessor, CARABAS-I, but with a number of major changes to improve system performance.

The first generation system CARABAS-I was completed in 1992 and used during 1992-94 in a number of flight campaigns to investigate different applications, including deserts, forests and sea ice [1-4]. The experiences gained from these experiments motivated a major system upgrade. The first test flights with the new CARABAS-II system was performed in October-November 1996. This paper reports on results from the first flight campaign (second flight test) during BALTASAR-96 (Baltic Airborne SAR experiment).

CARABAS-II SAR SYSTEM

A number of special considerations have influenced the design of the CARABAS systems [5-6], e.g. the imaging principles of UWB SAR systems, and the presence of strong radio-frequency interference (RFI). Conventional principles for radar system analysis have been revisited and adapted to the system design of a UWB-VHF SAR. The CARABAS-II system parameters are summarised in Table 1.

Perhaps the most important improvement is the new wideband antenna system. In order to retain low ohmic losses, the length of the antenna needs to be close to half the wavelength. In the CARABAS-I antenna design, antenna elements were contained in two canvas sleeves trailing behind the aircraft. This proved to be a less successful design causing both aerodynamical and electrical problems. The new rigid design for CARABAS-II is shown in Fig. 1, with the two Kevlar push booms mounted in front of the nose of the aircraft. The antennas are designed to provide essentially horizontal polarisation and omni-directional illumination across the 20-90 MHz band. Each boom is 8 m long with the active 5 m length extending in front of the nose and with a boom separation of 1.85 m. Both antennas are fed during transmission and a delay line is used to tilt the antenna beam to the left or right-hand side of the flight track. On receive, the signal from each antenna are simultaneously recorded in two parallel receiver channels.

Another important system improvement is the digital waveform generation which facilitates a flexible waveform design. The transmit waveform uses a large time-bandwidth product signal which increases average transmitted power but also enables narrow-band frequency notches and thus avoiding tele-conflict problems.

Similar to the CARABAS-I design, the instantaneous bandwidth of the receiver is small compared to the 70 MHz bandwidth in order to obtain a large dynamic range. The latter is important since strong intentional transmitters (TV, FM etc.) are present in the 20-90 MHz band which must not saturate the receivers. The transmit waveform consists of a number of pulses with varying centre frequencies in order to cover the full bandwidth. Each receiver has an instantaneous bandwidth of 2 MHz, the AD-converter provides 14 bits with 5 MHz sampling rate, and the 1 kHz dynamic range is 88 dB. With the two parallel receivers, the maximum data rate is 160 Mbit/s.

The large dynamic range is traded for a reduced swath width since the minimum PRF is set by the Doppler bandwidth of the ground echo. This becomes of critical concern when operating the system at 5-10 km altitude, and a novel frequency hopping technique is used which provides a PRF matched to the linearly increasing Doppler bandwidth as the centre frequency increases. This technique enables incidence angles out to about 60° to be covered at 10 km altitude. Furthermore, it has the advantage of providing a uniform signal-to-noise ratio in the image spectral domain which minimises processor matching loss. In fact, it provides essentially the equivalent to a "ramp filter" which otherwise is applied during processing to level the final image spectrum.

0-7803-3836-7/97/$10.00 © 1997 IEEE

During the first flight tests in October-November 1996 the system operated in a coherent-on-receive mode. The transmitted signal was therefore inserted into the receivers and this reference was used to extract the phase information for pulse compression. In early 1997, the system was upgraded to be fully coherent, i.e. with a stable phase through the entire system.

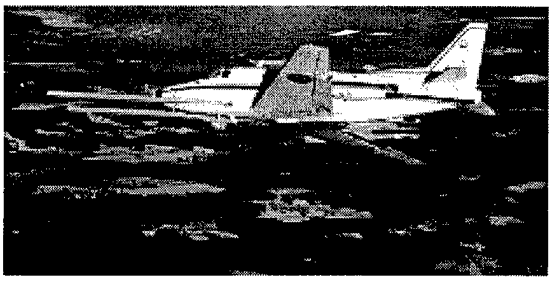

Figure 1. The Sabreliner aircraft with the antenna system for CARABAS-II (Courtesy: FMV:Prov).

Table 1. CARABAS II SAR parameters.

Aircraft	Rockwell Sabreliner
Nom. Altitude	1500-10000 m
Nom. Ground speed	100-130 m/s
Antenna	2 wideband dipoles
Frequency Band	20-90 MHz
Polarisation	Horizontal
Pulse coding	linear/non-linear FM
TX Peak Power	500 W
TX Notch Depth	30 dB
RX Bandwidth	2 x 2 MHz
RX Dynamic Range	88 dB
PRF	1-10 kHz
Number of frequency steps	1-256
ADC Sampling Rate	2 x 5 MHz
ADC Quantisation	2 x 14 bit
Data rate	< 160 Mbit/s
Tape Recorder Capacity	240 Mbit/s
Cassette Capacity	> 28 min

BALTASAR-96

The BALTASAR-96 campaign involved two airborne SAR systems, the CARABAS SAR and the DLR E-SAR (X- and P-band modes only). Both systems acquired radar data during 13-14 November close to the city of Karlskrona in southern Sweden. The main objectives of the experiment is to study counter-measures and military target signatures, particularly concealed in dense foliage, but also to support development of forestry applications. The experiment included one day over a coastal area and one day over an inland area. A total of 40 flight passes with E-SAR and 13 with CARABAS was completed.

The CARABAS data collection resulted in 11 successful passes despite it being only the second radar test flight. All passes were conducted at a nominal flight altitude of 2150 m, except one pass at 5 km altitude.

Unfortunately, the E-SAR raw radar data was corrupted due to a grounding problem in the tape recorder, so that only real-time processed imagery is available. The E-SAR flights will be repeated during May 1997.

SYSTEM CALIBRATION

The first processed images revealed artifacts caused by the pulse compression algorithm. Strong scatterers produced excessive paired-echo sidelobes in range due to periodic amplitude and phase ripple in the reconstructed wideband spectrum. These appear with a spacing of 80 m corresponding to the fundamental frequency step of 1.875 MHz which was used. The linear distortion in each sub-band are essentially duplicated at each new centre frequency which results in a periodic modulation across the spectrum. The distortion in each sub-band must therefore be accurately characterised and compensated in order to achieve full performance after pulse compression.

The acquired data also indicated fluctuations in the pulse reference due to cross-talk in the high-power switch. The reference pulse is therefore not a suitable correlation reference for pulse compression although it has successfully been used to retrieve the unknown phase in the coherent-on-receive data.

After the initial flight tests, the system was taken out of the aircraft and calibration measurements were performed in the lab to characterise each sub-band with a transfer function. The subsequent pulse compression used this set of measurements achieving almost full performance. A modified waveform with more uniform spectral characteristics will be used in the upcoming flight tests to further improve performance.

The calibration requirement to achieve low paired-echo sidelobes is quite demanding. At present, the sidelobe ratio has been measured to -30 dB corresponding to 0.5 dB of amplitude or 3° of phase ripple. This should normally be sufficient except for extremely strong nadir echoes which may require up to 50-60 dB of suppression. An example of residual paired-echo sidelobes emanating from strong nadir echoes is shown on the left-hand side of the image in Fig. 2.

PROCESSING RESULTS

After RFI filtering, pulse compression, wideband reconstruction, the final image is formed by azimuth focusing including motion compensation based on DGPS data. Figs. 2

and 3 show images from two passes which have been processed using a range migration algorithm. The two images essentially cover the same area but with different incidence angles. Linear bright features are typically power lines, fences, or ditches. Extended dark areas are open fields and bright areas are forest-covered. The forests in this region consists mainly of spruce (40%) and beech (40%) and with typical stem volumes ranging between 250 and 400 m^3/ha [7]. Note the essentially uniform character of the forest in Fig. 2, in contrast to Fig. 3 which shows a range of signatures over different forest areas. This implies that larger incidence angles are preferred for forestry application.

Fig. 4 show a small image chip centred on a 5-m trihedral. It has been processed using a global bakprojection technique in order to assess the resolution which can be achieved. The measured resolution is about twice the theoretical value, which is believed to be caused by uncompensated antenna characteristics. A summary of image quality parameters based on analysing trihedrals is given in Table 2.

Table 2. Image quality parameters

Resolution	9 m^2
Paired-echo PSLR	-30 dB
Noise-equivalent σ°	-30 dB
Noise-equivalent σ	-20 dBm^2

REFERENCES

[1] A. Gustavsson et al., "The Airborne VHF SAR System CARABAS," Proc. IGARSS'93, Tokyo, 18-21 August 1993, pp. 558-562, 1993

[2] H. Hellsten et al., "Ultra-Wideband VHF SAR - Design and Measurements," Proc. Aerial Surveillance Sensing, Orlando, 4-6 April , SPIE vol. 2217, pp. 16-25, 1994

[3] B. Larsson et al., "CARABAS - an Airborne VHF SAR System," Proc. 2nd International Airborne Remote Sensing Conference and Exhibition, San Fransisco, CA, 24-27 June 1996, vol. 2, pp. 365-373, 1996

[4] H. Israelsson et al., "Retrieval of Forest Stem Volume using VHF SAR," IEEE Trans. Geosci. Remote Sensing, vol. 35, pp. 36-40, 1997

[5] H. Hellsten et al., "Development of VHF CARABAS II SAR," Proc. Radar Sensor Technology, Orlando, FL, 8-9 April 1996, SPIE vol. 2747, pp. 48-60, 1996

[6] L.M.H. Ulander and H. Hellsten, "A New Formula for SAR Spatial Resolution," AEÜ Int. J. Electron. Commun., vol. 50, pp. 117-121, 1996

[7] F. Walter, G. Smith, P. Dammert, L.M.H. Ulander, "BALTASAR-96, Skogsdatarapport," in swedish,1997

Figure 2. CARABAS image (3.8 x 1.2 km^2) from 14 Nov 1996 and pass 2, illustrating residual paired-echoes from strong nadir returns on the left-hand side. Processed band is 40-60 MHz and resolution is 6 x 7 m^2. Incidence angle varies between 26° (top) and 47° (bottom).

Figure 3. CARABAS image (2.8 x 2.0 km^2) from 14 Nov 1996 and pass 5, illustrating the main experiment area. Processed band is 40-60 MHz and resolution is 5 x 7 m^2. Incidence angle varies between 44° (top) and 62° (bottom). A quarter-circular signature array with a 5-m trihedral at its centre is visible in the image centre.

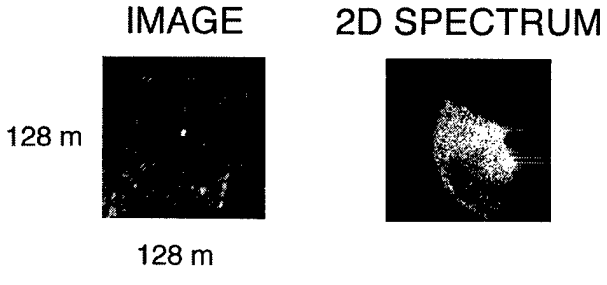

Figure 4. Image chip centred on a 5-m trihedral deployed on an open field. Processed band is 20-82.5 MHz and aperture angle is 96°, corresponding to a theoretical area resolution of 4.2 m^2 [6]. The measured resolution is 8.9 m^2. The image spectrum is uniformly illuminated except for a low gain area corresponding to the rear direction and 60-75 MHz. The cause of the latter is presently unknown.

Modelling of VHF Radar Backscattering from Forests Based on Radiative Transfer

Hans Israelsson and Jan Askne
Chalmers University of Technology
Department of Radio and Space Science, S-412 96 Göteborg, Sweden
telephone: +46-31-7721000
fax: +46-31-164513
E-mail: hans.israelsson@emw.ericsson.se

Lars Ulander
Swedish Defence Research Establishment
Department of Sensor Technology, PO Box 1165, S-581 11 Linköping , Sweden
telephone: +46-13-318000
fax: +46-13-318100
E-mail: ulander@lin.foa.se

Abstract -- The CARABAS system is a wide band SAR, that operates at VHF frequencies (20-90 MHz). The image information includes a higher dynamic range in the radar backscattering from forested areas of varying stem volume, than what has been found using conventional microwave SAR. A modified MIMICS model has been used to model the radar backscattering at VHF. The various terms in the solution have been added coherently, taking the variation with height above ground and the phase shift of the ground reflection into account. The results show an improved agreement with measured data.

INTRODUCTION

The CARABAS VHF (20-90 MHz) SAR-system was developed by the Swedish Defence Research Establishment. It is a wide band airborne SAR system that operates at HH-polarisation. The radar frequency band corresponds to wavelengths of 3.3 m to 15 m, which approximately matches the geometrical sizes of the major forest canopy components. The first radar test flights were performed in 1992. Currently the CARABAS II system, that is an upgraded version, is tested. One of the major improvements of CARABAS II is a new antenna system. Flight campaigns over forested terrain are carried out during 1997.

Test Site

The data that are used in this report were however collected in a campaign using the original CARABAS system. The test area was located on the island of Öland in southern Sweden. The area includes a mixed deciduous forest, that contains various forest stands of stem volumes in the range of 20-210 m^3/ha.

The results from the images acquired over forested areas demonstrated an improved dynamic range of the radar backscattering coefficient representing various biomass classes [1], compared to conventional microwave SAR systems. This phenomenon at VHF can be explained by an increased penetration of the radar energy into the forest canopy. At microwave frequencies, on the other hand, the backscattered signal is generated by scattering from the most upper part of the forest canopy. The scattering from the top layer becomes more predominant at forest stands with high biomass, and the backscattering coefficient gets saturated. Thus there is an apparent potential in using VHF SAR to monitor and assess forest biomass.

METHOD

In this paper, our approach is to model the radar backscattering from the forest canopy at VHF. In a number of publications, the radiative transfer method has been used to model the radar signal in the microwave frequency band (1-10 GHz). The results often agree reasonably well with measured data. The approximations and assumptions, that are made in the radar transfer model are apparently not crucial at microwave frequencies.

The most common way to solve the radiative transfer formula is to use the first order iterative solution. The solution is then obtained as various terms, describing the scattered intensity. The terms correspond to first order interactions among horizontal canopy layers.

In this paper, we have used the MIMICS model [2]. MIMICS divides the forest canopy into two different horizontal layers. The upper layer (the crown layer) includes the branches of various sizes and the leaves. The lower layer (the trunk layer) contains the trunks. Below the two layers, the ground is represented by a rough semi infinite homogenous dielectric material. The solution thus mainly consists of four terms that account for the first order interaction between the ground and the crown layer, and two terms that describe the interaction between the ground and the trunk layer.

In MIMICS the ground interaction is simplified, by adding the specular ground reflection and the canopy scattering incoherently. Hence the terms are added by means of intensity, and the consequence of the dihedral enhancement of the scattering is ignored.

0-7803-3836-7/97/$10.00 © 1997 IEEE

- crown direct backscattering
- ground-crown backscattering
- crown-ground backscattering
- ground-crown -ground backscattering
- ground-trunk backscattering
- trunk-ground backscattering

Modification of MIMICS

To include the effect of multi path scattering, we add the four terms of the solution, that are generated from crown scattering, coherently taking the phase shift of the ground reflection and the varying path lengths of the wave propagation into account. Besides, the two terms generated by trunk scattering are added coherently. The two resulting terms are then added by means of intensity.

The total backscattering coefficient then theoretically depends on the branch height above the ground, *h*. The total backscattering varies periodically versus branch height and the height average of the backscattered power increases compared to the original incoherent addition of the terms.

$$\sigma = \left\{\sqrt{\sigma_{cr.}} + \left(\sqrt{\sigma_{cr.gr.}} + \sqrt{\sigma_{gr.cr.}}\right)e^{-j(2kh\cos\theta+\angle R)} + \sqrt{\sigma_{gr.cr.gr.}}\,e^{-j(4kh\cos\theta+2\angle R)}\right\}^2 + \left(\sqrt{\sigma_{tr.gr.}} + \sqrt{\sigma_{gr.tr.}}\right)^2 \quad (1)$$

The dielectric constants of wood material and soil at VHF, at the moisture contents of interest, were found in the literature [3, 4].

The analytical scattering model of the individual cylinders, describing the branches and the trunks, is a high frequency approximation, that is close to the limit of validity at the radar frequencies of interest. At VHF, the cylinder lengths are of the same order of magnitude as the radar wavelength. Besides, electromagnetic coupling among the canopy components is neglected in the radiative transfer approach. These problems are addressed in another session of this conference [5], where the approximate model is compared to numerical FDTD calculations.

RESULTS

In Figure 1, the various resulting terms of the first order radiative transfer solution are shown, as MIMICS is applied in a straightforward manner, without the modifications described above. The scattering from the crown is predominant. Since the scattering from a horizontal cylinder becomes almost isotropic in the plane of incidence at HH- polarisation, the crown-ground backscattering terms exhibit reductions of intensitiy, that correspond to the Fresnel reflection coefficient.

If the phase shifts of the ground reflection and the phase shifts of the various lengths of propagation are taken into account, the resulting total radar backscattering coefficient shows a behaviour, that is strongly dependent on branch height. In Figure 2, this is illustrated at 50 MHz, together with the average number and the original MIMICS result.

In Figure 3, the results from the modified MIMICS approach are shown versus radar frequency, together with results from CARABAS measurements. The coherent results are obtained from averaging over various branch heights. The accuracy of the radiometric calibration in the images is within ±1 dB in the middle of the CARABAS band and somewhat worse at the outer parts. The calibration was performed using the responses from horizontal dipoles. The angle of incidence is 60°.

Conclusion

The results that have been processed in the study show that the main CARABAS results can be well explained by minor extensions of the MIMICS model. The major part of the backscattered energy is generated by crown scattering. To account for the multi path scattering, the varying path lengths and the phase shifts of the ground reflections have to be considered.

REFERENCES

[1] H. Israelsson, L. M. H. Ulander, J. Askne, J. Fransson, P.-O. Frölind, A. Gustavsson, and H. Hellsten, "Retrieval of Forest Stem Volume Using VHF SAR," *IEEE Transactions on Geoscience and Remote Sensing*, vol. 35, pp. 36-40, 1997.

[2] F. T. Ulaby, K. Sarabandi, K. McDonald, M. Whitt, and M. C. Dobson, "Michigan microwave canopy scattering model," *International Journal of Remote Sensing*, vol. 11, pp. 1223-1253, 1990.

[3] G. I. Torgovnikov, *Dielectric Properties of Wood and Wood-Based Materials*. London: Springer-Verlag, 1993.

[4] Å. Blomquist, "Betydelsen av topografi och elektriska egenskaper hos jordytan," Försvarets Forskningsanstalt 1974.

[5] L. M. H. Ulander, T. Martin, and H. Israelsson, "Numerical Studies of Forest Backscatter in the VHF-band," presented at IGARSS'97, 1997.

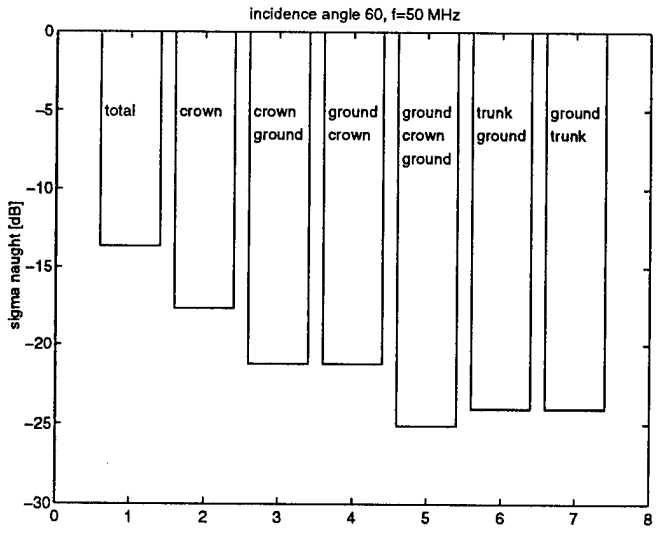

Fig.1 The various solutions from predictions using MIMICS without modifications.

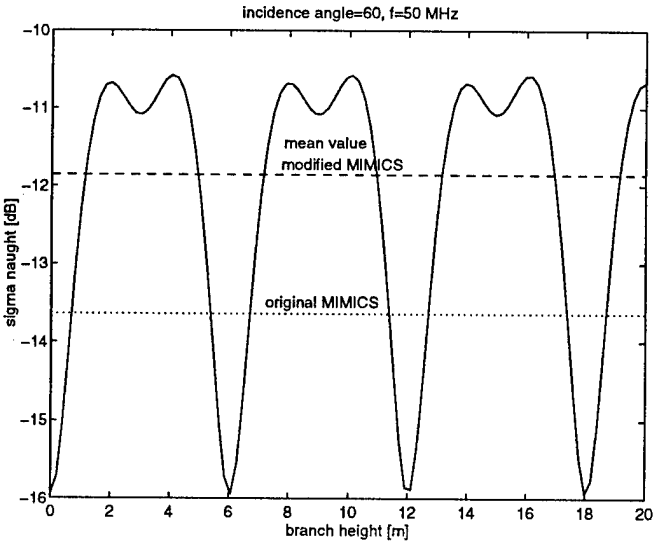

Fig.2 The total radar backscattering as a function of branch height above ground.

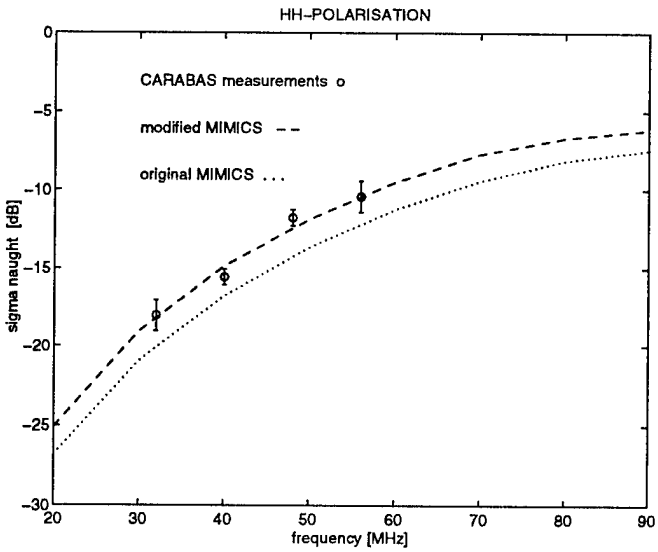

Fig.3 The coherent and the incoherent results together with CARABAS measurements versus radar frequencies. The error bars denote the radiometric accuracy of the CARABAS data.

Radar Backscatter from Boreal Forest in Winter

Martti Hallikainen, Marko Mäkynen, Jouni Pulliainen, Tommi Vänskä
Laboratory of Space Technology, Helsinki University of Technology
P.O. Box 3000, FIN-02015, Finland
Telephone +358-9-451 2371, Fax +358-9-451 2898, E-mail Martti.Hallikainen@hut.fi

Abstract -- The Helsinki University of Technology Scatterometer (HUTSCAT) was used to collect airborne data on radar backscatter from a variety of forest types and land-use categories in the Sodankylä test site, northern Finland. HUTSCAT operates at C and X band, VV, HH, VH, and HV polarization. Four incidence angles were used: 23, 30, 37, and 45 degrees off nadir. HUTSCAT measures the backscatter as a function of distance, thus allowing separation between contributions from the tree canopy and the ground. Measurements were conducted under dry snow, wet snow, and snow-free conditions. Backscatter contributions from the snow/ground and the trees, and the capability of various channels to produce forest canopy information is discussed.

TEST SITE AND DATA SETS

Test site

The Sodankylä test site is located in northern Finland (67.4 N, 26.6 E). It is a typical low-relief northern boreal forest area with pine as the dominant tree type. The maximum stem volume is 200 m^3/ha. The distribution of land use categories is available from a digital land-use map. The total length of the HUTSCAT test lines is 9345 m.

The following forest classes (abbreviations for Figs. 1-3 in brackets) and snow conditions are considered in this paper:

- Clear-cut areas (Cc)
- Pine 0 - 50 m^3/ha (P25)
- Pine 50 - 100 m^3/ha (P75)
- Pine 100 - 150 m^3/ha (P125)
- Mixed 50 - 100 m^3/ha (M75).

- Dry snow (January 19, 1993)
- Wet snow (May 6, 1993)
- Snow-free ground (May 14, 1993).

Airborne data set

Our airborne HUTSCAT scatterometer measures the target backscatter, with a range resolution of 65 cm, for eight channels: 5.4 and 9.8 GHz, VV, VH, HV and HH polarization. This measurement series is conducted within a time period of 16 ms. The HUTSCAT ranging capability allows investigation of the relative contributions from the ground (including both direct backscatter and tree-ground reflections) and the tree canopy. Four incidence angles were used in Sodankylä: 23, 30, 37, and 45 degrees off nadir.

The technical configuration of HUTSCAT in the Sodankylä campaign covers well that of ERS SAR (5.3 GHz, VV polarization, incidence angle 23 degrees), fairly well that of Radarsat (5.3 GHz, HH polarization, incidence angle 20 to 60 degrees), and partly that of the Shuttle-borne SIR-C/X-SAR (polarimetric at 1.25 and 5.3 GHz, VV polarization at 9.6 GHz, incidence angle 20 to 60 degrees).

HUTSCAT measures the backscattering coefficient once per meter along the flight track. All results were averaged over 25 meters in order to simulate the spatial resolution of spaceborne SAR sensors. The cross-polarized (XP) results are shown as average values from VH and HV polarizations.

Ground truth and weather conditions

The Finnish Environment Institute measured the snow thickness, density, water equivalent, layering, and the relative spatial coverage. On January 19 the temperatures of the snow surface and bottom were -10 C and -1 C, respectively. The water equivalent along the test lines varied between 102 and 182 mm and the snow mean density was 0.22 g/cm^3.

The mean daily air temperature was above 0 C since April 22 and on May 6 it was 4 C. Since May 2 also the minimum air temperature was above 0 C. The snow water equivalent along the test lines was around 100 mm. The snow was wet.

On May 14 the mean air temperature was 2 C and the maximum value 5 C. The test lines were free of snow.

RESULTS AND DISCUSSION

Backscatter contributions from ground and trees

Fig. 1 shows the difference between the direct backscatter from the tree canopy and the total contribution from the snow/ground, (including both direct backscatter and tree-ground reflections). For the dry snow situation, ground backscatter dominates for all channels and incidence angles. Under wet snow conditions, ground backscatter dominates for all like-polarized channels at 23 degrees, but only for forest type P25 at 45 degrees. Based on our experimental data, the general behavior of the difference is determined by four phenomena. First, backscatter from the snow-covered ground decreases when the snow gets wet. Second, direct backscatter from the trees increases when the canopy temperature rises above 0 C. Third, canopy backscatter slightly increases with increasing incidence angle. Fourth, ground backscatter decreases with increasing incidence angle.

0-7803-3836-7/97/$10.00 © 1997 IEEE

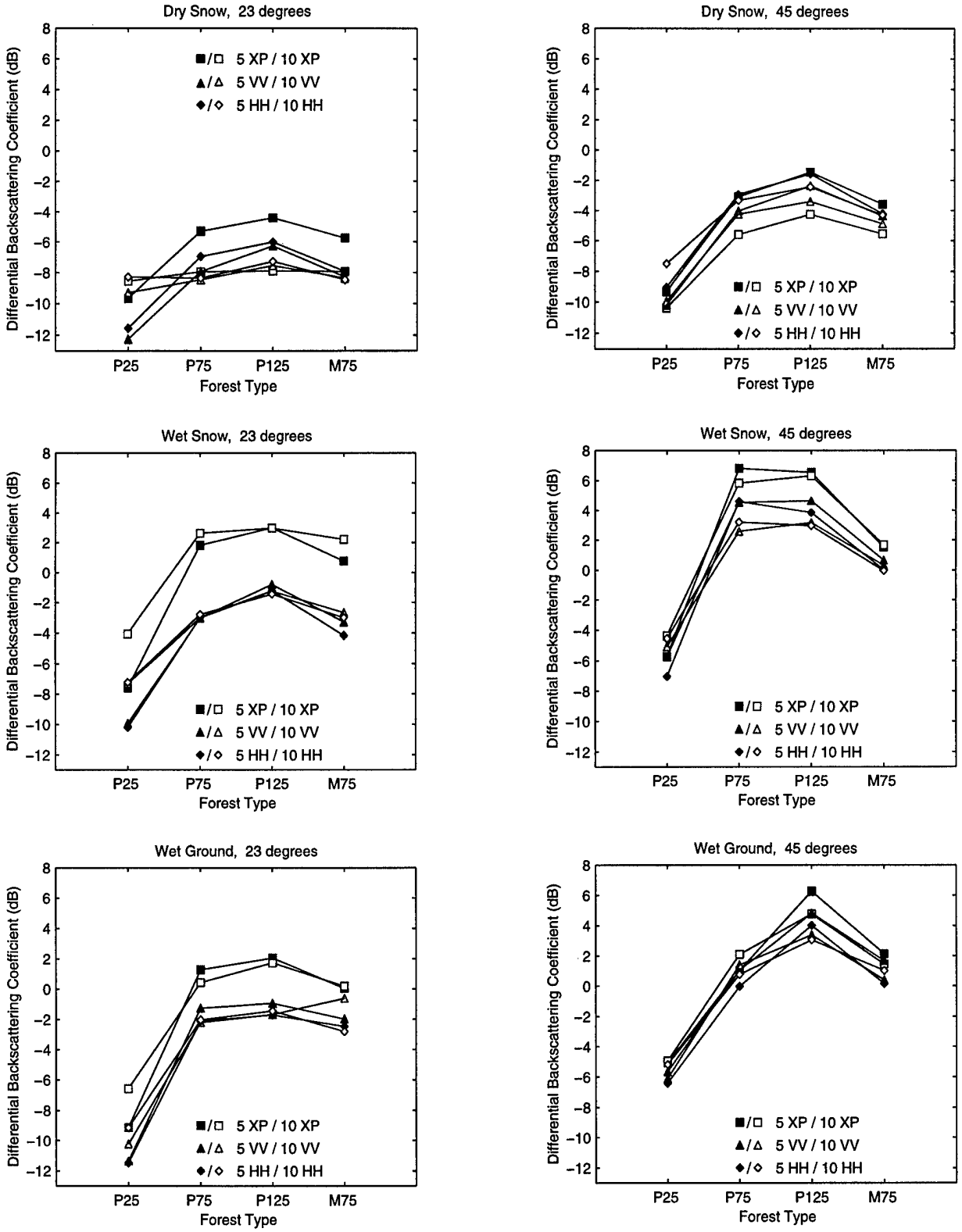

Fig. 1. Observed difference between direct backscatter from the tree canopy and contribution from the ground (including trunk-ground reflections). Results for VV, HH, and cross-polarization (XP) at C and X band, incidence angles 23 and 45 degrees, are shown. Pine forest is denoted by P and mixed forest by M. The average stem volume (m^3/ha) follows the tree type abbreviation.

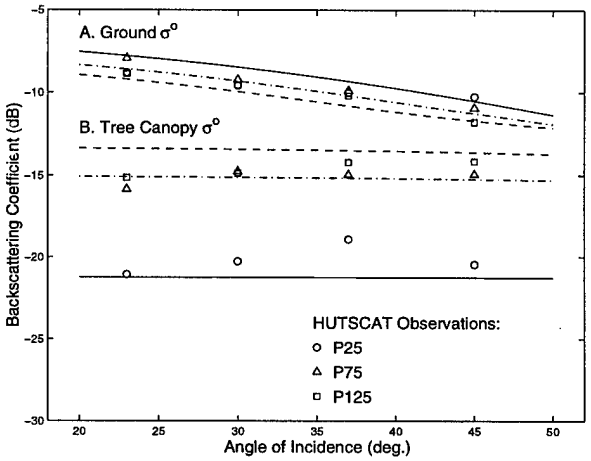

Fig. 2. Comparison of measured and calculated values for the backscattering coefficient of tree canopy and ground as a function of incidence angle (5.4 GHz, VV pol., dry snow).

The computational method [1] used in Fig. 2 assumes that the backscatter contribution from the snow-covered ground behaves as it does for snow-free ground. The moisture levels of canopy and snow/ground have been optimized to fit the experimental data. The backscatter contribution from the tree canopy is assumed not to depend on the incidence angle. The results in Fig. 2 suggest that this assumption may not be valid.

Behavior of total backscattering coefficient

The difference between the backscattering coefficient for forest type P125 and clear-cut areas is shown in Fig. 3. The results indicate that, for an incidence angle of 23 degrees, the difference for VV and HH polarization is positive only for dry snow conditions. For wet snow and snow-free conditions, discrimination of pine forest from clear-cut is not feasible, if like-polarization is employed. The use of like-polarization at X band instead of C band does not improve the discrimination capability. The cross-polarization mode at both C and X band provides reliable discrimination between the two categories for all snow/ground conditions, assuming that enough independent samples are available.

The use of a high incidence angle (45 degrees) improves the discrimination capability substantially, especially for like-polarization, and C band is slightly better than X band. The highest difference, 5.5 dB, between the two categories in Fig. 3 is obtained under wet snow conditions using C band, cross-polarization mode, and an incidence angle of 45 degrees.

CONCLUSIONS

Under dry snow conditions, backscatter contribution from the ground dominates over that from the tree canopy for the investigated boreal forest types at C and X band, incidence angles 23 to 45 degrees. Under wet snow and snow-free conditions, the dominance of the backscattering contribution from the tree canopy increases with increasing stem volume and incidence angle. The capability of radar to discriminate forest from clear-cut was observed to improve with increasing incidence angle. The use of cross-polarization at C and X band provides better discrimination than like-polarization.

REFERENCE

[1] Pulliainen, J., P. Mikkelä, M. Hallikainen, J-P. Ikonen, "Seasonal dynamics of C-band backscatter of boreal forests with applications to biomass and soil moisture estimation," IEEE Trans. Geoscience and Remote Sensing, vol. 34, no. 3, pp. 758-770, 1996.

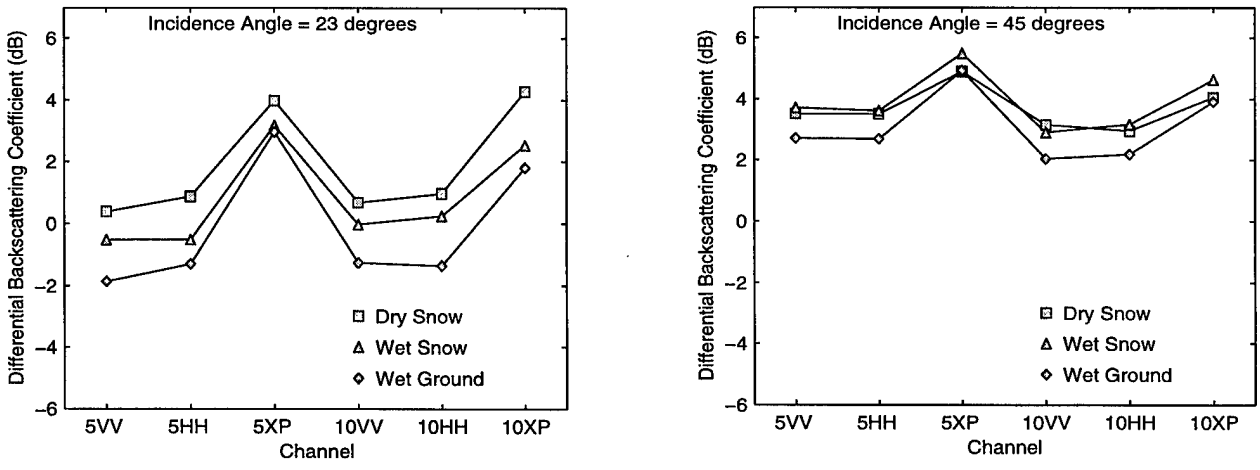

Fig. 3. Observed difference between the backscattering coefficient for pine forest (average stem volume 125 m^3/ha) and clear-cut for VV, HH, and cross-polarization (XP) at C and X band. Results are shown for incidence angles 23 and 45 degrees.

Air/Sea/Land Interaction in the Coastal Zone Seen by Satellite RAR and SAR

Leonid Mitnik and Vyacheslav Lobanov
Pacific Oceanological Institute, FEB RAS, 43 Baltiyskaya St., Vladivostok 690041, Russia
Tel: 7-4232-312-854/Fax: 7-4232-312-573/E-mail: mitnik%dan32@poi.marine.su

Ming-Kuang Hsu
Department of Oceanography, National Taiwan Ocean University, Keelung 20224, Taiwan, R.O.C.
Tel: 886-2-462-2192, ext 6313/Fax: 886-2-462-3073/E-mail: hsumk@ind.ntou.edu.tw

Ruo-Shan Tseng
Department of Marine Resources, National Sun Yat-Sen University, Kaohsiung 80424, Taiwan, R.O.C.
Tel: 886-7-525-2000 ext 5033/Fax: 886-7-525-5033/E-mail: rstseng@cc.nsysu.edu.tw

Kun-Shan Chen
Center for Space and Remote Sensing Research, National Central University, Chung-li, Taiwan, R.O.C.
Tel: 886-3-4227151/Fax: 886-3-425-4908/E-mail: dkschen@csr760.csrsr.ncu.edu.tw

ABSTRACT

Satellite real aperture radar (RAR) and synthetic aperture radar (SAR) images having different spatial resolution together with relevant remote and in situ data are used to study the specific features of the coastal environment off Taiwan, the southern Kuril Islands and Sakhalin. Radar signatures of the atmospheric (lee waves, orographic vortices, wind shadows, etc.) and oceanic (island wakes, eddies, etc.) phenomena express themselves in radar images via spatial variations in the surface wind, current and film fields. They change the surface roughness and hence radar image intensity.

INTRODUCTION

The space-time structure of the hydrophysical and meteorological fields becomes more complicated as the land is approached. This is due to influence of coastal orography and indented coastal line, distinction between land and sea temperatures, river runoff, changing bottom topography, variable tidal currents, etc. As a result, the significant changes of air and water parameters are observed over short distances and time periods.

Obstacles in the form of headlands, islands, coastal and underwater mountains change a structure of air or/and water flow. Character of this interaction depends on form, size and number of the obstacles, their relative position, velocity and stratification of flow, etc. Under the set of conditions, regular structures in the form of waves, vortices, vortex streets are observed in the lee of the obstacles. These features have been the topic of a large body of theoretical and laboratory and field experimental research [1-5]. Satellite and airborne optical images of the coastal areas and isolated islands have revealed the diversified regular mesoscale structures both in the atmosphere (in cloud field) and in the ocean (in sea surface brightness (suspended matter) field). The satellite radar images also permit the disturbances occurring in the air and water flows to be visualized under definite wind speeds.

The dynamic oceanic phenomena manifest themselves in a field of sea surface roughness. These manifestations represent the anomalous states of the sea surface as opposite to a "normal" state when its roughness is determined by the surface wind only. Appearance of the anomalous states on radar images is caused by modulation of the Bragg-scale wind waves by the variable currents directly and/or indirectly, for example, through redistribution of surface film concentration.

The atmospheric mesoscale phenomena (such as lee waves, orographic vortices, land breeze, wind shadows, roll and cellular convection, etc.) are also imprinted on the surface roughness field since they modulate horizontal surface wind. Sometimes the radar signatures of the atmospheric and oceanic phenomena are similar in appearance.

A possibility to observe the phenomena on their surface imprints depends on environmental conditions (first of all, on wind speed), magnitude of the small scale wave modulation, radar characteristics. Satellite scatterometer does not allow the air/sea/land phenomena to be observed due to pure spatial resolution. X-band real aperture radar (RAR) on a board of the Okean series satellites has a spatial resolution of about 1-3 km within a swath width of 460 km and a high sensitivity to wind speed variations. This has enabled the imprints of the lee waves, vortex streets and other mesoscale atmospheric processes to be observed simultaneously with synoptic wind field [6]. The oceanic phenomena were also found on the RAR images using mainly drifting ice as a tracer. The variations of sea surface roughness associated with the oceanic dynamics were registered occasionally [7].

C-band ERS-1/2 SAR has a spatial resolution of 25 m within a swath width of 100 km. Thus it is the best suitable to reveal the fine details of air/sea/land interaction and their relationships with mesoscale processes in the atmosphere and with mesoscale and large scale processes in the ocean.

0-7803-3836-7/97/$10.00 © 1997 IEEE

ATMOSPHERIC PHENOMENA

Satellite radar observations over the ocean revealed the periodic variations of surface roughness associated with roll convection, lee waves and other atmospheric phenomena [5,6]. The reason is that these phenomena manifest themselves as the variations of the surface wind (and other atmospheric parameters). Satellite visible and IR observations allow to estimate the arrangement of the wave crests and wavelength of the periodic phenomena using the cloud patterns. However, when air humidity does not reach a saturation level in upward rising areas of the atmospheric circulation clouds do not form and detection of rolls and lee waves becomes impossible.

Fig.1 shows an Okean RAR image of the Kuril Basin taken during cold air outbreak. The southeastward winds with a velocity of 12-15 m/s were observed in the Okhotsk Sea. Thus wind direction in the lower troposphere was close to normal to the mountain ridges on Siretoko Peninsula (1), Kunashir (2) and Iturup (3). The average maximum height of the mountains is about 1200-1500 m. They have a white tone on the image.

Several systems of alternating light (or gray) and dark bands are seen in the lee of the Kuril Islands. These features are the surface imprints of the atmospheric lee waves which were formed from interaction of air flow with the mountains (Fig.1). The quasi-periodic structures are well pronounced. Wind shadows downstream the highest peaks and east of Hokkaido are also readily apparent. The wavelength Λ of the lee waves southeast of Kunashir is about 9.5 km.

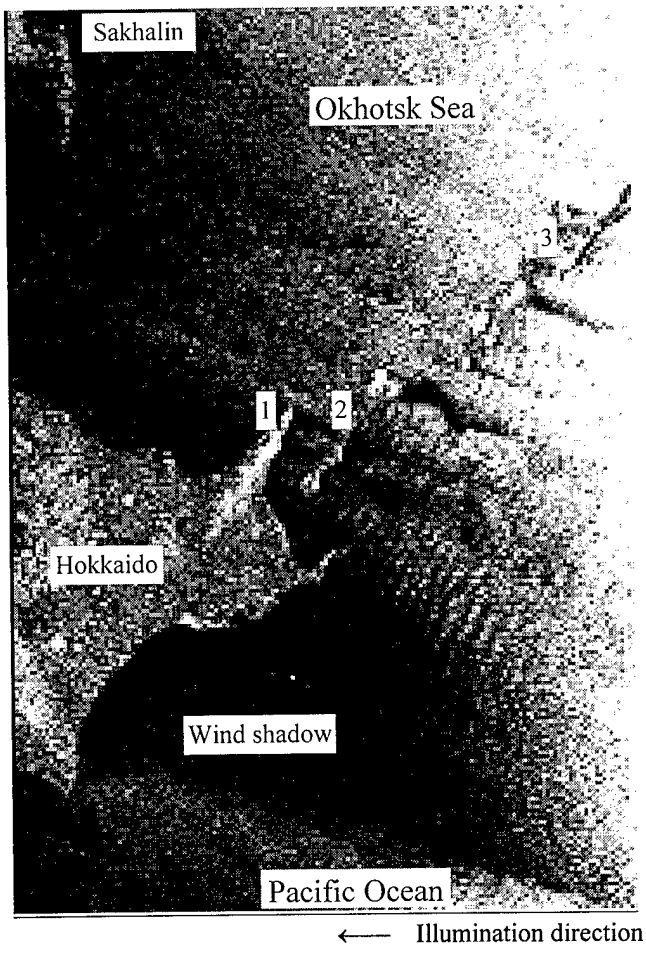

Fig.1. Okean RAR image (460 km x 700 km) acquired on 18 December, 1988, at 0345 UTC.

The surface imprints of the vortex-streets with a length of more than 170 km are seen in the wake of Dokuchaeva (1486 m) and Tyatya (1822 m) volcanoes on the northern Kunashir. Several geometrical parameters (the separation between the vortices with the same and opposite circulation, between the vortex chains with opposite rotation, etc.) can be determined from the image. They can be used to estimate the atmospheric parameters at given width and height of the obstacles [1].

A spatial resolution of a RAR is inadequate to observe the fine details of wind field. Consider Okean RAR and ERS-1 SAR images of the lee waves east of the southern Sakhalin (Fig.2). The waves in the lee of Krilion Peninsula (1) over the Aniva Bay (2), in the lee of Tonino Peninsula (3) and also over the Terpeniya Bay (4) have weak radar contrasts on the RAR image and are barely perceptible (Fig.2a). Their $\Lambda \approx 9$km.

The SAR image shows the clearly defined lee waves with $\Lambda \approx 1.7$ km, wind shadows, slicks, the features associated with depth variations south of Tonino Peninsula (3), etc. (Fig.2b).

OCEANIC PHENOMENA

The diversified expressions of coastal circulation were found on the SAR images especially near headlands, around islands and in bays. Fig. 3 depicts the island wake in the form of von Karman vortex street. This kind of vortex-shedding from a small obstacle is often seen in the island wakes [3,4].

A chain of vortices 1 is located almost parallel to the coast

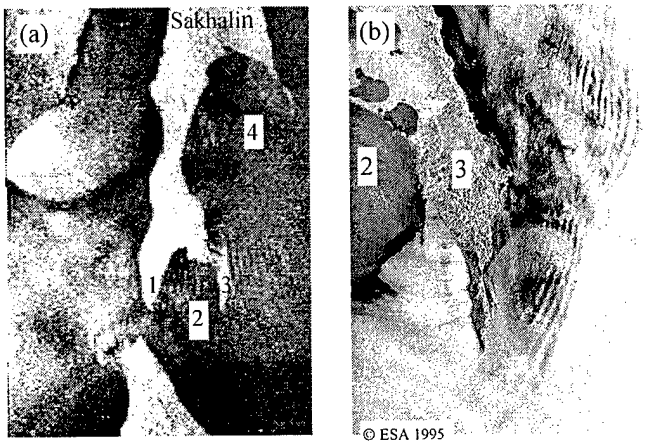

Fig.2. Atmospheric lee waves east of the southern Sakhalin: (a) Kosmos-1766 RAR image (460 km x 700 km) acquired on 12 September, 1987 at 12:15 UTC and (b) ERS-1 SAR image (80 km x 100 km) acquired on 30 May, 1995, at 01:16 UTC.

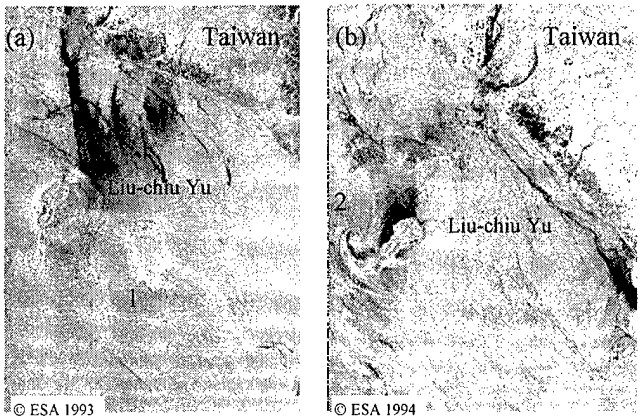

Fig. 3. Surface imprints of the island wake on the ERS-1 SAR images (28 km x 38 km) acquired on 29 November, 1993 at 02:31 UTC (a) and 7 April, 1994, at 14:24 UTC (b).

and characterized by an enhanced backscatter (Fig.3a). It is similar to an imprint of the atmospheric vortex street in Fig.1. The length of Liu-chiu Yu which determines the length scale L [3] is 4.5 km. The wavelength of the vortices is about 10 km and the separation between them is about 2-3 km. These values depend on the island wake parameter $P = UH^2/K_zL$, where U is velocity of flow, H is water depth and K_z is the vertical diffusion coefficient [3]. From Chinese Navy Chart No. 0340, velocity of southeastward flood current is 1-1.5 kn northwest of the island. The close values were obtained near the island by observations of a GPS buy. The chart also shows rips around the island (apart its southeast side) and to the north of it. On the SAR image the rips stand out sharply against the surrounding waters.

The change of current direction is accompanied by generation of the alternating anticyclonic and cyclonic vortices 2 (Fig.3b). An anticyclone near the coast has the most detailed characteristics: a dark center surrounded by bright circle with one large and one small "tails" extending outward from the vortex's boundary. The tails are clearly visible due to increased roughness. The observed vortices are connected with one another by their tails, like the vortex street generated by obstacles in laboratory flow visualization experiments [2].

Superposition of radar signatures of the atmospheric (dark bands in the center caused by the lee waves with $\Lambda \approx 2$ km, wind shadows) and oceanic (eddies, gray and light narrow bands in the lower right corner, slicks, etc.) phenomena is shown in Fig.4. The wind speed was 5 m/s from northwest.

CONCLUSION

Analysis of the RAR and SAR satellite data can reveal important information regarding the mesoscale phenomena and processes in air/sea/land system in the coastal zone and estimate their spatial evolution. The integration of radar, visible, infrared and in situ observations will be extremely useful in furthering the understanding of the variability of geophysical parameters which is typical of the coastal areas.

Fig. 4 ERS-1 SAR image (100 km x 100 km) of Aniva Bay acquired 14 May, 1995, at 01:19 UTC.

ACKNOWLEDGMENTS

This research has been sponsored by the National Science Council through research grants NSC-84-2611-M019-009 and NSC-85-2611-M019-011 K2.

REFERENCES

[1] "Manual on Usage of Satellite Data in Weather Analysis and Forecast, " I.P. Vetlov and N.F. Vel'tishchev, Eds. Leningrad: Hydrometeoizdat, 1982, 300pp. (in Russian).

[2] M. van Dyke, "An Album of Fluid Motion, " Stanford, California: Parabolic, 1982, 175 pp.

[3] C. Pattiaratchi, A. James, and M. Collins, "Island wakes and headland eddies: a comparison between remotely-sensed data and laboratory experiments," J. Geophys. Res., vol. 92, pp. 783-794, 1987.

[4] P.A. Davis and L.A. Mofor, "Observation of flow separation by an isolated island," Int. J. Remote Sensing, vol. 11, pp. 767-782, 1990.

[5] W. Alpers, "Measurement of mesoscale oceanic and atmospheric phenomena by ERS-1 SAR," Radio Science Bulletin, No 275, 1995, pp. 14-22.

[6] L.M. Mitnik and S.V. Viktorov (editors), "Radar Sensing of the Earth's Surface from Space, " Leningrad: Hydrometeoizdat, 200 pp., 1991 (in Russian).

[7] L.M. Mitnik and V.B. Lobanov, "Reflection of the oceanic fronts on the satellite radar images," in Oceanography of Asian Marginal Seas, K. Takano, Ed. Amsterdam: Elsevier, 1991, pp. 85-101.

Remote Sensing Analysis of Submerged Coral Reefs: Applications for Integrated Coastal Management in Fiji

Ellsworth LeDrew, Drew Knight, & Heather Holden

Faculty of Environmental Studies,
Department of Geography
University of Waterloo, Waterloo, Ontario, Canada N2L 3G1
VOX:519 888 4567 X2783
FAX: 519 888 6768
e-mail: ells@watleo.uwaterloo.ca

ABSTRACT

Current approaches to mapping submerged coral ecosystems by remote sensing techniques is largely confined to the identification of general reef features in shallow tropical waters. Technical difficulties in compensating for the attenuation of radiance through the water column, as well as an incomplete understanding about the specific spectral features of coral and other substrates under normal and stressed conditions has limited mapping and assessment procedures. This paper reports on recent developments in mapping submerged coral assemblages in Fiji using satellite imagery and in situ field measurements. An accurate and replicable procedure is proposed to quantify the spectral response of various corals and other submerged substrates to determine biodiversity and stress indicators for mapping and assessing coral ecosystems at site specific and regional locations. Applications of the approach in establishing baseline information, assessing environmental change and managing linked systems within an integrated coastal management framework are highlighted.

INTRODUCTION

Coral reefs are considered to be the oceanic equivalent of the tropical rainforests in terms of their biodiversity, complexity and net primary production. Interconnected coastal ecosystems composed of coral reefs and mangroves, seagrass beds, beaches, estuaries and marine waters have historically been the basis for subsistence, security and culture of local peoples throughout the developing world[1]. In addition, these coastal ecosystems constitute an important renewable resource for a wide range of other contemporary development uses such as settlement, transportation, fisheries, aquaculture, forestry, mining, industry, waste disposal and tourism.

The purpose of this paper is to report on recent developments for mapping coral stress using remotely sensed imagery and in situ field measurement techniques in Fiji. The objective is to develop an objective and repeatable procedure for mapping submerged coral reefs from satellite and airborne digital imagery. The applications of this approach in the broader area of integrated coastal management (ICM) is also discussed with a particular focus on coral ecosystems.

THE APPROACH IN FIJI AND INITIAL RESULTS

Studies by LeDrew et al.[2,3] have been directed toward resolving the technical issue of water column attenuation and applying the resultant image data to management issues. These studies integrate remote sensing satellite image analysis with in situ radiation field measurements primarily from SCUBA and ship based dropsonde techniques. The initial objective is to retrieve reasonable spectral signatures of submerged corals from satellite image analysis to create maps of coral biodiversity and stress. Preliminary field sessions were undertaken in three regions in Fiji: Savusavu Bay off Vanua Levu in the summer of 1994, in the Beqa Lagoon off Vita Levu in August of 1995 and 1996 and at various locations around offshore islands throughout the Bligh Waters in August 1996. The sites in Fiji were selected largely on the basis of personal experience, the availability of reef areas with a variety of reef structures and the logistical support provided by the Project Ocean Search program of Jean-Michel Cousteau Productions in 1994.

For all sites, measurements of optical properties of several water columns in deep water and over coral heads were taken with a dropsonde spectral radiometer (Profiling Reflectance Radiometer, PRR, from Biospherical Instruments Inc.). The measurements were for irradiance (downward solar flux) and radiance (upward reflected flux)

0-7803-3836-7/97/$10.00 © 1997 IEEE

in several discrete spectral bands that correspond to those of the SeaWiFs oceanographic satellite. The sounding locations were determined by a Global Positioning System. Sonar depths were observed and turbidity was measured at sample points throughout the water column of many of the soundings. Data analysis involved calculating the attenuation of irradiance at various depths along the dropsonde profile, and deriving reflectance spectra for a variety of submerged corals and debris surfaces. Using a transformation discussed in LeDrew and Holden (this volume) the bottom reflectance can be retrieved from the satellite data with some confidence without depth information.

The resultant map is illustrated in Figure 1 for the Beqa Lagoon, which is the remnant of a large ancient caldera that forms a barrier reef that encloses a volcanic island. The variety of coral formations within the lagoon provides a diverse sample population for study at a scale appropriate for image analysis. A SPOT satellite image with a normal linear stretch enhancement (Figure 1a) is the typical false colour display used in terrestrial applications. The only evidence of the corals is the exposed seaward edge of the barrier reef. In Figure 1b a grey-scale map of bottom reflectance is superimposed for the water areas. There is clearly increased information within the caldera that corresponds to known coral heads and dive sites. Additional results of this work to date have been reported in LeDrew et al.[2,3] Peddle et al.[4,5] and Holden et al.[6]

APPLICATIONS FOR INTEGRATED COASTAL MANAGEMENT

The increasing scope and magnitude of impacts and environmental change in coastal environments, particularly coral reefs, demands the development of new approaches to delineate features, monitor change and manage resources more effectively.

Integrated coastal management (ICM) has been proposed as a comprehensive, interdisciplinary, intersectoral, and adaptive approach for addressing complex issues concerning the conservation and sustainable development of coastal resources. It encompasses dynamic processes related to planning, assessment, community participation and co-management and evaluation. Such decision making approaches must reflect the complex and interconnected dynamics of coastal ecosystems. Islands and island nations (such as Fiji) are inherently coastal environments and, as such, require a high degree of integrated coastal management.

Perhaps one of the greatest impediments to the implementation of ICM plans is the requirement for accurate and replicable scientific data sets that can be used as a basis for informed decision making. Wells[7] has suggested that there should be a stronger role for science in the management of reef systems by increasing basic knowledge, providing better evidence for environmental change and the development of more science based management approaches. We concur with this approach and provide some examples to illustrate the utility of remote sensing and in situ techniques for the integrated management of coral reefs and associated ecosystems.

Establishing Baseline Information

Reliable maps and baseline data on global or regional reef ecosystems is extremely limited. International efforts such as ICLARM's ReefBase, and the World Conservation Monitoring Centre's (WCMC) Global Coral Reef Mapping Program are important efforts to map and assess the global distribution of reef resources and associated ecosystems but they are based upon exiting data of variable reliability. The mapping procedure introduced in this paper could potentially enhance these and other associated databases through an accurate, replicable and rapid assessment of submerged reefs delineated on a regional scale. This would have significant impact. Examples of applications that will benefit from replicable coral ecosystem data include the delineation of previously uncharted reefs, establishment of administrative boundaries for political and management purposes, oil spill contingency planning, charting navigation hazards, assessing new fishing grounds, and examining candidate areas for eco-tourist resorts and parks and protected areas.

Although Fiji has the second longest continuous stretch of coral reef in the world, little systematic mapping of the coastal environment has been undertaken. The procedure outlined above is well suited for mapping the geographical distribution of barrier, fringing, platform and patch reef types in Fiji. Such maps could be shared by a wide range of coastal zone researchers, planners and managers as baseline information to complement existing data sources and as a means to facilitate dialogue among the diverse users of coral ecosystems. These enhanced maps of submerged reefs (as illustrated in Figure 1b) are powerful visual tools for display and communication and can be readily understood by coastal zone planners and the general public alike. The conversion into reflectance spectra maps indicative of reef morphology will generate applications by the scientific community for research and training. They will also provide a focus for discussion of ecosystem dynamics and the impact of human-induced stressors.

Assessing Environmental Change

The South Pacific Regional Environment Programme has recommended a series of precise studies on recent coastal changes in Fiji related to the impacts of climate change and sea level rise[8]. Such studies should quantify rates of coastal change for various coastal environments as a basis for future planning. We believe with further developments and precision in the mapping analysis, reliable indi-

cators of coral biodiversity and stress can be determined from satellite and airborne digital imagery. Widespread coral bleaching has been linked to changes in ocean temperature and radiation regimes associated with strong EL Niño/Southern Oscillation episodes since the early 1980's,[9] with more recent events resulting in significant coral bleaching at greater depths than had previously been observed. Therefore accurate mapping of submerged reefs could form the basis of 'State of the Environment' reports for monitoring the health of regional reef ecosystems in Fiji and elsewhere. As a result, coral reef ecosystems could become one of the most important quantitative indicators of global climate change and variability[10].

Similarly, this approach could be used to map and assess the impacts associated with sea level rise and related stresses on other ecosystems highly intertwined with coral reefs, notably shorelines, mangroves and sea grass communities. It is questionable whether the offshore reefs in Fiji could respond so effectively to predicted sea-level rise that their present role in protecting Fiji's coasts from erosion and supplying their inhabitants with a variety of seafood can be sustained[8]. To date, however, few quantitative studies have been made. Estimates indicate that there has been an average rate of coastal inundation of 15 cm/year over the past 80 years. This is most likely attributable to sea level rise[8]. For coastal villages this poses significant problems as they are typically located along narrow coastal plains that have a critical shortage of low flat land. In Beqa, for example, scenarios of sea-level rise estimate that 79% of the villages and 100% of the mangroves could be inundated with a 3.5m rise in sea-level [high estimate for a global warming][11]. Inundation of the offshore reef would increase wave activity on the shoreline and result in further erosion of the shoreline.

CONCLUSIONS

Current approaches to mapping submerged coral ecosystems is largely confined to the identification of general reef configuration in shallow water based on image statistics rather than spectral discrimination. Technical difficulties in compensating for the attenuation of radiance through the water column as well as incomplete understanding about the spectral characteristics of specific coral and algae species, background debris and sand surfaces, in addition to changing water quality conditions under normal and stressed environments has limited the advancement of this procedure. Preliminary results however indicate that remotely sensed data can be used to determine the spectral response of corals with some confidence in tropical waters up to a depth of 10 metres, provided that there are optical measurements of the water properties from which to measure the diffuse volume attenuation coefficient. Subsequent research will concentrate on the collection of hyperspectral data at depth for a variety of coral, algae, debris and sand surfaces under various water quality and environmental conditions. Further work will also apply an image processing procedure identified as Spectral Mixture Analysis to the image data to estimate subpixel surface types at greater resolution for use in more precise coral mapping procedures[4].

The need for remote sensing technologies to identify, map and assess coral assemblages and impacts is urgently needed, particularly in over 100 developing countries that utilize coral reefs and related ecosystems as an important renewable resource. We suggest that a replicable and quantifiable mapping procedure for delineating submerged corals and related ecosystems will have considerable significance for studies of ecological stress, pollution abatement, natural and human-induced climate change and for the planning and management of coastal ecosystems.

This mapping approach and consideration of a Beqa Lagoon Biosphere Reserve or similar protected status within an ICM framework would complement the various regional environmental initiatives underway in the Pacific such as the 1997 Pacific Year of the Coral Reef, the South Pacific Biodiversity Conservation Program, SPREP's Integrated Coastal Zone initiatives, as well as other National Environmental Management Strategies (NEMS) in Fiji to ensure that important coastal areas are identified and managed for conservation and sustainable development purposes. Such an approach would permit quantitative information to be available to decision makers for understanding reef ecosystems and assessing environmental change. Ultimately this approach would advance the strategies of environmental conservation and sustainable development which are relatively new concepts for Pacific island governments[12]. On a global scale, the approach will follow the call issued for the International Year of the Reef-1997 (launched at the 8th International Coral Reef Symposium held in Panama in June, 1996) for the scientific community to enhance research efforts in coral reef assessment and monitoring to provide a more complete understanding of the status of the world's reefs.

ACKNOWLEDGMENT

Funding for the preliminary field research was provided by the Natural Sciences and Engineering Research Council of Canada (NSERC) as an Operating Grant awarded to Ellsworth LeDrew. The support of the Faculty of Environmental Studies and the Waterloo Laboratory for Earth Observation at the University of Waterloo is also gratefully acknowledged. The authors are grateful to John Morrow of Biospherical Instruments for the loan of the PRR instruments, and Marnie Laing for technical support in the field.

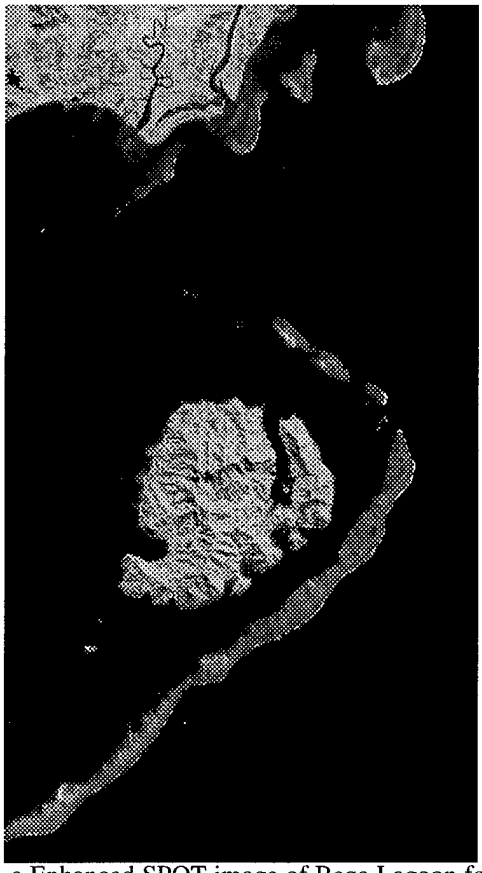

Figure 1.a Enhanced SPOT image of Beqa Lagoon for August 7, 1990

Figure 1.b SPOT image of Beqa Lagoon for August 7, 1990 with greyscale rendition of bottom reflectance superimposed upon Figure 1.a

REFERENCES

1. Kenchington, R., Coral-reef ecosystems: a sustainable resource. Nature and Resources, 21(2) (1985) 18-27.

2. LeDrew, E.F., Holden, H., Morrow, J., Murphy, R. & Bour, W., Mapping of coral ecosystem stress from landsat TM and SPOT imagery with in situ optical corrections. 3rd Thematic Conference on Remote Sensing of Marine and Coastal Environments, Seattle WA., 1995, pp. 211-219.

3. LeDrew, E.F., Holden, H., Morrow, J. & Murphy, R, Mapping coral ecosystem stress in Fiji from SPOT imagery with in situ optical correction, 18th Canadian Remote Sensing Symposium, Proceedings, 1996, pp. 581-583.

4. Peddle, D. R., LeDrew, E. F. & Holden, H., Spectral mixture analysis of coral reef abundance from satellite imagery: an empirical water depth correction using in situ profile spectra, 3rd Thematic Conference on Remote Sensing of Marine and Coastal Environments, Seattle WA. 1995, pp. II-563-575.

5. Peddle, D. R., LeDrew, E. F. & Holden, H., Remote sensing of coral reef abundance and depth from SPOT image spectral mixture analysis and ocean profile spectra, Fiji, 18th Canadian Remote Sensing Symposium, Proceedings, 1996, pp. 555-558.

6. Holden, H., Peddle, D. & LeDrew, E. F., Fluorescence as a potential indicator of coral health, Proceedings IGARSS'96, Lincoln, Nebraska.

7. Wells, S. M., Science and management of coral reefs: problems and prospects. Coral Reefs, 14 (1995) 177-181.

8. SPREP (South Pacific Regional Environment Programme), Integrated Coastal Zone Management Programme for Western Samoa and Fiji Islands. Assessment of Coastal Vulnerability and Resilience to Sea-Level Rise and Climate Change Case Study: Yasawa Islannds Fiji Phase II: Development of Methodology , SPREP, March 1994.

9. Dunbar, R.B. & Cole, J.E., Coral Records of Ocean-Atmosphere Variability, NOAA Climate and Global Change Program, Special Report # 10, 1993, 38pp.

10. Glynn, F. W., Coral reef bleaching in the 1980's and possible connections with global warming, Trends in Ecology and Evolution, 6 (1991) 175-179.

11. UNDP (United Nations Development Programme), Implications of Expected Climate Changes in the South Pacific Region; An Overview. eds., Pernetta, J.C. & P. J. Hughes. UNEP Regional Seas Reports and Studies, UNEP, No. 128, 1990.

12. Miles, G., Fuavao, V. & Smith, A., Implementing Agenda 21; oceans and the Barbados outcomes in the Pacific region. Ocean & Coastal Management, 29(1-3) (1995) 125-138.

LANDCOVER CLASSIFICATION USING ERS SAR/INSAR DATA OVER TROPICAL AREAS

Nicolas Stussi, Soo Chin Liew, Leong Keong Kwoh, Hock Lim,
Centre for Remote Imaging, Sensing and Processing (CRISP)
National University of Singapore, Lower Kent Ridge Road, Singapore 119260, Republic of Singapore
e-mail: crsns@leonis.nus.edu.sg, url: http://www.crisp.nus.sg

Janet Nichol, Kim Chuan Goh
Division of Geography, National Institute of Education
Nanyang Technological University, 469 Bukit Timah Road, Singapore 259756, Republic of Singapore
e-mail: nicholj@nievax.nie.ac.sg

Abstract -- In this study, we present a classification method using both optical and SAR data in order to perform landcover classification. First, different relevant parameters are derived from ERS-SAR data using multitemporal and interferometric analysis. Optical data are then used to define a set of training areas in order to perform a supervised classification. The results of classification using these techniques are compared with existing landuse maps and information derived from SPOT and Landsat data. We point out the usefulness of the coherence γ_{tandem} component for this application. Moreover, we show that $\Delta\gamma$ (difference between γ_{tandem} and $\gamma_{35\text{-}day}$) can give additional useful information for the classification process.

INTRODUCTION

SAR data appears to be very useful to supplement the lack of optical data, especially over tropical areas which are highly affected by an important cloud coverage.
It has been shown that a multitemporal analysis of SAR data allows to monitor changes in landcover using the backscatter change intensity. Nevertheless, this technique is not sufficient for landuse classification.

It has been demonstrated in [1] for boreal forest and in [3,4] for tropical forest that the coherence component derived from an interferometric pair gives additional useful information for landcover classification.
In this paper, we present a supervised classification method using both optical data and radar information derived from SAR and INSAR data.

First, we summarize the different steps to derive a serie of parameters (signatures) from both amplitude and complex data. Results obtained using this method will be discussed. Finally, limitation and future improvement of the method will be pointed out.

PROCESSING TECHNIQUES

Post Processing on Amplitude Images

Different parameters are derived from amplitude images SAR.PRI:

. backscattering coefficient σ^0
. backscatter intensity change $\Delta\sigma^0$ between 2 dates
. texture

First, an edge-preserving filter (Gamma-MAP) is performed on each amplitude image in order to significantly reduce the speckle within the image.
Then, backscatter intensity change $\Delta\sigma^0$ could be estimated correctly from two PRI images as follow:

$$\Delta\sigma^0_{dB} = 10 \cdot \log\left(\frac{\bar{I}_2}{\bar{I}_1}\right) \qquad (1)$$

Where $\bar{I}$ is the intensity of the signal after filtering.
Texture parameters (variance and entropy) are estimated in the image using the Grey-level Co-occurrence Matrix within large window (15x15).

Interferometric processing:

Only the coherence component derived from the interferometric pair is used. To generate the interferogram, the two complex images must be first co-registered to within 0.1 pixel accuracy. A first coarse registration is realised using a series of ground control points. The lack of bright and clear targets over tropical areas increases the difficulty to find a good set of GCP's. Fine registration is then perform using correlation both on amplitude and phase.

The degree of coherence γ for each pair (s_1, s_2) of co-registered complex values s_1, s_2 is given by

$$\gamma = \frac{\langle s_1 s_2^* \rangle}{\sqrt{\langle s_1 s_1^* \rangle \cdot \langle s_2 s_2^* \rangle}} \qquad (2)$$

with:
$$\langle s_1 s_2^* \rangle = \frac{1}{N} \cdot \sum_{i=1}^{N} s_{1,i} \cdot s_{2,i}^* \qquad (3)$$

The value N should be sufficiently large (e.g.: 3x12 or 4x16 pixels window in range and azimuth) to have a good estimation of the degree of coherence [7].

Baseline values plays an important role on the overall coherence level. It has been demonstrated in [5] that the degree of coherence decreases when the baseline increases. For this reason, we have selected interferometric pairs with

0-7803-3836-7/97/$10.00 © 1997 IEEE

baseline less than 300m to reduce the effect of baseline decorrelation.

A first study has been conducted to access the quality of the interferograms that can be generated over tropical areas. These results show that the degree of coherence in a tandem mode can serve as a reliable discriminator between vegetation and non-vegetation. It appears to be useless in the case of the 35-day repeat pass due to a high level of temporal decorrelation [5].

Nevertheless, change in coherence level $\Delta\gamma$ between tandem and 35-day repeat pass ($\Delta\gamma = \gamma_{tandem} - \gamma_{35\text{-}day}$) gives also an additional useful information.

METHODOLOGY

The main idea of our method (fig. 1) is to use all available information (signatures) derived from SAR and INSAR data to perform the classification.

From amplitude and complex SAR data, we can construct a vector of information I of n-order. The number n of discriminators depends on the number of SAR images taken into account for the analysis. Typically, a set of SAR data using one tandem pair and one SLC acquired 35-day later gives the following components:

$$I = [\sigma^\circ_1, \sigma^\circ_2, \Delta\sigma^\circ_{21}, texture_1, texture_2, \gamma_{tandem}, \Delta\gamma] \quad (4)$$

Where $\Delta\gamma$ refers to difference between γ_{tandem} and $\gamma_{35\text{-}day}$; σ°_1 and σ°_2 are related to the 2 amplitude images (35 days of interval).

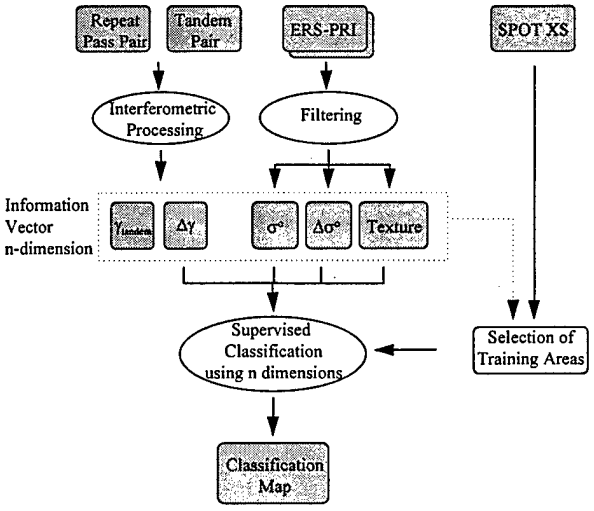

Fig. 1 : Graph of the classification method

First, a series of training areas are selected from the SPOT XS image, providing a representative set for the different types of landuses found in the image. In our study, 5 training areas are chosen corresponding to primary forest, rubber, oil palm plantation, rice and bare soil. Then, a supervised classification is performed on the SAR components (vector I) using the previous training set.

TEST SITE AND DATA

Our test site is located in the coastal region of central Sumatra in the Jambi province, Indonesia. This site has a wide variety of landcover types ranging from mangrove, swamp forest, primary and secondary forests and agricultural land including rice, coconut, rubber and oil palm. The region has been undergoing rapid deforestation with the logging of commercially exploitable timber and the conversion of forest to agricultural land. A set of optical data composed of two SPOT XS data (1996) and one Landsat TM data (1989) are used for the classification process. These data, in conjunction with a landcover map of 1:100 000 scale realised in 1992, are also used to validate the results of the classification. Both SAR.SLC and SAR.PRI data are used in this study for multitemporal and interferometric analysis. A set of ERS-PRI data acquired over one year (oct 95 to december 96) are used for multitemporal studies. Interferometric pairs acquired during tandem mission (April-June 1996) are used to derive the coherence components.

RESULTS

The behaviour of the degree of coherence versus the backscattering coefficient is first analysed in order to demonstrate the usefulness of both components.

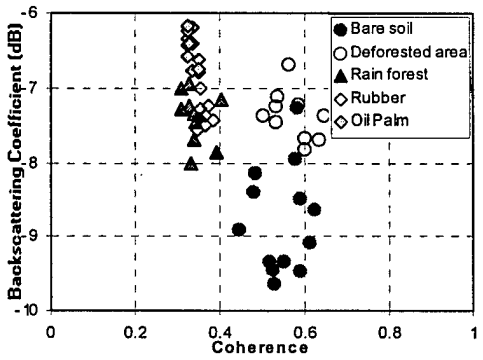

Fig. 2: Behaviour of coherence (tandem pass) as a function of σ° for various landcover types.

Fig. (2) points out the good discrimination between vegetated (forest, plantation, cultivated areas) and non-vegetated areas (bare soil and deforested areas) using coherence. An example is given in fig. (3) and fig. (4) corresponding to a logging area, where an intensive deforestation takes place. The coherence image shown in fig. (4) presents a good contrast (sharp edges) between forested (γ=0.3) and non-forested (deforested) areas (γ=0.6). This image can be compared with the amplitude image shown in fig. (3) where σ° is almost constant.

Nevertheless, different types of landuses could not be separated using only the coherence component. For example, oil palm plantation and rubber give the same degree of coherence. In this case, the backscattering coefficient σ° can then be used to discriminate these two types of landcovers. Unfortunately, primary forest and rubber could not be separated using both γ and σ°.

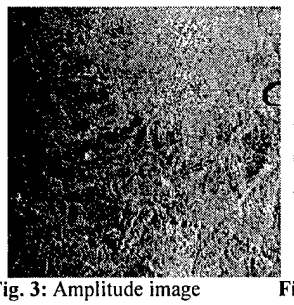

Fig. 3: Amplitude image (May 96)

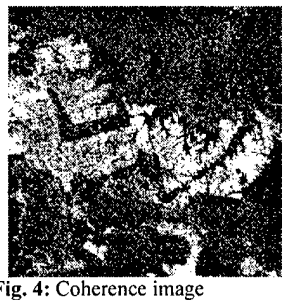

Fig. 4: Coherence image (tandem pass, May 96)

The backscatter intensity change between two images acquired at different dates could also be used as another relevant discriminator. On the one hand, the latter allows to distinguish the growth rate between different cultivated areas. On the other hand, he can inform on the landcover changes between dry and wet seasons (plantation versus primary forest). For instance, rice can be easely distinguish over one ERS cycle due to a rapid growth (typically 3 months).

The same analysis can be conducted using the coherence change index $\Delta\gamma$. The latter measures the variation of the temporal decorrelation between the two interferometric pairs ($\Delta\gamma = \gamma_{tandem} - \gamma_{35\text{-}day}$). This signature appears to be relevant for discriminating landcovers with the same backscatter behavior ($\Delta\sigma^o$ almost constant). The use of this parameter needs to be investigated further.

Nevertheless, our results shows that texture parameters appear to be similar for different landcover types. In this case, we can concluded that texture should not be considered as a relevant parameter in the classification process (simplification of vector I).

Fig. 5: Coherence image (tandem pass, May 96)

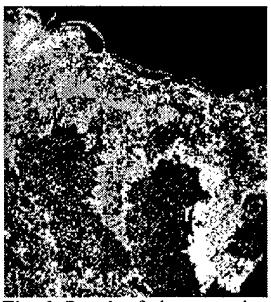

Fig. 6: Result of the supervised classification

Fig. (5) shows the coherence image (tandem mode) obtained over an area mainly composed of swamp forest (bottom) and cultivated areas (rice, coconut, rubber). We can see a good discrimination between swamp forest (dark areas in the center, γ=0.3) and cultivated areas located along the coast (γ ranges from 0.4 to 0.6). Rice appears with a high coherence level due to the early stage of growth.

The result of the classification process using our method is presented in fig. (6). The swamp forest (black) is clearly discriminated from the cultivated areas. Rubber (light grey) appears at the boundary. Moreover, rice (white) is correctly classified. Coconut appears in grey (between the swamp forest and the coast). Nevertheless, some areas are misclassified (bottom left) mainly due to the heterogeneity of the landcover (forest, rubber).

DISCUSSION / CONCLUSION

It has been demonstrated that multitemporal study in combination with interferometric analysis can give useful information for landcover classification. The coherence component appears as a relevant discriminator for this application. We have based our method on the use of a vector of information of n-order, composed of a series of parameters (signatures) derived from SAR and INSAR data: γ_{tandem}, $\Delta\gamma$, σ^o, $\Delta\sigma^o$ and texture. Optical data is then used to define a training set in order to control the supervised classification.

Tandem pair is more appropriate for this kind of study, in order to reduce the temporal decorrelation of the signal. However, small baselines are required to avoid a degradation of the overall coherence level (baseline decorrelation). Nevertheless, the change in coherence calculates from both tandem and 35-day repeat pass can give additional useful information for the classification process.

Nevertheless, sensitivity to biomass remains low with C-band. Moreover, L-band appears to be more suitable for this type of application. To significantly improve the results of the classification, combination of both ERS and JERS-1 data should be used for this application. Backscattering coefficient and backscatter change intensity could then be derived from JERS-1 data, and combined with coherence components extracted from ERS interferometric pair.

REFERENCES

[1] U. Wegmuller and C.L. Werner, "SAR Interferometric Signatures of Forest", *IEEE Trans. Geosci. Remote Sensing,* Vol. 33, no. 5, 1995, pp 1153-1161.

[2] H.A. Zebker and J. Villasenor, "Decorrelation in Interferometric Radar Echos", *IEEE Trans. Geosci. Remote Sensing,* Vol. 30, no. 5, 1992, pp 950-959.

[3] N. Stussi, L. K. Kwoh, S. C. Liew, K. Singh, H. Lim, "ERS-1/2 Interferometry: Some Results on Tropical Forest", FRINGE 96, Zurich, Switzerland, October 1996.

[4] N.Stussi, et al., "Landcover Classification using ERS SAR/INSAR data on Coastal Region of Central Sumatra", *3rd ERS Symposium*, March 17-21, 1997, Florence, Italy

[5] N. Stussi, et al., "Quality Assessment of Coherence Between 35-day and Tandem Modes in ERS-1/2 Interferometric Studies", *IGARSS'97*, August 3-8, 1997, Singapore

Preliminary Study on Development and Management Information System on China Coastal Resources Environment

Jiang Xingwei
National Marine Data and Information Service
93 Liuwei Road, Hedong District
Tianjin 300171, P.R. China
Tel: 86-22-24300881 Fax: 86-22-24304408
E-Mail: JXWNET@V7610.TISTI.AC.CN

Yun Caixing
State Key Lab. of Estuarine and Coastal Research
East China Normal University
3663 North Zhongshan Road, Shanghai 200062
Tel/Fax: 86-21-62546441

Abstract

With population movement to coast, the three major issues faced by our world--the population, resources and environment, become more and more severe in the coastal areas. Therefore, the rational utilization, development and protection of the coastal resources environment have been paid specific attention in the global sustainable development. The population of China occupies 22% in the world. In China, the population of the coastal areas (the population density is about 415/km^2) is the 40% of that of the whole country. And the gross output value of industry and agriculture in the coastal areas of China occupies the 64.7% in the whole country. In recent years, The policy of reform and opening outside have speeded the progress of the industrialization and urbanization of the eastern coastal area in China, which has made both the economy and population thereof growing rapidly. The population movement to coast has resulted in the deterioration of the natural resources and environment thereof in a certain degree, such as the loss of cultivated land, drying up of the coastal wet land, deterioration of the fishery resources, pollution of the water resources, etc. This will affect the future life of people and the sustainable development of social economy. Through the discussion on the development and management information system of China coastal resources environment, the paper tries to find the scientific way of the coordinative development of the population, resources, environment and social economy for the coastal areas on the developing countries.

I. Urgent Need for the Development and Management Information System on China Coastal Resources Environment

The coastal zone has always been being the area with the most active development by man because of the rich resources thereof. As a large ocean-related developing country, China is prominent in the development and utilization of coastal zone. China has the continental coastline of 18,000km and the island coastline of about 14,000km. There are over 6500 islands with the area of each over 500m^2. So China has vast seas and oceans and rich marine resources. Since the reform and opening outside, the development and utilization of marine resources have been growing rapidly in China. The growth of

0-7803-3836-7/97/$10.00 © 1997 IEEE

the marine economy is averagely 17% in the 1980s and it increases progressively by 20% per year in the 1990s. It is estimated that the output value of marine industries will reach 500 billion or so. It will become an important component of the national economy. However, the rapid development of the coastal areas also results in a series of issues needing prompt solution. The issues are major in the following aspects:

- Contradiction between the population movement to coast and the marine space resources ;
- Contradiction between the development of coastal city chain and the energies and communications;
- Deficiency of the fresh water resources;
- Pollution from land sources and ecological environment protection;
- Marine aquaculture and stock enhancement industry and the distribution of the coastal industries;
- Contradiction between reclaiming land from sea and protecting littoral wetland;
- Rational distribution of the harbors and the coastal engineerings;
- Development of coastal oil and gas resources and monitoring of oil pollution;
- Comprehensive development of river mouth delta and estuary;
- Reduction to a minimum of the loss caused by natural disasters in the coastal areas.

The issues mentioned-above limit to a certain extent the development of social economy in the coastal areas. In order to resolve these issues, the integrated management has to be strengthened. A effective plan for the integrated management of the coastal zone must be drafted on the basis of mastering clearly and sufficiently such data thereon as the natural features, economics and society. The development and management information system on coastal resources environment has to be set up to provide these data.

II. Establish Mode of the Development and Management Information System on Coastal Resources Environment

The development and management information system on China coastal resources environment can be established with three levels according to the different requirements of the national macro-adjustment and -control, the regional management and the local development.

1. National level system

Major functions: establishing the basic information system on the national coastal resources environment (1:500,000~1:1,000,000).

System products: distribution features of main marine resources, environmental conditions, human society, development of ocean-related economics.

2. Provincial (municipal) level system

Major functions: establishing the provincial or municipal information system on coastal zone planning and management (1:100,000~1:250,000).

System products: basic situations of the coastal population, resources, environment and social economics; sea functional zoning, use control of sea areas, asset assessment of marine resources, development plan of coastal zone, etc..

3. Prefectural (county) level system

Major functions: establishing the special-subject information system or the development information system on the typical regions (1:5,000~1:50,000)

System products: assessment of coastal ecological environment, development and management of coastal resources, assessment of coastal engineering construction, etc..

III. Application of RS, GIS, GPS Technologies in Development and Management Information System of Coastal Resources Environment

1. Remote Sensing (RS)

(1) Resources environment monitoring and data update

- Earth Observation Satellite: monitoring on the variations of coastal land coverage and utilization, vegetation coverage.
- Meteorological Satellite: used for monitoring the turbidity of waters, water surface temperature, and so on.
- Ocean Color Satellite: laying stress on the monitoring of the content and distribution variation of suspended sediment, chlorophyll, yellow substance and pollutants.
- Topography Satellite: used for surveying the sea surface features, sea wave, etc.
- Radar-Satellite: laying stress on environmental elements of the marine dynamics.
- Aerial remote-sensing: laying stress on the variation of coast and detail land survey, etc..

(2) Resolution selection

- Temporal resolution (0.5--26 days)
- Spatial resolution (1m--1.1km)
- Spectral resolution (10nm--100nm)
- Radiation resolution (8--12bit)

(3) Sensor Improvement

- High-Resolution Photoimaging Sensor (CCD camera)
- Imaging Spectrometer (10nm spectral resolution)
- Synthetic Aperture Radar (SAR)
- Laser Radar (LADAR)

2. Geographic Information System (GIS)

- Establishing the spatial data base on coastal resources and environment;
- Establishing the comprehensive analysis and assessment models and developing expert decision-making auxiliary system;
- submitting compounded information products.

3. Global Positioning System (GPS)

- Positioning and navigation of satellite and aerial remote-sensing;
- Correction and recovery of remote-sensing image and establishing the spatial coordinate of image elements;
- Definition of the monitoring points on land and at sea, selection of the position of training site for ground target classification, etc..

Status of the Development of an *In situ* Plankton Monitor

Dr. Walton Campbell, Joann Nault, and R.A. Warner
National Oceanic and Atmospheric Administration (NOAA)
National Ocean Service (NOS)
Office of Ocean Resources, Conservation and Assessment (ORCA)
1305 East-West Highway, 9th floor
Silver Spring, Maryland 20910-3281
telephone: 301-713-3000 / facsimile: 301-713-4384
email: walt@dolfun.nos.noaa.gov, jo@dolfun.nos.noaa.gov, and warner@caribe.nos.noaa.gov

Abstract -- The majority of the world's population lives and is employed along its shorelines and is economically dependent upon the activities of its coastal facilities. Development of methods to determine the spatial and temporal extent of changes in the health of coastal ecosystems within sufficient time to take effective management and mitigation actions is essential to effective environmental stewardship. The phytoplankton populations of coastal waters are very sensitive indicators of current environmental health and productivity because their nutritional and water clarity requirements are quite specific. These primary producers are the first step of the marine food web and thus, most of the rest of the coastal ecosystem (water quality, organisms which consume algae directly and their consumers, etc.) relies upon a healthy and balanced phytoplankton community.

Routine synoptic *in situ* monitoring of phytoplankton by labor-intensive ship operations is rapidly being replaced by satellite borne ocean color instruments, such as the ADvanced Earth Observing Satellite (ADEOS)/Ocean Color and Temperature Scanner (OCTS). However, frequent *in situ* calibration of data from diverse water masses is necessary to develop and maintain algorithms which correctly relate the data provided by remote sensing instruments to the *in situ* geochemical parameters.

INTRODUCTION

The successful deployment of NASA's experimental 5 channel NIMBUS-7 satellite with its Coastal Zone Color Scanner (CZCS) instrument provided a brief glimpse of the potential benefits to be obtained from a satellite-borne ocean color scanner. Attempts to calibrate the CZCS met with limited success because the sensor functioned only intermittently from 1978 - 86 and much of the *in situ* data collected depended upon costly, occasional research cruises. Attempts to derive an "ocean color index" using the NOAA TIROS/AVHRR instrument, have produced algorithms which have found only very limited applicability to most coastal environments due to limited spectral resolution of its two visible spectrum channels. With the successful 1996 launch of Japan's ADEOS satellite with its OCTS instrument, the dearth of space-borne color sensors is at an end. This should be soon followed by the launch of Orbital Science's Seastar (scheduled for June 18, 1997), and Japan's ADEOS II/ GLI (scheduled for 1998), and EOS-AM/MISR and MODIS instruments.

We have designed and are constructing a moored instrument package that will collect frequent chlorophyll and size distribution spectra from the same *in vivo* sample. A Turner Designs model 10-AU fluorometer has been modified and integrated with a modified Spectrex model PC-2000 laser particle counter into a watertight buoy housing This buoy will enable the characterization of chlorophyll containing phytoplankton [1,2] as well as distinguishing, the size spectra associated with these chlorophyll concentrations. This will facilitate identification of population genera/species relationships for calibration of the ocean color satellite instruments to algal biomass and net primary productivity. Fluorometric measurements for chlorophyll-a are very sensitive [3] and therefore are popular methods of determining phytoplankton abundance. But, problems remain in standard fluorometry techniques distinguishing chlorophyll-a fluorescence from that emitted from chlorophyll-b, accessory pigments, and other particulate and dissolved fluorescing compounds [4]. To obtain species-related information on the chlorophyll-a containing material quantified above, we will determine particle size spectra from within the same *in vivo* sample, [5, 6].

IN SITU INSTRUMENT

This field instrument has been designed to address the problems of *in situ* biofouling by the incorporation of magnetic rail-gun technology. This novel approach should minimize the necessity of the more commonly employed solutions to this problem of either frequent manual maintenance preformed on remote field instruments [7] or the use of extremely toxic chemicals on optical surfaces [8]. The rail-gun technology sampling subsystem provides for programmable, simultaneous window cleaning and sample rate/volume control.

0-7803-3836-7/97/$10.00 © 1997 IEEE

REMOTELY SENSED DATA

Remotely sensed data from ocean color sensors mounted on polar orbiting satellites, such as the OCTS on the Japanese satellite will be used in conjunction with the *in situ* data collected from the moored buoy described above. Calibration algorithms for the satellite sensor will be derived from these *in situ* data taking advantage of methods discussed in [9, 10, 11].

FIELD WORK

We have chosen waters south of Florida for field testing and evaluation due to the proximity of both case I and case II water masses, in the open ocean/Gulf Stream and within Florida Bay respectively: Fig. 1. In the region of South Florida, each ADEOS/OCTS image usually contains data from both water masses in a single orbital swath. This sampling strategy will minimize differences in sun angles, insolation, atmospheric attenuation/backscatter, and processing modes as well as make for more efficient field deployment efforts.

SUMMARY

At the time of writing, the instrument is being assembled, tested and readied for field deployment in June 1997. With the operational supply of OCTS imagery data, it is anticipated that preliminary calibration coefficients for Atlantic case I and case II waters will be forthcoming shortly thereafter. The combination of simultaneous chlorophyll fluorescence and particle size spectra will provide more accurate assessments of *in situ* primary producers. The use of magnetically coupled, through-the-cuvette-wall sampling control should make for a low-cost, maintenance free, autonomous, chlorophyll spectrum buoy design without the use of expensive manual labor or environmentally toxic chemicals.

Figure 1. Study Area.

REFERENCES

[1] Bricaud, A., C. Roesler, and J.R.V. Zaneveld, 1995. In situ methods for measuring the inherent optical properties of ocean waters. Limn. Oceanogr. 40: 393-410.

[2] Jeffrey, S.W.,and G.F. Humphrey, 1975. New spectrophotometric equations for determining chlorophylls a, b, andc1 in higher plants, algae and natural phytoplankton. Biochem. Physiol. Pflanzen 167: 191-194.

[3] Holm-Hansen, O., C.J. Lorenzen, R.W. Holmes and J.D. Strickland, 1965. Fluorometric determination of chlorophyll. J. Cons. Cons. Int. Explor. Mer 30: 3-15.

[4] Welschmeyer, N.A., 1994. Fluorometric analysis of chlorophyll a in the presence of chlorophyll b and pheopigments. Limnol. Oceanogr. 39:1985-1992.

[5] Stamm, A.J. and T. Svedberg, 1925. The use of scattered light in the determination of the distribution of size particles in emulsions. J. Am. Chem. Soc., 47: 1582-1596.

[6] Plank, W.S., J.R.V. Zaneveld, and H. Pak, 1973. Distribution of suspended matter in the Panama basin. J. Geophys. Res. 78: 7133.

[7] Martini, M.A. and W.J. Strahle, 1993. Multi-sensor system for coastal environments. Sea Technol. 34: 49-53.

[8] Butman, B. and D.W. Folger, 1979. An instrument system for long-term sediment transport studies on the continental shelf. J. Geophys. Res. 84: 1215-1220.

[9] Cullen,J.J., C.M. Yentsch, T.L. Cucci and H.L. MacIntyre, 1988. Autofluorescence and other optical properties as tools in biological oceanography, 149-156. In Ocean Optics 9, Proc. SPIE 925.

[10] Bhargava, D.S. and D.W. Marriom, 1991. Effects of suspended particle size and concentrations on reflection measurements. Photogram, Eng, Remote Sensing. 57: 519-529.

[11] Morel, A., 1988. Optical Modeling of the Upper Ocean in Relation to Its Biogenous Matter Content (Case I Waters). J. Geophys. Res. 93: 10749-10768.

Microbial Particles and Oceanic Optics: Where Do We Go Next?

Dariusz Stramski
Marine Physical Laboratory
Scripps Institution of Oceanography
University of California, San Diego
9500 Gilman Drive
La Jolla, CA 92093-0701
tel. (619) 534-1802/stramski@mpl.ucsd.edu

Abstract -- Achieving a detailed understanding of the roles played by various types of microbial particles in oceanic optics is a prerequisite to advancing remote sensing of water component concentrations and improving bio-optical models beyond their present one-parameter, chlorophyll-based description of very complicated and variable situations. We now have information available on the single-particle optical properties of various microbial species and a numerical radiative transfer model that is computationally efficient and accurate enough to permit extensive studies of light fields within and leaving the water as particle types, concentrations, and optical properties are systematically varied. A new approach combining a database of single-particle optical properties and radiative transfer modeling is very promising because it identifies bio-optical relationships and details which are not resolved by common correlational models parameterized in terms of chlorophyll concentration alone.

INTRODUCTION

The optical remote sensing estimation of co-existing concentrations of various organic and inorganic components in aquatic environments is contingent upon precise knowledge of the spectral optical cross sections for these components. This requires coordinated research in which the development of retrieval algorithms is conducted in tandem with determinations of the optical properties of aquatic components. In addition to pure water itself, several general categories of optically significant components can be distinguished, such as planktonic organisms, organic detritus, mineral particles, gas bubbles, and dissolved materials. The retrieval of component concentrations from satellite measurements of water-leaving spectral radiances depends upon the degree to which the components influence the absorption and scattering properties of natural waters and our ability to quantify these influences.

• This work was supported by the ONR Environmental Optics Program (grant N00014-95-1-0491) and NASA Ocean Biogeochemistry Program (grant NAGW-3574).

CHLOROPHYLL-BASED PARAMETERIZATION

It is well recognized that in the upper layers of the open ocean, usually termed case 1 waters [1], the optical properties and their variability are associated largely with phytoplankton and co-varying materials. This assertion along with early observations suggesting that the chlorophyll *a* concentration (*Chl*) in the surface waters could be deduced from measurements of upwelling light emerging from the sea [2] have had an enormous impact on the developments in the area of optical and satellite oceanography in the last two decades. One of the most important events at the beginning of this time period was the launch of the proof-of-concept mission of the Coastal Zone Color Scanner (CZCS) on Nimbus-7 in 1978 [3]. Since then much effort in ocean optics has been focused on developing bio-optical relationships for case 1 waters using a parameterization of sea water composition in terms of chlorophyll concentration alone. It has been shown that changes in *Chl* are accompanied by more or less systematic variations in the inherent optical properties (IOPs) and apparent optical properties (AOPs) of the ocean, such as the spectral absorption coefficient, the scattering coefficient, the diffuse attenuation coefficient for downwelling irradiance, and ocean reflectance [4, 5, 6]. The empirical correlations between *Chl* and optical properties have formed the basis of bio-optical models that predict IOPs and AOPs given *Chl*, or vice versa, including the retrieval of chlorophyll concentrations from remote-sensing spectral reflectances.

Although such chlorophyll-based bio-optical models may often satisfactorily predict average values as obtained from water samples taken at many locations and times, these models say nothing about the optical variability observed in different water samples, which have the same chlorophyll concentration. As a result of such optical variability, any particular measured chlorophyll concentration can frequently differ by a factor of two or so from the value predicted from bio-optical models, for example from the ratio of remote-sensing spectral reflectances. These variations may become even larger in case 2 waters, which include most coastal areas of the world's ocean where components other than phytoplankton and their derivatives are optically significant (e.g., resuspended sediments, terrigenous particles or dissolved organic matter).

0-7803-3836-7/97/$10.00 © 1997 IEEE

MICROBIAL PARTICLES AND OPTICS

In order to explain this seemingly unpredictable variability in the correlational, chlorophyll-based bio-optical models we must consider the detailed composition of sea water. Part of this variability is certainly due to the wide range of planktonic microorganisms including chlorophyll-bearing phytoplankton themselves. It seems clear that an improved understanding of the marine optical environment can be gained if we progress beyond the overly simplified parameterization of sea water composition in terms of chlorophyll concentration alone. The most rigorous approach should consider the optical properties of every species of aquatic components present in a water body, as well as the possible intraspecies variability in these properties. In regard to planktonic microorganisms such an approach should include the detailed composition of species, each one having distinct optical properties of its own, as well as the intraspecies variability in the optical properties. Because of the wide variety of species in natural waters, this approach must, in practice, be reduced to a certain number of appropriately selected species or taxa that realistically represent the mix of all microbial particles which affect the marine optical environment.

The relationship between microbial particles and oceanic optics is schematically depicted in Fig. 1. This figure emphasizes major biological-optical interactions that occur in the upper ocean. The bulk inherent optical properties (IOPs) of sea water depend on the optical properties of microbial particles at the level of both single cells and the entire planktonic community. The IOPs have, in turn, an influence on the apparent optical properties and light field characteristics within the water body and leaving the water, such as the remote-sensing reflectance. The optical properties of the entire planktonic community may vary as a result of changes in species composition, concentration and size distribution. The single-cell optical properties of any given species, usually termed the optical cross-sections, may vary as a result of physiological adaptation, which generally involves changes in cell size and refractive index. All these variations in microbial optical properties are induced by varying environmental conditions (e.g., physical-chemical fields such as temperature and availability of nutrients, and light field feedback on biology) as well as interactions within the planktonic community itself (e.g., prey-predator interactions).

It is obvious that, prior to applying any rigorous approach (extending beyond a simple chlorophyll parameterization) to the study of the marine optical environment, it is essential to examine the optical properties of various microbial species and how these properties respond to varying conditions of growth. Recent progress in two research areas have made it possible to initiate a new approach that combines a database of microbial optical properties and radiative transfer modeling [7, 8]. First, there has been a considerable progress in acquiring comprehensive information about both the absorption and scattering properties of different types of microbial particles, from the smallest bacteria to various nanoplankton species [9-20]. Second, a numerical radiative transfer model (Hydrolight 3.0), that is both accurate and computationally efficient enough to permit extensive studies of oceanic light fields as particle types, concentrations, and optical properties are systematically varied, has been developed [21].

Reference [7] describes the database of single-particle optical properties of five types of microbial particles covering the size range from ~ 0.05 μm (viruses) to ~ 10 μm (nanoplanktonic chlorophytes). Not only information about the magnitude and spectral behavior of various optical properties at the level of single particle, but also data about particle size and refractive index are included, which is critical in understanding of particle optics. Importantly, all single-particle optical properties required to carry out simulations with the radiative transfer model are included (i.e., spectral cross sections for absorption and scattering as well as spectral scattering phase functions).

Reference [8] shows how powerful a combination of such a database and radiative transfer modeling is in the study of oceanic optics. Specifically, the radiative transfer simulations showed the capability of this approach for separating and analyzing the contributions of individual microbial components to various measures of the light field, such as scalar irradiance, diffuse attenuation of irradiance, and remote-sensing reflectance. These simulations also showed how different microbial compositions of two water bodies can give considerably different remote-sensing reflectances, even though the chlorophyll concentration is the same in each of the water bodies. In other words, these results demonstrated that variability in chlorophyll concentrations obtained from remotely-sensed ocean color signals can be explained by the detailed composition of sea water.

In contrast to correlational, chlorophyll-based bio-optical models derived from statistical analysis of field data, this more rigorous approach leads to the development of a mechanistic model of the marine optical environment. To utilize such a mechanistic approach to its fullest potential requires creating a comprehensive database of the optical properties of marine particles. The present database [7] must be expanded to include more microbial species from various size ranges. The optical information about mineral particles and detritus is also needed to represent the natural assemblages of marine particles more realistically. The development of such database is a difficult and laborious task; it is nevertheless a worthwhile effort from which we shall continue to reap the benefits with the passage of time.

It is obvious that the ultimate database cannot include every species, but instead a manageable number of particulate components must be chosen. The selection of the components can be based on two simple criteria. First, the sum of selected particulate components should account

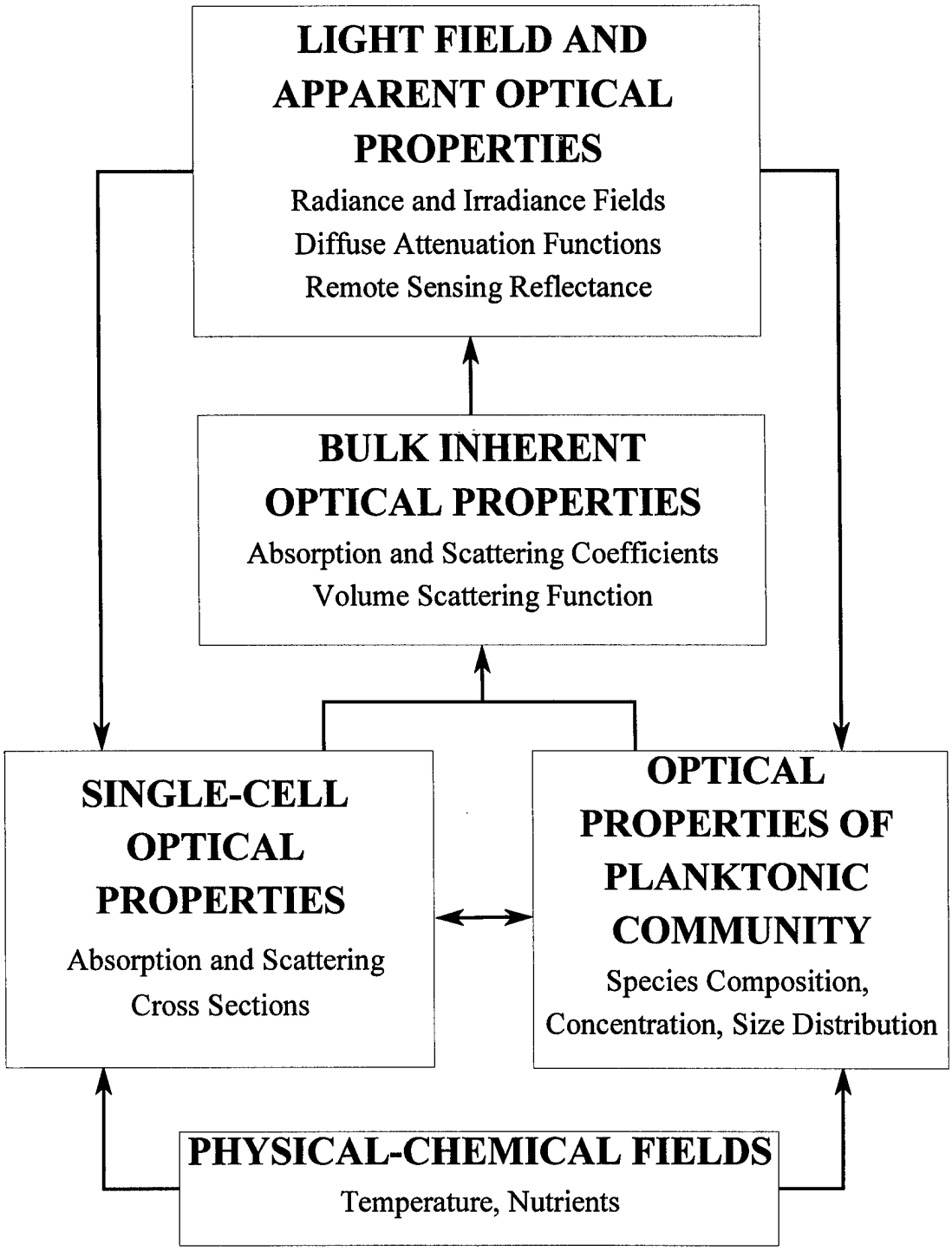

Fig. 1. Biological-optical interactions in the upper ocean.

for the total bulk optical properties of a water body as accurately as possible and, second, each of the particulate components should play a specific, well-defined role in the marine ecosystem. The latter criterion is important for the linkage of optical information with biological and ecosystem models. It is expected that each particulate component will generally include multispecies assemblages of similarly sized particles which have similar optical properties and functions in the marine environment. As an example, heterotrophic bacteria, including many different species of similarly sized microorganisms which are all heterotrophs, can be considered as one such distinct component. Similarly sized and pigmented photoautotrophic microorganisms can form separate components, etc. Some planktonic species or taxa with unique optical properties (for example, coccolitophores) will likely require consideration as separate components.

The further development of the database of single-particle optical properties is currently underway. It is anticipated that the next version of the database will be completed soon. This version will be based on information collected in recent years by several investigators through laboratory experiments with heterotrophic bacteria and twenty two different species and strains of marine phytoplankton, from the smallest prochlorophytes (~ 0.6 μm in size) to microplanktonic species of about 30 μm in size [10, 12, 16, 17, 18, 19, 20]. In combination with radiative transfer modeling, this database will provide a powerful means to study the effects of microorganisms on oceanic optics with unprecedented detail.

REFERENCES

[1] A. Morel and L. Prieur, "Analysis of variations in ocean color", Limnol. Oceanogr., 22, pp. 709-722, 1977.

[2] G.L. Clarke, G.C. Ewing, and C.J. Lorenzen, "Spectra of backscattered light from the sea obtained from aircraft as a measurement of chlorophyll concentration", Science, 167, pp. 1119-1121, 1970.

[3] W.A. Hovis et al., "Nimbus-7 coastal zone color scanner: system description and initial imagery", Science, 210, pp. 60-63, 1980.

[4] R.C. Smith and K. S. Baker, "Optical classification of natural waters", Limnol. Oceanogr., 23, pp. 260-267, 1978.

[5] H.R. Gordon and A. Morel, "Remote assessment of ocean color for interpretation of satellite visible imagery - A review", Lecture notes on coastal and estuarine studies, Springer-Verlag, 114 pp., 1983.

[6] A. Morel, "Optical modeling of the upper ocean in relation to its biogenous matter content (case I waters)", J. Geophys. Res., 93, pp. 10749-10768, 1988.

[7] D. Stramski and C.D. Mobley, "Effects of microbial particles on oceanic optics: A database of single-particle optical properties", Limnol. Oceanogr., 42, 1997, in press.

[8] C.D. Mobley and D. Stramski, "Effects of microbial particles on oceanic optics: Methodology for radiative transfer modeling and example simulations", Limnol. Oceanogr., 42, 1997, in press.

[9] A. Bricaud and A. Morel, "Light attenuation and scattering by phytoplanktonic cells: A theoretical modeling", Appl. Opt., 25, pp. 571-580, 1986.

[10] A. Bricaud, A.-L. Bedhomme, and A. Morel, "Optical properties of diverse phytoplanktonic species: experimental results and theoretical interpretation", J. Plankton Res., 10, pp. 851-873, 1988.

[11] A. Morel and Y.-H. Ahn, "Optical efficiency factors of free living marine bacteria: influence of bacterioplankton upon the optical properties and particulate organic carbon in oceanic waters", J. Mar. Res., 48, pp. 145-175, 1990.

[12] D. Stramski and D.A. Kiefer, "Optical properties of marine bacteria", Ocean Optics X, SPIE Proc., 1302, pp. 250-268, 1990.

[13] D. Stramski and A. Morel, "Optical properties of photosynthetic picoplankton in different physiological states as affected by growth irradiance", Deep-Sea Res., 37, pp. 245-266, 1990.

[14] A. Morel and Y.-H. Ahn, "Optics of heterotrophic nanoflagellates and ciliates: A tentative assessment of their scattering role in oceanic waters compared to those of bacterial and algal cells", J. Mar. Res., 49, pp. 177-202, 1991.

[15] D. Stramski and D.A. Kiefer, "Light scattering by microorganisms in the open ocean", Prog. Oceanogr., 28, pp. 343-383, 1991.

[16] Y-H. Ahn, A. Bricaud, and A. Morel, Light backscattering efficiency and related properties of some phytoplankters", Deep-Sea Res., 39, pp. 1835-1855, 1992.

[17] A. Morel, Y.-H. Ahn, F. Partensky, D. Vaulot, and H. Claustre, "Prochlorococcus and Synechococcus: A comparative study of their optical properties in relation to their size and pigmentation", J. Mar. Res., 51, pp. 617-649, 1993.

[18] D. Stramski and R.A. Reynolds, "Diel variations in the optical properties of a marine diatom", Limnol. Oceanogr., 38, pp. 1347-1364, 1993.

[19] D. Stramski, G. Rosenberg, and L. Legendre, "Photosynthetic and optical properties of the marine chlorophyte *Dunaliella tertiolecta* grown under fluctuating light caused by surface wave focusing", Mar. Biol., 115, pp. 363-372, 1993.

[20] D. Stramski, A. Shalapyonok, and R.A. Reynolds, "Optical characterization of the oceanic unicellular cyanobacterium *Synechococcus* grown under a day-night cycle in natural irradiance", J. Geophys. Res., 100, pp. 13,295-13,307, 1995.

[21] C.D. Mobley, Light and water. Radiative transfer in natural waters, San Diego: Academic Press, 1994, 592 pp.

Light Absorption Measurements of Aquatic Particles: Status and Prospects

Stelvio Tassan
SAI , CEC Joint Research Center, Ispra Establishment, 21020 Ispra, Italy, 0332 789128, stelvio.tassan@jrc.it
B. Greg Mitchell
Scripps Institution of Oceanography, La Jolla CA 92093-0218, USA, 619 534 2687, gmitchell@.ucsd.edu
Dariusz Stramski
Marine Physical Laboratory, Scripps Institution of Oceanography,
La Jolla, CA 92093-0238, U.S.A., 619 534 1802, stramski@mpl.ucsd.edu
Annick Bricaud
Laboratoire de Physique et Chimie Marines, CNRS and Universite P. and M. Curie,
BP 8, 06238 Villefranche-sur-Mer, France, annick@ccrv.obs-vlfr.fr

INTRODUCTION

Optical models in support of environmental or biogeochemistry studies using remote sensors require precise description of the individual contributions of the various substances contained in the upper water layers. This implies a demand for accurate measurements of optical properties, such as the light absorption coefficient of particulate matter suspended in aquatic environments, which includes phytoplankton, organic and inorganic detritus.

Oceanographers use two basic approaches to measure absorption by marine particles. First, in situ instruments such as the ac-9 from WetLabs, Inc., if deployed with and without a particle filter, provide estimates of particulate absorption at several discrete wavelengths as a difference between the measured total absorption and the measured absorption by soluble materials. This approach became available only a few years ago owing to recent development of appropriate instrumentation [1]. The second approach involves concentration of particles on filters with subsequent absorption measurements in the laboratory using standard dual-beam laboratory spectrophotometers. This approach has been used for many years and most data now available on absorption by marine particles has been collected that way. In this paper we will not address in situ measurements; our attention will be focused solely on the latter approach.

Although in recent years considerable progress has been achieved, a general consensus on the most effective methodology for measuring particulate absorption has not been reached. In view of the importance of the topic, the NASA SeaWiFS Project Office sponsored a workshop, held at the Scripps Institution of Oceanography in December 1996, to address methodological issues. The goal of the workshop was to compare measurement protocols adopted by various laboratories, to assess and analyze different methodologies from the point of view of accuracy, ease of use, and practicality, and to provide recommendations for improving the measurements. The present paper briefly reviews some of the methodological issues for measuring light absorption by aquatic particles that were addressed at the workshop. More complete discussion of the workshop results is anticipated to be published in the near future as a contribution to the NASA SeaWiFS Technical Memorandum series.

STANDARD TRANSMITTANCE (T) METHOD

Since the first use some 30 years ago [2, 3], light-transmission measurements on particles retained on glass-fiber filters have been the most common technique for the determination of the light absorption spectrum of particles sampled from aquatic environments. The light-transmission measurements are usually performed by dual-beam spectrophotometers where the light transmitted through the particle-retaining filter is compared with the light transmitted through an unused "reference" filter. The experimental raw data are expressed in terms of the dimensionless optical density (OD), also called absorbance, which is equal to the base 10 logarithm of the inverse transmittance. The spectral range in these measurements covers the visible region and it often extends to the ultraviolet and near infrared.

The use of glass-fiber filters offers one major advantage and one major disadvantage. The advantage is that the filtration allows one to concentrate particles that are naturally too dilute to measure with standard spectrophotometers. A major challenge is the fact that particles are embedded within a highly scattering medium which causes an increase in the optical pathlength resulting in enhancement of the measured optical density. Therefore, one of the most important problems which must be solved is the quantification of the pathlength amplification factor, often referred to as the β factor following the terminology of Butler [4], so that the apparent absorbance can be transformed to standard physical units.

BETA CORRECTION

Quantitative empirical expressions to correct the light-transmission measurements of filter-retained particle

0-7803-3836-7/97/$10.00

absorption for the dependence of β on the measured optical density were first derived by Mitchell and Kiefer [5] with subsequent modifications by Mitchell [6]. A review of more recent work on this subject may be found in [7]. In brief, the correction procedure involves the conversion of the optical density values measured on the filter (ODf) into optical density values of a hypothetical suspension (ODsus) that has the same geometrical pathlength as the filter sample. The geometrical pathlength of the filter sample, X, is simply calculated as the ratio of the volume filtered to the clearance area of the filter. Once ODsus corresponding to a given measured ODf is determined, one can then calculate the absorption coefficient (in 1/m) from the following equation: $a = 2.3\ ODsus/X$. This procedure is applied to each wavelength which eventually yields the spectrum of the absorption coefficient.

After proper scaling for the true geometric pathlength, the enhanced value of ODf compared to ODsus represents the pathlength amplification factor. Almost all work that has been done so far on this relationship is based on laboratory experiments with phytoplankton cultures. It was proposed that this relationship can be expressed in terms of a quadratic equation for a data set that included phytoplankton species ranging in size from 1 μm to 15 μm, and polystyrene beads [6]. The best fit relationship was: $ODsus = 0.392\ ODf + 0.665\ ODf * ODf$. Other investigators have found similar fits, within the anticipated error of the methodology, for phytoplankton larger than 1 μm [7, 8, 9, 10]. However, there is also evidence that this relationship may exhibit significant differences if we consider various species separately [8, 10]. Reference [8] determined much larger β for Prochlorophyte picoplankton species smaller than 1 μm, with the corresponding best fit relationship: $ODsus = 0.291\ ODf + 0.051\ ODf * ODf$. This result suggests a dependence of β on particle size, but one must be aware that there are potentially greater errors in measuring OD for the small Prochlorophytes, because their size is similar to the wavelength of visible light so that their volume scattering function will have relatively more scattering at large angles which are not collected by the instrument measuring optics. More studies on the β amplification factor are needed, as this correction is one of the important sources of error in the particulate absorption estimates retrieved from the filter-pad measurements. The information available at the present time indicates that the assumption of a single relationship ODsus vs. ODf may be inappropriate.

SCATTERING ERROR

In addition to uncertainties associated with the β correction algorithm and its possible natural variability, there is another very important obstacle in achieving accurate absorption measurements of ODsus and ODf. The problem is that no perfect instrument is now available which would provide a very accurate measurement of absorption by scattering samples, including samples of aquatic particles in suspension or on filters. The instruments we use (standard laboratory dual beam spectrophotometers with integrating sphere or scattered transmission accessories) provide a measure of absorption that consists of the true absorption and the fraction of scattered light which is not collected by the measuring optics. If uncorrected for, or if corrected for improperly, this scattering loss may be a source of significant error in the estimates of particulate absorption. Two sources of scattering error must be considered. First, there may be uncompensated scattering losses in the ODf, and second, there are certainly errors in the standard estimate of ODsus since integrating spheres or scattered transmission accessories can not collect all light scattered by a suspension. For accurate pathlength amplification correction, scattering corrections should be made on the ODsus and ODf used to determine the β correction factors.

In principle, the full requirements to accurately account for scattering losses are to measure absorption with an instrument whose geometrical configuration is exactly-defined and known, and to know the spectral volume scattering function (VSF) of the sample. Unfortunately, such full information is never available in routine measurements, primarily because of the lack of the capabilities to determine the VSF. One is thus forced to correct the absorption measurements for scattering error using simplified assumptions about the scattering losses. One of the most common correction procedures is the wavelength-independent correction. This procedure involves subtraction of a constant value from all spectral values of the measured optical density. This constant value is determined at the so-called null reference wavelength in the near infrared where the absorption by particles is assumed to be zero. Of course, this "null point" assumption can be a source of yet another error because some particles in natural assemblages may absorb in the near infrared. Although both the scattering losses may exhibit some significant spectral dependence and the "null point" assumption is questionable, this simple wavelength-independent correction is commonly used to correct the measurements made on both suspensions (ODsus) and filters (ODf).

Two significant methodological advances have recently been published: one proposes a correction for scattering losses in conjunction with the use of the T method [9]; the second describes a technique to transfer the particles to non-scattering glass slides [11] which eliminates the need to correct for pathlength amplification.

TRANSMITTANCE-REFLECTANCE (T-R) METHOD

Tassan and Ferrari [9] expanded the standard T method by including additional measurement of the light reflected by the filter-retained particles. This technique is referred to as the transmittance-reflectance (T-R) method. In this method, the optical density of the particles is derived from measurements of the light transmitted and reflected by the filter-retained particles. The measurements are carried out using an integrating-sphere attachment to the dual-beam spectrophotometer. The data analysis is performed by a theoretical model that eliminates the effect of light backscattering by the particles. This technique is especially suited to situations where light scattering losses for the transmittance mode of the measurement are expected to be large (e.g. samples from coastal waters with high inorganic sediment load). However, because the T-R method is more complex than the standard light-transmission measurement, it requires more effort in minimizing the experimental errors.

Tassan and Ferrari also used a different procedure for the determination of the ODsus vs. ODf relationship. This procedure involves measurements carried out on filter-retained particles (T-R method) and particulate suspension, before and after elimination of the pigment absorption by addition of the oxidizer NaClO (see below for details on the NaClO treatment). Provided that the change in scattered light loss caused by the addition of NaClO to the particle suspension is not significant (assumption supported by experimental and computational evidence), the difference of the optical densities measured before and after the treatment is due only to light absorption. Both ODsus and ODf, used to estimate the pathlength amplification, are presumably better corrected for the error due to light scattering than the same quantities obtained by the standard procedures. On the other hand, the standard method offers the advantage of greater simplicity for practical applications, with a reduced number of experimental error sources.

FILTER-TRANSFER-FREEZE (FTF) TECHNIQUE

Recently a new technique for measuring light absorption by aquatic particulate has been proposed [11]. This technique has been adapted (with some modifications) from the filter-transfer-freeze (FTF) technique developed for microscopic observations [12]. It consists of concentrating particles into a 0.2 μm polycarbonate membrane filter, transferring the filtered material to a glass microscope slide using liquid nitrogen freezing, and finally, measuring the particle absorption spectrum on the slide mounted in the spectrophotometer at the entrance of an integrating-sphere. This procedure avoids the problems associated with the β amplification factor because the particles are not embedded in a highly scattering medium, but instead are retained on transparent glass. The measured optical density spectra are generally in good agreement (within few percent) with the corresponding particle suspension spectra. The overall uncertainty is expected to be below that of measurements on filter-retained particles (mainly because of the lack of the uncertainty associated with the β factor). The time required to complete the FTF measurement is not significantly longer than the time required for the standard T measurement. Although the method has been tested successfully on various algal species and natural samples, one of the possible limitations of the FTF is that the transfer efficiency may not be perfect or sufficiently good for all types of particles. This question must be addressed in further tests. Another limitation at the present time is that the common use of methanol extraction of pigments to estimate detrital absorption [13] is not practical since a parallel sample must be filtered, extracted, and transferred and it is not easy to validate the transfer efficiency of methanol extracted natural particles. Therefore numerical or statistical decomposition methods [14, 15, 16] for separating phytoplankton from detritus are recommended if the FTF procedure is used.

PHYTOPLANKTON VS DETRITAL ABSORPTION

It is of great interest to be able to partition the total particulate absorption into the contribution by phytoplankton and all other particles referred to here as detritus (although this fraction may actually include absorption by heterotrophic microorganisms as well). The partitioning into phytoplankton and detritus is usually obtained experimentally by measuring absorbance of filter-retained particles before and after methanol extraction [13]. This procedure assumes that the treatment has no significant effect on the light scattering by the particles. Also, while methanol extraction is effective for most algal pigments, it fails to extract phycobiliproteins which are present in the ubiquitous cyanobacteria as well as other species including cryptophytes.

A recently proposed procedure, based on the oxidizing action of sodium hypochloride [9], eliminates the pigment absorption by chemical oxidation. It is effective with all phytoplankton types tested (including phycobiliprotein-containing species), either in water suspension or retained on any kind of filter (also cellulose membranes that are dissolved by methanol). The last feature permits the use of NaClO with the 0.22 mm Millipore membrane, to measure the light absorption of small phytoplankton cells or other particles that pass through the standard GF/F glass-fiber filter. Although for best results the NaClO amount and exposure time should be matched to the specific case, the method allows wide tolerance margins. The possibility that NaClO produces new light-absorbing substances was extensively tested. Results to be published in the NASA Workshop report show that there is no appreciable

contamination caused by these substances in the wavelength range 400-750 nm. One must still explore the lowest wavelength limit for NaClO use in the UV region, where some artifacts were found, especially below 350 nm.

Neither method for the elimination of pigment absorption is completely satisfactory since they also can remove the absorption of detrital pigments (e.g. phaeopigments or other detrital pigments generated by grazing), and possibly also some components of the organic detritus. Further, they may modify the light scattering properties of the particulates. This possibility would not affect the pigment optical density derived by the T-R method, since each measurement is individually corrected for light scattering, but it could introduce a systematic error in the pigment optical density obtained by the standard T method if particle scattering is significant compared to scattering by the filter itself (a situation that certainly occurs when the samples have large inorganic sediment load). Alternatively, the discrimination can be achieved using a numerical decomposition method, based on shape analysis of the absorption spectrum [15, 16].

CONCLUSION

The main open problems for estimating particulate absorption with standard bench-top spectrophotometers include quantitative specification of the pathlength amplification factor (β factor) and proper consideration of errors in absorption estimates due to light-scattering by the particles. The observed variability of β with particle type calls for a more careful determination and use of this function. An immediate research priority is to determine if differences that have been observed for cells whose size approximates the wavelength of visible light (e.g. Prochlorophytes) result from increased scattering errors in the estimate of ODsus or ODf, increases in the pathlength amplification, or a combination of both. Also the possible wavelength dependence of the pathlength amplification should be investigated. If scattering errors are either insignificant (particulate assemblages with relatively weak scattering at large angles) or can be minimized with improved methods (e.g. T-R method) it may still be impossible to specify corrections for measurements on filter-retained particles with general validity, because of the possible dependence of the β function on particle type. Thus it may become essential, for accurate work, to determine β for each experimental campaign covering a specific water "type". This prospect implies significant effort that may be impractical for routine work. The absorption error caused by light scattering (particularly backscattering) is an important issue for applications to water containing large amounts of inorganic particles (coastal zone, coccolithophore blooms, etc.). More work is required to understand possible scattering errors associated with the use of the standard T method, as well as the effects of scattering errors on the determination of pathlength amplification corrections.

Regarding instrumentation, an integrating-sphere attachment for dual beam spectrophotometers is highly recommended, in principle, because of its good optical geometry and flexibility for measurements on suspensions or filter-retained particles, the latter in both light-transmission and reflection mode. However, we found during the absorption workshop that the agreement between different manufacturers was not ideal, so careful consideration must be given to the choice of instrumentation. The standard transmittance measurement, although based on a simplified theoretical model, has few error sources and does not require the expensive integrating- sphere attachment (but development of pathlength amplification corrections does require some type of scattered transmission accessory to estimate ODsus). Thus, in situations where the load of strongly scattering inorganic particles is low (oceanic case 1 waters), the simple T method, using published algorithms, may still be an adequate option. The more laborious methods which correct for the effect of light backscattering (T-R method) or eliminate the need to determine β (FTF method), have a sounder theoretical basis. These recently developed methods need further testing for complete assessment of the effectiveness and optimization of the experimental details. The possibility of merging the two methods could be explored.

The available procedures for the discrimination of pigment from detritus absorption are not completely satisfactory (e.g. imperfect selectivity). The asset of methanol extraction is its low sensitivity to the treatment parameters (solvent amount and time); the advantage of NaClO oxidation is the wider application field, including particle suspensions and particles retained on cellulose filters and the effective elimination of absorption by phycobiliproteins.

ACKNOWLEDGMENT

The preparation of this review was supported in part by the NASA SeaWiFS Project.

REFERENCES

[1] C. Moore, J. R. V. Zaneveld and J. C. Kitchen, "Preliminary results from an *in-situ* spectral absorption meter", Ocean Optics XI, Proc. SPIE 1750, 1992, pp.330-337.

[2] C. S. Yentsch, "Measurement of visible light absorption by particulate matter in the ocean", Limnol. Oceanogr. 7, 1962, pp.207-217.

[3] H. G. Truper and C. S. Yentsch, "Use of glass fiber filters for the rapid preparation of in vivo absorption spectra

of photosynthetic bacteria", J. Bacteria 94, 1967, pp.1255-1256.

[4] W. L. Butler, "Absorption of light by turbid materials", J Optical Soc. America 52, 1962, pp.292-299.

[5] B. G. Mitchell and D. A. Kiefer, "Chlorophyll a specific absorption and fluorescence excitation spectra for light limited phytoplankton", Deep-Sea Res. 35(5), 1988, pp.639-663.

[6] B. G. Mitchell, "Algorithms for determining the absorption coefficient for aquatic particulate using the quantitative filter technique", in Ocean Optics 10, Proc. SPIE 1302, 1990, pp.137-148.

[7] J. S. Cleveland and A. D. Weidemann, "Quantifying absorption by aquatic particles: A multiple scattering correction for glass-fiber filters", Limnol. Oceanogr. 38, 1993, pp.1321-1327.

[8] L. R. Moore, R. Goericke and S. W. Chisholm, "Comparative physiology of Synechococcus and Prochlorococcus: influence of light and temperature on growth, pigments, fluorescence and absorption properties", Mar. Ecol. Prog. Ser.116, 1995, pp.259-275.

[9] S. Tassan and G. M. Ferrari, "An alternative approach to absorption measurements of aquatic particles retained on filters", Limnol. Oceanogr. 40, 1995, pp.1358-1368.

[10] B. Arbones, F. G. Figueiras and M. Zapata, "Determination of phytoplankton absorption coefficient in natural seawater samples: evidence of a unique equation to correct the pathlength amplification on glass-fiber filters", Mar. Ecol. Prog. Ser. 137, 1996, pp. 293-304.

11] K. Allali, A. Bricaud, M. Babin, A. Morel and P. Chang, "A new method for measuring spectral absorption coefficients of marine particles", Limnol. Oceanogr. 40, 1995, pp.1526-1531.

[12] C. D. Hewes and O. Holm-Hansen, "A method for recovering nanoplankton from filters for identification with the microscope: The filter-transfer-freeze (FTF) technique", Limnol. Oceanogr. 28, 1983, pp.389-394.

[13] M. Kishino, N. Okami and S. Ichimura, "Estimation of the spectral absorption coefficients of phytoplankton in the sea", Bull. Marine Sci. 37, 1985, pp.620-633.

[14] J. H. Morrow, W. S. Chamberlain and D. A. Kiefer, "A two-component description of spectral absorption by marine particles", Limnol. Oceanogr. 34, 1989, pp.1500-1509.

[15] A. Bricaud and D. Stramski, "Spectral absorption coefficients of living phytoplankton and non algal biogenous matter: A comparison between the Peru' upwelling area and the Sargasso Sea", Limnol. Oceanogr. 35, 1990, pp.562-582.

[16] C. S. Roesler, M. J. Perry and K. L. Carder, "Modeling *in-situ* phytoplankton absorption from total absorption spectra in productive inland marine waters", Limnol. Oceanogr. 34, 1989, pp.1510-1523.

Retrieval of Liquid Water Distribution in Convective Clouds Using Microwave Computerized Tomography

L.P.Bobylev

Nansen International Environmental and Remote Sensing Centre
Korpusnaya Str. 18, 197110 St. Petersburg, Russia
phone: +7 812 235 74 93, fax: +7 812 230 79 94
E-mail: nansen@sovam.com

Abstract -- A new method of retrieving liquid water content (LWC) fields in convective clouds is proposed. It is based on microwave radiometric sounding of clouds using computerized tomography principles. The fundamentals of the method are described; a possible scheme of cloud sounding from an aircraft is proposed. The potentialities of the method are assessed, for which purpose the necessary numerical experiments have been perfomed. In the mathematical sense, the method proposed leads to the solution of an inverse problem. For its solution, a modified iterative method based on algebraic retrieval algorithms has been used. The results of the numerical experiments are presented. The convergence of the iterative process is investigated, and the effect of noise in the initial radiometric data, the number of scanning positions and sounding directions on the accuracy of the retrieval of the method proposed is demonstrated.

Keywords: microwave remote sensing, computerized tomography, convective cloud,liquid water content

Information on the liquid water content (LWC) distribution in convective clouds is of exceptional importance for cloud seeding and for theoretical and applied studies in cloud physics. In principle, this information can be obtained by a new promising technique in remote sensing of cloudy atmosphere - that of passive microwave computerized tomography (PMWCT). Basically, the PMWCT is a product of application of principles and mathematical apparatus from computerized tomography to microwave radiometric measurements and their data analysis. In the present study such a tomographic method is proposed and its capabilities assessed from numerical simulation of a retrieval of LWC distribution through a given section of convective cloud. The simulation is initialized using the data on thermal microwave radiation of this cloud as measured from different positions and directions.

The method proposed makes it possible to retrive the distribution of LWC in a certain section of a convective cloud from its microwave emission measured from several positions in different directions.

Let the microwave radiometer be installed on an aircraft flying under a cloud (Fig.1). Scanning is perfomed upwards in the vertical plane, with different positions of the aircraft under the cloud.

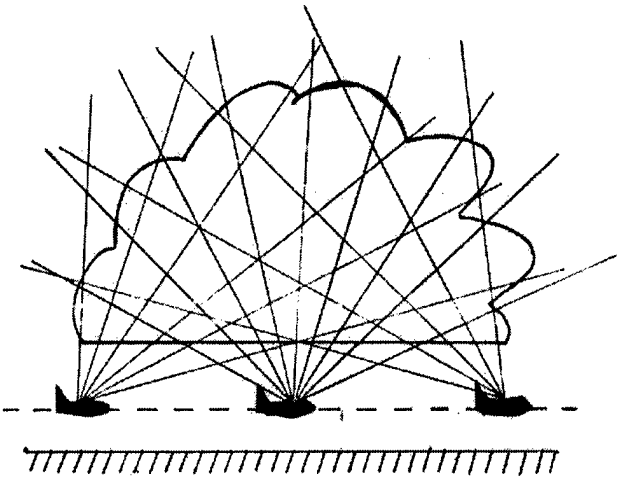

Fig.1. Scheme of sounding of a convective cloud with a microwave radiometer installed on an aircraft.

The fundamental principle forming the basis of computerized tomography (CT) methods is that of retrieval of the internal structure of an object from its projections. In mathematical terms, this is reduced to the retrival of a two-dimentinal function from its integrals taken along various directions. For the problem of the retrival of LWC fields, such integrals are the values of the cloud total liquid water content (TLWC) determined form microwave radiometric measurements in relevant directions:

$$W_k = \int_{L_k} w_k(l)dl, \qquad k=1,2,...,K \qquad (1)$$

where L_k is the length of the k-th ray within the cloud, K is the total number of rays, $w_k(l)$ is the distribution of LWC along the k-th ray (direction) of sighting (the procedure of transition from antenna temperature values registered by the radiometer for each direction of sounding to the values of the cloud TLWC in these directions is described in [1]).

By measuring the cloud microwave emission at different position of the aircraft (radiometer) in various directions, we obtain, as a result, a set of TLWC values which are integrals

0-7803-3836-7/97/$10.00 © 1997 IEEE

along the LWC field in relevant directions. Presenting the problem in a discrete form, one can eventually pass over to a large system of simultaneous linear equations. To solve it, we proposed a modified iterative procedure based on well-known in computerized tomography algebraic reconstruction techniques. The procedure is described in detail in [1]. Information on the boundaries of the reconstructed cloud section is used as a priori data; it can be obtained using other methods.

We consider the results of numerical simulation experiments investigating the procedure proposed. In these experiments, the reconstructed cloud section is given (its boundaries) and the initial LWC field for a given section. After that, the measurement process is modeled, as well as the transition from the antenna temperature values to the cloud LWC. Then the LWC field is retrieved in a given cloud section. The entire scanned field is subdivided into a large set of equal rectangular elements - cells.

The initial retrived LWC field is given by way of simple weighted statistical averaging:

$$w_{ij}^{o} = \sum_{k=1}^{K} \frac{W_k}{L_k} s_{ijk} \Big/ \sum_{k=1}^{K} s_{ijk} \qquad (2)$$

Here w^{o}_{ij} is the initial LWC value in the ij-th cell, s_{ijk} is the path of the k-th ray within the ij-th cell.

The iterative procedure is perfomed which is continued until the value $\sum_{k=1}^{K}\left(\Delta W_k^q\right)^2$ reaches the level of random noise in the initial radiometric data, or until the value ceases to decrease (W^q_k is the discrepancy between the "measured" and retrived at the q-th iteration values of the cloud TLWC in the k-th direction).

The error of retrival of the LWC field can be determined as:

$$\delta = \sum_{i,j}^{I,J}\left(w_{ij} - \hat{w}_{ij}\right)^2 \Big/ \sum_{i,j}^{I,J}\left(w_{ij} - w_{ij}^{o}\right)^2 \qquad (3)$$

where w_{ij} is the "precise" (given) LWC value in the ij-th cell, $\hat{w}_{ij}$ is the LWC estimate obtained as a result of reconstruction. At $\hat{w}_{ij} = w_{ij}^{o}$, this error equals 1, and as the retrieved LWC field approaches the initial one, it tends to 0.

Besides, the error of reconstruction of the LWC field can be characterized by the mean-square error (MSE) of the retrived field in comparison with the "true" (given) one.

In the course of the numerical experiments, a homogeneously distributed noise was introduced in the additive way into the initial TLWC values. The noise level was varied. To ensure the convergence of the iterative procedure smoothing of local LWC values was made according to a scheme suggested in [2]. The sceme is described in detail in [1]. It should be noted that the procedure is a certain filter regularizing the non-correct multidimensional inverse problem under examination.

To illustrate the results obtained, we consider the reconstruction of a test LWC field presented in Fig.2a. This is a 2-cell asymmetrical LWC field. The maximum LWC in the cells is 1 and 2.5 g/m^3, respectively. Fig.2b shows the LWC field reconsrtucted over three scan positions from an aircraft. 700 rays have been used for the retrieval, the noise in the initial radiometric data was 30%. Fig.2c shows the reconstruction error field (the difference between the true and reconstrauted LWC values). The MSE of the reconsrtuction is 0.09 g/m^3.

Fig. 3a presents the dependence of the retrieval error on the number of iterations, which characterizes the convergence rate of the iterative process. In the case of 2,3 and 8 scan positions, from an aircraft, 700 rays (sounding directions) have been used; in the case of 15 positions - 280 rays. The noice was 30%. It follows from the Figure that the retrieval process converges more rapidly with 3 and 8 scan positions.

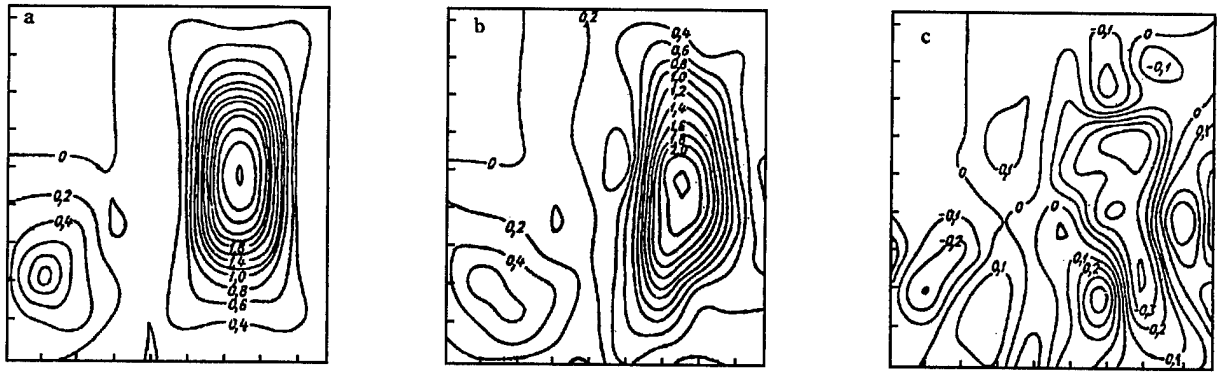

Fig.2. An example of the LWC field reconstruction in the section of a convective cloud: (a) the initial test LWC field (g/m3); b) the reconstructed field; c) the reconstruction error field.

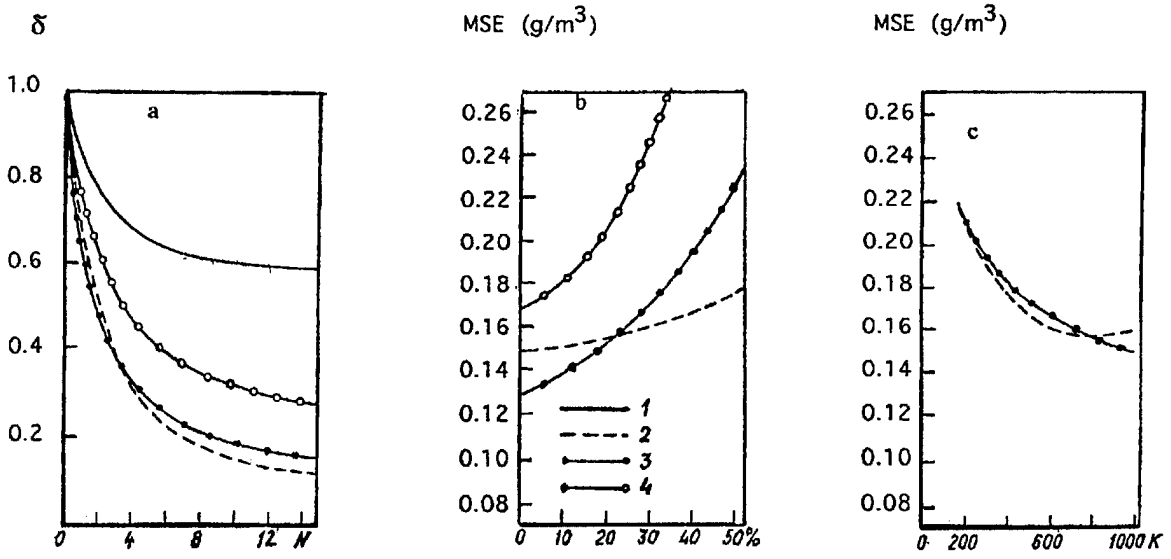

Fig.3. LWC field reconstruction errors: a) dependence of retrieval error on the number of iterations; b) dependence of the MSE of the reconstruction on the noise in the initial radiometric data introduced in the algorithm; c) dependence of the MSE of the reconstruction of the LWC field on the number of rays (equations) used. (1 - 2 scan positions; 2 - 3 positions; 3 - 8 positions; 4 - 15 positions).

Fig.3b presents the dependence of the MSE of the reconstruction on the noise in the initial radiometric data introdused in the algorithm. It can be noted that, in spite of the natural increase of the MSE of the reconstruction, the algorithm is stable enough with respect to the noise in the initial data and yields a reconstruction of a satisfactory quality even with rather high levels of noise.

Finally, Fig.3c shows the dependense of the MSE of the LWC field retrieval on the number of the "rays" (equations) used. The noise level is also 30%. It can be very well seen that, as the number of equations grows, the MSE of the reconstruction is at first decreasing rapidly, than slower. This can be accounted for by the fact that the introduced noise plays more negative role in comparison with the positive role of useful information on the LWC field incoming from new additional sounding directions.

It should be said in conclusion that the paper shows the good prospects of using passive microwave computerized tomography (PMWCT) for retrieval of LWC fields in convective clouds. Even with three scan positions (e.g.,from an aircraft upwards), a good enough quality of retrieval of LWC fields can be achieved. The retrieval error can there be not more than 10% of the maximum LWC value in the cloud section.

REFERENCES

[1] Stepanenko V.D., Shchuckin G.G., Bobylev L.P., Matrosov S.Yu., Microwave Remote Sensing in Meteorology, Leningrad: Gidrometeoizdat, 1987, 284p.

[2] Herman, G.T., Image Reconstruction from Projections. The Fundamentals of Computerized Tomography, New York: Academic Press, 1980

Low Cost Digitalization of an X-band, non Coherent Weather Radar

Gaspare Galati[1] , Giorgio Russo[1] , Guillame Dargaud[2] , Gabriele Pavan[1]

[1] Università degli Studi di Roma "Tor Vergata" and Centro "Vito Volterra"
Via della Ricerca Scientifica 00133, Roma - Italy -
Phone: +39 6 72591, Fax: +39 6 2026266, e-mail: galati@disp.utovrm.it
[2] Istituto di Fisica dell'Atmosfera (IFA/CNR)

Abstract: Meteor 200 is an X-band non coherent weather radar completely implemented by means of analog technology. To enhance his operation, a processing system based on a digital signal processing board in a personal computer has been devised. The system has been realized using a low cost Digital Signal Processor (DSP) Printed Circuit Board based on the TMS 320 C30 (Texas Instruments) device and supplied by the radarmeteorology group of the IFA/CNR (Institute for Atmospheric Physics/National Council of Research, Italy). The printed circuit board accepts as an input the radar trigger, the radar video and the clock; the latter can be internal or external to the radar. The board performs A/D conversion, acquisition and processing of radar signals from 500 to 900 range bins per sweep; the processing permits the computation of reflectivity factor by azimuth averaging either on log scale, or on (reconstructed) linear scale, or both. In this way a flexible signal processing is obtained, very suited to research purposes. The architecture has been implemented in his hardware and software parts and some test results have been obtained.

THE METEOR 200 WEATHER RADAR

Meteor 200 is an X- band analog weather radar derived from the ORION family of tracking radars (designed and manifactured by the company Selenia, Roma, Italy) and very much used in the past for weather analysis around both civilian and military airports and for research purposes. An IFA/CNR Meteor 200 has been installed on Tor Vergata area, south west of Rome, for cooperative research of IFA/CNR and of Tor Vergata University.

The main characteristics of Meteor 200 are shown in Tab.1.

As any analog weather radar, Meteor 200 is unable to do quantitative measurements as reflectivity factor and rainfall rate: the only output is an analog video and the operational controls to the radar system are manually adjusted by a console. Two displays show the Plan Position Indicator (PPI), the Range Height Indicator (RHI) and the Range Elevation Indicator (REI).To perform estimates of the reflectivity, then radar must be " digitized".

Meteor 200 Parameters	
ANTENNA	Parabolic Reflector
Reflector Diameter	2 m
Beam Width	1.25°
Gain	41 dB
TRANSMITTER	Magnetron
Power	200 kW peak, 140 W ave.
Pulse width (short - long)	0.5 μs - 3 μs
Pulse Repetition Frequency	1200 Hz (s.p.)- 240 Hz (l.p.)
Operating Frequency	9345-9405 MHz (9375 nom.)
RECEIVER	Logarithmic

Tab. 1 Meteor 200 specifications.

THE DSP BOARD

A new digital radar acquisition has been designed employing a PC430F board based on the DSP floating point device TMS 320 C30. The DSP device TMS 320 C 30 is a 32 bits device at a clock frequency of 32 MHz. C-language compiler, debugger tools and library allow an easy programming. It has a 12 bit A/D converter on the chip.

The main components of the PC430-F card are shown in Fig. 1.

As input signals the circuit board accepts:
1) the analog radar signal (analog input channel in Fig. 1);
2) external clock (max. 10 MHz);
3) external trigger (radar PRF).

The analog input is converted in digital format by the 12 bit A/D converter. The sampling frequency and the acquisition mode are adjusted setting the 82C54 timers.

The board is employed to achieve simultaneously:
- the A/D conversion;
- the pulse integration;
- the radar signal processing (estimate of the reflectivity on log or linear scale);
- the registration of the reflectivity matrix on the Personal Computer (PC) (hard disk, RAM).

Simultaneous operations are possible using a double buffer; in this way, while the first buffer is filled with samples coming from the FIFO (4 Kword), the second sends data to the processing routine. After processing data are sent to the PC.

0-7803-3836-7/97/$10.00 © 1997 IEEE

The instruction cycle time is 60 ns (i.e. 16.6 MIPS that can be extended to 33 MIPS by parallel operation). The RAM has 2 Kword on chip, the ROM , 4Kword.

A shared memory called Dual Port RAM, DPR, with dimension 128Kword is the interface between the board and the Personal Computer.

A memory expansion (8 Kword), faster than DPR, stores the samples of the acquisited signals and the "look up table" allowing linearization of the receiver characteristics, as explained later.

The functions are implemented as follows:

- acquisition and processing of radar signals by means of a software running on the PC430-F board and compiled by the C-compiler C30 and the assembly compiler ASM30.
- Storage of the data matrix containing the estimate of the radar reflectivity factor for each resolution cell by a software running on the Personal Computer and compiled by the Visual C/C++ , using the HSA RTL library.

In such a way an efficient parallel operation has been achieved.

SIGNAL PROCESSING

Purpose of signal processing is to estimate the radar reflectivity for each resolution cell, with azimuthal integration to reduce the variance of the estimate. The processing functions, shown in Fig. 2, are described in the following.

The radar echo, with power $P_{dBm,in}$, is the input to the logarithmic receiver, whose output voltage, V_{out}, has a dynamic range from 0 to 2.5 V. The A/D converter on the board has an input dynamics of 10 V (-5, +5 V or 0, 10 V). In order to avoid a video amplifier, a reduction of the accuracy of the digital representation of signals has been accepted with an operation equivalent to a 10 bit converter, in which the maximum output of the radar (i.e., 2.5 V) corresponds to the digital value 1024.

The characteristics of the logarithmic receiver is well approximated by a straight segment in the plane: input power (dBm) - output voltage (V), -110 dBm corresponding to 0 V and - 30 dBm corresponding to 2.5 V.

After A/D conversion, processing continues in parallel, i.e. on the digitized signal samples and on the same samples linearized by means of a look up table written in the fast expanded memory to avoid further charge of the CPU of the board. The comparison between reflectivity estimated in linear scale and in logarithmic scale can give information about the type of radar target.

The ensuing phase of the processing (Processing 1 of Fig. 2) is the azimuthal integration to reduce the variance of the estimate. The number of integrated pulses, K, is a system parameter (note that the antenna of METEOR 200 rotates at 1, 2, ... 5 RPM corresponding to 250, 125,... 50 pulses in the beam in the short pulse mode and 50, 25,...10 pulses in the long pulse mode).

The final processing (Processing 2 of Fig. 2) uses the weather radar equation to evaluate the radar reflectivity factor Z, both in logarithmic and in linear scale; in the logarithmic scale, the bias due to the logarithmic law before averaging is corrected by subtraction of a fixed quantity.

The equation implemented to determine the reflectivity factor (dBZ) is the following:

$$Z_{dBz} = -104.5783 + 20\log(R_{Km}) + 0.078125 \cdot \overline{P}_{num,dBm}$$

where R_{Km} is the distance (in Km) of the resolution cell under examination and $\overline{P}_{num,dBm}$ is the average power in dBm after the integration of pulses.

ANALYSIS OF THE RESULTS

Before using the PC 430-F board connected to a radar system it is necessary to test the acquisition and all other functional blocks; this test is done sending known signals (as close as possible to the rain echo) to the board and subsequently analyzing the output by debugger tools.

A suitable signal generation system, based on another Personal Computer with the AT-MIO 16E card, supplies the relevant test input. The LabWindows-CVI software supplies a graphic interface to allow the user to change the parameters of the generated signals, i.e. trigger, clock, number of integrated pulses K, output rate, dimension of the radar cell, characteristics of the receiver.

The following types of test have been done:

- Performance analysis and optimization. The aim is to find the parameters of the acquisition and processing software that guarantee the best performance of the board in the various operating conditions of the radar. Moreover, to find the most critical functions of the software, i.e. the ones calling for more CPU time, and to optimize them.
- Acquisition and processing tests. The aim is to check that acquisition and processing are done correctly. To this end, the following trials have been done

  - processing of a deterministic signal with known amplitude and repetition frequency (sawtooth and others);

  - processing of a Rayleigh-distributed random signal and comparison of its statistics with the theoretical ones;

  - comparison between the processing performed by the PC 430F board and the processing performed by the Personal Computer with the same input data.

A sample result is shown in Figs. 3 and 4. A rain echo (i.e. a Rayleigh-distributed signal), with constant intensity equal to 20 dBZ, has been generated by means of the AT-MIO16E (LabWindows/CVI) board. The simulated echo power at the input of the radar receiver is proportional to $1/r^2$ (r being the distance).

After the simulation of the whole reception and processing chain described in Fig. 2, an estimate of the reflectivity (both in linear and in logarithmic scale) is obtained. Statistical analysis (with computation of mean value and of standard deviation) of data show good agreement with the theoretical values.

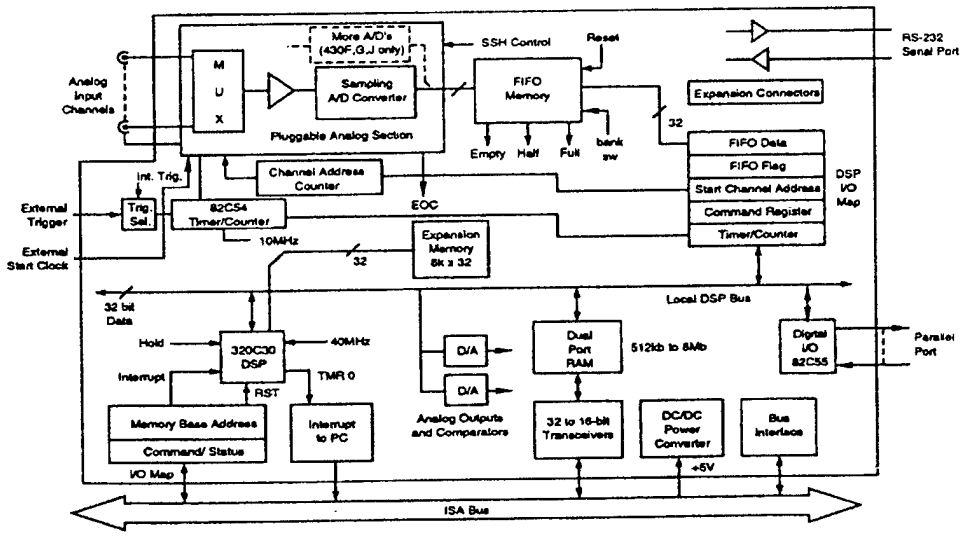

Fig.1 Block diagram of the PC430-F board.

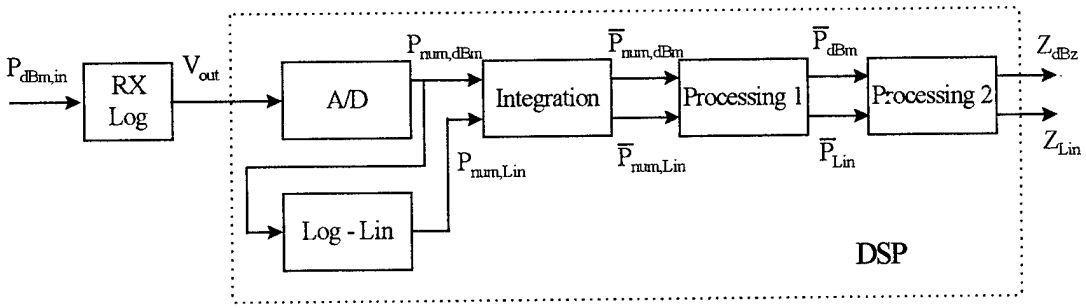

Fig. 2 Block diagram of the signal processing.

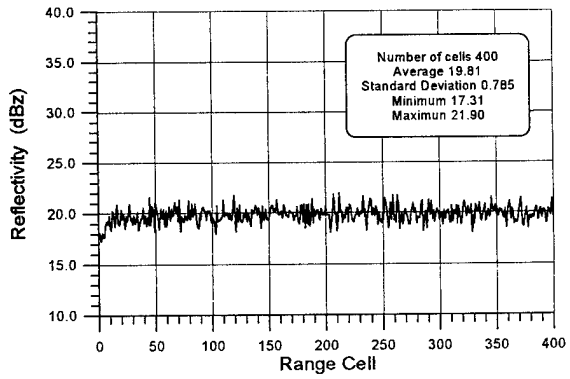

Fig. 3 Estimate of the reflectivity by the PC430F board (Z=20 dBz).for a signal generated by the AT-MIO 16E board, log scale.

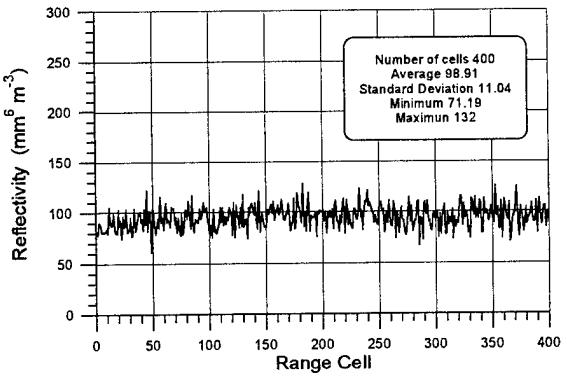

Fig. 4 Estimate of the reflectivity by the PC430F board (Z=100 mm^6 m^{-3}) for a signal generated by the AT-MIO 16E board, linear scale.

ACKNOWLEDGEMENT

The authors wish to thank the IFA / CNR for making this work possible: the radarmeteorology group of IF A (in particular Dr. Gorgucci) selected and provided the PC 430F board and Dr. Mastrantonio and Mr. Viterbini provided very useful help in the development of the system.

Environmental Quality and Changes: A View From NDVI in Hong Kong

Tung Fung
Department of Geography
The Chinese University of Hong Kong
Shatin, New Territories
Hong Kong
Phone: (852)-2609-6535
Fax: (852)-2603-5006
email: tungfung@cuhk.edu.hk

ABSTRACT

Normalized difference vegetation index (NDVI) has been a common tool for the studies of vegetation vigor and multitemporal land cover changes. While it can reflect these on a per-pixel basis, aggregating NDVI on planning units allow us to study environmental quality and changes in terms of the amount and condition of vegetation and green space in a city. In this study, NDVI images were extracted from multitemporal SPOT images from 1987 to 1995 in Hong Kong. NDVI mean values were aggregated at the tertiary planning unit (TPU) level and studied. They are highly associated with high NDVI features such as woodland and high scrub. They have a high correlation with crowdedness within the city. TPU of constant increase and decrease in NDVI mean values reveal the effect of new landscape design and the pressure of urban encroachment respectively.

INTRODUCTION

Rapid economic development and urban expansion has brought prosperity to the metropolitan city of Hong Kong in the last three decades. Yet, there has been critical concern about her environmental quality due to pressure exerted by the increases in population, vehicles, urban land conversion and inevitably increases in sewage, waste and air pollutants. The Royal Observatory has reported a decreasing visibility in the last 30 years. The Environmental Protection Department of the Government is also closely monitoring the quality of air and water. Most of these data, however, are based on point stations scattered in the territories of Hong Kong. It is difficult to capture an entire image of the environment. Undoubtedly, remote sensing data can alleviate this problem.

Most satellite remote sensors acquire spectral data in the visible and near infrared bands. There has been many studies in the application of these data in the modelling and monitoring of water quality and aerosal content in the air. In cities built with concrete and asphalt, an important component in assessing environmental quality is the amount and quality of green space. Remote sensing imagery, e.g. color infrared air photographs has long been used to study housing quality and differentiate housing types [1]. Most cities evolve through encroaching on the surrounding rural areas. How these rural green areas change and the rate at which they reduce in time are important information for urban planning and management. On the other hand, the provision of a substantial area of green space is essential to the livelihood within the city.

Vegetation indices derived from satellite imagery have been used in studying canopy characteristics such as biomass, leaf area index, productivity and vegetative land cover [2]. In this paper, normalized difference vegetation index (NDVI) derived from SPOT HRV data is used to study the rapidly changing environment of Hong Kong. It also attempts to explore the possibility of using multitemporal NDVI data aggregated at tertiary planning unit (TPU) level as an indicator of environmental quality with particular reference to the amount and condition of vegetation.

DATA AND METHODOLOGY

Four SPOT HRV multispectral data acquired on 01/14/1987, 12/21/1991, 12/16/1993 and 02/05/1995 were available for the study. All images were acquired during the dry season. They were geometrically corrected with reference to the Hong Kong metric grid system. Digitized topographic map sheets at 1:20,000 scale from the Government Land Information Centre was available for the selection of ground control points. All images were resampled at 20m X 20m spatial resolution. The entire image dimension was 3000 X 2400 pixels. For temporal analysis, the images were radiometrically adjusted using a relative calibration method [3]. Since the 1993 image had the smallest incidence angle and the best quality, it was chosen as the reference image. A total of 19 points representing scene-invariant dark and bright objects such as concrete playground in parks, beaches, airport runway were chosen for deriving the regression models. NDVI for individual images were then derived in real format.

CONVENTIONAL CHANGE DETECTION ANALYSIS

Most land cover change detection analyses are operated on a per-pixel basis. Through comparing the magnitude and direction of changes in digital numbers, change detection techniques are able to highlight areas of change or identify the nature of change by yielding a from-to matrix via image classification. In this paper, two conventional change detection techniques were also applied.

(1) Image differencing

Image differencing is the simplest and effective change detection techniques in detecting changes from images. Three differenced images were produced for the analysis:

$DIF_{9593} = NDVI_{95} - NDVI_{93}$ (Fig.1)
$DIF_{9391} = NDVI_{93} - NDVI_{91}$
$DIF_{9187} = NDVI_{91} - NDVI_{87}$

(2) Principal components analysis (PCA)

Principal components analysis is also commonly used for change detection. Applying the linear transformation to a merged multitemporal data, minor PCs are able to identify areas of changes. In this study, the 4 NDVI images were subject to a PCA. Table 1 illustrates the eigenstructure of the PCs.

Table 1 Eigenstructure of Principal Components

	PC1	PC2	PC3	PC4
$NDVI_{95}$	0.4525	-0.3798	-0.5096	-0.6257
$NDVI_{93}$	0.4708	-0.2963	-0.3086	0.7716
$NDVI_{91}$	0.5199	-0.2807	0.7999	-0.1051
$NDVI_{87}$	0.5508	0.8302	-0.0728	-0.0464
eigenvalue	5448.85	90.66	68.45	36.81
% var	73.82	9.52	8.27	6.07

These change detection images are effective in locating areas of changes which incur a significant change in the NDVI values. For the differenced images, a white tone identifies areas of increase in NDVI e.g. reclamation, vegetation regrowth after hill fire, whilst a dark tone reveals the reversed pattern e.g. reduction in vegetation amount due to land conversion or hill fire. Differenced images of different periods reflect the extent of reclamation and land conversion for urban expansion of those corresponding periods. For the PCs, similar information is extracted. PC2 highlights changes between 1987 and the 1990s. PC3 locates changes between 1991 and 1993/95 whilst PC4 reveals more recent changes between 1993 and 1995.

It can be shown that conventional change detection techniques are effective in identifying salient changes which involves substantial changes in NDVI values and extensive areas. Nevertheless, the study of changing environmental quality in terms of the amount and condition of vegetation may involve changes which are subtle and less abrupt.

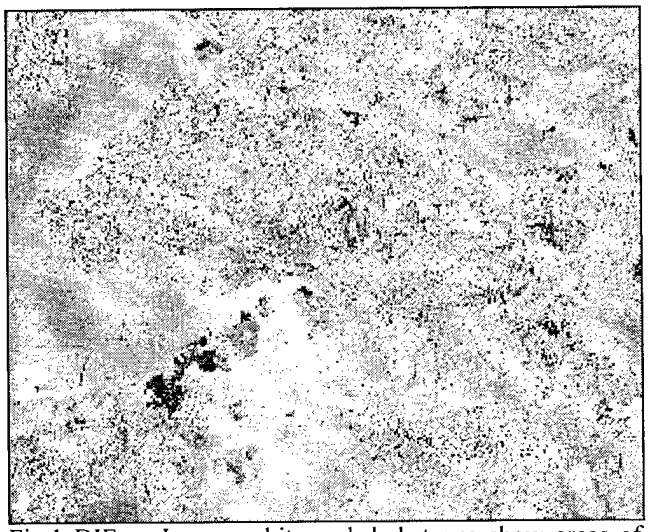

Fig.1 DIF_{9593} Image: white and dark tones show areas of land cover changes

NDVI at TERTIARY PLANNING UNIT

The mean values of NDVI within each TPU was computed from images of different years. Basically, the resultant image expresses NDVI at an aggregate level. TPU with luxuriant features of high NDVI values such as woodland should have a a high mean value. In old urban areas where vegetation is scarce and thus low NDVI values, the mean value is low.

In order to examine the relationship between the NDVI mean values and land covers, an ecological database published by the World Wide Fund for Nature in 1993 [4] was used to study with the 1991 NDVI mean values. This ecological database was produced based on air photo interpretation with 16 land cover classes. The proportion of each land cover was yielded for each TPU. A stepwise multiple regression model was established for the 1991 NDVI mean values as follows:

$NDVI_{TPU91}$ = 0.1726
+ 0.0046 high scrub
+ 0.0018 high scrub/grass
+ 0.0031 woodland
+ 0.0034 plantation
- 0.0025 water
- 0.0036 high density urban
- 0.0082 barren land

The r^2 is 0.9115. This model proved that the NDVI mean values at TPU level is highly and positively associated with high NDVI vegetative features in particular high scrub and woodland whilst other low NDVI vegetative features such as grass and low scrub are not significant.

The NDVI mean data was also studied in terms of its relationship with social areas. Based on the 1991 population census, 24 demographic, social and economic variables were extracted for a factor analysis. Seven factors were extracted and labelled as: 1. purchasing power; 2. working population; 3. household size; 4. elderly population; 5. crowdedness; 6. young family and 7. home ownership. A simple correlation analysis among these factors and the 1991 NDVI mean data shows that most factors have a low correlation except Factor 5 crowdedness which r is -0.6314 (significant at 0.05). Primarily, old and highly densed urban areas are more crowded where less vegetation is found. This result shows that the NDVI mean data can be an important indicator for the study of social area as well.

Lastly, to study the changing environment, the four NDVI mean data were compared. Undoubtedly, the NDVI mean values of many TPU fluctuates between years. It is however important to identify those TPU where there had been a constant trend of increase or decrease in the NDVI mean values. Fig.2 illustrates these two groups of TPU. Unlike the conventional change detection analysis, aggregating NDVI at TPU level reveals that areas of constant increase in NDVI mean values scattered within the old urban areas. These areas more or less reflect the urban renewal effect under which new housing estates were constructed with an improved landscape design and more green vegetation planted. In contrast, many TPU in the New Territories experienced a constant decrease in NDVI mean values which are mostly rural areas undergone urban land conversion and highway construction.

CONCLUSION

Conventional change detection techniques are able to highlight the exact location of land cover changes based on NDVI images. Aggregating NDVI data to planning units allow integrated studies with census and other socioeconomic data. In this study, it reveals the impact of urban land development on rural area as well as the effect of improved landscaping in existing urban area which are not effectively discerned in conventional change detection analysis.

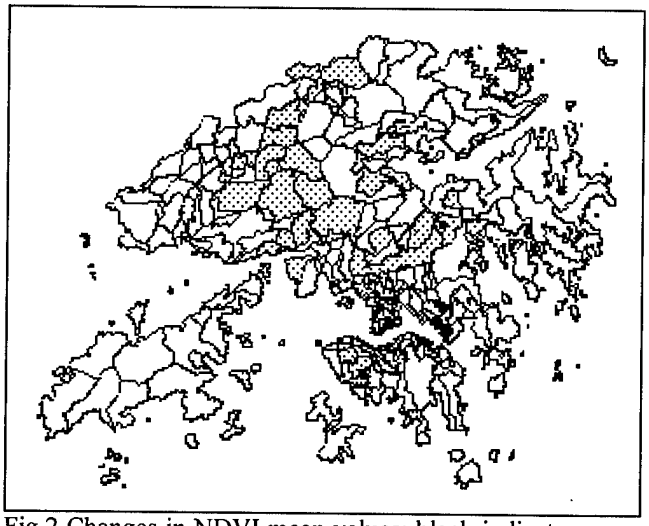

Fig.2 Changes in NDVI mean values: black indicates areas of constant increase; shaded pattern indicates areas of constant decrease.

ACKNOWLEDGMENTS

This research is supported by Hong Kong UPGC earmarked research grant CUHK9/93H.

REFERENCES

[1] C.P. Lo, *Applied Remote Sensing*, Longman, New York, 1986.

[2] J.R. Jensen, *Introductory Digital Image Processing: a Remote Sensing Perspective*, 2nd edition, Prentice-Hall, New Jersey, 1996.

[3] D.W. Eckhardt, J.P. Verdin, and G.R. Lyford, "Automated Update of an Irrigated Lands GIS Using SPOT HRV Imagery", *Photogrammetric Engineering and Remote Sensing*, 56 (11), 1515-1522, 1990.

[4] J.M. Ashworth, R.T. Corlett, D. Dudgeon, D.S. Melville and W.S.M. Tang, *Hong Kong Flora and Fauna: Computing Conservation*, World Wide Fund for Nature Hong Kong, Hong Kong, 1993.

Urban Planning Using Data Fusion of Satellite and Aerial Photo Images

Philip Cheng[1] and Thierry Toutin[2]

[1] PCI Enterprises 50 West Wilmot St. Richmond Hill, Ont, Canada, L4B 1M5
Phone (905)764-0614 / Fax (905)764-9604 / Email: cheng@pci.on.ca

[2] Canada Centre For Remote Sensing, 588 Booth Street, Ottawa, Ont, Canada, K1A 0Y7
Phone (613)947-1293 / Fax (613)947-1385 / Email: toutin@ccrs.emr.ca

Abstract - Urban planning using data fusion of different satellite and aerial photo images can be very useful. However, multisource data fusion requires geometric and radiometric processing, adapted to the nature and characteristics of the data. In this way the best information available from each image is preserved in the composite image. With the increased resolution of satellite and aerial photo images (5m and less), the off-nadir viewing angle of the satellite sensor (greater than 20 degrees), and the multi-source data available (such as SPOT, RADARSAT, and IRS), a general and accurate photogrammetric method which can deal with different satellite images and an accurate photogrammetric method for aerial photos are needed. For satellite images, a rigorous method developed at the Canada Centre for Remote Sensing (CCRS), Natural Resources Canada, which takes into account the nature of the data can be used. For aerial photos, the method of space resection by collinearity can be used. This paper will presents data fusion results using SPOT, RADARSAT, IRS satellite images and an aerial photo. The results are sharp and precise, which enables a better and easier interpretation for urban planning.

INTRODUCTION

The improvement in the speed and affordability of computers, the increased resolution of scanned aerial photos and satellite images, and the integration of cartographic features with GIS data (raster and vector) have revolutionized the process of topographic mapping. A growing number of applications require the co-registration and fusion of different satellite images and/or aerial photos with maps. This requires geometrically corrected images, accurately registered to a common reference system and pixel spacing. Therefore, the knowledge about the viewing geometry and the DEM is required. The correction process is called orthorectification, and the resulting image-based map is the orthoimage. Because they are planimetrically correct, orthoimages can be used as maps for direct measurements of distances, angles, positions, and areas without the necessity of corrections for image or terrain induced distortions. The combined orthoimages together with ground truth information can significantly improve data extraction and collection in areas such as urban planning.

Urban planning using digital aerial photos has become very popular in the past several years. The biggest obstacle with satellite images for urban planning was the resolution. The highest resolution commercial satellite available was SPOT (10m panchromatic). However, in the past several years, new satellites with higher resolution were launched. For example, the IRS-1C satellite with 5.8m panchromatic resolution, and the RADARSAT satellite with 8-9m resolution in fine beam mode. In addition, satellites with higher resolution (such as the EarlyBird satellites with 3m and 1m resolution) will be launched in future. With the high resolution satellites available, it is now possible to use satellite images for urban planning.

There are several advantages to creating orthoimages using satellite images for urban planning: (1) a satellite image covers a much bigger area in comparing to an aerial photo. Hence, less costs and less ground control points (GCPs) are needed, and (2) for areas which are always covered with clouds, the use of SAR imagery (which penetrates through clouds) can eliminate this problem.

0-7803-3836-7/97/$10.00 © 1997 IEEE

In order to create accurate orthoimages from satellite or aerial photos, several factors have to be considered: (1) the accuracy of the geometric modelling relating the uncorrected image coordinate to the ground reference; (2) the accuracy of the ground control points; and (3) the availability of the DEM and its quality. This paper mainly focuses on the geometric modelling of satellite and aerial photo images.

GEOMETRIC MODELLING

For scanned airphotos, space resection by collinearity is the preferred method of determining the parameters of exterior orientation. This is a purely numerical method that simultaneously yields six independent parameters expressing the space position and angular orientation of a tilted aerial photo. To utilize this method, the calibrated focal length of the camera lens and a minimum of three GCPs with X, Y, and Z ground coordinates must be known. This method permits the use of a redundant number of GCPs; hence, least squares computational techniques can be used to determine most probable values for the six parameters. In addition, the method can be extended to multiple blocks of photos by using a simultaneous bundle adjustment method. Details of the collinearity method can be found in [1].

For satellite images, the collinearity condition used is based on principles related to photogrammetry, orbitography, geodesy and cartography developed at CCRS [3]. This model is based on the collinearity method which reflects the physical reality of the complete viewing geometry and reflects the following distortions that may occur during image formation:

1. distortions due to the platform (position, velocity, and orientation);
2. distortions due to the sensor (orientation, integration time, and field of view);
3. distortions due to the Earth (geoid, ellipsoid, and relief); and
4. distortions due to the cartographic projection (ellipsoid, and cartographic reference)

The greatest advantage of this satellite modelling method is that it has been applied to VIR data (Landsat, SPOT, IRS, MOS), as well as SAR satellite data (ERS, JERS-1, SIR-C and RADARSAT) and can easily be modified to support other satellite and airborne sensors. The model adjusts simultaneously if more than one input image is used, which improves the relative accuracy of the positioning of superimposed images. Based on good quality GCP coordinates, the accuracy of this modelling was proven to be one-third of a pixel for VIR satellite images and one resolution cell for SAR images. The algorithm has been tested at the CCRS and Canada Centre for Topographic Information and meets the specifications of Canada's National Topographic Database to update digital topographic data at 1:50000 scale using SPOT panchromatic data. More details of the method can be found in [2,3].

Both aerial photo and satellite geometric modelling methods have been implemented into PCI's OrthoEngine photogrammetric and satellite edition software packages. The packages include data input, GCP collection, geometric model calculation, orthoimage generation, and mosaicking. In addition, the packages can be executed on most workstations and personal computers.

TEST IMAGES

To test the method using satellite images and aerial photo, four different satellite images and one aerial photo of Irvine, California were used.

- a raw panchromatic SPOT-HRV (10.0m resolution)
- an orbit-oriented IRS-1C (5.8m resolution resampled to 5.0m pixel spacing)
- a georeferenced RADARSAT fine beam (9.0m resolution resampled to 6.25m pixel spacing)
- a 1:60000 scale aerial photo scanned at 300 dots per inch (5.0m pixel spacing)

PCI's OrthoEngine packages were used to test the method. Ten GCPs and seven independent check points (ICPs) were collected from each image using USGS 1:24,000 scale maps. The ICPs were collected inside the area bounded by the GCPs and were not used in determining the geometric model and its parameters.

RESULTS

Table 1 shows a summary of the results using the GCPs and ICPs. The RMS residuals of the GCPs are within 1 pixel and the RMS errors of the ICPs are within 1 to 2 pixels. It should be noted that in this test the accuracy of the geometric modelling is limited by the accuracy of the GCPs obtained from the maps. The good results reflect the advantage of using the photogrammetric method which globally corrects the entire image and takes into consideration the distortions due to relief. With the accuracy of the results, it is possible to perform data fusion of different satellite image and aerial photos for urban planning with accuracy of about 5m.

CONCLUSIONS

It has been shown that data fusion using photogrammetric methods for satellite images and aerial photos can produce accurate results. To create orthoimages for data fusion, the model developed at CCRS can be used for different satellite images, and the space resection by collinearity method can be used for aerial photos. With the high resolution and accuracy of the orthoimages, the results can be used in areas such as urban planning.

ACKNOWLEDGMENTS

The authors would like to thank PCI Enterprises for providing all the support for this work. CCRS for providing the satellite modelling algorithms and technical assistance, RADARSAT International, SPOTIMAGE, and EOSAT company for providing the satellite images.

REFERENCES

[1] Wolf, Elements of Photogrammetry With Air Photo Interpretation and Remote Sensing, 2nd Ed., McGraw-Hill Book Co., 1983.

[2] Th. Toutin, "Multisource data fusion with an integrated and unified geometric modelling", EARSel Advances in Remote Sensing, Vol. 4, No. 2-X, 1995.

[3] Cheng and Th. Toutin, "High Accuracy Data Fusion of Satellite and Airphoto Images", 1995 ACSM/ASPRS Annual Convention & Exposition Technical Papers, Charlotte, North Carolina, Feb. 27-Mar 2, 1995.

Table 1: Geometric modelling results using ground control points (GCPs) and independent check points (ICPs) with photogrammetric methods for different satellite images and aerial photo.

Image	Aerial Photo		IRS		SPOT		RADARSAT	
GCP RMS Residual (m)	2.9	4.5	1.7	4.2	4.6	3.4	3.2	3.0
MAX Residual(m)	-0.2	7.6	-2.6	8.1	8.1	2.1	6.5	1.7
ICP RMS Error (m)	6.6	6.5	8.4	5.0	6.7	7.4	5.2	6.6
MAX Error(m)	4.4	-8.8	6.0	-9.3	5.4	7.9	-6.0	9.9

Information System for Monitoring the Urban Environment Based on Satellite Remote Sensing: Shanghai as an Example

Yun Zhang
Department of Cartography, Free University of Berlin
Arno-Holz-Str. 12, D-12165 Berlin, Germany
Tel.: +49 30 8383892, Fax.: +49 30 8386739, Email: yzhang@fpk.tu-berlin.de

Abstract -- A software package was developed for the purpose of monitoring the urban environment. It was tested in the entire urban area of Shanghai using TM and SPOT pan data. The water areas, houses, skyscrapers and green areas in the city were extracted. The TM and SPOT pan data were merged through different methods and compared. The accuracy of the extracted water areas is over 95% and that of the recognized skyscrapers is over 90%. The user accuracy of the extracted houses was increased by 30% and that of green areas by 11% .

INTRODUCTION

Satellite remote sensing is used world wide for the observation of the macroscopic environment of the earth providing continuous and actual information in a cost and time saving method. Despite numerous attempts satellite image data have unfortunately not been successfully applied to the detailed observation such as monitoring of the urban environment and its changes. The reasons for it are:

- The objects in urban areas are very complicated and they are shown more through their structures than through their spectral reflection properties.
- The spatial resolution of satellite image data is currently too crude to interpret the urban relationships.
- The digital classification of spatial features is still a difficult problem to solve [1, 2]. This has made the application of satellite remote sensing for use in urban investigation more or less impossible.

Without current data of the urban environment situation an environment-friendly urban planning is hardly possible. Satellite remote sensing has displayed tremendous potential to obtain these data, especially as far as it is concerned that satellite data with up to 1 m spatial resolution are going to be available in the near future [2, 3]. The problem is just that the digital classification of spatial features need to be improved [4]. For this purpose a specific software package has been developed in this project, which consists of several digital processes such as merging of multisensor data, spectral analysis, texture analysis, segmentation and pattern recognition for the purpose of classifying objects according to their spatial features.

This software package is compatible with the program ERDAS-IMAGINE. By combining the two programs a suitable information system for monitoring the urban environment has been developed.

The developed software package was tested in the entire urban area of Shanghai, China, (about 30 km × 30 km) using Landsat TM data and SPOT pan data as source data.

EXAMPLES OF THE SPECIFIC FUNCTIONS OF THIS SOFTWARE PACKAGE

Completion of water areas

In most cases water areas in urban regions cannot be completely extracted through multispectral classification. This is due to: (1) Many areas (e.g. shadows, dark roofs, damp places) display similar spectral features as water on the images, no matter which band combination is used; (2) Rivers in a city are frequently not broad enough, consequently not all the pixels of the rivers clearly display the spectral feature of water. Fig.1 shows the result of the multispectral classification of TM data. It is obvious that: (1) Many housing areas

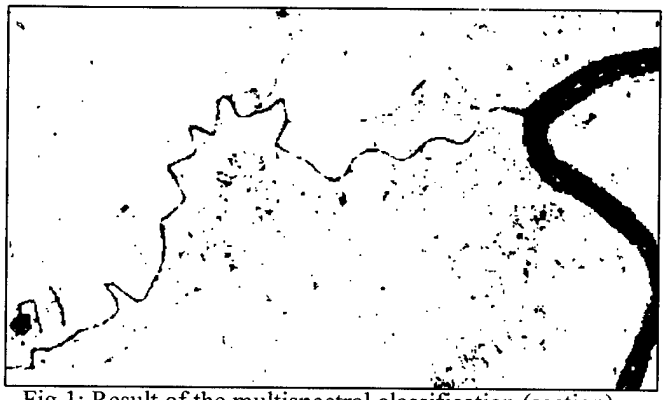

Fig.1: Result of the multispectral classification (section)

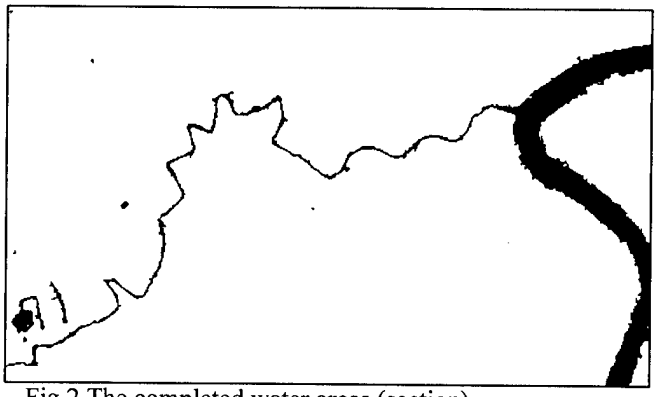

Fig.2 The completed water areas (section)

0-7803-3836-7/97/$10.00 © 1997 IEEE

were wrongly classified as water; (2) The small river was not continuously extracted; (3) In the big river there are false islands due to some ships being there. By using this software the water areas were completed (Fig.2): (1) The areas wrongly extracted as water were eliminated and the genuine water areas (ponds) remained; (2) The small broken river was linked together; (3) The false islands in the big river disappeared.

Separation of noises from houses

At the same time as buildings were extracted through the multispectral classification of the merged TM and SPOT pan image, numerous noises were also extracted, because both of them display similar spectral reflection (Fig.3). Through an additional processing with texture analysis the noises were separated from the buildings (Fig.4).

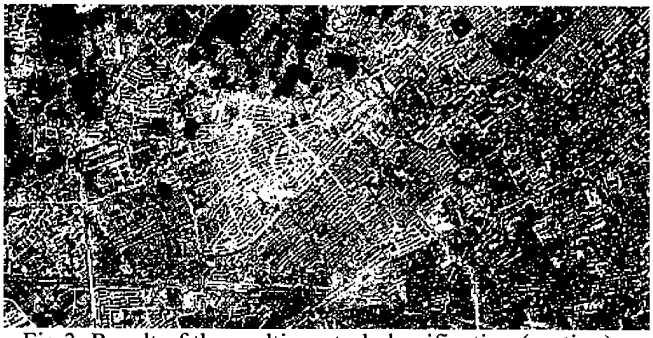

Fig.3: Result of the multispectral classification (section)

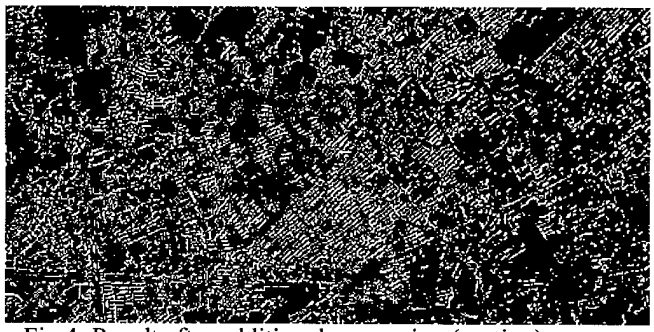

Fig.4: Result after additional processing (section)

Methods for merging of multisensor images

A well merged satellite image of TM and SPOT pan brings tremendous information for the observation of the urban environment. Besides the most frequently used IHS merging method, this software package also contains three other merging methods for different investigative purposes. They are PCS method (Principal Component Substitution), RVS method (Regression Variable Substitution) and SVR method (Synthetic Variable Ratio). The comparison of the merged images (Fig.5) shows that the color of the image merged through SVR method is the closest to that of the original TM image and their spatial resolution is not lower than the images merged through other methods. But the image merged through IHS method seems to be more suitable for the purpose of image mapping.

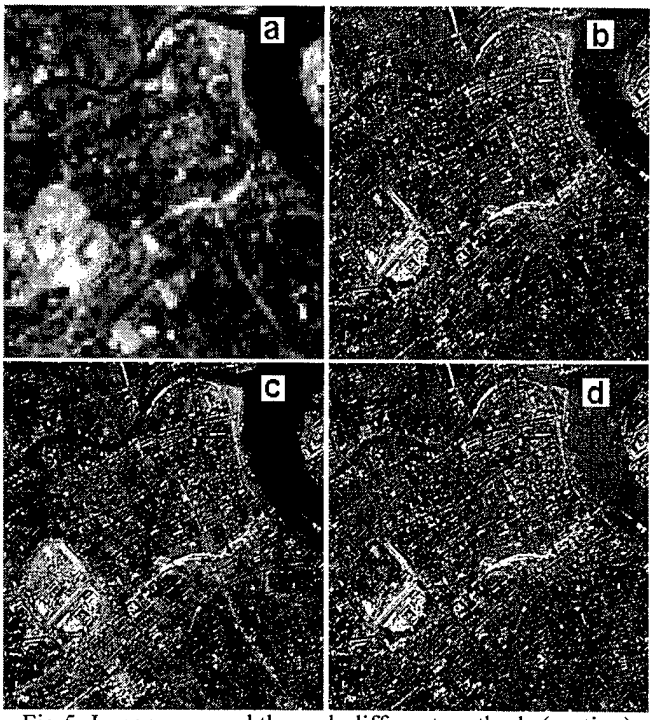

Fig.5: Images merged through different methods (section)
(a) TM image, (b) IHS image, (c) SVR image, (d) PCS image

Improvement of green areas

There is usually a problem that the extracted green areas in a city are larger than they actually are through multispectral classification. This is especially problematic in the classification of street green, because in this case the part of mixed pixels is especially large. With a suitable operation through the new software the accuracy of the result can be increased (Fig.6).

Fig.6: City green of Shanghai (section)

Recognition of skyscrapers

This software package also contains a method of skyscraper recognition, which can extract most of the skyscrapers in the city from SPOT pan image (Fig.7).

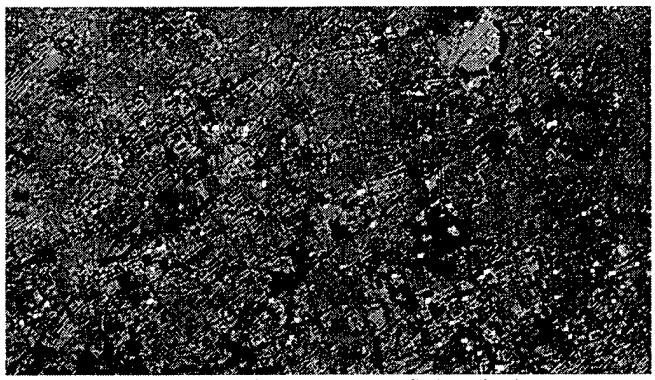

Fig.7: The extracted skyscrapers (red) (section)

Change detection of urban development

Through logical combination of the special functions of this software package various uses for the monitoring of urban environment can be developed. One of the uses is, for example, the change detection of urban development (Fig.8). The result is much more detailed than the normal change detection through multispectral classification.

Fig.8: Dynamic state of building development (section). The brightest parts are buildings (yellow) and infrastructures (white) from 1982 to 1989. Other buildings were built before 1982.

ACCURACY ASSESSMENT

Accuracy assessments were carried out for all the results before and after the accuracy improvement.

After the completion of water areas, rivers with breaks till 12 pixel long were linked together and the largest deviation is one pixel. All noises in the large water areas were eliminated. All the 19 multispectrally classified ponds in the city remain. Only one small noise area was wrongly kept as pond, while thousand of noise areas were eliminated. The accuracy of pond extraction is 95%.

In the accuracy assessment of house extraction, 400 random points in each of three areas with 400×600 pixels were assessed. The average user accuracy of the extracted houses has climbed from 58,78% to 86,09% after the improvement, and the average Kappa statistic was increased from 0,5423 to 0,8519. Both were increased by 30%.

5 aerial photos were used for the accuracy assessment of the green areas. The average user accuracy of the extracted green areas was increased from 51,4% to 62,4%. The improvement is more than 10%.

Visual check on aerial photos and merged TM-SPOT images shows that over 90% skyscrapers extracted through the automated recognition are correct. Only in some special cases other objects can be wrongly recognized as skyscrapers.

CONCLUSION

It is obvious that the accuracy of the results in this study is still not high enough for a detailed urban investigation and for large-scale GIS applications. Nevertheless, the results of this study are very useful for a rapid estimation of urban environment situation and city development, especially for the metropolitan cities of developing countries.

It can be expected that such methods will have a bright future because satellite data with up to 1 m spatial resolution are going to be available soon. With the new very-high-resolution satellite data it should be possible that by using the methods of this study even more urban environment information can be automatically extracted and the extraction accuracy considerably increased.

ACKNOWLEDGMENTS

It is with great appreciation that I thank Prof. Dr. J. Albertz, Department of Photogrammetry and Cartography, Technical University of Berlin, and Prof. Dr. U. Freitag, Department of Cartography, Free University of Berlin, for the support during the research. The used TM and SPOT pan images are supplied by Prof. Anxin Mei, Remote Sensing Institute, East China Normal University, Shanghai.

References:

[1] J. Albertz, Grundlagen der Interpretation von Luft- und Satellitenbildern: ein Einführung in die Fernerkundung, Darmstadt: Wiss. Buchgesellschaft, 1991.

[2] L. W. Fritz, "The Era of Commercial Earth Observation Satellites," Photogrammetric Engineering & Remote Sensing, January 1996, pp. 39-45.

[3] W. Stoney, "Data Summary," Executive Summary: Land Satellite Information in the Next Decade "The Would Under a Microscope", published by American Society for Photogrammetry and Remote Sensing, 1996, pp. 19-59.

[4] P. Gong, D. J. Marceau, P. J. Howarth, "A Comparison of Spatial Feature Extraction Algorithms for Land-Use Classification with SPOT HRV Data," Remote Sensing of Environment, 40, 1992, pp. 137-151.

Investigation of the North-East Monsoon Characteristics in the Region of South East Asia using ERS Wind Scatterometer Data

Yongqiang Guo, Jiaping Toh, Zhiyong Melvin Zhang
Swiss Cottage Secondary School, Secondary 4E1 & 4E2
No. 3 Bukit Batok St. 32, Singapore 659322, Tel: 65-563 7173

I-I Lin, Victor H.S. Khoo
Centre for Remote Imaging, Sensing and Processing (CRISP),
Faculty of Science, National University of Singapore,
Singapore 119260, Tel: 65-772 7908, Fax: 65-775 7717
E-mail: crslinii@nus.sg

Abstract --The north-east (NE) monsoon which occurs every year from November to February is a cyclical wave-like air mass that blows from the Asian continent to Indian Ocean, South East Asia and Australia. The cold winter in the Asian continent create a high pressure area and concurrently, hot southern hemisphere summer over most part of Australia constitute to a relatively low pressure area. This causes the cold and strong wind to blow from the north-east direction of Asian continent to low pressure region. Our region is affected by the monsoon in many ways, such as drought, floods etc.. Traditionally, there are very little observation, especially in the open ocean, so we need to use remote sensing satellites such as the European Remote Sensing Satellite (ERS) which equipped with a wind scatterometer to detect wind velocity over the ocean. Scatterometry measurements provides near surface wind information which is important for safe routing of ships, design of off-shore platforms and coastal defences [2]. Data from 1st February 1996 to 14th February 1996 were collected. With the use of PV-WAVE software, we generated visual displays of the wind condition from the scatterometer data. By analysing the visual displays we were able to observe general wind field changes during one surge event of the north-east monsoon.

INTRODUCTION

The objective of this project is to investigate the characteristics of the north-east monsoon winds using scatterometer data. Monsoon winds are well-developed over Asia and its direction is reversed completely from one season to another. Monsoon occur in the sub-tropics, especially where land masses form roughly East-West coastlines. They are not single, aberrant storms, like hurricanes, but cyclical wave-like air masses that move into the Asian continent from the sea during the northern-hemisphere summer and flow back to the sea in winter.

The scatterometer is a device mounted on some remote sensing satellites used to measure sea surface winds and their direction. Knowledge of wave and wind conditions is important for activities such as safe routing of ships and design of off-shore platforms and coastal defences.

THE NORTH-EAST MONSOON

The word monsoon is originated from the Arabic word "mausim" which literally means season. Monsoon is most often applied to the seasonal reversals of wind direction along the shores of the Indian ocean, especially in the Arabian Sea, that blow from the south-west during one half of the year and from the north-east during the other.

Rapid heating in the hot summer (July) over most parts of India creates a low pressure area. In the southern hemisphere, the winter season creates a high pressure area over the continent of Australia. The winds therefore blow from the Australian high pressure across the equator to the Asian low pressure. In Australia, it blows out as the south-east monsoon. As it crosses the equator, it is deflected to the right and reaches India and South-East Asia as the south-west monsoon and crosses Japan and China as the south-east monsoon. Rapid cooling in the cold winter (December) over most parts of India and Central Asia creates a high pressure area. While in the southern hemisphere, the summer season creates a low pressure area over the continent of Australia. The winds are now reversed and blow from the Asian high pressure to the Australian low pressure. In Asia, it blows out as the north-east monsoon. As it crosses the equator, it is deflected to the left and reaches Australia as the north-west monsoon [3].

The north-east monsoon is important to South-East Asia countries located south of about 10°N because it brings about 50% of the annual rain of these countries [1]. The people of these countries depend heavily on the monsoon rains for agriculture and many other activities. There are three driving mechanisms of monsoons [1]:-

0-7803-3836-7/97/$10.00 © 1997 IEEE

(1) The differential heating of the land and ocean and the resulting pressure gradient that drives the winds from high pressure to low pressure.
(2) The swirl introduced to the winds by the rotation of the earth.
(3) Moist processes that determine the strength, vigour, and location of the major monsoon precipitation by storing, redistributing, and selectively releasing, in the vicinity of the heated continents, the solar energy arriving over most of the tropics and subtropics.

MEASUREMENT OF THE WIND VECTOR

The scatterometer on ERS is used to estimate the wind speed and direction over a 500km swath, with a 50km resolution, over a 25km grid. It has three antennae which generate radar beams looking 45° forward, sideways and 45° backward with respect to the satellite's flight path. By analysing the backscatter from its three antennae, the satellite is able to deduce the wind velocity. The backscatter is mainly due to the reflections caused by surface roughness. If the viewing surface is smooth, the sensor receives virtually no return. In order for the satellite to deduce the wind speed and wind direction, the information form the backscatter is input into a complex mathematical model which then calculates the relative wind speed and wind direction of the area.

One of the most obvious use of this information is in the meteorological analysis of the weather. Some natural phenomenon such as cyclones and hurricanes may be impossible to analyse using the "traditional techniques", but with the help of remote sensing satellites, such spectacular wonders of nature can now be analysed. Such analysis may provide a way for us to predict which areas may be affected by such hazards and planned for emergency procedures during such a crisis. The data is also incorporated in mathematical models to improve their accuracy. Although the scatterometer was mainly used for measuring open ocean winds on large scales, it has been found to give useful data in coastal and enclosed sea areas.

INTERPRETATION OF SCATTEROMETER DATA

The interpretation was done around the South-East Asia region as that is our 'home' area. Our visual displays are based on a longitude of 25 °S to 25 °N and a latitude of 80°E to 140°E. Data from 1st February to 14th February 1996 was used in the analysis. With the use of PV-WAVE software we generated visual display of the wind conditions from the scatterometer data. By analysing the visual displays we were able to observe general wind field changes during one surge event, which is a sudden increase in the wind velocity. At the beginning of the surge, the wind in the South China Sea began to grow in magnitude from less than 5m/s on the 5th February 1996, to 12m/s on the 9th. The wind speed decreases back to 5m/s on the 13th. This observation is supported by comparing with the weather records from the Meteorological Service of Singapore.

The coloured band on the visual displays represents the path of the satellite. Unfortunately, the black and white print-out of this paper does not reflect the colour differences. The different colours represent different wind speed. The hot colours represent higher wind speed while the cool colours represent low wind speed. Below are the visual displays we generated representing the event of the cold surge.

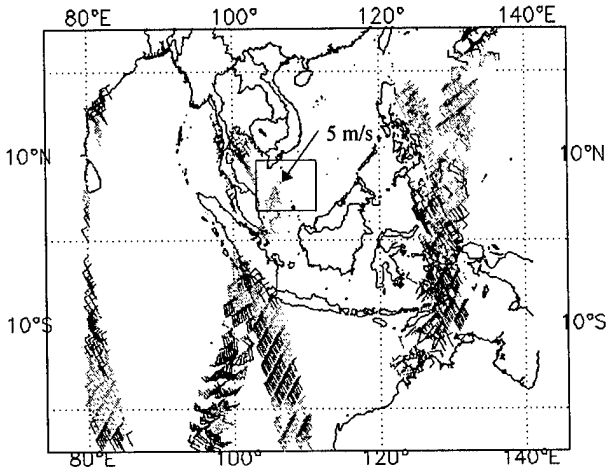

Fig 1: 5th February 1996 - Beginning of the cold surge.

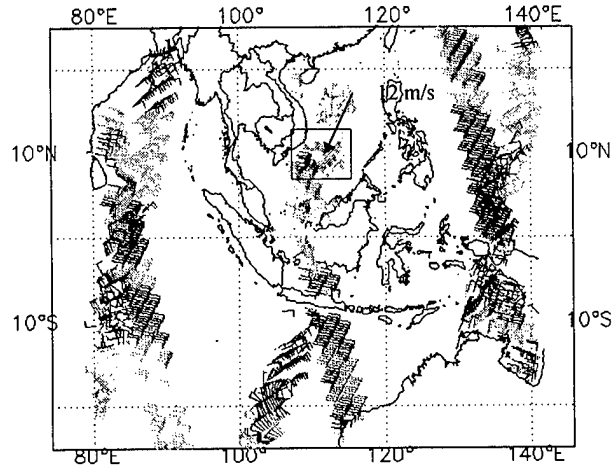

Fig 2: 9th February 1996 - Peak wind velocity during the surge.

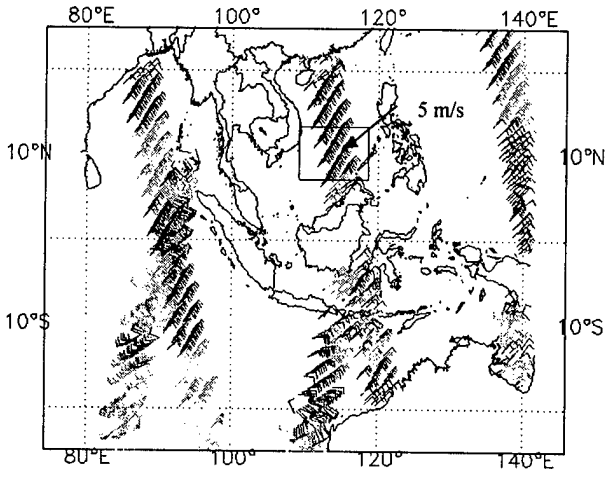

Fig 3: 13th February 1996 - End of the cold surge.

In the course of our analysis, we also found the occurrence of a tropical cyclone (centred at 117°E, 18°S) near the north-west coast of Australia. The wind distribution of the cyclone is resolved clearly by the wind scatterometer data as high resolution (25km) wind vectors are provided. The cyclone is clockwise. Maximum wind speed of more than 20m/s is observed at the centre and decreases outwards to about 10m/s where the ambient wind is about 5m/s. Fig 4 shows the location of the cyclone. Fig 5 which focus on the cyclone, shows the direction of the wind turning clockwise and the highest wind speed in the centre (yellow region, arrow point) and gradually decreasing outwards.

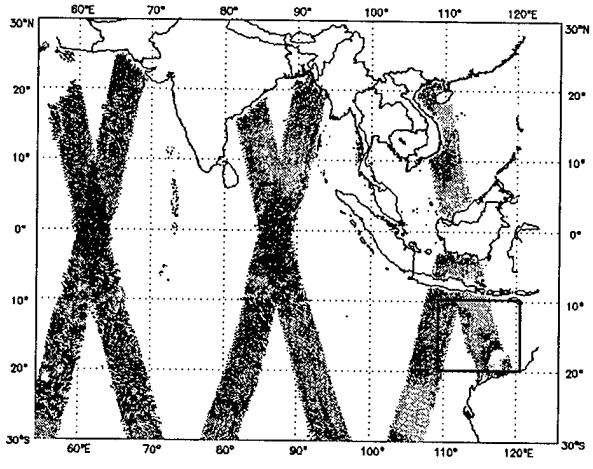

Fig 4: Cyclone spotted at north-west coast of Australia.

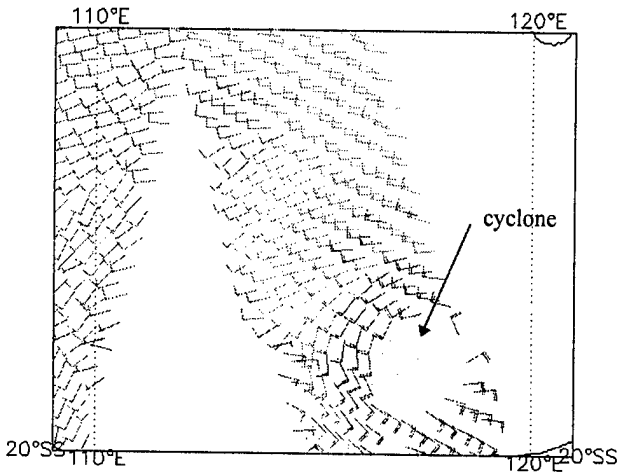

Fig 5: Clockwise cyclone with high wind speed at the centre.

CONCLUSION

We have shown the application of the wind scatterometer on board the ERS, in observing the monsoon winds. It gives us a better understanding of the wind field conditions during monsoon. We would be able to detect the temporal changes of the wind speed during a cold surges. We would be able to see the formation and movement of tropical cyclones as the wind scatterometer data has a resolution of 25km.

ACKNOWLEDGMENTS

We thank Dr. Dayalan Kasilingam from CRISP, NUS for providing us the technical supports. We also grateful to the National Science and Technology Board (NSTB) of Singapore for sponsoring us in the School Adoption Scheme in NUS.

REFERENCES

[1] Fein, Jay S. and Stephens, Pamela L., 1987, "Monsoons", John Wiley & Sons, New York.

[2] Hastenrath, Stefan, 1991, "Climate Dynamics of the Tropics", Kluwer Academic Publishers, Netherlands.

[3] McCurry, Steve, 1993, "Monsoon", C.S.Graphics, Singapore.

Remote Sensing Education Resources on the World Wide Web

S. Sivaprakash, Junjie.Ng, N. L. Teo,
Swiss Cottage Secondary School, Secondary 4E1,
Bukit Batok Street 32, Singapore 659322, Tel: (65)563 7173

Victor H. S. Khoo, S. C. Liew
Centre for Remote Imaging, Sensing and Processing (CRISP),
Faculty of Science, National University of Singapore,
Lower Kent Ridge Road, Singapore 119260
Tel: (65)771 5069, Fax: (65)775 7717, E-mail: phyliew@nus.sg

Abstract -- The objective of this project is to create a compilation of educational resources in remote sensing accessible through the World-Wide Web (WWW). This compilation will be useful to anyone interested in learning about remote sensing. Educators might also find it useful as a place to locate useful resources for teaching courses in remote sensing. The remote sensing web resources were organized into several categories in our web pages. These categories include (1) Remote Sensing Missions, (2) Remote Sensing Applications, (3) Notes on Remote Sensing and (3) Interesting Images. We hope to provide a one-stop web page for accessing educational resources in remote sensing on the world wide web.

INTRODUCTION

Many Remote Sensing web sites have been created by Remote Sensing institutions such as NASA, ERS etc. but not many sites contain information suitable for beginners. The information contained in the sites is not categorized. Many new users are likely to be overshelmed by the large amount of available information and confused by the way the information is presented. By compiling and categorizing these web sites, they can be made easy for beginners. Teachers can make used of them as teaching aids. The Remote Sensing topics can be made interesting for those who are new in the area of Remote Sensing. A comprehensive web page is therefore needed so that information about Remote Sensing can be located easily and efficiently. The web-page we are developing will have links to other sites so that the user is able to get further facts from them.

The hyper text based language used in the making of web pages allows easy cross referencing. Linking between web pages located at different sites around the world becomes transparent to the user. Useful resources such as missions, descriptions, sensors technical data, lecture notes, sample images and examples of remote sensing images can be located in the web sites of major remote sensing institutions.

OBJECTIVE

The main objective is to compile an educational resources about remote sensing in the WWW and make it available through a comprehensive web page. It is tailored to suit even those who have no background on remote sensing. By doing so people around the world will now know more about remote sensing. Those who have already have an idea on remote sensing can widen their knowledge on the subject through our web page. The user can gain access to various well known web sites around the world.

COMPILATION

The educational resources on remote sensing were complied by using the existing net search facilities such as Magellan and Yahoo and by visiting the web sites of major remote sensing institutions such as NASA, NOAA, USGS, ESA, CCRS, NASDA and CNES. These sites provide links to many other remote sensing related sites. Relevant sources of remote sensing lecture notes and tutorials were obtained through the World Wide Web. Materials gathered from the sites were studied by us to select the relevant information and classify them into the following categories: beginners, intermediate and advanced. During the process of compilation, we also collected satellite images, addresses of various sites and necessary graphics for our web page. Other information obtained for our site were applications of remote sensing, remote sensing missions and interesting images. After essential information had been gathered, they had to be presented in a ordered manner.

The programming language used to write the web page is the Hyper Text Mark-up Language (HTML). This is one of the common programming languages used to program web pages.

0-7803-3836-7/97/$10.00 © 1997 IEEE

HOME PAGE DESCRIPTION

The remote sensing web resources were organized into several categories in our web pages. The main home page is a user-friendly menu pointing to our other sub-pages as well as a starter for those who wish to learn about remote sensing. Some basic aspects of remote sensing are covered. The main page points to the following sub pages: (1) Remote Sensing Missions (2) Remote Sensing Applications (3) Interesting images and (4) Notes on Remote Sensing. Short descriptions of each sub-page are listed in the following paragraphs:

(1) In Remote Sensing Missions, the major satellite remote sensing missions are described. Links to the major satellite operators are provided.
(2) In Remote Sensing Applications, the uses of satellite remote sensing in areas such as oceanography, meteorology, forestry, agriculture and environmental management are introduced. Links are established to other web sites that contain materials describing real world applications of remote sensing.
(3) In the Interesting Images section, links to images which reveal special features or acquired during important events (e.g. volcanic eruption) are collected.
(4) In Notes on Remote Sensing, principles of optical remote sensing and radar remote sensing are described with links to lecture notes and tutorials available on the World Wide Web. Here we have categorized these resources into beginners, intermediates and advanced levels. Users will find it easy to locate their references according to their needs and levels.

Fig 1 shows part of the main homepage created with the sub-topics listed.

CONCLUSION

The web site on remote sensing educational resources will be useful to those who are new to the field of remote sensing as well as those who wish to know more. By classifying and presenting information on mission descriptions, notes and tutorials, sample images and examples of applications of remote sensing we hope to promote the interest in remote sensing and to provide a one-stop web-page for accessing the relevant educational resources available in the maze of world wide web.

ACKNOWLEDGMENT

The first three authors are students of the Swiss Cottage Secondary School, Singapore. This project was undertaken as part of the School Adoption Scheme organized by the National Science and Technology Board and the Ministry of Education, Singapore to promote interest in science and technology among the students. We would like to thank the Principal of Swiss Cottage Secondary School and Dr. Diana Ang for their help and support in the project.

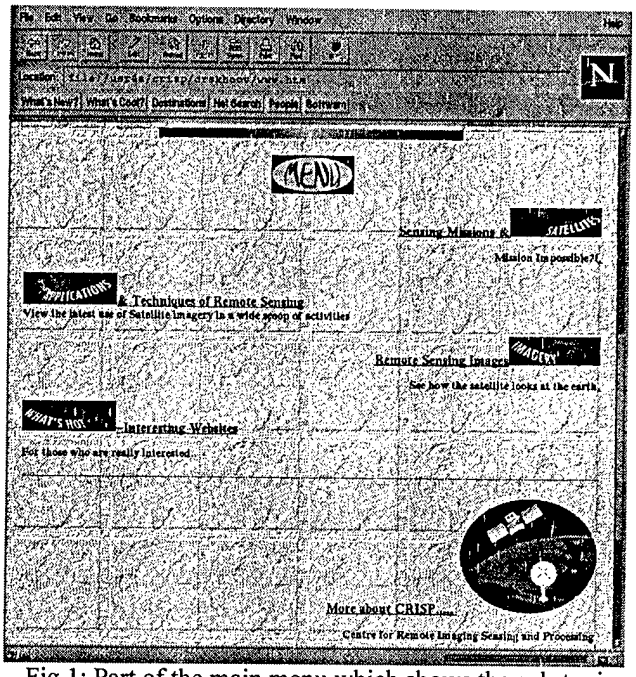

Fig 1: Part of the main menu which shows the sub-topics.

National GIS Training Program: Korean Experiences

Kiwon Lee, Ho-Geun Lee and Min Soo Kim

GIS Lab./SERI
P.O. Box 1, Yusung, 305-600, Korea
Tel: +82 42 869 1464, FAX: +82 42 869 1479
E-mail: {kilee, leehg, mskim}@seri.re.kr

Abstract: Korean GIS training program, supported by government, was established in 1996. The main purpose of this training program is to expand GIS-mind, being capable of initiating public accessibility with respect to broad scope of GIS, one of most prominent information systems in the information age. In this paper, practical aspects to execute and to derive national GIS training program are comprehensively discussed: Basic strategy, Three types of course curricula, and One year results based on questionnaires given to course attendants. Total duration of this training program is four-year to 1999; therefore, precious experiences obtained during this first year of 1996 works as useful and significant resources for further progress in Korean GIS activities as well as GIS education; furthermore, it is thought that Korean experiences are regarded as informative ones to other country-wide GIS training programs in preparation stage, in developing stage, or in executing stage.

Introduction

Since mid-1980s, Korean government had recognized GIS (Geographic Information System) capabilities to national-wide urban and regional planning project, digital mapping project, and environmental research project; therefore, they had financially supported GIS-related applications in various fields. From early 1990s, the main GIS researches have been gradually moved into GIS software development task under the title of so-called NGIS (National GIS) project and national-wide larger projects related to GIS database.

Since then, it has been also pointed out that the wide expansion of GIS-mind and the non-profitable GIS training programs should be also necessary to later various applications of GIS software products generated from NGIS project in late 1998. Therefore, National GIS training program was motivated from late 1995 by Systems Engineering Research Institute (hereafter referred to as SERI), one of governmental-supported institutions for GIS-related researches in Korea.

Comprehensive planning for National GIS training program was first performed by GIS research department within SERI, and several practical aspects are considered, in this planning stage: contemporary Korean GIS activities, lecturer/teacher or exercise resources produced in Korea, and Prerequisite understanding level of potential attendants of GIS training courses, in consideration of other country-wide generalized GIS training strategies [4], [5], and [6]. With this background and surveyed data, GIS training program was implemented as three courses in 1996: decision-maker course (2 days), manager course (10 days), and user course (15 days). Meanwhile, other long-term courses such as GIS analyst course (4 weeks) and GIS programmer course (6 months) are supposed to be started from 1997. In this paper, educational contents of each course are presented and the followed results based on questionnaires given to course attendants are also presented.

Strategy for National GIS Training Program

Distinguished National GIS training program from profitable training program, many aspects, which composed of broad scope of GIS understanding, are taken into account for program setting: Training courses and materials, Training curricula, GIS software and hardware including peripheral, Educational project scenario and demonstrative materials. While, most GIS-related fields are the important educational contents of GIS training units, especially overlapping fields among them.

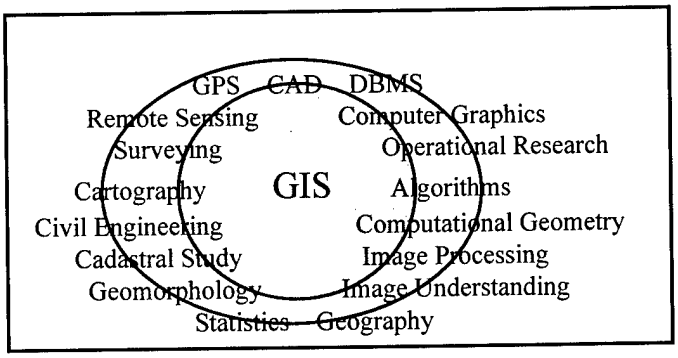

Fig. 1. Proposed educational contents for GIS training program, in association with other research fields, assembled and modified from other related resources [1], [2], [3], [8], [9] and [10].

Setting of Korean GIS Training Center

Based on reconnaissance survey for GIS training program

0-7803-3836-7/97/$10.00 © 1997 IEEE

during seven months, January to July, in 1996, educational facilities including GIS-hardware, softwares, and peripherals were built within Korean GIS Training Center, Yusung-district, Taejon-city, located in the mid-region of South Korea.

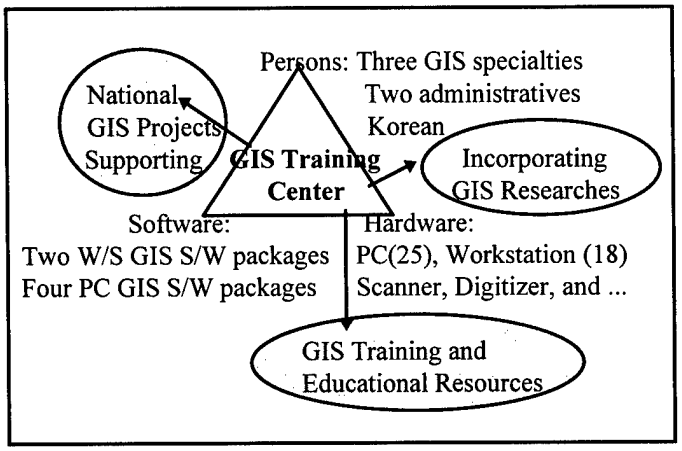

Fig. 2. Components of Korean GIS training center and its expected roles to Korean GIS activities.

Curricula of Proposed Three GIS courses

Three GIS training courses for decision-maker (Table 1), manager (Table 2) and user were provided, and course title or main scope were modified from Keller and Frank [7].

Basically, the executing strategies for these programs are as follows: To broaden GIS-mind for on-going or potential GIS projects and its academic/technical aspects for prospective GIS employment, To introduce state-of-the-art domestic GIS activities, and To execute practical GIS training for researchers involved in on-going GIS project.

Each courses' targets and design strategies is as follows. Decision Maker course is designed for persons who are charged jobs holding administrative decision-making competency of on-going GIS projects or holding heading initiatives of GIS projects in their organizations, and those who charged jobs capable of directly influencing of major trends of their GIS projects. While, manager course is designed for persons who are charged jobs for development/application planning and managing and scheduling of GIS project. User course is designed for persons who are charged jobs for operational task towards a given GIS project. We first intended to set the restricted course in the consideration of registering student's status and need (Table 4), as possible as total training schedule permitted. To last course at December, 1996, all attendant of decision maker course (5 times), manager course (3 times), and user course (2 times) were recorded as 102 persons, 57 persons, and 30 persons, respectively.

Table 1. Educational contents of GIS Decision Maker

Content / Day	Subject
Day 1	1. Overview of GIS (2 hr.)
	2. Seminars on GIS cases I and II of foreign countries (4 hr.)
	3. Cost/Benefit analysis (1 hr.)
Day 2	4. Seminar on Korean GIS cases I, II, and III (6 hr.)
	5. Total discussion (1 hr.)
Total 14 hr. (Lecture: 3 hr., Seminar: 10 hr., Discussion: 2hr.	

Table 2. Educational contents of GIS user course

Content / Day	Subject	Topic
Day 1	1. Overview of GIS	1) Definition/History of GIS 2) Trend of GIS 3) Data Structures of GIS 4) Exercise I
Day 2	2. Data Acquisition	5) Principles of Remote Sensing 6) Image Processing 7) Principles of GPS 8) Scanning/Digitizing Mapsets 9) Coordinate Geometry 10) Exercise II
Day 3	3. Map Projection and Map Analysis	11) Map types 12) Map Analysis Method 13) Map Projection Types 14) Coordinate Systems 15) Cartographic Transformation 16) Exercise III
Day 4	4. GIS-DBMS	17) Fundamentals of DBMS 18) Principles of Spatial DB 19) Exercise IV
Day 5	5. Spatial Analysis	20) Spatial Analysis Functions 21) GIS operators 22) Terrain Analysis 23) Network Analysis 24) Exercise V
Day 6	6. Presentation of GIS-output	25) Computerized Mapping 26) Design of GIS-output 27) Exercise VI
Day 7	7. Management/ Strategy for GIS projects	28) GIS project planning 29) Management of GIS Implementation
Day 8	8.Demonstration of Case Studies	30) Korean Case Study I 31) Korean Case Study II 32) Korean Case Study III
Day 9	9. On-site Studies	33) Visiting other GIS-site
Day 10	10. Total discussion	
Total 66 hr. (lecture: 48 hr, exercise: 18 hr, other: 10 hr)		

Meanwhile, Table 3 and table 4 are summary of attendants' job or affiliation, pre-knowledge level for GIS, and their utilizing stage.

Table 3. Summary of student's affiliations and jobs, in per cent

Item / Course	Types of affiliations				
	p	g	c	a	o
Decision maker	39.2	19.5	27.5	11.8	2.0
Manager	33.3	24.6	35.1	7.0	0.0
User	43.3	13.4	33.3	10.0	0.0

Note: p (provincial organization or equivalent), g (governmental organization or equivalent), c (company), a (academic institute or university, and o (others)

Table 4. (a) Pre-knowledge level by self-evaluation before taking GIS course, and (b) Their utilizing status of GIS project or research

(a)

Rank / Course	1	2	3	4	5
Decision maker	3.3	12.0	37.0	29.3	18.4
Manager	0.0	0.0	33.3	33.3	29.2
User	0.0	0.0	4.2	50.0	45.8

Note: 1 (highest) ← 5 (lowest)

(b)

Item / Course	A	D	P	N/A
Decision maker	14.2	22.8	54.3	8.7
Manager	6.3	22.9	54.2	16.7
User	8.3	16.7	66.7	8.3

Note: A (Application stage), D(Developing stage), and P(Planning stage)

Results

Course results are obtained from questionnaire given to all course attendants. As well, these results and their descriptive comments are reflected to further process to set up the next GIS training program.

Overall evaluation with respect to all courses appeared over 77 % as indicating their high satisfaction and usefulness for their works, than previously expected: decision-maker (84.8 %), manager (81.2 %) and user (66.7 %). At Table 5, other aspects of GIS training program are presented: educational contents, lecturing method and hands-on practice materials and textbooks.

Table 5. Summary of course results, in percent, based on questionnaire given to all attendants

(a)

Item / Course	Overall evaluation				
	1	2	3	4	5
Decision maker	18.5	66.3	15.2	0.0	0.0
Manager	10.4	70.8	18.8	0.0	0.0
User	16.7	50.0	25.0	8.3	0.0

(b)

Item / Course	Educational Contents				
	1	2	3	4	5
Decision maker	6.5	64.1	27.2	2.2	0.0
Manager	8.3	52.1	35.4	4.2	0.0
User	4.2	45.8	37.5	12.5	0.0

(c)

Item / Course	Lecturing method by lecturers				
	1	2	3	4	5
Decision maker	4.3	67.4	25.0	3.3	0.0
Manager	14.6	45.8	29.2	8.3	2.1
User	4.2	29.2	54.2	12.5	0.0

(d)

Item / Course	Practice materials and texts				
	1	2	3	4	5
Decision maker	N/A				
Manager	0.0	25.0	52.1	25.8	2.1
User	0.0	25.0	37.5	37.5	0.0

Note: 1 (very good), 2 (good), 3 (fair), 4 (poor), and 5 (very poor)

Concluding Remarks

Main courses of Korean GIS training program in future and educational contents are presented at Table 6. In this setting, the first year experiences are fully reflected and the following preparation works or researches are currently carrying out by Korean GIS specialties concerned. Especially, three courses in 1996 are consistently opened, but course duration is shorten in consideration of other long-term training courses.

Table 6. Proposed GIS courses in future

Item / Course	Course Duration	Remarks
Decision maker	2 days	same as 1996
Manager	5 days	same as 1996, but shorten duration
User	10 days	same as 1996, but shorten duration
GIS Analyst	5 weeks	GIS workshop (5 days) GIS Database Workshop (5 days) GIS Tool I (5 days) GIS Tool II (5 days) GIS Planning Workshop (5 days)
GIS Lecturer	6 weeks	GIS Analyst (5 weeks) Pedagogy (5 days)
GIS Applications	4 weeks Each	Land Information Systems AM/FM Environment Information Systems GIS in Transportation or Other applications dependent upon needs and current issues
GIS Programmer	6 months	Introduction to GIS (3 weeks) C/C++ Programming (4 weeks) Algorithm (2 weeks) Database (3 weeks) System Development (3 weeks) GIS-tool (3 weeks) Software Development (6 weeks)

According to the first experiences acquiring from GIS training program, GIS training program seems to possess lots of advantages as one of effective Nation-wide programs in these information ages, compared with other information systems. In addition, established GIS training program plays an important role to promotion of GIS research and development.

Finally, it was thought that Korean experiences are regarded as informative ones to other country-wide GIS training programs in preparation stage, in developing stage, or in executing stage.

References

[1] D. J. Unwin, et al., "A syllabus for teaching geographical information systems", International Journal of Geographic Information Systems, vol. 4, 1990, pp.457-465.

[2] J. Star and J. Estes, "Geographic Information Systems: An Introduction, Prentice-Hall, Englewood Cliffs, 1990, 251p.

[3] J. T. Coppock, 1992, "GIS Education in Europe", International Journal of Geographic Information Systems, vol. 6, 1992, pp.333-335.

[4] K. K. Kemp and A. U. Frank, Toward consensus on a European GIS curriculum: the international post-graduate course on GIS, International, Journal of Geographic Information Systems, vol. 10, 1996, pp.477-497.

[5] M. Batty, D. F. Marble, and A. G. Yeh, "Training Manual on Geographic Information Systems in Local Regional Planning, United Nations Center for Regional Development", Nagoya, Japan, 1995, 260p.

[6] M. F. Goodchild, and K. K. Kemp, "NCGIA education activities: the core curriculum and beyond", International Journal of Geographic Information Systems, vol. 6, 1992, pp. 309-320.

[7] P. C. Keller and A. U. Frank, "Issues to consider when developing of selection a GIS curriculum", Proc. of GIS '90 symposium, Vancouver, 1990, pp.527-533.

[8] S. Aronoff, 1989, "Geographic Information Systems: Management Perspectives", WDL publications, Ottawa, 1989, 286p.

[9] W. E. Huxhold and A G Levinsohn, A. G., "Managing Geographic Information System Projects", Oxfold University Press, New York, 1995, 247p.

[10] W. R. Jr. Gordon and N. M. Soubra, "Geographical information systems and planning in the USA: selected municipal adoption trends and educational concerns", International Journal of Geographic Information Systems, vol. 10, 1992, pp.477-497.

Issues of WWW-based Data Visualization in the Earth System Science Classroom

Farzad Mahootian, Ph.D., Earth System Science Community Co-Investigator
Gonzaga College High School, 19 Eye St., N.W., Washington D.C. 20001, USA
(202)966-8588, fax (202)336-7164
farzad@circles.org

INTRODUCTION AND BACKGROUND

Earth system science (ESS) is a holistic study of the Earth. ESS marshals the resources a variety of scientific and technical fields to explore interactions among the Earth's component subsystems in order to understand the Earth as a system, to explain Earth dynamics and Earth evolution, and to address the problem of the affects of human actions on global change. We have begun to understand that because the Earth is a system, our local actions have global effects, that human society has the power to change the world, for better or worse. It is of great importance, both for the sake of the Earth and for the sake of our own future, to understand the Earth for what it is: a complex system of interlaced and interacting subsystems.

In order to investigate the Earth system, teachers and students need access to expertise in a broad variety of disciplines: chemistry, physics, computer science, biology, mathematics, statistics, and political science. A variety of relatively new skills are also required: networked computing, tools and techniques for retrieving, visualizing, and analyzing remote sensing data, and building dynamic systems models. The question of visualization of remote sensing data became a central issue in curriculum development efforts of the Earth System Science Community (ESSC), a three-year project supported by NASA's Information Infrastructure Technology and Applications and High Performance Computing and Communication programs.

The thrust of the curriculum development effort was to enable students and teachers to conduct investigations in global change topics using remote sensing data gathered by NASA and other science agencies. The curriculum was project-based [1], with the intention of producing an authentic and living sense of understanding and participation in science research [2], [3]. Students and teachers were to collaborate on-line with their peers in other schools, and with scientists/mentors in universities and government science agencies. In this effort students and teachers become researchers and learn to design and carry out a research strategy, involving the proposal and articulation of a hypothesis, the building of a system model, and the search, retrieval, manipulation, visualization and analysis of appropriate data. Students conclude their research by testing their hypothesis with available data, using visualization software, and information available in print and on-line. Finally, students communicate the results of their research by publishing their reports, data, data products, and systems models. To date, over sixty reports have been published on the project website (http://www.circles.org/).

The curriculum content and pedagogy was designed and implemented during the 1993-94 pilot phase in adherence to the science strategy of NASA's Mission to Planet Earth, and to the (U.S.) National Research Council's National Science Education Standards (NSES) which were in draft form at the time [4].

THE ESSC PROJECT IN RETROSPECT

The original purpose of the Earth System Science Community was to build an investigation-oriented Earth system science curriculum in which high school and university students could conduct research projects on global change issues using Earth observation data and information over the Internet. Three integrated components were proposed: 1) an Earth system science curriculum, 2) an information system over the Internet to support the curriculum and access to remote sensing data, and 3) a pilot community of educators, students and scientists who would help define requirements for improving the curriculum and information system.

While the first two goals were achieved with a significant degree of success, it has become clear that the requirements of a successful on-line community were underestimated. In this respect, the main lesson learned was that, with proper encouragement and cultivation, communities can grow organically from a pre-existing nutritive substrate. The "substrate" here refers to long-term institutional commitment to supporting innovative (i.e., non-traditional) courses and teachers. A paradigm case of such commitment is represented in the (U.S.) National Science Foundation's *"systemic initiatives"* for science education reform. But in the absence of such a substrate, the simple influx of temporary dollars for teacher training and partial release time is an insufficient and ineffectual way to build on-line communities.

In retrospect, the ESSC project would have done better to focus on only one component, with a secondary focus on the collaborative development of a second one. Community-building over the Internet requires special expertise and attention: it does not simply emerge from the provision of the first two components. As it turned out, the ESSC made valuable contributions in its development of a curriculum and an information system capable of producing graphical answers to scientific questions about data.

VISUALIZATION IN SCIENCE AND EDUCATION

A. Introduction

The two most difficult aspects of teaching ESS are the visualization, analysis, and interpretation of data, on the one hand, and the use and construction of system models on the other. System modeling, in the ESS context, is the topic of another paper in this volume ("System Thinking and System Modeling in the Earth System Science Classroom").

0-7803-3836-7/97/$10.00 © 1997 IEEE

B. Visualization and the Construction of Knowledge

To paraphrase the great 18th century German epistemologist, Immanuel Kant, "models without data are empty, and data without models are blind." In Kant's theory of knowledge [5], "categories of understanding" (i.e., causality, composition, etc., which collectively lay the foundation for the "laws of nature") provide conceptual connectivity to the "forms of perception" (i.e., the ordering principles of space and time, which apply to all objects and events). Scientific consciousness, according to Kant, is constructed by one's appropriate use of the categories of understanding in association with the forms of perception. In his philosophy, Kant demonstrated that all knowledge is an active, on-going construction. In this respect the contemporary "constructivist" theory of learning [6] finds its ancestry in Kant's philosophy.

In the context of our discussion, the forms of perception are analogous to the archives of data of the Earth's systems, and the categories of understanding are embodied in our system models. These two moments in the process of knowledge are complementary. They are coupled within a feedback loop: novel features of the data, as revealed by visualization, force review and re-examination of the system model. Conversely, a novel model will send researchers back to the data archive to test the model's prediction.

The tapestry of knowledge is woven in the space created by the tension between model and data-- this dynamic tension stimulates the growth of scientific consciousness. That visualization is essential to the cognitive development of science has been noted in the philosophy and history of science [7], and by education theorists [8]. The term "scientific visualization" has recently acquired an exclusively technical meaning: "a set of display techniques used by scientist for the analysis of data... an image or animation in which numeric values in data sets are represented visually as colors, shapes, or symbols" [3]. It is clear, however, that the benefit of concretizing *both* abstract concepts *and* data by means of visualization satisfies more than merely aesthetic or heuristic needs [9]. The role of image, metaphor and analogy in the history of scientific discovery, from Plato through Kekule and Kelvin, is well-documented [10].

The CoVis project at Northwestern University has amply shown that science education can only benefit from the adaptation of the powerful tools and techniques of scientists, specifically scientific visualization and communications [11].

PROTOTYPE EARTH SYSTEM VISUALIZER (ESV)

To understand the Earth as a system researchers need to investigate interactions among the variety of data gathered by Earth observing instruments. Whether the researcher is novice or expert, designing an Earth system science research plan requires the efficient browsing of large volumes of data for a variety of parameters with extended spatio-temporal coverage. Scientists have access to a variety of tools and technicians to browse these data and decide on a research plan. This is not the case in the education context: students in high school and undergraduate settings often do not have access to a team of programmers and data visualization experts. And while the time and expertise available to students is limited, their requirements for creating a research plan are generally the same as those of the scientist: efficient browsing of large volumes of data for a variety of parameters with extended spatio-temporal coverage. A list of major obstacles to intercomparison studies of Earth system parameters includes: a) broad variety of data formats, b) variety of spatio-temporal resolutions, c) enormous file sizes, d) georeferencing, e) incomplete, poor, or highly specialized documentation, f) mastery of visualization software.

An example may serve to illustrate this issue. Students in my ESS class wanted to investigate the relationship between stratospheric ozone and phytoplankton pigment concentration to see whether diminishing ozone values have an effect on phytoplankton populations. A preliminary examination of data from NASA's TOMS and CZCS missions indicated coincident temporal and spatial coverage but different spatial resolutions, and different data formats. The necessity of reformatting and regridding the data was not beyond the students' understanding, but certainly beyond the limitations of time and expertise available to them.

The Earth System Visualizer (ESV) is designed to meet the challenges posed by research-oriented Earth system science courses. The ESV will also satisfy the general needs of research planning, at a preliminary level, by enabling users to visualize and intercompare data from a variety of parameters.

A. Selection of Parameters

Twelve parameters, with seven years of global coverage, were selected from the International Satellite Cloud Climatology Project (ISCCP-C) for the prototype phase of the ESV: 1) surface temperature, 2) ozone, 3) surface reflectance, 4) surface pressure, 5) snow and ice cover, 6) high level cloud amount, 7) high level cloud top pressure, 8) middle level cloud amount, 9) middle level cloud top pressure, 10) low level cloud amount, 11) low level cloud top pressure, 12) total cloud amount.

B. Selection of Plot Types

The selection of these plot types is based on requests made over the last three years by ESSC students. More complex plot types, which allow the user more flexibility, may be included in the next version. Users specify single location, or a rectangular region. The seven plot types are 1) pseudo-color map, 2) contour map, 3) overlay of contour on color map, 4) two-parameter scatter plot, 5) two-parameter time series at one location, 6) one-parameter time series at two locations.

C. User Interface

Simplicity, ease of use, and enhanced metadata documentation are essential elements of the ESV prototype interface. Because of the limitations of forms over the World Wide Web, the ESV interface consist of a sequence of three screens, through which the user specifies parameters, plot

type, spatial and temporal coverage of the data visualization. Brief tutorials on plot types are available for the novice user. If the ESV is continued, future Java versions will incorporate clickable maps, more plot types, and provide ready access to tutorials, enhanced metadata, complete metadata, all from a single screen. For an technical overview of the prototype, see the ESV website, www1.ecologic.net/avesda2/html/.

RECOMMENDATIONS

The ESV is a simple prototype. It can be readily duplicated in a variety of settings, using a variety of database and visualization software applications. The ESV uses the Informix Universal Server as the DBMS, and IDL as the visualization application. In that the ESV uses a small fraction of the capabilities of Informix and IDL, it represents a case of technological overkill-- given the context for which the ESV was constructed, namely: browsing and preliminary analysis of data by students. For such purposes, any network-savvy relational database coupled with compatible visualization software would do the job. Advanced capacity to respond to data requests involves issues of design more than it involves technological capability. The ESV quickly and efficiently delivers well documented data products that represent a broad array of data over a relatively long period of time. This is the minimum that a web-based visualization system should offer. Most laboratories could make their data available in such a manner with a small investment of time and expertise. It is a matter of perceived priority. In the past two years advances have been made by many government and academic research institutes to put their data on-line in manner accessible to the non-specialist. NOAA (e.g., ClimViz), NASA (GSFC, JPL, etc.), and a variety of university labs have made great volumes of data much more accessible, but they still have room for improvement.

The direction of future web-based visualizers is indicated in the CoVis series of Weather, Climate and Greenhouse Effect Visualizers [12]. These are learning environments that, like the ESV, are built on existing research-grade visualization tools, and provide the middle school audience with a friendly and supportive interface. Their most recent development, Climate Watcher, allows the user access to a broader array of data sets: physical and human geographic data is present. A future release, called World Watcher, *will integrate climate modeling with data visualization*, and allow the student to create "what if" scenarios that are based on a climate model coupled with climate data. The data are not blind, nor is the model empty. The World Watcher will also allow the student to *import* data into the system [13]. This will greatly increase the student's sense of participation and have a significant impact on learning. The World Watcher represents the future wave of meaningful interactivity with WWW-based visualization systems.

To conclude: future application design of WWW-based visualization systems requires attention to the following minimal set of features:

- appropriate, documentation of graphs and data products
- user-appropriate (i.e., "enhanced") metadata
- variety of plot types
- availability of derived data and data fusion products
- variety of levels of resolution (i.e., low to medium)
- reasonable file size, appropriate to desktop computing
- variety of downloadable formats
- significant data importation capabilities

REFERENCES

[1] Blumenfeld, Soloway, Marx, et al, "Motivating Project-Based Learning: Sustaining the Doing, Supporting the Learning," Educational Psychologist, 26 (1991), pp 369-398.

[2] Whitehead, A. N., The Aims of Education, New York: Macmillan, 1929.

[3] Edelson, D. C., "Realizing Authentic Science Learning through Adaptation of Scientific Practice," in Tobin, K., and Fraser, B., International Handbook of Science Education. Dordrecht: Kluwer, 1997 (in press).

[4] National Research Council, National Science Education Standards. Washington, D.C: National Academy Press, 1996.

[5] Immanuel Kant, The Critique of Pure Reason (1781). Translated by N. K. Smith. New York: St. Martin's, 1965.

[6] Yager, R.E., "The Constructivist Learning Model," The Science Teacher, September 1991.

[7] Miller, A. I., "Visualization Lost and Regained: The Genesis of the Quantum Theory in the Period 1913-27," in On Aesthetics in Science, J. I. Wechsler, Ed., Cambridge: MIT Press, 1978.

[8] Gordin, D. N. and Pea R. D., "Prospects for Scientific Visualization as an Educational Technology," Journal of the Learning Sciences, 4, 249-279.

[9] Tufte, E., Visual Explanations: Images and Quantities, Evidence and Narrative, Cheshire, CT: Graphic Press, 1997.

[10] Miller, A. I., Insights of Genius: Imagery and Creativity in Science and Art. New York: Springer-Verlag, 1996.

[11] The catalog of available CoVis papers are located at, http://www2.covis.nwu.edu/papers/Papers.html

[12]http://covis.atmos.uiuc.edu/geosciences/visualization/visualizers.html

[13] Personal communication with Daniel Edelson, CoVis and SSciVEE PI, Department of Computer Science, Northwestern University, Evanston Illinois, USA, May 1997.

Temperature Corrrected Bootstrap Algorithm

Joey C. Comiso and H. Jay Zwally
Laboratory for Hydrospheric Processes, Code 971
NASA/Goddard Space Flight Center, Greenbelt, MD 20771
Tel: 301-286-9135, FAX: 301-286-1761, e-mail: comiso@joey.gsfc.nasa.gov

Abstract -- A temperature corrected Bootstrap Algorithm has been developed using Nimbus-7 Scanning Multichannel Microwave Radiometer data in preparation to the upcoming AMSR instrument aboard ADEOS and EOS-PM. The procedure first calculates the effective surface emissivity using emissivities of ice and water at 6 GHz and a mixing formulation that utilizes ice concentrations derived using the current Bootstrap algorithm but using brightness temperatures from 6 GHz and 37 GHz channels. These effective emissivities are then used to calculate surface ice temperatures which in turn are used to convert the 18 GHz and 37 GHz brightness temperatures to emissivities. Ice concentrations are then derived using the same technique as with the Bootstrap algorithm but using emissivities instead of brightness temperatures. The results show significant improvements in areas where ice temperature is expected to vary considerably such as near the continental areas in the Antarctic, where the ice temperature is colder than average, and in marginal ice-zones.

INTRODUCTION

The most important parameter derived from satellite data that has been used for sea ice cover studies is ice concentration. Ice concentration is used to calculate the extent and actual area of the ice pack which are useful for assessing the state of the ice cover and its seasonal and interannual variabilities [1,2,3]. It is also used to characterize the marginal ice zones, the divergence zones, and polynya areas in relation to air-sea-ice interaction and heat flux studies.

Ice concentration has been defined as the percentage of open water within the field of view of the sensor. In the late spring and summer period when surface air temperatures are above freezing and open water are distinctly free of ice, the definition is exact. In the winter, the definition is not as clearcut because under freezing conditions, open water surfaces undergoes continuous transition to grease ice through pancakes or nilas (depending on the state of the ocean), and to young and the thicker ice types. During this time period, the emissivity of the surface changes from that of open water to that of thick ice.

Ice concentrations are derived using a mixing formulation because of the large footprint (>25km) of the satellite sensors [4,5,6,7]. Because of the high correlation of data from the different channels [7,8], the number of surfaces that can be unambiguously classified by SMMR data is three: two ice types and open water. The most dominant ice types are first year ice and multiyear ice which are found in the seasonal and the perennial ice regions, respectively. These two ice types have been shown to have distinctly different emissivities but the emissivity values can overlap [9,10]. The third type, which is abundant in leads, polynyas and marginal ice zones, is generally called thin ice but can be grease ice, pancake, or nilas. The ice concentration algorithms do not handle the thin ice types well because the emissivity is not well defined as stated earlier. But some have tried to calculate concentrations of thin ice in high ice production areas like the Bering Sea [11,12] where thick ice with snow cover is assumed to be minimal. In most ice algorithms, three surfaces (first year, multiyear , and open water) are used in a mixing formulation to derive ice concentration. In the Bootstrap algorithm, the high correlation of the emissivities of the different ice surfaces in some sets of channels is utilized and within the footprint of the sensor, the surface is assumed to be either ice or water. The presence of thin ice within the footprint, causes an error, the magnitude of which depends on thickness or emissivity [13].

The Bootstrap algorithm [14] makes use of two sets of channels: the HV37 set, consisting of the horizontally and vertically polarized data at 37 GHz, and the V1837 set, which makes use of the vertically polarized 18 and 37 GHz data. The HV37 set is generally insensitive to spatial variations in surface temperature and is most effective in the perennial ice regions while the V1837 is found to be most effective in the seasonal sea ice regions. The concurrent use of the two sets provides optimum accuracy in the retrieval of global sea ice parameters although the second set shows more sensitivity to surface temperature as described in [14]. In this paper, we present a technique that overcomes the latter weakness.

TEMPERATURE INDEPENDENT TECHNIQUE

The Nimbus-7 SMMR sensor has dual polarized channels at 5 frequencies ranging from 6 GHz through 37 GHz. The 6 GHz data have not been used for ice concentration algorithms, although they provide the largest contrast between open water and ice at this frequency, because of its large footprint (about 70 by 150 km). The latter causes some of the important features of the ice cover to be smeared out.

0-7803-3836-7/97/$10.00 © 1997 IEEE

This channel, however, provides good ice temperature information since it is least affected by snow cover and other surface effects. Knowing the effective emissivity, ε_s, of the surface, the average physical temperature of the surface, T_s, within the field of view of the sensor, can be calculated from

$$T_s = T_B/\varepsilon_s \qquad (1)$$

Since the field of view generally has both ice and water, the emissivity of the surface, ε_s, in the field of view of the sensor is derived using the mixing formulation given by

$$\varepsilon_s(6)=(1-C)\varepsilon_w+(C)\varepsilon_I \qquad (2)$$

where ε_w and ε_I are the emissivities of water and ice, respectively, while C is calculated using the Bootstrap technique but with 6 GHz data used instead of 18 GHz data. The use of the 6 GHz data to calculate C minimizes the effect of different footprint sizes which sometimes lead to errors. The emissivities at 18 GHz and 37 GHz are then calculated from (1) using T_s and the satellite observed brightness temperatures. Scatter plots of 18 GHz(V) versus 37 GHz(V) data points for both brightness temperatures and emissivities are shown in Fig. 1a and 1b. In the plots, the data points along line AD has been identified to correspond to those in consolidated ice regions while data points along OW are from open water regions. The plots are similar but the clustering of data points in the emissivity plot is better defined than those of the brightness temperature plot because the scatter of points due to spatial changes in ice temperature is minimized.

The new algorithm uses the same procedure as that described in [14,15] to derive ice concentration, but with emissivities substituted for brightness temperatures. The technique utilizes the line AD, as shown in the plots as reference for ice emissivity, and a point at O as a reference for open water. Although the emissivity of the open ocean has a substantial range as indicated by the spread of points along OW, the emissivity of water within the pack is close to O and less variable because of calm surface conditions. The ice concentration at each point B in the plot, is thus given by the ratio OB/OT, where T is the intercept of the lines OB and AD. The location of T changes from one data point to another and is determined by finding the common root of two linear equations corresponding to lines OB and AD.

The use of emissivities eliminate the error due to spatially varying surface temperatures since the latter is already incorporated in the formulation. However, the use of a constant value for emissivities of ice and water causes an error in the retrieval of ice temperature. To assess quantitatively the size of this error, histograms of brightness temperatures at 6 GHz in consolidated ice area are studied. The histograms show that the standard deviation of the brightness temperatures within the ice pack is about 3K. This produces about a 1% error in the value of the emissivity and about 3% error in ice concentration. This is an upper limit in the error since the standard deviation already includes spatial variations in temperature.

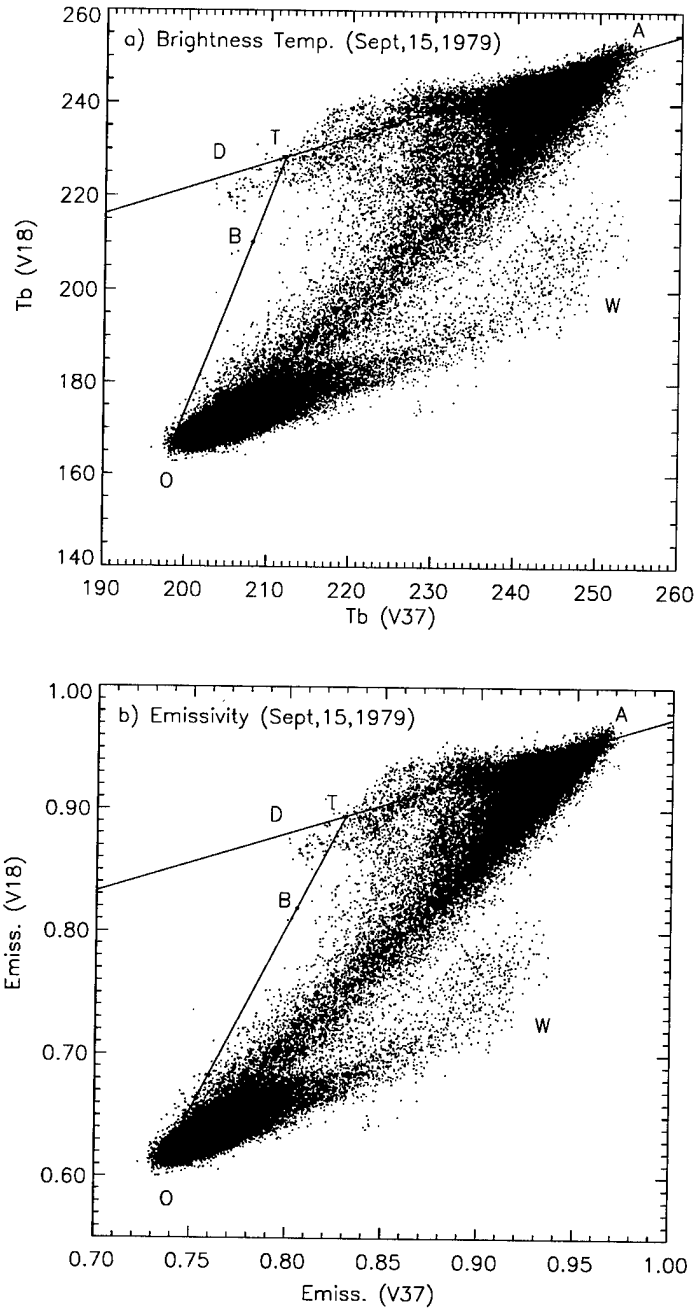

Figure 1. Scatter plot of 18 GHz versus 37 GHz data using (a) brightness temperatures, and (b) effective emissivities.

DERIVED ICE CONCENTRATIONS AND ICE TEMPERATURES

The algorithm is tested using SMMR data because the more current Special Scanning Microwave Imager (SSMI) does not have the 6 GHz channel used to obtain surface ice temperature. Using the procedure described above, coded ice concentration map for September 15, 1979 is shown in Fig. 2a. This ice concentration map was derived using vertically polarized 6 GHz data in combination with 37 GHz data as discussed earlier. The higher contrast in the brightness temperature of ice and water at 6 GHz compared to that at 18

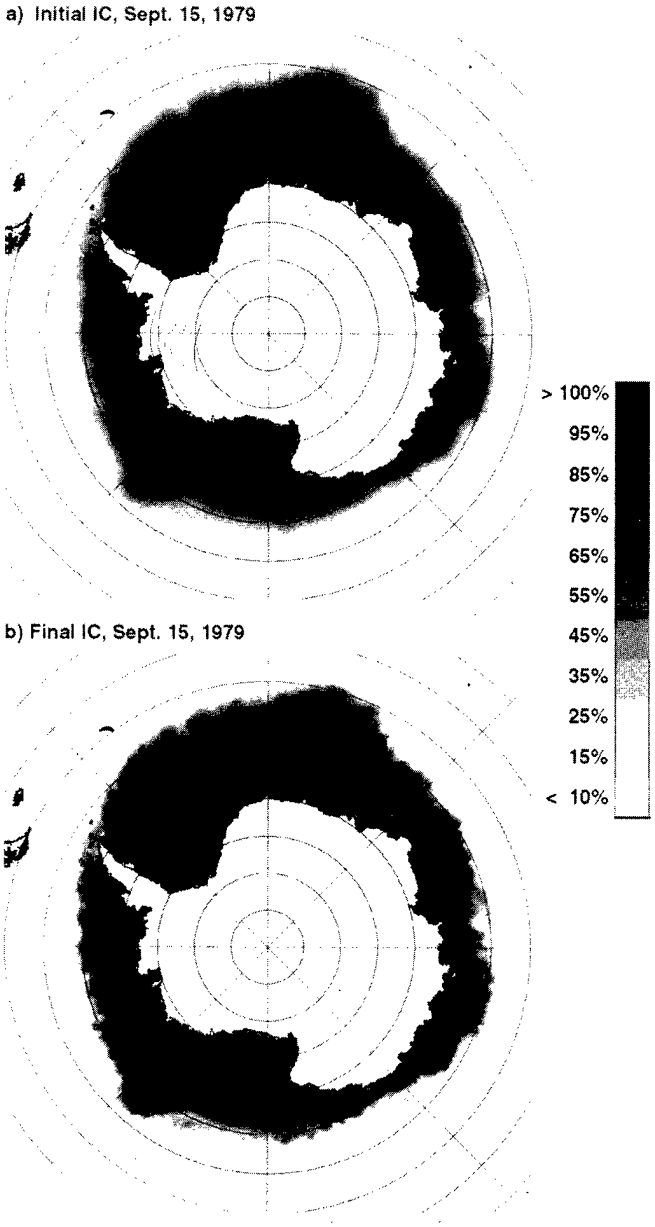

Fig. 2 (a) ice concentration used as initial value for (2); and (b) final ice concentration.

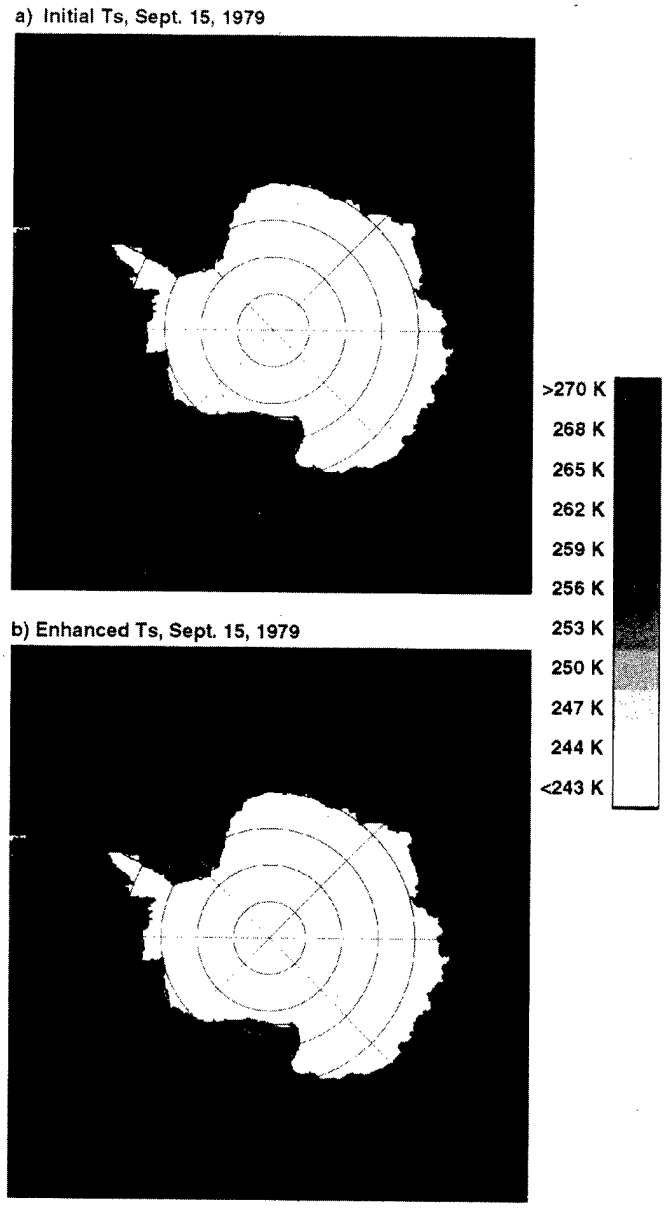

Figure 3. Surface ice temperatures: (a) initial map, and (b) final map.

GHz provides more accurate ice concentration but details in the ice cover are lost because of coarser resolution. The use of this ice concentration data also provides better ice temperature values especially near the marginal ice zone, where mismatches due to different resolutions sometimes occurs.

An ice concentration map using emissivities at 18 GHz and 37 GHz is shown in Figure 2b. The map is similar to that of Figure 2a, but provides more details associated with the better resolution of the 18 GHz than the 6 GHz data (e.g., the Cosmonaut polynya at 45° E). The initial surface temperature map derived is shown in Figure 3a and is used to derive the first V1837 ice concentration map. The surface temperature is re-calculated using ice concentrations from the latter create the final V1837 ice concentration map presented in Figure 2b. The final step is done to improve the matching of the satellite pixels which are taken at different resolutions. The final ice concentration map is very similar to the first V1837 ice concentration map with values differing by generally less than 3%.

Ice concentration maps in the Arctic region are also derived for both Bootstrap and the new algorithm and the results are presented in Figure 4. In the Central Arctic, the ice cover does not change much because of the use of the HV37 set which, as discussed in [14], already account for spatial variations in surface ice temperature. Again, the biggest improvement occurs in cold and almost snow free areas of the seasonal sea ice region.

Overall, the new algorithm enhanced by the use of the 6 GHz channel provides a better characterization of the ice cover than the regular Bootstrap algorithm. The physical surface ice temperatures derived are also realistic. The difference between the initial and final values for ice temperatures are probably mainly due to differences in footprint sizes of the channels used and also in the ice concentration input.

DISCUSSION AND CONCLUSIONS

An algorithm has been developed that makes use of 6 GHz, 18 GHz, and 37 GHz passive microwave data to derive ice concentrations. The use of this set of channels provides a means to enhance the accuracy of the retrieved products, especially in regions where the exclusive use of vertical polarization data is desired. Vertically polarized data are preferred to horizontally polarized data because of less sensitivity to angular dependence, layering, wetness, and other effects [16]. However, the use of vertically polarized data alone causes larger sensitivity (than a combined version) to spatial changes in ice temperature. Such weakness is overcomed by the concurrent use of the 6 GHz data to calculate surface ice temperatures which are used to derive emissivities that can be used to derive a more tempe-

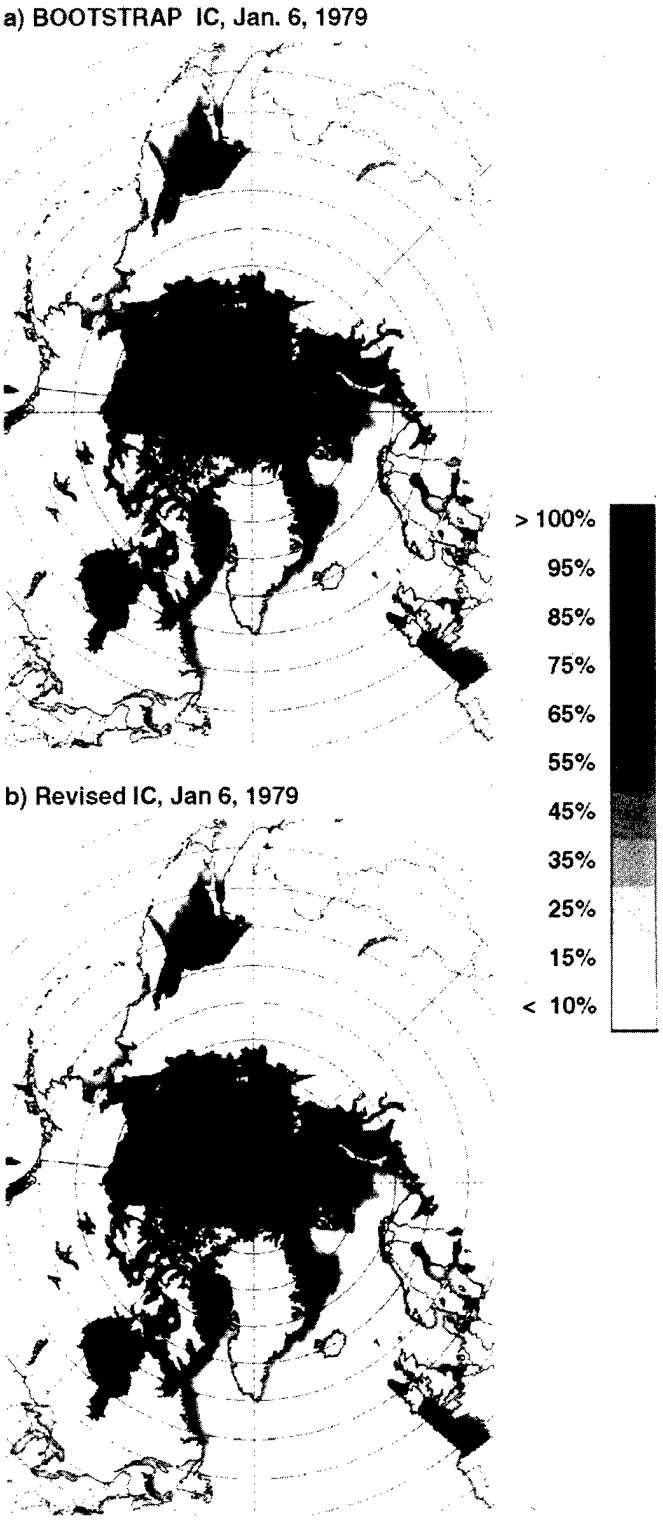

Figure 4. Arctic ice concentratrations using (a) the Bootstrap and (b) the enhanced Bootstrap technique.

rature insensitive and therefore more accurate ice concentration product.

Generally, the ice concentrations from the new technique provide qualitatively similar results to those of the Bootstrap algorithm.. They differ mainly in regions where the ice temperatures are considerably different from average values such as the coastal regions around Antarctica. Although the spatial variation of ice temperature in the Antarctic has been observed to be small, with standard deviation of about 2K [13], the ice temperature near the continent can be substantially lower than average because of the dominance of new and young ice with little of no snow cover.

In this study, we show that reasonably accurate values for ice temperature are obtainable from 6 GHz data. We also show that the ice temperature data can be used to calcuated emissivities that in turn can be used to improve accuracies of current ice concentration maps. Since the sample data set used is that from SMMR, we expect substantial improvements with the advent of AMSR data, because of much better resolution (i.e., 45 by 55 km for AMSR compared with 70 by 150 km for SMMR at 6 GHz). Some of the problems associated with mismatches in footprint sizes will be minimized and we expect further improvements in the accuracy of derived ice concentrations and ice temperatures.

ACKNOWLEDGMENTS

We are grateful to Rob Gersten of Hughes STX for programming and analysis support. This research was funded by the NASA Cryosphere Program and EOS-PM AMSR project.

REFERENCES:

[1] H.J. Zwally, J.C. Comiso, C.L. Parkinson, W. J. Campbell, F. D. Carsey, and P. Gloersen, "Antarctic Sea Ice 1973-1976 from Satellite Passive Microwave Observations," NASA Spec. Publ. 459, 1983, 206 pp..

[2] Parkinson, C. L., J. C. Comiso, H. J. Zwally, D. J. Cavalieri, P. Gloersen, and W. J. Campbell, "Arctic Sea Ice 1973-1976 from Satellite Passive Microwave Observations," NASA Spec. Publ. 489, 1987, 295 pp..

[3] Gloersen P., W. Campbell, D. Cavalieri, J. Comiso, C. Parkinson, H.J. Zwally, "Arctic and Antarctic Sea Ice, 1978-1987: Satellite Passive Microwave Observations and Analysis," NASA Spec. Publ. 511, 1992, 402 pp..

[4] E. Svendson, K. Kloster, B. Farrelly, O.M. Johanessen, W.J. Campbell, P. Gloersen, D. Cavalieri, and C. Matzler, "Norwegian remote sensing experiment: evaluation of the Nimbus 7 scanning multichannel microwave radiometer for sea ice research," J. Geophys. Res., vol. 88, pp. 2781-2792, 1983.

[5] Swift, L. Fedor, and R.O. Ramseier, "An algorithm to measure sea ice concentration with microwave radiometers," J. Geophys. Res., vol. 90, pp. 1087-1099, 1985.

[6] Cavalieri, P. Gloersen, and W.J. Campbell, "Determination of sea ice parameters with the Nimbus 7 SMMR," J. Geophys. Res., vol. 89, pp. 5355-5369, 1984.

[7] Comiso, "Characteristics of Winter Sea Ice from Satellite Multispectral Microwave Observations, " J. Geophys. Rev., vol. 91, pp. 975- 994, 1986.

[8] Rothrock , D.R. Thomas, A.S. Thorndike, "Principal component analysis of satellite passive microwave data over sea ice," J. Geophys. Res., vol. 93, pp. 2321-2332, 1988.

[9] Gloersen, W. Nordberg, T.J. Schmugge, T.T. Wilheit, and W.J. Campbell, "Microwave signatures of first year and multiyear sea ice," J. Geophys. Res., vol. 78, pp. 3564-3572, 1973.

[10] Grenfell, "Surface-based passive microwave studies of multiyear sea ice," J. Geophys. Res., vol. 97, pp. 3485-3502, 1992.

[11] Wensnahan, G.A. Maykut, T.C. Grenfell, D.P. Winebrenner, "Passive microwave remote sensing of thin sea ice using principal component analysis," J. Geophys. Res., vol. 98, pp. 12,453-12,468, 1993.

[12] Cavalieri, "A passive microwave technique for mapping new and young sea ice in seasonal ice zones," J. Geophys. Res., vol. 99, pp. 12,561-12,572, 1994.

[13] Comiso, J.C, T.C. Grenfell, M. Lange, A. Lohanick, R. Moore, and P. Wadhams, "Microwave remote sensing of the Southern Ocean Ice Cover," Chapter 12, Microwave Remote Sensing of Sea Ice, (ed. by Frank Carsey), Washington, D.C.: American Geophysical Union, 1992, pp. 243-259.

[14] Comiso, "SSM/I Concentrations using the Bootstrap Algorithm", NASA RP 1380, 1995, pp. 1-40.

[15] Comiso, and H. J. Zwally, "Polar Microwave Brightness Temperatures from Nimbus-7 SMMR, Time Series of Daily and Monthly Maps from 1978 to 1987," NASA RP1223, 1989.

[16] Matzler, R.O. Ramseier, E. Svendsen, "Polarization effects in sea ice signatures," IEEE J. Oceanic Eng. OE, vol. 9, pp. 333-338, 1984.

Wave Dispersion by Frazil-Pancake Ice from SAR Imagery

P.Wadhams†, G. De Carolis*, F.Parmiggiani° and M.Tadross†
† Scott Polar Research Institute, Cambridge CB2 1ER, (U.K.)
ph. +44-1223-336542 fax +44-1223-336549 e-mail: pw11@cam.ac.uk
* ITIS-CNR, P.O. Box 11, Matera (Italy)
ph. +39835-377282 fax +39835-339027 e-mail: decarolis@asimt0.mt.asi.it
o IMGA-CNR, via Gobetti 101, 40129 Bologna (Italy)
ph.+3951-639 8009 fax +3951-639 8132 e-mail: parmi2@ghibli.imga.bo.cnr.it

Abstract – On the basis of a theory of wave propagation from open sea in frazil-pancake ice developed in Wadhams [1], a project was carried out, during 1994-96 under the EU Environment Programme, to map ice thickness from SAR imagery in the Odden Ice Tongue, Greenland Sea.

Ground truth data (ice thickness and composition, wind stress and local wave spectrum, etc.) were available from a field experiment carried out in the Odden during April 1993. Twenty six high-resolution SAR images for the same period and covering the same area were acquired and processed.

A first, "simple", procedure was developed to perform spectral analysis in order to obtain the change of wavelength and angle of refraction of the dominant wave entering the ice field. Ice thickness values derived from the theory were larger than those measured during the field experiment.

The inversion scheme presented by Hasselmann et al. [2] was then utilized to retrieve the ocean spectrum from the SAR spectrum. This was done for three scenes (April 3 and 10, 1993) for which wave spectra from buoy data were available.

Variations of wavelength and propagation direction of the dominant wave systems are analyzed before and after they enter ice zones in order to: i) evaluate the optimal conditions occurring for spectral changes detection with the ERS SAR system; and ii) gain more insight into applicability limits of the inversion algorithm when applied to sea-ice scenes.

INTRODUCTION

In the years 1994-96, under the EU Environment Programme, we have carried out a project whose aim was the mapping of ice thickness from SAR imagery in the Odden Ice Tongue, Greenland Sea.

Odden is an ice tongue which usually develops during winter, just east of the main East Greenland ice edge, between 72-74°N latitude, and often curves round to the northeast, reaching east of 0°.

The nature of Odden is of special interest because it is believed that ice production in this region provides a salt flux which helps to trigger the mid-gyre convection occurring during winter. It is therefore particularly important to study the ice volume and growth rates in Odden.

In the winter of 1993 Odden developed entirely in the form of locally-grown frazil and pancake ice. A field experiment was carried out in the region in April 1993 as part of the EU-sponsored ESOP programme (European Subpolar Ocean Programme, [3]). The research ship "Polarstern" was in the Odden on 3 and 10 April and made measurements of ice thickness and composition, wind stress and local wave spectrum. This field measurements provided a validation opportunity to test a remote sensing technique which yields ice thickness in frazil and pancake ice using ocean wave dispersion as a proxy [4].

SAR WAVE SPECTRA

Synthetic aperture radar (SAR) can detect ocean waves and swell within a sea ice cover when this is composed of frazil or pancake ice (which is the case of the Odden region). This kind of ice regime was studied by Wadhams and Holt [4] in relation to a Seasat SAR image of the Chukchi Sea. Wave number spectra were derived from subscenes of the image and demonstrated refraction and a wavelength change with increasing penetration into the icefield. The results were compatible with a theory for wave dispersion in a frazil slick based on mass loading of the water surface by the ice, and the authors showed that wavelength changes in such an icefield can thus be used to calculate the thickness of the frazil-pancake ice cover.

The relationship which links k_w and k_i, the wave numbers in open water and ice, is:

$$k_i = k_w/(1 - c\ h\ r\ k_w) \tag{1}$$

where h is the thickness of the frazil or pancake layer, c is the average ice concentration within it and $r = \rho_i/\rho_w$, with ρ_i and ρ_w being ice and water densities.

The ice thickness h is then obtained from (1):

$$h = \frac{(k_i - k_w)}{c\ r\ k_i\ k_w} \tag{2}$$

0-7803-3836-7/97/$10.00 © 1997 IEEE

It should be noted that more complex theories of wave dispersion in frazil ice are being developed, which incorporates the viscosity of the ice layer.

The analysis of SAR images was performed on 26 full resolution SAR-PRI scenes of the ERS-1 of the Oddenn region, of the period 1-15 April 1993.

A first, "simple", analysis procedure was developed, consisting of the following steps: i) geo-location and geo-reference of each image onto a UTM map projection; ii) extraction of a line of 15 full resolution windows, 512×512 pixel size, going from the open sea toward and inside the ice field in the image; iii) wave spectra computation on the 15 windows (by means of the Optical Fourier Transform); and iv) contour plot and peak detection of wave spectra.

This kind of analysis gives the change of wavelength and angle of refraction of the dominant wave entering the ice field. Ice thickness values derived from (2) were larger than those measured during the field experiment.

INVERSION SCHEME

The SAR imaging of waves is a strongly non linear process. Because of the 180° directional ambiguity and the azimuthal cut-off, directional wave spectra can be estimated from SAR image spectra only using a first guess spectrum. The inversion scheme proposed in [2] was implemented for cartesian SAR spectra like those obtained from SAR-PRI images of ERS-1 [5]. The algorithm, written in IDL language, exploits the information provided by a guess wave spectrum in order to increase the information lacking in SAR data. An iterative procedure is used to extract wave information included in SAR data on the basis of the *a priori* wave spectrum. The inversion scheme includes a module for updating the guess spectrum from the retrieved wave spectrum after the last iteration step [2]. This is an interesting feature of the algorithm which enables the final retrieved spectrum to deviate from the initial guess when the latter is poor [2,5]. In order to increase the performance of the inversion algorithm in reproducing SAR spectra features, an interpolation module, which computes the updated guess spectrum on a coarser resolution of the wavenumber domain, was introduced. This module works as a smoothing filter on SAR spectra sampling variability and noise. The effects of the filter are spectral increments going added to the wave spectrum at each iteration step.

RESULTS AND DISCUSSION

Inversion results refer to the SAR image acquired on April 10 (orbit: 9077, frame: 1521). A directional wave spectrum was collected by a buoy deployed in a location inside the SAR scene but some time before the satellite pass. Various full resolution windows were extracted both in open and ice covered sea at increasing incidence angle and their spectra were computed. The quality of the results was evaluated considering both the global square error ϵ^2 and the correlation C between the real and simulated SAR spectra, as well as the cut-off wavelength measured on the simulated SAR spectra. The combination of these parameters gives an overall criterion to evaluate the performances of the inversion scheme. While ϵ^2 and C values should approach 0 and 1, respectively, the simulated cut-off wavelength should be as close as possibile to that estimated on the measured SAR spectrum. In Table 1 are reported: i) the dominant retrieved wavelength, and its direction of propagation, in the wavenumber domain (including wavelengths between 100 and 700 m); ii) the final square errors; iii) correlation; iv) simulated cut-off wavelength versus measured one on the real SAR spectrum; and v) incidence angle of the extracted windows. Windows # 1 and 6 refer to open sea spectra showing results which appear questionable. The reason may be that the first guess spectrum was collected inside the ice field, the high frequency part of the wave spectrum being affected by the presence of ice. Window # 2 (sea) shows very good results, as it was extracted close to the ice edge. Window # 3 was selected around the location where the buoy was deployed.

Fig. 1 shows the SAR scene under analysis with the indication of the site of the extracted windows. Fig. 2 shows two examples of spectra as they result from the inversion scheme outlined above.

ACKNOWLEDGMENTS

This work was supported by the European Union under contract no. EV5V-CT94-0440 of the Environment Programme.

REFERENCES

[1] Wadhams, P., The seasonal ice zone. In *The Geophysics of Sea Ice* (ed. N. Untersteiner), Plenum, New York, 1986, 825-991.

[2] S. Hasselmann, C. Bruning, K. Hasselmann and P. Heimbach (1996). "An improved algorithm for the retrieval of ocean wave spectra from synthetic aperture radar imagery", *J. Geophys. Res.*, vol. 101 (C7), 16615-16629.

[3] Wadhams, P. (1994). The European Subpolar Ocean Programme (ESOP). Proc. Oceanology '94, Brighton, Mar. 8-11, 1994, Spearhead, London.

[4] Wadhams, P. and B. Holt (1991). Waves in frazil and pancake ice and their detection in Seasat synthetic aperture radar imagery. J. Geophys. Res., vol. 96(C5), 8835-8852.

[5] G. De Carolis, "Inversion of ERS-1 SAR ocean spectra into wave spectra. Algorithm description.", *ITIS-CNR Tech. Report 96/8*, 1996.

Table 1

w #	Field	α	λ	ϕ	ϵ^2	$C(\%)$	ρ
1	sea	19.94	187.91	40.23	0.24	88.00	238/300
2	sea	20.90	150.85	45.00	0.11	95.39	289/287
3	ice	21.62	145.30	50.53	0.21	93.54	266/262
4	ice	22.13	172.00	53.74	0.21	92.85	256/257
5	ice	23.69	160.00	53.13	0.18	93.81	264/264
6	sea	25.60	265.74	48.37	0.64	74.22	101/320

where: α = SAR incidence angle; λ = wavelength of the dominant wave; ϕ = dominant wave direction versus range direction; ρ = ratio between cut-off wavelengths in the simulated and in the real spectrum.

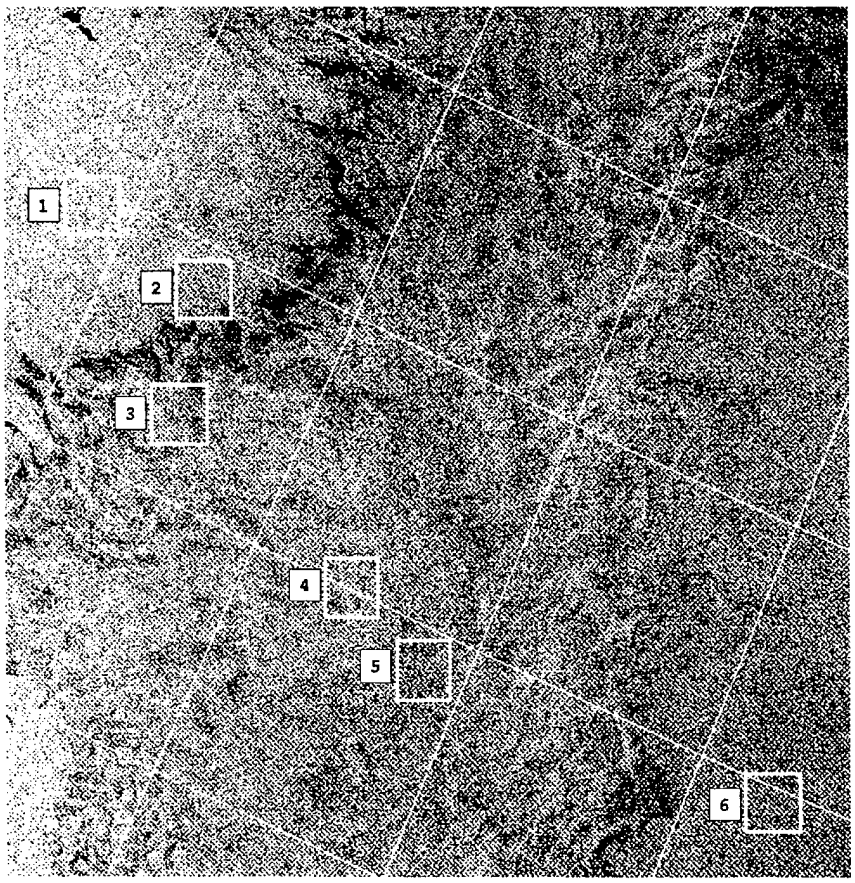

Fig. 1. SAR scene of April 10, 1993 (orbit: 9077, frame 1521) with the indication of the site of the extracted windows.

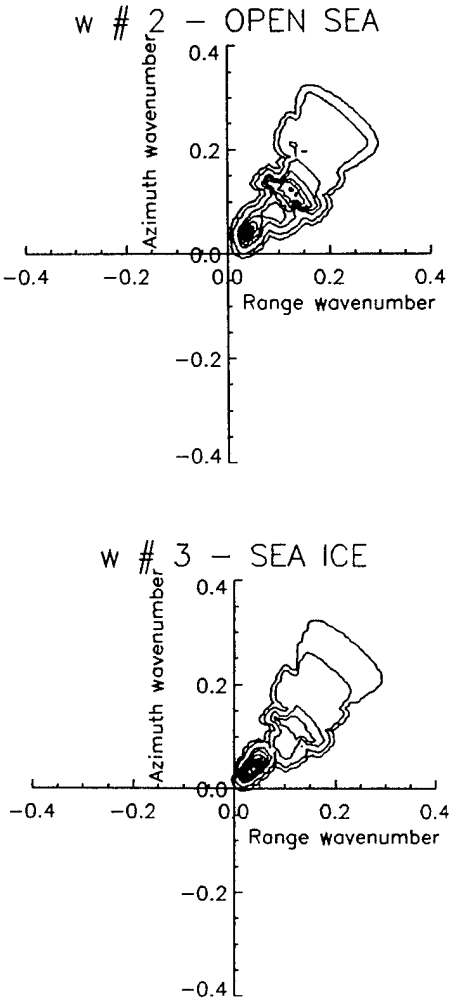

Fig. 2. Examples of inverted wave spectra within open sea (upper) and sea-ice (lower). Effects of wave propagation into sea ice is evident for wavenumbers larger than 0.1 m^{-1}.

Multiresolution Signal Representation for Phase Unwrapping and Interferometric SAR Processing

Richard Bamler[1]
Gordon W. Davidson[2]

[1]German Aerospace Research Establishment (DLR), German Remote Sensing Data Center (DFD)
Oberpfaffenhofen, D–82234 Wessling, Germany
phone: +49–8153–28–2673, fax: +49–8153–28–1420, e–mail: Richard.Bamler@dlr.de

[2]Glenayre, 1570 Kootenay St.
Vancouver, B.C., V5K 5B8, Canada
phone: (604) 293–4399, fax: (604) 293–4317, e–mail: gdavidso@glenvan.glenayre.com

Abstract — Phase unwrapping requires – implicitly or explicitly – phase gradient estimates for phase reconstruction. An asymptotically unbiased local frequency estimator based on multiresolution signal representation is presented. The proposed estimator is able to automatically trade–off resolution against estimation error. It is shown that interferometric SAR processing can be improved by employing a smoothed version of the unwrapped phase. Particularly, a novel method for slope–adaptive spectral shift filtering is introduced.

INTRODUCTION

Phase unwrapping conceptually consists of two steps: (1) estimation of phase gradients from the interferogram and (2) integration of the gradient estimates. The presence of noise and undersampling causes gradient estimates to be aliased, so that the measured gradient field is nonconservative, leading to a path dependent integration and errors in the constructed phase surface. Aliasing errors occur between points of nonzero curl of the phase gradient field, or residues, and phase unwrapping algorithms attempt to exclude the aliasing errors from the integration process either by branch–cuts in a path–following integration [1], or by zero–weights in weighted least squares or related algorithms [3], [4], [5].

The most commonly used procedure to estimate phase gradients is to take the phase differences of adjacent samples and wrap them into the principal interval of –0.5 ... +0.5 cycles. It has been shown that these estimates are biased towards lower values in the unavoidable presence of decorrelation noise and may lead to underestimation of terrain slopes [6], [7]. Hence, phase gradient (or: local frequency) estimation is worth being investigated for phase unwrapping.

In this paper we present improvements and extension to a previously published asymptotically unbiased phase gradient estimator based on multiresolution techniques [11], [12] (not to be confused with 'multi–grid' techniques [5]). We will further show, how a low resolution version of the unwrapped phase supports interferogram processing; in particular a new slope–adaptive wavenumber–shift filter will be introduced.

This short paper can only highlight a few aspects of a more detailed publication [13].

REVIEW OF MULTIRESOLUTION FREQUENCY ESTIMATION

The phase gradient estimator using wrapped phase differences of adjacent samples suffers from its small estimation window of 2x2 samples, leading to a high probability of aliasing. As mentioned above, aliasing errors add a bias to slope reconstruction, since it is more likely to 'loose' a fringe cycle when integrating up a noisy phase ramp than to 'win' a fringe.

As an alternative to wrapped phase differences, local fringe frequencies, f, can be estimated over larger windows of the complex interferogram [2]. The choice of the window size requires a trade–off between resolution and aliasing bias. To overcome this problem, multiresolution frequency estimation uses the benefits of both large and small windows. Conceptually, this is illustrated in fig. 1, in which $z(i,k)$ represents the interferogram. The largest window #3, corresponding to the lowest resolution, is used to obtain an estimate of an average frequency over the window, f_3, which is then used to flatten the phase over the next smaller window #2, or next higher resolution, by a complex multiply. The frequency then estimated from window #2 is the difference frequency $\delta_2 = f_2 - f_3$ where f_2 is the frequency that would have been estimated from window #2, without the complex multiply. This procedure of successive interferogram flattening is continued until the highest resolution level. The sum of difference frequencies is the frequency estimate f_0, corresponding to the smallest desired estimation window size. Since each estimation is of a rel-

0-7803-3836-7/97/$10.00 © 1997 IEEE

atively small difference frequency, the effect of slope on the estimation is approximately removed.

Although many methods of local frequency estimation could be used [2], it is desired to employ a computationally efficient method and one that gives a robust estimate in the presence of phase variation over a large window. For this reason, we use a modification of a spectral centroid estimator given by the phase of the autocorrelation function at the lag of 1 sample [9]. The estimated centroid of the spectrum (e.g. in the i –direction), at resolution level n , is

$$f_n^i = \arg\left\{\sum_i \sum_k z^*(i,k)\, z(i+1,k)\right\}/2\pi$$

where the summation extends over the estimation window. At the highest resolution level, the frequency estimate is $f_0^i = \arg\{z^*(i,k)\, z(i+1,k)\}/2\pi$ which is simply a calculation of the wrapped phase difference.

An advantage of this approach is that the computation of the above summation has an efficient, quad–tree–like hierarchical implementation. From the different possible multiresolution representations a scheme as the one from fig. 2 has proven to be well suited for SAR interferograms: Here, the original sample grid spacing is maintained for the first two summation layers, which allows for the modifications described below.

The accuracy of the frequency estimator can be improved at the expense of computation time by additionally employing lags of 2 and 3 samples.

Fig. 3 shows histograms of multiresolution phase gradient estimates and those obtained as wrapped differences of adjacent samples for a phase ramp of 0.25 cycles per sample and a moderate coherence. Clearly, multiresolution phase gradient estimates are unbiased while the conventional ones are restricted to the principal interval and, hence, their expectation value is smaller than the true slope.

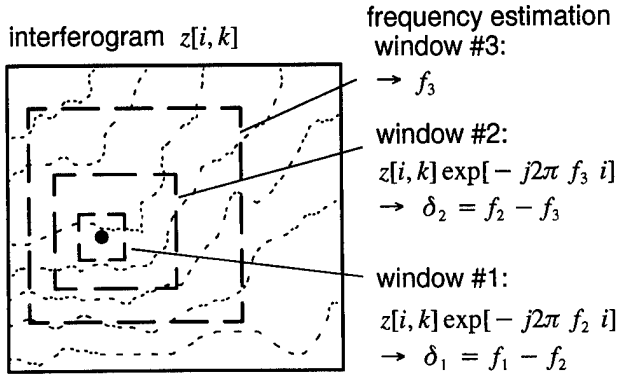

Figure 1: Multiresolution frequency estimation

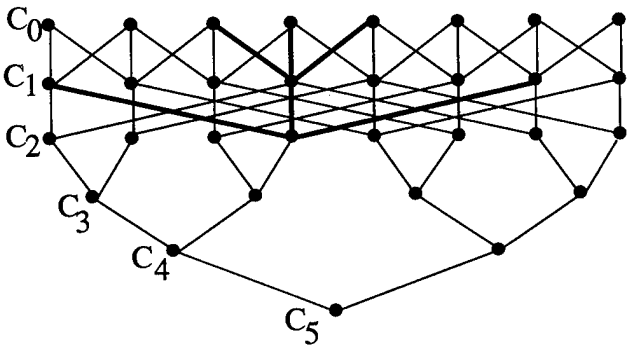

Figure 2: Hierarchical implementation of multiresolution frequency estimation (1–D example)

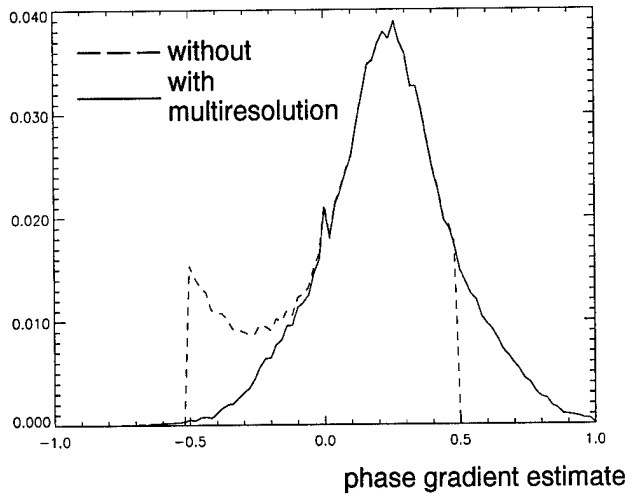

Figure 3: Histogram of frequency estimates with and without multiresolution, terrain phase slope = 0.25 cycles per sample, coherence = 0.7

ADAPTIVE MULTIRESOLUTION FREQUENCY ESTIMATOR

The proposed method readily provides frequency estimates at arbitrary resolution levels. E.g. the estimate at resolution level m is found by accumulating the difference frequencies, starting at the lowest resolution ($n = N$) up to level m (rather than going down to $n = 0$):

$$f_m = \sum_{n=m}^{n=N} \delta_n$$

In the *adaptive* multiresolution approach, the curl of the 2–D frequency field is computed at each resolution level, to decide whether the difference frequencies from the current and higher resolutions should be accumulated. At the point (i,k) in the

n 'th resolution level, let $f_n{}^i(i,k)$ and $f_n{}^k(i,k)$ be the frequency components in the i and k directions, and the curl $r_n(i,k)$ is computed as

$$r_n(i,k) = f_n^i(i,k) + f_n^k(i+1,k) - f_n^i(i,k+1) - f_n^k(i,k)$$

If one or more of the frequency estimates are aliased, a relatively large value of $|r_n(i,k)|$, close to one, results. Also, with local frequencies estimated over larger windows, the curl is affected by noise in the frequency estimates and is not necessarily an integer, as it is in the calculation of residues from adjacent phase samples. In the algorithm, at points where the magnitude of the curl exceeds a threshold, the frequency differences are only accumulated up to the lower resolution level. Thus, in the adaptive multiresolution resolution method, the required window size for frequency estimation is adjusted automatically to the local interferogram quality at every point.

APPLICATIONS OF SMOOTHED PHASE

Finally, the multiresolution frequency estimates may be input to a least squares reconstruction (LSE) for phase unwrapping. Although the result may be already considered an acceptable reconstruction, we propose to first reconstruct a smoothed version $\tilde{\phi}(i,k)$ of the phase. This is obtained by setting the aforementioned threshold in the adaptive multiresolution estimator conservatively low. Then noise and high frequency detail will be suppressed. In the following we will show how such a smooth phase can be used to improve interferogram processing.

Interferogram Flattening

Any phase unwrapping algorithm benefits from a pre–flattened interferogram. Hence, it makes sense to subtract the reconstructed smooth phase $\tilde{\phi}(i,k)$ from the interferogram before further processing (e.g. multi–looking) the data and unwrapping the residual details. Fig. 4 compares the phase errors for a scene unwrapped using smooth phase subtraction to the unwrapping result without flattening. The used scene was simulated from a fractal terrain containing zero–coherence water surfaces. The coherence was slope dependent and ranged from 0.0 (water) to 0.7 (flat terrain).

Coherence Estimation

Coherence estimates are known to be biased if the estimation widow is to small. On the other hand, the window size is limited by the local fringe frequency. Flattening the interferogram prior to coherence estimation facilitates the design of the estimator.

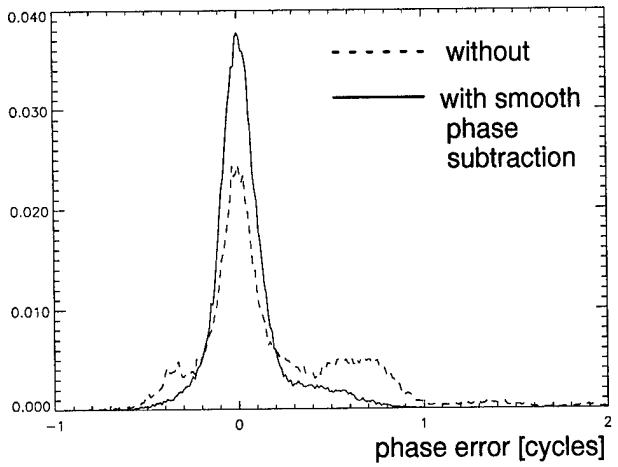

Figure 4: Histogram of unwrapped phase errors

Slope–Adaptive Spectral Shift Filter

The ground range reflectivity wavenumber spectrum is mapped into the SAR range signal spectrum according to the sine of the local incidence angle [8]. Hence, the two SAR images (taken at slightly different angles) contain partially different wavenumber components of the scattering surface, an effect known as wavenumber shift [8]. To avoid decorrelation the range spectra of the two SAR images must be truncated such that non–common wavenumbers are discarded. The amount of spectral shift is identical to the local fringe frequency and does not only depend on the baseline but also on local terrain slope. For optimal processing a *slope–adaptive* filter is required. The smooth phase $\tilde{\phi}(i,k)$ provides information about terrain slope and allows for an efficient implementation of such a filter, rather than a spatially varying, space–domain filter kernel.

Since the local spectral shift is equal to the local fringe frequency, multiplying each of the complex SAR images by complex exponentials of the smooth phase $\tilde{\phi}(i,k)$ performs a spatially varying range frequency shift of the image spectrum, such that the spectral components that are not represented in the other image get shifted outside the range system bandwidth. Then, a simple low–pass filter implemented in the frequency domain removes the uncorrelated parts of the spectrum for each image (fig. 5). Because of the spatially varying frequency shift implied in $\tilde{\phi}(i,k)$, the filtering of uncorrelated parts of the spectrum adapts to the local slope. Fig. 6 demonstrates the improvement in interferogram coherence due to adaptive spectral shift filtering. Although the difference in the histograms seems not to be dramatic, a close examination of the interferogram shows, that especially the critical up–slopes benefit from the filter; in those areas the number of residues are clearly reduced.

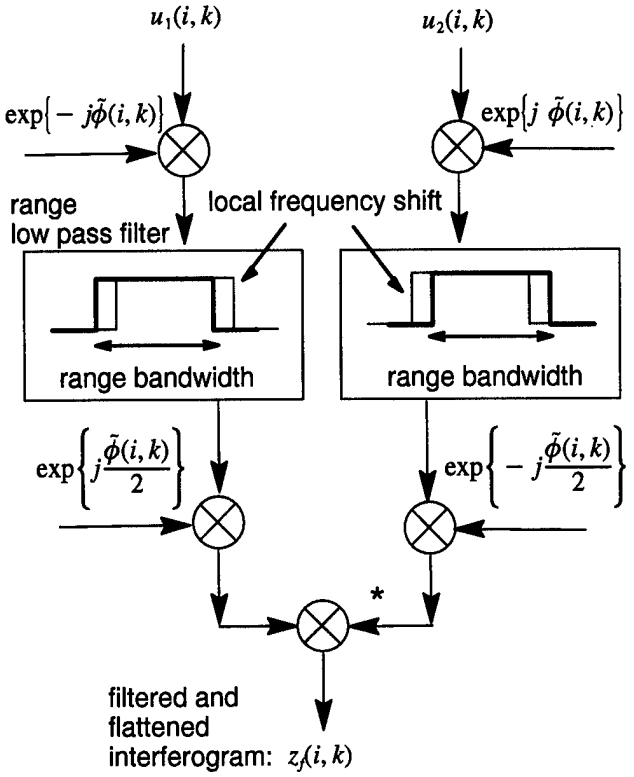

Figure 5: Slope–adaptive spectral shift filter

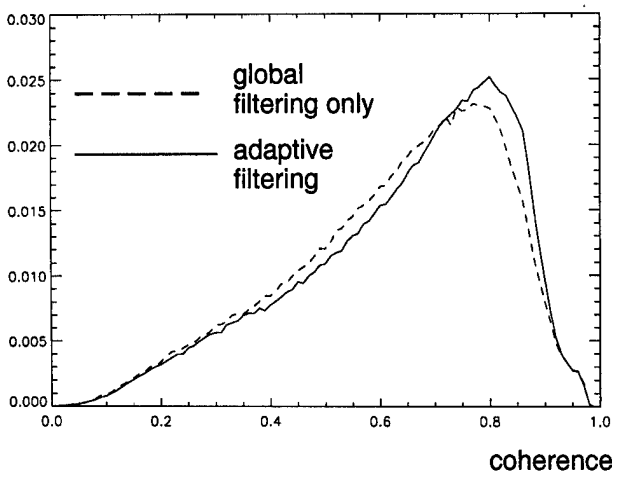

Figure 6. Histogram of coherence of real ERS–scene before and after slope–adaptive spectral shift filtering.

REFERENCES

[1] R. M. Goldstein, H. A. Zebker, and C. L. Werner, "Satellite radar interferometry: two–dimensional phase unwrapping," Radio Science, vol. 23, pp. 713–720, 1988.

[2] U. Spagnolini, "2–D phase unwrapping and instantaneous frequency estimation," IEEE TGRS, vol. 33, pp. 579–589, 1995.

[3] D. C. Ghiglia and L. A. Romero, "Robust two–dimensional weighted and unweighted phase unwrapping that uses fast transforms and iterative methods," JOSA A, vol. 11, pp. 107–117, 1994.

[4] G. Fornaro, G. Franceschetti, R. Lanari, "Interferometric SAR phase unwrapping using Green's functions," IEEE TGRS, vol. 34, pp. 720–727, 1996.

[5] M. Pritt, "Phase unwrapping by means of multigrid techniques in interferometric SAR," IEEE TGRS, vol. 34, pp. 728–738, 1996.

[6] R. Bamler, N. Adam, G. W. Davidson, D. Just, "Noise–induced slope distortion in 2–d phase unwrapping by linear estimators with applications to SAR interferometry," submitted to IEEE TGRS, Jan. 1996.

[7] R. Bamler, G. W. Davidson, "On the nature of noise in 2–D phase unwrapping," in: Microwave Sensing and Synthetic Aperture, Proc. SPIE, vol. 2958, pp. 216–225, 1996.

[8] F. Gatelli, A. Monti Guarnieri, F. Parizzi, P. Pasquali, C. Prati, F. Rocca, "The Wavenumber Shift in SAR Interferometry," IEEE TGRS, vol. 32, pp. 855–865, 1994.

[9] S. N. Madsen, "Estimating the Doppler centroid of SAR data," IEEE Trans. AES, vol. 25, pp.134–140, 1989.

[10] P. Pasquali, "Generation of height maps with interferometric SAR (in Italian), Ph.D. thesis, Technical University of Milano, 1995.

[11] G. Davidson, R. Bamler, "A multiresolution approach to improve phase unwrapping", in: Proc. IGARSS'96, pp. 2050–2053, 1996.

[12] G.W. Davidson, R. Bamler, "Robust 2–D phase unwrapping based on multiresolution", in: Microwave Sensing and Synthetic Aperture, Proc. SPIE, vol. 2958, pp. 226–237, 1996.

[13] G.W. Davidson, R. Bamler, "Multiresolution phase unwrapping for SAR interferometry, submitted to IEEE TGRS, Dec. 1996.

Phase Unwrapping by Fusion of Local and Global Methods

A. Reigber[1] and J. Moreira[2]

[1] DLR, Deutsche Forschungsanstalt für Luft- und Raumfahrt e.V., D-82230 Oberpfaffenhofen, Germany. Tel/Fax: (49)8153-282367/281135 Email: Andreas.Reigber@dlr.de

[2] Aerosensing Radarsysteme GmbH, D-82230 Oberpfaffenhofen, Germany. Tel/Fax: (49)8153-281542/281543, Email: Joao.Moreira@dlr.de

Abstract – This paper addresses a new PU algorithm based on the fusion of a region growing and an iteratively working 2-D least-square PU. By the mutual support of the two algoritms it is possible to combine the advantages of both and to eliminate the errors occuring if each one is working independently. The resulting unwrapped phase is characterised by a local stability gained from the contribution of the global method as well as the global stability given by the local method. The performance of the presented PU fusion is significantly better in comparison to the performance of the conventional methods.

Introduction

Across-track SAR interferometry is a potential tool to measure surface topography. The extraction of the absolute phase from the measured interferometric phase (phase unwrapping) is one important task in the interferometric processing procedure. Phase unwrapping problems occur from aliasing errors due to phase noise caused by low coherence and undersampling phenomena because of locally high fringe rates. Several PU algorithms based on different approaches are described in the literature. Global working PU algorithms are powerful in the local reconstruction of the unwrapped phase, but with the disadvantage of error propagation from decorellated parts of the image into high coherent areas. A loss in global stability is the result. In contrary local PU algorithms perform well in areas with sufficent high coherence. Local bounded propagation errors can occur in low coherent areas, but for the remaining parts a global height stability is derived. The combination of a robust representative of each sort of PU finally offers the possibility to exploit the advantages of both algorithms and therefore to improve the quality of the result.

Phase unwrapping methods

A simple and fast solution of the two-dimensional PU problem is the global working Least-Square Algorithm described in [1]. This algorithm is based on the minimisation of the differences between the partial derivatives of the wrapped and the unwrapped phase function [2] by solving a poisson equation with boundary conditions of the form:

$$\frac{\partial^2}{\partial x^2}\Phi(x,y) + \frac{\partial^2}{\partial y^2}\Phi(x,y) = \rho(x,y)$$

where Φ is the unwrapped phase and ρ the second order derivative of the wrapped phase. If the phase is affected by noise the phase slopes are always underestimated [4] and the LS-algorithm cannot reconstruct the full height of the underlying topography. These errors from decorrelated parts of the image also propagate into areas with high coherence. The result is a global distortion of the final absolute phase.

This problem is not present in the local approach. A fast and robust solution for local phase unwrapping are region growing algorithms like those in[3]. The basic idea of these kind of algorithms is the following: The pixels around an already solved region which have a sufficent number of unwrapped neighbour pixels are decided to be growth pixels. From the unwrapped phase values a predication of the absolute phase Φ_p is made providing to add the correct 2π-multiple to the growth pixels:

$$\Phi_{uw} = \Phi_p + \arctan(e^{i\Phi_{gr} - i\Phi_p})$$

The sucess of this method depends strongly upon the path chosen to perform the unwrapping and on the quality of the predication. Unwrapping errors are minimized by starting at pixels of high data quality or coherence and then relaxing the coherence limit step by step. At a certain critical coher-

0-7803-3836-7/97/$10.00 © 1997 IEEE

ence limit the algorithm starts to be unstable and wrong 2π-jumps are made.

Fusion of global an local PU

Looking at the differences between the orginal phase and the LS-solution a phase pattern can be observed which shows the global distortion of the obtained absolute phase (Fig. 3). This error matrix can now be unwrapped using the region growing algorithm. Because a local method always gives a correct solution we are able by this means to estimate and to correct exactly the error of the global algorithm. After reaching the critical coherence limit for the RG, the error can be interpolated into the unresolved parts. After this the final absolute phase can simply be obtained by adding the unwrapped error matrix to the LS solution.

The advantage of this advance is that it is now no longer necessary to reconstruct the heavily decorrelated parts with the local method. In these areas the global approach is more powerful. By iteratively unwrapping the differences of the original phase and the preliminary result it is possible to reach locally the correct phase gradient even in extremely low coherent areas. To bate the problem of the underestimation and allow a faster convergence to the correct slope it seems to be necessary to reduce the phase noise by boxcar filtering in every iteration step. We determined that with this method usually after 16 iterations no further improvement of the solution could be observed.

Another important step is to minimize the coherence limit of the RG-algorithm. The used coherence map has a strong influence on the unwrapping path chosen by the RG method. As we found out the best results can be obtained with coherence map calculated directly from the phase values using

$$\gamma = \langle e^{i\Phi} \rangle_N,$$

where $\langle \ldots \rangle$ stands for the expectaion value. By using an increasing number of necessary unwrapped neighbours in the search for the growth pixels and a bigger predication window for lower coherence it is possible get faultless results until a critical coherence of 0.3. Below this limit our algorithm is not stable and locally bounded errors may occur. At this point normally the greatest part of the image is reconstructed.

The result is now characterised by the perfect reconstruction in areas with $\gamma > \gamma_{krit}$ given by the local method and an approximately correct solution

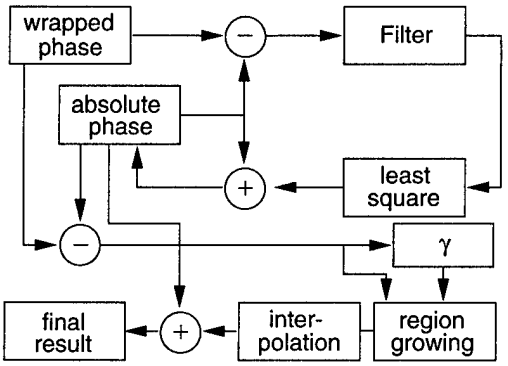

Figure 1: Scheme of the fusion algorithm, default value for the absolute phase is zero

in the resting parts gained from the global unwrapping. A shematic representaion of our algorithm is shown in Fig. 1.

Experimental results

The effectiveness of this new method has been verified among other things using an interferogram generated from ERS-1 data around Athens,Greece. A portion of 1k x 1k pixels is shown if Fig. 2. This SAR interferogram has been chosen because of its low coherence (in medium 0.45) and the partly steep topography in this area. The error pattern obtained from only the global method is shown in Fig. 3. In contrary to this the final result (Fig. 4,5) shows for the most parts an ideal reconstruction of the absolut phase. We also compared the DEM obtained from this unwrapped phase with an available

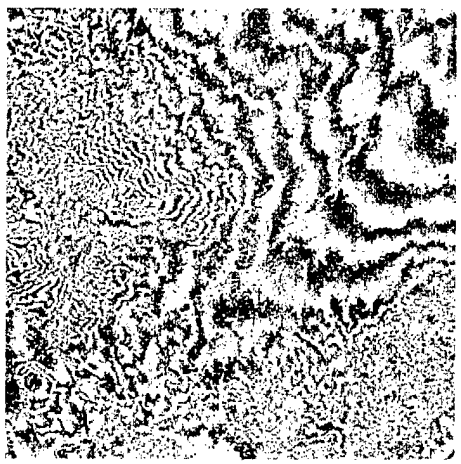

Figure 2: Phase of the interferogram, before unwrapping

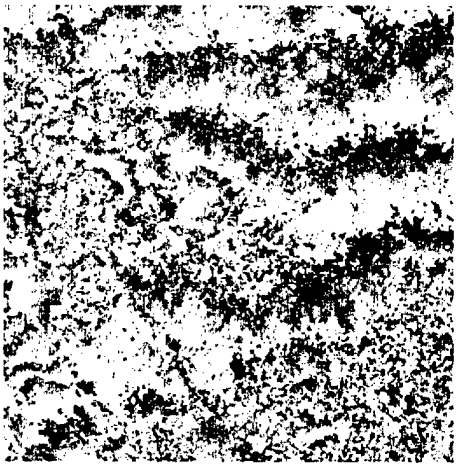

Figure 3: Residual error fringes of the LS solution

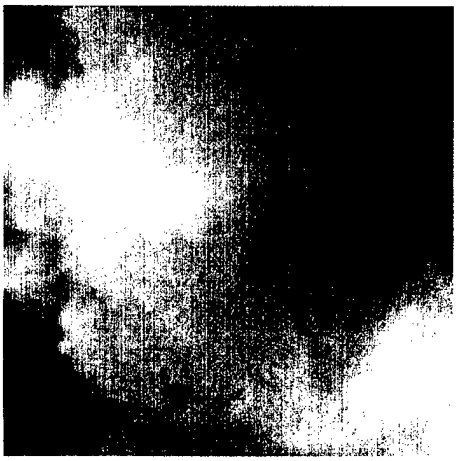

Figure 4: Result of the fusion algorithm

DEM from ground measurements. The absolute error is always below 15m in the parts solved by the region growing algorithm. The height in the globally unwrapped mountains is around 100m below the true height of 1700m. This is due to the slope underestimation in these decorrelated areas. The quality of results obtained on simulated data is about the same (not shown)

Also an interesting point is the time cosumption of the algorithm. For the presented example we needed 9.5 min for the 16 global iteration, 7 min for the region growing algorithm and 1 min for the interpolation on a Pentium PC. For a whole ERS scene the total computation time was around 10 hours. This acceptable speed makes the algorithm useable for operational work.

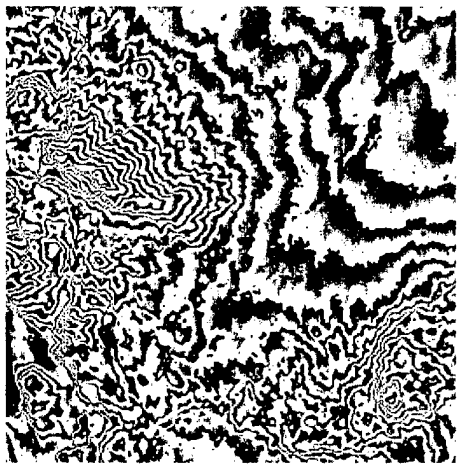

Figure 5: Filtered and rewrapped result of the fusion algorithm

Conclusions

We have developped a new phase unwrapping method which combines the advantages of both the global and the local methods. It can handle interferograms which are partly very noisy without any distortion of the resulting absolute phase. Also extremely decorrelated parts are approximately reconstructed without influence to the surrounding. Also because of its only moderate time consumption this fusion PU seems to be a ideal solution for the repeat-pass interferometry.

References

[1] M.D. Pritt, J.S. Shipman, "Least-Squares Two-Dimensional Phase Unwrapping using FFT's", IEEE Trans. Geos. and Remote Sensing, Vol. 32, No. 3, pp. 706-708, 1994

[2] D.C. Ghiglia, L.A. Romero, "Robust two-dimensional weighted and unweighted phase unwrapping that uses fast transforms and iterative methods", J. Opt. Soc. Am. A, Vol. 11, No. 1, pp. 107-117, 1994

[3] W. Xu, I. Cumming, "A Region Growing Algorithm for InSAR Phase Unwrapping", Proc. of IGARSS'96, pp. 2044-2047, 1996

[4] R. Lanari et al., "Generation of Digital Elevation Models by using SIR-C/X-SAR Multifrequency Two-Pass Interferometry: the Etna Case Study", IEEE Trans. Geos. and Remote Sensing, Vol. 34, No. 5, pp. 1097-1114, 1996

Comparison of Path-Following and Least-Squares Phase Unwrapping Algorithms

Mark D. Pritt
Lockheed-Martin Federal Systems
700 N. Frederick Ave., 181/2A34, Gaithersburg, Maryland 20879
Tel: 301-240-4336 Fax: 301-240-7190 E-mail: mark.pritt@LMCO.COM

Abstract — This paper presents a comparative analysis of eight phase unwrapping algorithms that, in the opinion of the author, encompass the current "state of the art" in phase unwrapping. Four of the algorithms are path-following algorithms, and four are least-squares algorithms. The algorithms are described, and their characteristics, such as execution time and memory requirements, are summarized. The results of the algorithms on eight phase unwrapping problems are then presented, and recommendations for how to use the algorithms in practice are given.

INTRODUCTION

Over the past decade or so, a profusion of phase unwrapping algorithms has appeared. It is very difficult to assess the merits of each algorithm and to compare them with one another, partly because many of the algorithms are difficult to implement correctly. As a result, very little has been published that compares the algorithms in a systematic manner.

This paper presents a comparative analysis of eight phase unwrapping algorithms, which have been categorized into *path-following* and *least-squares* algorithms. Path-following algorithms use localized pixel-by-pixel operations to unwrap the phase, while least-squares algorithms minimize a global measure of the differences between the gradients of the wrapped input phase and those of the unwrapped solution. The algorithms were selected for evaluation because they are mature and (except for one algorithm) generally successful on the phase unwrapping problems that arise in SAR interferometry (IFSAR). We briefly describe each algorithm along with the key details that are commonly overlooked in their implementation. We then summarize a number of characteristics: the average execution time, the memory requirements, whether or not the algorithm requires a "quality" map or mask to guide the unwrapping process, and whether or not the algorithm explicitly identifies "residues" (phase inconsistencies) [1]. After presenting the results of the algorithms on eight phase unwrapping problems, we conclude with recommendations for how to use the algorithms in practice.

ALGORITHMS

The following eight algorithms are examined in this paper:

1. *Goldstein:* Goldstein, Zebker and Werner's residue and branch cut algorithm [1]
2. *Quality:* Quality-guided algorithm [2–4]
3. *Mask Cut:* Mask cut algorithm [5]
4. *Flynn:* Flynn's minimum weighted discontinuity algorithm [6]
5. *FFT/DCT:* FFT- or DCT-based unweighted least-squares algorithm [7,8]
6. *PCG:* Preconditioned conjugate gradient (PCG) algorithm [7]
7. *Multigrid:* Multigrid algorithm [8]
8. *L_p-norm:* Minimum L_p-norm algorithm [9]

1. Goldstein's Algorithm

This algorithm identifies the residues in the wrapped phase data and "balances" them with branch cuts. It uses a nearest-neighbor heuristic to find a configuration of branch cuts, the sum of whose lengths is approximately minimal. The reader is referred to [1] for a description of the algorithm. It is necessary to emphasize two points to ensure a proper implementation of the algorithm: 1) Whenever a residue is encountered during the search, it is always connected by a branch cut to the "current" residue, even if the residue has already been joined by a prior branch cut. 2) If a pixel on the border of the array is encountered during the search, a branch cut is placed to the border, which serves to balance the residues. The algorithm is very fast, requires little memory, and generally unwraps phase data correctly. Its shortcoming is that it does not use information in the phase data, other than the locations of the residues, to guide the placement of the branch cuts. In particular, it does not use a quality map or mask to indicate where the corrupted phase values lie.

2. Quality Algorithm

This algorithm does not identify residues at all. Rather than depending on branch cuts, it relies completely on a quality map to determine the order in which the phase data are unwrapped. It begins at a "seed" pixel and "grows" a region of unwrapped pixels, beginning with the highest-quality pixels and ending with the lowest-quality. The resulting unwrapping path depends on the quality map. The best results have been obtained with quality maps defined by the correlation coefficients or phase derivative variances [8]. There are many ways to enhance the algorithm: multiple seed pixels, techniques to "seam" unwrapped regions together, threshold relaxation, pixel classification, etc. [2–4]. None of these enhancements were used in the present study, however. Good results were obtained with the basic algorithm described above.

3. Mask Cut Algorithm

This algorithm can be regarded as a cross between Goldstein's algorithm and the quality-guided algorithm. Like Goldstein's algorithm, it identifies residues and joins them with

0-7803-3836-7/97/$10.00 © 1997 IEEE

"branch cut" structures (actually masks) that interdict the unwrapping path to prevent the encircling of unbalanced residues. Like the quality-guided algorithm, it grows the masks based on the quality value of each pixel. It follows the lowest quality pixels from one residue to another until the residues are balanced [5].

4. Flynn's Minimum Discontinuity Algorithm

This new algorithm works with or without a quality map. It finds the unwrapped surface that is congruent to the wrapped phase and whose discontinuities (neighboring pixels whose difference exceeds π radians in magnitude) are minimal in some sense. The algorithm utilizes a tree-growing approach that traces paths of discontinuities in the intermediate unwrapped surface, detects the paths that form loops, and adds multiples of 2π to the phase values enclosed by the loops to reduce the number of discontinuities. It performs this process iteratively until no more loops are detected. The process is guaranteed to converge to an optimal solution [6].

5. FFT/DCT Algorithm

This algorithm solves the unweighted least-squares phase unwrapping problem [7,8] by means of FFTs or discrete cosine transforms (DCTs). Because the algorithm unwraps *through* rather than *around* the residues in the phase data, the result can be corrupted by these residues. The result tends to be accurate locally but not globally. For this reason, the algorithm is unacceptable for most applications. It is useful, however, when one desires a "quick look" at the unwrapped data.

6. PCG Algorithm

This algorithm overcomes the limitations of the unweighted least-squares algorithm by introducing weights to mask out the corrupted phase values [7]. A postprocessing congruence operation [10] is necessary for accurate results, and the algorithm works best with binary-valued weights (i.e., quality mask).

7. Multigrid Algorithm

This algorithm solves the weighted least-squares equation by means of multigrid techniques [8]. Like the PCG algorithm, it works best with binary-valued weights, and it requires the postprocessing congruence operation of [10], but it is generally faster, especially on problems that have discontinuities or shear. The algorithm requires an *ad hoc* procedure for restricting the weights to the coarse grids [8]. On some types of problems, the coarse weights can isolate portions of the phase data, thereby resulting in an incorrect unwrapping. For this reason, the PCG algorithm appears to be more reliable in practice.

8. Minimum L_p-norm Algorithm

This algorithm iterates on the PCG algorithm to find a solution whose gradients agree with those of the wrapped phase data in the sense of a minimum L_p-norm [9]. The most useful value of the parameter p appears to be p=0, which causes the gradients of the solution to differ from those of the wrapped phase data in as few places as possible. Because the algorithm generates its own data-dependent weights, it works with or without a quality map. The memory and execution time requirements are very high due to its doubly iterative structure.

ALGORITHM CHARACTERISTICS

Table 1 lists some characteristics of the algorithms. The algorithms are ranked in order of their average execution times, which are given for an array size of 1024 x 1024 on an IBM RS/6000 workstation. The FFT/DCT algorithm and Goldstein's algorithm are the fastest. They also have the lowest memory requirements. The last two columns of the table indicate whether or not the algorithm requires a quality map or mask (an entry of *y/n* indicates the algorithm works with or without a quality map) and whether or not the algorithm explicitly identifies residues. Flynn's minimum discontinuity algorithm and the minimum L_p-norm algorithm work with or without a quality map. These two algorithms have the highest average execution times and the highest memory requirements. Interestingly, only two algorithms (Goldstein's algorithm and the mask cut algorithm) explicitly identify residues.

PHASE UNWRAPPING EXAMPLES

The algorithms were tested on the following eight phase unwrapping examples, many of which have appeared in the published literature. (Space limitations preclude their appearance here.)

a. Actual IFSAR data from [9,10]
b. Magnetic resonance imaging (MRI) data of human head from [9]
c. MRI data of human knee from [9]
d. Simulated IFSAR data of terrain around Isolation Peak, Colorado from [10]
e. Simulated IFSAR data of terrain around Long's Peak, Colorado (similar to example *d*)
f. Sheared planes data from [7,8]
g. Spiral shear data (similar to example *f*, except that the lines of shear are curved instead of straight)
h. Noise-corrupted sheared planes data (example *f* corrupted with Gaussian-distributed noise)

Table 1. Characteristics of the algorithms

Algorithm	*Execution Time*	*Memory Required*	*Quality Map?*	*Residues ?*
FFT/DCT	23 sec	1 array	n	n
Goldstein	30 sec	3 arrays	n	y
Quality	3 min	4 arrays	y	n
Mask Cut	4 min	4 arrays	y	y
Multigrid	6 min	5 arrays	y	n
PCG	10 min	5 arrays	y	n
Flynn	20 min	7 arrays	y/n	n
L_p-norm	2 hr	8 arrays	y/n	n

These examples encompass a broad range of the typical problems encountered in phase unwrapping problems. Example *c* contains an excessive amount of background noise, while example *f*, although noise-free, contains a line of sharp discontinuity. Example *a* contains large patches of noise that a phase unwrapping algorithm must unwrap around, while example *e* suffers from a slight overall decorrelation due to a deliberately induced image misregistration.

Quality maps and masks for all of the algorithms were computed automatically (i.e., without human intervention) by means of the methods described in [8]. Because of its corruption with noise, example *h* did not allow the computation of a good quality map. As a result, only three algorithms, which did not require a quality map, could unwrap it correctly.

ALGORITHM RESULTS

Table 2 lists the results of the algorithms on the eight phase unwrapping examples. The algorithms are ranked in order of the number of examples they unwrapped correctly. An entry of *y* signifies a successful unwrapping, *n* indicates failure, and *(y)* indicates there were only minor errors in the unwrapping. Flynn's minimum discontinuity algorithm and the minimum L_p-norm algorithm were the only ones that unwrapped all of the examples correctly (although they did exhibit minor errors on example *d*.) While the quality-guided algorithm was the only one that unwrapped example *d* flawlessly, it could not unwrap example *h* due to the lack of a good quality map. The results of the mask cut and PCG algorithms were comparable to those of the quality-guided algorithm. Goldstein's algorithm failed on examples *d* and *e* due to the bad placement of a branch cut between two regions of layover. By comparison, the use of a quality map by the mask cut algorithm enabled it to confine its branch cuts within (rather than between) the regions of layover. The multigrid algorithm failed on example *d* because the zero weights (quality mask) isolated regions of the phase when they were restricted to the coarse grids. The FFT/DCT algorithm failed on all of the examples, as expected.

Which algorithm should be used in practice? The answer depends on the characteristics of the phase unwrapping problem at hand. It is recommended that Goldstein's algorithm be tried first, because it has very simple user inputs (e.g., no quality map is required), it is very fast, and it is generally successful in practice. When it fails, the user is usually warned by examining the placement of branch cuts. If a good quality map is available or can be derived from the data (by means of the techniques of [8], for example) then the quality-guided, mask cut or PCG algorithms should be tried. If the problem is very difficult, because of a large amount of noise, for example, then Flynn's minimum discontinuity algorithm or the minimum L_p-norm algorithm can be tried. Although these algorithms take much longer to execute, they can sometimes "crack" tough phase unwrapping problems on which the other algorithms fail.

A more detailed analysis of the algorithms, along with their C language source code implementations and techniques for evaluating the unwrapped results, will appear in an upcoming book [11].

REFERENCES

[1] R. M. Goldstein, H. A. Zebker and C. L. Werner, "Satellite radar interferometry: two-dimensional phase unwrapping," Radio Sci., vol. 23, pp. 713-720, 1988.

[2] D. J. Bone, "Fourier fringe analysis: the two-dimensional phase unwrapping problem," Applied Optics, vol. 30, pp. 3627–3632, 1991.

[3] H. Lim, W. Xu and X. Huang, "Two new practical methods for phase unwrapping," Proc. IGARSS, Firenze, Italy, pp. 196–198, 1994.

[4] W. Xu and I. Cumming, "A region growing algorithm for InSAR phase unwrapping," Proc. IGARSS, Lincoln, Nebraska, pp. 2044–2046, 1996.

[5] T. J. Flynn, "Consistent 2-D phase unwrapping and absolute values information," Proc. IGARSS, Lincoln, Nebraska, pp. 2057–2059, 1996.

[6] T. J. Flynn, "Two-dimensional phase unwrapping with minimum weighted discontinuity," J. Opt. Soc. Amer. A, in press.

[7] D. C. Ghiglia and L. A. Romero, "Robust two-dimensional weighted and unweighted phase unwrapping that uses fast transforms and iterative methods," J. Opt. Soc. Amer. A, vol. 11, no. 1, pp. 107–117, 1994.

[8] M. D. Pritt, "Phase unwrapping by means of multigrid techniques for interferometric SAR," IEEE Trans. Geosci Remote Sens., vol. 34, no. 3, pp. 728–738, 1996.

[9] D. C. Ghiglia and L. A. Romero, "Minimum L_p-norm two-dimensional phase unwrapping," J. Opt. Soc. Amer. A, vol. 13, pp. 1–15, 1996.

[10] M. D. Pritt, "Congruence in least-squares phase unwrapping," Proc. IGARSS, Singapore, 1997.

[11] D. C. Ghiglia and M. D. Pritt, *Two-dimensional phase unwrapping: theory, algorithms and software*, in press.

Table 2. Results of the algorithms on the eight examples

	Examples							
Algorithm	*a*	*b*	*c*	*d*	*e*	*f*	*g*	*h*
Flynn	y	y	y	(y)	y	y	y	y
L_p-norm	y	y	y	(y)	y	y	y	y
Quality	y	y	y	y	y	y	y	n
Mask Cut	y	y	y	(y)	y	y	y	n
PCG	y	y	y	(y)	y	y	y	n
Goldstein	y	y	y	n	n	y	n	y
Multigrid	y	y	y	n	y	y	y	n
FFT/DCT	n	n	n	n	n	n	n	n

Congruence in Least-Squares Phase Unwrapping

Mark D. Pritt
Lockheed-Martin Federal Systems
700 N. Frederick Ave., 181/2A34, Gaithersburg, Maryland 20879
Tel: 301-240-4336 Fax: 301-240-7190 E-mail: mark.pritt@LMCO.COM

Abstract — Least-squares phase unwrapping algorithms minimize the squares of the differences between the gradients of the wrapped input phase and those of the unwrapped solution. These algorithms seem to lack the accuracy of some path-following algorithms, however, even when weighted least-squares techniques are used to mask out corrupted phase values. The reason for this is that least-squares solutions are not congruent to the wrapped input phase. We introduce a congruence operation that forces any solution to be congruent to the wrapped input phase. This operation dramatically reduces the errors and renders least-squares solutions as accurate as those from path-following algorithms.

LEAST-SQUARES PHASE UNWRAPPING

Phase unwrapping is a key processing step in synthetic aperture radar interferometry (IFSAR) [1]. A number of phase unwrapping algorithms adopt a weighted least-squares approach in which the gradients of the solution are fit to the phase gradients [2,3]. The weights, which are used to mask out corrupted phase values, can be computed automatically from the correlation coefficients or the phase derivative variances [3].

The presence of residues (i.e., inconsistencies) [1] in the phase data presents problems for all phase unwrapping algorithms. These residues present special problems for least-squares algorithms. *Unweighted* least-squares algorithms underestimate (on average) the magnitudes of the gradients of the solution when noise-induced residues are present. The presence of large numbers of residues in regions of SAR layover and shadow corrupt the solution to a significant degree [2,3]. *Weighted* least-squares solutions, such as those produced by the PCG algorithm [2] or the multigrid algorithm [3], overcome this problem by zero-weighting the regions of layover and shadow, thereby preventing the residues in these regions from corrupting the solution. These residues, along with scattered residues that lie outside the corrupted regions, can still affect the solution, although to a lesser degree. The result is that the weighted least-squares algorithms generally lack the accuracy of path-following algorithms such as Goldstein's branch cut algorithm [1].

Fig. 1 shows the wrapped phase data from an IFSAR experiment. The regions of decorrelated (i.e., noisy) phase are induced by radar shadow and layover. Most of the residues lie within these regions. One does not expect a phase unwrapping algorithm to unwrap these regions correctly, but one does expect the phase data *outside* these regions to be unwrapped correctly. Fig. 2 shows the weights, with the zero weights shown as black pixels, used to mask out the corrupted regions so they do not affect the unwrapping. This mask was generated by the phase derivative variance algorithm of [3]. Fig. 3 shows the errors (i.e., differences from the correct result produced by the algorithm of [1]) in the unwrapped solution produced by the PCG algorithm. The various shades of gray indicate the magnitudes of the errors, with white indicating no error and black indicating errors of 2π radians or more. The figure shows that the errors are substantial throughout the image, even outside the regions of corrupted phase.

CONGRUENCE

The following question arises: can anything be done to improve the accuracy of the weighted least-squares algorithms?

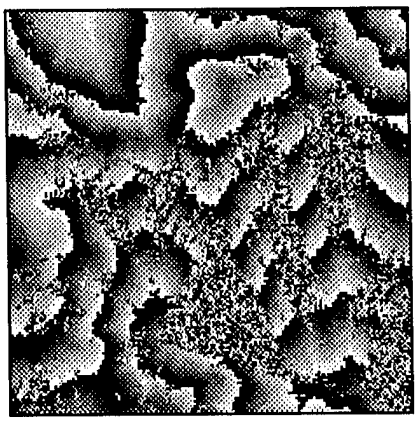

Fig. 1. Wrapped phase of IFSAR data. Notice the large patches of corrupted (noisy) phase).

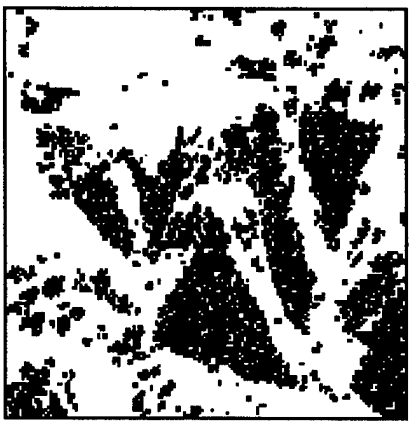

Fig. 2. Zero weights for masking out the regions of corrupted phase.

0-7803-3836-7/97/$10.00 © 1997 IEEE

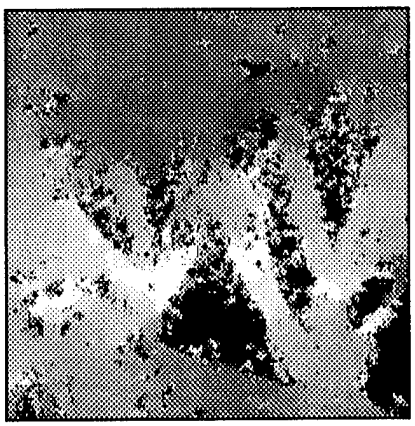

Fig. 3. Errors in the unwrapped results of the PCG algorithm *without* the congruence operation.

The answer is yes. Unlike the solutions produced by path-following algorithms, weighted least-squares solutions are not *congruent* to the wrapped phase. That is, if one rewraps the solution, the resulting phase is not identical to the wrapped input phase. This is because the least-squares formulation minimizes the *squares* of the differences between the gradients of the solution and the phase. Ordinarily one desires a congruent solution. Congruence can be achieved by means of a carefully defined "postprocessing" operation that subtracts the solution from the wrapped input phase, rewraps the result, and then adds it to the solution.

In terms of continuous functions, the postprocessing congruence operation is defined as follows. Given the unwrapped surface $\varphi(x,y)$ and the wrapped phase $\psi(x,y)$, define the *congruence* $\varphi'(x,y)$ of $\varphi(x,y)$ by

$$\varphi'(x,y) = \varphi(x,y) + \mathcal{W}[\psi(x,y) - \varphi(x,y)], \qquad (1)$$

where the wrapping operator $\mathcal{W}(\cdot)$ wraps the values of its argument into the range $(-\pi,\pi]$ by adding or subtracting an integral multiple of 2π radians. It is easy to verify that the surface $\varphi'(x,y)$ is congruent to the wrapped phase $\psi(x,y)$.

This simple congruence operation is unsatisfactory in the presence of noise, however, and it must be modified. A simple example will serve to illustrate this point. Let $\psi(x,y)$ be the wrapped phase of the function $f(x,y) = x$, and suppose a phase unwrapping algorithm has produced the unwrapped solution $\varphi(x,y) = x + \pi + \varepsilon(x,y)$, where $\varepsilon(x,y)$ is a zero-mean, Gaussian noise function with any fixed, small, nonzero variance. For simplicity, assume $|\varepsilon(x,y)| < \pi$. Observe that the rewrapped function $\mathcal{W}[\psi(x,y) - \varphi(x,y)]$ is equal to $\mathcal{W}[-\pi - \varepsilon(x,y)]$, which in turn equals $\pi - \varepsilon(x,y)$ when $\varepsilon(x,y) \geq 0$, and $-\pi - \varepsilon(x,y)$ otherwise. If we apply the simple congruence operation defined by (1) to the surface $\varphi(x,y)$, the result will be the function

$$\varphi'(x,y) = \begin{cases} x + 2\pi, & \varepsilon(x,y) \geq 0, \\ x, & \varepsilon(x,y) < 0. \end{cases} \qquad (2)$$

Thus, the congruent solution $\varphi'(x,y)$ does *not* equal the function $f(x,y) = x$. In fact, it is extremely discontinuous!

The desired solution $\varphi'(x,y) = x$ can be obtained by adding the constant $-\pi$ to $\varphi(x,y)$ *before* performing the congruence operation. This example illustrates a simple yet important fact: the congruence operation defined by (1) is *not* a linear operator. The example also suggests the correct way to define the congruence operation. The congruence of a given function $\varphi(x,y)$ should be defined by adding a constant h to it *before* applying (1), where h is chosen to minimize the number of discontinuities in the result.

ALGORITHM

We now shift to discrete functions and present the algorithm for the postprocessing congruence operation. This operation computes the congruence of the surface function φ_{ij} that represents the unwrapped solution of the wrapped phase ψ_{ij}. The algorithm approximates the optimal value of the constant h by a series of simple tests. The integer N, which controls the accuracy of the approximation, equals 10 in our implementation. The discontinuities that are counted in the loop are defined to be the neighboring grid points whose differences exceed π radians in magnitude.

Postprocessing Congruence Operation

for $k = 0$ to $N-1$
  Let $h = 2\pi k/N$.
  Compute the function $\varphi_{ij} + h + \mathcal{W}(\psi_{ij} - \varphi_{ij} - h)$.
  Let D_k be the number of discontinuities in this function.
end
Define the congruence to be the function computed above for the value k that minimizes D_k.

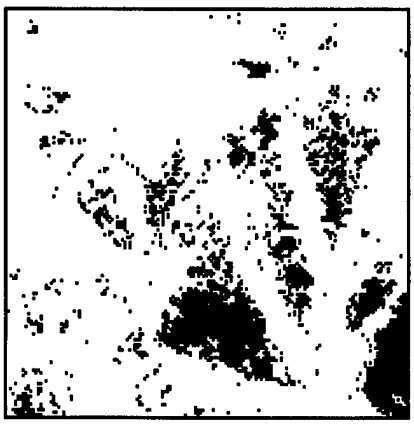

Fig. 4. Errors in the unwrapped results of the PCG algorithm *with* the congruence operation.

EXAMPLES

Fig. 4 shows the errors in the unwrapped solution produced by the PCG algorithm when the postprocessing congruence operation is applied. As can be seen, this operation reduces the errors dramatically. They are now confined to the regions of corrupted phase. Outside these regions, the PCG algorithm and the algorithm of [1] produce exactly the same (correct) unwrapped surface.

Fig. 5(a) shows the wrapped phase of simulated IFSAR data of the terrain around Isolation Peak, Colorado. Fig. 5(b) shows the weights that were generated by the phase derivative variance algorithm of [3] to mask out the decorrelated regions. Fig. 6(a) shows the errors in the unwrapped solution produced by the PCG operation without the postprocessing operation. Fig. 6(b) shows the errors after this operation is applied. As in the previous example, the congruence operation drastically reduces the errors and produces the correct unwrapped solution exclusive of the decorrelated patches (with the exception of the two very small regions in the upper right portion of the figure).

ACKNOWLEDGMENTS

Dennis C. Ghiglia of Sandia National Labs provided the phase data of Fig. 1. Michael J. Roth of the Johns Hopkins Applied Physics Lab provided the phase data of Fig. 5(a).

REFERENCES

[1] R. M. Goldstein, H. A. Zebker and C. L. Werner, "Satellite radar interferometry: two-dimensional phase unwrapping," Radio Sci., vol. 23, pp. 713-720, 1988.

[2] D. C. Ghiglia and L. A. Romero, "Robust two-dimensional weighted and unweighted phase unwrapping that uses fast transforms and iterative methods," J. Opt. Soc. Amer. A, vol. 11, no. 1, pp. 107–117, 1994.

[3] M. D. Pritt, "Phase unwrapping by means of multigrid techniques for interferometric SAR," IEEE Trans. Geosci. Remote Sens., vol. 34, no. 3, pp. 728–738, 1996.

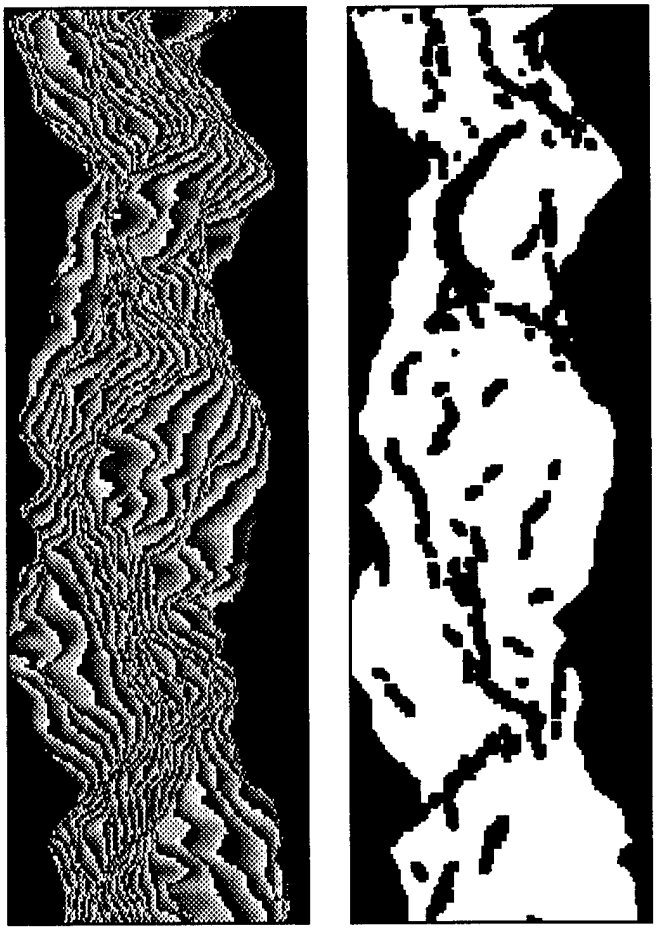

(a) (b)

Fig. 5. (a) The wrapped phase data for the simulated IFSAR example. (b) The zero weights used to mask out the decorrelated regions for the PCG algorithm.

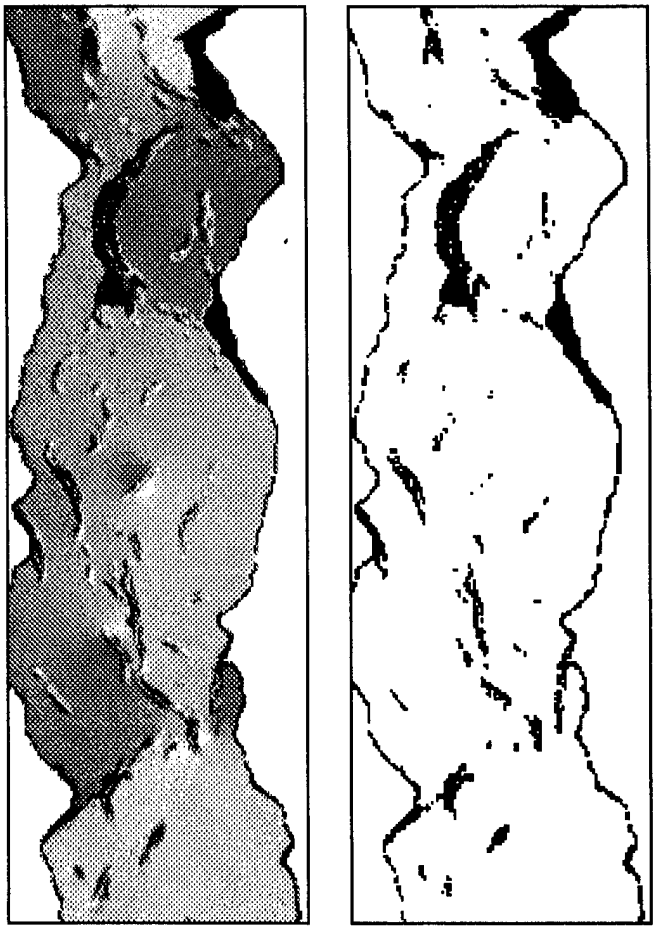

(a) (b)

Fig. 6. Errors in the unwrapped results produced by the PCG algorithm (a) *before* and (b) *after* application of the postprocessing congruence operation.

HOW GLOBAL AND LOCAL PHASE UNWRAPPING TECHNIQUES ARE CONNECTED

G. Fornaro[1], G. Franceschetti [1,2], R. Lanari[1], E. Sansosti[1], M. Tesauro[2]

[1] Consiglio Nazionale delle Ricerche, *Istituto di Ricerca per l'Elettromagnetismo e i Componenti Elettronici (I.R.E.C.E.)*, Via Diocleziano 328, 80124 Napoli, Italy.
☎ +(39)-81-5704945 fax +(39)-81-5705734 email: {fornaro, lanari, sansosti}@irece1.irece.na.cnr.it

[2] Università di Napoli, Federico II, *Dipartimento di Ingegneria Elettronica*, Via Claudio 21, 80125 Napoli, Italy.
☎ +(39)-81-7681111 fax +(39)-81-5934438 email: {francesc, manlio}@irece1.irece.na.cnr.it

Abstract -- The connection between local and global Phase Unwrapping procedures is discussed; they are both based on line integration of an estimate of the original phase gradient: the former performs the integration along a single path, the latter averages results of integration along all possible paths. The overall analysis is extended to weighted algorithms.

INTRODUCTION

Phase Unwrapping (PhU) consists of retrieval of the original (unwrapped) phase φ starting from the corresponding restricted (wrapped) phase φ_m in the $(-\pi,\pi)$ interval. Two-dimensional PhU is a problem encountered in different research and application areas; in the remote sensing field it has been deeply investigated because of its application to Synthetic Aperture Radar Interferometry (IFSAR).

Two-dimensional PhU techniques are implemented along two steps [1-4]:

(1) generation of an estimate **s** of the unwrapped phase gradient from wrapped data φ_m; and

(2) integration of the computed estimate **s**.

The first step is generally implemented by computing the gradient of the wrapped phase, say $\nabla\varphi_m$, and then chopping away the spikes due to the wrapped phase discontinuities. The obtained vector field $\mathbf{s}=\langle\nabla\varphi_m\rangle$ may be a corrupted estimate of the true phase gradient $\nabla\varphi$ if critical areas (layovers, undersampled areas, shadows and/or low coherency regions) are present: in this case the vector field **s** is not a true gradient and the relation $\nabla\varphi=\mathbf{s}$ is no more valid.

The second step is broadly referred to as PhU and can be performed along two lines:

(1) local integration [1]; or

(2) global integration [2-4].

In the first method the unwrapped phase is computed by integrating, starting from a fixed point P_0, the estimated phase gradient **s** over a path connecting all the points of the image [1]:

$$\varphi(\mathbf{r})=\varphi_0+\int_{P_0}^{P(\mathbf{r})} dc\,\mathbf{s}(\mathbf{r})\cdot\hat{\mathbf{c}}\ ,\quad \varphi_0=\varphi(P_0) \tag{1}$$

wherein $\hat{\mathbf{c}}$ is the unit vector along the integration path. This procedure can be directly implemented if the above mentioned constraints of low phase variation and high SNR values are met all over the image. If these conditions are not satisfied we will have an error that propagates along the whole integration path. The use of branch cuts (which interconnect residua of opposite polarity) to exclude critical areas from the integration path is then necessary [1].

The algorithms of the second method are based on a global integration operation carried out again on the estimated phase gradient. The Least Squares (LS) procedure, presented in [3], is based on the minimization of the squared distance between the vector field **s** and the desired true gradient of the unknown unwrapped phase:

$$\|\mathbf{s}-\nabla\varphi\|^2=\min\ . \tag{2}$$

An elegant solution to eq. (2) is provided by [2,4]:

$$\begin{aligned}\varphi(\mathbf{r}')=&-\iint_S dS\,\mathbf{s}(\mathbf{r})\cdot\nabla g(\mathbf{r}'-\mathbf{r})+\\&+\oint_C dc\,\varphi(\mathbf{r}_C)\frac{\partial g(\mathbf{r}'-\mathbf{r}_C)}{\partial n}\ ,\quad \mathbf{r}'\in S,\end{aligned} \tag{3}$$

0-7803-3836-7/97/$10.00 © 1997 IEEE

where S is the (planar) domain under investigation, C its boundary contour and $g(\mathbf{r})$ is the Green's function for the unbounded domain [2]:

$$\nabla^2 g(\mathbf{r}) = \delta(\mathbf{r}). \tag{4}$$

The solution provided by applying eq. (3) is referred to as the Green's Function method.

In the presence of identified critical areas it is possible to exclude them from the integration operation, similarly to the local approach, by using the so called weighted techniques. The weighted LS algorithms are based on the minimization of the following functional [3]:

$$\left\| w\nabla\varphi - ws \right\|^2 = \min \tag{5}$$

wherein w is a weighting function set to zero in the region to be excluded (weighted areas) and to one elsewhere.

CONNECTION BETWEEN GLOBAL AND LOCAL TECHNIQUES

Eq. (1) provides a definite phase value $\varphi(\mathbf{r})$ at any point $P(\mathbf{r})$ by direct integration along the chosen path. This value is either exact or wrong, depending on the path.

The LS method, eq. (2), apparently does not exhibit any connection between the retrieved phase, $\varphi(\mathbf{r})$, and the integration path. To explore this point we start from its solution via eq. (3), wherein the Green's function is given by [2]

$$g(r) = \frac{1}{2\pi}\ln\left(\frac{1}{r}\right) \quad , \tag{6}$$

and

$$\nabla g(r) = -\frac{1}{2\pi}\frac{\hat{\mathbf{r}}}{r} \quad . \tag{7}$$

We use polar coordinates for evaluating eq. (3) and we have:

$$\begin{aligned}\varphi(0) &= \oint_C dc\,\varphi(r_M,\theta)\frac{\hat{\mathbf{r}}\cdot\hat{\mathbf{n}}}{2\pi r_M} - \int_0^{2\pi} d\theta \int_0^{r_M} r dr s(r,\theta)\cdot\frac{\hat{\mathbf{r}}}{2\pi r} = \\ &= \frac{1}{2\pi}\int_0^{2\pi} d\theta\,\varphi(r_M,\theta) - \frac{1}{2\pi}\int_0^{2\pi} d\theta \int_0^{r_M} dr s(r,\theta)\cdot\hat{\mathbf{r}} = \\ &= \frac{1}{2\pi}\int_0^{2\pi} d\theta \left[\varphi(r_M,\theta) + \int_{r_M}^{0} dr s(r,\theta)\cdot\hat{\mathbf{r}} \right], \quad r_M \in C\end{aligned} \tag{8}$$

where the origin of coordinates has been set at the retrieved phase point $\mathbf{r}' = 0$, $|\mathbf{r}' - \mathbf{r}| = r$ and $r_M = r_M(\theta)$, see fig. 1.

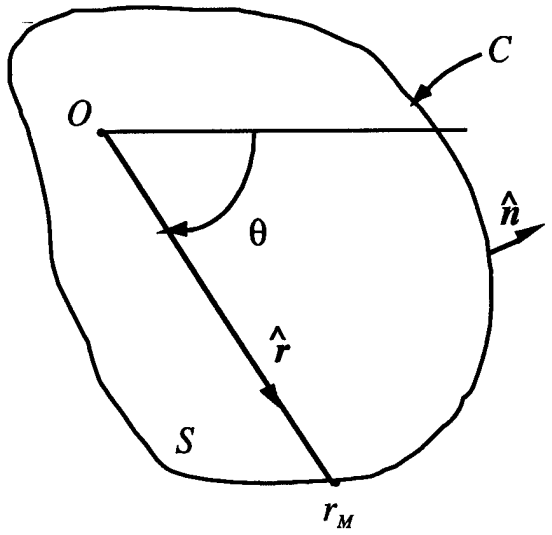

Fig. 1 Relevance of the use of Green's first identity in polar coordinates.

The phase value at $\mathbf{r}' = 0$ is the mean value of the line integrals over all the paths in all the directions θ departing from $\mathbf{r}' = 0$. As a matter of fact, the inner integral represents the line integral on a straight path connecting the point $\mathbf{r}' = 0$ (where we want to evaluate the phase) to the boundary along a fixed direction θ; $\varphi(r_M,\theta)$ is the value on the border taken as the initial value of the phase; the outer integral computes the mean value of the inner expression, which is θ-dependent. In absence of any critical area, the line integrals generate all the same value because all the paths are equivalent. In this case s is a true gradient, the line integral is independent from the path and its value can be obtained from the values that the phase assumes on the end point of the integration interval:

$$\varphi(0) = \frac{1}{2\pi}\int_0^{2\pi} d\theta\left[\varphi(r_M) + \varphi(0) - \varphi(r_M)\right]. \tag{9}$$

Accordingly, the average coincides with the value that we would obtain if a single line integral were evaluated (local integration). When critical areas are present in the investigated domain, any integration carried out through a path crossing these areas will generate an incorrect value (integer multiple of 2π). The mean operation reduces the error on the retrieved phase as much as the number of incorrect paths is decreased.

THE WEIGHTED CASE

In this case the global integration operation is performed on a multiconnected domain instead of a single connected one, wherein the additional boundaries are generated by the excluded critical areas (see fig. 2). In this case we have to add the additional boundary contour, say $C_1 = C^+ + C^-$, in eq. (3) (see fig. 2):

$$\varphi(\mathbf{r}') = -\iint_{S-W} dS\mathbf{s}(\mathbf{r})\cdot\nabla g(\mathbf{r}'-\mathbf{r}) + \\ + \oint_C dc\,\varphi(\mathbf{r}_C)\frac{\partial g(\mathbf{r}'-\mathbf{r}_C)}{\partial n} + \\ + \oint_{C_1} dc\,\varphi(\mathbf{r}_C)\frac{\partial g(\mathbf{r}'-\mathbf{r}_C)}{\partial n} \qquad \mathbf{r}' \in S \tag{10}$$

where C_1 consists of a close line around the weighed zone W. By using again polar coordinates, we have now:

$$\varphi(0) = \varphi_{2\pi-\Delta\alpha}(0) + \\ + \frac{1}{2\pi}\int_{\Delta\alpha} d\theta\left[\int_{r_M}^{r_{C^+}} dr\mathbf{s}(r,\theta)\cdot\hat{\mathbf{r}} + \int_{r_{C^-}}^{0} dr\mathbf{s}(r,\theta)\cdot\hat{\mathbf{r}}\right] + \\ - \frac{1}{2\pi}\int_{\Delta\alpha} d\theta\,\varphi(r_{C^+},\theta) + \frac{1}{2\pi}\int_{\Delta\alpha} d\theta\,\varphi(r_{C^-},\theta) + \\ + \frac{1}{2\pi}\int_{\Delta\alpha} d\theta\,\varphi(r_M,\theta), \tag{11}$$

wherein $\varphi_{2\pi-\Delta\alpha}(0)$ can be evaluated via eq. (8) applied to all points not included in the angular sector $\Delta\alpha$. After some mathematical manipulations eq. (11) can be rewritten in the following form:

$$\varphi(0) = \varphi_{2\pi-\Delta\alpha}(0) + \\ + \frac{1}{2\pi}\int_{\Delta\alpha} d\theta\left[\varphi(r_M,\theta) + \int_{r_M}^{r_{C^+}} dr\mathbf{s}(r,\theta)\cdot\hat{\mathbf{r}} + \right. \\ \left. + \left(\varphi(r_{C^-},\theta) - \varphi(r_{C^+},\theta)\right) + \int_{r_{C^-}}^{0} dr\mathbf{s}(r,\theta)\cdot\hat{\mathbf{r}}\right] \tag{12}$$

The first term in eq. (12), inside the square brackets, is the initial value; the second one accounts for the integration of s along the radial path from the outer boundary contour to the inner one; the third term is the phase jump across the excluded area: this term substitutes the integral within the weighted area where the gradient is incorrectly estimated; the fourth term is the integration of s over the remaining path. The outer integral represents the mean operation (over the angular sector $\Delta\alpha$) of the summation of the above mentioned path following integrals. Eq. (12) shows that weighted algorithms reach the correct phase value if weighting functions are properly set. On the contrary if we miss some weights, the error will be reduced by the mean operation.

In ref. [2] it is also shown that the required phase on the boundaries can be estimated from the measured data by solving a Fredholm equation of the second kind. This consideration suggests a new PhU weighted algorithm [4]:

(1) evaluation of the unwrapped phase on the boundaries by solving a Fredholm equation,

(2) evaluation of the unwrapped phase by using eq. (10).

Efficient techniques for solving the first point are under study.

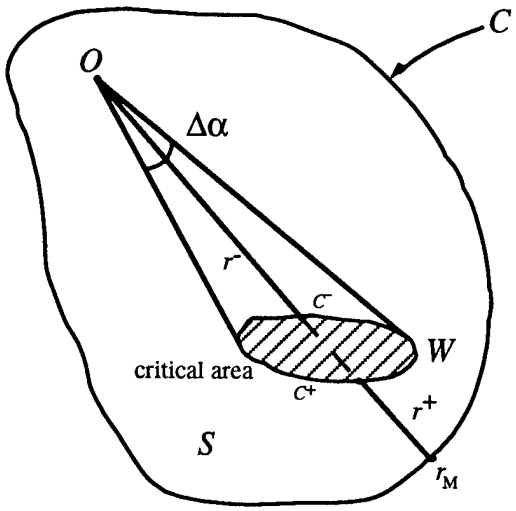

Fig. 2 Multiconnected domain.

REFERENCES

[1] R. M. Goldenstein, H. A. Zebker, and C. L. Werner, "Satellite Radar Interferometry: Two-dimensional Phase Unwrapping," *Radio Sci.* **23**, pp. 713-720, (1988).

[2] G. Fornaro, G. Franceschetti, and R. Lanari, "Interferometric SAR Phase Unwrapping using Green's Formulation," *IEEE Trans. Geosci. Remote Sens.* **34**, pp. 720-727, (1996).

[3] D. C. Ghiglia and L. A. Romero, "Robust Two-dimensional Weighted and Unweighted Phase Unwrapping that uses Fast Transform and Iterative Methods," *J. Opt. Soc. Am. A* **11**, pp. 107-117, (1994).

[4] G. Fornaro, G. Franceschetti, R. Lanari and E. Sansosti, "Robust phase unwrapping techniques: a comparison", *J. Opt. Soc. Am.* A **13**, pp. 2355-2366, (1996).

Modeling Water Surface Reflectance Signatures and In-Water Irradiance Profiles in Shallow Tropical Waters Influenced by Bottom Reflectance

Charles R. Bostater, Jr.
Division of Marine & Environmental Systems
College of Engineering,
Florida Institute of Technology
150 West University Blvd.,
Melbourne Florida, 32937
407-768-8000, x7113, bostater@probe.ocn.fit.edu

Abstract -- The two flow equations have been solved using Cauchy type boundary conditions so as to form a pair of coupled equations for use in a coupled atmosphere-water-bottom reflectance optical model to simulate the surface or subsurface reflectance, in-water irradiance profiles and in-water reflectance profiles in optically shallow or deep waters with or without a wind roughened surface. The model results presented here utilize clear water absorption and backscatter coefficients, and bottom reflectance as a function of wavelength. The bottom reflectance is characteristic of a tropical sea grass, sand & silt and Elkhorn coral, and a dead reef system in order to evaluate the nature of the underwater light climatology. The analytical model results are compared to a hyperspectral Monte-Carlo model. The Monte Carlo model also suggests a subsurface maximum in the intensity of light in optically shallow waters which is predicted by the analytical model.

INTRODUCTION

The two-flow equations for irradiance transfer used for simulating the below or above surface water reflectance in this paper are derived from the radiative transfer equation in a source free medium. The two-flow equations without the specular component (the Case I model), and with specular light (the Case II model) were then derived from the RTE and their solutions have been described by Bostater, Ma, McNally, Gimond and Lamb (1995). Although the solutions have been modified to demonstrate their utility in modeling the effects of a layered water column, the results presented in this model are those derived from the solutions with a specular component under low wind conditions for a homogeneous water column depth.

Analytical Remote Sensing Irradiance Model

The two-flow equations used are represented by a set of 3 coupled ordinary differential equations which are decoupled by the method of substitution into a set of second order differential equations. The two flow equations can be written as:

$$\frac{d}{dz}Ed(z) = -(a+b)Ed(z) + bEu(z) + cEs(z) \ , \quad (1)$$

$$\frac{d}{dz}Eu(z) = (a+b)Eu(z) - bEd(z) - cEs(z) \ , \quad (2)$$

and:

$$\frac{d}{dz}Es(z) = -\alpha Es(z) \ . \quad (3)$$

In the above equations, the assumption is made that the coefficients a, b, and c are depth independent and intrinsic or quasi-inherent optical properties, not apparent optical properties. In other words, they are not assumed a function of the light field.This assumption simplifies the solutions while still describing the fundamental physics as can be seen from the model results. It is a trivial matter for one experienced in solving these types of equations to show that mathematically unique solutions exist when boundary conditions are specified as follows. At the surface Ed(z), and Es(z) are given by values specified at z = 0 or Es(0) and Ed(0). In addition, 2 boundary solutions of the Cauchy type are specified as $\frac{d}{dz}Ed = \beta d$ at z = 0 and $\frac{d}{dz}Eu = \beta u$ at z = h. Note that these slope terms can be specified in terms of the original equations in (1) and (2) above. The solution technique assumes that the exponential solution of (3) allows for complete absorption of direct light at or before z=h due to the in-water attenuation processes inherent in absorption and backscatter or from absorption due to the bottom substrate. The last boundary condition utilized is Eu(h) where h = z is the depth of the water column and is specified from the relation Rb(h) = Eu(h)/Ed(h). Thus, Eu at z=0 can be predicted. All terms in the above are specified as a function of wavelength, λ except coordinate z. The solutions to the above with calculated downwelling diffuse irradiance Ed or indirect light, and the downwelling specular or collimated irradiance or Es from a simple marine atmospheric model due to Gregg and Carder (1990) is used to simulate the reflectance just above or below the water surface as a function of wavelength. In addition, the model predictions utilize

0-7803-3836-7/97/$10.00 © 1997 IEEE

wavelength dependent values of a and b from Smith and Baker (1981), and specified bottom reflectance signatures reported by Bostater (1992). The model takes into account the specular and diffuse reflectance at the sea surface, refraction of light through the air water interface and internal diffuse reflectance of light as it upwells from the water-air interface.

Hyperspectral Monte-Carlo Model

The Monte Carlo model is a recently developed hyperspectral model that predicts reflectance signatures using the same signatures for a, b, and Rb, as a function of wavelength. This model utilizes information contained in a scattering coefficient s=bs + fs, a scattering phase function and a concentration dependent absorption coefficient to estimate an optical pathlength. This length scale or pathlength is used to determine a probabilistic (uniform) distribution of photon pathlengths before an absorption or scattering event occurs. This information is then used to calculate the number of absorption, backscatter or forward scattering events at depth and then summed for the total number of events within a defined number of water column layers. The results can then be used to predict the vertical distribution of irradiance as well as to predict a Monte Carlo reflectance signature. Similar to the analytical irradiance model, effects of the air-sea interface is taken into effect, e g. specular and diffuse reflectance and refraction as well as bottom reflectance on a column depth z=h meters for any number of specified homogeneous water column layers.

MODEL RESULTS & COMPARISONS

Analytical Model Comparisons

Fig. 1 shows measured *in-situ* bottom reflectance signatures collected with a SE590 in an underwater case made for the solid state spectrograph. Signatures were collected in clear tropical water locations in the Caribbean Sea. Signatures include a sandy bottom (sand), turtle grass (grass), dead coral (deadre), Elkhorn coral (elk), and a sand-silt(sandsl) bottom

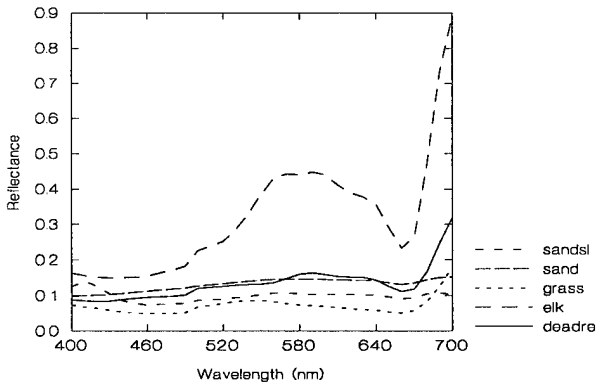

Fig. 1.In-situ measured bottom reflectance signatures.

These bottom reflectances are used as input into the coupled analytical model. Fig. 2 shows the resulting vertical profile of upwelling irradiance in the water column as a function of depth at 490 nm using the Elkhorn coral bottom reflectance signature for a 10 m water depth, Julian day 173 and zenith angle of approximately 60 degrees. In all simulations, the absorption and scattering is linearly dependent on the number of absorbers and scatterers (water quality concentrations). The conversion

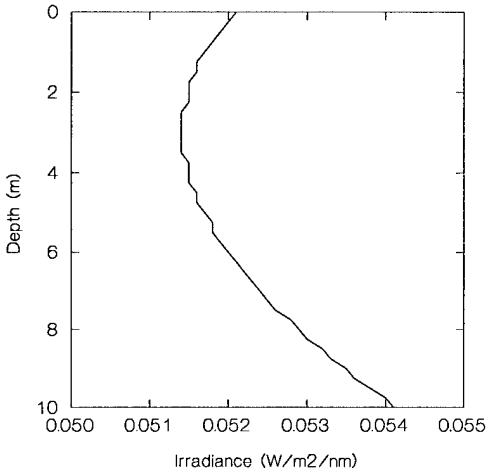

Fig. 2 Predicted upwelling irradiance influenced by elkhorn coral bottom reflectance in a clear water and 10m depth.

coefficient used was 2.85*b and the beam attenuation coefficient was set equal to the sum of a plus 53*b. Fig. 2 and Fig. 3 indicates a subsurface maximum of upwelling irradiance,

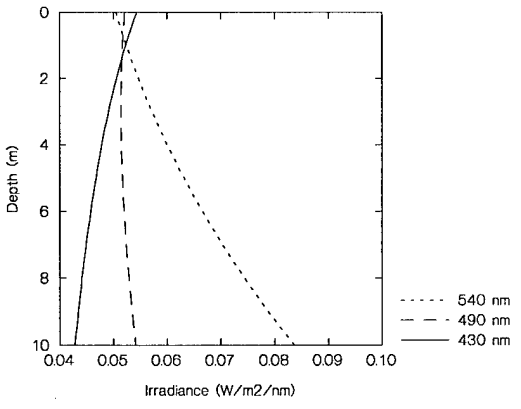

Fig. 3 Vertical distribution of upwelling irradiance (Eu) as a function of λ. Note the change as a function of depth.

or Eu(z) predicted from the model. Fig. 3 indicates that the shape of Eu(z) is wavelength dependent as expected. This indicates the need for careful considerations when interpreting *in-situ* measurement protocols and instrument performance. Fig. 4 shows the influence of different water column depths influenced from the bottom reflectance of a dead coral reef bottom type on the above surface reflectance at the 480 nm range.

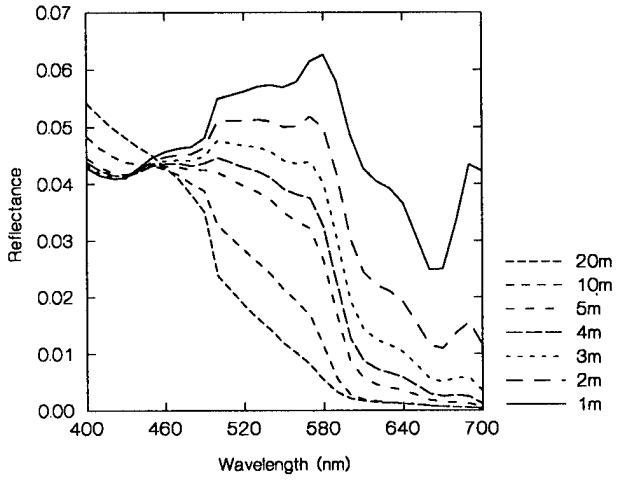

Fig. 4 Influence of varying the water depth on the predicted surface reflectance (480nm) influenced by a dead reef bottom.

Note the hinge point is shifted to the blue end of the spectrum compared to Fig. 5 for live Elkhorn coral reflectance.

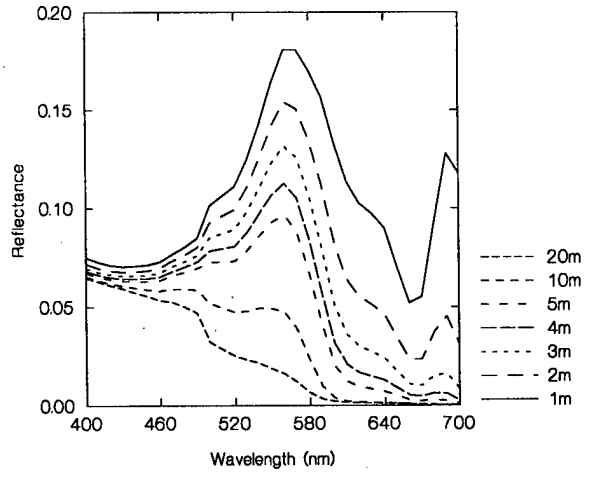

Fig. 5 Modeled reflectance using elkhorn coral bottom type.

Note the characteristic exponential decreasing reflectance similar to clear oceanic waters such as Gulf Stream waters or deeper Caribbean waters near the northern coast of Venezuela (Bostater, 1992). Note the water has a predicted broad flat region compared to Fig.5. Also note the lack of a hinge point due to the presence of the live coral bottom reflectance. Now Fig. 6 shows the influence of a sea grass bottom type on the water surface reflectance.

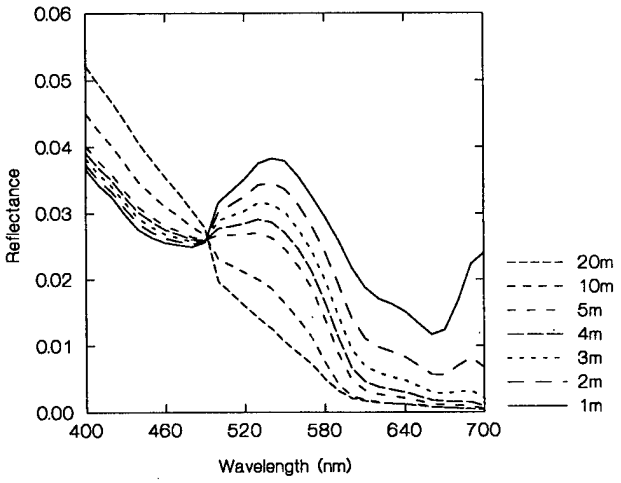

Fig. 6 Comparison of the influence of a sea grass bottom type. to sea grass or live coral bottom reflectance.

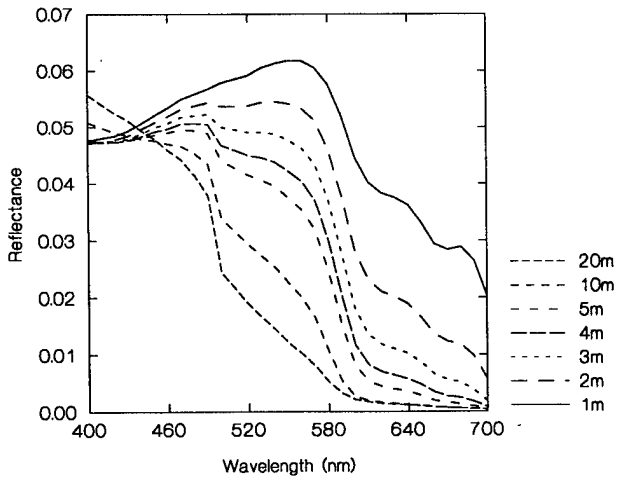

Fig. 7 Bottom reflectance influenced by a white sand bottom.

Note the unique characteristic of a white sand bottom as a function of water depth. Fig 8. shows the unique character of a mixed sand and silt bottom reflectance as a function of different water depths. Note the hinge point is no longer predicted compared to the extreme blue shift in the previous figure.

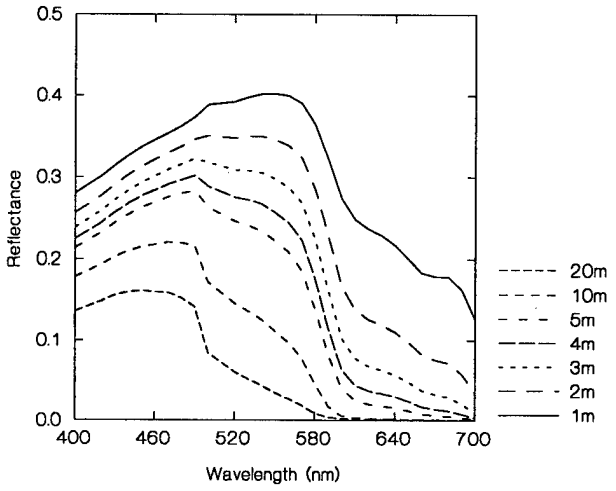

Fig. 8 Predicted surface water surface reflectance for a mixed sand and silt bottom reflectance type for various water depths.

Hyperspectral Monte Carlo Model Comparisons

Results for shallow waters (3 m) from this model suggests a more linear relative *in-situ* irradiant energy photon flux profile as suggested by Fig. 9 for clear water and no wind with a bottom reflectance value for Elkhorn coral at 490 nm.

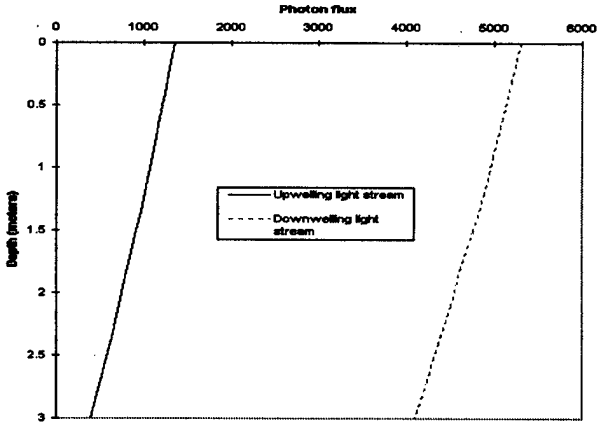

Fig. 9 Monte Carlo model results at 490 nm for a 3m water column influenced by Elkhorn coral. Note no characteristic exponential decay with low concentrations of absorbers and scatters.

These results suggest that actual measurements in shallow waters that indicate a linear or subsurface increase in reflectance or irradiance may indeed be representative of actual underwater light climatology. This result can be compared to the Monte Carlo model results for deeper waters as shown in Fig. 10.

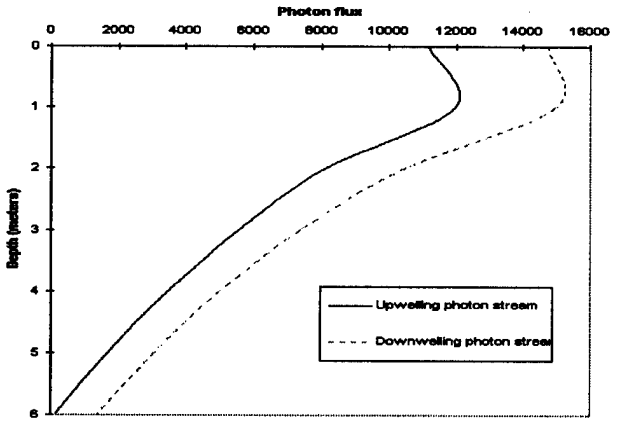

Fig. 10 Relative exponential *in-situ* irradiance photon flux for deeper water predicted from a Monte Carlo model influenced by Elkhorn coral bottom reflectance at 490 nm in clear water.

SUMMARY & CONCLUSIONS

Modeled surface reflectance signatures suggest the strong wavelength and depth dependence of waters influenced by bottom reflectance. An analytical model as well as a Monte Carlo model produce similar results and suggest that remote sensing data of bottom types as well as *in-situ* irradiance profiles will be strongly influenced by water depth. Thus, the extreme importance in accurate and reliable bottom depth measurements in applications where passive remote sensing of coral reefs are considered. Probable future solutions to this need will likely depend upon laser based techniques from airborne platforms due to the small spatial requirements for remote sensing of tropical coral reef diversity.

ACKNOWLEDGMENTS

Students M. Gimond, T. McNally and W. Ma are thanked for their assistance. This work has been funded by NASA, NOAA and NSF. S & C Services and KB Science & Eng. are thanked for making necessary equipment available.

RFERENCES

[1] Bostater, C., 1992, Remote sensing methods using aircraft and ships for estimating optimal bands & coefficients related to ecosystem responses, ERIM, First Thematic Conference on Remote Sensing for Marine & Coastal Environments, p.1051-1062.

[2] Smith, R., Baker, K., 1981, Optical properties of the clearest natural waters, Applied Optics, 20:177-184.

[3] Bostater, C., W. Ma, T. McNally, Gimond, M., Lamb. A., 1995, Application of a remote sensing model, SPIE 2586:32-43.

[4] Gregg, W., Carder, K., 1990, A simple spectral solar irradiance model for cloudless marine atmospheres, Limnology & Oceanography, 35(8):1657-1675.

Analysis of the Diffuse Attenuation Coefficients for Radiance and the Implications for Retrieval of the Spectral Signature of Submerged Tropical Corals

E. LeDrew, H. Holden
Waterloo Laboratory for Earth Observations
University of Waterloo
Waterloo, On N2L 3G1
VOX: 519 888 4567 2783
FAX: 519 888 6768
e-mail: ells@watleo.uwaterloo.ca

Abstract

This is the International Year of the Reef, yet the basis for reef mapping is existing Admiralty charts and air photos. We need the spectral information of airborne or satellite digital imagery to retrieve information regarding the stress on corals that may be caused by climate variability or change, and/or pollutant stress. The challenge is to adjust the digital imagery for the optical attenuation through water to depth with corrections that will vary with the density of intervening sediment or plankton.

In this paper we report on a study in Fiji in which we measured the vertical profiles of the diffuse attenuation coefficient for the downwelling irradiance and upwelling radiance in the SeaWiFS channels. We have over forty profiles over coral reefs, debris surfaces, and sand surfaces, as well as 'blue water' with depths far beyond the range of the 100 metre cable for the dropsonde radiometer. We derive an algorithm for determination of the bottom reflected radiance independent of image characteristics.

INTRODUCTION

Although corals are generally well adapted to the normal low-stress environments in the tropics, they are exceedingly vulnerable to environmental change, so strict resource management is necessary to ensure growth and survival. They are susceptible to a wide range of stress conditions caused by anthropogenic activities such as siltation from increased runoff, industrial and agricultural pollution, coastal development, coral mining, intensive recreational use, military activities and mineral exploitation (1). In addition, natural stresses, such as extreme changes in temperature, salinity and exposure to ultraviolet radiation, which may be related to El Niño events, may also damage coral ecosystems (2).

It is crucial that a numerative and replicable means for mapping and monitoring the stress of coral on a regional basis be developed. The potential key to such a mapping technique is the spectral transformation of the coral as it becomes 'bleached' from stress. In the surface tissues of all reef-forming corals are masses of photosynthetic zooxanthellae that nourish the coral polyps, or individual coral animals. The zooxanthellae leave the coral under duress, leaving the white calcium carbonate skeleton.

Traditionally, judgment of coral health has relied on the naked eye's ability to detect a loss of colouration. Although this may be reliable for severe bleaching, a determination that normally "pale" colonies are bleached can be extremely arbitrary, especially given natural variations in pigmentation. Radiometric data from optical remote sensors may provide the basis for confident demarcation of bleached reefs. In this paper we discuss a model for the determination of the spectral reflectivity of submerged corals.

The analysis is based upon the optical attenuation coefficient, which is a function of the absorption and scattering properties of the water. This attenuation coefficient, κ, is defined by Beer's Law as:

$$I_\lambda = I_{0,\lambda} \exp(-\kappa_\lambda D) \qquad (1)$$

Where D is the depth, I_λ is the irradiance at depth, and $I_{0,\lambda}$ is the spectral irradiance at the surface.

The most frequently measured and reported diffuse attenuation coefficient is k_{Down} (calculated from downwelling irradiance), although k_{Up} (calculated from upwelling radiance) is also possible (3). Attenuation can be assessed in different ways, but the best estimations are obtained from in situ irradiance measurements (6).

STUDY AREA

The field work for this research was conducted within a 390 km2 region called the Beqa Lagoon in Fiji (from 15°23° S to 177° E178° W) and a series of locations amongst islands in the Bligh Waters to the east. Measurements were conducted in the winters of 1995 and 1996.

0-7803-3836-7/97/$10.00 © 1997 IEEE

PROCEDURE

The optical properties of Beqa Lagoon waters were measured with a dropsonde radiometer (Profiling Reflectance Radiometer, PRR, from Biospherical Instruments Inc.) which has six bands representing SeaWiFS channels at 412, 443, 488, 510, 560, 665 nanometers.

In total, 40 vertical profiles were taken over the two years of field work. A GPS provided the geographic location of each of the profile stations, and a hand held sonar device measured water depth.

In addition, a SPOT HRV multispectral satellite image of Beqa Lagoon was acquired through programming for 9 August 1995 and, from the archives, for August 8, 1991. The first two bands of the SPOT satellite image correspond to the 560 and 665 nm wavebands of the PRR field data.

An atmospheric correction was performed on the image. The digital numbers were converted to radiance values at the top of the atmosphere following (7), and this value was entered into the 6S two-stream atmospheric correction package (8), along with other atmospheric parameters, to retrieve the equivalent surface reflectance.

RESULTS AND DISCUSSION

Deriving the Bottom Reflectance

In existing models for bottom reflectance derived from imagery, one or a combination of the following assumptions are made:

•attenuation coefficients are the same in relevant bands

•upwelling radiance is characterized by the downwelling irradiance diffuse attenuation coefficient.

•the ratio of the bottom reflectances in two bands is the same for all bottom types within a given scene

•the upwelling radiance plotted for two bands provide parallel populations when plotted for specific bottom reflectances

•internal reflection or Raman scatter is not a factor.

In the following we focus on the top 10 metres of the radiance profiles for cases with the surface far below ten meters. We have shown elsewhere that the attenuation coefficient profiles are not constant with depth and tend to change significantly below 10 metres, and indeed appears to indicate multiple scattering and Raman effects as the bottom is approached (4).

Eight soundings from 1996 are plotted in Figure 1 for the 560 nm (SPOT channel 1) vs 665 nm (SPOT 2) bands in the upper 10 meters. The August 17a sounding is for blue water with a depth beyond the limit of the ship's sonar. Upon examination of the cases, there appear to be three populations, and the profiles for each population are approximately parallel to each other. One group is from the Beqa Lagoon, another group is from islands in the Bligh Waters, and another dropsonde (August 15e) is for a completely overcast case.

If we assume that the profiles would be parallel within a region, and assume that we had a profile measured for a deep water reference point, the perpendicular distance between the lines at a particular point would be the difference in upwelling radiance, at that depth. The issue is to remove the depth constraint. Following the clue of (5) who applied a different procedure to image statistics, we rotate the profiles. A general rigid transformation is applied to the profile for August 6c in Figure 2.

$$x_{new} = x \cos \alpha + y \sin \alpha - h \quad (2)$$

$$y_{new} = -x \sin \alpha + y \cos \alpha - k \quad (3)$$

are the transformation equations that result from a rotation through α followed by a translation of h and k.

The rotated curve is approximately parallel to the x axis at y = 0. The solid line is the straight line approximation to the transformed curve. The delta symbol represents a reflectance from the SPOT image over a coral reef in the Beqa Lagoon. The diamond is that point with the same transformation applied. This would represent straight line parallel to the x axis at displacement of 0.05 units. This, logically, is the displacement in bottom reflectant radiance at some unknown depth. It would be the reflectance from the coral reef at
that depth.

CONCLUSIONS

We have made a proposal for a transformation that will provide bottom reflected radiance that is based upon a dropsonde profile of the diffuse attenuation coefficient of the upwelling radiance, and is independent of scene statistics such has been the case in previous studies. The SPOT image statistics can be converted into reflected radiances from the bottom with this transformation, without depth information, which is often an unknown in developing tropical nations that harbour the greatest tropical coral densities that are under potential duress.

ACKNOWLEDGMENTS

This research was supported by an NSERC grant to Ellsworth LeDrew. The authors are grateful to John Morrow of Biospherical Instruments for the loan of the PRR instruments, and to Drew Knight and Marnie Laing for technical support in the field.

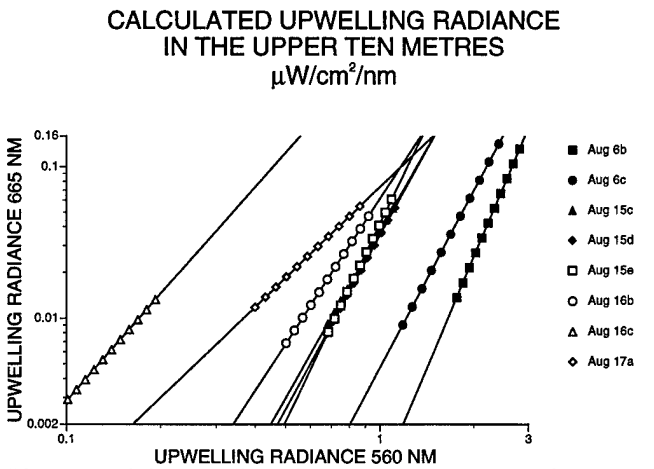

Figure 1. Eight soundings for the upper 10 metres from 1996

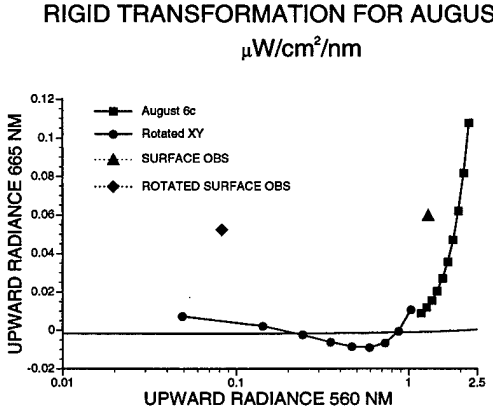

Figure 2. Rigid transformation for the profile of August 6c and a selected surface observation within the lagoon.

References

[1]Fagoonee, I. (1986) Remote sensing techniques for coral reef studies. International Symposium on Remote Sensing of Environment. 1: 439450

[2]Glynn, P. (1991) Coral reef bleaching in the 1980's and possible connections with global warming. Trends in Ecology and Evolution. 6:175179.

[3]Gower, J. (1981) Oceanography from space. New York: Plenum Press.

[4]LeDrew, E.F., H. Holden, D. Peddle, D. Knight, J. Morrow , 1996,"Spectral Measures of Coral Ecosystem Stress Derived from SPOT Satellite Imagery", Eco-Informa, Global Networks for Environmental Information, Lake Buena Vista, Florida.

[5]Lyzenga, D. (1978) Passive remote sensing techniques for mapping water depth and bottom features." Applied Optics. 17: 379383.

[6]Maritorena, S. (1996) Remote sensing of the water attenuation in coral reefs: a case study in French Polynesia. International Journal of Remote Sensing. 17: 155166.

[7]Markham, B. and Barker J. (1986) Landsat MSS and TM postcalibration dynamic ranges, exoatmospheric reflectances and atsatellite temperatures." EOSAT: Landsat Technical Notes.

[8]Vermote, E., Tanre D., Deuze J., Herman M., and Morcrette J. (1994) 6S user guide." NASA Goddard Space Flight Center.

ENVIRONMENTAL MONITORING OF THE VENICE LAGOON USING MIVIS DATA

Alessandro Barducci, Ivan Pippi
C.N.R. - I.R.O.E. "Nello Carrara"
Via Panciatichi, 64 - 50127 FIRENZE - ITALIA
Tel: 0039-55-4235277 - Fax: 0039-55-410893 - E-mail: pippi@geodec.iroe.fi.cnr.it

INTRODUCTION

MIVIS is one of the most promising instruments for airborne hyperspectral remote sensing. It provides 102 channels operating at high resolution in the visible, near and thermal infrared spectral ranges. This sensor is flown by the 'LARA Project' of the CNR on a CASA 212/200 aircraft.

In December 1995, a measurement campaign was performed over the Venice lagoon in order to infer the sensor performance in environmental monitoring applications. This campaign was also supported by in situ measurements.

The acquired data were firstly processed to assess the image quality, the sensor reliability and performance. Possible patterns of spatially structured noise as well as the signal-to-noise ratio were assessed.

Remotely sensed data are also affected by atmospheric scattering, absorption and thermal emission. Based on a radiative-transfer model utilising the MODTRAN computer code [1-3], we performed the image correction from atmospheric effects.

The corrected data have been used for the following applications: water quality assessment, vegetation status in the zones nearby the lagoon, evaluation of the impact of human activities on the environment.

The obtained results are shown and discussed.

NOISE ANALYSIS

Noise analysis has been splitted into different parts following the different characteristics shown by various noise kinds. We recognise three different image noise types: 1) spatially coherent noise, 2) spatially incoherent noise, and 3) spike noise. The first noise kind has a partially deterministic nature, and produces regular image patterns. Due to this characteristic, the effects of spatially coherent noise could theoretically be corrected [4]. The second one is originated by a fully stochastic process, and does not show any spatial structure or order into the affected image. Usually, it also is the main limitation to the signal-to-noise ratio (SNR) of the concerned image. Spike noise also has a casual nature, and shows a large amplitude perturbation of the signal revealed in a limited amount of image pixels. Our analysis has been focused on the algorithms which allow us to make quantitative determinations of the image SNR, and on restoration techniques that can filter spatially coherent noise structures. The work has been addressed to the study of remotely sensed data acquired by multispectral optical systems (e.g.: MIVIS).

Removing Spatially Coherent Noise

Useful multispectral imaging systems devoted to the remote sensing of Earth's surface often operate in whisk-broom mode. Due to imperfections in the scanning mechanism, images acquired by such sensors are generally affected by a standard scan-line shaped noise, as shown in Fig.1. It is to notice that this kind of noise is spectrally incoherent, which means that the noise pattern changes according to the considered spectral band. Therefore, this noise not only affects the radiance spatial distribution into the concerned image, but it systematically modifies also the spectrum of each image pixel. As a consequence removal of spatially coherent noise is a primary task for any remote sensing application.

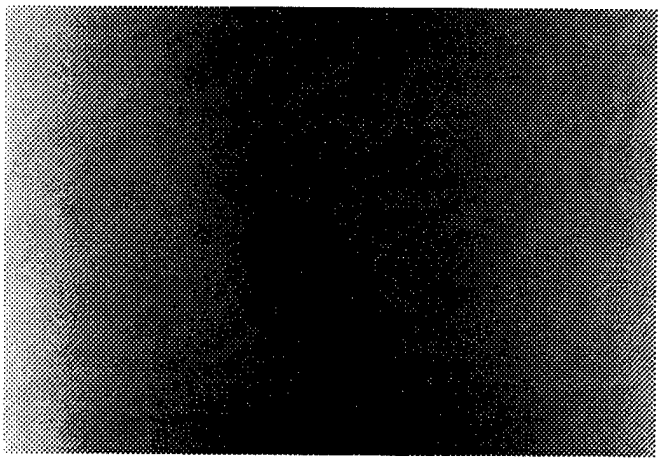

Fig.1:MIVIS image acquired in band 2 over open sea.

The main tool used to detect spatially coherent noise is the Fast Fourier Transform algorithm (FFT). In fact, the power spectrum of an image acquired by a scanning system reveals some vertical bars or straight lines which are the counterparts of the aforementioned line-shaped noise.

0-7803-3836-7/97/$10.00 © 1997 IEEE

It can be shown that a particular subset of the Hough transform (identified by the image integrals over the noise structures, i.e.: the image scan-lines) carries a lot of information about the spatial distribution of coherent noise. Let p represent such a subset:

$$p(y,\lambda) = \int I(x,y,\lambda)dx \qquad [1]$$

being I the image value, λ the band wavelength, and x the horizontal image co-ordinate. Due to averaging accomplished by Eq.1 the profile p could be supposed at a first approximation to be independent on the imaged scene. As long as this hypothesis holds true p only reflects the coherent noise pattern, and the restored image $G(x,y,\lambda)$ could simply be obtained by the I to p ratio. However, only rarely this hypothesis will be true, because the scene may be differently composed in each image scan lines. Then, we suppose that the lower spatial frequency components of the profile p are only due to scene variations while higher frequencies are exclusively induced by coherent noise. Under this condition, the p components only due to scene variations can be extracted and represented by the smoothed profile s defined by:

$$s(y,\lambda) = \frac{\int_{-\delta}^{\delta} p(y+\xi,\lambda)d\xi}{2\delta} \qquad [2]$$

In Eq.2 δ is the half-width of the averaging window, whose value should empirically be found. The p-to-s ratio should then depend only on the noise pattern, while it should be insensitive to the effective scene composition. This ratio is denoted by c:

$$c(y,\lambda) = \frac{p(y,\lambda)}{s(y,\lambda)} \qquad [3]$$

and can be used to estimate the corrected image G as:

$$G(x,y,\lambda) = \frac{I(x,y,\lambda)}{c(y,\lambda)} \qquad [4]$$

Let us note that G has meanly the same pixel-spectra as the original image I. This valuable property is related to the circumstance that by definition the value of c averaged over an image-window larger than δ always is 1 at any window position x_o,y_o.

The depicted procedure has been applied to images gathered by MIVIS and other scanning optical systems often employed in remote sensing campaigns. Obtained results have been excellent, and often the noise patterns have been fully rejected. We have also verified that our algorithm for coherent noise removal does not modify the pixel spectrum.

Signal-to-Noise Ratio

As stated the signal-to-noise ratio is mainly limited by the incoherent image noise. Since this disturbance cannot be removed it is more important to give a quantitative estimate of it, which is important for sensor comparison and characterisation. In our work the image SNR has been evaluated by taking the mean-to-standard deviation ratio over homogeneous image regions. This procedure has been applied to images already corrected for coherent noise effects, while raw data have been processed considering a single scan-line at a time. This option cut off possible influences of coherent noise on the computed SNR.

The obtained results show MIVIS images to have a SNR equal to 500, with progressive performance degradation towards the longer available wavelengths (Thermal Infrared range).

VENICE LAGOON MONITORING

As already stated in 1995 a measurement campaign has been performed over the Venice Lagoon. Fig.2 shows a MIVIS image acquired in the 7th spectral band (0.562 μm). The image was not corrected neither for atmospheric effects nor from coherent noise patterns, which are partially visible over the sea.

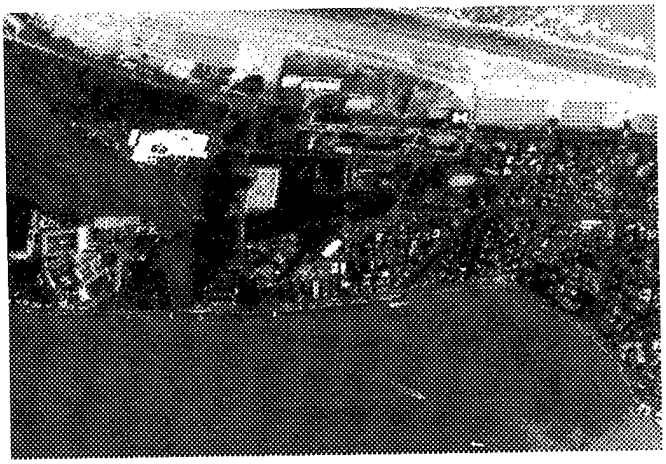

Fig.2: MIVIS image of Venice Lagoon (raw data) acquired in band 7 (0.562 μm).

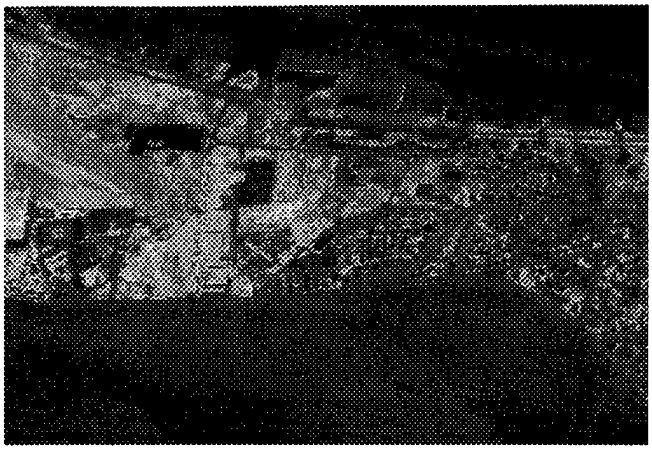

Fig.3: NDVI. Normalised difference between bands 20 (0.821 μm) and 13 (0.682 μm).

Fig.4: Image (band 20) enhancement by equalisation histogram.

After correction for atmospheric effects the acquired MIVIS images were processed with various algorithms in order to map vegetation and other significant environmental parameters. Fig.3 shows an example of this processing, realised by computing the modulus between bands 20 (0.821 μm) and 16 (0.682 μm). This calculation is closely related to the NDVI index, which holds a lot of information about vegetated areas. Fig.4 shows an example of image enhancement applied to a MIVIS image. It is to notice the large amount of details and spatial structures (e.g.: marine waves) held into the processed image. This circumstance indicates the good sensor performance, which is also confirmed by our measurement of the SNR which is greater than the one obtained with standard remote sensing equipment.

CONCLUSIONS

Our work has been aimed to study the environmental applications of multispectral images remotely sensed by airborne and spaceborne sensors. A great drawback encountered in using such images was the presence of spatially coherent noise patterns which affect the images and dim any pixel spectrum. The paper has shown that this problem may be overcome by means of an algorithm which utilises a particular subset of the image Hough transform. This algorithm has been shown to be able to reject coherent noise without changing the mean pixel spectra.

The major problem found when using multispectral data is however due to the lack of reliable theoretical models for processing the amount of acquired spectral data. In fact, only models specifically developed for low spectral resolution sensors are today available.

REFERENCES

[1] J. C. Wright, "Accuracy of LOWTRAN 7 and MODTRAN in the 2.0-5.5 μm region", *Applied Optics*, vol. 33, No. 9, pp., 1994.

[2] Berk A., Bernstein L. S. and Robertson D. C., "MODTRAN: a moderate resolution model for LOWTRAN 7", Rep. GL-TR-89-0122, 1989.

[3] F. X. Kneizys, E. P. Shettle, L. W. Abreu, J. H. Chetwynd, G. P. Anderson, W. O. Gallery, J. E. A. Selby and S. A. Clough, "Users Guide to LOWTRAN 7", Air Force Geophysics Laboratory, Rep. No. AFGL-TR-88-0177, 1988.

[4] A. Barducci, and I. Pippi, "MIVIS Evaluation for Hyperspectral Monitoring of the Environment", Europto II, 26-28 September, Paris, France, SPIE vol. 2585, 1995.

Analysis of Radar Response from Urban Areas*

Bruce Forster , Catherine Ticehurst and Yunhan Dong

School of Geomatic Engineering, The University of New South Wales
Sydney, 2052, NSW, Australia.
Telephone + 612 385 4172, Facsimile + 612 313 7493
email: b.forster@unsw.edu.au

Abstract - The output from regular mapping and monitoring of urban areas provides an important source of information for urban planners and decision makers. The use of remotely sensed data to provide this information has been successful in particular environments but has had only limited success in tropical zone countries where cloud and rain often restrict the useful acquisition of visible/infrared image data on a regular basis. In many cases, and particularly in east Asia, these are precisely the areas that most need the data. A number of researchers have examined the potential of using radar images to overcome these problems, because at the wavelengths used (X to P), radar is not affected by cloud or rain.

Urban areas are a spatially complex mixture of both natural and built surfaces whose spectral and geometric properties are many and varied. Buildings for example, cause significant backscatter when irradiated by microwave radiation, which is dependent on wavelength, polarisation and incidence angle of the radar beam, and roughness, dielectric properties and size, shape and orientation of the buildings and their surface facets. To some extent all combinations of specular and diffuse backscatter are a function of the height and width of buildings, and thus give rise to the possibility of using backscatter as a measure of the bulk density of the built environment.

Equations for backscattering mechanisms , often found in urban environments, are well known. These are for example, facets, point scatterers, dihedral and trihedral corner reflectors, cylinders and wedges. This paper examines the theoretical relationships between urban morphology and remote sensing response at radar wavelengths, provides some preliminary results on measures of urban classification using AirSAR quad polarised radar data from test sites over the city of Sydney, Australia, and proposes a solution to the problem of backscatter variation due to building orientation.

INTRODUCTION

Maintaining up-to-date information on urban growth, to allow adequate planning for physical and social infrastructure, is both costly and time consuming using traditional field and airphoto methods. Since the launch of the first Landsat remote sensing satellite, in 1972, many attempts have been made to use satellite and airborne remotely sensed data to classify and monitor urban areas in cities of both developed and developing countries [1]. The use of remotely sensed data to provide this information has been successful in particular environments but has had only limited success in tropical zone countries where cloud and rain often restrict the useful acquisition of visible/infrared image data on a regular basis. In many cases, and particularly in east Asia, these are precisely the areas that most need the data. A number of researchers have examined the potential of using radar images to overcome these problems, because at the wavelengths used (X to P), radar is not affected by cloud or rain. Recent papers [2] and [3] have documented the history of the use of radar in urban areas and the relationship between radar response patterns and bio- and geophysical parameters of urban areas. Researchers [4], [5] and others, have examined the potential for using radar, and integrated radar and optical data to overcome the problems of urban monitoring, with some satisfactory results. Most urban radar research to date, however, has relied on the traditional remote sensing methods of interpretation or classification of the amplitude of the response either from single or multi-wavelength images. Little effort has been made to understand the complex interaction of radar with urban type cover nor to extract relevant urban parameters from the data on the basis of this understanding.

Radar backscatter is dependent on surface dielectric and roughness properties, and particularly in a built environment, on orientation of facets, presence of dihedral corner reflectors (formed by the intersection of horizontal and vertical built features) and trihedral corner reflectors (formed by two orthogonal vertical walls and the ground). Double and triple bounce scattering from geometric structures are also important mechanisms in urban areas [6]. To some extent all combinations of specular and diffuse backscatter will be a function of the height and bulk of buildings, and thus give rise to the possibility of using backscatter as a measure of the vertical dimensions and size of the built environment. Increased corner reflector backscatter resulting from larger buildings should also result in a phase difference between the HH and VV backscattered field. Corner reflector effects can also create problems in classification, because the backscatter is strongly dependent on building orientation with respect to the radar azimuth direction. It is suggested that this may be overcome using combined multi-azimuth radar data or calculation of the corner reflector effect.

However it is only in relatively recent times that regularly available data from satellite borne synthetic aperture radar systems have become available on a regular basis., and make it possible for their integration into urban monitoring programs. These include Almaz (Russian), ERS-1 & 2 (European Space Agency), JERS-1 (Japan), and Radarsat (Canada). In addition data from airborne quad-polarised, multi-wavelength radar systems are now available over a number of sites around the world, including the city of

* This work was supported by the Australian Research Council.

0-7803-3836-7/97/$10.00 © 1997 IEEE

Sydney, Australia, where some recent urban related research has been undertaken [7], [8].

RADAR BACKSCATTER MEASURES

Buildings cause significant backscatter when irradiated by microwave radiation, which is dependent on wavelength, polarisation and incidence angle of the radar beam, and roughness, dielectric properties and size, shape and orientation of the buildings and their surface facets. Surface roughness occurs in a relatively small range (of the order of centimetres) for built surfaces, and building materials, with reasonably constant density and moisture content (low), should have a near constant (or easily determinable) relative permittivity and loss factor. Thus it may be assumed that variation in the measured backscatter will be predominantly due to antenna orientation with respect to the built geometry, for constant wavelength and polarisation. However in addition, larger buildings will tend to have more metallic components, such as in reinforced concrete, which will also increase the radar backscatter.

Equations for backscattering mechanisms, often found in urban environments, are well known. These are for example, facets, point scatterers, dihedral corner reflectors, cylinders and wedges. For all mechanisms, both diffuse and specular backscatter (both single and multiple bounce) will increase with increasing built structures, as the height, width, projected area and number of facets increase per unit area. For specular scattering this will also be dependent on the building orientation with respect to the radar beam orientation. For example, for dihedral corner reflectors, the maximum backscatter occurs when the angle between the flight direction and the building orientation is 0°, and the radar incident angle is 45°, for both vertical and horizontal polarisations. It can be given by

$$\sigma_{max} = 8 \pi b^2 L^2 / \lambda^2$$

where σ is the radar cross section (backscatter), b and L are the dimensions of the vertical component of the corner (effectively the vertical dimensions of the building) and λ is the radar wavelength. This maximum value will reduce as the incident angle changes, as a function of the projected area of the corner in the direction of the radar beam, and will also reduce as the angle between the radar range direction and building orientation changes from a right angle, and will reduce to a minimum at an approximate angle of 22.5° [9].

A recent study over Sydney [8] used SIR-B data to examine the average backscatter from different urban land use areas. The results showed that the average response for residential areas was lower than that of commercial areas, while the industrial areas had the highest return (for equivalent relative orientation angles). Here residential areas have smaller buildings and thus smaller dihedral reflectors, and generally materials of low dielectric constant (brick or timber walls and tiled roofs). Commercial buildings are usually more dense than residential buildings, are larger both in floor area and height, and contain more metal acting as structural support and as cladding. Industrial buildings in the subject area consisted of large (large and many dihedral reflecting corners) buildings mostly clad in metallic materials, which are conductors with a high dielectric constant, thus scattering most of the radiation at the surface, generating a very strong backscatter at particular orientation angles. The residential class was examined further to show the relationship between the backscatter and building orientation. The backscatter response value was highest when the angle (f) between the normal to the street and the radar look direction was zero, and decreased to a minimum at f equal to 22°. For values of f above 20° the backscatter varied little with phi. These results were similar to that obtained in [9].

A model has been developed [8] to give the expected backscatter from a group of buildings of user defined size, shape, material (including surrounding ground surfaces) and radar parameters. Existing formula, giving the backscatter for a dihedral corner reflector and a rectangular facet, were adopted into the model. The model is currently able to predict the backscatter from a simple building of rectangular shape with either a flat or a sloping roof. Results from the model show that the roof facet and front wall facing the antenna are the dominant contributors to the backscatter. Fig. 1 shows the backscatter with respect to ϕ for both residential and industrial type buildings, for each component of the building, as well as the total backscatter. The oscillations in the backscatter for both building types are due to phase differences as the distance the wave travels between the extremes of the object leads to either constructive or destructive interference. These oscillations become more frequent as the building size increases. The present model is being expanded to calculate the backscatter from a group of buildings of the same size, shape and material, and backscatter response from trees, essentially volume scattering, are also being integrated into the model. Finally the model is being further developed to allow the calculation of the polarised signature of a particular urban class.

RADAR POLARISATION SIGNATURES AND PHASE DIFFERENCE

Multipolarised radar provides much more information than individual cross or co-polarised radar. The received backscatter can be described by the polarisation signature which shows the co-polarised or cross-polarised return as a function of the transmitting polarisation. The polarisation of a wave can be described by its ellipticity and orientation angle [10]. A polarised wave may also be described as containing a vertical and horizontal component separated by a phase difference. A perfectly conducting dihedral corner reflector undergoes a phase shift of 180° during reflection, whilst a smooth (specular) surface undergoes almost no phase shift. These are commonly termed double and single bounce, or even and odd bounce scattering mechanisms. The polarisation signature contains valuable information for determining the characteristics of a surface. Trees, for example, can give a high cross-polarised response due to depolarisation by randomly oriented leaves, which may help to distinguish between some residential and commercial classes, since residential areas are more likely to contain a higher proportion of trees, both in gardens and along roads. In addition single storey residential areas are more likely to be dominated by single bounce or facet back scattering (from sloping roofs) when the incidence angle is normal to the roof, which occurs at about 30°, while larger buildings are dominated by double bounce or dihedral corner reflection from horizontal road/vertical building corners.

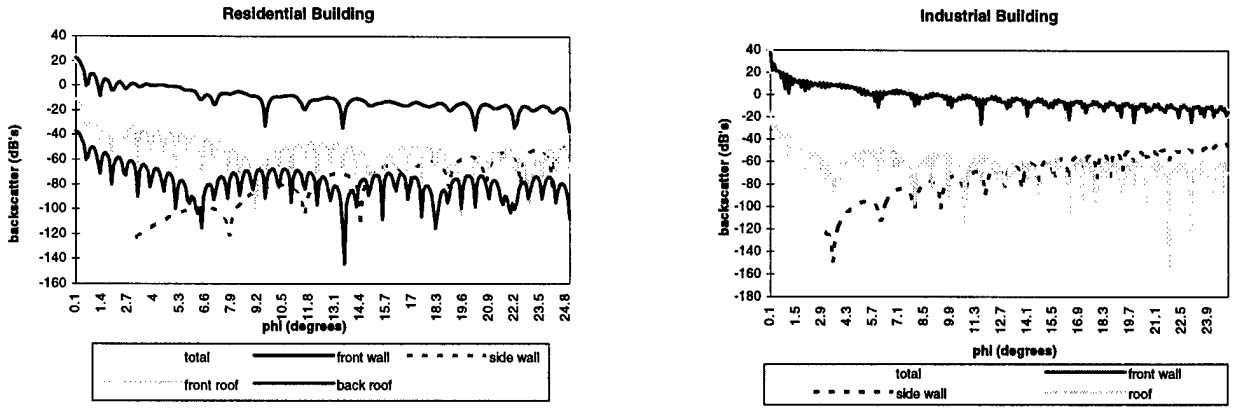

Figure 1: Modelled backscatter as a function of ϕ for each component of residential and industrial buildings, and their total.

In a recent study using AirSAR airborne data over Sydney [7], good classification results were obtained when a combination of single, double and cross-polarised scattering images, derived from P-band quad-polarised data, were used in the classification process. Residential, commercial, water, open grassed and treed areas were well separated. However these results were still dependent on the look direction angle and the incidence angle with respect to the major orientation of buildings and roof facet slopes. A method to decompose radar polarisation signatures has also been developed [11, 12]. In the model the backscatter was considered to consist of single (odd), double, Bragg and cross backscattering components, and the Mueller matrix was considered to be the sum of the Mueller matrices of these four scattering mechanisms.

The approach was applied to different categories of AirSAR (P, L and C quad-polarised data) images including forest, farmland, ocean and urban areas. The reconstructed polarisation signatures were found to coincide very well with the observed signatures. Fig. 2 shows the measured and simulated polarisation signatures (P-band) for a residential area, and their differences. For all cover classes examined, the accuracy of decomposition was found to be more than 95% for linear polarisations (HH and VV) and more than 85%, in most cases, for any other polarisation. Analysing the results of the decomposition it was found that double bounce scattering dominated the response from commercial areas, with a lesser percentage from residential areas. However in residential areas the percentage of odd or single bounce scattering was higher than all other land use categories, apart from grassland, and there was a significantly higher cross-polarised return from residential areas, compared to commercial areas due to increased vegetation volume scattering. Odd bounce scattering was also a higher percentage, for both residential and commercial, when VV return was compared with HH return. It was considered that polarimetric image classification would be improved using these optimal decomposition techniques, in addition to the traditional discriminators (co- and cross-backscattering coefficients, ratios of different backscattering coefficients, and phase difference).

REDUCTION OF CORNER REFLECTOR EFFECTS

In many applications of radar images the corner reflector effect can cause confusion in interpretation and classification. Here it is appropriate to reduce or eliminate these effects. This can be achieved in two ways. Firstly by imaging the area from two distinctly different azimuths, so that the effect appears in one image but not in the other, or secondly by accounting for building orientation to reduce the recorded backscatter to a value that does not include the corner reflector effect. The first approach can be achieved using an ascending and descending satellite image of the same area. For spaceborne radar in a sun synchronous orbit, the two paths will have a heading difference of approximately 22°. Thus what will cause corner reflection in one image will not do so in the other image, following the conclusions of [9]. Current research is using an ascending and descending ERS-1 image over Sydney to study this effect. The two images have been registered, and the following rule has been applied to eliminate the dihedral corner reflection effects. *If bright in A and not in B, replace with B. If bright in B and not in A, replace with A. If approximately the same, replace with the mean of A and B* Preliminary results show that a less confusing, more interpretable, single image results from this process. High backscatter that is not due to corner reflector effects, such as a metal dome, are not affected by this procedure. Further studies however are ongoing. It should be noted that the registration of the two radar images are a critical part of the procedure. As the images record the area from directions approximately opposite to each other the relative height displacement effects will be almost doubled making registration of the two images extremely difficult. This is particularly so for ERS-1 data, with a small look angle of approximately 23°. A solution to the problem was achieved by applying terrain height correction procedures via an intermediary Landsat TM image of the same area.

The second approach has theoretical appeal but has not yet been achieved in practice. It requires firstly the estimation of the orientation of built features with respect to the incoming radar. When this angle is more than 20° from the normal to the building alignment, no change is required. For angles less than 20° the measured backscatter can be reduced by the corner reflector effect, as calculated using the dihedral corner reflector equation. Recent research [13] has developed an algorithm to extract the per pixel

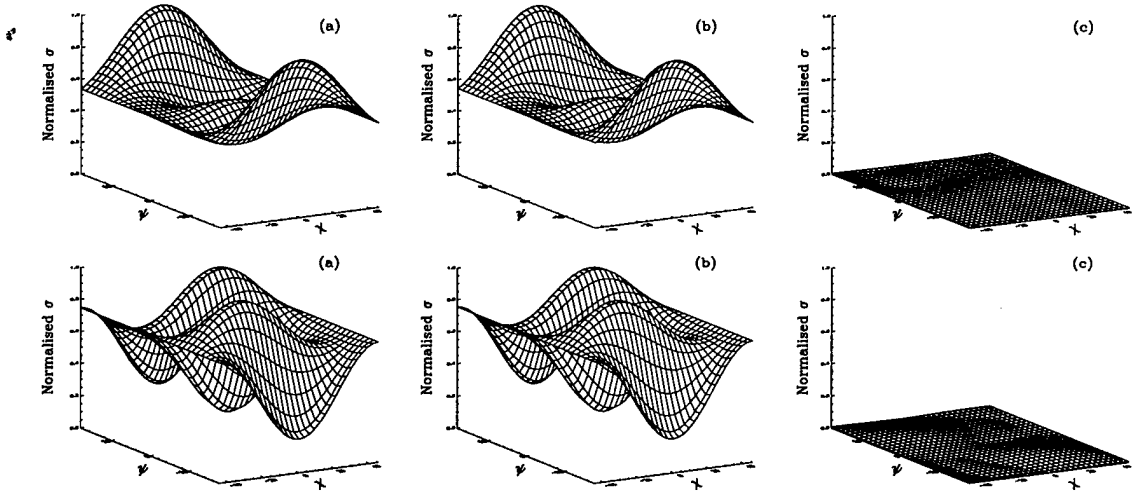

Figure 2: Polarisation signature (top: co-polarisation and bottom: cross-polarisation) comparison using the measured and simulated Mueller matrices for residential areas in Sydney at P-band: (a) measured, (b) simulated, and (c) absolute difference.

orientation of linear features from a digital image. In an urban area these are generally roads which normally parallel the building orientation. To date the algorithm has been applied to a Landsat TM image and simulated test data with very good results. Its application to a radar image has not yet achieved the same success due to higher levels of noise inherent in radar data.

SUMMARY AND CONCLUSIONS

An overview of theory, preliminary research results and some conceptual ideas have been presented with regard to the use of radar image data for monitoring urban areas. With the rapid growth of cities around the world, there is a consequent need for reliable , repetitive monitoring of these areas to allow appropriate planning and decision making. While further research is required on the work described in this paper, it would appear that the use of radar image data holds promise for the future.

REFERENCES

[1] Forster, B.C., "An examination of some problems and solutions in monitoring urban areas from satellite platforms," Int. J. Rem. Sen., vol.6, pp. 139-151, 1995.

[2] Henderson, F.M. and Xia, Z-G., "SAR applications in human settlement detection, population estimation and urban land use pattern analysis: A status report," IEEE Trans. on Geoscience and Remote Sensing, vol. 35, no. 1, pp. 79-85, January 1997.

[3] Xia, Z-G. and Henderson, F.M., "Understanding the relationships between radar response patterns and the bio- and geophysical parameters of urban areas," IEEE Trans. on Geoscience and Remote Sensing, vol. 35, no. 1, pp. 93-101, January 1997.

[4] Forster, B.C., "Evaluation of combined multiple incidence angle SIR-B digital data and Landsat MSS data over an urban complex," Proc. 7th Inter. Sym. Rem. Sen. for Resources Dev. and Envir. Man., Netherlands, pp. 813-816, Aug. 1986.

[5] Haak, B.N., "L-and X-band like-and cross-polarized synthetic aperture radar for investigating urban environments," Photo. Eng. and Rem. Sen., vol. 50, no. 3, pp. 331-340, 1994.

[6] Nasr, J.M. and Vidal-Madjar, D., "Image simulation of geometric targets for space borne synthetic aperture radar," IEEE Trans. Geoscience and Rem. Sen., vol. 29, no. 6, pp. 986-996, 1991.

[7] Dong, Y., Forster, B.C. and Ticehurst, C., "Decomposition of radar polarisation signatures from built and natural targets," International Archives of Photo. and Remote Sensing, vol. XXXI, part B7, pp.196-203, 1996.

[8] Ticehurst, C., Forster, B.C. and Dong, Y., "Using backscatter images for classifying and determining the bulk density of the urban environment," Int. Archives of Photo. and Remote Sensing, vol. XXXI, part B7, pp. 709-713, 1996.

[9] Hardaway, G., Gustafson, G.C. and Lichy, D., "Cardinal effect on Seasat images of urban areas,". Photo. Eng. and Rem. Sen., vol. 48, no. 3, pp. 399-404, 1982.

[11] Dong, Y., Forster, B.C. and Ticehurst, C., "Polarimetric image classification using optimal decomposition of radar polarization signatures," Proc. IGARRS'96, Lincoln, Nebraska, pp. 1556-1558, May 1996.

[12] Dong, Y. and Forster, B.C., "Understanding of partial polarisation in polarimetric SAR data," Int. J Rem Sens, vol. 17, no.12, pp. 2467-2475, 1996.

[13] Dong, Y., Forster, B.C. and Ticehurst, C., "Street orientation and recognition in Landsat TM imagery," submitted for publication.

Road Network Extraction from Airborne Digital Camera Images: A Multi-Resolution Comparison

P. Gong
Center for Assessment and Monitoring of Forest and Environmental Resources
Department of Environmental Science, Policy, and Management
151 Hilgard Hall, University of California, Berkeley, Ca 94720-3110
Tel. (510) 642-5170 Fax. (510) 643-5098 Email: gong@nature.berkeley.edu

J. Wang
Department of Geography
University of Western Ontario, London, Ontario, Canada

Abstract – As image resolution increases from 10-30 m to 0.5-2 m, road networks will appear to be narrow areas rather than thin lines. This becomes a challenge for traditional linear analysis methods based on mask operations but creates an opportunity for classification based methods. We experimented with an advanced linear analysis, gradient direction profile analysis, and a few classification algorithms including a maximum classification, clustering and a contextual classifier for road network extraction using airborne digital camera data acquired over Livermore, California with approximately 1.6 m spatial resolution. Results indicate that both the linear extraction and image clustering algorithms worked reasonably well. Best road network results have been obtained by applying the linear extraction algorithm to a morphologically filtered image that was generated by combining the near infrared (NIR) and red (R) image bands through NIR/R+NIR. With this method, the correctly extracted road pixels account for 78.7% of the total road pixels obtained from image interpretation with field verification. The image clustering method resulted in 74.5% correctly extracted road pixels. When experimenting with the images resampled at approximately 3 m and 5 m resolution, the best overall accuracies for road extraction decreased to 74.6% and 61.6%, respectively.

INTRODUCTION

Road network changes constantly at many rural-urban fringe areas due to urban expansion. Urban planners and decision makers on land use development often have obsolete land use information because operational mapping methods based on manual interpretation of aerial photographs usually take a year or two to complete from the time of aerial photography. Research efforts have been made to develop computer analysis algorithms for road network extraction [1-2] and land-use mapping [3] from satellite images. On 10-30 m spatial resolution satellite images, roads are linear features represented by valleys or ridges of brightness. Wang and Liu [4] grouped 4 types of line extraction methods that could be applied to road network extraction. They are (1) gradient operator and mask convolution method, (2) gradient direction profile analysis (GDPA) method, (3) mathematical morphology analysis method, and (4) knowledge-based method. Because the contrast between a road and the image background varies both spatially and spectrally, the use of multispectral data helps reduce road ambiguity.

Among various satellite and airborne sensing technologies, it is now possible to have high geometric and radiometric quality digital camera images on airborne platforms with spatial resolutions at the sub-meter level. In addition, 1-4 m resolution satellite imagery will soon become available and high spatial resolution digital can be obtained by scanning aerial photographs. In a study of road networks extraction from scanned color-infrared films from aerial photography, Benjamin and Gaydos [5] claim that 3 m spatial resolution is most suitable for road network extraction in Cupertino, California. They applied clustering and editing instead of the more sophisticated line extraction algorithms to scanned data resampled to different spatial resolution (1-5 m). Since most roads in urban areas are wider than 5 m, road networks become narrow areas rather than brightness valleys or ridges on images with pixel sizes smaller than 5 m by 5 m. At a spatial resolution better than 5 m, it is possible to extract road network with classification methods.

Our questions are:

- how well can traditional linear extraction algorithms perform when applied to those high spatial resolution images?
- to what extent, can classification methods be used for road network extraction purposes?
- how can methods in the two different paradigms be used to complement each other for improved road network extraction and land use classification?

This paper presents some of our efforts toward answering the first two questions. The objective was to compare classification methods with line extraction algorithms for road network extraction from digital camera images resampled at different spatial resolutions. A supervised per-pixel classification, a clustering, and a cover-frequency based contextual classification method were applied to classify an

0-7803-3836-7/97/$10.00 © 1997 IEEE

airborne digital camera image. A few road cover types were included in each classification. A gradient direction profile analysis algorithm was also applied to the same image. Road extraction results are presented and discussed.

STUDY SITE AND DATA

The study site is located on the east border (121°43' W, 37°41' E) of City of Livermore, California. On June 30, 1995, an imaging system consisting of 4 Kodak DCS-200 cameras was used on board of an aircraft to acquire multispectral images over the study area. The four cameras simultaneously acquired images at 450 nm, 550 nm, 650 nm, and 850 nm, respectively, with a band width of 80 nm. The single-band images from individual cameras were then geometrically corrected and resampled to form a multispectral data set. The spatial resolution is approximately 1.6 m.

ROAD EXTRACTION METHODS AND ACCURACY ASSESSMENT

Road network extraction methods generally involve five steps: data preprocessing, obtaining initial road network, noise removal, thinning, and pruning. The purpose of image preprocessing is to enhance road network features for subsequent analysis. We undertook grey-level dilation filtering to the original image. It is essentially an operation in search of maximum from a local neighborhood defined by the structuring element [6]. Moving a 3 X 3 kernel over a grey-level image, we assign the maximum grey-level value to the pixel at the kernel center. Noise removal is to remove from the initial road networks relatively small patches of pixels that have been identified as road segments. Pixel patches smaller than a certain size are removed from the initial road network image. Thinning reduces the detected road network from a few pixels wide to one pixel in width. Pruning removes short-branches of dead-end roads according to their lengths.

Gradient Direction Profile Analysis

The GDPA algorithm used in [1] was selected for use in this study. This algorithm first finds the greatest gradient direction for each pixel using the brightness values in a 3 by 3 neighborhood. A pixel is considered as a candidate road pixel if its greatest gradient exceeds a limit, T_d, specified by the analyst. The algorithm then searches among the candidate road pixels for pixels at ridge tops or valley bottoms of grey levels by modeling grey level profiles along the greatest gradient direction centered at each candidate pixel. The modeling is achieved through polynomial curve fitting along the gradient direction profile. The grey-level ridge top or valley-bottom positions are found through profile derivative and curvature analysis. The length of a profile, L, is specified by the analyst and the curvature of the polynomial function must be greater than a specified value, T_k. An initial road network is extracted from an image by adjusting the three parameters, T_d, L and T_k. Details on GDPA is found in Wang et al. [1].

Image Classification and Clustering

To classify roads from the digital camera image, we employed a clustering algorithm, a supervised maximum likelihood classifier and a cover-frequency based contextual classifier. The clustering algorithm is ISODATA (iterative self organizing data analysis technique). The cover-frequency based contextual classifier is found in [3]. It first converts the original image to a land-cover map using a regular per-pixel maximum likelihood classification (MLC) algorithm, or a grey-level vector reduced image with a grey-level vector-reduction algorithm, or a cluster map through clustering. The algorithm then extracts frequencies of land cover, cluster, or grey-level vector from a neighborhood of a pixel and uses the frequencies in classification of land uses or discrimination of road types for that pixel. The size of the pixel neighborhood is specified by the analyst. The contextual classification requires supervised training to determine the frequencies for each class. The same training set was used for both the maximum likelihood classification and the contextual classification.

We used 8 classes in the supervised classification. They include four types of road covers according to different road surface colors and materials, new asphalt, older asphalt, concrete and railroad. The other 4 cover types are residential, industrial, well irrigated grass land and dry grass land. We selected training areas for the 8 land-use classes and used the maximum likelihood classifier and the contextual classifier to classify the imaged area.

Image Resampling

All image resampling methods can be achieved through image convolution. To resample the 1.6 m resolution data to coarser resolutions, we compared the four different image resampling methods. As expected image averaging had the greatest effects in blurring the edges or linear features as image resolution degrades. Edges and linear features were better preserved in the resampled images generated by the remaining three resampling methods and those resampled images looked very similar. Therefore, we tested the linear extraction algorithms using the images resampled to 3 m and 5 m resolutions with the nearest neighbor method. We did not apply classification methods to the resampled images because as discussed in the introduction images with coarser spatial resolution would be less useful for road network classification.

Accuracy Assessment

Three measures can be calculated for the quantitative comparison [4].

Let N_{ce} be the number of correctly extracted road pixels; N_{tr} be the number of true road pixels; and N_{te} be the total number of extracted road pixels:

overall accuracy = N_{ce} / N_{tr}

commission error = $(N_{te} - N_{ce}) / N_{tr}$

The overall accuracy is the fraction of pixels correctly extracted as roads. The commission error is the number of pixels incorrectly extracted as road pixels divided by the number of true road pixels.

RESULTS

We applied the GDPA algorithm to each band of the original image and some derivatives of the images. The best result with the GDPA algorithm has been achieved using an image that combines the ratio between the near infrared and red band with the near infrared band, [band 4/band 3] + band 4. The newly generated image suppressed the shade and shadow in the original image through image ratioing, while the brightness of the vegetation portion of the image was enhanced. We then applied dilation filtering to the band combination image for 3 iterations. The initial road network was extracted from the dilated image (Td=1.0, L=5, Tk=3.0.

With the image classification approaches, no preprocessing was applied to the original images. The four bands of image were clustered using ISODATA resulting in 49 clusters. After a cluster by cluster examination, we selected those clusters corresponding to road networks. All road network clusters were merged to form an initial road network map, which was further processed by noise removal, thinning and pruning, and resulted in a final road map. Supervised MLC classification was also performed on the original four bands. Similarly, noise removal, thinning and pruning were applied to produce a final road map. The final road network results obtained from MLC and from the clustering algorithm are similar. The clustering algorithm picked up more road details, particularly the rail roads, than the MLC method. It also included more non-road artifacts in the final result.

The cluster map was also used as the basis for the contextual classification. Classified road results were used as the initial road networks for subsequent noise removal, thinning and pruning. We used a 9 by 9 pixel neighborhood size to generate cover frequencies in the contextual classification. We did not attempt to find an optimal window size for the classification. Generally, a large window size would remove more road details particularly when the road is relatively narrow. While a small window size would results in more unwanted details.

Table 1 lists some of the accuracy assessment results. With the 1.6 m resolution image, the best overall accuracy, 78.7%, is obtained by the GDPA method from the image specially enhanced (b4 + b4/b3). The second best is achieved by the clustering method (74.5%). However, both methods have relatively high commission errors. The lowest overall accuracy is from the contextual classification results but the commission error is the lowest.

Table 1. Performance evaluation of different road network extraction results

Images	Overall accuracy(%)	Commission error
band4	59.8	1.010
clustering	74.5	0.845
contextual	49.5	0.476
MLC	68.4	0.659
b4+b4/b3	78.7	0.984
band4 (3m)	66.0	0.951
b4+b4/b3 (3m)	74.6	0.832
band4 (5m)	53.5	0.882
b4+b4/b3 (5m)	61.6	0.693

ACKNOWLEDGEMENT

We are grateful to the assistance in field work by Miss Cynthia Cowen. The research is partially supported by an NSERC research grant to J. Wang.

REFERENCES

[1] Wang, J.F., P. M. Treitz and P.J. Howarth, 1992. Road Network detection from SPOT imagery for updating geographical information systems in the rural- urban fringe, *Int. J. Geographical Information Systems*, Vol. 6, No. 2:141-157.

[2] Gruen, A. and H.H. Li, 1995. Road extraction from aerial and satellite images by dynamic programming, *ISPRS Journal of Photogrammetry and Remote Sensing*, Vol. 50 No. 4:11-20.

[3] Gong, P. and P. J. Howarth, 1992. Frequency-based contextual classification and grey-level vector reduction for land-use identification. *Photogrammetric Engineering and Remote Sensing*, 58(4):423-437.

[4] Wang, J.F. and W. Liu, 1994. Road detection from multispectral satellite imagery, *Canadian Journal of Remote Sensing*, Vol. 20, No. 2:180-189.

[5] Benjamin, S., and L. Gaydos, 1990. Spatial resolution requirements for automated cartographic road extraction, *Photogrammetric Engineering and Remote Sensing*, Vol. 56, No. 1: 93-100.

[6] Sternberg, S.R., 1986. Grayscale morphology, *Computer Vision, Graphics, and Image Processing*, 35:333-355.

On the surface roughness characterization for SAR data analysis.

F. Mattia (1), J.C. Souyris (2), T. Le Toan (2),
D. Casarano (3), F. Posa (3), M. Borgeaud (4)

(1)ITIS-CNR, c/o CGS-ASI Loc. Terlecchia, I 75100 Matera (Italy)
tel. +39 835 377282, fax. +39 835 339027, e-mail: Mattia@asimt0.mt.asi.it
(2) CESBIO, 18 av. Edouard Belin bpi 2801, 31401 Toulouse Cedex 4,
(3) Politecnico di Bari, via Amendola 77, I 70100 Bari (Italy)
(4) ESA, ESTEC-XEP. P.O. Box 299, 2200 AG Noordwijk, The Netherlands

Abstract The objective of this paper is to investigate the possibility of achieving a more realistic description of natural surfaces for microwave remote sensing purposes. By analyzing measured profiles, non stationary effects which cannot be accounted for in the classical description of roughness are underlined. Subsequently, an expansion of *1/f* processes in terms of wavelet orthonormal basis is used to derive a possible description of natural roughness.

INTRODUCTION

In the context of remote sensing applications, surface roughness has been traditionally described as a zero mean Gaussian stationary random process with a concurrent autocorrelation function. The assumption of stationarity implies that there exists a fundamental spatial scale, identified by the correlation length (*l*), which characterizes the horizontal roughness properties of the process. Vertical roughness is represented by the profile height std (*s*). Although this statistical description offers a simple way of characterizing natural roughness, experimental results have always been found to have a critical variability in the estimation of surface parameters, especially regarding the correlation length. Previous works (see for example [1]) have presented natural soils showing *self similarity* properties, i.e. their geometrical properties are invariant to spatial scale transformations. For this reason, they cannot be characterized by a unique fundamental spatial scale.

The purpose of this paper is to present a possible mathematical description of isotropic *self similar* surfaces in terms of *1/f* random processes. Future work will assess the possibility of incorporating such a description in e.m. models.

As a preliminary step, we present some experimental results obtained by analyzing roughness profiles measured during two ground campaigns conducted in Europe. Subsequently, a brief introduction to the theory of *1/f* processes is given. In particular, a *Karhunen-Loève* expansion of *1/f* processes in terms of orthonormal wavelet basis [2] is used to model isotropic natural surface properties. The concurrent autocorrelation function is derived and its properties are illustrated.

EXPERIMENTAL DATA SET

Roughness profiles acquired over two different test sites in Europe have been analyzed in order to investigate the presence of non stationary effects in the natural roughness behavior. To achieve this, for each profile classical roughness parameters, namely *s* and *l*, have been calculated over different spatial scales. The first experimental data set has been collected during the second *SIR-C/X-SAR* mission over the Matera (Italy) test site. The profiles have been measured by means of a needle-like profiler *3 m* long with an horizontal resolution of *1.5 cm.* Figure 1 shows both *s* and *l* parameters for the smoothest field, estimated over *90 cm*, *180 cm* and *270 cm.* For the s parameter, no clear trend can be concluded whereas, in the case of the correlation, there is a clear increasing trend. Such an effect cannot be accounted for in the classical roughness description. The second experimental data set has been acquired during the three day repeat cycle of ERS1 (early 1994). During that period, the European Space Agency has supported an extensive ground data acquisition over a flat area in Middle Zeeland (The Netherlands). Profiles *1.5 m* long have been measured by means of a laser profiler having a horizontal resolution of *0.5 mm,* over fields having different roughness states. Roughness parameters have been analyzed on two different scales.: *1 m* and *1.5 m.* As an example, figure 2 shows the obtained estimates in the case of the smoothest field. For both parameters the average of the estimated values is increasing as a function of the scale under consideration. The increase is slower in the case of *s* than *l*. Due to the limited length of the analyzed profiles the increasing trend cannot be considered as fully prove. However, present observations are not in contradiction with the assumption that natural roughness possesses *self similarity* properties. Further experimental investigations aimed at measuring longer profiles are required to
definitely demonstrate whether or not natural roughness have *self similar* properties.

0-7803-3836-7/97/$10.00 © 1997 IEEE

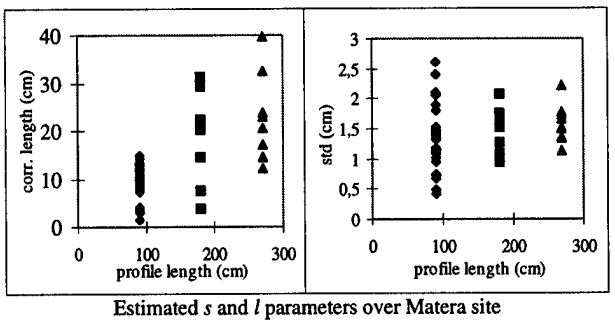

Estimated *s* and *l* parameters over Matera site

Fig.1

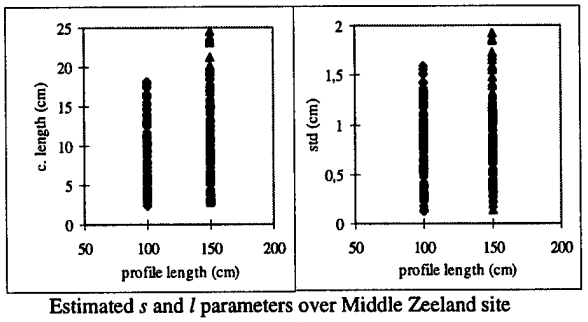

Estimated *s* and *l* parameters over Middle Zeeland site

Fig.2

In the present paper we assume natural surfaces are *self similar* and, in the following section, we present a possible mathematical description of such surfaces in terms of *1/f* processes.

1/f RANDOM PROCESSES

The *1/f random processes* are usually characterized, over an arbitrary wide spectral bandwidth Δf, by a power spectral density $S(f)=\frac{\sigma^2}{f^\nu}$ with $1\le\nu\le 3$. The expression for $S(f)$ indicates that, if the frequency bandwidth covers all the infinite interval of positive frequencies, then $S(f)$ no longer is an integrable function in the L^2 space. Consequently, it will not represent a valid power spectral density expression in the theory of stationary random processes. A classical example of *1/f* process is the fractional *Brownian motion*. In order to assess the potential of *1/f processes* to describe natural roughness, a simulation of one dimensional *fractional Brownian motion process,* based on *the successive random addition algorithm* has been implemented. One profile made of *30000* points (*300 m* assuming steps of *1 cm*), with a Hurst exponent *H=0.2* and a profile height *std* of *1.5 cm* has been generated. Then, a statistical analysis has been performed over sub-profiles of different lengths. Sub-profiles of *2.4 m*; *12 m* and *60 m* have been considered. Fig. 3, shows the *std*s and correlation lengths estimated over the different sub-profiles.

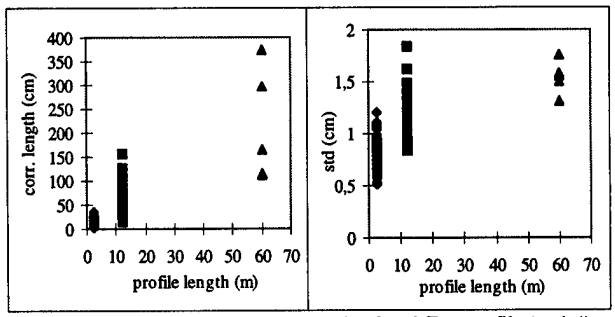

Estimated *s* and *l* parameters over a simulated fBm profile (ν=1.4)

Fig.3

Both the estimated *std*s and correlation lengths are increasing as a function of the sub-profile length. It can be shown that this effect is due to the non stationary behavior of the *fractional Brownian process.* Moreover, it should be noted that the increase of *std* versus profile length, is much smaller than for correlation length. It may explain why experimental data concerning short sub-profiles do not clearly indicate a non stationary effect in the case of standard deviation (see fig. 1). A mathematical tool of interest for *1/f random process* analysis has been recently proposed by Wornell [2]. It consists of a Karhunen-Loève expansion rule of *1/f processes* in terms of orthonormal wavelet bases. More precisely, it has been demonstrated that *1/f-like processes* can be decomposed over a wavelet basis. The coefficients of the decomposition are uncorrelated random variables with a given variance structure. Wornel has demonstrated the following theorem: *Consider any orthonormal wavelet basis* $\Psi_n^m(r)=2^{m/2}\Psi\left(2^m r-n\right)$ *with Rth-order regularity for some* $R\ge 1$. *Then the random process constructed via the expansion*

$$Z(r)=\sum_{m=-\infty}^{+\infty}\sum_{n=-\infty}^{+\infty} z_n^m\Psi_n^m(r) \qquad (1)$$

where the z_n^m *are a collection of mutually uncorrelated, zero mean Gaussian random variables with variances*

$$var\ z_n^m=\sigma_0^2\,2^{-\nu m} \qquad (2)$$

for some parameter $0<\nu<2R$, *has a time averaged spectrum*

$$S(f)=\sigma_0^2\sum_m 2^{-\nu m}\left|\Psi\left(2^{-m}f\right)\right|^2 \qquad (3)$$

that is nearly 1/f, i.e.

$$\frac{\sigma_L^2}{|f|^\nu}\le S(f)\le\frac{\sigma_H^2}{|f|^\nu} \qquad (4)$$

for some $0<\sigma_L^2\le\sigma_H^2<\infty$, *and has octave-spaced ripple, i.e. for any integer k*

$$|f|^\nu S(f)=\left|2^k f\right|^\nu S\left(2^k f\right) \qquad (5).$$

Such a mathematical description may be assumed to be a more realistic mathematical model for isotropic natural surfaces (i.e. $r=\sqrt{x^2+y^2}$).

SURFACE MODEL

When an e.m. wave is impinging on a random surface it is sensitive to surface geometrical features only over a finite range of scales. For this reason, surface details below, $L_1=\frac{\lambda}{10}$ and higher than, at maximum, the resolution cell $L_2= N \lambda$ can be disregarded. For e.m. scattering purposes, this implies that a consistent approximation for natural surface is:

$$Z_M(r)=\sum_{m=-M_1}^{+M_2}\sum_{n=-\infty}^{+\infty} z_n^m \Psi_n^m(r) \qquad (6).$$

$Z_M(r)$ is a cyclostationary process [2] having finite variance and a spatial averaged spectrum given by:

$$S_M(f)=\sigma_0^2 \sum_{m=-M_1}^{+M_2} 2^{-\nu m}\left|\Psi\left(2^{-m} f\right)\right|^2 \qquad (7).$$

The M_i i=1,2 values can be obtained by noting that $\forall r>0$ it is possible to find one M_0 and one r_0 such that $r=2^{M_0} r_0$ *with* $1\le r_0\le 2$ [2]. Then:

$$M_i=\pm\log_2\left(\frac{r_i}{L_i}\right) \text{ with i=1,2} \qquad (8)$$

By applying a Fourier transform to (7), the following autocorrelation function is obtained:

$$R_M(\tau)=\sigma_0^2 \sum_{m=-M_1}^{M_2} 2^{-m(\nu-1)} R_\Psi(2^m\tau) \qquad (9)$$

where $R_\Psi(\tau)=\int_{-\infty}^{+\infty}\Psi(\zeta)\Psi(\zeta+\tau)d\zeta$. Equation (9) correspond to a stationary process, valid within a finite range of spatial scales. This property may be very useful for incorporating such a roughness description in an appropriate asymptotic e.m. model. The expression of $R_M(\tau)$ depends on three parameters: σ_0; ν and the number of spatial scales taken into account (i.e. $M=M_2+M_1$). σ_0 clearly determines the value of the profile height *std* (i.e. $R_M(0)$). ν governs the shape of the function. The M parameter behaves has a magnification factor for the function shape. Figure 4 displays the normalized autocorrelation function (ACF) (i.e. $\frac{R_M(\tau)}{R_M(0)}$)

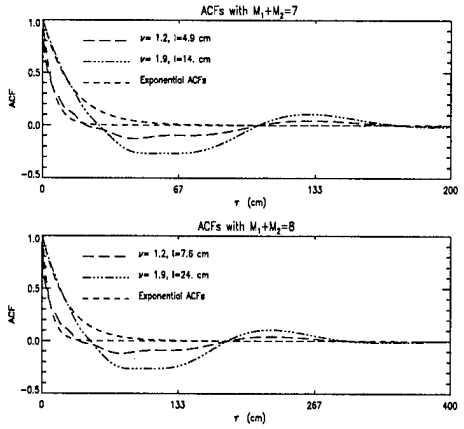

Derived Autocorrelation function
Fig.4

for $\nu=1.2$ and $\nu=1.9$.Two different ranges of spatial scales are considered. The first range corresponds to a finer resolution of *1 cm* and a coarser resolution of *128 cm* (i.e. $M_1=0$ and $M_2=7$). The second one has the same finer resolution but a coarser resolution equal to *256 cm*. For both cases, the corresponding exponential ACF has been superimposed. The family of wavelet considered here is the 12^{th}-order Daubeschies wavelet basis. As can be seen, eq. (9) has an exponential shape close to the origin and far from the origin it has an oscillatory behavior.

CONCLUSIONS

In this paper, the problem of a realistic mathematical description of natural roughness has been addressed. Experimental data set collected over different sites in Europe have shown non stationary effects. A description of such effects may be given using *1/f* processes. A *Karhunen-Loève* expansion of *1/f* processes in terms of orthonormal wavelet basis has been used to derive a possible mathematical model for natural roughness. Future work will be dedicated to incorporating such a description in suitable asymptotic e.m. models.

ACKNOWLEDGEMENT

This work has been supported by ESA -ESTEC under contract n.12008/96/ND/NB

REFERENCES

[1] Sayles, R.S., Thomas, T.R., "Surface Topography as a nonstationary random process", Nature, vol. 271, Febr. 1978
[2] Wornell, G.W., "Wavelet-Based Representation for the *1/f* Family of Fractal Processes," Proc. IEEE, vol. 81, Oct. 1993

Electromagnetic Scattering Interaction Between a Dielectric Cylinder and a Slightly Rough Surface

Tsenchieh Chiu and Kamal Sarabandi
Department of Electrical Engineering and Computer Science
The University of Michigan, Ann Arbor, MI 48109-2122
Tel:(313) 936-1575, Fax:(313) 747-2106
Email: tcchiu@engin.umich.edu

INTRODUCTION

In radar remote sensing of vegetation, accurate scattering models that can describe the interaction of electromagnetic waves and vegetation-covered terrain is of great importance. The common approach is to regard the vegetation-covered surfaces as a random collection of dielectric particles with canonical geometries, such as cylinders representing stems and branches and thin dielectric disks representing leaves, above a half-space dielectric medium with rough interface representing the ground. Most scattering models developed for this problem are based on single scattering properties of the scatterers. In these models, the scattering interaction among the vegetation particles and the vegetation particles and the rough surface are ignored. In more advanced models, such as radiative transfer (numerical or second-order iterative solutions), the scattering interaction among scatterers are accounted for assuming that the particles are in the far-field of each other. This is not an accurate model because most vegetation structures contain large particles (tree trunk, long branches, main stem for grasses) whose length are comparable to the vegetation layer thickness and are much larger than the wavelength. In these cases the near-field interaction, as opposed to far-field interaction, must be taken into account. Experimental results indicate that although the first-order scattering models are capable of predicting the co-polarized backscatter adequately, they are not able to predict the cross-polarized backscatter to within a desirable accuracy.

In this paper, an analytical solution that can predict the near-field interaction between a scatterer and a rough surface is presented. This solution is derived using a recently developed technique which is based on the reciprocity theorem [1]. This approach is very efficient since only the current distribution of isolated scatterers are needed to evaluate the interaction in the far-field region. In specific, the second moments of backscatter fields are provided for a circular dielectric cylinder above a slightly rough surface with inhomogeneous dielectric profile. The accuracy of the theoretical formulation is verified by conducting polarimetric backscatter measurements from a lossy dielectric cylinder above a slightly rough surface. Excellent agreement between the theoretical prediction and experimental results are obtained.

THEORETICAL ANALYSIS

In this section, the scattering formulation for a dielectric cylinder above a slightly rough surface which includes the near-field interaction between the cylinder and the rough surface is presented. The geometry of the scattering problem is shown in Fig. 1. The pertinent dimensions and orientation angles are specified in Fig. 2. By inspection, the backscatter from this composite target can be decomposed into four scattering terms: 1) direct backscatter from the cylinder ($\mathbf{S}^c$), 2) direct backscatter from the rough surface ($\mathbf{S}^r$), 3) cylinder-surface scattering ($\mathbf{S}^{cr}$), and 4) surface-cylinder scattering ($\mathbf{S}^{rc}$). $\mathbf{S}^c$ can be calculated easily using a semi-exact solution which is based on the eigen-function expansion and the physical optics approximation [2]. To calculate $\mathbf{S}^r$, the complete second-order solution presented in [3] is applied. The challenge here is to calculate $\mathbf{S}^{cr}$ and $\mathbf{S}^{rc}$ analytically. This is done using a recently developed technique which is based on the reciprocity theorem [1]. This method is extremely efficient and provides the interaction between the cylinder and rough surface up to the second order. The second-order scattered field from the cylinder which is illuminated by the scattered field of the rough surface is computed from

$$\hat{p} \cdot \mathbf{E}_{2c} = \int_{V_r} \mathbf{J}_r \cdot \mathbf{E}_{ec} dv$$

where $\mathbf{J}_r$ is the volumetric current induced in the rough surface by the incident wave in the absence of the cylinder, and $\mathbf{E}_{ec}$ is the scattered field from the cylinder when excited by an elementary current located at the observation point in the absence of the rough surface. The induced current in the rough surface is calculated by replacing the top rough layer with an equivalent polarization current above a dielectric half-space. The formulation of this equivalent current is obtained iteratively using a perturbation method [3]. The closed-form near-field solution for $\mathbf{E}_{ec}$ is obtained using the stationary phase technique, and its formulation can be found in [1]. After tedious algebraic manipulations which is beyond the scope of this paper, analytical expressions for the elements of the scattering matrix of surface-cylinder interaction are obtained.

0-7803-3836-7/97/$10.00

The solution for the RCS can be calculated from:

$$\frac{\sigma_{pqpq}}{4\pi} = |S_{pq}^{c} + S_{pq}^{rc(0)} + S_{pq}^{cr(0)}|^2 + \sigma_{pqpq}^{r0}\frac{A}{4\pi} + \langle |S_{pq}^{rc(1)} + S_{pq}^{cr(1)}|^2 \rangle \triangle^2 + 2\,Re\left\{ \langle S_{pq}^{r(1)} (S_{pq}^{rc(1)} + S_{pq}^{cr(1)})^* \rangle \right\} \triangle^2 + 2\,Re\left\{ (S_{pq}^{c} + S_{pq}^{rc(0)} + S_{pq}^{cr(0)}) \langle (S_{pq}^{rc(2)} + S_{pq}^{cr(2)}) \rangle^* \right\} \triangle^2 \qquad p,\, q \in \{h,\, v\}\,,$$

where A is the illuminated area, and σ_{pqpq}^{r0} is given by:

$$\sigma_{pqpq}^{r0} = \lim_{A\to\infty} \frac{4\pi}{A} \left\{ \left\langle |S_{pq}^{r(1)}|^2 \right\rangle \triangle^2 + \left[\left\langle |S_{pq}^{r(2)}|^2 \right\rangle + 2Re \left\langle S_{pq}^{r(1)} S_{pq}^{r(3)*} \right\rangle \right] \triangle^4 \right\}.$$

Here $S_{pq}^{r(1)}$, $S_{pq}^{r(2)}$, and $S_{pq}^{r(3)}$ are the first-, second-, and third-order backscattering matrix elements of the rough surface. Explicit expressions for σ_{pqpq} and the scattering matrix elements are rather lengthy and reported in [3].

SIMULATION AND EXPERIMENTAL RESULTS

Data simulation has been performed to investigate the importance of the contribution from the interaction between cylinders and rough surfaces. In Fig. 3, the ratios of the zero-order to the complete first-order backscattering solution excluding the direct backscatter form rough surface are plotted versus incidence angle. The length, radius, and dielectric constant of the cylinder are 0.71m, 0.385cm, and 43.4+i13.2 at 1.25 GHz, respectively. The cylinder is placed right above a rough surface with $ks = 0.1$, $kl = 2.0$ having exponential correlation function. The RCSs are calculated at six different cylinder tilt angles (β): 2^o, 4^o, 6^o, 8^o, 10^o, and 12^o. The RCS for each tilt angle is the average of the radar cross sections calculated at every 10^o of the azimuth angle (α). Basically, azimuthal symmetry is assumed uniform distribution over $[0, 2\pi)$. The zero-order solution includes scattering from the cylinder and the cylinder ground-bounce interaction for a flat surface. Fig. 3(a) and Fig. 3(b) show that, for the co-polarized scattering, the zero-order solution is sufficient except when the incidence angle is close to normal incidence. As shown in Fig. 3(c), the cylinder-rough-surface interaction is significant for the cross-polarized scattering. It is found that as the tilt angle increases, the cylinder-rough-surface interaction becomes less important.

Ignoring the cylinder-rough-surface interaction, the main source of the cross-polarized backscatter is the rough surface alone (second-order and higher-order perturbation terms). Fig. 4(a) compares the cross-polarized backscatter of the rough surface and the rough-surface-cylinder for different values of β assuming a cylinder density 1 cylinder/m^2. While the cross-polarized backscattering from the rough surface ($ks = 0.1$ and$kl = 3.0$) alone decreases rapidly as the incidence angle increases, the total backscattering increases. Fig. 4(b) shows a similar phenomenon as the number density of vertical cylinders increases.

To examine the validity of the scattering formulations, backscatter measurements were performed polarimetrically using the indoor bistatic facilities of the Radiation Laboratory at the University of Michigan. In these experiments, an X-band stepped frequency radar with the center frequency 9.25 GHz and the bandwidth 1.5 GHz was used. The experimental setup is shown in Fig. 5. A lossy circular cylinder was made by filling a circular cavity in a Styrofoam block with water. The radius and length of the water cylinder were 0.83 cm and 11 cm, respectively. A computer-generated Gaussian random rough surface with $ks = 0.2$ and $kl = 0.9$ was made by milling the surfaces of floral foam blocks, and then they were soaked with water. Because of the gravity, the water content at the top of the layer was found to be around 30%. The water content is assumed to increase linearly to nearly 100% at 0.5 cm below the top rough layer. The dielectric constant of water calculated from Debye formula was found to be 53.4 + i 39.3.

Fig. 6 shows the measured and theoretical cross-polarized RCS of the rough surface with and without the water cylinder. The inclusion of the cylinder does increase the cross-polarized backscattered field significantly. Note that the interaction of a vertical cylinder with flat surface does not produce any cross-polarized backscatter.

REFERENCES

[1] Sarabandi, K. and P.F. Polatin, "Electromagnetic Scattering from Two Adjacent Objects," *IEEE Trans. Antennas Propagat.*, vol. 42, no. 4, pp. 510-517, 1994.

[2] Sarabandi, K., *Electromagnetic Scattering from Vegetation Canopies,* Ph.D. dissertation, the University of Michigan, Ann Arbor, 1989.

[3] Sarabandi, K. and T. Chiu, "Electromagnetic Scattering from Slightly Rough Surfaces with Inhomogeneous Dielectric Profiles," to be published by *IEEE Trans. Antennas Propagat.*.

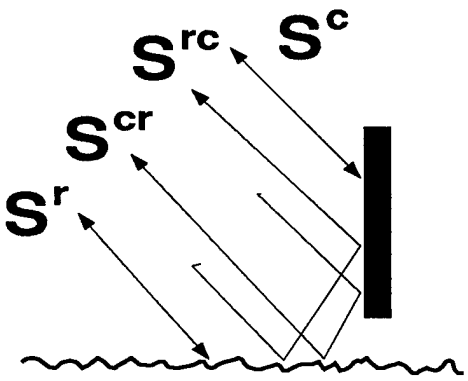

Figure 1: Configuration of the scattering problem.

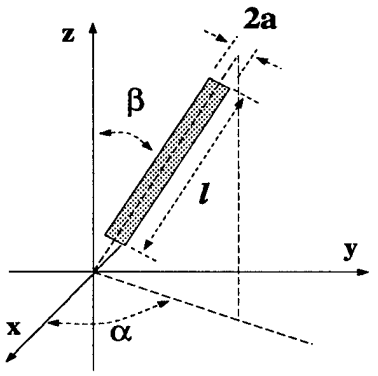

Figure 2: The dimension and orientation of a cylinder.

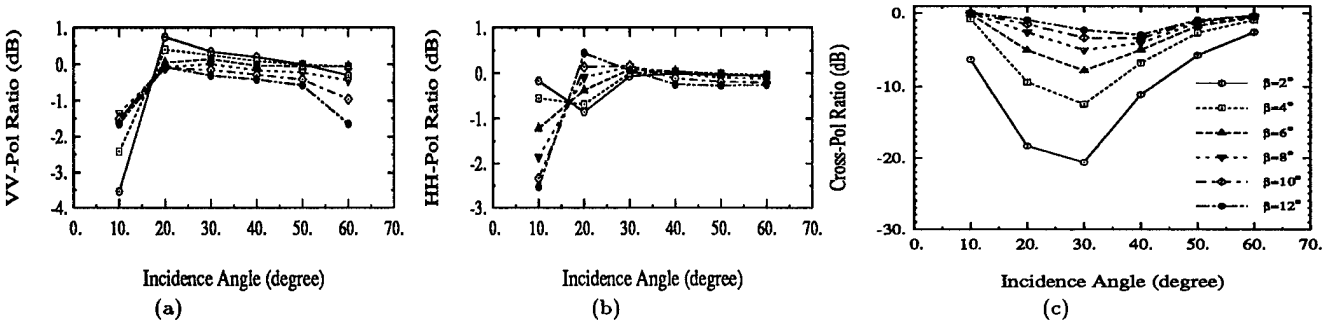

(a) (b) (c)

Figure 3: The ratio of the zero-order to the complete first-order for (a) vv-polarized, (b) hh-polarized, and (c) cross-polarized RCS.

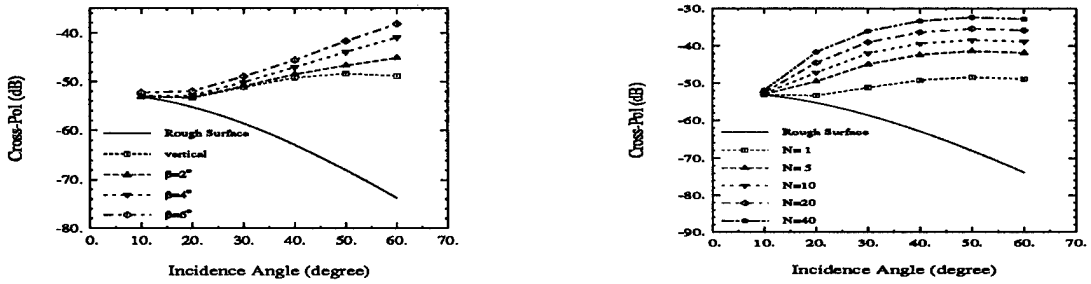

(a) (b)

Figure 4: The effect of the cylinder-rough-surface interaction on the cross-polarized scattering. The direct backscattering from rough surface alone (σ^0_{pq}) is also plotted for comparison.

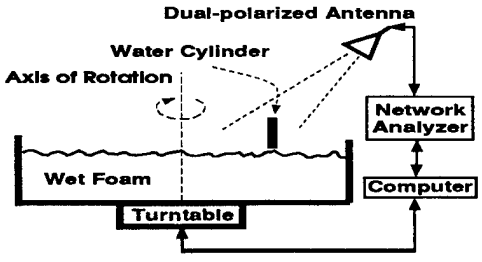

Figure 5: The experimental setup.

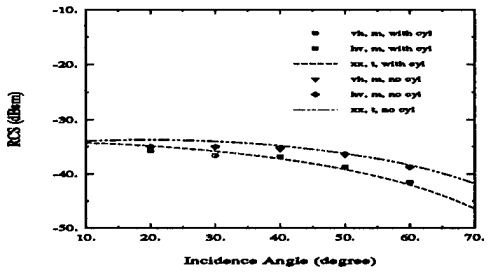

Figure 6: The cross-polarized RCS of the water cylinder above the rough surface at 9.25 GHz. The RCS of the rough surface alone ($\sigma^0_{pq}A$) is also shown for comparison.

Experimental Validation of Surface Scattering and Emission Models

P. Coppo[1], S. Lolli[2], G. Macelloni[3], G. Nesti[4], P. Pampaloni[3], R. Ruisi[3], D. Tarchi[4]

[1] Centro di Telerilevamento a Microonde, Firenze, Italy.
[2] Dipartimento di Fisica Superiore, Università di Firenze, Italy.
[3] IROE-CNR, Via Panciatichi, 64, 50127 Firenze, Italy. Tel. 39-55-4235-205, Fax. 39-55-4235-290, e-mail: microrad@iroe.fi.cnr.it
[4] IRSA-Advanced Techniques, JRC-CEE, Ispra, Varese, Italy.

Abstract -- Backscattering and emissivity measurements carried out on three experimental dielectric models, characterized by random surfaces with different statistics, have been compared with simulations obtained with the Integral Equation Model.

INTRODUCTION

The use of electromagnetic models in the study of microwave scattering and emission from soil can contribute to better understand the interaction between the electromagnetic fields and surfaces, and to develop inversion algorithms for soil moisture content and surface roughness retrieval. On the other hand it is well known that scattering and emission problem from random surfaces presents simple analytical solutions only for a limited number of cases (e.g.: Small Perturbation SP, Physical Optics PO, Geometrical Optics GO, Integral Equation Model IEM)which correspond to some combinations of roughness parameters and observation wavelengths [1, 2]. Validations of these approximate methods have been carried out in the 1D- case by using exact numerical methods (Method of Moment and MonteCarlo) and experimental data collected on conducting surfaces [3].

In this paper we describe the results of the research carried out at the European Microwave Signature Laboratory (EMSL) of the Joint Research Center of Ispra, Italy, for validating IEM by measuring backscattering and emission from experimental models realized with the same surface and dielectric characteristics used in the electromagnetic models.

This work was partially supported by the Italian Space Agency - ASI

THE EXPERIMENT

Three different experimental models, composed by an artificial dielectric with permittivity changing from 5.1 + j 1.4 at 1.5 GHz to 3.8 + j 0.9 at 18 GHz, have been tested. All the models had azimuthal isotropic random surfaces, two of them were characterized by a Gaussian correlation function with a correlation length (l) of 6 cm and a height standard deviation (s) equal to 0.4 cm ("smooth" surface) and 2.5 cm ("rough" surface) respectively. A third model, characterized by an intermediate roughness degree (s = 0.9 cm, and l = 3.0 cm), had been realized with a composite (Gaussian-exponential) correlation function. The sample under test was contained in a cylinder of 2 m in diameter and 0.4 m depth.

The polarimetric scattering measurements were carried out on the sample placed in the center of the EMSL anechoic chamber (radius 10 m) at various incidence and scattering angles between 10 and 50 degrees. A frequency stepped CW mode (step =11.25 MHZ) in the range 1.5 - 18 GHz was used, applying a full polarimetric calibration in the monostatic configuration and a simple "Response & Isolation" correction in the bistatic case. Range gating in time domain was applied to data to isolate the response of the target under investigation from the residual response of the chamber. The Half Power Beamwidth (HPBW) of the frequency dependent antenna pattern was larger than the target size on the whole frequency range. A power correction term, obtained by integrating the actual antenna response over the illuminated area, was applied to compensate for antenna pattern variation[4].

The scattering matrix of the target was measured in the plane of incidence (vertical polarization plane) both in monostatic and bistatic mode for different incidence and scattering angles. Independent samples were obtained by rotating the target in azimuth to obtain uncorrelated data at a given frequency and averaging in the frequency domain over a window larger than one correlation length. The azimuth autocorrelation function ACF showed that a step of 5° is sufficient to obtain

0-7803-3836-7/97/$10.00 © 1997 IEEE

independent samples at low frequency limit. As expected, at higher frequencies, the signal decorrelated faster. The frequency ACF of experimental data had a correlation length l_f (frequency) equal to 300 MHz rather close to the expected theoretical value for the range of target dimensions (220 MHz).

Outdoor emission measurements were worked out on the same targets at 6.8, 10.5 and 36.6 GHz, horizontal and vertical polarizations, at incidence angles between 20 and 60 degrees. The microwave radiometers were portable, battery operated, self-calibrated systems with a horn antenna for each frequency channel and an internal calibration based on two loads at different temperatures. Calibration checks in the range 30 K - 300 K were carried out during the experiments by means of absorbing panels (Eccosorb AN74 and VHP8) of know emissivity and temperature, and recording clear sky emission with the addition of a calibrated noise source coupled to the antenna. Sky emission was periodically measured by means of a reflecting plate placed above the target and subtracted from the total emission. The achieved measurement accuracy (repeatability) was better than ±1.0 K, with an integration time of 1 sec. The beamwidth of the corrugated conical horns was 20° at -3 dB and 56° at -20 dB for both frequencies and both polarizations. The distance between antenna and target was arranged to meet the conditions of far field operation at an observation angle $\theta = 45°$ from a height of 120 cm. The surface tempearure was measured with a thermal infrared sensor placed on the same boresight of microwave radiometers.

EXPERIMENTAL RESULTS AND COMPARISON WITH THE IEM MODEL

The combination of the surface parameters with the frequency range of the sensors allowed one to cover a large part of validity range of electromagnetic models. The experimental data have been compared with simulations obtained with the Integral Equation Model (IEM) implemented for single scattering , the model has a wider validity range than other approximations and reproduces the results of Small Perturbation Method (SPM) at low frequencies and Geometrical Optics (GO) or Physical Optics (PO) models at high frequencies.

The comparison has been carried out considering the behavior of the backscattering coefficient measured at HH and VV polarization and at various incidence angles as a function of frequency for the different surfaces. As an example Fig 1 shows the backscattering coefficient of the 'smooth' surface measured at HH polarization and for incidence angles $\theta = 10°$, 20° and 30°. We see that the model well reproduces experimental data on the whole frequency range for $\theta \leq 20°$, whereas at $\theta = 30°$ model and experimental data are in agreement only up to 8 GHz, at higher frequency experimental data tend to a constant value, whereas the model predicts a decrease of backscattering as the frequency increases. Similar results have been obtained at VV polarization.

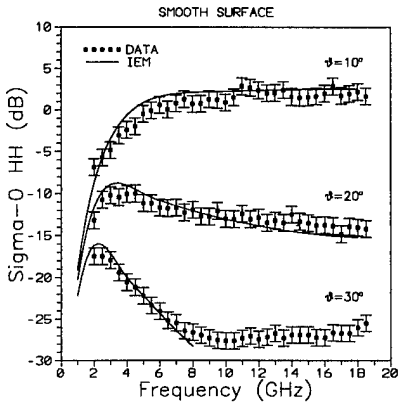

Figure 1 - Smooth surface (s = 0.4 cm, l = 6 cm). Comparison of simulated (IEM continuous line) and measured (points and error bars) backscattering coefficient at HH polarization and at $\theta = 10°, 20°$, and 30°.

An example of the results obtained on the rough surface is shown in Fig. 2 which represents $\sigma°_{HH}$ the as a function of frequency at incidence angle $\theta = 30°$. For this surface the variation with the incidence angle is very small.

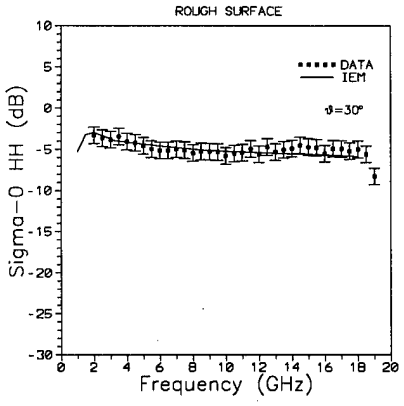

Figure 2 - Rough surface (s = 2.5 cm, l = 6 cm). Comparison of simulated (IEM continuous line) and measured (points and error bars) backscattering coefficient at HH polarization and at $\theta = 30°$.

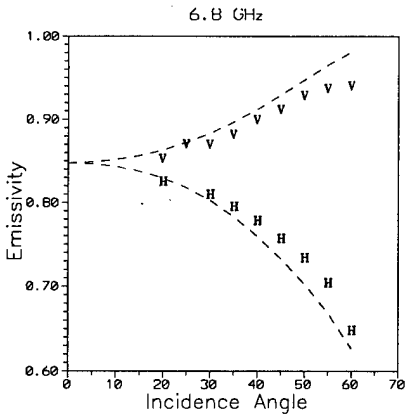

Figure 3 - Smooth surface (s = 0.4 cm, l = 6 cm). Comparison of simulated (IEM - continuous line) and measured (labels) emissivity at 6.8 GHz (V = vertical polarization, H = horizontal polarization).

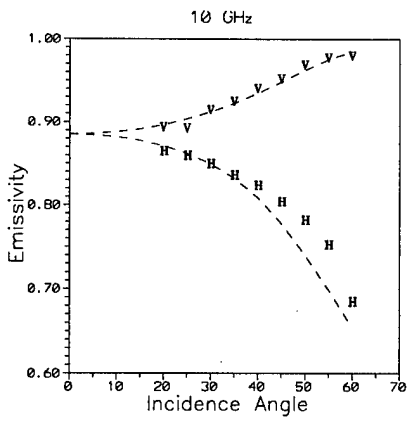

Figure 4 - Smooth surface (s = 0.4 cm, l = 6 cm). Comparison of simulated (IEM - continuous line) and measured (labels) emissivity at 10. 6 GHz (V =vertical polarization, H = horizontal polarization).

Model emissivity has been obtained from the bistatic scattering coefficient on the basis of energy conservation law [1], according to the equation :

$$e(\theta,\phi) = 1 - \frac{1}{4\pi\cos\theta}\int_0^{2\pi}\int_0^{\pi/2}\sigma^{o}(\theta,\ \phi;\ \theta_s,\ \phi_s)\ \sin\theta_s\ d\theta_s\ d\phi_s$$

The approximate value of emissivity has been obtained by the ratio between microwave and infrared brightness temperatures. A comparison of measured and predicted emissivity values at 6.8 GHz and 10.6 GHz for the 'smooth' surface is represented in Figs 3 an 4. We see that the model slightly underestimates the horizontal component of emissivity at both frequencies and overestimates vertical component at 6.8 GHz.

CONCLUSIONS

The comparison between the measurements on the dielectric target and the model calculations has confirmed that the Integral Equation Model has a wider range of applicability with respect to other classical approximations (Small Perturbation, Geometrical and Physical Optics). The simulated backscattering coefficient is in agreement with the measured one within the limits of experimental errors except for frequencies higher than 8 GHZ when the incidence angle is higher than 30 degrees. In the latter case, as the frequency increases, the measured backscattering tends to a constant value, whereas model prediction indicates a decrease.

Emission measurements and model simulations confirm the expected increase of emissivity (and the decrease of the polarization difference) as frequency and roughness increase.

REFERENCES

[1] L. Tsang, J. Kong and R. Shin, Theory of Microwave Remote Sensing, J. Wiley & Sons, 1985.

[2] A. K.Fung, Microwave scattering and emission models and their applications, Artech House Inc., Boston 1994

[3] A. K.Fung , A.J. Blanchard, and M.F. Chen, "Polarization properties in random surface scattering, Progress in Electromagnetic Research, Polarimetric Remote Sensing", J. Kong Editor, Elsevier , New York, 1990

[4] G. Nesti, P. Pampaloni, P. Coppo, M. Hallikainen, M. Mancini, P. Troch and M. von Shonermark, "Experimental research at EMSL on scattering properties of non vegetated terrains," Proc. International Geoscience and Remote Sensing Symposium, IGARSS'95, Firenze (Italy), T. Stein Editor, pp. 2020-2022, 1995

Discontinuity Adaptive MRF Model For Remote Sensing Image Analysis

P.C. Smits and S.G. Dellepiane
University of Genoa - Department of Biophysical and Electronic Engineering
Via all'Opera Pia 11A, I-16145 Genova - Italy
smits@dibe.unige.it, silvana@dibe.unige.it

Abstract - In this paper, an approach is presented for the analysis of synthetic aperture radar (SAR) images that preserves better fine structures and borders in the image than classical methods. The method uses the discontinuity adaptive MRF label model combined with an observation model based on a gamma distribution. This resulted in a new algorithm that is more suited to the segmentation of SAR images if one is interested in preserving details. Examples are given using real SAR data.

INTRODUCTION

Remote Sensing exists by the virtue of the physical and/or economic constraints that prevent human beings from exploring certain regions in person. Although many sophisticated instruments have been developed in order to relief the human observer from this task, the hunger for information seems more than ever unsatisfyable, and the more types of information can be extracted from remote sensing images, the more economical attractive these data become.

Segmentation and classification of remote sensing images can be formulated as ill-posed problems. Although the quality of many modern (remote sensing) imaging sensors is such that these problems are not too ill-posed, this situation changes in cases where one wants to extract types of information for which the sensor has not been build in the first place.

In order to tackle these ill-posed problems in the cases where the sensor is not optimized for the task that the end-user wants it to use for, a-priori constraints or other sources of information are important for the regularization of the problem. In this article, we focus on the problem of SAR intensity image processing for land-cover mapping; the regions may have geometrically difficult shapes, such as fine structures and critical borders between classes, that are obscured by the typical speckle noise.

Markov Random Field (MRF) models can be powerful instruments for solving ill-posed problems because of their ability to define the interaction between the pixels in the image. They are often formulated in terms of energy, and allow specific a-priori knowledge to be incorporated in the model. For an up-to-date and comprehensive discourse on MRF in computer vision applications the reader is referred to [1].

This paper builds on two lines of research reported in the literature. One concerns aspects related to the statistics of SAR intensity data, and the other relates to recent developments in the use of more precise MRF models. The novelty of this paper is the combination, on the one hand, of a discontinuity adaptive (DA-) MRF model that accounts for small structures and discontinuities as proposed in [2], and on the other hand of an image model based on the Gamma distribution [3].

In the approach proposed in this paper, an MRF approach is utilized in which regularization constraints like smoothness are encoded into an energy following a probabilistic route. Basically, the approach consists of two terms. One term is the observation model, which defines the relation between the observed intensity data and the underlying reality expressed in image labels or classes. The second term is a regularizer, and penalizes the irregularities according to the a-priori smoothness constraint encoded in it.

OBSERVATION MODEL

In this section, we are concerned with the observation model, i.e., the relation between the intensity data I and our image labels L.

In the literature agreement exists on the gamma distribution being one of the most suitable statistical models for SAR data. The distribution for multilook intensities can be modeled as ([3]):

$$p(I_s / L_s) = \frac{N^N I_s^{N-1}}{\langle I \rangle_l^N \Gamma(N)} \exp\left(-\frac{N I_s}{\langle I \rangle_l}\right), \quad (1)$$

where s is the index for the location, I is the intensity of the SAR data, L the label, N the number of independent one-look samples used to form each multilook intensity sample I_s and $\Gamma(N) = (N-1)!$. Assuming that the multilook intensity samples are mathematically independent, as do (Rignot and Chellappa, 1993), the joint distribution of $\boldsymbol{I}_s = \{I_t\}_{t \in N_s}$ is approximated by the product of the marginal distributions as

$$p(\boldsymbol{I}_s / L_s) \propto \exp\left[-MU_1(\boldsymbol{I}_s / L_s)\right],$$

This work was supported by the European Community program Training and Mobility for Researchers (Marie Curie Fellowship) under contract ERBF MBICT 95257.

0-7803-3836-7/97/$10.00 © 1997 IEEE

where M is the number of pixel elements contained in the neighborhood N_s. Limiting the model to the information present at the location of the pixel, we obtain (2):

$$U_1(I_s / L_s) = \frac{NI_s}{\langle I \rangle_{L_s}} - (N-1)\log(I_s) + N\log\left(\langle I \rangle_{L_s}\right).$$

DISCONTINUITY ADAPTIVE MRF MODEL

In this article, the strength and shape of the smoothness constraint is modified according to the local image content. The DA-MRF model for image analysis [2] has proven to be a valuable alternative to the classical MRF model. Without going too much into detail, we follow [2] in the definition of the DA-MRF model for the Gaussian situation first, and than optimize the model for use in SAR image analysis.

Li's [2] review on finding solutions to the problem of over-smoothing, focusing solely on the smoothness priors, resulted in the so-called *discontinuity adaptive* smoothness model. Using Gaussian observation statistics, Li comes to the following updating scheme:

$$f_i^{(t+1)} \leftarrow f_i^{(t)} - 2\mu\left\{\chi_i\left|f_i^{(t)} - d_i\right| - \lambda\sum_{r\in N_i}\left(f_r^{(t)} - f_i^{(t)}\right)h\left(f_r^{(t)} - f_i^{(t)}\right)\right\} \quad (3)$$

where $f_i^{(t)}$ is the estimated true image label at location i at time t, d_i the observation, and $h(\cdot)$ the so-called adaptive interaction function (AIF) which defines the interaction between the images sites i and its neighbours $r \in N_i$. μ is the update strength, and is chosen constant during the optimization process. At each iteration, the label of each pixel is updated based on the contextual information in the label image at the previous itaration. The updating process, which is a deterministic relaxation; possible stop criteria are a fixed number of iterations, or a threshold for the number of changes from one iteration to another.

DA-MRF WITH GAMMA MODEL

Derivation of the gamma-adapted updating scheme: Since the approach of Rignot and Chellappa deals with classification rather than with segmentation, the values of L_s in (2) are class indexes and have a semantic value rather than a quantitative one. In order to "translate" the quantitative values of $f(x)$ to qualitative ones, it is proposed to substitute the class indexes with the mean class-intensity values:

$$\langle d \rangle_{f_i} = f_i. \quad (4)$$

Following the mathematical derivation of (2) in [2], and substituting the Gaussian data distribution with the Gamma distribution

$$U_1(d_{i,j} / f_{i,j}) = \frac{Nd_{i,j}}{f_{i,j}} - (N-1)\log(d_{i,j}) + N\log(f_{i,j})$$

we can use use the deterministic gradient based minimization method to obtain the following updating scheme:

$$f_s^{(t+1)} \leftarrow f_s^{(t)} - \mu\left\{\left[\frac{N\left(f_s^{(t)} - d_s\right)}{\left(f_s^{(t)}\right)^2}\right] - \lambda\sum_{r\in N_s}\left(f_r^{(t)} - f_s^{(t)}\right)h\left(f_r^{(t)} - f_s^{(t)}\right)\right\} \quad (5)$$

Choice of the Adaptive Interaction Function: The regularizer takes effect when $\lambda > 0$. Its strength depends on the qualitative and quantitative shape of the AIF, basically determined by h_γ. For the experiments that follow, the AIF was chosen to be $h_\gamma = \left(1 + |\eta|/\gamma\right)^{-1}$ in both the x and y directions. The main reason is that it allows bounded but non-zero smoothing at discontinuities, useful properties when analyzing speckle images. Additional advantages are that the resulting energy function is convex and that the algorithm becomes computational efficient.

EXPERIMENTAL RESULTS

Parameter settings: Table I should give the reader an idea about the influence of the various parameters. The suggested value for a 4 look SAR intensity image. The value of γ depends on the level of detail required. The lower this value, the higher the level of detail present in the result.

Data description: In order to assess the usefulness of the proposed method, experiments have been done on portions of a 4-Look SAR intensity image (HH polarization) of a Flevoland (NL) scene, acquired during the Maestro I campaign in 1989. The original test image is shown in Fig. 1.

Comments on results: Some experimental results are reported in Fig. 2. Fig. 2a shows that, applying a low λ value, the final result tends to convert to the original data. With an increasing λ, clustering of regions gets stronger (Fig. 2b).

Table I. Parameters and their suggested values.

	Function	Filtering	Segmentation
λ	Relation between observation and regularization model	0.001	0.01
γ	Choice of regularization strength.	0.1-3	0.1-3
μ	Update strength (optimization procedure)	50	50

DISCUSSION AND CONCLUSIONS

In this paper, an approach has been presented for the analysis of synthetic aperture radar (SAR) images that uses the discontinuity adaptive MRF label model in combination with a Gamma-observation model. This resulted in a new algorithm that is more suited to the processing of SAR images if one is interested in preserving details. The clustering effect of regions with homogeneous back scatter signals is principally determined by mainly two parameters whose function is easy and intuitively to understand.

The advantages of the method is that its implementation is straightforward and it's execution fast.

Results on various real-world data sets, of which one has been presented in this paper, have shown that the method proposed is a useful tool for the analysis and interpretation of SAR images. However, it is stressed that at the end of the day it remains the end-user to decide what level of detail is required.

Since the spectral content of the original image is preserved by the choice of the image class labels, the approach could be of benefit in image compression.

REFERENCES

[1] Li, S.Z. (1995b), Markov Random Field modeling in computer vision, Springer Verlag, New York.

[2] Li, S.Z. (1995a), Discontinuity-adaptive MRF prior and robust statistics: a comparative study, IEEE Trans. on Pattern Analysis and Machine Intelligence 17(6), 576-586.

[3] Rignot, E., Chellappa, R. (1993). Maximum a posteriori classification of multifrequency, multilook, synthetic aperture radar intensity data, J. Opt. Soc. Am. A, Vol. 10, No. 4, pp. 573-582.

[4] Goodman J.W. (1975), Statistical properties of laser speckle patters,î in Laser Speckle and related phenomena, J.C. Dainty, ed., Vol. 9 of Topics in Applied Physics (Springer Verlag, New York, 1975), pp. 9-75.

[5] Smits P.C. and S. Dellepiane (1996), "Information fusion in a Markov Random Field based image segmentation approach using adaptive neighbourhoods," 13th Int. Conf. on Pattern Recognition, Vienna, August 1996, pp. 570-575.

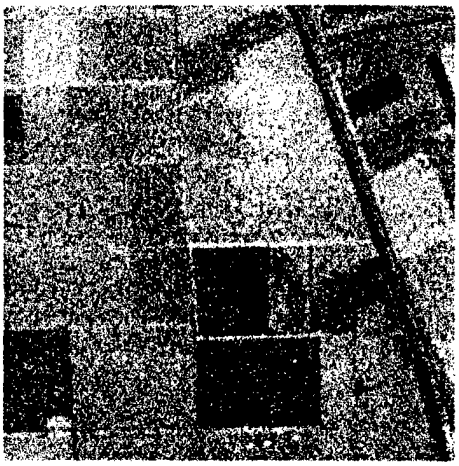

Fig. 1. Original image. 256x256 portion of a Flevoland 4 look SAR intensity image (HH polarization).

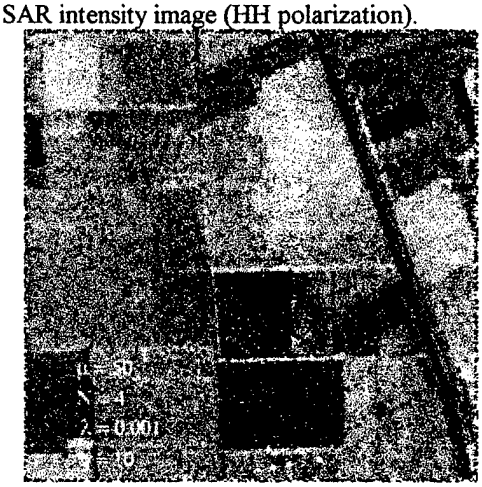

a.

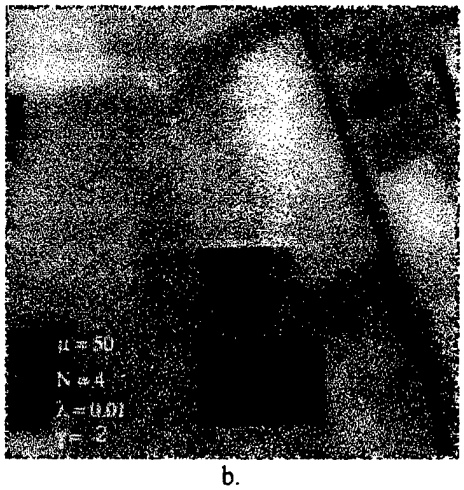

b.

Fig. 2. Results. a) Low λ: little filtering. b) As λ becomes larger, the clustering effect is stronger. All results in the image were obtained after 100 iterations.

Application of Adaptive Filters for Multisensoral Image Fusion

Klaus Steinnocher

Austrian Research Centre Seibersdorf - Department for Environmental Planning
A-2444 Seibersdorf, Austria
Tel: +43-2254-780-3876 / Fax: +43-2254-780-3888 / Email: steinnocher@arcs.ac.at

Abstract -- Today's remote sensors offer a wide variety of image data with different characteristics in terms of geometric, radiometric and spectral resolution. Although the information content of these images might be partially overlapping the complementary aspects represent a valuable improvement for information extraction. To exploit the entire content of multisensoral image data appropriate techniques for image fusion are indispensable.

The objective of this paper is to introduce an image fusion method based on adaptive filters. The method is applied to panchromatic and multispectral image data acquired by the Indian Remote Sensing Satellite IRS-1C. In order to evaluate the quality of the fusion process the merged images are compared to the results of the Intensity-Hue-Saturation and the Principal-Component-Substitution merging procedures.

INTRODUCTION

Image fusion in a general sense can be defined as „the combination of two or more different images to form a new image by using a certain algorithm" [1]. Multisensoral image fusion combines the information acquired by different sensor systems, to benefit from the complementary information inherent in the single image data. A comprehensive review on this topic is given in [2]. For the remainder of this paper we will concentrate on the fusion of multisensoral optical image data with different spatial and spectral resolutions. High resolution data of this kind are typically acquired from single platforms carrying two optical sensors providing panchromatic images with a high spatial resolution and three multispectral bands with a lower spatial resolution. Current examples of these platforms are SPOT, IRS-1C and MOMS-02. In the near future a number of sensor systems with similar characteristics will be launched [3].

Common methods for merging multispectral bands with the corresponding panchromatic image are component substitution techniques, such as Intensity-Hue-Saturation (IHS) or Principal-Component-Substituition (PCS) procedures [4]. These techniques are valuable for producing improved image maps for visual interpretation tasks, as they strongly enhance textural features. On the other hand they can cause significant distortions of the spectral properties of the merged images. In order to better preserve the multispectral information, new methods have been developed recently, such as the generalized Component Substitution Technique [5], the Radiometric Method [6] and the Multiresolution Multisensor Technique [7].

ADAPTIVE IMAGE FUSION

Fusion of multiresolution optical image data aims at the derivation of multispectral images providing the high spatial resolution of the panchromatic image. The perfect result of such a process would be an image that is identical to the image the multispectral sensor would have observed, if it had the high resolution of the panchromatic sensor. Such an image would allow to differentiate at least all objects that are detectable in the panchromatic image. An approximation of the desired result can be obtained by extracting objects from the panchromatic image and "fill" them with the corresponding average multispectral information. Similar techniques have been successfully used for integrating spectral image data with vector layers in a GIS [8]. The drawback of this method for multi-image fusion lies in the requirement of a consistent set of object borders. Although the requirement can be fullfilled through segmentation of the panchromatic image it would need computational intensive and time consuming preprocessing.

As an alternative we introduce the Adaptive Image Fusion (AIF) method that uses local object edges instead of image segments. We assume that an image object Z is represented by a set of neighbouring pixels z_i, whose values are Gaussian distributed: $z \sim N(\mu_Z,\sigma_Z)$. This assumption of normality is generally reasonable for common spectral response distributions [9]. We furthermore assume that the standard deviation σ_z within an object Z is linearly related to the standard deviation of the image noise σ by the mean μ_z of the observed values z_i within the object:

$$\sigma_z = \mu_z \sigma \qquad (1)$$

In the local neighbourhood of an object edge we will therefore find two distributions, each representing one of the neighbouring objects. To seperate these objects, i.e., to

This work was funded by the Austrian Mininstry for Science and Traffic, Vienna (*GZ 79.061/2-II/5/95*).

0-7803-3836-7/97/$10.00 © 1997 IEEE

assign each pixel to one of these objects, adaptive filter techniques can be used. These filters have been successfully applied to image data for noise reduction, in particular for suppression of speckle in SAR imagery. We have chosen the modified sigma filter as it matches the assumptions given above.

The *sigma filter* averages only those pixels in a local window which lie in a two sigma range of the central pixel value [10]. All other pixels are assumed to belong to another distribution, i.e., they represent a neighbouring object. As this filter is based on the assumption that the central pixel is in fact the mean of its Gaussian distribution, it might not include all relevant pixels in the averaging process. A more general approach, the *modified sigma filter* [11], averages all pixels, which could belong to the same distribution as the central pixel without knowing the actual mean of this distribution. Thus, areas with a low standard deviation, i.e. objects, will be smoothed, while areas of a high standard deviation, i.e. areas containing object edges, are split in seperate objects.

For the image fusion approach multispectral bands are included in the filter process. The selection of pixels which belong to the same distribution is performed on the panchromatic image, whereas the averaging is done also in the multispectral band. This leads to a better delineation of objects in the multispectral images without significantly changing their spectral information.

APPLICATION

The AIF algorithm was applied to a multisensoral image acquired by the Indian remote sensing satellite IRS-1C. This system provides panchromatic images with a spatial resolution of 5.6m (PAN), and three multispectral bands (green, red and near infrared) with a resolution of 23.5m (LISS-2/3/4). The commercially available scenes are radiometrically preprocessed, panorama corrected and resampled to a pixel size of 5m and 25m, respectively. The acquired scene (path 30, row 35, quadrant A) was taken on August 9, 1996 and covers an area of approximately 70x70 km^2 located in Upper Austria (centered on 13°35'E / 47°58'N). The images were geocoded to the Austrian geodetic reference system. The multispectral bands were resampled to 5m pixel size to match the resolution of the panchromatic image.

Application of AIF requires knowledge of the standard deviation of the image noise σ. As suggested in [11] it can be calculated from the image itself by inversion of (1). The local mean and standard deviation values are derived from a moving 5x5 window. From the resulting σ-values histogram the mode was taken as an estimate for the overall value of σ. Applying this value the adaptive fusion was performed seperately for each multispectral band applying a 5x5 window, thus leading to a synthetic multispectral image stack.

COMPARISON OF METHODS

To assess the efficiency of the AIF method a comparison with standard component substitution techniques was performed. For the standard merging the IHS and the PCS merging procedures from the ERDAS Imagine software package [12] were used. In both cases a histogram match was performed before substitution to adjust the panchromatic image to the intensity image and the first principal component, respectively.

The assessment focusses on how far the radiometry of the multispectral images is distorted by the merging procedure. It is based on the idea that a synthetic image once degraded to its original resolution should be as identical as possible to the original image. This property is estimated by comparing the mean values and standard deviations of and the correlation coefficients between the degraded and the original images [13].

To produce the degraded images the merging results were averaged applying a 5x5 filter kernel and resampled to 25m pixel size. Table I presents the results of the comparison between the degraded images and the original data. The first column shows the global mean (μ) and standard deviation (σ) of the original multispectral bands. The columns entitled 'abs.' give the respective values of the merged products. The relative differences, entitled 'Δ', are derived from the absolute differences divided by the mean of the original data.

The results of AIF show no significant differences in the mean values, but the standard deviation is slightly reduced. This is due to the averaging performed during the merging process. IHS merged images show a higher deviation in the mean values and an increase of the standard deviation resulting from the inclusion of textural information from the panchromatic image. PCS merged images are significantly different from the original image data. Their pixel values are by no means comparable to the input data.

Comparison of the correlation coefficients leads to similar results (see Table II). It can be clearly seen that the AIF images correlate highly with the original data, whereas the correlation between IHS and PCS merged images and the original images is significantly lower. In particular, the near infrared band has no correlation with the original image.

Table I: Statistics of differences between original and degraded image bands

image-bands		original image	AIF		IHS		PCS	
			abs.	Δ (%)	abs.	Δ (%)	abs.	Δ (%)
LISS-2	μ	89.4	89.5	0.17	90.2	0.88	73.0	-18.34
green	σ	22.3	21.1	-5.38	25.9	16.14	24.6	10.31
LISS-3	μ	31.9	32.0	0.34	32.3	1.13	20.6	-35.42
red	σ	13.5	12.8	-5.18	14.7	8.89	14.0	3.7
LISS-4	μ	100.9	101.1	0.14	98.9	-2.0	143.6	42.3
nir	σ	27.5	25.0	-9.09	19.9	-27.6	6.8	-75.3

CONCLUSION

A new method for the fusion of high resolution panchromatic images and lower resolution multispectral images was introduced. The AIF method sharpens object edges present both in the panchromatic and the multispectral images. Edges only appearing in the multispectral bands are slightly smoothed, whereas edges only appearing in the panchromatic image have no influence on the merged product. Comparison with the IHS and PCS merging procedures demonstrates the benefits of the new method. Whereas local texture is stronger enhanced applying the former methods, the latter significantly better conserves the multispectral information. This is due to the fact, that from the panchromatic image only object edges are used in the merging process rather than including the actual pixel values as performed in the standard methods. This leads to the conclusion that the AIF method improves subsequent numerical processing of the merged images. It is particularly useful as a preprocessing method for classification procedures based on multivariate normal distributions such as maximum likelihood classification. Current research focusses on the application of AIF for merging optical and SAR data and on the evaluation of the benefit of AIF for multispectral classification.

Table II: Correlation coefficients

bands	AIF	IHS	PCS
LISS-2	0.97	0.89	0.92
LISS-3	0.98	0.95	0.91
LISS-4	0.96	0.82	0.30

REFERENCES

[1] J. L. Van Genderen and C. Pohl, "Image fusion: issues, techniques and applications," *Proc. EARSeL Workshop Intelligent Image Fusion*, Strasbourg, France, 1994.

[2] C. Pohl, "Geometric aspects of multisensor image fusion for topographic map updating in the humid tropics," *ITC Publication*, Number 39, Enschede, Netherlands, 1996.

[3] G.R. Carlson and B. Patel, "A new area dawns for geospatial imagery," *GIS World*, vol. 10, no. 3, pp. 36-40, 1997.

[4] P.S. Chavez, S.C. Sides and J.A. Anderson, „Comparison of three different methods to merge multiresolution and multispectral data: Landsat TM and SPOT panchromatic," *Photogrammetric Eng. Remote Sensing*, vol. 57, no.3, pp. 295-303, 1991.

[5] V.K. Shettigara, "A generalized component substitution technique for spatial enhancement of multispectral images using a higher resolution data set", *Photogrammetric Eng. Remote Sensing*, vol. 58, no.5, pp. 561-567, 1992.

[6] A.H.J.M. Pellemans, R.W.L. Jordans and R. Allewijn, "Merging multispectral and panchromatic SPOT images with respect to the radiometric properties of the sensor," *Photogrammetric Eng. Remote Sensing*, vol. 59, no.1, pp. 81-87, 1993.

[7] B. Zhukov, M. Berger, F. Lanzl and H. Kaufmann, "A new technique for merging multispectral and panchromatic images revealing sub-pixel spectral variation", *Proc. IGARSS'95*, Florence, Italy, pp. 2154-2156, 1995.

[8] L.L. Janssen, M.N. Jaarsma and E.T. van der Linden, "Integrating topographic data with remote sensing for land-cover classification," *Photogrammetric Eng. Remote Sensing*, vol. 56, no.11, pp. 1503-1506, 1990.

[9] T.M. Lillesand and R.W. Kiefer, "Remote sensing and image interpretation," New York: Wiley & Sons, 1994.

[10] J.S. Lee, „A simple speckle smoothing algorithm for synthetic aperture radar images," IEEE Trans. Syst., Man, Cybern., vol. 13, pp. 85-89, 1983.

[11] D. M. Smith, "Speckle reduction and segmentation of synthetic aperture radar images," Int. J. Remote Sensing, vol. 17, no. 11, pp. 2043-2057, 1996.

[12] Erdas, "Erdas Field Guide," ERDAS Inc., Atlanta, GA, USA, 1994.

[13] T. Ranchin, L. Wald, M. Mangolini and C. Penicand, "On the assessment of merging processes for the improvement of the spatial resolution of multispectral SPOT XS images," *Proc. Int. Conf. Fusion of Earth Data*, Cannes, France, pp. 59-67, February 1996.

CLASSIFICATION AND FEATURE EXTRACTION OF HYPERDIMENSIONAL DATA USING LOOC COVARIANCE ESTIMATION[1]

Jon Atli Benediktsson, Jon Ingi Ingimundarson, and Johannes R. Sveinsson

Engineering Research Institute
University of Iceland
Hjardarhaga 2-6, 107 Reykjavik, Iceland
E-mail: benedikt@verk.hi.is

ABSTRACT

New methods for processing of multisource and hyperdimensional data are discussed both in terms of feature extraction and classification. An extension to decision boundary feature extraction (DBFE) is proposed. The extension is based on a recently developed covariance estimator, the leave one out covariance. The extended decision boundary method is tested on a multisource remote sensing and geographic data set.

1. INTRODUCTION

A problem with using conventional multivariate statistical approaches for classification of hyperdimensional and multisource data is that these methods rely on having nonsingular (invertible) class-specific covariance matrices for all classes. When n features are used, the training samples for each class must include at least $n+1$ different samples so that the sample covariance matrices will be nonsingular. Therefore, the sample covariance matrices may be singular in hyperdimensional cases involving limited training samples.

Related to the above problem, feature extraction is very important for multisource and hyperdimensional data. Here, the recently proposed DBFE method is investigated [1]. Lee and Landgrebe have proposed a parametric version of the DBFE which is based on using sample covariance matrices for the individual classes to determine the decision boundary. However, for multisource and hyperdimensional data the estimates of the sample covariance matrices can become singular as described above. Therefore, it is important to find other ways of estimating the covariance matrices to determine the decision boundary for the DBFE method. Here we propose a new version of the DBFE which is based on the leave one out covariance (LOOC) method introduced by Hoffbeck and Landgrebe [3]. The LOOC method does not need as many samples for covariance estimation as the sample covariance approach but always gives nonsingular covariance matrices.

The paper is organized as follows. First the DBFE approach is briefly reviewed, then the LOOC method is reviewed in relation to DBFE. Experimental results are given for feature extraction and classification of multisource data from a forest area in Canada. Finally, conclusions are drawn.

2. DECISION BOUNDARY FEATURE EXTRACTION

In [1],it was shown that discriminantly informative features and discriminantly redundant features are related to and can be extracted from the decision boundary. It was also shown that discriminantly informative feature vectors have a component which is normal to the decision boundary at at least one point on the decision boundary. Further, discriminantly redundant feature vectors are orthogonal to a vector normal to the decision boundary at every point on the decision boundary. By considering the *effective decision boundary* only, the number of features can be significantly reduced while achieving almost the same classification accuracy as in original feature space [1].

In [1], the effective decision boundary is estimated in original feature space using an estimate of the sample covariance matrices for the individual classes. The feature extraction is based on these covariance estimates, and if not enough samples are available, the covariance matrices can become inaccurate. Inaccurate sample covariance matrices can lead to errors in determining the effective decision boundary, and consequently the feature extraction based on DBFE is effected.

[1]This research is supported in part by the Icelandic Research Council and the Research Fund of the University of Iceland.

0-7803-3836-7/97/$10.00 © 1997 IEEE

Table 1: Training and Test Samples for Information Classes in the Experiment on the Anderson River Data.

Class #	Information Class	Training Size	Test Size
1	Douglas Fir (31-40m)	971	1250
2	Douglas Fir (21-30m)	551	817
3	Douglas Fir + Other Species (31-40m)	548	701
4	Douglas Fir + Lodgepole Pine (21-30m)	542	705
5	Hemlock + Cedar (31-40m)	317	405
6	Forest Clearings	1260	1625
	Total	4189	5503

3. STATISTICS ESTIMATION IN MULTISPECTRAL ANALYSIS

Usually, there are not enough training samples available in remote sensing. Therefore, significant inaccuracy can result in the estimation of the mean vectors, M_i, and covariance matrices, Σ_i, for the individual classes. This problem becomes more severe as the number of features increases.

As it turns out, with limited training samples, discriminant functions which do not contain many parameters may provide improved classification results even though they result in simpler decision boundaries. Hoffbeck and Landgrebe [3] proposed a covariance estimator which provides this advantage. This covariance estimator examines mixtures of the sample covariance, diagonal sample covariance, common covariance, and diagonal common covariance [2]:

$$C_i(\alpha_i) = \begin{cases} (1-\alpha_i)diag(\Sigma_{i|k}) + \alpha_i\Sigma_{i|k} & 0 \le \alpha_i \le 1 \\ (2-\alpha_i)\Sigma_{i|k} + (\alpha_i - 1)S_{i|k} & 1 \le \alpha_i \le 2 \\ (3-\alpha_i)S_{i|k} + (\alpha_i - 2)diag(S_{i|k}) & 2 \le \alpha_i \le 3 \end{cases}$$

where *diag* is the diagonal operator, the subscript $i|k$ denotes that the quantity is computed without sample k, and S is the common covariance matrix, computed by averaging the class covariances across all classes [2]. The variable α_i is a mixing parameter that determines which mixture is selected.

The value of the mixing parameter α_i is selected so that the best fit to the training samples is achieved, in the sense that the average likelihood of left-out samples is maximized. The technique is to remove one sample, estimate the mean and covariance from the remaining samples, then compute the likelihood of the sample which was left out, given the mean and covariance estimates. Each sample is removed in turn, and the average log likelihood is computed. Several mixtures are examined by changing the value of α_i, and the value that maximizes the average log likelihood is selected. This optimization criterion is referred to as the leave one out covariance (LOOC) method.

Here, the LOOC method is incorporated with the parametric DBFE method, i.e., the class specific covariance matrices in the DBFE method that are used to determine the decision boundary in full feature space, are estimated using LOOC estimation. Using this approach, the DBFE method will become more robust.

Table 2: Eigenvalues for LOOC-DBFE Analysis.

# of Features	Eigenvalue	Proportion	Accumulation
1	4.136	33.66	33.66
2	2.869	23.35	57.01
3	1.979	16.11	73.12
4	1.672	13.61	86.72
5	0.800	6.51	93.23
6	0.265	2.16	95.39
7	0.167	1.36	96.75
8	0.100	0.81	97.56
9	0.095	0.76	98.32
10	0.054	0.44	98.76
11	0.045	0.37	99.13
12	0.029	0.23	99.37
13	0.019	0.16	99.53
14	0.014	0.12	99.65
15	0.013	0.11	99.76
16	0.008	0.07	99.83
17	0.007	0.06	99.89
18	0.006	0.05	99.94
19	0.003	0.03	99.97
20	0.002	0.01	99.98
21	0.001	0.01	99.99
22	0.001	0.01	100.00

4. EXPERIMENTAL RESULTS

The data used in the experiment, the Anderson River data set, are a multisource remote sensing and geographic data set made available by the Canada Centre for Remote Sensing (CCRS) [3]. Six data sources were used: Airborne Multispectral Scanner (11 spectral data channels), Steep Mode SAR (4 data channels), Shallow Mode SAR (4 data channels), Elevation data (1 data channel), Slope data (1 data channel), Aspect data (1 data channel). The ABMSS and SAR data were detected during the week of July 25 to 31, 1978. Each channel comprises an image of 256 lines and 256 columns. All of the images are spatially co-registered with pixel resolution of 12.5 m.

There are 19 information classes in the ground reference map provided by CCRS. In the experiments, only the six largest ones were used, as listed in Table 1. Here, training samples were selected uniformly, giving 10% of the total sample size. Test samples were then selected randomly from the rest of the labeled data.

The proposed LOOC-DBFE analysis was performed on the data. The eigenvalues of the LOOC decision boundary feature matrix are shown in Table 2. From the table it can be seen that approximately 99% of the variance

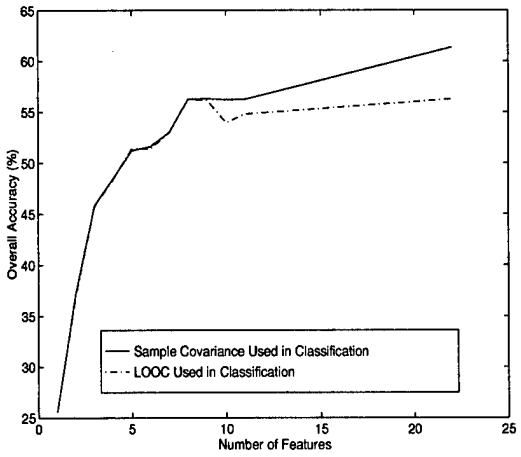

Figure 1: Training Accuracies as a Function of the Number of Features in the LOOC-DBFE Analysis.

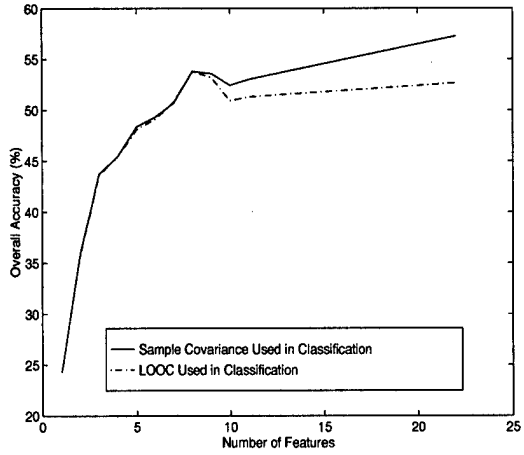

Figure 2: Test Accuracies as a Function of the Number of Features in the LOOC-DBFE Analysis.

in the data was preserved in 11 features, and about 96% in 6 features. The maximum likelihood algorithm (ML) for Gaussian data [4] was trained on the LOOC-DBFE transformed data with a different number of input features. For each feature set, both the conventional sample covariance matrices and the LOOC estimated covariance matrices were used in classification. The classification results for the LOOC-DBFE are shown in Figures 1 (training) and 2 (test). From the figures it can be seen that there was about 4% decrease in overall training and test accuracies when 11 input features were used instead of 22. Then, the classification accuracies stayed approximately the same when the data were reduced to 8 features. However, the performance decreased again about 4% in terms of training and test accuracies when 6 features were used instead of 11. From Figures 1 and 2 it is clear that similar results were achieved for using the LOOC method in classification as the commonly used sample covariance method. The main reason for this could be that in the experiments reported here there was not truly a paucity of training samples.

5. CONCLUSION

An extension to decision boundary feature extraction (DBFE) has been proposed. This extension is based on using leave one out covariance (LOOC) estimation. The proposed approach will make the DBFE method more robust and is especially useful in hyperdimensional spaces where limited training data are available. Here this approach was tested on a multisource remote sensing and geographic data set. The approach showed promise but should be more appropriate on hyperdimensional data which can be assumed to be truly Gaussian.

ACKNOWLEDGEMENTS

The authors are very grateful to Dr. Joseph Hoffbeck of AT&T, Prof. Chulhee Lee of Yonsei University, Prof. David A. Landgrebe and Mr. Larry Biehl of Purdue University for their invaluable assistance in preparing this paper. The Anderson River SAR/MSS data set was acquired, preprocessed, and loaned by the Canada Centre for Remote Sensing, Department of Energy Mines, and Resources, of the Government of Canada.

6. REFERENCES

[1] C. Lee and D.A. Landgrebe, "Feature Extraction Based on Decision Boundaries," *IEEE Transactions on Pattern Analysis and Machine Intelligence*, vol. 15, no. 4, pp. 388-400, April 1993.

[2] J. Hoffbeck and D.A. Landgrebe, "Covariance Matrix Estimation and Classification with Limited Training Data," *IEEE Transactions on Pattern Analysis and Machine Intelligence*, vol. 18, no. 7, pp. 763-767, July 1996.

[3] D.G. Goodenough, M. Goldberg, G. Plunkett, and J. Zelek, "The CCRS SAR/MSS Anderson River Data Set," *IEEE Transactions on Geoscience and Remote Sensing*, vol. GE-25, no. 3, pp. 360-367, 1987.

[4] J.A. Richards, *Remote Sensing Digital Image Analysis*, 2nd Edition, Springer Verlag, New York, N.Y., 1993.

Comparison of Land Cover Indices of AVHRR Data

Takako Sakurai-Amano, Joji Iisaka* and Mikio Takagi
Institute of Industrial Science, University of Tokyo
7-22-1 Roppongi, Minato-ku, Tokyo, Japan 106
Tel:+81-3-3402-6231 ex.2643/Fax:+81-3-3423-2834/takako@tkl.iis.u-tokyo.ac.jp
Tel:+81-3-3479-0289/Fax:+81-3-3402-6226/takagi@tkl.iis.u-tokyo.ac.jp
***Pacific Forest Centre, Forestry Canada, Natural Resources Canada**
506 West Burnside Rd., Victoia, British Columbia, Canada V8Z 1M5
Tel:+1-250-363-0797/Fax:+1-250-363-0797/jiisaka@pfc.forestry.ca

Abstract -- We have compared NDVI and the Feature Mixing Model as a practical semi-quantitative measure of daily vegetation. In the comparison, we used AVHRR data for a warm, humid and relatively flat eastern China. While NDVI only gives a general trend, the results obtained using the Feature Mixing Model directly gives a more plausible picture of the vegetation of the corresponding terrain.

INTRODUCTION

Daily broadcasting of global land-cover information with weather forecasts is the best way to inform global environmental changes to the general public. Of the many satellite remote-sensing data, NOAA-AVHRR data is best suited for this purpose because of its long term operation, wide area coverage, short revisit cycle, affordable data processing loads, and data availability,

NDVI is often used to describe global changes in vegetation, but how its values correspond to the physical terrain is not very clear. While NDVI is relevant in investigating biomass, precipitation and some ecological phenomena in arid and semi-arid areas [1], its values in more humid areas vary day to day. Maximum compositing partly removes atmospheric effects [2], but the original GVI weekly composites sometimes need to be composited over a longer period (3-4 weeks) , which sacrifices time resolution.

On the other hand, the Feature Mixing Model [3,4,5] operates on a simple concept. Since it directly relates to terrain features, the model is independent of atmospheric conditions as long as their effects are linear. In previous studies, we investigated the potential of the Feature Mixing Model as applied to AVHRR data for eastern Asia [6,7]. We found that daily vegetation ratios calculated by the Feature Mixing Model using the sum of all daily scattergrams instead of individual daily scattergram were more plausible than daily NDVI values. In this study, we further investigated the method by applying it to a relatively flat area of eastern China in three periods of six consecutive days in May and July, 1995, and compared the results with NDVI.

FEATURE MIXING MODEL

We often observe a typical triangular pattern in scattergrams of visible and near IR terrain spectra of various optical sensors, including AVHRR. A corner high in IR and low in visible spectra corresponds to thick vegetation, a second corner high in both visible and IR spectra to inorganic materials, and a third corner low in both visible and IR spectra to dark objects such as water bodies and shadows. According to the Feature Mixing Model, a radiance space defined by two spectral bands is transformed into a triangular space defined by the linear sum of "vegetation," "inorganic materials," and "dark objects" as shown schematically in Fig. 1. The observed digital count T_1 and T_2 of channel 1 and 2 are given as follows using the digital counts and proportions of "pure" vegetation V_i, α, "pure" inorganic materials I_i, β, and "pure" dark objects D_i, γ.

$$T_1 = \alpha V_1 + \beta I_1 + \gamma D_1 , \quad (1)$$

$$T_2 = \alpha V_2 + \beta I_2 + \gamma D_2 , \quad (2)$$

where $$\alpha + \beta + \gamma = 1 . \quad (3)$$

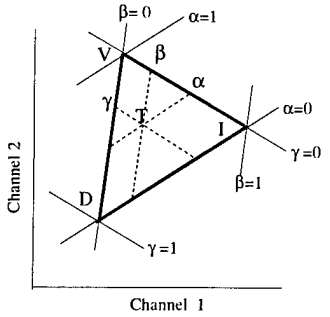

Fig. 1. Feature Mixing Model

It is then possible to solve α and β :

$$\alpha = \frac{(I_2 - D_2)(T_1 - D_1) - (I_1 - D_1)(T_2 - D_2)}{(I_2 - D_2)(V_1 - D_1) - (I_1 - D_1)(V_2 - D_2)}, \quad (4)$$

$$\beta = \frac{(I_1 - D_1)(T_2 - D_2) - (I_2 - D_2)(T_1 - D_1)}{(I_2 - D_2)(V_1 - D_1) - (I_1 - D_1)(V_2 - D_2)} . \quad (5)$$

0-7803-3836-7/97/$10.00 © 1997 IEEE

We should note that (4) and (5) for observed digital counts and albedo are the same as long as the correction is linear.

We further define the following normalized ratios, which are independent of shadows (or water), to compare the values of different locations :

$$\alpha' = \frac{\alpha}{\alpha+\beta} \quad \text{and} \quad \beta' = \frac{\beta}{\alpha+\beta} \ . \qquad (6)$$

EXPERIMENT

We used channel 1 and channel 2 data of NOAA-14 AVHRR observed at University of Tokyo (See Fig. 2). The data were then radiometrically and geometrically corrected using 0.01° intervals. The test area was the relatively flat region of eastern China (114-124°E and 30-38°N). The test dates were May 4-9, May 22-27, and July 17-22, 1995.

Cloud masks were created as follows: 1) threshold the channel 1 image at the values of 180, 160, and 140; 2) take areas above 180 as core cloud areas; 3) include point-like and line-like features above 160 attached to the core area; 4) include point-like and line-like features above 140 attached to the above area; 5) include small areas (tentatively set to less than 30000 pixels) enclosed in clouds; and 6) dilate the areas by 8 pixels to include the cloud shadows. Even applying this cloud mask, we sometimes observe the effect of clouds far outside the cloud mask.

Vertices of the triangle in the Feature Mixing Model were defined as follows: 1) eliminate small noise from the scattergram of cloud screened channel 1 data through thresholding; 2) eliminate isolated point-like features; 3) determine the dark object point $\mathbf{D}(D_1,D_2)$ from a reasonably populated pixel group among the lowest channel 2 pixel groups; 4) define the **D-V** line as the highest slope and the **D-I** line as the lowest slope to cover the main lobe; and 5) define the **V-I** line as the highest line roughly parallel to the bottom line of the main lobe. When it was difficult to define a triangle, the scattergram of the minimum channel 1 composite and the corresponding channel 2 composite spectra for the previous week or month was used.

RESULTS AND DISCUSSION

Fig. 4 and Fig. 5 are α' and NDVI of May 5, 1995. Since the day offered probably the best conditions of the year for NDVI, both show similar trends except for mixed forests in the bottom of the images (around 31°N) and a wheat growing region in the upper left of the images. The scattergram of the day could be referred to understand such a discrepancy (see Fig.3). Area A of the scattergram corresponds to the wheat growing region and area B corresponds to the southern forests. Using the thin triangle, it is easy to see in the Feature Mixing Model scheme that the proportion of the vegetation at B is higher than that at A. In the NDVI scheme (the dotted line corresponds to the highest NDVI value), as A and B are almost aligned on a line from the origin, they show us similar (actually NDVI values at A is slightly higher than those at B). Thus α' values directly gives a plausible picture where the vegetation in the southern forest is thicker than that of the wheat growing region of China, although verification with independent ground information is needed.

The maximum NDVI during the period of May 4-9 is similar to the NDVI of May 5 because the day was so clear. We define the minimum channel 1 composite for α' to minimize the cloud covered area during the same period. The result from the minimum channel 1 composite for α' is also similar to the α' of May 5 but with less cloud coverage.

Among the observations in this study other than those above are: 1) Daily NDVI tends to give poor results in July and in a more cloudy day in May. The maximum NDVI

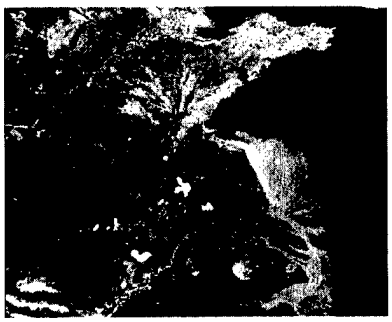

(a)

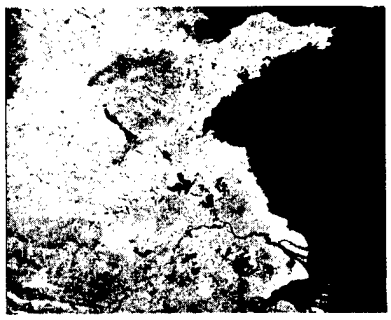

(b)

Fig. 2. Original spectra of May 5, 1995 (a) channel 1 (b) channel 2

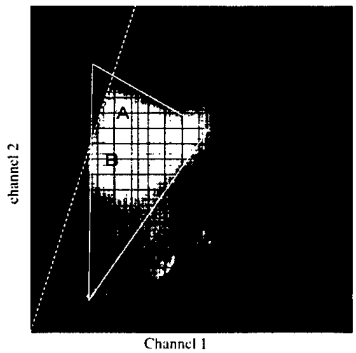

Fig.3 Scattergram of Fig. 2.

method gives much better results. 2) Daily α' for the Feature Mixing Model gives more stable results. 3) α' obtained from the minimum channel 1 composite method slightly improves the values but greatly reduces the cloud coverage. 4) Daily α' can be determined fairly consistently from the previous weekly or monthly composites of the scattergram.

The concept of the Feature Mixing Model is very simple and straightforward. The key to using the Feature Mixing Model lies in how to define daily triangle when clouds cover the key areas. If we are satisfied with several levels of vegetation, we can calculate daily α' using the triangle obtained from the weekly (or monthly) minimum channel 1 composite method instead of daily triangle. However, daily α' may not be even needed because, first, vegetation does not usually change such a short time span and, second, the variable cloud cover will create too many patches of missing information. Weekly vegetation can be estimated from the minimum channel 1 composite image and the corresponding channel 2 image. When applying the Feature Mixing Model to a much larger region, we need to define a triangle for each group of seasonally similar climate zones, and find conversion factors among the different groups.

CONCLUSION

We have compared NDVI and the Feature Mixing Model and obtained daily vegetation in warm and humid eastern China. While NDVI only shows a general trend and needs a further complicated analysis to relate to the amount of vegetation of the corresponding terrain, the results of the Feature Mixing Model directly gives a plausible picture, although there is a need to verify the results using ground data. Weekly minimum channel 1 composite image and the corresponding channel 2 image stabilize the results from the Feature Mixing Model and minimize missing information caused by clouds.

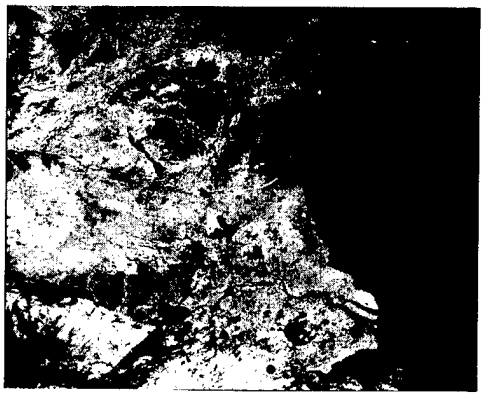

Fig. 4. Vegetation ratio α' for May 5, 1995. Roundish black areas which do not appear in Fig.5 are cloud masks.

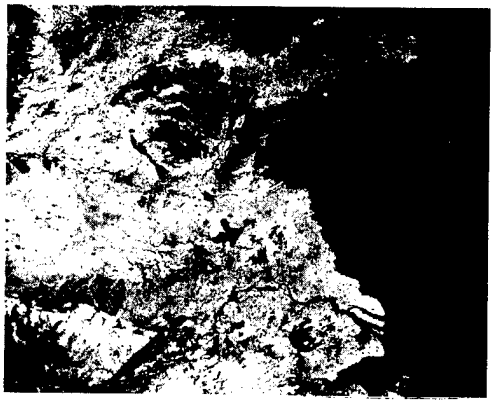

Fig. 5. NDVI for May 5, 1995

ACKNOWLEDGMENT

The authors wish to thank Dr. Zhog-Chao Shi and Tiam-En Chen for providing information on the test area

REFERENCES

[1] C. J. Tucker, "History of the use of AVHRR Data for Land Application," in Advances in the Use of NOAA AVHRR Data for Land Applications, G. D'Souza, A. S. Belward and J-P. Malingreau, Eds. Dordrecht/ Boston/London: Kluwer Academic Publishers, 1993, pp. 1-19.

[2] B. N. Holben, "Characteristics of maximum-value composite images from temporal AVHRR data," Int. J. Remote Sens. Vol. 7, pp. 1417-1434 , 1986.

[3] J. Iisaka, H. Yoshimori, Y. Yasuda, and Y. Emori, "Phenomena modeling of remotely sensed data by image rationing," Proc. the 15th Int. Symp. on Remote Sensing of Environment, pp.1127-1140, Ann Arbor, 1981

[4] M. Fukuhara, S. Hayashi, Y. Yasuda, Y. Emori and J. Iisaka, "Extraction of Soil Information from Vegetated Area", IBM Tokyo Scientific Center Report, pp. 1-19, November, 1979.

[5] J. Iisaka, E. Amano, and T. Sakurai-Amano, "Automated forest clearcut detection from TM data," Proc. 26th Int. Symp. of Environmental Monitoring and 17th Symp. of Can. Remote Sens. Soc., 4 pages, Vancouver, 1996

[6] T. Sakurai-Amano, J. Iisaka and M. Takagi, "A Feature Mixing Model for AVHRR Data," Proc. Int. Symp. Remote Sens., pp. 50-55, Chedu, Korea, October, 1996.

[7] T. Sakurai-Amano, J. Iisaka and M. Takagi, "An Environ- mental Index from AVHRR Data", IIS Forum, pp. 1-6, Univ. of Tokyo, February, 1997

Monte Carlo Simulations of Scattering of Electromagnetic Waves from Dense Distributions of Nonspherical Particles

Leung Tsang
Department of Electrical Engineering
University of Washington
Seattle, WA 98195

K.H. Ding, and S.E. Shih
Research Laboratory of Electronics
Massachusetts Institute of Technology
Cambridge, MA 02139

Abstract – In a dense, discrete random medium, the propagation and scattering of waves are not only affected by the individual properties of the particles such as sizes, shapes and permittivities, but also by the group properties such as the statistics of relative particle positions and relative orientations. In this paper, we investigate the interactions of electromagnetic waves with a dense medium consisting of spheroidal particles with random or aligned orientations. A multiple scattering formulation based on the volume integral equation and method of moments is developed. A shuffling process is used to generate the positions of densely packed spheroids within a cubic box. The scattering results are averaged over many realizations. Numerical results are presented for the extinction rates to illustrate the polarimetric scattering properties and the differences of scattering properties between nonspherical and spherical particles.

INTRODUCTION

In microwave remote sensing, one often encounters densely packed media such as snow, soil, gravel etc. In a dense, discrete random medium, the propagation and scattering of waves are not only affected by the individual properties of the particles such as sizes, shapes and permittivities, but also by the group properties such as the statistics of relative particle positions and relative orientations. In previous papers [1-5], we have studied the propagation and scattering of waves in densely packed spheres using analytical methods [1], Monte Carlo simulations [2,3], and experimental measurements [4,5]. In this paper, we perform Monte Carlo simulations of scattering by densely packed spheroids. In dense media that occur in nature, such as snow terrain, the ice grains are nonspherical. Scattering of electromagnetic waves by nonspherical particles also give important polarimetric signatures.

We use a shuffling algorithm [6] to generate the positions of densely packed spheroidal particles within a cubic box. The shuffling process consists of a succession of trial moves in which the coordinates and orientations of particles are selected and changed by the combination of random displacements and rotations. In the course of simulation, we have to know the size, shape, and position of each spheroid. Also, we have to know whether any pair of spheroids overlap each other. To do this, we have used the contact function for two arbitrary spheroids [7]. Given the centers, sizes, and orientations of a pair of spheroids, the numerical value of this function is less than 1 if they overlap, otherwise they do not. The scattering of electromagnetic waves by a system of randomly distributed and oriented spheroids is solved via the volume integral equation approach. The method of moments [8] is applied to convert the integral equation into a matrix equation which is then solved iteratively for each realization of spheroids. The scattering results are averaged over many realizations. Numerical results are presented for the extinction rates to illustrate the polarimetric scattering properties and the differences of scattering properties between non-spherical and spherical particles.

MULTIPLE SCATTERING FORMULATION

Consider an incident electric field $\overline{E}_{inc}(\overline{r})$ impinging upon N number of randomly positioned and oriented small spheroids (Figure 1). Spheroid j, centered at $\overline{r}_j$, occupies region V_j, and has permittivity ϵ_j, $j = 1, 2, \ldots, N$. The discrete scatterers are embedded in a background medium with permittivity ϵ.

The total electric field can be obtained via a volume integral equation

$$\overline{E}(\overline{r}) = \overline{E}_{inc}(\overline{r}) + k^2 \sum_{j=1}^{N} \int_{V_j} d\overline{r}' \, \frac{g(\overline{r}, \overline{r}')}{\epsilon} \overline{P}_j(\overline{r}') - \sum_{j=1}^{N} \overline{\nabla} \int_{V_j} d\overline{r}' \, \frac{\overline{\nabla}' g(\overline{r}, \overline{r}')}{\epsilon} \overline{P}_j(\overline{r}') \quad (1)$$

where $g(\overline{r}, \overline{r}')$ is the scalar Green's function, and $\overline{P}_j(\overline{r})$ is the polarization density inside particle j,

$$\overline{P}_j(\overline{r}) = (\epsilon_j - \epsilon)\overline{E}_j(\overline{r}) \quad (2)$$

To solve (1) by the method of moments, we expand the eclectic field $\overline{E}_j(\overline{r})$ inside the jth spheroid in term of a

0-7803-3836-7/97/$10.00 © 1997 IEEE

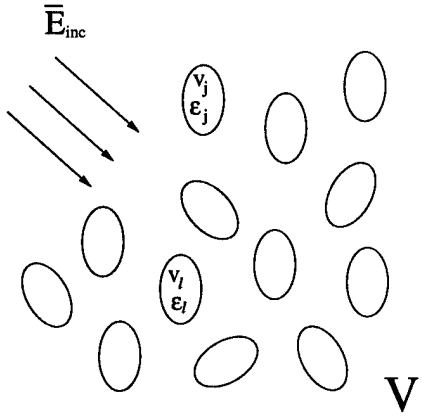

Figure 1: An electric field $\overline{E}_{inc}(\overline{r})$ incidents upon N non-overlap, small spheroids that are randomly positioned and oriented in a volume V.

set of N_b basis functions $\overline{f}_{j\alpha}(\overline{r})$

$$\overline{E}_j(\overline{r}) = \sum_{\alpha=1}^{N_b} a_{j\alpha}\overline{f}_{j\alpha}(\overline{r}) \tag{3}$$

where j is the particle index and α is the basis function index. Since the spheroid is small, we can choose the basis functions to be the electrostatic solution of a spheroid. The first three basis functions are those of the dipole solutions and the next five are those of quadrupole solutions. If the particles are closely packed, the near field interactions have large spatial variations over the size of a spheroid that may induce quadrupole fields inside the spheroid. However, the non-near field interactions have small spatial variations over the size of a spheroid and only induce dipole fields inside the spheroid.

Substituting (3) into (1), we get

$$\overline{E}(\overline{r}) = \overline{E}_{inc}(\overline{r}) + \sum_{j=1}^{N}\sum_{\alpha=1}^{N_b} a_{j\alpha}\overline{q}_{j\alpha}(\overline{r}) \tag{4}$$

with

$$\begin{aligned}\overline{q}_{j\alpha}(\overline{r}) &= k^2\int_{V_j} d\overline{r}'\; g(\overline{r},\overline{r}')\overline{f}_{j\alpha}(\overline{r}')(\epsilon_{rj}-1) \\ &- \overline{\nabla}\int_{V_j} d\overline{r}'\; \overline{\nabla}' g(\overline{r},\overline{r}')\cdot\overline{f}_{j\alpha}(\overline{r}')(\epsilon_{rj}-1)\end{aligned} \tag{5}$$

being the electric field induced by the polarization $\overline{P}_j(\overline{r})$ of spheroid j, and $\epsilon_{rj} = \epsilon_j/\epsilon$. Of particular importance is the internal field created by $\overline{P}_j(\overline{r})$ on itself. Because of the smallness of the spheroid, an electrostatic solution can be sought and we have, for $\overline{r}$ in V_j,

$$\overline{q}_{j\alpha}(\overline{r}) \cong C_{j\alpha}\overline{f}_{j\alpha}(\overline{r}) \tag{6}$$

Note that an approximation sign is used in (6) to indicate the low frequency approximation.

Applying Galerkin's method to (4), we obtain

$$\begin{aligned}a_{l\beta} &= \int_{V_l} d\overline{r}\;\overline{f}_{l\beta}(\overline{r})\cdot\overline{E}(\overline{r}) \\ &= \frac{1}{(1-C_{l\beta})}\left[\int_{V_l} d\overline{r}\;\overline{f}_{l\beta}(\overline{r})\cdot\overline{E}_{inc}(\overline{r})\right. \\ &+ \left.\sum_{\substack{j=1\\ j\neq l}}^{N}\sum_{\alpha=1}^{N_b} a_{j\alpha}\int_{V_l} d\overline{r}\;\overline{f}_{l\beta}(\overline{r})\cdot\overline{q}_{j\alpha}(\overline{r})\right]\end{aligned} \tag{7}$$

Equation (7) contains full multiple scattering effects among the N number of spheroids under the small spheroid assumption. After the coefficients $a_{l\beta}, l = 1,2,\ldots,N$ and $\beta = 1,2,\ldots,N_b$ are solved, the far field scattered field in the direction (θ_s,ϕ_s) is express as

$$\begin{aligned}\overline{E}_s(\overline{r}) &= k^2\frac{e^{ikr}}{4\pi r}(\hat{v}_s\hat{v}_s+\hat{h}_s\hat{h}_s)\sum_{j=1}^{N}\sum_{\alpha=1}^{N_b} a_{j\alpha}(\epsilon_{rj}-1) \\ &\cdot\int_{V_j} d\overline{r}'\; e^{-i\overline{k}_s\cdot\overline{r}'}\overline{f}_{j\alpha}(\overline{r}')\end{aligned} \tag{8}$$

where $\hat{k}_s = \sin\theta_s\cos\phi_s\hat{x} + \sin\theta_s\sin\phi_s\hat{y} + \cos\theta_s\hat{z}$, $\hat{v}_s = \cos\theta_s\cos\phi_s\hat{x}+\cos\theta_s\sin\phi_s\hat{y}-\sin\theta_s\hat{z}$, and $\hat{h}_s = -\sin\phi_s\hat{x}+\cos\phi_s\hat{y}$.

PARTICLE PLACEMENT ALGORITHM

In the simulation study of randomly placed objects, various particle placement algorithms, such as Metropolis shuffling and sequential deposition, have been applied to generate realizations of particle positions [7]. In this paper, a shuffling process is applied to generate the positions of densely packed spheroids.

We consider N spheroidal particles that are randomly placed in a simple cubic cell. Periodic boundary conditions are employed such that the central primary cell containing the N particles is surrounded by the periodic images of itself. In our Monte Carlo simulations, the N spheroids in the initial configurations are placed in close contact and aligned, but without overlap with each other. In such an initial set-up, we are able to create cases of higher fractional volumes. The shuffling process consists of a succession of trial moves in which we attempt to change the coordinates and orientations of particles by the combination of random displacements and rotations. During the course of simulation, in order to select the allowed new locations and orientations of particles, we have to check if any pair of spheroids overlap. This is carried out via a contact function F_{AB} for any two particles A and B with the following property [7]:

$$F_{AB}(\overline{r}_A,\Omega_A;\overline{r}_B,\Omega_B)\begin{cases}<1 & \text{if A and B overlap}\\ =1 & \text{if A and B touch}\\ >1 & \text{if A and do not overlap}\end{cases} \tag{9}$$

where $\overline{r}_A,\Omega_A$ and $\overline{r}_B,\Omega_B$ are the positions and orientations of particle A and particle B, respectively. Such a

contact function for a pair of non-penetrable spheroids has been derived for the study of non-spherical molecular fluid [7]. In this manner, we proceed to create a series of non-overlap configurations of spheroids. The adjustments of random displacements and rotations is such that 50% of the attempted moves are accepted.

SIMULATION RESULTS

We perform Monte Carlo calculation of scattering from a random distribution of N spheroidal particles of the same size with semi-axes $a = b$ and $c = ea$, where e denotes the elongation of particle. The permittivity of particle is $\epsilon_s = 3.2\epsilon_o$. In the simulations, $N = 1000$ spheroids are placed within $N_r = 50$ test volumes according to the process described in the previous section. The spheroids can be randomly oriented or aligned. The scattered field is solved using (8). Through the computation of coherent field by averaging over N_r realizations, we can obtain the incoherent scattered fields which are thus applied to calculate the extinction rate [2,3].

In Figure 2, we illustrate the normalized extinction coefficients as a function of fractional volume for a medium consisting of vertically aligned spheroids with $ka = 0.2$, and $e = 2$. In such a medium, a vertically polarized electromagnetic wave (results denoted by squares) has a higher scattering loss than that for a horizontally polarized wave (results denoted by circles). The extinction rates are also compared with those of media with randomly oriented spheroids (results denoted by triangles) of the same size and elongation, and media with spherical particles (results denoted by crosses) of $ka = 0.2$, and $e = 1$. The medium with randomly oriented spheroids predicts an attenuation between vertical and horizontal cases. On the other hand, the spherical case predicts a much less attenuation than spheroidal case, since each sphere has a smaller volume compared with spheroid, even though the medium assumes same fractional volume. Figure 3 demonstrates the extinction rates as a function of particle elongation for media with vertically aligned spheroids of $ka = 0.2$, and $f_v = 20\%$. It shows that the spheroid with longer elongation ratio predicts a larger attenuation due to its larger particle volume.

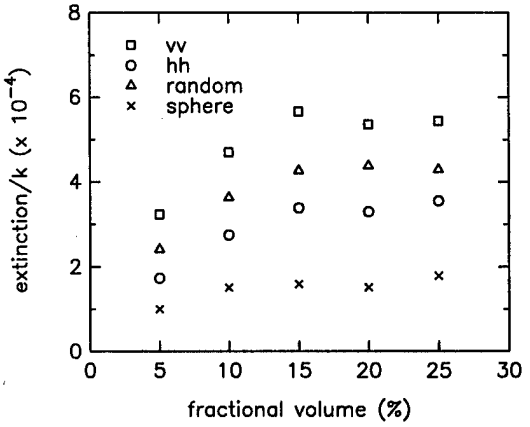

Figure 2: Extinction rate as a function of fractional volume for spheroids of $ka = 0.2$, and $e = 2$. The calculations are based on Monte Carlo simulations.

REFERENCES

[1] L. Tsang, J.A. Kong, and R.T. Shin, *Theory of Microwave Remote Sensing,* Wiley-Interscience, New York, 1985.

[2] L. Tsang, C.E. Mandt, and K.H. Ding, "Monte Carlo simulations of extinction rate of dense media with randomly distributed dielectric spheres based on solution of Maxwell's equations," *Optics Letters,* Vol. 17, pp. 314-316, 1992.

[3] L. Zurk, L. Tsang, K.H. Ding and D.P. Winebrenner, "Monte Carlo simulation of the extinction rate of densely packed spheres with clustered and nonclustered geometries," *J. Opt. Soc. Am. A,* Vol. 12, pp. 1772-1781, 1995.

[4] A. Ishimaru, and Y. Kuga, "Attenuation constant of coherent field in a dense distribution of particles," *J. Opt. Soc. Am.,* Vol. 72, pp. 1317-1320, 1982.

[5] C.E. Mandt, Y. Kuga, L. Tsang, and A. Ishimaru, "Microwave propagation and scattering in a dense distribution of spherical particles: experiment and theory," *Waves in Random Media,* Vol. 2, pp. 225-234, 1992.

[6] K.H. Ding, C.E. Mandt, L. Tsang, and J.A. Kong, "Monte Carlo simulations of pair distribution functions of dense discrete random media with multiple sizes of particles," *J. Electro. Waves Applic.,* Vol. 6, pp. 1015-1030, 1992.

[7] J.W. Perram, and M.S. Wertheim, "Statistical Mechanics of Hard Ellipsoids. I. Overlap Algorithm and the Contact Function," *J. Comp. Phys.,* Vol. 58, pp. 409-416, 1985.

[8] R.F. Harrington, *Field Computation by Moment Methods,* MacMillan, New York, 1968.

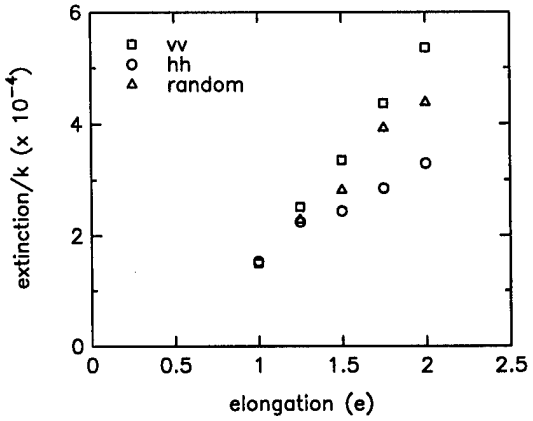

Figure 3: Extinction rate as a function of particle elongation for spheroids of $ka = 0.2$, and $f_v = 20\%$. The calculations are based on Monte Carlo simulations.

A Finite Difference Time Domain (FDTD) Simulation of Electromagnetic Wave Propagation and Scattering in a Partially Conducting Layered Earth

John Calhoun
Hughes Aircraft Company — Mukilteo Operations
6500 Harbour Heights Parkway, Mukilteo, Washington
Telephone (425) 356-3293/FAX (425) 356-3183/E-mail jcalhoun@atk.com

SUMMARY

A Finite Difference Time Domain (FDTD) simulation of electromagnetic propagation in partially conducting layers was performed. The simulation was constructed to model the case of a source antenna in close proximity to the earth's surface with receiving antennas both in the ground and on the earth's surface. The objective of the modeling and simulation was the prediction of the back scattered temporal and spatial waveforms from various objects buried in the partially conducting subsurface layers of the earth.

In our investigation we performed three primary modifications to the simulation code. First, the code was ported from a mainframe computer to a Sun work station. This involved splitting the simulation into a data calculation phase and an interactive data display phase. During the calculation phase, all the simulation results are computed to create time histories of the total electromagnetic field in a region of space which included both the source antenna and all the receive antenna locations. The receive antennas were located both on the surface of the earth as well as buried within the subsurface layers of the earth. The calculation phase creates a large matrix of time histories of the transmitted, scattered and total electromagnetic fields at all the sampled receive locations. An interactive display module was developed using MATLAB on the Sun workstation to view the results of the simulation.

The second extension of the simulation code was the incorporation of coherent transmit and receive waveforms into the simulation. An analytic formulation of the transmit pulse into real and imaginary parts allows coherent signal generation and analysis. This permits the calculation of both amplitude and phase information for the incident, scattered and total electromagnetic fields during the calculation phase of the simulation.

The third modification to the simulation code was the inclusion of the capability to place multiple scattering objects within the subsurface layers. The objects were allowed to be partially conducting and to have random statistical distributions of both size and spatial location. This represents a first attempt at providing simulation results for a simple two media model of an inhomogeneous layer.

The simulation results to be shown include a variety of antenna and scattering object locations for various combinations of layered earth models. The results are shown as color plots of the two dimensional maps of the electromagnetic fields as well as a pseudo animation of the two dimensional spatial maps. These pseudo animation results were obtained by sampling the hard copy color outputs of the simulation and display and combining them into a temporal record which approximates the time history animation results obtainable using the interactive display module.

The matrix of simulation results of the complex values of the vector E and H fields may be processed with signal processing algorithms to create detection maps and image reconstructions. The model produces time histories of the complex field values at all points in the simulation volume. Since the field values are coherent, the data created by the simulation may be processed with temporal and spatial signal processing algorithms to develop simulated results of particular earth models and scattering object geometries. This allows the creation of performance predictions of candidate signal sensing and processing approaches for the detection of man made objects buried in the earth. A proposed sensing and processing system is described which allows the detection and imaging of man made buried objects.

BASIC FDTD MODEL EQUATIONS

The basis of the model equations to be used in this investigation are Maxwell's Equations expressed in a discrete representation so that numerical approximations to the various incident, reflected and scattered fields may be computed using digital computers. These discretized Maxwell Equations form the foundation of the Finite Difference Time Domain (FDTD) approach to the solution of electromagnetic propagation problems. The basic set of computer code which was used as a starting point for this investigation was provided as the output of the Doctoral dissertation of Roberts [1] from Ohio State University. The original work on the discretization of Maxwell's equations was accomplished by Yee [2].

EXTENSIONS OF THE FDTD MODEL

For this investigation it was desired to characterize the electromagnetic fields scattered from simple geometric objects in a multilayered earth with antennas in close proximity to the surface of the earth. The end objective of the investigation was to determine signal transmission, reception and processing techniques for use with Ground Penetrating Radar when used to locate man made objects embedded in a layered earth. The extensions to the code were developed to allow the

0-7803-3836-7/97/$10.00 © 1997 IEEE

investigation of possible test geometries and test equipment for a GPR experiment. The simulations were used to predict the potential for obtaining information concerning buried man made objects using multiple GPR transmitter and receiver locations. The signal generation and processing approach consisted of coherent pulse generation and received signal processing and optimum combination of the multiple received signals.

ANALYTIC SIGNAL REPRESENTATION

In order to represent transmit and receive signals as a complex quantities, we modified the FDTD code to include transmit pulses expressed in the form of narrow band complex signals, such that a transmit signal is defined as $s(t) = a(t)\{\cos[\omega t+\Phi(t)] + j\sin[\omega t+\Phi(t)]\}$. This allows a pulse at center frequency w to be generated such that there is an amplitude, associated with the envelope function a(t), as well as a phase $\Phi(t)$. All computations are performed as complex quantities and the outputs are available as complex values or as magnitude and phase. This enhancement of the FDTD code was included to allow the simulation and processing of coherent GPR data. The magnitude and phase information is displayed using the interactive display module on the Sun workstation. The objective of this modeling was the prediction of the complex waveforms of the received back scattered electromagnetic fields to allow the use of multiple antenna coherent sensing systems. Examples of this type of sensing system include beamforming systems and inverse imaging systems.

MULTIDIMENSIONAL VISUALIZATION MODULE

In order to investigate the effects of changing test equipment capabilities, target geometries, earth electromagnetic propagation parameters and signal processing algorithms, we developed a multidimensional Visualization Module using MATLAB, implemented on a Sun workstation. This module allows analysis and visualization of the electromagnetic field data at a single point in space as a function of time, as well as at a single time or multiple times at several points in space. Screen displays and hard copy color plots are produced of two dimensional maps of the electromagnetic fields in operator selected horizontal or vertical planes. In addition, a three dimensional spatial map may be output at an instant of time. The two and three dimensional maps may also be viewed as animated time histories of the electromagnetic fields.

RESULTS OF SIMULATIONS OF WAVE PROPAGATION AND SCATTERING IN MULTI-LAYERED MEDIA

Simulation results are presented for a basic experiment conducted in a volume which varied from 1.5 to 2.5 meters wide by 2 to 2.5 meters long by 2 meters deep. Multiple layers, multiple object positions, multiple antenna positions and multiple soil types were investigated. A typical sampled time history of the results is shown in Figure 1. Additional results will be shown during the oral presentation.

DEVELOPMENT OF A TWO MEDIA RANDOM INHOMOGENEOUS LAYER

In order to model an inhomogeneous soil layer we modified the FDTD code to include the capability to include several spherical scattering objects with a random distribution of both size and location. A common complex permitivity was assumed for all of these spherical scatterers. For our simulation we chose a case with all scatterers of the same radius and with a uniform distribution in location. Various complex permitivities were assigned to the scatterers. This provided a simple two media representation of an inhomogeneous layer. Sample results of this investigation are shown in Figure 2. Additional results will be shown during the oral presentation.

CONCLUSIONS AND RECOMMENDATIONS

The primary purpose of this investigation was the development of a tool for the planning and analysis of coherent GPR experiments to determine the location and imaging of size, shape and material properties of buried man made objects. Capabilities have been expanded in the areas of coherent signal representation, transmit and receive signal multidimensional visualization and wave propagation and scattering in inhomogeneous layers. The tool is at a stage of development that can support experiment planning and development of novel image processing schemes, especially employing coherent GPR. Experiments are planned which will employ this simulation tool in the near future.

ACKNOWLEDGMENTS

The author would like to express his thanks to Laura Johnston for the implementation of the FDTD modifications and to Tony Luk for the development of the Multidimensional Visualization Module.

REFERENCES

[1] R.L. Roberts, "Analysis and Theoretical Modeling of GPR Polarization Data," PhD Dissertation, The Ohio State University, 1994.

[2] K.S. Yee, "Numerical solution of initial boundary value problems involving Maxwell's equations in isotropic material," IEEE Trans. Anten. Propa., v. AP-14, No. 3., p302-307, 1966.

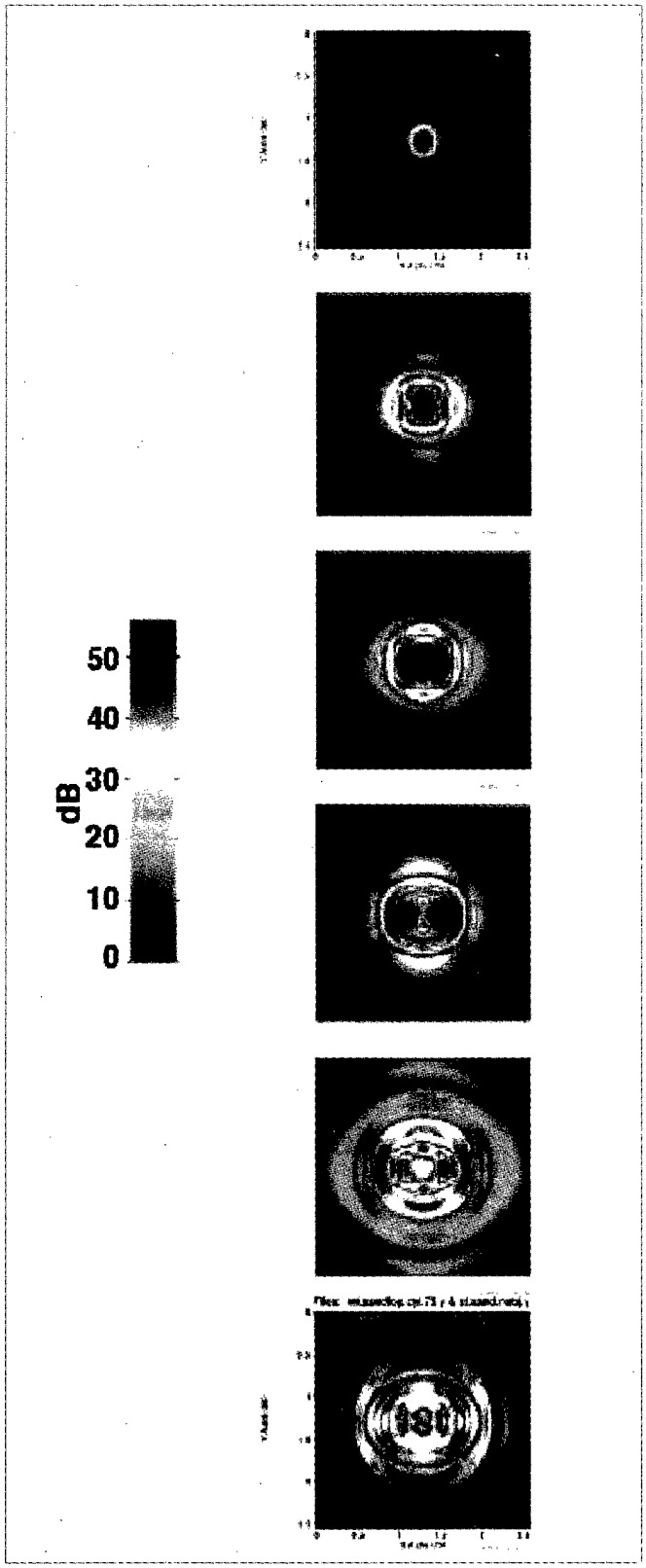

Figure 1. Time History of Scattering From a Cylindrical Object in a Layered Media of Sand, Intermediate, and Clay. The Cylinder is in the Top Sand Layer at 0.7m Depth.

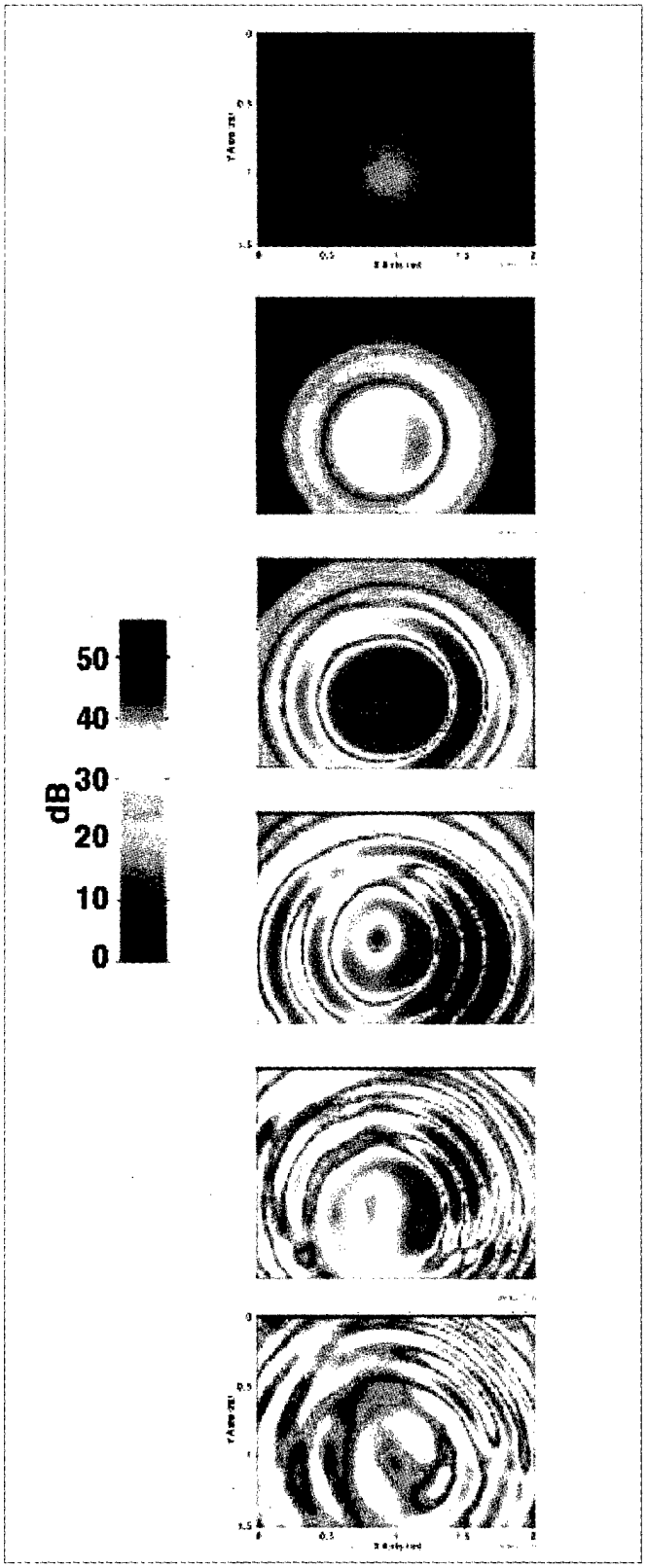

Figure 2. Time History of 2 Media With a Cylinder Target at 1m Depth. Spherical Scatters Have $\sigma = 0.0266$, $\varepsilon = 6.83$. Background Layer Has $\sigma = 0.0133$, $\varepsilon = 6.83$. Receive Antenna on Earth Surface. (σ is conductivity, ε is permittivity)

Complex Permittivity Measurements of Two Conifers

A. Franchois[1], R. Lang[2], Y. Piñeiro[1]

[1] **Advanced Techniques, SAI JRC 21020 Ispra (Va), Italy**
Tel/Fax: +39 332 789131/5772, E-mail: Ann.Franchois@jrc.it
[2] **EECS, George Washington University, Washington DC 20052, USA**

Abstract Complex permittivity measurements in the frequency range 1 - 10 GHz of two conifers, a 5.0 m high Balsam Fir and a 1.9 m high Spruce, are presented. With the large amount of measurement data it is possible to establish representative average values for the various parts of the considered trees.

INTRODUCTION

Measurements of the complex permittivity

$$\epsilon_r(\omega) = \epsilon_r^{'}(\omega) - j\epsilon_r^{''}(\omega) \qquad (1)$$

of two conifers, a 5.0 m high Balsam Fir and a 1.9 m high Spruce, were performed in the frequency range 1 - 10 GHz, within the frame of a polarimetric scattering and imaging experiment conducted in June 1996 in the European Microwave Signature Laboratory (EMSL) [1]. This also comprised a careful measurement of the trees' geometry by R. Landry of the Canadian Centre for Remote Sensing (CCRS), which will serve together with the complex permittivity data to construct 3D computer models of the trees. The huge set of data thus collected will be used to test microwave forest backscatter models, forward attenuation algorithms, and 3D reflectivity imaging algorithms.

This paper shortly describes the complex permittivity measurement method and presents measurement results for the various tree parts, such as new and first year needles, branches from different tree heights, and trunk sections. For the branches and trunks different layers from the phloem into the xylem were measured. Representative average values are also proposed.

MEASUREMENT METHOD

Set-up and procedure

A HP8510B Network Analyzer (NA) based reflection coefficient measurement method with an open-ended coaxial probe - a piece of 3.6 mm semirigid coaxial cable without flange - was used. The probe was connected to a HP85134 Test Port Cable which allows flexion without loss of accuracy. The position of cable and probetip, against which the tree samples were pressed, remained unchanged during the measurements. The small diameter of the probetip was advantageous in assuring a good contact with heterogeneous or small sized samples. Each measurement was repeated three times in a row, with interruption of the contact probetip-sample, and was accepted only if the standard deviation was sufficiently small. The time needed for such a sequence was typically 30 s.

Prior to the measurements a standard S_{11} calibration (short, open, matched load) was performed at the end of the flexible Test Port cable. Parasitic reflections at the cable-probe connector interface were gated out with the time gating feature of the NA. The resulting reflection coefficient measurements were referred to a measurement of the probe open into air. Measurements of known reference liquids were done from time to time as a check during the tree measurements and also served for the determination of the probetip capacitance.

Complex permittivity extraction

Lumped element models for the probetip-material discontinuity have been discussed abundantly in the literature, e.g. [2, 3, 4]. We use a frequency dependent shunt capacitor $C(\omega)\epsilon_r$, where the value of $C(\omega)$ is determined at each frequency of interest by means of a calibration with known reference liquids.

The ratio Γ of the complex reflection coefficients for the probe terminated by the material and by air is then expressed as

$$\Gamma = \left(\frac{1 - j\omega Z_0 C\epsilon_r}{1 + j\omega Z_0 C\epsilon_r}\right)\left(\frac{1 + j\omega Z_0 C}{1 - j\omega Z_0 C}\right), \qquad (2)$$

where $Z_0 = 50\Omega$ is the line impedance, and ϵ_r is given by

$$\epsilon_r = \frac{1 - \Gamma + j\omega Z_0 C(1+\Gamma)}{j\omega Z_0 C[1 + \Gamma + j\omega Z_0 C(1-\Gamma)]}. \qquad (3)$$

Small relative errors in the factor $\omega Z_0 C$ lead to equally small relative errors in ϵ_r when $\omega Z_0 C \ll 1$.

Neglecting the second order terms in (2) yields a simplified expression, used by some authors (e.g. [5])

$$\epsilon_r = 1 + \frac{(1-\Gamma)}{j\omega Z_0 C(1+\Gamma)}. \qquad (4)$$

However, using this approximation introduces significant differences even at frequencies lower than 10 GHz for

0-7803-3836-7/97/$10.00 © 1997 IEEE

tree parts with high water content such as needles, active xylem and phloem. In this paper all complex permittivity results were obtained with (3).

Determination of probetip capacitance

For the determination of $C(\omega)$ we have used (2), where $\Gamma(\omega)$ are measured values and where $\epsilon_r(\omega)$ is a model for the reference liquid. Writing (2) as a second degree equation in C

$$\epsilon_r(1-\Gamma)\omega^2 Z_0^2 C^2 + j(1-\epsilon_r)(1+\Gamma)\omega Z_0 C + 1 - \Gamma = 0, \quad (5)$$

and solving the real or imaginary part for $C_r(\omega)$ or $C_i(\omega)$ respectively, or the complex equation for a complex $C_c(\omega)$, one expects to find values which are in close agreement if (2) and the reference liquid model are sufficiently accurate. Values for C_r, C_i and C_c obtained from experimental data using methanol show a close agreement (Table I); when using butanol, the values show differences of 20 %, probably due to uncertainties on the butanol model. In this paper we use the real part of C_c with methanol as reference liquid.

Freq. [GHz]	Ref. liquids	C_r [fF]	C_i [fF]	C_c [fF]
1	methanol	21.5	21.1	$21.2 - j0.15$
5.5		20.2	20.3	$20.25 + j0.03$
10		20.9	20.8	$20.9 - j0.06$
1	butanol	22.7	25.9	$24.0 + j1.6$
5.5		20.2	27.0	$24.5 + j3.3$
10		22.7	30.1	$27.6 + j3.5$

Table I: Probetip capacitance at 1, 5.5 and 10 GHz with different computation schemes

For methanol we used a Cole-Cole dispersion model [6] with temperature dependent expressions for the LF and HF limit permittivities $\epsilon_{r,s}(T)$ and $\epsilon_{r,\infty}(T)$ and for the relaxation time $\tau(T)$,

$$\epsilon_{r,met.} = (4.95 - 0.022T) + \frac{(39.2 - 0.22T) - (4.95 - 0.022T)}{1 + j\omega 10^{-3}(80.5 - 1.17T)^{0.964}}, \quad (6)$$

where the frequency is expressed in GHz, the relaxation time in ps and the temperature in °C. The time dependent expressions were obtained by a linear fit to the data of [7] in the temperature range 10-40°C. For butanol we used the two component Debye dispersion model reported in [5].

MEASUREMENTS FOR TREES

The 5.0 m high Balsam Fir was approximately 21 years old and the 1.9 m high Spruce was approximately 6 years old. Both trees were bought planted in pots. Prior to the complex permittivity measurements they were kept for some time in an artificial environment (the EMSL anechoic chamber) for the scattering experiments, with exposure to a constant artificial illumination (thus no day-night cycle). The Balsam Fir had been watered abundantly during 2 weeks. The complex permittivity measurements were done in parallel with the tree vectorization, a procedure of complete geometric inventory which requires the destruction of the tree. For the Balsam Fir this destruction was spread over 2 days - with the removal of the branches on day one and the sawing up of the trunk on day two -, while for the Spruce everything was completed in one day. Measurements were always performed immediately after the removal of the sample from the tree. An overview of the samples, their height above ground and dimensions is given in Table II. Results for these samples are now discussed.

Tree Part	Height [mm]	Length [mm]	Diameter [mm]
Balsam Fir			
Needles	various	≈ 21	≈ 1.2
br97	420	1275	13.6, 4.5*
br75	1280	1012	19.5,5.2*
br67	2090	1000	15.6, 6.5*
br66	3800	590	9.5, 6.2*
tr0	0	-	110
tr1	1300	-	80
tr2	2300	-	58
tr3	3300	-	37
Spruce			
Needles	various	≈ 13	≈ 0.6
br36	250	550	8.0,2.9*
tr0	0	-	31
tr1	500	-	23
tr2	1000	-	13
tr3	1500	-	8

Table II: Position and dimensions of the tree samples (* values for bottom and top of branch)

Trunks

A conifer trunk consists of a bark, a phloem and a cambium layer surrounding the active and passive xylem [8], see Fig.1. The cambium is a thin reproduction layer which generates new active xylem on its interior side and phloem on its exterior side. The active xylem is several annual rings wide and is made of tracheids (spindle-shaped

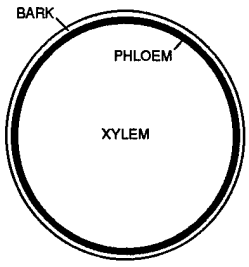

Figure 1: Schematic cross-section of a trunk

cells) for transportation of water in the upward direction. The width of these cells is larger for xylem formed during spring (early wood) than during autumn (late wood). The phloem, typically a few mm thick, transports water with assimilates downward. Since sections were sawed from the trunks, the transportation of liquids in phloem and xylem was stopped, but the water content remained. Measurements were performed a few cm away from the sawing sections - which were drier - with the probe in the radial direction (pointing to the trunk center) and going progressively inward by carefully pealing off layers.

For the Balsam Fir the complex permittivity as a function of the distance from the trunk center at 1 GHz is shown for section tr1 on Fig.2. These data are mean values of three subsequent single measurements and the error bars are the standard deviations. The maximum value for $\epsilon_r^{'}$ occurs - also for the other trunk sections of the Balsam Fir as well as for higher frequencies - at the interface between phloem and active xylem. This interface was measured by applying the probe against a piece of phloem pealed off the xylem. For the xylem the data fluctuate over short distances varying from about $\epsilon_r = 30 - j6$ to $\epsilon_r = 12 - j2$ on Fig.2. This is probably due to the seasonal variations. We suggest mean values for the phloem, the part of the xylem which corresponds to about six outer annual rings and the inner xylem. For the other trunk sections less measurements were done inside the xylem but similar values are obtained as for tr1. At 10 GHz the trend is toward lower values (about -10) for $\epsilon_r^{'}$ and higher values (about $+3$) for $\epsilon_r^{''}$.

For the Spruce the phloem permittivity increases with the height of the section (from about $\epsilon_r = 40 - j9$ to about $\epsilon_r = 55 - j17$ at 1 GHz). Xylem data are available for the outer surface and at the center of each section, ranging - at 1 GHz - from $\epsilon_r = 37.5 - j10$ to $\epsilon_r = 44 - j12$ and from $\epsilon_r = 17.3 - j3.7$ to $\epsilon_r = 26 - j5.7$ respectively. There is no apparent dependence of these values on height, and a model for the xylem based on single mean values may be used.

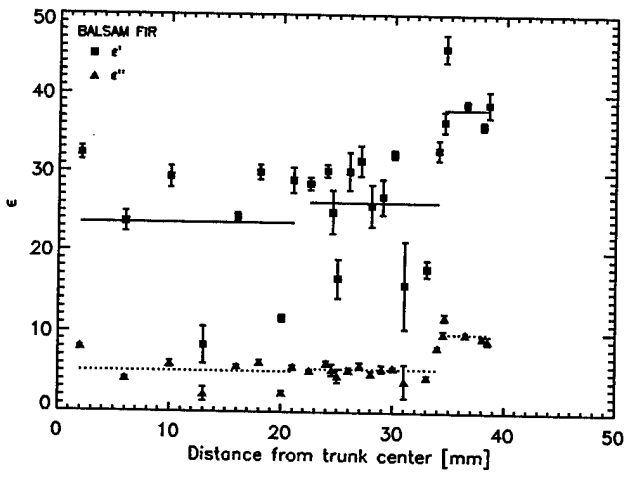

Figure 2: ϵ_r across trunk section tr1 of the Balsam Fir at 1 GHz. Mean values for 3 concentric regions are indicated by plain and dotted lines

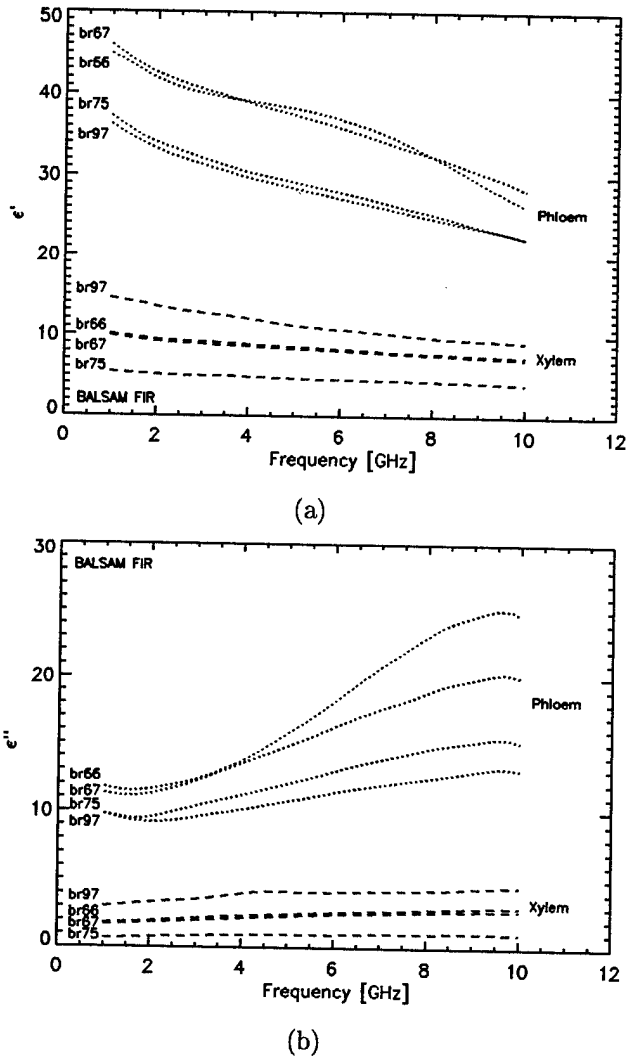

Figure 3: $\epsilon_r^{'}$ (a) and $\epsilon_r^{''}$ (b) for phloem and xylem of 4 branches of Balsam Fir

Branches

The morphology of a branch is similar to that of a trunk. We performed measurements on both sides of the phloem and on the outer surface and at the center of the xylem, each time at the bottom, middle and top of the branch. Data for the outer surface of the phloem and for the center of the xylem of branches br97, br75, br67 and br66 of the Balsam Fir are presented on Fig.3. For the phloem ϵ_r is higher for top branches than for bottom ones. The data

for branch br36 of the Spruce lie in the same ranges as those of the Balsam Fir.

Needles

Bright green new needles, which are located at the outer surface of the tree, and darker first year needles from different tree heights were measured. Therefore, several tens were arranged in parallel in a circular clamp which was then tightened firmly. The upper or lower ends sticking out of the clamp were removed yielding a smooth measurement surface and the superfluous liquid was wiped off. The effect of drying of the sample surface became important after roughly 5 minutes.

Fig.4 shows complex permittivity data as a function of frequency for needles taken from three branches of the Balsam Fir, br75, br67 and br66. The plain curves, one for each branch, are the mean values of 3 subsequent single measurements, indicated by the dots. The new needles have significantly higher values than the old needles, and present together with the cambium the maximum values for this tree. On the other hand, variations from branch to branch are rather small such that we suggest to model new and old needles with single values regardless of their position in the tree. Such mean values and standard deviations at 1 and 10 GHz, derived from the 9 single measurements, are also indicated on Fig.4.

For the Spruce measurements were performed for new and old needles from the top and bottom parts of the tree. Here no such clear distinction is present between new and old needles, although the new needles from the top have a little higher value. We suggest to use one single mean value: 31.8 ± 3 and 20.5 ± 2 for $\epsilon_r^{'}$ at 1 and 10 GHz, and 8.15 ± 0.7 and 13.6 ± 2 for $\epsilon_r^{''}$ at 1 and 10 GHz. The role of the needles in the tree scattering process is especially important for the higher frequencies.

CONCLUSION

Complex permittivity measurements of various parts of two conifers, a Balsam Fir and a Spruce, were presented. For the trunks data are available across layers from the phloem to the xylem center, at different trunk heights. There are similarities between the trunk data for both trees. Data for branches - measured in the same way as the trunks - and for new and old needles from different tree heights are also available. Representative ranges and mean values were proposed. For the Balsam Fir a significant difference exists between the values for the new and old needles, while this is not the case for the Spruce.

REFERENCES

[1] R. H. Lang, "A Tree Scattering Experiment," *EMSL Newsletter*, no. 9, pp. 1–3, November 1996.

[2] E. C. Burdette, F. L. Cain, J. Seals, "In Vivo probe measurement technique for determining dielectric properties at VHF through microwave frequencies," *IEEE Trans. Microwave Theory Techn.*, vol. 28, pp. 414–427, April 1980.

[3] M. A. Stuchly, M. M. Brady, S. S. Stuchly, G. Gajda, "Equivalent circuit of an open-ended coaxial line in a lossy medium," *IEEE Trans. Instrum. Measurement*, vol. 31, pp. 116–119, June 1982.

[4] M. A. El-Rayes, F. T. Ulaby, "Microwave dielectric spectrum of vegetation - part I: experimental observations," *IEEE Trans. Geosci. Remote Sensing*, vol. 25, pp. 541–549, September 1987.

[5] D. R. Brunfeldt,*Portable Dielectric Probe Instruction and Operating Manual*, Applied Microwave Corp. Lawrence, Kansas 66046.

[6] A. R. von Hippel, *Dielectric Materials and Applications*. London: Artech House, 1954.

[7] B. P. Jordan, R. J. Sheppard, S. Szwarnowski, "The dielectric properties of formamide, ethanediol and methanol," *J. Phys. D: Appl. Phys*, vol. 11, pp. 695–701, 1978.

[8] P. J. Kramer, *Water Relations of Plants*. London: Academic Press, 1983.

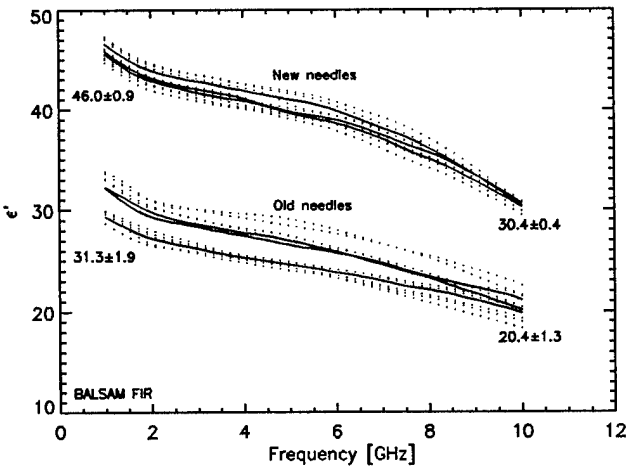

(a)

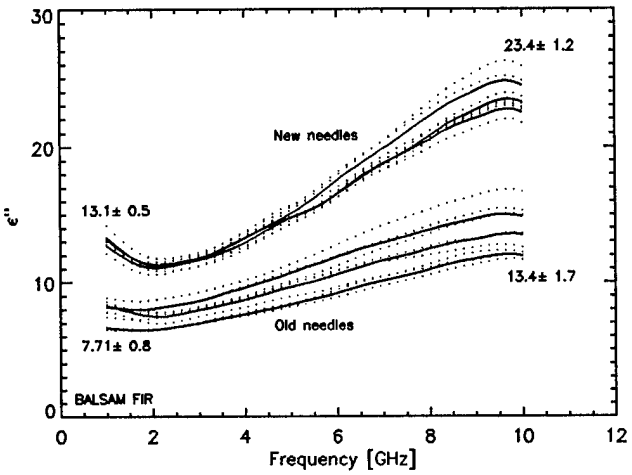

(b)

Figure 4: $\epsilon_r^{'}$ (a) and $\epsilon_r^{''}$ (b) for new and old needles of 3 branches of Balsam Fir.

3D ELECTROMAGNETIC MODELING USING STAGGERED FINITE DIFFERENCES

Gregory A. Newman and David L. Alumbaugh
Sandia National Laboratories
P.O. Box 5800, Albuquerque NM 87185-0750
Tel: (505) 844-8158; Fax (505) 844-7354
Email: ganewma@sandia.gov

ABSTRACT

The method of finite differences has been employed to solve a variety of 3D electromagnetic (EM) forward problems arising in geophysical applications. Specific sources considered include dipolar and magnetotelluric (MT) field excitation in the frequency domain. In the forward problem, the EM fields are simulated using a vector Helmholtz equation for the electric field, which are approximated using finite differences on a staggered grid. To obtain the fields, a complex-symmetric matrix system of equations is assembled and iteratively solved using the quasi-minimum method (QMR) method. Perfectly matched layer (PML) absorbing boundary conditions are included in the solution and are necessary to accurately simulate fields in propagation regime (frequencies > 10 MHz). For frequencies approaching the static limit (< 10 KHz), the solution also includes a static-divergence correction, which is necessary to accurately simulate MT source fields and can be used to accelerate convergence for the dipolar source problem.

INTRODUCTION

For too long the interpretation of frequency-domain electromagnetic data arising from complex geologic media has been limited by the lack of interpretation tools. It is only within the last few years that the ability to model and invert complex 3D EM data is emerging. A key reason for this development has been the application of efficient finite-difference methods to the forward modeling problem.

Over the last five years, we have developed solutions to the 3D EM forward problem for frequency-domain applications ([1] and [2]). Progress has proceeded on several fronts, including the development of a fast 3D finite difference modeling code for both dipolar and MT or natural source (plane wave) fields. Key features of the forward modeling code is its ability to simulate fields from the propagation to diffusion regime (radar to inductive EM), the inclusion of the perfectly matched layer absorbing boundary conditions necessary to reduce the size of the model domain and accurately simulate wave propagation, and the ability to model 3D variations in electrical conductivity, dielectric permittivity and magnetic permeability. The modeling code also includes a static-divergence correction, which is necessary to insure accurate MT results. In this talk, we will review our efforts in forward modeling.

THE FORWARD PROBLEM

Theory

Assuming a time harmonic dependence of $e^{i\omega t}$ where $i=\sqrt{-1}$, the vector Helmholtz equation for the electric field given by [1] is written here as

$$\nabla_e \times \mu_o/\mu \nabla_e \times \mathbf{E} + \omega\mu_o(\sigma + i\omega\varepsilon)\mathbf{E}=\mathbf{S} \qquad (1)$$

In this expression the electrical conductivity, magnetic permeability and dielectric permittivity are denoted by σ, μ and ε respectively, where μ_o is the magnetic permeability of free space. Specification of the source vector **S**, which includes the appropriate boundary conditions, determines whether dipolar or natural source (MT) field excitation is to be simulated. For dipolar source fields we have, for a total-field formulation

$$\mathbf{S} = -i\omega\mu_o \mathbf{J_p} - i\omega \nabla_h \times (\mu_o/\mu \mathbf{M_p}), \qquad (2)$$

where $\mathbf{J_p}$ and $\mathbf{M_p}$ are current densities for the impressed electric and magnetic dipole sources, and Dirichlet boundary conditions are assumed with the tangential electric fields set to zero on the model domain boundary. Sometimes a scattered field formulation is desired because of accuracy considerations [2]. In this case we have

$$\mathbf{S}=-i\omega\mu_o[(\sigma-\sigma_p) + i\omega (\varepsilon-\varepsilon_p)]\mathbf{E_p}-i\omega\mu_o\nabla_h\times[(\mu-\mu_o)/\mu\mathbf{H_p}], \quad (3)$$

where p designates background or primary values which are easy and fast to compute, such as a whole space. With a scattered field formulation the electric field, **E**, in equation (1) is replaced by a scattered electric field, $\mathbf{E_s}$, where we impose the boundary condition that tangential $\mathbf{E_s}$ be zero on the boundary of the model domain. The total electric field is then given by the expression $\mathbf{E_t} = \mathbf{E_p} + \mathbf{E_s}$. In order to simulate natural source fields, **S** is set to zero everywhere, except at points where tangential

0-7803-3836-7/97/$10.00 © 1997 IEEE

electric-field boundary values are specified. These boundary values arise from vertically propagating plane waves in layered or 2D geologic media assigned at the boundaries of the 3D problem.

The modified differential operators in equation (1) are defined by

$$\nabla_e = \mathbf{i}\, 1/e_x\, \partial/\partial_x + \mathbf{j}\, 1/e_y\, \partial/\partial_y + \mathbf{k}\, 1/e_z\, \partial/\partial_z$$

and (4)

$$\nabla_h = \mathbf{i}\, 1/h_x\, \partial/\partial_x + \mathbf{j}\, 1/h_y\, \partial/\partial_y + \mathbf{k}\, 1/h_z \partial/\partial_z,$$

where e_j and h_j for $j = x,y,z$ are complex coordinate stretching variables which stretch the x ,y and z coordinates and define the PML absorbing boundary conditions originally developed by [5], but are in a form developed by [6] for ease of implementation.

When equation (1) is approximated with finite differences using the staggered grid due to [7], a linear system results in which the matrix is complex symmetric. This system can be efficiently solved iteratively using Krylov sub-space methods, including the quasi minimum residual (qmr) method. The reader is referred to [1] and [2] for the details on how these solvers are implemented. Once the electric fields are determined, the magnetic fields can be determined from Faraday's law, by numerically approximating the curl of the electric field at various nodal points and interpolating either the electric or magnetic field nodal values to the point of interest.

Even with the benefits of a staggered grid, which implicitly enforces the auxiliary divergence conditions on the current density,

$$\nabla_h \cdot \{(\sigma + i\omega\varepsilon)\,\mathbf{E}\} = \nabla_h \cdot \mathbf{S}/\, i\omega\mu_o, \qquad (5)$$

it is often necessary to explicitly enforce this condition through a static-divergence correction at frequencies approaching the static limit. The correction adds a term to the electric field such that equation (5) is identically satisfied and is alternated with a series of qmr iterations on equation (1). All the details on how to implement this correction procedure for either scattered and total fields can be found in [8], [9] and [10].

MT Simulations

In Figure 1, we demonstrate the 3D code's capability to simulate magnetotelluric fields which are useful in crustal investigations of the earth. The top part of the figure shows a conductive block, 2 km thick, residing in an earth with three layers. The 3D results are plotted at 1 Hz in terms of apparent resistivity and phase, given by the following formula

$$\rho^{TE} = |E_y/H_x|^2/\omega\mu_o \qquad (6)$$

$$\rho^{TM} = |E_x/H_y|^2/\omega\mu_o \qquad (7)$$

and

$$\theta^{TE} = \tan^{-1}\,[\mathrm{Im}(E_y/H_x)/\mathrm{Re}(E_y/H_x)\,] \qquad (8)$$

$$\theta^{TM} = \tan^{-1}\,[\mathrm{Im}(E_x/H_y)/\mathrm{Re}(E_x/H_y)]. \qquad (9)$$

The notation TE and TM stand for transverse electric and magnetic and denote responses produced by inducing electric and magnetic fields perpendicular to the strike direction of the model. For a half-space model, the apparent resistivity will equal that of the half space, while the phase will be 45 degrees. To verify the results, we have compared the 3D responses with two 2D codes; one based on finite elements [11] and the other on finite differences that we recently developed. In the 2D case the block model is assumed to possess infinite strike length, while in the 3D case it is 80 km. Comparisons between the different codes are quite good. It must be noted that to obtain accurate 3D results a static divergence correction, as discussed above, was required for this simulation.

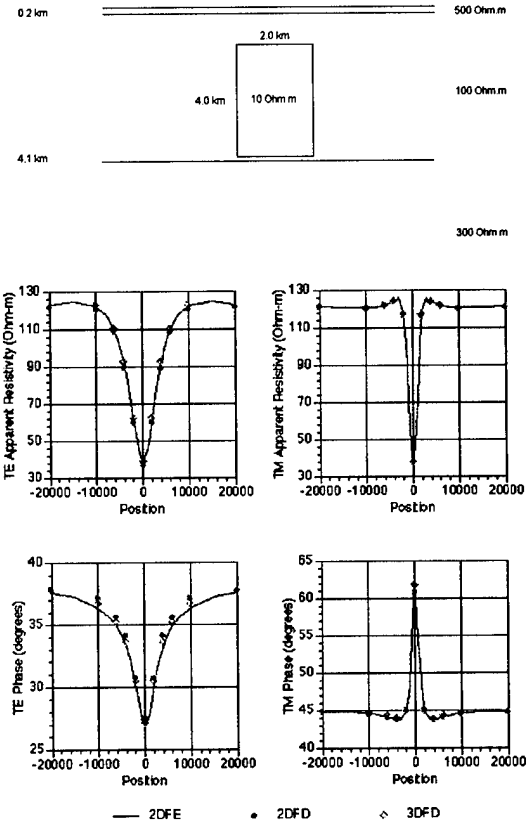

Figure 1. Comparison between 3D and 2D codes for a MT simulation at 1 Hz at the earth's surface.

The Need for PML Boundary Conditions

[1] has shown the need of the PML absorbing boundary conditions when simulating propagating fields in the frequency domain. To summarize the results, the complex stretching parameters are assigned a value of $1 + a - i\,b$. On the internal portions of the mesh, $a = b = 0$ such that the modified Helmholtz equation reduces to the normal form. Near edges of the mesh e_i and h_i are allowed to vary over several cells, but only in the direction that is perpendicular to the boundary. For example, along the $+z$ boundary $e_x = e_y = h_x = h_y = 1$ and only $e_z = h_z$ are allowed values of a and b that differ from zero. Some guidelines for selecting the PML stretching coordinates can be found in [1].

Figure 2 shows a simulation where the horizontal and vertical magnetic field arising from a vertical magnetic dipole and calculated on a 120 x 120 x 120 mesh for the three layer model is indicated in panel a). Resistivities of the layers are 1373, 76, 1000 Ω.m and 6, 41 and 1 are their dielectric properties relative to free space. The thickness of each layer is 1.1 and 0.9 meters. The 3D results and have been plotted against the 1D solution based on Sommerfield integrals. It is immediately evident in panel b) that the 3D solution without the PML boundary condition begins to break down at about 15 MHz, and we can assume that this is due to reflections due to the mesh boundaries contaminating the solution. Doubling the size of the cells along the mesh boundaries, that is using real grid stretching, does not help matters. Panel c) shows that poor results occur when a real stretching parameter a = 1.0 is employed along 25 cells of each boundary. However, when complex grid stretching is employed the results are much better. Panel d) shows results that when a stretching parameter of b = -0.6 is employed along 25 cells of each boundary, the fields calculated with the 3D solution match those of the 1D solution almost exactly. In panel e) we demonstrate how absorbing boundaries can be applied to shrink the size of the mesh. In this case a 72 X 72 X 72 mesh was used along with b=-2.0 applied for 10 cells along each boundary. Notice that both the 3D and 1D calculations coincide. This example fully illustrates the utility of the PML boundary conditions as they not only allow one to accurately simulate wave propagation, but also allow the mesh size to be significantly reduced and results in much smaller run times.

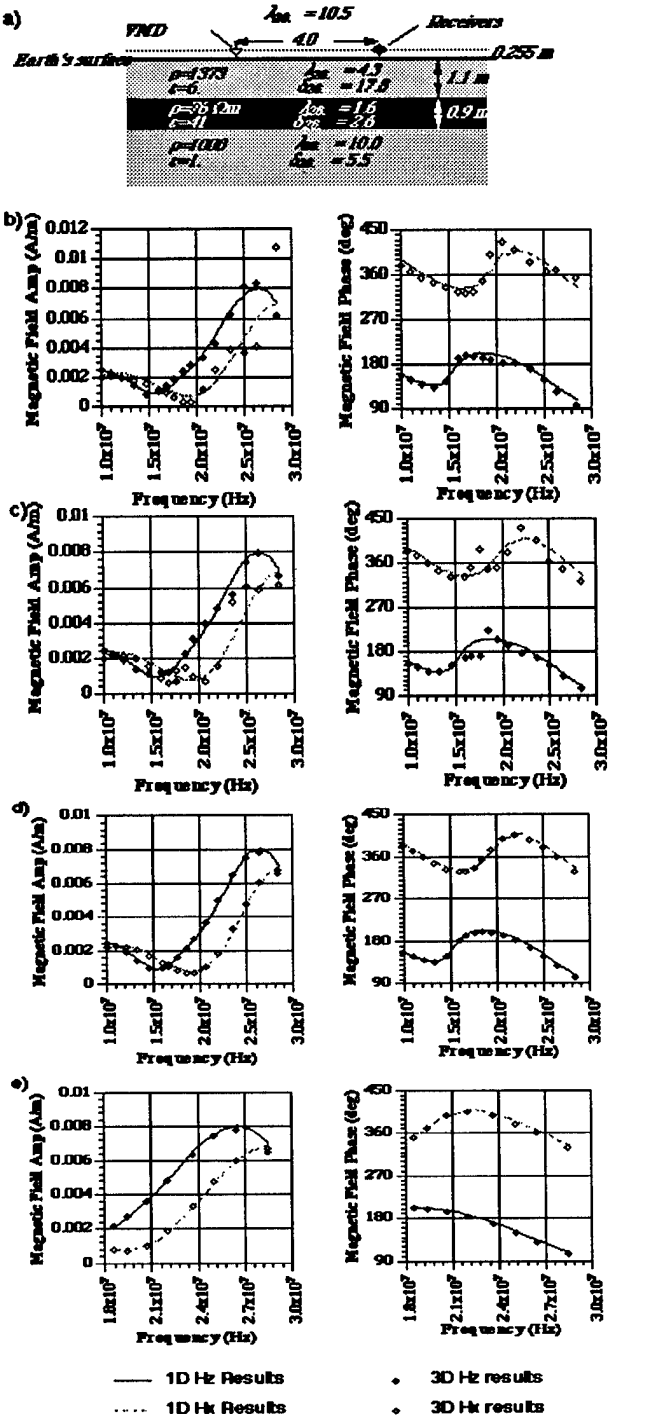

Figure 2. 1D model used to verify the need for PML absorbing boundary conditions. Note that the magnetic permeability has been set to that of free space. At the top of the figure we also have included wavelengths and skin depths in the respective layers. See text for panel explanation.

ACKNOWLEDGMENTS

This work was performed at Sandia National Laboratories, which is operated for the United States Department of Energy (DOE). Funding for the work was

provided by DOE's office of Basic Energy Sciences, Division of Engineering and Geoscience, under contract DE-AC04-94AL85000.

REFERENCES

[1] Alumbaugh D. L., Newman G. A., Prevost L., and Shadid, J. N., 1996, Three-dimensional wideband electromagnetic modeling on massively parallel computers: Radio Science, **31**, 1-23.

[2] Newman G. A., and Alumbaugh D. L., 1995, Frequency-domain modeling of airborne electromagnetic responses using staggered finite differences: Geophysical Prospecting, **43**, 1021-1042.

[3] Newman G. A., and Alumbaugh D. L., 1997, Three-dimensional massively parallel electromagnetic inversion - I. Theory: Geophysical Journal International, **128**, 345-354.

[4] Alumbaugh D. L., and Newman G. A., 1997, Three-dimensional electromagnetic inversion - II. Analysis of a crosswell electromagnetic experiment: Geophysical Journal International, **128**, 355-363.

[5] Berrenger J., 1993, A perfectly matched layer for the absorption of electromagnetic waves: Journal of Computational Physics, **114**, 185-200.

[6] Chew W. C., and Weedon W. H., 1994, A 3D perfectly matched medium from modified Maxwell's equations with stretched coordinates: Microwave Optical Technology Letters, **7**, 599-604.

[7] Yee K. S., 1966, Numerical solution of initial boundary problems involving Maxwell's equations in isotropic media: IEEE Transactions on Antennas and Propagation, **AP-14**, 302-309.

[8] Newman G. A., and Alumbaugh, D. L., 1996, Electromagnetic modeling of subsurface 3D structures: Presented at the International Geoscience and Remote Sensing Symposium (IGARSS), Omaha, Nebraska.

[9]Alumbaugh D. L., and Newman G. A., 1996, Electromagnetic modeling of perfect conductors in an arbitrary host, 66th Society of Exploration Geophysicists Annual Meeting, Extended Abstracts, 978-981, Tulsa OK.

[10] Smith T., Conservative modeling of 3D electromagnetic fields; Part I: Properties and error analysis: Geophysics, **61**, 1308-1318.

[11]Wannamaker P. E., Stodt J. A., and Rijo L., 1987, A stable finite element solution for two-dimensional magnetotelluric modeling: Geophysical Journal Royal Astronomical Society: **88**, 277-296.

3D ELECTROMAGNETIC INVERSION USING CONJUGATE GRADIENTS

Gregory A. Newman and David L. Alumbaugh
Sandia National Laboratories
P.O. Box 5800, Albuquerque NM 87185-0750
Tel: (505) 844-8158; Fax (505) 844-7354
Email: ganewma@sandia.gov

ABSTRACT

In large scale 3D EM inverse problems it may not be possible to directly invert a full least-squares system matrix involving model sensitivity elements. Thus iterative methods must be employed. For the inverse problem, we favor either a linear or non-linear (NL) CG scheme, depending on the application. In a NL CG scheme, the gradient of the objective function is required at each relaxation step along with a univariate line search needed to determine the optimum model update. Solution examples based on both approaches will be presented.

INTRODUCTION

Because of computational demands, inversion of frequency-domain electromagnetic data arising from complex geologic media has only been a dream. In fact it is only within the last few years that the ability to model complex 3D geology in a forward sense is now emerging. Since modeling complex geology is no longer a barrier, this has also opened up the ability to image it. Important applications of the new imaging technology are now arising in environmental waste characterization and resource exploration.

Within the last two years, we have developed solutions to the 3D inverse problem for frequency-domain applications ([1], [2], [3] and [4]), where 2.5 and 3D imaging codes have been used to reconstruct the conductivity within the subsurface. The inversion codes include an efficient finite-difference forward-modeling algorithm which is necessary to compute predicted data and model sensitivities at high discretization levels, and hence we are able to image complex geological media. In this talk, we will review our efforts in inversion employing iterative conjugate gradients methods.

THE INVERSE PROBLEM

Regularized Least Squares

All least squares solutions begin by minimizing the difference between observed and predicted data, often subject to some sort of constraint needed to stabilize the inversion process. In underdetermined problems, which we consider here, stability is provided with Tikhonov regularization, where only smoothly varying models are sought. Let's divide the earth into M cells and assign to each cell an unknown conductivity value. Further let $\mathbf{m}$ be a vector that describes these values, which is of length M. We now form an objective functional, φ, which combines the data error and model smoothness in the following fashion:

$$\varphi = \sum_{j=1}^{N} \{ (d_j^{obs} - d_j)/\varepsilon_j \}^2 + \lambda \, \mathbf{m}^T \mathbf{W}^T \mathbf{W} \, \mathbf{m}. \quad (1)$$

In equation (1) the terms that describe the observed and predicted data are d_j^{obs} and d_j, where the summation is over N data points. We also weight the data errors in equation (1) by the standard deviations of the observed data, ε_j. This gives noisy data smaller weight when forming φ.

The parameters that dictate model smoothness are the regularization matrix $\mathbf{W}$, which consists of a finite difference approximation to the Laplacian (∇^2) operator and the tradeoff parameter, λ, which is used to control the amount of smoothness to be incorporated into the reconstruction. Different strategies for selecting λ can be found in [1] and [5].

In small scale inverse problems it may be feasible to determine the minimum of equation (1) with a brute force search in parameter space. For large scale problems, such as ours, this is not an option. Instead, what is typically done is to set the gradient of the objective function, $\nabla\varphi$, with respect to the model parameters to zero, and find by some economical means those model parameters that satisfy $\nabla\varphi = 0$. Because the predicted data depend on the model, $\mathbf{m}$, in a non-linear fashion we are forced to solve $\nabla\varphi = 0$ using an iterative method.

Derivation of the Jacobian Matrix Elements

Model sensitivity or Jacobian matrix elements play a critical role in the inverse solution and efficient manipulation of these elements is essential for a robust inverse solution. Following the derivation of [1], we derive the model sensitivity elements by first considering a single predicted data point, d_j, consisting of either the electric or magnetic fields. Consider, for example, the x-

0-7803-3836-7/97/$10.00 © 1997 IEEE

component of the magnetic field at location j, which can be represented as

$$H_{xj} = {}^{h}\mathbf{g}^{t}_{j(x)}\mathbf{E}. \quad (2)$$

In this expression **E** is an electric field vector arising from a 3D earth model and has dimension of NTx1, where NT represents the number of electric field unknowns that are determined from the finite difference forward solution for a given source and discrete frequency [6]. The vector ${}^{h}\mathbf{g}^{t}_{j(x)}$ is an interpolator vector for the x-component of the magnetic field at the jth measurement point and is of dimension 1xNT (t here denotes the transpose operator). This vector will interpolate the sampled fields on the forward modeling grid to the measurement point and numerically includes a curl operator that is applied to the electric field. With this definition an element of the Jacobian matrix is written for the x-component of magnetic field as

$$\partial H_{xj}/\partial m_k = {}^{h}\mathbf{g}^{t}_{j(x)}\,\partial\mathbf{E}/\partial m_k. \quad (3)$$

From the forward problem [6] shows that the electric fields are determined from the linear system,

$$\mathbf{KE} = \mathbf{S}, \quad (4)$$

where **K** is the sparse finite-difference stiffness matrix with 13 non-zero entries per row and depends linearly on the electrical parameters we desire to estimate. Because the forward problem can specify boundary conditions and sources that depend on the model parameters, the source vector, S, can also depend on the model parameters. Thus differentiating equation (4) with respect to m_k yields,

$$\partial\mathbf{E}/\partial m_k = \mathbf{K}^{-1}(\partial\mathbf{S}/\partial m_k - \partial\mathbf{K}/\partial m_k\mathbf{E}). \quad (5)$$

The derivatives $\partial\mathbf{S}/\partial m_k$ and $\partial\mathbf{K}/\partial m_k$ in equation (5) are rapid to compute analytically; the interested reader is referred to [1] for the specific details. Finally, an element of the Jacobian matrix for the x-component of magnetic field can be written as

$$\partial H_{xj}/\partial m_k = {}^{h}\mathbf{g}^{t}_{j(x)}\,\mathbf{K}^{-1}(\partial\mathbf{S}/\partial m_k - \partial\mathbf{K}/\partial m_k\mathbf{E}). \quad (6)$$

Similar expressions can be derived for the other electric and magnetic field components.

Inverse Solution via Conjugate Gradients

Because of the size of the 3D inverse problem, direct methods cannot be used to repeatedly invert a full least-squares system matrix involving model sensitivity elements. However, gradient methods are feasible. The steepest-descent method is the most widely known of the gradient methods. Unfortunately the method usually converges very slowly near the minimum of the objective functional. A better approach can be the conjugate-gradient (CG) method. Linear and non-linear CG schemes are known and we have investigated both types for the 3D EM inverse problem.

Linear Conjugate Gradients

Minimization of equation (1) with respect to **m**, given a background model $\mathbf{m}^{(i)}$ needed to linearize the problem for iteration (i), yields the model update,

$$\mathbf{m} = [(\mathbf{DA}^{(i)})^{t}(\mathbf{DA}^{(i)}) + \lambda(\mathbf{W})^{t}(\mathbf{W})]^{-1}(\mathbf{DA}^{(i)})^{t}(\mathbf{D}\delta\mathbf{d}^{(i)}) \quad (7)$$

with

$$\delta\mathbf{d}^{(i)} = (\mathbf{d}^{obs} - \mathbf{d}^{(i)} + \mathbf{A}^{(i)}\mathbf{m}^{(i)}), \quad (8)$$

where the weighting matrix, **D**, is diagonal and consists of the reciprocal of the data standard deviations. The Jacobian matrix is denoted by $\mathbf{A}^{(i)}$ in the above expressions and its individual elements are given from the derivation above. The fact that the Jacobian matrix and the predicted data, $\mathbf{d}^{(i)}$, depend on the iteration count implies that they must be re-computed after each model step.

Linear conjugate gradients can be applied directly to linear systems that are symmetric positive definite, including the least squares normal equations given by equation (7). In a linear conjugate gradient method, all one needs is one matrix-vector multiplication per relaxation step. However, because the matrix given by this operation is $[(\mathbf{DA}^{(i)})^{t}(\mathbf{DA}^{(i)}) + \lambda(\mathbf{W})^{t}(\mathbf{W})]$, there are several other matrix-vector multiplications to be considered. First, the matrix product of $(\mathbf{DA}^{(i)})^{t}$ with $\mathbf{DA}^{(i)}$ requires two matrix-vector multiplications. In addition, the regularization-matrix product with its transpose requires two more matrix-vector multiplications. Since the latter matrix-vector multiplications are easy to implement and compute, no further elaboration will be given to them here.

For the Jacobian matrix-vector multiplications, $\mathbf{DA}^{(i)}$ and $(\mathbf{DA}^{(i)})^{t}$, we have

$$\mathbf{y} = \mathbf{DA}^{(i)}\mathbf{u} \quad (9)$$

and

$$\mathbf{z} = (\mathbf{DA}^{(i)})^{t}\mathbf{y}, \quad (10)$$

where **u** is an arbitrary real vector, known as a CG search direction vector. Because the data weighting and Jacobian matrices are real (we treat real and imaginary components of the data separately), the vector **y** is real with dimension 2N, where N is the number of complex data points used in the inversion. The vector **z** is real since the model parameters are assumed to be real valued. [1] give compact and

computationally efficient forms for the two matrix-vector multiplications for dipolar source fields, which are also used to treat the matrix-vector multiplications given in equations (7) and (8), i.e. $\mathbf{A}^{(l)}\mathbf{m}^{(l)}$ and $(\mathbf{DA}^{(l)})^t$ $(\mathbf{D}\delta\mathbf{d}^{(l)})$, which are needed to initialize the CG solver at each iteration of the inversion.

In addition to the forward solutions necessary to determine **E** for each source and frequency, the matrix-vector multiplications in equations (9) and (10) require solving a series of forward problems corresponding to the total number of unique data measurements locations, where

$$\mathbf{v}_j^t = \mathbf{g}_j^t \mathbf{K}^{-1}, \tag{11}$$

or since $\mathbf{K}^t = \mathbf{K}$ [1],

$$\mathbf{K}\,\mathbf{v}_j = \mathbf{g}_j. \tag{12}$$

A unique measurement location comprises the interpolator vector $\mathbf{g}_j$, which is based on the measurement of a specific field component or data type made at the site, independent of the source. Thus the total number of forward solutions needed for each model update is given by $N_{tx} + N_{rx}$, where N_{tx} and N_{rx} are the total number of sources and unique receiver positions used in the inversion at a given frequency. Note that multiple frequency data will require additional forward solutions for both the source and unique receiver positions.

To launch the inversion using the linear CG approach, we assume an initial background model and compute the predicted data for all the different sources. At the first iteration the matrix-vector multiplications needed to solve the linear least-squares system of equations are computed and equation (7) is solved using the linear CG method. We proceed to the next iteration if the data error (sum of squared errors) is above the estimated noise of the data set. If this is true the model is linearized again about the new model **m**, new predicted data and electric fields are computed from the updated background model, and the new model update is determined once the tradeoff parameter is specified.

A 3D inversion scheme using linear conjugate gradients has been successfully applied to crosswell 20 kHz electromagnetic data collected at the Richmond Field Station near Berkeley, California [2]. By comparing images of the data collected before injection of 50 000 gallons of salt water, a 3D image of the plume has been developed, which shows the location of zones of maximum permeability surrounding the injection well through which the salt water has migrated (Figure 1). A resolution analysis has determined that the location of the plume is fairly accurate. As this example clearly demonstrates, diffusive EM fields posseses the ability to map permeability changes in the subsurface.

Nonlinear Conjugate Gradients

We have found that the linear CG scheme discussed above is optimal when many sources are employed as in a crosswell survey. For natural source fields (magnetotelluric applications) there is, however, a better approach based on non-linear conjugate gradients.

To use non-linear conjugate gradients for solving $\nabla\varphi = 0$ demands that we make two subsidiary calculations at each iteration of the procedure. First we calculate the gradient of the objective functional in equation (1)

$$\nabla\varphi = \nabla\varphi_d + \lambda\nabla\varphi_m, \tag{13}$$

where φ_d and φ_m are functionals that relate to the data misfit and the model constraint. Second we minimize φ along a specified ray, that is, find the value of α that minimizes the expressions $\varphi(\mathbf{m} + \alpha\mathbf{u})$ for specified model parameters **m** and conjugate search direction **u**.

Consider first computing a specific element of $\nabla\varphi_d$ and let us define the difference between observed and predicted data as

$$\Delta d_j = \{(d_j^{obs} - d_j)/\varepsilon_j\}, \tag{14}$$

thus

$$\partial\varphi_d/\partial m_k = -2 \sum_{j=1}^{N} \Delta d_j \; \partial d_j/\partial m_k. \tag{15}$$

Therefore, in general, we can then write from equation (6)

$$\partial\varphi_d/\partial m_k = -2 \sum_{j=1}^{N} \Delta d_j \; \boldsymbol{g}_j^t \cdot \mathbf{K}^{-1}(\partial S_1/\partial m_k - \partial\mathbf{K}/\partial m_k\mathbf{E}) \tag{16}$$

where the interpolator vector $\boldsymbol{g}_j^t$ is based on the data type. Evaluation of $\nabla\varphi_m$ leads to

$$\nabla\varphi_m = 2\mathbf{W}^t\mathbf{W}\mathbf{m}. \tag{17}$$

It is now possible to show that the number of forward solves needed to evaluate the gradient in equation (16) is only two for each source and frequency. One solve is needed to obtain the electric fields **E** of a specified source and another solve is needed to compute the fields arising from the following source

$$\mathbf{g}^t = -2 \sum_{j=1}^{N} \Delta d_j \, \boldsymbol{g}_j^t. \tag{18}$$

Fields for this source distribution are obtained following equations (11) and (12).

Extension of equation (16) to include multiple sources is easy, where the gradients for a full set of data are just the sum of gradients for each independent source position and frequency. Thus the total number of forward modeling applications necessary to evaluate (16) is twice the number of sources at each discrete frequency.

Because a line search is needed to minimize $\varphi(\mathbf{m} + \alpha\mathbf{u})$, this will require additional forward solutions. [7] provides a number of strategies to carry out the line search, where the number of forward modeling applications varies. A reliable approach to conduct the line search is to use both functional and derivative information at two points, fit a cubic through these points and step immediately to the minimum. The number of forward modeling applications required for this type of line search is four per frequency. However, half of the required information is already known due to the previous model update. Thus only two additional applications of the forward modeling code at each source and frequency are required.

Listed below is an outline of the nonlinear CG method based on the algorithm [8] that will be used in this analysis:

(1) choose $\mathbf{m}_{(1)}$ and select $\mathbf{u}_{(1)} = -\nabla\varphi(\mathbf{m}_{(1)})$
(2) find $\alpha(i)$ that minimizes $\varphi(\mathbf{m}_{(i)} + \alpha(i)\,\mathbf{u}_{(i)})$
(3) set $\mathbf{m}_{(i+1)}=\mathbf{m}_{(i)}+\alpha(i)\,\mathbf{u}_{(i)}$) and $\mathbf{r}_{(i+1)} =-\nabla\varphi(\mathbf{m}_{(i+1)})$
(4) $\beta_{(i+1)} = \max\{(\mathbf{r}_{(i+1)}^{T}\mathbf{r}_{(i+1)}-\mathbf{r}_{(i+1)}^{T}\mathbf{r}_{(i+)})/\mathbf{r}_{(i)}^{T}\mathbf{r}_{(il)}\,,\ 0\}$
(5) $\mathbf{u}_{(i+1)} = \mathbf{r}_{(i+1)} + \beta_{(i+1)}\,\mathbf{u}_{(i)}$
(6) Stop when $|\,\mathbf{r}_{(i+1)}\,|$ is sufficiently small, otherwise go to step (2).

The convergence of this scheme can also be accelerated by including preconditioning. The interested reader is referred to [9] for the details.

ACKNOWLEDGMENTS

This work was performed at Sandia National Laboratories, which is operated for the United States Department of Energy (DOE). Funding for the work was provided by DOE's office of Basic Energy Sciences, Division of Engineering and Geoscience, under contract DE-AC04-94AL85000.

REFERENCES

[1] Newman G. A., and Alumbaugh D. L., 1997, Three-dimensional massively parallel electromagnetic inversion - I. Theory: Geophysical Journal International, **128**, 345-354.

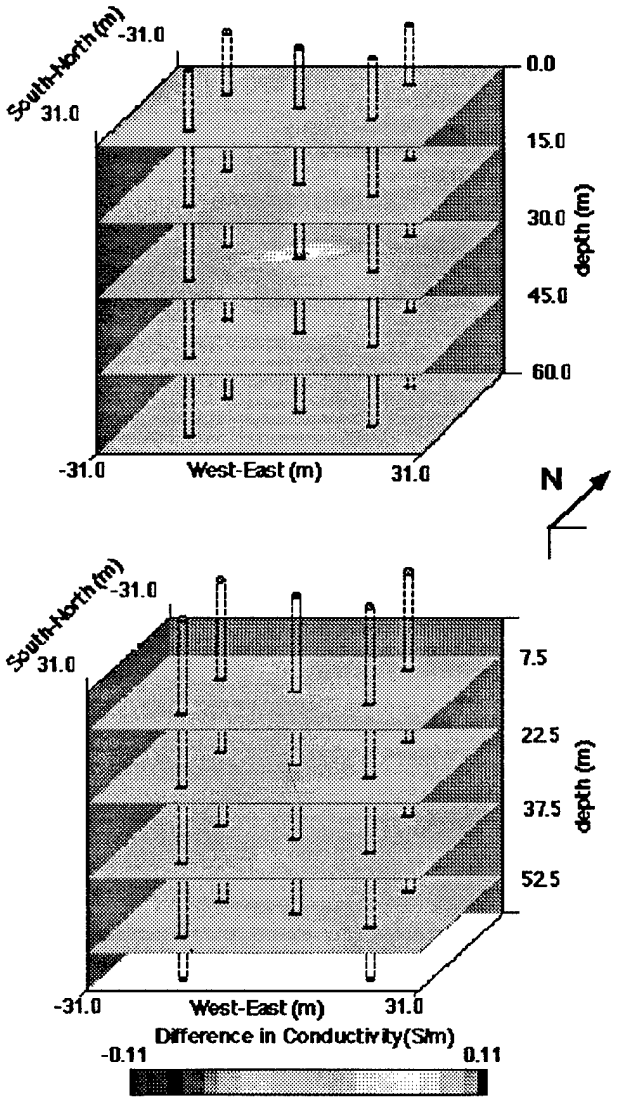

Figure 1. Difference image between pre- and post-injection of 50,000 gallons of 1 Ω.m saltwater near 30 m depth. Two views of the same reconstruction are included such that horizontal slices, showing how the conductivity has changed, can be shown at nine different depths, with the back and left-side panels showing how the change varies continuously with depth. The four observation wells are shown surrounding the injector well shown at the center. Vertical magnetic field receivers were deployed in the observation well from the surface to 60 m depth at 5 m intervals. An 18.5 kHz vertical magnetic dipole was used as the transmitter and was placed in the injector well. The transmitter was moved in 2.5 m increments from 5 to 60 m depth in the crosswell experiment. Refer to [2] for additional details. Notice that the salt-water plume is clearly observed in the difference image near 30 m depth.

[2] Alumbaugh D. L., and Newman G. A., 1997, Three-dimensional electromagnetic inversion - II. Analysis of a crosswell electromagnetic experiment: Geophysical Journal International, **128**, 355-363.

[3] Newman G. A., and Alumbaugh D. L., 1997, 3D Electromagnetic Modeling and Inversion on Masively Parallel Computers: In Press, In *3D Electomagnetics*, Investigations in Geophysics Series, Society of Exploration Geophysicists, Tulsa OK.

[4] Alumbaugh, D. L., and Newman, G. A., 1997b, 3-D electromagnetic inversion for environmental site characterization, In R. S. Bell, editor, Proceedings of the Symposium on the Application of Geophysics to Engineering and Environmental Problems, SAGEEP '97, March 23 to 26, 1997, Reno, NV., Environment Engineering Geophysical Society, Wheat Ridge, CO, 355-364.

[5]Wang T., Orstaglio M., Tripp A., and Hohmann G., 1994, Inversion of diffusive transient electromagnetic data by a conjugate-gradient method: Radio Science, **29**, 1143-1156.

[6] Alumbaugh D. L., Newman G. A., Prevost L., and Shadid, J. N., 1996, Three-dimensional wideband electromagnetic modeling on massively parallel computers: Radio Science, **31**, 1-23.

[7]Acton F. S., 1970, *Numerical Methods that Work*, Harper and Row, New York.

[8] Polyak E., and Ribiere, 1969, Note sur la convergence des méthods conjugées: Rev. Fr. Inr. Rech. Oper., 16, 35-43.

[9] Shewchulk, J., R., An introduction to the conjugate gradient method without agonizing pain: School of Computer Sciences, Carnegie Mellon University, Pittspurg, PA. Electronic copy of the article is available by anonymous FTP to WARP.CS.CMU.EDU (IP address 128.2.209.103) under the file name quake-papers/painless-conjugate-gradient-ps.

INVERSION OF 6FF40 INDUCTION TOOL MEASUREMENT USING THE DISTORTED BORN ITERATIVE METHOD

Siyuan Chen* and Weng Cho Chew

Electromagnetics Laboratory
Center For Computational Electromagnetics
Department of Electrical and Computer Engineering
University of Illinois
Urbana, IL 61801

W. D. Kennedy

Mobil Exploration and Producing Technical Center
P.O.Box 819047
Dallas, TX 75381-9047

Abstract

In this paper, the Gauss-Laguerre method is used to perform the Sommerfeld integration for obtaining the response of 6FF40 in layered lossy media. The distorted Born iterative method is used to reconstruct the profile from the measurement data. The results show good agreement with those obtained by using other methods.

1. Introduction

The 6FF40 is a long-used industry-standard tool for the estimation of oil reserves [1,2]. This instrument can be used to measure the formation resistivity. It is based on the electromagnetic induction principle and uses a symmetrical six-coil antenna array. The response of these arrays can be adequately represented by modeling the subsurface as a one-dimension horizontally layered media. The main challenge is to calculate the Sommerfeld integration. Because of the damped kernels, we can use the Gauss-Laguerre method to perform the integration efficiently. By choosing the parameter properly, less than fifteen integration points yields accurate results.

We are interested in the reconstruction of the formation from the measurement data. Since the receiver signal is a nonlinear function of the formation conductivity, we have to solve a nonlinear inverse problem. The solution can be found by using Newton's method. We first give the initial values and then linearize the equation in each step. The Distorted Born Iterative Method (DBIM) can provide this approach and has a second order convergence. In our case, even though the formation is complicated, the results converge after five to six iterations with error less than 0.1 percent.

2. Formulation

2.1. Forward Problem

The induction tool is an axisymmetric measurement where no azimuthal variation of the conductivity is assumed. The 6FF40 is a coil array with three transmitters and three receivers as shown in Figure 1.

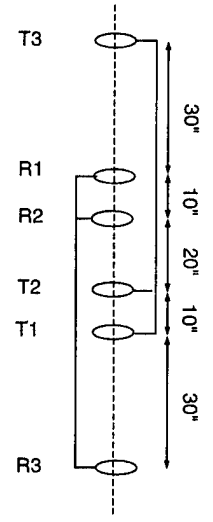

Fig.1 The 6FF40 array

Each transmitter can be simulated as a small electric current loop antenna and the E_ϕ component satisfies the following equation [3]

$$\left(\frac{\partial}{\partial\rho}\frac{1}{\rho}\frac{\partial}{\partial\rho}\rho+\frac{\partial^2}{\partial z^2}+k^2\right)E_\phi =$$

0-7803-3836-7/97/$10.00 © 1997 IEEE

$$-i\omega I\mu_0\delta(\rho-\rho')\delta(z-z'), \quad (1)$$

where

$$k^2 = i\omega\mu(\sigma - i\omega\epsilon). \quad (2)$$

The solution of Equation (1) can be written in the form of a Sommerfeld integral as :

$$E_\phi = \Big(-\frac{IA\omega\mu}{4\pi}\Big)\int_0^\infty J_1(k_\rho\rho)\frac{{k_\rho}^2}{k_{nz}} \times F(z,z',k_\rho)\,dk_\rho, \quad (3)$$

where A is the area of the small electric current loop and $F(z,z',k_\rho)$ is a function which depends not only on the k_ρ but also on z and z', as well as the conductivity of each layer. Since only the field on the axis is of interest and the frequency is low, Equation (3) can be simplified as

$$E_\phi = \Big(-\frac{IA\omega\mu}{4\pi}\Big)\int_0^\infty \frac{{k_\rho}^3\rho'}{2k_{nz}}F(z,z',k_\rho)\,dk_\rho. \quad (4)$$

To obtain the response of the 6FF40, we evaluate the integration numerically. Because of the damped kernel, it can be done by using the Gauss-Laguerre method. For convenience, we let $x = k_\rho/c$ and rewrite (4) as

$$E_\phi = \frac{IA\omega\mu\rho'}{8\pi c^4}\int_0^\infty e^{-x}\Big(\frac{x^3e^{-x}F(z,z',x)}{k_{nz}}\Big)\,dx. \quad (5)$$

By properly choosing the parameter c, we can control the variation of the kernel, and hence, use no more than fifteen points to capture all the variations.

The 6FF40 has three transmitters and three receivers, so the total response can be obtained by a superposition of nine transmitter-receiver pairs. In induction logging, we use the effective conductivity rather than electromagnetic field to describe the measurement data. By using the geometrical factor theory [2], we establish a linear relationship between the E_ϕ and the effective conductivity σ_e as

$$\sigma_e = \frac{-4\pi V}{I\omega^2\mu^2\pi^2{\rho'}^4\sum_{i=1}^3\sum_{j=1}^3\frac{T_jR_i}{L_{ij}}}, \quad (6)$$

where $V = 2\pi\rho' E_\phi$. T_j and R_i are the numbers of turns wound on the mandrel of radius ρ' and L_{ij} is the distance between the transmitter and receiver.

2.2. Inverse Problem

To reconstruct the profile from the measurement data, we use the distorted Born iterative method. Generally, the E_ϕ field which is excited by the transmitter j and received by receiver i can be written as the following integral equation [3,4]

$$g(r_i,r_j',\epsilon) = g^{inc}(r_i,r_j',\epsilon_b) + \int g(r_i,r'',\epsilon_b)g(r'',r_j',\epsilon_b)\delta k^2\,dr'', \quad (7)$$

where

$$\delta k^2 = \omega^2\mu(\epsilon-\epsilon_b) \simeq i\omega\mu(\sigma-\sigma_b), \quad (8)$$

$$g(r'',r_j',\epsilon_b) = \frac{i\rho_j'}{2}\int_0^\infty \frac{k_\rho}{k_z}J_1(k_\rho\rho'')J_1(k_\rho\rho_j') \times F(z'',z',k_\rho)\,dk_\rho. \quad (9)$$

For convenience, we choose the effective conductivity as the variable which is given by

$$\sigma_e = \sum_{i,j} t_{ij}g(r_i,r_j',\epsilon). \quad (10)$$

Consequently, we rewrite the integral equation (7) as

$$\sigma_e = \sigma_{e,b} + i\omega\mu\int \delta\sigma(r'') \times \sum_{ij} g(r_i,r'',\epsilon_b)g(r'',r_j',\epsilon_b)t_{ij}\,dr''. \quad (11)$$

Since we already know the the position of each layer, the integration with respect to z'' can be evaluated analytically. If we assume

$$\delta\sigma(z'') = \sum_{n=1}^N a_nB_n(z''), \quad (12)$$

where

$$B_n(z'') = \begin{cases} 1, & -d_n < z'' < -d_{n-1}, \\ 0, & \text{otherwise}, \end{cases} \quad (13)$$

then the integral equation can be writen as

$$\sigma_e = \sigma_{e,b} + \sum_{n=1}^N a_ni\omega\mu\int_{-d_n}^{-d_{n-1}} dz''\int_0^\infty d\rho'' \times \sum_{i,j} g(r_i,r'',\epsilon_b)g(r'',r_j',\epsilon_b)t_{ij}. \quad (14)$$

The above measurement can be performed at different sonde locations, so we can write the discretized integral equation in a set of linear equations as

$$\sigma_{e,l} = \sigma_{b,e,l} + \sum_{n=1}^{N} a_n c_{ln}, \tag{15}$$

or in the matrix form

$$\delta\boldsymbol{\sigma}_e = \bar{c} \cdot a, \tag{16}$$

where $\delta\boldsymbol{\sigma}_e = \boldsymbol{\sigma}_e - \boldsymbol{\sigma}_{e,b}$.

To solve the above equation, we use the Tikhonov regularization procedure and obtain the following equation [3]

$$\bar{c}^{\dagger} \cdot \delta\boldsymbol{\sigma}_e = (\bar{c}^{\dagger} \cdot \bar{c} + \lambda\bar{I}) \cdot a. \tag{17}$$

Equation (17) can be solved with the help of the conjugate gradient method. λ is the regularization parameter and can be chosen to be zero in our case. In the spirit of DBIM, the newly obtained conductivity can be used as the background for the next iteration, and the above procedure can be repeated until convergence is reached.

3. Numerical Results

To show the damping property of the integrand in Equation (5), we calculate it by using different c. The results are shown in Figure 2 and Figure 3, from which we can see that ten to fifteen points are enough to capture all the variations.

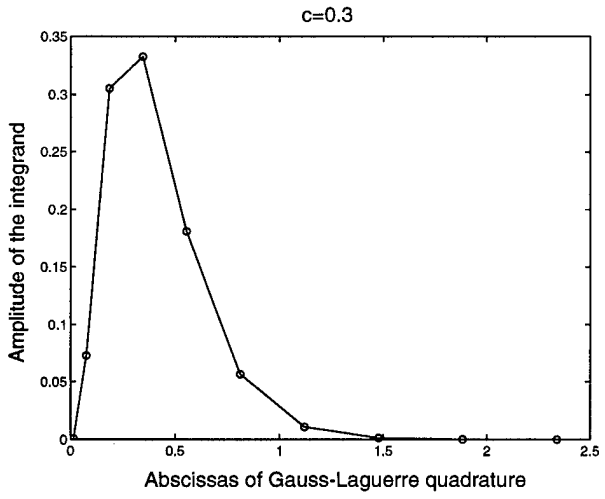

Fig.2 The amplitude of the integrand with $c = 0.3$.

Based on the above analysis, we calculate the response of 6FF40. The model we used is an Oklahoma benchmark resistivity profile and the results are shown

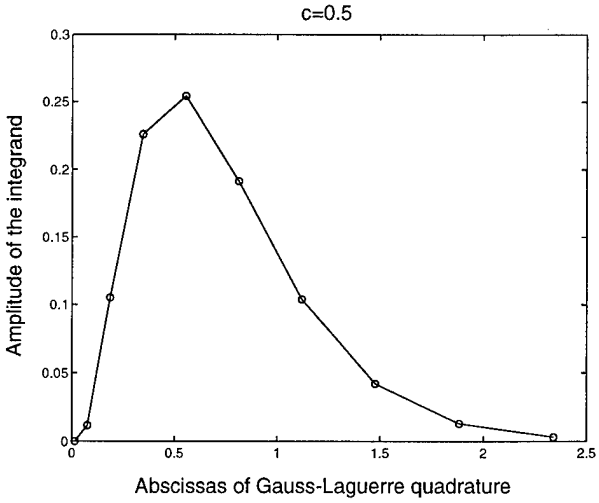

Fig.3 The amplitude of the integrand with $c = 0.5$.

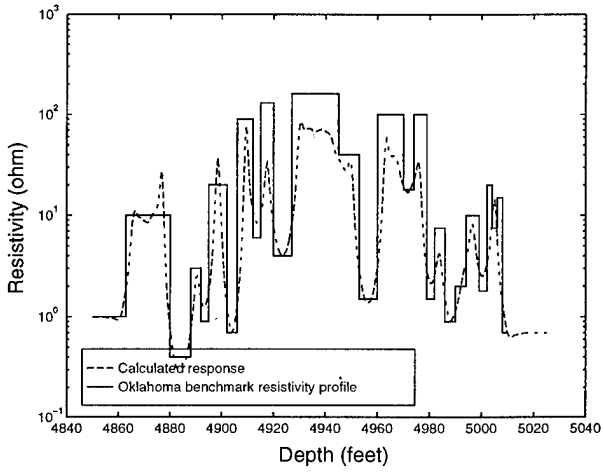

Fig.4 The Oklahoma benchmark resistivity profile and the 6FF40 response.

in Figure 4. Additional techniques with skin-effect correction and three-point deconvolution [5] are also used to obtain the final results [1].

The results show good agreement with the data provided by Mobil company and the code is two to three times faster than the one using the fast Hankel transform (FHT) method [1].

We have applied the DBIM to solve the inverse problem for the 6FF40. First, the forward code is used to generate synthetic data for the Oklahoma benchmark resistivity profile and then give an initial guess of a homogeneous formation. Finally, DBIM is used to obtain the correction to the initial guess. The newly obtained profile is used as the background conductivity and the same procedure repeated again. After five iterations, the solution

converges with error less than 0.1 percent. The reconstructed profile at different iteration are shown in Figure 5 and Figure 6.

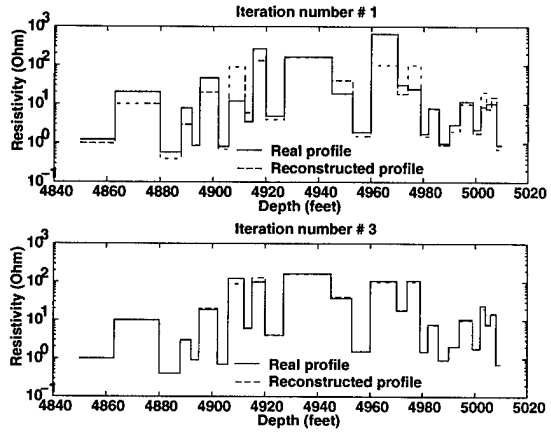

Fig.5 The reconstructed profile at 1 and 3 iterations

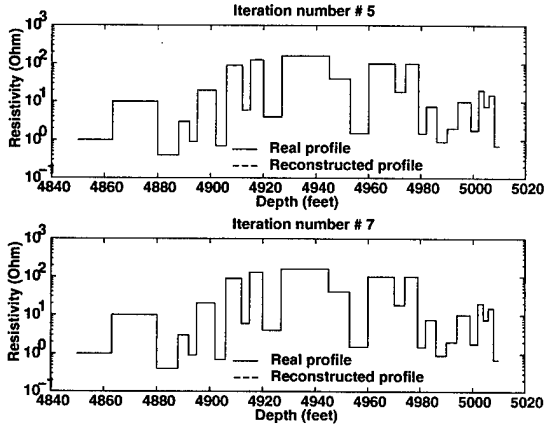

Fig.6 The reconstructed profile at 5 and 7 iterations

We have also investigated another model with 7 layers. The solution converges faster than the former one and only takes three iterations.

4. Conclusion

We have demonstrated the use of Gauss-Laguerre integration together with the DBIM to solve both the forward and inverse problem for the induction tool 6FF40. They are proven to be very effective in this case. When we solve the inverse problem, a negative conductivity profile sometimes ensues in the first several iterations. This is understood as Gibbs' phenomenon [4]. These negative values should be removed before they are used in the next iteration as the background conductivity.

5. References

[1] W. D. Kennedy, R. H. Hardman, "Rapid and accurate method for the computation of one-dimensional 6FF40 induction log responses in horizontally layered media", Submitted to *Geophysics.*

[2] J. H. Moran, K. S .Kunz, "Basic theory of induction Logging and application to study of two-coil sondes", *Geophys.*, vol. 27, no. 6, pp. 829-858, 1962

[3] W. C. Chew, "*Waves and Fields in Inhomogeneous Media*", Chapter 2 and Chapter 9, IEEE press, 1995.

[4] W. C. Chew, Q. H. Liu, "Inversion of induction tool measurements using the distorted Born iterative method and CG-FFHT", *IEEE Trans. Geoscience and Remote Sensing*, vol. 32, no. 4, July 1994.

[5] L. C. Shen, "Effects of skin-effect correction and three-point deconvolution on induction logs", The Log Analyst, July-August issue, p. 217, 1989.

A New Numerical Method for Large-Scale Complex Media: The PSTD Algorithm

*Q. H. Liu**

Klipsch School of Electrical and Computer Engineering
New Mexico State University
Las Cruces, NM 88003, USA
Phone: (505) 646-5976; Fax: (505) 646-1435
Email: qhliu@nmsu.edu

ABSTRACT

Conventional finite-difference time-domain (FDTD) methods are very inefficient for simulations of electromagnetic wave propagation in large-scale complex media. This is mainly because of the low-accuracy associated with the spatial discretization in the FDTD methods. As a result, even for a moderate size problem, a large number of cells (typically 10–20 cells per wavelength) are required to obtain reasonably accurate results. This requirement becomes much more stringent for large-scale problems since the dispersion error grows rapidly with the propagation distance. We recently developed a pseudospectral time-domain (PSTD) method which requires only two cells per wavelength regardless of the problem size. In terms of the spatial discretization, this method is an optimal time-domain solution since it has an infinite order of accuracy in the spatial representation. For a problem of size 32 to 512 wavelengths in each dimension, the PSTD method is at least 4^D–32^D times more efficient than the FDTD method (where D is the dimensionality of the problem). For larger problems, the advantage of the PSTD method becomes even more profound. Therefore, the PSTD method is ideal for simulations of electromagnetic wave propagation in large-scale complex media.

1. INTRODUCTION

Large-scale complex media are encountered in many applications. The simulation of electromagnetic wave propagation in such media is a great challenge even with modern supercomputers. For example, with the conventional FDTD methods, a large-scale 3-D problem of size $128\lambda \times 128\lambda \times 128\lambda$ is apparently still beyond the reach of modern supercomputers.

This work addresses the important problem of simulating large-scale three-dimensional problems for subsurface radar applications in complex media. The most popular method in simulations of subsurface radar applications is the Yee's finite-difference time-domain (FDTD) method. In this method, the spatial and temporal derivatives in Maxwell's equations are approximated by finite differences within a staggered grid. Hence the FDTD method has a second-order accuracy in both spatial and temporal derivatives. Numerical experiments show that accurate results for even a problem of moderate size require a fine discretization of about 10–20 cells per wavelength at the highest frequency being simulated. This stringent requirement severely limits the size of problems solvable on a computer with a given memory and computation speed.

We develop a pseudospectral time-domain (PSTD) method which allows a coarse discretization of only two cells per wavelength, drastically increasing the size of problems solvable. The PSTD method uses a fast Fourier transform (FFT) algorithm, instead of finite differences in the conventional FDTD method, to represent spatial derivatives. Since the Fourier transform has an infinite order of accuracy, it requires only two cells per wavelength as dictated by the Nyquist sampling theorem. The wraparound effect, a major limitation caused by the periodicity assumed in the FFT, is removed by using Berenger's perfectly matched layers. For large three-dimensional problems, the PSTD algorithm is orders of magnitude more efficient than the FDTD methods in terms of computer memory and computation time.

2. THE PSTD ALGORITHM

Using a coordinate-stretching variable $e_\eta = a_\eta + i\frac{\omega_\eta}{\omega}$ to incorporate perfectly matched layers for conductive media [5], we derive the split Maxwell's equations ($\eta = x, y, z$)

$$a_\eta \epsilon \frac{\partial \mathbf{E}^{(\eta)}}{\partial t} + (a_\eta \sigma + \omega_\eta \epsilon)\mathbf{E}^{(\eta)} + \omega_\eta \sigma \int_{-\infty}^{t} \mathbf{E}^{(\eta)} dt = \frac{\partial}{\partial \eta}(\hat{\eta} \times \mathbf{H}) - \mathbf{J}^{(\eta)}, \quad (1)$$

*This work was supported by a Presidential Early Career Award for Scientists and Engineers (PECASE) through EPA and by Sandia National Laboratories under the SURP program.

0-7803-3836-7/97/$10.00 © 1997 IEEE

$$a_\eta \mu \frac{\partial \mathbf{H}^{(\eta)}}{\partial t} + \mu \omega_\eta \mathbf{H}^{(\eta)} = -\frac{\partial}{\partial \eta}(\hat{\eta} \times \mathbf{E}) - \mathbf{M}^{(\eta)}, \quad (2)$$

where $\mathbf{E} = \sum_{\eta=x,y,z} \mathbf{E}^{(\eta)}$ and similarly for other field components. Equations (1) and (2) consist of a total of 12 scalar equations, since both $\mathbf{E}^{(\eta)}$ and $\mathbf{H}^{(\eta)}$ have two scalar components perpendicular to $\hat{\eta}$.

The FFT algorithm is used to represent the spatial derivative in (2) to yield

$$a_\eta \mu \frac{\partial \mathbf{H}^{(\eta)}}{\partial t} + \mu \omega_\eta \mathbf{H}^{(\eta)} = \hat{\eta} \times \mathcal{F}_\eta^{-1}\{ik_\eta \mathcal{F}_\eta[\mathbf{E}]\} - \mathbf{M}^{(\eta)}, \quad (3)$$

where $\mathcal{F}_\eta$ and $\mathcal{F}_\eta^{-1}$ denote forward and inverse Fourier transforms in the η direction which are calculated by FFT's. A similar result can be obtained for (1). As seen from above, the PSTD method is used to approximate the spatial derivatives of the tangential field components which are continuous even at the material discontinuities (except at the boundary of a perfect conductor, which requires further research). This smoothness guarantees the effectiveness of the PSTD method even for media with discontinuities.

In contrast to the standard Yee's algorithm, the PSTD method uses a spatially centered grid where all field components are located at the same points. This provides an important advantage over the Yee's algorithm since the material properties are not altered by the presence of the staggered grid. The temporal grid, however, is staggered in the same way as in the FDTD method. In the PSTD algorithm, perfectly matched layers are implemented at the outer edge as the absorbing boundary condition to eliminate the wraparound effect.

For simplicity, we analyze the dispersion relation and the stability condition of the PSTD algorithm for a plane wave in a homogeneous, non-conductive medium. The dispersion relation for a propagating plane wave is given by the propagating wave as

$$k = \frac{2}{c\Delta t} \sin \frac{\omega \Delta t}{2}. \quad (4)$$

According to the Nyquist sampling theorem, the FFT algorithm provides exact representation for $|k_\eta| \leq \pi/\Delta\eta$, where $\Delta\eta$ is the cell size in the $\hat{\eta}$ direction. Therefore, as long as $\omega\Delta t/2 \ll 1$, (4) reduces to the exact dispersion relation for the plane wave. The stability criterion of the PSTD scheme can be derived from the dispersion analysis as

$$\frac{c\Delta t}{\Delta x} \leq \frac{2}{\sqrt{D}\pi}. \quad (5)$$

where D is the dimensionality. Given the same cell size Δx, the stability criterion in (5) for the PSTD algorithm is more stringent than that for the FDTD method only by a factor of $\pi/2$. However, considering the fact that for the same accuracy, the FDTD method requires much finer cells than the PSTD algorithm, the time step for the PSTD algorithm can be chosen equal to or larger than that in the FDTD method.

3. NUMERICAL RESULTS

Figs. 1(a) and 1(b) compare the dispersion relations in the FDTD, MRTD (multiresolution time-domain) [6], and PSTD algorithms with the exact dispersion relation for a one-dimensional problem. The relative error in the normalized wavenumber $K = k\lambda_{min}$ is shown as a function of the normalized frequency $W = \omega\lambda_{min}/c$ (where λ_{min} is the minimum wavelength corresponding to the highest frequency). The grid density (number of cells per minimum wavelength λ_{min}) is 8 and 32 for the second-order FDTD algorithm in Figs. 1(a) and 1(b), respectively. However, for the MRTD, PSTD, and the 14th-order FDTD algorithms, the grid density is 2 for both Figs. 1(a) and 1(b). It is seen that as the grid density increases from 8 to 32, the second-order FDTD algorithm significantly improves the accuracy in its dispersion relation. The relative error in K becomes comparable to that in the 14th-order FDTD algorithm with a grid density of 2. The accuracy of the newly developed MRTD algorithm with a grid density of 2 is comparable to that in the second-order FDTD algorithm with a grid density of 8.

It is observed that among all the curves in Figs. 1(a) and 1(b), the PSTD algorithm with a grid density of 2 has the highest accuracy in dispersion. The small dispersion error comes from the approximation in temporal derivative. Indeed, the PSTD algorithm is an optimal time-domain solution in the sense that it requires the minimum spatial sampling rate while maintaining the highest accuracy in its dispersion relation.

This advantage of the PSTD algorithm is important for simulating large-scale complex problems. To illustrate this point, the propagation of electromagnetic waves in a three-layer one-dimensional problem is simulated in Fig. 2. An air layer is surrounded by a dielectric background with $\epsilon_r = 4$, and the layer interfaces are at $x = 3$ and $x = 6$ m. A source exciting E_y is located at $x = 9.6$ m, and the propagation of waves is simulated over a long distance from $x = 0$ to $x = 153.6$ m (or about $512\lambda_{min}$). It is well known that for the FDTD algorithm to obtain accurate results, the grid density has to be increased with the increasing size of the problem. Figs. 2(a) and 2(b)

show that with a receiver at $x = 15.0$ m, or $468\lambda_{min}$ away from the source, even with a grid density of 16, the FDTD algorithm has a large dispersion error. The maximum relative error in the waveform is about 26%. As also shown in Figs. 2(a) and 2(b), with an increased grid density of 32, the relative error in waveform decreases to 8.5%, still too high to be acceptable for many applications. However, with the PSTD algorithm, even with a grid density of 2, the waveform is accurate to within 0.8%, as shown in Figs. 2(c) and 2(d).

Earlier we found that for a moderate problem size of 32λ in each dimension, the PSTD algorithm is about 4^D times more efficient than the FDTD method, where D is the dimensionality of the problem. From the above example, it is seen that when the problem size is increased to 512λ in each dimension, the PSTD algorithm is at least 32^D times more efficient than the FDTD method. For a three-dimensional problem of size $512\lambda \times 512\lambda \times 512\lambda$, it suggests that the PSTD method is at least 30,000 times more efficient than the FDTD method.

4. CONCLUSIONS

We have developed a pseudospectral time-domain (PSTD) algorithm to simulate electromagnetic waves in inhomogeneous, conductive media. This optimal time-domain algorithm requires only two cells per wavelength because the Fourier transform (through an FFT algorithm) is used to represent spatial derivatives. The wraparound effect caused by the use of FFT is eliminated by using Berenger's perfectly matched layers (PML). Numerical experiments show that for a comparable accuracy, the PSTD algorithm is 4^D–32^D times more efficient than FDTD methods (D is the dimensionality of the problem) for a problem of size 32λ to 512λ in each dimension. The advantage of the PSTD algorithm becomes even more profound for larger problems. The PSTD method is ideal for parallel computation of large-scale problems since both the FFT and the PML are well-suited for parallelization.

REFERENCES

[1] Q. H. Liu, "A spectral-domain method with perfectly matched layers for time-domain solutions of Maxwell's equations," 1996 URSI Meeting, Baltimore, MD, July 1996.

[2] Q. H. Liu, "The PSTD algorithm: a time-domain method requiring only two cells per wavelength," *Microwave Opt. Tech. Lett.*, vol. 10, no. 6, June 1997.

[3] S. A. Orszag, "Comparison of pseudospectral and spectral approximation," *Stud. Appl. Math.* , vol. 51, pp. 253–259, 1972.

[4] J.-P. Berenger, "A perfectly matched layer for the absorption of electromagnetic waves," *J. Computational Physics*, vol. 114, pp. 185–200, 1994.

[5] Q. H. Liu, "An FDTD algorithm with perfectly matched layers for conductive media," *Micro. Opt. Tech. Lett.*, vol. 10, no. 2, pp. 134–137, 1997.

[6] M. Krumpholz, and L. P. B. Katehi, "New prospects for time domain analysis," *IEEE Microwave Guided Wave Lett.*, vol. 5, no. 11, pp. 382–384, 1995.

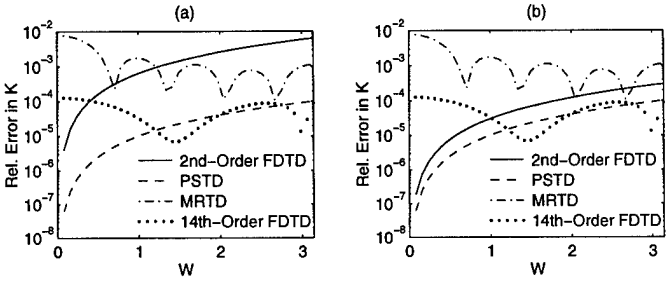

Fig. 1. Relative dispersion errors in the PSTD, MRTD, second-order FDTD, and 14th-order FDTD algorithms. The grid density is two cells per wavelength in PSTD, MRTD, and the 14th-order FDTD algorithms, while 8 and 32 cells per wavelength for the second-order FDTD in (a) and (b), respectively.

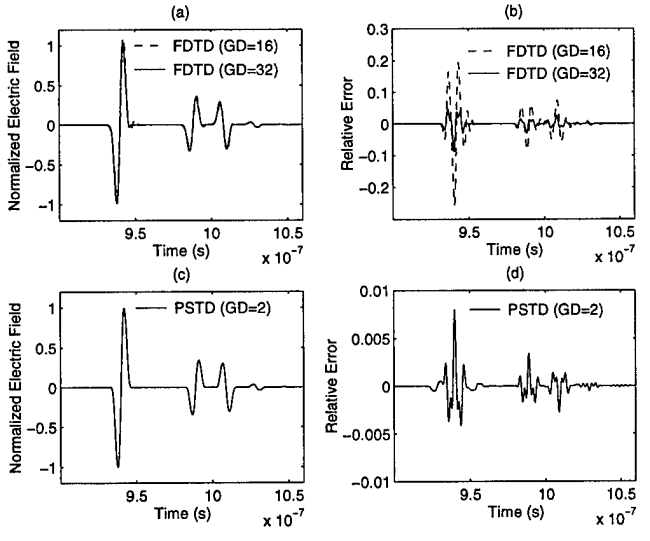

Fig. 2. PSTD and FDTD results at 140.4 m (or $468\lambda_{min}$) away from the source. Waveforms (a) and their relative errors (normalized with the peak value) (b) from the FDTD algorithm with a grid density of 16 and 32, respectively. Waveform (c) and its relative error (d) from the PSTD algorithm with a grid density of 2.

3D PML-FDTD Simulation of Ground Penetrating Radar on Dispersive Earth Media

F. L. Teixeira[†1], W. C. Chew[†2], M. Straka[‡], M. L. Oristaglio[*], T. Wang[*]
[†]Center for Computational Electromagnetics, Department of Electrical and Computer Engineering
[‡]National Center for Supercomputing Applications
University of Illinois, Urbana IL 61801-2991 USA
[1]fteixeir@cspark.ece.uiuc.edu, [2]w-chew@uiuc.edu
[*]Eletromagnetics Department, Schlumberger-Doll Research, Old Quarry Road, Ridgefield, CT 06877 USA

Abstract—**A 3D finite-difference time-domain simulation of ground penetrating radar (GPR) is described. The soil material is characterized by inhomogeneities, conductive loss and strong dispersion. The dispersion is modelled by a N-th order Lorentz model and implemented by recursive convolution. The Perfectly Matched Layer (PML) is used as an absorbing boundary condition (ABC). This formulation facilitates the parallelization of the code. A code is written for a 32 processor system. Almost linear speedup is observed. Results include the radargrams of buried objects.**

I. INTRODUCTION

Transient electromagnetic measurements usually require large bandwidths to resolve structures of interest. In addition, at the operating frequency range of GPR (50MHz-1GHz), soil materials can be strongly dispersive. These two facts imply that any realistic numerical simulations of GPR on these conditions should include dispersive effects.

Two recent developments in FDTD method make more feasible the direct simulation of the time domain response of EM fields in complex, dispersive media in open space. The first one is the family of techniques developed to incorporate dispersion into existing FDTD schemes. One of these is the recursive convolution technique [1]. It reduces the electric field convolution with the permittivity to a recursive relation which is updated iteratively. The dispersion is modelled by a Lorentz model which includes the Debye dispersion as a special case. The Lorentz model is causal, being consistent with the Kramers-Kronig relations. The second recent development on the FDTD method is the introduction of the Perfectly Matched Layer (PML) as an absorbing boundary condition (ABC) to simulate an open space [2,3]. Apart form its numerical efficiency, one of the major advantages of the PML over previously proposed ABCs when simulating dispersive media is that its absorption properties hold independently of the frequency, thus not requiring the knowledge of the dispersive nature of the propagating field.

This work is supported by Air Force Office of Scientific Research under MURI grant F49620-96-1-0025, Office of Naval Research under grant N00014 -95-1-0872, and National Science Foundation under grant ECS93-02145.

In this work, these two developments are combined to achieve a more realistic simulation of GPR. The PML implementation is based on the coordinate stretching approach [3].

II. FORMULATION

The generalized Maxwell's equations [3] for a PML medium read as:

$$\nabla_\sigma \times \vec{E} = i\omega\vec{B}, \qquad \nabla_\sigma \times \vec{H} = -i\omega\vec{D} + \sigma\vec{E}, \tag{1}$$

where $\nabla_\sigma = \hat{x}\frac{1}{s_x}\partial_x + \hat{y}\frac{1}{s_y}\partial_y + \hat{z}\frac{1}{s_z}\partial_z$, and $s_\zeta(\zeta) = a(\zeta) + i\frac{b(\zeta)}{\omega}$ are the complex stretching variables. The vacuum is a special case of a PML. The interface between two PML media is reflectionless in the continuum space for all frequencies and angles of incidence [2,3]. The time domain equations are obtained after a field splitting as follows:

$$-(a_\zeta\partial_t + b_\zeta)\vec{B}_{s_\zeta} = \partial_\zeta\hat{\zeta}\times\vec{E}, \tag{2}$$

$$(a_\zeta\partial_t + b_\zeta)\vec{D}_{s_\zeta} + a_\zeta\sigma\vec{E}_{s_\zeta} + b_\zeta\sigma\int_0^t \vec{E}_{s_\zeta}(\tau)d\tau = \partial_\zeta\hat{\zeta}\times\vec{H}, \tag{3}$$

where ζ stands for x, y and z. For an inhomogeneus, dispersive (non-magnetic) medium, $\vec{B}_{s_\zeta}(\vec{r},t) = \mu\vec{H}_{s_\zeta}(\vec{r},t)$ and $\vec{D}_{s_\zeta}(\vec{r},t) = \epsilon(\vec{r},t) * \vec{E}_{s_\zeta}(\vec{r},t)$. A Lorentzian medium is modeled by a complex susceptibility [1]

$$\hat{\chi}(\vec{r},t) = \sum_{p=1}^{P} i\gamma_p(\vec{r})e^{(-\kappa_p\omega_p - i\beta_p)t}u(t). \tag{4}$$

In the above, P is the number of species, $\beta_p^2 = (1-\kappa_p^2)\,\omega_p^2$, $\gamma_p(\vec{r}) = [\epsilon_s(\vec{r}) - \epsilon_\infty(\vec{r})]\,\frac{\omega_p G_p}{\sqrt{1-\kappa_p^2}}$, $\sum_{p=1}^{P} G_p = 1$, and $\epsilon(\vec{r},t) = \epsilon_0\epsilon_\infty(\vec{r})\delta(t) + \epsilon_0\Re e\,[\hat{\chi}(\vec{r},t)]$.

To characterize a Lorentz dispersion the condition $\kappa_p < 1$ must hold. The Debye dispersion is a specialization of the above with $\kappa_p > 1$ and the conditions $\Im m(\beta_p) < 0$ and $\Im m(\gamma_p) < 0$. It can be cast into a more familiar form:

$$\hat{\chi}(\vec{r},t) = [\epsilon_s(\vec{r}) - \epsilon_\infty(\vec{r})]\sum_{p=1}^{P}\frac{\lambda_p}{\tau_p}e^{-\frac{t}{\tau_p}}u(t), \tag{5}$$

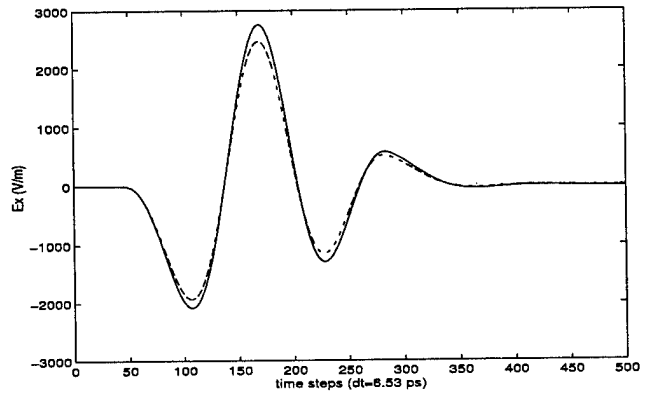

Fig. 1. Pseudo-analytical solution (dashed line) vs. FDTD solution (solid line).

with $\sum_{p=1}^{P} \lambda_p = 1$. By substituting (3) and the expression for $\epsilon(\vec{r}, t)$ in the constitutive relation and letting $t = l\Delta_t$, one arrives at:

$$\vec{D}^l = \epsilon_0 \epsilon_\infty \vec{E}^l + \epsilon_0 \sum_{p=1}^{P} \Re e \left[\hat{\chi}_p^0 \vec{Q}_p^l \right], \tag{6}$$

where $\vec{Q}$ is an auxiliary vector defined as: $\vec{Q}_p^l = \vec{E}^l + \vec{Q}_p^{l-1} e^{(-\kappa_p \omega_p - i\beta_p)\Delta_t}$, for $l > 0$. For $l = 0$, $\vec{Q}_p^0 = 0$. Replacement of time derivatives by finite differences in (4) and subsequent rearrangement for time-stepping gives:

$$\vec{B}_{s_\zeta}^{l+\frac{1}{2}} = -\Omega_\zeta^{-1} [\Delta_t (\partial_\zeta \hat{\zeta} \times \vec{E}^l) - a_\zeta \vec{B}_{s_\zeta}^{l-\frac{1}{2}}], \tag{7}$$

$$\begin{aligned} \vec{E}_{s_\zeta}^{l+1} = \tilde{\Omega}_\zeta^{-1} [\Delta_t (\partial_\zeta \hat{\zeta} \times \vec{H}^{l+\frac{1}{2}}) + \\ a_\zeta \vec{D}_{s_\zeta}^l - \sigma b_\zeta \Delta_t \vec{F}_{s_\zeta}^l - \Omega_\zeta \epsilon_0 \vec{P}_{s_\zeta}^l], \end{aligned} \tag{8}$$

where $\vec{P}^{l-1} = \sum_{p=1}^{P} \Re e \left[\hat{\chi}_p^0 \vec{Q}_p^{l-1} e^{(-\kappa_p \omega_p - i\beta_p)\Delta_t} \right]$, $\vec{F}_{s_\zeta}^l = \vec{F}_{s_\zeta}^{l-1} + \Delta_t \vec{E}_{s_\zeta}^l$, $\Omega_\zeta = a_\zeta + \Delta_t b_\zeta$, $\tilde{\Omega}_\zeta = \Omega_\zeta \alpha \epsilon_0 + a_\zeta \sigma \Delta_t$, and $\alpha \equiv \epsilon_\infty + \sum_{p=1}^{P} \Re e \left[\hat{\chi}_p^0 \right]$. The spatial discretization is done via the usual Yee scheme.

III. NUMERICAL RESULTS

To validate the 3D PML-FDTD algorithm, the field from an electric dipole above a conductive, dispersive half-space was solved pseudo-analytically by a numerical evaluation of Sommerfeld integrals for many excitation frequencies. The resultant frequency domain solution was then multiplied by the source pulse spectrum and inverse Fourier-transformed.

Fig. 1 shows the results using both formulations for a vertical electric dipole above a two-species Lorentzian half-space medium. The source and receiver coordinates are $(25,25,35)\Delta_x$ and $(15,25,25)\Delta_x$, respectively (Δ_x = 4.24 mm). The interface is at $z = 30\Delta_x$. The half-space has $\epsilon_s = 50$, $\epsilon_\infty = 5$, $\sigma = 0.3$ S/m, and Lorentz frequencies $\omega_1/2\pi = 2 \times 10^8$ Hz and $\omega_2/2\pi = 5 \times 10^8$ Hz. Also, $G_1 = 0.4$, $\kappa_1 = \kappa_2 = 0.5$. The PML has a 7 layer quadratic-profile. The excitation is a derivative of the Blackmann-Harris (BH) window function with $f_c = 1.0$ GHz. The Courant factor used is 0.8 for a time step of $\Delta_t = 6.53$ ps. The total simulation domain (including the PML layers) is a 50×50×50 grid. The receiver is deliberately buried in the half-space to make the results more sensitive to its dispersive properties. The comparison shows a good agreement between the formulations. Any differences may be attributed to inherent modelling errors such as the finite size of dipole source, the discrete approximation of Maxwell's equations and reflections due to the discretization of the PML.

The example of a GPR response consisted of a metal pipeline buried in soils with different moisture contents. The parameters for the dispersion model are obtained through a fitting of the experimental data by a two-species Debye model [4]. The experimental data used is the one reported in [5] for the Puerto Rico type clay loams. Table 1 gives the model parameters for different moisture contents. The transmitting and receiving dipoles are parallel to the metal pipe, with the former located at $(15,25,55)\Delta_x$ (Δ_x = 5 cm). The response is taken at the same y and z coordinates, but with an off-set in x varying from 0.1 m to 2.5 m. The interface is at $z = 55\Delta_x$. The pipe is buried 2 m deep and is 6 inches in diameter. The source pulse is the BH pulse with $f_c = 200$ MHz. The dielectric constant and conductivity for the non-dispersive example were taken as those at $f_c = 200$ MHz. Figs. 2–4 show that, as the moisture content is increased, the pipe echo appears later and is subject to a stronger attenuation.

A version of the code has been parallelized to run on a 32-processor SGI R10000. Fig. 5 shows the speed of the code (running a two-species dispersive model) for 1000 time steps as a function of the number of active processors. The speed is defined as the inverse of the real time on an empty machine (single-user). The problem size is 50 × 50 × 50. An almost linear speed-up up to 12 processors is observed. For this problem size, not much more speed-up past 12-15 processors is expected due to the communication overhead and load imbalance between the processors. However, for problems sizes beyond 50 × 50 × 50, increased speed-up can be expected with a larger number of active processors on this 32-processor machine.

Table 1

%	ϵ_∞	ϵ_s	σ(mS/m)	λ_1	τ_1(nsec)	τ_2(nsec)
2.5	3.20	4.25	0.397	0.71	2.71	0.108
5.0	4.15	6.55	1.11	0.75	3.79	0.151
10.0	6.00	9.50	2.00	0.79	3.98	0.251

Debye-model parameters of the Puerto Rico type clay loams as a function of moisture content.

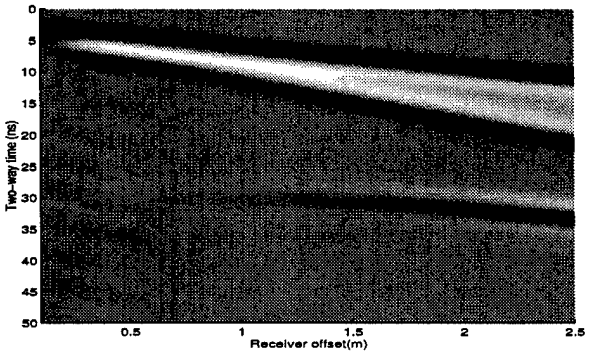

Fig. 2. FDTD simulation of the common-source radargram of a metal pipe buried on dispersive soil with 2.5 percent of moisture.

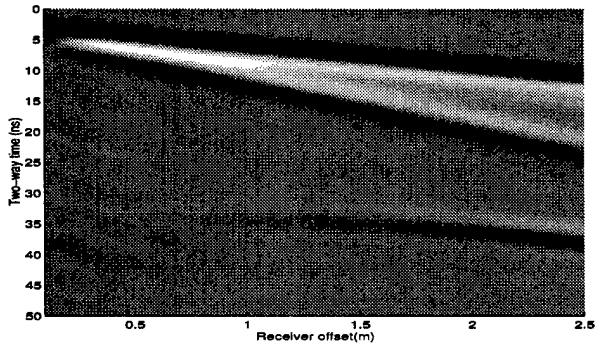

Fig. 3. FDTD simulation of the common-source radargram of a metal pipe buried on dispersive soil with 5 percent of moisture.

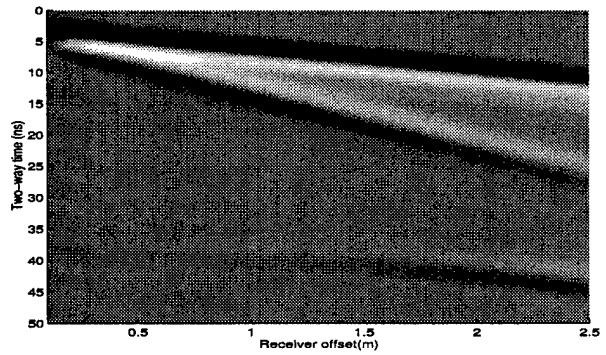

Fig. 4. FDTD simulation of the common-source radargram of a metal pipe buried on dispersive soil with 10 percent of moisture.

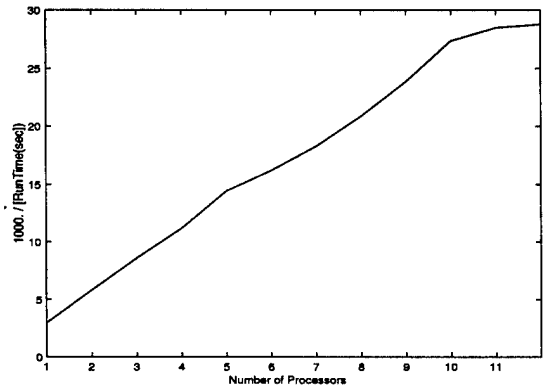

Fig. 5. Speedup of the code for 1000 time steps for different number of processors.

IV. CONCLUSION

A 3D PML-FDTD simulation of GPR on dispersive soils is described. The dipersive effect is modelled by Lorentzian and Debye terms and incorporated in the FDTD algorithm using recursive convolution. The PML implementation is based on the coordinate stretching approach. The results show that dispersion has a significant effect on the measured response, corroborating the need of its inclusion in realistic simulations of GPR on dispersive soils. The parallel version of the code shows an almost linear speed-up.

REFERENCES

[1] R. Luebbers, F. Hunsberger, "FDTD for N-th Order dispersive media," *IEEE Trans. Antennas Propagat.*, vol. 40, pp.1297-1301, 1992.

[2] J. Berenger, "A Perfect Matched Layer for the Absorption of Electromagnetic Waves," *J. Comput. Phys.*, vol. 114, pp.185-200, 1994.

[3] W. C. Chew, W. Weedon "A 3D Perfect Matched Medium from Modified Maxwell's Equations with Stretched Coordinates," *Microwave Opt. Tech. Lett.*, vol. 7 , pp.599-604, 1994.

[4] T. Wang, M. Oristaglio, W. C. Chew "Finite Difference Simulation of Ground Penetrating Radar on Dispersive Soils," SDR-EMG Research Note, 1995.

[5] J. Hipp, "Soil Electromagnetic Parameters as Functions of Frequency, Soil Density and Soil Moisture," *Proc. IEEE*, vol. 62, pp.98-103, 1974.

Title: The International Space University: Its Missions and Programs

Sunita Bali
International Space University
Parc D'Innovation, Bld Gonthier D'Andernach
67400. Illkirch. France
Tel:+33 3 88 65 54 30
Fax: +33 3 88 65 54 47
E-mail: bali@mss.isunet.edu

Abstract-- Space programs are a global undertaking of humanity in which cultural diversities can flourish and produce innovative solutions to world problems. The International Space University was founded in 1987 to respond today's challenge in space sector. ISU is dedicated to the development of space technology for peaceful purposes by offering its unique programs such as: Summer Session Program, (SSP) Masters in Space Studies, (MSS) and Professional Development Program (PDP), and International Symposium. With its innovative approach and unique programs, ISU educates the space professionals required by the international space community. Its mission continues to expand through employing new teaching methods through the publication of educational material, in various media, growing from its unique programs.

INTERNATIONAL SPACE UNIVERSITY AND ITS MISSIONS

The future development of any country depends on its ability to engage in successful partnership with other countries around the world. The International Space University (ISU) is an innovative, global, interdisciplinary, international and intercultural space-oriented educational institution devoted to:

- the education, in space-related fields, of professionals of all discipline, (education and training)
- the creation and expansion of knowledge (research and advanced studies) and the training of researchers
- the exchange and dissemination of knowledge and ideas (outreach) to serve the world community dedicated to: the development of space-related activities for peaceful purposes; the improvement of life on Earth, and the expansion of life into space by inspiring those leaders and innovators who will promote the application of space technology in areas such as communication, education, science, health care, meteorology and management of resources for initiating sustainable development of all nations, and who will guide humanity beyond the next frontier.[1]

ISU as an international, non-profit organization founded in1987 by Peter Diamandis, Todd Hawley and Bob Richards. Its programs began with 10-week Summer Sessions, the first of which was held in 1988 and which are now well established, successful annual events.

ISU's Central Campus is located in Strasbourg, France, operating within a network of 25 Affiliate institutions in 14 countries and in partnership with numerous governmental agencies and industry around the world

PROGRAMS, OBJECTIVES AND DISCIPLINES

ISU education and training programs cover all disciplines relevant to space programs and their applications with a strong emphasis of interdisciplinary studies. The necessary fundamental knowledge in technical and non-technical and the interactions between these disciplines makes ISU programs unique. Various skills in the field of communication, teamwork, research, problem solving, decision making in multicultural environment are very important part of Summer Session Program and the Master of Space Studies. These programs also include theme days, seminars and workshops which bring together

[1] ISU Mission
Accepted by the ISU Board of Trustees

0-7803-3836-7/97/$10.00 © 1997 IEEE

international experts from industry, government and academia to discuss contemporary and future issues and developments in the space arena. Visits to industry, research establishments and the centers of professionals interest offer opportunities for first-hand observation of space applications and hardware.

Objectives

Bearing in mind these requirements, the curriculum MSS treats all major space-related disciplines - both technical and non-technical - and their inter-relationships within the framework of an integrated program. With its distinctive interdisciplinary, international and intercultural character and global perspective, the MSS program offers a broad and challenging course for personal and professional development. For experienced professionals, the MSS program strengthens both management and technical skills potentially leading to career advancement, a career shift within the space sector, or a career move into the space sector. Building upon the individual's current knowledge and past experience, the MSS also enables students to develop new expertise in a second field of space activity.

Disciplines:

- Business and Management of space programs
- Command, control and communications Systems
- Earth Observation (Remote Sensing, Geographic Information Systems)
- Earth-oriented Space Applications (telecommunications, Global Positioning Systems, Global Navigation Systems)
- Launch Vehicles and Transportation Systems
- Law and policy of space activities
- Mission Analysis and Systems
- Orbital Systems
- Space and Society (education, ethics, history, philosophy)
- Space Architecture
- Space Life Sciences
- Space Physical Sciences
- Space Resources and processing under Microgravity

All these elements are adapted to fit the structure and time-frame of each program.

The Summer Session Program (SSP)

It is an intensive ten-week course offered since 1988 is hoisted by institutions in different countries each year, covers the fundamental aspects of all major space-related disciplines, both technical and non-technical. Till now 1055 individuals from 65 countries have participated in the SSP. The 1997 SSP will be held in Houston, Texas. Moreover the curriculum reflects:

- the need in the future development of space activities to promote interdependence and cooperation as the driving forces for future accomplishments in space
- the importance of integrated and interdisciplinary learning,
- the development of space applications fro the benefit of all humanity

The curriculum includes workshops to develop skills in specific areas, with hands-on experience and case-studies. Each year SSP Design Projects, completed by the participants, offer innovative solutions to international conferences around the world.

The academic program has evolved over the years and will continue to develop and change as space activity progresses.

The ISU network, which developed through the Summer Sessions, provides an invaluable resource of highly skilled and enthusiastic individuals. Many alumni have benefited from the network on obtaining employment.

The ISU SSP has proved to be an exceptional opportunity for students and faculty to network with professional colleges and international leaders in space research, development and applications. The Summer Session alumni, faculty members, visiting lecturers and members of the host community have contributed to creating a professional network facilitating access to information and exchanges which have been successful in advancing various projects.SSP also provides a uniquely rich human experience by learning about and appreciate the cultures of their colleagues.

The Master of Space Studies (MSS)

The First Master of Space Studies began on 04 September 95 with students from around the world to Strasbourg, France to accomplish an 11-month graduate course. The international space programs require participants with adequate knowledge to deal with the issues that arise when developing, operating and using such programs-political, legal, financial, social, technological and scientific. They must be able to collaborate in a context where many national and disciplinary perspective may be in conflict.

The MSS is a unique degree course preparing graduates and young professionals to respond to the current and future demands of the space sector, especially in the applications of space technology.

The Master of Space Studies (MSS) is an eleven-month program which takes place at the Strasbourg Central Campus. From September 1997, the program will be offered in modules, which may either be taken in one academic year, or built up over two or a maximum of 3 years. A twelve week professional placement period at ISU Affiliate or at another institution, in different parts of the world is a very important part of MSS as a regular individual guidance and advice from an academic adviser is provided. The aim is to enable students to pursue original work in their main field of interest as well as contribute to a project in their host institution during their professional training. The Team Design Project enables to develop teamwork skills in a multinational environment. It gives an opportunity to propose innovative solutions to current problems.

The Annual International Symposium, focusing on the same topic as the Team Project, is an important opportunity fro MSS students to develop professional networking contacts. The first ISU International Symposium, an annual event, was held in Strasbourg in February 1996 on the subject of "Space of Service t o Humanity" and the theme of the 1997 Symposium is "New Space Markets". which is to held in Strasbourg from 26-28 May 97.

Professional Development Program (PDP)

A newly-established Professional Development Program (PDP) offers short courses, seminars for more senior professionals in the field of space and its applications. Participants gain an understanding of how different countries and cultures operate in the space arena. These courses emphasize the international and interdisciplinary components of the chosen theme. Five courses were offered to 100 participants in 1996. Some short courses and workshops offered by ISU provide an opportunity to meet and learn with people from many regions of the world who wish to broaden their outlook and deepen their understanding of key issues. The goal of the Professional Development Program is to provide with a full understanding of the space arena: policy, regulations, and business, as well as marketing, finance and technology. Further, the aim is to stimulate creative thinking and provide the tools and information necessary to develop and maintain new space-related products

The PDP is an outgrowth of ISU experience over the last decade, drawing expertise from over 400 international and government partners, as well as a network of 25 Affiliates in recognized institutions of higher learning from 14 countries. The expertise of the people in these organizations is packed into the Professional Development Program, along with new and innovative approaches to enhance the productivity and cost-effectiveness.

ISU Network

The network of ISU participants has produced a cacophony of global interaction, collaboration in business, research, and projects. Using the internet as a forum for discussion and flow of ideas, global ties are made and maintained. Companies regularly send ISU alumni to manage their branch offices around the world and there by capitalize on the ISU Network.

Through all these activities ISU is helping to develop a body of internationally-minded professionals with the breath and depth of knowledge needed for leadership and management of current and future space endeavors. ISU recognizes the importance of such individuals in creating, implementing and using space activity for practical applications, for scientific exploration and for the spirit of human adventure.

Title: Project SUN (Students Understanding Nature)

Dr. Gilbert Yanow
NASA/Jet Propulsion Laboratory (JPL)
4800 Oak Grove Dr., Mail Stop CS-530, Pasadena, CA 91109
Voice: (818) 354 6916, FAX: (818) 354 8080, email: gilbert.yanow@jpl.nasa.gov
Dr. Adrian Herzog
California State University, Northridge (CSUN)
18111 Nordhoff St., Physics and Astronomy Dept., Northridge, CA 91330
Voice: (818) 677 3931, FAX: (818) 677 3234, email: adrian.herzog@csun.edu

BACKGROUND

Project SUN was initiated via a small grant from NASA's Mission to Planet Earth. It was designed to be an educational program that was driven by scientific requirements. The basic science aim is to produce long term, scientifically valid, time resolved, survey data of Earth surface solar radiation in both the visible and erythemal UV (see below) ranges. At the same time, this data is correlated with detailed local weather information. The student teams aim to produce data good enough to allow eventual peer reviewed publication.

Educationally, Project SUN's goal was to allow students to learn science via on-the-job training; that is learn science by doing real science. In addition to the survey effort, students are encouraged to use the data collected for their own research interests. Project SUN also sought to elevate the appreciation of scientific research in the minds of teachers and students.

APPROACH TO SCHOOLS

Interested teachers and their classes are given a brief presentation on the need for the long term study of both the visible and ultraviolet solar surface radiation. If they wish to join the project, it is suggested that it be done via a "research team" that will be long term, just as the athletic teams are. However, above all, the scientific data they will produce must be of "professional" quality or the project will be a failure.

If they request to become part of Project SUN, they are given further hands-on training, a SUN kit (visible light pyranometer, special filter UV sensor, interfaces, software, test instruments and handbook). The school must supply old computers that can be used as dedicated data loggers (Apple, Macintosh, soon PC). The school is then allowed all the time they feel they may need to develop their skills, with periodic support calls to the teacher.

DEVELOPMENT OF A RESEARCH TEAM

The key to success for the school and Project SUN is the teacher. If the teacher is "hands-on" i.e., an amateur radio operator, amateur astronomer, computer buff, etc.,then he or she will be able to solve the problems that always arise in research (broken wires etc.) and the team will succeed. The time it takes for school teams to be able to start contributing data varies from a few weeks to many months, again depending usually on the teacher.

INSTRUMENTATION AND SOFTWARE

Visible Light Pyranometer

Visible light is detected using a Silicon Cell Pyranometer that was designed by G. Yanow [1] [2]. While the instrument is made for the project, its commercial cost would be less than $75. Test units have been sent to the National Renewable Energy Lab., U.S. Dept of Energy, for evaluation. This instrument was judged to be able measure the visible light spectrum to an accuracy of 4.2% [3]. Other types of pyranometers that are in the price range of $2000 have a typical accuracy of about 3.5%. An instrument that can measure within 5% is considered acceptable. In practice, each school is given a refurbished and re-calibrated unit each year.

UV Sensor

The measurement of surface ultraviolet light is a far more complicated problem than the visible. It was decided to measure the UV radiation in the same manner that the UV Index is predicted. That is, based on the research done on how humans are effected by radiation in the UVA and UVB spectral regions [4]. The results of this research are illustrated in Fig. 1.

The curve shows the importance of the various UV wavelengths in their damaging effects on humans. The most sever injury comes from the UVB region (290-315 nm). However, the Earth's ozone, water vapor, smog, etc. greatly attenuate this radiation before it reaches the surface. There is much more UVA (315-400 nm) than UVB at ground level. The result is that during the summer months the UVA radiation can contribute 15-20% of skin damage [5]. It should also be noted that the published "UV index" is based on this Erythema Action Spectra curve.

0-7803-3836-7/97/$10.00 © 1997 IEEE

Project SUN uses a filter type UV sensor made by Vital Technologies, Bolton, Ontario Canada, their model BW20.

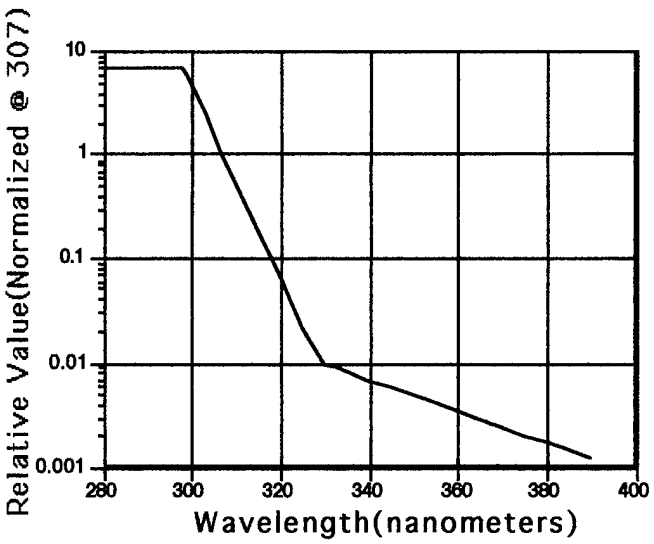

Fig. 1 Erythema Action Spectra

The BW20 was designed for Project SUN, but also now serves a wide global market. The transmission function in the filter of the BW20 very closes matches this response curve. In addition, tests at the National Institute for Standards and Technology (NIST) have shown the Vital filters to be very stable. The BW20's are also re-calibrated annually.

Calibration

The visible light pyranometers are calibrated against a Yankee TSP-1 Total Solar Pyranometer. The BW20 UV sensors are calibrated against the Vital Technologies Laboratory model BW100.

The calibration procedures are the same for both the visible and UV instruments. Data is taken comparing the SUN units against the standards every two minutes from the time period of 10:00 AM to 2:00 PM, on relatively clear days, for five days. An average calibration constant is then determined for each instrument. The standard deviation of the data must be the order of a few percent or less or the procedure is repeated until the correct tolorance is met.

The visible light is calibrated in units of watts/square-meter and the UV in milliwatts/square-meter. Note: a UV index of 1 is 25 milliwatts/square-meter--a data recording of 250 milliwatts/square-meter is therefore a UV index of 10.

However, there is currently a problem in the world of UV calibration. The Canadians first came out with a calibration based on detailed data they had taken. NIST now has also presented a calibration standard. Unfortunately, the two standards differ by about 25%, with the Canadian giving a higher reading of UV index. The current UV index predictions are based on the Canadian standard. Since this daily prediction is one of the "reality checks" used by the SUN research teams, the project has opted to stay with the Canadian standard for the time being.

Interfaces and Software

When the computers that are used as dedicated data loggers are old Apple IIe's, (two needed) modified Vernier Software (Portland OR.) VIU interfaces are used. When the data logger is made from an older Macintosh (one needed), the Vernier Serial Interface is used. Both of these units give 12 bit accuracy in the range of 0-5 VDC. In the future, researchers will be able to used older IBM's or compatibles with a Vernier serial interface.

The data logger programs, in all cases, are from Vernier Software. Yanow[2] has written conditioning software that combines the solar and UV data with a location header and local weather conditions of the day. When the data is posted in graphical form on the Home Page, four curves are presented with the locale and weather data; the visible light profile, the erythema UV profile, a profile of the ratio of visible to UV (to illustrate the skewing of the black body curve) and the predicted profile of the solar zenith angle for the location.

OPERATIONS

Overall Project

As said, Project SUN was started as a NASA/JPL pilot program. The Physics and Astronomy Dept. of the CSUN, has now formed a partnership with JPL to improve and expand the effort both in the U.S.A. and internationally. CSUN will take the lead in maintaining the Home Page and managing the data. JPL will support the instrumentation, the calibration and continue to develop the experimental protocols. JPL and CSUN will jointly do the training and analyze the data.

Current Status

At the time of presentation, Project SUN has six schools in the Los Angeles area, one in the San Diego area, one in Michigan, one in Western Australia, one in Indonesia and one in Japan. With the help of CSUN and additional financial support (to be developed jointly by CSUN and JPL) the number of schools could greatly be increased over the next and following years.

Research Protocols

The obligation of each research team is to take SUN data at

least two days per week during the school year (special arrangements are made for the vacations times). The other days of the week, the teams are encouraged to carry out research programs of their own. Examples of this independent research have been projects to determine if a locale could develop enough electricity via photocells to support themselves, studies to determine the types of clouds that produce enhanced surface effects via cloud optics, and the correlation between humidity and UV reading. Examples of data are shown in following four figures. The conditions for the day were a maximum temperature of 97.7 degrees F, 30% relative humidity, a clear sky, with a 18 mile per hour wind from the west.

GUILDFORD GRAMMER SCHOOL, PERTH W.A. 21.NOV1995

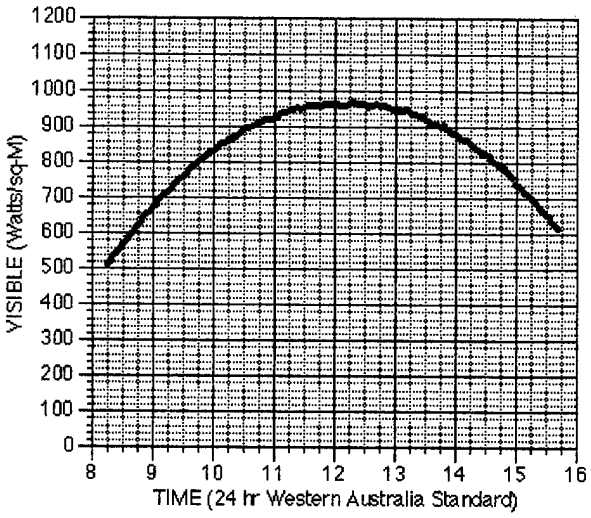

GUILDFORD GRAMMER SCHOOL, PERTH W.A. 21 NOV 1995

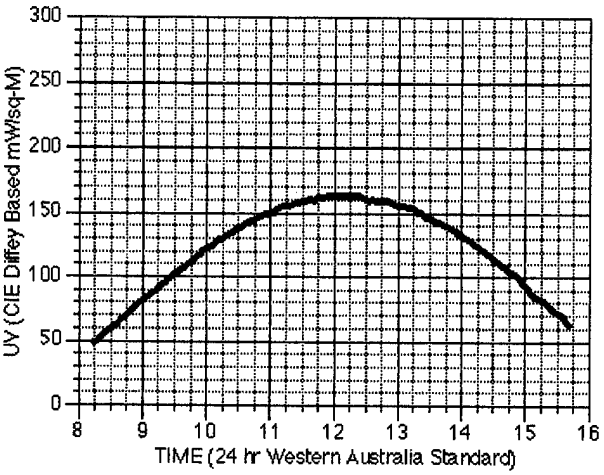

GUILDFORD GRAMMER SCHOOL, PERTH W.A. 21 NOV 1995

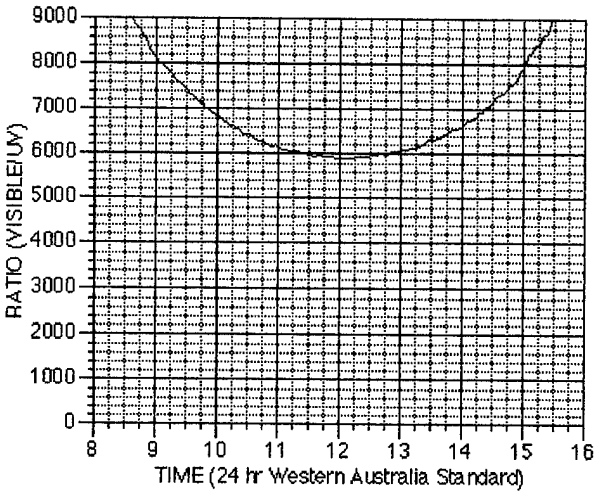

GUILDFORD GRAMMER SCHOOL, PERTH W.A. 21 NOV 1995

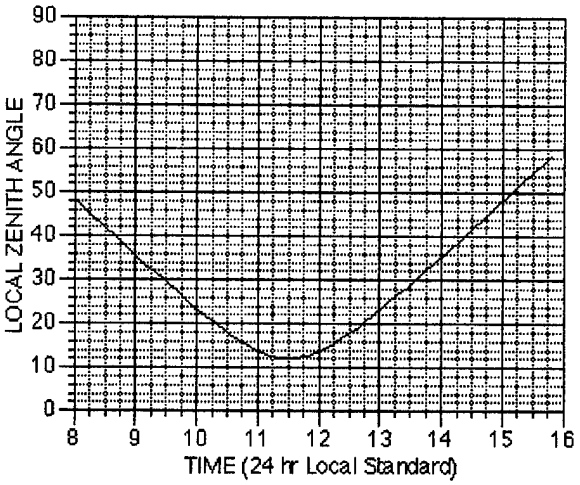

[1] Yanow, G.,"Inexpensive Pyranometer", NASA Tech Briefs. 20, 6, June 1996.

[2] Project SUN Home Page,http://sunshine.jpl.nasa.gov.

[3] Metrology Laboratory, "BORCAL 94-2", National Renewable Energy Laboratory, June 10, 1994.

[4] McKinlay, A.F. and Diffey, B.L. "A Reference Action Spectrum for Ultraviolet Induced Erythema in Human Skin", Human Exposure to Ultraviolet Radiation: Risks and Regulations, pp 83-7, 1987.

[5] Diffey, B.L., "Solar Ultraviolet Radiation Effects on Biological Systems", Review in Physics in Medicine and Biology 36(3):299-328, 1991.

The CSU-Chill Fully Polarimetric S-Band Weather Radar Facility: Providing Research Experience to Undergraduates

V. N. Bringi and V. Chandrasekar
Colorado State University
Fort Collins, CO 80523

Abstract - For the past six years Colorado State University has been providing research experience to undergraduates in electrical engineering using the CSU-CHILL radar facility as a focal point. Typically, 8 -10 sophomore/junior students from various universities in the U.S. are selected for the ten-week summer program which is funded by the National Science Foundation. This paper describes briefly the capabilities of the CSU-CHILL radar and the chase van validation efforts conducted during the summer of 1996. The CSU-CHILL radar is a national facility for advanced research in remote sensing of weather phenomena and is open to investigators from all universities.

INTRODUCTION

The CSU-CHILL radar is operated by Colorado State University as a national facility for conducting advanced research in remote sensing of weather phenomena, and for providing educational experience to students in Electrical Engineering (EE) and Atmospheric Science (ATS). The radar facility is funded via a cooperative agreement with the U. S. National Science Foundation and, currently, we are in our 7th year of a ten-year continuing agreement which began in 1990 with total funding of $5.0 million. The radar facility is unique because of its fully polarimetric/Doppler measurement capabilities largely developed during the last two years. It is the only one of its kind operated by a university in the United States.

DATA SOURCES

CSU-CHILL Radar

The radar facility is located near Greeley, CO about 30 miles from the main campus of Colorado State University. Table 1 gives the system characteristics of the radar. The radar is designed as a two transmitter/two receiver system. The use of two separate channels, one for horizontal polarization and one for vertical polarization, avoids the use of a high power polarization switching device to switch the transmitted polarization state between H and V states on a pulse-by-pulse basis. The use of two receivers permits the simultaneous measurement of the copolar and cross-polar backscattered signals. Thus, by alternately transmitting H and V-polarized pulses, the backscatter matrix is measured:

$$S = \begin{bmatrix} S_{hh} & S_{hv} \\ S_{vh} & S_{vv} \end{bmatrix}$$

The radar processor, computes in real-time, the following quantities: radar reflectivity at H-polarization (Z_h), the differential reflectivity (Z_{dr}), and the copolar correlation coefficient (ρ_{hv}) between the HH and VV returns. In addition, the terms $<S_{hh}\,S_{vh}^*>$ and $<S_{vv}\,S_{hv}^*>$ are computed where angle brackets denote time-averaging. In summary, the processor computes three real terms of the polarimetric covariance matrix, i.e., $<|S_{hh}|^2>$, $<|S_{vv}|^2>$ and $<|S_{hv}|^2>$, and three complex terms, i.e., $<|S_{vv}\,S_{hh}^*|>$, $<S_{hh}\,S_{vh}^*>$ and $<S_{vv}\,S_{hv}^*>$.

REU Experience

The Research Experience for Undergraduate (REU) program is funded by the National Science Foundation and is currently in its sixth year at Colorado State University. During the summer of 1996, students were involved in an intensive effort to gather in-situ data on hydrometeors within storm cells that could be compared against simultaneously measured radar parameters such as Z_h, Z_{dr}, LDR, φ_{dp}, and ρ_{hv}. One goal was to assess the accuracy of φ_{dp} as a measure of rain intensity, and the other was to assess the utility of Z_h, Z_{dr}, LDR and ρ_{hv} in detecting hail and estimating hail severity. Two chase vans were especially instrumented to collect hydrometeor data. Students assisted with various aspects of the instrumentation. The first van (see Fig.1) called "Hailstone" was installed with a roof-mounted hail collection funnel (1m in diameter) for manual collection of hailstones which were "quenched" in cold hexane and placed in dry ice. The hailstones were later photographed with a digital camera and special software was written to analyze the size and shape distributions. A large number of time-resolved samples were collected with sizes ranging from 1-5 cm. The Hailstone van was also equipped with a Young capacitance raingage which was interfaced to a PC. Rain accumulations were recorded every few seconds.

The second van (see Fig. 2) called "Austria" was installed with the 2D-video disdrometer obtained on lease from Joenneum Research, Graz, Austria. This instrument is a newly developed precipitation gage working on the basis of two line scan video cameras. Particles falling through the 10 cm x 10 cm opening on the top of the van appear as a dark silhouette against a bright background. Fig. 3 shows a sample from the display program that is available in real-time to the operator.

0-7803-3836-7/97/$10.00 © 1997 IEEE

Students were trained to operate the instrument, to calibrate it using calibration spheres, and to trouble-shoot the optical alignment under rather adverse conditions.

Both vans were equipped with GPS receivers interfaced to a laptop computer and a transceiver unit which transmitted the lat/long data to a base unit at the radar. Van tracks were overlaid on the radar PPI displays.

Examples of Data Collected

On 6 July 1996, the two vans were directed by the radar operator to intercept a severe storm cell containing intense rain mixed with hail up to 1.7 cm in diameter. Each van was manned by two students. Based on radar-based storm cell movement and speed, the vans were directed to locations that would intercept the storm core. On this day the van operators had only a few minutes to set up the instrumentation and start data collection. Students were thus exposed to a stressful environment and had to make, at times, critical judgement calls to ensure that high quality data were collected. Fig. 4a shows the rainfall accumulation profile using the Young capacitance gage. Fig. 4b shows the rainrate profile computed using a finite impulse response (FIR) filter designed by one of the students (Mr. Andy Shroyer). The data show intense rainrates up to 150 mmh^{-1} maximum. Fig. 5 shows sample photographs of the collected hailstones. Time-resolved hailstorm samples were collected at approximately two minute intervals over the duration of this event. Such datasets are invaluable in testing radar-based algorithms for rainrate and hail severity.

ACKNOWLEDGMENTS

The authors acknowledge the participation of the 1996 REU students, in particular, Mr. Andy Shroyer of Colorado State University, Mr. Scott Grahm and Mr. Mike Lundahl of N. Arizona University and Mr. Vivek Goyal of Penn State University. Drs. John Hubbert and John Beaver of Colorado State University played key roles in training the REU students and in directing the chase van operations. The CSU-CHILL facility is supported by NSF cooperative agreement ATM-9500108 supplemented by cost sharing funds from the State of Colorado. The REU program was funded by the NSF via EEC-9322446. The cooperation of Joanneum Research, Graz, Austria, in particular, Mr. Michael Schonhuber, Mr. Urban and Professor Randeu are acknowledged. Funds for the chase vans were provided by DOD grant DAAH04-94-G-0420, and by the Rome Laboratory of the USAF under contract F30602-96-C-0119.

Table 1. System Characteristics of the CSU-CHILL Radar

Antenna	
type	fully steerable, prime focus parabolic reflector
size	8.5 meters in diameter
feed	scalar horn
3 dB beamwidth	1.0 degrees
directivity	45 dB
sidelobe level (any ϕ-plane)	≤ -27 dB
cross-polarization level (any ϕ-plane)	≤ -30 db
polarization radiated	horizontal or vertical
Transmitter	
type	klystron, modernized FPS-18
wavelength	10.7 centimeters
peak power	700 - 1000 kW
pulse width	steps of 0.1 µs up to a maximum of 1.0 µs
PRT	800 - 2500 µs
max. unambigous range	375 kilometers
max. unambigous velocity	± 34.3 m/s
Receiver	
noise figure	0.7 dB
noise power	− 114 dBm
typical bandwidth	750 kHz
transfer function	linear
dynamic range	90 dB, 0 - 60 dB IAGC in 12 dB steps

Variables Available

- Reflectivity at Horizontal Polarization (Zh)
- Differential Reflectivity (Zdr)
- Mean Doppler Velocity ($\bar{v}$) and Spectral Width (σ_v)
- Differential Phase between Horizontal and Vertical States (ψ_{dp})
- Copolar Correlation Coefficient ($\rho_{hv}(0)$)
- Linear Depolarization Ratio (LDR)
- Doppler Spectra from FFT Processing
- I, Q and log(P) for every pulse in time series mode (up to 150 gates)

Fig. 1 Hailstone van with Andy Shroyer and Scott Graham

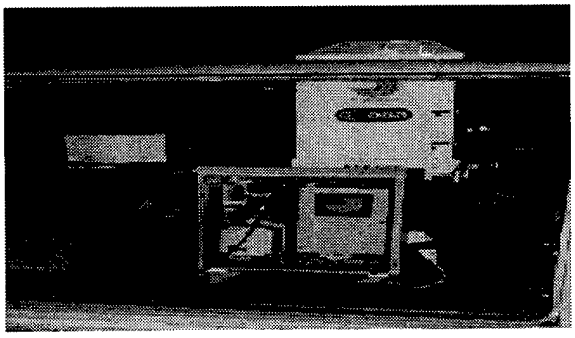

Fig.2 2-D video distrometer

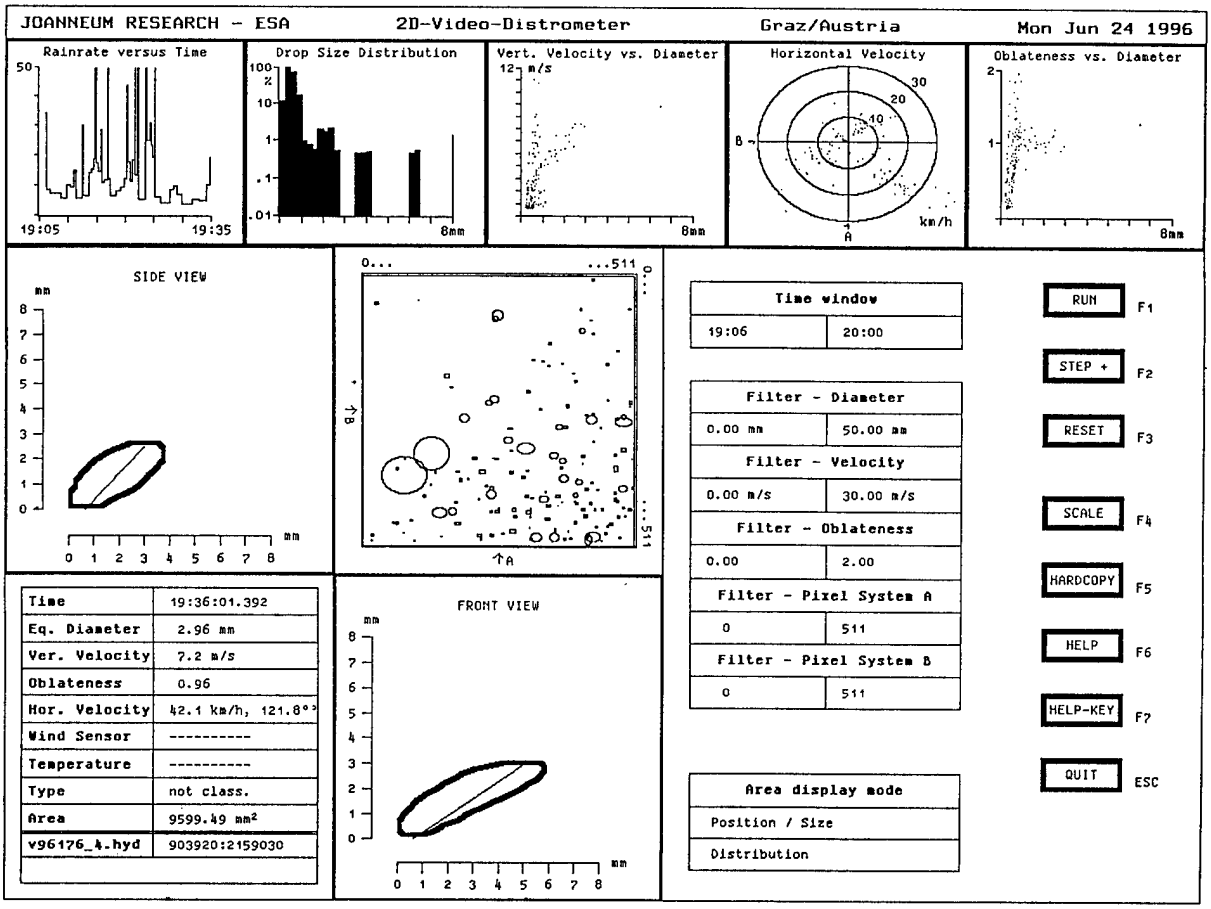

Fig.3 Real-Time Display from 2D-video disdrometer.

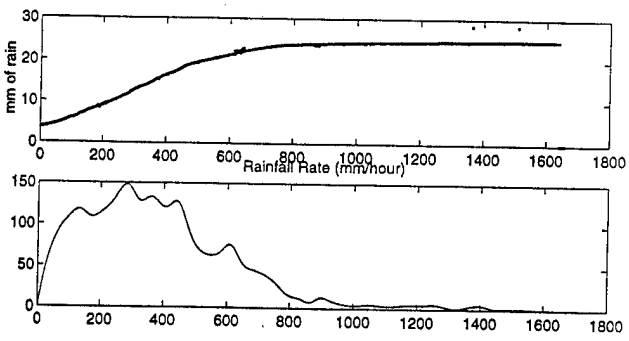

Fig.4 Top panel is rain amount(mm) vs. time(sec)
Bottom panel is rain rate(mm/hr)

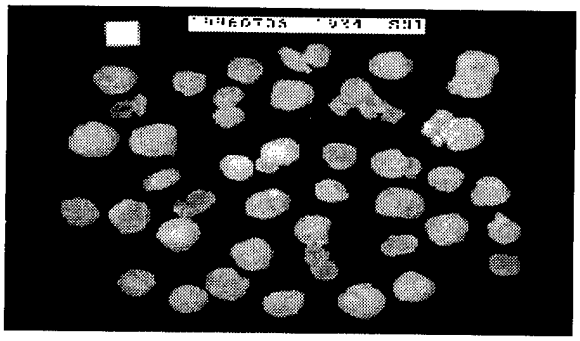

Fig.5 Sample of hail images

Using the World Wide Web for Distributed Learning: Two Examples

J. W. Skiles*, Johnson Controls World Services, NASA Ames Research Center (ARC); Kenneth D. Kennedy, College of San Mateo (CSM), William B. Rundberg, CSM; and David L. Peterson, Ecosystem Science and Technology Branch, ARC.
*Corresponding Author: Mail Stop 239-20, NASA Ames Research Center, Moffett Field, CA 94035-1000 USA. tel: 415/604-3614; fax 415/604-1088, e-mail: jskiles@mail.arc.nsas.gov

Abstract -- This paper details two projects that use the World Wide Web (WWW) for dissemination of curricula that focus on remote sensing. 1) Presenting grade-school students with the concepts used in remote sensing involves educating the teacher and then providing the teacher with lesson plans. In a NASA-sponsored project designed to introduce students in grades 4 through 12 to some of the ideas and terminology used in remote sensing, teachers from local grade schools and middle schools were recruited to write lessons about remote sensing concepts they could use in their classrooms. Twenty-two lessons were produced and placed in seven modules that include: the electromagnetic spectrum, two- and three-dimensional perception, maps and topography, scale, remote sensing, biotic and abiotic concepts, and landscape change. Each lesson includes a section that evaluates what students have learned by doing the exercise. The lessons, instead of being published in a workbook and distributed to a limited number of teachers, have been placed on a WWW server, enabling much broader access to the package. This arrangement also allows for the lessons to be modified after feedback from teachers accessing the package. 2) Two-year colleges serve to teach trade skills, prepare students for enrollment in senior institutions of learning, and more and more, re-train students who have college degrees in new technologies and skills. A NASA-sponsored curriculum development project is producing a curriculum using remote sensing analysis and Earth science applications. The project has three major goals. First, it will implement the use of remote sensing data in a broad range of community college courses. Second, it will create curriculum modules and classes that are transportable to other community colleges. Third, the project will be an ongoing source of data and curricular materials to other community colleges. The curriculum will have these course pathways to a certificate; a) a Science emphasis, b) an Arts and Letters emphasis, and c) a Computer Science emphasis. Each pathway includes course work in remote sensing, geographical information systems (GIS), computer science, Earth science, software and technology utilization, and communication. Distribution of products from this project to other two-year colleges will be accomplished using the WWW.

UNDERSTANDING THE BIOSPHERE FROM THE TOP DOWN

The National Aeronautics and Space Administration (NASA), because of its mandate, has a particular way of viewing the earth. The office at NASA Headquarters responsible for actually studying our planet is called Mission to Planet Earth (MTPE). The perspective of MTPE is to use sensor technology and instrument platforms, be they satellites or aircraft, to gather vast amounts of information about Earth without physically touching the Earth. Thus, this is called "remote sensing".

The information so gathered is used to infer how the mechanisms and processes of the earth system work. Judicious surface observations (ground truthing) are carried out to verify the inferences. In this way local-to-global studies are done, but they are unique because only rarely are measurements made on the ground.

Project Purpose

In proposing this project, the project team had one major question: Can the biosphere (that part of our planet where life is found) be viewed pedagogically from space down to the surface using lessons, designed for grade-school students, to teach children about the earth system? The answer was thought to be "yes" especially if teachers were involved in writing the lessons. The project team thought that by presenting the study of the biosphere as a whole, from the top down, using remote sensing technology, students would perceive the biosphere as containing interlinked environments and organisms. This structure, the team expected, would aid students when they are introduced later to concepts like, for example, trophic levels and energy flow within an ecosystem and in the biosphere. It was also expected that students would learn the elements of the physics involved in remote sensing, the ideas of measuring things from a distance, the difference between two and three dimensional representation, and the other ideas and concepts the lesson authors specify in their exercises.

Eight teachers from culturally diverse areas of the communities near Ames Research Center produced 22 lessons for this curriculum with the help of NASA staff. The lesson topics were fit into seven different topical modules that include the electromagnetic spectrum, 2-dimensional and 3-dimensional perception, maps and topography, scale concepts, remote sensing, biotic and

0-7803-3836-7/97/$10.00 © 1997 IEEE

abiotic concepts, and landscape changes. A diagram of the modules is shown in Fig. 1.

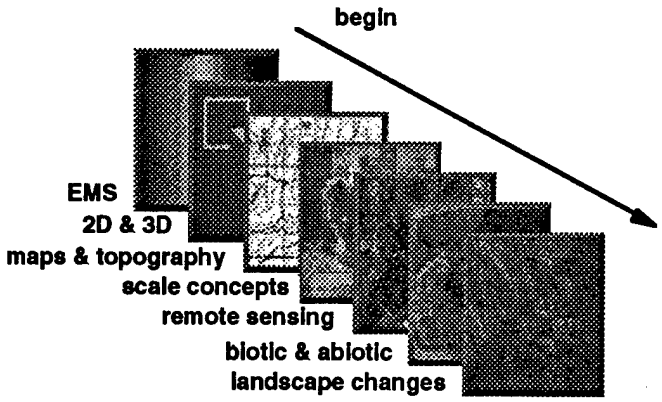

Fig. 1. A conceptual chart of the modules included in the Understanding the Biosphere from the Top Down project.

While each lesson and each module may be used separately and generally stands alone, students without a remote sensing understanding should start with one or more of the lessons devoted to the electromagnetic spectrum (EMS). Then students should do the lesson devoted to 2-dimensional and 3-dimensional perception. A lesson on maps and topography should follow and then students should study the concept of scale.

The teachers who wrote the lessons in this package were greatly intrigued by remote sensing. As such, they wrote a number of lessons that deal with aspects of that discipline. In order to understand what one sees in a remotely sensed image, one needs (in part) to know what features on the ground are or were alive and what features never were alive; this is the difference between biotic and abiotic and one of the modules in the package has students determine what is abiotic and abiotic in a school-yard scene. The last module deals with landscape change.

Instead of producing a workbook for teachers that would have limited distribution and be difficult to revise, the twenty-two lessons have been converted to hypertext markup language (html) for inclusion on a World Wide Web (WWW) home page making them accessible to teachers worldwide. Remote sensing imagery, graphics, and figures that accompany the lessons have been scanned or digitized and placed in the appropriate lessons. The URL for the WWW page is: http://geo.arc.nasa.gov. Click on "What's New!" and then on "Top Down Education Project". The package may also be accessed from NASA's Spacelink maintained at Marshall Space Flight Center under the heading "Additional Resources".

The lessons were written by teachers for teachers, so many contain instructions about advanced preparation and planning that must be done before the students are given the tasks to perform. The lessons are not a specific set of instructions, but rather are guidelines to be used and modified as needed by each teacher to fit into unique classrooms. It is up to each teacher to use these lessons at appropriate places in their school's curriculum. Teachers with motivated students may wish to have those students download the lessons and work directly from the computer.

Benefits Of World Wide Web Distribution

By implementing a World Wide Web on-line distribution of the Top Down teacher guides and by counting the number of hits to the web page, it is possible to determine who is visiting the material. By examining the IP numbers of those who hit the page, it becomes obvious that the guides can be accessed from people around the world. (To date, the web page has been visited by persons in Japan, Germany, the Netherlands, Austria, Great Briton, Canada, and the United States.)

Further, by placing the materials on the web, updates and corrections can be made to exercises without printing the guides over. Teachers may visit the site repeatedly, downloading only those lessons for which they have need at the time.

Grade school teachers and advanced grade-school students are the customers for this product. They can access the lessons as needed, check for revisions periodically, and because an e-mail address is supplied in the package for the project PI, ask questions about the lessons and the project. A further benefit is that NASA has not had to pay for printing 10,000 copies of the guides nor for distribution. Nor does NASA need to print corrections, updates, or revisions to the lessons as these are added to the source displayed on the World Wide Web.

ACTES: AN ASSOCIATE OF ARTS IN COMMUNITY COLLEGES FOR TRAINING IN EARTH SCIENCE

This project (sponsored in part by NASA) has three major goals. The first is the implementation of the use of remote sensing data in a broad range of community college courses. Second, it is creating curriculum modules and classes that are transportable to other community colleges via WWW technology. Third, at the end of the three-year project, a WWW server will have been established that will be an ongoing source of data and curricular materials to other community colleges.

The objectives for the project include the development of a teaching laboratory, a curriculum, transferable classes using remote sensing, technical reading and writing, an occupational certificate based on specified courses, and dissemination of the materials by publicly accessible techniques.

An additional objective expected to be achieved is that as a result of taking the proposed sequence of courses,

students will show comprehension of and ability to use the scientific method in using data, forming testable hypotheses and constructing "ground truthing" experiments. This objective will be achieved through the use of mapping exercises for San Mateo County, and using Geo-Positioning System (GPS) techniques and Geographical Information System (GIS) data layering and display.

The result of the implementation of this curriculum will be hands-on learning for students whether they are at a two-year college for an AA degree, retraining to improve their job skills, taking classes to satisfy requirements for four-year colleges, or any combination of these options. The expectation is that these students will be able to continue their education in the remote sensing/GIS area at a senior college, or move into entry level positions at local companies where remote sensing and GIS technologies are used, or have valuable skills to append to their resumes.

A sequence of courses has been established at CSM for students wishing to earn an AA in this area of expertise. Titles of each of the five courses and short descriptions of each follow:

Introduction to Earth Systems Analysis - An introduction to several topics. Students learn about coordinate systems, scale, map projection systems, use of the Internet as a resource, remote sensing (RS), image manipulation, GPS concepts, and the construction of WWW pages.

Spatial Analysis in Geographic Information - Students learn principles of cartography including coordinate systems, projections, scale, layering in maps, and the use of applications such as ArcView, NIH Image.

GPS, GIS and Image Processing - Students gain extensive experience with software packages (ArcView, NIH Image, Vista Pro, MapInfo, Photoshop, GPS software from Trimble) which they use to study GIS and GPS concepts.

Remote Sensing Technology and Processing - Students learn about different remote sensing instruments (Thematic Mapper, Spectron), the remote sensing platforms on which the instruments are deployed (satellite, aircraft, hand-held), the resolution and scale of the images the instruments produce, and the features and limitations of each instrument. Students learn image classification techniques, classified image display and interpretation techniques, and explore the means, locations, and costs of acquiring sensor images.

Laboratory Practicum - This is a laboratory activity or collection of activities where students use skills and concepts from the above listed classes in individual projects. A typical activity will be to determine a target and objective, examine images of the target with respect to the objective, construct conjectures as appropriate, ground-truth where possible, and develop a report of the project findings and conjectures and place the report on the WWW. The real applications addressed in this practicum, while based in San Mateo County in northern California, will be typical of communities almost anywhere in the country and perhaps across the globe.

By taking this course sequence, students will be able to identify, use, and analyze basic data structures from the point of view of sensor data, data base organization, and data representation; students will be able to acquire data by a range of techniques including downloading from the Web, use of CD-ROM, scanner, and satellite transmitted data. Students will also have a basic understanding of sensor technology and remote sensing concepts, and will be able to acquire and use data from remote sensing sources.

Benefits Of World Wide Web Distribution

The World Wide Web is an integral part of the ACTES project where it is used two ways in particular: 1) it is a medium for the distribution of materials that are products of the project and include items such as course materials and learning modules; 2), it is an instruction medium for students.

At the completion of the project, colleges throughout the world will be able to download developed materials from the ACTES WWW site and use them for their own related course work and programs. These materials will include course outlines, classroom exercises, individual lessons, and supporting graphics and images.

It is expected that instructors will be able to choose which lessons to use that will enhance existing courses or that they will download materials for entire courses. Revisions made to the project materials from feedback by users will be done quickly and allow anyone who can access the ACTES WWW site immediate updates to the curriculum.

The ACTES materials may be accessed at the WWW URL:
http://www.smcccd.cc.ca.us/smcccd/csm/actes/actes.html.

Title: "Winds of Change", the NSCAT CD-ROM

Dr. Gilbert Yanow
NASA/Jet Propulsion Laboratory (JPL), Educational Affairs Office
4800 Oak Grove Dr., Mail Stop CS-530, Pasadena, CA 91109
Voice: (818) 354 6916, FAX: (818) 354 8080, email: gilbert.yanow@jpl.nasa.gov

BACKGROUND

NASA now requires every project have a public and educational outreach component. The educational side of this outreach must be based on the needs and requirements of the educational community. The NASA Scatterometer project, NSCAT, is one of the projects that has led the way in this approach to outreach. This was a major departure from what had been done before at JPL. NSCAT was the first JPL project to develop what they have called a "high density" educational product. The "density" of Winds of Change will become self evident in the reading of this paper. The NSCAT project came to the JPL Educational Affairs Office (EAO) to form a partnership in the development of this CD-ROM and associated plans.

APPROACH

The Core Team

Initially the EAO formed what was called a "Core Team". This team was composed of active classroom teachers representing all the grade levels, university educational evaluators and teacher trainers, curriculum specialists and writers, media developers, educational consultants, representatives from the California State Dept. Of Education and NSCAT engineers and scientists. It took several meetings for this varied group to develop a common language, but once this was done (educators learned science and engineering terms and the scientists and engineers learned educational terminology), the design for the NSCAT educational product evolved.

Basic Design

The Core Team, based on focus groups inputs at teacher meeting and many private interviews, decided on the following design criteria:

- Aim the product at middle school, with the subject matter of Global Climate, to have the widest audience,.
- Write a teacher resource, but in a way that students could also use directly.
- Use the "web" suggested by our educational consultant, Mr. Bruce Payne [1], to make sure the product was thematic and interdisciplinary.
- Make sure the materials aligned with educational guidelines [2] [3] [4].
- Use a CD-ROM as a high density media, but with a very simple "point and click" interface.
- The final product must be machine independent.
- Develop a systems approach with an evaluation, distribution and follow-on strategy.

EDUCATIONAL DESIGN

Winds of Change Overall Structure

The structure of Winds of Change is illustrated in Fig.1.

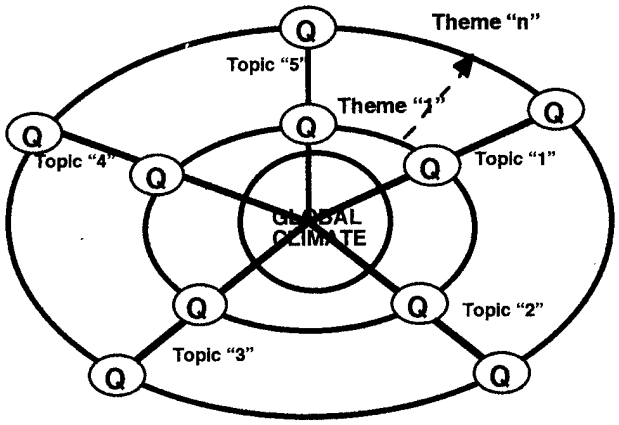

Fig.1 Winds of Change Basic Structure

The concentric ellipses are major themes that come from the educational references, slightly modified from focus group inputs. In the case of Winds of Change, eight major themes were used, (1) Scale and Structure, (2) Measurement, (3) Energy, (4) Systems and Interactions, (5) Patterns of Change, (6) Evolution, (7) Stability and (8) Human Interaction .

The radiating spokes are interdisciplinary subjects. Five were chosen for Winds of Change, (1) Atmosphere, (2) Weather, (3) Climate, (4) Living Things and (5) Oceanography. Wherever a topic and theme intersect, a major question is asked that will be the direction of a whole battery of resource materials. In the case of the intersection of Weather and Structure, the question asked was, "What is Weathers".

Navigating Winds of Change

The navigation system of Winds of Change is either menu or graphical, point and click. When Winds of Change is booted up (on either a Macintosh or IBM compatible machine) the user has three basic menu choices, to find out about how, why and who developed Winds of Change, to get

0-7803-3836-7/97/$10.00 © 1997 IEEE

more background materials on the NSCAT project or to use the curriculum resource. If the curriculum resource is chosen, Fig.1, with all the eight themes and five topics appears on the screen.

The user then points and clicks on the topic desired. The screen zooms in to this one spoke, allowing much more detailed examination. As the cursor is moved to the intersection of the chosen topic and theme, the major question appears. To zero in on a question, the user clicks on it.

A resource panel then appears on the screen, allowing the user to pick from four types of information, (1) background materials, (2) classroom activities, (3) still images or (4) quicktime movies. All the resources may be electronically copied to an other media (disk, hard drive, etc.) or sent to a printer (color or black-and-white). The background and activities are in the form of PDF files. The images can also be expanded on the screen to be used for classroom presentations on a large monitor.

In this way, the teacher can build up the materials needed to teach a unit based on the specific question in one of many ways. Students can use the materials directly as part of independent study research projects. When this the method of use of Winds of Change, it is suggested that students use a journal, printed or electronic, to record and present their work.

The number of pages of background materials, activities, still photos and quicktime movies various from question to question. Usually, there are from 7-12 pages of background materials, 3-6 classroom activities, 5-21 still images and from 0 -9 movies. In the case of the example stated, "What is Weather", there are 7 pages of background, 5 activities, 21 still images and 9 movies.

For the three topics of weather, atmosphere and oceanography, there are a total of 194 pages of background materials, 106 activities, 247 still images and 80 quicktime movies.

FIELD RESULTS AND FORMAL EVALUATION

Field Results

The CD-ROM was released in two stages or versions. "Version I" had three "spokes" implemented, atmosphere, weather and oceanography. Approximately 5000 Winds of Change, Version I have been distributed over the last year. Version II is complete with all five topics and is at the time of writing being distributed.

The main complaints from the users of the first version were to do with installation of Adobe Acrobat for the reading of the PDF files. These problems have been fixed with Version II. Users (educators, teachers and students) in response to the subject materials and content for both versions have been very positive.

Formal Evaluation

Version I was sent to the Mid-Continent Regional Educational Laboratory (McREL) in Aurora, CO, U.S.A. for formal evaluation. McREL did this evaluation on two levels: an evaluation by professional curriculum developers and a parallel evaluation by a group of mentor teachers. In addition, McREL did an alignment of a compendium of the various national standards with the materials on the first version of Winds of Change (only the topics of atmosphere, weather and oceanography). There were a large number of areas they examined, e.g. introductory materials, background information, classroom activities, images, movies, self-directed activities, most appropriate uses, etc.

The teachers gave the materials, based on all the various parameters, a mean rating of 5.4 out of a perfect score of 7. The teachers commented that they especially liked the information, the organization, the activities and the supporting visuals.

The Professional writers gave the first version of Winds of Change an average total rating of 4.5, but noted that the quality of materials in Winds of Change compares favorably with the quality of other middle school science curricula. The professionals liked the combination of text, visuals and activities, the organization and the consistency of format. It was also noted that Winds of Change would have application to high school science, especially 9th grade Earth Science.

The professional evaluators expressed some concern that the teacher level vocabulary might be above the student users. However, the NSCAT project worked with many teachers who reported (about 50% of teachers) they had their students use the Winds of Change for self study. No teacher ever reported that their students had problems with the reading level.

The alignment of the first version of the CD-ROM with the national standards was also reveling. The information is summarized in Fig. 2.

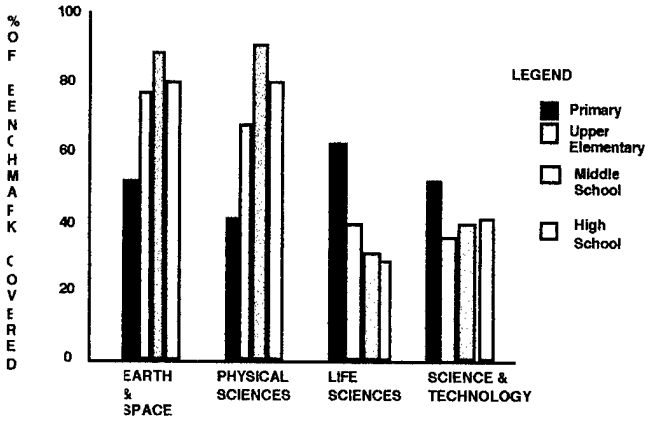

Fig. 2 Standards Alignment

What was found surprising was the large amount of standards that Winds of Change covered beyond the targeted grade levels and subjects areas. At the present time McREL is doing the alignment for the last two "spokes", Climate and Living Things. The standards alignment will be even more impressive at that time.

DISTRIBUTION PLAN

The decision was made early in the development of Winds of Change that the CD-ROM that the distribution be done in a "targeted" manner. That is, be distributed, free of charge, at national or regional educator meetings with a large attendance of teachers representing the designed grade levels and subjects. Direct requests from teachers were also honored.

Teachers who are given Winds of Change are requested to fill in a "No Cost Order Form" or register as an official user. This information will be used later for a long term evaluation of the product. NSCAT now has thousands of teachers in this data base.

ENHANCEMENTS OF WINDS OF CHANGE

The Educators Information and Exchange Home Page

As part of the CD-ROM section of the overall NSCAT Home Page [5] is the Educators Information and Exchange area. Educators who use this page can order Winds of Change electronically. The Standards Alignment is also presented on this page. Educators can "click" to one of the main 18 McREL science standards. Once a major standard is chosen, the user clicks to a set of sub standards, based on details of subject and grade level (K-2, 3-5, 6-8 and 9-12). When a particular substandard is chosen, this page will reference all the background materials, activities, images and movies that can be used to teach this standard. In this way a teacher can decide a path of use of Winds of Change. In future this page will also allow teachers to exchange ideas and methods of use of Winds of Change via a password protected user forum.

FOLLOW ON ACTIVITIES

New Internet Student Activities

Over the next year, several major activities will be instituted as part of the NSCAT Home Page that will make use of NSCAT data. Examples of these activities are "Sail the Seas". Using the wind data and "value added science products" of NSCAT coupled with ocean current data from the TOPEX/POSEIDON mission, students will plan a sailing voyage from Australia to North America. Part of this activity will be for the students to investigate what stops will be made on this trip and develop information about these ports and countries.

"Wind and Weather" will be an investigation of correlating the NSCAT wind data with weather maps and observed circulation patterns. Students will gain an understanding of the ways the world's winds influence global weather.

A World Wide Student Research Project on Possible Precursor Effects of El Nino

Working with research scientists, modified tables of NSCAT data for "sensitive" NSCAT" cells (50 kilometer squares of the ocean surface) of the tropical south Pacific will be presented on the home page. Schools, from anywhere in the world, that wish to participate with this project, will form long term research teams that will "adopt" specific NSCAT cells. These student research teams will carry out long term investigations of the time resolved wind direction, wind speed and ocean currents for these areas. The initial aim of this research will be to establish the range and observed behavior of these parameters during normal weather patterns. When a group of student research teams find data that falls outside of this norm, they will work with each other and the NSCAT project to see if these observations are indicative of a precursor effect of a coming El Nino.

[1] Private Communications

[2] Project 2061, American Association for the Advancement of Science (1993), *Benchmarks for Science Literacy.*

[3] National Research Council (1996), *National Science Standards.*

[4] California Department of Education (1990), *Science Framework for California Public Schools: Kindergarten Through Grade12.*

[5] http://winds.jpl.nasa.gov

Landuse Study of the Sentosa Island using SPOT Images

L. Zhao (a), F. Y. Tan (a), W. Quek (a), P. Chen (b) and S. C. Liew (b)

(a) Swiss Cottage Secondary School, Sec 4E1, Bukit Batok Street 32, Singapore 659322

(b) Centre for Remote Imaging, Sensing and Processing, National University of Singapore,
Lower Kent Ridge Road, Singapore 119260
Tel: (+65) 7723220, Fax: (+65) 7757717, Email: phyliew@nus.edu.sg

Abstract -- The objective of this project is to study the change in land cover of the Sentosa island and to assess the condition of the vegetations existing on the island using SPOT images. Two SPOT multispectral sub-scenes of the island acquired in Feb 94 and Aug 96 were used in the study. The two images were first co-registered using common ground control points. For each image, the vegetation was characterized by the normalized difference vegetation index (NDVI). The change in the state of vegetation was assesed by the change feature image. Unsupervised classification was done on the image of 1996 and the change feature image separately. The land cover classes in 1996 and the changes between the two images were obtained from the classified images.

INTRODUCTION

Remote sensing provides a technique of mapping and mornitoring natural resources. It is a valuable tool in the detection and identification of landuse/land cover changes over large areas. Land cover changes are caused by natural processes and human activities. Much work has been done in analyzing and classifying land use/land cover and vegetation types using LANDSAT, SPOT, AVHRR AND ERS/JERS SAR data [1] [2] [3] [4]. The details that can be identified and the accuracy of such analysis depend on the nature of the analyzed region as well as the temporal, spectral and spatial resolution.

The objective of this project is to assess the capability of multitemporal analysis of SPOT data, to identify land cover changes of the Sentosa island, a holiday resort island lying half a kilometre south of the Singapore main island, and to assess the condition of the vegetations existing on the island using SPOT images. Despite the rapid development of attractions, golf courses and theme parks on the island, a significant part of the island is still under the cover of dense tropical forest.

METHODS

Two multispectral SPOT images acquired in Feb 1994 and Aug 1996 were used in this study. The methods can be described as follows:

1. Atmospheric correction: The atmospheric scattering causes haze and reduces the contrast ratio of image. To correct the haze effect in each band, the minimum value obtained from the histogram was substracted from all the DNs in the band.

2. Registration: The two images were co-registered by using common set of ground control points, a first-order polynomial warp function and cubic convolution resampling.

3. Masking: The sea around the island was masked out.

4. Histogram matching: A grey level transformation was applied to all three bands in the 1994 image to match their histograms to tho respective bands of the 1994 image. The two images after histogram matching are shown in Fig.1 and Fig. 2.

5. Computation of vegetation index

$$NDVI=(NIR-RED)/(NIR+RED)$$

$$RVI = NIR/RED$$

NDVI has been shown to be highly correlated with parameters associated with vegetation conditions such as vegetation density and cover[5], green leaf biomass[6]. In this study, the NDVI and RVI images were created from the histogram-matched images of 1994 and 1996, which were expressed as NDVI94 , NDVI96, RVI94 and RVI96. From these index images, the interpretability can be enhanced. RVI and NDVI values of nonvegetated, build-up areas are consistently low, while that of perennials are consistently high .

6. Change feature extraction: The ratio NDVI96/NDVI94 was used to generate change feature image. In this ratio image, values close to one indicate little or no change. Large positive values in the change image indicate an increase. Conversely, the pixels with low values indicate decrease.

7. Unsupervised classification: The image of 1996 and the above change feature image were classified separately in order to identify the land cover classes in 1996 scene and the changes

0-7803-3836-7/97/$10.00 © 1997 IEEE

between the two images. An unsupervised classification was performed using ISODATA clustering. The ISODATA clustering algorithm selects a set of original centroids evenly spaced along the range of the spectral values for the whole image. A 98% convergence threshold was specified for the unsupervised classification in this study. The statistics from the resulting clusters were used as training statistics for classification of the whole image using a maximum likelihook classifier.

8. The result was checked by field survey.

RESULTS AND DISCUSSION

In the classification of 1996 scene, the image was classified using three XS band and RVI96. Seven main land cover classes were distinguished in the classified image (Fig. 3), which are forest, golf courses, reclaimation area, bare soil land, built-up areas, lake and beach. The change-detection image (Fig. 4) provides information about land cover changes. From the studies that had been done, some major changes can be observed in the classified image. The area used for golf course was increased in 1996 compared with 1994. The vegetation in the reclaimed area was increased. There are some minor changes in the bare land areas near the Fantasy Island, more vegetation are grown in that area ,comparing the 96 scene with the 94 scene. The changes can be observed from Fig. 4.

CONCLUSIONS

The results indicate that multitemporal satellite remote sensing is an useful approach for identifying and monitoring the state of land use. Methods based on multitemporal NDVI features derived from SPOT data are viable in distinguish vegetation from nonvegetation area.

Studies indicate that the technology can provide valuble information with respect to land use and change detection.

ACKNOWLEDGMENT

The first three authors of this paper are students of the Swiss Cottage Secondary School, Singapore. This project was done during their vacation attachment at the Centre for Remote Imaging, Sensing and Processing. The attachment was part of the School Adoption Scheme organized by the National Science and Technological Board in conjunction with the Ministry of Education, Singapore to promote interest in science and technology among secondary school students. The authors wish to thank the Principal of Swiss Cottage Secondary School for his support of the project.

REFERENCES

[1] Hans Rasch, "Mapping of Vegetation, Land Cover, and Land Use by Satellite--Experience and Conclusions for Future Project Applications", Photogram. Eng. Remote Sens. pp.265-271, 1994.

[2] Pol R. Coppin and Marvin E. Bauer, "Processing of Multitemporal Landsat TM Imagery to Optimize Extraction of Forest Cover Change Features", IEEE Trans. Geosc. Rem. Sens., vol. 32, pp. 918-927, 1994.

[3] Shahzanan R. Shaker and Yousif Ali Hussin, "A Comparison Between Optical and Microwave Satellite Data in Monitoring Tropical Land Use Changes", IEEE IGARSS95, pp.1532-1534, 1995.

[4] G. M. Foody and R. A. Hill, "Classification of Tropical forest classes from Landsat TM Data", Int. J. Rem. Sens., 17(12):2353-2367, 1996.

[5] J. P. Ormsby, B. J. Choudhury, and M. Owe, "Vegetation spatial variability and its effect on vegetation indices", Int. J. Rem. Sens. , 8(9):1301-1306, 1987.

[6] C. J. Tucker, "Red and Photographic infrared linear combinations for monitoring vegetation", Rem. Sens. Environ, 8: 127-150, 1979.

Fig 1. 1994 Feb Scene, histogram matched to 1996 Aug scene

Fig. 2 1996 Aug Scene

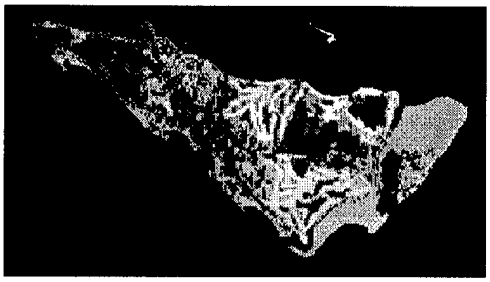

Fig. 3 Classification map based on the three XS band and RVI96 band

Fig.4 Classification based on NDVI Changes
red: large increas, green: moderate increase,
grey: no change, blue: masked out area

Evaluation of elevation derived from interferometric SAR data with DEM

Masafumi Iwamoto*, Takahiko Fujisaka*,
Chiaki Satoh**, Kyosuke Kawabata** , and Yoshihisa Hara**
* Mitsubishi Electric Corporation, Information Tecnology R&D Center
** Mitsubishi Electric Corporation, Kamakura Works
5-1-1 Ofuna,Kamakura-shi, 247 JAPAN
Email : iwamoto@rsd.isl.melco.co.jp TEL : +81-467-41-2523 FAX : +81-467-41-2519

Abstract -- Interferometric SAR is a stereoscopic method to obtain contours of ground elevation. A lot of studies have been done to derive the elevation map from SAR data, however, only few studies have been reported to examine the difference between the elevation map and DEM (Digital Elevation Model). In this paper, we compare the surface elevation map derived from interferometric SAR data with DEM, and evaluate the error distribution of the elevation map. The root mean squared error is found to be 33 m, and it agrees with the absolute vertical accuracy of DEM. The error distribution is also evaluated, and is verified to be approximately gaussian. The large errors tend to appear locally at shadowed or steep sloped area, where phase noise or phase unwrapping error is large.

1.INTRODUCTION

In recent years, a lot of studies have been done about interferometric SAR (Synthetic Aperture Radar) data processing. As the ground elevation is calculated by exploiting the phase difference between two SAR images of the same site, the phase unwrapping is the indispensable process for interferometric SAR. It is also suggested that the accuracy of elevation map depends crucially on the phase unwrapping algorithm [1] [2] [3]. Two popular techniques for phase unwrapping are the least squares approach [4] and branch cut method [5] [6]. The least squares approach is fast and fully automatic ,but errors can be large because of its sensitivity to noise and the assumed boundary condition used. The branch cut method sometimes requires manual operation, but this algorithm has a great advantage of the small error compared to the least squares approach [7].

In this paper, the elevation map is derived from ERS-1 (European Remote Sensing Satellite) SAR images using the branch cut method. The algorithm is modified to automate and reduce the elevation error. The elevation map is compared with DEM (Digital Elevation Model) and the error distribution is evaluated.

2. THE SURFACE ELEVATION MAP

The process of interferometric SAR to derive the elevation map consists of three steps. These are the registration of two images, the calculation of an interferogram, and the phase unwrapping. An example of the interferogram is shown in Fig.1.

The phase unwrapping is required, because the phase difference of an interferogram is moduro 2π, and phase field must be unwrapped to obtain its absolute value at every pixel before it is used to retrieve the ground elevation. As there are two popular techniques to phase unwrapping, the least squares approach and the branch cut method, we adopted the latter one because of the small error.

The branch cut method search the points where the phase inconsistency occurs. These singular points have the values of +/-1, and are called "residues" on the analogy of the theory of complex functions. The residues with opposite sign are paired

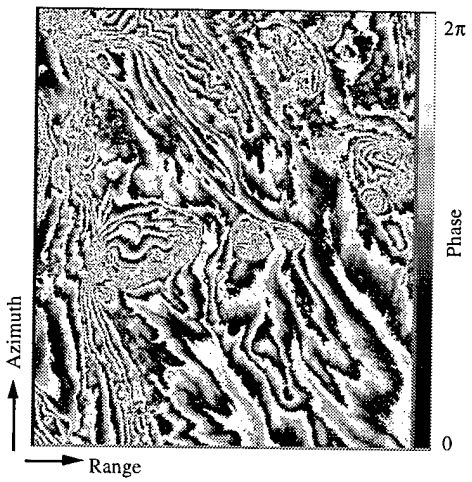

Figure 1. Interferogram.

0-7803-3836-7/97/$10.00 © 1997 IEEE

and joined to draw a "branch cut" line. Then the phase unwrapping is carried out by integrating the phase along a path without crossing any branch cut lines, and the phase of each pixel is defined uniquely. However, errors occur due to the ambiguity of the residue connection. It is not easy to find the appropriate connections, when a large number of residues appear in the image, and the manual operation is sometimes required.

The algorithm is improved to automate the process and to reduce the error. First, the residues are paired using the nearest neighbor method. And then, the simulated annealing is applied. The residues are re-connected on the basis of a sum of the length of branch cut lines. The single residues are driven away from the center of the image, and are connected to the boundary.

The surface elevation map is derived from ERS-1 SAR images over an area of Philip Smith Mountains, Alaska. The parameters of the images are shown in Table.1. The size of the image is about 37 km by 28 km. The phase is unwrapped using the modified branch cut method, and converted to the elevation map as shown in Fig.2(a).

3. THE ERROR DISTRIBUTION

The elevation map derived from interferometric SAR is compared with DEM, and the error distribution is evaluated. Before comparing, the elevation map has to be converted into the same format as that of the DEM, because the elevation map contains not only foreshortening distortion and vertical offset, but also differences from the DEM in position, direction, and spatial resolution. The foreshortening distortion is compensated on the basis of the elevation map itself, and the others are adjusted using a small area of the DEM. The registration is conducted to minimize the root mean squared error of height between the surface elevation map and the DEM.

We use a 1-degree DEM supplied by USGS (United States Geological Survey). Its horizontal spacing is 3-arc seconds by 6-arc seconds, and the absolute accuracy of elevation data is 30 m. The contour map of the DEM is shown in Fig.2(b), and the parameters are shown in Table 2.

Fig.3 shows the elevation error between the surface elevation map by interferometric SAR and the DEM. The large errors tend to appear locally at shadowed or steep sloped area, where phase noise or phase unwrapping error is large. It means a special merit of the branch cut method not to propagate the local error.

The root mean squared error is evaluated, and is found to be 33 m, which agrees with the absolute vertical accuracy of the DEM. The error distribution is also evaluated, and is verified to be approximately gaussian as is shown in Fig.4. The evaluated results are summarized in Table 3.

Table 1: SAR data parameters.

Orbit number	1029,1072
Site position	68.7 N , 150.9 W
Repeat interval	3 Days
Baseline	233.5 m
Image size (Az. x Rng.)	12800 x 2048 pixel
Resolution (Az. x Rng.)	3.9m x 19.5m

Table 2: DEM parameters.

Data spacing	South-North	3 arcsec (90.9 m)
	East-West	6 arcsec (62.2 m)
Data size	South-North	1201
	East-West	601
Accuracy	Horizontal	130 m (90%)
	Vertical	+/-30 m (90%)

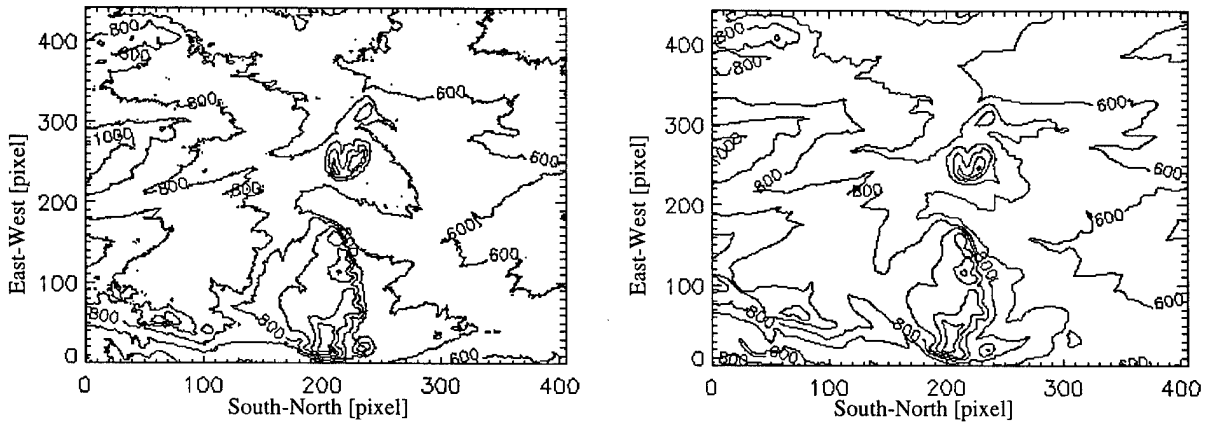

(a) Map derived from the interferometric SAR (b) Map from the DEM (Courtesy of USGS)

Figure 2. Contour maps (Interval: 100m).

4.CONCLUSION

The accuracy of the surface elevation map derived from interferometric SAR is evaluated. The phase of the interferogram is unwrapped using the modified branch cut method, and the elevation map is compared with the DEM of USGS.

The error distribution of the elevation map is evaluated, and is verified to be approximately gaussian. The root mean squared error is also evaluated, and is found to be 33m, which agree with the absolute vertical accuracy of DEM.

These results show the effectiveness of the interferometric SAR approach to derive the ground elevation map. However, we still have some points to be improved in the phase unwrapping algorithm, because the cost of calculation is too large.

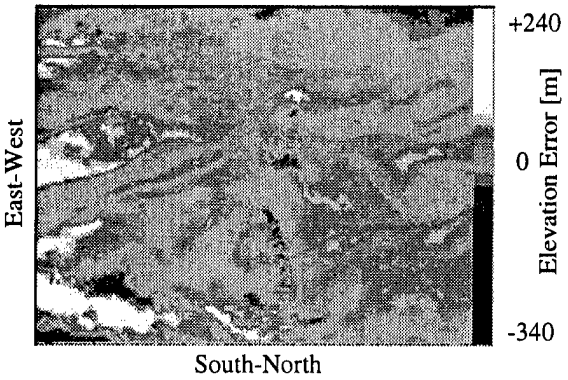

Figure 3. Elevation error.

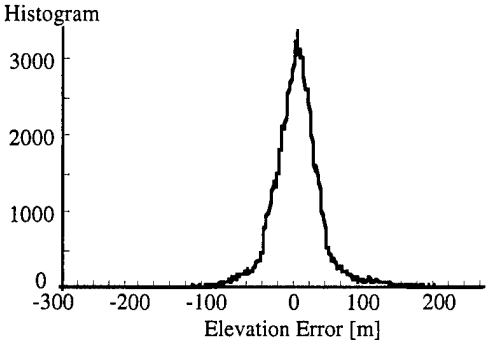

Figure 4. Histogram of elevation error.

Table 3: Evaluated results.

Evaluated area	Size	36.9 x 27.5 km
	Minimum height	460 m (DEM)
	Maximum height	1220m (DEM)
Elevation error	Average	4.2 m
	Standard deviation	33.4 m
	Prob. of under the 30m	74.9 %

REFERENCES

[1] Q.Lin, J.F.Veseccky, H.A.Zebker, "New Approaches in Interferometric SAR Data Processing", IEEE Trans.GRS, Vol.30, No.3, pp.560-567, 1992.

[2] Li,Fuk, K.Goldstein,R.M., "Studies of Multibaseline Spaceborne Interferometric Synthetic Aperture Radars" , IEEE Trans.GRS, Vol.28, No.1, pp.88-97, 1990.

[3] Rodriguez, E.Martin,J.M., "Theory and design of interferometric synthetic aperture radars", IEE Proceedings-F, Vol.139, No.2, pp.147-159, 1992.

[4] D.C.Ghiglia, L.A.Romero, "Robust two-dimensional weighted and unweighted phase unwrapping the usesfast transforms and iterative methods" , J.Opt.Soc.Am.A, Vol.11, No.1, pp.107-, 1994.

[5] R.M.Goldstein, H.A.Zebker, C.L.Werner, "Satellite radar interferometry: Two-dimensional phase unwrapping", Radio Science, Vol.23, No.4, pp.713-720, 1988.

[6] H.A.Zebker, C.L.Werner, P.A.Rosen, S.Hensley, " Accuracy of Topogrpahic Maps Derived from ERS-1 Interferometric Radar" , IEEE Trans.GRS, Vol.32, No.4, pp.823-836, 1994.

[7] C.Satoh, K,Kawabata, Y.Hara, M.Iwamoto, T.Fujisaka, Y.Zhang, Y.E.Yang, C.C.Hsu, L.Wang, K.H.Ding, J.A.Kong, "Differential SAR Interferometry using JERS-1 data" , SPIE's 11th Annual International Symposium on Aerospace / Defence Sensing Simulation and Controls, in press.

Applicability of Category Decomposition for the Fusion of Multi-Resolution Data

Shoji Takeuchi and Asako Inanaga
Remote Sensing Technology Center of Japan
Roppongi First Bldg.8F, 1-9-9, Roppongi, Minato-ku, Tokyo 106, Japan
Tel:+813-5561-8778, Fax:+813-5561-9542, E-mail:takeuchi@restec.or.jp

Abstract -- The authors tested the applicability of category decomposition method based on the linear mixture model for the fusion of multiple-resolution satellite data such as Landsat-TM and NOAA-AVHRR. The goal of the application of this method is to estimate the mixing ratio of different categories within one pixel of the lower-resolution data using the classification result of the higher-resolution data, which is considered to be useful for the extrapolation of the information from the higher-resolution data over the wider coverage of the lower-resolution data. The authors tested the estimation accuracy by two kinds of decomposition methods, the maximum likelihood estimation and the minimum distance estimation and also by the multiple regression method. The experimental results showed that the most adequate estimation was obtained by the category decomposition based on the minimum distance estimation.

1.INTRODUCTION

Data fusion using plural images with different ground resolution is one of the promising method for the practical application of satellite remote sensing data because the latest and future satellites such as current ADEOS, IRS and next SPOT board multiple-resolution sensor systems. One of the merits of multiple-resolution sensor data is that they can complement each other in resolution and coverage. One of the feasible approach using this complementary aspect is the method called "scaling", in which the information on the mixing ratio of different landcover categories obtained from the higher-resolution data is extrapolated in a wider area which the lower-resolution data may cover.

The authors studied the feasibility of this scaling using a category decomposition approach together with a multiple regression approach. As the category decomposition method, two kinds of estimation methods, the maximum likelihood estimation and the minimum distance estimation based on the linear mixture model were used. As the test data set for multiple-resolution, a simulated data set using Landsat-TM and a real data set using TM and NOAA-AVHRR were used to evaluate the estimation accuracy of the occupation rate of mixed categories within one pixel of the lower-resolution data.

2. METHOD

2.1 Category Decomposition

Resent studies (i.e. Matsumoto et al) have reported the effectiveness of the maximum likelihood estimation based on the assumption for the normal distribution of the multispectral data belonging to each land cover category. This method considers the variance of the training data as well as their mean vectors. The authors applied this maximum likelihood estimation (ML) together with the minimum distance estimation (MD), in which only the mean vector is considered.

As the spectral mixing model of plural landcover categories, the following linear mixture model is used,

$$I_i = \sum_{k=1}^{N} B_k A_{ki} \qquad \sum_{k=1}^{N} B_k = 1 \tag{2.1}$$

where I_i is the observed variable of band i of the mixel, B_k the occupation rate of category k in the mixel and A_{ki} the representative value of category k in band i.

In ML, I_i is supposed to be the normal distribution with the mean A_i and the variance σ_i^2 as follows,

$$A_i = \sum_{k=1}^{N} B_k A_{ki}^* \qquad \sigma_i^2 = \sum_{k=1}^{N} B_k^2 \sigma_{ki}^2 \tag{2.2}$$

where A_{ki}^* and σ_{ki}^2 are the mean value and variance of category k in band i respectively. The optimal combination of B_k can be estimated by minimizing the following likelihood Q(I),

$$Q(I) = -\sum_{i=1}^{M} \ln P(I_i) \tag{2.3}$$

$$P(I_i) = \frac{\exp\{-(I_i - A_i)^2 / 2\sigma_i^2\}}{\sigma_i (2\pi)^{1/2}} \tag{2.4}$$

Due to the assumption of (2.2), the spectral band should be non-correlated each other. Therefore the original data are transformed to an orthogonal spectral data by the principal component analysis (PCA).

In MD, the optimal combination of B_k is estimated by minimizing the following Euclid distance D^2,

$$D^2 = \sum_{i=1}^{M} (I_i - A_i)^2 \tag{2.5}$$

The MD does not consider the variance of the training data and only the mean vector is used.

In both of above two category decomposition methods, the optimal combination of B_k was estimated by searching all the possible combinations of B_k with the step of 10 percent occupation rate.

2.2 Multiple Regression

Another approach for the estimation of mixing ratio of landcover categories is the direct estimation by the multiple regression (MR) using the linear combination of multispectral data as follows,

0-7803-3836-7/97/$10.00 © 1997 IEEE

$$B_k = \sum_{i=1}^{M} a_{ki} I_i + C_k \qquad (2.6)$$

where a_{ki} is the regression coefficient for category k and band i and C_k is the constant.

3. EXPERIMENTAL RESULT

3.1 Test Data Set

Two kinds of data sets were generated at the Kanto Plain including Tokyo Metropolis which coverage was about 70 Km by 70 Km.

One was the simulated TM data set, in which the lower-resolution (LR) data were generated by averaging TM data. The higher-resolution (HR) data was TM data itself with 28.5 m resolution. The resolution of the LR-data is 684 m, which is nearly same as that of OCTS of ADEOS. By considering of the spectral bands of AVNIR of ADEOS, only first four bands of TM were used for simulation. In this simulated data set, the spectral bands are identical between the LR and HR data.

The second data set was the combined data of two real data, Landsat-TM and NOAA-AVHRR observed on the same day. AVHRR data were used as the LR-data with 1.1 Km resolution. As the spectral bands of AVHRR are different from those of TM, the spectral bands are different between the LR and HR data. As the spectral bands for the LR-data, the first two AVHRR bands (visible and near-infrared bands) were used.

3.2 Landcover Classification

Landcover classification was performed to the HR-data (TM data) by the maximum likelihood classifier (MLC). The original TM four bands data were transformed to two principal components by PCA. The landcover categories were Urban, Bare-soil (abbreviated as Baresl), Grass (including agricultural fields), Forest and Water. After the classification, the numbers of existing categories were counted within the area corresponding to one pixel of the LR-data to get the occupation rate for each category within one pixel of the LR-data.

3.3 Generation of Training Data

The training data which represent the spectra of each landcover category are quite important for category decomposition. For the simulated TM test data set, two kinds of training data sets were tested, one was the same training data set as that used for MLC of TM and the other was the training data set which was generated using the classified image by MLC. In the latter training data set, all the pixel values of TM data (after PCA) corresponding to the same category were collected in the classified image and the mean vector and variance were re-computed.

The above two training data sets were tested with ML and MD. The result was that the estimation error by the second training data set was always smaller in both ML and MD. This result suggests the importance of the representativeness of the spectra of training data.

3.4 Result by Simulated Data Set

Fig.1 shows the estimation results of occupation rate of mixed landcover categories by ML, MD and MR using the simulated TM test data set. Water1 and Water2 correspond to sea water and river water respectively. As Urban and Forest were sometimes confused with Water1 or 2, another case which neglected Water category was also tested. From Fig.1 it is clear that the worst one is ML. For MD and MR, it is difficult to select better method only from the result of Fig.1.

A possible reason why ML resulted in the worst errors is that the variances of the training data were not estimated accurately because the training data were collected from whole test areas where the spectral variety exists due to many subsets of the same landcover category. This spectral variety will reduce if one landcover category is divided into several sub categories according to their spectral variations. However, in this case, the number of categories to be decomposed increases, which may cause bigger errors for the estimation of their occupation rate.

3.5 Result by Real Data Set

Only MD and MR were tested using the real TM-AVHRR data set. One reason to abandon ML is the result of Fig.1. Another reason is the difficulty to generate proper training data set for ML. As the spectral bands are different between the HR and LR data, it is necessary to reconstruct training data using the LR-data. As almost of the pixels of the LR-data are mixel condition, it is considered difficult to estimate accurate variance from the mixel-like spectral data.

The mean vector was estimated from quasi-pure pixels which occupation rate for same category is more than 90 percent. For some landcover categories like Grass, it was still difficult to find such a pure pixel. For these categories, the regressive estimates was computed using the following residuals of band values,

$$R_{i,n} = I_i - (\sum_{m=1}^{L} A_{mi} * B_m) \qquad (3.1)$$

where $R_{i,n}$ is the residual of band i for category n and m means the major categories which mean vectors can be estimated from pure pixels. By the regression between $R_{i,n}$ and B_n, $R_{i,n}$ when B_n is 100 percent is the mean value of band i for category n. However, the category with very small occupation rate like Water2 was still impossible to estimate the mean vector by the regression and it was neglected finally.

Fig.2 shows the result for the real TM-AVHRR data set by MD and MR. As Water2 was neglected, the water category was only one (Water). The case in which Water was neglected was also tested. For both cases, MR was slightly better than MD.

3.6 Distribution Pattern of Occupation Rate

Although the previous result suggests the slightly better result for MR than for MD, the actual distribution patterns should be also considered. According to the inspection of the distribution patterns of estimated occupation rate by MD and MR, it was clearly verified that the estimated patterns by MR always resulted in fuzzy patterns with less contrast compared with the estimated patterns by MD. This fuzziness is considered to be the fundamental characteristics of the regression in order to get the smallest error. Therefore, by considering this fuzziness of

MR, MD is considered to be the best method among ML,MD and MR.

3.7 Effect of Step for Occupation Rate

In ML and MD, the step of 10 percent occupation rate was used to estimate the optimal combination of B_k. This step value seems to be large and actually the step value brings quantization error. However, actual quantization error for 10 percent step is theoretically 2.89 percent, which is relatively smaller than the actual estimation errors. In addition the test with a reduced step of 5 percent was performed and the result was only 0.4 percent reduction of the estimation errors. This result suggests that the step value has less effect on the estimation errors.

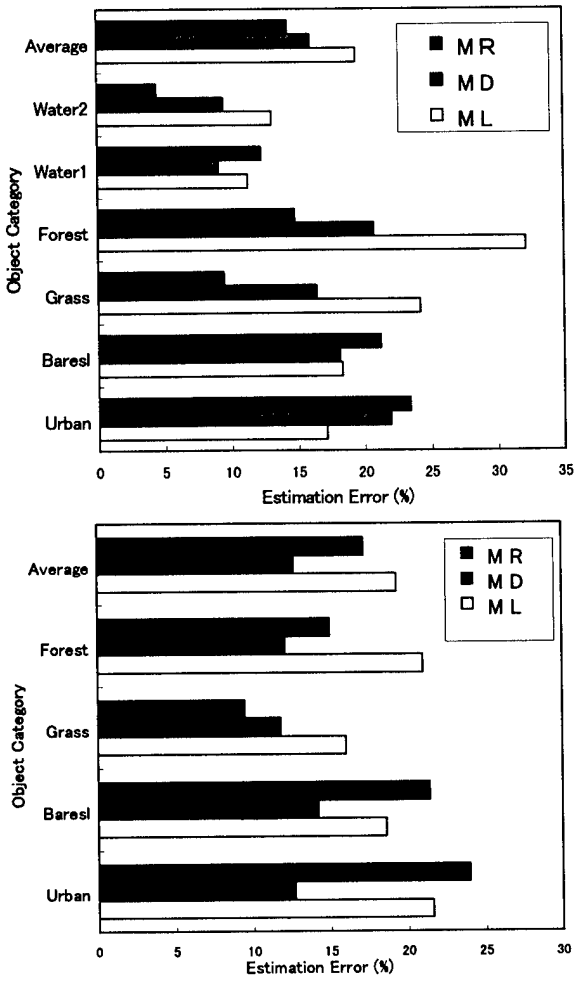

Fig.1 Estimation accuracy by Maximum Likelihood (ML), Minimum Distance (MD) and Multiple Regression (MR) for simulated TM multiple-resolution data set. The upper graph shows the result for six categories and the lower graph shows the result for four categories excluding Water.

4. CONCLUSION

The above experimental results suggest the feasibility for applying category decomposition approach for the fusion of multiple-resolution sensor data obtained from current and future Earth observation satellites. For practical utilization of the scaling technique described in this paper, it is still necessary to evaluate the effect by the variety of spectra due to wide coverage of the LR-data. Especially the effect of atmosphere should be corrected to obtain uniform spectra over whole area of the coverage of LR-data. These studies should be continued to obtain a practical methodology to utilize the multiple-resolution sensor data effectively.

REFERENCES

[1] M.Matsumoto, K.Fujiku et al, "Category Decomposition based on Maximum Likelihood Estimation,"(Japanese), Journal of the Japan Society of Photogrammetry and Remote Sensing, Vol.30,No.2,pp25-34, May 1991.

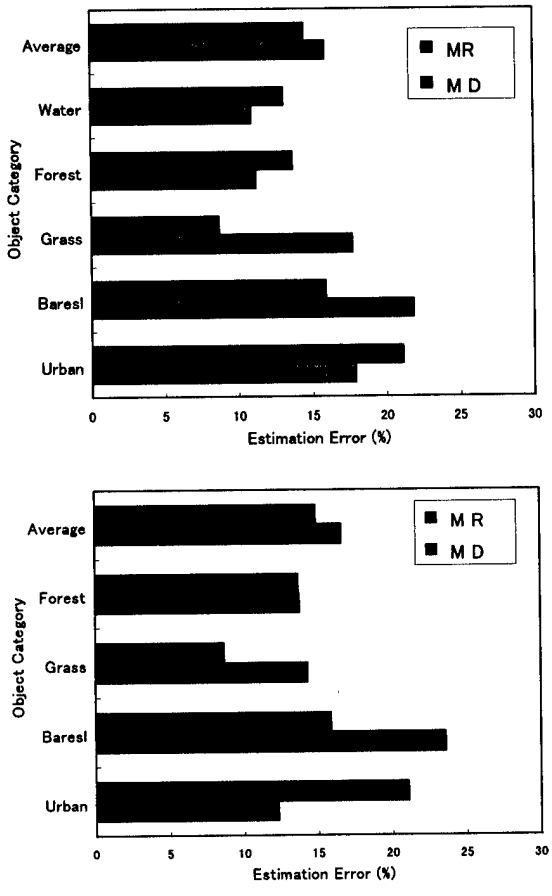

Fig.2 Estimation accuracy by Minimum Distance (MD) and Multiple Regression (MR) for the real TM-AVHRR multiple-resolution data set. The upper graph shows the result for five categories and the lower graph shows the result for four categories excluding Water.

Estimation of Topographic Effects in NVI data obtained from Satellite Images

T. Kusaka and M. Sakane
Kanazawa Institute of Technology
7-1 Nonoichi-machi Ishikawa 921, Japan
Tel: +81-762-48-1100 Fax: +81-762-94-6727
E-mail: kusaka@manage.kanazawa-it.ac.jp

Abstract -- The topographic effects in Normalized Vegetation Index (NVI) data obtained from Landsat TM data and NOAA AVHRR data are estimated. It is assumed that the topographically induced radiance variations can be estimated by the cosine of the angle, γ, between the direction of the sun and the local surface normal. Digital terrain data sampled with the grid width 50m are used to evaluate γ. By comparing NVI data derived from satellite data with γ-data, the following results were obtained: (1)The correlation between NVI and VI data derived from Landsat TM data and γ-data is high. (2)The correlation between NVI data derived from NOAA AVHRR data and γ-data is also significant.

INTRODUCTION

The global vegetation index data (GVI data) produced from NOAA AVHRR data have been utilized by many researchers. However, in attempting to derive the vegetation index related to the intrinsic properties of ground objects from satellite-level data over mountainous terrain, the problem is more complex, because solar illumination conditions vary remarkably one target to another due to the topography. Since the vegetation index is obtained from the ratio of radiance values in two channels, visible and near infrared channels, in general, it is considered that topographic effects, which are radiance variations caused by the topography, will be reduced when the optical thickness of the atmosphere is thin [1]. However, the sensor receives the radiance due to multiple reflections of light by adjacent terrain [2]. And shadows cast by adjacent terrain are contained in the range of one pixel of low resolution satellite data. This indicates that the global vegetation index data will be modulated significantly by topographic effects.

In this study, we estimate the topographic effects in Normalized Vegetation Index (NVI) data obtained from Landsat TM data and NOAA AVHRR data. It is assumed that the topographically induced radiance variations depend on the cosine of the angle, γ, between the direction of the sun and the local surface normal [2]. The influence of topographic effects on the NVI data derived from satellite data can be evaluated by comparing spatial variations of NVI data with those of γ. We use digital terrain data (DTD) sampled with the grid width 50m to evaluate the values of γ.

VEGETATION INDEX

The vegetation index (VI) is defined as the ratio of radiances received by the sensor in two channels, visible and near infrared channels, i.e., VI = X2 / X1, where X1 is the radiance value at the visible channel and X2 the radiance value at the near infrared channel. The normalized vegetation index (NVI) that is usually called the normalized difference vegetation index (NDVI) is also defined as NVI = (X2 - X1) / (X2 + X1). If the optical thickness of the atmosphere is very thin, and the ground cover is a three-dimensionally varying surface with Lambertian reflectances, then X1 and X2 would be proportional to γA1 and γA2, respectively, where A1 and A2 are surface reflectances at the visible and near infrared channel. In this case, we see that VI and NVI do not depend on γ, that is, they are not modulated by the topographic effect. However, the radiances recorded by satellite sensors involve the additive path radiance and the diffusely transmitted radiance reflected off the background outside the target object because of the scattering of light in the atmosphere. Therefore, VI and NVI will be a function of γ.

VARIATIONS OF TOPOGRAPHICALLY INDUCED VEGETAION INDEX

Digital terrain data and γ -data

We used digital elevation data produced by Geographical Survey Institute of Japan whose grid width is 50m. For study site, we selected the mountain region near Kanazawa city in Japan. The terrain elevation in this region is lower than 3000m. The values of γ, which is the cosine of the angle between the direction of the sun and the local surface normal, were computed at every grid point of DTD. Thus obtained data set will be referred to as γ -data.

VI and NVI estimated from the reduced Landsat TM data

The NDVI derived from NOAA AVHRR data is commonly used in monitoring the vegetation in the global environment. The instantaneous field of view (IFOV) of NOAA AVHRR is coarse and the received signals by AVHRR will include

0-7803-3836-7/97/$10.00 © 1997 IEEE

radiances reflected by surface objects at different slopes. On the other hand, the high resolution Landsat TM image is very useful in observing the local change of vegetation. Therefore, the radiance variations in one pixel of AVHRR data will be inferred from the averaged TM data over the corresponding area to the IFOV of the NOAA AVHRR. This is why the Landsat TM image is transformed to the reduced image with the almost same resolution as the NOAA AVHRR data.

We first extracted a 512*512 pixel area from Landsat TM data taken on October 10, 1987. The azimuth angle of the sun was 50° and the azimuth angle 145°. Since the grid width of DTD we used is slightly coarse, as compared with the ground resolution of TM data, we interpolated the grid width of DTD to the 30m grid interval to compute γ -data. The Landsat TM image was accurately registered to the γ -data by means of geometric transform using ground control points. Next, we computed the averaged count levels over the 37*37 pixel area in the original TM image to create the reduced TM image, and obtained VI and NVI from the values of TM bands 2 and 4 in the reduced TM image. The values of γ were also averaged over the 37*37 pixel area in γ -data. Hereafter, this reduced γ -data will be referred to as Γ-data. Figs.1 and 2 show the shaded relief images of NVI data and Γ-data, respectively. We can see from Figs.1 and 2 that two images show the similar pattern. A plot of the values of VI, NVI and Γ-data from a traverse of 13 pixels along the 315th line in Fig.1 is shown in Fig.3. In Fig.3 the values of NVI and Γ are multiplied by 127 and those of VI by 24. As seen from Fig.3, the variations of NVI and VI are strongly correlated to those of Γ. This means that the values of NVI and VI obtained from the reduced TM image are significantly modulated by topographic effects. Fig.4 shows the variations of count levels of bands 2 and 4 in the reduced TM image and Γ-data at the same line as shown in Fig.3. We can see that the count levels at TM band4 are large and show the strong correlation with the variations of Γ, while the count levels at TM band 2 are not enough large to contain the variations of Γ.

VI and NVI obtained from NOAA AVHRR

We used the DTD covering 40km*50km mountainous area to compute Γ-data, and used the channels 1 and 2 of AVHRR data taken on May 10, 1990, August 19, 1991 and November 30, 1991 to evaluate NVI and VI. The zenith angles of the sun at the corresponding date were 28, 34 and 66 degree. The values of the computed VI and NVI were normalized by using maximum and minimum values of VI and NVI, i.e., normalized NVI=255*(NVI-Min(NVI))/(Max(NVI)-Min(NVI)). Figs.5 and 6 show the shaded relief images of NVI obtained from AVHRR data on Nov. 30, 1991and Γ-data, respectively. We can see from Fig.5 that two images show similar shaded patterns in the same as Figs.1 and 2. The variations of NVI, VI and Γ at the 10th line in Fig.5 are also shown in Fig.7. As seen from Fig.7, the values of NVI and VI vary correlatively with those of Γ. This means that the values at channel 2 are enough large to involve the variations of Γ. On the other hand, the reflectance of vegetation at channel 1 is small and so the values of channel 1 do not include the variations of Γ as shown in Fig.8.

CONCLUSIONS

We obtained the following results, by comparing NVI and VI data derived from satellite data with γ-data obtained from digital elevation data.

(1)The correlation between NVI and VI data derived from Landsat TM data and Γ-data is high.

(2)The correlation between NVI and VI data derived from NOAA AVHRR data and Γ-data is also significant.

This means that the count levels at the near infrared channel in Landsat TM and NOAA AVHRR data show the high correlation with Γ-data, while the count levels at the visible channel are not enough large to show the variations of Γ.

This study was supported by the Grant-in-Aid for Scientific Research on Priority Areas (No. 08241222) of the Japanese Ministry of Education, Science, Sports and Culture.

REFERENCES

[1] T.Kusaka, et al., Signature variations due to atmospheric and topographic effects on satellite MSS data over rugged terrain, Proc. IGARSS'88, pp.825-828, 1988

[2] T.Kusaka & Y.Kawata, Atmospheric and topographic correction of satellite data over mountainous terrain, Proc. IGARSS'94, pp.58-60, 1994

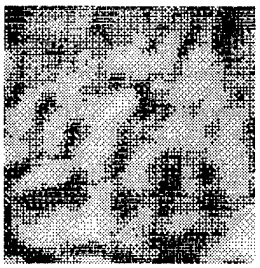

Fig.1 NVI data obtained from the reduced TM data

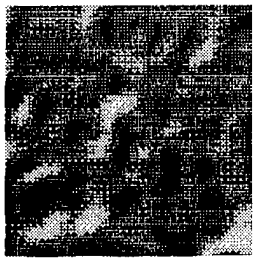

Fig.2 Γ-data in the test area

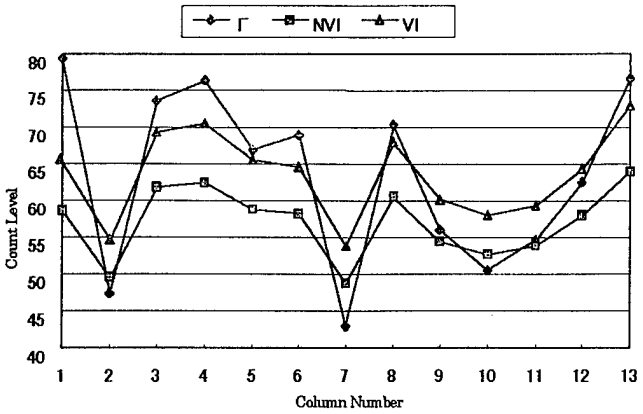

Fig.3 Variations of NVI, VI and Γ values at the 315th line in Fig.1

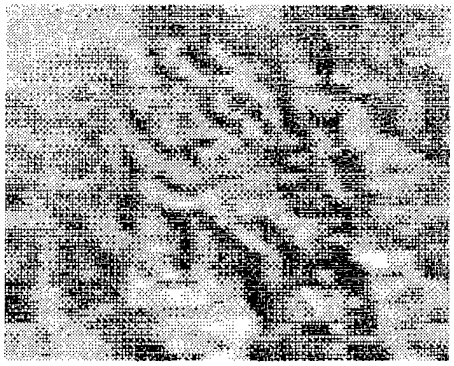

Fig.6 Γ-data at the same date as shown in Fig.5

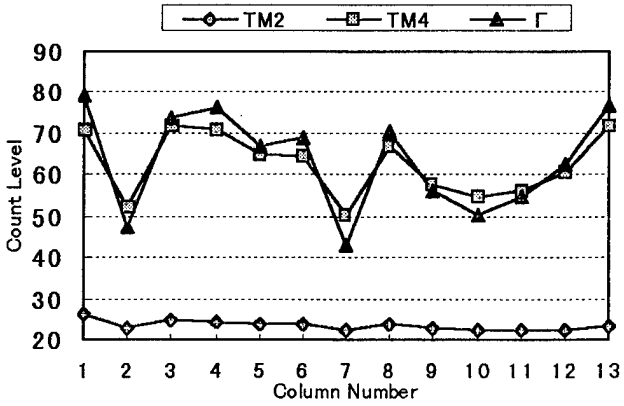

Fig.4 Count levels of bands 2 and 4 in the reduced TM image and Γ-data at the same line as shown in Fig.3

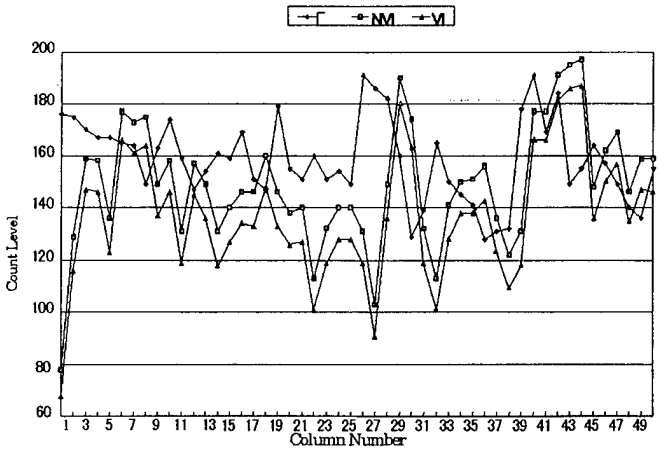

Fig.7 Variations of NVI, VI and Γ values at the 10th line in Fig.5

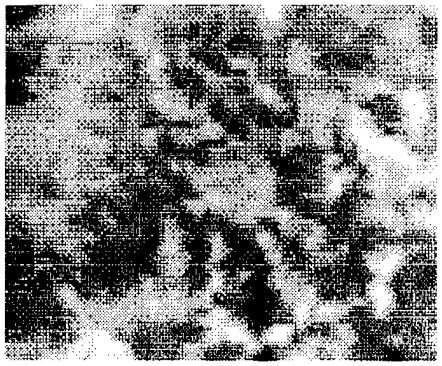

Fig.5 Shaded relief image of NVI obtained from AVHRR data on Nov. 30, 1991

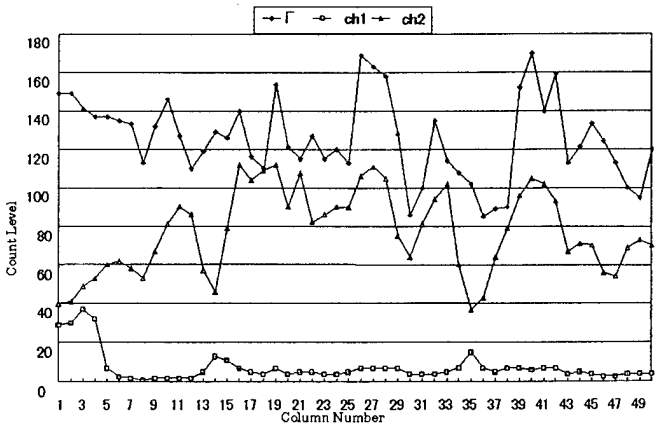

Fig.8 Count levels of channels 1 and 2 in NOAA AVHRR data and Γ-data at the same line as shown in Fig.7

A Method for Object-Oriented Feature Extraction from Hyperspectral Data — Generation of New Channels by Fusion of Data —

Sadao Fujimura and Senya Kiyasu
The University of Tokyo, Graduate School of Engineering
Department of Mathematical Engineering and Information Physics
7-3-1 Hongo, Bunkyo-ku, Tokyo 113, JAPAN
Phone: +81-3-3812-2111 ext.6900, Fax: +81-3-5689-7354
E-mail: fuji@k2.t.u-tokyo.ac.jp

Abstract — Extracting significant features is essential for processing and transmission of a vast volume of hyperspectral data. Conventional ways of extracting features are not always satisfactory for this kind of data in terms of optimality and computation time. We present an object-oriented feature extraction method designed for supervised classification. After all the data are reduced and orthogonalized, a set of appropriate features for prescribed purpose is extracted as linear combinations (fused channel) of the reduced components. Each dimension of hyperspectral data is weighted and fused according to the extracted features, which means the generation of new channels from hyperspectral data. Results of feature extraction are applied to evaluating the performance of sensors and to designing a new sensor.

INTRODUCTION

Recently the dimension of remotely sensed data becomes higher and higher because of higher spectral resolution, increasing number of sensors, and multi-temporal observations. Airborne Visible Infrared Imaging Spectrometer (AVIRIS), for example, has 224 spectral bands in the 0.4 - 2.5μm region [1]. In order to efficiently obtain necessary information from these hyperspectral data, or to transmit the data through a communication channel, the quantity of data must be reduced. This can be achieved by extracting significant features.

We present here a feature extraction method designed for object-oriented supervised classification. In classification of data we have some kind of objectives or intention. Therefore we introduce subjective significance explicitly into feature extraction. The purpose of our feature extraction is to extract a set of features which optimally separate one class from another among a particular set of important classes.

One of the conventional methods of feature extraction utilizes an exhaustive search for selecting the best subset of sensor channels [2]. However, when it is applied to hyperspectral data, astronomical computation time is required to evaluate all the combinations of channels. Hyperspectral data contain useful information in many channels at the same time. Therefore it would be better to fuse the data from many dimensions and generate new channels to extract important information. Principal component analysis [3] or canonical analysis [4] are the methods which can be used for fusing many dimensions of data. Though they extract features which yield high average separability among classes, they are not always suitable for object-oriented classification, because they are not selected from the viewpoint of particular discrimination. Our method extracts appropriate features as linear combinations of reduced and orthogonalized components obtained by principal component analysis. Each feature is determined successively by considering the distance from the significant classes until the distance satisfies a condition.

The results of feature extraction can be applied to evaluating the current sensors' efficiency and/or designing new sensors for a specific purpose. We will also show an example of evaluation and designing of sensors.

PRINCIPLE OF FEATURE EXTRACTION

Description of Data

We assume that we can get training data for almost all the classes in an image and can estimate the characteristics of the classes.

We denote N dimensional hyperspectral data by a vector $\mathbf{y} = (y_1, \cdots, y_N)^t$ and suppose that they are classified into one of, say, n classes. Then, $\mathbf{y}$ can be decomposed into class mean $\mathbf{y}_a$ and within-class dispersion $\mathbf{y}_e$ as $\mathbf{y}_{ij} = \mathbf{y}_{a_i} + \mathbf{y}_{e_{ij}}$ $(i = 1 \sim n,\ j = 1 \sim m_i)$, where $\mathbf{y}_{ij}$ is j-th data of class i. We write the covariance matrix of $\mathbf{y}$, $\mathbf{y}_a$ and $\mathbf{y}_e$ as $\mathbf{C}_{yy}$, $\mathbf{C}_a$ and $\mathbf{C}_e$ respectively. Here, we assume that $\mathbf{C}_e$ of each class is identical.

Feature Extraction

Here, we consider a case where several important classes should be discriminated from all the other classes. We use a measure of separability between two classes and extract the features which maximize the separability of a particular pair of classes that we wish to discriminate.

Our method consists of two steps of processing: pre-processing and feature extraction. In the pre-processing, hyperspectral data $\mathbf{y} = (y_1, \cdots, y_N)^t$ are reduced and normalized to m $(m \ll N)$ components $\mathbf{z} = (z_1, \cdots, z_m)^t$ by

0-7803-3836-7/97/$10.00 © 1997 IEEE

a linear transformation $\mathbf{z} = \mathbf{A}^t\mathbf{y}$. From the assumption on $\mathbf{C}_e$ that the within-class dispersion is the same for all the classes, they are normalized into m dimensional spheres after transformation. This makes the space uniform: this means that the distance measured in terms of variance does not have directionality in the space.

In the second step, features are successively extracted [5] until there remains no class which has distance from the particular classes less than the minimum distance obtained so far. Feature extraction is done by determining sub-space in the feature space: that is, by making a linear combination of $\mathbf{z}$ as $\mathbf{a}^t\mathbf{z}$, where $\mathbf{a}$ is an m dimensional weight vector which we call here feature vector. The procedures for determining successive feature vectors is as follows:

(1) Set an optimal feature vector $\mathbf{a}_1$ between the two nearest classes among the prescribed classes.
(2) Evaluate the separability on $\mathbf{a}_1$ for all the combination of the prescribed classes.
(3) If there is any pair of prescribed classes which does not have enough separability, set an additional feature vector $\mathbf{a}_2$ perpendicular to $\mathbf{a}_1$ between them.
(4) Features are successively extracted until all the distance among the prescribed classes are larger than the minimum distance obtained so far.
(5) Apply the procedures (2)~(4) to the distance among the prescribed and the other classes.

A feature ${\mathbf{a}_i}^t\mathbf{z}$ is equivalent to $(\mathbf{A}\,\mathbf{a}_i)^t\mathbf{y}$, because $\mathbf{z} = \mathbf{A}^t\mathbf{y}$, where $(\mathbf{A}\,\mathbf{a}_i)$ means the factor for weighting each dimensions of the spectral data. Each dimensions are fused according to the extracted features $(\mathbf{A}\,\mathbf{a}_i)$ to generate new channels for object-oriented classification.

EXPERIMENTAL RESULTS OF FEATURE EXTRACTION

We acquired data for four growth-stages of tree leaves (A~D: from young to fallen), soil, stone and concrete by using a ground-based imaging spectrometer which we developed. We obtained 411 dimensional data from the sensor and used for the experiments. For estimating the mean and the variance of each class, 45 training data were used for each class. Averaged relative reflectance is shown in Fig. 1. In the following, the covariance matrices of the classes are assumed to be identical.

After reducing and normalizing the data to 7 orthogonal components, features were extracted from one to another. Here we selected classes A and B as those significant to be classified. Two features shown in the form of the weighting factors in Fig. 2 are extracted. This figure shows how we weight and fuse the data and generate new channels sufficient for classifying classes A and B. The first feature is set between A and B, and the second is set between A and C.

The test data of 196 samples for each class were classified by using linear discriminant functions. The classification accuracy was compared with that by canonical analysis. Fig.3 shows the accuracy for classes A and B in terms of the number of features, which is about 35% (one feature) and 18% (2 features) higher than that by canonical analysis.

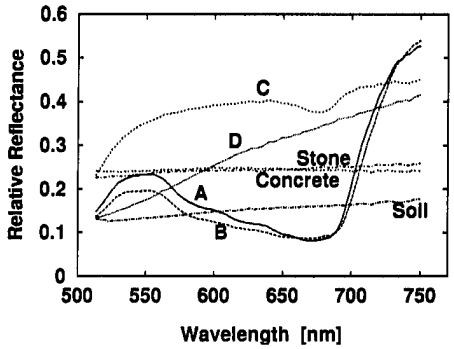

Fig. 1 Spectral reflectance of objects (A~D : Leaves of plant)

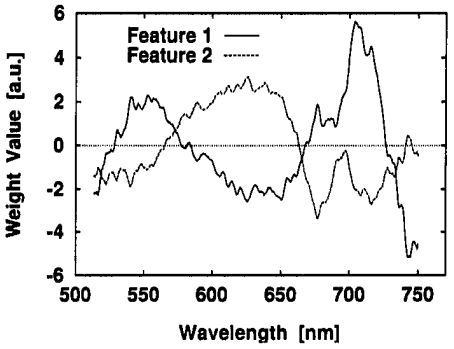

Fig. 2 Weighting factors for the significant classes A and B

APPLICATION TO SENSOR EVALUATION AND SPECTRAL BAND DESIGN

We applied the result of feature extraction to the evaluation of performance of sensors, which are evaluated by classification accuracy of significant classes.

Hyperspectral data acquired are separated into two groups, and object-oriented features are extracted using the first half of the data. The other half of the data are classified by using the extracted features and by using the spectral bands of a sensor under consideration. The performance is evaluated according to the accuracy of classification.

In order to show the method, we picked up the subset of the bands from the Coastal Zone Color Scanner (CZCS). Because of the limited coverage for wavelength of acquired data, only three out of the six CZCS's spectral bands (bands 2,3 and 4) were used for experiments. Fig. 4 shows the classification accuracy by the three bands of CZCS, and by the extracted features. The former was lower than

the latter by about 9% when the number of bands was three. Thus, we can know that the performance of the three bands of CZCS is not sufficient for classifying the classes A and B.

We also applied the extracted features for designing spectral bands. The features indicate how we give the weight and fuse the data as we mentioned before. The magnitude of extracted features are suppose to be suggesting informative spectral regions. Therefore, it is reasonable to allocate spectral bands to the regions where the magnitude of extracted features is high.

An example of bands allocated to the prominent regions of extracted feature is shown in Fig. 5. Classification accuracy using these bands is shown in Fig. 6. When the number of bands is three (band 3, 4 and 5 in Fig. 5 were used), the accuracy of classification was as high as by the extracted features themselves.

CONCLUSIONS

We have proposed a feature extraction method for object-oriented classification of hyperspectral data. By extracting features, hyperspectral data are fused and new channels are generated. The method was tested using 411 dimensional hyperspectral data for two prescribed significant classes. It was found that classification accuracy of the particular classes increased compared with classification using the features extracted by canonical analysis. We have showed a method to apply the extracted features to evaluating the performance of current sensors and to designing band of new sensors. It was shown that the spectral bands of sensors can be improved for a specific purpose by designing them according to the extracted features. Extension of this method to extracting quantitative information efficiently and accurately from hyperspectral data are subjects for a future study.

REFERENCES

[1] G.Vane, "First results from the Airborne Visible/ Infrared Imaging Spectrometer (AVIRIS)," Proc. of SPIE, vol.834, pp.166-174, 1988.

[2] D.A.Landgrebe, "Useful Information from Multispectral Image Data: Another Look," in Remote Sensing: The Quantitative Approach, P.H.Swain and S.M.Davis, Eds. McGraw-Hill, 1978, pp.358-361.

[3] P.J.Ready and P.A.Wintz, "Information Extraction, SNR Improvement, and Data Compression in Multispectral Imagery," IEEE Trans. Comm., vol. COM-21, pp.1123-1131, 1973.

[4] R.A.Schowengerdt, Techniques for Image Processing and Classification in Remote Sensing, Academic Press,1983, pp.159-167.

[5] S.Fujimura and S.Kiyasu, "Significance-Weighted Feature Extraction from Hyper-Dimensional Data," Proc. of SPIE, vol.2318, pp.63-68, 1994.

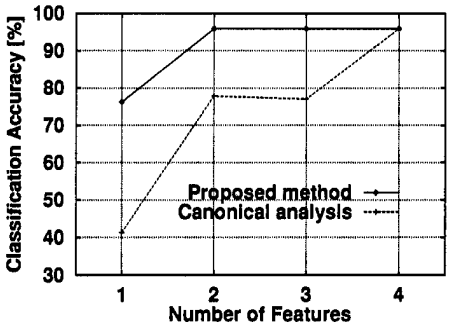

Fig. 3 Classification accuracy of calsses A and B versus number of features

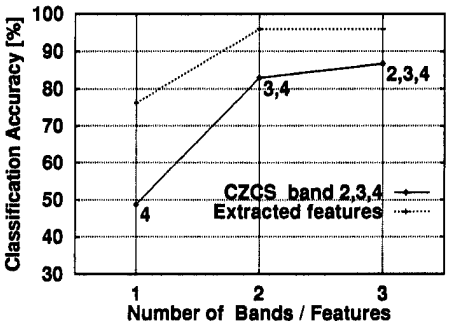

Fig. 4 Classification accuracy by bands 2, 3 and 4 of CZCS and by extracted features

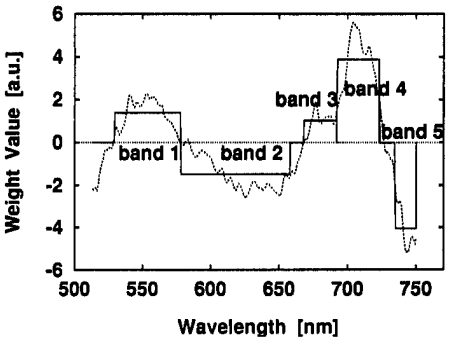

Fig. 5. Five spectral bands designed for new sensors using extracted features
(Rectangular weights approximating feature 1)

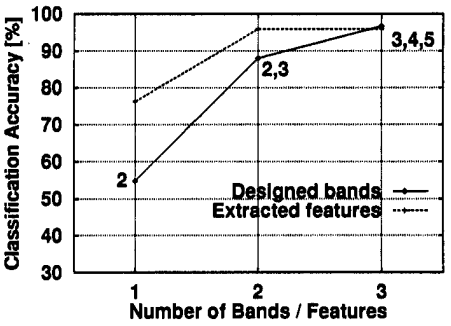

Fig. 6. Classification accuracy by designed bands

BAYESIAN FEATURE SELECTION FOR CLASSIFYING MULTI-TEMPORAL SAR AND TM DATA

Y. Yamagata and H. Oguma
National Institute for Environmental Studies
Onogawa 16-2 Tsukuba 305 JAPAN
Tel:+81-298-50-2545 Fax:+81-298-50-2572
Email:yamagata@nies.go.jp

Abstract – Remotely sensed imagery data from various satellite sensors are now available for environmental monitoring. However, due to the difficulty in surveying, it is not easy to obtain a sufficient number of training data for classifying these high dimensional imagery data. In order to make use of these imagery data, it is necessary to develop a classification method which can attain a high classification accuracy only using a limited number of training data. In this study, we have tested the bayesian approaches which integrate feature selection and model averaging in the classification process. The experiments are conducted using bayesian neural networks, gaussian process, and maximum likelihood for classifying wetland vegetation types using multi-temporal LANDAT/TM, JERS1/SAR, and ERS/SAR data. The results shows that the bayesian approaches work well for classifying these imagery data, and especially the gaussian process has a very high accuracy which outperforms other methods for classifying the sensor fusion data using JERS1/SAR and LANDSAT/TM.

INTRODUCTION

In order to accurately classify the multi-temporal sensor fusion data, it is necessary to use many training data to determine the parameters of the classification model. However, the number of training sample is often limited for the environmental studies such as wetland monitoring due to the difficulty in field investigation[1)2)].

Feature extraction and selection method is often used to circumvent this problem[3)]. By using these methods, with the process of cross validataion[4)], we can reduce the parameters of the model. However these methods are not free from underfitting problem. Namely, there is a danger that the model is so simplified that it can not describe the difference between the classes sufficiently. The selected model also has an uncertainty because the choice is depending on the training data. Thus the model might not be optimal for real data classification.

In stead of selecting a model, bayesian approach integrate the process of model selection and model averaging[5)6)]. Bayesian model calculate the posterior probability of each model with different parameters and integrate the model estimations by using these posterior as the weight for the model. Thus bayesian approach is free from overfitting and underfitting without reducing the features. As we need not separate the training the data for cross validation, we can make use of the limited number of training data without loosing the generality of the model.

In this study, in order to see how the bayesian approach enhance the classification performance, we have conducted classification experiments using bayesian methods and compared with the conventional maximum likelihood method. Here, bayesian neural networks[7)] and gaussian process[8)] were employed as the bayesian classification method. These methods are tested for classifying the wetland vegetation types using multi-temporal LANDSAT/TM, JERS1/SAR, and ERS1/SAR data.

DATA AND METHODS

In the experiments, 13 scenes of LANDSAT/TM (Fig.1), JERS1/SAR (1993/4/3, 1996/5/21, 1993/6/30, 1993/8/13), and 4 scenes of ERS1/SAR (1993/4/29, 1993/6/3, 1993/8/12, 1993/10/21) data were used for the classification after the geometric corrections to 20m resolution.

Classification were conducted for 9 classes of wetland vegetation types (Alder, Alder/Reeds, Sphagnum, Pools, Trifoliata, Reed, Sedge/Reed, Sedge). 100 training data for each class were sampled and the accuracy was tested using 100 test data.

The classification were conducted using the following 3 methods,

1) Maximum Likelihood

Multidimensional gaussian distribution with different covariance matrix was assumed for each class, and the matrixes were estimated from the training data and the class of the test data were predicted using maximum

0-7803-3836-7/97/$10.00 © 1997 IEEE

likelihood method.

2) Bayesian Neural Networks

One hidden layer of the neural networks with the nodes of twice the number of input variables were used. All the parameters are given the priors and the posterior are calculated for the training data. The model prediction were then integrated over the parameter space with the posterior as weights.

3) Gaussian Process

By introducing the latent variables $y_0^{(i)},\ldots,y_{K-1}^{(i)}$ for classes, the classification problem can be transformed to a regression problem. Then, the latent variables are modeled using gaussian process which is defined by the covariance function.

$$Cov[y_k^{(i)}, y_k^{(j)}] = \eta_k^2 \exp(-\sum_{u=1}^{p} \rho_{ku}^2 (x_u^{(i)} - x_u^{(j)})^2) + \delta_{ij} J$$

where, $x_u^{(i)}$ is the p input variables, i, j is the over the training data, η_k and ρ_{ku} are hyper parameters, and the J is a jitter term to stabilize the calculation.

Then the prediction for the test data can be calculated as,

$$E[y_k^{(n+1)} | y_k^{(1)},\ldots,y_k^{(n)}] = \mathbf{k}_k^t \mathbf{C}_k^{-1} \mathbf{y}_k$$

Finally, using the bayesian approach, the predictions are integrated over the parameter space by the Markov Chain Monte Calro methods as,

$$\int P(y_k^{(n+1)} | x^{(n+1)}, \theta) P(\theta | D) d\theta \cong \frac{1}{N} \sum_{t=1}^{N} P(y_k^{(n+1)} | x^{(n+1)}, \theta^{(t)})$$

RESULTS

1) The 13 LANDSAT/TM scenes were classified separately by the 3 methods and the accuracy (classification error %) were compared. The result in Fig. 1 shows that the gaussian process was superior to the maximum likelihood in 9 cases and the accuracy was higher more than 5% in 6 cases.

2) Multi-temporal JERS/SAR and ERS1/SAR have been classified by changing the speckle noise filter. The filters used were FRS(Frost), Lee, MAP, MED(Median). The result in Fig. 2 shows that the MAP and MED filter perform well for both JERS1/SAR and ERS1/SAR data. Both of gaussian process and bayesian neural network were superior to the maximum likelihood in 6 cases, however the increases in accuracy were less than 3 %. On the other hand the accuracy was greatly improved for the sensor fusion data of JERS1 and ERS1. The accuracy of gaussian process and bayesian neural network was higher than the maximum likelihood around 10%.

3) The classification accuracies are compared for the 3 combinations using LANDSAT/TM, JERS1/SAR, and ERS1/SAR data.
   a) The 3 TM scenes acquired in June, August, and November are overlaid successively and classified. The result were shown in the left hand side of Fig.3. This shows that the gaussian process performed better as the number of the scenes increases.
   b) NDVI(Normalized Difference Vegetation Index) were calculated for 13 LANDSAT/TM scenes and was also combined with both the JERS1/SAR and ERS1/SAR. The result in the middle of Fig.3 shows that the only bayesian neural network increased the classification accuracy for this combination.
   c) The scene acquired in August which showed the highest accuracy was overlaid with the JERS1/SAR and ERS1/SAR scenes. The result in the right side of Fig. 3 shows that the JERS1/SAR information greatly improve the accuracy more than 5% and especially the gaussian process attained the highest accuracy of all.

REFERENCE

1)Y. Yamagata and Y. Yasuoka : Unmixing Wetland Vegetation Types by Subspace Method Using Hyperspectral CASI Image, International Archives of Photogrammetry and Remote Sensing, XXXI, 781/787 (1996).

2)J. P. Hoffbeck and D. A. Landgrebe : Classification of Remote Sensing Images Having High Spectral Resolution, Remote Sensing Environment, 57, 119/126 (1996).

3)T. Y.Young and K.-S. Fu eds. : Handbook of Pattern Recognition and Image Processing, Academic Press, (1986)

4)D.Michie, D.J.Spiegelhalter and C.C.Taylor eds. : Machine Learning: Neural and Statistical Classification, Ellis Horwood, (1994)

5)B. D. Ripley : Pattern Recognition and Neural Networks, Cambridge University Press, (1996)

6)A. E. Raftery : Bayesian Model Selection in Social Research, Sociological Methodology, (1995)

7)R. M. Neal : Bayesian Learning for Neural Network, Springer-verlag, (1996)

8)R. M. Neal : Monte Carlo Implementation of Gaussian Process Models for Bayesian Regression and Classification, Technical Report, Department of Statistics, University of Toronto, No.9702, (1997).

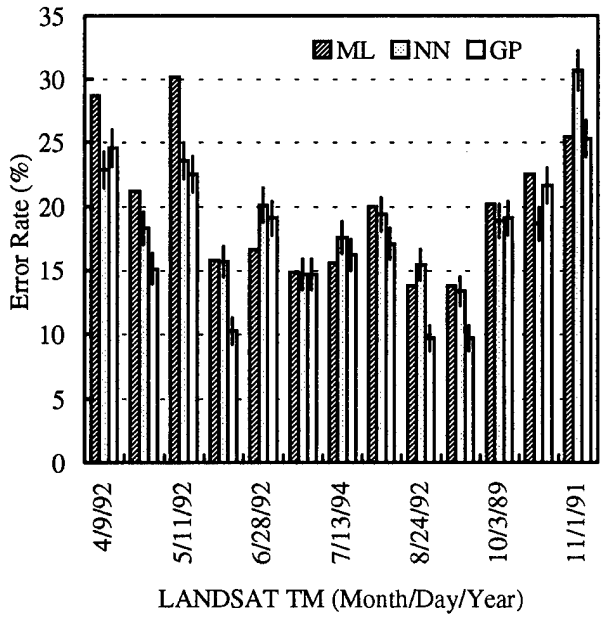

Fig. 1 Classification accuracy comparison for each LANDSAT/TM data.

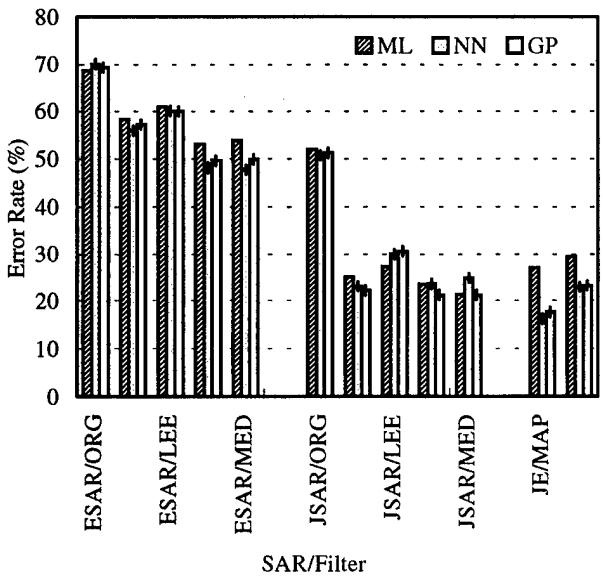

Fig. 2 Classification accuracy comparison for JERS1/SAR and ERS1/SAR data with speckle noise filters.

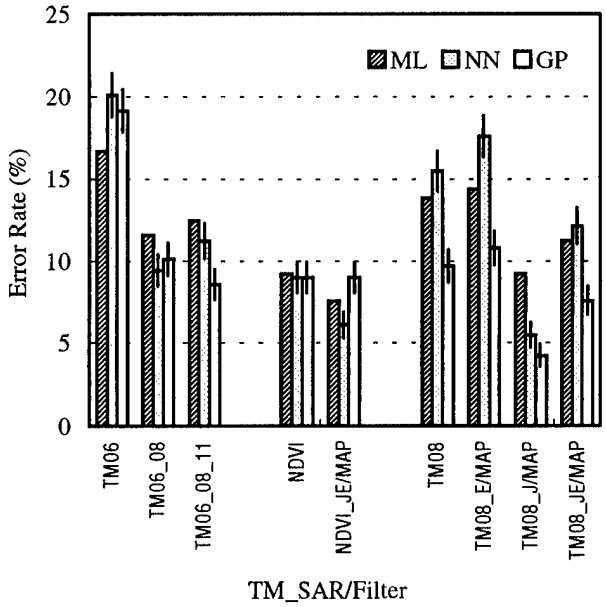

Fig. 3 Classification accuracy comparison for various combinations of LANDSAT/TM, JERS1/SAR, ERS1/SAR data.

Rainfield Detection Comparison In Small Regions With Particular Microclimatic Characteristics Using Meteosat And SSM/I Navigated Images

Enrico Piazza (member, IEEE), Pier Franco Pellegrini, Maurizio Tommasini

Dipartimento di Ingegneria Elettronica, University of Florence,
Via di S. Marta, 3- 50139 Firenze - Italy
Tel. +39-55-4796267, Fax. +39-55-494569, E-Mail: *labtel@ing.unifi.it*

Abstract: Research trend in future years is oriented towards the development of integrated systems, which collect information on the forecasting and detection of high intensity rain on a given region. These information generally come from various sensors.
In this paper a work based on different sensed data from satellite is presented.
All satellite data immages are geometrically geolocated by both solving the actual orbit equations and by the means of polinomial maps and ground control points.

INTRODUCTION

The rain rate comparison here reported takes into account data coming from Meteosat and DMSP satellite
The rain rate algorithm use the threshold method in the case of the IR images while a whole lot of different techniques have been tested for the rain rate retrieval from SSM/I data.
SSM/I data have been obtained directly from NOAA-NGDC (National Geophysical Data Center) distribution archives while the Meteosat Images was received directly by the PDUS (Primary Data User Station) receiving station operated by University of Florence and PIN-Prato Ingegneria, This station is a twin digital receiver able to gather data also from polar satellites such as the NOAA serie.
The rainfall results are compared with those obtained at the ground from a series of raingauges belonging to the the Italian National Hydrographic Service placed along the investigated area.
Here follows a case study about the flooding of small rivers in the north of the Tuscany Region. This event is pretty interesting because the local orography encourage the formation of rapidly developing events with an hard intensity. These microclimatic behaviours are common especially in the summer time.

PROCESSING SOFTWARE

The AmEDIT software has been developed as a suite of computer programs in a modular way. Thus it is possible to add new functions just by changing or adding new modules. It may handle data coming from Meteosat MVIRI (Meteosat VISible and IR Imager) radiometer as well as NOAA (National Oceanographic and Atmospheric Administration) AVHRR (Advanced Very High Resolution Radiometer), DMSP (Defense Meteorological Satellite Program) SSM/I (Special Sensor Microwave/Imager) radiometers and ground rain gauges. The output of this software is represented as resampled and interpolated images with a common pixel grid, mainly in a standard projection map.

COMMON MAP PROJECTION

To obtain a map in a common cartographic projection the Mercatore one has been used. It has the advantages of being a conformal transformation with perpendicular grid. The following formula is used:

$$m = a_0 \ln(\tan(\pi/4 + lat/2)) - a_1 \sin(lat) - a_2 \sin^3(lat) + - a_3 \sin^5(lat) \quad [min]$$

where the coefficients are computed for an earth eccentricity taken by the WGS-84 ellipsoid:

$e=0.08181901$
$a_0 = 3437.74677078$ [min];
$a_1 = 23.01348$ [min];
$a_2 = 0.05135343$ [min];
$a_3 = 0.00020626673$ [min].

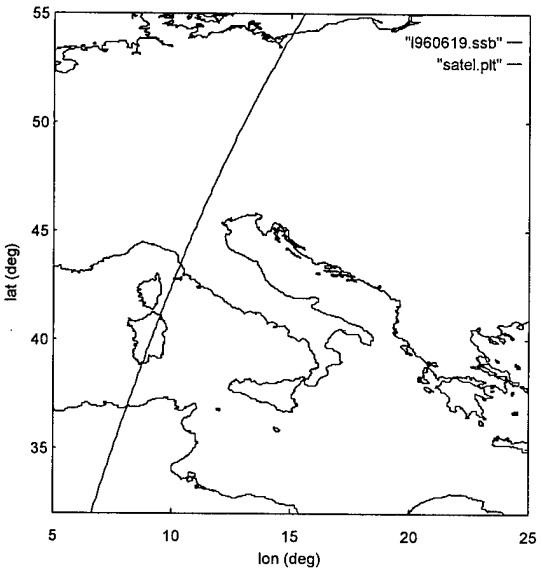

Fig. 1 - Trace of the subsatellite point relative to the analized DMSP orbit superimposed to a map of Europe sampled from a map by Italian Navy Idrographic Institute.

The digital map used was produced by sampling coastlines of the Italian Navy Idrographic Institute, Map Number 340/INT 301 scale 1:2,250,000 (41 deg 30' N) Mercatore projection, Datum ED50, after conversion to WGS84 (see Fig. 2)

RAIN RATE ESTIMATION

The rain rate comparison here reported takes into account data coming from Meteosat and DMSP satellites.
In the case of the IR images from the Meteosat, the rain rate algorithm use the threshold method (NAWT) [1].

0-7803-3836-7/97/$10.00 © 1997 IEEE

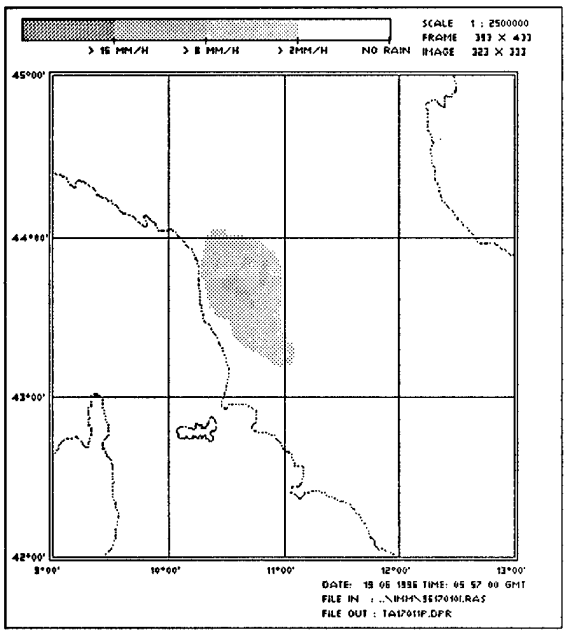

Fig. 2 - The rain rate algorithm, in the case of the IR images from the Meteosat, use the threshold method (NAWT). It shows a precipitation area larger than the actual one and placed much more south.

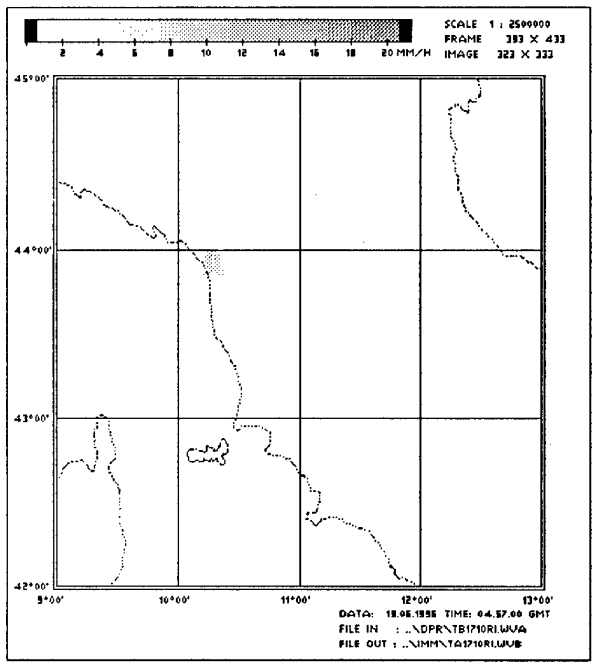

Fig.3 - Example of the rain rate retrieval from SSM/I data. The algorithm is the Calval one.

This method first extract the top of the clouds temperature from the IR Imagery and the temperature histogram. Then consider a cloud with area A defined by the 235 K isotherm and with temperatures $T_{50\%}$, $T_{10\%}$ and T_{min} defining the coldest 50% area, coldest 10% area and minimum temperature respectively.

A whole lot of different techniques have been tested for the rain rate retrieval from SSM/I data [2][3].

The AmEDIT software has presently modules for up to 15 different algorithms:

- Adler (2 versions);
- Grody;
- Ferraro (2 versions);
- Ferryday (2 versions);
- Calval (3 versions);
- Barrett;
- Linear (2 versions);
- Smith (2 versions).

SATELLITE DATA SOURCES

SSM/I data are not directly available but they have to be gathered from agencies such as NOAA, which submit data to a pre-processing and distribute them. The here used data are in standard XDF (eXternal Data Format) and have been obtained directly from NOAA-NGDC (National Geophysical Data Center).

Meteosat Images was received by the PDUS (Primary Data User Station) receiving station operated by University of Florence and PIN-Prato Ingegneria, This station is a twin digital receiver able to gather data also from polar satellites such as the NOAA serie.

GROUND DATA VALIDATION

The rainfall results are compared with those obtained at the ground from a series of raingauges belonging to the the Italian National Hydrographic Service placed along the investigated area. (see Fig. 4). The raingauges have provided reilable measurements over the whole investigated area and with no time gaps.

A comparison between the numerical values has highlighted that the satellite estimation is far more lower than the gauge one even if in the SSM/I it is closer to the true.

In the examples, see. Fig. 5, the precipitations mesaurement in the hours around 6 UTC at the gauge was 150 mm/h while the SSM/I one was 12 mm/h (Fig. 3) and Meteosat was 8 mm/h (Fig. 2). it should be noted that gauge integrates over a small area and a long period of time, on the contrary satellites integrate over a large area in a short period of time.

Our work at present and for the next future is oriented in build a data base of the various events that occourred. This for Meteosat, SSM/I and raingauges. It is useful for a correct interpretation of satellite data about the particular area under analysis.

Results are of general interest also over differnt areas with different orographic characteristics.

CASE STUDY: THE VERSILIA FLOOD

Here follows a case study about the flooding of small rivers in the north of the Tuscany Region. This event is pretty interesting because the local orography encourage the formation of rapidly developing events with an hard intensity (see Fig. 5). These microclimatic behaviours are common

especially in the summer time when intense evaporation they cannot be scattered because of the presence of the mountains chain. Thus it can lead to the formation of cumulus clouds that can in turn deal to intense precipitation for little periods of time and over small areas.

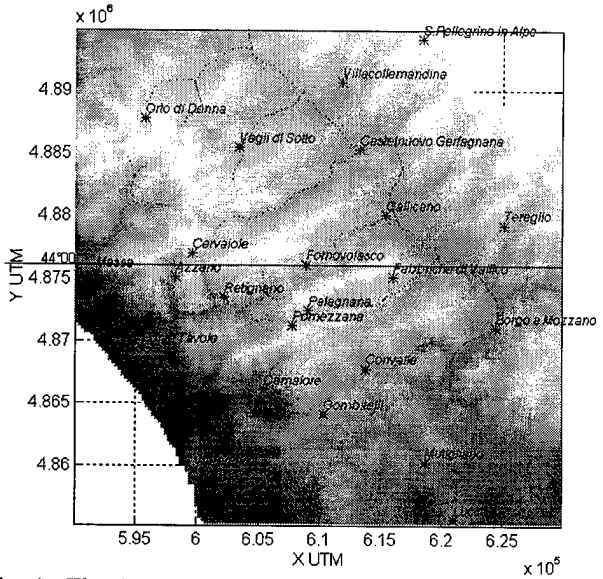

Fig. 4 - The Automatic recording stations placed in the north of Tuscany. The horizontal line is the 44th parallel. The grey shades show the orography of the region.

In the case of the Versilia Flooding, the period of time was particularly long giving no time to rivers to waste the fallen water. More, SSM/I D-Matrix algorithm, showed no wind over the sea, so the clouds didn't move during the precipitation event.

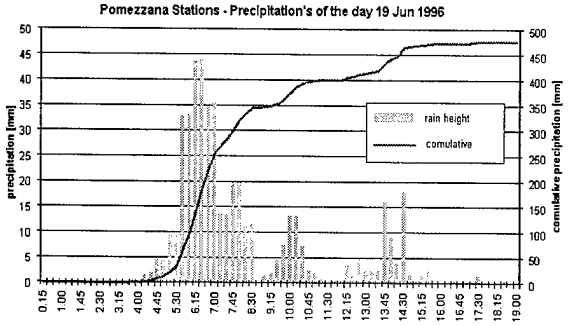

Fig. 5 - Precipitation height recorded at the Pomezzana Station. It show a very high peak around 6:00 UTC (that's 7.00 Local Time). Position of the station: 10°21'35" E, 43°59'50" N

CONCLUSIONS

Result here reported confirm that with the microwaves data it is possible to obtain rain rate values accurate in both values confidence and location, but with poor spatial resolution. On the contrary, IR data give higher spatial resolution and a continuous monitoring of the observed area but with just qualitative values of both rain rate and location. It must be noted that the centers of the two area are displaced over about 50 Km and only partially overlapped (see Fig. 6) this is due to the different phisical parameter measured by the sensor: Top of clouds temperature in the IR and the scatterig due to the micrometeores in the microwaves. Nevertheless the multisensor methods, applied regularly to the same region can give good forecasting of the high intensity, dangerous, events

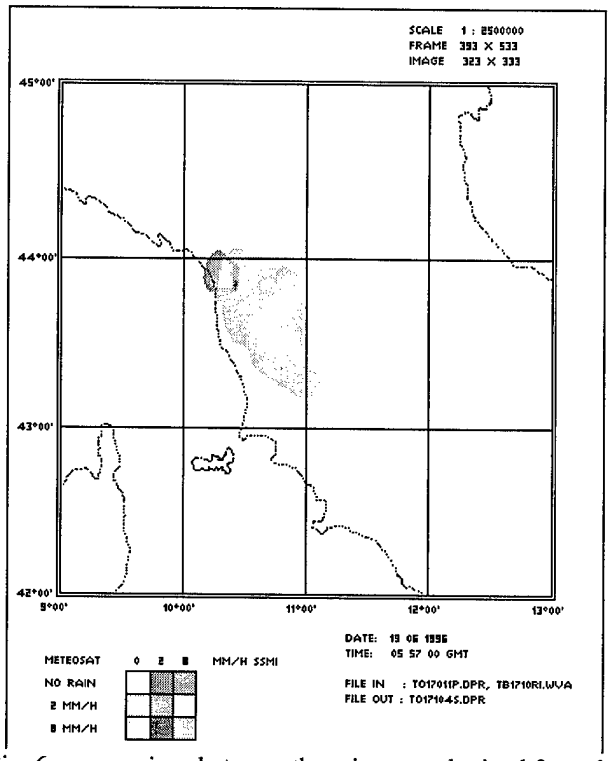

Fig. 6 - comparison between the rain rates obtained from the SSM/I sensor and the Meteosat IR sensor.

REFERENCES

[1] Levizzani V., Poreti F., Prodi, "Operational Rainfall Estimation Using Meteosat Infrared Imagery: An Application in Italy's Arno River Basin-It's Potentials and Drawbacks", ESA Journal, Vol 14, Pag. 313-323, 1990

[2] EC, Barrett, and M.J. Beaumont, "Satellite Rainfall Monitoring: an Overview", Remote Sensing Review, vol. 11, pp. 23-48, 1994.

[3] Burns B.A., Flender F., Heygster G., Hunewinkel T., And Künzi K., "Evaluation of Algorithms for Retrieval of Rain Rate with Passive Microwave Radiometers", University Of Bremen-Istitute Of Enviromental Phisic, Final Report, August 1994.

Geosynchronous Technology Infusion Studies

L. Hilliard, D. Jenstrom, D. Chesters, P. Racette
National Aeronautics and Space Administration
Goddard Space Flight Center
Greenbelt, MD 20771
http://www701.gsfc.nasa.gov/ags/ags.htm

Abstract -- NASA and NOAA are now sponsoring Advanced Geosynchronous Studies (AGeoS), technology work that will lead to the next generation of space sensors located in geosynchronous orbit.

INTRODUCTION

In the early 1990's, NASA commissioned a Geostationary Earth Observatory (GEO) team [1] to study the utility of environmental observations from geostationary orbit. This GEO study concluded that: "In many respects, the polar-orbiting instruments study the effects of processes, whereas the geostationary instruments can study the process itself."

Indeed, research in climate change consists of determining how the long-term changes affect short-term processes, and how those altered short-term processes, in turn, establish new long-term behavior. Because the diurnal cycle drives so many energetic short-term processes, it is necessary to directly measure rapidly changing components like winds, clouds, aerosols and precipitation on a global scale. While a polar-orbiting satellite can observe the entire globe at high resolution, it cannot resolve the diurnal cycle. While a geosynchronous satellite can resolve the diurnal cycle, it is limited about one-quarter of the earth's surface. Therefore, a combination of remote sensing data from both platforms yields a synergistic system for studying both the processes and the resulting changes in weather and climate.

For the last 25 years, National Oceanic and Atmospheric Administration (NOAA) has been flying Geosynchronous Operational Environmental Satellites (GOES) to observe weather. In the mid-1990's, a new generation GOES imager and infrared Sounder came on-line with accurate radiometric calibration and earth-location, with performance similar to the NOAA polar-orbiting instruments.

Up to the early 1980's, NASA's Operational Satellite Improvement Program (OSIP) orchestrated changes in the NOAA satellites [2]. Since that time, there is a next-generation National Polar-Orbiting Environmental Satellite System (NPOESS) being planned, but there is no corresponding effort to infuse advanced technology into the GOES program for improved weather and climate monitoring, or to coordinate the polar- and geo-systems [3]. To deal with this issue, an AGeoS team has been formed to consider improvements in future GOES missions[4].

NASA's Mission to Planet Earth (MTPE) has developed a low earth orbit imager called the Moderate Resolution Imaging Spectrometer (MODIS) carrying 36 spectral channels from 0.4 to 13.3 μm in wavelength [5]. MTPE will also fly, on the Earth Observing System (EOS) missions, microwave sensors that probe to lower levels of the atmosphere when clouds are present. With similar imaging and sounding data from geostationary orbit, numerical modelers would have access to the diurnal drivers of climate change.

In addition to imaging and sounding, AGeoS will consider requirements for a lightning mapper, more efficient ground distribution and autonomous spacecraft control systems, spaceborne architecture tradeoffs (i.e. constellation studies), and the science algorithms associated with all of these enhancements so they can be effectively used by the scientific community. To address all of these issues joint NASA/NOAA Management and Science Teams have been established to oversee the AGeoS effort. This report briefly describes the initial steps being taken to investigate the high priority geosynchronous measurement needs identified so far.

IMAGER

Using current technology, it is possible to build a GOES imager agile enough to provide continental U.S. coverage synchronized to the national weather radars and also several full-disk images every hour. NASA-Goddard Space Flight Center has studied the Geosynchronous Advanced Technology Environmental System (GATES) [6] as one way to deliver full-disk images in all the MODIS spectral window channels.

The GATES imager study shows that recently developed technologies are sufficient to create a geosynchronous imaging system that will likely meet or exceed all known National Weather Service (NWS) next generation GOES imaging needs while simultaneously providing valuable climate imaging data. Some of the key technologies are photovoltaic long wave detectors, large focal plane arrays with high performance readout circuitry, wide field large aperture optics, stable and thermally conductive mirrors and composite structure, high-repeatability full spectrum calibration, reliable and low-vibration mechanical coolers, loop heat pipes, very high speed communication and processing systems, automated image registration and resampling algorithms, and highly autonomous operation.

Many of these technologies are, however, unproven in space to the degree required by GOES. Of chief concern is the large degree of cost, schedule, and performance risk involved in integrating many new technologies into a precision sensing system. Demonstrating that these components will work together in a calibrated system and

provide the required quality of science and weather data is critical for infusion into an operational program.

AGeoS is investigating the pros and cons of various geosynchronous imaging techniques through a series of trade studies that will be used to focus technology development and demonstration activities. A laboratory testbed will likely be developed that will integrate the technologies together as a first step in evaluating mutual compatability. This testbed will also be valuable in developing streamlined performance verification techniques to reduce the cost and risk of flight instrument integration and test.

Certain system level technology issues such as proof of techniques to overcome the geosynchronous solar environment, and proof of sufficient performance and reliability to meet GOES operational needs must await actual demonstration in geosynchronous orbit to be truly resolved.

INFRARED SOUNDER

In 1996, the GATES-2 studies looked for a high spectral resolution infrared (IR) sounder design that could coordinate measurements with a microwave (MW) sounder from a single geosynchronous IR/MW platform. An MIT Lincoln Laboratory IR interferometer sounder concept uses a 65K 6 x 6 photovoltaic HgCdTe Focal Plane Array. For compatibility with the microwave sounder, the GATES-2 IR sounder concept used a 22 cm aperture with an internal nodding mirror. Nodding compensates for spacecraft scan motion that is being used to raster the infrared and microwave field-of-view over the earth disk.

AGeoS will be taking a broader look at geosynchronous infrared sounding techniques and will be initiating technology development and demonstration activities. Key technology issues will be the evaluation of various types of interferometers and spectrometers for their viability in geosynchronous earth sensing, the use of large focal plane arrays to increase ground coverage rate, evaluation of calibration requirements and techniques, and issues surrounding synchronized operation with a microwave sounder. The latest subsystem technologies will be evaluated, some of which are being developed for NASA's New Millennium Program (NMP). NASA's Strategic Enterprise for Atmospheric Science at Langley Research Center will play a major role in this study.

MICROWAVE SOUNDER

The GOES satellites currently have no microwave frequency sounder on board. Thus, current IR sounding techniques are limited by clouds. In NOAA's vision of the future, co-registered infrared and microwave sounders will do the temperature profiling and water vapor tracking required for predicting severe storm activity. The Geosynchronous Microwave Sounder Working Group (GMSWG) has proposed a microwave sounder [7].

The least mature of the technologies being considered in the next generation geostationary platforms are related to microwave sounding. Feasibility studies for performing microwave sounding from a geostationary orbit were performed in the 1970's [8]. The study found that placing a large aperture antenna to realize reasonable spatial resolution and developing reliable low noise receivers sensitive enough for sounding measurements were of greatest challenge. Today, these challenges still represent the barriers to realizing a geostationary microwave sounder.

The current strawman configuration being considered is derived from recommendations from the GMSWG. The design uses twelve channels centered about four frequencies at 118 GHz, 183.31 GHz , 380 GHz and 425 GHz. A two meter aperture provides a resolution of 20 km at the two highest frequencies, the maximum spatial resolution deemed useful by the GMSWG. Of particular challenge is obtaining 10 micron surface accuracy across the aperture to obtain better than 90% beam efficiency at the higher frequencies. Numerical modeling of the structural integrity of a composite antenna design is in progress. Determining the influences of thermal loading on aperture efficiency is of key consideration.

The highest priority technology need is to develop low noise receiver components at the submillimeter wave channels of 380 GHz and 425 GHz. The previous work in space science [9] plus additional development of planar diode mixer components at 557 GHz have established a good approach to this challenge. A research grant has been provided to the University of Virginia to build breadboard front end devices and matching circuits to demonstrate low noise performance at 380 and 425 GHz. Precision machining for integrated feedhorns and resonant cavities will be made repeatable using a new plastic molding process developed by the University of Virginia. Flying these technologies on an aircraft instrument will provide relevant data for assessing these new channels.

LIGHTNING MAPPER

A low earth orbit lightning mapper, the Optical Transient Detector, is currently on orbit, and a similar instrument will be flying on board the Tropical Rainfall Measurement Mission (TRMM) scheduled for launch later this year. However, these measurements do not provide the capability to continuously monitor specific storms or storm systems. Clearly, geosynchronous orbit provides the best vantage point for continuous monitoring of regions of interest. Data from a geosynchronous lightning mapper will be especially useful in concert with other measurements of water in the atmosphere.

Modern solid state mosaic focal planes have enabled these scientific instruments to be low impact on system weight and volume budgets. The prime technology challenge for a geosynchronous lightning mapper will be the development of the real time event processor that can extract the momentary differences in intensity of a lightning event. The Marshall Space Flight Center will be leading this investigation.[10]

ADVANCED GROUND SYSTEMS

The infusion of advanced instruments into the GOES program will significantly increase the downlink data rate to a level that is beyond the capability of the current GOES ground station and data distribution system. This study will investigate new ground station and data distribution architectures for delivery of advanced data products to users.

The investigation of advanced ground systems must take into account synergism with the MTPE products acquired in low earth orbit. A subset of the climate data must be compatible with the daily data requirements used by the National Weather Service (NWS) forecast models. A technology demonstration mission would allow NWS data products to merge with minimal disruption to the operational system.

GOES CONSTELLATION STUDIES

The GATES studies suggested that technology demonstrations should be accomplished with a series of small scale missions to minimize cost and risk. Perhaps this architecture is also best for the future fleet of operational satellites. Of prime concern for infusion of technology into the operational GOES program is how technology can be used to make the space segment as cost efficient and flexible as possible while providing improved and expanded measurements. This constellation study will investigate the issues and options surrounding large-satellite versus small-satellite versus hybrid architectures.

SUMMARY

The AGeoS team has used the mutual interest of the NASA/MTPE and NOAA/GOES programs to define the objectives of a technology infusion study. With the point designs that came from early studies sponsored by NASA, more system and technology trades have been uncovered. AGeoS technology mile-stones include laboratory testbeds, aircraft instruments, and flight demonstrations achieved through a NASA pathfinder program such as the NMP or the Earth System Science Pathfinder (ESSP) program. Investigations infusing new technology and measurements into the GOES program will come through constellation and ground system studies.

REFERENCES

[1] NASA "The Geostationary Earth Observatory (GEO): A Report by the Earth Science Geostationary Platform Science Steering Committee (ESGPSSC), MSFC, September 1994.

[2] U.S. Congress, Office of Technology Assessment, "The Future of Remote Sensing from Space: Civilian Satellite Systems and Applications", OTA-ISC-558 (Washington, DC: U.S. Government Printing Office, July 1993), p. 38.

[3] U.S. Congress, General Accounting Office, "Planning for the Geostationary Satellite Program Needs More Attention", GAO/AIMD-97-37, March 1997.

[4] Price, R. "Advanced Geosynchronous Studies" Interoffice Memorandum: Associate Director of MTPE to Director of GSFC, November 15, 1996.

[5] National Aeronautics and Space Administration, Earth Observing System Reports: Volume IIb, "Moderate Resolution Imaging Spectrometer", 1986, p. 45.

[6] Chesters D., D. Jenstrom, "GATES – a small, agile imaging satellite prototype for GOES-R", SPIE Proceedings, Denver Colorado, August 1996.

[7] Blackwell W.J., D. H. Staelin, "Comparative performance analyses of passive microwave systems for tropospheric sounding of temperature and water vapor profiles" SPIE Proceedings, Denver Colorado, August 1996.

[8] Goodwin, F.E., R.E. Graves, M.S. Hersman, M. Luming, "Geosynchronous Microwave Atmospheric Sounding Radiometer (MASR) Feasibility Study, Final Report, "Hughes Ref. No. D8647 SCG 80039R, January 1978.

[9] Tolls,V., and G. Melnick et. al., "The Submillimeter Wave Astronomy Satellite", SPIE Proceedings, Vol. 2268, 1994.

[10] Christian, H.J., R.J. Blakeslee, S.J. Goodman, "The Detection of Lightning from Geostationary Orbit", J. of Geophysical Research, vol.94, No. D11, pp. 13,329-13,337, September 30,1989.

TECHNOLOGIES FOR FUTURE REMOTE SENSING SYSTEMS

Authors : C. Dionisio, M. Oricchio, F. Mura
Alenia Aerospazio
via Saccomuro 24, Rome
00131 Italy
tel: +39 41512138; fax: +39 4191391

ABSTRACT

This paper presents the results of a study carried out for ESA by Alenia Aerospazio, regarding the identification the future (2005-2010) Earth Observation (EO) market, requirement, concepts, architecture and technologies.

1. INTRODUCTION

With the aim to identify new concepts , architecture and technologies for the implementation of 2010 services, ESA assigned a study to a team of Industry and Universities leaded by Alenia Aereospazio. The consortium is composed of: Alenia Aerospazio (I), University of Naples (I), MDA (C) and ESYS (GB).

The study results are summarized in this paper, presenting how from the market analysis we are passed to the system design, the technology selection, the cost evaluation and the business plan preparation. The studied system is dubbed Future Earth Observation System (FEOS).

2. MARKET ANALYSIS

After the market study exploited by ESYS a set of services has been identified for FEOS:

- On-demand near real-time data access: user can request a data set or a product and receive it after 7 hours. Typical applications are: all weather all time mapping, law enforcement, oil spillage detection, disaster detection and monitoring, pollution control, etc.
- standard products: products can be accessed by selecting application and area of observation, then intelligent S/W agents find data and remote computing resources.
- Continuos data delivery: special areas are routinely observed and product delivered to the user via multimedia satellite or ATM backbone

Direct data reception: users receive processed data directly from the satellite by a S-band link.

The market analysis result shows that revenues for 600-2000 MECU/y can be captured if a suitable architecture of services is settled.

3. REQUIREMENT

From the market analysis have been derived a set of mission and services requirements for a future EO system to be deployed in 2010 .

Requirement	Value/feature
global access time (GAT)	< 7 hours
all weather/day-night capability	need SAR
high spatial resolution (HSR) images	<0.5 m optical <1 m SAR
pointing accuracy	< 3.8 10E-3°
images geolocalization	<1 m
programmable swath dimension	>10 Km for HSR
3-D images in both optical and MW bands	stereo+ SAR interferometry
MTI capability	option
multispectral capability	0.4-2/3-5/ 8-11μm
service life time	15-20 years
direct access to satellite by users	X band
direct gruond Rx	• full raw data (2Gb/s) • processed data (2Mb/s)
service availability	> 0.95
low implementation and operation cost	commercial rules applicable

The parameter GAT includes the time between the user request and the delivery of the information at the user facility. It is composed of: the time needed for mission

0-7803-3836-7/97/$10.00 © 1997 IEEE

planning and commanding, the space segment revisit time (fixed lower than 6 h.) and the data processing and dissemination time.

4. SYSTEM ARCHITECTURE AND TECHNOLOGIES

The first comment to the requirement is that the global acceess and the high revist time can be achieved only by a constellation of satellites in LEO orbit. Than the all weather, around the clock observation need a microwave imaging sensor, tipically a SAR (Synthetic Aperture Radar). The future technology (the system is designed for 2010) shall permit the implementation of small satellite (< 300 Kg) embarching high resolution sensors.
The system architecture, see fig 1. is based on the following ideas:
- use small satellite in costellation
- implement both optcal and SAR sensors
- accomodate single payload on the s/c , so to minimize s/c weight and optimize constellation orbital planes
- decrease optical satellite orbit altitude to reduce payload complexity. This choise is payed with an increase of the number of satellites in the orbit plane but it is supposed that what should be minimized is the cost of the sensor
- use automatic remote stations for receiving the sats measurement data, process and transmit them via multimedia satellite the products.
- command and control the constellation by a single station and multimedia sats as TT&C relay.

ORBIT SELECTION
Starting from the assumption to design an instrument which can access a field of regard comprised within the 15°-55°, then the SAR satellite selected orbit (~ 410 Km, dawn - dusk) gives a global access time of 14 hours with a single orbital plane and 5 satellites. By a second orbit plane shifted of 92.9° (noon orbit) the time is reduced to 7 hours. Altenatively, if both sides of the satellite nadir trace can be accessed by roll-axe tilting or two antennas, two orbital planes with four satellite allow a global revisit time of 6 hours.
The optical sat orbit was selected to stay as low as 280 Km. With a +/- 35° sensor tilt capability , we need 5 sats to achieve 24 hours revisit time.

SAR SENSOR DESIGN
In order to explore new technical solution it was studied SAR design at Ku and Ka frequencies. The Ka design is almost impraticable due to the high atmospheric attenuation but the Ku sensor is really very attractive . First it is possible to met the spatial resolution requirement without steering the antenna beam because of the reduced antenna dimension requirement (2m x 1m) than we can implement single pass interferometry embarching two antennas on a single sat with a 60m lenght boom, now perfectly feasible.
The transmit power is in the order of 4 Kw for a 20 dB sigma nougth. The use of advanced technology like:
- ultralightweight panel
- foldable/ inflatable structure
- miniaturized T/R modules (HBT,pHEMT)
- multifunctional structure
- fotonic technology (OBF..)
- smarts and MEMS
- 3D MCM
- advanced computer architecture with ASIC for dedicated functions like data compression; shall lead to an instrumet design with a weight of about 60 Kg and a power consumption of 425 watts.

OPTICAL SENSOR DESIGN
Different concepts have been studied for the optical sensor design based on conventional and innovative approaches. At the end the most innovative has been selected whose main mirror is composed of a mosaic of deployable segments. Each segment is built with ultralightweight graphite and embedded with smart materials to compensate for distorsions. The budgets are: 30 Kg for weight and 60 watts for power.
Enabling tecnologies are:
- segmented deployable structure
- improved crycooler
- improved detectors and FPA

SATELLITE DESIGN
The future satellite design shall be performed around a single processing architecture to support the functions of sat control, navigation and attitude control.
High on board autonomy shall permit faults detection and recovery, orbit maintenance, pointing, high tlc level. This reduce the operation cost, the risks of errors and increase the payload operability.
Of great importance is the on-board power generation obtained by more powerfull solar cells (multijunction, concentrators, etc.) deployed by inflatable or hybrid techniques.
Electrical propulsion is a mandatory choise at 280 Km because of high propulsion efficiency. An improved fuel efficiency of 25 times is expected in the near future. Our optical sat

need 350 Watts more for this propulsion system.
Finally lightweight structure based on very high modolus CFRP will imply a 8-14% less weight.

GROUND SEGMENT DESIGN
The ground segment is based on a Central Mission Planning and Control Center which provides constellation control and plan the user requests. The satellite transmit the data to the Acquisition station distribuited along the World, 15 are enough to cover the lands. They receive the data automatically at very high data rate (2 Gbps) and retransmit or the data itself or the near real time elaborated products to the users via a multimedia sats or via the ground based B-ISDN with the INTERNET service. In pratice, it shall be possible for a single user receive the information via a cheap, standard portable multimedia terminal everywhere in the globe. Key technologies come from multimedia word and are: nomadic computing, intelligent agents and networks.

7. CONCLUSIONS

An overall mission cost has been estimated, based on previous experiences in GLOBALSTAR and COSMO programs, see figure 2. For a 15 years mission 4000 MECU are needed to settle the service but if the market expectations are maintained the mission is very profitable.

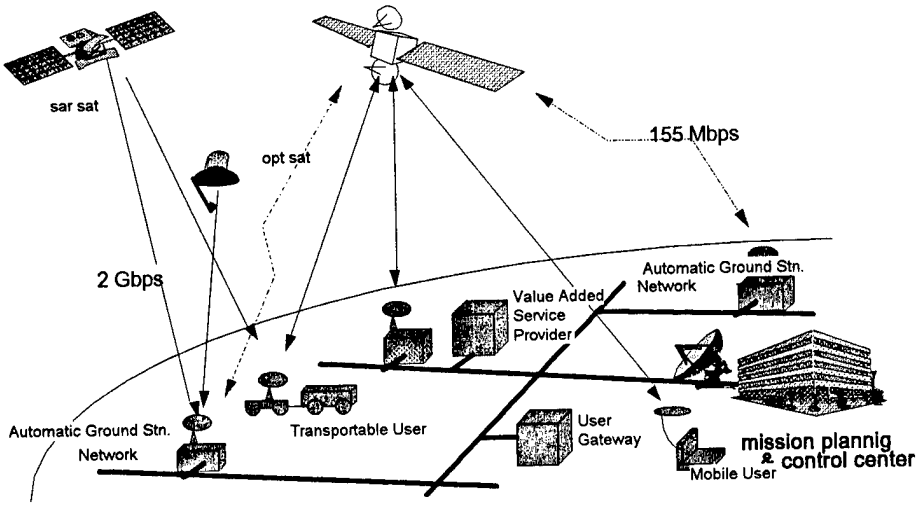

figure 1. Overall system architecture

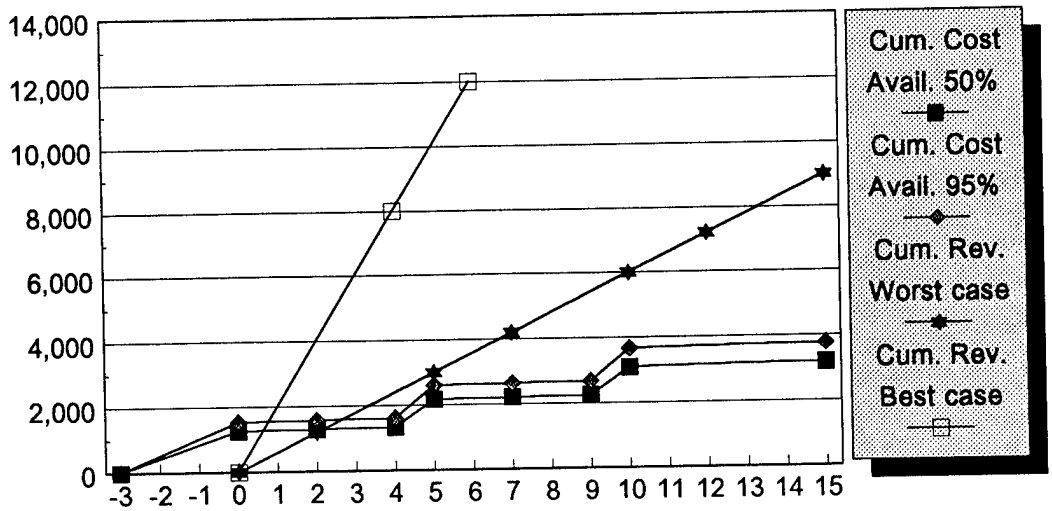

figure 2. Cost revenues summary (MECU)

An outlook for European Spaceborne Synthetic Aperture Radar

Christoph Heer, Semir Mahdi*
G. Angino, Andrea Torre**
*** Dornier Satellitensysteme D-88039 Friedrichshafen, Germany**
Telephone +49 7545 84319 / Fax +49 7545 84177
**** Alenia Aerospazio-Space Division, via Saccomuro 24, 00131 Roma**
Telephone +39 641511 / Fax +39 641512102

OVERVIEW

Two complementary future SAR instruments to be carried on separate platforms have been studied by the European Space agency (ESA). (1) CLIMACS, a modest-resolution, global monitoring SAR. (2) NGSI, a high resolution, flexible viewing SAR. CLIMACS will provide a long-term, uninterrupted global monitoring of land and ice surfaces with high temporal, high radiometric resolution. NGSI will be an all-purpose sensor providing synoptic views of selected scenes. The NGSI study goal was the definition of future technology developements.

In parallel, the German Space Agency (DARA) is funding the development of an active antenna demonstrator (DESA) in order to promote further technological developments.

NEXT GENERATION SAR INSTRUMENT

System Aspects and Requirements

The instrument is a fully polarimetric, dual frequency sensor operating simultaneously at X -and L-band and is suitable for long term repeat pass interferometry. The instrument is compatible with the ARIANE V launcher, the orbit altitude is 600 km. The most demanding requirement is the fully polarimetric operation in a high resolution imaging mode providing a swath width of at least 80 km at an incidence angle of 15 deg. The purity of the fully polarimetric image is defined via the Stoke Scattering Operator Bias (SSOB) required to be less than +/-10%. Due to international frequency band allocations, the system bandwidth is limited to 85 MHz resulting in a range resolution of 5m for incidence angles of 21 deg. and higher. During the study, the original azimuth resolution requirement of 5m was changed to 7.5m in order to improve the fully polarimetric swath width. The measurement sensitivity of the sensor is defined via the Noise Equivalent Sigma Zero (NEQSZ) being better than -21 dB at X-band, and - 29 dB at L-band. The radiometric stability is required to be less than 0.4 dB. In order to allow long-term repeat pass interferometry, the phase drift rate of the instrument should be less than 0.2 deg/sec. Basically, five different modes of operation are defined. High resolution (5m) images are required in the fully polarimetric mode, the co- or cross-polar mode, the alternating polarisation mode and the wave mode.

Additional ScanSAR modes provide high (5m), medium (100m) and low (500m) resolution images.

The maximum radar raw data rate from the 8-bit A/D converter of 4x 1.25 Gbps requires data reduction and compression schemes as well as on-board data processing.

Trade-off Results

For each of the investigated frequency band (X, C, S, and L-band), six different rf-power generation and distribution concepts have been traded-off with respect to power consumption, mass, complexity and calibration feasibility. The concepts are: (1) Central tx/rx signal generation and reception. (2) Central tx and Subarray level rx concept. (3) Subpanel level tx/rx concept. (4) Row level tx/rx concept. (5) Subpanel level tx and Subarray level rx concept. (6) Subarray level tx/rx concept.

For the X-band, the fully active concept (6) with rf power generation and reception on subarray level via T/R modules has been selected. For the L-band, the row level concept (4) has been selected where each row is fed by a single transmit and receiving unit containing redundant HPAs and LNAs.

Antenna Design

Each antenna is divided into 5 mechanical panel and into 40 subpanel. The subarray length is 0.35m at X-band and 0.7m at L-band resulting in a total length of the antenna of 14m. In elevation, 32 rows are necessary to meet the fully polarimetric ambiguity ratio requirement of 20 dB and the Stokes Matrix Operator Bias requirement of +/-0.1. At X-band, each of the 1280 T/R modules provide about 6.5 W rf peak o/p power. At L-band, 450 W per T/R unit is required. In total, the instrument consumes 4.6 kW DC power. Due to a structural integrated design, the mass of the X-band antenna is 370 kg only. No structural integrated design has been performed for the L-band resulting in an antenna mass of 1177 kg. The X-band radiators are wave guides in metalled CFRP providing low loss (< 0.3 dB) and high polarisation isolation (35 dB). Similar performance can be achieved at L-band, where four stacked patches with suspended dielectric skins form one subarray.

Instrument Performance

With the chosen instrument design, all requirements could be met. The high resolution, fully polarimetric swath width (first swath) is 80 km and ranges from 15 to 22.5 deg. incidence angle. The correspondent first swath for single polarisation is 125 km wide and provides the same sensitivity of NEQSZ < -21 dB.

0-7803-3836-7/97/$10.00 © 1997 IEEE

Stokes Scattering Operator Bias

Another demanding requirement is due to the SSOB. The polarisation state of a plane wave can be described by its Stokes' vector. The scattering process is described by the Stokes' Scattering Operator (SSO) relating the incident wave with the scattered one. The Stokes' Scattering Operator Bias (SSOB) is the difference between the SSO as expected exclusively from the scattering process and the measured SSO including instrument errors like antenna leakage in polarisation and channel imbalance. In the general case of an unique scatterer the 4*4-matrix of the SSO consists of 7 independent variables, four amplitudes and three relative phases, resulting into nine relations among the elements of the SSO. Due to the assumed symmetry of the scattering process of HV and VH, the SSOB consists of seven different non-zero elements, including the normalised E0,0 element being unity in any case. An example of the elements of the SSOB is shown in fig. 1-1 for the first swath.

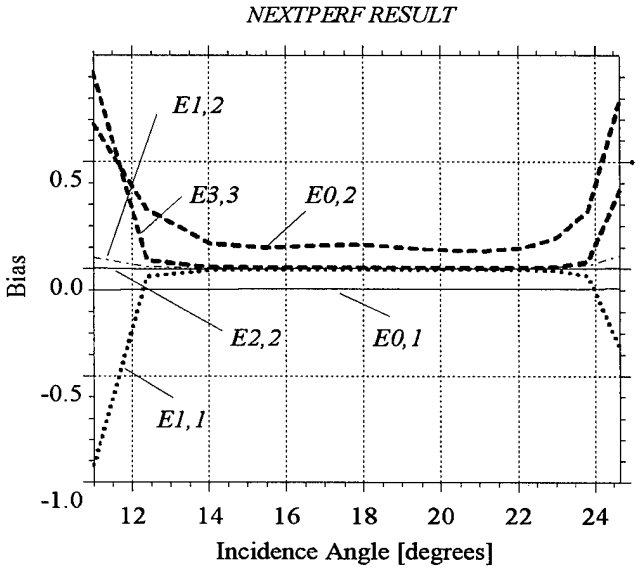

Fig. 1-1: Relevant elements of the SSOB

The main contribution to the SSOB is due to polarisation leakage in the antenna mainlobe region. The requirement of SSOB<+/-0.1 could be met over the whole swath with a channel imbalance of 0.4 dB in gain and 5 deg. in phase for each, the tx and the rx path. The antenna cross-pol level is assumed to be -35 dB.

DESA BASED SAR INSTRUMENT

Background

The objective of the DESA project (DEmonstrator SAr) is the definition and building of one flight representative electrical panel of an active antenna envisaged for an X-band SAR instrument. Necessary technologies will be developed and tested in order to reduce technological risks for future projects. Main emphasis is put on the T/R module and antenna radiator design. Based on the DESA technical parameters and the requirements drawn to current and possible future instruments as ERS-1, SIR-C/X-SAR, NGSI and CLIMACS, a reference SAR (SAR-R) is designed in order to demonstrate its performance.

Antenna Design

The SAR-R antenna is divided into 5 mechanical panel, each mechanical panel carries 6 electrical panel. An electrical panel consists of 30 subarrays with a length of 0.4m resulting in a total antenna size of 12m x 0.7m. Two classes of T/R modules (high and low power modules) are connected to the subarrays in order to provide some fixed antenna amplitude taper in the tx case. In the centre region of the antenna (row 8 to 23), 16 high power modules are assembled whereas the outer rows 1 to 7 and 24 to 30 are fed by the low power modules. In total, 5.4 kW rf peak power is generated by the HPAs. Due to the low loss of the active antenna, the radiated rf peak power is 3.8 kW. The receive path loss including all elements between the radiator and the LNA is 1.94 dB. The Noise Figure of the LNA itself is 1.1 dB.

Calculated Performance

With respect to NGSI, the geometric resolution of DESA is increased to 5m x 6.5m due to the increased chirp bandwidth (100 MHz instead of 83 MHz) and the reduced antenna length (12m instead of 14m). The total difference in system gain is 2.83 dB. For this reason, the width of the first swath over which the sensitivity requirement is met is 65 km only. This is shown in fig. 1-2.

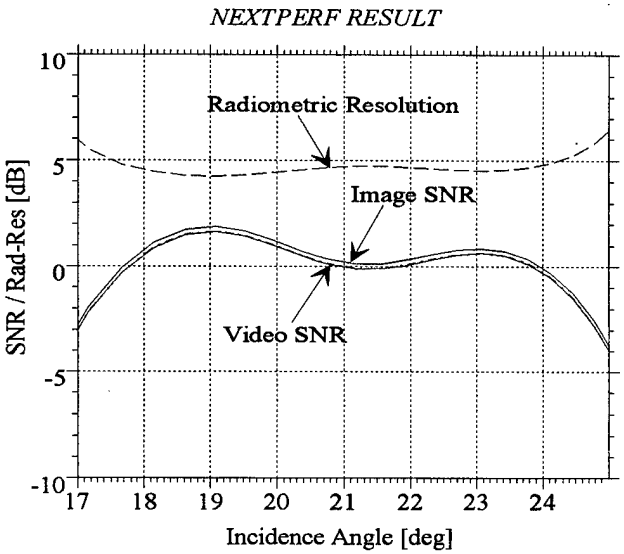

Fig. 1-2: DESA Sensitivity across first swath.

Note, an image signal to noise ratio of 0 dB corresponds to an Noise Equivalent Sigma Zero of -21 dB. The actual

instrument performance is summarised in table 1-1 where the range of incidence angle over which the requirement is met is given.

Table 1-1: DESA actual instrument performance

	Ambiguity free Swath (23 dB)	Sensitivity Swath (-21 dB)	Ground Coverage
Swath-1	15-25 deg.	17.8-24 deg.	65 km
Swath-2	23-32 deg.	24-30.7 deg.	78.9 km
Swath-3	30.2-39 deg.	30.5-38.2 deg.	102.4 km
Swath-4	37.5-43.5 deg.	38.2-43 deg.	73.1 km
Swath-5	43-46 deg.	42.4-47 deg.	60.1 km
Swath-6	45.5-50 deg.	45.6-49.8 deg.	77.3 km

THE CLIMACS INSTRUMENT

The mission is intended for the Climate study of Land surfaces and Ice using Microwave ACtive Sensing (CLIMACS). Possible companion instruments for inclusion on the CLIMACS mission include a medium resolution imaging spectrometer and an along track scanning radiometer (ATSR). The CLIMACS initial performance requirements are reported in Table 1

Table 1-2: Main requirements parameters

Parameter	Value
Coverage	Global within 3 to 5 days
Orbit	Polar, sun-synch. Altitude 500-850 km
Frequency	2 or 3 among P,L,C,X
Polarisation	HH and VV
Spatial resolution	250-1000 m
ISLR	> 20 dB
PSLR	> 25 dB
Ambiguity ratio	> 20 dB
Radiometric accuracy	< 0.6 dB
Radiometric Stability	< 0.3dB (image) < 0.5dB (mission)
Channel imbalance	< 0.5 dB
Mass	< 200 kg
Antenna size	12 m * 2.6 m
Power consumption	< 150 w
Reliability	0.9
Platform	ERS-1 or JERS-1 types

Trade-off

Many concepts were considered during the trade-off study, mainly: Conventional SAR, Multiple SAR, ScanSAR, Low PRF ScanSAR, Multiple Beam ScanSAR. The selected system is the ScanSAR mode which synthesises a good coverage with an easy implementation.

Baseline

The instrument baseline, selected from two options (4 and 5- subswaths system) and two design concepts (Blass matrix or phase shifters), consists of a dual frequency instrument at L and X band. Dual pol mode (HH and VV) is implemented at L-band; the X-band SAR implements a single pol mode (HH or VV). The selected concept shall have a radiometric resolution of 0.4 dB with a spatial resolution of $2x2km^2$. A ScanSAR mode with a total swath of 420 km and four subswaths is selected. For L-band we opt for the 4 scan cycle system, which then reduces to 2 scans for each polarisation. For the X-band a single scan timing cycle is assumed.

Instrument design

The proposed instrument architecture consists of:

1. centralised HPA plus Blass matrix for the X-band. The antenna is split in 12 electrical panel (grouped in six mechanical panels if accommodation in the Ariane 4 fairing is considered) each one with its Blass matrix. To synthesise the required beams and to avoid the losses due to the intrinsic non-orthogonality of the beams, the beams are grouped two by two and realised by two different Blass matrices for each electrical panel.

2. the L-band antenna is split in six electrical panels (one HPA and LNA per panel; six mechanical panels). The required four beams are grouped two by two. Each group is realised by a Blass matrix. Polarisation switches are set between the Blass matrix and the radiator to select the required polarisation.

CONCLUSION

The study of the NGSI demonstrate that a fully polarimetric dual frequency SAR mission appears to be feasible from a technical point of view. Even the large size of the L-band antenna of 14m x 5.7m can be accommodated in the spacecraft. Nevertheless, mass, power and size are still the critical parameters. A structurally integrated design should be done in order to reduce the large mass of the L-band antenna as it has been done for the X-band antenna.. Higher dc to rf power efficiency for the X-band T/R modules as well as for the L-band SSPA units are required.

For the DESA based SAR-R instrument, the geometric resolution is improved at the expense of the NEQSZ swath width. The single polarised and shortened active antenna saves mass and simplifies the spacecraft accommodation. The present X-band T/R module technology provides acceptable instrument performance.

The CLIMACS study results give the design of a low resolution, wide swath, dual-frequency and dual-polarisation instrument. The semi-active ScanSAR design results in a total dc power consumption of 460 Watt only, the total mass is estimated to be 329 kg. Due to the fixed ScanSAR operational scenario, the instrument stability could be increased by the use of a Blass matrix.

Future Operational Spaceborne Synthetic Aperture Radar System Considerations

Dr. Erich Velten, Christoph Heer
Dornier Satellitensysteme D-88039 Friedrichshafen, Germany
Telephone +49 7545 84319 / Fax +49 7545 84177

INTRODUCTION

This paper summarises the system design aspects which can be incorporated in a future operational SAR instrument. This instrument will generate high resolution images useful for commercial applications, Earth science, civilian and military applications. The presented baseline concept considers a two frequency, multi-polarised instrument with combined h/w in the central electronics subsystem. Nevertheless, the modular design provides the flexibility to realise a stand alone instrument for each frequency band.

Mission design summary

- 600 km sun synchronous, near-circular orbit with high inclination. Complete coverage at the equator after 7 days in wide swath mode.
- Swath selection within 15 - 55 deg. incidence angle.
- L-band, fully polarimetric SAR with multiple resolutions and swath width capabilities.
- X-band, dual polarimetric SAR with multiple resolutions and swath width capabilities.
- Principle modes of operation:
  - Spotlight
  - High resolution Stripline
  - Wide swath ScanSAR
  - Wave mode
  - Single, dual and fully polarisation
  - Repeat pass interferometry capability
- Antenna electronic beam steering in elevation and azimuth.
- Digital chirp generation and digital filtering for optimised performance.
- Antenna size and polarisation
  - X-band 10m x 0.70m, HH,HV,VV,VH (dual. pol.)
  - L-band: 10m x 3.24m, HH,HV,VV,VH (quad. pol.)
- Data handling
  - Data compression
  - On board processing
  - Solid State Mass Memory of 3x75 Gbit
  - Typical data rate of 3x330 Mbps
- Maximum DC Power
  - X-band: 2850 W
  - L-Band: 1050 W
- Mass
  - X-band: 550 kg
  - L-band: 650 kg

RADAR DESIGN

The radar baseline design considers state of the art technology resulting in excellent instrument performance. Alternatively, certain technology developments can be expected in the next decade providing either further increased instrument performance and/or may result in a relaxation of the requirements to be drawn to the launcher and the spacecraft service module. Both aspects will impact the overall mission cost. For example, the manufacturing cost of an advanced dual polarised wide band patch radiator will be significant lower than a radiator realised with slotted wave guides. Furthermore, higher dc to rf efficiency of the T/R modules will reduce the required total dc power and hence will reduce the size and mass of the solar panels and batteries. These aspects are discussed in the following with respect to the baseline radar design.

Baseline radar design

In the transmit chain of the instrument, a digital chirp generator offers the required flexibility in terms of bandwidth and chirp characteristics for optimum performance. The maximum system bandwidth is 100 MHz resulting in a range resolution of better than 5m.

The power loss in the transmit chain is mainly determined by the tx/rx drop-in circulator. Present state of the art technology guarantees a loss as low as 0.4 dB.

In the receiver chain, two switchable analogue filters do account for different modes of operation, e.g. a high resolution stripline mode and a low resolution wide swath mode. An A/D converter with a maximum clock frequency of 200 MHz is followed by a programmable digital filter which matches the signal bandwidth to the radar measurement geometry and required resolution. Data reduction and on board processing capability is considered as baseline. The receive path loss is again determined by the tx/rx drop-in circulator plus the isolator and limiter required for LNA protection. A total loss of 1.3 dB is achievable. The noise figure of the LNA is measured to be 0.9 dB in X-band and 0.6 dB in L-band.

The two SAR antennae comprise fully distributed T/R modules on subarray level (fully active antenna) in order to provide maximum antenna beam pointing and shaping flexibility as well as high instrument reliability. The dc to rf efficiency of the T/R module is >20 % in X-band and >25 % in L-band.

0-7803-3836-7/97/$10.00 © 1997 IEEE

X-band antenna design

The X-band antenna is a dual polarised phased array split into three mechanical panels. Each mechanical panel consists of 8x2 subpanels. The size of a subpanel is about 42cm x 35cm and carries 16 T/R modules. In summary, the antenna consists of 24 subarray columns in azimuth and 32 rows in elevation resulting in 768 high power efficient T/R modules of 7 W peak output power each. The subarray is made of slotted wave guide in CFRP technology with a subarray loss of 0.5 dB. The mass of this subsystem is about 450 kg including structure and network.

L-band antenna design

The L-band antenna is a dual polarised patch array split into three mechanical panels. Each mechanical panel consists of 4x2 subpanels. The size of a subpanel is about 84cm x 160cm and carries 9 T/R modules. In summary, the antenna consist of 12 subarrays columns in azimuth and 18 rows in elevation resulting in 216 high power efficient T/R modules of 10 W peak output power each. As for X-band, the power loss of a patch array is 0.5 dB. The mass of this subsystem is about 550 kg including structure and network.

Calibration

Real time in orbit internal calibration of the instrument is realised via an optical delay line. A portion of the transmit pulse is coupled out at the output of each T/R module, summed up via the calibration network and delayed by a fibre optic delay line. The delay time is just the length of the transmit pulse duration which then allows to feed back this calibration signal into the T/R module front end for closed loop calibration.

System Performance

The following tables 1-1 and 1-2 summarise the system and instrument key parameters of the baseline design relevant for single look processing. Alternatively, multiple looks can be processed in order to obtain improved radiometric resolution at the expense of geometric resolution.

Table 1-1: Instrument characteristics:

TX pulse length	10..50 µs
TX bandwidth	max. 100 MHz
Range of PRF	1000...4000 Hz
Antenna size (X-band)	10m x 0.7m
T/R o/p power	7 W peak
Total dc-power	2.65 kW
Antenna size (L-band)	10m x 3.24m
T/R o/p power	10 W peak
Total dc-power	865 W
Total instr. mass:	1200 kg
Total instr. dc power	3.9 kW

The instrument performance tabulated below is derived for an incidence angle of 35 deg. and a single polarisation case as an example.

Table 1-2: Typical instrument performance:

Modes of operation:	Spot-light mode	High resol. strip	Low resol. strip	High resol. Scan	Low resol. Scan
range resol. [m]	3	5	22	35	100
azim. resol. [m]	3	5.6	22.5	33.5	100
Noise equiv.σ^0					
-X [dB]	-26	-22.5	-28.5		
-L [dB]	-31	-27.5	-33.5		
Ambiguity ratio [dB]	22	25			
Swath width					
-X [km]	38 x 4	74		400	400
-L [km]	54 x 28	64		400	400

The calculated image performance over the swath is shown in fig.1-1 and fig.1-2 for the high resolution stripline mode at X-band. The distributed target ambiguity suppression is better than 25 dB over the range of incidence angle from 31° - 38°. The noise equivalent sigma zero (where snr > 0 dB) is better than -22.5 dB over a range of 32.5° - 38.5°, resulting in a performance swath width of 74 km.

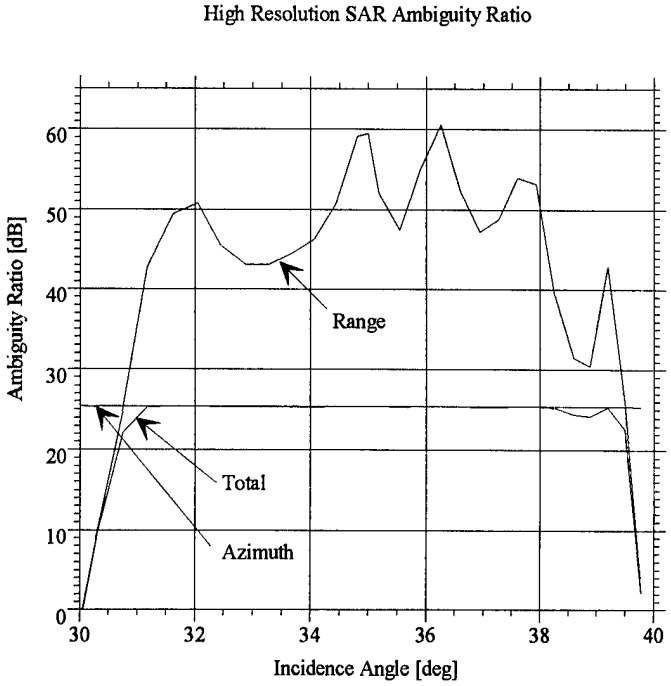

Fig. 1-1: Example of ambiguity ratio

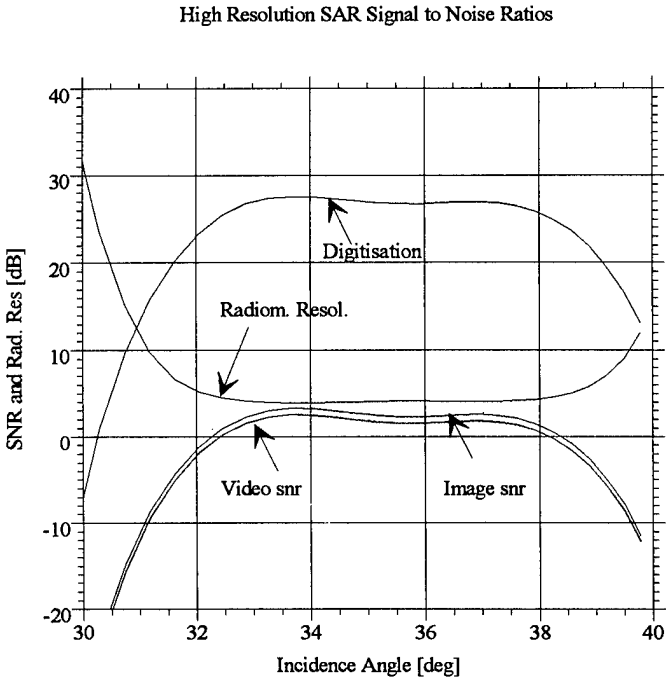

Fig. 1-2: Example of signal to noise ratio

Interferometry

The phase interferogram obtained from two SAR images of the same area relevant to two different look angles is a powerful technique for the generation of digital elevation models. The availability of multi-frequency information permits drastic improvements of the phase unwrapping procedure required to recover the original phase. In general, low frequency interferometric images (e.g. L-band) have a low decorrelation which leads to high coherence even for areas with dense vegetation. The phase unwrapping is considerably simpler as for high frequency images which in general show much better height resolution.

In combination, high accurate digital elevation model can be efficiently processed.

Operational considerations

The application of high resolution SAR's should not be limited by the instrument raw data rate even for a system providing 3 receive channels, i.e. X-band (dual pol.), L-band (quad pol.). In general, the data rate impacts the system mass and dc-power as well as the operation time due to the required on-board data storage capacity. Considering an operational profile where about 15 scenes per orbit will be imaged, the typical amount of data per scene is approximately 3x5 Gbit only. A raw data compression factor of 2.5 is applied.

The length of a scene is considered to be 100 km for the stripline mode. Typical ScanSAR data rates are between 25 to 65 Mbps. Taking into account a defined loss in the image quality, higher raw data reduction factors (e.g. 5..10) can be applied such that continuous operation of the ScanSAR mode becomes possible with just one single down link opportunity per orbit. For this, the required on board storage capacity is below 3x60 Gbit.

Further data reduction can be achieved by the compression of the on-board processed image data (on-board processing) leading also to a possible concept of small and flexible de-centralised ground stations.

For continuous ScanSAR operation, the available primary power may become a limiting factor. If one considers only single polarisation operation at L-band and reduced sensitivity at X-band (e.g. -23 dB instead of -28 dB), the total instrument dc power will drop from 3.9 kW to 1.7 kW.

For the high resolution stripline mode, the average power per orbit is reduced by the relatively short operation times. Assuming the same operational profile as before, the average dc-power over an orbit of 100 min. is below 200 W including a stand-by power of approximately 60W.

In order to reduce the effort and costs inherent with mission operation, the instrument itself can overtake some of this activities. For example, an automatic gain control (AGC) first tested during the SIR-C/X-SAR mission is one step towards autonomous operation. The AGC analyses the digitised radar raw data (square law detection) and controls the receiver gain in front of the ADC accordingly.

At its end, only user defined requirements as for example the target location, instrument mode and ground station location will be up-linked to the satellite. The actual satellite and radar setting parameters as e.g. pointing and antenna pattern optimisation are derived and performed on-board.

Further improvements

As an alternative to this baseline design, the system bandwidth could be increased up to 500 MHz which would provide very high resolution images of about 0.5m x 0.5m resolution when combined with a spotlight mode. For this, the antenna radiator will be a patch array which offers the advantage of a wide bandwidth, low mass and low production cost. In order to compensate for the lower sensitivity inherent to wide bandwidth operation, either the T/R module peak output power or the total number of T/R modules can be increased for example by reducing the length of the subpanels. The increase in the total dc power can be compensated for by high efficient T/R module (e.g. efficiency > 30% at X-band, > 35% at L-band). Applying those high efficient T/R modules to the current baseline design presented before, the total dc power saving would be 32%.

Next-Generation Coherent Radar Depth Sounder for Measurement of Greenland Ice Sheet Thickness

J. Legarsky, T. Chuah, and S.P. Gogineni
The University of Kansas, Radar Systems and Remote Sensing Laboratory
2291 Irving Hill Road, Lawrence, KS 66045, USA
913/864-7736 (T) - 913/864-7789 (F) - legarsky@rsl.ukans.edu

Abstract -- The mass balance of the Greenland ice sheet plays an important role in the rise of the Earth's sea level. Rising sea levels over the last century led to the initiation of a program by NASA to measure the surface elevation and thickness of the Greenland ice sheet.

The University of Kansas with its radar depth sounder participates in the Greenland ice sheet measurements. The airborne depth sounder measures surface elevation and the thickness of the ice sheet. Over the past several years, we have made improvements to the depth sounder. During the 1996 field experiment the depth sounder performed to its theoretical limit. We collected a large volume of data and supplied the processed data to scientists worldwide.

Having achieved the theoretical performance of the depth sounder, we wished to improve our measurements further and also to minimize the physical dimensions of the depth sounder system. We designed and built a Next-Generation Coherent Radar Depth Sounder (NG-CORDS) using today's technology to obtain a compact design as well as improved performance. We implemented the design using radio frequency integrated circuits (RFICs) and microwave monolithic integrated circuits (MMICs). The complete RF module is easily contained within a 8"x10.17"x4" enclosure.

Tests of the laboratory performance of NG-CORDS show the improved performance over the previous depth sounder. At the time of writing, the NG-CORDS will fly on a NASA P-3 over the Greenland ice sheet in May 1997. From the May 1997 field experiments, we expect to see the improved performance of the NG-CORDS. One mark of improved performance will be the imaging of the ice sheet internal layers through the entire ice sheet.

In this paper, we present the NG-CORDS system and experimental results.

INTRODUCTION

The mass balance of the Greenland ice sheet plays an important role in the rise of the Earth's sea level. The sea level has increased over the last century. NASA initiated a program to measure the surface elevation and thickness of the Greenland ice sheet. Remote sensing instruments, such as airborne altimeters and radio echo sounders, provide a safe, inexpensive, effective means of obtaining these ice parameters.

RFICs and MMICs have become commercially available at affordable prices [1]. Advances in recent years resulted in faster, inexpensive computers and signal-processing chips. We designed, tested and built a radar depth sounder using RFICs, MMICs, and state-of-the-art computer and signal processing cards. We named this radar the *N*ext-*G*eneration *C*Oherent *R*adar *D*epth *S*ounder (NG-CORDS). We use the NG-CORDS to measure the ice thickness of the Greenland ice sheet. Currently, we provide the best ice thickness measurements of the Greenland ice sheet known using the NG-CORDS.

THE NG-CORDS SYSTEM

NG-CORDS is a mirror version of the *I*mproved *C*oherent *A*rctic and Antarctic *D*epth *S*ounder (ICARDS) [2] that we used to measure ice sheet thickness over the past several years. NG-Cords uses ICs in place of connectorized components and it uses a state-of-the-art digital system. Its electrical performance is better than ICARDS, due to the availability of low-cost RFICs and MMICs and a wide selection of available IC specifications and packages. Table 1 summarizes the basic radar parameters. Fig. 1 shows the block diagram of NG-CORDS. The entire system consists of three basic elements: 1) the antennas; 2) the analog section; and 3) the digital section. The antennas are the same as the ICARDS antennas.

The analog section is contained within a rack-mountable chassis and performs all analog operation from transmit to receive. There are three user ports in the analog section: 1) test port; 2) STC port; and 3) PRF port. These ports are provided for ease of monitoring and understanding the real time display of radar data. The analog section generates an RF-chirp pulse of 1.6-μs duration with a peak power of 200 W for transmission through the transmit dipole array. The backscattered echoes are coupled to the analog section from the receive dipole array. These echoes are amplified, compressed and demodulated into video I and Q signals. These two signals, plus a system-oscillator-derived 37.5 MHz clock signal are used as input signals to the digital section. The 37.5 MHz clock signal from the analog section and the PRF signal from the digital section synchronize the operation of the entire radar system. The analog section of NG-CORDS combines the transmitter and receiver, their triggering circuits, and the power amplifier of ICARDS. The transmitter, receiver and their triggering circuits are integrated into a module that we called the RF module. The transmitter consists of a CW generation and power-dividing subsection, a

0-7803-3836-7/97/$10.00 © 1997 IEEE

limiting subsection, a pulse amplification and shaping subsection, and a power amplifier subsection.

The digital system is contained within a rack-mountable chassis. Here, the I and Q signals are digitized by two 12-bit A/D converters sampling at 18.75 MHz. These sampled data are coherently and/or incoherently integrated. These, plus the display of the post-integration results in A-scope form and 64-level gray-scale radio echogram, are carried out in real time. GPS information, acquired through the COM1 port, and the digitized backscattered data are stored on the hard disk of the digital section for subsequent processing. The timing of NG-CORDS operation is essentially the same as ICARDS, except that the STC is sweeping from 0 to 1.2V.

EXPERIMENTAL RESULTS

Mapping internal ice layers is very important in radio echo sounding (RES) of ice. Internal ice layers are also important to glaciologists. Fig. 2 shows a radio echogram recorded near the NGRIP site. This radio echogram was used to aid in deciding the location for the *N*orth *GR*eenland *I*ce Core *P*roject (NGRIP) drill site. The echogram shows there is no internal layer undulation [3]. Also, by following the layers, N. Gundestrup [4] believed he had identified the deepest visible layer to be 97 kyrs old, just a little above the 120- to 130-kyrs-old Eemian layer. The Eemian layer is important in the potential solution of the controversial question of whether there was an abrupt warming during that time.

Fig. 3 shows a radio echogram of the Petermann Glacier. The thickness, location of the grounding line and location of the calving front of the glacier can be identified from the echogram. This echogram merged with the airborne *A*ltimeter *T*opographic *M*apper (ATM), can be used to study the drainage of ice from the vast ice sheet of Greenland [5].

CONCLUSIONS

Sea level rise, which affects inhabitants of the Earth, has led to a major research interest in the mass balance of the ice sheets. NASA responded by initiating a program to measure the elevation and thickness of the Greenland ice sheet. Airborne laser altimetry and radio echo sounding provide methods for obtaining the ice parameters. The NASA P-3 flight lines are controlled by specific task-orientated missions from year to year. Every five years the flights are repeated. The NG-CORDS is an instrument that provides reliable measurements of the ice thickness.

REFERENCES

[1] Cohen, E.D., "The impact of the U.S. MIMIC program on technology and applications," *Technical Report, Advanced Research Projects Agency*, 1995.

[2] Chuah, T.S., *Design and Development of a coherent radar depth sounder for measurements of Greenland ice sheet thickness*, D.E. Dissertation, The University of Kansas, Lawrence, Kansas, USA, 1-158, 1996.

[3] Dahl-Jensen, D., N. Gundestrup, K.R. Keller, S.J. Johnsen, S.P. Gogineni, C.T. Allen, T.S. Chuah, H. Miller, S. Kipstuhl, E.D. Waddington, "A search in North Greenland for a drill site," in press, *J. of Glaciology*, 1997.

[4] Gundestrup, N., University of Denmark, personal communication, 1996.

[5] Jezek, K.C., S.P. Gogineni, T.S. Chuah, "Dynamics of the Petermann Glacier," unpublished monograph, 1996.

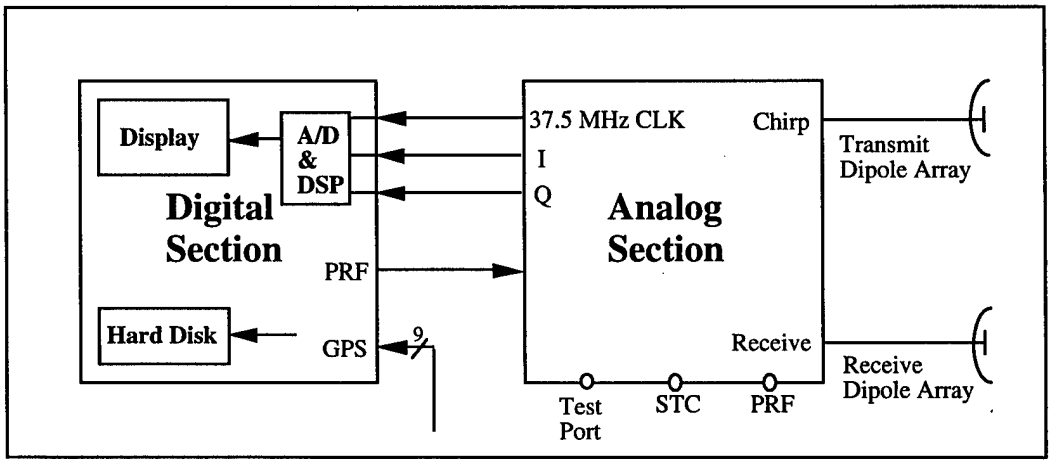

Figure 1. Block diagram shows the NG-CORDS configuration.

Table 1: Basic NG-CORDS Parameters

Description	Characteristic	Units
Radar Type	Pulse Compression	---
RF Carrier Frequency	150	MHz
RF Up-Chirp Bandwidth	17.00	MHz
Transmitted Pulse Width	1.6	μs
Compressed Pulse Width	60	ns
Peak Transmit Power	200	W
PRF	2.3, 4.6, 9.2, 18.4 (selectable)	KHz
Receiver Dynamic Range	93	dB
STC Dynamic Range	38	dB
Number of Coherent Integrations	selectable to 64,000	---
Number of Incoherent Integrations	selectable to 64,000	---
Baseband I & Q Bandwidth	10	MHz
A/D Dynamic Range	12-bit, 72	dB
Sampling Period	53.3 (18.75 MHz)	ns
Sampling Delay	selectable to 300 μs	---
Pixel Window in Ice (range)	4.494	m
Antennas	4-element λ/2 dipole arrays	

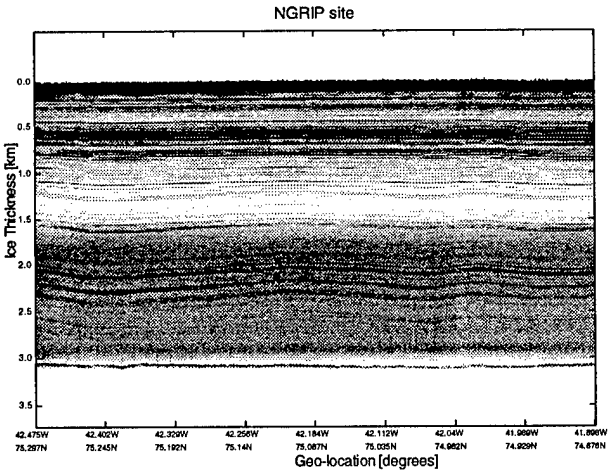

Figure 2. Radio echogram recorded near the NGRIP site.

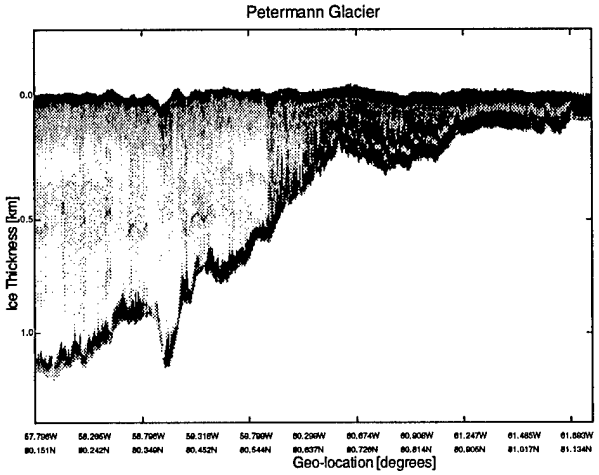

Figure 3. Radio echogram recorded over the Petermann Glacier.

A New Airborne Remote Sensing Platform for Acquiring Spatial and Radiation Information

Liu Zhen Li Shukai

Institute of Remote Sensing Applications, Chinese Academy of Sciences
PBX 9718, Beijing 100101, PRC. Tel:+86-10-6491-9232 Email:sfdirsa@public3.bta.net.cn

ABSRTACT--With the development of Global Position System(GPS) and Inertial Navigation System(INS), the precise position and attitude parameters of airborne platform can be obtained. The new system, such as INSAR and Scanning Laser Ranger(SLR), are excellent equipment for acquiring the relative height of earth objects. At the same time optical remote sensing sensor makes rapid progress. It is time to integrate these system into a new one, which can provide high accurate DEM and remote sensing image synchronically.

INTRODUCTION

The system, which integrates differential GPS receiver, INS, SLR and Infrared Sensor(IS), is loaded on a specially developed platform. The infrared optical axis of IS and that of SLR are coupled in the same virtual axis, so every SLR point fit in a pixel of inferred image accurately. DEM is generated form INS, GPS and SLR data. Because SLR point fit in a pixel of inferred image accurately, every DEM data have a corresponding image pixel. The result of test in North China proves that good quality DEM, geocoding images, ortho-images and 3D perspective images can be obtained in several hours after flying. Obviously, the system can save more money and time than the old method can. It has the advantage than INSAR in that the data processing need not super computer such as Cray, Sun workstation is enough. Although INSAR has more high accuracy of relative height, to generate interfergram from INSAR data is a time consuming job and the accuracy of DEM is unsatisfied without GCP.

STRUCTURE OF SYSTEM

The system includes two subsystems: System of Data Acquisition (SDA), System of Data Processing (SDP).

The SDA is composed of differential GPS receivers, INS, IS, SLR and a set of recorder and power system. A special platform was developed, on which sensors of SLR, IS, and INS were loaded. The deformation of the platform is limited in $15''$, so SLR, IS, and INS have the same parameters of position and attitude. The function of SDA is to receive, gather and record the data of GPS, INS, SLR, IS.

The function of SDP is to input the data from DAS and to output different degree digital products, such as DEM, geocoding-image, ortho-image, 3D perspective image. The

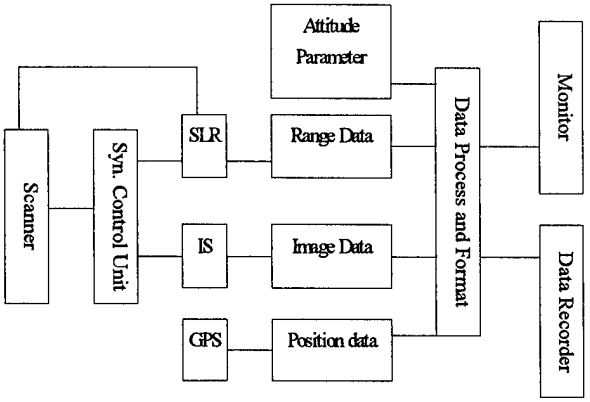

Figure 1 System of Data Acquisition

network , which is composed of Sun 20 workstation and 5 PCs, is the SDP software platform. A special soft package was developed.

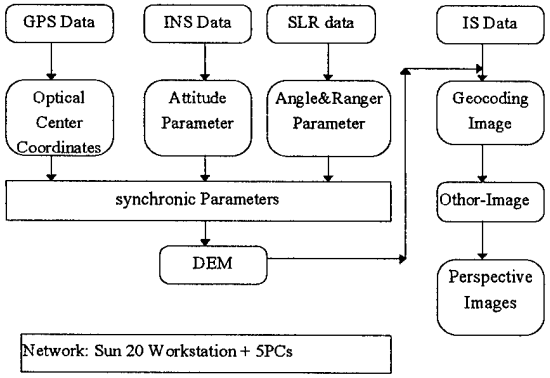

Figure 2 System of Data Processing

TEST AND RESULT

Test Site: Datangshan test site locate at Changping County, Beijing, north edge of North China plain, $116°18'45''$–$116°22'30''$E, $40°10'40''$–$40°12'30''$N. It cover 25 km. There is a hill which is 120 meter high In test site.

CONCLUSION AND DISCUSSION

The spatial quality of Datangshan hill image(Pic 1) is very poor, it is impossible to correct the image by use of GCPs since at least over hundred GCPs need. Pic.3 is the DEM of test site by use of the new system. Picture2 are geocoding images after correction. The time from receiving data to generation of all picture is in 2 hours. The result is satisfied.

Eleven control point were used in evaluating the spatial accuracy of the system.

$$u(X,Y,H) = (6.479,9.605,2.897)$$
$$\sigma(X,Y,H) = (8.825,10.695,6.002)$$

It is conclude that there is obvious system error in flying direction, which is caused by the unsatisfied accuracy of the INS. The error of the system is bigger that aero-cameral, which is cause by the propagation and accumulation of error of sub-systems. There are a lot of research to be conducted:

- Improve the accuracy of INS, GPS .
- Analysis how the error propagate and accumulate.
- Develop new algorithm for the data process to meet the real- time requirement.

ACKNOWLEDGEMENTS

We thanks all people conduct different research in the project, they are Prof. Xue Yongqi, Prof. Guo Huadong, Prof. Qian Yuhua, Mr. Liu Tong, Mr. You Hongjian, Dr. Jiang Yuesong, Mr. Chen Jiping, Mr. Shen Zaixun, Miss Ma Jingzhi, Mr. Jin Dondhua, Mr. Su Rong, Dr. Shao Hui, Mr. Liu Jianmin.

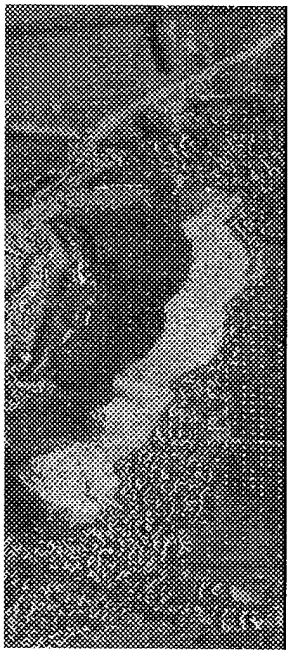

Pic. 1 Datangshan Image

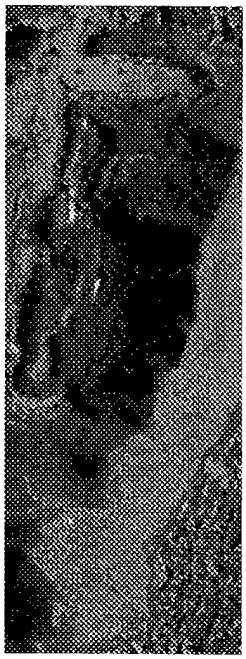

Pic. 2 Datangshan Geocoding Image

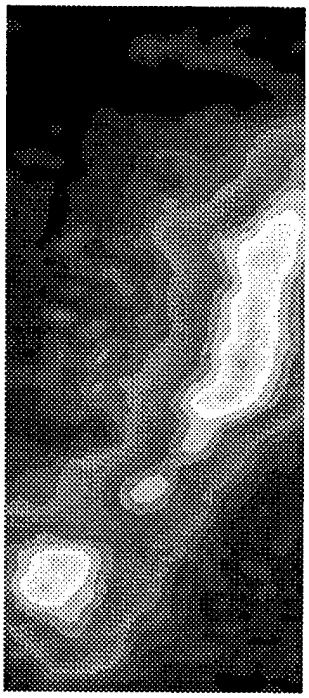

Pic. 3 Datangshan Hill DEM

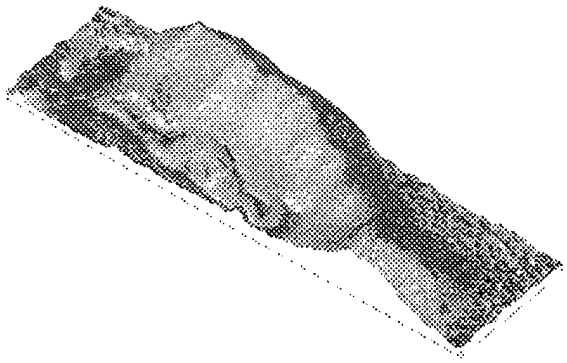

Pic. 4 Datangshan Hill Perspective Image

Combined High-Resolution Active and Passive Imaging of Ocean Surface Winds from Aircraft

A.J. Gasiewski and J.R. Piepmeier
School of Electrical and Computer Engineering
Georgia Institute of Technology, Atlanta, GA 30332-0250
(404) 894-2934; (404) 894-2984
ag14@prism.gatech.edu; gt2930b@prism.gatech.edu

R.E. McIntosh, C.T. Swift, J.R. Carswell, W.J. Donnelly, and E. Knapp
Microwave Remote Sensing Laboratory
University of Massachusetts, Amherst, MA 01003
(413) 545-4858; FAX: (413) 545-4652
mcintosh@ecs.umass.edu; klemyk@ecs.umass.edu; carswell@alex.ecs.umass.edu;
donnelly@alex.ecs.umass.edu; knapp@alex.ecs.umass.edu

E.R. Westwater, V.I. Irisov, and L.S. Fedor
NOAA Environmental Technology Laboratory, Boulder, CO 80303
(303) 497-6527; (303) 497-3577
ewestwater@etl.noaa.gov; virisov@etl.noaa.gov; lfedor@etl.noaa.gov

D.C. Vandemark
Laboratory for Hydrospheric Processes
NASA Goddard Space Flight Center, Wallops Island, VA 23337
(757) 824-2038; (757) 824-1036
vandemark@gsfc.nasa.gov

Abstract – A unique complement of passive and active microwave imaging and sensing instruments for observing ocean surface emission and scattering signatures were integrated onto the NASA Wallops Flight Facility's Orion P-3B aircraft (N426NA) for the purpose of studying the signature of ocean surface winds. The complement included: (i) a four-band (X, K, Ka, and W) tri-polarimetric scanning radiometer (PSR) (ii) a C-band ocean surface scatterometer (CSCAT), (iii) a Ka-band conical-scanning polarimetric radiometer (KASPR), (iv) a nadir-viewing Ka-band polarimetric radiometer, (KAPOL) (v) a 21- and 31-GHz zenith-viewing cloud and water vapor radiometer (CWVR), and (vi) a radar ocean wave spectrometer (ROWS). The above Ocean Winds Imaging (OWI) complement was flown during January-March, 1997 over the Labrador Sea. Conically-scanned brightness temperature and backscatter imagery were observed over open ocean for a variety of wind speeds and cloud conditions. Presented herein are the results of a preliminary intercomparison of data from several of the OWI instruments.

1. INTRODUCTION

Aircraft and satellite measurements have pointed to the possibility of building passive microwave sensors to measure both ocean surface wind speed and direction using the anisotropic nature of the emission from a wind-driven ocean. Such measurements would likely complement and improve upon wind vector maps available from active instruments (e.g., the NASA scatterometer - NSCAT). The need for complementarity is particular acute in high-wind conditions. Accordingly, the primary goal of the Ocean Winds Imaging (OWI) experiment was to collect data to verify the utility of passive polarimetric ocean wind vector sensing in high seas, with secondary goals being to better characterize the thermal emission and scattering signatures of a wind-driven ocean surface. The complement was flown under a variety of meteorological conditions in coordinated patterns over both ocean buoys along the eastern U.S. coast near Virginia and an instrumented research vessel - the *R.V. Knorr* - within the Labrador Sea. Local overflights of several NOAA ocean buoys near Wallops Island, VA and within the Gulf of Maine, and an extensive set of overflights of the Knorr located in the Labrador Sea during March 1-10, 1997 within the vicinity of 57°N, 53°W were performed. The conditions represented a wide range of surface wind speeds, cloud and water vapor states, and fetch lengths.

The OWI complement included two active radar scat-

0-7803-3836-7/97/$10.00 © 1997 IEEE

terometers for measuring both Bragg and specular return (University of Massachusetts' C-band Scatterometer - CSCAT and the NASA/Wallops Flight Facility's Ku-band Radar Ocean Wave Spectrometer - ROWS), two passive polarimetric imaging radiometers for imaging the upwelling thermal emission from the ocean surface (Georgia Institute of Technology's Polarimetric Scanning Radiometer - PSR and the UMASS Ka-band Scanning Polarimetric Radiometer - KASPR), and precision fixed-beam radiometers for measuring the sub-track upwelling polarimetric emission from the ocean surface (the NOAA Environmental Technology Laboratory's Ka-band polarimetric radiometer - KAPOL) and the above-track thermal emission from clouds and water vapor (the NOAA/ETL Cloud and Water Vapor Radiometer - CWVR). The complement also included a GPS dropsonde package (provided by the National Center for Atmospheric Research) for measuring subtrack P,T,Q, and wind vector profiles, and several video cameras for recording ocean foam and cloud conditions. This paper provides a preliminary intercomparison of some scan-averaged data from the Labrador Sea deployment.

2. EXPERIMENT DESCRIPTION

Flight patterns used in the OWI experiment consisted primarily of straight and level transects forming "hex cross" patterns (Fig.1). The hex cross pattern allowed $\sim$ 30 km flight lines crossing the surface truth site at three different approach angles. Ship measurements included bulk meteorological quantities, ocean surface wind speed and direction, surface heat flux, long-wave directional spectra, and atmospheric profiles parameters via rawindsondes. Typical overflight altitudes were $\sim$ 5.5 km. A detailed description of the OWI sorties, including a discussion of the prevailing meteorological and sea conditions, the data observed by the various OWI sensors, the coincident data available from various sources, and the engineering and logistical issues encountered during the experiment, can be found in [1].

3. RADIOMETER OBSERVATIONS

The PSR consists of a gimbal-mounted scanhead drum containing four total power radiometers operating at 10.7, 18.7, 37, and 89 Ghz [2]. Each radiometer measures the first three modified Stokes' parameters ($T_v = \langle |E_v|^2 \rangle$, $T_h = \langle |E_h|^2 \rangle$, and $T_U = 2\Re\langle E_v E_h^* \rangle$). A two-axis stepper-motor drive system allows the radiometer scanhead to be positioned at arbitrary azimuth and elevation angles. External hot and ambient calibration loads are view once per scan to provide absolute radiometric calibration. Analog detection hardware is used to measure the orthogonal-polarized brightness temperatures T_v and T_h. A bank of three-level digital correlators operating at 1 GS/sec is used for the measurement of T_U and for redundant measurements of T_v and T_h.

Fig. 2 shows calibrated X-band vertical and horizontal brightness temperature variations observed during conical scans with a 53.1^o incidence angle. Each plot is an average of several complete (360^o) azimuthal scans observed during three hex-cross transects oriented in N-NE, W, and S-SE directions and flown on March 4, 1997 from 1502-1548 UTC. The brightness imagery have been corrected for roll and pitch variations using an empirical limb brightening function derived from a series of cross-track scans that were performed during banked turns. The radiometric noise was reduced by averaging to $\sim$ 0.8 K for each of $\sim$ 280 azimuthal points.

The plots show a distinctive 3-5 K up-wind/downwind anisotropy with second harmonic dependence with consistent phases between transects. The wind was reported by the Knorr to be from 270^o at 15 m/secs with gusts to 18 m/sec, 4.8 m swell from 275^o. It is seen that the second harmonic content of the horizontal channels is significantly greater than that of the vertical channels. A similar harmonic distribution has been observed in both SSM/I data [3] and in simulations using an asymmetric wave geometrical optics (AWGO) model [4].

The 37-GHz KAPOL instrument was oriented in a nadir-staring configuration. A ferrimagnetic switch facilitated the observation of three linear polarizations (along track at 0^o, and $\pm 45^o$ from along-track) from which the first three Stokes parameters were computed according to $T_I = T_{45} + T_{-45}$, $T_Q = 2T_0 - T_{45} + T_{-45}$, and $T_U = T_{45} - T_{-45}$. The sensitivity of the KAPOL radiometer was $\sim$ 0.03 K for 1 second integration time.

At nadir, any polarization signatures (as seen in the second and the third Stokes parameters) can originate only from ocean surface anistropies. Such signatures can be seen in the KAPOL data observed during the three crossing transects of the hex cross. Fig. 3 shows a time record of T_I illustrating strong variations ($\gtrsim$ 10 K) due to the presence of the clouds between the aircraft and the sea surface. In contrast, T_Q and T_U show that noise due to clouds is mostly absent. Four strong variations in T_Q and T_U are related to rolls encountered during aircraft's turns. The absence of cloud signatures in T_Q and T_U is a result of the non-polarized nature of the phase matrix for electrically small cloud particles.

It is noted, however, that the mean levels of T_Q and T_U change in between aircraft turns as a result of changes in the polarization basis of the instrument. Such baseline data can thus be used to determine the apparent direction of the wind by estimating the predominant direction of the

polarization anisotropy. Fig. 4 shows recovered vectors of the brightness anisotropy along the hex-cross flight tracks obtained using a two-parameter (amplitude and phase) second harmonic fit to T_Q and T_U values. In these calculations, the KAPOL data was averaged over 30 seconds, and a 180^o directional ambiguity was resolved using in-situ wind measurements from the aircraft ($\sim 280^o$). The estimates compare well with reported surface winds measured by the Knorr and with the average surface winds measured using four GPS dropsondes released by the P-3 along a flight line in the vicinity of the hex-cross ($280^o \pm 15^o$ at 17 ± 1.5 m/sec).

The zenith-looking 21 and 31 GHz CWVR was similarly used to observe the impact of cloud emission reflected in the upwelling polarimetric ocean signatures. By flying beneath a broken cumulus cloud base on January 27, 1997, it was observed that warm perturbations of 3-4 K in the CWVR channels caused by clouds were strongly correlated with warm perturbations in the upwelling T_I as measured by KAPOL. However, the measurements of T_Q and T_U were virtually unaffected by the clouds.

4. RADAR OBSERVATIONS

The CSCAT radar [5] provided 360^o azimuthal scans of normalized radar cross-section simultaneously at incidence angles of 21^o, 31^o, 41.5^o, and 52^o. An example of an NRCS scan along with CMOD4 model fits is shown in Fig. 5 for the four incidence angles. Wind speed and direction estimates using CMOD4 curve fitting [6] during the period from 1447 to 1642 UTC resulted in consistent estimates of wind speed (15.5 m/sec average value) and direction (Fig. 6) for all four incidence angles. These wind speed and direction estimates are similarly in excellent agreement with the available surface truth.

ROWS data for the period from 1600-1642 UTC were similarly constant. Estimated sea surface parameters using the ROWS data [7] indicate a wind speed at 10 meters height $U_{10} = 13.34 \pm 0.95$ m/s, in reasonable agreement with both Knorr, dropsonde, and CSCAT observations. The ROWS data also indicate a significant wave height of 4.66 ± 0.31 m and RMS slope (at Ku-band) of 0.0438 ± 0.0024, consistent with high well-developed seas. These additional surface statistics are presently unavailable from the above active and passive instruments. ROWS will also be providing directional swell estimates for evaluating long-wave impact on the passive measurements.

5. SUMMARY

The above preliminary intercomparisons support the notion that active and passive remote sensing instruments can both be used to estimate wind direction. Indeed, excellent self-consistency among the variety of passive, active and contact sensors in both wind speed and direction was observed during the OWI experiment. Further intercomparisons are being made to determine the specific limitations of passive wind vector sensors in space. To expand the range of wind conditions for which data is available, additional deployments of the OWI complement of instruments are being planned in conjunction with instrument development studies in support of the NASA's EOS and the National Polar-Orbitting Operational Environmental Satellite System (NPOESS).

ACKNOWLEDGMENTS

The authors would like to thank R. Davidson, J. Baloun, and M. Tucker of the Raytheon Corporation for the design and fabrication of critical aircraft components; P. Bradfield, G. Postell, and the pilots and crew of N426NA for their outstanding help during the field campaign; and Drs. M. Van Woert of the U.S. Office of Naval Research, B. Douglas of the NASA/Headquarters Physical Oceanography Program, and S. Mango of the NPOESS Integrated Program Office for their support. GT acknowledges support from ONR grant NOOO14-96-1-0716, NPOESS IPO contract SMC 185-96-N0109, and NASA grant NAGW 4191; UMASS acknowledges support from ONR grants N00014-96-1-0698 and N00014-95-1-1034; NOAA/ETL acknowledges partial support from NOAA/NESDIS under contract MIPR-FY7615-96-NO243.

REFERENCES

[1] A.J. Gasiewski, J.R. Piepmeier, R.C. Lum, M. Klein, D. DeBoer, E.R. Westwater, V. Irisov, L. Fedor, C.T. Swift, R.A. McIntosh, J. Carswell, W.J. Donnelly, E. Knapp, and D. Vandemark, "Ocean Winds Imaging (OWI) experiment final report on NASA/WFF Orion P-3 integration and Labrador Sea field measurements", Tech. Rep., Georgia Institute of Technology, May 1997.

[2] J. R. Piepmeier and A. J. Gasiewski, "Polarimetric scanning radiometer for airborne microwave imaging studies", in *Proc. 1996 Int. Geosci. and Remote Sens. Symp. (IGARSS)*, University of Nebraska, Lincoln, NE, 1996, pp. 1688–1691.

[3] F. J. Wentz, "Measurement of oceanic wind vector using satellite microwave radiometers", *IEEE Trans. Geosci. Remote Sens.*, vol. 30, no. 5, pp. 960–972, September 1992.

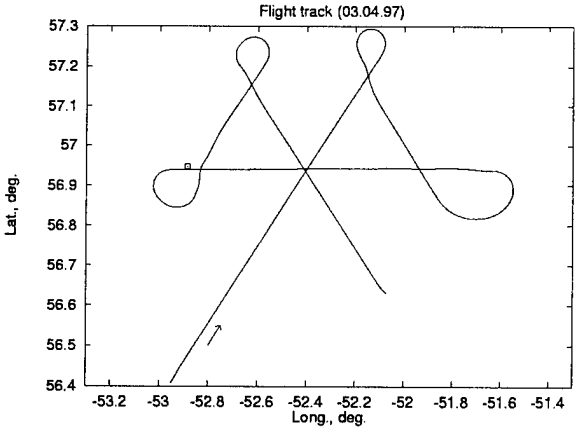

Figure 1: Hex-cross flight pattern used during OWI/Labrador Sea observations of ocean-surface anisotropies on March 4, 1997.

[4] D. B. Kunkee and A. J. Gasiewski, "Simulation of passive microwave wind-direction signatures over the ocean using an asymmetric wave geometrical optics model", *Radio Science*, vol. 32, no. 1, pp. 59–78, January-February 1997.

[5] J. R. Carswell, R. E. McIntosh, S. C. Carson, F. K. Li, G. Neumann, D. J. McLaughlin, J. C. Wilkerson, and P. G. Black, "Airborne scatterometers: Investigating ocean backscatter under low- and high-wind conditions", *Proceedings of the IEEE*, vol. 82, no. 12, pp. 1835–1860, 1994.

[6] European Space Agency, "CMOD4 model description", Electrosciences Report ER-TN-ESA-GP-1120, European Space Agency, 1993.

[7] D. Vandemark, F.C. Jackson, E.J. Walsh, and B. Chapron, "Airborne measurements of ocean wave spectra and wind speed during the Grand Banks ERS-1 SAR Wave Experiment", *Atmosphere-Ocean*, vol. 32, no. 1, pp. 143–178, 1994.

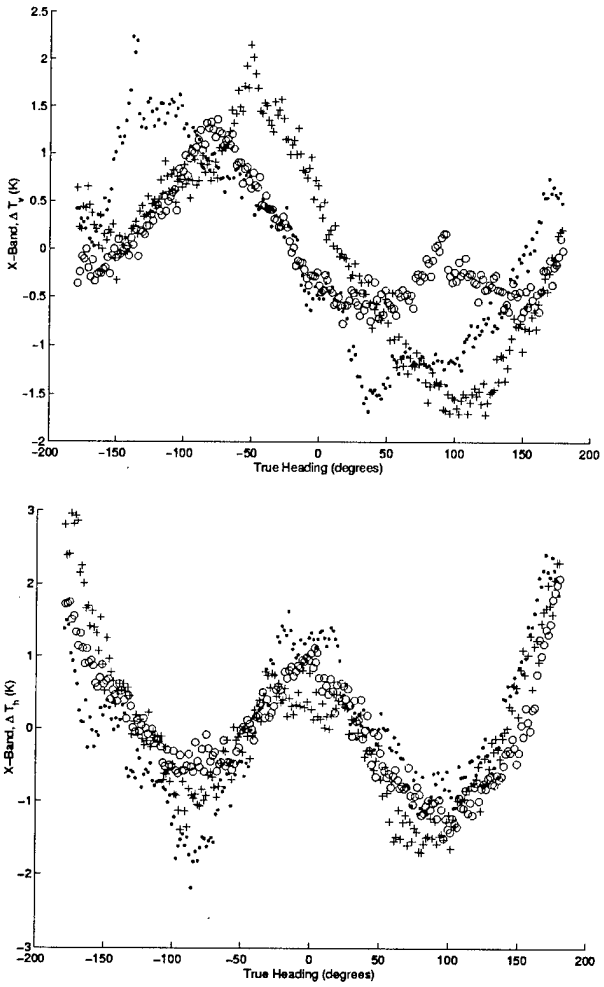

Figure 2: Calibrated PSR X-band azimuthal scans for a series of straight transects referenced to true north.

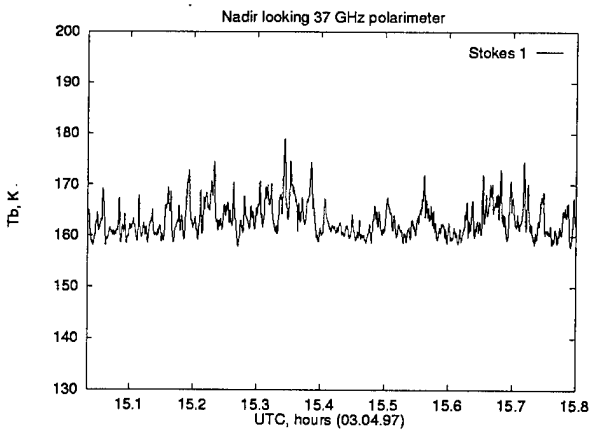

Figure 3: First Stokes parameter as observed using KAPOL during three transects of the hex-cross pattern in Fig. 1.

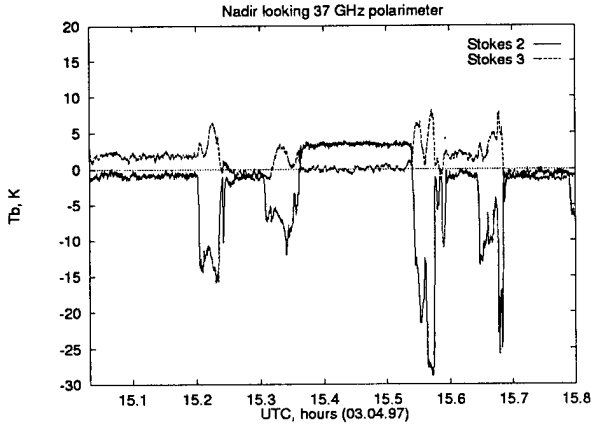

Figure 4: Second and third Stokes parameters as observed using KAPOL during three transects of the hex-cross pattern in Fig. 1.

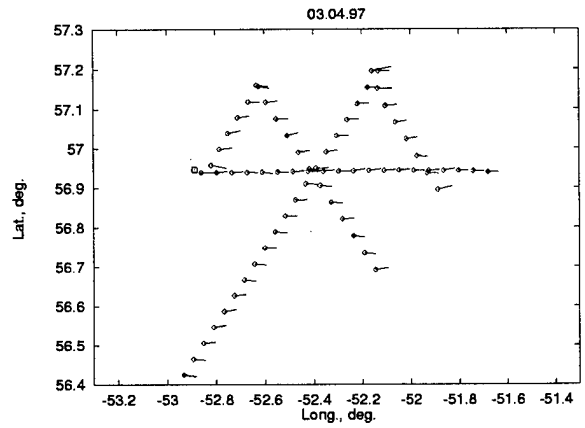

Figure 5: Ocean surface wind anisotropy vector determined from KAPOL data.

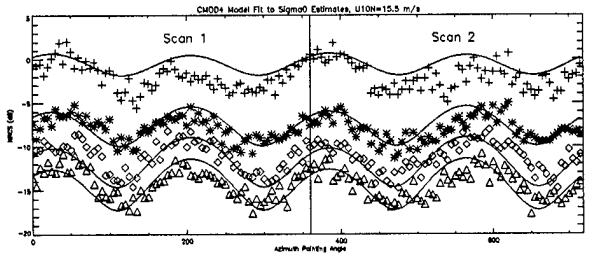

Figure 6: Azimuthal scans of normalized radar cross section observed at four incident angles using CSCAT.

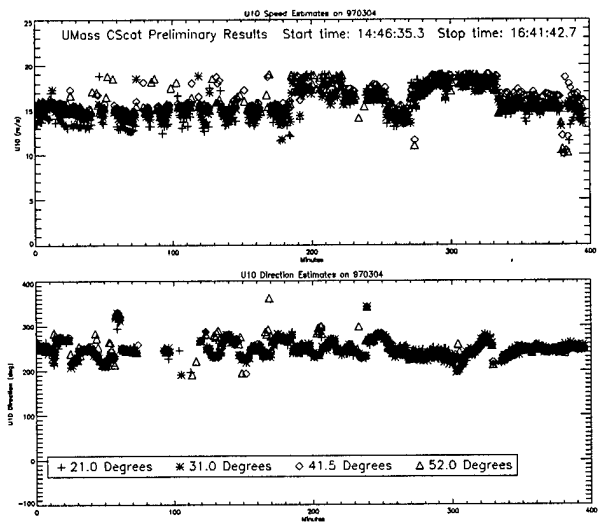

Figure 7: Estimated wind speed and direction using CSCAT data and the CMOD4 inversion model.

High-resolution Multiband Passive Polarimetric Observations of the Ocean Surface

Jeffrey R. Piepmeier and Albin J. Gasiewski
School of Electrical and Computer Engineering
Georgia Institute of Technology, Atlanta, GA 30332-0250
(404) 894-2984; (404) 894-2934; FAX (404) 894-4641
gt2930b@prism.gatech.edu; ag14@prism.gatech.edu

Abstract – A multiband microwave polarimetric scanning radiometer (PSR) was operating during January-March, 1997 over the Labrador Sea and the Atlantic Ocean aboard the NASA/WFF P-3B aircraft. Conically-scanned brightness temperatures were observed over open ocean for a variety of wind speeds and cloud conditions. Presented here are several illustrations and applications of data obtained during the Labrador Sea experiment.

INTRODUCTION

A versatile new airborne microwave imaging radiometer, the Polarimetric Scanning Radiometer (PSR), has been developed for the purpose of obtaining polarimetric microwave emission imagery of the Earth's oceans, land, ice, and clouds and precipitation [1]. In early 1997, the PSR was integrated onto the NASA Wallops Flight Facility P-3B Orion (N426NA) in conjunction with the Ocean Winds Imaging (OWI) Labrador Sea experiment. During the Labrador Sea deployment, conical, cross-track, and fixed-angle stare scanning modes where used to obtain calibrated brightness temperature data over a wind-driven ocean. Here, data from the experiment is used to illustrate the various scan modes available using the PSR.

INSTRUMENT DESCRIPTION

The PSR consists of a set of four tri-polarimetric ($T_v \sim \langle|E_v^2|\rangle$, $T_h \sim \langle|E_h^2|\rangle$, $T_U \sim 2\Re\langle E_v E_h^*\rangle$) radiometers housed within a cylindrically shaped gimbal-mounted scanhead. The scanhead contains an 80486 PC, an eight-channel digital correlator bank, and four total-power tri-polarimetric radiometers. The radiometric bands measured are X (10.6-10.8 GHz), K (18.5-18.9 GHz), Ka (36-38 GHz), and W (86-92 GHz). These bands are selected to provide sensitivity to clouds, precipitation, and surface features over almost one decade of microwave spectrum at octave intervals. The radiometer antennas are orthogonal linearly-polarized corrugated feedhorns with grooved rexolite lenses. A single dual-band antenna is used for the X- and Ka-band channels. Antenna diameters are chosen to provide beamwidths of 8^o (for both X- and K-bands) and 2.3^o (for both Ka- and W-bands.) Main beam efficiencies are greater than 0.95 and on-axis cross-polarization discrimination exceeds 27 dB. Fig. 1 is a video image showing the PSR in the P3 bomb-bay – the antenna lenses are clearly visible. The scanhead is rotatable by the positioner so that the radiometers can view any angle within 70^o elevation of nadir and any azimuth angle (a total of 1.32π sr solid angle), as well as external hot and ambient calibration targets. This configuration supports conical, cross-track, along-track, fixed-angle stare, and spotlight scan modes.

LABRADOR SEA EXPERIMENT

During the Labrador Sea experiment, the PSR was operated in three scan modes (conical, cross-track, and fixed angle stare) over ocean, land, and sea ice. The conical scan mode was used over ocean to obtain azimuthal scans of the wind-driven surface. The cross-track mode was used to estimate elevational brightness temperature profiles, and the fixed angle stare mode was used to obtain views of the cold sky for an extra calibration point.

Conical scanning

Azimuthal variations of the wind-driven ocean surface were observed using the conical scan mode. For a single straight and level flight track on March 4, 1997, nineteen azimuthal scans were averaged to arrive at a mean azimuthal signature for vertical and horizontal polarizations at X- and K-bands. The surface conditions according to the *R.V. Knorr* were winds from 270^o at 15 m/s gusting to 17 m/s with a 5-meter swell from 275^o. Fig.s 2-5 show the brightness temperature variations for the four channels. The signatures display the expected $sin(\phi)$ and $sin(2\phi)$ variations as observed in both SSM/I data [2] and in simulations using an asymmetric wave geometric optics model [3]. Furthermore, the variations exhibit the expected phase associated with an upwind brightening in T_v and a null in T_h.

Cross-track scanning

A useful function for computing pitch and roll corrections to brightness temperatures is the derivative of brightness temperature with respect to elevation angle. Although $dT_B/d\theta$ can be computed using radiative trans-

0-7803-3836-7/97/$10.00 © 1997 IEEE

Band	Polarization	$dT_B/d\theta$ (K/^{o})
X	V	1.83
X	H	-1.02
K	V	2.36
K	H	-0.87
Ka	V	2.25
Ka	H	-0.71
W	V	-0.58
W	H	1.06

Table 1: Elevation brightness correction coefficients (winds at 15 m/s, cloud ceiling at 2km.)

fer theory, an in-situ measurement is invaluable due to specific surface conditions and cloud layers that are not easily characterized for inclusion in a radiative transfer model. Performing cross-track scans coupled with an aircraft spiral maneuver allows the entire hemisphere of surface incident angles to be sampled. From this data set an azimuthally averaged brightness temperature elevation profile is easily produced. Having executed this a number of times during the deployment, an example from March 4, 1997 is reported here. Sea surface conditions are identical to those reported in the previous section. Additionally, upon aircraft descent, the cloud tops are observed at two km altitude. A plot for T_v at Ka-band is given in Fig. 6. This curve is calculated by averaging ten cross-track scans as the aircraft executed a partial circle banked at 20^o. The slope of this curve at 53.1 degrees from nadir yields the desired $dT_B/d\theta$ for aircraft attitude correction of conically scanned brightness temperature data taken at the standard SSM/I incident angle. The values of these correction coefficients are shown for all PSR bands at vertical and horizontal polarizations in Table 1.

Fixed-angle stare

Physical temperature gradients and the off normal incidence view angle of the hot and cold calibration targets cause the emission temperatures of the loads to be slightly lower than the measured physical temperatures. This causes an additional unknown, an effective emissivity of the targets, in the calibration relationship. The emission temperature of a calibration load in thermal equilibrium is

$$T_{emiss} = T_{amb} + \epsilon_{eff}(T_{load} - T_{amb}),$$

where T_{emiss}, T_{amb}, and T_{load} are the emission temperature, ambient temperature, and load's heatsink temperature, respectively. With a third calibration data point, the additional parameter may be determined. This third point must be taken in-situ when the aircraft is at normal operational altitude and the microwave absorbing material is in thermal equilibrium. Above the clouds, the view of a cold sky presents itself as an excellent third calibration point. With the antennas pointed to 60^o above aircraft nadir, the aircraft rolls an additional 60^o, resulting in a look at the cold sky 30^o above the horizon (or 120^o from nadir.) The cold sky look coupled with hot and cold calibration load looks forms a three point data set. The optimal value of ϵ_{eff} is found by varying this parameter to affect a minimum sum of squared-errors for a best-fit line through the three calibration points. For the flight on March 7, 1997, the effective emissivity is estimated to be approximately 0.7 for all channels. This is reasonable considering the strong temperature gradients expected within the microwave absorber which comprises the calibration targets.

CONCLUSION

In conclusion, these data excerpts from the Labrador Sea deployment demonstrate the usefulness of a scanning polarimetric radiometer for ocean wind studies. Further work remains in data processing, particulary the calibration and processing of the correlation channel for determination of T_U, for further understanding of passive high wind-speed signatures. Future deployments of the PSR are planned to provide an expanded data base with which to study ocean and atmospheric thermal emission.

ACKNOWLEDGMENTS

The authors wish to thank C. Campbell, E. Thayer, R.C. Lum, M. Klein, and D. DeBoer for their assistance in the PSR integration and operation phases; and are grateful for support from the following organizations: U.S. Office of Naval Research (grants N00014-95-1-0426 and N00014-95-1-1007), NASA Headquarters (grant NAGW-4191), and the NPOESS Integrated Program Office (contract SMC 185-96-N0109).

REFERENCES

[1] J. R. Piepmeier and A. J. Gasiewski, "Polarimetric scanning radiometer for airborne microwave imaging studies", in *Proc. 1996 Int. Geosci. and Remote Sens. Symp. (IGARSS)*, University of Nebraska, Lincoln, NE, 1996, pp. 1688–1691.

[2] F. J. Wentz, "Measurement of oceanic wind vector using satellite microwave radiometers", *IEEE Trans. Geosci. Remote Sens.*, vol. 30, no. 5, pp. 960–972, September 1992.

[3] D. B. Kunkee and A. J. Gasiewski, "Simulation of passive microwave wind direction signatures over the ocean using an asymmetric-wave geometrical optics model", *Radio Science*, vol. 32, no. 1, pp. 59–77, 1997.

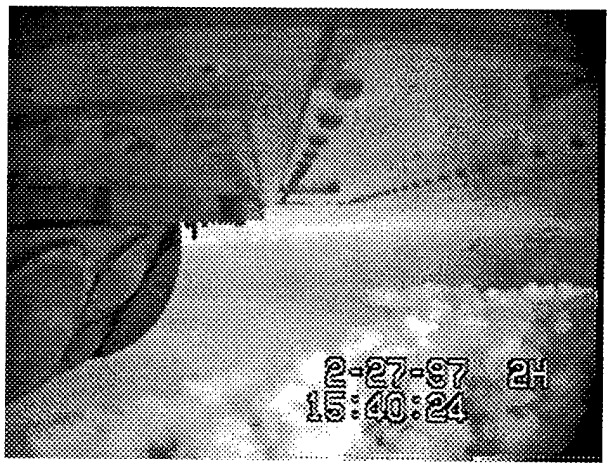

Figure 1: PSR on NASA WFF P3-B, aft view.

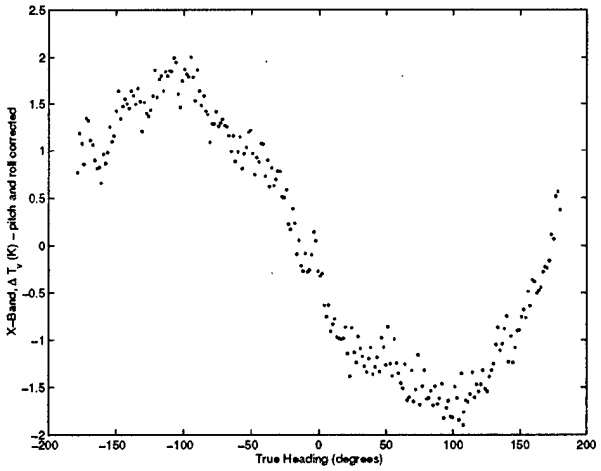

Figure 2: X-band ΔT_v averaged over 19 azimuthal scans. The wind direction is reported to be from -90^o .

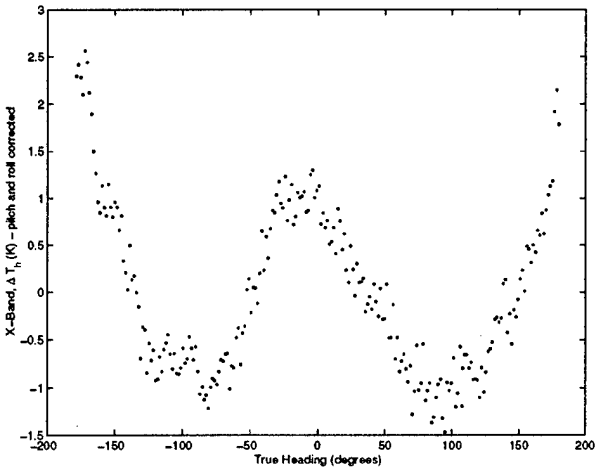

Figure 3: X-band ΔT_h averaged over 19 azimuthal scans.

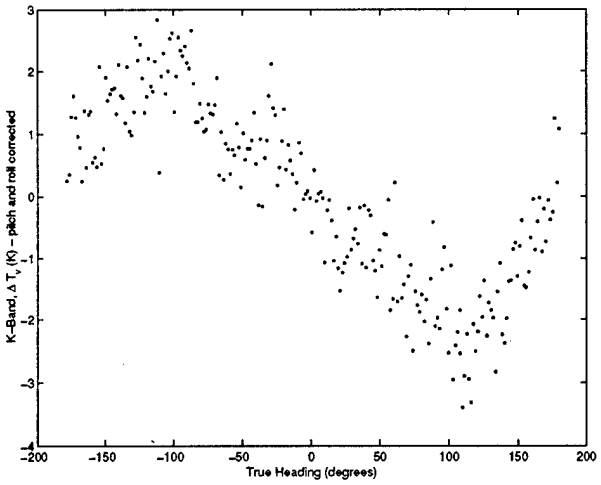

Figure 4: K-band ΔT_v averaged over 19 azimuthal scans.

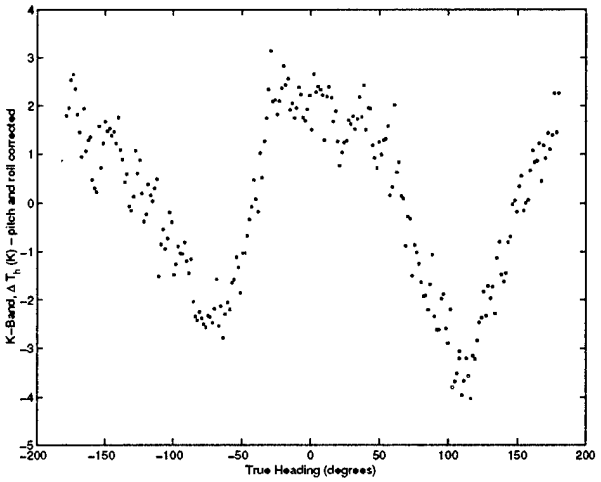

Figure 5: K-band ΔT_h averaged over 19 azimuthal scans.

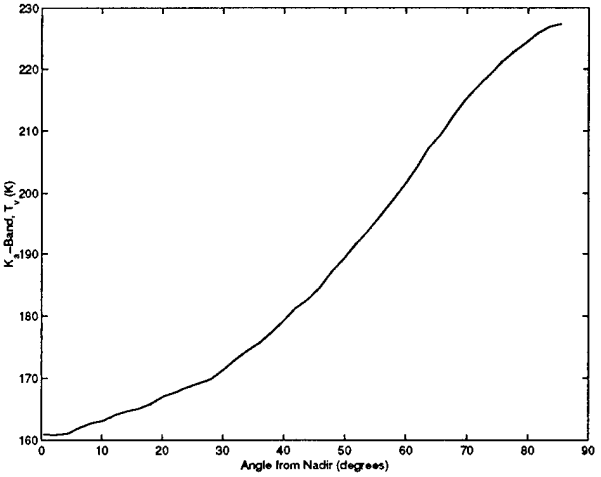

Figure 6: Ka-band T_v elevational profile.

Multi-Frequency Polarimetric Microwave Ocean Wind Direction Retrievals

Paul Chang[2], Peter W. Gaiser[1], Karen St. Germain[1] and Li Li[3]

[1] Naval Research Laboratory, Washington DC 20375-5351; (202)767-8253; (202)767-9194 FAX; gaiser@vaxusr.nrl.navy.mil; Corresponding Author
[2] NOAA/NESDIS/Office of Research and Applications, Washington DC 20233; (301)763-8231; (301)763-8020 FAX; chang@orbit.nesdis.noaa.gov
[3] Jet Propulsion Laboratory, Pasadena, CA 91009; (818)354-8349; (818)354-9476 FAX; li.li@jpl.nasa.gov

INTRODUCTION

The ocean wind velocity plays an important role in meteorology, oceanography, climatology, and military operations. Recent work and advancements in polarimetric radiometry suggest that it is possible to retrieve the complete ocean wind vector passively by measuring the radiometric Stokes parameters.

The Naval Research Laboratory (NRL) and the Jet Propulsion Laboratory (JPL) have conducted several aircraft campaigns from 1994-1996 using polarimetric microwave radiometers to measure the ocean surface wind direction. The first flights in 1994 used the JPL 19 and 37 GHz polarimetric radiometers, which measure the first three Stokes parameters (I, Q, U). In 1995, NRL added 10.8 GHz polarimetric radiometer and a dual polarization 22 GHz radiometer. In 1996, NRL modified the 10.8 GHz radiometer to measure all four Stokes parameters simultaneously. The experiments collected data at a variety of incidence angles during circle flights over National Data Buoy Center (NDBC) buoys, which were used for *in situ* data. The NDBC buoys reported the wind speed and direction with accuracies of ±1 m/s and ±10° [1]. In 1995, the buoys used were limited to those reporting every 10 minutes; the 1994 data were collected at buoys reporting hourly. Because there were no buoys near Hurricane Juliette, dropsondes were used for the necessary ground truth. Lastly, four flights were flown in November, 1996, out of NASA/Wallops Flight Facility (WFF) on the NASA/WFF P-3. These polarimetric brightness temperatures, together with *in situ* buoy wind data, verified the presence of a strong wind direction signal.

EXPERIMENT AND DATA ANALYSIS

The NRL 10.8 GHz polarimetric radiometer (hereafter, the 10 GHz) was first flown in the Fall'95 WINDRAD flight experiment along with the NRL 22 GHz dual-polarization radiometer and the JPL 19 and 37 GHz polarimetric radiometers on the NASA DC-8. At that time, the 10 GHz could measure only the first three Stokes parameters by sequentially measuring four polarizations, vertical, horizontal and ±45°. It is necessary to measure left- and right-circular polarization to derive the fourth Stokes parameter *V*. In 1996, NRL modified the 10 GHz system to make this possible. Previous polarimetric radiometer designs either could not measure *V* or could measure either *U* or *V*, but not both. This modification is important to understand better how the Stokes parameters relate to one another and the ocean surface.

To illustrate the effect of incidence angle and the potential value of the *V* term, Figure 1 plots *U* and *V* at 45° and 65°, both in ~13 m/s winds. The *U* signal changes in shape and magnitude from 45° to 65°; V increases significantly in magnitude and has a dominant second harmonic. At 65°incidence angle, the peak-to-peak value of *V* is approximately equal to that of *U*. These data are qualitatively consistent with the preliminary geophysical model developed by Wilson and Yueh [2].

The 10 GHz polarimetric channel provides important data needed to understand better the ocean surface conditions driving the wind vector signature. This channel is also important for accurate wind retrievals in higher wind speeds and in the presence of clouds and precipitation. These adverse conditions currently limit the effectiveness of the SSM/I sensor. The 1995 flight campaign included wind conditions ranging from 3–24 m/s, with the majority of the measurements being made below 10 m/s. Figure 3 shows 10 GHz *U* data, the third Stokes parameter, at three different wind speeds. Notice that the strength of the signal decreased as the wind speed increased from 14m/s to 24 m/s. Data from the JPL 19 and 37 GHz radiometers exhibited similar behavior. We have seen that the wind direction signal has increased as a function of wind speed up to 15 m/s. The 1995 data set includes only three high wind sets (14,15, and 24 m/s) and the 1996 winds peaked near 15 m/s.

Therefore, we intend to collect more polarimetric data in high wind conditions, particularly near hurricanes, to either verify or refute the behavior seen in Figure 2.

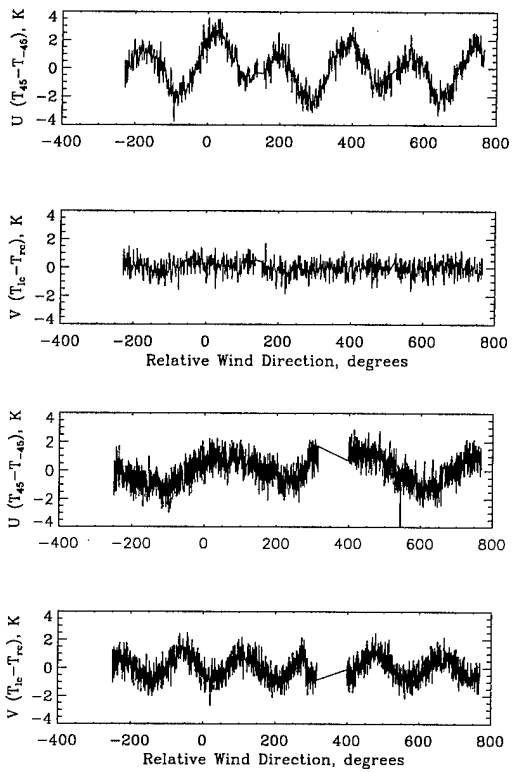

Figure 1. The third and fourth Stokes parameters (U and V) at 45° (top two plots) and 65° (bottom two plots) incidence angle from the NRL 10.8 GHz polarimetric radiometer.

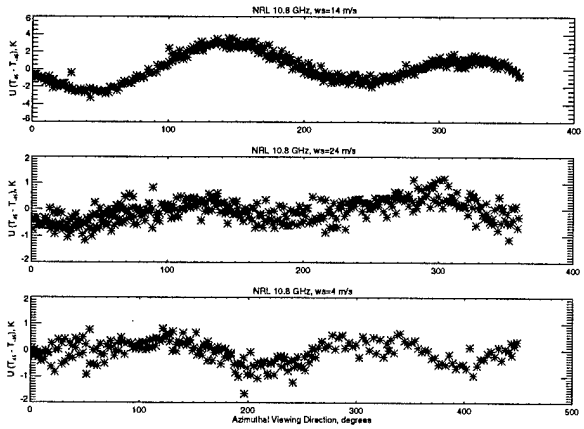

Figure 2. NRL 10.8 GHz U data (third Stokes parameter) at wind speeds of 14, 24, and 4 m/s The sky conditions ranged from scattered clouds to thin clouds. Each plot depicts overlaid data from multiple circles.

WIND DIRECTION RETRIEVALS

To evaluate the effectiveness of passive polarimetric data for retrieving the ocean surface wind direction, we developed a series of neural network (NN) retrieval algorithms using various combinations of data channels for each incidence angle. All the retrievals in this study use one-look geometry and only the results for wind direction are discussed because wind speed determination is a well established operational capability. Furthermore, 10 GHz data were not used in these retrievals because there are considerably less data at 10 GHz than at the other frequencies. Table 1 summarizes the scenarios considered and the RMS error of the wind direction retrieval, where the buoy measurements were taken as truth.

The scatter plot in Figure 3 illustrates the wind direction retrieval performance obtained with a NN algorithm using T_v, T_h and U at 19 and 37 GHz, and T_v, and T_h at 22 GHz, at 55°. It is important to realize that there is no ambiguity in these direction retrievals. The appendix contains plots of all the scenarios for which retrievals were developed.

The 22 GHz radiometer was added to the instrument suite because atmospheric water vapor resonates at 22.235 GHz. Thus, this channel is very sensitive to water vapor and is often used to measure it. To examine the importance of using 22 GHz in these retrievals, we trained NN models with and without the 22 GHz data. The two scatter plots showing 65° results in Figure 7 are representative of the improvement seen by including this frequency. The 22 GHz data accounts for noise in the signals due to variations in the tropospheric water vapor, thus reducing the scatter in the retrievals. On average, retrievals using only 19 and 37 GHz polarimetric data have approximately 33% higher RMS error.

In addition to the results discussed above, the NN retrievals developed for this study reveal other interesting behaviors. One sees that having two polarimetric channels (U terms) improves retrieval performance, especially at 45° and 65°. Using 37 with either 19 or 22, but not both gives mixed results, with the 19 retrievals working best at 45° and 55°. For cases including all wind speeds, the performance is best when T_v, T_h and U at 19 and 37 GHz, and T_v, and T_h at 22 GHz are used. It is important to emphasize that these retrievals did not consider combinations which include 10 GHz data. It is possible that 10 GHz will provide more improvement than 19 GHz, because of better atmospheric penetration. One other trait that is evident in Table 1 is that for every case, 45° produced the highest error. This is significant because the raw data and the harmonics suggest that a 45°

incidence angle data has the highest signal-to-noise ratio (SNR) of the three angles considered in this study. Possible explanations for this incongruity are (1) noisier raw data due to less stable aircraft bank angles during circle flights, and (2) greater sensitivity to other surface variables such as wave height and sea surface temperature.

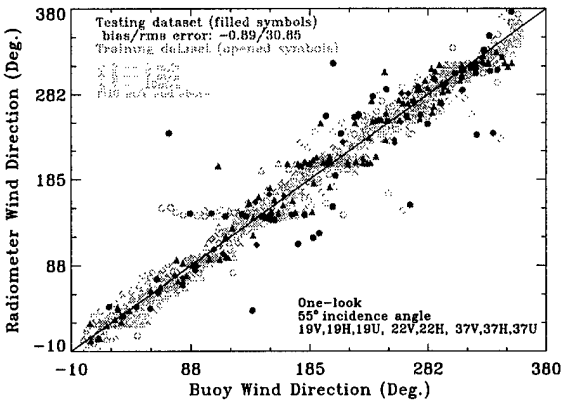

Figure 3. One-look wind direction retrievals at 55° incidence angles.

CONCLUSIONS

This study has demonstrated that unambiguous wind direction retrievals can be made using passive microwave polarimetric data. These retrievals perform best with polarimetric data from at least two frequencies and 22 GHz vertical and horizontal polarization data to account for atmospheric water vapor. The overall performance of the NN models developed for this work is very good, and suggests that a polarimetric microwave radiometer is a viable alternative to a scatterometer. This study also demonstrated that a 10.8 GHz polarimetric radiometer is capable of measuring a wind direction signature. Furthermore, 10 GHz measurements of *V* have shown this to be a unique signal, strong enough at some incidence angles to be comparable to *U*.

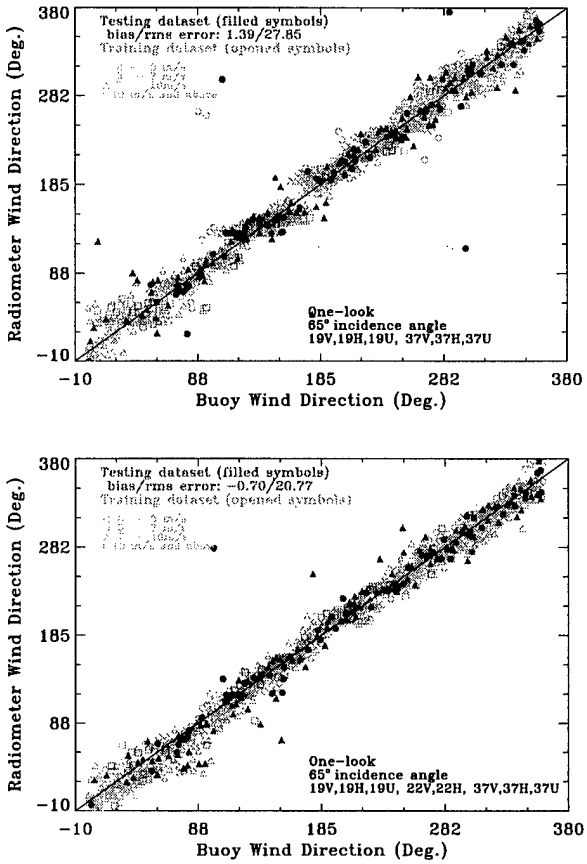

Figure 4. One-look wind direction retrievals at 65° illustrating the value added by the 22 GHz vertical and horizontal polarization data.

[1] I. Palao, "The National Data Buoy Center homepage", Technical report, National Oceanic and Atmospheric Administration, http://seaboard.ndbc.noaa.gov.

[2] W. J. Wilson and S. H. Yueh, "Ocean wind direction measurements using passive polarimetric radiometers", JPL Publication 96-6, 1996.

Table 1 Wind Direction Retrieval RMS Errors

	19 V,H,U 22 V,H 37 V,H,U	19 V,H 22 V,H 37 V,H,U	19 V,H,U 37 V,H,U	19 V,H 37 V,H,U	22 V,H 37 V,H,U	19 V,H,U 22 V,H 37 V,H,U w > 5m/s
45°	31.6	51.0	43.0	50.3	55.8	27.0
55°	30.9	29.8	39.1	37.2	44.2	**12.4**
65°	**20.8**	24.2	27.9	39.5	22.1	**13.8**

Development of a Sea Surface Temperature Algorithm for the ADEOS II/AMSR

John Galloway, Mark Goodberlet, Calvin Swift
Microwave Remote Sensing Lab
Knowles Engineering Building, University of Massachusetts at Amherst, Amherst, MA 01003
T: (413) 545-2463, F: (413) 545-4652, galloway@alex.ecs.umass.edu

Abstract – This paper describes ongoing development of an operational algorithm for retrieval of sea surface temperature (SST) from brightness temperature measurements made using the Advanced Microwave Scanning Radiometer (AMSR) system on the ADEOS II satellite.

INTRODUCTION

The desire to estimate sea surface temperature (SST) variation on a global scale drives the effort described in this paper. Prior systems such as the Advanced Very High Resolution Radiometer (AVHRR) and Special Sensor Microwave Imager (SSM/I), provide some global coverage of this field, but most have suffered from a lack of coverage due to atmospheric interference. The SSM/I system has provided information on an operational basis on the wind speed at the ocean surface [1]. Allocation of the frequencies covered by the AMSR system involved, among other requirements, the choice of two lower frequency channels which should be more sensitive to changes in SST (see figure 1), and less susceptible to atmospheric influences. Initial work to use SSM/I data to generate a similar algorithm for SST estimates has indicated a reasonable chance of success in that regard (see figure 2).

The present effort focuses on algorithm development using data from the AMSR, included on the ADEOS-II satellite, to provide global maps of SST to the research community. Specific goals of this development effort include provision of an operational SST algorithm with an accuracy of $\pm$ 0.5 °C for the AMSR, and determination of the spatial and temporal resolution expected for such SST estimates. The rest of this paper discusses the approach being taken to obtain this algorithm and establish the expected accuracy prior to the launch of the ADEOS-II satellite.

ALGORITHM DEVELOPMENT APPROACH

The approach being used is similar to that used to provide operational wind speed estimates for the SSM/I system. First, an SST algorithm appropriate for the SSM/I system will be determined, including a correction for wind driven modulation of the SST estimates. The modulation of brightness temperature due to wind speed over the ocean has been observed in the SSM/I data and reported in [2]. The D-matrix technique provides estimates of a parameter, SST for instance, from multiple measurements (buoy SST values) and a matrix of values established by multiple linear regression. In the case of the SSM/I brightness temperatures for the 19.35, 22.235, and 37 GHz channels, the expression for SST using the D-matrix method is:

$$SST = \sum_{i=0}^{N-1} D_i T_i, \qquad (1)$$

where the T_i values are the brightness temperature measurements and the D_i values are the D-matrix parameters.

The buoy and SSM/I data currently in hand include many of the NOAA buoys used for development of the GSW wind speed algorithm and satellite data from DMSP spacecraft F11 and F13 during 1995 and part of 1996. The coverage in time for the F11 satellite includes the period from Julian day 228 in 1994 to the end of 1995. The F13 archives cover the period from Julian day 123 in 1995 to day 213 in 1996. The list of buoys currently being used may be found in table I. The data from 1995 for both the buoys and satellite will be used to generate D-matrix parameters for an initial SST algorithm. The criteria for collocating the SSM/I brightness temperature and buoy SST measurements include a maximum separation of 25 km and 30 min between the measurements. Estimates of the wind speed and direction to be used to remove wind modulation from the SST estimates will be provided by the ERS-1 system aboard the ADEOS satellite.

After establishing an SST retrieval algorithm for the SSM/I case, the radiative transfer equation (RTE) will be used to extend the SSM/I results to the frequencies included in the AMSR. First, the RTE will be used to correct the SSM/I channels to properly simulate the AMSR channels. Then a simulated data set for the AMSR will be produced using the values of SST from the SSM/I algorithm.

ALGORITHM VALIDATION

Comparison between SST values from the SSM/I and AMSR algorithms and buoy and AVHRR SST measurements provide the basis for evaluation and validation of the algorithms. The difference between the 1996 buoy SST measurements and the SSM/I SST estimates will be analyzed to establish some of the factors influencing the error budget in the SSM/I SST estimates. The comparison between AVHRR estimates of SST and this initial algorithm will establish the expected accuracy without removal of the effect of wind speed modulation. Use of wind speed data from the ERS-1 system aboard the ADEOS-I satellite is expected to provide the information needed to remove wind effects from the initially determined D-matrix. The revised D-matrix algorithm for the

This work is supported by the ADEOS-II Secretariat, Earth Observation Research Center, National Space Development Agency of Japan

0-7803-3836-7/97/$10.00 © 1997 IEEE

SSM/I will then be characterized in terms of RMS difference and mean offset between the SSM/I and AVHRR SST estimates.

The AMSR algorithm developed from the SSM/I algorithm using the RTE will also be compared with NOAA buoy data to determine the expected error in the AMSR case. A climatological model for the wind will be used to provide the correction for the wind modulation of these SST estimates.

Instrument-Based Validation

Further validation of this D matrix is expected from measurements to be undertaken using NASDA's Airborne Microwave Radiometer (AMR). Measurements of the brightness temperature across the Kuroshio current using AMR will provide the data necessary to establish the accuracy of the proposed SST algorithm. This validation will include appropriate correction for the difference in atmospheric influence on the AMR and AMSR measurements.

Conclusions

Prior work with SSM/I data indicated the likelihood of successful development of an SST algorithm for that instrument. The inclusion of two lower frequency channels in the AMSR design enables greater sensitivity to SST changes with lesser dependence on atmospheric effects. The use of the approach outlined in this paper provides a pre-launch characterization of the quality of the proposed SST algorithm for the AMSR. This characterization involves the establishment of an equivalent SSM/I algorithm with well determined error budget and conversion of the SSM/I coefficients to AMSR equivalent coefficients using the RTE and climate wind models. Finally, pre-launch validation and characterization of the AMSR SST algorithm will be provided by the AMR measurement of the Kuroshio current.

Acknowlegements

This effort has been made possible by the assistance of Dr. Paul Chang at NOAA/NESDIS, who provided access to the 1995 and 1996 SSM/I data and AVHRR data. The NOAA buoy data was obtained from the archive maintained by the NOAA National Oceanographic Data Center.

References

[1] M. A. Goodberlet and C. T. Swift, "Remote Sensing of Ocean Surface Winds With the Special Sensor Microwave/Imager", *Journal of Geophysical Research*, vol. 94, no. C10, pp. 14547–14555, October 1989.

[2] F. J. Wentz, "Measurement of oceanic wind vector using satellite microwave radiometers", *IEEE Transactions on Geoscience and Remote Sensing*, vol. 30, pp. 960–972, 1992.

TABLE I

List of buoy names and locations. Buoy names prepended with a bullet are those which appeared originally in [1].

Buoy Name	Latitude (N)	Longitude (E)	Climate Code
32302	-18.00	274.90	tropics
41018	15.00	285.00	tropics
• 51002	17.19	202.17	tropics
• 51004	17.44	207.49	tropics
• 51003	19.14	199.20	tropics
• 51001	23.40	197.73	low-latitude transition
• 42002	25.89	266.43	mid-latitude
• 42001	25.93	270.35	mid-latitude
• 42003	25.93	274.08	mid-latitude
41010	28.90	281.50	mid-latitude
• 41006	29.32	282.66	mid-latitude
• 41002	32.29	284.76	mid-latitude
46025	33.75	240.93	mid-latitude
46053	34.24	240.15	mid-latitude
46023	34.25	239.33	mid-latitude
46054	34.27	239.55	mid-latitude
41001	34.70	287.41	mid-latitude
46028	35.76	238.13	mid-latitude
46042	36.75	237.59	mid-latitude
46059	37.98	230.00	mid-latitude
• 44004	38.46	289.31	mid-latitude
46022	40.76	235.50	mid-latitude
• 46006	40.87	222.46	mid-latitude
• 44011	41.08	293.42	mid-latitude
• 46002	42.53	229.74	mid-latitude
• 44005	42.90	291.06	mid-latitude
• 46005	46.08	229.00	mid-latitude
• 46003	51.85	204.08	mid-latitude
• 46001	56.29	211.82	arctic
• 46035	56.96	182.27	arctic

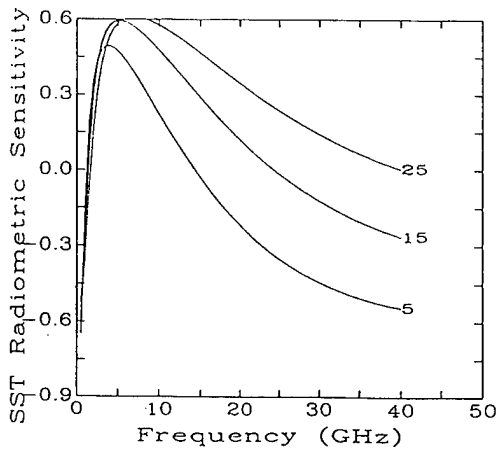

Fig. 1. Plot of SST radiometric sensitivity (defined as change in surface brightness temperature caused by a 1 °C change in SST) as a function of frequency for vertical polarization. Different curves indicate 5, 15 and 25 °C SST. A beam incidence angle of 53° and ocean salinity of 36 ppt were also assumed.

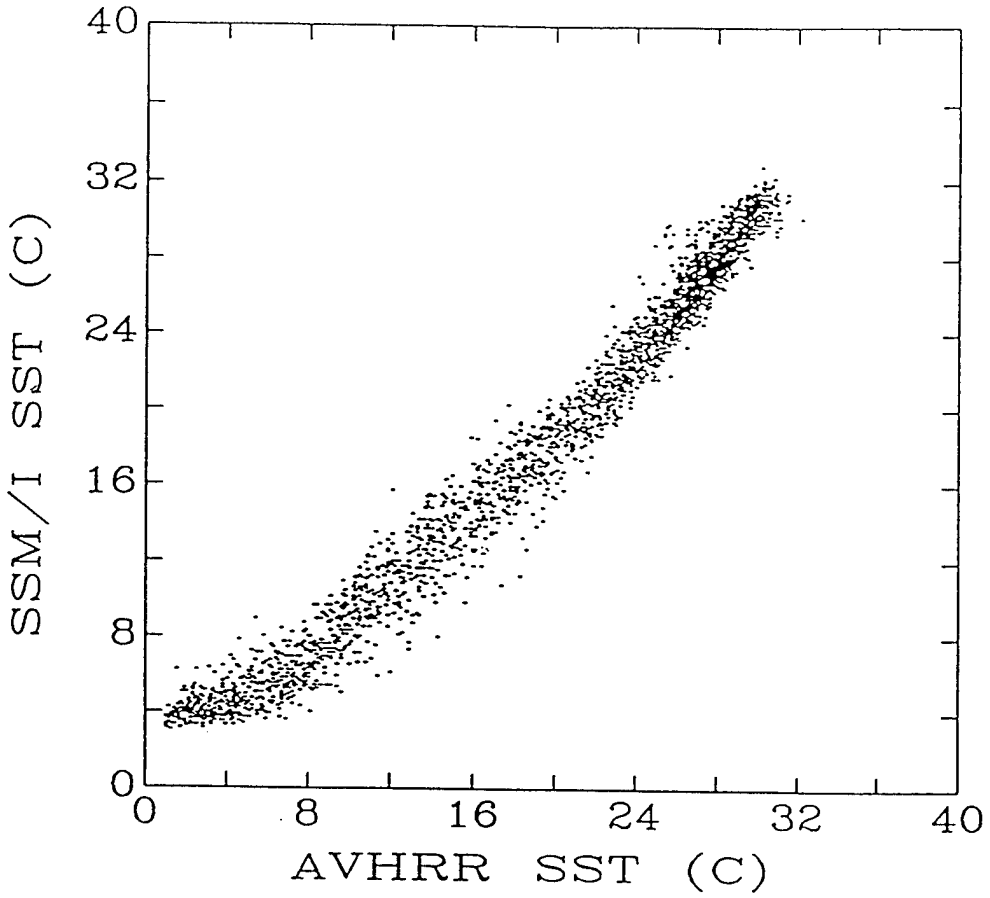

Fig. 2. Scatter plot of SSM/I and AVHRR SST estimates. This data was from the February 1988 portion of the data base used to develop the GSW ocean surface wind speed algorithm.

Estimation of Ocean Wave Height from Grazing Incidence Microwave Backscatter

Joseph R. Buckley andJohann Aler
Department of Physics, Royal Military College of Canada
PO BOX 17000 STN FORCES, KINGSTON ON CANADA K7K 7B4
tel: (613) 541-6000 ext 6275 / fax: (613) 541-6040 / e-mail:buckley-j@rmc.ca

Abstract -- When waves on the ocean surface are viewed with a ship-borne marine radar, their height is not directly related to either the magnitude of the microwave backscatter field or the magnitude of the modulation of this field in this grazing incidence regime.

We have performed some validation tests of a model [1] which theoretically related the statistics of the ratio of illuminated to shadowed areas through the viewing geometry to the significant height of the waves causing the shadowing. Using a subset of the data collected by two different digital marine radars on the Sea Truth and Radar Systems Experiment of December, 1994, we calibrated the model against measured wave heights, and then validated it using the remaining data from the radars and other independent wave height estimations. Significant wave heights in these experiments ranged from less than one to greater than 5 metres.

We found reasonable agreement between our inferred wave height extracted from radar imagery and heights estimated by other means when the sea conditions were moderate and not too complex. Scatter in the results was not inconsistent with the statistical variability expected from the sampling statistics.

The model failed under conditions of crossing seas, where it overpredicted the wave height, and when the measured wave height was a significant fraction of the radar scanner height, where the model exhibited asymptotic behaviour and underpredicted the actual wave height.

INTRODUCTION

The use of marine radar as an instrument to estimate ocean wave length and propagation direction has long been established. [2], [3]. The results of several wave spectral intercomparison experiments have shown that marine radar reproduces the shape of the wave spectrum better than other measurement technologies, especially under severe sea states [4]. The estimation of wave height from marine radar imagery however has been a more difficult problem. The root of the difficulty is that the intensity of backscatter in a marine radar image is associated with the concentration of capillary (1-5cm) waves on the sea surface, and the number of these is related to the wind stress, not to the wave height. The larger scale waves enter the problem only as the mechanism by which the backscatter field is modulated. Far from the radar, where the incidence angle is less than the wave slope, the sides of waves farther from the radar are shadowed from the radar and are therefore invisible. In this region, the intensity of the modulation is unrelated to the height of the waves Reference [1] proposed a model for estimating wave height in this region based on geometric optics and a theoretical model of sea surface elevation. Initial attempts to validate this model [7], [8], met with some success, but were hampered by lack of a sufficiently controlled data set and calibrating data. In this report, we extend their work to better and more varied data sets, with more calibrating data, and with some statistical investigation of theesults.

THEORY

Reference [1] described that, at grazing (<2°) incidence, a radar image of the sea surface consists of bright patches of reflection from the visible portions of the waves facing the radar ("islands"), separated by shadowed regions of no radar reflection ("troughs"). A statistical description of the proportions of these "islands" to the "troughs" leads to an estimate of the sea state, in terms of significant wave height. The only tunable parameter in the model is the probability of illuminatioP_0.

DATA

Data appropriate for the testing of this theory have been collected by both the Marine Microwave Research Group of the Physics Department, Royal Military College of Canada (RMC) and by MacLaren-Plansearch Ltd. (MPl) of Halifax, NS, Canada in the Sea Truth and Radar Systems experiment (STARS) which took place on the southern Grand Banks of Newfoundland in December, 1994. On this cruise, several other sources of wave height data were available for calibration and validation purposes [9]. Other sources of experimental data not reported here have been used with results similar to those described in this paper,

The RMC radar system and its data have been described in [3], and the MPl system in [10]. Fig. 1. shows a typical radar backscatter image from the RMC radar.

0-7803-3836-7/97/$10.00 © 1997 IEEE

Figure 1: Typical radar image of ocean surface waves. December 3, 1994

Islands and troughs were extracted from the radar imagery through a sequence of steps which, with some experimentation, proved to be relatively statistically stable. These steps were, in sequence: i) to threshold each image just above the receiver's noise floor, ii) to regularise the shape of the islands through a morphological "closing" transformation, iii) to establish the direction of wave propagation through a principal component analysis of either the image or its 2-D spectrum, iv) to coalesce four adjacent radial lines in that direction, with an OR operation in the transverse direction and v) to determine the resultant island and trough lengths in each image.

CALIBRATION

Calibration of the RMC radar data used those image sets for which there were corresponding Directional Waverider™ estimates of the significant wave height. The general technique of calibration was to use island / trough pair lengths extracted from these images, and the known significant wave height to calculate what P_0 value would have been required for that particular island / trough length to produce that particular wave height. All individual values that showed no significant deviation from the mean were averaged to produce the single value most representative of the data set. The result was a value of P_0= 0.350 which was used in all subsequent wave height calculations. Using this value to estimate the wave heights gave a relative error of 11% on December 2 and 16% on December 3. Therefore this is the value we used for the validation trials.

A similar procedure was followed for the MPl radar, but with a differentP_0 value.

VALIDATION

The calibrated relationships for estimating wave height from marine radar backscatter imagery were validated with independent data sets. In the case of the STARS experiment, we used hindcast estimates of wave height from the Canadian Spectral Ocean Wave Model (CSOWM) [11] to compare with radar predictions. The validation was carried out for time periods different from those used in the calibration press.

Inherent in the validation attempt was the assumption that to P_0 value, once calibrated for a particular radar in a particular observing geometry, should not change. Therefore the validation for the RMC radar was run using the P_0 value established in the calibration phase of the STARS experiment.

Fig. 2 shows the results of the wave height validation for both the RMC and MPl radar data throughout STARS. This figure shows that, for days 336 and 337 (December 2 and 3), the RMC radar and the model agree fairly well. On day 338 the radar severely overestimates the wave height as predicted by the model. For a while early on day 339 they agree again, but then the radar again severely overpredicts the wave height On day 341, through the middle of a storm, the radar underpredicts the wave height, but by day 342 the two are in agreement again.

In this figure we see that, in the region where the RMC radar performed most poorly, on day 338, the MPl radar was not collecting data, so no comparison an be made. On the other day of poor performance, day 341, the RMC radar underpredicted less than did the MPl radar, although neither did an adequate job of prediction.

DISCUSSION

The model [1] of estimation of significant wave height from marine radar backscatter shadowing statistics appears to be valid for a range of sea conditions when calibrated with independent wave height data. The estimation procedure provided accurate results in cases where there is only one wave propagation direction (monochromatic sea), when the waves are not too large with respect to the antenna height, and when the island / trough pairs are clearly defined. These conditions are met under moderate wind conditions when there is no significant swell present.

The wave height algorithm is ultimately dependent on the ratio of island length to trough length. When the islands are smaller than they ought to be, the wave height prediction is too large. When the islands are too large, the wave heights are too small. Cases where the prediction does not work can be attributed to imaging situations where the imaging model breaks down.

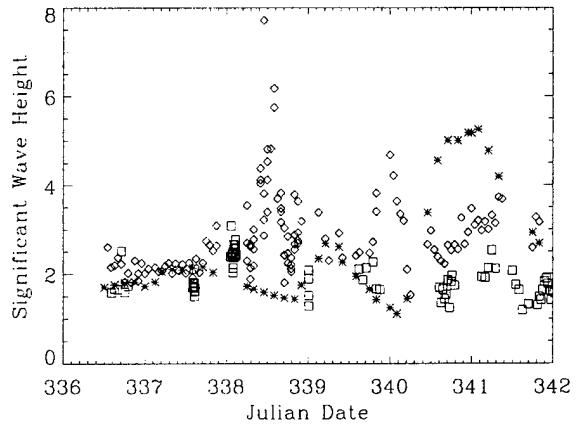

Figure 2: Validation Comparison of the RMC and MPl Radars. ◊ indicates RMC radar data, ❑ indicates MPl radar data, ✱ indicates CSOWM predictions.

During the severe storm of December 6, both radars significantly underpredicted the wave height. We observed that, as the storm was building, the island to trough ratio initially decreased as expected, then reached a limiting value. Either the model [1] for the shape of the sea surface is not valid for the storm-state ocean as the wave profiles may no longer be well represented or the geometrical optics illumination assumption breaks down when the wave height is a significant fraction of the antenna height. We are continuing our investigation of this phenomenon using data from other experiments.

Under conditions where the wind speed is very low (perhaps < 5 ms^{-1}) even large waves are very poorly imaged. This lack of backscatter may be attributed to the lack of capillary waves on the surface. Very little can be done under these circumstances. It is not possible to extract information from an image which contains none.

Even if the islands and troughs are well-defined, significant discrepancies in the calculated wave heights were noted in cases where the wave field is complex. A simple model using two or more interfering sine wave fields shows that mean island length will decrease under conditions of crossing seas. Under these conditions the measured island lengths are "too small" and therefore the estimated wave heights are too large.

Complex, multi-modal seas are commonplace in the Canadian offshore. The problem of correctly extracting island lengths from imagery of these states is important in the continued evolution of this form of wave height estimation. A principal thrust of our continuing research will be to estimate wave heights under these conditions correctly.

ACKNOWLEDGEMENTS

This work was sponsored by the Academic Research Programme of National Defence Canada under grant 3705-908, and by the National Energy Board, as part of Project 6B2044 of the Panel on Energy Research and Development.

REFERENCES

[1] Wetzel, L.B., "Electromagnetic Scattering from the Sea at Low Grazing Angles", in Surface Waves and Fluxes, G.L. Geernaert, and W.J. Plant, eds. Kluwer Academic Publishers, Dordrecht, The Netherlands, 1990.

[2] Young, I., W. Rosenthal, and F. Ziemer, "Three Dimensional Analysis of Marine Radar Images for the Determination of Ocean Wave Directionality and Surface Currents". J.Geophys. Res**90:** pp 1049-1059, 1984.

[3] Buckley, J. R., M. Allingham, and R. Michaud, "On the Determination of Directional Sea Surface Spectra from Marine Radar Imagery". Atmosphere-Ocean, 32(1), pp. 195-213, 1994.

[4] Dobson, F. W., S. D. Smith, R. J. Anderson, P. W. Vachon, D. Vandemark, J. R. Buckley, M. Allingham, M. Khandekar, R. Lalbeharry and E. Gill. "The Grand Banks, ERS-1 SAR Wave Experiment" EOS, Trans. Am.Geophys. U., 74(4),pp41,44-45, 1993.

[5] Ziemer, F. "Directional Spectra from Shipboard Navigation Radar During LEWEX" in Directional Ocean Wave Spectra, R.C. Beal, ed. The Johns Hopkins University Press, Baltimore, MD., 1989

[6] Plant, W.J. "The Modulation Transfer Function: concept and applications" in Radar Scattering From Modulated Wind Waves G.J. Komen and W.A. Oost, eds. Kluwer Academic Publishers,Dordrecht, The Netherlands. 1988.

[7] MacLaren Plansearch Limited, "Development of a Wave Height Measuring Algorithm for Marine Navigation Radar" Report to National Research Council Canada (NRC). Halifax, Nova Scotia. MPL Ref. # 007262, 1995.

[8] Henschel, M. D., J.R. Buckley and F.W. Dobson, "Estimates Of Wave Height From Low Incidence Angle Sea Clutter" 4th International Conference on Wave Hindcasting and Forecasting, Banff, AB, October, 1995.

[9] Vachon, P. W., C. Bjerkelund, J. Buckley, J. Campbell, F. W. Dobson, A. L. Gray, H. Johnsen and R. Lalbeharry. "Validation of SAR Ocean Wave Measurements: ERS-1 and CV-580 Cross-spectra and CV-580 Along-Track InSAR" International Geoscience and Remote Sensing Symposium. Lincoln, Nebraska, May, 1996 pp 1155-1157., 1996.

[10] Trask, J, M. Henschel, and B. Eid, "Analysis of Marine Radar Image Spectra Collected During the Grand Banks ERS-1 SAR Waves Experiment" Atmosphere-Ocean, 32(1), pp. 215-236. 1994.

[11] Khandekar, M. L., and R. L. Lalbeharry. "A Brief Overview of Environment Canada's Operational Ocean Wave Model" 3rd International Conference on Wave Hindcasting and Forecasting, Montreal, PQ, May, 1992.

Calibration of a High Resolution Airborne 3-D SAR

J. Dall, J. Grinder-Pedersen, S. N. Madsen

Danish Center for Remote Sensing, Dept. of Electromagnetic Systems
Technical University of Denmark, B-348, DK-2800 Lyngby, Denmark
Phone: +45 4525 3800, Fax: +45 4593 1634, E-mail: jd@emi.dtu.dk

Abstract — The potential of across-track interferometric (XTI) synthetic aperture radar (SAR) for producing high resolution 3-D imagery has been demonstrated by several airborne systems including EMISAR[1], the dual frequency, polarimetric, and interferometric SAR developed at the Dept. of Electromagnetic Systems (EMI). In order to achieve a high geodetic fidelity when using such systems operationally, calibration procedures must be applied. Inaccurate navigation data and system parameters as well as system imperfections must be accounted for. This paper presents theoretical models describing the impact of key error contributors on the measured terrain elevation. The models are used in estimating calibration parameters on the bases of distributed targets with known elevation. Finally, the calibration procedure is applied to EMISAR data collected by the Danish Center for Remote Sensing (DCRS[2]), and the stability of the estimated parameters is examined in order to assess the general utility of the procedure.

INTRODUCTION

Many airborne XTI systems are capable of producing 3-D imagery with height resolutions on the order of one meter, i.e. the stochastic height noise of these systems is about one meter. However, often systematic errors hamper the absolute accuracy of the generated digital elevation models (DEMs) unless multiple ground control points (GCPs) are used to correct the data. The need of such points complicates automation of the processing procedures, and it even prevents production of calibrated 3-D imagery in remote areas without GCPs.

The systematic errors can be divided into three different classes, viz. those originating from

- insufficient navigation system accuracy
- insufficient system parameter knowledge
- system imperfections

Navigation data of importance are the roll angle and the platform position which directly couples to the absolute pixel position. The system parameters include the channel delay, the channel phase shift including the phase ambiguity number, the baseline length and angle. The errors of the first two classes cause calibration errors that vary slowly and monotonously in the range direction. The system imperfections on the other hand give rise to errors of more complicated character. The imperfections addressed in this paper are multi-path propagation introduced by on-aircraft reflections and channel leakage [1]. Both cause oscillating phase errors and hence height errors that are generally not monotonous.

By setting up models relating the parameters of the error contributors to the systematic height errors, calibration parameters can be estimated from distributed targets with known elevation [1], e.g. a sea surface with waves giving the signal-to-noise ratio required to have sufficiently low height noise.

This calibration procedure has been applied to XTI data acquired with EMISAR in 1996. A total of 6 scenes from 3 different missions have been calibrated in order to examine the stability of the estimated parameters and to assess the general utility of the procedure.

In 1995 the L- and C-band polarimetric capabilities of EMISAR were supplemented with an XTI capability by adding two flush mounted C-band antennas in front of the wing. This antenna installation provides a baseline with a length of B = 1.14 m and an angle of $\alpha_p = 34°$ from the platform horizontal. The antennas are fully polarimetric, so either HH or VV polarized XTI data can be collected. Since the antennas are connected via the switch matrix also used for polarimetry the system can be operated in multiple XTI modes:

- single baseline (transmit on one antenna, receive on both);
- double baseline (sequentially transmit and receive on one antenna then transmit and receive on the other)
- dual baseline (sequentially transmit on one antenna and receive on both, then transmit on the other and receive on both, thus collecting both double and single baseline data).

EMISAR is flown on a Danish Air Force Gulfstream G-3 twin engine jet aircraft which is typically operated at 25.000 ft when XTI data are collected. The navigation system includes INSs as well as a P-code GPS system.

[1] Development of EMISAR has been supported by the Thomas B. Thriges Foundation, the Danish Technical Research Counsil (STVF), the Royal Danish Air Force (RDAF), the Technical University of Denmark, the Joint Research Centre (JRC) and by the Danish National Research Foundation.
[2] The Danish Center for Remote Sensing is finansed by the Danish National Research Foundation.

0-7803-3836-7/97/$10.00 © 1997 IEEE

MODELS

Assuming that the Earth curvature can be neglected i.e. the SAR is at an altitude H above a flat reference plane, and that the baseline is much smaller than the slant range R, then the unwrapped interferometric phase is given by

$$\phi=\phi_1-\phi_2=-\gamma\cdot\sin(\theta-\alpha),\ \gamma=2\pi pB/\lambda \quad (1)$$

where θ (>0) is the line-of-sight angle with respect to the nadir direction and α is the baseline angle. Thus $\theta-\alpha$ is the angle between the baseline normal and the line-of-sight direction, and $B\sin(\theta-\alpha)$ is the baseline component in the line-of-sight direction. p = 1 in the single baseline mode and p = 2 in the double baseline mode.

The terrain height h and the ground range c are given by

$$h=H-R\cdot\cos(\theta) \quad (2)$$

$$c=R\cdot\sin(\theta) \quad (3)$$

The impact of navigation data errors is easily found from (1-3). The height sensitivity to a platform altitude error is trivial

$$\frac{\partial h}{\partial H}=1 \quad (4)$$

and since the resulting baseline angle α equals the platform baseline angle α_p plus/minus the roll angle α_r (right/left looking SAR), the sensitivity to a platform roll error is

$$\frac{\partial h}{\partial \alpha_r}=\frac{\partial h}{\partial \theta}\bigg|_{H,R}\frac{\partial \theta}{\partial \alpha}\bigg|_{\phi,B}\frac{\partial \alpha}{\partial \alpha_r}=R\cdot\sin(\theta)\cdot 1\cdot(\pm 1)=\pm c \quad (5)$$

The influence of erroneous system parameters is also found from Eqs. 1-3. The impact of an α_p error is the same as that of an α error (the opposite for a left-looking SAR). The sensitivities to a baseline length error and a phase error are

$$\frac{\partial h}{\partial B}=\frac{\partial h}{\partial \theta}\bigg|_{H,R}\frac{\partial \theta}{\partial B}\bigg|_{\phi,\alpha}=R\cdot\sin(\theta)\frac{\tan(\theta-\alpha)}{B}=\frac{c\phi}{B\sqrt{\gamma^2-\phi^2}} \quad (6)$$

$$\frac{\partial h}{\partial \phi}=\frac{\partial h}{\partial \theta}\bigg|_{H,R}\frac{\partial \theta}{\partial \phi}\bigg|_{B,\alpha}=R\cdot\sin(\theta)\frac{1}{-\gamma\cdot\cos(\theta-\alpha)}=\frac{-c}{\sqrt{\gamma^2-\phi^2}} \quad (7)$$

The channel delay errors impacts the estimation of the absolute phase, which in turn impacts the unwrapped phase according to (7).

The remainder of this section addresses the third class of errors, those originating in system imperfections. Fig. 1 shows an on-aircraft reflection point located on the line connecting the two interferometry antennas. The signals propagating between an antenna and a target via this point is delayed and attenuated before it is added to the direct signal. By using the approximation $1+ae^{j\phi} = 1+a\cdot\cos\phi+ja\cdot\sin\phi \approx e^{ja\cdot\sin\phi}$, where $a\ll 1$ is the attenuation factor of the delayed signal, it can be shown that in all three operation modes the phase error caused by on-aircraft multi-path propagation can be expressed as

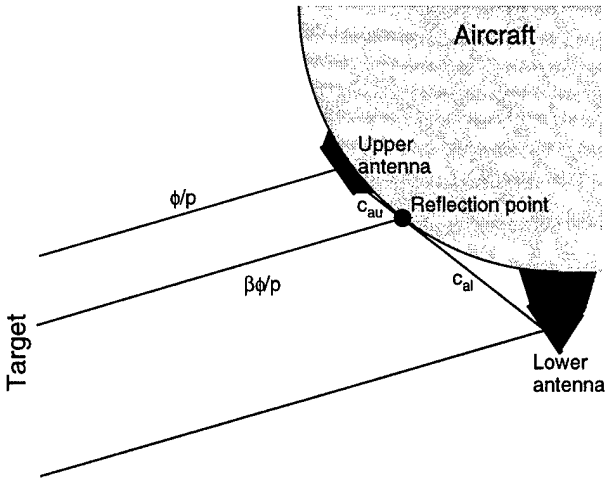

Fig. 1 On-aircraft multi-path. All propagation phases are one-way phases, and the phases to the target are differential with respect to the lower antenna. $c_x = a_x e^{j\phi_x}$.

$$\phi_A=-pa_l\cdot\sin\left(\beta\cdot\phi/p+\phi_{al}\right)-pa_u\cdot\sin\left((1-\beta)\cdot\phi/p-\phi_{au}\right) \quad (8)$$

βB is the baseline from the lower antenna to the reflection point.

Fig. 2 outlines the switch matrix needed in XTI systems offering single, double, and dual baseline operation. The intended signal paths are indicate in black, the leakages in gray. In the figure the switch is set for transmission on the upper antenna. Note that the complex constants representing the leakages depend on the setting of the switch as indicated by the last subscript (upper transmit: u, lower transmit: l). Using the above-mentioned approximation in combination with Fig. 2 it can be shown that the phase errors for double baseline, single baseline upper transmit, and single baseline lower transmit are

$$\phi_d=-a_{etu}\sin\left(\phi/2+\phi_o+\phi_{tu}-\phi_{etu}\right)-a_{eruu}\sin\left(\phi/2+\phi_o+\phi_{ru}-\phi_{eruu}\right)$$
$$-a_{etl}\sin\left(\phi/2+\phi_o-\phi_{tl}+\phi_{etl}\right)-a_{erll}\sin\left(\phi/2+\phi_o-\phi_{rl}+\phi_{erll}\right) \quad (9)$$

$$\phi_u=-a_{eruu}\sin\left(\phi+\phi_o+\phi_{ru}-\phi_{eruu}\right)-a_{erlu}\sin\left(\phi+\phi_o-\phi_{rl}+\phi_{erlu}\right) \quad (10)$$

$$\phi_l=-a_{erul}\sin\left(\phi+\phi_o+\phi_{ru}-\phi_{erul}\right)-a_{erll}\sin\left(\phi+\phi_o-\phi_{rl}+\phi_{erll}\right) \quad (11)$$

These three phase errors can be expressed in a generic form $\phi_L = a\cdot\sin(f\phi+o)$ which is used subsequently.

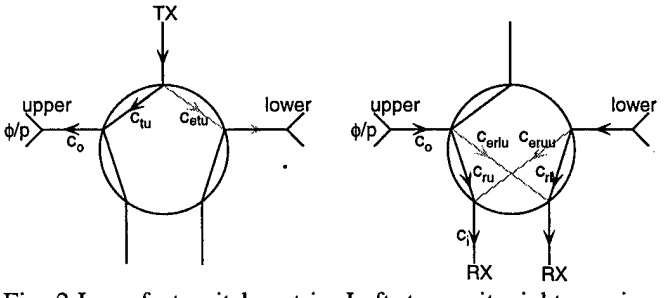

Fig. 2 Imperfect switch matrix. Left: transmit, right: receive. $c_x = a_x e^{j\phi_x}$.

CALIBRATION PROCEDURE

According to Fig. 2 the measured phase is

$$\phi_m=\phi+p\cdot\phi_o+(p-1)(\phi_{tu}-\phi_{tl})+(\phi_{ru}-\phi_{rl})+\phi_i+\phi_a+\phi_L \qquad (12)$$

The measured navigation and system parameters are: $H_m=H+\Delta H$, $\alpha_{rm}=\alpha_r+\Delta\alpha_r$, $\alpha_{pm}=\alpha_p+\Delta\alpha_p$, and $B_m=B+\Delta B$. Using these parameters the measured height becomes

$$h_m=h+\frac{\partial h}{\partial\phi}(\phi_m-\phi)+\frac{\partial h}{\partial H}\Delta H+\frac{\partial h}{\partial\alpha_r}\Delta\alpha_r+\frac{\partial h}{\partial\alpha_p}\Delta\alpha_p+\frac{\partial h}{\partial B}\Delta B \qquad (13)$$

First the calibration procedure interprets the difference between this height and the true height $h=h_{ref}$ of a reference surface as a phase error which according to (7) is given by

$$\Delta\phi=\frac{\partial\phi}{\partial h}(h_m-h_{ref})=p\cdot\phi_o+(p-1)(\phi_{tu}-\phi_{tl})+(\phi_{ru}-\phi_{rl})+\phi_i$$
$$+\phi_a+\phi_l+\sqrt{\gamma^2-\phi^2}\left(-\frac{\Delta H}{c}\pm\Delta\alpha_r-\Delta\alpha_p\right)-\phi\frac{\Delta B}{B} \qquad (14)$$

Note that $\Delta\phi\neq\phi_m-\phi$ because $\Delta\phi$ also includes terms introduced when the impacts of the other system parameter errors and navigation data errors are interpreted as phase errors.

Next the calibration procedure plots $\Delta\phi$ as a function of ϕ_m (ϕ is not known). Unlike the first three phase terms in (14), which are constants, and the altitude, roll and baseline terms, which are slowly varying functions of ϕ (and hence ϕ_m), the two multi-path terms are very sensitive to the shift caused by substituting ϕ_m for ϕ. In this context it is worth noting that $\phi_L(\phi_m)$ does not depend on ϕ_o, as ϕ_L according to Eqs. 9-11 is a function of $\phi+p\phi_o=\phi_m-(p-1)(\phi_{tu}-\phi_{tl})+(\phi_{ru}-\phi_{rl})+\phi_i-\phi_A-\phi_L$.

Finally, the procedure estimates the calibration parameters by fitting the curve forms of the terms in (14) to $\Delta\phi(\phi_m)$. For a typical EMISAR geometry Fig. 3 plots these terms as functions of ϕ and the figure illustrates that the estimation is ill-conditioned as, for instance, a combined phase and roll error is fairly indistinguishable from an altitude error.

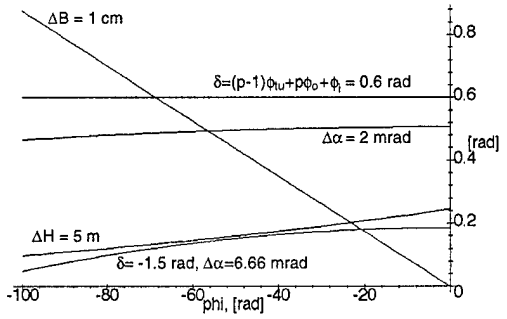

Fig. 3 Examples of $\Delta\phi$ contributors.

EMISAR CALIBRATION

This section shows some results based on six EMISAR data sets from three different flights, all collected over sea surfaces. The two interferometric channels are processed simultaneously and motion compensated to a common reference line, [2]. The processor also includes automatic determination of the absolute phase, [3]. The output products include co-registered amplitude data, height map, correlation map, and for calibration runs also absolute phase maps. The output data sets are orthorectified to a spherical (s, c, h) coordinate system, [4]. Usually output products are generated at 5 or 10 m ground range pixel spacing.

The processing includes an amplitude, phase, and delay calibration based on signals from three internal calibration loops exercised just before and after every mapping. This internal calibration facility, which was originally intended for polarimetric calibration [5], covers the phase terms c_{tu}, and c_{ru} but not ϕ_o.

Fig. 4 shows $\Delta\phi(\phi_m)$ for the six double baseline scenes after calibration of altitude, roll and phase. Baseline calibration was not included. The standard deviation of the roll and phase corrections are 1.8 mrad and 0.3 rad, respectively. (The latter is 0.1 rad when a single outlier is removed, while it is 0.5 rad without internal calibration. The internal calibration in turn drifts less than 0.05 rad from pre-map to post-map.) Since the figures correspond to height errors on the order of ten meters it is concluded that altitude, roll and phase must be calibrated on a scene by scene basis to achieve meter level accuracies. In Fig. 4 the slowly oscillating ϕ_A sinusoidal (first term, $\beta<0.5$) is superimposed the faster ϕ_L sinusoidal. Table 1 lists the mean and standard deviation for the amplitude, frequency and offsets of these sinusoidals. The amplitudes correspond to height oscillations of a few meters and to an aircraft reflection suppression of -20 dB and a switch isolation of -40 to -30 dB. The ϕ_L frequency of 0.5 is consistent with (9), and the ϕ_A frequency of 0.11 corresponds to β = 0.23 and hence a reflection point βB = 26 cm from one antenna. The offsets vary less than 2 percent of the sinusoidal periods and the amplitudes are also stable, so a fixed multi-path calibration can be applied to multiple scenes.

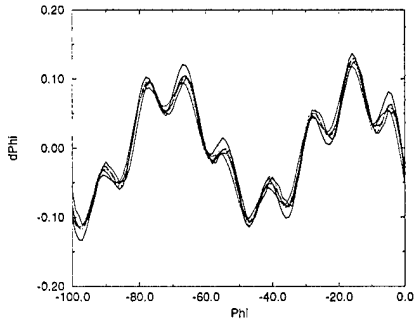

Fig. 4 $\Delta\phi(\phi_m)$ after calibration of the navigation parameters and the system parameters.

Table 1 Statistics for the multi-path phase terms.

	amplitude, a [mrad]	frequency, f [rad^{-1}]	offset, o [rad]
ϕ_A (β<0.5 term)	86 ±2	0.11 ±0.00	3.3 ±0.05
ϕ_L	36 ±4	0.50 ±0.00	3.1 ±0.2

When the estimated sinusoidals are eliminated the second ϕ_A term appears. It has a somewhat smaller amplitude and, as expected, a frequency corresponding to 1-β.

One of the six data sets was collected in dual baseline mode. The frequencies of the sinusoidals extracted from the two single baseline products have proved to be twice that of the corresponding double baseline product, in accordance with Eqs. 8-11. Also, the amplitude of the ϕ_A phase error differs by a factor of two is as expected from (8).

CONCLUSION

Accurate calibration is crucial for the generation of XTI products having not just a high resolution but also a high geodetic fidelity. Calibration based on ground control points is not easily automated and such points are rarely available in remote areas. This paper has presented a model-based calibration procedure using distributed targets with known elevation. The model includes navigation parameters, system parameters, and system imperfections. Errors from these three classes contribute to the EMISAR data, the calibration of which has been reported in this paper.

While the work with calibration procedures continues at DCRS, the EMISAR system is being upgraded in order to reduce the need of calibration. The navigation system, and in particular its attitude accuracy, will be improved, and a switch matrix with better isolation has been ordered.

REFERENCES

[1] S.N. Madsen, N. Skou, K. Woelders, and J. Granholm, "EMISAR Single pass Topographic SAR interferometer modes", International Geoscience and Remote Sensing Symposium, IGARSS'96, pp. 674-676, Lincoln, Nebraska, USA, May, 1996.

[3] David R. Stevens, Ian G. Cumming, and A. Lawrence Gray, "Options for Airborne Interferometric SAR Motion Compensation", IEEE Trans. GRS, vol. 33, pp. 409-420, March 1995.

[4] S.N. Madsen, "On absolute phase determination techniques in SAR interferometry", SPIE conference proceedings, Orlando, Florida, April 1995.

[5] Søren N. Madsen and Howard Zebker, "Imaging Radar Interferometry", Chapter 6 in Manual of Remote Sensing, Vol. III, 1997, in press.

[6] J. Dall, N Skou, E. Lintz Christensen, "Pulse-based Internal Calibration of Polarimetric SAR", IGARSS'94, 1994 International Geoscience and Remote Sensing Symposium, California, USA, August 1994.

The Mount Etna Case Study: A Multisensor View

R. Horn, K. P. Papathanassiou, A. Reigber, R. Scheiber (DLR - Institut fuer Hochfrequenztechnik),
P. Hausknecht, P. Strobl, R. Boehl (DLR - Institut fuer Optoelektronik),
M. Scheele, R. Reulke, W. Baerwald (DLR - Institut fuer Weltraumsensorik),
German Aerospace Research Establishment (DLR), P. O. Box 11 16, D-82234 Wessling, Germany
Tel.: +49-8153-28-2384, Fax: +49-8153-28-1449, Email: ralf.horn@dlr.de

G. Puglisi, M. Coltelli (CNR - Istituto Internazionale di Vulcanologia (I.I.V.)),
G. Fornaro (CNR - Istituto di Ricerca per L'Elettromagnetismo e i Componenti Elettronici (I.R.E.C.E.)),
Consiglio Nazionale delle Ricerche (CNR), Italy

Abstract -- Three DLR institutes, forming the cluster „Sensorik fuer Fernerkundung & Navigation", and two italian CNR institutes, I.R.E.C.E. and I.I.V., agreed on carrying out a joint airborne multisensor campaign in the Mt. Etna area in summer 1996. The site is of high geological interest. The deployment of an experimental SAR (E-SAR), a multispectral optical scanner (DAIS) and a wide angle stereo camera (WAAC) resulted in a number of unique data sets, which allow the analysis of the synergy between optical and microwave sensors with regard to the application.

INTRODUCTION

Mt. Etna is located on the eastern margin of the island Sicily, Italy, close to Catania, the second largest city of the island. The volcanic cone has a basal diameter of 40 km and an elevation of 3350 m, hence it is the highest mountain in the central mediterranean region. The volcano (Fig. 1) lies on the boundary between the African and European plates, on the crossing of three regional fault systems that deeply cut the Earth's lithosphere. This tectonic arrangement produces a peculiar stress field that allows a continuous rising of basaltic magma from the Earth mantle since about half a million years [1].

Mt. Etna is the most active volcano in Europe, and it has the world's longest documented record of eruptions. Historical lava flows cover a large part of its surface; in addition several volcanic structures like calderas, sector collapses, rift zones and regional fault systems are exposed as well. The occurrence of these features makes Mt. Etna an ideal site to evaluate the performance of airborne multisensor systems.

International teams of scientists conducted an airborne multisensor experiment in the Mt. Etna area in July 1996. The site is of high geological interest. Its topography is very well known - a precise elevation model derived with photogrammetric methods exists. The geology of the site is best known to the scientists at I.I.V.. Moreover, the area shows volcanic activity, which is continuously monitored. These characteristics justified the big effort the german and italian partners undertook. The objectives of the experiment are:

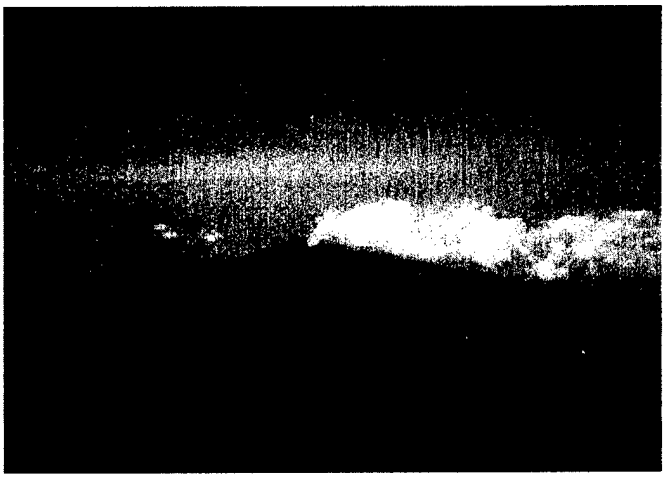

Figure 1: Aerial photo of Mt. Etna taken during flight in July 1996. A view from southwest at 5700 m altitude.

- The generation of a high precision DEM using airborne microwave and optical sensors,
- The retrieval of surface parameters using radar polarimetry and optical spectrometry,
- The investigation of the synergy potential of optical and microwave sensors, and, finally,
- The exploration of the limits of airborne differential SAR interferometry.

This paper revises the activities during the experiment phase, gives an overview of the sensor systems employed and summarizes the present status in data processing and evaluation.

THE EXPERIMENT

Two main test sites were defined in the Mt. Etna region. One covers the cone of the volcano (Area A) and the second a valley southeast of the etna summit (Area B: Valle del Bove). Area A extended over 3 km in ground range and was 12 km long. Its central axis was oriented by 20° with respect to North. Area B had a size of 3 km by 8 km and was oriented east-west (almost

0-7803-3836-7/97/$10.00 © 1997 IEEE

perpendicular to area A). In July 1996 DLR and I.I.V./ I.R.E.C.E. placed 14 corner reflectors (90 cm) in both areas. They were meant as passpoints mainly for the airborne SAR sensor to control the radiometric and geometric processing accuracy, but could also be used by the stereo camera under good conditions. The position of each reflector was measured by differential GPS in the WGS 84 reference system. DLR transferred two of its Dornier DO228 aircrafts, one equipped with the Experimental SAR (E-SAR), and the other with two optical systems, the Digital Airborne Imaging Spectrometer (DAIS 7915) and the 3 line Wide Angle Airborne Camera (WAAC), for one week to Catania airport (Fig. 2). Their task was to acquire data over the same test areas almost simultaneously for the analysis of topographic and physical surface parameters. Again differential GPS was employed to position the aircrafts with best achievable accuracy. For that purpose a GPS reference station was set up at the I.I.V. in Catania.

Seismic activity was continuously monitored at I.I.V.. Ground truth, i.e. surface roughness, soil moisture and conductivity, was collected by one team. A second team measured the relative reflectance of reference targets with a field spectro-meter to control the calibration of the DAIS sensor. An extensive GPS survey of the volcano cone was carried out to gain information about topographic changes due to volcanic activity. During the mission Mt. Etna showed continuously increasing activity climaxing with an eruption two days after the campaign on July 21, 1996. Data acquisition was extended for one day to capture at least a part of this period.

SPECTRAL GROUND TRUTH MEASUREMENTS

As an in-flight calibration, to validate the laboratory spectral calibration and to control for uncertainty in the input data for atmospheric correction [2] a ground-truth campaign was carried out in parallel to the DAIS overflights. The instrument used was an ASD FieldSpec FR Spectrometer (courtesy of Geo-Forschungszentrum Potsdam, Germany) with a nominal spectral range from 350-2500 nm.

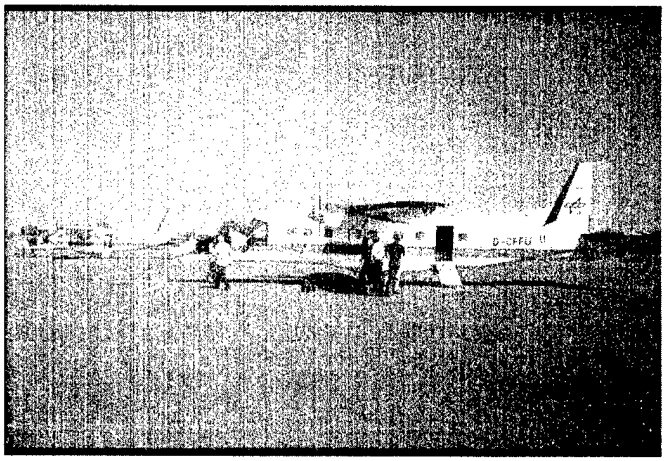

Figure 2: Two DLR airplanes of type DO228 stationed at Catania airport.

THE AIRBORNE SENSOR SYSTEMS

The Experimental Airborne SAR - E-SAR

The E-SAR is a multi-frequency SAR system mounted on board a Dornier DO 228 aircraft, which is owned and operated by DLR. At present the radar is operational in P-, L-, C- and X-Bands with selectable vertical or horizontal antenna polarization. SAR interferometry and SAR polarimetry are new functional modes of the radar established during 1996. A radar front-end for both across and along track single-pass SAR interferometry in X-Band was integrated. Additional antenna mounts were attached to the right hand side of the aircraft for both configurations. The mechanical baselines are approx. 130 cm (across track (XTI)) and 80 cm (along track (ATI)). Switched from pulse to pulse both antennas in either configuration (XTI or ATI) are transmitting and receiving radar signals with vertical polarization. The received SAR raw data is formatted in the E-SAR High Density Tape Format and recorded on high density digital cartridges (HDDC) at rates up to 128 Mbit/s. A SONY Digital Instrumentation Recorder allows continuous data recording up to 6 hours 40 minutes at 32 Mbit/s. In flight a real-time 'Multi-Look'-SAR-Processor converts the raw data to high resolution imagery of good quality, which is recorded on Exabyte tape [3].

The Digital Airborne Imaging Spectrometer - DAIS

The Digital Airborne Imaging Spectrometer DAIS-7915 is a 79 channel high resolution optical spectrometer which collects information from the surface of the Earth in the 0.4 - 12.3 µm wavelength region while scanning from an aircraft. It electronically processes this data into digital format consisting of 16 bit words, which are recorded on a tape cartridge. The DAIS scan mechanism is a Kennedy type where a cubic polygon mirror scans the terrain below through the opened window hatch in the bottom of the aircraft. DAIS is operated onboard DLR's Dornier DO 228 aircrafts and has a swath angle of 26°, which is covered by 512 pixels per scanline. The instantaneous field of view (IFOV) currently used is 3.3 mrad, giving a typical pixelsize of 10 m from a flight altitude of 3000 m above ground [4]. Please refer to recent publications [5] or the World Wide Web (http://www.op.dlr.de/DAIS) for further information.

The Wide Angle Airborne Camera - WAAC

At DLR a miniaturised Wide-Angle Optoelectronic Stereo Scanner (WAOSS) was developed for the Russian Mars-96 mission. Preflight tests of this camera led to demands for a more flexible camera, suitable for airborne imaging applications. Hence, the Wide-Angle Airborne Camera (WAAC) was developed based on this camera concept. The WAAC is a three line stereo scanner working in the push-broom mode. The im-

age is generated within the image plane of a single lens by means of three CCD lines. With the knowledge of aircraft motion stereo image processing is possible. The received image strips are stored on SCSI II device. For airborne applications the mass (4.5 kg), volume (L:285 x W:190 x H:202 mm) and power consumption (15 W) are of high importance. For camera control and image as well as gyro data collection only a PC is required. The camera is fixed mounted in the aircraft's tail and the aircraft axis coincides with the camera axis. The aperture angle of the camera lens is 80 degree and the number of pixels is 5184 with an IFOV of 0.3 mrad. For a typical height of 3000 m the ground resolution is about 1 m. The spectral responsiveness is different for nadir and backward / forward line. The nadir line is sensitive from 0.45 to 0.7 μm and the backward / forward line from 0.6 to 0.8 μm [6].

FIRST RESULTS

DAIS Data

The DAIS data displayed in Fig. 3 and 4 show a scene covering the 'Valle del Bove' from west to east, an area of about 2.7 km x 10 km. The recent lava stream from the 1993 eruption can be clearly identified as ending at the lower right, where the village of Zaffarena is located. Fig. 3 is a combination of the spectral channels 15 (735 nm), 12 (686 nm) and 5 (564 nm), where any (even sparsely) vegetated area shows up in light gray shades. The various uncovered lava streams exhibit very dark (fresh) to grey (older, already started to weather) colours. The white areas in the middle are clouds.

Fig. 4 displays another false colour combination (converted to grayscale) using the spectral channels 74 (8622 nm), 35 (1606 nm) and 12 (686 nm). Channel 74 is located in the thermal Infrared and mainly determined by the surface temperature. Clearly visibly are areas of obviously higher temperature in the 'Valle del Bove' lava flow, where through cracks in the surface the lower, warmer lava can be seen. However, higher temperature can also mean that the location was exposed to sunshine and has heated up, shaded areas will show up less intense. The effect of these temperature differences causes one to see an almost 3-dimensional effect at certain craters.

Multisensor Images

A combination of optical DAIS data and L-band E-SAR data can be seen in Fig. 5, the displayed area is about 1.8 km x 8 km, therefore slightly less than in the previous images. Like in Fig. 4 the channel 74 (8622 nm) is giving thermal information. The L-Band crosspolarized SAR image provides surface and structural information, as can be seen in the 'Valle del Bove' lava stream. Channel 30 (1001 nm), which is located in the near infrared, enhances vegetated areas.

A fusion of image data of the three sensors WAAC, E-SAR & DAIS can be seen in Fig. 6. It shows the Mt. Etna summit region from south to north displayed from left to right. The underlying WAAC image (3) covers an area of about 12 km x 4.8 km, the pixel size is about 1 m x 1 m near the summit of Mt.Etna. The white areas are clouds. The DAIS channels 75 (9455 nm), 36 (1637 nm) and 15 (740 nm) are combined to image no. 2 left of the centre. Note the clouds displayed in light gray. Intensity differences caused by different surface temperatures show up in different gray tones. On the left side and covering the summit caters an E-SAR data set (1) is merged over the WAAC image. The X-Band interferometric SAR phase information is combined with the image intensities and results in the displayed fringes image. The contours correspond to isoheight lines.

SUMMARY

Although data evaluation is not yet completed, the first results, shown here, already demonstrate the synergy potential of optical and microwave remotely sensed data. The fusion of different sensor data allows us to combine their specific advantages and to solve the inherent problems, which limit the performance of the individual sensor system. This improves the thematic interpretation especially for geological applications - the main point of the experiment.

REFERENCES

[1] M. Coltelli et al., *SIR-C/X-SAR Interferometry over Mt. Etna: DEM Generation, Accuracy Assessment and Data Interpretation*, DLR-Forschungsbericht 95-48, 1996.

[2] R. Richter, "Atmospheric Correction of DAIS 7915 Hyperspectral Image Data", *SPIE Proc.*, Vol. 2758 pp. 390-399, 1996.

[3] R. Horn, "The DLR Airborne SAR Project E-SAR", *Proc. of IGARSS Symposium*, Lincoln, Nebraska, 1996.

[4] S. H. Chang, M. J. Westfield, F. Lehmanm, D. Oertel, R. Richter, "79 - Channel Airborne Imaging Spectrometer", *SPIE Proc.*, Vol. 1937, pp. 164 - 172, 1993.

[7] P. Strobl et al., "DAIS System Performance, First results from the 1995 Evaluation Campaigns", *Proc. 2nd International Airborne Remote Sensing Conference and Exhibition*, San Francisco, Vol. II pp. 325-334, 1996.

[6] R. Sandau, A.Eckardt, "The Stereo Camera Family WAOSS/WAAC for Spaceborne/Airborne Applications", *International Archives of Photogrammetry and Remote Sensing*, Vol. XXXI, part B1, pp. 170-175, 1996.

ACKNOWLEDGEMENTS

The authors wish to thank all their colleagues, who helped to make this a successful experiment, and G. Krueger of GFZ-Potsdam for his support to the ground truth measurements. Very special thanks go to Mt. Etna for his constructive and not destructive contribution to this work.

Figure 3: DAIS false colour image of 'Valle del Bove' (Area B) converted to grayscale. Scene size approx. 2.7 km by 10 km. Channels 15, 12 and 5.

Figure 4: DAIS false colour image of 'Valle del Bove' (Area B) converted to grayscale. Scene size approx. 2.7 km by 10 km. Channels 74, 35 and 12.

Figure 5: Overlay of DAIS and E-SAR data of 'Valle del Bove'. DAIS channels 74 and 30, E-SAR L-Band, crosspolarized. Scene size 1.8 km by 8 km.

Figure 6: The Mt. Etna summit region (Area A). Overlay of an E-SAR X-Band In-SAR image (1) and a DAIS image (2) on top of a WAAC image (3).
Scene size: 12 km by 4.8 km (no. 3).

Feature Extraction for Neural Network Classifiers Using Wavelets and Tree Structured Filter Banks

Johannes R. Sveinsson, Jon Atli Benediktsson and Omar Hilmarsson

Engineering Research Institute, University of Iceland,
Hjardarhagi 2-6, Reykjavik, IS-107, Iceland
E-mail: sveinsso@verk.hi.is, benedikt@verk.hi.is

ABSTRACT

Two feature extraction methods are considered for neural network classifiers. The first feature extraction method is based on translation-invariant wavelet transformation. The wavelet transformation transforms a signal from the time domain to the scale-frequency domain and is computed at levels with different time/scale-frequency resolution. The second feature extraction method is based on tree structured multirated filter banks. The tree structured filter banks can be tailored for multisource remote sensing and geographic data. In experiments, the proposed feature extraction methods for neural networks performed well in classification of multisource remote sensing and geographic data.

1. INTRODUCTION

Representation of input data for neural networks is important and can significantly affect the classification performance of neural networks. The selection of input representation is related to the general pattern recognition process of selecting input classification variables which strongly affect classifier design. This means if the input variables show significant differences from one class to another, the classifier can be designed more easily with better performance. Therefore, the selection of variables is a key problem in pattern recognition and is termed feature selection or feature extraction [1]. Feature extraction can, thus, be used to transform the input data and in some way find the best input representation for neural networks.

For high-dimensional data, large neural networks (with many inputs and a large number of hidden neurons) are often used. The training time of a large neural network can be very long. Also, the training methods for neural networks are based on estimating the weights and biases for the networks. If the neural networks are large, then many parameters need to be estimated based on a finite number of training samples. In that case, overfitting can possibly be observed, that is, the neural networks may not generalize well although high classification accuracy can be achieved for training data. Also, for high-dimensional data the curse of dimensionality or the Hughes phenomenon [1] may occur. Hence, it is necessary to reduce the input dimensionality for the neural network in order to obtain a smaller network which performs well both in terms of training and test classification accuracies. This leads to the importance of feature extraction for neural networks, that is, to find the best representation of input data in lower dimensional space where the representation does not lead to a significant decrease in overall classification accuracy as compared to the one obtained in the original feature space. However, few feature extraction algorithms are available for neural networks.

Several authors have proposed the use of neural networks for feature extraction [2],[3],[4]. All these authors concentrate on proposing neural networks which do feature extraction. In contrast, in [5] linear feature extraction based on the decision boundary feature extraction method for neural network is used and compared to different feature extraction methods in classification of multisource data.

In this paper two feature extraction methods, based on translation-invariant wavelets and IIR filter banks, for neural networks classifiers are discussed and applied in classification of multisource remote sensing and geographic data.

2. FEATURE EXTRACTION

2.1. Translation-Invariant Wavelets

The wavelet transform (WT) can be implemented by the tree structure shown in Figure 1. Each stage of the structure is shown in Figure 2. The signal being processed is low-pass and high-pass filtered and down-sampled by 2. Every time down-sampling is performed, the signal length is reduced by 2. The output from the low-pass branch goes

This work was supported in part by the Research Fund of the University of Iceland and the Icelandic Research Council.

0-7803-3836-7/97/$10.00 © 1997 IEEE

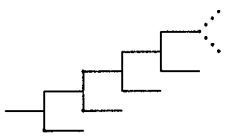

Figure 1: The tree structure for both the wavelet and multirate filter bank transformation

through the same process of filtering and down-sampling.

One of the major shortcomings of the WT is its sensitivity to translation. This mean that the wavelet coefficients of the translated signal will not be time/index-shifted versions of the coefficients of the unshifted signal. Consequently, in feature extraction with WT the quality of the representation depends on where, for instance, discontinuities are positioned in the signal. In [6] Liang and Parks used the algorithm by Beylkin [7] to compute the WT for all possible circular shift of a signal. By choosing a cost function, the minimal cost wavelet coefficients of the shift were select using a binary tree search algorithm. Then, the wavelet coefficients together with the translation to which they correspond completely represented the original signal. This algorithm is translation invariant in the sense that no matter how the input is shifted it gives the same wavelet coefficients. The cost function chosen for this application was the vector entropy, given by

$$\mu(x_n) = -\sum_n \left|\frac{x_n}{\|x\|}\right|^2 \log_2 \left|\frac{x_n}{\|x\|}\right|^2 \qquad (1)$$

for a sequence, $\{x_n\}$, of signals.

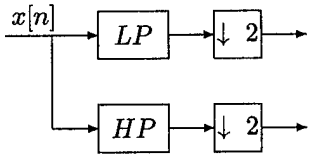

Figure 2: One stage in the wavelet transformation.

2.2. Multirated Filter Banks

The tree structured filter bank transformation is depicted in Figure 1 and each stage of the transformation is shown in its polyphase form using the butterfly computation of DFT (or 2-point DFT) in Figure 3. The signal being processed is low-pass and high-pass filtered and down-sampled by 2. The output from the low-pass filter goes through the same process as the original signal of filtering and down-sampling. The building elements of the filter bank transformation are two-channel all-pass based IIR quadrature mirror filters (QMF) [8]. The same all-pass filters $A_0(z)$ and $A_1(z)$ are used for all stages of the transformation. The low-pass and high-pass filters of the two-channel all-pass IIR QMF bank are given by

$$\begin{aligned} H_{LP}(z) &= \tfrac{1}{2}[A_0(z^2) + z^{-1}A_1(z^2)] \\ H_{HP}(z) &= \tfrac{1}{2}[A_0(z^2) - z^{-1}A_1(z^2)]. \end{aligned} \qquad (2)$$

In this application, one of the all-pass filters, $A_0(z)$, was chosen to be a pure delay, i.e., $A_0(z) = z^{-1}$ and hence the filters $H_{LP}(z)$ and $H_{HP}(z)$ have approximately linear phase in their passbands. Here the other all-pass filter was chosen as the first order filter $A_1(z) = \dfrac{0.375 + z^{-1}}{1 + 0.375z^{-1}}$.

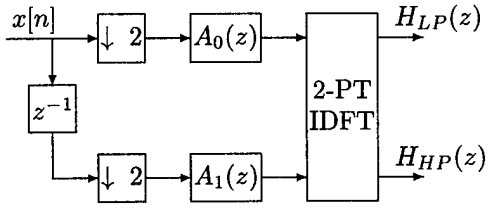

Figure 3: One stage in the filter bank transformation

3. EXPERIMENTAL RESULTS

The data used in the experiment, the Anderson River data set, are a multisource remote sensing and geographic data set made available by the Canada Centre for Remote Sensing (CCRS) [9]. Six data sources were used: Airborne Multispectral Scanner System (11 spectral data channels), Steep Mode Synthetic Aperture Radar (SAR) (4 data channels), Shallow Mode SAR (4 data channels), Elevation data (1 data channel), Slope data (1 data channel), and Aspect data (1 data channel). The AMSS and SAR data were detected during the week of July 25 to 31, 1978. Each channel comprises an image of 256 lines and 256 columns. All of the images are spatially co-registered with a spatial resolution of 12.5 m.

There are 19 information classes in the ground reference map provided by CCRS. In the experiments, only the six largest ones were used, as listed in Table 1. Here, training samples were selected uniformly, giving 10% of the total sample size. Test samples were then selected randomly from the rest of the labeled data.

The number of features for the data was 22 so it was necessary to add zeros to the data so that the number of features became 32. Eight-tap Daubechies wavelet filter (i.e., D_8) [10] was used in the translation-invariant wavelet transformation. The conjugate gradient perceptrons (CGP) with one hidden layer was trained on the wavelet translation-invariant transformed and filter bank transformed input data with a different number of feature. In

Table 1: Training and Test Samples for Information Classes in the Experiment on the Anderson River Data.

Class #	Information Class	Training Size	Test Size
1	Douglas Fir (31-40m)	971	1250
2	Douglas Fir (21-30m)	551	817
3	Douglas Fir + Other Species (31-40m)	548	701
4	Douglas Fir + Lodgepole Pine (21-30m)	542	705
5	Hemlock + Cedar (31-40m)	317	405
6	Forest Clearings	1260	1625
	Total	4189	5503

Table 2: Classification Accuracies for Translation-Invariant Wavelet.

# of Features	Overall Training Accuracy	Overall Test Accuracy
2	42.71	42.58
4	51.58	51.46
8	58.42	57.92
16	69.00	66.83
32	73.10	70.20

each case, the number of hidden neurons was twice the number of input feature. The classification results are listed in Table 3 for the translation-invariant WT and in Table 4 for the filter bank transformation. From these tables it can be seen that about 4 per cent decrease in overall training and test accuracies when 16 input features were used instead of 32. When less the 16 feature were used, the classification accuracies decreased more significantly.

4. CONCLUSIONS

Two feature extraction methods, based on translation-invariant wavelets and IIR filter banks, for neural networks classifiers are proposed and applied in classification of multisource remote sensing and geographic data. The methods showed promise but should be more appropriated on data which have number of feature that need not be zero padded. Also, the choice of the cost function for the translation-invariant wavelets is important. The cost function should be chosen such that the parameters of the classifier and feature extractor are jointly optimized.

Table 3: Classification Accuracies for Tree Structured Filter Bank.

# of Features	Overall Training Accuracy	Overall Test Accuracy
2	47.24	47.28
4	53.01	52.61
8	57.29	56.98
16	71.47	68.84
32	75.50	72.82

5. REFERENCES

[1] K. Fukunaga, *Introduction to Statistical Pattern Recognition*, 2nd edition, Academic Press, NY, 1990.

[2] J. Lampinen and E. Oja, "Distortion Tolerant Pattern Recognition Based on Self-Organizing Feature Extraction," *IEEE Transactions on Neural Networks*, vol. 6, pp. 539-547, 1995.

[3] J. Mao and A.K. Jain, "Artificial Neural Networks for Feature Extraction and Multivariate Data Projection," *IEEE Transactions on Neural Networks*, vol. 6, pp. 296-317, 1995.

[4] E. Oja, "PCA, ICA, and Nonlinear Hebbian Learning," *Proceedings of the International Conference on Artificial Neural Networks (ICANN '95)*, held in Paris, France, on 9 -13 Oct., pp. 89-94, 1995.

[5] J. A. Benediktsson and J. R. Sveinsson, "Feature extraction for multisource data classification with artificial neural networks," *Int. J. Remote Sensing,* vol. 18, no. 4, pp. 727-740, 1997.

[6] J. Liang and T.W. Parks, "A translation-invariant wavelet representation algorithm with applications," *IEEE Trans. on Signal Processing,* vol. 44, pp. 225-232, 1996.

[7] G. Beylkin, "On the representation of operation in bases of compactly supported wavelets," *SIAM J. Numer. Anal.,* vol. 29, pp. 1716-1740, 1992.

[8] T.Q. Nguyen, T.I. Laakso, and R.D. Koilpillai, "Eigenfilter approach for the design of allpass filters approximating a given phase response," *IEEE Trans. on Signal Processing,* vol. 42, pp. 2257-2263, 1994.

[9] D.G. Goodenough, M. Goldberg, G. Plunkett, and J. Zelek, "The CCRS SAR/MSS Anderson River Data Set," *IEEE Transactions on Geoscience and Remote Sensing*, vol. GE-25, pp. 360-367, 1987.

[10] I. Daubechies, *Ten Lecture on Wavelets*, SIAM, USA, 1992.

Development of a New Automated Land Cover Change Detection System from Remotely Sensed Imagery based on Artificial Neural Networks

Xiaolong Dai and Siamak Khorram
Computer Graphics Center, North Carolina State University
Campus Box 7106, Raleigh, North Carolina 27695 - 7106, USA
Tel: (919)515-3430 Fax: (919)515-3439 Email: xdai@unity.ncsu.edu, khorram@ncsu.edu

Abstract -- The research in this paper is designed to develop and implement the algorithms for an automated spatial change information extraction system from remotely sensed imagery based on artificial neural networks. First, we investigate the suitability of the application of neural networks in automated change detection using TM imagery and its related network design problems unique to change detection. We then develop a neural networks-based change detection system using back-propagation training algorithm. This trained network is then able to efficiently detect land cover changes and provide complete information about the nature of change. Based on our experiments, it has been proven that this technique is successful and has immense implications on land cover change detection and quantification at all levels of applications ranging from local to global in scale.

Introduction

Given the current techniques available, remote sensing provides the most feasible approach to regional and larger scale land cover change detection. Many interactive change detection techniques are in practice today. However, the majority of the techniques themselves can only provide a binary change mask and classification procedures must then be applied to multitemporal images in order to obtain the categorical information of multidate land covers. Besides, analysts have to manually process many critical tasks related to image processing, feature extraction, and feature delineation such as image registration, threshold tuning, change identification. Therefore, a reliable and automated change detection system that can provide complete land cover changes is crucial in environmental remote sensing and its regional or global implementation.

Usually, change detection involves pattern identification of a pair of spatially registered images acquired on the same ground area at two different times. Based on the functions of the current change detection techniques, we can classify them into two broad categories: (1) change mask development (CMD); (2) categorical change extraction (CCE). In CMD, changed and non-changed areas are separated by a preset threshold according to the spectral characteristics of images. The types of changes are unknown directly from these techniques and need to be identified by further pattern recognition techniques. Most change detection methods fall into the first category, such as *Image Differencing, Image Ratioing, Image Regression, etc.* In CCE, explicit categorical changes are detected directly based on the spectral reflectance of the data. There are mainly three CCE techniques: *Change Vector Analysis, Post Classification Comparison, and Direct Multidate Classification.* However, there are major problems associated with these techniques: the accuracy of *Post Classification Comparison* technique is critically dependent upon the two individual classifications and the dependency information between the two images is ignored [1]; in the *Direct Multidate Classification,* it is difficult to develop ground-corresponding training sites from both images and accurately estimate the transitional probabilities of changes. To solve these problems associated with current change detection techniques, we investigate the use of neural networks in change detection system.

Fundamentals of Backpropagation Neural Networks

Artificial neural networks are large networks of individual processing elements which are interconnected and running in parallel. They are designed to perform a specific pattern recognition task by specifying their architecture: the input layer, the output layer, the hidden layers, the number of processing elements in each layer, the network topology, and the weight of each connection [2]. The ultimate goal of neural network training is to minimize the cost or error function for all possible examples through the input-output relation. The network in this study is trained using the backpropagation procedure [3] that iteratively adjusts the coupling strengths in the network, which is expressed in the following equation:

$$\Delta w(n+1) = -\eta \frac{\partial E}{\partial w} + \alpha \Delta w(n) \qquad (1)$$

where E is the square of error between the desired output and actual output; $\Delta w(n+1)$ and $\Delta w(n)$ are the weight changes at step $(n+1)$ and step n, respectively; η, the *learning rate*, is the percentage of the step taken towards the minimum error in each iteration; α, the *momentum*, averages the weight changes themselves rather than averaging the derivatives. The method of adaptive learning rates is used [4].

Neural Network-based Change Detection System: Experimental Design

The experimental design includes both architectural and

This work was supported by Cray Research, Inc. and North Carolina Supercomputing Center under the 1997 Cray Grant Program.

0-7803-3836-7/97/$10.00 © 1997 IEEE

parametric selection of neural network-based change detection system. In the following, we investigate the methodology and the basic architectural elements of a neural network-based land cover change detection system: network input, network output, network architecture, and network training parameter and procedures.

Network Input: Data Input Structure and Encoding

The input data for change detection consist of two different images of the same area acquired at different times which have been spatially aligned by image registration. The simplest structure for data input is to read one multispectral pixel into the network at a time and the pixels of the whole image are processed sequentially on a pixel-by-pixel basis. If only the non-thermal TM bands are used and no ancillary data are presented, this scheme requires 12 input nodes. The pixel values of images presented to the network are scaled to the range of 0 to 1 to avoid the use of a scale or shift factor every time the sigmoid activation function is evaluated and reduce floating point computations.

Network Output: Change Encoding and Extraction

Due to large number of change combinations unique in change detection, the output encoding for a land cover change detection system is a challenging task because there are k^2 change combinations for a k-class classification scheme. The natural way to encode the output classes is to use one output node per cover change class, which is called *direct encoding*. One of solutions to reduce the number of output nodes is to use *binary encoding* [5]. For a classification scheme with less than 5 classes, we recommend using *direct encoding*. For a classification scheme with more than 10 classes, use of *binary encoding* is suggested. The output values of the network are continuous and need to be coded to represent final change classes. The simplest way to assign a class to the input data is to choose the class of the output node with the highest value.

Network Architecture

While the structure of the first and last layers of the neural network is controlled by input and output, the number of hidden layers and their size must be determined experimentally. Generally for classification of single-date imagery, a three layer fully connected network is sufficient [6]. For complex classification, like change detection with large change combinations, we found that a four-layer network with arbitrary decision boundaries achieves the best results in terms of the square error at convergence and the generalization ability. The architecture of the four-layer feed-forward network considered in the present research is shown in Fig. 1. The network parameters such as learning rate and momentum, termination rule, and the number of nodes in each hidden layer are determined by experiments.

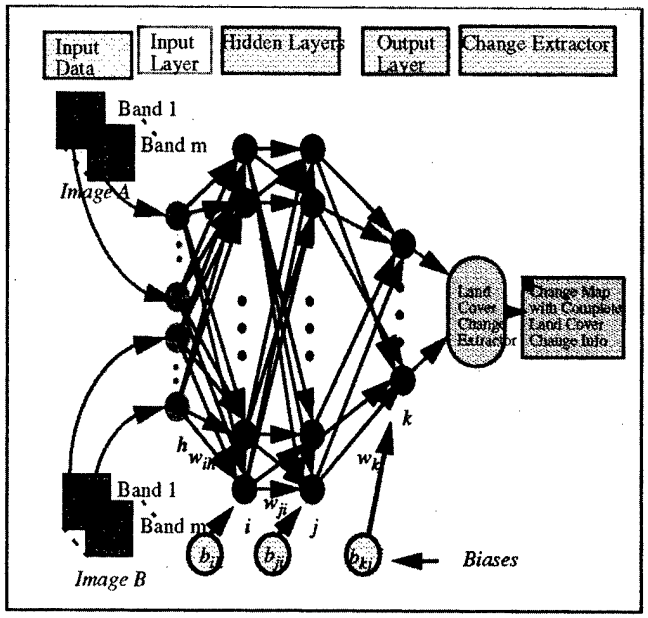

Fig. 1 Neural network architecture for a change detection system

Data Sets and Experimental Results

Description of the Data Sets and Classification Scheme

The imagery data used to develop and test the neural network-based land cover change detector correspond to the surroundings of Wilmington, North Carolina. Two Landsat TM images of this area are used: one collected in Winter 1988 (T_b) and the other in Winter 1994 (T_{b+1}). Fig. 2 (a) and (b) shows the standard false color composites of these two images, respectively. The six non-thermal TM bands was used in change detection. Therefore, the neural network has 12 input nodes. A 512×512 portion of the data was used for land cover change detection experiments.

The desired output is a classified change map according to a variation of the standard land use/land cover classification scheme proposed by Anderson *et al.* [7]. The classifications in this study exclude snow and tundra, and combine agricultural and urban land into a single category. The final

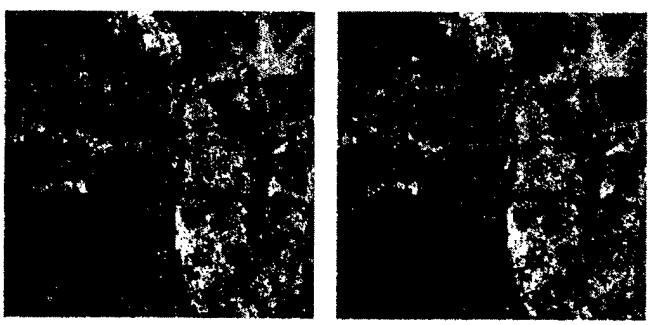

(a) Winter 1988 (b) Winter 1994

Fig. 2 False color composites of the study area: Wilmngton, North Carolina.

classes are: (1) forest; (2) agriculture/bare/urban (ABU); (3) cypress/wet deciduous scrub/marsh (CWM); and (4) water. Using direct output encoding scheme, each land cover transition is represented by one output node. Therefore, there are sixteen output nodes in the proposed system.

Development of Training Data and Test Data

For each class in both images, 200 samples were randomly chosen from the training data for each class per date. In neural networks-based change detection, the condition of ground-corresponding for the training data of each change combination can be relaxed to different ground locations in each image as long as it belongs to the correct classes since there is no need to assume the distributions of the data and to estimate the change probabilities from the training data. Thus, 3200 samples of input-output pairs were produced for training and testing the neural networks. These samples were further divided into two groups: 1600 samples for network training and 1600 samples for testing the trained network.

Experimental Results

The training and test data were presented to the neural network in the form of vectors derived from spectral signatures, with one value per input item presented and one per output change class. The initial learning rate was set to 0.001, with adaptation every epoch in batch training, and the rate of learning rate increase to 1.07 and the rate of learning rate decrease to 0.7. The momentum was set to 0.00005. With these parameters set, the remaining parameters are the number of nodes in the two hidden layers. We started from 12-36-36-16 configuration and found that a configuration of 12-36-48-16 achieved the best results. The change detection accuracy of the trained network for the training samples was 100%. Applying the trained network to the 1600 test samples leads to a change detection accuracy of 98.9%. The trained change detection network was then used as a feed-forward network to detect changes. The resulting land cover change map is shown in Fig. 3. 1183 pixels were then randomly selected and used to evaluate the accuracy. The overall accuracy of neural network-based change detection is 95.6% comparing to 86.5% for post classification comparison.

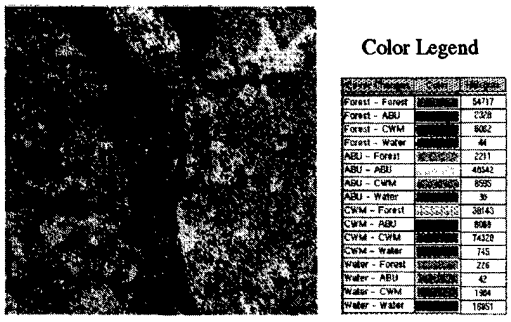

Fig. 3 Change map with complete land cover changes produced by the neural networks-based change detection technique.

Discussions and Conclusions

The neural network model for digital change detection show great potential as a change detection technique from remotely sensed imagery. We summarize the advantages of this method as follows: (1) It is superior to the statistical-based techniques in terms of change detection accuracy since it makes use of the time dependency between the data at two times; (2) Multisource data can be easily added in the system just by adding additional input nodes; (3) This method can provide complete categorical land cover changes; (4) Since it is distribution-free, it is not necessary to develop training sets which have to be extracted from the same ground locations; (5) The trained change detection nets can be used as feed-forward network, like a hard-wired circuit, which has an implication of real-time operation in regional or global applications. The backpropagation is one of the important training algorithms that are mathematically tractable but it is computationally complex and needs lengthy training time. Given the time-consuming nature of the network training and the needs for fast or even real-time operation in global change monitoring, it is worthwhile to pursue artificially intelligent methods in the effort of change detection.

References

[1] Coppin, P. R. and M. E. Bauer, "Digital change detection in forest ecosystems with remote sensing imagery," *Remote Sensing Reviews*, vol. 13, pp. 207-234, 1996.

[2] Gopal, S. and C. Woodcock, "Remote sensing of forest change using artificial neural networks," *IEEE Trans. on Geoscience and Remote Sensing*, vol. 34, no. 2, pp. 398-404, March 1996.

[3] Rumelhart, D. E., G. E. Hinton, and R. J. Williams, "Learning internal representations by error propagation," in *Parallel Distributed Processing: Explorations in the Microstructure of Cognition, Volume 1: Foundations*, The MIT Press, Cambridge, MA, pp. 318-362, 1986.

[4] Smith, M., *Neural Networks for Statistical Modeling*, Van Nostrand Reinhold, 1993.

[6] Paola, J. D. and R. A. Schowengerdt, "A review and analysis of backpropagation neural networks for classification of remotely-sensed multi-spectral imagery," *Int. J. Remote Sensing*, vol. 16, no. 16, pp. 3033-3056, 1995.

[5] Benediktsson, J. A., P. H. Swain, and O. K. Ersoy, "Neural network approaches versus statisitical methods in classification of multisource remote sensing data," *IEEE Trans. Geosci. Remote Sensing*, vol. 28, pp. 540-551, July 1990.

[7] Anderson, J. R., E. E. Hardy, J. T. Roach, and R. E. Witmer, "A land use and land cover classification system for use with remote sensing data," *USGS Prof. Paper 964*, 28p, 1976.

Characterisation Of Agricultural Land Using Signal Processing And Cognitive Learning Techniques

Graham M.Herries[1], Thomas M. Selige[2],
Landscape Analysis and Geo-Information Systems Group, Institute of Biomathematics and Biometrics,
GSF- National Research Centre for Environment and Health, D-85758 Oberschleissheim, Germany.
[1]+44 1924 370495 herries@gsf.de [2]+49 89 3187 2255 selige@gsf.de

Abstract -- This paper presents the application of Neural Networks and Singular Value Decomposition to agricultural land use classification.

Neural Networks (NN) have been found to have good generalization properties [1] and their use is becoming increasingly prevalent in the field of remote sensing [2]. However, there are a number of problems where neural networks do not necessarily provide an optimum solution, these include mixed pixel analysis, sub-class characterization and parameter extraction for use in bio-physical models. Typically the application of NN techniques to remote sensing involves using one NN to classify a large number of land-cover classes [3]. The authors have found this approach to be inefficient and inaccurate, a modular approach is therefore implemented which is more flexible. SVD has previously been used to classify agricultural species with accuracy's approaching 95% and has also been used to characterise sub-classes of Winter Wheat [4]. SVD and key vector analysis also enable parameters such as yield to be directly correlated with the output vectors. A holistic classification process has been developed by the author's which uses the best elements from neural networks and SVD.

This paper applies these techniques to optical airborne data at varying resolution from 1m to 5m resolution. The area used for this work is a research farm in Bavaria, Germany, which comprises of a highly dynamic terrain with small field units. High resolution land-use maps and yield data have been produced for the research farm, using GPS equipment attached to crop harvesters. These maps are used to validate the results produced by the various techniques.

INTRODUCTION

Current classification techniques were developed for satellite data having a typical resolution of 30m. Modern satellite sensors will produce resolutions of 5m. At this resolution features that were not present at coarser resolutions become apparent and problematic. New classification techniques are required to deal with these problems and to manage the increased quantity of data. Fundamental to the development of new techniques is the collection of accurate ground-truth data, to enable results to be correlated with actual features. Airborne scanners are becoming frequently used for high resolution surveying of interesting regions or eco-system monitoring. They have an advantage in their ability to produce images of very-high resolution which can be used to aid the development of new techniques and verify classification accuracy's.

NEURAL NETWORKS

Backpropagation (BP) and its many variants are commonly used neural network training techniques for supervised classification in remote sensing [2] [3]. They can and frequently are treated as 'black boxes' with respect to the training data sets and initialisation and learning parameters. However, their are a number of problems with BP algorithms which necessitate careful selection of training patterns and learning parameters.

PROBLEMS WITH BACKPROPAGATION

There are two main problems with the BP training algorithm. The first is that the algorithm works well on simple data sets but as the data set becomes more complex, the performance of BP rapidly falls off. The error function E(w), becomes littered with local minima, the global minima often being dominated and difficult to converge on. The computational time can increase dramatically and the success of the training algorithm can often be hindered by becoming trapped in local minima. Modifications to the BP algorithm such as Adaptive Learning Rate, Weight Decay and Momentum, have recently been introduced to counteract this problem. Unfortunately, using a high value of momentum may get you out of a minima, but there is no indication if the next minima found is better or worse than the one which has just been left [5].

The second problem is that BP is sensitive to initial conditions caused by randomly choosing weights and biases in the initialisation procedure [5]. In practical terms this means that the ANN will initially begin training on different parts of the error surface. This problem is not likely to seriously affect the performance when the data set is relatively simple, but does cause serious degradation as the complexity increases. The random initialisation of the ANN is the reason why the initial sum squared error (SSE) differs at the start of each training period and the training period itself, measured by the number of epochs, is variable. Generally, the shorter the training time the closer to the global minima on initialisation.

The selection of the training set can have a significant effect on the training and overall result for the network. Land-use classes need to be selected with care, as mixed class training samples will cause the network to become unstable. In a situation where identical or very similar spectral responses are presented to a network to represent different classes, this will cause the network to oscillate. A bad side effect is that if there are a large number of classes then it may

0-7803-3836-7/97/$10.00 © 1997 IEEE

not be noticeable that the network is having problems distinguishing these 2 classes. It is quite probable that the network will train to a good overall sum-squared error, but in reality the error for the 2 classes is high and the other classes have become over-trained and have lost their generalisation capabilities. This will yield a very poor network that has little use when applied to other data.

Neural networks that have good generalisation capabilities can classify sample data sets of very similar type accurately. However, when they are used in an operational scenario, the results produced are very poor. This is often caused by the prevalence of mixed pixels, variations in growth and unknown classes within images.

MODULAR NEURAL NETWORK APPROACH

To counter some of these problems a modular NN approach has been proposed and implemented. This modular approach necessitates having a NN for each class. Although this may seem to be excessive it produces greater flexibility and can reduce training times significantly [6]. If a new class is required then all that has to be done is to train a new network to discriminate the class, all the other networks do not have to be re-trained. Due to the networks being less complex they comprise of only a few neurons and thus train very quickly and minimise on the global minima very well.

SINGULAR VALUE DECOMPOSITION

SVD represents a powerful numerical technique for the analysis of multivariate data. SVD can be used as a preliminary stage in most types of multivariate analysis, and can greatly increase the computational efficiency of linear techniques such as key vector analysis, and non linear techniques such as cluster analysis and neural network analysis. SVD is also an extremely effective technique for the reduction of white noise. The inherent attributes of the SVD technique may have a considerable influence on the dataset (Herries, 1995a). The SVD technique has not been included within this paper as its mathematical description is well documented [2] [7].

DATA ACQUISITION

The images used for this study were a set of multispectral images generated using a Daedalus ATM airborne scanner. This scanner produces 11 channels of different wavelengths.

The Daedalus airborne scanner was mounted in a DO228 aircraft and flown over the experimental farm at an altitude of 450 meters. This produced an effective pixel resolution of 1m. The image has been panoramically corrected. The image was acquired on the 4th July 1994 at 12.00am.

The Daedalus image was then subsequently resampled and geo-referenced with an Orthophoto of 80cm resolution, a yield map and a digital elevation model. This produced images with a pixel resolution of 80cm.

Scheyern experimental farm is managed under the project Forschungsverbund Agrarökosysteme München, which is a co-operation between GSF - Forschungszentrum für Umwelt und Gesundheit and several institutes of the Technische Universität München. The site is situated about 40 kilometers north of Munich in a hilly landscape derived from tertiary sediments. The area amounts to 143 ha. (10% pasture, 90% cropland). It illustrates the typical problems of an intensively farmed landscape: Erosion, soil compaction and contamination of ground water. The area covered by the experimental farm has a very dynamic terrain and is situated between 450 and 490 meters above sealevel. The land cover types are representative of much of Western Europe. Cultivation is more difficult on the slopes and erosion is much higher. The annual precipitation is approx. 833 millimeters.

RESULTS

Fig.1, shows a false colour composite of the Daedalus image resampled to 80cm resolution. This was then resampled again to 5m resolution and used with the neural and SVD techniques to produce estimations of yield and mixed pixel quantities within certain known field units.

Fig.2, shows pixel mixing between gravel and winter wheat. The dark areas represent high levels of winter wheat within each pixel and the light areas represent gravel being present within the pixel at a proportion equal to its intensity. The path is present on the top edge of the field unit to show pure gravel in those pixels.

Fig.3, shows the results of classifying the 80cm Daedalus image with SVD and key vector analysis. To produce this map two areas were selected that contain known yield quantities 8.29 t/ha and 4.92 t/ha. The SVD was computed and a key vector generated. This key vector was then applied to the field unit shown and the results show the relative proportions of yield within the field unit. Light areas represent high yield tending towards 8.29 t/ha and dark areas represent low yield tending towards 4.92 t/ha.

Fig.4, shows the actual yield map for this field unit. This was generated by using a GPS system attached to a harvester. The dark areas represent low yield. The area labeled A in Fig.1, is clearly noticeable in all the figures. This is caused by a localised increase in gravel content in the soil, which reduces plant growth and therefore yield. It is possible to see in Fig.2, that the pixels in this area contain a modest gravel quantity, which is being characterised using the spectral response of these pixels.

CONCLUSIONS

The images show that these techniques can be used to characterise land-use of varying resolution to a high degree of accuracy. The SVD and key vector analysis techniques are excellent for characterising mixed pixels into their constituent components and these techniques can also be used to generate yield maps directly, or indirectly when used with regression techniques.

The thrust of this work is to develop modern classification techniques to classify imagery for use in real applications. The techniques are being developed alongside an extensive ground truth and imagery collection regime.

It is envisaged that these techniques will be used to generate parameters for inclusion into a number of environmental risk models, currently being developed at GSF.

The classification results for this work are extremely good and are well correlated with the ground truth data.

There are a number of improvements that are planned which should increase the robustness, efficiency and accuracy of the results. There is an extensive plan of future work.

ACKNOWLEDGMENT

The images were kindly provided by the Institute of Optoelectronics, DLR-German Aerospace Research Establishment, Oberpfaffenhofen, Germany. The Image processing software, XDIBIAS, was kindly supplied by DLR and Max Fruth GmbH.

REFERENCES

[1] R.,Lippmann, "An introduction to computing with neural nets", IEEE ASSP Magazine, Vol. 2, pp. 4-22, 1987.

[2] J.A.Benediktsson, P.H.Swain, and O.K.Ersoy, "Neural network approaches versus statistical methods in classification of multisource remote sensing data". IEEE Trans. Geosci. Rem. Sens., Vol. 28, no. 4, pp. 540-552, 1990.

[3] I.Kanellopoulos, A.Varfis, G.Wilkinson and J.Megier , "Land-cover discrimination in SPOT HRV imagery using an artificial neural network - a 20-class experiment", Int. J. Rem. Sens., Vol. 13, pp. 917-924, 1992.

[4] G.Herries, S.Danaher, and T.Selige, "Characterisation of agricultural land using singular value decomposition", In Proceedings of Remote Sensing for Agriculture, Forestry, and Natural Resources, E.T. Engman, G.Guyot, C.M.Marino, Paris, p.2, 26-28 September 1995.

[5] G.Herries, A.Murray, S.Danaher, and T.Selige, "Classification of remote sensing imagery using genetic algorithms and neural networks", In ProceedingsImage and Signal Processing for Remote Sensing II, J.Desachy, Paris, p.200, 25-27 September 1995.

[6] G.Herries, S.Danaher, and A.Murray, "Characterisation of forestry species - a comparison using singular value decomposition (SVD) and artificial neural networks (ANN)". IEE Conference on Image Processing and it's Applications, 1995.

[7] S.Danaher, and E.O'Mongain, "Singular Value Decompos1ition in multispectral radiometry". International Journal of Remote Sensing, Vol. 13, no. 9, pp. 1771-1777, 1992.

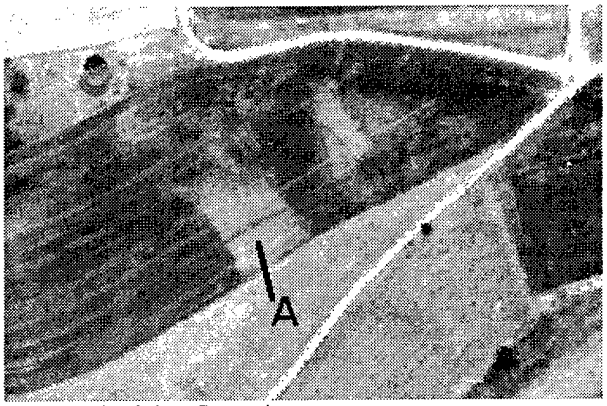

Figure 1 False Colour Composite

Figure 3 SVD Yield Map 80cm

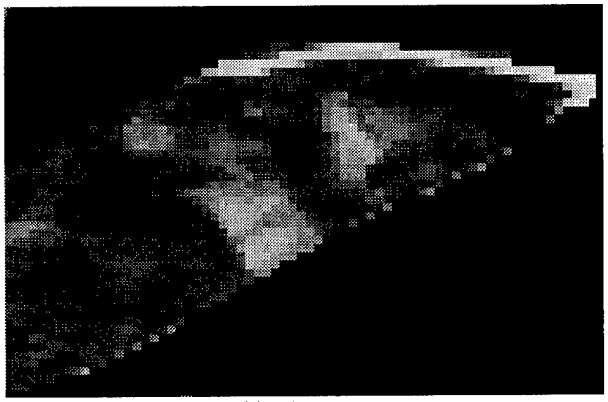

Figure 2 Mixed Pixel Quantities 5m

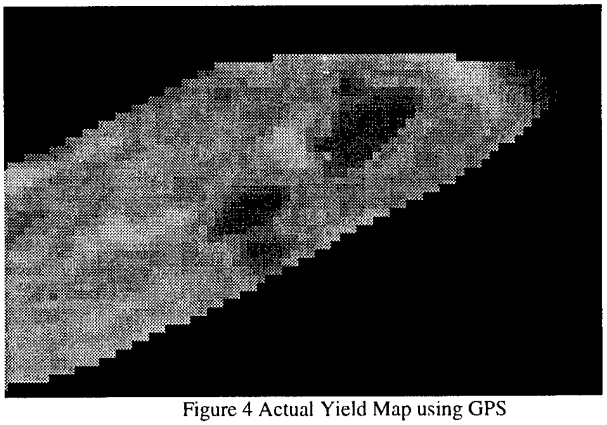

Figure 4 Actual Yield Map using GPS

Prediction of the Upwelling Phenomenon at the Northwest African Atlantic Coast — a connectionist approach

Stefan K.T. Kriebel*
Marine Environment Unit of the Space Applications Institute
Joint Research Centre of the European Commission
TP 690 — 21020 Ispra (VA) — Italy
Phone: ++39/332/78-5935 — Fax: ++39/332/78-9034
Email: stefan.kriebel@jrc.it

Abstract — This article presents a connectionist approach based on artificial neural network technique for the prediction of coastal upwelling in a study window off the northwest African coast. The prediction approach is based on the correlation of the coastal wind and the sea surface temperature anomalies during upwelling events. This correlation is first investigated by theoretical studies with a 3-dimensional Atlantic circulation model to obtain more information about the process. Then the correlation is approximated with an artificial neural network adapted with time series of the local wind and the upwelling sea surface temperature index.

The ANN prediction result varies with the seasons. It is within a range of $\pm 1K$ for seasons with little coastal upwelling dynamics (winter, spring) and within a range of $\pm 4K$ for dynamic seasons (summer and autumn).

MOTIVATION

Coastal upwelling (CU) is a transient, 3-dimensional meso scale-process with distinct variations along the coast [4] which leads to horizontal anomalies of physical, chemical, and biological properties. With upwelling waters anorganic matter is transported from subsurface layers into the euphotic layer where the biological primary production is triggered by solar radiation which generates phytoplankton abundance. Hence CU regions have an enhanced biological productivity and are well known as rich fishery areas.

One of the main approaches for studying the CU phenomenon is the development of two and three dimensional ocean hydrodynamic models. Such models are successfully applied for determining basic features of the CU phenomenon in different areas of the ocean [6].

The main drawback of the modelling approach, especially of three dimensional models, is the model complexity which usually prohibits a straightforward operational use.

In this work a portable connectionist approach with artificial neural networks (ANN) is applied on the northwest African CU region, based directly on time series representing the CU dynamics.

STUDY WINDOW

As a study window an quadratic area off the northwest African coast is chosen with the upper left corner at $[24°N, 23°W]$ and the lower right corner at $[19°N, 16°W]$. This window is located mainly along the Mauretanian coastline and is characterized by almost permanent CU with regular seasonal and small interannual variations [5].

Further the coastline in the study window is oriented from north to south and thus parallel to the prevailing trade winds in this area. The offshore water flow induced by the trade winds [2], generates a water divergence which is compensated by a vertical water flow from subsurface layer into the surface layer [4], see Fig. 1.

Moreover, the bathymetry in the study window is regular and almost not distorted by (underwater) islands. The shelf is flat and enhances CU due to its so-called guiding effect [4].

The dominating near surface water flow in this area is directed equatorwards throughout the year. The undercurrent in the study area are also stable throughout the year and is directed polewards [4].

DATA

The main driving forces for the ocean circulation are the wind stress, the net heat and the salt fluxes. Additionally, the response of the coastal ocean to these surface fluxes depends significantly on the topography, coastline, and thermohaline stratification. These geographical factors originate physical processes like internal Kelvin waves, nonlinear instabilities, and local vorticity, which interact locally with the CU phenomenon [6].

To facilitate the prediction task the following assumption is done: no change of topography, coastline, and thermohaline stratification along latitude, within the study window. This is not restrictive in the study window for reasons explained in the previous section.

*also: Fakultät für Informatik, Technische Universität München, D-80290 München, Germany, email: kriebel@informatik.tu-muenchen.de

0-7803-3836-7/97/$10.00 © 1997 IEEE

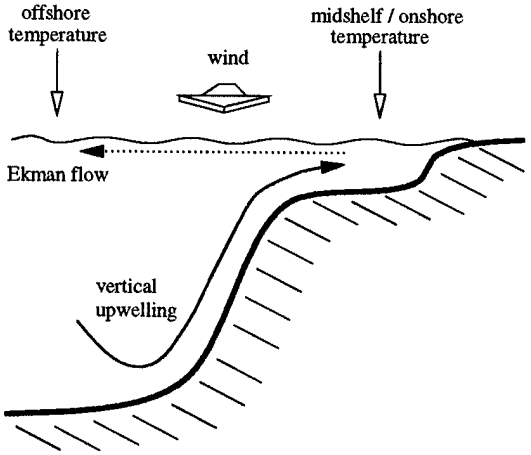

Figure 1: Schematics of coastal upwelling – The wind component parallel to the coastline causes a horizontal water divergence offshore in the surface layer which is compensated by upwelling water from subsurface layers.

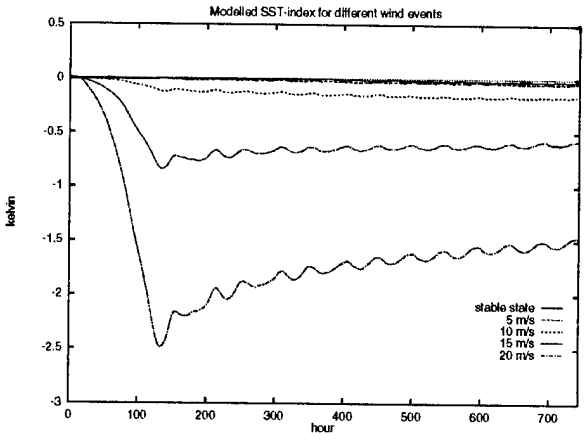

Figure 2: Modelled SST index for samples of wind events – Variations of the force of unidirectional wind events induce significant variations in the resulting SST index signal.

ECMWF (European Centre for Medium range Weather Forecast) daily wind data is used as exogenous parameter. It has a spatial resolution of 1.125° in latitude and longitude and is used from 1986 to 1991.

AVHRR (Advanced Very High Resolution Radiometer) derived SST index data is used as prediction target. The SST index is defined as the difference of the midshelf (also onshore) SST and the SST 500 *km* offshore [5], see Fig. 1. The original temporal resolution of AVHRR data is daily but is first averaged, due to cloud contamination, to a resolution of 4 values per month and then interpolated [7] to asure continuity in the time series which is important for ANN applications. The spatial resolution of the AVHRR data is about 0.05° in longitude and latitude.

THEORETICAL ANALYSIS

The theoretical analyses with the 3-dimensional circulation model ISPRAMIX [1] were done to further investigate the dynamics of the upwelling process and also the correlation of local wind events with the SST index. The wind time series, and so the Ekman upwelling index [4], is found to compare well with the large-scale pattern of the SST index [5].

To make the different experiments comparable, artificial initial conditions are introduced throughout the theoretical analyses. A circulating wind vector with a speed of 2 $\frac{m}{s}$, a period of 48 hours, and stable net heat flux with daily variations provide stable initial conditions for at least 744 hours (31 days).

Wind vectors of different durations, speeds, and directions were superimposed on the initial conditions. In Fig. 2 the dynamics of the SST index for equatorwards winds of 5, 10, 15, and 20 $\frac{m}{s}$ velocity and superimposed for 5 days is depicted as an example. It can be seen that the function to be estimated for the prediction is nonlinear which emphasis the application of an ANN as nonlinear stochastic modelling tool.

Further experiments showed a maximum and a minimum value in the amplitude of the SST index for continuous wind events, limited by the water temperature in upper boundary layer depth and the SST itself. Moreover, the wind history was found to be important as permutated wind events generated different final SST index signals. Also a correlation in the order of the power of 3 was found for the wind and the SST index which is subject of current research.

PREDICTION

The goal is to adapt an ANN to the nonlinear transfer function $\mathcal{G}$ in equation 1 which describes the nonlinear dependencies (see section DATA) between the wind history $\vec{w}$ of length $|\vec{w}| = l$, and the SST index at time t, SST_t^i,

$$SST_t^i = \int_{t-l}^{t_0} dt \; \mathcal{G}\,(t_0 - t\,,\, w_t). \qquad (1)$$

A 3 layer feedforward ANN [3] is adapted to $\mathcal{G}(t_0 - t, w_t)$ with the supervised backpropagation learning algorithm. The ANN architecture comprises 7 input neurons, 14 hidden neurons, and 1 output neuron.

The number of input units is determined by the autoregression coefficients of the wind time series which converge to zero at lag 10 days. At lag 7 days the autocorrelation coefficient is 0.2. The temporal variations of the coastal wind have typically periods of 5 to 10 days. Within this time scale occur the local CU pulsations forced

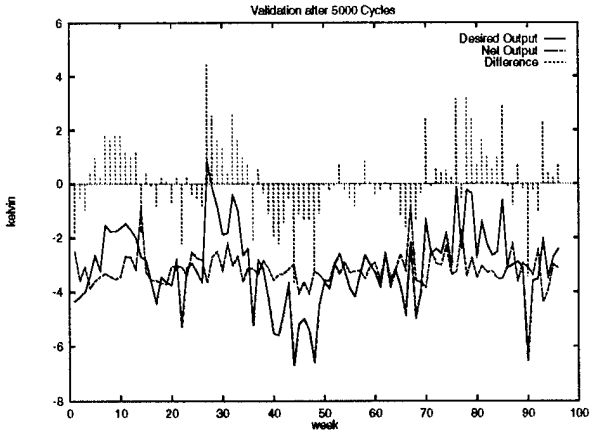

Figure 3: CU prediction with an ANN – The prediction result of the SST index is depending on seasonal variability of the CU dynamics. The impulses along the x-axis show the prediction error.

by the local winds [4]. The sampling rate of the SST index time series is also 7 days.

The number of hidden units is guestimated according the trade off of a minimimum number to avoid overfitting of the ANN to the training data but still to keep the ability to adapt to the general temporal patterns (generalisation) [3]. The number of output units is determined by the prediction task.

In Fig. 3 the ANN prediction for 1990 and 1991 (48 values per year) is depicted after training with the data from 1986 - 1989. The training was stopped after 5000 training cycles. It can be seen that the prediction error (drawn as impulses along the 0 line) has a seasonal variability. The prediction result is within a range of $\pm 1K$ for winter and spring which are known as the less active CU seasons. The variation of the prediction for the main CU season is $\pm 4K$.

The ANN adapts well to the transfer function $\mathcal{G}$ for certain periods of the year where the SST index signal shows little dynamics and fails for other periods with higher dynamics.

CONCLUSION

The seasonality of the prediction error leads to the conclusion that one single ANN is overloaded to adapt to the seasonal variability of the CU dynamics. A possible way to achieve better prediction results based on ANN technique is to devide the prediction according the obvious results gained. The different seasons of CU dynamics can be predicted by different ANN which are then put together to an ANN with hierarchical and/or modular architecture.

A problem of this approach is the requirement of a big amount of training samples in order to achieve good approximation of an ANN to a nonlinear transfer function. But with a seasonal seperation of the prediction the amount of data is further reduced.

The application of hierarchical and/or modular ANNs and of model generated training data is subject of current research.

ACKNOWLEDGMENTS

This work was supported by a Ph.D. fellowship of the European Commission's Human Capital and Mobility program. Further, the work was influenced by many fruitful discussions with Dr. W. Eifler and Dr. E. Demirov.

REFERENCES

[1] W. Eifler and W. Schrimpf. ISPRAMIX, a Hydrodynamic Program for Computing Regional Sea Circulation Patterns and Transfer Processes. Technical report, Joint Research Centre, 1992.

[2] V.W. Ekman. Upwelling. *Ark. Mat. Astron. Fys.*, 12(1), 1905.

[3] John Hertz, Anders Krogh, and Richard G. Palmer. *Introduction to The Theory of Neural Computation.* Santa Fe Institute Studies in the Science of Complexity. Addison-Wesley Publishing Company, 1991.

[4] E. Mittelstaedt. Upwelling regions. In Jürgen Sündermann, editor, *Oceanography*, chapter 7, pages 135–166. Springer-Verlag, 1986.

[5] Leo Nykjær and Lieve van Camp. Seasonal and interannual variability of coastal upwelling along northwest Africa and Portugal from 1981 to 1991. *Journal of Geophysical Research*, 99(C7):14.197–14.207, 1994.

[6] James J. O'Brien, R. Michael Clancy, Allan J. Clarke, Michel Crepon, Russell Elsberry, Tor Gammelsrød, Malcolm MacVean, Lars Petter Röed, and J. Dana Thompson. Upwelling in the ocean: Two-and three-dimensional models of upper ocean dynamics and variability. In Eric Bradshaw Krauss, editor, *Modelling and Prediction of the Upper Layers of the Ocean*, chapter 11, pages 178–228. Pergamon Press, 1977.

[7] Carlos Villacastin. Interpolation of AVHRR derived SST coastal upwelling index. *unpublished*, 1997.

Polarimetric SAR Speckle Filtering and Its Impact on Classification

J.S. Lee(1), M.R. Grunes(1) and G. De Grandi(2)
(1) Remote Sensing Division, Code 7263, Naval Research Laboratory
Washington DC 20375-5351, USA , Tel: (202) 767-2004, Fax: (202) 767-5599
Email: lee@scimg.nrl.navy.mil, grunes@imsy1.nrl.navy.mil
(2) European Union Commission Joint Research Center 21020 ISPRA (VA) Italy
Tel: 39 332 789823, Fax: 39 332 789073, Email: gianfranco.degrandi@jrc.it

Abstract -- Speckle reduction of polarimetric SAR imagery has been studied using several different approaches. Most of these approaches exploited the statistical independence between HH, HV and VV channels. The statistical characteristics, such as correlation between channels, and polarimetric signature preservation, were not addressed. This paper proposes a new approach in polarimetric SAR filtering. This new approach emphasizes introducing no cross-talk, preserving polarimetric properties and statistical correlations between channels. In addition, the image sharpness is better maintained. The impact of using this polarimetric speckle filtering on terrain classification is also studied. NASA/JPL Les Landes polarimetric P-Band and C-Band SAR data is used for illustration.

INTRODUCTION

Speckle appearing in SAR images is due to the coherent interference of waves reflected from many elementary scatterers. Speckle complicates the image interpretation problem by reducing the effectiveness of image segmentation and classification. Many algorithms have been proposed to reduce the speckle effect [1]. For polarimetric SAR, the speckle reduction problem is more complicated, because of the difficulty of dealing with the cross product terms. *Novak and Burl* [5] derived the polarimetric whitening filter by optimally combining all elements of the polarimetric covariance matrix to produce a single speckle reduced image. *Lee et al.* [2] proposed two algorithms that produced speckle reduced HH, VV and HV images by using a multiplicative noise model and minimizing the mean square error. The off-diagonal terms of the covariance matrix were not filtered. *Goze and Lopes* generalized *Lee*'s approach to include all elements of the covariance matrix for one-look imagery. The main deficiencies of these approaches are that they introduce cross-talk between channels and polarimetric properties are not carefully preserved. In addition, the utilization of statistical independence between polarization channels altered the statistical correlation. In this paper, a new approach is proposed to overcome these deficiencies.

Polarimetric Covariance Matrix

For monostatic radar, the polarimetric scattering information can be represented by a complex vector, $u^T = [S_{hh}, S_{hv}, S_{vv}]^T$ or a complex covariance matrix:

$$C = uu^T = \begin{bmatrix} |S_{hh}|^2 & S_{hh}S_{hv}^* & S_{hh}S_{vv}^* \\ S_{hv}S_{hh}^* & |S_{hv}|^2 & S_{hv}S_{vv}^* \\ S_{vv}S_{hh}^* & S_{vv}S_{hv}^* & |S_{vv}|^2 \end{bmatrix}$$

SAR data are frequently multi-look processed for speckle reduction and data compression by averaging several neighboring 1-look pixels.

$$Z = \frac{1}{n}\sum_{k=1}^{n} C(k)$$

where C(k) is the kth 1-look sample. The Z matrix is a Hermitian matrix. The statistics of Z has been extensively studied and found to have a complex Wishart distribution (*Lee et al* [4]). The other representation is the Stokes's matrix, which is a real 4x4 symmetrical matrix. The terms of the Stokes' matrix are a linear combination of terms from the covariance matrix. Speckle filtering should reduce speckle of all terms in the Covariance matrix. The diagonal terms of Z can be characterized by a multiplicative noise model. The off-diagonal terms contain noise neither multiplicative nor additive. Filtering the off-diagonal terms properly remains a difficult problem to address.

Basic Principle of the New Approach

1. To avoid cross-talk, each element of the covariance matrix has to be filtered independently in the spatial domain.
2. To preserve polarimetric properties, each term of Z should be filtered in a manner similar to multi-look processing by averaging the covariance matrices of neighboring pixels. All elements should be filtered by the same amount.
3. To preserve features, edge sharpness and point targets, the filtering is done by weighting the covariance matrix of the center pixel with the mean of covariance matrix from selected neighboring pixels using the local statistics filter [1].

THE POLARIMETRIC SAR SPECKLE FILTER

The boxcar filter has the deficiency of smearing edges, and degrades image quality. The proposed polarimetric SAR

filter uses edge-directed non-square windows and applies the *Lee*'s local statistics filter. The edge-directed window and the weights are computed using the span (total power) image. The same edge-directed window is then used to compute the mean and variance for each element of the covariance matrix, and the same weights are then applied. Thus, the polarimetric information is preserved in homogeneous areas, and cross-talk between channels is avoided. Also, the image sharpness is maintained, because of the use of edge-directed windows. The filter operates in a 7x7 moving window, and follows these basic steps:

1. Edge-directed window selection: one of eight edge-directed windows as shown in Fig.1 is selected to filter the center pixel. Using the span image, the edge direction is computed following the procedure of *Lee*'s refined filter[3]. The window is divided into 3x3 sub-windows and their means are computed. Edge direction is detected by a simple edge-mask using the sub-means. The edge masks used here are

$$\begin{bmatrix} -1 & 0 & 1 \\ -1 & 0 & 1 \\ -1 & 0 & 1 \end{bmatrix} \begin{bmatrix} 0 & 1 & 1 \\ -1 & 0 & 1 \\ -1 & -1 & 0 \end{bmatrix} \begin{bmatrix} 1 & 1 & 1 \\ 0 & 0 & 0 \\ -1 & -1 & -1 \end{bmatrix} \begin{bmatrix} 1 & 1 & 0 \\ 1 & 0 & -1 \\ 0 & -1 & -1 \end{bmatrix}$$

Sobel or Prewitt edge detectors are not used for this operation, because they are not accurate in detecting noisy edge direction. The maximum absolute value selects the edge direction. The edge directed window is selected based on the closeness of the center sub-mean with the two sub-means in the edge-direction. The span image is used, because of its lower speckle noise level.

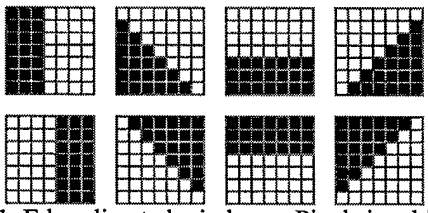

Fig. 1 Edge-directed windows. Pixels in white are used in the filtering computation.

2. The local statistics filter using the multiplicative noise model is then applied. Let y_0 be the span pixel value. The filtered pixel value is computed by

$$\hat{y} = \overline{y} + k(y_0 - \overline{y})$$

$$k = \frac{var(y)}{var(y_0)} = \frac{var(y_0) - \overline{y}^2 \sigma_v^2}{var(y_0)(1+\sigma_v^2)}$$

where $\hat{y}$ is the filtered pixel value, $\overline{y}$ and $var(y_0)$ are the local mean and variance computed in an edge-directed window. The σ_v is the standard deviation of the multiplicative noise. For 4-look imagery, $\sigma_v = 0.5$.

3. The same k value and the same window number obtained from step 2 are used to filter the whole covariance matrix including the off-diagonal terms. The filtered covariance matrix is

$$\hat{Z} = \overline{Z} + k(Z - \overline{Z})$$

where each element of $\overline{Z}$ is the local mean computed using the same edge-directed window.

4. The covariance matrix can be converted into Stokes' matrix, if desired.

EXPERIMENTAL RESULTS

NASA/JPL AIRSAR P and C-Band polariemtric SAR imagery of Les Landes is used for illustration. This scene contains many homogeneous forested areas with several age classes of trees. This data is 4-look processed. Fig. 2 shows the original and filtered P-band HH SAR images. It shows that speckle has been reduced and image sharpness preserved.

(a) Original P-band HH image

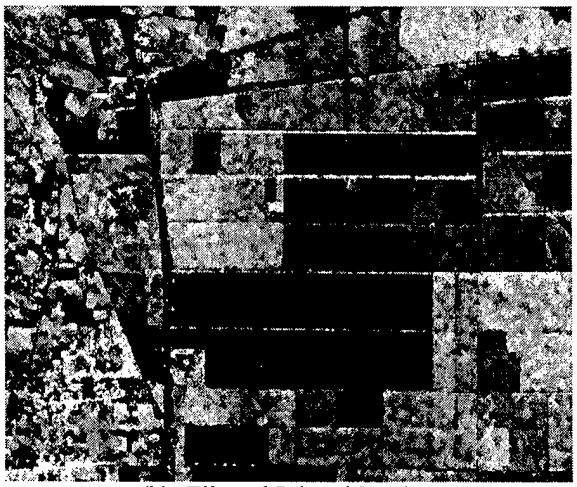

(b) Filtered P-band HH image

Fig. 2 The HH image was used as an example to show the effectiveness of this algorithm in speckle reduction while preserving edge sharpness.

Polarimetric Properties Preservation

To evaluate the preservation of polarimetric information, we used the homogeneous areas to generate the polarization signatures (van Zyl, 1987). Excellent agreement between signatures from the original and filtered data indicates the robustness of this filtering algorithm even using contour plots for comparison. We also compared the averaged covariance matrix over several homogeneous areas. Again, the results are good even for the off-diagonal terms.

Statistical Information Preservation

The objective is to maintain the statistical information similar to multi-look processing. We have investigated the filtered correlation coefficient between HH and VV, and found that this filter can achieve filtering results similar to an additional 25-look processing, but without the deficiencies of straight averaging.

THE IMPACT ON CLASSIFICATION

The Les Landes P- and C-band data is used for classification using the Bayes Maximum Likelihood classification algorithm [4]. We have tested the classification by dividing the classes into four and seven classes. The seven classes are 1) Bare soil, 2) 5-8 years old trees, 3) 8-11 years old, 4) 11-14 years old, 5)15-19 years old, 6) 33-44 years old and 7) > 41 years old. The correct classification rates are listed in Table 1 for classification based on P-band, C-band, and combined P and C-band data.

Table 1 Comparison of correct classification rates using the original and the filtered data

CLASS	1	2	3	4	5	6	7
P-Band ,Orig.	99	78	33	52	44	25	19
P-Band, Filter	100	95	82	93	89	55	41
C-Band, Orig.	71	13	20	34	27	10	10
C-Band, Filter	100	42	37	60	70	26	26
P & C, Orig.	99	81	45	58	51	29	22
P & C, Filter	100	97	84	96	97	63	49

The improvement in classification using the filtered data is quite striking. The classification accuracy using the original data is not acceptable, especially for C-band. Typically, the correct classification rates are nearly doubled for class 3 through class 7.

This improvement is mainly because speckle filtering enhances the separation of all polarization channels and of phase differences. To clearly visualize this effect, we plot the histograms of the original and the filtered HH polarization for four classes, as shown in Fig. 3. The distributions become more concentrated for filtered data than for original data. Similar effects are shown in phase difference histograms. Fig. 4 shows the HH and VV phase differences using the original data and the filtered data. Even though the phase difference terms were not directly filtered, the filtering of off-diagonal terms makes the phase difference distribution more concentrated.

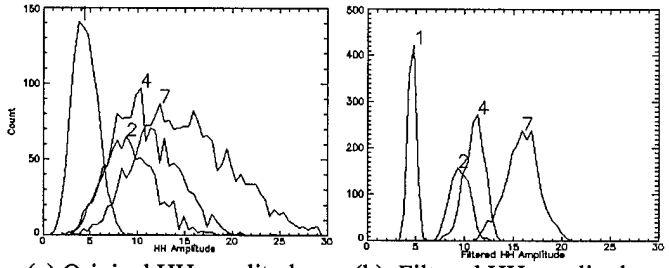

(a) Original HH amplitude (b) Filtered HH amplitude

Fig. 3 Histograms of HH distributions of four classes. The filtering enhances the separation of classes.

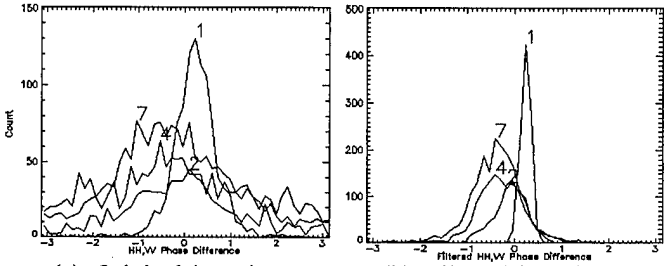

(a) Original $\phi_{HH} - \phi_{VV}$ (b) Filtered $\phi_{HH} - \phi_{VV}$

Fig. 4 Histograms shows the filtered phase difference distribution becoming more concentrated.

CONCLUSION

A new approach has been adopted to develop a polarimetric SAR speckle filter that preserves radiometric and polarimetric properties, and maintains the statistical characteristics similar to multi-looking processing. The effect of polarimetric speckle filtering on terrain type classification is quite dramatic in boosting classification performance. JPL AIRSAR data is used for illustration.

Acknowledgment:

This work was supported by ONR under 6.1/6.2 funding.

REFERENCES

[1] J.S. Lee, et al., "Speckle Filtering of SAR Images: A Review", *Remote Sensing Reviews,* vol. 8, 313-340, 1994.

[2] J.S. Lee, M.R. Grunes and S.A. Mango, 'Speckle Reduction in Multipolarization and Multifrequency SAR Imagery," *IEEE Trans. GARS* Vol. 29, 535-544, 1991.

[3] J.S. Lee, "Refined filtering of Image Noise Using Local Statistics," CVGIP, vol. 15, 380-389, 1981.

[4] J.S. Lee, M.R. Grunes and R. Kwok, "Classification of Multi-look Polarimetric SAR Imagery Based on Complex Wishart Distribution," *Int. J. Remote Sensing*, vol. 15, no. 11, 2299-2311, 1994.

[5] L.M. Novak and M.C. Burl, "Optimal Speckle Reduction in Polarimetric SAR imagery," *IEEE AES,* v26-2, 1990.

The principles of polarimetric filtering

Shaun Quegan[1] and Jesper Schou[2]
[1]Sheffield Centre for Earth Observation Science [2] Danish Centre for Remote Sensing
[1]University of Sheffield, Hicks Building, Sheffield S3 7RH, UK.
Tel: +44 114 222 23778 Fax: +44 114 222 3809 Email: S.Quegan@sheffield.ac.uk
[2]Dept. Electromagnetic Systems, Technical University of Denmark, Building 348, DK-2800 Lyngby, Denmark

Abstract: - Filtering can be used either to reconstruct the information bearing parameters in polarimetric images or to produce intensity images with reduced 'speckle'. These two approaches are analysed through the product model, using both model-free and model-specific texture, and performance criteria described.

INTRODUCTION

Filtering of polarimetric images can be carried out for two purposes: (i) to use the multi-channel information in order to enhance the perceived **structure** in the imagery; (ii) to provide improved local estimates of the **parameters** characterising the data. The information being sought in these two cases is quite different. In the first case, polarimetric information is discarded in order to form a one-dimensional 'projection' of the data with reduced speckle compared to a single look image. In the second, a true reconstruction of the data is required, preferably taking account of image structure.

Both approaches must be based in the statistical properties of the data. It has been suggested on theoretical and empirical grounds that a viable data model for the scattering matrix data $\boldsymbol{S}$ is [1]

$$\boldsymbol{S} = T\boldsymbol{Y} \tag{1}$$

Here we assume that $\boldsymbol{S} = (S_{hh}, S_{hv}, S_{vv})^t \equiv (S_1, S_2, S_3)^t$ is a 3-vector corresponding to calibrated single frequency polarimetric data, T is a positive scalar texture variable, for which $\langle T^2 \rangle = 1$, related to fluctuations in the number of scatterers and $\boldsymbol{Y}$ is a zero-mean complex Gaussian random variable. Since T and $\boldsymbol{Y}$ are independent, it can be seen that

$$C_{ij} = \langle S_i S_j^* \rangle = \langle T^2 \rangle \langle Y_i Y_j^* \rangle = \langle Y_i Y_j^* \rangle \tag{2}$$

so that the covariance matrix of $\boldsymbol{Y}$ can be estimated from the observed covariance matrix, C.

RECONSTRUCTION FILTERING

The data model (1) implies that polarimetric filtering in order to recover the statistical information-bearing elements has the task of estimating 9 real parameters for $\boldsymbol{Y}$ (3 real channel powers and 3 complex correlation coefficients) and whatever number of parameters is necessary to describe T (this depends on the texture model [1]; in the commonly used gamma distributed model for T, just a single order parameter is needed). We can recognise three cases:

(i) Textureless, $T \equiv 1$. Then C carries all the information and its maximum likelihood estimate (MLE) is the sample covariance matrix [2].

(ii) Model-free texture. The covariance matrix can be estimated without assuming any distributional form for T using a minimum mean square error (MMSE) approach for the real 9-vector, $\boldsymbol{Y}_c$,

$$\boldsymbol{Y}_c = \left(|Y_1|^2, |Y_2|^2, |Y_3|^2, \mathrm{Re}(Y_1 Y_2^*), \mathrm{Im}(Y_1 Y_2^*), \mathrm{Re}(Y_1 Y_3^*), \mathrm{Im}(Y_1 Y_3^*), \mathrm{Re}(Y_2 Y_3^*), \mathrm{Im}(Y_2 Y_3^*)\right) \tag{3}$$

with a similar definition for S_c. Then the MMSE filter has the form

$$\hat{\boldsymbol{Y}}_c = \langle \boldsymbol{Y}_c \rangle + \left(I_9 - \left[\langle T^4 \rangle - 1\right] \langle \boldsymbol{Y}_c \rangle \langle \boldsymbol{Y}_c^t \rangle C_S^{-1}\right) \frac{\boldsymbol{S}_c - \langle \boldsymbol{S}_c \rangle}{\langle T^4 \rangle} \tag{4}$$

where I_9 is the 9 × 9 identity matrix. In this form, all the terms can be directly estimated from the observed data. The mean vector $\langle \boldsymbol{S}_c \rangle = \langle \boldsymbol{Y}_c \rangle$ can be estimated from a window surrounding the pixel of interest. In order to estimate $\langle T^4 \rangle$, note that

$$\frac{\langle S_c(i) S_c(j) \rangle}{\langle S_c(i) \rangle \langle S_c(j) \rangle} = \langle T^4 \rangle \frac{\langle Y_c(i) Y_c(j) \rangle}{\langle Y_c(i) \rangle \langle Y_c(j) \rangle}. \tag{5}$$

0-7803-3836-7/97/$10.00 © 1997 IEEE

Since $\boldsymbol{Y}$ is Gaussian, the normalised moment on the RHS of (5) can be readily calculated. When $i = j$ with $1 \le i \le 3$, it takes the value $(1 + 1/L)$ for L-look data.

Finite sampling effects in (4) may cause the estimate of $\langle T^4 \rangle$ to be less than 1, despite the fact that $\langle T^4 \rangle \ge 1$ in the population, which leads to negative estimates of the powers in the channels. Since this indicates an artefact of the sampling, $\langle T^4 \rangle$ should be constrained to be the maximum of 1 and the value supplied by (5).

Assessing the overall performance of this filter is not easy, but Figure 1 shows how it sharpens the phase difference distribution in a forested region of AirSAR data as window size increases. By contrast, in untextured (Gaussian) data, the filter has no effect on the phase distribution [3].

(iii) Model-based texture. If the distribution of T is known, a full MLE solution can be attempted. In practice, even for the gamma distributed model for T, the solution is non-analytic and approximate methods must be used [4]. Alternatively, the texture variable can be estimated separately using a maximum a posteriori approach, with solution given as the positive root of

$$\nu T^4 + \left(3L - \nu + \tfrac{1}{2}\right)T^2 - L\,tr\left(C^{-1}\overline{C}\right) = 0 \qquad (6)$$

for L-look data. Here ν is the order parameter of the gamma distribution which must be estimated, like C, from a surrounding window, possibly using the MMSE methods described above. The quantity $\overline{C}$ is the observed sample covariance matrix and *tr* denotes trace. This is the multi-look polarimetric equivalent of the single channel gamma MAP filter [5].

STRUCTURE FILTERING: SPECKLE REDUCTION

Speckle is essentially a single-channel concept; it expresses the variability in an estimate of σ° at each pixel due to the uniform distribution of phase. This hinders the recovery of scene structure, such as point target or edge detection, and hence numerous methods have been developed to reduce its effects. For single channels, speckle reduction and parameter reconstruction are essentially the same thing. However, when dealing with polarimetric data, we can instead form an 'intensity' image, J, from a linear combination of channels, $\boldsymbol{w} = R\boldsymbol{z}$, by

$$J = \sum_{i=1}^{M} |w_i|^2 = \boldsymbol{w}^\dagger \boldsymbol{w} = \boldsymbol{z}^\dagger A \boldsymbol{z} = tr\left(A\boldsymbol{z}\boldsymbol{z}^\dagger\right) \qquad (7)$$

where $A = R^\dagger R$ is Hermitian. Note that here we allow M channels and a generalised data vector $\boldsymbol{z}$ since the results are generally applicable ($M = 3$ and $\boldsymbol{z} = \boldsymbol{S}$ for polarimetry). This discards the polarimetric information but can produce an image with reduced 'speckle' compared to a single channel. Since this method takes weighted averages of channels, not spatial averages, it should preserve resolution (but see below). The normalised variance of J, $V_J = \mathrm{var}(J)/\langle J \rangle^2$, is minimised when $A = \alpha C^{-1}$, where α is an arbitrary constant and C is the complex covariance matrix [1, 6]. This minimum value is

$$V_J(\min) = \langle T^4 \rangle \left(1 + \frac{1}{M}\right) - 1 \qquad (8)$$

for the textured case, which reduces to just $1/M$ in the Gaussian case. For L-look data providing a sample covariance matrix, $\overline{C}$, this result can be generalised: the minimum variance image is given by

$$J = tr\left(C^{-1}\overline{C}\right) \qquad (9)$$

and $V_J(\min)$ is as in (8) but with the first term on the RHS multiplied by $1/L$. This assumes a constant value of the texture variable across each of the independent looks in the multi-look data. No analytic solution is known if texture varies with look. Although this technique appears to preserve resolution, in practice the need to form a local estimate of C causes energy spread and resolution is lost [3].

The above method of reducing speckle requires access to the full covariance matrix, but also of interest are methods using just intensity data. In this case, the matrix A in (7) is chosen to be diagonal, with diagonal terms A_1, A_2 and A_3, equivalent to a vector $\boldsymbol{A} = (A_1, A_2, A_3)$. The general effects of a filter of this type can be effectively displayed when the like and cross-polarised channels are uncorrelated and untextured. Then

$$V_J = \frac{Var(J)}{\langle J \rangle^2} = \frac{1}{L}\,\frac{1 + 2\gamma|\rho|^2 A_3 + \gamma^2 A_3^2 + \varepsilon^2 A_2^2}{\left(1 + \varepsilon A_2 + \gamma A_3\right)^2} \qquad (10)$$

where A_1 has been set to 1, $\gamma = \langle |S_3|^2 \rangle / \langle |S_1|^2 \rangle$, $\varepsilon = \langle |S_2|^2 \rangle / \langle |S_1|^2 \rangle$ and ρ is the HH-VV complex correlation coefficient. Figure 2 indicates regions in the (A_2, A_3) plane where $V_J < L^{-1}$ (so that speckle is reduced) or $V_J > L^{-1}$ (so that speckle is enhanced). The boundary

between the two regions is indicated in Figure 2 by the solid curves. In general, the normalised variance is minimised when

$$A = \kappa C_I^{-1}\sigma \qquad (11)$$

where $\sigma^t = (C_{11}, \ldots C_{MM})$ and C_I is the covariance matrix of one-look intensity:

$$C_I(i,j) = \langle I_i I_j \rangle - \langle I_i \rangle \langle I_j \rangle = |C(i,j)|^2 . \qquad (12)$$

The constant κ is arbitrary. For L-look textured data the value of the minimum normalised variance is

$$V_J(\min) = \langle T^4 \rangle \left(1 + \frac{1}{L\sigma^t C_I^{-1}\sigma} \right) - 1 \qquad (13)$$

Under the conditions of Figure 2 this global minimum has the value

$$V_J(\min) = \frac{1}{L} \times \frac{1+|\rho|^2}{3+|\rho|^2} \qquad (14)$$

which is achieved when A is any multiple of the vector $\left(1/\sigma_1,\ \left(1+|\rho|^2\right)/\sigma_2, 1/\sigma_3\right)^t$. Setting $A_1 = 1$, the minimum therefore occurs at $A_2 = \left(1+|\rho|^2\right)\varepsilon^{-1}$, $A_3 = \gamma^{-1}$ as noted on Figure 2. Note that any positive filter weights give speckle reduction, but the degree of reduction depends on the covariance structure, and may vary over the image. More general weightings (for example those provided by a principal components analysis) may cause very significant speckle enhancement.

REFERENCES

[1] C.J. Oliver and S. Quegan, Information in SAR Images: Methods and Models for Understanding SAR Data, Artech House, 1997.

[2] N.R. Goodman, "Statistical analysis based on a certain multivariate Gaussian distribution (an introduction)", Ann. math. Stat., vol.34, pp. 152-177, 1963.

[3] J. Schou, Validation of filters and statistical models, Short Course report, University of Sheffield/Technical University of Denmark, 1997.

[4] R.J.A. Tough, D. Blacknell and S. Quegan , "A statistical description of polarimetric and interferometric synthetic aperture radar data", Proc. R. Soc. Lond. A, vol.449, pp.567-589, 1995.

[5] A. Lopes, E. Nezry, R. Touzi and H. Laur, "Structure detection and statistical adaptive speckle filtering in SAR images", Int. Jnl. Remote Sensing, vol.14, pp. 1735-1758, 1993.

[6] L.M. Novak, M.C. Burl and W.W. Irving, "Optimal polarimetric processing for enhanced target detection", IEEE Trans. AES, vol.29, pp.234-244, 1993.

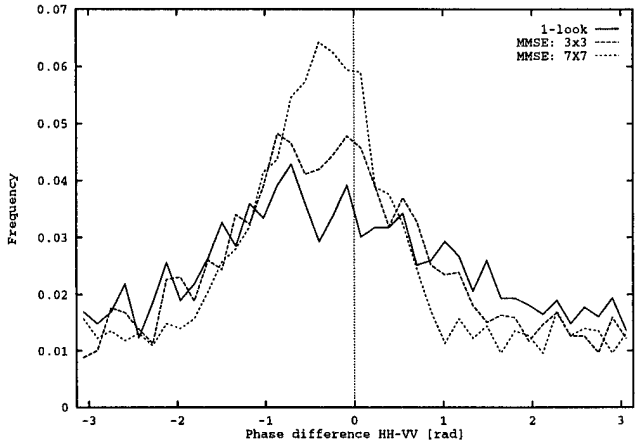

Figure 1: $\phi_{HH\text{-}VV}$ for single-look AirSAR data, from a forested area and using the MMSE filter with a window size of 3 x 3 and 7 x 7 pixels respectively.

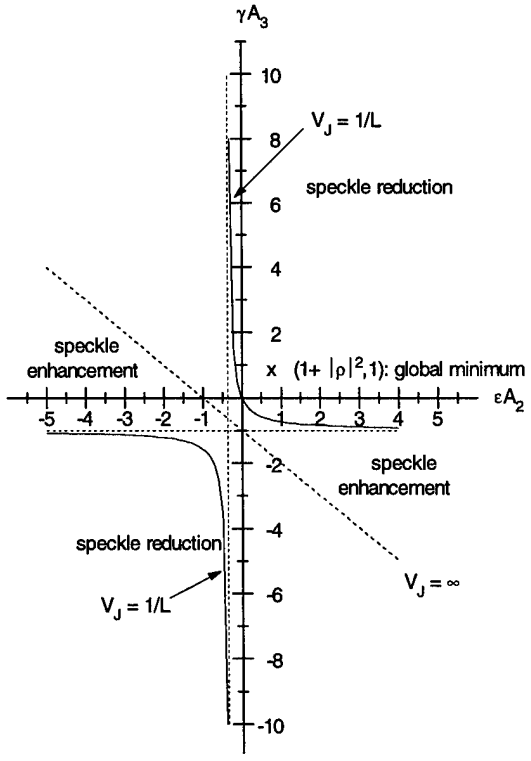

Figure 2:Effects of linear intensity filtering on speckle.

Optimal Bayesian Texture Estimators for Speckle Filtering of Detected and Polarimetric Data

Armand Lopès[1)], Jérôme Bruniquel[1)], Franck Séry[1)], & Edmond Nezry[2)]

[1)] **CESBIO (CNES/CNRS/UPS) Bpi 2801, 18 Av. Edouard Belin, 31401 Toulouse Cedex 4, France**
[2)] **PRIVATEERS N.V. Company, Saint Martin, Netherlands Antilles**
[1)] **phone:(33) 5.61.55.85.39; fax: (33) 5.61.55.85.00; email: Armand.Lopes@cesbio.cnes.fr**

Abstract. For surfaces satisfying the "product model", the sample Covariance Matrix (CM) is the product of a positive scalar random variable μ representing texture and a mean CM representing the polarimetric properties of the surface. The Maximum Likelihood (ML) estimator of μ is given by the Multilook Polarimetric Whitening Filter (MPWF). The ML estimator satisfies the well known multiplicative speckle model. For the multiplicative model, we analyze the optimality of the texture estimators by using decision theory and Bayes approach. We develop a new estimator for Gamma distributed texture. The *A Posteriori* Mean (APM) estimator is radiometrically unbiased and has the smallest Mean Square Error (MSE) of all estimators. The Gamma-MAP estimator, on the contrary, is radiometrically biased, but it preserves the textural contrast better.

1. INTRODUCTION

The texture of polarimetric clutters is frequently modeled as a positive scalar multiplicative random variable μ. This variable modulates the mean covariance matrix (CM) $\boldsymbol{C}_{zh}$, which represents the polarimetric properties of the surface [1]-[4].

$$\boldsymbol{C}_z = \mu\, \boldsymbol{C}_{zh} \tag{1}$$

Equation (1) represents what would be the ideal unspeckled data $\boldsymbol{C}_z$. The same relation holds for the speckled multilook sample CM $\boldsymbol{\Sigma}_z$ of the backscattered vector ${}^t\mathbf{z}=(E_{hh},E_{hv},E_{vh},E_{vv})$:

$$\boldsymbol{\Sigma}_z = \frac{1}{L_o}\sum_{m=1}^{L_o} \mathbf{z}_m\, {}^t\mathbf{z}_m^{*} = \mu\, \boldsymbol{\Sigma}_{zh} \tag{2}$$

This is the so called "product model". The probability density function (pdf) of the sample CM $\boldsymbol{\Sigma}_{zh}$, for a homogeneous clutter, is the complex Wishart pdf [2],[5]. For a textured surface, the conditional pdf of $\boldsymbol{\Sigma}_z$ is:

$$p_{\Sigma}(\boldsymbol{\Sigma}_z/\mu\boldsymbol{C}_{zh}) = \frac{L_o^{pL_o}\,|\boldsymbol{\Sigma}_z|^{L_o-p}\exp(-L_o\frac{1}{\mu}\mathrm{Tr}(\boldsymbol{C}_{zh}^{-1}\boldsymbol{\Sigma}_z))}{\pi^{p(p-1)/2}\,\Gamma(L_o)\ldots\Gamma(L_o-p+1)\,\mu^{pL_o}\,|\boldsymbol{C}_{zh}|^{L_o}} \tag{3}$$

where L_o is the Equivalent Number of Independent Look (ENIL) and p is the number of channels (p=4 or p=3 for reciprocal data). A well known class of clutter satisfying these conditions is the class of K-distributed surfaces, with Gamma pdf:

$$p_{\mu}(\mu) = \frac{\alpha^{\alpha}}{\Gamma(\alpha)\bar{\mu}}\left(\frac{\mu}{\bar{\mu}}\right)^{\alpha-1}\exp(-\alpha\frac{\mu}{\bar{\mu}}) \qquad \mu \geq 0 \tag{4}$$

For a normalized texture random variable, the mean value $E_{\mu}(\mu)=\bar{\mu}$ is equal to one. α is the heterogeneity (or order) parameter. In the general case, the texture may have any distribution.

The Maximum Likelihood (ML) per pixel estimator of the normalized texture μ is derived from (3). We have shown that it is equal to the normalized Multilook Polarimetric Whitening Filter (MPWF) [2],[3]

$$\hat{\mu}_{ML} = \frac{1}{p}\mathrm{Tr}(\boldsymbol{C}_{zh}^{-1}\boldsymbol{\Sigma}_z) = \frac{1}{p}z_{MPWF} \tag{5}$$

We also have shown that the ML estimator satisfies the well known multiplicative speckle model

$$\hat{\mu}_{ML} = \mu \,.\, \frac{1}{p}\mathrm{Tr}(\boldsymbol{C}_{zh}^{-1}\boldsymbol{\Sigma}_{zh}) = \mu \,.\, F \tag{6}$$

where the random variable F is the speckle and has a Gamma pdf with mean value $E_F(F)=1$ and ENIL (order parameter) $L=pL_o$. The ML estimator is a sufficient statistic and the data $\boldsymbol{\Sigma}_z$ can be reduced to $\hat{\mu}_{ML}$ without loss of textural information. It is also unbiased, i.e., $E_F(\hat{\mu}_{ML}) = \mu$. In addition its variance reaches the Cramer-Rao lower bound $\mathrm{var}(\hat{\mu}_{ML}) = \mu^2/pL_o$. It is thus an efficient estimator of the normalized texture μ. Equation (6) shows that the problem of normalized texture estimation is analogous to the problem of radar reflectivity R estimation under the multiplicative model, when the observed intensity I and the mean radar reflectivity $E_R(R)$ are given

$$I = R.F = \mu\, E_R(R).\, F \tag{7}$$

where $I=|E_{pq}|^2$ and F are the backscattered field intensity and the speckle intensity for the pq polarization, respectively. Estimating R is equivalent to estimating $\mu = R/E_R(R)$. In the latter case the ML estimator $\hat{\mu}_{ML} = I/E_R(R)$ does not bring any improvement unlike the polarimetric estimator, which is less speckled. For the latter, the ENIL is p times greater than the initial value L_o.

Usual speckle filters convert the data I (the ML estimator) into a filtered (estimated) value $\hat{R}$. In the next sections we develop a method which generalizes both problems and we establish a new optimal bayesian texture estimator. We compare it to some well-known speckle filters such as the Linear Minimum Mean Square Error (LMMSE) and the Maximum *A posteriori* (MAP) filters.

0-7803-3836-7/97/$10.00 © 1997 IEEE

2. OPTIMAL BAYESIAN TEXTURE ESTIMATORS

In [2] we have derived some texture estimators based on the sufficient statistic $\hat{\mu}_{ML}$, which takes into account some prior knowledge on μ. This can be the range (minimum and maximum values), or the exact expression of the texture pdf. If the prior knowledge is that μ is uniformly distributed over the range $[0,+\infty[$, the MAP estimator reduces to the ML estimator. A less arbitrary pdf for μ is given by the Maximum Entropy (ME) method. The ME pdf for a positive random variable, whose mean value is known, is the Exponential pdf. The Exponential pdf is a particular case of the Gamma pdf with a=1. We have observed that it is radiometrically biased with $E(\hat{\mu}_{Exp\text{-}MAP.}) < \bar{\mu}$. This study confirms this observation. This is not the case for the Gamma-*A Posteriori* Mean (APM). The APM, described bellow, is the MMSE Bayes estimate.

2.1 The decision theory and the Bayes estimators.

For a continuous variable, the decision rule, defining an optimal per pixel texture estimator, is a function $\hat{\mu}_f = f(\hat{\mu}_{ML})$ of the data which must optimize some criteria. For instance the estimator may minimize a cost (loss) function $C(\hat{\mu}_f, \mu)$ which penalizes erroneous estimations $\hat{\mu}_f$ of the true value μ. Several cost functions can be used: the usual square error (quadratic function of the euclidian distance), the Dirac error and the less used abolute error criterion (linear function of the distance) [6]:

$$C_{SE}(\hat{\mu}_f, \mu) = (\hat{\mu}_f - \mu)^2 \quad (8a)$$

$$C_{DE}(\hat{\mu}_f, \mu) = 1 - \delta(\hat{\mu}_f - \mu) \quad (8b)$$

$$C_{AE}(\hat{\mu}_f, \mu) = |\hat{\mu}_f - \mu| \quad (8c)$$

In the case of random variables $\hat{\mu}_f$ and μ, the loss function is also random. The average loss over all possible observations is called the risk function:

$$\mathbf{R}_{C,f}(\mu) = E_{ML}(C(\hat{\mu}_f, \mu)) = \int_0^\infty C(f(\hat{\mu}_{ML}), \mu).p(\hat{\mu}_{ML}|\mu)\, d\hat{\mu}_{ML} \quad (9)$$

For each particular value or range value of μ, we can have a particular function f which minimizes $\mathbf{R}_{C,f}(\mu)$. This is not easy to handle. Moreover the true value μ is not known *a priori*. The Bayes approach allows to solve (regularize) this problem by giving a criterion based on the prior knowledge. The prior pdf $p_\mu(\mu)$ can be interpreted as the degree of belief one has about the possible values of the unknown variable. The risk function can be weighted by the prior degree of belief to penalize the less probable texture values. The mean risk of using the function f,

$$E_\mu(\mathbf{R}_{C,f}(\mu)) = \int_0^\infty \mathbf{R}_{C,f}(\mu)\, p(\mu)\, d\mu), \quad (10)$$

is called the posterior risk. The optimal estimate minimizes it. The mean risk can be written as $E_\mu(\mathbf{R}_{C,f}(\mu)) = E_{ML}[E_\mu(C(\hat{\mu}_f, \mu)|\hat{\mu}_{ML})]$. The quantitiy in the brackets is the posterior cost, given the observation $\hat{\mu}_{ML}$. The optimal function f is the one which minimizes it for each $\hat{\mu}_{ML}$.

$$\hat{\mu}_{opt} = \arg_f \{\min E_\mu(C(\hat{\mu}_f, \mu)|\hat{\mu}_{ML}) \text{ for each } \hat{\mu}_{ML}\} \quad (11)$$

2.2 Optimal texture estimators for various cost functions

By using the cost funtions in (8) and minimizing the mean posterior cost (11), the Bayes estimators are given by

$$\hat{\mu}_{MMSE} = E_\mu(\mu|\hat{\mu}_{ML}) = \hat{\mu}_{APM} \quad (12a)$$

$$\hat{\mu}_{MMDE} = \arg_\mu\{\max p(\mu|\hat{\mu}_{ML})\} = \hat{\mu}_{MAP} \quad (12b)$$

$$\hat{\mu}_{MMAE} = \arg_\mu\{P(\mu|\hat{\mu}_{ML}) - \frac{1}{2} = 0\} = \hat{\mu}_{APMed} \quad (12c)$$

where $P(\mu|\hat{\mu}_{ML})$ is the *a posteriori* cumulative density function (cdf). The estimators are all particular statistics of the *a posteriori* pdf $p(\mu|\hat{\mu}_{ML})$: the mean (*A Posteriori* Mean APM), the mode (MAP) and the median value (APMed), respectively. Among them, the MAP and APM are used. The MAP can be often more easily derived than the APM [6].

3. THE MMSE ESTIMATOR FOR EXPONENTIALLY OR GAMMA DISTRIBUTED TEXTURE

The Gamma-MAP estimator has been already established [7]. The Gamma-APMed can be obtained numerically. It lies between the MAP and the APM, whose analytical expression can be derived and is given by

$$\hat{\mu}_{G^-APM} = \sqrt{i_o}\frac{K_{\alpha-L+1}(\sqrt{i_o})}{K_{\alpha-L}(\sqrt{i_o})}\frac{1}{2\alpha}\bar{\mu}, \qquad i_o = \frac{4\alpha L\hat{\mu}_{ML}}{\bar{\mu}}, \quad (13)$$

where $K_n(x)$ is a modified Bessel function of order n. This expression can be applied to detected intensity data by using I instead of $\hat{\mu}_{ML}$, and $E_R(R)$ instead of $\bar{\mu}$. The MAP estimate is always smaller than the APM and the Linear MMSE (Kuan filter) estimates.

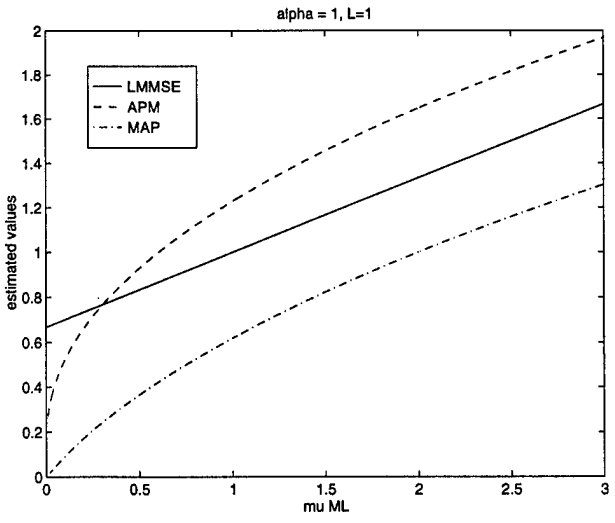

Figure 1 - Estimation functions $\hat{\mu}_f = f(\hat{\mu}_{ML})$ of the LMMSE, APM and MAP estimators for α=1 and L=1.

3.1. Radiometric bias and Mean Square Error

The mean radiometric error (bias) for the estimator $\hat{\mu}_f$ is defined by $\Delta\hat{\mu}_f = E(\hat{\mu}_f)-\bar{\mu}$. It is zero for the LMMSE estimator. For the APM estimator, it is easy to show that

$$\Delta\hat{\mu}_{APM} = \int_0^{\infty} \mu\, p(\mu)\, d\mu\ ) - \bar{\mu} = 0 \qquad (14)$$

This is not the case for the Gamma-MAP estimator, which is biased toward lower values (Fig. 2). The APM has naturally the smaller MSE (Fig. 3). The LMMSE estimator is only sub-optimal. This is due to the restriction to a linear estimation function. On the opposite, the MAP is the better on the *a posteriori* probability criterion.

3.2 Variance and variation coefficient CV

A surprinsing and unexpected fact is that the variance and coefficient of variation (CV) of all estimators are smaller that the true values, $var(\mu)= \bar{\mu}^2/\alpha$ and $CV_{\mu}^2 = 1/\alpha$, respectively. This means that these estimators reduce the texture dynamics. But the MAP preserves the textural contrast better, especially for small ENILs (Fig. 4). It is therefore the most adapted for optimal intensity summations with textural compensation [8]. The differences between the APM and the MAP estimators are reduced when the ENIL increases. The bias of the Gamma-MAP becomes small, the estimator's MSE decrease and the estimator's variances reach the true value.

5. CONCLUSIONS

In this study, we have analyzed optimal texture estimators for the multiplicative speckle model using decision theory and Bayes approach. We have established the Gamma-APM estimator which is the MMSE estimator for Gamma and exponentially distributed texture. The APM is radiometrically unbiased, but the MAP preserves the texture dynamics better. The ML classification for polarimetric data and homogeneous surfaces [5] can be applied to textured surfaces by using the per pixel $\hat{\mu}_{ML}$ or $\hat{\mu}_{EXP\text{-}APM}$ estimators.

REFERENCES:

[1] S. Quegan, and I. Rhodes, "Statistical models for polarimetric data: consequences, testing and validity", *IJRS* 16 n°7, 1183-1210, 1995.

[2] A. Lopès, and F. Séry. "Optimal Speckle Reduction for the product model in Multilook Polarimetric SAR Imagery and the Wishart Distribution", *IEEE Tr.on GRS* 35 n°3, May 1997.

[3] A. Lopès, J. Bruniquel, and F. Séry, "Optimal summation and whitening filter for speckle reduction in multilook and polarimetric image processing", *Proc. EUSAR'96 Conference,* Königswinter Germany, pp. 77-80, , 26-28 March 1996.

[4] I.R. Joughin, D.B. Percival and D.P. Winebrenner, "Probability density functions for multilook polarimetric signatures", *IEEE Tr. on GRS* 32 n°3, 562-574, May 1994.

[5] J.S. Lee, M.R. Grunes, and R. Kwok., "Classification of multilook polarimetric SAR imagery based on complex Wishart distribution", *IJRS* 15 n°11, 2299-2312, 1994.

[6] M. Schwartz, L. Shaw, "Signal processing: discrete spectral analysis, detection and estimation", *Mc Graw Hill*, 1975.

[7] A. Lopès, E. Nezry, R. Touzi, and H. Laur, "Structure detection and statistical adaptive speckle filtering in SAR images", *IJRS,* Vol.14 n°9, 1735-1758, 1993.

[8] J. Bruniquel, and A. Lopès, "Multivariate optimal speckle reduction in SAR imagery", *IJRS*, Vol.18 n°3, 603-627, 1997.

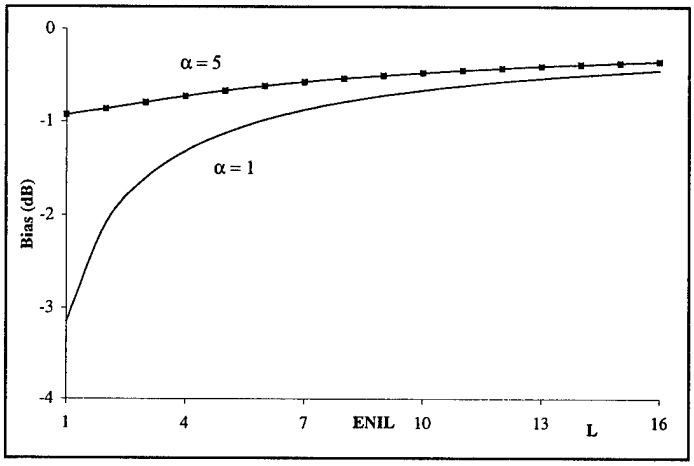

Figure 2 - Bias of the Gamma-MAP relative to the ENIL L.

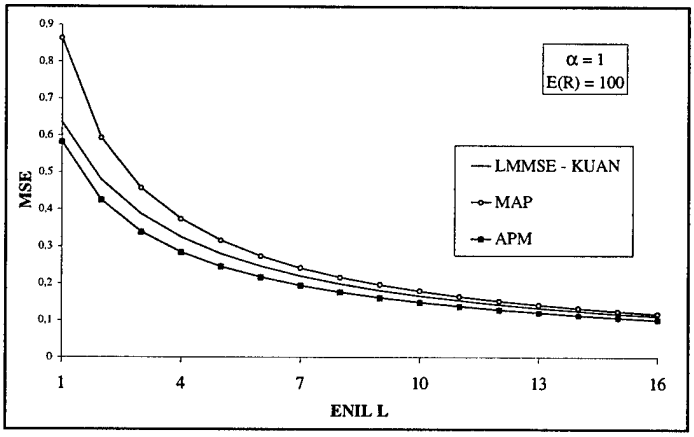

Figure 3 - MSE of the 3 estimators normalized by $E^2(R)$.

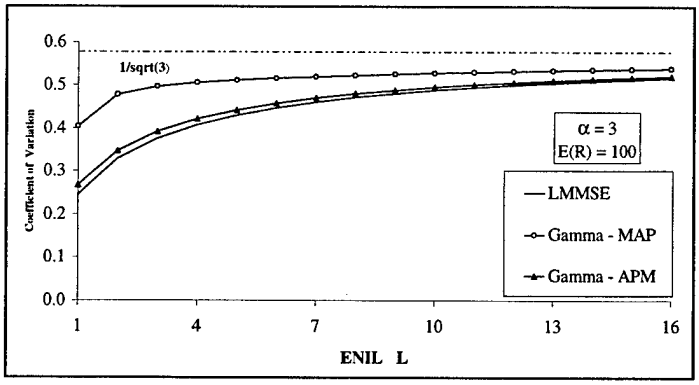

Figure 4 - Coefficient of Variation of the 3 estimators.

Radar Reflectivity Estimation Using Multiple SAR Scenes of the Same Target: Technique and Applications.

G.F. De Grandi (1), M. Leysen (1,3), J.S. Lee (2), D. Schuler (2)
(1) European Commission Joint Research Centre - Space Applications Institute - 21020 Ispra (VA) Italy
Tel.: +39 332 789823 Fax: +39 332 789073 Email: gianfranco.degrandi@jrc.it
2) Remote Sensing Division, Code 7263, Naval Research Laboratory, Washington DC 20375-5351, USA
Tel.: (202) 767-2004, Fax: (202) 767-5599, Email: schuler@imsy1.nrl.navy.mil, lee@imsy1.nrl.navy.mil
(3) VITO Flemish Institute for Technological Research Boeretang 200 B-2400 Mol Belgium
Tel.+ 32 14 33 58 85, E-mail leysenm@vito.be

ABSTRACT

An investigation on techniques to estimate the underlying reflectivity in a time series of SAR images is presented in this paper. The topic has interesting implications for a wide range of radar remote sensing applications where the time evolution of the ecosystem is of importance. Focus will be given here to a thematic application - monitoring of the tropical forest - which is one of the major R/D activities within the European Commission TREES project, and which offered the motivation to develop the approach presented here. The theory behind two statistical estimators, which were previously proposed by one of the authors, and that are used in the present study, is briefly summarized. Implementation issues which are specific to the case at hand are then discussed. Finally some results are presented, based on simulated SAR images and an ERS-1 time series acquired over the tropical forest in West Africa. The results highlight the performance of the filters, in terms of speckle suppression and restoration of the image texture. At this stage of our research we can already conclude that the approach has a high potential for radar remote sensing applications; the key point is that it allows for the reconstruction of the underlying radar reflectivity time evolution at the full spatial resolution of the signal but with a dramatic improvement of the signal to noise ratio; the way is thus paved for reaching unprecedented results in the visual or automatic interpretation of SAR imagery.

RATIONALE

We present in this paper an investigation on techniques to estimate the underlying reflectivity in a time series of SAR images. In our case the motivation for this research effort stems from a particular thematic application - tropical forest monitoring - but the approach presented here has certainly deep implications for a wider range of radar remote sensing applications (e.g. crop yield prediction, flooded area monitoring, burnt scar detection, forest seasonality), and will be in general useful when the ecosystem dynamic evolution must be tracked. Tropical forest monitoring is the objective of the European Commission TREES (Topical Ecosystem Environment monitoring by Satellites) project, in whose framework this study was initiated.

The potential of space-borne microwave sensors, such the SAR on board the ESA ERS space-craft, for obtaining large - continental - scale radar maps of the tropical forest has been recently investigated by the SAI MTV unit [1]. One of the problems that surfaces here and in similar studies is that discrimination of certain types of vegetation - such as primary and secondary forest - are not always possible using only intensity values; a contextual measure is needed, such as texture. In turn conventional texture measures are quite ineffective in the case of ERS imagery, and therefore an approach to detect structures at different scales based on a wavelet multi-resolution decomposition was proposed [2]. This approach offers an ideal framework to deal with multi-scale texture, but suffers from the contamination of speckle noise in SAR images. Therefore especially in order to deal with small scales - at the order of the ERS PRI pixel spacing e.g. 12.5 - suitable techniques to extract the underlying radar reflectivity from noise must be found. Conventional speckle filters use the spatial local statistics.in the neighbourhood of a pixel and therefore tend to smooth - or even worse corrupt - texture at small scales. The approach presented here allows us to achieve an excellent signal to noise ratio at the original signal spatial sampling, and therefore paves the way for reaching unprecedented results in the visual or automatic interpretation of SAR imagery over the tropical forest.

ESTIMATORS

From the statistical signal processing point of view we can attack the time series reflectivity estimation problem along two lines: assuming a model only for the noise component and restricting the embedded signal to be stationary; characterizing the signal by a state or dynamical model (e.g. Gauss-Markov). To the first category belong estimators such as the Linear Minimum Mean Square Error LMMSE (e.g. Wiener filters); these estimators solve with a relatively low computational complexity the filtering problem - estimation of reflectivity at measurement times t_i based on present and past data only - and the smoothing problem - estimation based on future data also. To the second category the Kalman filter, and other adaptive FIR

0-7803-3836-7/97/$10.00 © 1997 IEEE

filters, which are typically used in process control. These techniques add complexity both under the computational and the signal modelling point of view, but are very attractive because they lend themselves to the solution of the interpolation and the prediction problem, which would allow us to extend the radar reflectivity estimation to times where no real data acquisition was performed. Clearly this is of utmost importance for certain applications, such as crop monitoring or multi-sensor data fusion. Work in this direction is under way at the JRC SAI MTV and NRL.

We will limit our discussion in this paper to two estimators belonging to the first category, which were originally introduced by one of the authors [3]. Both filters are linear minimum variance estimators and assume a multiplicative noise model: $z_i = x_i v_i \quad i = 1 \ldots n$ where v_i is the noise with unit mean and standard deviation σ_v and x_i is the reflectivity to be estimated.

The first estimator, which will be referenced as optimum weighting, considers an unbiased linear estimation of the reflectivity at time t_0 as a weighted sum of the signals in the time series:

$$\hat{x}_{t0} = \sum_{1}^{n} \alpha_i z_i \frac{E[z_{t0}]}{E[z_{ti}]} \qquad \text{(EQ 1)}$$

The weights α_i are found by imposing the minimum variance of the reflectivity and the additional condition that for homogeneous areas:

$$x_i = E[x_i] \qquad \text{(EQ 2)}$$

This means that the optimum weighting algorithm will reconstruct in an optimal way the reflectivity only if it is taken from a uniform distribution (fully developed speckle regime); for areas with a fluctuating population of scatterers within the resolution cell, which give rise to a K-distribution for the amplitude backscattered signal, (the reflectivity is Gamma distributed) the estimator would not be minimum variance.

The second estimator considered here is a vector extension of the classical Lee filter [4]. In this case the linear estimator is:

$$\hat{x} = A\bar{x} + Bz \qquad \text{(EQ 3)}$$

where $\hat{x}, z, \bar{x}$ are now n-vectors and the matrices A, B are chosen as to minimize the reflectivity variance. Solutions of (2) and (3) are given in [3].

The difference between the two approaches is, from an intuitive point of view, that the optimum weighting filter uses the local spatial statistics only to balance differences in reflectivity between images at different times; the estimation of the reflectivity $\hat{x}$ is simply achieved through condition (2), assuming a uniform distribution. The vector Lee filter uses the local spatial statistics also to improve the estimate of $\hat{x}$ in the case of non-homogeneous areas through (3).

Applications of the above mentioned estimators to our case requires careful consideration of the two following aspects: SAR time series acquisition geometry and local statistic estimation.

IMPLEMENTATION ISSUES

The technique we are describing is based on the assumption that the same resolution element on the ground is illuminated by the radar beam in the same way, and corresponds to the same coordinates in the image plane (sampled signal) in all images of the time series. The backscattered signal can of course change from one time to the next due to a change in the dielectric and geometrical properties of the elementary scatterers, but should not change due to a different position of the resolution element with respect to the radar. Therefore proper spatial co-registration of the SAR images in the time series is of paramount importance. This in turn means that overlapping orbits should be chosen in the SAR acquisition phase, to minimize effects due to differences in the local incidence angle. These differences would affect both the displacement of features due to topography, and the radar cross section.

The local statistic estimation is also a crucial point. Local statistic is estimated using small windows centred around the pixel of interest. The window size is related to the variance of the estimator. For instance the standard error on the expected value $E[z]$ which appears in (1) can be roughly estimated for ERS PRI 3 looks amplitude data considering fully developed and correlated speckle. In order to achieve a standard error on the mean of 5% a 17x17 window is required. On the other hand a typical problem in local estimators is that the population in the window should be homogeneous - edges, fine structures and point targets must be detected. The two contrasting requirements call for a filter implementation using adaptive windows in size, shape and detection algorithm.

One additional point to consider in our case is the statistical non-uniformity due to changes in the target throughout the time series: for instance an homogeneous area can become split into two regions (and create an edge) if part of the backscattered signals is enhanced by a meteorological event. Therefore the adaptive window algorithm must be applied separately for each resolution element and each data set in the time series. At the time of writing a fully adaptive local statistic estimator has been implemented for the optimum weighting algorithm. The following restrictive hypothesis (suggested by the thematic application) is done: fine structures (such as roads, rivers) and man-made targets (strong targets) are stationary in time. The local estimator tries at first to use a large (typically 17x17 window) if the area is homogeneous (the normalized second moment is used as a discriminator). If the area is non-homogeneous then a series of detectors using progressively smaller windows are used to locate edges, fine structures or point targets. The correlation coefficient between pairs of

images in the series is used efficiently as one of the discriminators. In the case of extended edges when the window can be partitioned into homogeneous subsets, the algorithm indicated in [4] is used.

RESULTS AND DISCUSSION

Simulation

In order to evaluate in a controlled way the results of the filtering process and to benchmark different approaches a simulated SAR time series was generated using a Monte Carlo approach. The simulated images contain homogeneous areas with fully developed un-correlated speckle, corresponding to a 3 looks amplitude signal. Within an image two areas with different random reflectivity are generated to simulate an extended linear edge. Also the reflectivities are changed throughout the time series in such a way as to simulate cases where left and right reflectivities around an edge change with the same sign or with opposite sign. The latter case is in particular critical, because it would cause artifacts using a simple fixed window estimator. Also a fine linear feature with low reflectivity (mimicking the case of a river), and a strong point target (simulating a house roof) are inserted in the images.

An example of simulated SAR time series is reported in Fig. 1. Two frames out of 18 are shown. Results obtained using the optimum weighting filter with the adaptive window local statistic estimator are reported in Fig 1-c while results using the vector speckle filter and a fixed 7x7 local estimator are shown in Fig. 1-b. On a visual basis, problems related to the small estimation window in the vector filter case are readily apparent in the homogeneous areas. The estimation error gives rise to a typical "cardboard" effect, which is visible in most products by speckle filters based on local statistic. On the other hand the adaptive window gives a smooth reconstructed reflectivity (see Fig. 1-c). Also some bright and dark spots (which we could call shot noise) are appearing throughout the image in the case of the vector filter; they are probably due to numerical instabilities in the computation of the inverse covariance matrix (see equation B.8 in [3]); but further investigation on this phenomenon must be carried out. In general mean reflectivity values, and the non-stationary structures in the images are well reconstructed for both filters. Values for the one point statistic on one homogeneous area are reported in Table 1. It can be observed how the optimum weighting algorithm achieves a better signal to noise ratio.

TABLE 1.

	Mean	*SD*	*ENL*
PRI	279.60	83.59	3
Vector	279.72	27.55	28
Opt. W.	279.80	21.27	47

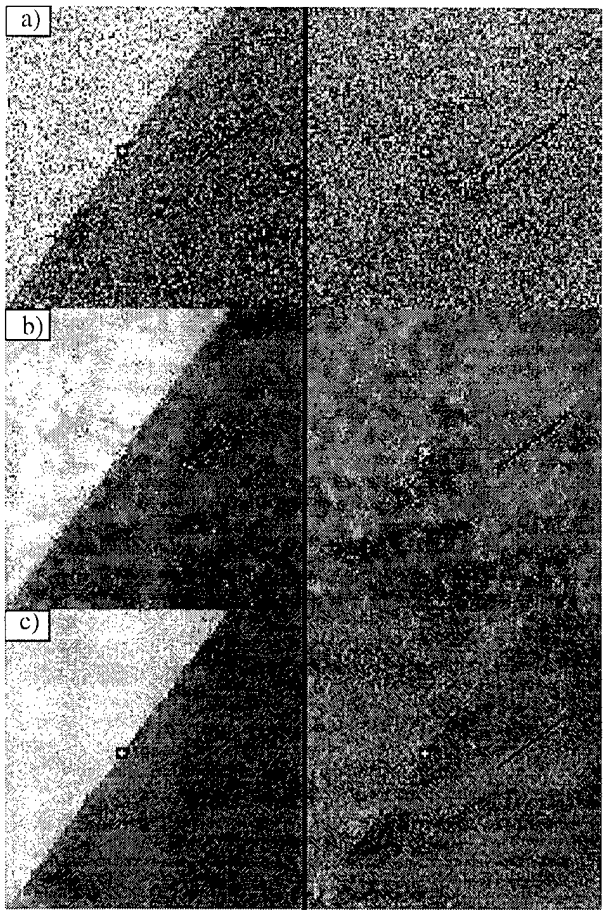

Fig. 1 - Simulated SAR multi-temporal (18) images a); results using the vector speckle filter b) and the optimum weighting filter c).

Multi-temporal ERS-1 SAR images

The multi-temporal estimation technique is undergoing a full validation and fine tuning in the context of the TREES project using a stack of 18 ESA ERS-1 SAR images of a test site situated in the Ivory Coast, West Africa. The images were acquired from April 1992 to November 1993 with a periodicity of 35 days and therefore cover a full seasonal cycle. The 18 acquisitions of the same nominal scene (track 259, frame 135) were taken from nearly identical orbital positions. The baseline differences in the data sets used are within a range of 2000m. This assures, together with the excellent spacecraft stability, that topography induced radiometric and geometric distortions are nearly the same in all images. The stack was co-registered (ground range shifts) using a two steps algorithm; at first the nominal corner points of the images are taken to compute coarse offsets, subsequently fine tuning is achieved by means of cross-correlation. The site was characterized by ground data collected during several field trips, and complementary optical data and SAR data are also available. It constitutes therefore a

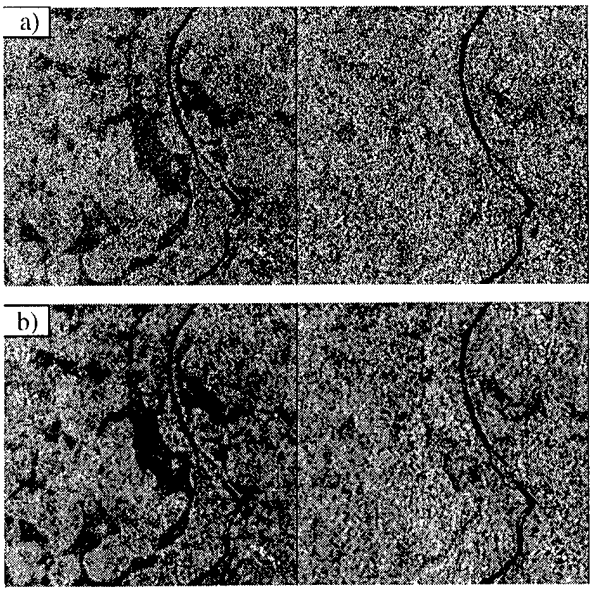

Fig. 2 - Radar reflectivity estimation in a time series of 18 ERS-1 PRI images of the Sassandra test site in West Africa. Two dates are shown: Feb. 93 and Apr. 92. Original PRI frames in a) and filtered frames in b).

solid platform to assess the relevance of the approach presented here.

An example of the results obtained so far is shown in Fig. 3. A window in the original PRIs stack was selected and processed using the vector filter, and the optimum weighting filter. The scene represents part of the site which is characterized by the natural transition zone between forest and savannah biomes. It is intersected from north to south by the Sassandra river with semi-deciduous forest of different density on either bank of the river.

Two dates in the time series are shown for the original ERS-1 image (Fig. 3.a) and the corresponding ones obtained by the filter (Fig. 3.b). The spectacular improvement that is achieved in terms of noise suppression and features enhancement is readily apparent from visual inspection of the images. Time variation of the underlying radar reflectivity are followed properly by the filter, and fine structures (the river) and strong targets (a village) are well retained.

In order to quantify the potential of the approach in terms of textural information extraction, averaged power spectra were computed in selected parts of the images. An example is shown in Fig. 3. The PRI spectrum (dashed line) is clearly dominated by the speckle noise and tends to be quite flat; whereas the spectrum of the filtered data (solid line) shows a characteristic $1/f$ trend in the frequency range corresponding to a spatial period up to 50m. This test points out the possibility of using a texture measure in a classification scheme, once the signal has been filtered, as it is discussed in [2].

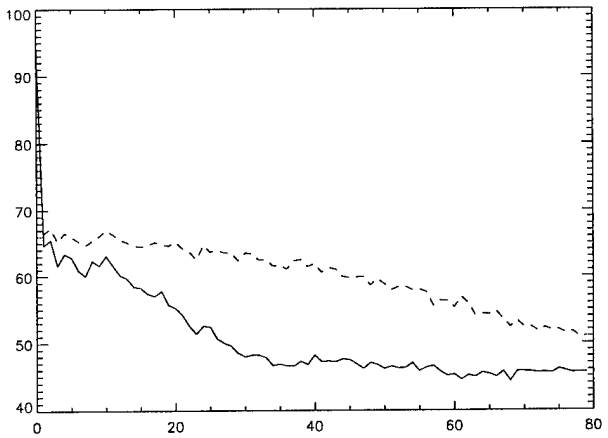

Fig. 4 - Power spectra (dB) of the PRI sample (dashed) and the corresponding vector filtered sample (solid).

CONCLUSIONS

The techniques and the results presented in this communication are still quite preliminary; work is under way at the JRC MTV and the NRL to refine the filters' performance, to fully assess the benefits form the thematic point of view, and to explore alternative ways to achieve the reflectivity restoration form the statistical signal processing point of view.

However at this stage of our research we can already conclude that the approach has a high potential for radar remote sensing applications; the key point is that it allows for the reconstruction of the underlying radar reflectivity time evolution at the full spatial resolution of the signal but with a dramatic improvement of the signal to noise ratio; the way is thus paved for reaching unprecedented results in the visual or automatic interpretation of SAR imagery.

REFERENCES

[1] G.F. De Grandi, J.P. Malingreau, M. Leysen, "The ERS-1 Central Africa Mosaic: A New Perspective in Radar Remote Sensing for the Global Monitoring of Vegetation", *submitted to IEEE Trans. on GARS, 1997.*

[2] M. Simard, F. De Grandi, K. Thomson, M. Leysen, "Sensitivity Analysis of ERS-1 SAR Signal to Multiscale Structures of the Tropical Forest by Means of the Wavelet Transform", *Proc. of the 3rd ERS Symp., Florence, 1997.*

[3] J.S. Lee, M.R. Grunes, S.A. Mango, "Speckle Reduction in Multipolarization Multifrequency SAR Imagery", *IEEE Trans. on GARS, vol. 29, no. 4, 535-544, July 1991.*

[4] J.S. Lee, "Refined Filtering of Image Noise Using Local Statistics", *Comp. Graphics and Image Proc. 15, 380-389, 1981.*

Control Systems Principles Applied to Speckle Filtering and Geophysical Information Extraction in Multi-Channel SAR Images

Edmond Nezry, Francis Yakam-Simen, Francis Zagolski, Iwan Supit

PRIVATEERS NV, Private Experts in Remote Sensing
42 De Weaver Drive, Philpsburg, Sint Marteen, Netherlands Antilles; c/o 21 via Carducci, 21027 Ispra, Italy
Phone/Fax: (+39) 332-781494; E-mail, via: http://www.treemail.nl/privateers/

ABSTRACT

Two new Bayesian vector speckle filters have been developed for multi-channel SAR images. Since these filters present the structure of data fusion control systems, their application is the first processing step of application-oriented control systems designed to exploit the synergy of SAR sensors.
We present such a control system, to retrieve soil roughness and soil moisture using ERS and Radarsat images.
Results show that the new speckle filters present convincing performances for speckle reduction, for texture preservation and for small scene objects detection. The retrieval of soil roughness and soil moisture through Bayesian data fusion of ERS and Radarsat data provides also valuable results.

1. INTRODUCTION

In the case of mono-channel SAR images, a Bayesian method, the Maximum A Posteriori (MAP) filter has already proved to be well-suited for the restoration of both the radar reflectivity and the textural properties of natural scenes [1].
In the case of multi-channel detected SAR images, as described in [1,2], the i^{th} component R_i (channel i) of the radar reflectivity vector R is obtained when:

$$\partial \mathrm{Ln}(P(I/R))/\partial R_i + \partial \mathrm{Ln}(P(R))/\partial R_i = 0 \quad \text{for } R_i = \hat{R}_{i\,MAP} \qquad (1)$$

where I is the speckled intensity vector available in the actual SAR data. $P(I/R)$ is the joint probability density function (pdf) of the speckle. $P(R)$ is the joint pdf of the radar reflectivity, introduced as statistical A Priori information in the restoration process. The first term of Eq. 1, (Maximum Likelihood) accounts for the effects of the compound imaging system. The second term (Maximum A Priori) represents our prior statistical knowledge of the imaged scene. In the Bayesian inference process, induction is influenced by the prior expectations allowed by the prior knowledge of $P(R)$. Also the non-linear system and scene effects are taken into account by the restoration process. Therefore MAP speckle filtering can be considered as a controlled restoration of R, where A Priori knowledge controls the inference process, and allows an accurate estimation of the radar backscattering coefficients σ°_i.

At this point, additional Bayesian processes can be designed to retrieve important geophysical parameters, in a cascade of control processes.

2. MULTI-CHANNEL SCENE MODEL

It is now well established that a Gamma pdf would be the most suitable representation of the first order statistical properties of a natural scene. However, to describe these properties as viewed by diverse SAR sensors (different scene physics) or at different dates (scene evolution), there is no analytic multivariate Gamma pdf available. In the following, we use a multivariate Gaussian pdf as analytic multi-channel (*i.e.* coupled) scene statistical model. This statistical model is convenient to preserve the mathematical tractability of the problem. In addition, the Gaussian model is still commonly used to describe the statistical properties of natural scenes.

3. SPECKLE MODELS AND MAP FILTERS

Let first consider the case of very different SAR sensors (very different wavelengths, for instance). In this case, it is justified to consider that the speckle is independent between the N image channels. Under this assumption, $P(I/R)$ can be modelled as a set of N independent Gamma distributions. Using this speckle model, the *Gamma-Gaussian MAP filter for multi-channel detected SAR images* (N channels) comes down to the resolution of a set of N scalar equations [2]:

$$\begin{aligned} & L_i\,(I_i/R_i^2 - 1/R_i) - {}^t(1_i).C_R^{-1}.(R-\langle R\rangle) \\ & - {}^t(R-\langle R\rangle).C_R^{-1}.(1_i) - 1/2\ \mathrm{Tr}[C_R^{-1}.\partial C_R/\partial R_i] \\ & + {}^t(R-\langle R\rangle).C_R^{-1}.\partial C_R/\partial R_i.C_R^{-1}.(R-\langle R\rangle) = 0 \end{aligned} \qquad (2)$$

where C_R is the covariance matrix of the scene, (1_i) is a vector where all components but the i^{th} are equal to zero, and the L_i are the Equivalent Numbers of Looks (ENL) of the individual SAR images.
Replacing the speckle model by the appropriate optical noise model in the concerned image channels, this filter adapts easily to the case of multi-channel optical and SAR images. Thus, the introduction of coupling between the scene statistical representations is already a data fusion process.
In the particular case of multi-date images acquired on repeat-pass by the same SAR sensor or of a set of images acquired

0-7803-3836-7/97/$10.00 © 1997 IEEE

by diverse SAR's with similar properties (only differences: polarization configuration, or slightly different incidence angles), the correlation of the speckle between SAR image channels must be taken into account to deal optimally with system effects in the series of images. In theory, $P(I/R)$ should be a multivariate Gamma pdf. Nevertheless, since such a pdf is not available analytically, another reasonable choice for $P(I/R)$ must be done for mathematical tractability: Lee [3] has shown that, in the case of multilook SAR images ($L>3$), $P(I/R)$ can be reasonably approximated by a Gaussian distribution. Under this assumption, the *Gaussian-Gaussian MAP filter for multi-channel detected multilook SAR images* is the set of equations [2,4]:

$$
\begin{aligned}
&{}^t(1_i).C_S^{-1}.(I-R) + {}^t(I-R).C_S^{-1}.(1_i) - 1/2\ \mathrm{Tr}[C_R^{-1}.\partial C_R/\partial R_i\ ] \\
&+ {}^t(R-\langle R\rangle).C_R^{-1}.\partial C_R/\partial R_i\ .C_R^{-1}.(R-\langle R\rangle) \\
&- {}^t(1_i).C_R^{-1}.(R-\langle R\rangle) - {}^t(R-\langle R\rangle).C_R^{-1}.(1_i) = 0 \qquad (3)
\end{aligned}
$$

where C_S is the covariance matrix of the speckle.

4. MAP FILTERS AND CONTROL SYSTEMS

These filters offer numerous advantages [2]: non linear image restoration, preservation of high spatial resolution through the correction of the effects of the compound multi-sensor imaging system, improvement of the probability of detection of thin scene structures due to both the diversity and redundancy aspects of information in all the channels.
Nevertheless, the most remarkable feature is that they present the structure of control systems. Both Eqs. (2) and (3) can be rewritten as Riccati's algebraic equations:

$$- A X - X\,{}^tA - Q + X\,{}^tC\,P^{-1}\,C\,X = 0 \qquad (4)$$

Eq. (4) represents the optimal controlled state reconstruction at constant gain of linear invariant processes (R and textures of the channels) perturbed by white noises (speckle, pixel spatial mismatch between channels). It can be shown that the scene A Priori model acts as a command, and that the covariance matrices act as multipoles or controls [4].

5. FILTERING OF ERS / RADARSAT DATA SET

This new filtering technique is evaluated on a couple of Radarsat (C-HH) and ERS-1 (C-VV) SAR images, acquired along descending passes within 4 hours on Feb. 13, 1996. A detail of these images, around the Schipol-Amsterdam airport in the Netherlands is shown in [4] (this issue).
The Radarsat and ERS SAR's operated at the same frequency from a very similar orbit (similar altitude and inclination angle), at similar angles of incidence. Thus, image superimposition is possible without geometrical corrections over wide areas. The two sensors differ only in polarization configuration. They are sensitive to similar physical properties of extended land areas, even if these properties do not contribute in the same amount to the backscattered signal. However, their different sensitivity to structural scene elements is of interest for the identification of these particular targets. In this context, it is therefore appropriate to use the new Gaussian-Gaussian MAP filter.
The filtered images are shown in [4] (this issue). Thin details (roads, point targets, field edges) are very well denoised and preserved. On the other hand, speckle noise is strongly filtered within the surrounding homogeneous agricultural fields (ENL=120 for Radarsat, ENL=100 for ERS). For both SAR's, the filtered images were found superior in quality to the images filtered using the mono-channel MAP filter [1] and the same structure detection algorithm [5].

6. BAYESIAN RETRIEVAL OF SOIL PARAMETERS

Haddad & Dubois [6] have developed a Bayesian estimation method of soil roughness and soil moisture. Although their method presents some built-in limitations (the imaginary part of the dielectric constant ε is not taken into account, no dependence on the surface correlation, *cf.* [7]), it is based on the same principle as our new filtering method and present common theoretical advantages.
Since our data are accurately filtered and calibrated, instead of the model presented in [6] we can use directly the soil backscattering empirical model of Dubois *et al.* [8]:

$$
\begin{aligned}
&\sigma^\circ_{HH} = m = M_1(\theta,\lambda)\ .\ f(\varepsilon,h) \qquad (5)\\
&\sigma^\circ_{VV} = n = M_2(\theta,\lambda)\ .\ g(\varepsilon,h)
\end{aligned}
$$

where θ is the wave incidence angle, λ is the radar wavelength, ε is the soil dielectric constant (related to soil type and moisture), and h is the r.m.s. height (soil roughness).
Using Bayes' theorem, the unnormalised conditional joint probability of (ε,h) verifies [6]:

$$P(\varepsilon,h|m,n) = P(\varepsilon,h) / [\ f(\varepsilon,h).g(\varepsilon,h)\ ]\ .\ P(M_1,M_2) \qquad (6)$$

The optimum unbiased estimator for $X \in \{\varepsilon,h\}$ that has minimum variance is the conditional mean [6]:

$$\hat{X} = \int X\ .\ P(\varepsilon,h|m,n)\ d\varepsilon.\ dh \qquad (7)$$

Finally, the dielectric constant is converted to volumetric soil moisture through a set of empirical curves [9].
With our data accurately filtered and calibrated, the nature of the randomness present in (m,n) can only be due to relief. Since our Netherlands area present negligible relief, $P(M_1, M_2)$, which depend primarily on the SAR frequencies and on the local incidence angles is reasonably assumed a Dirac distribution. This results in a straightforward estimation of $P(\varepsilon,h|m,n)$, *i.e.* a drastic simplification of the resolution process, and improves potentially estimation accuracy.
Results of this method, applied over the Netherlands, are shown in Figures 1 and 2. In February, the low or non-

existent vegetation layer does not affect significantly the retrieval of soil parameters over agricultural areas.
In addition, snow covered areas (lighter tones in the north of the scene, on Figs. 1 and 2), difficult to identify in the original SAR images, can be more easily identified.
The interest of the quantitative results (especially soil moisture) for the initialization of agro-meteorological and crop growth models has already been widely expressed. In addition, since soil roughness is also helpful to identify cultivated areas, such a result can also be used in photo-interpretation to support other agriculture applications such as crop surfaces estimation [10].

7. CONCLUSION

Two new Bayesian speckle filters have been developed for multi-channel SAR images, with very convincing results [4]. Combined with the two-points statistics based algorithm exposed in [5], these filtering techniques are able to produce filtered images without loss in spatial resolution. Within homogeneous areas, efficient speckle filtering enables the accurate estimation of σ° required by most remote sensing SAR applications such as the retrieval of soil parameters.
The major interest of this technique is that we apply pure control systems. This offers wide possibilities for the choice and the design of additional commands (statistical/physical models) for further data exploitation. In this view, speckle filtering should be regarded as the first step of integrated application oriented control systems rather than of processing chains.

ACKNOWLEDGMENTS

The ERS and Radarsat images have been provided by the European Space Agency (Pilot Project PE-FRNE2) and by the Canadian Space Agency (Pilot Project ADRO#581).

REFERENCES

[1] A. Lopes, E. Nezry, R. Touzi, H. Laur, 1993: "Structure detection and statistical adaptive speckle filtering in SAR images", *Int. J. Rem. Sens.*, Vol.14, n°9, pp.1735-1758.
[2] E. Nezry, F. Zagolski, A. Lopes, F. Yakam-Simen, 1996: "Bayesian filtering of multi-channel SAR images for detection of thin structures and data fusion", *Proc. of SPIE*, Vol.2958, pp.130-139, EUROPTO II, Taormina (Italy), 23-26 Sept. 1996.
[3] J.S. Lee, 1980: "Digital image enhancement and noise filtering by use of local statistics", *IEEE Trans. on PAMI*, Vol.PAMI-2, n°3, 165-168.
[4] E. Nezry, A. Lopes, F. Yakam-Simen, 1997: "Prior scene knowledge for the Bayesian restoration of mono- and multi-channel SAR images", *Proc. of IGARSS'97*, Singapore, 3-8 Aug. 1997, this issue.
[5] E. Nezry, M. Leysen, G. De Grandi, 1995: "Speckle and scene spatial statistical estimators for SAR image filtering and texture analysis: some applications to agriculture, forestry, and point targets detection", *Proc. of SPIE*, Vol.2584, pp.110-120, EUROPTO II, Paris (France), 25-29 Sept. 1995.
[6] Z.S. Haddad, P.C. Dubois, 1994: "Bayesian estimation of soil parameters from remote sensing data", *Proc. of IGARSS'94*, Vol.3, pp.1421-1423, Pasadena, 8-12 Aug. 1994.
[7] M.S. Dawson, A.K. Fung, M.T. Manry, 1995: "Tools for soil moisture retrieval from radar measurements", *Retrieval from bio- and geophysical parameters from SAR data for land applications*, pp.295-305, Toulouse, 10-13 Oct. 1995.
[8] P.C. Dubois, J. van Zyl, T. Engman, 1995: "Measuring soil moisture with imaging radars", *IEEE Trans. Geosc. Rem. Sens.*, Vol.33, n°4, pp.915-926.
[9] M. Hallikainen, F.T. Ulaby, M.C. Dobson, M.A. El-Rayes, L. Wu, 1995: "Microwave dielectric behaviour of wet soil, Part 1: Empirical models and experiment observations", *IEEE Trans. Geosc. Rem. Sens.*, Vol.GE-23, n°1, pp.25-34.
[10] E. Nezry, G. Genovese, G. Solaas, S. Rémondière, 1995: "ERS based early estimation of crop areas in Europe during the winter 1994/1995", *Proc. of the 2nd ERS Applications Workshop*, ESA SP-383, pp.13-20, 6-8 Dec. 1995.

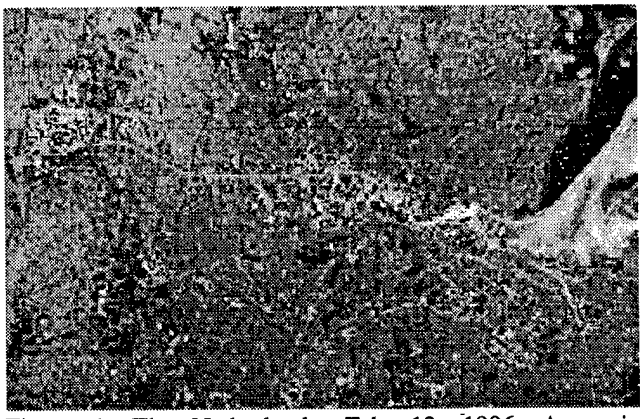

Figure 1: The Netherlands; Feb. 13, 1996. Area size: 38.5x24.5 km. Soil moisture map (ERS/Radarsat fusion).

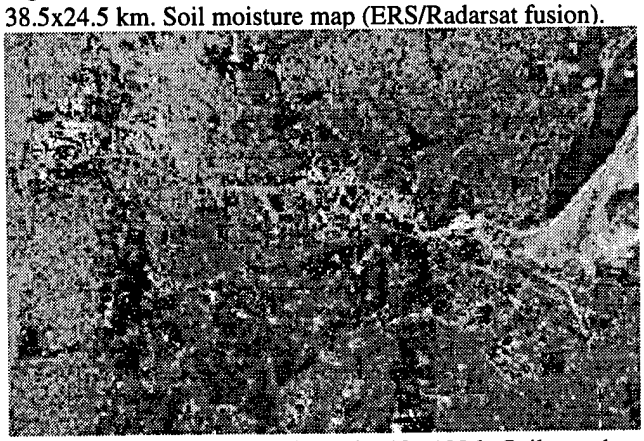

Figure 2: The Netherlands; Feb. 13, 1996. Soil roughness map (inversed LUT), using ERS / RADARSAT data fusion.

Multiresolution Adaptive Speckle Filtering: a Comparison of Algorithms

B. Aiazzi*, L. Alparone°, S. Baronti*, G. Borri°

*Istituto di Ricerca sulle Onde Elettromagnetiche "Nello Carrara" - CNR, via Panciatichi, 64, I-50127 Firenze, Italy
Phone: +39-55-4235-275; Facsimile: +39-55-410893; E-mail: baronti@iroe.fi.cnr.it
°Dipartimento di Ingegneria Elettronica, University of Florence, via S. Marta, 3, I-50139 Firenze, Italy
Phone: +39-55-4796-372; Fax: +39-55-494569; E-mail: alparone@cosimo.die.unifi.it

Abstract -- Speckle filtering in multiresolution frameworks is the key to extend spatial adaptivity also across scales. Several procedures based on wavelets and pyramids, in which the different resolutions are adaptively filtered, have been introduced for selective speckle smoothing with preservation of features and point targets. In this work, comparison tests on true and synthetic speckled images show significant advances of the *multi-* over the *single-scale* approach, especially for the pyramid based scheme proposed by the authors, where visual comparisons on SAR images show better texture preservation.

INTRODUCTION

Synthetic Aperture Radar (SAR) images are affected by speckle which appears as a granular signal-dependent noise, whose effect is to degrade the performance of image segmentation and classification algorithms. For this reason, several techniques have been developed for speckle reduction [1]. Adaptive spatial filtering based on local statistics is widely used, with the objective of smoothing homogeneous areas, in which speckle is fully developed, simultaneously preserving point targets and edges, in which SNR is higher [2]. One of the crucial points of spatial adaptive filtering is to find the most suitable neighborhood of each pixel, in which the features driving the smoothing algorithm will be estimated. A suited approach consists of adaptively modifying the shape and/or size of the local processing window at each pixel position, based on some local features (e.g., mean, variance, gradients), thereby determining the filter response. A different approach consists of taking a multi-resolution decomposition of the input image, and adaptively filtering each resolution layer, which exhibits a different SNR. Once all the resolutions, including the base-band, have been adaptively smoothed, a noise-free image may be achieved.

The wavelet transform has been employed for multi-resolution de-speckle, thanks to its capability to capture spatial features within frequency sub-bands. The most established approach consists of thresholding the absolute values of the wavelet coefficients based on a proper SNR measure of each sub-band [3]. Coefficients below the threshold are assumed to depend entirely on noise and are therefore discarded. The largest coefficients are retained and used to synthesize a noise-free image. However, textured artifacts are likely to be generated on homogeneous regions, as well as ringing effects along step edges and other structured impairments due to frequency aliasing. In addition, the signal-dependent nature of speckle is generally not considered in wavelet-based schemes.

A recent scheme of speckle filtering [4] has been designed starting from a set of multi-scale low-pass versions of the noisy image, considering the local variation coefficient. Since first-order statistics computed on multiple scales are related to second-order statistics (i.e., gradients) on a single scale, the scheme is substantially similar, although formally different, to the refined local statistics filter [5], introduced many years before, which represents a forerunner of multi-resolution speckle filtering, and is still unsurpassed among single-scale spatial filters [1], at least for not overly textured images.

Another adaptive multi-scale filter was proposed by the authors [6], who noticed that the band-pass frequency representation of Laplacian pyramids (LP) allows image structures to be mapped onto multiple scales without losing their connectivity, thus allowing to improve the efficacy of local statistics filtering. The noise model is easily retained by defining the LP as the ratio, instead of the difference, of two low-pass versions of the noisy image.

LLMMSE FILTERING

A *minimum MSE* filter based on *local linear* (i.e., first-order) statistics, referred to as LLMMSE filter, was also developed for a multiplicative noise model by Kuan *et al.* [7].

Denote with $G(m,n) = F(m,n) \times u(m,n)$ the observed pixel value, with $F(m,n)$ the noise-free image, and with $u(m,n)$ the multiplicative noise, independent of $F(m,n)$, stationary and uncorrelated, with unit mean and variance σ_u^2. The LLMMSE estimate of F at (m,n) may be approximated by

$$\hat{F}(m,n) \simeq \overline{G}(m,n) + \left[G(m,n) - \overline{G}(m,n)\right] \left(1 - \frac{\sigma_u^2}{C_v^2(m,n)} \right) \left(\frac{1}{1+\sigma_u^2} \right) \quad (1)$$

where $C_v(m,n) \approx \sigma_G(m,n)/\overline{G}(m,n)$, $\sigma_G(m,n)$ and $\overline{G}(m,n)$ being local standard deviation and average of G, respectively. Such features are evaluated on a suitable neighborhood of (m,n).

0-7803-3836-7/97/$10.00 © 1997 IEEE

MULTIRESOLUTION LLMMSE FILTERING

The Gaussian pyramid (GP) is a multiresolution image representation obtained through a recursive *reduction*, i.e., separable low-pass filtering and decimation by *2* along rows and columns of the image data set, which represents the zeroth level, up to a base band level K having size smaller by 2^K.

From the GP, a *Ratio Laplacian Pyramid* (RLP) [6] was defined to match the multiplicative nature of speckle noise. Each GP level up to $K - 1$ is pixel-by-pixel divided by its low-pass version, which is *expanded* (up-sampled and low-pass filtered) by *2*, to match the size of its underlying level. The ratio is taken to yield a pyramid whose levels are roughly *band-pass* image descriptions, but have nonzero mean [8].

For natural images, each layer of the RLP is characterized by an SNR that increases with scale. Therefore, adaptive LLMMSE filtering (1) may be tuned to the noise variance of the level (either *base-band* or *band-pass*).

The noise variance at the kth level of the RLP, $\sigma_u^2(k)$, $k = 0, \ldots, K-1$, including the base-band for $k = K$, is to be fed to (1), and can be computed from the frequency responses $R(\omega)$ and $E(\omega)$ of reduction/expansion filters, as shown in [8]:

$$\sigma_u^2(K) = \frac{\sigma_u^2}{4\pi^2}\cdot\left[\int_{-\pi}^{\pi}\left|\prod_{l=0}^{K-1} R(2^l\omega)\right|^2 d\omega\right]^2$$

$$\sigma_u^2(k) = \frac{\sigma_u^2}{4\pi^2}\cdot\left[\int_{-\pi}^{\pi}\left|\prod_{l=0}^{k-1} R(2^l\omega)\right|^2 d\omega\right]^2 + \frac{\sigma_u^2}{4\pi^2}\cdot\left[\int_{-\pi}^{\pi}\left|E(2^k\omega)\cdot\prod_{l=0}^{k} R(2^l\omega)\right|^2 d\omega\right]^2 - \frac{\sigma_u^2}{2\pi^2}\cdot\left[\int_{-\pi}^{\pi}|E(2^k\omega)|\cdot|R(2^k\omega)|\cdot\left|\prod_{l=0}^{k-1} R(2^l\omega)\right|^2 d\omega\right]^2 \qquad (2)$$

The noise-free GP at level $k < K$, namely $\hat{F}_k$, is recursively given as product of the filtered L_k, and the expanded $\hat{F}_{k+1}$, starting from $k = K - 1$. The complete block diagram is shown in Figure 1. Notice that, for $K = 0$, the scheme becomes plain LLMMSE filtering (1). The sizes of processing windows at each level k should be progressively reduced for increasing k: 9×9, 7×7, 5×5, 3×3, for a *4*-layers scheme ($K = 3$).

RESULTS AND COMPARISONS

Results of multi-resolution adaptive filters will be reported on both synthetic and true SAR images. Noisy versions of a test image have been produced from simulated speckle with unit mean, variance σ_u^2 and multi-look amplitude statistics.

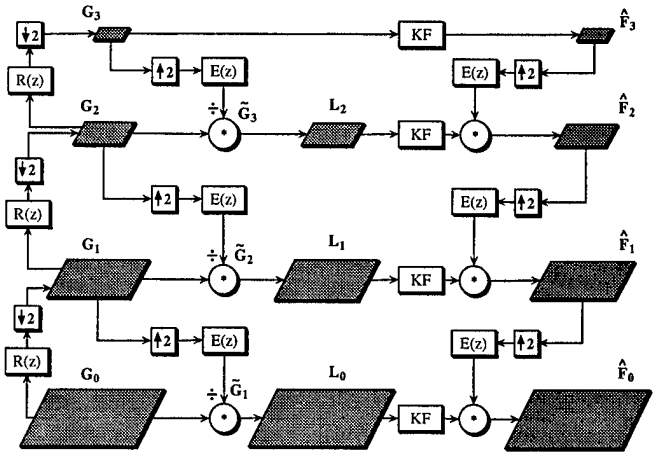

Figure 1. - Flowchart of Laplacian pyramid filtering scheme: *R(z) / E(z)* are reduction/expansion filters; KF is Kuan's filter.

SNR between noise-free and processed noisy versions are reported versus the number of equivalent looks, i.e., σ_u, in the plots of Figure 2. Wavelet-based [3] (WMF), Meer's [4], and refined Lee's [5] filters are compared with the pyramid scheme by the authors [6,8], referred to as MLPF. Kuan's filter [7] (i.e., MLPF with $K = 0$) is also included in the comparison. MLPF gives the best performance followed by Meer's, refined Lee's (comparable in average with WMF), and Kuan's filters. Notice that only MLPF attains a small improvement over Kuan's scheme for single-look images.

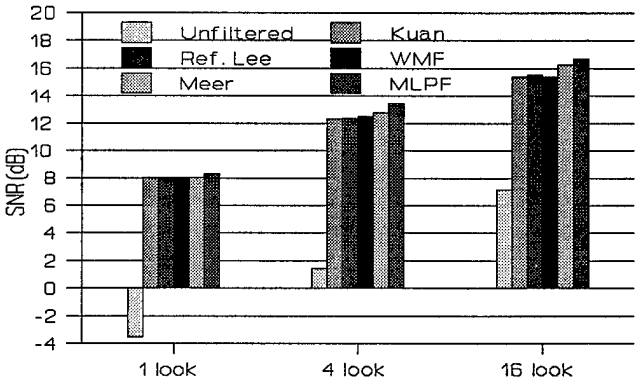

Figure 2. - SNR between noise-free and processed speckled versions of test image, for variable number of looks.

Figure 3 shows original and three processed versions of an *8-bit* detail from a NASA/JPL AIRSAR image (*4*-looks intensity) of the San Francisco Bay. All the algorithms are effective in selectively removing noise in proximity of step edges, contours and thin lines, without diminishing image sharpness, differently from Kuan's filter which is known to introduce blur and leave noisy edges. MLPF tries to find a balance between the above tendencies. Meer's and refined Lee's filters are similar, although the latter is more accurate.

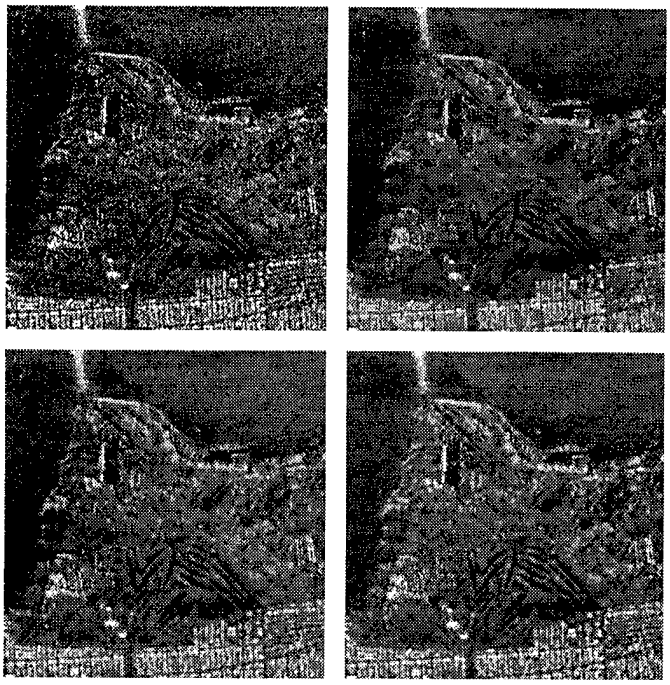

Figure 3. - A 256 × 256 detail from SAR image of San Francisco Bay (top-l); Lee's refined filter (top-r); Meer's filter [4] (bottom-l); 4-layer MLPF filter (bottom-r).

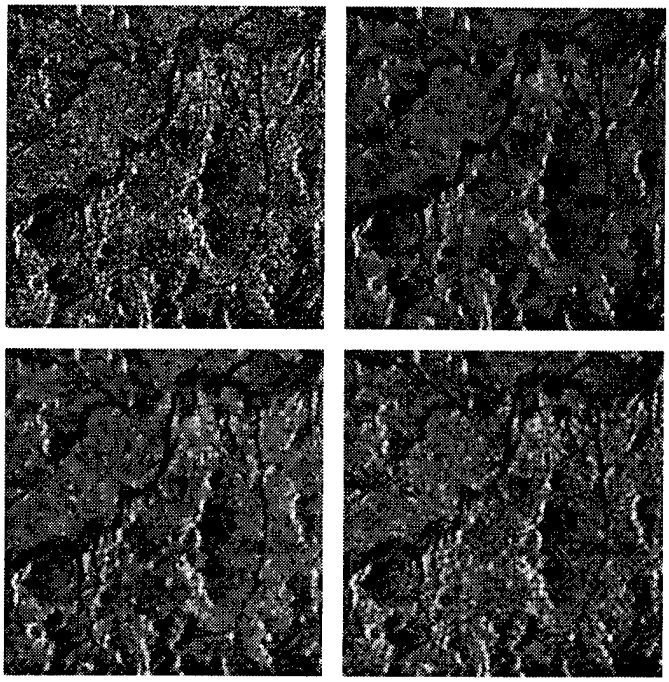

Figure 4. - A 256 × 256 detail from ERS-1 SAR image of Metaponto (top-l); Lee's refined filter (top-r); Meer's filter (bottom-l); 4-layer MLPF filter (bottom-r).

Despite its good SNR, visual results of WMF were omitted because of textured impairments due to wavelet synthesis.

Figure 4 shows an original and processed detail from an ESA ERS-1 spaceborne SAR image (*3*-looks amplitude) of a region near Metaponto, Southern Italy. In this case, texture preservation prevents full speckle reduction. MLPF seems to attain the best visual results, avoiding introducing artifacts.

CONCLUDING REMARKS

In conclusion, in objective tests the pyramid scheme is more efficient than the other schemes reviewed, providing a estimate of the *noise-free* original better by over *1.2* dB than that of the standard LLMMSE Kuan's filter. Comparisons with the other multiresolution schemes, as well as with Lee's refined filter, attest higher *SNR* and comparable visual quality.

Although all the mentioned schemes, except the wavelet-based one, perform quite well, the filter proposed by the authors is slightly superior, especially on textured scenes.

ACKNOWLEDGMENTS

The authors are grateful to Dr. J.-S. Lee for kindly providing test images, as well as for a number of suggestions.

Work carried out with grants of ASI-Italian Space Agency, within a project on multisource classification of land use.

REFERENCES

[1] J.-S. Lee, I. Jurkevich, P. Dewaele, P. Wambacq, A. Oosterlinck, "Speckle Filtering of Synthetic Aperture Radar Images: A Review," *Remote Sensing Reviews*, Vol. 8, pp. 313-340, 1994.

[2] A. Lopez, R. Touzi, E. Nezry, "Adaptive Speckle Filters and Scene Heterogeneity," *IEEE Trans. Geosci. Remote Sensing*, Vol. 28, No. 6, pp. 992-1000, 1990.

[3] K. Lebart and J.-M. Boucher, "Speckle filtering by wavelet analysis and synthesis," *Wavelet Appl. in Signal Image Process. IV, SPIE Vol. 2825*, pp. 644-651, 1996.

[4] P. Meer, R.-H. Park, and K. Cho, "Multiresolution Adaptive Image Smoothing," *CVGIP: Graphic Models Image Process.*, Vol. 56, No. 2, pp. 140-148, Mar. 1994.

[5] J.-S. Lee, "Refined Filtering of Image Noise Using Local Statistics," *CVGIP*, Vol. 15, No. 2, pp. 380-389, 1981.

[6] B. Aiazzi, L. Alparone, S. Baronti, G. Borri, C. Susini, "Multiresolution De-Speckle Based on Laplacian Pyramids," *Proc. IGARSS'96*, Lincoln, NE, pp. 411-413.

[7] D. T. Kuan, A. A. Sawchuck, T. C. Strand, P. Chavel: "Adaptive Noise Smoothing Filter for Images with Signal-Dependent Noise," *IEEE Trans. Pattern Anal. Machine Intell.*, Vol. 7, No. 2, pp. 165-177, 1985.

[8] B. Aiazzi, L. Alparone, S. Baronti, G. Borri, C. Susini, "Multiresolution adaptive noise filtering based on Laplacian pyramids," *SPIE Vol.2825*, pp. 632-643, 1996.

The Application of Wavelet Transform for Speckle Suppression in Radar Imagery*

Yunhan Dong[1], Bruce Forster[1], Anthony Milne[2] and Catherine Ticehurst[1]
[1]School of Geomatic Engineering, The University of New South Wales, Sydney 2052, Australia
Telephone: +61 2 9385 4209, +61 2 9385 4172, Facsimile: +61 2 9313 7493
Email: y.dong@unsw.edu.au, b.forster@unsw.edu.au
[2]Office of Postgraduate Studies, The University of New South Wales, Sydney 2052, Australia
Telephone: +61 2 9385 2731, Facsimile: +61 2 9385 3733, Email: t.milne@unsw.edu.au

Abstract — An effective algorithm for speckle noise smoothing using wavelet transform techniques is presented in this paper. Recursive wavelet transforms are used to gradually suppress speckle noise. It is found that this algorithm is more powerful compared to other existing filtering algorithms in terms of speckle suppression for synthetic aperture radar images. Examples show that the ratio of the original standard deviation to mean of about 0.30 (equivalent to 3-look images) can be reduced to 0.05–0.03 (equivalent to more than 100-look images), with a possible small sacrifice of losing some details and narrow edges.

INTRODUCTION

The existence of speckle noise in SAR (synthetic aperture radar) images greatly reduces their interpretability. References [1-3] have reviewed and evaluated a wide range of filtering techniques. It is known that, in theory, the intensity of speckle noise obeys a negative exponential distribution and is a multiplicative noise. In the case of one-look images, the standard deviation of the noise is equal to its mean. Consequently, noise-model-specific filters, such as the Lee's multiplicative model [4] which uses spatial statistics, the polarimetric whitening [5] and the Lee et al model [6] which use correlation statistics among multipolarization and/or multifrequency channels to suppress speckle, have been developed. On the other hand, non-noise-model-specific filters, normally developed for smoothing additive noise, such as median, sigma, mean, K-NN (k nearest neighbor averaging) geometric filters, as well as many of their modifications have also been extensively applied in speckle suppression in radar images.

The wavelet transform technique is used in this paper to suppress speckle noise in SAR images. It is implemented by convoluting a smoothing function with the original image in space, which can be viewed as a weighted averaging scheme. However, the wavelet transform has further advantages. First, the wavelet functions can be built systematically based on the data analysis. Second the multiscale transform is particularly adapted to characterize signals, so that the smoothed images can be obtained in designated scales for different purposes. If the wavelet function is chosen to be differentiable, the filtered signals are the smoother than those filtered by use of moving windows. Algorithms using moving windows calculate the current pixel value without direct consideration of the previous and following pixel values, so that the filtered signals cannot be as smooth as the signal filtered by the wavelet transform.

*This work was supported by the Australian Research Council.

WAVELET TRANSFORM FUNCTIONS

The discrete wavelet techniques have been used extensively in image data compression and reconstruction in recent years. It is shown in this paper, however, that the technique can also be used to suppress speckle in SAR images.

In numerical applications, the smoothing wavelet transform of $f(x)$ at the scale 2^j and at the position x is defined by the convolution product

$$S_{2^j}f(x) = f * \phi_{2^j}(x) \quad \text{with} \quad \phi_{2^j}(x) = \frac{1}{2^j}\phi\left(\frac{x}{2^j}\right) \quad (1)$$

where $*$ denotes one-dimensional convolution, $\phi(x)$ is referred to as a smoothing function and $\phi_{2^j}(x)$ is the dilation of $\phi(x)$ by a factor 2^j. The wavelet transform $S_{2^j}f(x)$ is, therefore, the signal function smoothed at the scale 2^j. The larger the scale, the less fluctuations remain.

Various smoothing functions designed for signals with additive noises can be used for speckle suppression in SAR images where the noise has a multiplicative structure. It has been shown that a signal with a multiplicative noise structure can be viewed as a signal with an additive noise structure [7]. The authors have tested some smoothing functions such as the Guassian function, Daubechies' function [8] and Zhou et al's function [9]. The Fourier transform function of the smoothing function used in this paper is,

$$\Phi(\omega) = \left(\frac{sin(\omega/2)}{\omega/2}\right)^4 \quad (2)$$

which has been found, when used in a recursive smoothing scheme, to give a slightly better performance.

For fast implementation of discrete algorithms, one can define the Fourier transform of the smoothing function $\phi(x)$ as [10],

$$\Phi(\omega) = \prod_{j=1}^{+\infty} H(\omega/2^j) \quad (3)$$

where $H(\omega)$ is a 2π periodic and differentiable function. Equation (3) implies

$$\Phi(2\omega) = H(\omega)\Phi(\omega) \quad (4)$$

From (3) and (2), we find the Fourier transform of the smoothing operator H to be

$$H(\omega) = cos^4(\omega/2) \quad (5)$$

The fast wavelet transform algorithms for one-dimensional signals, based on (4), can thus be written as,

$$S_{2^{j+1}} f = S_{2^j} f * h_{2^j} \qquad j = 0, 1, \cdots. \tag{6}$$

where h_{2^j} is the recursive smoothing operator at the scale 2^j. $S_{2^0} f$, the finest resolution, is the original signal.

The wavelet transform (6) can be viewed as a scheme of weighted averaging with different scales. Our goal is to suppress the noise as much as possible while maintaining the local features. That is, the fine scales might not suppress speckle enough and the coarse scales might smear local features too much. To overcome this problem, a recursive algorithm for the noise suppression is given as follows,

$$\begin{array}{l} j = 0 \\ \textit{While } (j < J) \\ \textit{If } (j \le j_0)\ h = h_{2^j}\ \textit{Else } h = h_{2^{j_0}} \\ S_{2^{j+1}} f = S_{2^j} f * h \\ j = j + 1 \\ \textit{End of While} \end{array} \tag{7}$$

where j_0 is a threshold, depending on how detailed the local features are to be maintained.

The one-dimensional fast wavelet transform algorithms can be extended to two-dimensions by substituting for (7) as follows,

$$S_{2^{j+1}} f(x, y) = S_{2^j} f(x, y) * *h(x)h(y) \tag{8}$$

where $**$ denotes two-dimensional convolution. Since the two dimensional convolution is a separable convolution of the rows and columns, the discrete FFT (fast Fourier transform) algorithm can be easily employed in programming.

EVALUATION OF RESULTS

Quantitative evaluation of a filter includes several criteria [1], among which the most important are,

1. preservation of the mean,
2. reduction of the standard deviation, and
3. preservation of edges.

A 512×512 NASA/JPL AirSAR C-band HH polarization intensity image, acquired over the South Alligator River region, Northern Territory, Australia, in 1993, is shown in Fig. 2. The five images filtered by K-NN, median, Lee's multiplicative, geometric and wavelet algorithms are also shown in the figure for comparison. Up to eight iterations are used for all five filtering algorithms. A threshold $j_0 = 1$ is used for wavelet transform. Since a moving window is required in the median, K-NN and Lee's multiplicative model filters, moving windows 3×3, 5×5 and 7×7 are recursively used. That is, the size of the moving window 3×3 is used in the first and then fourth iterations, the size of the moving window 5×5 is used in the second and fifth iterations, and so on. Table 1 gives the quantitative analysis for two uniform 50×50 pixel areas, representing a wet *Melaleuca* swamp, and mixed woodland, respectively, as shown in the figure. To observe the preservation of the mean, the mean of each area, normalized to its original mean, referred to as the normalized mean (NM), is used in the table. Therefore, the closer to 1 the NM, the better the preservation of the mean. Theoretically, only the wavelet transform filter guarantees the preservation of the mean. Another quantity shown in the table is the ratio of the standard deviation to mean (STM). The smaller the STM, the better the speckle suppression. It can be seen that the wavelet transform is the best in terms of speckle suppression. The STM of the original image, which is about 0.354, is reduced to about 0.030, equivalent to increasing the look number by a factor of $(0.354/0.030)^2 \approx 139$ in the multi-look processing. Fig. 1 depicts the change from grassland to forests, in a three dimensional view, using the original and filtered data. While the filtered data using the wavelet transform method are the smoothest everywhere, the median filtered data preserve sharp edges better.

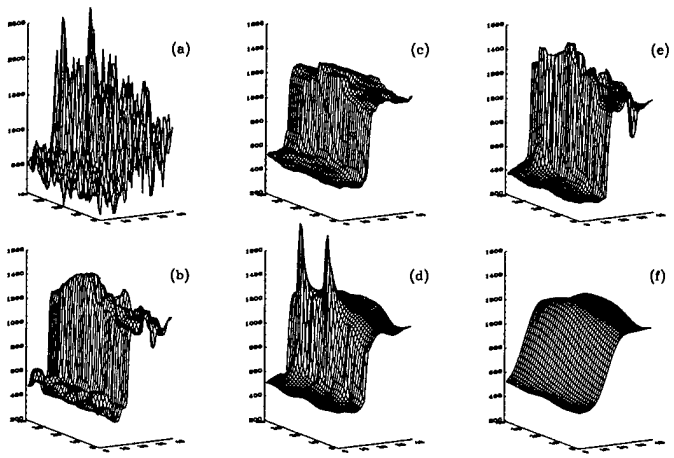

Figure 1: Three dimensional views of data changes from grassland to forests: (a) original, (b) K-NN, (c) median, (d) Lee's multiplicative, (e) geometric and (f) wavelet transform.

Table 1: Comparison of speckle suppression using different filtering algorithms for the JPL/NASA AirSAR C-band HH intensity data

	Area I		Area II	
Filter	NM	STM	NM	STM
Original	1.000	0.341	1.000	0.367
K-NN	0.974	0.108	0.959	0.121
Median	0.980	0.058	0.950	0.057
Lee's Multi	1.002	0.048	0.990	0.050
Geometric	1.020	0.105	1.021	0.099
Wavelet	1.006	0.025	0.996	0.034

REFERENCES

[1] Y. Huang, and J. L. Van Genderen, "SAR speckle reduction: A review of filtering techniques and an evaluation of filter performance," submitted to Int J of Remote Sensing for publication, 1996.

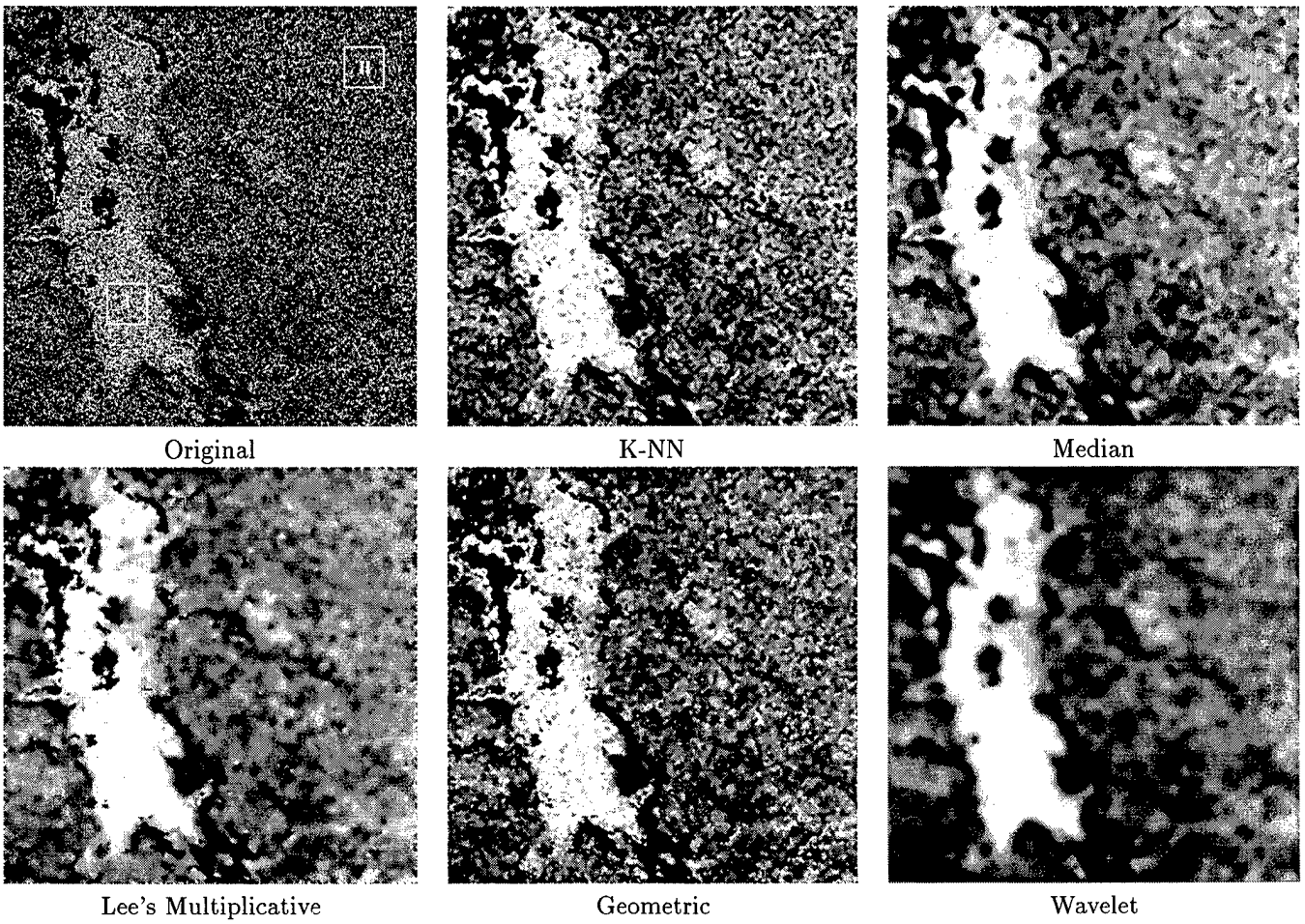

Figure 2: An original image and its five speckle suppressed companions filtered by the K-NN, median, Lee's multiplicative, geometric and wavelet filters, respectively. The original image is a 512 × 512 pixel NASA/JPL AirSAR C-band HH polarization intensity image.

[2] G. A. Mastin, "Adaptive filters for digital image noise smoothing: An evaluation," Computer Vision, Graphics, and Image Processing, vol. 31, pp. 103-121, 1985.

[3] P. Dewaele, P. Wambacq, A. Oosterlinck, and J. L. Marchand, "Comparison of some speckle reduction techniques for SAR images," Proceedings of IGARSS '90, pp. 2417-2412, 1990.

[4] J. S. Lee, "Speckle suppression and analysis for synthetic aperture radar," Optical Engineering, vol. 25, pp. 636-643, 1986.

[5] L. M. Novak, and M. C. Burl, "Optimal speckle reduction in polarimetric SAR imagery," IEEE Trans on Aerospace and Electronic Systems, vol. 26, pp. 293-305, 1990.

[6] J. S. Lee, M. R. Grunes, and S. A. Mango, "Speckle reduction in multipolarization, multifrequency SAR imagery," IEEE Trans on Geoscience and Remote Sensing, vol. 29, pp. 535-544, 1991.

[7] Y. Dong, B. C. Forster, A. K. Milne, and G. Morgan, "Speckle suppression using recursive wavelet transforms," Int J of Remote Sensing, in press, 1997.

[8] I. Daubechies, Ten Lecture Notes on Wavelets. Philadelphia: Society for Industrial and Applied Mathematics, 1992.

[9] J. Zhou, X. Fang, and B. K. Ghosh, "Smooth image segmentation via multiresolution analysis," in A. F. Laine, and M. A. Unser (Editors), Wavelet Application in Signal and Image Processing II, 27-29 July 1994, San Diego, California. Washington: SPIE, pp. 462-472, 1994.

[10] S. Mallat, and S. Zhong, "Characterization of signals from multiscale edges," IEEE Trans on Pattern Analysis and Machine Intelligence, vol. 14, pp. 710-732, 1992.

USE OF RADARSAT SCANSAR PRODUCTS FOR REGIONAL MAPPING IN SOUTHEAST ASIA

D.M. Nazarenko[1], G. Mitchell[2], and G.C. Staples[1]

(1) RADARSAT International Inc.
200 - 3851 Shell Road
Richmond, BC CANADA V6X 2W2
Email: dnazarenko@rsi.ca
Email: gstaples@rsi.ca

(2) RGI Resource GIS and Imaging Ltd.
1602 - 409 Granville Street
Vancouver, BC CANADA V6C 1T2
Email: gerry@pro.net

Abstract The RADARSAT SAR system has the unique ability to shape and steer the radar beam to permit imaging in numerous modes with varying image characteristics. Among these imaging modes, RADARSAT provides the first operational ScanSAR mode available on a satellite platform. Depending on the configuration, ScanSAR data can be acquired in nominal 300 or 500 kilometre swaths with 25 and 50 metre pixel spacing respectively.

The ScanSAR mode has proven to be an excellent tool for acquiring regional information, providing a means of rapidly and cost effectively mapping large areas while still retaining a high level of detail in the image product. In Southeast Asia the utility of this product has been translated into numerous regional mosaics which are being utilized in various resource development projects through the area.

This paper discusses ScanSAR image quality issues related to the production of regional scale mosaics, reviews the mosaicing process and finally addresses the application of these unique products. Examples of geocoded and ortho-rectified image mosaics will be illustrated.

1. INTRODUCTION

The RADARSAT program has been designed to provide operational functionality, first to meet Canadian earth observation requirements, and secondly, to address global earth observation requirements. As part of the process, considerable effort was spent addressing mission requirements from the perspective of data users [1],[2]. The results of this effort have been incorporated into the many elements of the RADARSAT system. Various aspects of the system have been described in considerable detail elsewhere [3],[4].

A unique feature of the RADARSAT system is the ScanSAR imaging mode which provides a useful wide area coverage capability. Although the image resolution is reduced, the ability to image large areas in a single pass provides an opportunity to effectively undertake broad area surveillance. In addition, it affords an opportunity for more frequent imaging than is normally possible. Figure 1 shows a full ScanSAR narrow scene (300 kilometre swath) of the Mekong Delta region of Vietnam.

Figure 1 ScanSAR Narrow image of Vietnam, acquired September 15, 1996. © Canadian Space Agency/Agence spatial canadienne.

2. SCANSAR IMAGE QUALITY

RADARSAT single-beam modes have a nominal swath width ranging from 50 km for Fine mode to 150 km for Wide mode. To achieve significantly wider swath widths in a single satellite pass, the ScanSAR imaging mode was developed. ScanSAR details are given elsewhere [3]. The

0-7803-3836-7/97/$10.00 © 1997 IEEE

ScanSAR mode is capable of operating in two combinations: ScanSAR Narrow gives a nominal 300 km swath width and ScanSAR Wide gives a nominal 500 km swath width (50 m and 100 m resolution respectively). Both modes combine single-beam Standard and Wide modes to produce the final 8-bit ScanSAR image.

To achieve the wide ScanSAR swath widths, the RADARSAT pulse repetition frequency (PRF) was modified, which also introduced nadir ambiguities near the edge of images with adjoining beams [5]. Beam overlaps were created between adjacent beams through PRF modification thus eliminating nadir ambiguities from all RADARSAT single-beam modes except Wide 3. Because of the beam-combining methods used to produce ScanSAR imagery, nadir ambiguities are to some degree present in all ScanSAR modes. The impact on the two ScanSAR Narrow modes is minimal since the ambiguity occurs in overlap region between the Standard and Wide modes. For one of the two ScanSAR Wide modes, however, the Wide 3 nadir ambiguity occurs in about the middle of the beam thus producing an unusually strong return in the azimuth direction. The impact on data quality on either side of the ambiguity is negligible.

Doppler centroid estimation (DCE) is the process of determining the Doppler frequencies corresponding to the Doppler spectrum of the received signal. Due to the burst structure of the data received during ScanSAR mode, DCE errors result in scalloping. Scalloping is a high frequency modulation along the image due to unbalanced Doppler filter placement, and manifests itself as banding in the azimuth direction. DCE errors also introduce geometric errors. If the Doppler filters have an error which is an integral number of PRF's, then feature location errors of about 5 km per PRF error will occur [6]. In addition, if the Doppler filters straddle a multiple of the PRF, ghosting (the appearance of the same feature at two different azimuth locations) with about 5 km azimuth displacement, has been reported [7]. Improvements in the DCE are ongoing during the ScanSAR qualification period.

Other ScanSAR image artifacts include radiometric imbalance between the beam modes that comprise the ScanSAR image. This radiometric imbalance is range dependent, and appears as a visible stripe where two beams join. Improved techniques to mosaic beam modes together have significantly reduced the radiometric imbalance. Cosmetic alterations of the ScanSAR imagery, similar in concept to antenna pattern corrections, have also been used, but at the expense of a slight reduction in overall radiometric fidelity.

Finally, RADARSAT incorporates an automatic gain control (AGC) that sets the recorded signal intensity when in imaging mode. Dark rangeward bands, that sometimes appear in the imagery, have been attributed to saturation of RADARSAT's 4-bit analog-to-digital converter [8]. The AGC is controlled using range samples 1025 to 3072. Therefore, for the case of an image acquired with low backscatter in the near range (water for example) and high backscatter in the far range (land for example), the far range portion will appear darker than it should; the reverse situation is also true, but rarely observed. Implementation of a scheme whereby the AGC can be turned off has virtually eliminated the AGC problem.

3. MOSAIC PRODUCTION

The ability to image large areas rapidly is an important benefit of the ScanSAR mode. This capability is being utilized routinely in Canada to assist in mapping large marine areas in support of shipping activities. However the combined advantages of wide area coverage and reliable access to data are also important in the tropical belt where it has been possible to create large regional mosaics in areas where up to date information is lacking.

This has been particularly important in Indonesia and other South East Asia countries where regional and country-wide mosaics have been prepared to support various resource development activities (Figure 2).

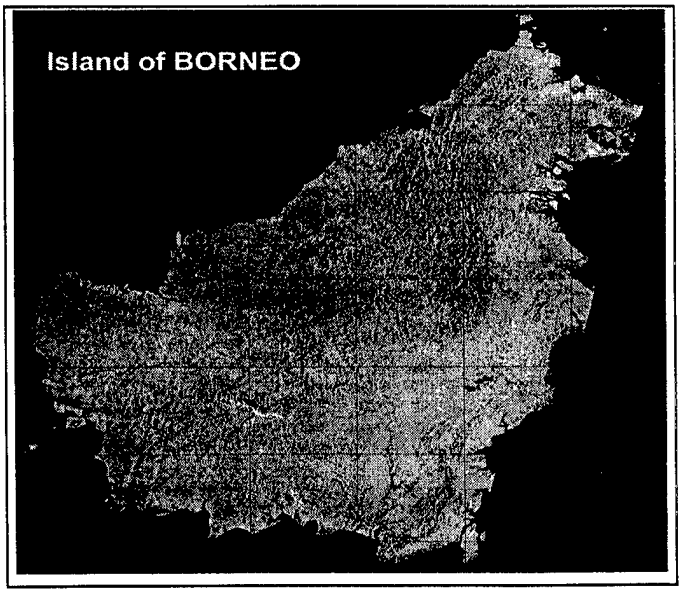

Figure 2 Mosaic of Borneo using ScanSAR Narrow imagery. © Canadian Space Agency/Agence spatial canadienne.

The SE Asia ScanSAR Narrow RADARSAT Mosaics are composed of multiple ScanSAR Narrow RADARSAT scenes which have been geometrically processed, enhanced and

merged into map oriented mosaics with 50 metre pixels. The mosaics are geometrically corrected to map coordinates in UTM projection. Assessment of the positional accuracy of the mosaics has shown them to be accurate to within 200M at sea level.

The ScanSAR Narrow radar signal intersects the earth's surface at an incidence angle which varies from 31° to 46° to vertical, across each ScanSAR scene leading to geometric distortions in the image. With the radar data geometrically corrected to sea level, the inclined RADARSAT signal results in the locations of radar returns from elevations above sea level being offset towards the satellite by a distance equal to the product of the cotangent of the angle of radar incidence and the elevation. For example, with a topographic elevation of 2,000 m and an incidence angle of 31°, the radar return is offset 3,300 metres towards the satellite from its correct map location. At 2,000 m elevation and an incidence angle of 46° the offset is 1,900 metres towards the satellite.

The topographic distortion of the RADARSAT data can be corrected using digital topographic data. Thirty arc second (approximately 1 km) resolution digital topographic data is available from SE Asia from NASA, via the US Geological Survey's EROS Data Centre in Sioux Fall South Dakota. The NASA digital topographic data can be used to correct the major, longer wavelength topographic distortions in the mosaics. In cases where more detailed topographic data is available the ScanSAR data can be rectified with this data yielding increased geometric fidelity.

4. SCANSAR APPLICATIONS

RADARSAT ScanSAR data is an effective tool for providing an overview of large areas. In the ScanSAR Narrow mode the 50m resolution provides sufficient detail to permit general assessment of land cover and ocean conditions while the Wide mode (100m resolution) is still adequate for coarser scale mapping. Key applications of the data to date have included the following:

- regional and country-wide mosaics for geological mapping
- general land cover mapping
- detection of naturally occurring marine oil seeps
- ship detection and sea ice mapping

5. CONCLUSIONS

Despite the image quality challenges presented by the ScanSAR product, the imagery has been used successfully for a variety of applications. It is expected that this use will increase particularly in areas where access to regional scale data is difficult or where routine monitoring is required.

REFERENCES

[1] Canadian Space Agency. *RADARSAT Mission Requirements Document*, RS-CSA-SP0001-NC, RADARSAT Program, 1991.

[2] Parashar, S., E. Langham, J. McNally, S. Ahmed, "RADARSAT Mission Requirements and Concept", *Canadian Journal of Remote Sensing*, Vol. 19, No. 4, November 1993.

[3] Raney, R.K., A.P. Luscombe, E.J. Langham, and S. Ahmed, RADARSAT. *Proceedings IEEE*, Vol. 79, No. 6, June 1991.

[4] Luscombe, A.P., I. Ferguson, N. Shepherd, D.G. Zimick, and P. Naraine, The RADARSAT Synthetic Aperture Radar Development. *Canadian Journal of Remote Sensing*, Vol. 19, No. 4, November-December 1993.

[5] Luscombe, A.P., Nadir Ambiguities in RADARSAT Imaging, Proceedings CEOS Workshop on RADARSAT Data Quality, Canadian Space Agency, St-Hubert, Canada, February, 1997.

[6] Gray, R., Doppler Centroid Estimation Errors and Image Quality, Report No. AS96-001 prepared for the Canadian Space Agency, July, 1996.

[7] Werle, D., RADARSAT SAR Azimuth Ambiguity Patterns - The Ghost Fleet of Halifax Harbour and Implications for Applications Work, Proceedings CEOS Workshop on RADARSAT Data Quality, Canadian Space Agency, St-Hubert, Canada, February, 1997.

[8] Vachon, P.W., A.L. Gray, and A.L. Luscombe, RADARSAT SAR Analog-to-Digital Converter Saturation, Proceedings 6th. Workshop of the Canadian Ice Working Group, Ottawa, Canada, November, 1996.

Using the RADARSAT SAR Versatility to Enhance Fine Resolution Imaging Capabilities

A. P. Luscombe,
SPAR Aerospace
21025 Trans-Canada Highway,
Ste-Anne-de-Bellevue, Quebec, H9X 3R2 Canada
Phone: 514 457-2150 (x3641) Fax: 514 425-3041
E-mail: aluscomb@spar.ca

D. A. Furseth,
RADARSAT International
3851 Shell Road, Suite 200
Richmond, BC V6X 2W2 Canada
Phone: 604 231-4912 Fax: 604 231-4900
E-mail: dfurseth@rsi.ca

S.K. Srivastava
Canadian Space Agency
6767 route de l'Aeroport
St. Hubert, Quebec J3Y 8Y9 Canada
Phone: 514 926-5133 Fax: 514 926-5167
E-mail: Satish.Srivastava@space.gc.ca

W.C. Jefferies,
RADARSAT Interational
75 McClelland Road
Cantley, Quebec J8V 2Y8 Canada
Phone: 819 827-3001 Fax: 819 827-1955
E-mail: bjefferies@rsi.ca

Abstract -- The RADARSAT SAR design includes a number of selectable and programmable features to provide the wide range of operational imaging modes, ranging from ScanSAR to Fine Resolution. The potential range of imaging capabilities which this versatile instrument could provide is significantly larger than is currently offered operationally, and additional modes are progressively being introduced to meet identified demand. This paper considers the fine resolution imaging capabilities, describing some additional options which are now available and suggesting further modes, with wider access and even finer resolution, which the instrument could provide in the future.

INTRODUCTION

Canada's RADARSAT-1 Earth observation satellite is the first civilian satellite Synthetic Aperture Radar (SAR) mission to include a wide range of imaging modes covering different swath widths, resolutions and imaging angles [1]. It is also the first civilian satellite SAR to offer a fine resolution imaging mode. These capabilities are provided through a SAR system which was designed to be very versatile in its operations, allowing selectable chirp bandwidth, pulse repetition frequency (PRF), timing parameters, and beam patterns and directions. With this degree of flexibility in the SAR operations, the potential range of imaging modes is considerably larger than is routinely used.

During the first year of RADARSAT operation, the greatest commercial demand has been for the Fine Resolution mode. This mode offers a resolution of better than 9 m in both range and azimuth, and with options for either real time data downlink or data recording and playback, this imaging capability is available for the entire globe. The RADARSAT system currently provides imaging options covering incidence angles from 36 to 48 degrees, with image swaths of 37 to 45 km width with recorded data or 49 to 57 km using the real time downlink.

Initially, a choice of five Fine Resolution Beam positions was offered by the order desk for routine operations, but it was found that this limited choice unnecessarily restricted the completeness, flexibility, and efficiency of the fine resolution coverage. In particular, it did not allow RADARSAT to operate optimally in providing fine resolution mapping and monitoring in cloud-covered equatorial regions. As an illustration of the effective use of the RADARSAT instrument's versatility, this paper explains how the ground segment was modified to operate the SAR so as to satisfy these fine resolution mapping requirements.

The paper also considers some further potential enhancements to fine resolution imaging capabilities, which could extend the range of incidence angles that can be imaged. These capabilities would also be provided with the existing versatile features of the design using the wide bandwidth pulse together with appropriate selections of beam pattern, PRF and timing parameters. This extended range of fine resolution incidence angles would give improved revisit frequency for monitoring applications, provide better choice in applications requiring specific imaging angles, and allow enhanced fine resolution stereo imaging.

RADARSAT SAR VERSATILITY

Three main features were included in the RADARSAT SAR design [2] to provide a wide range of imaging options:

o Elevation beamforming with 32 phase shifters across the antenna width and a fixed amplitude distribution. Sets of coefficients for 20 beams are stored on-board the satellite, any of which can be replaced by another set uplinked from the ground;

o A choice of pulse forms, with three preprogrammed chirps covering different bandwidths (including the 30 MHz chirp used for Fine resolution imaging) and a programmable pulse register. Filters and sampling rates corresponding to each of the pulse defined bandwidths are available in the receiver;

o Programmable timing parameters such as Pulse Repetition Frequency (PRF), receive window start time and duration.

With appropriate combinations of these parameters and functions, the SAR can be commanded to image in the operational imaging modes (Standard, Wide Swath, Fine Resolution, ScanSAR and Extended High and Low Incidence) which offer wide ranges of viewing angle, resolution and swath width. In the Fine Resolution mode, for example, the wide bandwidth (30MHz)

0-7803-3836-7/97/$10.00 © 1997 IEEE

options are selected for the pulse, filter and sampling rates. One of the five Fine Resolution Beams stored on-board the satellite is chosen to illuminate the required region, and the PRF and receive window duration and start time are set so as to give reception of signals from the required swath without exceeding the data rate limit and without interference from pulse transmissions or ambiguities from the nadir area.

AUGMENTING THE FINE RESOLUTION COVERAGE

The initial configuration of the RADARSAT system offered five beam positions in Fine Resolution mode, one for each of the beams stored on-board the satellite. Because the real time downlink permits a higher data rate than the on-board recorder, a longer receive window is used for the former. This gives coverage of a wider swath (49 to 57 km) for real time downlink than when using the on-board recorder (37 to 45 km). The initial five positions span an incidence angle range of 37 to 47 degrees and an accessibility swath of about 210 km. Real time swath positions overlap by more than 10 km, but with the narrower recorded swaths little or no overlap remains.

During the first year of RADARSAT operations, the Fine Resolution has been the most popular commercial imaging mode. Much of this interest and activity has been in cloud-covered equatorial regions where use of the on-board recorder was necessary. Experience with numerous projects in these regions revealed some practical difficulties in planning and implementing coverage schedules with recorded Fine Resolution imaging. These difficulties, as explained in [3], result from the absence of beam overlaps with the limited range of swath positions offered to users. An operation was therefore undertaken to define and implement some additional fine resolution imaging options to provide the required swath overlaps and overcome these problems. These additional options are now operationally available for users.

The main requirements for these Fine Beam additions were:

o that an overlap of at least 10km be provided between swath positions for both real time downlink and recorder operation,

o that quality be essentially the same as for existing options,

o that they could be tested and implemented quickly and easily, if possible without any modification to spacecraft software.

Various options were considered [3]. The solution that was adopted was the simplest to implement, requiring a change to only one parameter in the Payload Command Data (PCD): the receive window start time. With the additional choices that have been made available, there are now three swath positions available with each of the Fine Resolution Beams, with the additional two positions obtained by setting the receive window start time earlier and later than for the existing mode. For the recorder mode, the changes in the start time are ±60μs, and for the real time mode ±30μs. These values take into account the difference in receive window durations, and were set after consideration of the following performance aspects:

o All overlaps are at least 24km, and are approximately equal across the set of 15 recorder mode options.

o Nadir ambiguities are avoided with all swath positions, as indicated in Fig. 1, in which the ground range positions of the swaths (horizontal lines) are plotted against PRF. The diagonal bands on this plot indicate regions which cannot be imaged because returns coincide with pulse transmissions, and the single diagonal lines show the positions of nadir ambiguities.

Figure 1: Augmented Fine Beam Positions

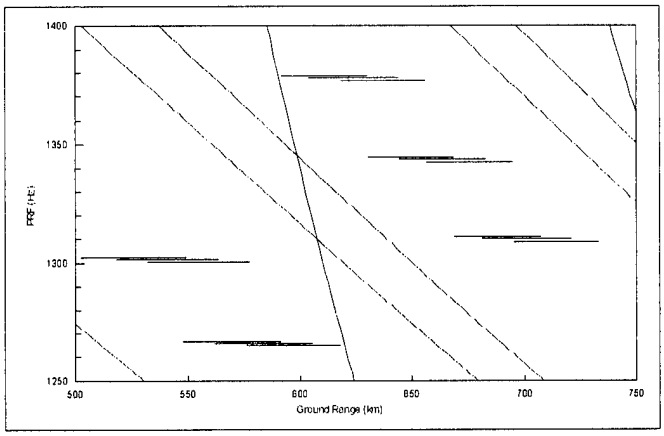

o Sensitivity, as characterised by Noise-Equivalent Sigma-Zero (NESZ), remains comparable to other current imaging modes. This aspect of performance is affected because the imaged area is now illuminated by a section of the beam further from the peak.

o Radiometric accuracy effects due to pointing uncertainties remain within budget limits. These effects are increased for the new positions because the coverage includes regions of greater gain slope in the antenna beam pattern, although less than for some of the other existing beams used operationally.

There are now a total of 15 swath positions available for any real time downlink image, and 15 positions for any recorded image. The widths and positions of these options are given in Table 1. The benefits of this wider range of options in mapping of Equatorial regions has been demonstrated in the early months of their availability.

	Real Time		Tape Recorded	
Beam Position (code)	Swath Width (approx.)	Incidence Angle Range (Degrees)	Swath Width (approx.)	Incidence Angle Range (Degrees)
Fine 1 Near (F1N)		36.4 - 39.5		36.3 - 38.9
Fine 1 (F1)	57 km	36.8 - 39.9	45 km	37.2 - 39.6
Fine 1 Far (F1F)		37.2 - 40.3		38.0 - 40.3
Fine 2 Near (F2N)		38.9 - 41.8		38.9 - 41.1
Fine 2 (F2)	56 km	39.3 - 42.1	42 km	39.6 - 41.8
Fine 2 Far (F2F)		39.6 - 42.5		40.3 - 42.5
Fine 3 Near (F3N)		41.1 - 43.7		41.1 - 43.1
Fine 3 (F3)	51 km	41.5 - 44.0	39 km	41.8 - 43.7
Fine 3 Far (F3F)		41.8 - 44.3		42.5 - 44.4
Fine 4 Near (F4N)		43.2 - 45.5		43.2 - 45.0
Fine 4 (F4)	50 km	43.5 - 45.8	37 km	43.8 - 45.6
Fine 4 Far (F4F)		43.8 - 46.1		44.4 - 46.1
Fine 5 Near (F5N)		45.0 - 47.3		45.0 - 46.8
Fine 5 (F5)	49 km	45.3 - 47.5	38 km	45.6 - 47.3
Fine 5 Far (F5F)		45.6 - 47.8		46.2 - 47.8

Notes:
1. These values are for a mid-latitude case with 800 km satellite altitude.
2. Incidence angles will change slightly (+/- 0.1 degrees) with scene latitude, primarily due to the change in altitude with latitude.
3. Product widths should be within approximately 1 km of stated width.

Table 1: Augmented Fine Resolution Parameters

ADDITIONAL FINE RESOLUTION CAPABILITIES

The additional fine resolution options described in the previous section were offered in order to support operations in mapping of Equatorial regions. The instrument is capable of providing many other additional modes, and these might be considered for implementation if they would also satisfy an identified customer need. Certain practical considerations would have to be taken into account, however, before that decision could be made:

o RADARSAT is an operational system with a large number of users depending upon its reliable operation. Implementation and testing of new modes should not disrupt routine operations.

o To ensure continuity, the improved capability should be compatible with the existing imaging modes and products.

o Changes to the Space Segment should be avoided if possible.

o Changes to operations and documentation in all elements of the ground segment (Mission Management Office, Network Stations, processors, products, etc.) should be minimized.

The additional capabilities that have already been provided are simple in concept, but still required significant changes in the ground segment operations. The image planning and payload command generation had to include the new options, for example, and product descriptions and identifications had to be modified in all processing, archiving, distribution and sales activities.

The following subsections identify further potential extensions to fine resolution capabilities, and explain how they could be provided using the versatile elements in the instrument design. In practice, however, these are only likely to become operational capabilities if they meet the criteria of need and practicality.

Extended Angular Accessibility

The Fine Resolution Beams currently provide access to a width of about 230km between incidence angles of about 36° and 48°. This region was chosen to take advantage of the inherently finer ground range resolution at higher incidence, and is at the far edge of the 500km Standard Beam accessibility region. The SAR can use the wide bandwidth pulse for imaging at any angle, however, and so finer resolution images could be obtained anywhere within the wider access region. (Azimuth resolution would be essentially the same as for the current modes, and ground range resolution would be better than 12m for all but the first 80km.) Of potentially even greater interest would be fine resolution imaging at higher angles, over the region currently covered with the High Incidence Beams, where the ground range resolution would be even finer (about 6m at 60° incidence). With these extensions from 20° to 60° incidence, total access is increased to about 800km.

These capabilities could be provided by uploading beams specifically designed to illuminate the required swaths. Because of the limited number of beam table locations available on the satellite, however, this is likely to require frequent replacement of beams and updating of information for all network stations.

A more practical approach, with only a small impact on imaging performance, is to use the fine resolution pulse with existing beams which were originally defined for use with the lower bandwidth pulses. Because of the higher sampling rate, the receive window and the imaged swath will be narrower for fine resolution imaging, but full accessibility can be achieved using two or more receive window start times with each beam.

Non-standard combinations of beam pattern and pulse have been demonstrated experimentally. To implement a full range of swath positions operationally would require significant modification in the ground segment (as indicated above), but could be considered if a major customer base were identified.

Finer Resolution Image Production

The current fine resolution images are produced with single-look, coherent processing across the full nominal pulse bandwidth in range and a Doppler bandwidth corresponding to about 95% of the antenna 3dB-beamwidth in azimuth. In both dimensions, a standard weighting (about 9dB taper) is applied in the processing. If some relaxations could be allowed for other aspects of image quality (principally, impulse response sidelobes and azimuth ambiguities), the system could provide even finer resolution in both dimensions. The principal change in the instrument operation is to use a higher PRF (but within duty cycle constraints for the amplifier). This would allow coherent processing to be performed over a wider Doppler bandwidth without causing high azimuth ambiguities. When this change in processing is combined with a significant reduction in weighting, reductions by as much as 30% in azimuth and 15% in range could be achieved.

SUMMARY

The RADARSAT SAR provides operational capabilities in a wide range of imaging modes. The Fine Resolution mode has proven to be the most popular mode for commercial customers during the first year of operations. Initially, a choice of only five swath positions was offered to users for fine resolution imaging, but this choice has now been expanded to 15 to provide the larger overlaps required to allow efficient mapping strategies. The additional capabilities were provided using the versatile features built into the instrument design. Further potential additional fine resolution modes have been identified to provide a much wider accessibility and even finer resolution. Operational implementation of these modes depends on there being an identified need, and on the practicalities of performing the necessary associated modifications in the ground segment.

References

[1] R.K.Raney, A.P. Luscombe, E.J. Langham and S. Ahmed, "RADARSAT", Proc. IEEE, vol. 79, pp. 839-849, June 1991.

[2] A.P. Luscombe, I. Ferguson, N. Shepherd, D.G. Zimcik, P. Naraine, "The RADARSAT SAR Development," Canadian Journal of Remote Sensing, vol. 19, pp. 298-310, Nov 1993.

[3] D.A. Furseth, A.P. Luscombe, W.C. Jefferies and S. Srivastava, "Using RADARSAT's Imaging Versatility to Improve Fine Resolution Mapping Capabilities", Proc. GER '97, Ottawa, Canada, May 25-30 1997.

RADARSAT Image Quality and Calibration Results

S. K. Srivastava[1], R. K. Hawkins[2], T. I. Lukowski[2], B. Banik[1], M. Adamovic[1]

[1]RADARSAT Operations, Canadian Space Agency
6767 Route de l'aéroport, Saint-Hubert, Québec, J3Y 8Y9, Canada
Tel: (514) 926-5133, Fax: (514) 926-5167, Email: Satish.Srivastava@space.gc.ca

[2]Canada Centre for Remote Sensing, Natural Resources Canada
588 Booth St., Ottawa, Ontario, K1A 0Y7, Canada
Tel: (613) 995-1067, Fax: (613) 947-1383, Email: Hawkins@ccrs.emr.ca

Abstract -- In this paper, we present an overview for the initial calibration of RADARSAT beams and modes, the elements of the operational calibration of RADARSAT data, progress to date in executing the calibration plan, and some general information on the image quality performance achieved to date.

INTRODUCTION

The Canadian Earth observation satellite, RADARSAT was launched on November 4, 1995. After commissioning, it was put into routine operation on April 1, 1996. Since then we have completed one year of successful operation, demonstrating and utilizing data for their intended applications. The overall requirements for image quality are laid out in the System Specification Document for RADARSAT [1]. This included consideration of radiometry, location fidelity, impulse response characteristics, as well as swath size and image sampling characteristics. The CEOS Working Group on Calibration and Validation conducted a three-day symposium on RADARSAT data quality in February, 1997 at the Canadian Space Agency; readers should consult the proceedings [2] for a more complete picture. In this paper, we are primarily concerned with the image quality and radiometric properties associated with the image products generated by the Canadian Data Processing Facility (CDPF). It was clear from our first considerations on the subject that data volume dictates that the only feasible model for the calibration of products from this operational satellite is to build that calibration into the product itself.

CALIBRATION MODEL

In this model, we needed to build into the satellite and ground segment operations the hardware and interfaces which would enable us to determine and update automatically in the processing chain as many as possible of the dynamically varying system parameters. Parameters which are provided or updated automatically for each processing sequence include the following:

- Spacecraft ephemeris data including: velocity and position vectors through predicted or reconstituted orbit information,
- Spacecraft attitude as deduced from Doppler frequency and interbeam radiometry characteristics,
- Transmitted power and receiver gain through the recording and subsequent processor analysis of the pulse replica information,
- SAR mode and beam configuration through appropriate normalizations in the processor,
- Antenna pattern mask placement, and range-dependent fall off in the received power across the swath.

More slowly varying properties or initialization parameters for the system would be determined off line, monitored in time, updated as required and fed back into the processing stream by the Mission Management Office (MMO). Those parameters which are deemed to be more slowly varying include:

- **Antenna pattern shape and absolute gain for the system** - the determination of the antenna pattern shape and overall system gain are described briefly in [3],
- **Range chirp phase characteristics** - are output by the processor with each image product using replica data. However, they were fixed early on in the mission and fixed parameters are used in the processing,
- **System noise** - is determined from a special calibration sequence in the spacecraft and processing in the CDPF and a thermal noise reference level (TNRL) is provided in the product. The levels for RADARSAT are considerably better than the specification. It is expected that the TNRL levels will soon be updated in the product.

The calibrated products generated by the CDPF are in terms of radar brightness β^0. Users retrieve this information from the Digital Numbers (DN's) through use of a Look Up Table included in the product as described in [4].

0-7803-3836-7/97/$10.00 © 1997

RESULTS

There are several aspects of image quality which are part of the operational "calibration" of RADARSAT which should be highlighted. These include:

- **Impulse Response Characterization**
- **Location Accuracy**

Parameters are determined from use of the RADARSAT Precision Transponders [5] and have been reported in detail elsewhere [6] to significantly exceed the system specification. A summary of the image quality performance for single beam products is given in Table 1.

There are problems in the ScanSAR processor in estimations of Doppler centroid and beam pointing. As a result, occasionally scalloping effects and visibility of beam boundaries are observed in products produced by the CDPF. Therefore ScanSAR products are not yet qualified. Work is in progress to correct or minimize these problems.

Table 2 is a chronology of progress to date and plans for the completion of the radiometric calibration of RADARSAT. Based on the measurements, for the beams calibrated to date we note the following from Table 3 which summarizes the worst case results during the Calibration Phase:

- RADARSAT beam pattern variation during the first year of operation seems to be small.

- RADARSAT calibration uncertainty seems to be dominated by the combined effects of placement of the antenna mask and apparent overall gain variations in the system.

- The greatest uncertainties are near the edges of the beams where the effects of roll pointing uncertainty in the satellite is highest. Roll uncertainties as high as 0.3 degrees have been observed. This is particularly important in ScanSAR.

The radiometric uniformity of ScanSAR images has improved remarkably with the updates to the constituent beam patterns (S5, S6, S7, W1, W2 and W3) which have occurred during the past year. It is expected that ScanSAR data quality will improve even more when the dynamic beam pointing algorithm will be updated in the CDPF since this will significantly improve matching in the interbeam region.

Table 1 Measured Image Quality Performance Summary

Parameter	Comparison with Specs
Ground range resolution	Better by 11.5%
Azimuth Resolution	Better by 8.4%
Range PSLR	Better by 1.0 dB
Azimuth PSLR	Better by 2.7 dB
Absolute Location Error	Better by 78%

Table 2 Chronology and Plan for Radiometric Calibration of RADARSAT

Dates	Activity	Significant Results
December, 1995 to March, 1996	Characterization and Qualification Phase	- Chirp Phase coefficients established (February, 1996). - Many final integration aspects corrected. - Some beams reduced in swath to exclude nadir ambiguity (March, 1996). - Single beam products in 500 km accessibility swath qualified in terms of swath and impulse response (April, 1996).
March, 1996 to July, 1997	Qualification and Calibration Phase	- SGF products for beams EH1-EH6 qualified in terms of swath and impulse response (August, 1996). - Shifted fine beams introduced (November, 1996). - Beams S1-S4 calibrated (November 27, 1996). - Beams S5-S7 and W1-W3 calibrated (February 14, 1997). - Products for beam EL1 qualified in terms of swath and impulse response (April, 1997). - Thermal noise references for all beams (to be established by May, 1997). - Calibration of currently available extended high and low beams (to be completed by July, 1997). - ScanSAR qualification and calibration (to be completed by July, 1997).

CONCLUSIONS

The image quality measurement results indicate that the RADARSAT System is meeting and exceeding its performance specifications. The operational objectives for producing radiometrically calibrated products for all beams and processing modes will soon be achieved for the CDPF. In fact a number of beams have already been calibrated as indicated in Table 2. The process has been long due to the large number of beams (22) and products available. We believe, however, that end users can count on high quality data that will serve their needs for quantitative measurements from RADARSAT products.

ACKNOWLEDGMENTS

The RADARSAT program owes its success to the vision and efforts of a very large group of dedicated people. Besides the authors, the team directly involved in measurements and maintenance of RADARSAT data quality consists of the following individuals: Bill Jefferies, RSI; Tony Luscombe, Spar Aerospace; Nick Shepherd, ALTRIX; Rob Gray, ALTRIX; and Caroline Cloutier, CCRS. The authors also thank other staff from CSA, CCRS and RSI for supporting the calibration activities.

REFERENCES

[1] RADARSAT System Specification", CSA Document RSCSA-SP0002, Rev C, 1996.

[2] Proceedings of a Committee on Earth Observations (CEOS) Workshop on RADARSAT Data Quality, LD Arsenault, Ed. Saint-Hubert, Canada: CSA, February 1997.

[3] T. I. Lukowski et al., "RADARSAT elevation antenna pattern determination," (These proceedings).

[4] NW Shepherd, Extraction of Beta Nought and Sigma Nought from RADARSAT CDPF Products, ALTRIX Systems Report AS97-5001, 9p., February 1997. This report is appended to [2].

[5] R. K. Hawkins, L. D. Teany, S. K. Srivastava and S. Y. K. Tam, "RADARSAT precision transponders," Advances in Space Research, in press [Presented at COSPAR'96, July 1996].

[6] S. K. Srivastava et al., "Calibration and image quality performance results of RADARSAT," Advances in Space Research, in press [Presented at COSPAR'96, July 1996].

Table 3 Measured Worst Case Radiometric Calibration Accuracy for Beams S1-S7 and W1-W3

Property	Unit	Central 80%		Whole Beam	
Beam Pointing Stability	[deg]	0.3		0.3	
Beam Pattern Stability	[dB]	0.2		0.2	
Processing Replica Error	[dB]	0.2		0.2	
Point and Distributed Target Pattern Agreement	[dB]	0.2		0.2	
Point and Distributed Target Level Agreement	[dB]	0.5		0.7	
Relative Accuracy within Scene	[dB]	0.8		1.04	
		Measurement	Mission Lifetime Goal	Measurement	Mission Lifetime Goal
Overall Accuracy[1]	[dB]	1.4	3.0	1.6	3.0

[1] Measurements performed with matched AGC setting and limited dynamic range.

A Preliminary Study of Phenological Growth Stages of Wetland Rice using ERS1/2 SAR Data

Saiful Bahari b. Abu Bakar and Abdul Talib b. Shaari
Malaysian Centre for Remote Sensing
CB100, 5th Floor
City Square Centre
Jalan Tun Razak
MALAYSIA
Tel:+603-2645640
Fax:+603-2645646

H. T. Chuah and H.T. Ewe
Faculty of Engineering
Telekom University
Bukit Bruang, Jalan Ayer Keroh Lama
Melaka
MALAYSIA
Tel:+606-2523420
Fax:+606-2318696

Abstract -- This paper investigates the suitability of use of space-borne multi-date SAR images (ERS1/2) for monitoring of growth stages of wetland paddy crops. Four study sites are selected in the Kedah State, Malaysia, which produces 39% of total paddy output in the country. The period of study is from April to September 1996, which covers the first cropping in the year. Groundtruth measurements on soil and paddy plants are conducted around the days of data acquisition. In general, the phenological growth stages of wetland rice can be classified into five main stages: soil preparation, germination, vegetative, ripening and harvest. Preliminary results indicate that space-borne radar imagery has a great potential for delineation and monitoring different growth stages of wetland rice.

INTRODUCTION

Rice is the staple food in Malaysia. The growing areas for paddy (*Oryza sativa*) form about 12.7% of total cultivated vegetation areas in the country. The identification and real-time monitoring of paddy areas is therefore essential for economic reasons. Traditionally this has been done by using optical remote sensing data such as SPOT. However, due to cloud cover over the country, year-round optical data are not possible. The use of microwave remote sensing technology is thus a logical choice. Some work has recently been reported on the use of ERS-1 data for rice monitoring in the temperate regions [1]. This paper reports on a similar investigation of the suitability of using SAR images to monitor the phenological growth stage characteristics of wetland rice in the tropical region. The study site is at Kedah, a Northern State in Peninsular Malaya, which accounts for 39% of total paddy fields (about 97,200 hectares during main season) in Malaysia [2]. Double cropping is practised in Malaysia, where the first cropping is planted around April and harvested around September; while the second cropping covers the period from October to February the following year. The images used are multi-date images from ERS 1/2. Although our initial plan also includes the use of RADARSAT data, we are unable to present those results in this paper at the point of writing. The main difficulty encountered is the rescheduling of the data acquisition by RADARSAT due to unforeseen circumstances. Groundtruth measurements are conducted around the day of data acquisition. These include moisture content of the soil, soil composition, water depth, plant height, plant density, sizes and moisture contents of leaves, stems and stalks. The study covered the period from April to September 1996. From our analysis, generally there is an increase in backscatter as the plant grows and the biomass increases. Then the backscatter saturates and drops as the plant matures and dries before harvest. Preliminary results indicate that backscatter returns vary with phenological growth stages of the paddy plants which can be divided into 5 main stages: Soil Preparation, Germination, Vegetative, Ripening, and Harvest [3]. This study shows that space-borne SAR images can be a useful tool for delineation and monitoring of paddy growing areas in a tropical condition.

FIELD WORK

Four paddy fields in the Kedah State had been selected for the study: Kampung Tanah Seratus (Lat. 6° 1' 50.5''N, Long. 100° 21' 53.1''), Kampung Rambai (Lat. 6° 2' 6.7''N, Long. 100° 27' 8''), Kampung Hutan Kandis (Lat. 6° 11' 1.4''N, Long. 100° 24' 33.1'') and Kampung Telok Jawa (Lat. 6° 13' 24.9''N, Long. 100° 19' 36.9''). 6 field trips were conducted during the period of study from April to September 1996 (i.e. on April 27, May 19, June 1, June 25, August 11, and September 15, 1996). During each field trip, the following groundtruth measurements were made at the sites, the positions of which were checked by a GPS system:

(a) composition and moisture content of soil
(b) average height of paddy crops above the soil
(c) moisture content and sizes of paddy plant constituents such as leaves and stalks
(d) weather conditions

At each site, measurements were done on 5 samples for 5 plots. Photographs of the sites were taken and properly documented. Table 1 gives a typical measurement results on the paddy plants for Kampung Tanah Seratus.

0-7803-3836-7/97/$10.00 © 1997 IEEE

Table 1:Typical Measured Data for Paddy Field at Kampung Tanah Seratus, Kedah State, Malaysia

Date	4.27	5.19	6.1	6.25	8.11	9.15
Average height above water (cm)	17.2	59	59.0	76.8	89.7	0
Average leaf width (cm)	0.42	0.88	0.9	1.1	1.13	0
Average leaf thickness (mm)	0.11	0.14	0.14	0.17	0.22	0
Average stalk diameter (cm)	0.4	0.4	0.5	0.6	0.6	0
Average of moisture content of plant (%)	76.2	_	79.8	75.2	53.2	0
Average No. of tillers in a 0.5m x 0.5 m plot	176	186	186	132	90	0
Average No. of leaves per tiller	4	8	8	5	4-5	0

RESULTS AND DISCUSSION

Figure 1 illustrates graphically the preliminary results of the study for Site 1: Kampung Tanah Seratus. Figure 1(a) gives the average radar backscatter coefficient σ^o from the wetland paddy fields based on ERS1 (for dates: 4.27.96 and 6.1.96), ERS2 (8.11.96 and 9.15.96) as well as RADARSAT data (8.21.96). σ^o is obtained using the following equation:

$$\sigma^o = 20 \log_{10} (DN) - K \quad \text{..... (1)}$$

where DN is the SAR image digital number, K= 63.43 dB (before 8.16.96) and K=59.68 dB (after 8.16.96) for ERS1 data; while K=60.92 dB (before 8.16.96) and K=59.75 dB (after 8.16.96) for ERS2 data.

All the images have been co-registered using SPOT Panchromatic data as reference. Note that σ^o from ERS1/2 are VV-polarization.

Figures 1(b) and (c) shows the average height and moisture content of the paddy crops, respectively; whereas Figure 1(d) gives the growth stages of paddy during the study period The following observations can be made:

(a) On 4.27.96, the paddy was at its germination stage. The soil was irrigated and the field was practically flooded with water. σ^o_{vv} is low since there is very little backscatter contribution from the water surface, and the plants are very small.

(b) On 6.1.96, after 45 days, the crops were in the vegetative phase. The moisture content of the plant was high and the average height of plant above the water level was about 59 cm. In this case, σ^o_{vv} is higher since there is more returns due to volume scattering with the plant constituents.

(c) During the field trip on 8.11.96, the crops were in the ripening/mature stage. The plant moisture content was lower than that on the previous trip, but the average height was taller. σ^o_{vv} is still high, indicating that plant moisture and plant height are two important factors that control the radar backscatter returns.

(d) On 9.15.96, the paddy crops had already been harvested, leaving behind bare soil that were ploughed and prepared for the second cropping in the year. The field was also covered with water. Again we note that σ^o_{vv} is relatively low compared to those at vegetative stage, or the ripening stage.

There is an immediate plan to concentrate on the use of RADARSAT data for our next phase of study.

CONCLUSION

From this preliminary study, the backscatter coefficient σ^o of the paddy fields from ERS1/2 do vary at different growth stages. The variation reflects the conditions/states of the plants and soil surfaces such as water content and height of plant. Thus there is a great potential for application of SAR images in delineation and monitoring of paddy fields. However, much detailed work needs to be done to compare and contrast, both qualitatively and quantitatively, σ^o and the physical conditions of the fields, through groundtruth measurements and simulations. This will enhance one's confidence in the use of such space-borne data.

REFERENCES

[1] Le Toan, T., L.F. Wang, Floury, N., K.H. Ding, J.A. Kong, M. Fujita and T. Kurosu, (1997), "Rice Crop Monitoring using ERS-1 Data based on Experiment and Modelling Results,", IEEE Trans. Geoscience & Remote Sensing, Vol. 35, No. 1, pp. 41-56.

[2] Ewe, H.T., H.T. Chuah, A. Ismail, K.F. Loh, and N. Nasruddin, (1995), "Paddy Crop Monitoring using Microwave Remote Sensing Technique,", *Geocarto International*, Vol. 10, No. 3, pp. 33-41.

[3] Rashid, Abdullah, *Padi (Paddy)*, Penerbit Prisma, Petaling Jaya, Malaysia, 1991.

ACKNOWLEDGMENT

The authors would like to thank the Agricultural Department of Kedah State for their assistance in carrying out the field work, and the Malaysian Centre for Remote Sensing for its financial support.

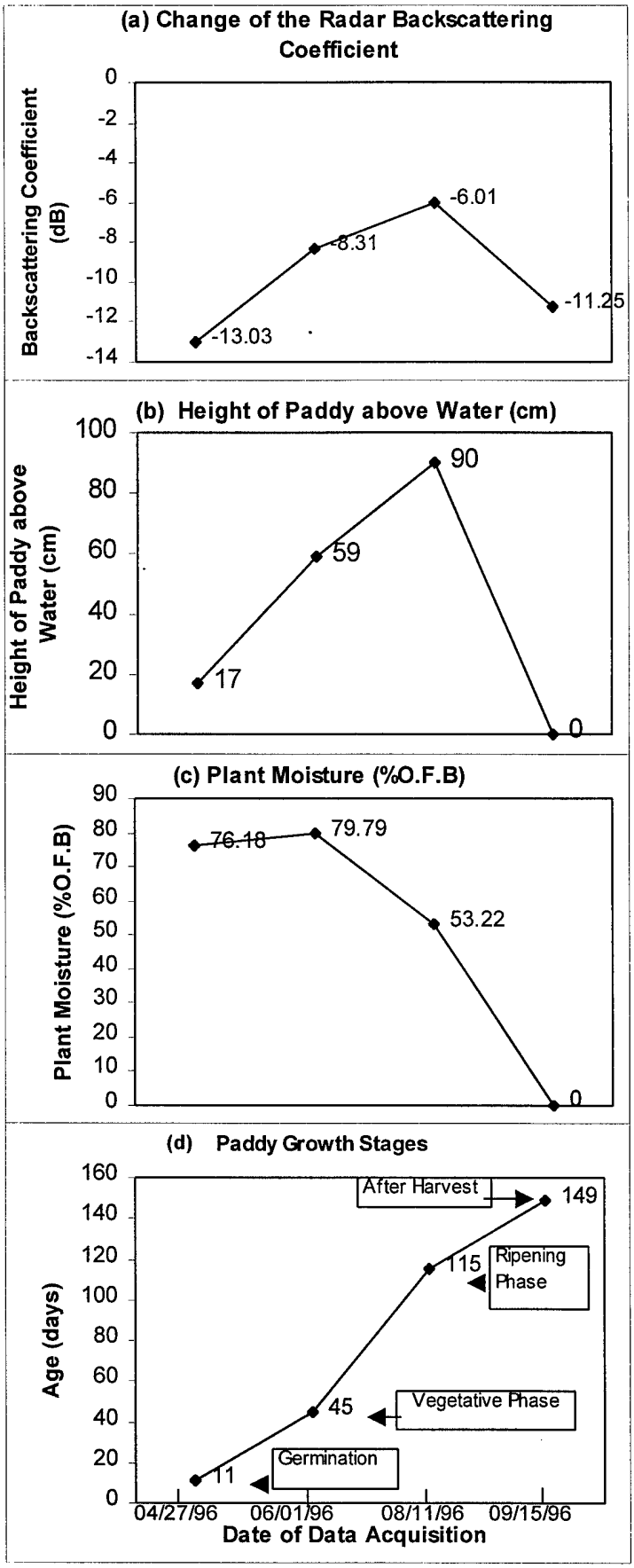

Fig 1: (a) Radar backscatter from ERS ½ Data (b) Average height of paddy crop above water level (c) Plant moisture(%O.F.B) (d) Phenological growth stages of paddy plant.

Effects of Within-Season Dielectric Variations on Terrain Classification Using SIR-C/X-SAR

Kathleen M. Bergen, M. Craig Dobson, Leland E. Pierce, Fawwaz T. Ulaby

The University of Michigan, Radiation Laboratory
Ann Arbor, MI 48109-2122 USA
FAX: +1-313-747-2106 email: kbergen@eecs.umich.edu

ABSTRACT

In this paper we investigate the sensitivity of the SIR-C/X-SAR instrument to within-season moisture perturbations for the Michigan Forests Test Site (MFTS). Precipitation events occurred at the conclusion of the October mission and thus analysis of the last four data-takes can demonstrate the relationships between SAR backscatter (σ°) and precipitation at each polarization and frequency. It is expected that backscatter is affected by incident precipitation and that the presence/absence of intercepted precipitation will be found to have the greatest impact at the shorter wavelengths and for vegetation classes characterized by low relative biomass. Four scenes for SRL-2 were acquired at a common viewing geometry (41° angle of incidence) and 24-hour revisit interval. The means and standard deviations are used to measure the sensitivity of feature vectors to intercepted precipitation and soil moisture content conditions. Differences are generated using the October 7 scene (taken before any precipitation events) as the baseline. T-tests are used to determine significance of the differences. Results show (1) that changes in σ° of agricultural fields are correlated with near-surface soil moisture and (2) changes in σ° of forested areas corresponds to senescence of deciduous foliage and the competing effects of intercepted precipitation on crown-layer attenuation. Typically, intercepted precipitation changes scattering mechanisms at shorter wavelengths (C-band) and mainly enhances attenuation at L-band. T-tests show these daily differences are commonly significant. Hence, land-cover classifications and biophysical retrieval algorithms must consider these sources of scene variability in σ°.

1. INTRODUCTION

SAR backscatter (σ°) from vegetation is a function of vegetation structural composition and its dielectric properties. Varying moisture conditions can affect σ°, and in this paper we investigate the sensitivity of the SIR-C/X-SAR instrument to a sequence of precipitation events which occurred at the Michigan Forests Test Site (MFTS) at the conclusion of the October 1994 mission. Here we analyze the last four data-takes of this mission to demonstrate the relationships between σ° and precipitation at each polarization and frequency and for different vegetation types. Regarding the latter, it is expected that low biomass vegetation classes such as short vegetation or young trees will be more sensitive to precipitation effect on σ°. Frequency/polarization combinations respond to moisture effects of different compartments. For example, for a forested area, at L-hh, soil moisture tends to dominate, at L-vv, crown effects, and at L-hv a mixture of crown, trunk and soil. In general, moisture drives up the σ°, as has been demonstrated by soil and vegetation moisture dielectric measurements [1-3]. However, this is not always the case, as it has been demonstrated with AIRSAR data that the presence of rain on conifer needles may decrease backscatter [4].

2. METHODS

Six features each for the four scenes were extracted for initial analysis: C-hh, hv, vv, and L-hh, hv, vv. X-SAR has not yet been analyzed but will be included. All data were processed by JPL and DLR to single-look complex values in slant range. Calibration values for antenna pattern correction and amplitude and phase are those provided by JPL and DLR. Data were orthorectified to a digital elevation model (DEM) interpolated from 1:100,000 DLG hypsography using a program developed jointly by VEXCEL Corporation and The University of Michigan Microwave Image Processing Laboratory. Data-takes were co-registered to the UTM grid using an automated registration program based on the correlation method [5].

Precipitation was recorded over the duration of the October mission. A network of rain gauges was distributed within the forest stands and in adjacent clearings. If we assume incident rainfall to be uniformly distributed, then the difference between recorded precipitation within and adjacent to the stands should be proportional to the rainfall intercepted by the vegetation. Precipitation events and amounts are summarized in Table 1.

Data-take 118.6 (Oct. 7) was taken before any precipitation occurred, and this provides a baseline from which to measure $\Delta\sigma^\circ$. Precipitation on Oct. 8 occurred during the over-flight of the MFTS; however, the rainfall was very scattered and would

0-7803-3836-7/97/$10.00 © 1997 IEEE

Table 1: Average Precipitation Oct. 7 - Oct. 10, 1994

Daily Precipitation (mm, stdev)				
	Oct. 7	Oct. 8	Oct. 9	Oct. 10
Clearings	0.0	1.45 (0.87)	10.31 (1.46)	4.09 (1.18)
Forest	0.0	1.10 (0.78)	8.65 (2.04)	2.29 (0.99)
Time of	none	during	during	before

have affected only some of the portions of the western part of the test site. Thus this image should show fairly minor, if any, moisture differences. On Oct. 9, rain occurred both before and during the over-flight, and throughout the MFTS. This image should show the effect of precipitation. Rain continued overnight, and while it had stopped by the time of the Oct. 10 over-flight, accumulated soil and vegetation moisture was at a peak for the sequence of scenes analyzed. Analysis of this image should show the greatest effect of precipitation.

Data were extracted from the overlap area of the four scenes for each of 45 forest test stands (each 200 x 200 m) and 27 agricultural fields using GIS polygons developed from a GPS survey which was also registered to the UTM grid. Means and standard deviations were extracted for each Level II or Level III land-cover class. Level II classes include short vegetation, northern hardwoods, aspen, lowland conifer, red pine, and jack pine. For red and jack pine, additional Level III classes based on basal area (lo BA, hi BA) were defined.

Differences were generated for each class type using the October 7 scene (taken before any precipitation occurrences) as a baseline and are calculated on a pixel-by-pixel basis as, e.g., Oct. 7 - Oct. 8. Means were also extracted for each individual stand/field and t-tests were done by class to provide a decision method to determine the significance of the $\Delta\sigma^\circ$. Further work will include extraction of X-SAR data and tests of the effect of precipitation on classifications. To determine the effect of $\Delta\sigma^\circ$ on classification, a classification will be done for the reference scene and then applied to each of the remaining three scenes. Classification accuracies can then be evaluated for each of the Level II classes.

3. RESULTS

Tables 2 and 3 give the mean σ° in dB by land-cover class for the October 7 reference scene and $\Delta\sigma^\circ$ in dB's for the remaining three scenes. $\Delta\sigma^\circ$ is generally less than 2 dB and positive with the significant exception of short vegetation (i.e., the agricultural fields). This decrease in backscatter for heavily vegetated areas corresponds to two factors: (1) the senescence of deciduous foliage, and (2) the effects of intercepted precipitation leading to either an increase in crown layer attenuation (most noticeable at L-band) and a competing increase in scattering by the crown layer (most noticeable at C-vv on October 9). The backscatter difference for the agricultural fields are correlated with observed change of near-surface soil moisture. the extent to which the observed differences in σ° are significant with respect to classification is evaluated using T-tests of the sample populations for each feature vector. These results are given in Tables 4 and 5 for L-and C-bands respectively. The T-tests show these daily differences are commonly significant, in particular at the shorter wavelength and under the greatest precipitation conditions (see Table 5). Therefore we expect that land-cover classifications and biophysical retrieval algorithms will need to consider these sources of scene variability.

4. NOTES TO TABLES 2-5.

(1) Note: N = N of pixels. (2) Note: N = N of test stands/fields. Red pine med and hi are combined into one category (hi); n. hdwds and aspen are combined to one category each. Lowland conifer results cannot be considered significant due to small sample size. Results significant to 0.10 are highlighted in bold.

5. REFERENCES

[1] McDonald, K.C., M.C. Dobson, and F.T. Ulaby, "Modeling Multifrequency Diurnal Backscatter From a Walnut Orchard, " *IEEE Trans. Geosci. Rem. Sens.* , Vol. 29, No. 6, pp. 852-863, Nov. 1991.

[2] Bergen, K.M., M.C. Dobson, L.E. Pierce, J. Kellndorfer, and P. Siqueira, *October 1994 SIR-C/X-SAR Mission: Ancillary Data Report Raco, Michigan Site*, Radiation Laboratory Technical Report 036511-6T, Radiation Laboratory, EECS Dept. The University of Michigan, Ann Arbor, MI, Dec. 1995b.

[3] Dobson, M.C., K. McDonald, F.T. Ulaby, and T. Sharik, "Relating the Temporal Change Observed by AIRSAR to Surface and Canopy Properties of Northern, Mixed Conifer and Hardwood Forests of Northern Michigan," *Proceedings of the Third Airborne synthetic aperture Radar (AIRSAR) Workshop*, Jet Propulsion Laboratory, Pasadena, CA, May 20-24, 1991, JPL Publication 91-30, pp. 34-43, August 1, 1991.

[4] Schowengerdt, Robert A., *Techniques for Image Processing and Classification in Remote Sensing*, New York : Academic Press, 1983.

[5] Bergen, K.M., M.C. Dobson, T.L. Sharik, I.J. Brodie, *Structure, Composition, and Above-ground Biomass of SIR-C/X-SAR and ERS-1 Forest Test Stands 1991-1994, Raco, Michigan Site.* Radiation Laboratory Technical Report, 026511-7-T, Radiation Laboratory, EECS Dept. The University of Michigan, Ann Arbor, MI, Oct. 1995a.

Table 2: Effect of precipitation on L-band σ° (1).

Class	N	Oct 7 (118.6)			Oct 8 (134.3)			Oct 9 (150.2			Oct 10 (166.1)		
		σ° L-hh	σ° L-vv	σ° L-hv	Δ L-hh	Δ L-vv	Δ L-hv	Δ L-hh	Δ L-vv	Δ L-hv	Δ L-hh	Δ L-vv	Δ L-hv
short veg	6386	-18.629	-17.231	-27.628	-0.174	-0.229	-0.074	-2.061	-0.448	-2.297	-3.298	-1.208	-3.608
red pine lo BA	467	-7.806	-10.895	-14.579	0.838	0.656	0.585	1.082	0.777	0.876	0.352	0.671	0.201
red pine med BA	116	-6.115	-9.640	-12.691	0.98	1.568	0.713	1.951	0.419	0.329	0.357	-0.526	0.508
red pine hi BA	516	-6.392	-8.338	-11.870	0.44	0.93	0.517	1.037	1.074	0.75	0.473	0.722	0.488
jack pine lo BA	1764	-8.698	-11.830	-15.623	0.969	0.297	0.698	0.982	0.196	0.715	0.174	0.322	0.181
jack pine hi BA	814	-7.233	-10.217	-14.069	1.074	0.773	0.856	1.226	0.623	0.674	0.313	0.439	-0.256
lowland conifer	180	-7.980	-9.053	-14.397	0.075	0.152	0.223	0.058	0.785	0.228	-0.425	0.522	-0.353
n. hdwd med BA	254	-8.300	-9.632	-14.364	1.266	0.238	0.332	2.104	1.073	0.684	0.864	0.674	0.227
n. hdwd hi BA	900	-8.239	-8.687	-13.510	0.488	0.942	0.918	1.163	1.363	1.542	0.624	1.408	0.661
aspen lo BA	212	-9.187	-10.194	-16.134	1.29	1.224	0.97	1.309	1.682	0.539	0.737	1.711	-0.539
aspen med BA	219	-8.116	-9.335	-14.320	0.701	0.688	0.093	1.089	1.168	0.505	-0.018	0.985	-0.505

Table 3: Effect of precipitation on C-band σ° (1).

Class	N	Oct 7 (118.6)			Oct 8 (134.3)			Oct 9 (150.2			Oct 10 (166.1)		
		σ^0 C-hh	σ^0 C-vv	σ^0 C-hv	Δ C-hh	Δ C-vv	Δ C-hv	Δ C-hh	Δ C-vv	Δ C-hv	Δ C-hh	Δ C-vv	Δ C-hv
short veg	6386	-11.847	-13.465	-19.376	0.464	0.222	0.286	-0.247	-1.183	-0.784	0.504	-0.254	-0.51
red pine lo BA	467	-10.216	-11.107	-15.997	-0.207	0.031	0.063	-0.089	-0.71	-0.34	0.48	0.645	0.595
red pine med BA	116	-9.727	-10.784	-15.103	0.635	1.152	1.806	0.484	-0.267	0.729	0.776	0.545	1.365
red pine hi BA	516	-9.287	-9.690	-14.276	0.332	0.61	0.318	0.36	0.006	0.67	1.387	1.397	1.574
jack pine lo BA	1764	-9.483	-10.625	-15.703	0.389	0.501	0.199	0.039	-0.088	0.338	0.908	0.684	0.885
jack pine hi BA	814	-8.526	-9.658	-14.021	0.376	0.284	0.835	0.246	-0.153	0.398	1.201	0.685	1.17
lowland conifer	180	-7.150	-7.989	-13.536	0.579	0.864	0.548	0.609	0.293	0.979	1.432	1.294	0.857
n. hdwd med BA	254	-8.594	-8.966	-14.984	0.965	0.211	-0.023	0.426	-0.35	-0.185	1.947	0.747	1.155
n. hdwd hi BA	900	-8.014	-8.140	-13.673	1.213	0.717	0.523	0.871	0.074	0.951	1.858	1.159	1.718
aspen lo BA	212	-9.360	-9.754	-15.082	0.315	0.079	0.459	0.095	-0.881	-0.207	1.051	0.381	1.222
aspen med BA	219	-8.892	-8.895	-13.598	0.343	0.442	0.978	-0.224	-0.047	0.928	0.82	1.524	1.879

Table 4: L-band: T-test p-values comparing sample populations of σ° on October 7 to the remaining three dates (2).

Class	N	Oct 8 (134.3)			Oct 9 (150.2			Oct 10 (166.1)		
		L-hh	L-vv	L-hv	L-hh	L-vv	L-hv	L-hh	L-vv	L-hv
short veg	27	0.84	0.54	0.89	**0.00**	**0.24**	**0.00**	**0.00**	**0.01**	**0.00**
red pine lo BA	5	**0.01**	0.37	0.35	**0.10**	0.31	0.23	0.46	0.36	0.67
red pine hi BA	8	0.21	0.22	0.22	**0.00**	**0.04**	**0.02**	0.37	0.45	**0.09**
jack pine lo BA	12	**0.05**	0.49	0.14	**0.04**	0.64	0.16	0.72	0.42	0.72
jack pine hi BA	5	**0.10**	**0.08**	0.24	**0.01**	0.19	0.12	0.55	0.40	0.51
lowland conifer	2	0.90	0.91	0.80	0.90	0.56	0.83	0.39	0.67	0.65
n. hdwd	8	0.19	0.14	**0.08**	**0.00**	**0.00**	**0.00**	0.12	**0.01**	0.18
aspen	5	0.38	0.25	0.63	**0.10**	**0.04**	0.64	0.79	0.14	0.62

Table 5: C-band: T-test p-values comparing sample populations of σ° on October 7 to the remaining three dates (2).

Class	N	Oct 8 (134.3)			Oct 9 (150.2			Oct 10 (166.1)		
		C-hh	C-vv	C-hv	C-hh	C-vv	C-hv	C-hh	C-vv	C-hv
Short Veg.	27	0.94	0.78	0.58	**0.00**	**0.00**	**0.00**	0.75	0.17	**0.05**
red pine lo BA	5	0.45	0.83	0.93	0.85	0.13	0.26	0.18	0.33	0.23
red pine hi BA	8	0.27	0.27	0.23	0.41	0.93	**0.02**	**0.00**	**0.01**	**0.00**
jack pine lo BA	12	0.18	**0.07**	0.54	0.93	0.71	0.29	**0.00**	**0.01**	**0.00**
jack pine hi BA	5	0.15	0.18	**0.10**	0.40	0.54	0.41	**0.00**	**0.00**	**0.02**
lowland conifer	2	0.50	0.27	0.43	**0.10**	0.55	0.11	0.16	0.13	0.22
n. hdwd	8	**0.00**	**0.02**	0.36	**0.00**	0.91	0.11	**0.00**	**0.00**	**0.00**
aspen	5	0.20	0.37	0.33	0.79	0.46	0.38	**0.07**	**0.00**	**0.01**

Scale Integration of Bi-Directional Reflectance Effects in Remotely Sensed Vegetated surfaces

D.W. Burgess, J.R. Dymond, D. Pairman, J.D. Shepherd
Landcare Research New Zealand Ltd.
PO Box 38-491, Wellington, New Zealand
Ph +64-4-569-0180, Fax +64-4-569-0181, E-mail burgessd@landcare.cri.nz

Abstract -- Researchers are becoming increasingly aware of the importance of characterising the anisotropic reflectance of vegetated surfaces for remote ground cover monitoring. View angle considerations are particularly important for wide field of view sensors such as the NOAA AVHRR series of instruments. Orbital constraints mean that it is difficult to adequately sample the domain of viewing and illumination geometries in order to build a model of the surface anisotropy.

This paper assesses the feasibility of applying a Bidirectional Reflectance Distribution Function (BRDF) derived from high resolution data (30cm), acquired with an aircraft mounted digital camera, over a number of vegetation classes, to the low resolution (1.1km) AVHRR observations. The validity of integrating data from these significantly different scales is discussed. Limitations on data comparison due to atmospheric and radiometric effects are also addressed.

INTRODUCTION

Over recent years researchers have become aware of the value of the data derived from multiple viewing angles over a given area of vegetation. The structure and state of a vegetated surface influences the way that light is reflected back to a sensor at different viewing positions. With a large number of views, it is possible to build a BRDF. There is significant interest in inverting BRDFs to retrieve biophysical parameters [1], [2], [3].

This new awareness of the anisotropy of the Earth's surface has led other researchers to seeks to remove the effect for the purposes of accurate monitoring of vegetation state over time [4], [5].

In order to derive a BRDF, it is necessary to obtain a large number of measurements over a wide range of viewing and illumination geometries. This is best achieved using a low altitude sensor where a range of measurements can be made in a relatively short period of time, and problems such as atmospheric contamination and non-homogeneity are eliminated. However, with regard to monitoring land surface state on a regional, or even global scale, satellite remote sensing is the only practical alternative. We are therefore faced with the challenge of making the most of each distinct data source : surface anisotropy characterised via a BRDF derived from ground based data; and accurate monitoring capabilities from a wide field of view, frequent revisit space-based sensor such as the NOAA/AVHRR instrument. In this paper we begin to assess whether a low altitude BRDF can be used to characterise the the angular effect in a AVHRR data set.

METHOD

AVHRR data was collected over the Southern hemisphere summer of November 1996 - February 1997. Band 1 (660 nm) samples were taken over three forest test sites. These samples included a range of viewing and illumination geometries and were oriented 30 to 40 degrees from the principal plane[1].

A BRDF model, derived for the same ground cover types, based on data from an aircraft mounted digital camera, was used and reflectances were calculated for geometries corresponding to the satellite samples. The satellite measurements were compared to the modelled reflectances.

BRDF Model Description

The model used was developed by Dymond and Qi [6]. It calculates the radiance of a dense vegetation canopy as the product of three functions

$$L = S(\theta,\phi)H(\alpha,\theta)B(\alpha) \qquad (1)$$

The S function represents the proportion of canopy seen as sunlit, excluding the hotspot. The hotspot function, $H(\alpha,\theta)$, corrects the S function for the higher probability of seeing sunlit leaves near to the anti-solar point. The B function represents the average radiance of sunlit leaves. These functions are given by

$$S(\theta,\phi) = \frac{\cos\theta}{\cos\theta + (\sigma_\theta/\sigma_\phi)\cos\phi}$$

$$H(\alpha,\theta) = \begin{cases} 2\exp(-\tan(\alpha/2)/h\theta) & \alpha < \pi/2 \\ 2\exp(-\tan(\pi/4)/h\theta) & \alpha \geq \pi/2 \end{cases}$$

$$B(\alpha) = \frac{4\rho E}{3\pi^2}(\sin\alpha + (\pi/2 - \alpha)\cos\alpha)$$

[1] The principal plane is the plane in which the sun and viewing directions are the same or separated by 180 degrees

0-7803-3836-7/97/$10.00 © 1997 IEEE

where θ is the sun zenith angle; ϕ is the off-nadir view angle; α is the phase angle; σ_θ and σ_ϕ are the average projected leaf area in the sun and view directions respectively; h is a constant which is proportional to the leaf length divided by the distance between leaves [7]; ρ is the leaf reflectance; and E is the radiant flux density of the sunlight. The model essentially has two parameters, h and ρE, and a function, $\sigma_\phi/\sigma_\theta$, to be determined.

The model was tested by fitting it to densely-sampled, multi-view radiance measurements of pine forest (*Pinus radiata*) and pasture (*Lolium spp*), taken at a sun zenith angle of 59^0, and then making radiance predictions for multiple views at a sun zenith angle of 20^0. Comparison of predicted with measured radiances showed that the model out-performed the linear Roujean et al.model [4] and the non-linear Verstraete et al. model [9]. The improvement is due to two factors: the hotspot function has a sun zenith angle dependence; and the S function allows the average projected leaf area to vary with off-nadir view angle.

AVHRR Data Acquisition and Preprocessing

All afternoon passes of the NOAA-14 satellite were received and archived at Landcare Research NZ Ltd., Wellington, New Zealand. The scenes were manually cloud screened and rectified to the New Zealand metric map grid using automatic chip matching and manual refinement.

Test sites were chosen in the central North Island of New Zealand. Two sites were pine forest (*Pinus radiata*) and one was beech forest (mixed *Northofagus fusca* and *Northofagus menziesii*). They were all mature stands with closed canopies.

In order to avoid pixel mixing, the sample locations were reverse mapped into the raw imagery and 3 x 3 pixel samples were extacted. Allowing for sub pixel cloud contamination and misregistration, the lowest value pixel was selected for processing. It was calibrated using updated calibration coefficients from NOAA.

AVHRR top of atmosphere radiances were atmospherically corrected using the 6S computer code [10] to produce surface reflectances. The atmospheric profiles input to this code were monthly climatoglical mean profiles of pressure, temperature, water vapour and ozone, obtained at the National Institute of Water and Atmosphere Research (NIWA) facility at Lauder in Central Otago, New Zealand. Aerosol optical depth was also estimated from preliminary sun photometer investigations taken at this site.

Lake Taupo, a large lake in the central North Island of New Zealand, was used as a dark target to investigate accuracy of the atmospheric correction. AVHRR data was gathered over the lake and the calibration and atmospheric correction procedures were applied as outlined above. It was anticipated that accurate preprocessing would yield a consistent near-zero reflectance irrespective of view zenith angle, except for forward scattered geometries where specular reflection would lead to sun glint off the water. Initial results showed a small overestimation of atmospheric effects, leading to backscatter reflectances being slightly depressed. An improved lake reflectance was obtained assuming no atmospheric aerosols (see Fig. 1). Some variation in the measured reflectance is still visible in this data. Since the sample was taken in the middle of a large lake, errors due to misregistration are unlikely to cause this variability. We therefore conclude that the variation is due to day to day variations in the atmospheric profile which have not been taken into account.

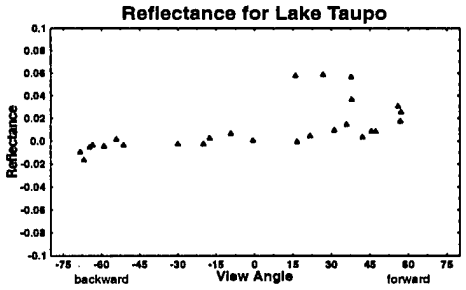

Figure 1: Lake Taupo reflectances

RESULTS

Figure 2 shows both the measured and the modelled results for the three test sites. Although there is still some variability in the measured reflectances, there is agreement between the measured and modelled values in terms of magnitude and trends exhibited.

Measured reflectances are consistently higher in the forward scatter direction. This may be due to incorrect atmospheric correction but this seems unlikely in view of our dark target results. Although some of the lake measurements in the forward scatter direction were affected by sun glint (reflectances of 0.4 - 0.6), others with similar view zenith angles had relative azimuth angles[2] large enough (> 220 degrees) to avoid this. These samples showed relatively consistent near-zero reflectance. It is therefore likely that the model is slightly underestimating the forward scatter reflectances.

DISCUSSION

There are a number of other considerations that need to be taken into account when comparing the measured and modelled results. .

- In order to obtain samples from a wide range of view angles, some very oblique views were processed. According to [11], at a view zenith angle of 60 degrees, an AVHRR pixel is approximately 2km by 4km in size. Although every effort was made to find large homogeneous test sites, these were on

[2] The relative azimuth angle is the angle between the solar and view azimuths

average only 4km by 4km. Small misregistrations would therefore lead to pixel contamination.

- The 6S atmospheric correction code is limited to view zenith angles of less than 60 degrees and solar zenith angles of less than 50 degrees. Some of our backscatter samples have geometries very close to this and are therefore not reliably corrected.

In light of these factors we feel that the results are extremely encouraging and warrant further investigation.

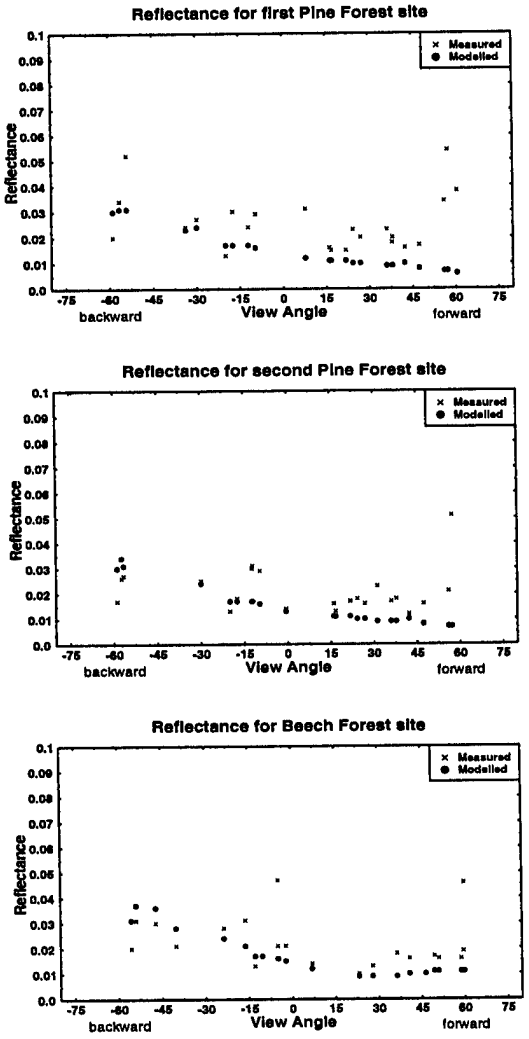

Fi

gure 2 : Measured and modelled results

CONCLUSION

The agreement between the measured AVHRR samples and the low altitude BRDF modelled values suggests that there is a future for this approach. We would like to extend this work into the near infrared by comparing AVHRR band 2 measurements with an enhancement to this BRDF model that incorporates multiple scattering.

These results suggest that is a realistic possibility to develop a cover-type specific angular correction for AVHRR data based on low altitude measurements.

REFERENCES

[1] N.S. Goel and D.E. Strebel, "Inversion of Vegetation Canopy Reflectance Models for Estimating Agronomic Variables. I. Problem Definition and Initial Results Using Suits Model", Remote Sensing of Environment, vol. 13, pp. 487-507, 1983.

[2] J. Qi, F. Cabot, M.S. Moran and G. Dedieu, "Biophysical Parameter Estimation Using Multidirectional Spectral Measurements", Remote Sensing of Environment, vol. 54, pp. 71-83, 1995.

[3] J.L. Privette, W.J. Emery and D.S. Schimel, "Inversion of a Vegetation Reflectance Model with NOAA AVHRR Data", Remote Sensing of Environment, vol. 58, pp. 187-200, 1996.

[4] J.-L. Roujean, M. Leroy and P.Y. Deschamps, "A Bidirectional Reflectance Model of the Earth's Surface for the Correction of Remote Sensing Data", J. Geophysical Research, vol. 97, no. D18, pp. 20,455-20,468, December 20, 1992.

[5] M. Leroy and J.-L. Roujean, "Sun and View Angle Corrections on Reflectances Derived from NOAA/AVHRR Data", IEEE Trans. On Geoscience and Remote Sensing, vol. 32, no. 3, May 1994.

[6] J.R. Dymond and J. Qi, (in press), "Reflection of visible light from a dense vegetation canopy - a physical model", Agric. For. Meteorol.

[7] B. Hapke, "Bidirectional reflectance spectroscopy: 4. The extinction coefficient and the opposition effect", Icarus, vol. 67, pp. 264-280, 1986.

[9] M.M. Verstraete, B. Pinty and R.E. Dickinson, "A physical model of the bidirectional reflectance of vegetation canopies 1. Theory." J. Geophysical Research, vol. 95, pp. 11,755-11,765, 1990.

[10] E. Vermote, D. Tanré, J.L. Deuzé, M. Herman and J.J. Morcrette, "Second Simulation of the Satellite Signal in the Solar Spectrum", User Guide Version 0, April 18, 1994, Laboratoire d'Optique Atmosphérique, Université des Sciences et Technologies de Lille, Villeneuve d'Ascq Cédex, France, 1994.

[11] S.N. Goward, B. Markam, D. G. Dye, W. Dulaney and J. Yang, "Normalized Difference Vegetation Index Measurements from the Advanced Very High Resolution Radiometer", Remote Sensing of Environment, vol. 35, pp. 257-277, 1991.

Airborne SAR in an End-to-End System for Sustainable Forest Management

H. Greidanus, D.H. Hoekman[2], R.J.A. Grim[3], W.J. Looyen[4]
TNO Physics and Electronics Laboratory
P.O. Box 96864, 2509 JG Den Haag, The Netherlands
tel. +31-70-3740441, fax +31-70-3280961, e-mail greidanus@fel.tno.nl
2: Wageningen Agricultural University; 3: Fokker Space; 4: NLR

Abstract -- An end-to-end information system for forest mapping and monitoring is discussed, in which the data are obtained from many available sensors. The role of airborne SAR in such a system is emphasized. User groups are identified, as well as their requirements, the system concept, and aspects of the implementation.

INTRODUCTION

Export of timber is of large economic importance for many tropical countries. In view of international agreements, there exists a commitment after the year 2000 to export timber obtained from the sustainably managed exploitation of forests. To ensure availability of operational tools for monitoring and management of the extensive tropical forest areas after the year 2000, it is necessary to install on relatively short term operational forest monitoring and management systems. These systems will be able to draw for a large part on remote sensing data, from satellites and from aircraft. In general, optical data could provide much of the required information; however, especially in tropical regions persistent cloud cover can pose severe problems. For this reason, SAR (Synthetic Aperture Radar) data are used. In addition, radar data can give information on forest presence, type and condition, and interferometric radar data can be used to produce elevation models. In the recent past, pre-operational flights have been performed with airborne SAR systems. Based on the outcome of these experiments, decisions can be made concerning the configuration of an adequate operational forest monitoring system.

Since the information needed by forest users and managers will have to come from a variety of sources in a reliable way, it is necessary to integrate the entire process between data reception and information delivery into a complete 'end-to-end' system. This paper reports on a study resulting in a system concept for an end-to-end operational forest monitoring system. The 'end-to-end' system refers to the complete chain of elements that will gather, process and present the information required by a user.

BOUNDARY CONDITIONS

There are several important boundary conditions that have to be taken into account in defining and developing an end-to-end system. The output and performance of the system has to determined based on user requirements; the users will have to be involved in both the definition and the development of the system. For maximum acceptance and cost effectiveness in the development phase, the system will have to build upon the existing infrastructure. It is important to recognize different user groups, each with their own specific requirements. There are four: (1) The system operators, cf. in the form of a commercial or government service; they will run the system, direct the operations, and deliver the output. (2) Forest exploitation organizations; they will use the system to plan and monitor their operations, and to demonstrate that the exploitation is within the limits of their concession. (3) The government, for verification of the concession holders' activities and for releasing new concessions. And (4) independent NGO's, for verification of the proper implementation of the international conservation criteria and guidelines such as those from ITTO. In addition to the users, numerous other parties are involved in the acceptance and development. These will include manufacturing industries, commercial services, research institutes, universities and government bureaus, who will share amongst them the required expertise, capabilities and responsibilities in the fields of forestry, remote sensing, SAR, operations, manufacturing, technology development and management.

THE END-TO-END SYSTEM

The end-to-end forest monitoring and management system should be based on advanced observation techniques. The system will comprise the following elements:

- Space segment (optical, radar and infrared).
- Air segment (one or more aircraft with camera, SAR sensor, real-time SAR processor, navigation/motion registration and data storage).
- Ground segment (data reception, handling, processing, archiving and distribution). Under processing can be recognized: optical processing, SAR processing, interferometric processing, DEM (Digital Elevation Model) extraction, georeferencing, radiometric calibration and thematic processing.
- Support segment (planning, operations, maintenance, ground truthing, education and training, research, system upgrading).

The information products that are output of the system can be divided into four categories:

0-7803-3836-7/97/$10.00 © 1997 IEEE

1. Mapping for land use and vegetation type. This is required at scales of 1:250,000 to 1:25,000.
2. Forest fire monitoring. This can be implemented by fire detection, assessment of fire damage, and detection of dry areas. Also partially underground coal fires are an issue in this respect.
3. Monitoring of indicators for sustainable forest management. This needs to be implemented by the ability to map individual tree crowns, degree of canopy closure, skid trails and reforestation.
4. Advanced products. This refers to products which are at the moment not yet defined, but these will include timber volume and tree height.

These information products impose specific demands on the data, which, in turn, can be addressed by specific sensors. Only a combination of sensors is able to cover the full spectrum of user needs. An overview is given in Table 1.

Table 1. Products, data requirements and sensors.

Application	Data	Sensor
Mapping 1:250.000	Multi-channel 25 m resolution	Optical and SAR satellite
Mapping 1:100.000	Multi-channel 20 m resolution	Optical and SAR satellite
Mapping 1:50.000	Multi-channel 10 m resolution	Optical and SAR satellite, or airborne SAR
(Logging) road network	Single channel 3-10 m resolution	Airborne SAR *or* aerial photography
Mapping 1:25.000	Multi-channel 3-5 m resolution (multi-look) interferometric *or* optical	Airborne SAR *or* aerial photography
Forest fire detection	Infrared low resolution	Infrared satellite
Forest fire monitoring (1:15.000)	Short wave single channel 3 m resolution	Airborne SAR, directed by satellite
Monitoring indicators of sustainable management (1:5-10.000)	Short wave (X or C) high resolution (2x2x2 m 10-look) interferometric *or* optical	Airborne SAR *or* aerial photography
Advanced	? (Multi-frequency high resolution interferometric polarimetric) ?	Airborne SAR

Satellite data can be used for large-scale overviews, with which airborne operations can be directed to gather more detail. Subsequently, once detailed information is known about an area, the frequently available satellite data can be used to monitor for changes. For satellite data, the system can presently draw upon LANDSAT and SPOT for optical; on NOAA-AVHRR or ERS-ATSR for infrared; and on ERS, JERS and RADARSAT for radar. In the future, most of these data sources will have comparable successors; also the possibility of dedicated satellite missions for tropical forest management must not be discounted.

An operational and economically viable airborne SAR system will have to comply with a number of criteria (in addition to the requirements from Table 1). It will have to: - have a reasonably wide swath, in combination with a limited range in incidence angle; - have an on-board quick-look facility; - have a large baseline (i.e. distance between the two interferometric antennae); - be robust and easily maintainable; - be suited for use on small aircraft; - and its platform will have to be able to fly at high altitude (up to 8 km at least). For airborne SAR, some of the products of Table 1 can be delivered by sensors that are nowadays available, although almost all of these are not truly operational. For the high-resolution products, at present there are no operational systems available at all, and these will have to be developed. It is possible to design SAR systems, on the basis of present-day commercially available technology, that attain the specifications needed. The parameters of one such a system are listed in Table 2. This concerns a single system that can operate in two modes: a high-resolution interferometric mode for use of monitoring indicators of sustainable management, and a medium resolution polarimetric mode, with one interferometric channel, for mapping at 1:25.000 scale.

Table 2. SAR system parameters for a system that simultaneously covers two of the requirements of Table 1. Incidence angles depend on altitude but always fall within the quoted range. Data rates are such that one recorder suffices.

Mode	High-resolution interferometric	Medium resol. polarimetric interferometric
Altitude	5-8 km	5-8 km
Max. velocity	145 m/s	145 m/s
Baseline	1.4 m	1.4 m
Channels	2	4
Slant range resolution	0.6 x 0.6 m (Range x Az)	1.2 x 0.6 m (Ra x Azimuth)
Ground resolution	2.0 m @ 11 look	3.0 m @ 12 look
Height accuracy	< 2. 0 m	< 2.0 m
Ground swath	7.9 km	7.9 km
Incidence angle	40° - 67°	40° - 67°
Band width	250 MHz	125 MHz
Max. data rate	29 Mbyte/s	29 Mbyte/s

Of course, it is also possible to implement each requirement in a different system, which may be more economical in practice if these systems need to be used much. The high data rates will result in large amounts of data; this puts a very heavy load on all subsequent activities, such as processing,

archiving and analysis. A single channel radar image at 2 m resolution amounts to a data volume of 10 Gbyte/Mha (Million hectare), while the intermediate single-look complex data needed to derive the associated DEM is an order of magnitude more, and the raw data is 25 times as much. A polarimetric image at 5 m resolution amounts to some 5 Gbyte/Mha. The most stringent requirement of Table 1 is the 2m, 10-look resolution (also in terms of radar hardware); although this requirement is technically feasible, if it can be relaxed (even to 2.5 m or 3 m) then system cost and complexity will be significantly reduced. However, the need to discern individual tree crowns seems at the moment to imply this requirement.

Because the final information products will be the result of a combination of the data from various sensors, and because of the very high data rates, the ground segment will be of considerable complexity. There is the choice between a centralized facility or a network of decentralized ones. From the point of view of data access and local availability, the latter would be preferable; however, archive integrity, the complex processing and analysis, and the need to combine data from different sources favor a centralized facility. This choice will also be influenced by the existing infrastructure. The software needed for the ground segment may be composed of commercially available packages, customized for the operational environment and overlaid with a shell for proper data and user interfacing. The information products should have a data format which conforms to international commercial standards. Commercially available PCs and UNIX-based workstations may be used, extended with accelerator boards for some of the computationally intensive tasks such as the SAR processing. With the nowadays available hardware, a limited number of workstations suffices to cover the processing demands of the ongoing forest monitoring operations of a medium-sized country.

IMPLEMENTATION

Implementation of an end-to-end system will have to be based on the existing infrastructure, the availability of sensors that partially cover the data requirements, the lack of those that would cover them in full, and the milestone of the year 2000. Between now and 2000, existing airborne SAR systems can be used for mapping down to scales of 1:15.000, together with data from existing satellites and aerial photography operations. At the same time, a new dedicated high-resolution airborne SAR system can be developed. From 2000 onwards, this system will then be available for mapping at scales of up to 1:10.000. After 2005, other and more advanced airborne SAR systems will become available to address the more advanced applications such as tree and height timber volume estimation. Airborne SAR systems can be designed to operate in various modes, each suited for a particular application. In defining new systems, other applications besides forest management should be taken into account, such as general mapping, agriculture and coastal zone management. This will positively influence the cost/benefit ratio and the acceptance.

REFERENCES

[1] D.H. Hoekman, "Radar monitoring system for sustainable forest management in Indonesia", these proceedings.

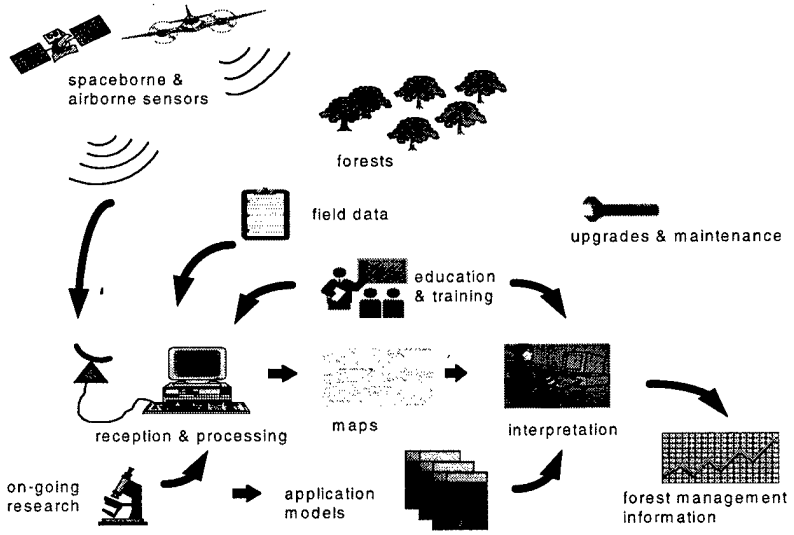

Figure 1. Impression of an end-to-end information system for forest management.

Comparing accuracy of satellite- and airborne remote sensing data in the retrieval of forest stand attributes

Juha Hyyppä, Mikko Inkinen, Hannu Hyyppä, Marcus Engdahl, Martti Hallkainen

Helsinki University of Technology, Laboratory of Space Technology
Otakaari 5 A, FIN-02150 Espoo, Finland
Phone: +358-9-4514775, Fax: +358-9-4512898, Email: Hyyppa@ava.hut.fi

Abstract - Recent advances in developing remote sensing methods for forest inventory have suggested a good potential for the use of multi-source, multi-dimensional remote sensing data. This paper describes results of the retrieval of stem volume, basal area, and mean height utilizing the following remote sensing data: Landsat TM, SPOT Pan and XS, ERS-1/2 PRI and SLC, airborne data from imaging spectrometer AISA, radar-derived forest canopy profiles (obtained with HUTSCAT), and aerial photographs. Ground truth data consist of 40 spruce-dominated and mixed stands, which have been carefully measured using about 10 relascope sample plots in each stand. Multivariate data analysis techniques were applied. The results suggested that 1) radar-derived stand profiles seemed to be the most accurate data source for forest inventory, 2) combining ERS-1/2 coherence images with Landsat TM improved estimation accuracy, 3) Landsat TM was a more accurate data source than other satellite data (SPOT Pan and XS, ERS-1/2 intensity and coherence images), 4) principal component analysis was found to be a good technique with this dataset to derive predictor variables from AISA data (30 channels with high multicollinearity), 5) higher coherence was obtained for winter images than summer images due to snow-covered ground.

INTRODUCTION

Conventional forest inventory is both expensive and time-consuming. In theory, remote sensing methods offer a good alternative and/or a supporting method for traditional forest inventory and, therefore, remote sensing applications in the estimation of biomass and stem volume have been intensively investigated during the last few years (e.g. [1],[2],[3],[4],[5]). The feasibility of remote sensing data at visible, near-infrared, infrared and microwave spectral bands has been studied for both small- and large-area forest inventory. Digital satellite, e.g. Landsat TM, have even been applied with success for operational large-area applications, such as national forest inventories [6]. Recently, progress has been made to combine both microwave and visible/infrared data sets to fully exploit the potential of both approaches. A multi-source remote sensing data for forest inventory can be used to improve the accuracy of remote sensing based estimates. Using conventional field inventory methods, the accuracy for main attributes, such as stem volume, is typically about 15 %.

The main objective of this study was to estimate the accuracy of each individual remote sensing data source on the retrieval of the following forest stand attributes: stem volume (m^3/ha), basal area (m^2/ha) and tree height (m), and to improve current methods by applying multi-source data sets.

MATERIAL

From the Kalkkinen test site, locating 130 km north of Helsinki, 40 homogeneous spruce-dominated and mixed stands were measured using about 10 relascope sample plots in each stand. Tree species and diameter at breast height (dbh) were recorded for each measured tree, determined with a relascope factor of 1. Age, dbh, and height were measured for the basal-area-median-tree of each sample plot. From these data mean tree height (m), basal area per hectare (m^2/ha) and stem volume per hectare (m^3/ha) were obtained for each stand basically as means of the sample plot values. Descriptive statistics of the 40 stands are depicted in Table 1. The applicability of the results with other stand conditions were not tested. In the future, the results will be obtained for all typical stand conditions covering thousands of hectares.

Table 1. Descriptive Statistics of Field Inventory Stands.

	Volume	*Basal area*	*Height*
Minimum	119.3 m^3/ha	13.1 m^2/ha	10.6 m
Maximum	330.6 m^3/ha	30.1 m^2/ha	25.4 m
Mean	222.5 m^3/ha	22.6 m^2/ha	20.3 m
Std.dev.	58.9 m^3/ha	4.5 m^2/ha	2.8 m

The remote sensing data set included satellite data from SPOT, Landsat, ERS-1/2, airborne data from imaging spec-

0-7803-3836-7/97/$10.00 © 1997 IEEE

trometer (AISA), airborne ranging radar (HUTSCAT), and digitized aerial photographs, Table 2.

Table 2. Remote Sensing Data.

Imaging spectrometer AISA	Measured on 10 June 1996 using the AISA spectrometer of the Finnish Forest Research Institute (METLA), resolution 1.6 m (across-track) and 2.4 m (along-track), geometric and radiometric rectification was done by METLA, spectral range 466-870 nm.
Aerial photographs	Photographed on 8 June 1996, with scale of 1:20 000, digitized and orthorectified into pixel size of 0.85m.
Radar profiles	Measured on 22 November 1996, using helicopter-borne ranging scatterometer HUTSCAT with polarization modes HH, VH, HV, and VV at an incidence angle of 23° off nadir, center frequency 5.4 GHz, range resolution 0.65 m, spatial resolution (at tree tops) 8 m, flight line spacing was 100 m.
SPOT Pan/XS	Acquisition date 24 August 1996, processing level 1B.
Landsat TM	Acquisition date 24 August 1996, system corrected mini-scene.
ERS-1/2	5 SLC pairs and corresponding ERS-1 PRI images obtained via ERS tandem AO project AOT.SF301 during summer 1995 and spring 1996.

METHODS

The coherence images were produced from ERS-1/2 Tandem SLC images using the ISAR-Interferogram Generator software developed in Politecnico di Milano. The ISAR-software is distributed free of charge to the members of the ESA Fringe Group. ISAR software co-registers the two SLC images to the required sub-pixel accuracy, subtracts the flat terrain phase term from the interferogram and performs common-band filtering in order to reduce baseline decorrelation. If needed, ISAR software also estimates the local directional slopes (the instantaneous frequency of the interferometric phase). In coherence estimation the ISAR software uses a Gaussian estimator window in order to reduce the deleterious effect of bright reflectors.

Satellite images were rectified using base maps and ground control points. Radar profiles corresponding to ground truth stands were determined using GPS-coordinates and corresponding time recorded during flight. In digitized aerial photographs, the effects of illumination variations within images were reduced by a regression method (Holopainen, 1995). After correcting the individual images, an ortho-photo mosaic was constructed.

The rectified and preprocessed data was analyzed using image processing, GIS and statistical software. The boundaries of the stands were imported from GIS to the image processing system. From each stand, statistical features such as mean, standard deviation, histogram and its shape, and ratio of different channels were calculated. Principal component analysis was applied to the 30-channel AISA image and a combination of all satellite images. All together, over 250 predictor variables were formed. Multiple regression models were built on these variables using best subset regression. All data were used for modelling. The criterion to eliminate variables was that all variables in the models should be significant ($p<0.05$).

RESULTS AND DISCUSSION

Table 3 shows the accuracy comparison of various data sources for standwise volume estimation. The results are summarized in the following.

- HUTSCAT-derived tree height estimates differed with 1.3 m standard deviation and 0.3 m systematic error from the ground truth data. The tree height estimation capability of HUTSCAT was superior to any other data source. Adding crown backscatter mean to the volume model, the standard error of volume estimates was only 28 m^3/ha (12 %).

- Within stand shadowing in aerial photographs, maybe typical to spruce stands, improved both height and volume estimation accuracy. Additionally, inadequate mosaicing and illumination correction resulted in dramatic deterioration of accuracy.

- Aerial photographs and AISA image gave second best accuracy of 15 % to 18 % to stem volume. Principal component analysis was successfully applied to AISA data, because signals of 30 AISA output channels correlated strongly with each other. The first principal component (PC) corresponded to overall variation in the image, the second PC to variation in the forest, and the third PC to striping effects in the images caused by unideal mounting of the sensor on the aircraft.

- The combination of ERS coherence image and LANDSAT TM image resulted in improved accuracy for all tested attributes. The ERS coherence based estimates were more accurate than SPOT Pan and XS based estimates.

Table 3. Accuracy comparison between various data sources for stem volume assessment

Data source	Predictors	R^2	SE (m^3/ha)
SPOT Pan	*mean intensity*	0.11	56.4 (25.3%)
SPOT XS	*mean intensity, ch 1*	0.21	53.2 (23.9 %)
Aerial mosaic	*mean of near-IR and green channels*	0.32	50.0 (22.5 %)
ERS	*mean of coherence 21-22 August*	0.32	49.4 (22.2 %)
Landsat TM	*mean of ch 6*	0.37	47.4 (21.3 %)
ERS/Landsat	*mean of ch 6, mean of coherence 21-22 August*	0.43	45.7 (20.6 %)
AISA*	*PC 2*	0.63	40.5 (18.7 %)
Aerial photo*	*mean of red and green channels*	0.78	35.0 (15.6 %)
HUTSCAT*	*mean height of the profile, crown backscatter at VH*	0.75	28.2 (12.3 %)

** The number of stands used for AISA, aerial photograph and HUTSCAT measurement varied slightly due to improper data acquisition. However, it was statistically tested that each ground truth data sets reprented the same distribution.*

- The coherence over boreal forests during winter was considerably higher than during other seasons perhaps due to wet snow conditions. Therefore, ERS Tandem interferograms acquired during winter seemed to be ideal for DEM generation over boreal forests.

- Summation of several normalized coherence images produced images suited better for land-use and forest classification than a single coherence image.

The relative accuracies are extremely good, mostly due to low variation of stands. Therefore also, the coefficients of determination are relative low. With larger number of stands and with larger variation, it is expected that coefficients of determination and SE (standard error) values will be higher than in Table 3.

ACKNOWLEDGMENT

The ERS-1/2 SLC images were provided by ESA as a part of the Tandem AO project AOT.SF301. The authors are grateful to Kai Mäkisara (METLA) for acquisition and preprocessing of AISA data and to Jari Varjo for design of the field inventory measurements and various valuable advices.

REFERENCES

[1] R.Päivinen, A. Pussinen, and E. Tomppo, "Assessment of boreal forest stands using field assessment and remote sensing", Proceedings of Earsel 1993 Conference "Operationalization of Remote Sensing", ITC Enshedene, The Netherlands, 19-23 April, 8p, 1993.

[2] U. Wegmüller, and C.L. Werner., "SAR interferometric signatures of forest", IEEE Transactions on Geoscience and Remote Sensing, Vol. 33, pp.1153-1161, 1995.

[3] E.S. Kasischke, N.L.Jr. Christensen, and L.L. Bourgeau-Chavez, "Correlating radar backscatter with components of biomass in loblolly pine forests", IEEE Transactions on Geoscience and Remote Sensing, Vol. 33, pp. 643-659, 1995.

[4] K.J. Ranson, G. Sun, B. Montgomery, and R.H. Lang,, "Mapping of boreal forest biomass using SAR", Proceedings of IGARSS'96 Conference, Vol. 1, Lincoln, Nebraska, May 27-31, 577-579, 1996.

[5] J. Hyyppä, J. Pulliainen, M. Hallikainen, and A. Saatsi, "Radar-Derived Standwise Forest Inventory", IEEE Transaction on Geoscience and Remote Sensing, Vol. 35, pp. 392-404, 1997.

[6] E. Tomppo, "Satellite image-based national forest inventory of Finland", International Archives of Photogrammetry and Remote Sensing, 28:419-424, 1991.

Application of Multitemporal ERS Synthetic Aperture Radar in Delineating Rice Cropping Systems in the Mekong River Delta

S. C. Liew[a], S. P. Kam[b], T. P. Tuong[b], P. Chen[a],
V. Q. Minh[c], L. Balababa[d] and H. Lim[a]

[a]Centre for Remote Imaging, Sensing and Processing,, National University of Singapore,
Lower Kent Ridge Road, Singapore 119260.
Tel: (+65) 7723220, Fax: (+65) 7757717, email: phyliew@nus.edu.sg
[b]International Rice Research Institute, P.O. Box 933, 1099 Manila, Philippines
[c]Department of Soil Science, Faculty of Agriculture, University of Can Tho, Can Tho, Vietnam
[d]Natural Resources Program, Asian Institute of Technology, Bangkok., Thailand

Abstract -- The aim of this study is to use multitemporal ERS-2 satellite synthetic aperture radar (SAR) images in delineating and mapping areas under different rice cropping systems in the Mekong river delta, Vietnam. Five change index maps were generated from the six images acquired between June and December, 1996. Using a 3-dB threshold, the pixels in each change index map were classified into one of three classes: increasing, decreasing or constant backscattering. The five change index maps were used to generate a composite map with 243 possible change classes. After discarding the minority classes, and merging the dominant classes with similar backscatter time series, the thematic classes of rice cropping systems practiced in the study area were delineated.

INTRODUCTION

The objective of this study is to use multi-temporal ERS-2 SAR data to delineate and map the spatial distribution of the various rice cropping systems in the Mekong River Delta. The results of our previous study within a test area of 100 km by 100 km which includes parts of Soc Trang and Bac Lieu provinces in the Mekong river delta, Vietnam using ERS-2 SAR scenes subsampled to 50 m pixel size have been reported. have been reported [1]. Single cropping and variations of the double cropping rice cultivating regions have been delineated by thresholding the change index maps derived from a series of seven multitemporal ERS-2 images. This method allows the discrimination of regions of different rice cropping systems over a broad area.

In this paper, we report the results of applying the similar technique to delineate rice cropping systems on a smaller scale. The test area is confined to a 12 km x 10 km region southwest of the town of Soc Trang in the Mekong Delta. Full resolution (12.5 m pixel size) Precision Image (PRI) products are used in this study. The rice cropping systems in this region are mainly the rainfed double cropping systems. Variations of this main system have been mapped using this technique.

There are three main rice seasons in the Mekong river delta (see Table 1). Two of the seasons (HT and M) coincide with the rainy season which typically starts in May and lasts until November. The three rice seasons, in various combinations governed by hydrology, rainfall pattern and availability of irrigation, constitute the variety of rice-based cropping systems practiced in the Mekong river delta [2]. The rainfed double cropping systems in this area are variations of the HT-M system, typically practiced in the salinity affected areas and in areas where irrigation is not available. The planting methods are mainly the direct seeding methods.

Table 1: Rice Seasons in the Mekong River Delta

	Season	Planting	Harvest
Dong Xuan (DX)	Winter - Spring	Nov/Dec	Feb/Mar
He Thu (HT)	Summer - Autumn	May/Jun	Aug/Sep
Mua (M)	Rainy Season	Jul/Aug	Dec/Jan

Various studies on the backscattering of radar from rice plants [3] indicate that the radar backscatter generally increases with time after planting during the vegetative phase when there is a rapid increase in plant biomass. The backscatter saturates at the reproductive phase of the growth cycle when the plants start flowering. The backscattering coefficient is found to increase from −16 dB or less at the beginning of the growth cycle when the field is inundated and there is little biomass in the field, to about −8 dB at the saturation level [3]. It should then be possible to monitor the rice growth stage by measuring the backscattering coefficient from the plants as a function of time if radar images are acquired at appropriate time intervals. ERS-2 SAR images can only be acquired in the same mode (either descending or ascending) at 35-day intervals. Although the backscatter time series obtained at 35-day intervals would not have sufficient temporal resolution to capture the rapid increase in biomass during the vegetative phase for the

0-7803-3836-7/97/$10.00 © 1997 IEEE

short growth duration rice, which is about 30 days, it would still be able to capture the changes in backscatter between the beginning of the planting cycle and the end of the reproductive stage. Generally, the beginning of a rice season would be identified by a low backscatter in the time series when the field was inundated while the end of the reproductive stage is characterised by a high backscatter.

IMAGE PROCESSING

Seven descending mode ERS-2 synthetic aperture radar images at 35-day repeat intervals were acquired (track 75, frame 3411 shifted down by 30% to cover areas of interest in Soc Trang and Bac Lieu provinces) during the following dates in 1996: May 5, Jun 9, Jul 14, Aug 18, Sep 22, Oct 27 and Dec 1.

The ERS-2 scenes were acquired and processed into the calibrated SAR Precision Image (PRI) format at the ground station of the Centre for Remote Imaging, Sensing and Processing (CRISP), Singapore. An edge-preserving speckle removal filter based on the adaptive Wiener filter for multiplicative noise was applied. Multitemporal colour composite images were then generated to show the changes in the backscattering coefficients during the rice growing seasons.

CLASSIFICATION METHOD

The classification method has been described in [1]. Maps of radar change indices (change in backscattering coefficient expressed in dB) for consecutive pairs of images were generated. A 3-dB threshold was then applied to each change index map to produce a threshold-change-index (TCI) map. For each TCI map, the pixels were classified as having a constant ($-3dB < CI < +3dB$), decreasing ($CI < -3dB$) or increasing ($CI > +3dB$) backscattering over the corresponding time period. Five TCI maps (covering the period from Jun 9 to Dec 1) were combined to give a total of 243 possible change classes. In the previous study [1] covering a larger area, the change classes were merged into thematic classes of rice cropping system on the basis of similarity in their time series of radar backscattering (σ_0 in dB) as well as their geographical distribution pattern, with the consideration of field knowledge about the type of rice cropping system that might be practiced in a particular geographical region. In this study, the same change signatures in the series of threshold change index maps were used in merging the change classes into thematic classes.

RESULTS AND DISCUSSIONS

An example of a multitemporal colour composite image of the test area is shown in Fig. 1. The multitude of colours illustrates the variety of rice cropping systems in the study area. The bright white area on the top right part of the image is the town of Soc Trang. The grey linear features are the linear settlements, homestead gardens and orchards along canals and roads where the backscattering coefficient remained relatively constant throughout the season. The rice areas appear in shades of reddish orange and green.

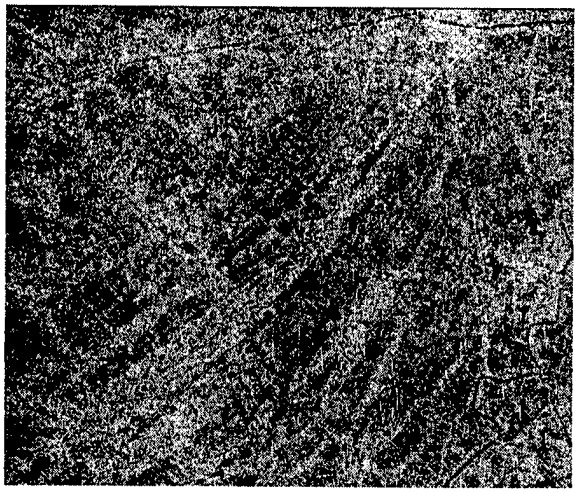

Fig. 1: Multitemporal SAR colour composite image of the test area (Red: May 5, Green: June 9, Blue: July 14, 1996)

The resulting thematic map of the rice cropping systems is shown in Fig. 2 while the time series of the change classes corresponding to these thematic classes are graphed in Fig. 3. The white areas Fig. 2 are the areas with relatively time invariant radar backscatter (see Fig. 3a). The magnitude of the back scattering coefficient is relatively high at about -7 dB, typical of vegetation with closed canopy structure.

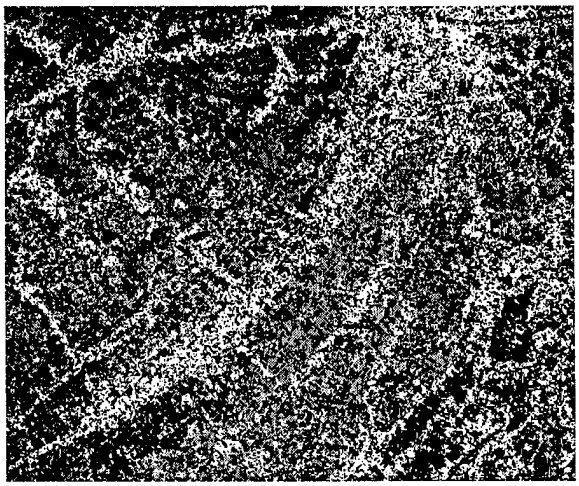

Fig. 2: Thematic map of rice cropping systems in the test area. The magenta, green and cyan regions are regions of three variations of the double crop rainfed HT-M system. The white areas are non rice areas with relatively stable radar backscatter over time.

Three variations of the double crop rainfed rice croping systems have been identified in this region. The magenta-coloured areas appear scattered, with some concentrations along the main road leading from Soc Trang to Bac Lieu. Ground observations indicate that the rainfed HT-M system is practiced in some parts of this area, where the dry direct-seeded HT crop is planted between May/June and Aug/Sep, followed by the Mua crop in Oct. The backscatter time series (Fig. 3b) is characterised by a distinct drop in σ on Oct 27, followed by a steep increase in backscatter. This increase is probably due to the *Mua* crop. The earlier part of the time series is relatively flat. The beginning of the HT crop in May/June is probably not sampled by any of the SAR images.

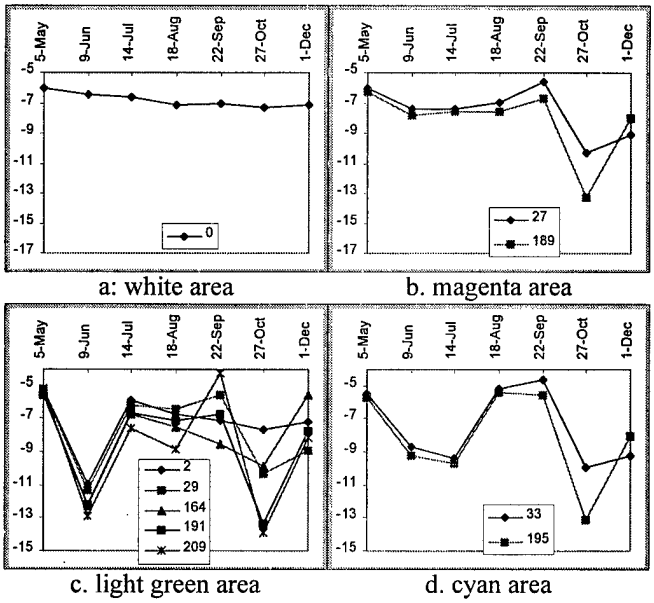

Fig. 3: Backscatter time series of the four thematic classes shown in Fig. 2.

The system practiced in the areas coloured light green in Fig. 2 is characterised by two distinct drops in the backscatter time series, i.e. on Jun 9 and Oct 27 (see Fig. 3c). These areas are lower-lying, the fields are flooded in June resulting in the drop in σ in the Jun 9 scene. The wet field conditions allow for wet direct seeding of the HT crop. The increase in σ after October corresponds with the *Mua* crop. On the other hand in the areas coloured cyan in Fig. 2, there is no distinct dip in σ in the backscatter time series (Fig.3d); there was no early season inundation of the rice fields. The HT crop is mainly dry direct seeded, hence the corresponding increase in backscatter between Jul 14 and Aug 18.. As is the case of the light green areas, the increase in σ after October corresponds with the *Mua* crop.

CONCLUSIONS

Three variations of the double crop rainfed HT-M systems have been identified and delineated in the study area by thresholding the change index maps derived from multitemporal SAR images followed by merging of the change classes into thematic classes using the same set of change signatures derived from a previous study [1] involving a much larger area than the present study. Our results indicate that this technique is also capable of delineating the rice cropping systems on a smaller scale.

REFERENCES

[1] S. C. Liew, S. P. Kam, T. P. Tuong, P. Chen, V. Q. Minh, L. Balababa, and H. Lim. "Delineation of rice cropping systems in the Mekong river delta using multitemporal ERS synthetic aperture radar," *Proc. 3rd. ERS Symposium,* Florence, 1997 (In press).

[2] T.P. Tuong, C.T. Hoanh and N.T. Khiem. 1991. "Agro-hydrological factors as land qualities in land evaluation for rice cropping patterns in the Mekong Delta of Vietnam," in P. Deturck and F.N. Ponnamperuma (eds.) *Rice Production on Acid Soils of the Tropics.* Institute of Fundamental Studies, Kandy, Sri Lanka.

[3] T. Le Toan, F. Ribbes, L.-F. Wang, N. Floury, K.-H. Ding, J. A. Kong, M. Fujita, and T. Kurosu, "Rice crop mapping and monitoring using ERS-1 data based on experiment and modeling results," *IEEE Trans. Geosci. Remote Sensing*, vol 35, pp. 41-56, 1997.

Combined ERS SAR and Optical Satellite Data for the Estimation of Forest Structural Attributes

G. Kattenborn*, E. Nezry**

*University Freiburg, Dep. Remote Sensing and Landscape Information Systems
Aschenbrennerstr. 18, D-79110 Freiburg, Germany, Phone (++49)761 800937, E-mail: kattenborn@t-online.de

**PRIVATEERS N. V., St. Maarten, Netherlands Antilles
c/o Via Carducci 21, I-21027 Ispra (Va), Italy, Phone (++39)332 781494, E-mail: edmond.nezry@iol.it,

Abstract -- ERS-1 acquisitions of the Black Forest test site in Germany from 1991 to 1993 were selected to cover a variety of seasonal and phenological stages. Multisensor analysis (ERS-1, SPOT) was performed using a forestry GIS data base from the regular forest taxation. It turned out that the C-VV band of ERS-1 is sensitive to age in young deciduous and coniferous forest stands of temperate zones. A synergetic relationship between optical and microwave data has been established. The combined data set provided a combination that allowed better differentiation of forest age classes, as compared to results obtained with the individual sensors.

INTRODUCTION

Compared to the capabilities of optical spaceborne sensors the information content of a single frequency SAR, such as the ERS-1 AMI may be limited for land and forestry applications. However, continuous spaceborne SAR coverage may provide more information than can be obtained with single or limited optical spaceborne observations.

The ability of microwaves to penetrate the outer part of forest canopies and be scattered by branches and trunks leads to the assumption that SAR sensors might be able to provide estimates of forest biomass or other stand attributes.

From that, the objectives of this study are to exploit multidate ERS-1 observations and a rich available ground truth data set in order to assess the information content of ERS-1 SAR data for forestry and other land applications, and especially to evaluate the potential for improved information extraction from multitemporal SAR data. Furthermore the combined use of optical and microwave spaceborne data should give insight into possible synergetic effects for qualitative and quantitative analysis of forest stands.

TEST SITE AND DATA

The study area (about 30x30 km) stretches from France over the fertile Rhine valley with its submediterranean climate and its variety of agricultural crops, vineyards and forests, to the city of Freiburg in the centre of the area. From there it passes the western slope of the Black Forest.

ERS-1 acquisitions (14 Single Look Complex (SLC) data sets) from 1991 to 1993 were selected to cover a variety of seasonal and therefore phenological stages. SPOT/XS from September 12, 1991 have also been used for the study. The overall processing chain applied to the ERS-1 (SLC) SAR was especially designed to monitor the changes occurring to the scene at a high spatial resolution [1].

Data analysis was made by selecting a wide range of well documented ground samples on flat terrain. *Analysis of multitemporal ERS-1 slant range SAR data* was conducted using 40 test areas (forest, agriculture, grassland) each greater than 2.5 ha. *After geocoding, the multisensor (ERS-1, SPOT) analysis* was performed using a forestry GIS from the inventory used for regular forest taxation in 1990 for a forest district (6000 ha, 960 forest stands).

VEGETATION DYNAMICS USING ERS-1

Grassland, agriculture and forest, vegetated areas characterising a landscape, were used to study phenological and seasonal influences on ERS-1 backscatter evolution. Fig. 1 shows a plot of the ERS-1 backscatter range, defined as the difference between maximum and minimum measured backscatter of all acquisitions, versus the average ERS-1 backscatter value of all measurements. Generally, different target groups can be distinguished. Woody plants/forests form a group with high backscatter and a low dynamic range of backscatter over the seasons. In this group conifers show the highest dynamic range while young stands show the lowest average backscatter. Herbaceous vegetation (grassland) has a low average backscatter and medium dynamic range. Agriculture has the highest dynamic range of backscatter due to the influence of cultivation practices. A separation of woody and herbaceous vegetation and also of different accumulations of biomass seems to be possible using this representation.

0-7803-3836-7/97/$10.00 © 1997 IEEE

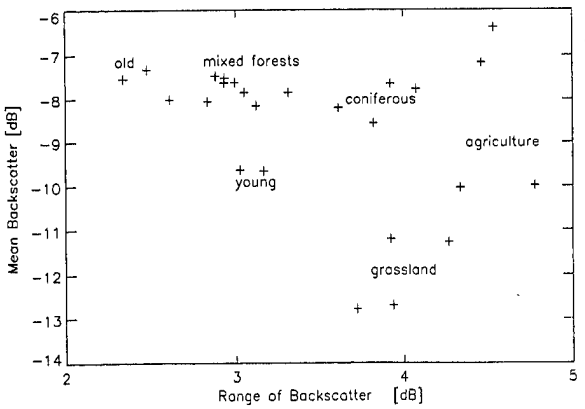

Fig. 1: Average ERS-1 backscatter versus range of ERS-1 backscatter of all ERS-1 acquisitions for different vegetated areas.

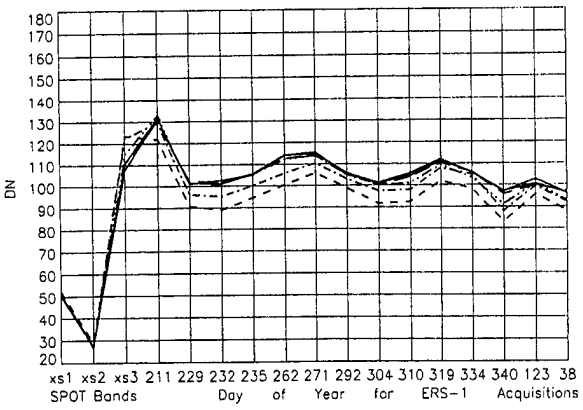

Fig. 2: SPOT reflectivity and temporal sequence of ERS-1 backscatter averaged for forest age classes 1-10, 11-20, 21-30, 81-90, 91-100, 101-110 years (bottom to top). For better comparison signatures are represented in digital numbers.

RETRIEVAL OF FOREST STAND ATTRIBUTES

After multisensor/multitemporal data fusion, the possibility of retrieval of forest stands attributes was investigated using GIS information and combined SPOT and ERS-1 data.

Since, according to the German forest taxation practice, biomass is not generally estimated for young forest stands, age information was considered for this study. The response of forest age classes to SPOT spectral bands and to the ERS-1 time series is depicted in Fig. 2. SPOT XS1 and XS2 bands show no apparent sensitivity to age of forest stands. The SPOT/XS3 band shows decreasing reflectance for increasing forest age. On the contrary, ERS-1 radar reflectivity increases with forest age, until saturation is reached after 30-40 years. A very interesting fact is, that this behaviour remains stable. Seasonal and environmental influences affect only, and almost in the same amount, the absolute mean level of radar reflectivity of forest age classes.

Capabilities of SPOT/XS3 and ERS-1 data for discriminating stands of different ages were examined by calculating the linear correlation coefficients between forest backscatter and age for four cases (Table 1):

- correlation between age (all age classes, from 1 to 160 years) and backscatter/reflectivity of forest stands, not differentiating species composition on polygon base,
- correlation between age (all age classes, from 1 to 160 years) and backscatter/reflectivity of forest stands, not differentiating species composition on pixel base,
- correlation between age (only age classes from 1 to 30 years) and backscatter/reflectivity of forest stands, not differentiating species composition on pixel base,
- correlation between age (only age classes from 1 to 30 years) and backscatter/reflectivity of the same stand type (i.e. same species or species composition) on pixel base.

As expected from Fig. 2, the low correlation coefficients obtained (Table 1) in the first two cases prove that neither SPOT nor ERS-1 allow complete discrimination of age classes from 1 to 100 years. In the last two cases, if only the first three age classes (from 1 to 30 years) are considered, then a very high correlation is observed between age and ERS-1 (all acquisitions) or SPOT/XS3 signals, for either not differentiating species composition or the example of a special stand type such as red oak.

The opposite signs of the correlation coefficients between forest backscatter and age class exhibited by SPOT/XS3 and ERS-1 indicate a possible synergy of both sensors for retrieval of forest stand age. Thus, a fusion of the data has been tried by simply using a ratio of the SPOT/XS3 image radiometry and the rescaled filtered ERS-1 amplitude.

These ratios of SPOT/XS3 to every ERS-1 acquisition were statistically evaluated by computing the linear correlation coefficients to age classes. Results are given in Table 2 for non-differentiating species composition and for a special stand type (ash). By showing fairly good correlations for forest age ranging from 1 to 100 years, the results in Table 2 indicate a superior sensitivity of this SPOT/X3 to ERS-1 ratio index to age classes compared to each single sensor.

Table 1: Correlation coefficients between backscatter of forest age classes (1-100 years) and age in one SPOT and 14 ERS-1 scenes on polygon base, on pixel base, on pixel base for the first three age classes (1-30 years) and on pixel base for the first three age classes of a red oak stand.

	[illegible]	Pixel Based		
	All Stand Types		[illegible]	
	1 - 100 Years	1 - 100 Years	1 - 30 Years	1 - 30 Years
SPOT/XS3				
12/09/91	- 0.09	- 0.43	- 0.91	- 0.98
ERS-1				
30/07/91	0.15	- 0.20	0.98	0.89
17/08/91	0.20	0.22	0.99	0.96
20/08/91	0.25	0.28	0.99	0.97
23/08/91	0.19	0.16	0.99	0.99
19/09/91	0.21	0.09	0.99	0.95
28/09/91	0.16	0.04	0.99	0.95
19/10/91	0.16	- 0.07	0.99	0.98
31/10/91	0.18	- 0.03	0.97	0.99
06/11/91	0.17	0.52	0.98	0.93
15/11/91	0.15	0.08	0.94	0.93
30/11/91	0.13	0.19	0.73	0.92
06/12/91	0.23	0.28	0.99	0.98
03/05/92	0.12	- 0.11	0.94	0.93
07/02/93	0.18	0.20	0.91	0.93

Table 2: Correlation coefficients between ratio of SPOT/XS3 and ERS-1 for 14 ERS-1 acquisitions of forest age classes 1-12 (1-120 years) and age without differentiation of ~~stand type and of forest age classes~~ 1-10 (1-100 years) and age of an ash stand on pixel base.

	Ratio SPOT XS3/ERS-1	
ERS-1 Acquisition	All Stand Types 1 - 100 Years	Ash 1 - 100 Years
30/07/91	- 0.75	- 0.67
17/08/91	- 0.77	- 0.75
20/08/91	- 0.76	- 0.75
23/08/91	- 0.75	- 0.77
19/09/91	- 0.80	- 0.77
28/09/91	- 0.78	- 0.78
19/10/91	- 0.75	- 0.66
31/10/91	- 0.76	- 0.74
06/11/91	- 0.82	- 0.86
15/11/91	- 0.79	- 0.87
30/11/91	- 0.78	- 0.75
06/12/91	- 0.87	- 0.82
03/05/92	- 0.77	- 0.83
07/02/93	- 0.79	- 0.89

SUMMARY AND CONCLUSIONS

The results of this study add to the growing evidence of the valuable capabilities imaging radars have for the studying and monitoring of forests due to the sensitivity of radar to a variety of processes in vegetation ecosystems and the proven synergy to optical satellite data.

Long term variations due to phenological and seasonal effects can be used to discriminate land use classes. Thus, high resolution monitoring of vegetated surfaces, forest conversion into cultivated or bare soils, or agriculture management seems to be possible using multitemporal ERS data.

The results from this investigation demonstrate that the C-VV band of ERS-1 is sensitive to age (and therefore closely related parameters such as tree height, woody biomass) in young deciduous and coniferous forest stands of temperate zones. This capability can be important for forest ecology studies. First, information about the growth dynamics of successional sequences on burned areas, clearings etc. can be important for prognosis about future growth and population development (patterns). Second, boreal forests are often characterised by low biomass levels, comparable to that of the young stands used in this investigation. Therefore, ERS-1 SAR could be sensitive to changes in these ecosystems.

A synergistic relationship between optical and microwave data has been established, allowing better differentiation of forest age classes, as compared to results obtained with the individual sensors. Age differences, however, are not directly detected. Rather, it is the different tree and stand characteristics (e.g. foliar vigor, quantity and distribution, tree height, stem and branch size, standing biomass and canopy structure) of differently aged stands which will result in different optical and microwave signatures.

ACKNOWLEDGEMENTS

This research and application work was conducted at the Joint Research Centre of the European Communities, Institute of Remote Sensing Applications, Advanced Techniques Unit within two CEC contracts: EARS-92-0004-FR, and a Visiting Scientist Contract.

REFERENCES

[1] Kattenborn, G., Nezry, E., De Grandi, G. and Sieber, A., 1993. High resolution detection and monitoring of changes using ERS-1 time series. Proc. of the Second ERS-1 Symp., Hamburg (Germany), 11-14 October 1993, ESA SP-361, pp. 635-642, January 1994.

Conference Author Index

D

E

F

K

L

M

N

T

U

V

W

X

Y

Z